Advances in Materials Science and Engineering

Advanced Materials for Promoting Sustainability

Lead Guest Editor: Gopal P.M.
Guest Editors: Kavi Mani and Petr Spatenka

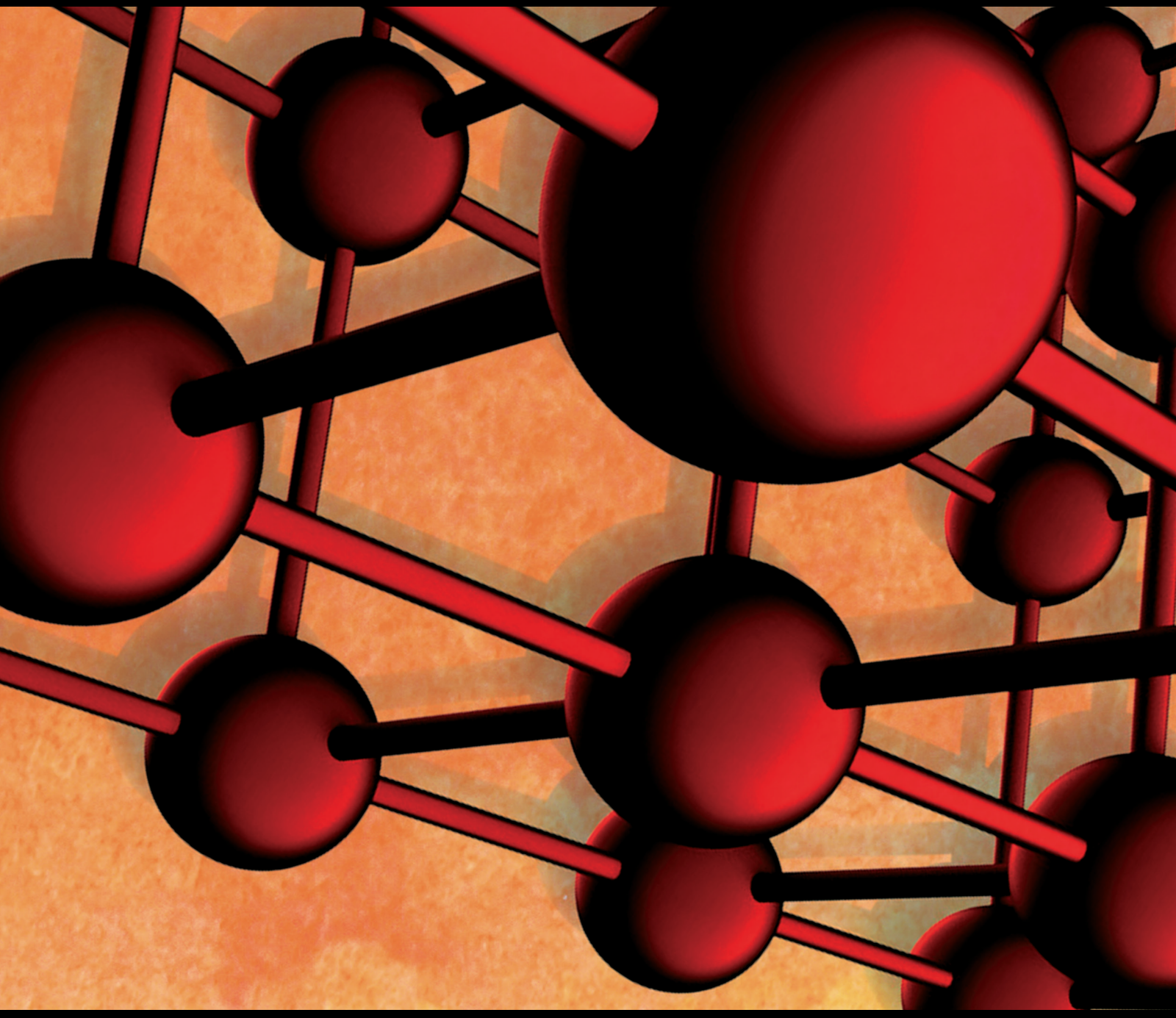

Advanced Materials for Promoting Sustainability

Advances in Materials Science and Engineering

Advanced Materials for Promoting Sustainability

Lead Guest Editor: Gopal P.M.
Guest Editors: Kavi Mani and Petr Spatenka

Contents

Contents

Contents

Hindawi
Advances in Materials Science and Engineering
Volume 2023, Article ID 6931291, 11 pages
https://doi.org/10.1155/2023/6931291

Research Article

Experimental Analysis on the Feasibility of Bamboo Reinforcement in Concrete Mix Design and Comparison with Steel Reinforced Concrete

R. Sivakumar,[1] R. Ganesan,[2] A. Latha,[3] Karan Moolchandani,[4] Anuj Kumar Sharma,[5] Sri Ram Krishna Mishra,[6] Farhan Khan,[7] Amit Kumar Yadav,[8] and Lijalem Ayele[9]

[1]*Department of Civil Engineering, E.G.S. Pillay Engineering College, Nagapattinam 611002, Tamilnadu, India*
[2]*Department of Civil Engineering, Saveetha School of Engineering, Saveetha Institute of Medical and Technical Sciences (SIMATS), Chennai 105, Tamilnadu, India*
[3]*Department of Civil Engineering, Panimalar Engineering College, Chennai 56, India*
[4]*Maulana Azad National Institute of Technology, Bhopal, MP, India*
[5]*Civil Engineering Department, Ramdeobaba College of Engineering and Management, Nagpur 440013, India*
[6]*Civil Engineering Department, Bhilai Institute of Technology Raipur, Kendri, Atal Nagar, Raipur, Chhattisgarh 493661, India*
[7]*Department of Civil Engineering, Rungta College of Engineering and Technology, Bhilai, Chhattisgarh 490024, India*
[8]*Central University of Jharkhand, Ranchi, India*
[9]*School of Mechanical and Industrial Engineering, Institute of Technology, Debre Markos University, Debre Markos 269, Ethiopia*

Correspondence should be addressed to Lijalem Ayele; ayele018@gmail.com

Received 20 July 2022; Revised 23 August 2022; Accepted 13 July 2023; Published 14 September 2023

Academic Editor: Pudhupalayam Muthukutti Gopal

Besides being chief construction ingredients, concrete and steel produce a high amount of CO_2, and high energy consumption promotes global warming. To evade this problem, green and low energy consuming alternative is required. Rapid growing time with the least period to attend optimum strength made bamboo a new immerging mainstream constituent in construction. Bamboo, as one of the probable alternate structural materials, not only promises a sustainable and sturdy option but also reduces the environmental carbon footprint. In this research, article authors replaced steel reinforcement in concrete with bamboo. To establish bamboo as a construction material, a concrete beam of 200 mm × 500 mm is made in which bamboo bars of diameter 20 mm are used with a variation of 1 to 4% of the reinforcement area. Various tests were performed to provide the feasibility of bamboo as construction materials after 28 days of curing, in which test results were found promising. The impact test shows only 25% of wear and tear. Also, bamboo reinforced concrete (BRC) without changing cross sections provided 50% axial compressive strength compared to steel reinforced concrete (SRC). However, in the tensile test, BRC outperformed SRC by providing 50% more resistance against tensile load. Authors also performed rate analysis between SRC and BRC to find that it almost reduces 18% of the cost at a small scale. Hence here, comparative research is provided, and the authors believe that it would pave the road on which forthcoming researchers will walk to reach the destination of finding an alternate, sustainable, and green construction material in the form of bamboo.

1. Introduction

In naming construction materials, concrete holds one of the top positions on the list. Concrete is generally made of cement, fine aggregate, coarse aggregate, and water. The reaction of cement components with water provides sufficient and required binding property with the strength of the concrete. Cement gets into smaller gaps existing between fine sand, filling the pore and providing impermeability to concrete. The property of binding different constituents of concrete initiated after adding water to concrete after that initial setting and hardening of concrete take place. This

process imparts strength to fine aggregate and makes it a solid mass. Fine aggregate fills the gaps between the coarse aggregate. They consist of silica grains in angular or rounded shapes. Allowing water through its pores helps to harden the cement, helping lower the shrinkage cracks. The reaction between cement constituents and silica of coarse aggregate made concrete a solid mass, providing resistance against crushing. However, the hardness of concrete also brings some problems in the structure as concrete shows a very brittle nature against loads. Concrete can easily withstand compressive load but have very poor ductility and provide little resistance against tensile load. To complement the properties of concrete, a ductile material is required to withstand with both forces and will show only ductile failure.

In the 19th century, researchers used steel bars as reinforcement for concrete. The selection of steel as a reinforcing material in compliance with some of its properties, i.e., steel is highly ductile. Young's modulus is equal for both compression and tension; it has high tensile strength compared with concrete, and most importantly the thermal coefficient of steel and concrete is almost identical, thus preventing bond failure between them [1–3].

However, the usability of cement and steel in construction has issues. The first and obvious issue is the weight of the structure, i.e., dead load. The high specific gravity of concrete and steel can make structures very heavy. This not only contributed to the calculation of load combinations for structure design but also increased the cost of structures. For heavy structures, it is likely to be noted that it suffers more in an earthquake. The second issue is not visible but is more concerning than the first issue and has a negative impact on the environment. The production sector of this constituent is one of the most polluting industries. Production of cement requires burning fossil fuels to burn the limestone and other ingredients to make clinker which later grinds to make cement. This process produces an enormous amount of CO_2. One ton of cement contributes 750 kg of CO_2 to the environment. Similarly, for steel, the production of 1 ton steel contributes 1.9 tons of CO_2 to the atmosphere. This is estimated as half a ton of CO_2 per person [4]. The third issue associated with these ingredients is that it is costly. The advancement of any country depends on the development of the infrastructure sector. Hence, rising cost of ingredients only contributes to problems rising for developing countries. Therefore, it is easy to say that headlong production and use of cement and steel adversely impact the atmosphere. Various problems, i.e., cost, degradation of cement, weight, and nonrenewability of each material, change the focus of the study to the more sustainable and ecofriendly options.

New studies show that using natural fibre, sustainable and green concrete technology can be developed [5]. In this area, past studied fibres are jute [6, 7], coconut coir [8, 9], sisal [10], babadua [11], date palm [12], bamboo [13], and bamboo fibre [14]. Although every fibre shows potential but rapid growth, attainment of optimum strength in a few years and lush amount of supply provide the bamboo fibre with little advantage over all other natural fibres.

Past studies report the notable mechanical and physical properties of bamboo [5]. Fast-growing, timber-like bamboo is associated with the grass family *Poaceae*. In just three years, it attains its optimum strength and maturity at the age of 5 years. The tensile strength of some bamboo species is the same as the yield strength of mild steel. Other than that, a six-time greater specific weight ratio is achieved by bamboo compared with steel. Bamboo can take a tensile and compressive load similar to steel, but the remarkable point is to notice that the required energy for producing 1 m^3 of steel is 50 times higher than bamboo. All these properties made researchers use bamboo in place of steel reinforcement [15].

Mansur and Aziz [6] use bamboo mesh in woven form with cement mortar. It is used to act as reinforcement. This study suggested that a significant increment had been seen in ductility and toughness. Using bamboo imparts a considerable increase in tensile, flexural, and impact strength. Akeju and Falade [16] research on the reduction of water absorption of bamboo by coating it with bitumen and sand. They used treated bamboo for reinforcement in column and beam member. Ghavami [15] enlightens that ultimate load carrying capacity is increased four times using bamboo as reinforcement with nonreinforced concrete. However, the author also provided suggestions that the bond strength of steel is higher for steel and concrete than that of bamboo with concrete, which made bamboo reinforced concrete (BRC) carry less tensile load. The author described the application of bamboo as a structural element using as a frame, beam, and shutter, which would be subjected to bending stress.

Prasad et al. [17] used low-cost panels for cheap houses using bamboo reinforced cement-sand mortar panels in hilly areas. Mats were made of bamboo and coated with bitumen, and a spray of sand was used for wall and roof elements. A plaster of 12 mm made with mixed cement: sand (1 : 6) is applied to both faces to bear stresses; however, no test was reported supporting that. Maity et al. [18] suggested the use of precast BRC wall panels. Lima et al. [19] performed the durability analysis by applying calcium hydroxide and tap water on BRC and stated that after 60 days of the continuous wetting and drying cycle, BRC did not show any variation in tensile strength and Young's modules.

Single and double beam using bamboo as reinforcement and column analysis were performed by Rahman et al. [20] and Salau et al. [21], respectively. It is stated by Terai and Minami [22] that RCC's formula to evaluate fracture behavior is sufficient to perform for BRC. Also, Yamaguchi et al. [23] used bamboo as main rebar and stirrups with flexural load and studied its performance.

Different studies, such as roofs' top by insertion of bamboo strips [24, 25], their behavior, and strengthening the bamboo by chemical treatments, regarding the use of bamboo as structural elements are performed [26]. Using bamboo pegs in reinforcements and also the bond between them, all are studied and elaborated on in past research studies [27–29].

Regarding carbon embodied energy, the manufacturing sector of both reinforcing materials shows significant differences positively towards bamboo. Embodied energy of bamboo columns is only 4–6 MJ/kg in comparison with medium carbon steel with an energy of 29–35 MJ/kg [30].

Similarly, the carbon footprint of steel is significantly greater than bamboo's, with 2.2–2.8 kg·CO_2/kg (equivalent kg of CO_2 per kg of the material) for medium carbon steel [30] and 0.25 kg·CO_2/kg for bamboo [31–33].

Authors in this research studied the bamboo called as Katang (*Bambusa bambos*) shown in Figure 1 available locally in Maharashtra. A thin layer of bitumen and sand is applied to protect it from corrosion and water absorption. Various tests were performed to find the different mechanical properties of bamboo and applied it as the main bar in the beam arrangement using bamboo sticks as stirrups. The test list and results are discussed below.

The authors' objective of this study is to investigate the different civil advantages of using bamboo as a reinforcing material in place of steel for making reinforced concrete sections. Past studies using bamboo reinforcement did alter the cross section of the concrete beam. The authors in this study intended to achieve the maximum compressive strength possible from bamboo reinforced sections compared with steel reinforced sections without altering the cross section of the concrete beam. Also, a cost analysis is performed by the authors in this study to compare the economic difference in steel reinforced and bamboo reinforced concrete sections.

Figure 1: Image of *Bambusa bambos* [34].

2. Experimental Program

Experimental program for bamboo reinforcement is depicted in a flow diagram in Figure 2.

2.1. Material Selection and Properties

2.1.1. Bamboo. For this study, we selected a bamboo species called *Bambusa bambos* or giant thorny bamboo locally available in Maharashtra state. In the local language, it is called Katang [35]. It is perennial *Poaceae* having a clump height of 20–35 m. It almost takes 12 years to reach maturity [36]. The interesting fact with bamboo is that it attains its maximum height in the very first year with a 30 cm growing rate per day [37, 38]. Specifications of *Bambusa bambos* are represented in Table 1.

2.1.2. Cement. While defining cement, the adhesive and cohesive property plays a key role. The property of cement assists in compacting different fragments together. For this study, we selected Portland pozzolana cement (PPC), which will later be used in making concrete. Different tests were performed to determine cement's properties, i.e., consistency (IS code 8112-1976), initial setting time (IS code 12269: 1987), final setting time (IS code 12269:1987), specific gravity of cement (IS code 2720- part 3), fineness modules (IS code 4031:1996 part 1), and soundness of cement using Le Chatelier's apparatus (IS code 4031-1996 part 2) and IS code 5514-1996. Different test results are tabulated in Table 2, and also chemical composition of cement is presented in Table 3.

2.1.3. Aggregate. Inert, inorganic, granular material having stones or stone-like solid is named as aggregate. Aggregate is a very chief ingredient in concrete making. It occupies about 3/4th of the volume of concrete. It provides required strength to the concrete structure, while cement is associated with particle binding. Changes in aggregate property can bring a change to the tangible property due to the large volume fraction. Aggregate also provides economical control to the concrete and also provides durability and stability in the concrete mix. Two types of aggregates are generally used in the concrete. They are described as follows:

(a) *Coarse Aggregate.* Aggregates retained on sieve no. 4 (4.75 mm) are predominantly named as coarse aggregates for the concrete-making process. The maximum size can be taken as large as 150 mm. Different properties of coarse aggregates used in this project are determined referencing IS code 383:1970. The different test results are shown in Table 4.

(b) *Fine Aggregate (Sand).* Aggregates those passed no. 4 sieve (4.75 mm) and retained on no. 200 sieve (75 microns) are considered fine aggregates. Fine aggregates fill the pores of coarse aggregates providing better load transfer property by creating better contact between particles. The various tests to analyze the properties of fine aggregates are used in this project, referencing IS code 383:1970, as described in Table 4.

2.1.4. Water. Water used to prepare different samples of concrete had been clean and free from impurities and dirt. No such foreign matter was presented in water, i.e., oil, salts, alkalis, and sugar. The pH value is greater than 6 for applied water in this study.

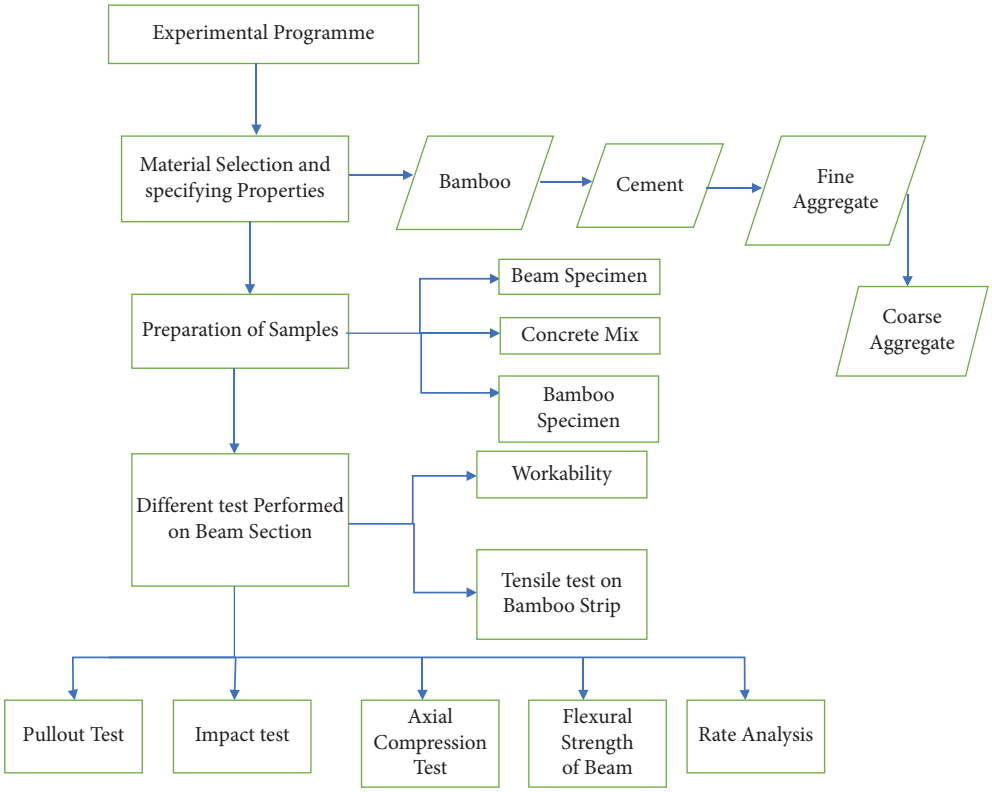

Figure 2: Flowchart of experimental program for bamboo reinforced beam (source: author).

Table 1: Specifications of *Bambusa bambos* (source: author).

Specification	Property
Full strength attaining period	3–5 years
Full maturity	12 years
Sustainable temperature	22–30°C
Habituality	Evergreen
Height	30 m
Edibility	Moderate

Table 2: Properties of PPC (source: author).

S. N.	Description of property	Value in PPC
1	Fineness (cm^2/gm)	3600
2	Normal consistency (%)	31
3	(a) Initial setting time (minute) (b) Final setting time (minute)	55 305
4	Soundness (mm)	2
5	Specific gravity	3.15

Table 3: Chemical constituent of PPC (source: author).

S. N.	Oxide	% in cement
1	SiO_2	19.71
2	Al_2O_3	5.20
3	Fe_2O_3	3.73
4	CaO	62.91
5	MgO	2.54
6	SO_3	2.72
7	K_2O	0.90
8	Na_2O_3	0.25
9	Miscellaneous	2.04

Table 4: Properties of course and fine aggregate (source: author).

S. N.	Property	Coarse aggregate	Fine aggregate
1	Fineness modules	7.098	2.493
2	Specific gravity	2.85	2.66
3	Water absorption	0.8%	1%

2.2. Sample Preparation

2.2.1. Bamboo. Bamboos were dried and cut into 3/4th inch (20 mm) wide and 7 ft 9 inches (2.36 m) long strips for the tests. Bamboo strips were treated by applying a bitumen coat and sprinkles of sand to them. The treatment is done to avoid the absorption of water when it is cast in the beam. Five points were selected to measure the distance. The effect of nodes was not present in the limited study of authors; hence, the effect of nodes was desired to be investigated. Samples were prepared so nodes would be at the center, and aluminum tabs were provided to protect bamboo from crushing. All assemblies are presented in Figure 3.

2.2.2. Concrete Mix. Concrete mix design is done to achieve suitable strength and durability. By selecting the proper ingredient, we ensure that concrete can perform up to our expectations. Concrete design mainly depends on four major factors: water/cement ratio, cement content, gradation of

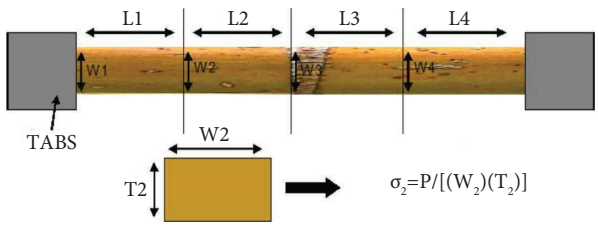

Figure 3: Assemblies for bamboo specimen preparation (source: author).

aggregate, and consistency. Determination of preparation of these four factors is known as concrete mix design. Based on experience, we adopted a 0.45 water/cement ratio but allowed water for absorption to increase the ratio to 0.509. The used proportion for desired concrete is 6 : 9 : 14, which provided mean compressive strength of 31 MPa. Final mix proportion and quantities of concrete are shown in Table 5, and concrete preparation is shown in Figure 4. From Figure 5, the X-ray diffractometer identified the presence of a noncrystalline substance in bamboo reinforced beam.

The slump test provided 100 mm of slump for this concrete mix.

2.2.3. Beam Preparation. The aim of the paper is to find the feasibility of bamboo as reinforcement can be achieved by comparing bamboo reinforced beams to the steel reinforced beam. The design of the beam was provided with 0.4 widths to depth ratio, the clear cover is between 45 mm for steel, and clear spacing is prepared with 25 mm or 1.33 times more than the biggest aggregate size. For the bamboo reinforced beam, 200 ∗ 500 mm size of the beam is selected where 20 mm of bamboo dia bar is provided. Clear cover and clear spacing each were provided with 40 mm. Bamboo bars were tied using bending wire. The beam and arrangement of r/f are shown in Figures 6 and 7, respectively.

2.3. Methodology and Experimental Investigation. After mixing the concrete in two batches, it was taken to the formwork. A 40 mm clear cover is placed at the bottom, and reinforcement is placed over it. Concrete was placed around the reinforcement, and rubber mallets were used as vibration tools to compact concrete. Also, steel rods were used to push down concrete so expulsion of air could occur. When all concrete was poured down, the top surface was finished with a smooth surface and curing was done after 24 hours of casting. Cylinders were also prepared for compression tests for a curing period of 7, 14, and 28 days. Strength was found according to that. Different mechanical properties, i.e., compressive strength, split tensile strength, and flexural strength of the sample, were found using the universal testing machine (UTM) at a constant loading rate of 120 KN/min.

3. Results

3.1. Workability. Slump test, compaction test, and Vee-Bee test (shown in Figure 8) and results were found to be high for the mix. It shows that the mix is workable, can be helpful for various desired applications, and can flow well in areas where congestion of ingredients occurs. The different results are shown in Table 6.

Table 5: Finale mix proportion and quantities for concrete (source: author).

Constituent	Mass used	Volume
Water	158.36 lit	
Cement	311.11 kg	1 m^3
Fine aggregate	739.148 kg	2.376 m^3
Coarse aggregate	1351.16 kg	4.34 m^3

Figure 4: Preparation of concrete (source: author).

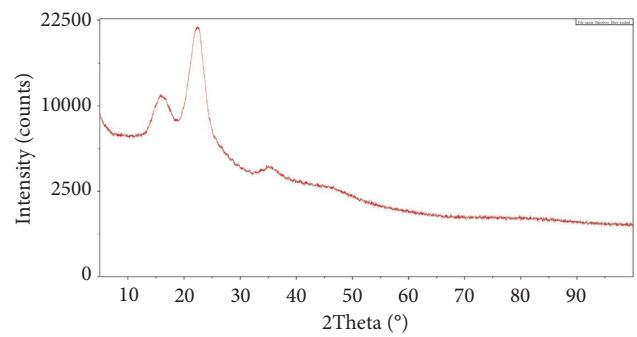

Figure 5: X-ray diffractometer of the bamboo reinforced beam (source: author).

Figure 6: Reinforcement arrangement (source: author).

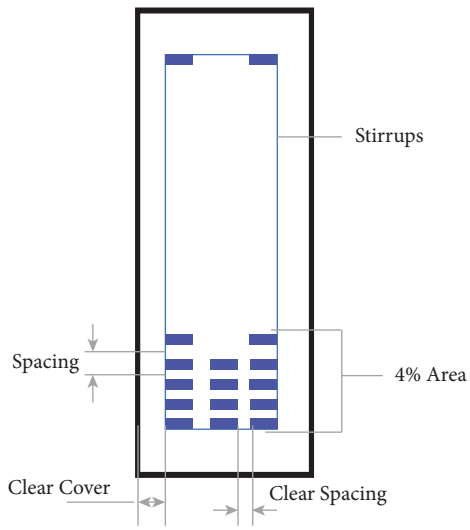

Figure 7: Beam arrangement (source: author).

Figure 8: Vee-Bee test setup (source: author).

Table 6: Workability test results (source: author).

Compaction factor test	0.89
Slump test	68 mm
Vee-Bee	13 sec

3.2. Tensile Test on Bamboo Strip. A tensile test was conducted to know the elastic parameter of reinforcement and ultimate strength (as shown in Figure 9). A total of three specimens were tested, and as the aim was to find the effect on bamboo's nodes, there was only one node in each sample. The measurement of thickness and width is taken from 3 points, and the average is taken for the calculation. It was noted that most of the failures have occurred on sample nodes. The resulting data are presented in Table 7.

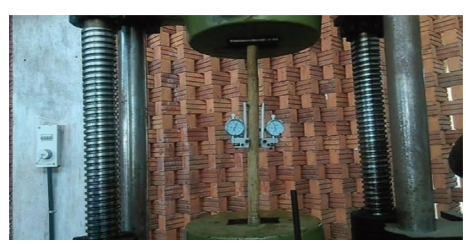

Figure 9: Tensile test setup for bamboo (source: author).

3.3. Pull-Out Test. For inner bonding strength calculation, cylinders were made. A total of 3 adhesives are taken: (a) plain bamboo, (b) Araldite, and (c) Araldite with binding wire. In concrete cylinders, 100 mm of strips are inserted. To calculate bond stress, formula $\tau b = F/\mathrm{SL}$ is used where F denotes pull-out load, s is the perimeter, and l is the inserted length, i.e., 100 mm. For every adhesive, three samples were made. Results are shown in Table 8. The analysis of the result provides data that Araldite with wire provides the best bond stress. The test represented that most failures happened due to slippage of the bamboo strip.

3.4. Impact Test. For the impact test sample, having clean aggregates dried in the oven at 105–110 to achieve constant weight after placing the sample in Los Angeles' machines, 20–30 rpm of rotation is achieved. After 15 minutes, the sample is removed and passed through the 1.75 mm sieve, indicating the percentage of samples passing after the test.

Table 7: Tensile test results (source: author).

S. N.	Length (mm)	Dia of bamboo specimen (mm)	Area (mm^2)	Ultimate load (KN)	Failure stress (MPa)	Strain
1	500.00	28	615.75	17.2	27.93	0.0080
2	510.00	26	530.9	13.8	25.99	0.0080
3	520.00	28	615.75	16.2	26.30	0.0076
		Average			26.74	0.0078

Table 8: Pull-out test results (source: author).

S.N.	Adhesive	Bamboo width (mm)	Bamboo thickness (mm)	Contact area per unit height (mm)	Pull-out load (KN)	Bond stress (MPa)	Avg. bond stress (MPa)
1	Plain bamboo	20.63	3.53	48.32	0.25	0.05	0.16
		22.71	3.10	51.62	1.34	0.26	
		21.85	4.67	53.04	0.99	0.19	
2	Araldite	23.47	3.47	53.88	1.94	0.36	0.31
		20.89	3.07	47.92	1.28	0.27	
		21.34	3.95	50.58	1.53	0.30	
3	Araldite with wire	22.81	2.95	51.52	1.96	0.38	0.50
		20.24	3.39	47.26	2.68	0.57	
		20.64	2.05	45.38	2.54	0.56	

The test data show that the weight of oven-dried sample was $w_1 = 1250$ gm, and the retained portion of the sample after the test was $w_2 = 937.5$ gm; hence, using the formula $W_1 - W_2/W_1 \times 100$, we calculated that the impact test shows only 25% of abrasion in the sample which is good.

3.5. Axial Compression Test. Axial compression tests for short columns were performed using columns of size 160 mm × 160 mm × 1000 mm. A total of 24 columns were casted for mix design of M20, 3 no. of each column for 4%, 6%, and 10% of reinforcement, and three plain concrete columns and RCC column with steel were cast for comparison purpose. From Table 8, Araldite and wire are used for maximum bond strength. The average of three is taken as axial compression for each column type. Because bamboo is a fibrous material, a higher amount of reinforced column with bamboo, i.e., 10%, can sustain with a comparison of steel reinforced column. Load deformation behavior is plotted in Figure 10, where the chart shows that bamboo r/f absorbs more energy. The same result was found in the study of Agrawal et al. [29].

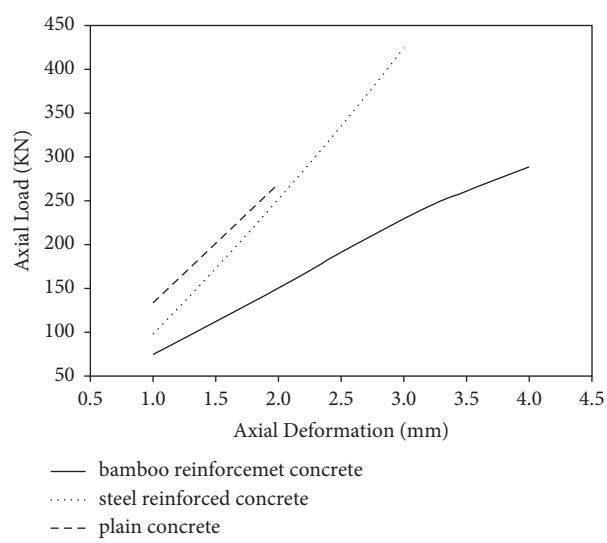

Figure 10: Load deformation behavior (source: author).

3.6. Flexural Strength of Beam. To compare flexural strength of SRC beam with 10% reinforced BRC beam, two beam specimens were made with three samples for each specimen prepared. The sizes were 700 mm × 150 mm × 150 mm. A lab test was performed after 28 days of curing according to IS 516, and average data are considered, suggesting that SRC is better in flexural about almost two times than BRC. The comparative data are represented in Table 9, and performing flexural test setup is shown in Figures 11 and 12, respectively.

3.7. Transverse Loading Test on Concrete Columns. From this test, the authors tried to find out the behavior of bamboo reinforced columns under the action of both axial and transverse loading. Nine samples were made for the transverse loading test: plain concrete, steel reinforced concrete, and bamboo reinforced concrete columns. Each constituent has three samples from which the average is taken as transverse loading. The test is performed under constant 10 KN of axial load. Different samples with different percentages of reinforcing

Table 9: Flexural strength comparison between SRC and BRC (source: author).

Reinforcement type	Length	Width	Depth	Load of failure	Flexural = ($3PL/2bd^2$) (N/mm^2)
SRC	700	150	150	14.53	4.536
BRC	700	150	150	7.34	2.25

Figure 11: Setup for flexural test (source: author).

Figure 12: Performing flexural test (source: author).

Table 10: Maximum transverse load sustain by columns (source: author).

S. N.	Material	Sample no.	Reinforcement percentage	Transverse load at failure (KN)	Average load (KN)	Maximum deflection (mm)	Average deflection (mm)
1	Plain concrete	1	—	9.89		5.61	
2	Plain concrete	2	—	9.62	9.87	5.21	5.34
3	Plain concrete	3	—	10.1		5.2	
4	RCC	1	0.78	13.98		5.96	
5	RCC	2	0.78	13.64	13.94	5.64	5.79
6	RCC	3	0.78	14.2		5.78	
7	BRC	1	4	11.2		4.9	
8	BRC	2	4	10.8	11.03	4.2	4.56
9	BRC	3	4	11.1		4.6	

material are presented in Table 10. Also, results occurring from these tests are presented in Table 10. Results indicate that steel reinforced column shows 13.94 KN of sustainability of transverse load and bamboo reinforced column shows 11.03 KN of transverse load. The comparison of both samples provides positively 80% of transverse load towards BRC than SRC.

Also, BRC concrete can sustain 11% of more transverse load than plain concrete. All results are plotted in the graph in Figure 13.

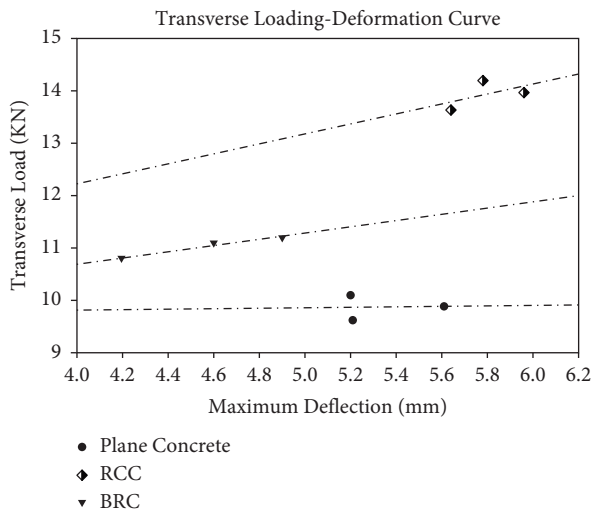

Figure 13: Transverse loading deformation curve (source: author).

Table 11: Rate analysis (source: author).

S. N.	Specimen	Materials	Per	Quantity	Rate (in rupee)	Cost (in rupee)
1	Steel reinforced concrete	Cement	Bag	1	385	385
		Fine aggregate	m^3	0.009325	2170	20.23
		Coarse aggregate	m^3	0.003475	1575	5.47
		R/F	kg	3.475	53.5	185.91
		Total				596.61
2	Bamboo reinforced concrete	Cement	Bag	1	385	385
		FA	m^3	0.009325	2170	20.23
		CA	m^3	0.003475	1575	5.47
		R/F	kg	0.68	17	10.52
		Araldite adhesive	kg	0.05	800	40
		Wire	Coil	1	23	23
		Bitumen	kg	0.05	35	17
		Total				501.22

3.8. Rate Analysis. The comparative rate analysis for both types of beam is presented in Table 11.

Hence, from the data, it is clear that BRC also reduces the cost of structure making by almost 18%.

4. Conclusion

This study tested the possible use and feasibility of bamboo as concrete reinforcement on different beam and column specimens. The study includes a bunch of tests, i.e., tensile test, pull-out test, axial compression test, flexural strength, and comparison on rates performed by authors. It is investigated and found that Araldite with wire exhibits higher bond strength for the pull-out test for the interface.

Tensile test on treated bamboo strip provided an average of 186.3 MPa of failure stress. Also, the impact test on the concrete mix provides only 25% of wear and tear in the Los Angeles test, which is quite good. The axial compression test suggests that columns with a higher percentage of bamboo as reinforcement provide more energy absorption. Each column shows brittle behavior and provides only a little warning before failure. However, the flexural analysis of SRC and BRC provides results that SRC is better in avoiding flexural failure almost by two times than the BRC beam. The authors also provide a rate analysis for SRC and BRC on the current price range and found that BRC reduces cost by almost 18%. Hence, authors believe that bamboo has the potential to become a sustainable and cheap building material as reinforcement and should perform experiments in future to further solidify outcomes from this study.

In this paper, the authors provide novelty in different points from previous studies. Authors replaced the conventional method of steel as a reinforcing material with bamboo reinforcement. Apart from all previous studies, this study focuses on Indian species of bamboo called Katang, which is found in the Maharashtra state of India. From studies of these species, we identified different engineering properties of bamboo listed above. In this paper, a special arrangement of bamboo reinforcement is studied for research purposes, i.e., the arrangement of nodes in the center of the span so that nodes take the maximum load. Without changing the cross section of the bamboo reinforced beam

compared to the steel reinforced beam, the authors achieved 50% more compressive strength than the steel reinforced beam. Also, the authors perform a cost analysis to clarify the objective of achieving a cheap alternative of steel reinforced concrete section.

5. Future Scope

The potential of bamboo as reinforcement is tried to justify in this study. Notably, bamboo reinforcement has some issues to rectify. First, to gain the same amount of compressive strength as steel reinforcement, a higher percentage of bamboo is required, which eventually increases the weight of the structure since a large area is required to fit the greater percent of bamboo. So, studies to reduce the weight of the structure can be carried forward. Also, the effect of clear cover for bamboo reinforced structures should be studied in future. A clear cover is provided to protect steel from corrosion, but bamboo is affected by the environment and can decay. So, optimum clear cover can be identified by future work. Also, the effect of hybrid reinforcement using steel and bamboo can be investigated in future.

Data Availability

The data used to support the findings of this study are included within the manuscript.

Conflicts of Interest

The authors declare that there are no conflicts of interest.

Authors' Contributions

All authors contributed to the study conception and design. All authors read and approved the final manuscript.

References

[1] Britannica Editors of Encyclopaedia, *Reinforced concrete*, Encyclopedia Britannica, Chicago, IL, USA, 2020.

[2] Testbook, "Why steel is commonly used as good reinforcing material," https://testbook.com/question-answer/why-steel-is-commonly-used-as-good-reinforcing-mat--608b996f60a98e0431df5c8d.

[3] Builderspace, "Why concrete is reinforced with steel the complete guide," https://www.builderspace.com/why-concrete-is-reinforced-with-steel-the-complete-guide.

[4] Columbia University, *Blogs*, Columbia University, New York, NY, USA, 2012.

[5] B. A. Akinyemi and T. E. Omoniyi, "Effect of moisture on thermal properties of acrylic polymer modified mortar reinforced with alkali treated bamboo fibres," *Journal of the Indian Academy of Wood Science*, vol. 15, no. 1, pp. 45–51, 2018.

[6] M. A. Mansur and M. A. Aziz, "A study, of jute f, bre reinforced cement composites," *International Journal of Cement Composites and Lightweight Concrete*, vol. 4, 1982.

[7] S. Chakraborty, S. P. Kundu, A. Roy, B. Adhikari, and S. B. Majumder, "Polymer modified jute fibre as reinforcing agent controlling the physical and mechanical characteristics of cement mortar," *Construction and Building Materials*, vol. 49, pp. 214–222, 2013.

[8] S. M. Islam, R. R. Hussain, and M. A. Z. Morshed, "Fiber-reinforced concrete incorporating locally available natural fibers in normal- and high-strength concrete and a performance analysis with steel fiber-reinforced composite concrete," *Journal of Composite Materials*, vol. 46, no. 1, pp. 111–122, 2011.

[9] M. Ali, A. Liu, H. Sou, and N. Chouw, "Mechanical and dynamic properties of coconut fibre reinforced concrete," *Construction and Building Materials*, vol. 30, pp. 814–825, 2012.

[10] T. Filho, R. Dias, F. D. A. Silva, and E. M. R. Fairbairn, "Durability of compression molded sisal fiber reinforced mortar laminates," *Construction and Building Materials*, vol. 23, no. 6, pp. 2409–2420, 2009.

[11] C. K. Kankam and B. Odum-Ewuakye, "Babadua reinforced concrete two-way slabs subjected to concentrated loading," *Construction and Building Materials*, vol. 20, no. 5, pp. 279–285, 2006.

[12] A. Kriker, G. Debicki, A. Bali, M. M. Khenfer, and M. Chabannet, "Mechanical properties of date palm fibres and concrete reinforced with date palm fibres in hot-dry climate," *Cement and Concrete Composites*, vol. 27, no. 5, pp. 554–564, 2005.

[13] K. Ghavami, "Ultimate load behaviour of bamboo reinforced lightweight concrete beams," *Cement and Concrete Composites*, vol. 17, pp. 281–288, 1995.

[14] H. S. Ramaswamy, B. M. Ahuja, and S. Krishnamoorthy, "Behaviour of concrete reinforced with jute, coir and bamboo fibres," *International Journal of Cement Composites and Lightweight Concrete*, vol. 5, 1983.

[15] K. Ghavami, "Bamboo as reinforcement in structural concrete elements," *Cement and Concrete Composites*, vol. 27, no. 6, pp. 637–649, 2005.

[16] T. A. I. Akeju and F. Falade, "Utilization of bamboo as reinforcement in concrete for low-cost housing," in *Proceedings of the engineering research for the industries*, pp. 10-11, Cape Town, South Africa, April 2001.

[17] J. Prasad, B. S. Pandey, R. Ahuja, and A. K. Ahuja, "Low cost housing for hilly regions using locally available material," *Asian J Civil Eng Build Hous*, vol. 6, no. 4, pp. 257–265, 2005.

[18] D. Maity, S. K. Behera, M. Mishra, and S. Majumdar, "Bamboo reinforced concrete wall as a replacement to brick and mud wall," *IE (I) J-AR*, vol. 90, pp. 5–10, 2009.

[19] H. C. Lima Jr., F. L. Willrich, N. P. Barbosa, M. A. Rosa, and B. S. Cunha, "Durability analysis of bamboo as concrete reinforcement," *Materials and Structures*, vol. 41, pp. 981–989, 2008.

[20] M. M. Rahman, M. H. Rashid, M. A. Hossain, M. T. Hasan, and M. K. Hasan, "Performance evaluation of bamboo reinforced concrete beam," *International Journal of Engineering & Technology*, vol. 11, no. 4, pp. 142–146, 2011.

[21] M. A. Salau, I. Adegbite, and E. E. Ikponmwosa, "Characteristic strength of concrete column reinforced with bamboo strips," *Journal of Sustainable Development*, vol. 5, no. 1, p. 133, 2012.

[22] M. Terai and K. Minami, "Fracture behavior and mechanical properties of bamboo reinforced concrete members," *Procedia Engineering*, vol. 10, pp. 2967–2972, 2011.

[23] M. Yamaguchi, M. Kiyoshi, and T. Koji, "Flexural performance of bamboo-reinforcedconcrete beams using bamboo as main Rebars and Stirrups," in *Proceedings of the Third*

International Conference on Sustainable Construction Materials and Technologies, p. E273, Kyoto, Japan, August 2013.

[24] D. N. Sri Murni Dewi, H. Suseno, and L. Susanti, "Increasing performance of bamboo reinforced concrete beam with addition of bamboo pegs on the reinforcements," *International Journal of Civil Engineering & Technology*, vol. 10, no. 1, pp. 724–734, 2019.

[25] S. Dewi and D. Nuralinah, "The recent research on bamboo reinforced concrete," *MATEC Web of Conferences*, vol. 103, p. 2001, 2017.

[26] J. A. Abdalla, B. S. Thomas, and R. A. Hawileh, "Use of hemp, kenaf and bamboo natural fiber in cement-based concrete," *Materials Today: Proceedings*, vol. 65, pp. 2070–2072, 2022.

[27] A. A. Banjo and E. O. Temidayo, "Repair and strengthening of bamboo reinforced acrylic polymer modified square concrete columns using ferrocement jackets," *Scientific African*, vol. 8, Article ID e00378, 2020.

[28] P. R. Mali and D. Datta, "Experimental evaluation of bamboo reinforced concrete beams," *Journal of Building Engineering*, vol. 28, 2020.

[29] A. Agarwal, B. Nanda, and D. Maity, "Experimental investigation on chemically treated bamboo reinforced concrete beams and columns," *Construction and Building Materials*, vol. 71, pp. 610–617, 2014.

[30] M. F. Ashby and D. Cebon, "Materials selection in mechanical design," *Journal de Physique IV*, vol. 3, no. C7, pp. C1–C7, 1993.

[31] P. van der Lugt, J. G. Vogtländer, J. H. van der Vegte, and J. C. Breze, *Life Cycle Assessment and Carbon Sequestration; the Environmental Impact of Industrial Bamboo Products*, World Bamboo Organization, Antwerp, Belgium.

[32] H. Archila et al., "Bamboo reinforced concrete: a critical review," *Materials and Structures*, vol. 51, no. 4, p. 102, 2018.

[33] H. Archila, S. Kaminski, D. Trujillo, E. Z. Escamilla, and K. A. Harries, "Bamboo reinforced concrete: a critical review," *Materials and Structures*, vol. 51, 2018.

[34] Guaduabamboo, "Bambusa bambos," https://www.guaduabamboo.com/blog/bambusa-bambos.

[35] Wikipedia, "Bambusa bambos," https://en.wikipedia.org/wiki/Bambusa_bambos.

[36] Feedipedia, "Node," https://www.feedipedia.org/node/496.

[37] K. Fern, "Notes from observations," *Tasting Etc at Plants For A Future and on Field Trips*.

[38] Tropical theferns, "Bambusa bambos," https://tropical.theferns.info/viewtropical.php?id=Bambusa+bambos.

Hindawi
Advances in Materials Science and Engineering
Volume 2023, Article ID 2391166, 12 pages
https://doi.org/10.1155/2023/2391166

Research Article

Waste Coir Nanofiller Fused Gallus-Gallus Fibres Reinforced PMC

V. Vijayan,[1] T. Sathish,[2] R. Saravanan,[2] Kuldeep Kumar,[3] Ganesh K. Jadhav,[4] V. Sharun,[5] R. Elangovan,[6] K. Chellamuthu,[7] Mandeep Singh,[8,9] and Aklilu Teklemariam[10]

[1]*Department of Mechanical Engineering, K.Ramakrishnan College of Technology, Trichy, India*
[2]*Department of Mechanical Engineering, SIMATS School of Engineering, Chennai 602105, Tamil Nadu, India*
[3]*Department of Civil Engineering, Punjab Engineering College, Sector-12, Chandigarh, India*
[4]*Department of Mechanical Engineering, Dr. D.Y. Patil Institute of Engineering Management and Research, Akurdi, Maharashtra, India*
[5]*Department of Mechanical Engineering, Panimalar Engineering College, Chennai 600123, India*
[6]*Department of Mechanical Engineering, Mookambigai College of Engineering, Kalamavur, Pudukkottai, Tamil Nadu 622502, India*
[7]*Department of Mechanical Engineering, K. Ramakrishnan College of Engineering, Trichy, India*
[8]*School of Mechanical and Mechatronic Engineering, Faculty of Engineering and Information Technology, University of Technology Sydney, Sydney, NSW, Australia*
[9]*School of Mechanical and Manufacturing Engineering, Faculty of Engineering, The University of New South Wales, Sydney, NSW 2052, Australia*
[10]*Department of Mechanical Engineering, Faculty of Manufacturing, Institute of Technology, Hawassa University, Awasa, Ethiopia*

Correspondence should be addressed to Aklilu Teklemariam; akliluteklemariam@hu.edu.et

Received 12 August 2022; Revised 28 November 2022; Accepted 4 April 2023; Published 29 May 2023

Academic Editor: Pudhupalayam Muthukutti Gopal

This research aims to increase the utility of globally and abundantly available waste natural fibres of Gallus-Gallus fibres coir waste from mattress and car seat manufacturing factories. The composite samples were prepared with a rally round of polyester resin of grade GP500 bio-epoxy by synthesizing specially treated Gallus-Gallus fibres selectively used for reinforcement and characterizing them through static and dynamic mechanical analyses to identify their wide range of applicability. The Gallus-Gallus fibres are preprocessed with sodium oxidative and a half per cent of potassium manganate (VII) chemical solution. The selective use includes 5 mm, 10 mm, 15 mm, and 20 mm length of the Gallus-Gallus fibre, and the quantity of reinforcement was 10%, 20%, and 30%. Five alternate layers of matrix and fibres, with vertical and horizontal orientation, are considered; 12 different samples of Gallus-Gallus fibres reinforced polyester polymer composites and a neat polyester composites were synthesized and characterized for moisture absorbability, tensile strength, tensile modulus, flexural strength, flexural modulus, wear resistance, and out-performed composites were included in microscopic examination and dynamic Mmchanical analysis. The interesting results are the preferred resin, supported for good surface finish, interface bonding, and totally in the enhancement of Composite properties. The composites are strong in tension (760.89 MPa) and sufficiently flexible (flexural modulus 5441.32 MPa), absorbed less moisture (5.8 g), high wear-resistant (least weight loss upon abrasion with a value of 0.1989 g), secured good results in dynamic analysis, and ensured homogeneous distribution of fibres in the matrix through a scanning electron microscopy image. The composites CPPC10, CPPC11, and CPPC12 performed well but composite CPPC12 outperformed.

1. Introduction

Globally, the availability of chicken feathers increases day-by-day multiple times due to the consumption of chicken flush through the wide variety of palatable tasty food styles and huge in volume. It was estimated that the feather disposal is 5–10 per cent of the weight of the chicken. Chicken feathers (Gallus-Gallus) contain 91% keratin protein. They are electrically and thermally low conductive materials and enhanced mechanical properties as fillers [1]. Some of the interesting results found in literature especially in the valorisation of chicken fibres were used as reinforcement materials in synthesizing composites. The authors in [2] used TPU-polyether resin as matrix and waste keratin Gallus-Gallus fibres (GGFs) as reinforcement (0%, 30%, and 60%) in synthesizing polymer composite through solvent-casting-evaporation method and investigated thermomechanical properties by dynamic mechanical analysis. Uniform distribution of fibres is ensured through SEM image [3]. RSO-polyurethane composite is synthesized in rubber seed oil-based polyurethane resin employed as a matrix in synthesizing 5%, 10%, 15%, 20%, and 25% weight percentage of Gallus-Gallus particles reinforced composites by the casting method. These composites were characterized by the test of hardness, moisture absorption, density tensile, and impact strength. It was found that an increase in hardness and tensile strength was observed in reinforcement from 15% to 25% and a decrease in the density and impact strength [3, 4] used polypropylene resin matrix in composing 5, 10, 15, and 20 wt.% Gallus-Gallus fibres in powder form reinforced in the matrix [5]. It was found that the reinforcement enhanced flexural and tensile properties but not impact strength. SR green epoxy 56 resin is used to compose an average length of 26 mm Gallus-Gallus fibres reinforced 60%, 70%, and 80% of weight fraction. They were characterized by thermal and acoustic insulation properties. The study [6] used the cellulose of butyl methylimidazolium chloride resin to compose curtain of hair, Gallus-Gallus, and wool reinforced composites and found that the reinforcement improved the mechanical properties. Alkali-treated Gallus-Gallus fibres are used to improve the mechanical properties of the composite [6] in which natural rubber was employed as resin/matrix [7]. Polylactic acid resin-based Gallus-Gallus particle of weight fraction, 2%, 5%, 8%, and 10% reinforced composites, reported that Gallus-Gallus fibres enriched the thermal stability of CFF/PLA composite. The studies [8, 9] also used Gallus-Gallus fibre fillers as heat insulation in Winter clothes. The study [10] synthesized glass/epoxy/Gallus-Gallus fibre hybrid composite for printed circuit board application and found that the dielectric constant of the composites decreased with fibre contents and similar to printed circuit board property achieved. The study [11] brought into play of poly-methyl methacrylate resin matrix to blend keratin fibres of Gallus-Gallus reinforced composite which resulted that the sign of the augment of storage modulus offers elevated stability, as replicated in the modulus behaviour, and reduction of Tan delta peak is a sign of the physically powerful interface. Waste SiC is utilized as filler material for preparing epoxy glass fibre composite and investigated the machinability in abrasive water jet machining by [12]. They used Taguchi and grey relation analysis to optimize the machining parameters. The study [13] recommended the green filler material for synthesizing the glass fibre epoxy composite through the compression moulding technique in which the 0.6 wt.% reinforcement outperformed. The study of [14] investigated the effects of oxygen plasma treatment on polyethylene matrix and found that higher flexural strength of 25.87 MPa was observed by the novel treatment but tensile strength was slightly reduced from 18.2 MPa to 17.7 MPa. The study [15] used benzoyl chloride treatment for the natural fibres of ramie and kenaf fibres; they optimized the weight percentage of fibres with Taguchi-based grey relational analysis and further optimized by TOPSIS technique [16]. The novelty utilized TiO_2 filler in the polymer composited and improved the tribological properties and reported that 40 wt.% SP/5 wt.% TiO_2 composition recorded good results. The study [17] recommended sodium bicarbonate treatment for natural fibres like jute fibre composites and found that such treatment improved the machinability of drilling [18]. Banana fly ash/sisal/pineapple composites are introduced and the wear parameters are optimized by GRA, and it is reported that the addition of filler materials and hybrid fibres with the polymer matrix results in increased friction.

Novelty of this research utilizes the used-waste of coir from the car seat and used bed and sofa set as nanofiller in fabricating novel composite. This research gives more importance on bio degradation after use so it utilizes grade GP500 bio-epoxy polyester resin to compile a composite matrix with Gallus-Gallus fibres reinforcement. The preprocessing of Gallus-Gallus fibres and special chemical treatment to refine the quality of Gallus-Gallus fibres and enhancement of their strengths. Investigation on the influence of the length of Gallus-Gallus fibres used and quantity of fibres reinforced in layer fashion composites. The originality can be claimed in the chemical solution prepared for processing and preprocessing of Gallus-Gallus fibres, composite matrix, and classifications of specially treated selective Gallus-Gallus fibrereinforced polyester polymer composites and use of nanofillers.

2. Materials and Methods

The use of Gallus-Gallus fibres as reinforcing elements in synthesizing hybrid composites is focused in this research.

2.1. Constituents of Composite. The Gallus-Gallus fibres are employed as reinforcement elements and the polyester resin of grade general purpose 500 bio-epoxy as matrix materials. The considerable properties of the matrix material are its casted laminate possesses tensile and flexural strengths that are 57 N/mm^2 and 85 N/mm^2, respectively. Their tensile modulus and flexural modulus are 3150 N/mm^2 and 3250 N/mm^2, respectively. Low volumetric shrinkage 7-8% and specific gravity 1.22. The Gallus-Gallus fibre physical and chemical properties are moisture absorption 16–20 wt%. Aspect ratio that is length to diameter ratio between the 30 and 50. The specific gravity of Gallus-Gallus fibre is 0.7 to 1.2 and the nature of rapidly degrade in highly alkaline environment (where pH value is 12.4), oven dried fibre recorded tensile strength about 70 MPa and young's modus up to 50 GPa, 43 : 100 for hardener and resin ration in wt%. The fast harder was used. The used coir from the waste car seat, waste

Figure 1: Fresh Gallus-Gallus fibres and waste coir powders.

bed, and sofa was first separated. That coir fibres were put into Soxhlet device; acetone, toluene, and methylated spirit were added in the ratio of 1 : 4 : 1 to dewax coir for 4 hours to 5 hours. Then, those fibres were extracted and dried at 380 K. After that such coir fibres were grinded multiple times and fine nanopowder is obtained. The average particle size was measured with use of nano ZS model Malvern particle size analyzer. It was in the range of 850 nm to 975 nm. Its chemical properties are 27.41% cellulose, 42% lignin, 14.63% hemicellulose, and 10.16% pectin/wax. The ultimate tensile stress was 106 to 175 MN/m^2 and Elongation was permitted up to 47%. Though polyester resin 20% weaker than bond made by epoxy, more fragile, they are useful, create low stress, and less expensive. Polyester resins are found working well along with epoxy since they are adequate adhesive [19]. The unsaturated polyester resin with epoxy unutilized to fabricate E-SiO_2 nanocomposites and achieve the amazing results of Shore A hardness increased by 14.0%, elongation at break by 86.80%, flexural stress by 86.81%, flexural strength by 69.18%, and Young's modulus by 37.03% [20].

2.2. Pretreatment of Gallus-Gallus Fibres. The fresh Gallus-Gallus fibres of various lengths were collected from the butcher shop or slaughter house shown in Figure 1. Those feathers were washed with running water. The cleaning solution was prepared as the distilled water is mixed with heated SDS solids in the ratio of 40 : 1 and a total of 10 litres as suggested [21–23]. The feathers were fed in the washing machine to agitate for 30 to 45 minutes with 50°C heated sodium dodecyl sulphate (SDS) solution. The SDS is used for bacterial decontamination in the Gallus-Gallus fibre. Then, those feathers were washed and agitated with plain distilled water for 15 minutes. After rinsing the feathers, they dried in sunlight for a day.

2.3. Chemically Treating Gallus-Gallus Fibres. The chemical solution was composed of with weight fraction of 5% caustic soda (sodium hydroxide, NaOH), five per cent of potassium permanganate VII, and the remaining ninety per cent distilled water. NaOH is a mandatory compound with potassium permanganate VII for the permanganate ion to react for the purpose (dermatitis, fungal infections, and so on). Then, the cleaned feathers were soaked in the solution for 10 hours. After that, the Gallus-Gallus fibres were washed in distilled water. Then, the washed Gallus-Gallus fibres were dried in sunlight for 48 hours. Hence, the Gallus-Gallus fibres were treated for refinement.

2.4. Hybrid Composite Samples Preparation. The compression moulding type synthesizes method is preferred. The percentage of specially treated Gallus-Gallus fibres (including nanofiller) varied four three levels as 10%, 20%, and 30% against the variation of the polyester matrix. The length of the Gallus-Gallus fibres varied in four levels from 5 mm to 20 mm with the step of 5 mm. The neat polyester was also prepared to validate the influence of specially treated Gallus-Gallus fibres and their contribution to the composite matrix. The neat polyester acts as a control specimen that is a benchmark specimen. The detailed research design is presented in Table 1. The layer arrangements are polyester/Gallus-Gallus fibres/polyester/Gallus-Gallus fibres/polyester. Hence, out of five layers, the Gallus-Gallus fibres are placed in the second and fourth layers. The percentage of contribution in the composite matrix is divided equally (as per research design allocation) for obtaining uniformity. For example, 90% polyester and 10% fibre (specially treated Gallus-Gallus fibres 8% and nanofiller 2%) are used for CPPC1, CPPC4, CPPC7, and CPPC10. The composite laminates CPPC2, CPPC5, CPPC8, and CPPC11 consists of 16% specially treated Gallus-Gallus fibres and 4% nanofiller) and the composite laminates CPPC3, CPPC6, CPPC9, and CPPC12 consist of 24% specially treated Gallus-Gallus fibres and 6% nanofiller. In those composites, respective lengthen fibres and polyester resin are distributed in layers as 30%, 5%, 30%, 5%, and 30% for a layer of first, second, third, fourth, and fifth, respectively.

2.5. Synthesize of Composites. The research design of synthesizing of proposed specially treated selective Gallus-Gallus fibres reinforced polyester polymer composites is detailed in Table 1. The coir nanofillers were mixed thoroughly with resin. Square shaped chromium-plated Mild steel moulds (of side 30 cm) were placed on the worktable of the compression testing machine (CTM). The wax was applied on the moulds for nonsticking of composite to mould and easy for releasing the composite from the mould. The selective length of Gallus-Gallus fibres was used as per research design in synthesizing a class of

Table 1: Research design.

Composites	PC*	CPP C1	CPP C2	CPP C3	CPP C4	CPP C5	CPP C6	CPP C7	CPP C8	CPP C9	CPP C10	CPP C11	CPP C12
Length of feather Gallus-Gallus fibres	—	5	5	5	10	10	10	15	15	15	20	20	20
Weight percentage of polyester	100	90	80	70	90	80	70	90	80	70	90	80	70
Weight percentage of Gallus-Gallus fibres	0	8	16	24	8	16	24	8	16	24	8	16	24
Percentage of waste coir nanoparticles	0	2	4	6	2	4	6	2	4	6	2	4	6

*Control specimen.

composite. The extreme layers are polyester in between layers and are alternate sequence appropriate long fibres and matrix material. Hence, out of five layers, the Gallus-Gallus fibres were placed in the second and fourth layers. After completing all five layers, the undried composite was compressed by compression testing machine (CTM). This causes the excess resin and air gaps/air bubbles removed from the composite and finished with uniform thickness. The composite was kept in CTM for 6 to 10 minutes and maintained the temperature of 120°C with a uniform load of compression of 2000 kg to avoid the bending while setting of composites [3]. After that, composites panel was allowed to dry on the rooftop for 5 to 6 days. In the same way, all 13 kinds of composite panels were synthesized. The chemical treatment of Gallus-Gallus fibres supports well in synthesizing the composites and found good bonding with the matrix. The surface finish of the composite was also found good.

2.6. Characterization of Moisture Absorbability. The samples were warmed up at 50 to 60 degrees Celsius for discarding the moisture content in the composite sample panels. Then, they were measured in all the dimensions and mass of each specimen. The specimens were immersed in the distilled water bath for 120 hours. The weight gain and dimensional gain were noted every 12 hours gap. The rapid improvements were observed in the first few observations and then gradually stabilized. On the last day, that is, the fifth day, no more improvement was found in dimensions as well as weight gain. Hence, it was understood that the test is almost complete. The final readings were used for estimating the net moisture absorbed in grams and elongation computations. The observations were graphically presented, analyzed, and discussed in the next section.

2.7. Characterization of Tensile Properties. The sample specimens for characterization of tensile properties are shown in Figure 2. A 400,000 N capacity Universal Testing machine was employed in this investigation. The specimen and testing procedure is followed as per ASTM D3039. In an inch wider, 10 inches long rectangular-shaped specimenand the gauge length was 6 inches. A gradual load of a millimetre per minute speed was set. The investigation was performed at room temperature and in the spring season. The sample specimens for this investigation are shown in Figure 3. The observations were graphically presented, analyzed, and discussed in the next section.

2.8. Characterization of Flexural Properties. The bendability of material is also a fundamental characteristic of a material. This is usually carried out in the position of a simply supported beam with a load on its midspan. That is, the reaction load at each endpoint and the loading at the middle point. The same universal testing machine is employed for this investigation and the loading speed was a millimetre per minute. A half an inch wider 6 inches long and 3 mm thicker specimens were used as per the standard of ASTM D790. The test was carried out at room temperature in spring atmospheric conditions. The observations were graphically presented, analyzed, and discussed in the next section.

2.9. Characterization of Tribological Property. The wear resistance is one of the tribological properties. The test (standard D4060-14) was carried out to characterize the Gallus-Gallus fibres reinforced polyester polymer composites and neat polymer composite in terms of wear resistance property. The Taber abrasers, Model ISE AO16 is employed in this investigation with a setting of revolution of turntable 1000 per minute for five hours for each 6.35 mm thick round sample with the surface area of 100 square millimetres. After 5 hours, the loss of weight of the specimens was measured for knowing the wear resistance of samples of each fibre length category and neat polyester composite. The observations were graphically presented, analyzed, and discussed in the next section.

2.10. Characterization of Properties Based on Dynamic Mechanical Analysis. The DMA Q800 V20.6 Build 24 is employed for executing the dynamic mechanical analysis in the composites. It is a kind of bending mode investigation. The 3 mm thick, $1/2'' \times 2\ 1/2''$ sized rectangular specimens were used. The heating rate of 4 degrees Celsius per minute is in the range of 28 to 230 degrees Celsius, and the vibration frequency is 1 Hz. Figure 4 shows results of the dynamic characterization. The observations were graphically presented, analyzed, and discussed in the next section.

The tensile tested specimen samples are shown in Figure 5. The special treatment of Gallus-Gallus fibres brings basic required strength into all kinds of composites. The detailed analysis and discussion of their characterization results were presented in the next section.

3. Results and Discussion

The 12 types of Gallus-Gallus fibres reinforced polyester polymer composites and neat polymer composites were

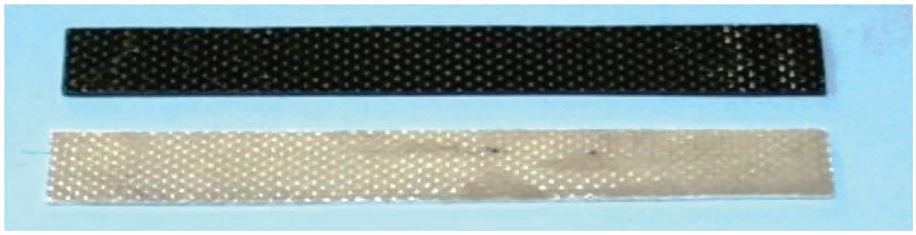

Figure 2: Tensile test specimen of specially treated selective Gallus-Gallus fibres reinforced polyester polymer composite and neat polymer composite.

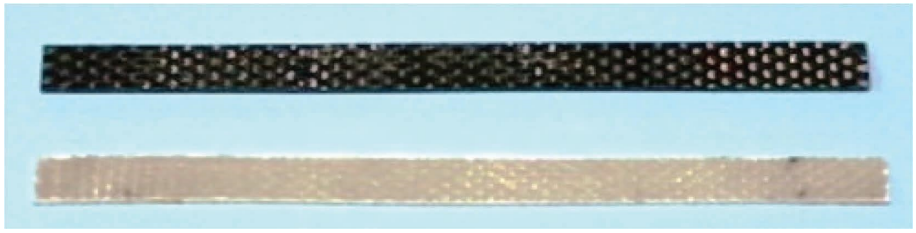

Figure 3: Flexural test specimen of specially treated selective Gallus-Gallus fibres reinforced polyester polymer composite and neat polymer composite.

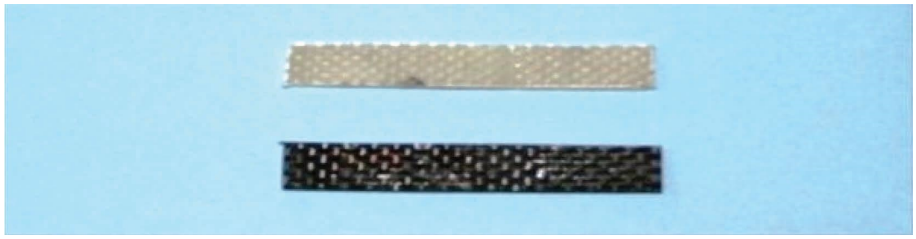

Figure 4: Dynamic mechanical analysis specimen of specially treated selective Gallus-Gallus fibres reinforced polyester polymer composite and neat polymer composite.

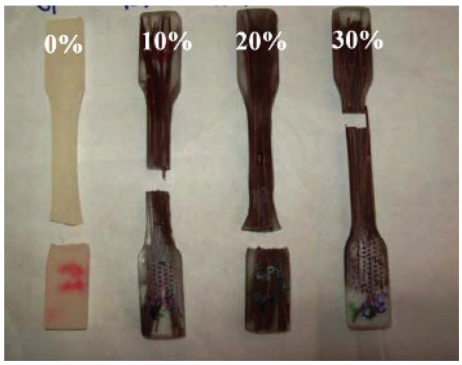

Figure 5: The tensile tested specimens of specially treated selective Gallus-Gallus fibres reinforced polyester polymer composite and neat polymer composite.

synthesized and characterized with static and dynamic mechanical analysis. Their observations are presented in this section as graphical outputs. In this section analysis of the results of the investigation is presented in detail. To evaluate the effectiveness of Vol. % of fibres and length of fibres used in Gallus-Gallus fibres reinforced polyester polymer composites, Tukey's multiple range test is employed for analyzing the results of static analysis. In MINITAB 17 software, the significance level of value is set as p less than 0.05. The comparative analysis is presented in this section sequentially.

3.1. Tensile Load-Based Characterization. The tensile test observations are presented in graphical form with Tukey test results in Figure 6. The test results reveal that neither neat polyester composite nor 5 mm and 20 mm long fibres used composites categories Gallus-Gallus fibres reinforced polyester polymer composites are strong. The preferable composite matrix (tensile strength is 16.5 MPa) is 80% polyester and 20% Gallus-Gallus fibres (with a selective length of 15 mm). The Tukey test results reveal that within the 10% fibre cases, the composite CPPC4 outperforms and the composite CPPC7 is more significant than composite CPPC1, composite CPPC4, and composite CPPC10 as per means of standard error ± SE at the level of $P \leq 0.05$. As logically compared to other wt% composites, the increase in tensile strength of 10 wt% composites is expected to increase up to composite CPPC7. This ambiguity in the result may be due to some inherent defects of synthesizing. The ostensible plunge in the tensile modulus was demonstrated in the case of 30 wt% fibre reinforced composites. The reason behind this fact is the lack of fibre dispersion.

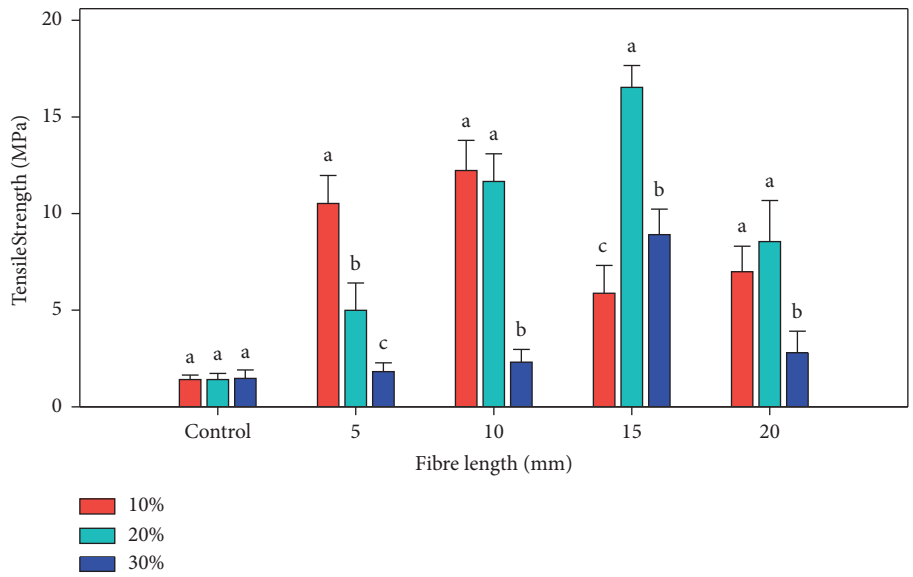

Figure 6: Tensile strength specially treated selective Gallus-Gallus fibres reinforced polyester polymer composites and neat polyester composite with Tukey test results.

The dispersion of fibres usually happens in the situation of fibre agglomeration. The neat composite has a tensile strength of 1.41 MPa.

In Figure 6, from left to right, the first three bars indicate control specimens, so no variation observed. The next 12 bars indicate the performance of composite specimen CPPC1 to CPPC12. It can be observed that within the 15% fibre cases, the composite CPPC8 outperformed. According to Tukey test results, the composite CPPC2 is more significant than composite CPPC4, composite CPPC6, and composite CPPC8 as per means of standard error ± SE at the level of $P \leq 0.05$. In the Tukey test results of 30% fibre cases, the composite CPPC3 is more significant than the control specimen than composite CPPC6, composite CPPC9, and composite CPPC12 as per means of standard error ± SE at the level of $P \leq 0.05$.

The tensile modulus of Gallus-Gallus fibres reinforced polyester polymer composite and neat polymer composite is shown graphically by the Tukey test result in Figure 7. In Figure 7, from left to right, the first three bars indicate control specimens so no variation is observed. The next 12 bars indicate the performance of composite specimen CPPC1 to CPPC12. It can be observed that the Tukey test results reveal that according to tensile modulus there is no significance as per the length of the fibres used, but the quantity of fibres used is significantly deferred as per means of standard error ± SE at the level of $P \leq 0.05$. The highest tensile modulus obtained for 10 mm long fibres used composites like CPPC4, CPPC5, and CPPC6. The CPPC5 found the highest value of 760.89 MPa compared to the tensile modulus of CP (213.32 MPa).

3.2. Flexural Test-Based Characterization. The flexural strengths of Gallus-Gallus fibres reinforced polyester polymer composite and neat polymer composite show graphically the Tukey test result in Figure 8. In Figure 8, from left to right, the first three bars indicate control specimens so no variation is observed. The next 12 bars indicate the performance of composite specimen CPPC1 to CPPC12. It can be observed that the increase of fibre content in the composite increases the flexibility; that is, flexural strength improved and the highest values were obtained for the composite CPPC12 (41.58 MPa) followed by CPPC11 39.35 MPa. The flexural strength of the PC is 29.14 MPa. In terms of flexural strength, the Tukey test results, it is understood that there is no significant difference between composite as per means of standard error ± SE at the level of $P \leq 0.05$. That is, all the prepared composites are sufficiently flexible.

The flexural modulus of Gallus-Gallus fibres reinforced polyester polymer composites and neat polymer composites is shown graphically with the Tukey test result in Figure 9. In Figure 9, from left to right, the first three points (same one over another) indicate control specimens, that is, variation observed. The next 12 points indicate the performance of composite specimen CPPC1 to CPPC12. It can be observed that the increase of fibre content in the composite increases the flexibility that improves flexural modulus and the highest values obtained for the composite CPPC12 (5441.32 MPa) followed by CPPC11 as 5278.95 MPa. The flexural modulus of PC is 2032.23 MPa. According to the flexural strength-based Tukey test result, it is understood that there is a significant difference of 10% fibre category composites (red) as per means of standard error ± SE at the level of $P \leq 0.05$, starting from 10 mm fibre length category and increased gradually with the increase of fibre lengths.

3.3. Wear Resistance-Based Characterization. The observation of weight losses Gallus-Gallus fibres reinforced polyester polymer composites and neat polymer composite is

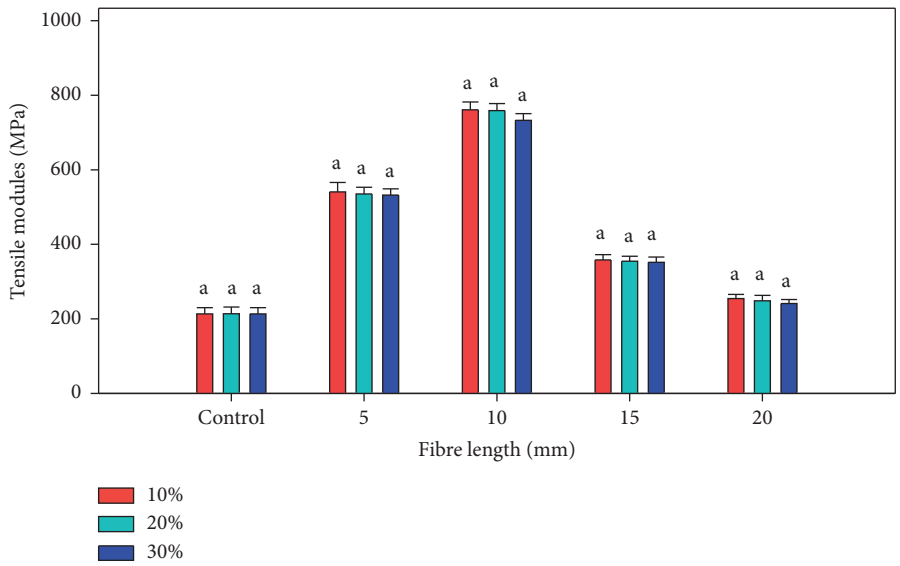

Figure 7: Tensile modulus specially treated selective Gallus-Gallus fibres reinforced polyester polymer composites and neat polyester composite with Tukey test results.

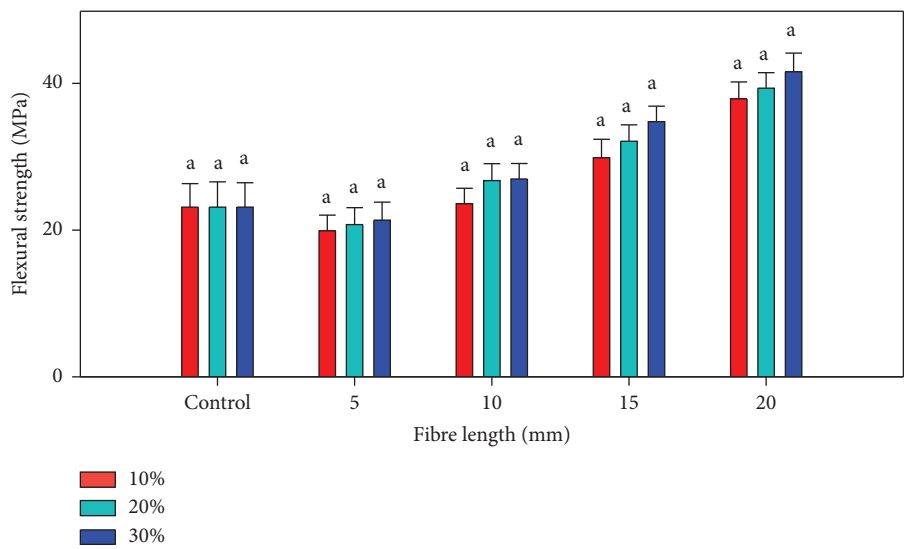

Figure 8: Flexural strength of specially treated selective Gallus-Gallus fibres reinforced polyester polymer composites and neat polyester composite with Tukey test results.

graphically presented along with Tukey test results in Figure 10. In Figure 10, from left to right, the first three points (same one over another) indicate control specimens, that is, variation is observed. The next 12 points indicate the performance of composite specimen CPPC1 to CPPC12. It can be observed that the special treatment on the Gallus-Gallus fibres supported well enhancements across all the fibre contents used. At lower weight fractions, the sample of CPPC1 (reinforced with 10 wt% (5 mm length of fibre)) had the most wear resistance because it had the least weight loss upon abrasion with a value of 0.1989 g among the treated CFF reinforced composites followed by samples containing 10 wt% (10 mm length of fibre) contents having increasing weight loss values of 0.2156 and 0.3998 g. A critical look at the graph revealed that the reinforcement of Gallus-Gallus fibres promotes wear resistance. So, wear resistance improves with the increase of vol. % of Gallus-Gallus fibres. The wear resistance is comparatively so much better than the no fibre reinforcement (neat polyester) had the least wear resistance and the overall highest weight loss value of 2.954 g. This indicates that the reinforcements improved the abrasion resistance of the developed composites.

3.4. Characterization of Moisture Absorption Property. The observation of net moisture absorbed by the Gallus-Gallus fibres reinforced polyester polymer composites and neat polymer composite in grams of weight gain is presented

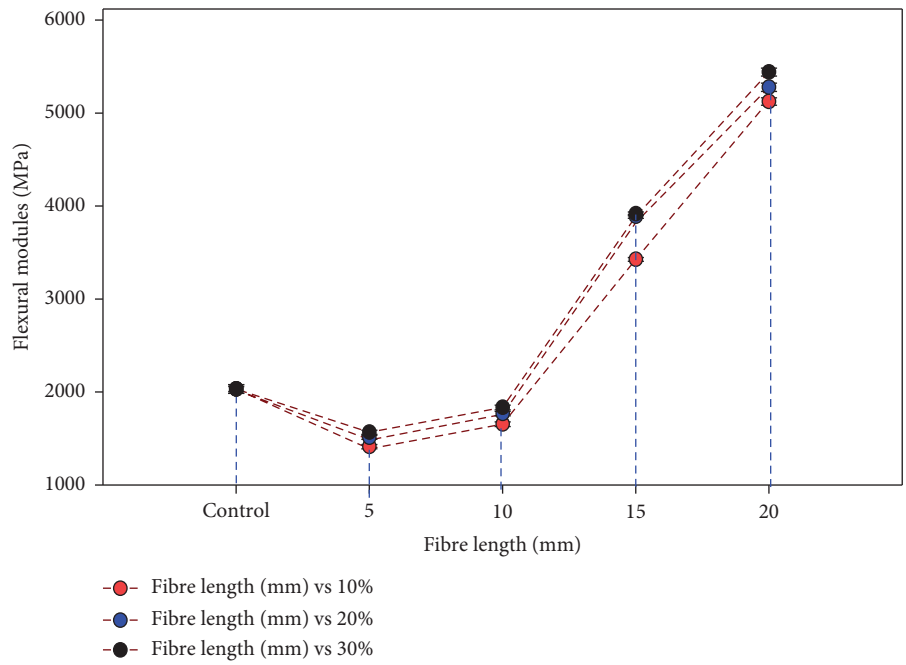

Figure 9: Flexural strength of specially treated selective Gallus-Gallus fibres reinforced polyester polymer composites and neat polyester composite with Tukey test results.

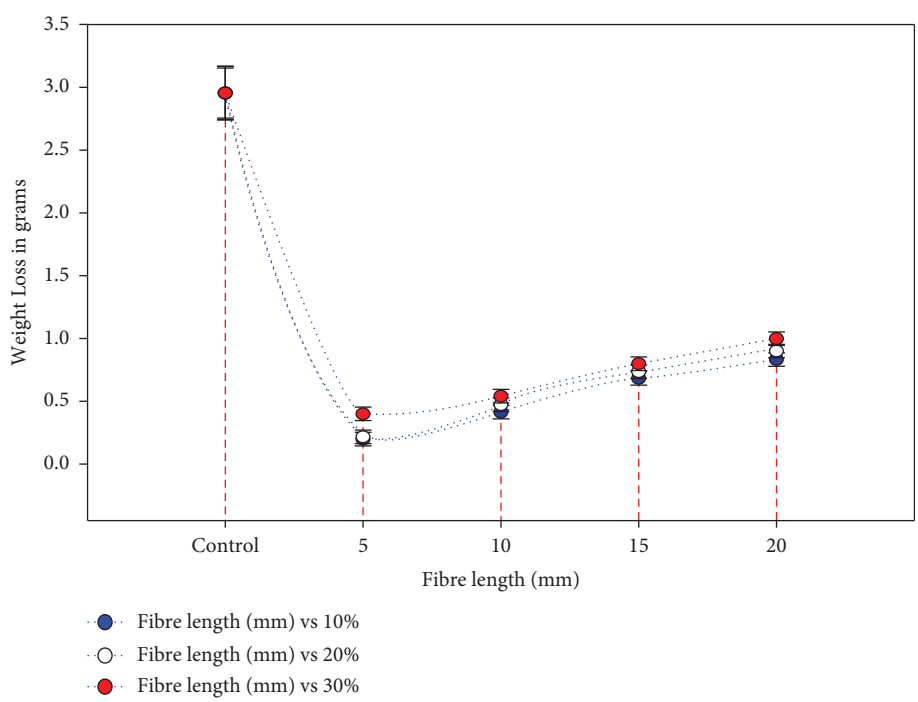

Figure 10: Wear property of specially treated selective Gallus-Gallus fibres reinforced polyester polymer composites and neat polyester composite with the Tukey test results.

graphically along with the Tukey test results in Figure 11. In Figure 11, from left to right, the first three bars indicate control specimens so no variation is observed. The next 12 bars indicate the performance of composite specimen CPPC1 to CPPC12. It can be observed that there are five groups such as neat composite, Gallus-Gallus fibres (length 5 mm, 10 mm, 15 mm, and 20 mm) reinforced polyester polymer composites. As per the Tukey test result, there are no significant differences in variation of fibres reinforcement in composites, but in a variation of the length of the fibres.

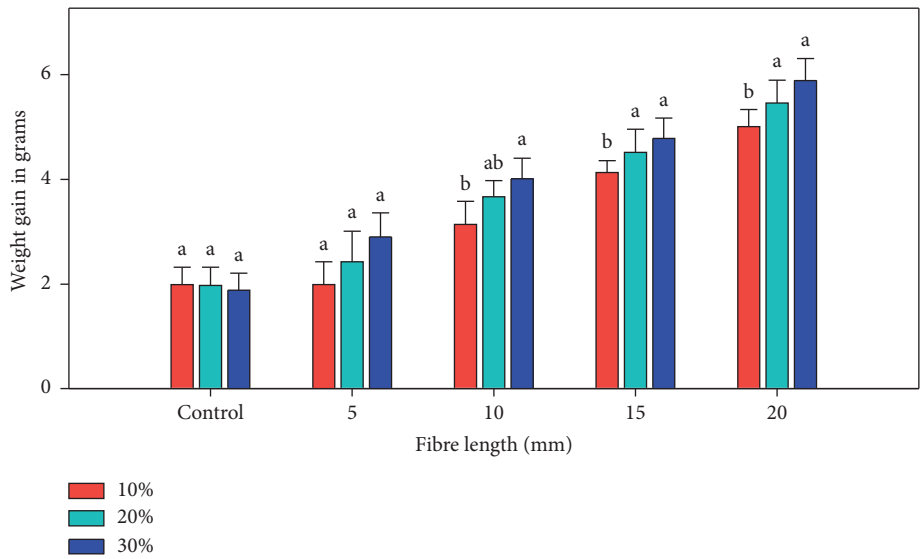

Figure 11: The moisture absorbability of specially treated selective Gallus-Gallus fibres reinforced polyester polymer composites and neat polyester composite with the Tukey test results.

In general, it is found that an increase in fibre content and an increase in the length of fibres are used directly in proportion to the weight gain by moisture absorption. The highest gain weight by composite CPPC12 by moisture absorption was 5.8 g.

3.5. Microscopic Analysis. The microscopic analysis was carried out employing the scanning electron microscopy test image of tested composite specimen of CPPC12. The uniform distribution of Gallus-Gallus fibres in the polyester matrix is ensured. The self-explanatory image of scanning electron microscopy is shown in Figure 12. The CFF in the SEM image meant chicken feather fibres (Gallus-Gallus fibres).

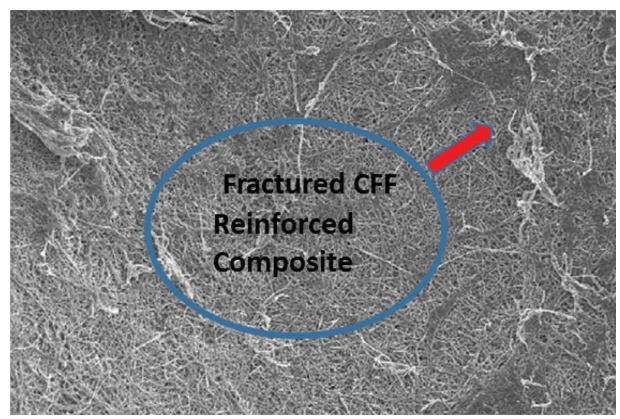

Figure 12: Scanning electron microscopy image of specially treated selective chicken feather fibres (CFF) reinforced polyester polymer composite of CPPC12.

3.6. Analysis of the Dynamic Mechanical Analysis-Based Characterization

3.6.1. Dynamic Mechanical Analysis for Storage Modulus (E'). Usually, the frequency of 1 Hz is maximum in a diverse natural fibre ratio in the storage module (E'), particularly the bio-composites. The storage modulus is indirectly proportional to tan delta. The dynamic mechanical analysis results of the storage module were statistically between the diverse natural fibres of CPPC12 composite. The values were significant at the maximum temperature of 90.27°C and it is significant with 20 wt% and 10 wt% composites of CPPC11 and CPPC10 with 89.58°C and 82.67°C, respectively. The storage modulus curves also illustrated that the biologically derived composites integration increases the E' values significantly.

3.6.2. Dynamic Mechanical Analysis for Loss Modulus (E''). The dynamic mechanical analysis curves (Figure 13) of the loss modulus showed that the fibres of composite CPPC12 reached maximum dissipation of mechanical energy with 362.0 MPa as compared to composite CPPC11 with 320.11 MPa, whereas CPPC10 with 318.29 MPa. It is also clearly evident that in the loss modules data, the consolidation of diverse types of bio-composite composition lands the extension of the loss modulus peak percentage, as a result of the amplification in procession separation.

3.6.3. Dynamic Mechanical Analysis of Composites Based on Tan Delta. The tan data results are displayed in Figure 13. The loss modulus to storage modulus is a ratio (E''/E') which is base for considering the damping results [21]. In general, combination of natural fibres ratio grades the behaviour of damping in bio-composites; it is generally owing to the shear-stress (τ) dosage with fibres combined in the company of energy of viscos-elastic indulgence on natural fibre matrix [12]. These experimental results support [1] chicken feather fibre (CFF) in the matrix of poly-lactic acid (PLA) improving

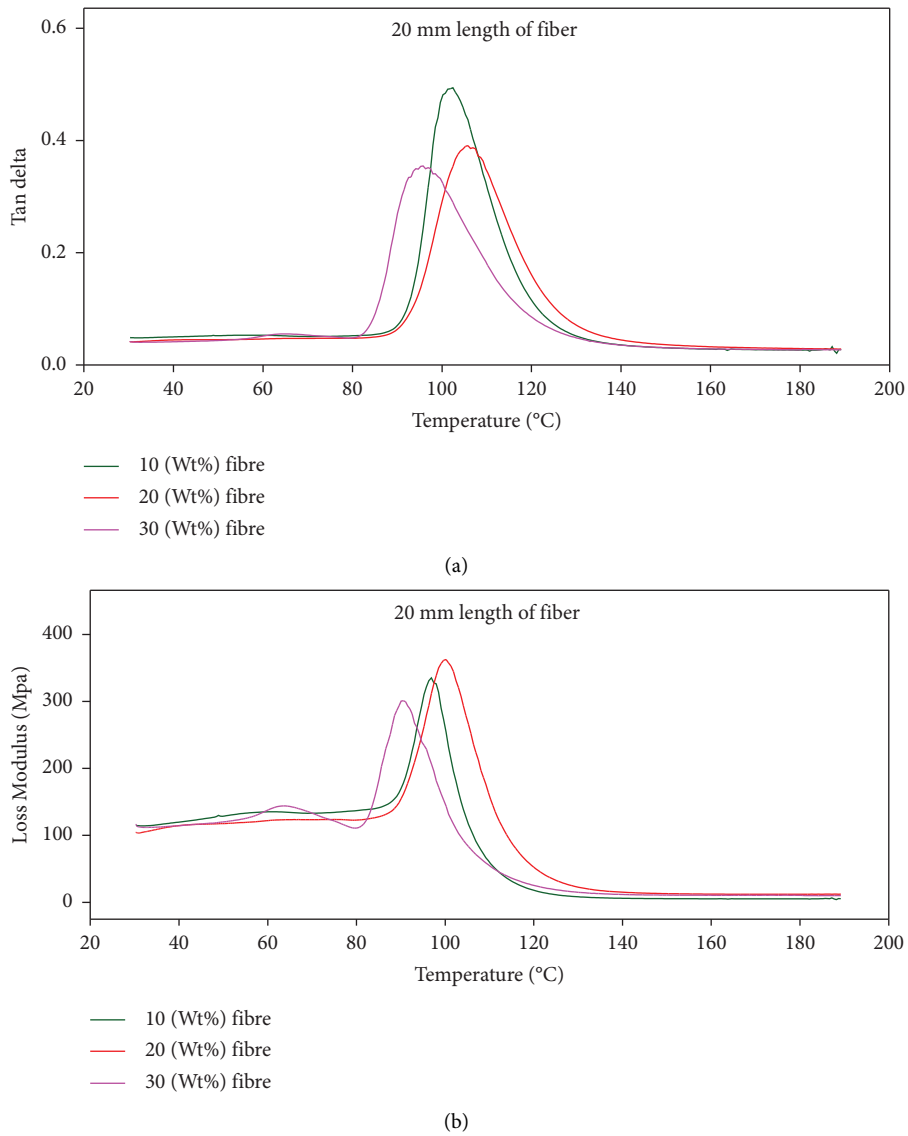

Figure 13: The results of dynamic mechanical analysis of specially treated selective Gallus-Gallus fibres reinforced polyester polymer composites CPPC10, CPPC11, and CPPC12. (a) Tan data. (b) Loss modules.

the maximum stiffness, that is, the tensile modulus of 4.2 GPa [8]. Chicken feather fibre reinforced composites improved the mechanical, thermal, and electric properties [24].

The above results in the CPPC12 composite, the significant peak area of 0.362 delivered at 89.62°C as compared to the CPPC11 composite (0.398 at 111.26°C) and CPPC10 Composites (0.526 at 105.16°C). Hence, it is clear that the storage modulus of the composites decreased with the increase of Gallus-Gallus fibres reinforcement; hence, the mechanical loss factor (tan delta) decreased with the increase of Gallus-Gallus fibres reinforcement. The sign of augment of storage modulus offers elevated stability, as replicated in the modulus behaviour, and reduction of Tan delta peak is a sign of physically powerful interface [10].

Chicken feather fibre (CFF) in the matrix of poly-lactic acid (PLA) improved the maximum stiffness, that is, trensile modulus of 4.2 GPa. Chicken feather fibre reinforced composites improved the mechanical, thermal, and electric properties. Gallus-Gallus fibres and jute fibre combined at 50/50 fibre wt% for highest impact strength [25]. Aluminum diethyl phosphinate, ammonium polyphosphate, reinforced thermoplastic polyurethane, and aluminum hypophosphite are used to enhance flame retardant properties of Gallus-Gallus fibres composite [26]. The Gallus-Gallus fibres associated with human hair fibre in unsaturated polyester resin matrix in which the composition human hair 40 (Wt.)%, Gallus-Gallus fibres 10 (Wt.)% remaining 50 (Wt.)%, matrix recorded 183 MPa flexural strength, and 108.3 MPa compressive strength [27].

4. Conclusions

This research focused on increasing the utility value of universally as well as abundantly available Gallus-Gallus fibres and waste coir fibres. The Gallus-Gallus fibres were

pretreated and specially treated with sodium and potassium manganate VII solution. The Gallus-Gallus fibres are selectively used in synthesizing composites in terms of wt% (10%, 20%, and 30%) as well as length (5 mm, 10 mm, 15 mm, and 20 mm) of Gallus-Gallus fibres. The waste coir powders were used as nanofillers. The specific outcomes are consolidated as follows:

Moisture absorption, depending upon the content of (Wt. %), specially treated selective Gallus-Gallus fibres in the composite matrix as well as the length of fibres used. Both are directly proportionate to the quantity of absorption of moisture. Although the maximum of 5.8 g weight gain found in 20 mm fibres used 30% Weight contributed CPPC12 composite.

The maximum tensile strength of 16.5 MPa was observed for composite CPPC10, that is, 80% polyester and 20% Gallus-Gallus Fibres of the selective length of 15 mm.

The highest tensile modulus obtained for 10 mm long fibres used composites like CPPC4, CPPC5, and CPPC6 which for CPPC5 tensile modulus was found highest as 760.89 MPa.

The highest flexural strength observed for the composite CPPC12 was 41.58 MPa and CPPC11 was 39.35 MPa.

The highest flexural modulus observed for the composite CPPC12 was 5441.32 MPa and then CPPC11 at 5278.95 MPa.

The maximum wear loss of 1.12 g was observed on the CPPC12 composite at 5000 rpm speed for 240 minutes of the tested specimen. Hence, the entire range of the proposed specially treated selective Gallus-Gallus fibres reinforced polyester polymer composites has good wear resistance

Based on the abovementioned results, the composites CPPC10, CPPC11, and CPPC12 are considered for microscopic examinations and dynamic mechanical analyses. The microscopic examination ensured the uniform distribution of selective Gallus-Gallus fibres in the polyester resin matrix. The dynamic mechanical analyses concluded that the mechanical loss factor that is tan delta decreased with the increase of Gallus-Gallus fibres reinforcement. That is, the augment of storage modulus offers elevated stability, as replicated in the modulus behaviour and reduction of tan delta peak is a sign of the physically powerful interface. Overall, the composite CPPC12 outperformed well.

The practical implications would be the utility value of Gallus-Gallus is focused on. The proposed composites properties are spread from sufficient strength to good strength, so a wide range of applications can be identified such as construction, doors, shelves, furniture, automotive, and upholstery.

Data Availability

The data used to support the findings of this study are included in the article. These are available from the corresponding author upon request.

Disclosure

The study was performed as a part of the Employment Hawassa University, Ethiopia.

Conflicts of Interest

The authors declare that there are no conflicts of interest regarding the publication of this paper.

Acknowledgments

The authors appreciate the technical assistance to complete this experimental work from Faculty of Manufacturing, Institute of Technology, Hawassa University, Ethiopia. The authors thank SIMATS School of Engineering, Chennai, and K. Ramakrishnan College of Technology, Trichy, for the support of draft writing, proof reading, and technical assistance.

References

[1] T. Tesfaye, B. Sithole, D. Ramjugernath, and T. Mokhothu, "Valorisation of chicken feathers: characterisation of thermal, mechanical and electrical properties," *Sustainable Chemistry and Pharmacy*, vol. 9, pp. 27–34, 2018.

[2] F. Pourjavaheri, F. Mohades, O. Jones et al., "Avian keratin fibre-based bio-composites," *World Journal of Engineering*, vol. 14, no. 3, pp. 183–187, 2017.

[3] O. Omorogbe, D. Yawas, I. Dagwa, I. Bakare, and M. Isa, "Physico-mechanical and micro-structural analysis of chicken feather particles reinforced rubber seed oil based polyurethane composites," *World Journal of Engineering*, vol. 10, no. 4, pp. 343–352, 2013.

[4] R. B. Choudary and R. Nehanth, "Effects of fibre content on mechanical properties of chicken feather fibre/PP composites," *Materials Today: Proceedings*, vol. 18, pp. 303–309, 2019.

[5] J. Bessa, J. Souza, J. B. Lopes et al., "Characterization of thermal and acoustic insulation of chicken feather reinforced composites," *Procedia Engineering*, vol. 200, pp. 472–479, 2017.

[6] C. D. Tran, F. Prosenc, M. Franko, and G. Benzi, "Synthesis, structure and antimicrobial property of green composites from cellulose, wool, hair and chicken feather," *Carbohydrate Polymers*, vol. 151, pp. 1269–1276, 2016.

[7] D. P. Sreenivasan, A. Sujith, and C. Rajesh, "Cure characteristics and mechanical properties of biocomposites of natural rubber reinforced with chicken feather fibre: effect of fibre loading, alkali treatment, bonding and vulcanizing systems," *Materials Today Communications*, vol. 20, Article ID 100555, 2019.

[8] S. Cheng, K.-T. Lau, T. Liu, Y. Zhao, P. M. Lam, and Y. Yin, "Mechanical and thermal properties of chicken feather fiber/PLA green composites," *Composites Part B: Engineering*, vol. 40, no. 7, pp. 650–654, 2009.

[9] N. Pasayev and O. Tekoglu, "The use of chicken feather fibers as filling material in Winter clothes for heat insulation purposes," *International Journal of Clothing Science & Technology*, vol. 31, no. 2, pp. 259–271, 2019.

[10] M. Zhan, R. P. Wool, and J. Q. Xiao, "Electrical properties of chicken feather fiber reinforced epoxy composites," *Composites Part A: Applied Science and Manufacturing*, vol. 42, no. 3, pp. 229–233, 2011.

[11] A. L. Martínez-Hernández, C. Velasco-Santos, M. de-Icaza, and V. M. Castaño, "Dynamical–mechanical and thermal analysis of polymeric composites reinforced with keratin biofibers from chicken feathers," *Composites Part B: Engineering*, vol. 38, no. 3, pp. 405–410, 2007.

[12] V. Kavimani, P. M. Gopal, K. R. Sumesh, and N. V. Kumar, "Multi response optimization on machinability of SiC waste fillers reinforced polymer matrix composite using taguchi's coupled grey relational analysis," *Silicon*, vol. 14, no. 1, pp. 65–73, 2022.

[13] V. Kavimani, P. M. Gopal, K. R. Sumesh, and R. Elanchezhian, "Improvement on mechanical and flame retardancy behaviour of bio-exfoliated graphene-filled epoxy/glass fibre composites using compression moulding approach," *Polymer Bulletin*, vol. 79, no. 8, pp. 6289–6307, 2022.

[14] K. R. Sumesh, J. Anton, P. Spatenka, and H. J. Sourkova, "Experimental studies on the influence of plasma treatment of polyethylene in carbon fiber composites: mechanical and morphological studies," *Polymers*, vol. 14, no. 6, p. 1095, 2022.

[15] S. Ganesh, S. Keerthiveettil Ramakrishnan, V. Palani, M. Sundaram, N. Sankaranarayanan, and S. P. Ganesan, "Investigation on the mechanical properties of ramie/kenaf fibers under various parameters using GRA and TOPSIS methods," *Polymer Composites*, vol. 43, no. 1, pp. 130–143, 2022.

[16] K. R. Sumesh, G. Saikrishnan, P. Pandiyan et al., "The influence of different parameters in tribological characteristics of pineapple/sisal/TiO2 filler incorporation," *Journal of Industrial Textiles*, vol. 51, no. 5, Article ID 8626S, 2022.

[17] P. Ravikumar, G. Rajeshkumar, P. Manimegalai, K. R. Sumesh, M. R. Sanjay, and S. Siengchin, "Delamination and surface roughness analysis of jute/polyester composites using response surface methodology: consequence of sodium bicarbonate treatment," *Journal of Industrial Textiles*, vol. 51, no. 1, pp. 360S–377S, 2022.

[18] S. Keerthiveettil Ramakrishnan, K. Vijayananth, G. Pudhupalayam Muthukutti, P. Spatenka, A. Arivendan, and S. P. Ganesan, "The effect of various composite and operating parameters in wear properties of epoxy-based natural fiber composites," *Journal of Material Cycles and Waste Management*, vol. 24, no. 2, pp. 667–679, 2022.

[19] M. Davallo, H. Pasdar, and M. Mohseni, "Mechanical properties of unsaturated polyester resin," *International Journal of ChemTech Research*, vol. 2, no. 4, pp. 2113–2117, 2010.

[20] X. Huang, Y. T. Guo, X. M. Yan, G. Q. Yin, and G. Z. Feng, "A new type of unsaturated polyester resin with epoxy functionalized nano-silica and dimer fatty acid: preparation and property," *Polymers for Advanced Technologies*, vol. 33, 2022.

[21] T. Tesfaye, B. Sithole, and D. Ramjugernath, "Valorisation of chicken feathers: recycling and recovery routes," in *Proceedings of the Sardinia 2017, 16th International Waste Management and Landfill Symposium. S Margherita di Pula, IWWG: International Waste Working Group*, p. 511, CISA Publisher, Sardinia, Cagliari, Italy, October 2017.

[22] T. Tesfaye, B. Sithole, D. Ramjugernath, and V. Chunilall, "Valorisation of chicken feathers: characterisation of physical properties and morphological structure," *Journal of Cleaner Production*, vol. 149, pp. 349–365, 2017.

[23] T. Tesfaye, B. Sithole, and D. Ramjugernath, "Preparation, characterisation and application of keratin based green biofilms from waste chicken feathers," *International Journal of Chemical Sciences*, vol. 16, no. 3, p. 281, 2018.

[24] R. A. Kurien, A. Biju, K. A. Raj, A. Chacko, B. Joseph, and C. P. Koshy, "Chicken feather fiber reinforced composites for sustainable applications," *Materials Today: Proceedings*, vol. 58, pp. 862–866, 2022.

[25] K. C. Jennifer, K. Saravanan, C. Kayalvizhi et al., "Study of impact strength properties of chicken feather fiber/jute fiber and its blends," *Journal of Natural Fibers*, vol. 19, no. 17, pp. 15238–15248, 2022.

[26] A. Mutlu and M. Dogan, "The effect of phosphorus-based flame retardants on the thermal and fire retardant properties of chicken feather/thermoplastic polyurethane biocomposites," 2022, https://assets.researchsquare.com/files/rs-1768236/v1/135c2362-62eb-498e-b5a0-434b5a870026.pdf?c=1656001934.

[27] T. Worku and S. Nachippian, "Development and analysis of human hair fiber and chicken feathers reinforced composite," 2022, https://assets.researchsquare.com/files/rs-1773566/v1/9f144276-b05d-4dab-83d5-3c41b1f06084.pdf?c=1656347835.

Hindawi
Advances in Materials Science and Engineering
Volume 2023, Article ID 4865273, 23 pages
https://doi.org/10.1155/2023/4865273

Review Article

An Overview of Current and Prognostic Trends on Synthesis, Characterization, and Applications of Biobased Silica

Belete Tessema,[1] **Girma Gonfa**,[1,2] **Sintayehu Mekuria Hailegiorgis**,[1,2] **and S. Venkatesa Prabhu**[1,2]

[1]*Department of Chemical Engineering, Addis Ababa Science and Technology University, Addis Ababa, Post Box 16417, Ethiopia*
[2]*Center of Excellence for Bioprocess and Biotechnology, Addis Ababa Science and Technology University, Addis Ababa, Post Box 16417, Ethiopia*

Correspondence should be addressed to Girma Gonfa; girma.gonfa@aastu.edu.et

Received 24 October 2022; Revised 21 December 2022; Accepted 5 April 2023; Published 26 April 2023

Academic Editor: Vijayananth Kavimani

Silica has shown numerous applications in different fields such as environmental, biomedical, agriculture, and even in chemical processing. However, due to high energy-intensive and cost-effective issues, researchers show interest to replace the conventional methods with biobased environmentally-friendly techniques for biosilica production from renewable biomass sources. Generally, silica is found to be available in amorphous and crystalline structures. For commercial purposes, silica is produced from alkyl orthosilicates ore that consists of polyethlydiorthosilicate, tetraethyl ortothosilicate, and tetramethyl orthosilicate. Another form of silica, silica gel, is produced from the selected resources of biomass, such as palm tree, wheat straw, maize leaves, teff straw, sugarcane bagasse, rice husk, rice straw, sugarcane leaf, oat husk, bamboo leaf, and corn cob. The production of biobased silica gel from agricultural residues is found to be a sustainable which receives a significant attention that can be replaced with inorganic-based silica gel for environmental concerns. Based on this context, there is a huge look for developing a process to produce biobased silica and silica gel from biomass resources with low energy utilization as promising alternatives to conventional methods. Keeping in view, current trends and methods for synthesis, the characterization of biobased silica and silica gel, as well as its wide prognostic applications were focused on a comprehensive review.

1. Introduction

Silica is a well-known material that is the most useful inorganic chemical compound for different industrial applications, such as environmental, biomedical, agriculture, and even in chemical processing. Commonly, it is found on the earth's crust and arises naturally as flint, sand, or quartz [1, 2]. Based on its structural characterization, silica gel has been found to be either amorphous or crystalline in appearance, which is observed as an inflexible 3-dimensional network of colloidal [3]. According to Kalapathy et al. [4], the structural character of the silica gel depends on its preparation method. Accordingly, it can also be categorized in aqua gel form, where the openings are occupied with water molecules in the xerogel aqueous phase, the openings are detached due to evaporation; besides, in the aerogel form, the solvent portion is detached by supercritical carbon dioxide. Biomass can be a potential source for the extraction of synthetic silica components such as silica gel. In such a way, biomass resources ash of rice husk [5], sorghum bagasse [6], teff straw [7], maize leaves [8], rice straw [9], wheat straw [10], sugarcane bagasse [11], sugarcane leaf [12], bamboo leaf [13] corn cob [14], and palm [1] are found to be potential feedstock. Sodium silicate is used in general to extract the silica from the residual ash of the feedstock [15]. Further, the produced silica is treated with different types of acid such as sulphuric acid [16], hydrochloric acid [17], nitric acid [18], and acetic acid [19] to turn it into gel. Several investigations have proven that the silica particles have numerous industrial applications, such as the synthesis of shear thickening fluid, as adsorbents, and inert material, even as potential catalyst [20–22]. Bageru and Srivastava [7]

and Mizer [5] have documented that the silica gel materials have a strong adsorption capacity due to its high surface area (700–800 m^2/g) with appreciable other physical properties. In specific, it exits excellent adsorption capacity on different organic compounds [23, 24]. The soluble forms of silicates derived from silica have remarkable industrial applications, especially, in pharmaceuticals and construction areas. The most common applications of liquid silicates are found in the development of ceramics [25, 26], concrete materials [27], glasses manufacturing [28], cement [29], delivery of biologically active ions [30], supercapacitors manufacturing [31], batteries [32], pharmaceuticals and cosmetics [33], detergents and adhesive agents [3, 4, 34]. Solid-state silica is used for various applications in the manufacturing of petroleum-derived products [35], fine-chemicals [36], biofuels [37], oil recovery [38], pollution abatement technologies and optical materials [4, 39], catalyst support [40], microfilters [41], thermal superinsulation [42], controlled release of drugs [23], and drug delivery systems for antibiotics [34, 43].

Silica particles have also been demonstrated for their outstanding performance in influencing plant metabolic activities [44]; it helps as a fertilizer to improve seedling growth rate, root development, and increase water retention [45] in plants. Moreover, silica gel exhibits several applications as adsorbent in chromatographic separation and removal of organic pollutants in water purification systems [46].

Commercially, silica can be produced from alkyl orthosilicates ore using the appropriate catalysts, such as polyethlydiorthosilicate, tetraethyl ortothosilicate, and tetramethyl orthosilicate [7]. Silica gel is prepared by acid precipitation method using sodium silicate solution, quartz, and soda ash at the elevated temperature. So far, the conventional methods, namely, precipitation [47], electrocoagulation [48], alkaline fusion [49], chemical vapor deposition [50], sol-gel [3, 51], fluidized bed technology [52], and hydrothermal methods [3] are employed traditionally for the production of silica gel. However, high-temperature calcination that reaches up to 1710°C is found to be one of the major drawbacks for silica gel production in the traditional existing methods [3, 49]. High-temperature reaction leads to energy-intensive process that has an adverse effect on developing an economically sustainable process for silica gel production and its marketing as well [10]. The conventional methods of producing silica gel limit its use in situations where product purity is not compromised because they contain contaminants such as heavy metals [6]. In addition, large-scale production of crystalline silica nanoparticles may release toxic matters into the working environment that may create unsafe working condition which causes occupational diseases, such as lung cancer and pulmonary tuberculosis [53].

Silica gel can be produced from renewable sources of selected biomass such as palm tree [1], wheat straw [10], maize leaves [8], teff straw [7], sugarcane bagasse [11], rice husk and rice straw [5, 9], sugarcane leaf [12], oat husk [54], bamboo leaf [13], and corn cob [14]. At present, agricultural residues receive significant attention as feedstock to produce silica gel due to sustainability, economic and environmental concern. However, developing a process for silica gel production with low energy and cost requirements using agricultural biomass material is still challenging [5, 7]. So far, different approaches for preparing silica gel from agricultural residues have been carried out, such as hydrothermal technique, chemical vapor deposition, combustion synthesis, sol-gel processing [7, 55, 56], and precipitation methods [39]. Upon the potential importance of silica and silica gel, this comprehensive review has been narrated to provide the different techniques used for the synthesis and characterization of biobased silica and its current and prognostic applications.

2. Biosilica

Silicon compounds are transferred from the roots to the shoots and deposited as the amorphous material SiO_2. Silica accumulations in the shoots of many plant species range from 0.1 to 10% [57]. Phytoliths are an accumulation of silicon in plants (amorphous hydrated silica) [58]. Usually, the concentration of stationary silicon compound is higher in older plant tissues, and the rate of build-up varies depending on the tissue. According to silicon accumulators makeup 7 out of 10 largely harvested crops. When compared with other natural systems, some crops have high silicon accumulation such as rice, sugarcane, and wheat that have ability to transfer more silicon from the soil. Therefore, plants, particularly crop wastes accumulate a lot of silicon, which might be thought of as an excellent source of biosilica [59]. Silica, produced from plant origins [60] has been identified to have better advantages compared to the silica obtained from synthetic or mineral sources. Such biobased silica can be synthesized using processes with less energy consumption, relatively simple, and environmentally friendly that do not require sophisticated infrastructure and costly reagents. The biobased silica powder obtained from plant sources comprises a slight amount of metal oxides which are considered impurities. However, the high purity silica at an affordable cost is an obligatory requirement. It has been clear that most waste by-products found from biomass residues create environmental concerns [5] such as attraction of pest and odor generation that might cause adverse effects on human health [61].

The studies conducted elsewhere revealed that the silica deposition in agricultural residues is significantly influenced by the availability and quantity of silicon present in the soil. The plant root system absorbs silicic acid from the soil and deposits it in the plant in the form of amorphous silica. Through the biological nature of the transpiration, silica deposition in the plant increase in all parts of the plants. Research outputs indicated that more water absorption could improve more silica deposition in the various plant components [20, 62, 63]. Currie and Perry [64] have reported that different plants were identified as significant contents of silica, such as wheat, rice, bamboo, sunflower, sorghum, and corn. Usually, silica has been deposited at leaves, stems, and other plants parts ranging from 0.1 to 10 w/w%. According to Currie and Perry [64] and Norsuraya et al. [61], present of silica content in agricultural residue can be varied with respect to species, season, plant maturity, and geographical location of the farm.

Table 1 presents the availability of silica composition in different agricultural residues reported by different investigators. From these observations, the presence of silica in various agriculture residues that vary from 46 to 95.5%; however, the composition depends on the type of biomass sources.

2.1. Biomass Source

2.1.1. Rice Husk and Straw. Rice husk has been investigated for its potential as an energy source as well as a source of silica [65]. Gu et al. [66] investigated in their research that rice husk ash is primarily made up of silica, which can be used in wastewater treatment and other industrial uses. Silica particle extraction from rice straw ash is a green approach that protects human health and the environment. The widely used process for producing silica in industries involves fusing sodium carbonate and quartz at high temperatures that range from 1700 to 2000°C for sodium silicate production, which is then precipitated with sulphuric acid to recover silica. Ma et al. [67] reported that 0.23 tons of carbon dioxide are released to the environment for every ton of silica produced, escalating the greenhouse impact. According to Carmona et al. [68] that rice husk contains around 20% minerals as well as organic compounds including cellulose, hemicellulose, and lignin, where silica makes up 94% of minerals, with the remaining 6% made up of aluminium oxide, potassium oxide, magnesium oxide, calcium oxide, and phosphorus oxide. The soil's composition varies from location to location depending on the kind of soil, fertilizers applied, and weather conditions [3]. Ramadhansyah et al. [69] observed that 93% of silica was gained from rice husk material. Moreover, from rice hulls contain 8.7–12.1% of silica content [70]. Trubetskaya et al. [71] report that the dry matter of rice husks contains a larger fraction of silica with 9.8%.

In yet another study, extracting high amount of silica using acid treatment method can be used to remove the presence of trace quantities of cations to increase the SiO_2 yield from the rice husk [70]. In such processes, the husk is subjected to calcination process followed by sodium hydroxide treatment in the preparation of sodium silicate. In order to control the size of nanoparticles, the aging time and temperature need to be adjusted during the reaction [72].

Rice straw differs from other cereal straws since it has high silica concentration and less lignin [73] and is referred to as a stem of plants [2]. In general, the stem is separated after harvesting rice grains and considered as by-product or biomass waste. It is found to be rich in silica. Different studies indicated that the silica content in the rice straw is comparatively higher than in other parts of the plants. Studies revealed that the composition of the rice straw ash content (13–20%), the percentages of cellulose (32–47%), hemicellulose (19–27%), lignin (5–24%), and other components (13–20%). Other ingredients in rice straw include silica, which makes up (60–80%) of the total weight. Owing to the silica content present in the ash obtained from rice straw, it can be considered a promising raw material for silica synthesis [2, 9]. Khaleghian et al. [74] reported that the content of rice straw ash has 10–17%; from this, around 75% is the silica content. The chemical makeup of rice husk and straw has been reported by different investigators are summarized in Table 2.

Studies revealed that the rice husk from India and Cambodia have almost the same composition in the SiO_2 content (80% and 80.18%, respectively) [76, 77]. Besides, the rice husk from China had 94.79% of SiO_2 content [75]. In this line, the rice husk obtained from Bangladesh [79], Brazil, Canada, and Malaysia also have better silica content, such as 89.86%, 92.9%, 97%, and 93.1%, respectively [59]. It is apparent that based on its geographical nature, SiO_2 content in the rice husk is found to be low in Cambodian and Indian-based rice husk.

After rice husk, one of another important origins for silica are rice straws. Accordingly, rice straw from Indonesia (84.60%) [9] and Italy (83.20%) [77] were observed to similar in their silica composition. While comparing to the SiO_2 content of rice straw from the China (73.26%) [75], Egypt (57.90%) [78], and Vietnam (50.68%) [77], the yield of SiO_2 for Indonesian's and Italian's rice straw were found to be high. Yet another climatic factors, such as humidity level, air quality, sun light exposure, use of fertilizers, soil nature, and farming conditions, can also be decided the amount of silica present in the agriculture residues [78]. However, the husk obtained from the rice plant, contains 1.6 times more silica than the rice straw because of the plant's accumulation mechanism as aforementioned. Schneider et al. support this result and they observed that the rice husk has 1.8 times more silica content than rice straw [77] because of the biomass features where they are geographically located, even the other components contents also found to be varied.

2.1.2. Sorghum Bagasse. The grasses of sorghum can store silica in the form of silicic acid that can be precipitated as amorphous silica, commonly, known as phytoliths [81]. They absorb silicic acid from the soil and deposit as solid silica in their leaves. This mineral, which makes up 1–10% of the dry weight of grass mass, increases the resistance of plant to various stressors. However, even such a mineralization process is still poorly understood that needs to be investigated in detail about the mechanism for increasing stress tolerance [82]. Bioresidues from the red grain sorghum husk comprise both organic and inorganic materials, such as cellulose, hemicellulose, lignin, Na, Ca, Mg, Fe, K, Mn, Al, and SiO_2 [83]. With reacting low concentration hydrochloric acid to the sorghum husk particles at pressurized temperature followed by calcination, silica phytoliths could be extracted [84]. According to Periasamy et al. [85], significant amount of pure silica (95%) and negligible amount of magnesium were found in this biomass [85]. Sweet sorghum (*Sorghum bicolor* (L.) moench) is one of the common crops Africa sub-Saharan. It is a subsistence crop that can grow at different climatic environments. It is primarily utilized for the preparation of bioethanol [6], food, fuel, fiber, and brewing. The sweet sorghum bagasse is left as a solid residue that remains after collection of its grains. Its

Table 1: Percentage of silica in ash produced by different biomass sources.

Feedstock	Silica content (%)	Different methods	Calcination temperature (°C)	Type of materials	Structural properties	Reference
Rice husk	97.44	Sol gel	850@3 hr	Silica gel	Amorphous	[5]
Sorghum bagasse	96.36	Sol gel	600@3 hr	Silica gel	Amorphous	[6]
Teff straw	91.80	Hydrothermal	900@2 hr	Silica	Crystalline	[7]
Maize leaves	93.00	Leaching	500@4.5 hr	Silica gel	Amorphous	[8]
Rice straw	84.60	Extraction	500@2 hr	Silica	Crystalline	[9]
Wheat straw	83.00	Sol- gel	550@4 hr	Silica gel	Amorphous	[10]
Sugarcane bagasse	81.60	Sol gel	550@1 hr	Silica gel	Amorphous	[11]
Sugarcane leaf	80.14	Sol gel	600@1 hr	Silica gel	Amorphous	[12]
Bamboo leaf	75.90	Extraction	950@1 hr	Silica gel	Amorphous	[13]
Corn cob	52.32	Sol gel	650@3 hr	Silica gel	Amorphous	[14]
Palm	46%	Leaching	800@0.5 hr	Silica gel	Amorphous	[1]

bagasse has been mostly used to prepare the reinforcing composites woods, silage feed, and pulp manufacturing for paper. Studies on the composition analysis of sweet sorghum bagasse reveal that the contents vary with respect to its genotype, environment, and plant maturity [86]. Sorghum plant has eight different types, and all types show a significant variance in the amounts of ash, silica, iron, and calcium. In all the types, silica is found to be in the range from 8.10 to 10.78% in the ash obtained from its roots. The amount of ash in the sheath and leaves varied similarly. The roots' silica concentration ranged from 4.37 to 5.72% [87].

2.1.3. Teff Straw. Teff grain is a specific source of traditional food in Ethiopia. The chemical analysis on teff straw, which is grown on different parts of Ethiopia has been demonstrated with different compositions of silica. However, the chemical composition of teff obtained from various agro-ecologies was observed to be similar [88]. Commercially, Teff straw is worthless in Ethiopia except for traditionally used for animals feed and mud house construction as a binder. In some provinces, it has been under taken to open air burning to discharge the nutrients as manure for further cultivation. Nevertheless, this approach could cause air pollution on the surrounding [7]. More than two million tons of teff straw are thrown out with the trash each year. These are plenty enough for the production of silica material. Recently, different studies were documented on the teff straw utilization for the purpose of producing biogas, biomethane [89], and removing toxic heavy metal such as Cr (VI) from aqueous solutions [90]. According to [7], thermal method had been used to obtain 91.82% of pure biosilica from the teff straw.

2.1.4. Wheat Straw and Husk. Wheat is one of the most widely grown crops, covering more than 20% of the global agricultural product [91]. Wheat grain has better protein. It contains unique physical and chemical properties. It is consumed by major populations in the world because of its better protein content as compared to cereal crops, rice, and maize. It has very good source of carbohydrates and minerals such as phosphorous, potassium, calcium, magnesium, iron, boron, and zinc [92]. Wheat husk is a biomass residue remained after harvesting and mostly used for the production of energy. Therefore, generating energy from wheat husk has great potential especially in the wheat producing countries. Wheat straw contains considerable amount of silica of about 9% that found in the form of hydrated which can be recovered as amorphous silica under a programmable burning condition [93].

In recent times, it is used as substrate for ethanol production in second generation process [94]. Waste biomass of the wheat straw is a promising renewable energy source in the forms of liquid, solid, and gas fuel. Additionally, when an agricultural by-product of wheat straw is burned, a significant content of SiO_2 can be obtained [95]. Besides, under a controlled burning condition, from the wheat straw can produced 10% ash, and from this ash can extract more than 70% of silica [96].

2.1.5. Bagasse and Leaves of Sugarcane. Sugar and ethanol are the most extensive commercial product prepared from sugarcane. A substantial amount of agricultural waste, such as straw and bagasse, are produced during the sugar-making process [11, 70]. Each ton of sugarcane is said to yield 200 kilograms of tips and straw and between 250 and 270 kg of bagasse, while processing the waste. The biomass created in the sugar manufacturing sector results in ash, which is either used as fertilizer or is just dumped in landfills. Therefore, the use of landfills causes some environmental and public health issues. Recently, construction industry led to employ the sugarcane waste ash instead of cement or sand. The sugarcane ash contains a substantial amount of silica. It could be a by-product with significant added value for different industries, such as tooth pastes and the rubber industry as strengthening agents [11].

The chemical makeup of different biomasses is shown in Table 3. According to these data, Wassie and Srivastava [99]; have reported that teff straw ash has a 52.23% silica [99]. However, Amibo et al. [98] observed the concentration of silica was observed to be 92.89% [98]. Ash from wheat husk comprised with 92.30% of silica [59]. From the studies documented by Alves et al., sugarcane bagasse has 72.74–81.60% of silica [11, 27]; besides, sugarcane leaf and wheat straw have showed, 80.14% and 73–73.15%, respectively. The level of the other inorganic by-products composition was found to be low.

Table 2: Composition of rice husk and rice straw ash by geographical location.

Chemical components	Composition in percent												
	References												
	[75]		[9]	[76]		[77]		[78]	[79]	[59]			[76]
	China		Indonesia	India	Cambodia	Italy	Vietnam	Egypt	Bangladesh	Brazil	Canada	Malaysia	India
	Rice straw	Rice husk	Rice straw	Rice husk	Rice husk	Rice straw	Rice straw	Rice straw	Rice husk				Rice husk
Silicon dioxide (SiO_2)	73.26	94.79	84.60	80	80.18	83.20	50.68	57.90	89.86	92.9	97	93.1	22.12
Aluminium oxide (Al_2O_3)	0.25	0.36	—	3.93	0.83	0.33	0.14	1.00	0.73	0.18	0.4	0.21	1.23
Ferric oxide (Fe_2O_3)	0.49	0.86	0.16	0.41	4.29	3.57	0.43	1.00	1.28	0.43	0.4	0.21	1.28
Calcium oxide	4.46	0.75	0.88	3.84	1.55	1.60	6.14	2.30	0.91	1.03	0.49	0.41	1.24
Magnesium oxide (MgO)	2.14	1.86	0.44	0.25	0.81	1.00	2.32	3.40	1.16	0.35	0.50	1.59	0.21
Sodium oxide (Na_2O)	0.93	0.39	—	0.67	—	—	—	—	—	0.02	1.12	—	—
Potassium oxide (K_2O)	13.46	1.86	6.39	1.45	3.89	2.73	21.11	14.60	—	0.72	3.0	2.31	—
Manganese oxide (MnO_2)	0.04	0.02	—	—	—	—	—	—	—	—	—	—	0.074
Phosphorus oxide (P_2O_5)	1.94	0.23	—	3.80	3.80	4.12	0.77	13.80	—	—	—	—	—
Sulfur trioxide (SO_3)	2.41	0.09	—	0.78	2.05	1.52	2.14	3.20	—	0.10	0.24	—	—
Titanium oxide (TiO_2)	0.05	0.02	—	—	—	—	—	—	—	—	—	—	—
Chlorine (Cl_2)	0.57	0.08	—	—	—	—	—	2.30	—	—	—	—	—
Other components	—	—	7.53	2.60	2.60	1.92	—	0.50	—	—	—	—	—
Loss on ignition [80]	—	—	—	8.56	—	—	—	—	4.26	—	—	—	73.87

Table 3: Composition of teff straw, wheat husk and straw, sugarcane bagasse, and leaf ash based on its geographical location.

Chemical components	Composition in percent								
	References								
	[97]	[98]	[99]	[59]		[100]	[59]	[11]	[12]
	Ethiopia			Bangladesh	Turkey	Pakistan	Bangladesh	Brazil	India
	Teff straw ash			Wheat straw	Wheat husk	Wheat straw	Sugarcane bagasse	Sugarcane bagasse	Sugarcane leaf ash
Silicon dioxide (SiO_2)	91.81	92.89	52.23	73	92.30	73.15	72.74	81.60	80.14
Aluminium oxide (Al_2O_3)	0.42	<0.01	1.55	3.90	—	—	5.26	7.94	0.89
Ferric oxide (Fe_2O_3)	0.71	0.23	9.74	1.75	0.647	1.67	3.92	2.31	0.51
Calcium oxide (Zhang et al.)	3.43	1.67	17.66	8.12	4.17	5.78	7.99	0.98	6.06
Magnesium oxide (MgO)	0.81	0.82	1.97	2.80	—	1.78	2.78	1.26	5.02
Sodium oxide (Na_2O)	0.74	<0.01		—	—	—	0.84	0.26	0.28
Potassium oxide (K_2O)	0.29	0.19	3.92	—	2.60	3.87	3.47	2.10	3.09
Manganese oxide (MnO_2)	—	<0.01	2.39	—	0.12	—	—	0.06	0.17
Phosphorus oxide (P_2O_5)	0.95	0.29	3.92	—	—	—	—	1.07	—
Sulphur trioxide (SO_3)	0.63	—	4.11	—	—	—	—	0.52	2.25
Titanium oxide (TiO_2)	—	<0.01	0.69	—	0.074	0.96	—	0.67	0.046
Chromium oxide (Cr_2O_3)	—	—	0.82	—	—	—	—	—	0.0067
Coper oxide (CuO)	—	—	—	—	0.052	—	—	—	—
Water (H_2O)	—	1.34	—	—	—	—	—	—	—
Chlorine (Cl)			0.38			—		0.36	0.69
Other components	0.21	—	—	—	—	—	—	—	—
Loss on ignition [80]	—	2.45	—	—	0.037	2.38	—	0.79	—

2.1.6. Corn Cob. Corn or maize is one of the well-known crops, which is frequently utilized as food in the world [3]. The waste material from the corn is corn cob husks. In corn cobs, silica considers the main inorganic component [101, 102]. It is obtained in huge amount from the production of corn processing as a waste. Normally, the by-products, corn cob, are stored and burned in an open area. Corn cobs contain notable amount of amorphous silica [56, 103], which could be converted into silica after burning in air and followed extraction using alkaline or acid solutions [103]. According to [3], the ash generated from corn cob comprises around 60% of silica. They have used a well-grounded powder to produce silica, silica nanoparticles, and silicates [3]. On other hand, the silica in corn plants is found to be accumulated in other parts of plants such as fruits, leaves, stems, seeds, and roots [39].

2.1.7. Bamboo. Bamboo is very famous biomass made by lignocellulosic material. Using bamboo, different value-added goods are attained. It is known to be nonwoody plant commonly produced by primary shoot. It has various uses, starting from different domestic products up to industrial utilization, such as nutrition, paper, pulp (textile, toys, medicine sector, and aircrafts [104]), and building materials [70]. However, the leaves obtained from the bamboo plants are often considered as waste materials that receives comparatively less attention. Nevertheless, it has some significance in terms of presence of silica compounds, which can be extracted and utilized [13]. Studies report that the silica content of ash obtained from the bamboo leaf after washed using acid was found to be significant [70]. Hence, bamboo has similar chemical composition that of wood, however, in terms of minor components, bamboo is known to be higher content compared to wood [104].

Chemical composition analysis reveals that constituents of bamboo fiber primarily consist of hemicelluloses, cellulose, and lignin. This contributes around 90% of total biomass of the bamboo. It is also found that the presence of the minor components such as tannins, fat, protein, pigments, pectin, resins, inorganic salts, ash, and waxes in the bamboo biomass. These ingredients are the key responsible for the physiological activity of bamboo. Generally, they are found in cavity of cells or special organelles [70].

2.1.8. Palm Mill Fly Ash. Palm oil is very famous which is produced from palm (*Elaeis guineensis*) [105]. In the view of silica-containing agrowastes, fly ash obtained from palm oil mill can be a potential resource [54]. Around four million tons of wastes are produced from palm oil mill per year in Malaysia, which is the largest world producer. In the palm oil processing, mills are utilized only 10% of the palm fruit bunches, whereas the remaining 90% are simply discarded [106]. During the combustion of residues, palm-oil-fuel-ash is found to be a by-product from processing of palm oil [107]. The solid waste consists of 15% shell and 85% fiber that are utilized as boiler fuel whereas the 5% fuel might be leftward as unburned material that generates ash. Alkaline extraction and sol-gel precipitation using sulphuric acid have been extensively used to produce silica that can be precipitated from palm oil ash. However, the process with the use of sulphuric acid requires a large volume of chemicals which makes the processing cost expensive. Recently, by another way, CO_2 is employed to reduce the amount of chemicals needed for this process. In addition, this method can destabilize the silica extract easily for the recovery of sodium hydroxide [54].

Table 4 demonstrates the biomass chemical composition. Where bamboo leaf ash contains silica with a range from 75.90 to 82.86% [109, 111], followed by ash from corn cob from 27.80 to 66.38% [59, 108, 111], and palm ash 40.60–63.60% [1, 59, 110]. The other by-products from the inorganic composition were at a lower level compared with the major components.

Ashes from bamboo leaves, maize cobs, and palm leaves were analyzed, and it was discovered that they included oxides of aluminum, sodium, calcium, potassium, iron, zinc, magnesium, titanium, phosphorus, sulphur, and chlorine.

3. Synthesis of Biobased Silica from Biomass Resources

3.1. Preparation of Biosilica from Selected Biomasses. Silica is extracted from different biomass sources using different extraction methods. Silica is extracted from the rice husk by two methods, extraction with alkaline solution, and sol-gel technique [5]. These methods are found to be economically feasible for the silica production [4]. According to [10], wheat straw is treated with hydrochloric acid in microwave digester. After removing the excess acid, it was calcinated at 550°C. Then, the fine white powder was obtained. Teff straw is also one of the most important silicas bioresources, while silica is synthesized from teff straw using hydrothermal method by refluxing with HCl at 80°C for 1 h. The prepared silica can be subjected to characterize using different techniques to understand the physical and chemical properties [7, 11]. Recently, the use of corn cob for the biosilica production is significantly concerned by most of the studies. Initially, corn cob is subjected to grind to obtain fine powder using size reduction techniques. In another way, silica is obtained from the ash of corn cob using the acid precipitation method [3]. In elsewhere, maize leaves are used for silica production using leaching method [8]. Sugarcane bagasse and leaves are another bioresource for biosilica [3, 70]. Palm tree ash also has been investigated for silica production by treating with acids. For this, appropriate concentration of sulphuric acid, hydrochloric acid, and nitric acid solution were widely used for silica extraction [1].

During acid extraction, the biomass residue was washed and dried after that the size of the residue treated by HCl solution. Then it was dried in over with temperature of 60°C for 24 h. Followed by subjected to burn in a furnace for 6 h at 800°C.

3.2. Preparation of Biosilica Nanoparticles from Selected Biomasses. A beaker was contained 5, 10, and 15% of NaOH solution and combined with rice husk ash. The mixture was

Table 4: Composition of corn cob, bamboo leaf, and palm ash by geographical location.

Chemical components	Composition in percent							
	Reference							
	[59] Bangladesh	[14] Nigeria Corn cob	[108] Indonesia	[109] India Bamboo leaf	[13] Indonesia Bamboo leaf	[59] Bangladesh Palm ash	[1] Malaysia Palm ash	[110] Malaysia Palm ash
Silicon dioxide (SiO_2)	66.38	47.78	27.80	82.86	75.90	63.6	45.50	40.60
Aluminium oxide (Al_2O_3)	7.48	9.40	5.70	1.14	4.13	1.6	5.40	3.71
Ferric oxide (Fe_2O_3)	4.44	8.31	4.69	0.32	1.22	1.4	3.26	15.74
Calcium oxide (Zhang et al.)	11.57	16.70	14.03	2.57	7.47	7.6	12.80	19.60
Magnesium oxide (MgO)	2.06	7.80	9.50	1.35	1.85	3.9	3.20	1.30
Sodium oxide (Na_2O)	0.41	1.89	—	0.18	0.21	0.1	—	—
Potassium oxide (K_2O)	4.92	5.42	18.49	3.27	5.62	6.9	23.30	13.80
Manganese oxide (Mn_2O_3)	—	2.70	—	—	—	—	—	0.28
Phosphorus oxide (P_2O_5)	—	—	—	—	—	—	5.38	2.73
Sulphur trioxide (SO_3)	—	—	—	—	1.06	—	—	0.44
Titanium oxide (TiO_2)	—	—	—	—	0.20	—	—	0.35
Other components	—	—	—	—	—	—	1.16	—

agitated for three hours. The residue is washed with distilled water after filtering the final mixture. The filtrate from this extraction is sodium silicate solution. The sodium silicate solution's starting pH was calculated. When a gel forms or condensation with an acid solution occurs, add HCl, and stir until pH 7 is reached. To describe the gel, it was filtered, rinsed with distilled water, and dried for three hours at 100°C [112]. In other investigations, wheat straw samples were burned off using a muffle furnace at 500°C for 8 hours before being subjected to reflux boiling in a 10 percent (v/v) aqueous solution of HNO_3. The samples were then completely cleaned with distilled water before being burned of 400, 500, 600, and 700°C, respectively. For this process porous silica nanoparticle was prepared [113].

3.3. Methods of Preparation. Silica is prepared from different biomass resources [2] using various methods such as hydrothermal technique, combustion synthesis, chemical vapor deposition, microbial hydrolysis processing [7], sol-gel processing [10, 11], and chemical vapor deposition [114].

3.3.1. Sol-Gel Method. Sol-gel is a process by which a transformation occurs in colloidal suspension of sol into gel through 3D interconnecting network. This process yields homogeneous and pure sol-gel. Sol-gel method can be further processed to get different forms of desired materials such as films, fibers, and powders in submicron forms [3]. In this method, suspension of concentrated hydroxide or metallic oxide (sol) is involved. The sol is dehydrated through evaporation which results in a semirigid mass, colloquially, and gel. In a controlled heating, the gelated material can produce pure and mixed oxides. The properties of a particular sol-gel network are related to different parameters, such as temperature, pH, reagent concentration, time of reaction, concentration of added catalyst, drying, and aging temperature. These factors are significantly affecting the condensation reactions and rate of hydrolysis [114]. The reaction is controlled by the reactants of alcohol, acid/base, and water. The particle size can be adjusted by precursor concentration, pH, and reaction temperature [3]. In general, the sol-gel technique requires important steps in order to obtain final metal oxides which comprise condensation, hydrolysis, and rate of drying. Accordingly, the metal precursor is taken to rapid hydrolysis reaction to produce solution of metal hydroxide. In the process, a condensation process leads to result in a 3D gel. By the end of the process, the gel product is dried, and converted to a xerogel [115].

Sol - gel method is the most extensive method and applied to prepare silica gel. Table 1 summarizes amorphous silica and the yield of silica gel from various biomass. To eliminate the volatile material from the sample, rice husk ash was calcined at 700°C for five hours. To create sodium silicate solution, rice husk ash that had undergone thermal calcination was extensively combined with alkali solution. Through the neutralization of a sodium silicate solution, silica can be produced. According to Ananthi et al. [18], the rice husks can be steeped in nitric acid and precipitated silica to achieve the maximum amount of sodium silicate solution [18].

According to [61], the silica gel content was leached out from the aqueous phase in the form of soluble sodium silicate according to

$$SiO_2\,(\text{Ash}) + 2NaOH \xrightarrow{\text{yields}} Na_2SiO_3 + H_2O \tag{1}$$

Then, silica gel was started to precipitate when the pH decreased to <10. The precipitation of silica gel has been carried out according to

$$Na_2SiO_3 + 2HCl \xrightarrow{\text{yields}} SiO_2 + 2NaCl + H_2O \tag{2}$$

The solution (sol) was aged in mother solution at room temperature for 20 hr and called silica gel [4].

Sol-gel method is able to produce thin and thick coating. It has the capacity of sintering at low temperatures (200–600°C). Sol-gel method is efficient with economic feasibility that can produce better-quality product. However, this method has some drawbacks, such as the product

resulted with residual hydroxyl and/or carbon groups. It needs long processing time. The use of organic solutions may result in handling of toxic [116]. The process flow for creating silica gel from agricultural waste is shown in Figure 1.

3.3.2. Hydrothermal Method. Hydrothermal process is a proven method for synthesis of nanomaterials. It is principally a solution reaction-based approach [117, 118]. This method generally carried out at elevated temperature and high pressure for crystal growth or crystal synthesis since the substances is insoluble in normal temperature of less than 100°C and pressure of less than one atmosphere. The elevated temperature of 250–300°C can produce the maximum ionic product. In most of the time, hydrothermal synthesis is carried out below the temperature of 300°C. However, the temperature about 374°C, and pressure, 22.1 MPa are found to be the critical condition. Studies showed that under supercritical condition, the dielectric constant, and solubility of compounds solvent properties can be changed dramatically.

Because water has a dielectric constant of 78 at ambient temperature, polar inorganic salts can be dissolved in it. The dielectric constant exhibits a decreasing trend while temperatures rise and an increasing trend while pressure falls. As a result, due to the enrichment of the reaction rate, and massive supersaturation produced by the theory of nucleation, supercritical water offers a potential reaction field for particle development, and lowering its solubility [119]. The hydrothermal process can produce crystalline segments that are unstable at their melting point. This process is suitable for growing crystals of excellent quality while maintaining good control over their alignment. Basically, the process via which metallic oxide units develops the process of creating metallic salt solutions, including hydrated metallic ions [119]. The hydrothermal process can produce crystalline segments that are unstable at their melting point. This process is suitable for growing crystals of excellent quality while maintaining good control over their alignment. Basically, there is the process via which metallic oxide units develops. It is used to create metallic salt solutions using hydrated metallic ions that hydrolyze to metal hydroxides and then continue to precipitate to metal oxides after dehydration. Hydrolysis is an electrostatic interaction between metallic ions and hydroxyl ions.

Hydrolysis method is proven to be more effective for determining the precise physical characteristics of novel compounds and multicomponent physicochemical systems under high pressure and temperature [114]. After acid refluxing, biomass material samples can be used to make biosilica components by hydrothermally decomposing the organic constituents in an electric muffle furnace. 50 grams of teff straw were placed in an electric muffle furnace and burned for two hours at different temperatures (500, 700, and 900°C) to produce ash. This experiment was conducted by Bageru and Srivastava. They noticed that the teff straw ash products include substantial amounts of biosilica components [7]. The availability of agricultural waste products that can be converted into silica material is shown in Figure 2. The yield of silica from various biomass is shown in Table 1 with the majority of this method's crystalline silica being created for further use.

3.3.3. Chemical Vapor Deposition Methods. Commercial nanoparticle material synthesis frequently uses chemical vapor deposition (CVD). For a technique of components exposed to one or more volatile pioneers, CVD is employed. The pioneers breakdown or react on the surface of the substrate to produce a tinny film or nonvolatile firm sum. The majority of its applications involve coating faces with thin films. CVD is also utilized to produce highly pure nanocomponents, powders, and to build resource combinations using penetration methods [3].

The chemistry is ludicrous and many different kinds of chemical reactions are intertwined due to the multipurpose environment of CVD [120]. Single-walled carbon nanotubes (SWNTs) are produced generally at lower temperatures of 600–900°C; however, higher temperatures of 900–1200°C reaction encourage the formation of SWNTs. On occasion, depending on the type of ingredients, carbon nanofibers and nanobeads are also produced. A recent study discovered that utilizing a superior nitrogen-pretreatment of the Fe-Mo/MgO reagent, thermal CVD could make SWNTs with substantially graphitized structure. Since it was concluded in the complete comment that nitrogen-pretreatment enhances catalytic activity and supports the development mechanism to manufacture elongated SWNTs, it is similarly formed, extremely graphitized SWNTs of enlarged size [114].

The method that has been used commercially to remove silica fine particles is one specific benefit of CVD [121]. However, the drawbacks of CVD include peculiar equipment and potentially hazardous gaseous unsatisfactory yields [3]. Another difficulty in the CVD manufacturing process is controlling the stage structure, particle diameter, and shape [114, 121]. Due to the gaseous undesirable products' high level of poisonousness, CVD requires specialized equipment.

This method of preparation involves depositing a thin layer of gaseous reactants on the substrate. By combining the gas molecules in a reaction chamber at room temperature, deposition is produced. A chemical reaction occurs when a heated substrate comes into contact with a gas mixture, and a thin film is produced on the surface. This thin layer can be kept and applied in numerous ways. The primary deciding factor in this method is the temperature of the substrate. This process produces evenly sized, exceptionally pure, and mechanically stable nanoparticles. Two drawbacks of CVD are the requirement for specialized equipment and the severe toxicity of the gaseous by-products [122].

3.3.4. Coprecipitation Method. Complications may be situated where this type of method is infrequently agrees to attain worthy macroscopic homogeneousness [123]. Its production includes suspension of compounds of precursor salt in media of aqueous followed by pH arrangement the precipitate in the solution [114]. For metallic compounds of two or more alignment the solubility of the constituents

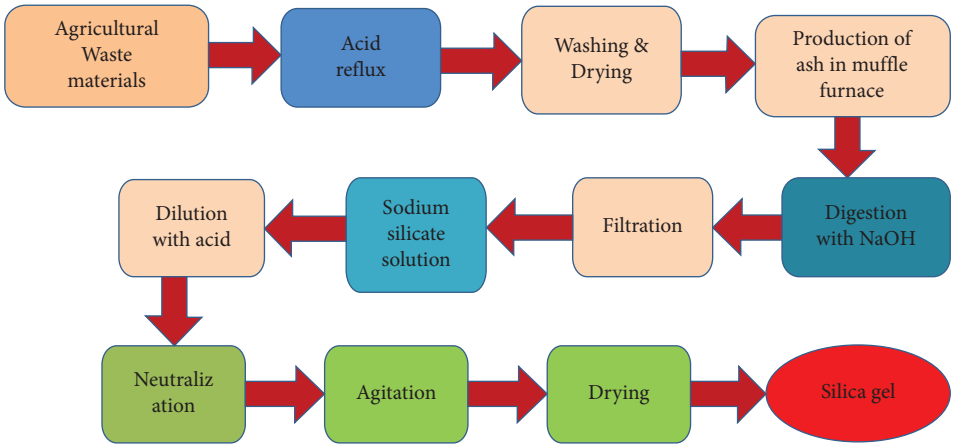

Figure 1: The process flow diagram for making silica gel from agricultural waste.

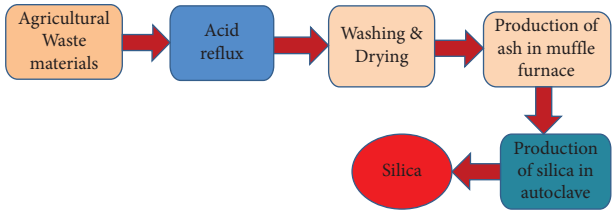

Figure 2: Schematic illustration of provision of agricultural waste materials converts into silica material.

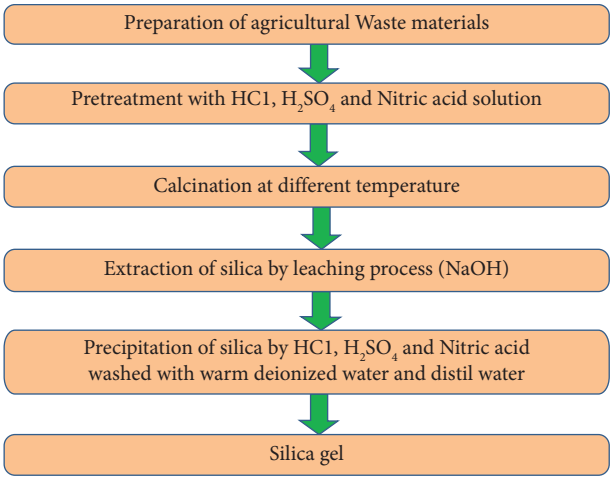

Figure 3: Schematic illustration of the silica gel extraction process.

differs depending on the precipitate which occurred during precipitation. Normally, for a condition of poor mixing or a slow precipitate in the reaction intermediate, the precipitate which shows a heterogenous and coprecipitation method is preferable one compared with other techniques [123]. For preparation of metallic oxide powders and ceramics material this method is preferred. Coprecipitation techniques preferred not only as a simple method but also easy for mixing of metallic ingredients which produces with a low temperature treatment with perfect stoichiometry [114]. To prepare molecular sieve for converting amorphous to crystalline constituents with better thermal stability, using hydrothermal treatments is preferred [123] rather than this method. Silica gel acquired from different biomass materials are presented in Table 1. Figure 3 presents a schematic illustration for silica gel extraction process.

3.3.5. Leaching Method. Leaching is nothing but eliminating constituent from solid through liquid withdrawal media. In this method, the natural solid form the preferred constituent spreads into the solvent. Three imperative parameters are found to be most important in leaching process that are solvent selection, interaction time, and temperature. Temperature must be attained to optimize production of bulk transfer and solubility. It can be distributed into two classes, namely, dispersed solid, and percolation. However, solids are contacted with the selected solvent in the classes of percolation and broadly used for exciting the solid quantity. Whereas, for dispersed classes usually the solid becomes grounded into small before adding into the selected solvent. Additionally, liquid is added into the quantity of solid and vice versa for the case of dispersed classes. To prepare metallic oxides of silica, nitric, hydrochloric, and sulphuric acids are widely applied [1, 8].

Temperature of 90°C is better than 80°C for leaching performance of silica from rice husk ash which increased from 92.40% to 99.30%. Similarly based on this performance the Fe_2O_3 decreased from 2.26 to 0.43% at 90°C. With the elevated temperature, the acid molecules gotten an additional kinetic energy, because of this the molecular movement greatly increment, which results the rate of chelating increased. In addition to this, the smaller the particle size of the rice husk which gain larger surface area exposed and making easier mass and heat transfer to the prepared husk powder thus contributing in increasing leaching rate [124]. Temperature and particle size are the main determinant factor to enhance leaching process effect.

Sol-gel, chemical vapor deposition, hydrothermal, and leaching are a few of the various reported approaches that have been summarized. Comparing the sol-gel approach traditional methods, there are a number of benefits. Sol-gel techniques sometimes include trade-offs for better control of

surface area, pore volume, and size dispersion. Additionally, it is superior to other conventional methods for generating high-quality materials that are homogeneous and pure at low temperatures.

4. Characterization

Synthesized biobased silica material derived from the selected biomass resource is characterized using different techniques. The major characterization techniques include Brunauer–Emmett–Teller (BET), transmission electron microscopes (Rodella et al.), X-ray fluorescence, X-ray diffraction (XRD) method, thermo gravimetric analysis, differential thermal analysis, Fourier transforms infrared spectroscopy, Raman spectroscopy, and scanning electron microscopes [125].

4.1. Brunauer–Emmett–Teller (BET). Adsorption is the process by which gas molecules or atoms attach to a surface. The exposed surface area, temperature, gas pressure, and the degree of gas-solid interaction all have an impact on how much gas is adsorbed. Because it is readily available in high purity and interacts strongly with the majority of materials, nitrogen is often used in BET surface area analysis [126]. In the BET method, where P is the system pressure and P_0 is the initial pressure, the specific surface area can be evaluated in the relative pressure range (P/P_0) of 0.05 to 0.25. The silica nanoparticles' pore volume was calculated using a pore size analyser using the nitrogen adsorption isotherm at a relative pressure P/P_0 of 0.3 measurements of the porous size distribution [66]. The nitrogen adsorption isotherm of rice husk ash at 77K is with a plateau near the relative pressure ($P/P0$) of 1.0 was not reached by the adsorbed volume of nitrogen on rice husk ash [127].

In studies elsewhere, Prempeh et al. [128] determined the surface area using the BET equation for pressures between 0.05 and 0.3 (P/P_0) is fitted on the data of adsorption in BET analysis the adsorptive gas of nitrogen at 77K for this the molecular cross section of it works with standards value of 0.162 nm^2. At 0.98 the relative pressure of total volume was determined. Using an indirect molecular adsorption technique, characteristics of the pore size can be determined.

Particle size reduction often supports adsorption, a surface phenomenon. Smaller biomass particles are said to have a higher ability for adsorption than bigger ones. Since adsorption capacity and BET surface area are directly inversely related, larger particles with more BET surface area should result in better removal rates [136]. The surface area, pore volume, and pore size of various types of silica gel, silica, and biomass ash are shown in Table 5. The generated ash from bamboo leaves had a maximum specific surface area of 667.95 m^2/g, a total pore volume of 58.4 ml/g, and an average pore diameter of 99.97 nm after being heated to 600°C for 4.5 hours. [134] following that, rice husk ash was discovered to have an average pore diameter of 1.98 nm, total pore volumes of 0.6464 ml/g, and a specific surface area of 653 m^2/g [135]. Silica obtained from the rice straw ash with surface area of 413 m^2/g, total pore volumes of 0.2 ml/g and 1.9 nm as the average diameter of the pore [133]. Similarly, the highest surface are of silica gel from teff straw with temperature 750°C at 2 h was found to be 305 m^2/g [98] afterward, sugarcane bagasse silica with a surface area of 265 m^2/g, total pore volumes of 0.425 ml/g, and an average pore diameter of 6.250 nm came in second [11].

4.2. X-Ray Diffraction (XRD). XRD method is known to be an effective technique which is used to determine the crystal structure of any materials [137, 138]. XRD analysis was conducted by comparing the diffraction lines of the samples with those in standard from the powder diffraction [125]. Based on this standard, XRD can determine the crystalline nature of particle of bigger size of 3–5 nm. The chemical phase configuration and the bulk materials of crystalline can be analyzed using XRD. XRD instrument have electromagnetic radiation which has a wave length size that ranges from 0.01 to 0.7 nm. This range is comparable with spacings of the lattice planes in crystalline form. The spacing size of metallic atoms always is between of 0.2-0.3 nm. X-ray photons are dispersed in a diverse way whereas the X-rays beam incident interrelates with the exact atom. When there is no change in incident photon and different photons of energy were scattered, and this revealed their elastic nature. The superposition of distributed waves and the advantageous behavior of wave phase interference are both possible. However, because of the phase, destructive interference cannot occur. The creation of periodic planes in coherent stutterers is caused by the atoms' crystalline planes. When different kinds of atomic planes are created by diffraction patterns, which provide information about how the atoms are arranged within crystals.

The amorphous nanosilica was discovered at the peak of 2 equal to 220 in the prepared rice husk ash at temperatures of 500, 700, and 1000°C. According to the silica activity index, the absence of the crystallin phase is largely supported by the lack of strong peaks that would have indicated the absorption of crystal structures that were organized. When rice husk is prepared sustainably at a lower temperature, potassium is found since there are no carbon peaks, and the material is porous. In contrast, the rice husk needs to be washed in acid solution prior to thermal treatment in order to primarily remove the potassium content and remove any fixed carbon from the raw materials. The particles' half-width of the peak can be calculated using (3) Scherer's formula.

Scherer's formula can be expressed as follows:

$$D = \frac{K * \lambda}{\beta * \operatorname{Cos}\theta}, \tag{3}$$

where K (constant) = 0.9 nm, $\lambda = 1.542$ Å (angstrom) by means of wavelength Cu-Kα and radian of β. The nanosilica materials were produced near to 7 nm, these results can be determined manually using the chart of XRD [139]. According to Bageru and Srivastava [7], the amorphous nanosilica was discovered at the peak of 2 equal to 220 in the prepared rice husk ash at temperatures of 500, 700, and 1000°C. According to the silica activity index, the absence of

Table 5: BET.

No	Biomass sources	Temperature (°C)	Surface area (m^2/g)	Total pore volume (cm^3/g)	Average pore size	References
1	Teff straw ash	500 @2 hr	52	—	—	[97]
		700 @2 hr	61	—	—	
		900 @2 hr	81		—	
3	Teff straw silica gel	750 @2 hr	305	—	—	[98]
4	Rice husk ash	850 @3 hr	72.26	—	—	[129]
2	Rice straw ash	850 @3 hr	94.53	—	—	
6	Corncob ash	850 @3 hr	203.03	—	—	
7	Rice husk ash	700 @5 hr	236.20	0.54	9	[130]
3	Rice husk silica	600 @2 hr	218	0.32	5.56	[131]
4	Sugarcane bagasse ash	550 @1 hr	1.50	0.0049	10.790	[11]
5	Sugarcane bagasse silica		265	0.425	6.250	
6	Coconut husk ash	600 @2 hr	56	0.14	—	[128]
7	Corncob ash		70	0.14	—	
8	Corn husk ash		91	0.21	—	
9	Rice husk ash	800–850	296.98	0.57	7.68	[132]
10	Rice straw ash		413	0.2	1.9	[133]
11	Bamboo leave ash	600@4.5 hr	667.95	58.4	99.97	[134]
12	Rice husk ash	700@4 hr	653	0.64647	1.98	[135]
13	Rice husk silica gel	650@ 6 hr	258		12.1	[76]
14	Sugarcane leaves ash	500@ 4.5 hr	323	0.41	5.0	[8]
15	Maize leaves ash		182	0.34	7.0	

the crystallin phase is largely supported by the lack of strong peaks that would have indicated the absorption of crystal structures that were organized. When rice husk was prepared sustainably at a lower temperature, potassium is found since there are no carbon peaks and the material is porous. In contrast, the rice husk needs to be washed in acid solution prior to thermal treatment in order to primarily remove the potassium content and remove any fixed carbon from the raw materials. The particles' half-width of the peak can be calculated using (3) Scherer's formula. It was found that purity of the biosilica increases with temperature. However, while increasing the temperature amorphous nature of the silica after 700°C was observed to lose, in case of Figure 4(b) by the hydrothermal method, the same was observed as result. In case of Figure 4(a) using the sol-gel method of potential virtually removes all other ingredients, and only amorphous biosilica is formed outside of the temperature range of 500–900°C, according to the XRD pattern [7, 97]. In addition to this, in Figure 4(c) the presence of silica, which is present as crystalline ash is shown by the significant peak detection at 20.9 and 26.6 in section (a). The extracted silica is primarily amorphous, as evidenced by the broad X-ray diffraction pattern in section (b), which is typical of amorphous materials. In general, it has been observed that the diffraction broad peak at theta = 22° suggests amorphous silica together with some crystalline silica in section (c) [111].

4.3. X-Ray Fluorescence Method. X-ray fluorescence (XRF) method is a nondestructive elemental analysis method that can be used for any material. This method is most applicable for pharmaceutical, environmental, forensic, industrial, and different scientific researches areas. XRF is used to determine the elemental concentration of contaminants or constituents based on peak's energy comparison using the element's binding energy. According to scientific research studies, X [140] have reported that the chemical composition of rice husk ash has been determined using XRF technique with sample in oxides forms of silica content of 95.6 wt%, 96.1 wt %, and 95.89 wt% at calcination temperatures of 400, 450, and 500°C, respectively. Based on XRF, it was observed that the commercial biosilica is found to be 98% pure. However, from the teff straw ash, the biosilica was met a good purity up to 92%, while the teff straw ash burnt at 900°C. For teff straw ash obtained at 500 and 700°C, concentration of biosilica was reported to be 85 and 91%, respectively [7].

4.4. Thermo Gravimetric Analysis. Thermo gravimetric analysis (TGA) is a method with modification in mass of samples to be examined through a rise in temperature at quantified with heating rate and vapor environment [141]. In the processing of TGA investigation, the loaded sample with the microbalance arm used for suspension of the small crucible of platinum. The oven temperature can be easily measured and examined. Investigation is supported by rising the temperature of sample, progressively in a flow N_2, Ar, He, and the sample weight can be schemed in contrast to temperature. Heating rate, the quantity of sample, flow of the carrier gas is some of the most affecting parameters. Investigation of materials of volatile, moisture content, and thermal stability are some of the major analyzations based on TGA. TGA techniques can also studied for the determination oxidation, chlorination, hydrogenation, and desorption/adsorption supported with reaction kinetics for

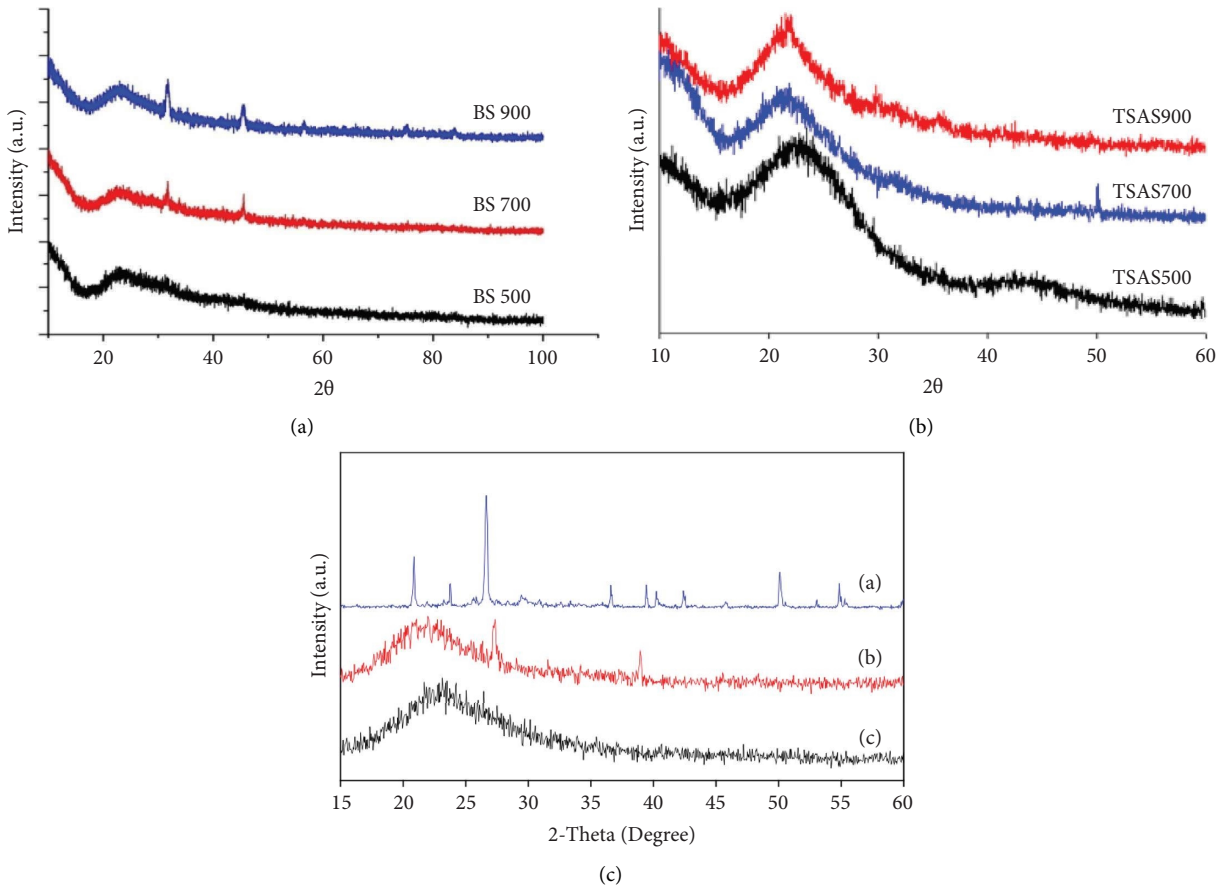

Figure 4: Schematic illustration of the XRD of (a) silica gel, (b) silica from teff straw, and (c) corn con ash, silica gel, and nanosilica gel [7, 97, 111].

gaseous reactions. Besides, the TGA techniques study can be applied for pyrolysis kinetics, for example, carbonization and sintering. The TGA analysis have been presented on the mass loss in temperature range of 230–520°C. During this range, the loss is much higher than the temperature range of 520–1000°C. The teff straw ash production was higher from 500 to 700°C than with temperature range of 700–900°C [7].

4.5. Differential Thermal Analysis. Differential thermal analysis works with the same rate of temperature difference between the reference and sample. In DTA analysis, identical thermal condition is used for heating the reference and sample in the same oven. Where on the period of heating, the reference and the sample temperature difference is checked. When the samples are undertaken changes in state, latent heat of the transition will be absorbed the sample temperature is differ from the reference materials. Then, the temperature is recorded for both of reference and sample materials. Along with temperature,the occurrence of change can be detected [142]. Bageru and Srivastava [7] have studied on the biosilica structures obtained from teff straw ash at 700°C. They have demonstrated that the size distribution is not uniform compared with 900°C of teff straw ash.

The derivative profile of DTGA indicates that the temperature rises gives a change of mass loss. Figure 2 presents of the thermograph finds three characteristics conditions in the process of decomposition. There are ranges of mass loss from 25 to 140°C. The initial weight loss upto of 5.87% was occured due to the loss of water. Between 150 and 350°C, the DTGA results have shown the highest peak. In this peak, the area of active pyrolysis was indicated. Gaseous volatiles can be released when hemicellulose and celluloses decomposed into smaller molecules. During this process carbon monoxide and carbon dioxide is released by the reaction carried out for removal of carbon and oxygen eliminated from the polymer materials. Totally, in this process, around 48.05% of the samples mass was eliminated. Between 350 and 500°C, the pyrolysis is called passive. In this stage, 20.14% of mass was out due to the composition process of lignin, so-called passive pyrolysis zone. Studies reported that the 20.14% of mass was released due to lignin combustion at this process. When temperature becomes 550°C the mass becomes stable the content of ash or the inorganic residue [143]. During this stage, the combustion practice happened in three phases: 68–281, 307–381, and 408–454°C. When the first two phases were described by speedy devolatilization, the sample weight lost was from 25.43 to 45.15% this loss was a high considerable amount. In

the DTG curves, the two distinct peak of mass loss indicated, whereas the third phase showed a slow process of degradation [128].

4.6. Methods of Fourier Transforms Infrared Spectroscopy. Methods of Fourier Transforms Infrared Spectroscopy (FT-IR) is a known as vibrational spectroscopy grounded on the occurrence molecular vibrations that can absorbs infrared radiation. This method provides information about the molecular structure of materials or compounds of functional groups [144]. The oxides and dioxides of the functional groups of biosilica are observed to be nearby 470, 800, and 1100 cm^{-1}. At the temperature of 900 > 700 > 500°C, as shown in Figure 5(a), the teff straw ash's areas and peak height display increase in corresponding order. In similar way the biosilica concentration order is improved with increasing temperature. Peaks of C=O found on 1400 and 1600 cm^{-1}, C-O on 2350 cm^{-1}, C-H on 2860, and 2930 cm^{-1} were detected as unburned with peak strength order these is due to the impurity of carbon. It is apparent that while increasing the temperature impurity of the carbon was also increased. The spectra with peak of all samples visibly show similar positions. In the same way which includes around 1100 cm^{-1} have a strong band, around 800 cm^{-1} have a sharp band of medium and on around 470 cm^{-1} have a strong band Si-O-Si asymmetric vibration have a strong absorption peaks at 1100 cm^{-1} and the higher ionic character of the Si-O group have a shear bands [7]. The symmetric stretching of vibrations of SiO_4 tetrahedral is due to the band at 800 cm^{-1} and the Si-O bending band vibrations occurred due to at 470 cm^{-1} [146]. The asymmetric stretching is found on the broad band between 3000 and 3700°C and whereas the silanol of O-H groups absorptions of the vibrations of bending in most of the time caused by physical absorption of water [147]. According to Figure 5(b), the vibration network of O-Si-O is connected to the band 463–475 cm^{-1}, while the symmetric stretching vibration network of O-Si-O was assigned to the band 791–807 cm^{-1}. Broadband at 1633–1645 cm^{-1} is due to O-H bond bending vibration from Si-OH silanol groups, while 3338–34,750 cm^{-1} is due to O-H bond stretching vibration from Si-OH silanol groups and are due to adsorbed H_2O molecules on the silica surface. Band 1071–1090 cm^{-1} was due to Si-O-Si irregular stretching vibration [145].

4.7. Methods of Raman Spectroscopy. The vibration and rotation modes of molecules were studied by Raman spectroscopy. Based on the Raman spectroscopy of each compound have exceptional spectrum for the case of the cross-reference. On the sample of the analysis a laser light is focused which is due to the vibration of molecule. Because of light scattering that results in shifting either down or up for the energy of photon laser will be in the form of excitation [148]. This method can be used for analyzing crystals and molecules of the internal structure [138]. This all based on phenomenon of scattering of electromagnetic radiation is carried out by molecules. Elastic or inelastic scattering is performed by molecules [138, 148].

4.8. Methods of Transmission Electron Microscopy. Transmission electron microscopy is a system detecting membrane surface. The magnification of TEM is around of 50 million which is suitable for nanometer scale measurements and more magnification compared with SEM [137]. Based on TEM information can the analysis can be made on surface area and texture-based topography, shape, and size of the particles based on morphology, arrangements of atoms of crystallographic, and elements and their relative amounts base on composition.

Rajaeiyan and Bagheri-Mohagheghi [149] have studied on nanoparticles of the image using TEM was carried out. The particles were synthesized by sol-gel and coprecipitation techniques strengthening at 1250°C. The alumina particles produced by coprecipitation system had the size of 10–50 nm of diverse shape which have been looked hexagonal of irregular or spherical. But, form the sol-gel method, having the size scattering of 10–20 nm showed more spherical which is for the case of nanoparticles of alumina.

4.9. Scanning Electron Microscopy. For analysis of membrane the morphology and topography data of the prepared membranes SEM is one of the essential methods. Additionally, for the case of porous material to determine the pore size method of SEM is most preferable one. In case of a compressed membrane to measure thickness of the selective layer SEM can be the appreciable method. In SEM, samples should be in form of solid and moisture free. Samples moisture can be evaporated because it works under vacuum and also the sample is electrically conductive if not coating by metallic component is preferable [137]. For dealing the electron microscopic structure SEM is the most used method. Surface area of the specimen can be scanned for focusing the formed image based on SEM technique. In this technique, the electron beam is also called as incident beam where 10 nm is detected. Furthermore, 1 μm and also in SEM instantaneously image is not formed where illuminating the whole part with a similar fashion with TEM. When the sample must be made thin in TEM for electron transition otherwise it will be scattered or absorbed. In nutshell, the SEM technique can overcome for this limitation [137, 138]. During the studies by Rajaeiyan and Bagheri–Mohagheghi [149], the particles image formed based on SEM from the analysis of the methods of sol-gel and coprecipitation was analyzed. In coprecipitation method strong agglomeration and varied size of the particle is formed where as in case of sol-gel method the particles showed a uniform particle distribution as well as elongated shape. Therefore, in sol-gel method the structure of gelatinous state is formed from the precursor which allowed alumina crystalline of free from agglomeration.

The SEM pictures in Figure 6 clearly reveal a difference, which can be seen in the textures of the biosilica samples prepared from teff straw. For example, in Figure 6(a) at 500°C particles' darker colour and larger size indicate the presence of carbon impurities that were left behind in the sample after incomplete combustion at 500°C compared

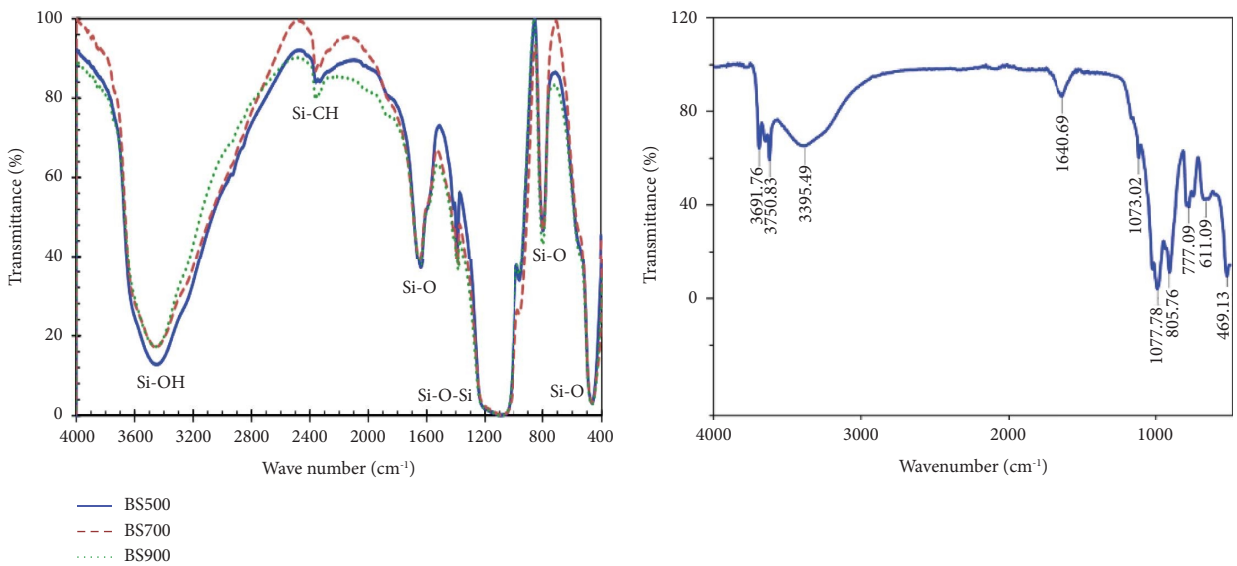

Figure 5: FTIR spectra of samples of biosilica produced synthetically from teff straw (a) [97] and palm kernel shell (b) [145].

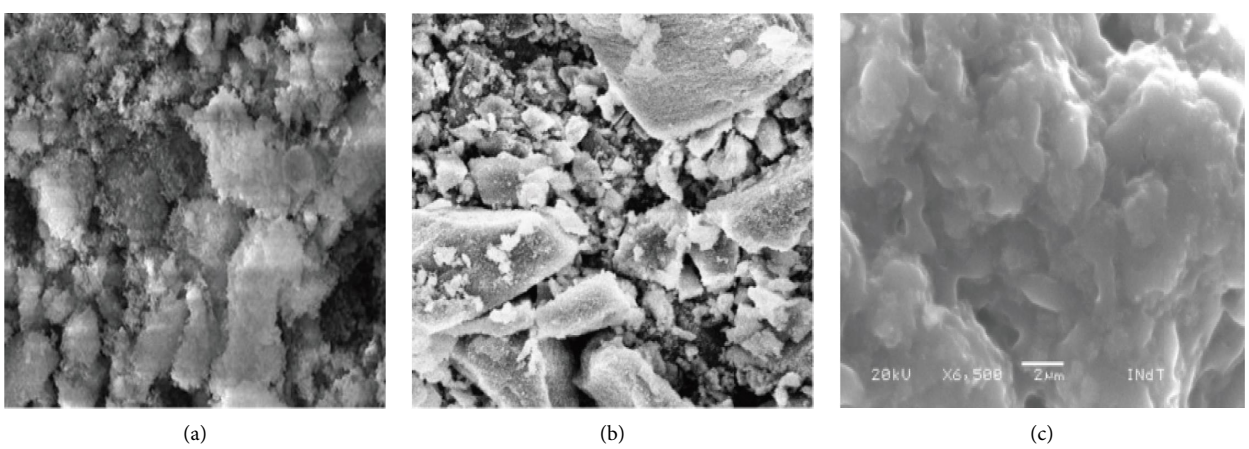

Figure 6: SEM examination of samples of biosilica made from teff straw (a) and (b) synthetically [97] and (c) silica gel from rice husk [15].

with biosilica prepared in Figure 6(b) at 700°C [97]. The micrograph of the rice husk ash instance demonstrates that individual silica grains were not visible. Instead, the silica formed uneven and cohesive surfaces by clustering into spherical clusters [15].

5. Applications of Silica Gel

Silica gel is one of the most significant inorganic materials that have been broadly known for stable and desirable properties with respect to temperature and mechanical influences [12]. Silica gel has been exploited potentially for raw materials to produce silicon carbide and soluble silicates. Both of these materials are used in different applications such as ceramics, electronics components, refractory industries, manufacture of glass, rubber tire filling material, chromatographic stationary phase, adhesive, components in the ceramic, detergent, and pharmaceuticals. As we know, the price of mineral silica is quite expensive. Hence, the use of biosilica has become better alternative for silicon chip manufacturing [13]. Hence, it needs an effective production of high value-added biosilica from a low-cost material that can be an alternate way compared with the conventional production method. Some of the major applications of silica gel were presented as follows.

5.1. Applications of Nanosilica. Recently, a significant amount of silica has been extensively used in different industries. In specific, nanostructured silica has a potential characteristic that is required for recent applications [150] for biosensors, bioimaging, drug delivery systems [3], drinking water, and wastewater treatment [46], CO_2 capture applications [151, 152], superhydrophobic coatings [153], toothpastes as a cleansing agent, reinforcing agent, anticaking agent in salts, cosmetics applications [11], uses as

a catalytic support in acetic acid steam reforming [19], in agricultural and environmental remediation potential applicability [38], and so on. In other, silica gel is commonly applied to absorb excess moisture present in the environment. It is put forefront of refrigerant drying, process industries, insulating glass industry, desiccant powder, and packaging desiccants [106]. Silica gel desiccant in sachets is considered to have a scavenger property for water [105].

Utilizing silica nanoparticles as reinforcement or filler in sophisticated composite materials is one of their most well-known uses. The capacity to achieve homogeneous filler dispersion, which affects how well silica-polymer nanocomposites perform overall, is one of its key features [121]. An essential step in preparing silica-polymer nanocomposites is the chemical modification of silica surfaces with organofunctional groups. It has been noted that surface changes promote the dispersion of silica nanoparticles inside the polymer matrix while also improving the affinity between the organic and inorganic phases [154]. In the concrete industry, silica nanoparticles have the potential to solve numerous technical problems relating to concrete materials and significantly improve the mechanical characteristics of concrete [155]. This nanomaterial also has effective since it has a significant pozzolanic activity [156]. Concrete and mortar materials can be benefited from the microstructure-improving effects due to the colloidal silica nanoparticle attachment [157].

5.2. Chemical Applications of Silica Gel. Typically, trialkoxysilanes with organo-substituted co-condensation or post-synthesis grafting are used to functionalize silica particles [158]. For instance, one of the most often used metals functionalized onto mesoporous silica nanoparticles for catalytic applications is aluminum. It was utilized to deliver drugs [159]. Titanium oxide and iron oxide are incorporated in produced silica nanoparticles. The synthesized substance was utilized in catalytic processes [160]. Silver nanoparticles based on silica have recently been created and will be utilized to treat *Mycobacterium tuberculosis* [161]. Similar to this, copper, silver, and copper hydroxy salt were employed to create the corresponding metallic silica nanoparticles, which displayed positive and encouraging outcomes when used as antibacterial agents [162].

5.3. Biomedical Application of Silica. A widely acknowledged characteristic currently being researched is the use of tailored nanostructures for the targeted administration of medications to patients [38, 163]. These nanostructures can serve as transporters and direct substances to particular organs or human tissues. Due to their large surface area and porous structure, mesoporous silica nanoparticles have gained considerable respect in this regard. Recently, these particles have been utilized as nanocarriers for the delivery of medications [164]. Additionally, the hydrophobicity of the medicines decreases absorption during oral administration. This is enhanced by utilizing silica nanoparticles as carriers for such hydrophobic medications, which have demonstrated encouraging outcomes when administered orally [163].

5.4. Agricultural Applications. A bioactive component called silica has been linked to fungicidal effects. Different investigations revealed that silica could increase the resistance against fungal diseases. It has been proven that the environmental stress and tolerance can increase; in nut shell, the productivity of crop significantly improves [165]. It has been demonstrated to boost the resistance of cucumbers to powdery mildew [166], in cucumbers and grapes [167, 168]. In the recent past, in vitro studies have also been performed to investigate the antifungal effect of silica, and in vitro inhibition of mycelial growth of several phytopathogenic fungi grown on potassium silicate amended media has been reported [165].

5.5. Applications for Food Preservation. Many fruits can be coated with hybrid films made of silica to extend their shelf life and keep fresher for longer [169]. It has been demonstrated that some fruits can prolong their shelf life dramatically. Fruit has a tendency to make you lose weight, better enzymatic activity, more reducing sugars, and a longer shelf life [170]. The addition of nanofillers such as silicate, clay, and titanium dioxide to biopolymers may enhance their mechanical and barrier qualities as well as provide additional uses as an antibacterial agent, biosensor, and oxygen scavenger in food packaging [171]. The bio-nanocomposite can be utilized as an active food packaging that can interact with the food in a number of ways, such as by releasing beneficial components such as antibacterial agents and antioxidant agents or by eliminating unfavorable factors such as oxygen or water vapor. Additionally, the bio-nanocomposite can be employed as smart food packaging that detects the features of the packaged food, such as microbial contamination or expiration date, and uses a mechanism to record and convey information about the product's quality or safety [170].

5.6. Industrial Applications. Silica nanoparticles are ideal for a variety of industrial applications due to their mesoporous structure and high surface area. Due to the exceptional qualities these particles exhibit, more and more people are turning to these applications. As an illustration, mesoporous silica-based nanofibers have demonstrated remarkable potential for immobilization and are thus an appropriate material for encapsulation [172]. Moreover, by encapsulating capsaicin using the same fiber matrix, the enzyme's stimulation activity was increased. This demonstrates the viability of employing mesopore silica nanoparticle fibers used for enzymatic encapsulation [173].

5.7. Environmental Applications. Due to their toxicity, inability to degrade, and long-lasting nature, heavy metals such as arsenic, copper, cadmium, chromium, nickel, zinc, lead, and mercury are important contaminants of fresh water reservoirs. These heavy metal ions are naturally present in the environment, but due to an increase in

industrial waste, their concentration is rising right now [174]. The harmful ions get into the food chain and ultimately get into people [175]. For instance, consuming too much zinc may result in health issues such as stomach pains, vomiting, and skin irritations, Ni concentrations above a certain level cause lung and kidney cancer [176]. Natural zeolites, naturally occurring silicate minerals, have been utilized extensively in place of manufactured resins to remove heavy metals from aqueous solutions due to their inexpensive cost and high availability [177]. Moreover, compared to controls, silica nanoparticles exposed to polluted plants absorbed more air lead [178].

5.8. Applications in Water Purification. Using silica nanoparticles, heavy metals can be removed from aqueous solutions. The same has already been demonstrated in a number of studies, supporting its use in the treatment of industrial effluent [179]. Additionally, silica nanoparticles have been demonstrated to reduce or completely eliminate the biological oxygen demand (Sahebi et al.). Compared to more traditional approaches that do not use silica nanoparticles, biological oxygen demand (BOD) activity is more effective [180]. To test their antibacterial effectiveness, synthetically made silver nanoparticles were mixed with silica nanoparticles. Furthermore, the temperature and organic matter content of nanoparticles had a significant impact on their antiviral activity. According to the study, silica linked nanoparticles may be used as antivirals to destroy viruses in wastewater [181].

5.9. For the Application of Semiconductor. The main component of the solar cell's semiconductor layer may be silica. The semiconductor is a substance with conductivity that is between that of an insulator and that of a conductor. The bandgap energy is the primary factor that determines how a semiconductor interacts with other materials. The difference between the valence band and the conduction band section, which defines the amount of transition energy required to convert the electron band from the valence band to the conduction band, is determined by the energy bandgap [182]. Bandgap energy for semiconductors ranges from 0 to 4 eV, whereas it is beyond 4 eV for isolators and below 0.5 eV for conductors [183]. Due to the leaps made by excited electrons, semiconductors are created as materials that support electric currents. The photovoltaic principle states that silicon crystalline base material is used to create solar cells because of its abundance, lack of toxicity, and high conversion efficiency [184].

6. Conclusions and Future Prospects

In this review paper, synthesis, characterization mechanisms, and application areas of biosilica were reviewed. Agricultural waste resources such as palm tree, wheat straw, maize leaves, teff straw, sugarcane bagasse, rice husk, rice straw, sugarcane leaf, oat husk, bamboo leaf, and corn cob can be used as a source of silica was presented. From these biomass sources, using different approaches such as sol-gel, hydrothermal, chemical vapor deposition, impregnation, electrodeposition, coprecipitation, and leaching method synthesizing of silica gel have been described briefly. Then, using different characterization mechanisms such as BET, XRD, TEM, and SEM were presented. Also, the multipurpose applications used in the form of catalyst, synthesis of shear thickening fluid, chemically inert material, strong adsorption capacity, ceramics, concrete materials, glass, cement, medicine, supercapacitors, batteries, cosmetics, detergents, adhesive agents, pharmaceutical, fine-chemicals, clean fuels, catalyst support, microfilters, thermal superinsulation, controlled release of drugs, and good option to deliver drugs of antibiotics were presented here. This review indicates that the results from agricultural wastes source of silica is an alternative one. Therefore, this form of silica basis will contribute benefits used for a low-cost input material, pure silica product, and environmentally-friendly.

Besides these, the subsequent features have a necessity to be addressed in upcoming mechanisms: (1) advance studies on agricultural leftover resulting biosilica in order to grow better-quality fresh adsorbent on behalf of removing organic and inorganic wastes from drinking and wastewater. (2) Development of a high-yield and cost-effective biosilica which replace an energy-intensive commercial sale product. (3) Biosilica products have their own merits such as the raw materials that are easily available, cost-effective, pure yield, and environmentally-friendly. (4) The merits and demerits of each preparation method of biosilica are still not clear. Consequently, scientists are quite challenged with incomplete consideration in this zone of biosilica preparation. On behalf of the advance argument on this fact of view, the reader can denote the reference presented now. (5) In emerging requirements for silica, there is an essential behalf of critical care over the outline of favourable directive that encourages the vast usage of used yields after leftover.

Data Availability

All data used in the findings of this study are included within the article.

Conflicts of Interest

The authors declare that they have no conflicts of interest.

Acknowledgments

This study was supported by Addis Ababa Science and Technology University.

References

[1] C. P. Faizul, C. Abdullah, and B. Fazlul, "Extraction of silica from palm ashvia citric acid leaching treatment," *Advances in Environmental Biology*, vol. 7, pp. 3690–3695, 2013.

[2] N. Permatasari, T. N. Sucahya, and A. B. Dani Nandiyanto, "Review: agricultural wastes as a source of silica material," *Indonesian journal of science and technology*, vol. 1, no. 1, pp. 82–106, 2016.

[3] S. Prabha, D. Durgalakshmi, S. Rajendran, and E. Lichtfouse, "Plant-derived silica nanoparticles and composites for biosensors, bioimaging, drug delivery and supercapacitors: a review," *Environmental Chemistry Letters*, vol. 19, no. 2, pp. 1667–1691, 2020.

[4] U. Kalapathy, A. Proctor, and J. Shultz, "A simple method for production of pure silica from rice hull ash," *Bioresource Technology*, vol. 73, no. 3, pp. 257–262, 2000.

[5] G. Mizer, *Optimization and Characterization of Silica Synthesized from Rice Husk*, Ph. D. Thesis, AAU Institutional Repository, Addis Ababa Uiversity, Addis Ababa, Ethiopia, 2019, http://etd.aau.edu.et/handle/123456789/20999.

[6] M. Mupa, C. Hungwe, S. Witzleben, C. Mahamadi, and N. Muchanyereyi, "Extraction of silica gel from Sorghum bicolour (L.) moench bagasse ash," *African Journal of Pure and Applied Chemistry*, vol. 9, 2015.

[7] A. B. Bageru and V. Srivastava, "Preparation and characterisation of biosilica from teff (eragrostis tef) straw by thermal method," *Materials Letters*, vol. 206, pp. 13–17, 2017.

[8] N. N. Maseko, D. Schneider, S. Wassersleben et al., "The production of biogenic silica from different south african agricultural residues through a thermo-chemical treatment method," *Sustainability*, vol. 13, no. 2, p. 577, 2021.

[9] A. Nandiyanto, T. Rahman, M. Fadhlulloh, A. Abdullah, I. Hamidah, and B. Mulyanti, "Synthesis of silica particles from rice straw waste using a simple extraction method," in *Proceedings of the IOP Conference Series: Materials Science and Engineering*, Bandung, Indonesia, November 2016.

[10] K. G. Patel, N. Misra, and R. R. Shettigar, "Preparation and characterization of silica gel from wheat straw," *International Journal of Chemical Engineering and Applications*, vol. 7, no. 5, pp. 344–347, 2016.

[11] R. H. Alves, T. V. S. Reis, S. Rovani, and D. Fungaro, "Green synthesis and characterization of biosilica produced from sugarcane waste ash," *Journal of Chemistry*, vol. 2017, Article ID 6129035, 9 pages, 2017.

[12] A. Arumugam and V. Ponnusami, "Modified SBA-15 synthesized using sugarcane leaf ash for nickel adsorption," *Modified SBA-15 synthesized using sugarcane leaf ash for nickel adsorption*, vol. 20, 2013.

[13] O. Olawale, "Ampel bamboo leaves silicon dioxide (SiO2) extraction. IOP conference series: earth and environmental science," *IOP Conference Series: Earth and Environmental Science*, vol. 141, 2018.

[14] P. Imoisili and S. Olusunle, "Extraction and characterization of amorphous silica from corn cob ash by sol-gel-method," *Chemistry and Materials Research*, vol. 3, no. 4, pp. 68–72, 2013.

[15] S. P. B. Lima, R. P. Vasconcelos, O. A. Paiva et al., "Production of silica gel from residual rice husk ash," *Química Nova*, vol. 34, no. 1, pp. 71–75, 2011.

[16] B. R. Moreira, M. C. Breitkreitz, R. Simister, S. J. McQueen-Mason, L. D. Gomez, and C. A. Rezende, "Improved hydrolysis yields and silica recovery by design of experiments applied to acid-alkali pretreatment in rice husks," *Industrial Crops and Products*, vol. 170, Article ID 113676, 2021.

[17] S. S. Hossain, L. Mathur, and P. Roy, "Rice husk/rice husk ash as an alternative source of silica in ceramics: a review," *Journal of Asian Ceramic Societies*, vol. 6, no. 4, pp. 299–313, 2018.

[18] A. Ananthi, D. Geetha, and P. Ramesh, "Preparation and characterization of silica material from rice husk ash–an economically viable method," *Chemistry and Materials Research*, vol. 8, no. 6, pp. 1–7, 2016.

[19] W. Guo, G. Li, Y. Zheng, and K. Li, "Nano-silica extracted from rice husk and its application in acetic acid steam reforming," *RSC Advances*, vol. 11, no. 55, pp. 34915–34922, 2021.

[20] R. M. Long, Y. Jiang, J. Q. Guo et al., "Synthesis of silica-based solid-acid catalyst material as a potential osteochondral repair model in vitro," *Frontiers in Bioengineering and Biotechnology*, vol. 9, p. 1200, 2021.

[21] N. Rodella, A. Bosio, R. Dalipi et al., "Waste silica sources as heavy metal stabilizers for municipal solid waste incineration fly ash," *Arabian Journal of Chemistry*, vol. 10, pp. S3676–S3681, 2017.

[22] M. Zarei and J. Aalaie, "Application of shear thickening fluids in material development," *Journal of Materials Research and Technology*, vol. 9, no. 5, pp. 10411–10433, 2020.

[23] H. Shi, J. Cui, H. Shen, and H. Wu, "Preparation of silica aerogel and its adsorption performance to organic molecule," *Advances in Materials Science and Engineering*, vol. 2014, Article ID 850420, 8 pages, 2014.

[24] W. Wei, H. Hu, X. Ji, Z. Yan, W. Sun, and J. Xie, "Selective adsorption of organic dyes by porous hydrophilic silica aerogels from aqueous system," *Water Science and Technology*, vol. 78, no. 2, pp. 402–414, 2018.

[25] V. A. Karelin, A. N. Strashko, A. Sazonov, and A. Dubrovin, "Obtaining the fine-grained silicon carbide, used in the synthesis of construction ceramics," *Resource-Efficient Technologies*, vol. 2, no. 2, pp. 50–60, 2016.

[26] Y. Zhang, M. Cao, Z. Yao et al., "Effects of silica coating on the microstructures and energy storage properties of BaTiO3 ceramics," *Materials Research Bulletin*, vol. 67, pp. 70–76, 2015.

[27] P. Salim and B. Prasad, "An investigation on the influence of silica fume on the properties of mineral admixture concrete," *International Journal of Civil Engineering and Technology*, vol. 9, pp. 1217–1227, 2018.

[28] K. Ibrahim, "Recycled waste glass powder as a partial replacement of cement in concrete containing silica fume and fly ash," *Case Studies in Construction Materials*, vol. 15, Article ID e00630, 2021.

[29] G. Chand, S. K. Happy, and S. Ram, "Assessment of the properties of sustainable concrete produced from quaternary blend of Portland cement, glass powder, metakaolin and silica fume," *Cleaner Engineering and Technology*, vol. 4, Article ID 100179, 2021.

[30] H. Zhu, K. Zheng, and A. R. Boccaccini, "Multi-functional silica-based mesoporous materials for simultaneous delivery of biologically active ions and therapeutic biomolecules," *Acta Biomaterialia*, vol. 129, pp. 1–17, 2021.

[31] K. Cendrowski, W. Kukułka, and E. Mijowska, "Silica nanospheres as a key process element in the Green engineering for the synthesis of carbon nanotubes as a supercapacitors additives," *Materials Research Bulletin*, vol. 146, Article ID 111620, 2022.

[32] J. Jang, J. Oh, H. Jeong, W. Kang, and C. Jo, "A review of functional separators for lithium metal battery applications," *Materials*, vol. 13, no. 20, p. 4625, 2020.

[33] A. Belostozky, S. Bretler, M. Kolitz-Domb, I. Grinberg, and S. Margel, "Solidification of oil liquids by encapsulation within porous hollow silica microspheres of narrow size distribution for pharmaceutical and cosmetic applications," *Materials Science and Engineering: C*, vol. 97, pp. 760–767, 2019.

[34] D. Camporotondi, M. Foglia, G. Alvarez et al., "Antimicrobial properties of silica modified nanoparticles,"

Microbial pathogens and strategies for combating them: Science, Technology and Education, vol. 2, pp. 283–290, 2013.

[35] G. Negi, S. Anirbid, and P. Sivakumar, "Applications of silica and titanium dioxide nanoparticles in enhanced oil recovery: promises and challenges," *Petroleum Research*, vol. 6, no. 3, pp. 224–246, 2021.

[36] L. L. Félix, J. M. Porcel, F. F. H. Aragón, D. G. Pacheco-Salazar, and M. H. Sousa, "Simple synthesis of gold-decorated silica nanoparticles by in situ precipitation method with new plasmonic properties," *SN Applied Sciences*, vol. 3, no. 4, pp. 443–510, 2021.

[37] A. F. Lee, "Catalysing sustainable fuel and chemical synthesis," *Applied Petrochemical Research*, vol. 4, no. 1, pp. 11–31, 2014.

[38] F. Akhter, A. A. Rao, M. N. Abbasi et al., "A comprehensive review of synthesis, applications and future prospects for silica nanoparticles (SNPs)," *Silicon*, vol. 14, no. 14, pp. 8295–8310, 2022.

[39] J. C. Védrine, "Heterogeneous catalysis on metal oxides," *Catalysts*, vol. 7, no. 11, p. 341, 2017.

[40] A. V. Borhade, D. R. Tope, and S. G. Gite, "Synthesis, characterization and catalytic application of silica supported tin oxide nanoparticles for synthesis of 2, 4, 5-tri and 1, 2, 4, 5-tetrasubstituted imidazoles under solvent-free conditions," *Arabian Journal of Chemistry*, vol. 10, pp. S559–S567, 2017.

[41] M. Youmoue, R. T. Tene Fongang, A. Gharzouni et al., "Effect of silica and lignocellulosic additives on the formation and the distribution of meso and macropores in foam metakaolin-based geopolymer filters for dyes and wastewater filtration," *SN Applied Sciences*, vol. 2, no. 4, pp. 642–720, 2020.

[42] S. Iswar, S. Galmarini, L. Bonanomi et al., "Dense and strong, but superinsulating silica aerogel," *Acta Materialia*, vol. 213, Article ID 116959, 2021.

[43] Y. Zhou, G. Quan, Q. Wu et al., "Mesoporous silica nanoparticles for drug and gene delivery," *Acta Pharmaceutica Sinica B*, vol. 8, no. 2, pp. 165–177, 2018.

[44] A. Rastogi, D. K. Tripathi, S. Yadav et al., "Application of silicon nanoparticles in agriculture," *3 Biotech*, vol. 9, no. 3, pp. 90–11, 2019.

[45] J. Liu, S. Ma, and L. Zang, "Preparation and characterization of ammonium-functionalized silica nanoparticle as a new adsorbent to remove methyl orange from aqueous solution," *Applied Surface Science*, vol. 265, pp. 393–398, 2013.

[46] M. Rashed, *Adsorption Technique for the Removal of Organic Pollutants from Water and Wastewater*, IntechOpen Limited, London, SW, UK, 2013.

[47] Y. Zhang, Z. Zhang, D. Feng et al., "Effect of microbubbles on preparation of precipitated silica by carbonization: physical-chemical structure, kinetic parameters and mass transfer characteristics," *Carbon Capture Science and Technology*, vol. 1, Article ID 100002, 2021.

[48] Y. G. Asfaha, A. K. Tekile, and F. Zewge, "Hybrid process of electrocoagulation and electrooxidation system for wastewater treatment: a review," *Cleaner Engineering and Technology*, vol. 4, Article ID 100261, 2021.

[49] S. N. Ishmah, M. D. Permana, M. L. Firdaus, and D. R. Eddy, "Extraction of silica from bengkulu beach sand using alkali fusion method," *PENDIPA Journal of Science Education*, vol. 4, no. 2, pp. 1–5, 2020.

[50] N. Li, H. Habuka, S. Ikeda, and S. Hara, "Silicon chemical vapor deposition process using a half-inch silicon wafer for Minimal Manufacturing System," *Physics Procedia*, vol. 46, pp. 230–238, 2013.

[51] S. T. Oyama, H. Aono, A. Takagaki, T. Sugawara, and R. Kikuchi, "Synthesis of silica membranes by chemical vapor deposition using a dimethyldimethoxysilane precursor," *Membranes*, vol. 10, no. 3, p. 50, 2020.

[52] M. Rozainee, S. Ngo, A. A. Salema, and K. Tan, "Fluidized bed combustion of rice husk to produce amorphous siliceous ash," *Energy for Sustainable Development*, vol. 12, no. 1, pp. 33–42, 2008.

[53] S. Murugadoss, D. Lison, L. Godderis et al., "Toxicology of silica nanoparticles: an update," *Archives of Toxicology*, vol. 91, no. 9, pp. 2967–3010, 2017.

[54] P. S. Utama, R. Yamsaengsung, and C. Sangwichien, "Production and characterization of precipitated silica from palm oil mill fly ash using CO2 impregnation and mechanical fragmentation," *Brazilian Journal of Chemical Engineering*, vol. 36, no. 1, pp. 523–530, 2019.

[55] H. Jung, H. Kwak, J. Chun, and K. Oh, "Characteristics of crystalline silica (SiO2) particles prepared by simple solution method using sodium silicate (Na2SiO3) precursor Journal of Physics: conference Series," 2018.

[56] A. Pieła, E. Żymańczyk-Duda, M. Brzezińska-Rodak et al., "Biogenic synthesis of silica nanoparticles from corn cobs husks. Dependence of the productivity on the method of raw material processing," *Bioorganic Chemistry*, vol. 99, Article ID 103773, 2020.

[57] K. E. Richmond and M. Sussman, "Got silicon? The non-essential beneficial plant nutrient," *Current Opinion in Plant Biology*, vol. 6, no. 3, pp. 268–272, 2003.

[58] H. Ehrlich, K. D. Demadis, O. S. Pokrovsky, and P. G. Koutsoukos, "Modern views on desilicification: biosilica and abiotic silica dissolution in natural and artificial environments," *Chemical Reviews*, vol. 110, no. 8, pp. 4656–4689, 2010.

[59] M. A. Salam, K. Ahmed, T. Hossain, M. S. Habib, M. S. Uddin, and N. Papri, "Prospect of molecular sieves production using rice husk in Bangladesh: a review," *International Journal of Chemistry, Mathematics and Physics*, vol. 3, no. 6, pp. 105–134, 2019.

[60] N. M. Cremaes, *Multifunctional Silica-Based Nanoparticles for Biomedical Applications*, Cora TDX, Manchester, UK, 2014.

[61] S. Norsuraya, H. Fazlena, and R. Norhasyimi, "Sugarcane bagasse as a renewable source of silica to synthesize santa barbara amorphous-15 (SBA-15)," *Procedia Engineering*, vol. 148, pp. 839–846, 2016.

[62] V. Meena, M. Dotaniya, V. Coumar et al., "A case for silicon fertilization to improve crop yields in tropical soils," *Proceedings of the National Academy of Sciences, India - Section B: Biological Sciences*, vol. 84, no. 3, pp. 505–518, 2014.

[63] M. Sahebi, M. M. Hanafi, A. Siti Nor Akmar et al., "Importance of silicon and mechanisms of biosilica formation in plants," *BioMed Research International*, vol. 2015, Article ID 396010, 16 pages, 2015.

[64] H. A. Currie and C. C. Perry, "Silica in plants: biological, biochemical and chemical studies," *Annals of Botany*, vol. 100, no. 7, pp. 1383–1389, 2007.

[65] Y. Liu, S.-S. Chen, A.-J. Wang, J.-J. Feng, X. Wu, and X. Weng, "An ultra-sensitive electrochemical sensor for hydrazine based on AuPd nanorod alloy nanochains," *Electrochimica Acta*, vol. 195, pp. 68–76, 2016.

[66] S. Gu, J. Zhou, C. Yu, Z. Luo, Q. Wang, and Z. Shi, "A novel two-staged thermal synthesis method of generating nano-silica from rice husk via pre-pyrolysis combined with

calcination," *Industrial Crops and Products*, vol. 65, pp. 1–6, 2015.

[67] X. Ma, B. Zhou, W. Gao et al., "A recyclable method for production of pure silica from rice hull ash," *Powder Technology*, vol. 217, pp. 497–501, 2012.

[68] V. Carmona, R. Oliveira, W. Silva, L. Mattoso, and J. Marconcini, "Nanosilica from rice husk: extraction and characterization," *Industrial Crops and Products*, vol. 43, pp. 291–296, 2013.

[69] P. Ramadhansyah, M. Salwa, A. Mahyun, B. A. Bakar, M. M. Johari, and C. C. Norazman, "Properties of concrete containing rice husk ash under sodium chloride subjected to wetting and drying," *Procedia Engineering*, vol. 50, pp. 305–313, 2012.

[70] A. Zamani, A. P. Marjani, and Z. Mousavi, "Agricultural waste biomass-assisted nanostructures: synthesis and application," *Green Processing and Synthesis*, vol. 8, no. 1, pp. 421–429, 2019.

[71] A. Trubetskaya, P. A. Jensen, A. D. Jensen, M. Steibel, H. Spliethoff, P. Glarborg, and F. H. Larsen, Comparison of high temperature chars of wheat straw and rice husk with respect to chemistry, morphology and reactivity," *Biomass and Bioenergy*, vol. 86, pp. 76–87, 2016.

[72] V. H. Le, C. N. H. Thuc, and H. H. Thuc, "Synthesis of silica nanoparticles from Vietnamese rice husk by sol–gel method," *Nanoscale Research Letters*, vol. 8, no. 1, pp. 58–10, 2013.

[73] P. Van Soest, "Rice straw, the role of silica and treatments to improve quality," *Animal Feed Science and Technology*, vol. 130, no. 3-4, pp. 137–171, 2006.

[74] H. Khaleghian, M. Molaverdi, and K. Karimi, "Silica removal from rice straw to improve its hydrolysis and ethanol production," *Industrial and Engineering Chemistry Research*, vol. 56, no. 35, pp. 9793–9798, 2017.

[75] X. Yao, K. Xu, and Y. Liang, "Comparing the thermophysical properties of rice husk and rice straw as feedstock for thermochemical conversion and characterization of their waste ashes from combustion," *Bioresources*, vol. 11, no. 4, pp. 10549–10564, 2016.

[76] R. Prasad and M. Pandey, "Rice husk ash as a renewable source for the production of value added silica gel and its application: an overview," *Bulletin of Chemical Reaction Engineering and Catalysis*, vol. 7, no. 1, p. 1, 2012.

[77] D. Schneider, S. Wassersleben, M. Weiß, R. Denecke, A. Stark, and D. Enke, "A generalized procedure for the production of high-grade, porous biogenic silica," *Waste and Biomass Valorization*, vol. 11, no. 1, pp. 1–15, 2018.

[78] H. A. Alyosef, A. Eilert, J. Welscher et al., "Characterization of biogenic silica generated by thermo chemical treatment of rice husk," *Particulate Science and Technology*, vol. 31, no. 5, pp. 524–532, 2013.

[79] M. Rashid, "Strength behavior of cement mortar assimilating rice husk ash," *International Journal of Advances in Agricultural and Environmental Engineering*, vol. 3, no. 2, 2016.

[80] A. Loiseau, V. Asila, G. Boitel-Aullen, M. Lam, M. Salmain, and S. Boujday, "Silver-based plasmonic nanoparticles for and their use in biosensing," *Biosensors*, vol. 9, no. 2, p. 78, 2019.

[81] V. M. Zancajo, S. Diehn, N. Filiba, G. Goobes, J. Kneipp, and R. Elbaum, "Spectroscopic discrimination of sorghum silica phytoliths," *Frontiers of Plant Science*, vol. 10, p. 1571, 2019.

[82] S. Kumar, Y. Milstein, Y. Brami, M. Elbaum, and R. Elbaum, "Mechanism of silica deposition in sorghum silica cells," *New Phytologist*, vol. 213, no. 2, pp. 791–798, 2017.

[83] K. Amutha and G. Sivakumar, "Analytical analysis of synthesized biosilica from bioresidues," *Spectrochimica Acta Part A: Molecular and Biomolecular Spectroscopy*, vol. 112, pp. 219–222, 2013.

[84] Y.-B. Im, R. Wahab, S. Ameen, Y.-S. Kim, O. Yang, and H.-S. Shin, "Synthesis and characterization of high-purity silica nanosphere from rice husk," *Journal of Nanoscience and Nanotechnology*, vol. 11, no. 7, pp. 5934–5938, 2011.

[85] V. S. Periasamy, J. Athinarayanan, and A. A. Alshatwi, "Extraction and biocompatibility analysis of silica phytoliths from sorghum husk for three-dimensional cell culture," *Process Biochemistry (Barking, UK)*, vol. 70, pp. 153–159, 2018.

[86] M. Wright, I. Lima, and R. Bigner, "Stability and use of sweet sorghum bagasse," *Sugar Tech*, vol. 19, no. 5, pp. 451–457, 2017.

[87] F. Lanning, T. Garabedian, Distribution of ash, calcium, iron, and silica in the tissues of young Sorghum plants," *Transactions of the Kansas Academy of Science*, vol. 66, no. 3, pp. 443–448, 1963.

[88] B. Haileselassie, S. Dargie, and A. Estifanos, "Mineral composition of grain and straw of tef (Eragrostis tef) grown on Vertisols," *Ethiopian Journal of Agricultural Sciences*, vol. 29, no. 2, pp. 83–91, 2019.

[89] A. Chufo, H. Yuan, D. Zou, Y. Pang, and X. Li, "Biomethane production and physicochemical characterization of anaerobically digested teff (Eragrostis tef) straw pretreated by sodium hydroxide," *Bioresource Technology*, vol. 181, pp. 214–219, 2015.

[90] B. Tadesse, E. Teju, and N. Megersa, "The Teff straw: a novel low-cost adsorbent for quantitative removal of Cr (VI) from contaminated aqueous samples," *Desalination and Water Treatment*, vol. 56, no. 11, pp. 2925–2936, 2015.

[91] S. Neu, J. Schaller, and E. G. Dudel, "Silicon availability modifies nutrient use efficiency and content, C: N: P stoichiometry, and productivity of winter wheat (*Triticum aestivum* L.)," *Scientific Reports*, vol. 7, no. 1, pp. 40829–40838, 2017.

[92] P. Mañas and J. De Las Heras, "Nutrient content in wheat grain and straw using sludge and compost from a wastewater treatment plant as a fertiliser," *Journal of the Science of Food and Agriculture*, vol. 98, no. 12, pp. 4707–4714, 2018.

[93] H. J. Naqvi, A. Saeed, A. Umair, and F. H. Shah, Precipitated silica from wheat husk," *Journal of the Pakistan Institute of Chemical Engineers*, vol. 39, no. 1, pp. 51–54, 2011.

[94] S. R. Collins, D. C. Radley, C. Schoen et al., "Variation in the chemical composition of wheat straw: the role of tissue ratio and composition," *Issue Brief (Public Policy Institute, American Association of Retired Persons)*, vol. 32, no. 1, pp. 1–9, 2014.

[95] V. Bartůněk, D. Sedmidubský, D. Bouša, and O. Jankovský, "Production of pure amorphous silica from wheat straw ash," *Green Materials*, vol. 6, no. 1, pp. 1–5, 2018.

[96] A. Goyal, H. Kunio, H. Ogata, M. Garg, A. Anwar, and M. Ashraf, "Synergic effect of wheat straw ash and rice-husk ash on strength properties of mortar," *Journal of Applied Sciences*, vol. 7, no. 21, pp. 3256–3261, 2007.

[97] A. B. Bageru and V. C. Srivastava, "Biosilica preparation from abundantly available African biomass Teff (Eragrostis tef) straw ash by sol-gel method and its characterization," *Biomass Conversion and Biorefinery*, vol. 8, no. 4, pp. 971–978, 2018.

[98] T. A. Amibo, S. M. Beyan, and T. M. Damite, "Production and optimization of bio-based silica nanoparticle from teff

straw (eragrostis tef) using rsm-based modeling, characterization aspects, and adsorption efficacy of methyl orange dye," *Journal of Chemistry*, vol. 2022, Article ID 9770520, 15 pages, 2022.

[99] B. Wei and S. Song, "Synthesis and characterization of nanosilica from teff straw," *Journal of Nano Research*, vol. 46, 2017.

[100] S. A. Memon, I. Wahid, M. K. Khan, M. A. Tanoli, and M. Bimaganbetova, "Environmentally friendly utilization of wheat straw ash in cement-based composites," *Sustainability*, vol. 10, no. 5, p. 1322, 2018.

[101] S. A. Ajeel and K. A. Sukkar, *Extraction High Purity Nanosilica Corn Cob by Modified Precipitation Technique*, Research Square, Durham, North Carolina, USA, 2021.

[102] F. S. Galindo, P. H. Pagliari, W. L. Rodrigues et al., "Silicon amendment enhances agronomic efficiency of nitrogen fertilization in maize and wheat crops under tropical conditions," *Plants*, vol. 10, no. 7, p. 1329, 2021.

[103] G. Deepana, D. Shobarajkumar, C. Subha, and S. Sasipriya, "Synthesis and characterization of silica from zea mays," *International Journal of Engineering Research and Technology*, vol. 8, no. 3, pp. 311–316, 2019.

[104] M. A. Azeez and J. I. Orege, "Bamboo, its chemical modification and products," *Bamboo Curr. Fut. Prosp*, vol. 25, 48 pages, 2018.

[105] A. S. H. Amarakoon and S. Navaratne, "Evaluation of the effectiveness of silica Gel desiccant in improving the keeping quality of rice crackers," *International Journal of Science and Research*, vol. 6, 2017.

[106] N. Nur Amalina Shairah Abdul Samat, S. Aishah Zulkafly, U. Zulaikha Kamarul Jaman, N. Syuhada Ahmad Zauzi, M. Rezaur Rahman, and R. Baini, "Characteristics analysis of bio-based silica extracted from sarawak palm oil waste," *International Journal of Engineering and Technology*, vol. 7, no. 18, pp. 94–96, 2018.

[107] M. Amran, G. Murali, R. Fediuk, N. Vatin, Y. Vasilev, and H. Abdelgader, "Palm oil fuel ash-based eco-efficient concrete: a critical review of the short-term properties," *Materials*, vol. 14, no. 2, p. 332, 2021.

[108] G. A. P. K. Wardhani, N. Nurlela, and M. Azizah, "Silica content and structure from corncob ash with various acid treatment (HCl, HBr, and Citric Acid)," *Molekul*, vol. 12, no. 2, pp. 174–181, 2017.

[109] S. Mohapatra, R. Sakthivel, G. Roy, S. Varma, S. Singh, and D. K. Mishra, "Synthesis of β-SiC powder from bamboo leaf in a DC extended thermal plasma reactor," *Materials and Manufacturing Processes*, vol. 26, no. 11, pp. 1362–1368, 2011.

[110] Z. Yahya, M. M. A. B. Abdullah, K. Hussin, K. N. Ismail, R. Razak, and A. V. Sandu, "Effect of solids-to-liquids, Na2SiO3-to-NaOH and curing temperature on the palm oil boiler ash (Si+ Ca) geopolymerisation system," *Materials*, vol. 8, no. 5, pp. 2227–2242, 2015.

[111] E. A. Okoronkwo, P. E. Imoisili, S. A. Olubayode, and S. O. Olusunle, "Development of silica nanoparticle from corn cob ash," *Advances in Nanoparticles*, vol. 5, no. 2, pp. 135–139, 2016.

[112] H. Agusnar, H. Agusnar, P. Sugita, and I. Nainggolan, "Preparation sodium silicate from rice husk to synthesize silica nanoparticles by sol-gel method for adsorption water in analysis of methamphetamine," *South African Journal of Chemical Engineering*, vol. 40, pp. 80–86, 2022.

[113] H. Chen, F. Wang, C. Zhang, Y. Shi, G. Jin, and S. Yuan, "Preparation of nano-silica materials: the concept from wheat straw," *Journal of Non-crystalline Solids*, vol. 356, no. 50-51, pp. 2781–2785, 2010.

[114] A. Mahapatra, *Fabrication and Characterization of Novel Iron Oxide/alumina Nanomaterials for Environmental Applications*, National Institute Of Technology, Rourkela, Odisha, India, 2013.

[115] H. M. Fahmy, A. M. Mosleh, A. A. Elghany et al., "Coated silver nanoparticles: synthesis, cytotoxicity, and optical properties," *RSC Advances*, vol. 9, no. 35, pp. 20118–20136, 2019.

[116] E. M. Modan and A. G. Plăiaşu, "Advantages and disadvantages of chemical methods in the elaboration of nanomaterials," *The Annals of "Dunarea de Jos" University of Galati. Fascicle IX, Metallurgy and Materials Science*, vol. 43, no. 1, pp. 53–60, 2020.

[117] Y. X. Gan, A. H. Jayatissa, Z. Yu, X. Chen, and M. Li, "Hydrothermal synthesis of nanomaterials," *Journal of Nanomaterials*, vol. 2020, Article ID 8917013, 3 pages, 2020.

[118] O. Schäf, H. Ghobarkar, and P. Knauth, "Hydrothermal synthesis of nanomaterials," in *Nanostructured Materials*, pp. 23–41, Springer, Berlin, Germany, 2004.

[119] H. Hayashi and Y. Hakuta, "Hydrothermal synthesis of metal oxide nanoparticles in supercritical water," *Materials*, vol. 3, no. 7, pp. 3794–3817, 2010.

[120] Y. M. Manawi, A. Samara, A. Samara, T. Al-Ansari, and M. Atieh, "A review of carbon nanomaterials' synthesis via the chemical vapor deposition (CVD) method," *Materials*, vol. 11, no. 5, p. 822, 2018.

[121] I. A. Rahman and V. Padavettan, "Synthesis of silica nanoparticles by sol-gel: size-dependent properties, surface modification, and applications in silica-polymer nanocomposites—a review," *Journal of Nanomaterials*, vol. 2012, Article ID 132424, 15 pages, 2012.

[122] T. Saeed, A. Naeem, T. Mahmood, and N. H. Khan, "Preparation of nano-particles and their applications in adsorption," in *Engineered Nanomaterials-Health and Safety*, IntechOpen, London, SW, UK, 2019.

[123] J. A. Schwarz, C. Contescu, and A. Contescu, "Methods for preparation of catalytic materials," *Chemical Reviews*, vol. 95, no. 3, pp. 477–510, 1995.

[124] F. C. Pa and W. K. Kein, "Removal of iron in rice husk via oxalic acid leaching process," in *Proceedings of the IOP Conference Series: Materials Science and Engineering*, Penang, Malaysia, November 2019.

[125] S. Sembiring and W. Simanjuntak, "X-ray diffraction phase analyses of mullite derived from rice husk silica," *Makara Journal of Science*, vol. 77, 82 pages, 2013.

[126] P. Raja and A. Barron, "BET surface area analysis of nanoparticles," *Chemistry LibreTexts*, vol. 9, 2019.

[127] R. S. Bakdash, I. Aljundi, C. Basheer, and I. Abdulazeez, "Rice husk derived Aminated Silica for the efficient adsorption of different gases," *Scientific Reports*, vol. 10, no. 1, pp. 19526–19612, 2020.

[128] C. O. Prempeh, S. Formann, T. Schliermann, H. B. Dizaji, and M. Nelles, "Extraction and characterization of biogenic silica obtained from selected agro-waste in Africa," *Applied Sciences*, vol. 11, no. 21, Article ID 10363, 2021.

[129] J. Wannapeera, N. Worasuwannarak, and S. Pipatmanomai, "Product yields and characteristics of rice husk, rice straw and corncob during fast pyrolysis in a drop-tube/fixed-bed reactor," *Songklanakarin Journal of Science and Technology*, vol. 30, no. 3, 2008.

[130] D. Dhaneswara, J. F. Fatriansyah, F. W. Situmorang, and A. N. Haqoh, "Synthesis of amorphous silica from rice husk

ash: comparing HCl and CH3COOH acidification methods and various alkaline concentrations," *International Journal of Technology*, vol. 11, no. 1, p. 200, 2020.

[131] R. A. Bakar, R. Yahya, and S. N. Gan, "Production of high purity amorphous silica from rice husk," *Procedia Chemistry*, vol. 19, pp. 189–195, 2016.

[132] B. Thongma and S. Chiarakorn, "Recovery of silica and carbon black from rice husk ash disposed from a biomass power plant by precipitation method," in *Proceedings of the IOP Conference Series: Earth and Environmental Science*, Malacca, Malaysia, August 2019.

[133] M. Hessien, M. Rashad, R. Zaky, E. Abdel-Aal, and K. El-Barawy, "Controlling the synthesis conditions for silica nanosphere from semi-burned rice straw," *Materials science and engineering: B*, vol. 162, no. 1, pp. 14–21, 2009.

[134] O. Olawale, "Bamboo leaves as an alternative source for silica in ceramics using Box Benhken design," *Scientific African*, vol. 8, Article ID e00418, 2020.

[135] A. Hassan, A. Abdelghny, H. Elhadidy, and A. Youssef, "Synthesis and characterization of high surface area nano-silica from rice husk ash by surfactant-free sol–gel method," *Journal of Sol-Gel Science and Technology*, vol. 69, no. 3, pp. 465–472, 2014.

[136] S. K. Deokar, S. A. Mandavgane, and B. D. Kulkarni, "Behaviour of biomass multicomponent ashes as adsorbents," *Current Science*, vol. 110, no. 2, pp. 180–186, 2016.

[137] Y. Alqaheem and A. A. Alomair, "Microscopy and spectroscopy techniques for characterization of polymeric membranes," *Membranes*, vol. 10, no. 2, p. 33, 2020.

[138] M. De, *Catalyst Science and Technology-Web Course*, NPTEL, Chennai, India, 2014.

[139] E. Rafiee, S. Shahebrahimi, M. Feyzi, and M. Shaterzadeh, Optimization of synthesis and characterization of nanosilica produced from rice husk (a common waste material)," *International Nano Letters*, vol. 2, no. 1, pp. 29–38, 2012.

[140] S. Yunusa, A. Ahmed, S. Bawa, J. Iyun, and M. Dauda, "Preparation of high grade silica from rice husk for zeolite synthesis," *Nigerian Journal of Basic and Applied Sciences*, vol. 24, no. 1, pp. 41–45, 2016.

[141] Z. Ma and F. Zaera, "Characterization of heterogeneous catalysts," *Surface and Nanomolecular Catalysis*, vol. 1, 37 pages, 2006.

[142] A. M. Zambrano Arévalo, G. C. Castellar, W. A. Vallejo Lozada, I. E. Piñeres Ariza, J. S. Valencia Ríos, and M. M. Cely Bautista, "Conceptual approach to thermal analysis and its main applications/Aproximación conceptual al análisis térmico y sus principales aplicaciones," *Prospect*, vol. 15, no. 2, pp. 117–125, 2017.

[143] D. F. Hincapié-Rojas, P. Pineda-Gomez, and A. Rosales-Rivera, "Synthesis and characterisation of submicron silica particles from rice husk," *Green Materials*, vol. 6, no. 1, pp. 15–22, 2018.

[144] S. A. Khan, S. B. Khan, L. U. Khan, A. Farooq, K. Akhtar, and A. M. Asiri, "Fourier transform infrared spectroscopy: fundamentals and application in functional groups and nanomaterials characterization," in *Handbook of Materials Characterization*, pp. 317–344, Springer, Berlin, Germany, 2018.

[145] P. E. Imoisili, K. O. Ukoba, and T.-C. Jen, "Green technology extraction and characterisation of silica nanoparticles from palm kernel shell ash via sol–gel," *Journal of Materials Research and Technology*, vol. 9, no. 1, pp. 307–313, 2020.

[146] S. J. Parikh, K. W. Goyne, A. J. Margenot, F. N. Mukome, and F. J. Calderón, Soil chemical insights provided through vibrational spectroscopy," *Advances in Agronomy*, vol. 126, pp. 1–148, 2014.

[147] L. B. Capeletti and J. H. Zimnoch, "Fourier transform infrared and Raman characterization of silica-based materials," *Applications of Molecular Spectroscopy to Current Research in the Chemical and Biological Sciences*, IntechOpen, London, SW, UK, 2016.

[148] A. A. Yaqoob, T. Parveen, K. Umar, and M. N. Mohamad Ibrahim, "Role of nanomaterials in the treatment of wastewater: a review," *Water*, vol. 12, no. 2, p. 495, 2020.

[149] A. Rajaeiyan and M. Bagheri-Mohagheghi, "Comparison of sol-gel and co-precipitation methods on the structural properties and phase transformation of γ and α-Al2O3 nanoparticles," *Advances in Manufacturing*, vol. 1, no. 2, pp. 176–182, 2013.

[150] H. J. Jung, H. Kwak, J. Chun, and K. K. Oh, Alkaline fractionation and subsequent production of nano-structured silica and cellulose nano-fibrils for the comprehensive utilization of rice husk," *Sustainability*, vol. 13, no. 4, p. 1951, 2021.

[151] H.-C. Fu, F. You, H.-R. Li, and L.-N. He, "CO2 capture and in situ catalytic transformation," *Frontiers in chemistry*, vol. 7, p. 525, 2019.

[152] Y. Wu and P. Li, "The potential of coupled carbon storage and geothermal extraction in a CO," *Geothermal Energy*, vol. 8, 2020.

[153] L. Xu, D. Zhu, X. Lu, and Q. Lu, "Transparent, thermally and mechanically stable superhydrophobic coating prepared by an electrochemical template strategy," *Journal of Materials Chemistry*, vol. 3, no. 7, pp. 3801–3807, 2015.

[154] H. Cao, S. Song and H. Cao, Strengthening of basalt fibers with nano-SiO2–epoxy composite coating," *Materials and Design*, vol. 32, no. 8-9, pp. 4180–4186, 2011.

[155] M. Alhawat, A. Ashour, and A. El-Khoja, "Properties of concrete incorporating different nano silica particles," *Materials Research Innovations*, vol. 24, no. 3, pp. 133–144, 2020.

[156] F. Sanchez and K. Sobolev, "Nanotechnology in concrete–a review," *Construction and Building Materials*, vol. 24, no. 11, pp. 2060–2071, 2010.

[157] Y. C. Flores, G. C. Cordeiro, R. D. Toledo Filho, and L. M. Tavares, "Performance of Portland cement pastes containing nano-silica and different types of silica," *Construction and Building Materials*, vol. 146, pp. 524–530, 2017.

[158] T.-H. Liou and C.-C. Yang, "Synthesis and surface characteristics of nanosilica produced from alkali-extracted rice husk ash," *Materials science and engineering: B*, vol. 176, no. 7, pp. 521–529, 2011.

[159] W. Zhao, J. Gu, L. Zhang, H. Chen, and J. Shi, "Fabrication of uniform magnetic nanocomposite spheres with a magnetic core/mesoporous silica shell structure," *Journal of the American Chemical Society*, vol. 127, no. 25, pp. 8916-8917, 2005.

[160] S. Shironita, K. Mori, T. Shimizu, T. Ohmichi, N. Mimura, and H. Yamashita, "Preparation of nano-sized platinum metal catalyst using photo-assisted deposition method on mesoporous silica including single-site photocatalyst," *Applied Surface Science*, vol. 254, no. 23, pp. 7604–7607, 2008.

[161] S. Montalvo-Quirós, S. Gómez-Graña, M. Vallet-Regí, R. C. Prados-Rosales, B. González, and J. L. Luque-Garcia, "Mesoporous silica nanoparticles containing silver as novel antimycobacterial agents against *Mycobacterium tuberculosis*," *Colloids and Surfaces B: Biointerfaces*, vol. 197, Article ID 111405, 2021.

[162] E. Soheyli, D. Azad, R. Sahraei, A. A. Hatamnia, A. Rostamzad, and M. Alinazari, "Synthesis and optimization of emission characteristics of water-dispersible ag-in-s quantum dots and their bactericidal activity," *Colloids and Surfaces B: Biointerfaces*, vol. 182, Article ID 110389, 2019.

[163] M. Manzano and M. Vallet Regí, "Mesoporous silica nanoparticles for drug delivery," *Advanced Functional Materials*, vol. 30, no. 2, Article ID 1902634, 2020.

[164] Y. Wang, Q. Zhao, N. Han et al., "Mesoporous silica nanoparticles in drug delivery and biomedical applications," *Nanomedicine: Nanotechnology, Biology and Medicine*, vol. 11, no. 2, pp. 313–327, 2015.

[165] V. Tyagi, S. Pandit, A. Sharma, and R. K. Gupta, "Extraction and characterization of silica from rice husk for use in food industries," *Extraction*, vol. 2, no. 4, 2017.

[166] J. F. Ma and N. Yamaji, "Silicon uptake and accumulation in higher plants," *Trends in Plant Science*, vol. 11, no. 8, pp. 392–397, 2006.

[167] P. Bowen, J. Menzies, D. Ehret, L. Samuels, and A. D. Glass, "Soluble silicon sprays inhibit powdery mildew development on grape leaves," *Journal of the American Society for Horticultural Science*, vol. 117, no. 6, pp. 906–912, 1992.

[168] J. Menzies, P. Bowen, D. Ehret, and A. D. Glass, "Foliar applications of potassium silicate reduce severity of powdery mildew on cucumber, muskmelon, and zucchini squash," *Journal of the American Society for Horticultural Science*, vol. 117, no. 6, pp. 902–905, 1992.

[169] H. Song, W. Yuan, P. Jin et al., "Effects of chitosan/nano-silica on postharvest quality and antioxidant capacity of loquat fruit during cold storage," *Postharvest Biology and Technology*, vol. 119, pp. 41–48, 2016.

[170] S. H. Othman, "Bio-nanocomposite materials for food packaging applications: types of biopolymer and nano-sized filler," *Agriculture and Agricultural Science Procedia*, vol. 2, pp. 296–303, 2014.

[171] J.-W. Rhim, H.-M. Park, and C.-S. Ha, "Bio-nanocomposites for food packaging applications," *Progress in Polymer Science*, vol. 38, no. 10-11, pp. 1629–1652, 2013.

[172] S. Miri, V. S. Raghuwanshi, P. C. Andrews, and W. Batchelor, "Composites of mesoporous silica precipitated on nanofibrillated cellulose and microfibrillated cellulose: effect of fibre diameter and reaction conditions on particle size and mesopore diameter," *Microporous and Mesoporous Materials*, vol. 311, Article ID 110701, 2021.

[173] T. Yamauchi, T. Saitoh, K. Shirai, K. Fujiki, and N. Tsubokawa, "Immobilization of capsaicin onto silica nanoparticle surface and stimulus properties of the capsaicin-immobilized silica," *Journal of Polymer Science Part A: Polymer Chemistry*, vol. 48, no. 8, pp. 1800–1805, 2010.

[174] A. Azimi, A. Azari, M. Rezakazemi, and M. Ansarpour, "Removal of heavy metals from industrial wastewaters: a review," *ChemBioEng Reviews*, vol. 4, no. 1, pp. 37–59, 2017.

[175] B. Merzouk, M. Yakoubi, I. Zongo et al., "Effect of modification of textile wastewater composition on electrocoagulation efficiency," *Desalination*, vol. 275, no. 1-3, pp. 181–186, 2011.

[176] F. Fu and Q. Wang, "Removal of heavy metal ions from wastewaters: a review," *Journal of Environmental Management*, vol. 92, no. 3, pp. 407–418, 2011.

[177] T. Motsi, N. Rowson, and M. Simmons, "Adsorption of heavy metals from acid mine drainage by natural zeolite," *International Journal of Mineral Processing*, vol. 92, no. 1-2, pp. 42–48, 2009.

[178] X. Yang, Z. Shen, B. Zhang et al., "Silica nanoparticles capture atmospheric lead: implications in the treatment of environmental heavy metal pollution," *Chemosphere*, vol. 90, no. 2, pp. 653–656, 2013.

[179] F. Akhter, S. Soomro, M. Siddique, and M. Ahmed, "Plant and non-plant based polymeric coagulants for wastewater treatment: a review," *Jurnal Kejuruteraan*, vol. 33, no. 2, pp. 175–181, 2021.

[180] M. Sibag, B.-G. Choi, C. Suh et al., "Inhibition of total oxygen uptake by silica nanoparticles in activated sludge," *Journal of Hazardous Materials*, vol. 283, pp. 841–846, 2015.

[181] S. Park, Y.-S. Ko, H. Jung, C. Lee, K. Woo, and G. Ko, "Disinfection of waterborne viruses using silver nanoparticle-decorated silica hybrid composites in water environments," *Science of the Total Environment*, vol. 625, pp. 477–485, 2018.

[182] E. Rafiee, S. Shahebrahimi, M. Feyzi, and M. Shaterzadeh, "The potential of rice husk ash for silica synthesis as a semiconductor material for monocrystalline solar cell: a review," in *Proceedings of the IOP Conference Series: Earth and Environmental Science*, Malang, Indonesia, August 2021.

[183] F. C. Lanning and T. Garabedian, "The effect of chemical treatment on the production of active silica from rice husk 18th international mining congress and exhibition of Turkey-IMCET," *Earth Environ. Sci*, vol. 733, 1963.

[184] A. Blakers, N. Zin, K. R. McIntosh, and K. Fong, "High efficiency silicon solar cells," *Energy Procedia*, vol. 33, pp. 1–10, 2013.

Hindawi
Advances in Materials Science and Engineering
Volume 2023, Article ID 2708776, 10 pages
https://doi.org/10.1155/2023/2708776

Research Article

Performance of Polymer Composite Constituted Cabinet Dryer Integrated within a Solar Flat Plate Collector

S. Raj Sachin,[1] **Anton M. Kuzmin**,[2,3] **Subramanian Krishnakumar**,[4] **Anandhan Jayaganthan**,[5] **and Yesgat Admassu**[6]

[1]*Department of Mechanical Engineering, Sanjivani College of Engineering, Kopargaon, Maharashtra 423603, India*
[2]*Department of Mechanization of Agricultural Products Processing, Ogarev Mordovia State University, Saransk 430005, Russia*
[3]*Plekhanov Russian University of Economics, 36, Stremyanny Ln, Moscow 117997, Russia*
[4]*Department of Mechanical Engineering, Gnanamani College of Technology, Namakkal, Tamilnadu 637018, India*
[5]*Department of Automobile Engineering, Sathyabama Institute of Science and Technology, Chennai, Tamilnadu 600119, India*
[6]*Defence University College, Bishoftu, Ethiopia*

Correspondence should be addressed to Yesgat Admassu; yesgat.admassu@dec.edu.et

Received 19 October 2022; Revised 8 December 2022; Accepted 4 April 2023; Published 20 April 2023

Academic Editor: Pudhupalayam Muthukutti Gopal

Generally, solar dryer cabinets are made up of sheet metals that are heavy, costly, tend to rust over time, and possess the high heat rate to the outer atmosphere. In order to overcome these drawbacks, this research urges to develop a natural fiber reinforced polymer-based cabinet dryer, specially designed and fabricated for the purpose of solar drying. Nylon is used as the matrix material and *Prosopis juliflora* in particulate form is used as the natural fiber reinforcement. The dryer cabinet was designed at industrial scale to dry 5 kg of ginger at a single setting. This work also studies the efficiency of the polymer composite cabinet integrated with a flat plate solar collector system that is coated with copper and black chrome attached to corrugated fins in between the absorber plate and storage medium. The FRP chamber was compartmented in its interior with aluminium perforated sheets and experimentation was performed to determine the efficiency of the composite cabinet based on reduction of heat loss from the system. The performance of the coating, storage medium materials, and overall storage efficiency were also studied. The FRP cabinet resulted in a moisture level less than 8.5% within 4–7 days. Exergy studies showed 75% efficiency and energy studies gave 25.5 kJ/kg peak readings of drying efficiency for a period ranging between 11 and 12 hours. This was a 75% increment in energy efficiency. Thermal degradation of the FRP material was found to be stable up to 300°C. The overall weight of the constructed polymer cabinet was 25% lesser than the conventional systems.

1. Introduction

Ginger is a popular spice and cash crop all over the world. India, China, Japan, Nigeria, and Indonesia are among the countries that grow it. India is the world's greatest producer and consumer of ginger, accounting for 32.75 percent of global output [1]. The consumption pattern shows that green ginger is used 50% of the time, dry ginger is used 30% of the time, and seed materials are used just 20% of the time. Dried ginger has a large market and is exported due to its medicinal characteristics, which are used to cure stomach aches, nausea, indigestion, asthma, and other ailments [2]. To avoid waste due to microbial and fungal attacks, the economically valuable spice must be dried effectively to achieve a very low moisture content. Drying has traditionally been crucial for preserving agricultural products and extending the shelf life of food [3]. Drying different food products can be carried out in a variety of ways. The traditional open-air drying method has a number of drawbacks. For limiting product deterioration and reducing drying time, numerous energy-based dryers are available. Due to the increasing cost of energy, traditional dryers and drying procedures are not cost effective [4, 5]. Drying has become an energy-intensive and unaffordable practice for farmers due to diminishing fossil fuel supplies and rising costs [6].

FRPs when compared with metals, avoid heat transfer to a greater extent. Polymer composites are sustainable and can be recycled during the end of their service life [7]. They also tremendously help in weight reduction when compared with the existing metal-based structures for solar dryers. Their ability to avoid rusting unlike metals and their inability of undergoing chemical reaction with the product that is to be dried or the fragments and evaporated vapours that are developed by the drying process makes them a significant material to be considered for the proposed application. The natural fiber reinforced plastics provide the cheapest method for fabricating FRPs [8]. Their strength to weight ratio has fascinated researchers to utilize them in versatile applications. Various natural fibers have also been studied for their heat transfer analysis [9]. *Prosopis juliflora* (PJ) is one of the very successful natural wood fibers that has proven high thermal stability and good mechanical character. Previous studies depict that PJ wood has very low moisture absorbance tendency, high thermal stability, and is also a very cheap source of reinforcement [10, 11]. Among the various sizes of natural fibers long, short, and powdered, the small-sized fibers have proven to show better thermal stability which is a key factor to the application that the composite in this research work is being developed for. Hence this research considers PJ as the reinforcement material in the particulate form. Table 1 portrays the chemical configuration of *Prosopis juliflora* natural wood fibers.

Various polymers in literature surveys have been developed by combining natural fibers for thermal-based applications to resist heat transfer. Nylon is selected in this research due to its complex polymeric structure giving it its rugged construction. It is one of the promising polymers that can withstand high temperatures and provides excellent abrasion and good work life [12]. These properties of nylon and PJ ensure a promising output. This project work is one of the first attempts made to fabricate a FRP-based composite cabinet dryer for the purpose of drying agricultural food products. This research examines the reduction of heat loss in the cabinet dryer chamber, the economic feasibility of the developed FRP cabinet, and experimental analysis to evaluate the performance for drying ginger targeting suitability for medium scale farmers and MSMEs. Mechanical properties of biodegradable film based polymers with natural fiber reinforcements have also proven to have shown outstanding performance along with thermal stability and thermal degradation characteristics [13–15].

Natural fiber reinforced composite materials are processed in many different methods based on the end application they are developed for [16]. Among the various methods of processing of polymers such as hand-layup, injection moulding, compression moulding, and in situ, large-sized slabs are found to be best produced using the compression moulding technique especially when natural fiber reinforcements are taken into consideration [17]. McHenry and Stachurski [18] have previously worked with nylon-reinforced eucalyptus wood fibers to fabricate a composite material specifically designed for a fluidized bed for mixing and moisture control applications. Reinforcement quantities of the wood fibers at 2.5, 5, and 7.5 wt % were considered amongst which the 2.5 wt% wood powder reinforced nylon composite had resulted with the highest mechanical characteristics. Morphological characterization had shown excellent adhesion of the wood fibers to the nylon polymer. Thermal degradation of the wood was initially at 120°C which had a drastic improvement of upto 230°C after it was melt mixed into a composite with nylon. A hot press was used to fabricate the composite slabs which resulted in excellent bonding of the matrix and reinforcement materials. Aydemir et al. [19] worked with Nylon 6 reinforced pine wood fibers and maple wood fibers individually to form composites for the automobile industry relating to hood fabrication applications. A 60# mesh size was used to obtain even sized wood particles which were reinforced into nylon at weight ratios of 5, 10, 20, and 30%. Heat-treated wood fibers and untreated wood particles were analysed during the study. Composite compounding followed by the injection moulding technique was followed for the fabrication of the composite specimens. TGA carried out on the composites showed a minimum thermal stability of 200°C for the untreated fibers and higher values for the heat-treated fiber-reinforced composites. Although rheological studies showed that the viscosity of the 20 wt% reinforced composites were very high, the mechanical properties were found to be best for the 20 wt% wood fiber-reinforced nylon composites for both the cases of pine wood and maple wood fibers.

The cabinet dryer is the most practically used space in a solar dryer system for drying farm products. Higher heat retention and low heat transfer from the outer atmosphere and vice versa should be maintained for greater efficiency of the dryer. These factors leads us to the practical thinking of FRP-based composites as an alternative for conventional metal-based walls of the dryer cabinet due to their extensive property of heat transfer resistance between mediums [6, 7]. In this research work, drying of ginger was undertaken to study and investigate the performance of the integrated composite cabinet with a solar flat plate collector.

2. Methodology

2.1. Experimental Design. The solar collector was fabricated to the following dimensions: 750 mm length, 450 mm width, and 180 mm·height; the dimension of the absorber plate was 700×400 sq·mm and 0.8 mm thick [14]. The schematic representation of the solar flat plate collector with a black chrome coated absorber plate is shown in Figure 1. A diverging portion is given at the collector's entry to allow consistent air transmission over the absorber plate, and a convergent pipe with a size of 125 mm length and 45 mm width was used to connect the collector and the drying chamber composite cabinet. The diagrammatical model of the complete setup connecting the dryer solar plate and the composite cabinet tower is represented in Figure 2.

A primary solar collector (0.75×0.45) m is positioned on top of the dryer, which is protected by a transparent glass cover. Forced convection provides fresh air, which is heated as it passes through the solar collector on its way to the drying chamber. It permits solar rays into the drying

Table 1: Chemical configuration of *Prosopis juliflora* natural wood fibers.

Plant/wood fibres	Cellulose (wt%)	Hemicellulose (wt%)	Lignin (wt%)	Wax (wt%)
Prosopis juliflora	61.65	16.14	17.11	0.61

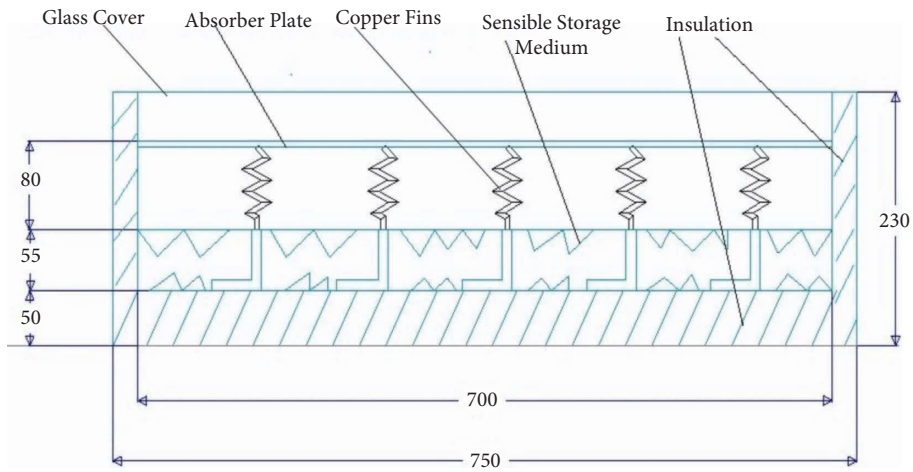

Figure 1: Design of the solar collector plate.

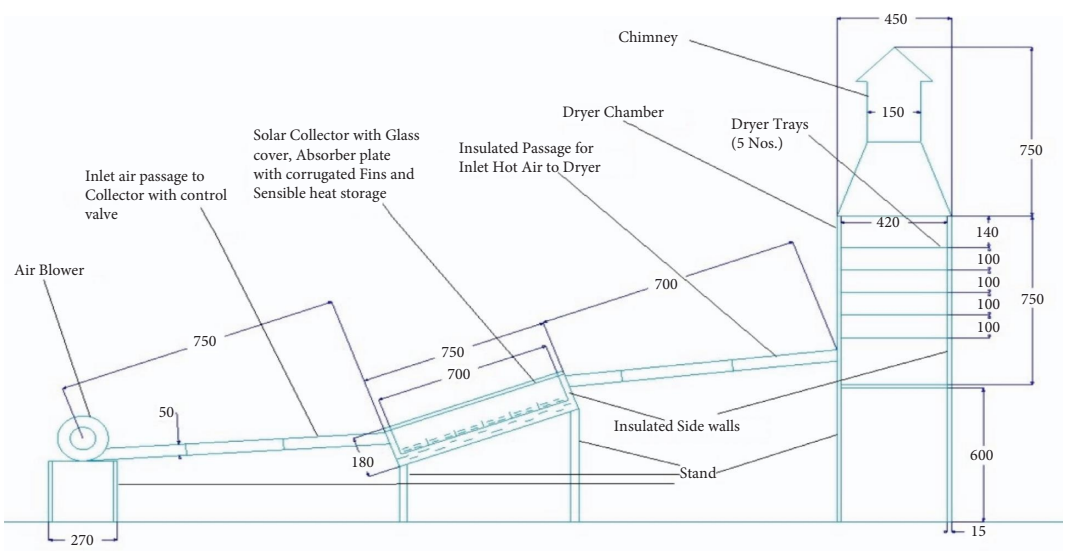

Figure 2: Schematic diagram of the complete experimental setup with the integrated composite dryer unit.

chamber, which speeds up the drying process due to the greenhouse effect. The dimensions of the composite drying chamber are 750 mm height and 450 mm width. Five trays at a distance of 100 mm each were designed and placed at equal intervals inside the composite chamber to facilitate loading of the food products. To allow for improved air circulation, the drying tray comprises of aluminium perforated sheets with a surface area of 380×380 sq·mm. On the sample holding mesh trays, ginger slices (5 kg each batch) with a moisture content of 621.5 percent d.b. were equally distributed. With an electronic balance scale, the weight of the material was carefully measured at predetermined time intervals to analyse the drop in mass due to dehydration. A PT-100 sensor thermocouple with an accuracy of 0.5°C was used to measure the temperature of the air at the inlet and outlet of the solar collector at regular time intervals. The composite dryer cabinet made of fiber-reinforced plastic (FRP) had a wall thickness of 10 mm. All direct experimental data that were noted manually and using sensors were tabulated and then provided as input to the Origin 8 version software to obtain precision graphical representations of the results.

2.2. Fabrication of the FRP Cabinet Material. Nylon 66 was obtained from the Central Institute of Plactic Engineering Technology at Hyderabad in India. The nylon was in tiny granular form in its virgin state. It had a specific gravity of

1.14 grams/cc and a melting point of 223°C as denoted by the supplier. PJ wood was initially obtained from Namakkal district in Tamil Nadu, India, and the wood was dried in a furnace at 80°C for 48 hours to get rid of moisture in the fibrils. Then, the wood was sized down using machinery as performed in previous experimental works by the authors [10, 15] and finally sieved using a 400# mesh size to obtain the equally sized fine powder. The powdered PJ was initially dry mixed with nylon granules in calculated weight fraction ratios of 80 : 20. The literature records that 20 wt% reinforcement of natural fiber particles into polymers deliver composites with the best mechanical character [8, 11]. Then, the dry mixed materials were blended using a twin screw extruder at 240°C and a rotary screw speed of 100 rpm. This process ensured that the nylon and the PJ fiber were blended with each other completely and were obtained in the form of composite pellets. These composite pellets were then placed in the compression moulding machine and fabricated into large slabs of dimensions 750 × 450 mm and uniform thickness of 10 mm. The compression moulding process was performed at a pressure of 6 bar and a temperature of 240°C for a period of 12 hours. The final product was then constructed into the outer layer walls of the drying cabinet using mechanical fixtures. Test specimens of the fabricated composite material were cut from the large slabs and were tested for thermal stability using thermogravimetric analysis (TGA) [15] and the water absorption rate to ASTM D570 [20].

2.3. Experimental Calculations

2.3.1. Determination of the Moisture Content of Ginger. The formulae used to calculate the wetness of ginger using the solar dryer system are tabulated in Table 2 and represented through equations (1–6). Physical errors such as fixed errors, manufacture errors, and random errors were considered while other parametric errors such as relative humidity, moisture loss, weight loss, solar intensity, and air velocity errors were also considered during the experimental phase.

2.3.2. Economic Analysis. Any system's economic viability is determined by doing an economic study of the system. It is critical to determine whether a new technology is economically viable before it can be successful and commercialized. In this study, a variety of economic variables were utilised to assess the economics of a hybrid sun-drying system. The total capital cost (C0) of the designed system is calculated using equation (7) [27]. The parameters and their respective formulae that were considered for the economic analysis of the drying system are tabulated in Table 3 and are represented thorough equations (8)–(10).

$$\text{CO} = \text{cost of materials used for fabrication of system} + \text{labour cost} \quad (7)$$

In Table 3, C0 is the fabricated dryer's capital cost in rupees, t is the dryer's life span (year), P is the daily benefits gained from the dryer in rupees, n is the number of days of operation per year (day), R is the repair and maintenance cost in rupees, and D is the discount rate (%).

3. Results and Discussion

The curve of dryer efficiency during drying is shown in Figure 3. The range of dryer efficiency during drying ginger was in the range of 4.16–46.72%, respectively. The average dryer efficiency of dried ginger was 28.96%, respectively. It can be seen that using higher drying temperature would increase the dryer efficiency. This happens because higher drying temperature used will generate more heat, which will increase the moisture uptake by drying air and speeds up the drying process. This will increase the dryer efficiency [28]. This research showed results that coincide with few previous studies. A solar LPG hybrid dryer applied for drying shrimps where the dryer efficiency was varied from 24.21 to 37.09%, with the average value of 29.93% [29]. A second study used cassava as the product to be dried. The dryer efficiency was found to be 30% with an increase from 16%. Drying temperature was increased from 40°C to 60°C [28, 29]. Another study reported an average dryer efficiency value of 27.1% during seaweed drying using a solar tray dryer [30].

3.1. Quality of Dried Ginger. Four quality parameters of dried ginger were tested in this experiment based on the following criterion: aroma test, fat content, ash content, and presence of moulds and insects during storage. During the quality test, there were no changes in aroma of the dried ginger. Also, no mould formation or insects was seen to develop and the nil traces of fungal formation were endured during storage of dried ginger. Both the fat and ash content of dried ginger have satisfied the range of their respective standard value. The fat content decreases with higher temperature (4.46% to 2.73%, for 40 to 60 degree, respectively). This happens because higher temperature will tend to deactivate the enzymes, thus halting the production of volatile fatty compounds and reducing the fat content [31]. However, drying helps to conserve the bioactive compounds and unsaturated fatty acids which are more adequate for consumption [32]. The drying behaviour of ginger was achieved maximum between 12 pm and 2 pm where the hot air was set at 60°C. The highest temperature recorded was 61°C. The moisture content of ginger decreased drastically with increased drying time and reached a constant value after due course of time.

3.2. Energy and Exergy Analysis. As incurred from the first law of thermodynamics, energy gain and energy utilised were estimated for the solar collector system, while exergy data were interpreted relating the second law of thermodynamics to govern the type of exergy losses, magnitude and the location during the drying process. Exergy loss was seen to be dominant at the final trays due to the low utilization of the available energy. Despite the energy utilization ratio and exergy efficiency of drying ginger varied from 15.3 to 25.4 kJ/kg and 57.5 to 78.95%, and the ginger was sufficiently dried between the temperature ranges of 40°C–60°C and

Table 2: Formulae used to calculate the wetness of ginger using the solar dryer system.

Equation number	Description/parameters	Formulas	References
(1)	The initial moisture content (M), m_i represents the mass of wet ginger in (g) and m_d represents the mass of dry ginger (g)	$M = (m_i - m_d/m_i) \times 100$	[21–24]
(2)	The amount of water content (W) removed	$W = M_i - M_f/100 - M_f \times W_o$	[21–24]
(3)	Instantaneous moisture content Mt is calculated for time '*t*'	$M_t = [((M_t + 1)W_t/W_o) - 1]$	[21–24]
(4)	The moisture ratio MR	$\mathrm{MR} = ((M_t - M_e)/(M_i - M_e))$	[21–24]
(5)	Since equilibrium moisture (Me) is very less compared to initial moisture	$\mathrm{MR} = (M_t/M_i)$	[25]
(6)	Drying system efficiency is a measure of a drying system's overall efficacy, indicating how well the input energy is used to dry the product; the energy usage for the blower can be used to calculate the forced convection dryer efficiency	$\eta_d = (\mathrm{WL}/A_s I + P_f)$	[26]

Table 3: Formulae used for the economic analysis of the drying system.

Equation number	Description/parameters	Formulas	References
(8)	Net worth (NW) of the drying system	$\eta_d = (\mathrm{np} - \mathrm{co}\alpha/d)\,((1+d)^t - 1/1+d)$	
(9)	Benefit-cost ratio	$\mathrm{BCR} = (\text{total benefit received per year/capital cost developed system})$	[26, 27]
(10)	Payback period (PP)	$\mathrm{PP} = (\mathrm{co}/(\mathrm{np} - \alpha\mathrm{co}))$	

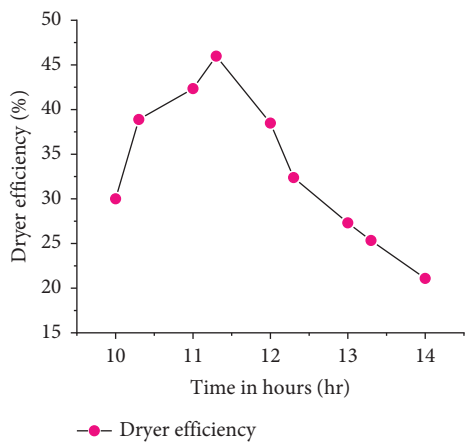

Figure 3: Dryer efficiency curve for drying ginger.

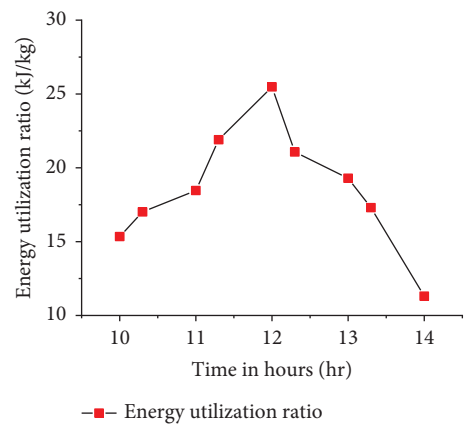

Figure 4: Variation of the energy utilization ratio with the dehydrating period.

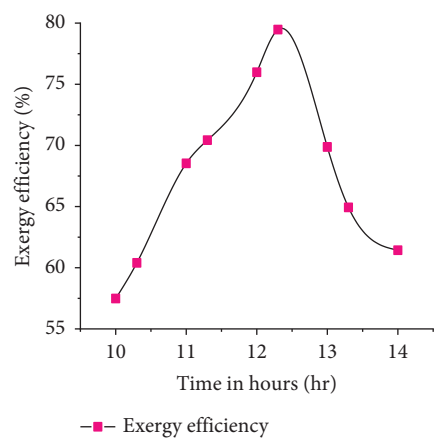

Figure 5: Variation of exergy efficiency with the dehydrating period.

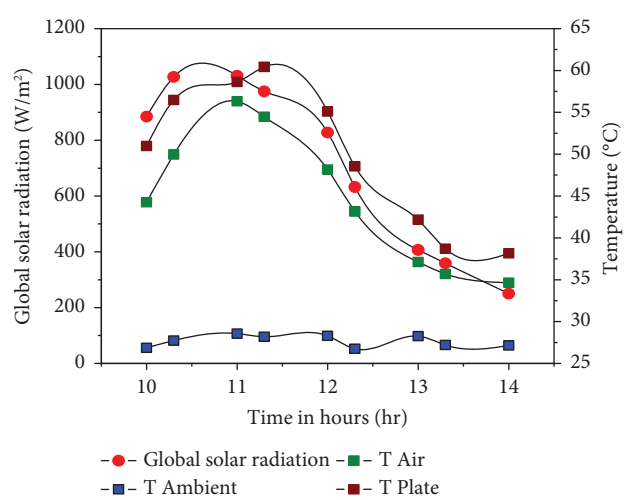

Figure 6: The profiles of temperature and solar intensity during solar drying of ginger.

36°C–63°C at a relative humidity of 1.243 m/s and an air flow time of 6 hours [33]. The reduced sun radiation during the evening hours was not taken into consideration since the literature states that the efficiency of the dryer cabinet since preheating using coarse aggregates help in reducing the heat loss. Hence, the exergy performance quantifies the energy loss in the solar-based system that is still based on the second law of thermodynamics. The energy and exergy performances are graphically depicted in Figures 4 and 5, respectively.

3.3. Economic Analysis of the Developed System. The created dryer's economic analysis and related factors are based on India's economic circumstances. For ginger drying, a cost-benefit analysis was conducted using the annualised cost technique. 5 kilograms of ginger took 6 hours to dry in a solar dryer. On a clear sunny day, 5 hours of drying time is available on average. For a year, 200 days were counted as clear sunny days. The solar dryer's capital cost is estimated to be Rs. 30,000. The solar dryer's annual repair and maintenance costs are calculated at 5% of the annual capital cost. Drying cost for 5 kg of ginger with a solar dryer was estimated to be Rs. 61 per day. In season, raw ginger costs Rs. 20 per kilogram. The amount of electricity required to dry 5 kg of ginger is 1.5 units. Dried ginger is worth Rs. 160 on the market, and the daily benefit from drying is Rs.77. The annual cost of a specially developed drying system for ginger is Rs. 21,700. The benefit-to-cost ratio of the solar dryer that was designed was found to be 2.41. The cost-benefit ratio was computed. The developed FRP cabinet dryer had a payback period of only 6 months. When compared with the conventional solar-drying hybrid system, the payback period is short. As a result, FRP solar drying systems are cost effective. The usage of a solar dryer cut the drying time in half. It can be seen from Figure 6 that the ambient temperature varied from 26 to 28.96°C while the solar intensity varied between 721.54 and 1027.72 W/m^2, with the average of 780.13 W/m^2.

Ginger drying was tested for thermal performance and drying qualities. The moisture content of ginger decreased from 83.3% to 10.41%, respectively, all on wet basis as shown Figure 7. The similar equilibrium moisture content results were reported by several research work on potatoes [34], tomatoes [35], bananas [36], and cucumbers [37]. The net benefit, benefit-to-cost ratio, and payback duration were

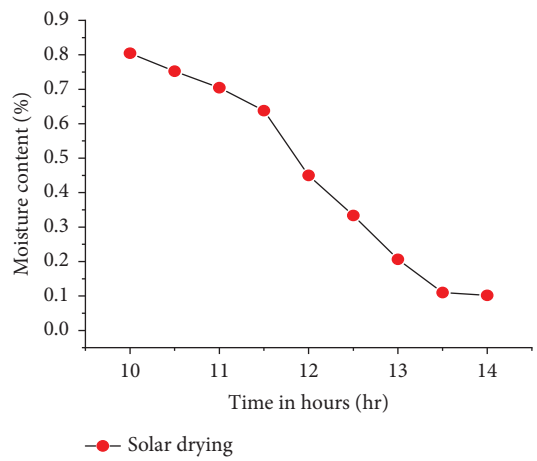

Figure 7: Drying characteristics of ginger with respect to drying time.

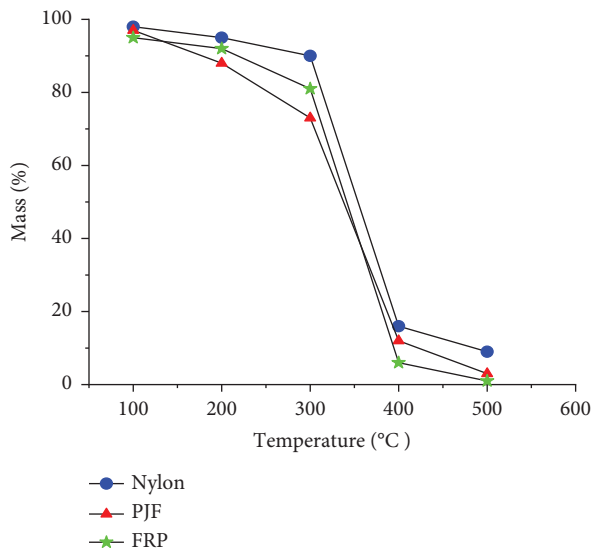

Figure 8: TGA curves of the cabinet dryer materials.

calculated using economic analysis and it proved the devices' economic viability.

3.4. Thermal Properties of the FRP. A minor amount consisting of a 50 milligram sample was taken from the developed composite material to carry out the thermal studies. The specimen was placed in the crucible of a thermogravimetric analyzer apparatus of Model: S11TG/DTA 6300 for analysing the thermal stability, thermal degradation initiation and progression, and the complete degradation with postresidue. All the properties of the specimens were analysed while maintaining the inner equipment environment with nitrogen gas. The variation of temperature was set at an increment rate of 5°C per minute. The testing was performed between the temperature range initiating from 20°C upto a maximum limit of 500°C [38]. Thermal stability of the composite was checked in comparison with plain nylon polymers as well as plain PJF wood powder. The thermal degradation of nylon was highest and addition of PJ wood powder as reinforcement acting like a thermal barrier similar to a ceramic wool reinforcement in an exhaust system [39]. Significant amount of thermal stability increment was noticed which was calculated to be sufficient enough for the described application. The maximum temperature of thermal stability of the composite material was 200°C beyond which marginal degradation showed reduction in a mass of the composite upto 80%. Further increment in the temperature showed abrupt degradation turning the mass of the composite from 80% to 10% at 400°C. Beyond this point minimal residue of the composite was found. The TGA curves are depicted in Figure 8.

Thermal properties of the FRP as tabulated in Table 4 were analysed. Thermal properties were found to be suitable at the maximum internal temperature held within the solar cabinet during the experimental phase when compared to other conventionally used materials. Hence while using the FRP walled cabinet dryer, it is not necessary to provide an additional layer of glass wool, which is a common practice followed while using sheet metal based dryer cabinets. Water

Table 4: Thermal properties of the PJ-reinforced nylon FRP composite.

Thermal conductivity	Melting point	Maximum service temperature	Vicat softening point	Thermal degradation
0.200–0.330 W/m-K	200–240°C	80–210°C	150–260°C	320°C

absorption carried out to ASTM D570 for a period of 24 hours showed a negligible absorption rate of 0.06%. This was due to the natural tendency of the fiber to absorb moisture.

4. Conclusion

(i) The thermal efficiency of the FRP cabinet dryer was found to be 12% more efficient than the conventional metal sheet based cabinet models and had an overall weight reduction of the equipment by 25%. The polymer cabinet dryer is one of the most hygienic and eco-friendly process.

(ii) Metal-based dryers can harm the food source due to toxicity that appears by reaction of chemicals between the metal and the ginger juice; it makes the food material less appetizing. This is prevented when the polymer cabinet is used as an alternative. It is also an economical and sustainable method of drying.

(iii) It can be concluded that the solar drying method introduced in this study is suitable for ginger as well as other food materials and much faster compared to other conventional methods, while still able to maintain the quality of product. The developed FRP cabinet dryer is more suitable to dry the agricultural products and it is environment friendly in terms of avoiding harmful gaseous reactions that may be emitted by the food products or the conventional sheet metal glass wool method. It is also found to be more economical and lighter in weight when compared with conventional solar dryer cabinets.

(iv) It was found that final moisture content of ginger dried between 40 and 60°C gives the best result. However, the maximum drying was achieved between 11 and 12 hours, which is much faster than other ginger-drying studies using other types of dryers. It is assumed that ginger drying takes place primarily during the falling rate period, as evidenced by the decreasing value of the drying rate over time.

(v) It was seen that the solar drying system made up of nylon and PJ combined composite reduces heat loss and does not affect the aroma of ginger. The exergy efficiency of the dryer varied from 19.1% to 78.8%. The overall energy efficiency of the dryer was 73.6% through which observations showed that 1000 grams of ginger had been efficiently reduced by mass weight to 369.77 grams after the drying period. This is considerably as effective as the heavy and costly metal-based dryers.

(vi) Energy values showed a peak at 26°C at a 12 hour time duration and exergy peaked at 80% for the respective time duration. Economic analysis revealed a benefit-to-cost ratio of 2.41. This proved increased energy savings for a calculated period of 6 months.

(vii) Thermal stability of the nylon-PJ composite material was stable upto 310°C beyond which degradation stated and the complete degradation took place at 400°C leaving behind a 5% residue at 500°C. This proves that the material is optimally suitable for the application that it was developed for.

Data Availability

All the data used to support the findings of this study are included within the article.

Conflicts of Interest

The authors declare that they have no conflicts of interest.

References

[1] R. K. Aggarwal, "Indirect solar drier for drying of hill products," *Assian Journal of Agriculture and Rural Development*, vol. 2, no. 2, pp. 201–205, 2012.

[2] A. R. Sundari Umyal, P. Neelamgam, and C. V. Subramanian, "Study and analysis of drying characteristics of ginger using solar drier with evacuated tube collectors," *Research Journal of Pharmaceutical, Biological and Chemical Sciences*, vol. 4, no. 3, pp. 1258–1267, 2013.

[3] I. Doymaz, "Air-drying characteristics of tomatoes," *Journal of Food Engineering*, vol. 78, no. 4, pp. 1291–1297, 2007.

[4] G. Gurlek, N. Ozbalta, and A. Gung, "Solar tunnel drying characteristics and mathematical modelling of tomato," *Journal of Thermal Science and Technology*, vol. 29, no. 1, pp. 15–23, 2009.

[5] M. Babu, S. S. Raj, and A. Valan Arasu, "Experimental analysis on Linear Fresnel reflector solar concentrating hot water system with varying width reflectors," *Case Studies in Thermal Engineering*, vol. 14, Article ID 100444, 2019.

[6] M. Babu, P. Sekhar Babu, S. S. Raj, and S. Saravanan, "Theoretical design, material study and material selection for compact linear Fresnel reflector concentrating system," *Materials Today: Proceedings*, vol. 45, no. 1, pp. 1671–1678, 2021.

[7] S. S. Raj, "Wood Plastic composite processing and mechanical characteristics – a brief literature review. Lecture notes in mechanical engineering," *Recent Advances in Manufacturing, Automation, Design and Energy Technologies*, pp. 269–276, Springer, Singapore, 2021.

[8] S. S. Raj, T. K. Kannan, M. Babu, and M. Vairavel, "Processing and testing parameters of PLA reinforced natural plant fiber composite materials – a Brief review," *International Journal of Mechanical and Production Engineering Research and Development*, vol. 9, no. 2, pp. 933–940, 2019.

[9] H. Takagi, A. Nakagaito, and K. Liu, "Heat transfer analyses of natural fibre composites," *WIT Transactions on The Built Environment*, vol. 137, pp. 237–243, 2014.

[10] S. S. Raj, T. K. Kannan, and R. Rajasekar, "Influence of *Prosopis Juliflora* wood flour in poly lactic acid- developing a novel bio- wood plastic composite," *Polímeros*, vol. 30, no. 1, Article ID e2020012, 2020.

[11] S. S. Raj, T. K. Kannan, M. Kathiresan, K. Balachandar, and S. Krishnakumar, "Why not stir casting for polymer composites? Investigations on Poly Lactic Acid based wood plastic composite," *Materials Today: Proceedings*, vol. 45, pp. 862–868, 2021.

[12] K. S. Randhawa and A. D. Patel, "A review on tribo-mechanical properties of micro- and nanoparticulate-filled nylon composites," *Journal of Polymer Engineering*, vol. 41, no. 5, pp. 339–355, 2021.

[13] M. K. Anton, A. S. Alexander, and S. R. Sachin, "Investigation of the orientational mechanical properties of biodgradable extrusion films based on polyolefins and beet pulp," *Materials Research Proceeding*, vol. 21, pp. 144–149, 2022.

[14] M. Augustus Leon, S. Kumar, and S. C. Bhattacharya, "A comprehensive procedure for performance evaluation of solar food dryers," *Renewable and Sustainable Energy Reviews*, vol. 6, no. 4, pp. 367–393, 2002.

[15] S. R. Sachin, T. K. Kannan, and R. Rajasekar, "Effect of wood particulate size on the mechanical properties of PLA bio-composite," *Pigment & Resin Technology*, vol. 49, no. 6, pp. 465–472, 2020.

[16] A. Gholampour and T. Ozbakkaloglu, "A review of natural fiber composites: properties modification and processing techniques, characterization, applications," *Journal of Materials Science*, vol. 55, no. 3, pp. 829–892, 2020.

[17] A. Lotfi, H. Li, D. V. Dao, and G. Prusty, "Natural fiber–reinforced composites: a review on material, manufacturing, and machinability," *Journal of Thermoplastic Composite Materials*, vol. 34, no. 2, pp. 238–284, 2021.

[18] E. McHenry and Z. H. Stachurski, "Composite materials based on wood and nylon fibre," *Composites Part A: Applied Science and Manufacturing*, vol. 34, no. 2, pp. 171–181, 2003.

[19] D. Aydemir, A. Kiziltas, E. Erbas Kiziltas, D. J. Gardner, and G. Gunduz, "Heat treated wood-nylon 6 composites," *Composites Part B: Engineering*, vol. 68, pp. 414–423, 2015.

[20] S. S. Raj, K. A. Michailovich, K. Subramanian, S. Sathiamoorthyi, and K. T. Kandasamy, "Philosophy of selecting ASTM standards for mechanical characterization of polymers and polymer composites," *Materiale Plastice*, vol. 58, no. 3, pp. 247–256, 2021.

[21] E. Elangovan and S. K. Natarajan, "Experimental research of drying characteristics of red banana in a single slope solar dryer based on natural and forced convection," *Food Technology and Biotechnology*, vol. 59, pp. 1–28, 2015.

[22] E. Elangovan and S. K. Natarajan, "Experimental study on drying kinetics of ivy gourd using solar dryer," *Journal of Food Process Engineering*, vol. 44, pp. 1–39, 2021.

[23] E. Elangovan and S. K. Natarajan, "Effect of pretreatments on drying of red dacca in a single slope solar dryer," *Journal of Food Process Engineering*, vol. 44, Article ID e13823, 2021.

[24] E. Elangovan and S. K. Natarajan, "Effects of pretreatments on quality attributes, moisture diffusivity, and activation energy of solar dried ivy gourd," *Journal of Food Process Engineering*, vol. 44, pp. 1–14, 2021.

[25] S. K. Natarajan, K. Sankaranarayanasamy, S. Ponnusamy et al., "Experimental comparative study on reduction in the moisture content of cucumber in a double slope solar dryer with open sun drying method," *Journal of Physics: Conference Series*, vol. 1276, pp. 1–6, 2019.

[26] V. Shanmugam and E. Natarajan, "Experimental investigation of forced convection and desiccant integrated solar dryer," *Renewable Energy*, vol. 31, no. 8, pp. 1239–1251, 2006.

[27] K. G. Sajith and C. Muraleedharan, "Economic analysis of a hybrid photovoltaic/thermal solar dryer for drying amla," *International Journal of Engineering Research and Technology*, vol. 3, no. 8, pp. 907–910, 2014.

[28] N. A. Aviara, L. N. Onuoha, O. E. Falola, and J. C. Igbeka, "Energy and exergy analyses of native cassava starch drying in a tray dryer," *Energy*, vol. 73, pp. 809–817, 2014.

[29] S. Murali, P. R. Amulya, P. V. Alfiya, D. A. Delfiya, and M. P. Samuel, "Design and performance evaluation of solar - LPG hybrid dryer for drying of shrimps," *Renewable Energy*, vol. 147, pp. 2417–2428, 2020.

[30] A. Fudholi, K. Sopian, M. Y. Othman, and M. H. Ruslan, "Energy and exergy analyses of solar drying system of red seaweed," *Energy and Buildings*, vol. 68, pp. 121–129, 2014.

[31] Q. Jun, A. Parag, D. M. Jacobs, R. M. Boom, and A. I. Maarten, "A systematic analysis on tomato powder quality prepared by four conductive drying technologies," *Innovative Food Science and Emerging Technologies*, vol. 54, pp. 103–112, 2018.

[32] A. Jelled, Â. Fernandes, L. Barros et al., "Chemical and antioxidant parameters of dried forms of ginger rhizomes," *Industrial Crops and Products*, vol. 77, pp. 30–35, 2015.

[33] R. Dhivagar, M. Mohanraj, K. Hidouri, and Y. Belyayev, "Energy, exergy, economic and enviro-economic (4E) analysis of gravel coarse aggregate sensible heat storage-assisted single-slope solar still," *Journal of Thermal Analysis and Calorimetry*, vol. 145, no. 2, pp. 475–494, 2021.

[34] S. K. Natarajan and E. Elavarasan, "Experimental investigation of drying potato for karaikal climatic condition," *IOP Conference Series: Earth and Environmental Science*, vol. 312, pp. 1–7, 2019.

[35] E. Elavarasan, Y. Kumar, R. Mouresh, and S. K. Natarajan, "Study of drying kinetics of tomato in a solar dryer," in *Current Advances in Mechanical Engineering*, pp. 349–358, Springer, Singapore, 2021.

[36] S. Anagh, E. Elavarasan, S. K. Natarajan, A. Anandu, and H. M. Senin, "Experimental investigation of drying kinetics of poovan banana under forced convection solar drying," in *Current Advances in Mechanical Engineering*, pp. 621–631, Springer, Singapore, 2021.

[37] E. Elavarasan, S. K. Natarajan, S. Anagh, A. Anandu, and H. M. Senin, "Experimental investigation of drying cucumber in a double slope solar dryer under natural convection and open sun drying," *Innovations in Energy, Power and Thermal Engineering*, pp. 41–52, Springer, Singapore, 2021.

[38] S. Sumathy Raj, T. Chellapandian, and B. Nanjappan, "Effect of glycerol on the properties of coconut oil cake reinforced poly(lactic acid)," *Polimery*, vol. 67, no. 2, pp. 61–66, 2022.

[39] C. S. Prasad, M. Babu, and S. S. Raj, "Thermal analysis on exhaust valve with thermal barrier material," *International research journal on automotive research technology*, vol. 1, no. 6, pp. 18–32, 2018.

Hindawi
Advances in Materials Science and Engineering
Volume 2023, Article ID 9089620, 14 pages
https://doi.org/10.1155/2023/9089620

Research Article

Stir Casting Processing, Mechanical, and Wear Behavior of AA2024 +10 wt. % Flyash +5 wt. % Graphite Hybrid Composite

S. Senthil Murugan,[1] M. Vigneshkumar,[2] M. John Iruthaya Raj,[3] Sivamani Selvaraju,[4] N. Vinayaka,[5] Srinivasan Murugan,[6] V. Vijayan,[7] and Addisalem Mekonnen[8]

[1]*Department of Mechanical Engineering, Rajalakshmi Engineering College, Chennai 602105, Tamilnadu, India*
[2]*Department of Mechanical Engineering, Sri Krishna College of Engineering and Technology, Coimbatore, Tamilnadu, India*
[3]*Department of Mechanical Engineering, Mar Ephraem College of Engineering and Technology, Marthandam, Tamilnadu, India*
[4]*Department of Engineering, University of Technology and Applied Sciences, Salalah, Oman*
[5]*Department of Aeronautical Engineering, Nitte Meenakshi Institute of Technology, Yelahanka, Bengaluru 560064, India*
[6]*Department of Mechanical Engineering, Mahendra Engineering College, Mahendrapuri, Mallasamudram, Namakkal 637503, India*
[7]*Department of Mechanical Engineering, K. Ramakrishnan College of Technology, Samayapuram, Trichy, Tamil Nadu, India*
[8]*Department of Mechanical Engineering, Faculty of Manufacturing Institute of Technology, Hawassa University, Hawassa, Ethiopia*

Correspondence should be addressed to Addisalem Mekonnen; addisalemm@hu.edu.et

Received 12 August 2022; Revised 10 October 2022; Accepted 25 November 2022; Published 9 February 2023

Academic Editor: Pudhupalayam Muthukutti Gopal

Metal matrix composites (MMCs) and their hybrid combinations are widely incorporated in research due to their enhanced mechanical properties and wear resistance. In this work, an investigation is made to fabricate AA2024 matrix flyash and graphite-reinforced hybrid composite for industrial applications and determine its suitability by performing testing and characterization. Tensile properties and compressive strength, wear resistance, fracture toughness, impact energy, and the hardness of the composites are evaluated. A tensile strength maximum of 300 MPa was achieved. Furthermore, the thermal analysis of a disc brake of this hybrid composite is performed using SOLIDWORKS software to identify the temperature distribution up to 469°K. The addition of flyash reinforcement shows the changes in properties with weight reduction. Although the content of graphite particles shows a deterioration in mechanical properties, it acts as a lubricant and reduces wear by friction and friction between the components. The coefficient of friction (COF) for the specimen is in the range of 0.1 to 0.3. The distribution of graphite and flyash is analyzed using the scanning electron microscope. It was found that the properties of the prepared composite are lesser than the base alloy AA2024, but the fabricated composite's density (2.07 g/cc) is lesser than the base alloy AA2024 (2.78 g/cc).

1. Introduction

The possibilities of obtaining a desirable blend of strength, rigidity, toughness, or specific weight using traditional materials are limited. Composite materials have gained significant attraction in recent times for overcoming these inadequacies and meeting the excessive requirements of today's technology. MMCs have considerably enhanced properties over conventional alloys, such as high specific strength, specific modulus, dampening capacity, and abrasion resistance [1]. Some of MMCs' physical properties, such as their lack of significant moisture absorption, reduced thermal conductivities, and resistance to most radiations, are also advantageous. Composites with low-density and low-cost reinforcing are becoming increasingly popular [2, 3]. Composites reinforced with flyash are anticipated to break through the cost barrier for broad use in automobile and light-duty applications [4]. As a result, it is anticipated that

integrating flyash particles into aluminium alloys leads to an effective application for the low-cost waste by-product and also the capacity to preserve energy-intensive consuming aluminium components [5]. Particulate reinforced aluminum matrix composites are gaining popularity due to their low cost and benefits such as isotropic characteristics and the ability to undergo secondary processing, allowing for the creation of secondary components [6]. Cast aluminum matrix particle reinforced composites offer higher specific strength, specific modulus, and wear resistance than unreinforced alloys [7]. The shortcoming of aluminium alloys is the minimal resistance to abrasive wear under low-lubrication conditions and their significant retention of the lubricating layer over the sliding surface, making tribological applications difficult. Aluminium graphite particle composites are self-lubricating composites that receive attention from researchers because of their remarkable anti-seizure effect, high thermal stability, excellent damping characteristics, and reduced friction coefficient [8]. This self-lubrication is caused by the shearing of graphite particles under the composite's sliding surface, which reduces shear stress, alleviates permanent deformation in the subsurface area, reduces the friction coefficient, and acts as a lubricant [9]. As a result, the development and retention of this tribo-layer on the sliding surface influence the materials' tribological behavior through material properties such as chemical composition, mode of fracture, and material thickness [10]. It is determined by the type of sliding surface, the atmosphere, and the amount of graphite content in the composite. It has been observed that increasing the graphite component in Al/graphite composites reduces the wear rate. However, there are claims that the wear rate increases with the graphite content owing to a reduction in the fracture toughness and hardness of composites [11]. Hence, extensive experimental research is required to analyze the effect of the inclusion of micron-size flyash and graphite with the matrix AA2024 wrought alloy.

The novelty of the paper is the hybrid combination of flyash with graphite reinforcement, and the aim of the present work is to fabricate the AA2024 aluminum matrix hybrid composite using the stir casting setup and to characterize the fabricated specimens, including the thermal analysis using SOLIDWORKS software.

2. Materials and Method

Aluminum AA2024 alloy is the matrix for the hybrid aluminum matrix composite in the current study. It is utilized in applications, which demand a high strength-to-weight ratio, in addition, to excellent fatigue resistance such as wings and fuselages in aircraft structures. The chemical composition of the alloy as per optical emission spectroscopy is presented in Table 1. Flyash is one of the wastes produced by coal burning. The principal elements of flyash are oxides such as SiO_2, Al_2O_3, and Fe_2O_3, which are present in the industrial by-product collected from the flue gas of coal-burning electric power plants. It is widely used by the construction industry for cost reduction in the manufacturing of concrete structures, bricks as well as road construction. The composition of different fly ashes is presented in Table 2. Graphite nature is soft and it has a lubrication property [11].

The stir casting method was utilized for the preparation of AA2024 metal matrix composite as both class-F flyash (100 grams = 10%), and graphite (50 grams = 5%) were the reinforcements. Figure 1(a) shows the stir-casting process. The fabrication of a composite involves the addition of dispersed phases into a molten matrix and subsequent solidification. Initially, the mold for the casting and the reinforcement particles at the required weight was preheated to 200°C in an oven. The aluminum AA2024 (1000 grams) was melted in the clay crucible in the furnace and followed by the addition of reinforcement into the molten matrix, which is at 680°C–700°C slowly with a rate of 1 gram per 20 sec. The temperature was ensured with a thermocouple and digital meter. During the stirring with a stirrer, the chemical reaction took place between the matrix alloy and reinforcement to develop homogeneous hybrid composites. The stir casting setup is utilized to achieve excellent mechanical properties owing to the increased interfacial bonding among the matrix and flyash through the vortex developed. Once the proper mixture is obtained, then the temperature is measured and the prepared composite was poured at the temperature of 780°C into the preheated mold (Figure 1(b)). Three molds are prepared for casting rods of a diameter of 20 mm, length of 300 mm, and length of 350 mm, as shown in Figure 1(c). The required specimens were cut from the cast for the characterization of microstructures, tensile, compression, and hardness testing. Wear rate analysis was also performed on the prepared specimens. The cast rods are first cut into various lengths according to the specifications. Now, the cut pieces are machined in the lathe. The specimen for the tensile test involves turning, facing, and chamfering. The specimens for the compression test and wear tests involve turning and facing. It is found that the density of the hybrid composite is lesser than that of the base alloy AA2024. Thus, the weight is automatically reduced. Theoretical and experimental density values of the hybrid composite fabricated are 1.97 g/cm^3, and 2.077 g/cm^3, respectively. These values are lesser than the density of AA2024 value of 2.78 g/cm^3.

3. Testing, Results, and Discussion

3.1. Tensile Test. In the tensile test, the specimens are subjected to uniaxial tension until failure. Figures 2(a)–2(d) show the tensile testing (ASTM E8 standard) of the prepared composite. The tensile sample for testing was prepared as per the standard given in Figure 2(a). The prepared tensile specimen and the specimen position in the testing machine are given in Figures 2(b) and 2(c), respectively. The tensile fractured specimens are shown in Figure 2(d). The neck formation was not seen on the specimens after tensile testing. The recorded stress and strain curve during tensile testing is given in Figure 3(a). The tensile testing result was almost the same for all three samples according to the stress vs strain curve. It showed the ultimate stress was around 300 MPa and the strain of around the 3.6–3.8 range. The

Table 1: Chemical composition of AA2024 matrix.

Element	Al	Cu	Fe	Mg	Mn	Si	Ti	Ni	Zn	Cr	Pb	Sn
%	91.95	4.63	0.35	1.4	0.6	0.41	0.05	0.01	0.2	0.38	0.04	0.03

Table 2: Composition of various fly ashes.

Component	Bituminous	Sub-bituminous	Lignite
SiO_2 (%)	20–60	40–60	15–45
Al_2O_3 (%)	5–35	20–30	20–25
Fe_2O_3 (%)	10–40	4–10	4–15
CaO (%)	1–12	5–30	15–40
LOI (%)	0–15	0–3	0–5

ultimate tensile and yield strength were observed and given in the bar chart shown in Figure 3(b). The values are noted for three specimens, and the average value is considered the final value. The average tensile and yield strengths were 297 MPa and 154 MPa, respectively. The composite strength is lesser than that of the AA2024 alloy. The reason is though the graphite and flyash reduce the weight of the composites, it decreases the composite strength. The strain hardening rate (h) was calculated based on the values of yield strength (YS), and tensile strength (TS) of the prepared casting. It decides the material ductility and is also an important property for engineering applications [12]. It can vary depending on the strain rate. The estimated YS/TS ratio and TS and YS difference are plotted in Figures 3(c) and 3(d), respectively. The decrease in this YS/TS ratio means an increase in tensile ductility. The value here is in the range of 0.5. Although all the samples have almost equal values, sample 1 shows the maximum ductility with a 0.513 ratio value. These values might be considered for the evaluation of the strain-hardening exponent of the composite. Similarly, the difference in tensile and yield strength has an impact on the plastic deformation of the castings. From the data, the values are in the range of 141 to 143 MPa. Here, sample 1 showed a maximum value of 143.8 MPa. According to Von Mises's statement, shear yield strength (τ) can be estimated by Von Mises's yield criterion (equation (1)) [13]. Maximum shear yield strength is 79 MPa for sample 2 and a minimum of 75.8 MPa.

$$\tau = 0.5\sigma_{ys}, \tag{1}$$

where "τ" is the shear yield stress in MPa, σ_{ys}-yield strength in MPa.

3.2. Compression Test. The compression test is conducted in the UTM (Universal Testing Machine). Here, the specimen is subjected to a uni-axial compression until failure. Compressive strength is the ability of a material to bear a compressive load tending to reduce its height. As per Figure 4(a), the compressive test specimen (100 mm × ϕ20 mm) was prepared as per ASTM E9 standard and the specimen is shown in Figure 4(b). The Specimen after the compressive test is shown in Figure 4(c), and the crack was found in the center of the specimens. The compressive test results are given in Figure 5(a). Figures 5(b) and 5(c) show the load vs displacement curve and stress vs strain curve for all three specimens, respectively. The ultimate compressive load and ultimate compressive strength are taken from the graphs generated for the specimens. The values are noted, and the average of the three values is considered the final value. The average ultimate load was 72.5 kN, and the average ultimate compressive strength was 267.3 MPa. It is found that the compressive strength gets reduced with that of the base alloy AA2024. During compressive testing, the maximum load was obtained as 80 kN, and the maximum compressive strength was recorded as 300 MPa. From the graph, the load obtained was in the range between 48 and 80 kN, whereas the stress value during compressive testing was in the range of 180 MPa–30 MPa, as per plots Figures 5(b) and 5(c). The crack was found in the compressed samples. The convex portion propagates cracks and was highly affected by the compressive load during the compression test.

3.3. Toughness Test. The toughness of the composite is determined by the Charpy impact test to analyze the amount of energy absorbed by the prepared casting during fracture. This study helps to study the ductile to brittle transition on the material. Here, the impact test was done on the prepared casting specimen (10 mm × 10 mm × 55 mm) shown in Figure 6(a). A V-notch was cut to a depth of 2 mm at the center. The Charpy impact test was taken for three specimens, and the impact energy was noted, as shown in Figure 6(b). The average value was around 1.52 kg·m. The toughness value gets reduced when compared to that of base alloy AA2024. The specimen subjected to impact is shown in Figure 6(c). The Rolfe Novak Barsom upper shelf correlation [14–16] is given in equation (2) [17]. Using this equation, the fracture toughness was calculated with impact energy. The recorded fracture toughness values are given as a bar chart in Figure 6(d). The values were in the range of 24.8 to 25.4 MPa·m$^{1/2}$. The average fracture toughness was about 24.99 MPa·m$^{1/2}$.

$$\left(\frac{K}{Y_s}\right)^2 = 5\left[\left(\frac{I}{Y_s}\right) - 0.05\right], \tag{2}$$

where "K" is fracture toughness (MPa·m$^{1/2}$) [18], "Y_S" is yield strength (MPa), and "I" is impact energy (kg·m)

3.4. Hardness Test. A hardness test is performed to determine the ability of the composite material to withstand indentation [19]. The Rockwell hardness test (B scale) is used in our current study to determine the hardness, which is based on the depth of penetration of an indenter. The indentation on the specimen is shown in Figure 7(b). The hardness value is taken at three different spots. The average of the three values is taken as the final value and shown in

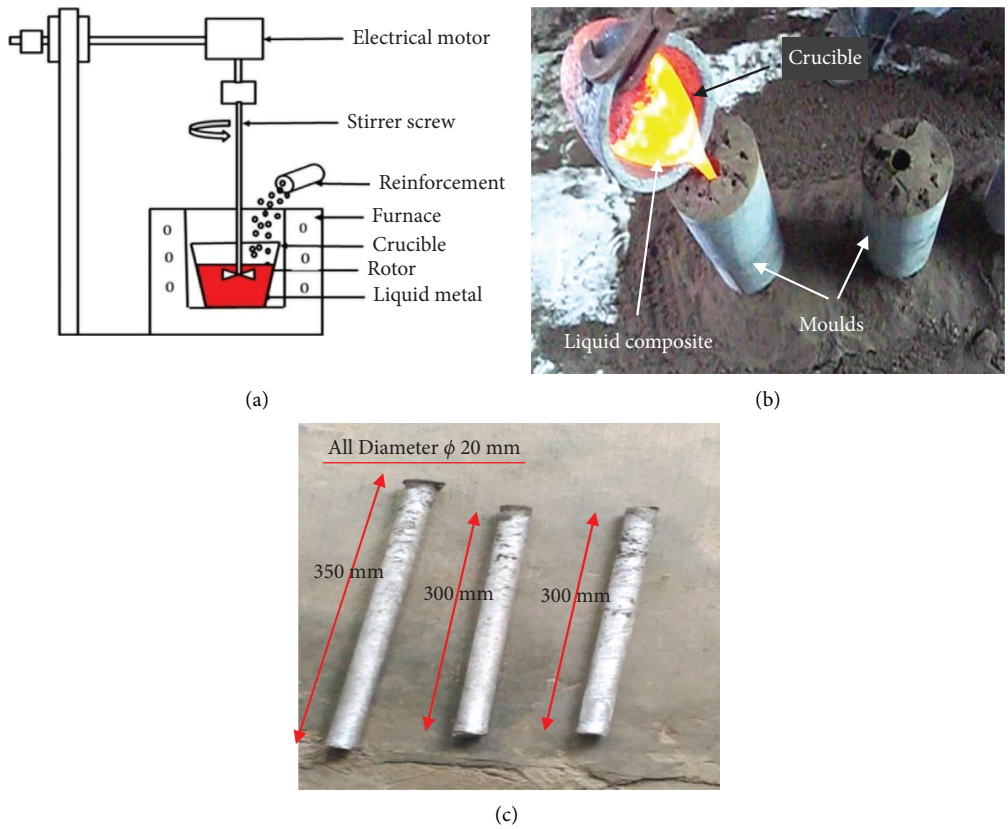

Figure 1: (a) Schematic of stir casting; (b) composite pouring; (c) prepared composite castings.

Figure 7(c) for samples 1, 2, and 3. It was found that the hardness of the hybrid composite was lesser than that of the base alloy AA2024. An average of 63HRB hardness was recorded.

3.5. Wear Test. The tribological experiments were conducted at a temperature of 30°C using the pin-on-disc apparatus seen in Figure 8(a). The tests were carried out at a 500 rpm sliding speed, a 20 N applied force, and a distance of 1000 m. For the wear test, pins having a diameter of 10 mm and a height of 30 mm were employed, as indicated in Figure 8(a). The specimen for wear testing is given in Figure 8(b). The surface of the pin was polished, as shown in Figure 8(c), and was rotated against a disc. The specimen after the wear testing is shown in Figure 8(d). The wear rate was determined by observing the loss of weight during the testing. A digital weighing scale with an accuracy of 0.1 mg was used to determine the weight of each specimen. Weight loss is defined as the difference in weight of the test specimen before and after testing. A graphite lubricating coating covers the whole worn surface, eliminating direct interaction between the pin and disc and lowering the friction coefficient significantly. The friction coefficient and wear rate for three distinct specimens were determined, and the final result was calculated using the average of the three data. It is found that wear properties have shown improvement due to the addition of graphite. The wear rate and friction coefficient values are presented in Table 3. The coefficient of friction (COF) was calculated using (3) [20], where the applied load/normal force (L_a) in "N" was 20 N and the frictional force (F_f) in "N."

$$\mathrm{COF} = \frac{F_f}{L_a}. \tag{3}$$

By physically examining the test specimens before and after wear testing, the changes in the cross-sectional area of the specimens were easily comprehended. Very few weight losses (in grams) were observed among all three specimens. The composite (sample 1) showed higher COF. A higher COF means that more/higher F_f was present. Here, the COF was less than 0.5, and its range was 0.1 to 0.3. If the COF value is greater than 1, it means that the normal force is weaker than the friction. Here, the addition of graphite reduced the COF value. From the results, low COF showed a high wear rate.

Figure 9 provides the relationship of frictional force over sliding distance during the wear analysis of all three samples. For sample 1, the frictional force reached 6.5 N; whereas it reached for samples 2 and 3 to 5.7 N and 3.2 N, respectively. COF and wear rate are the functions of sliding distance [21]. The wear rate and the weight loss values are low for high frictional force. There are not many variations in the frictional forces in the due course of the period while increasing the sliding distance from 300 mm onwards. The value might be changing according to the changes in the applied load.

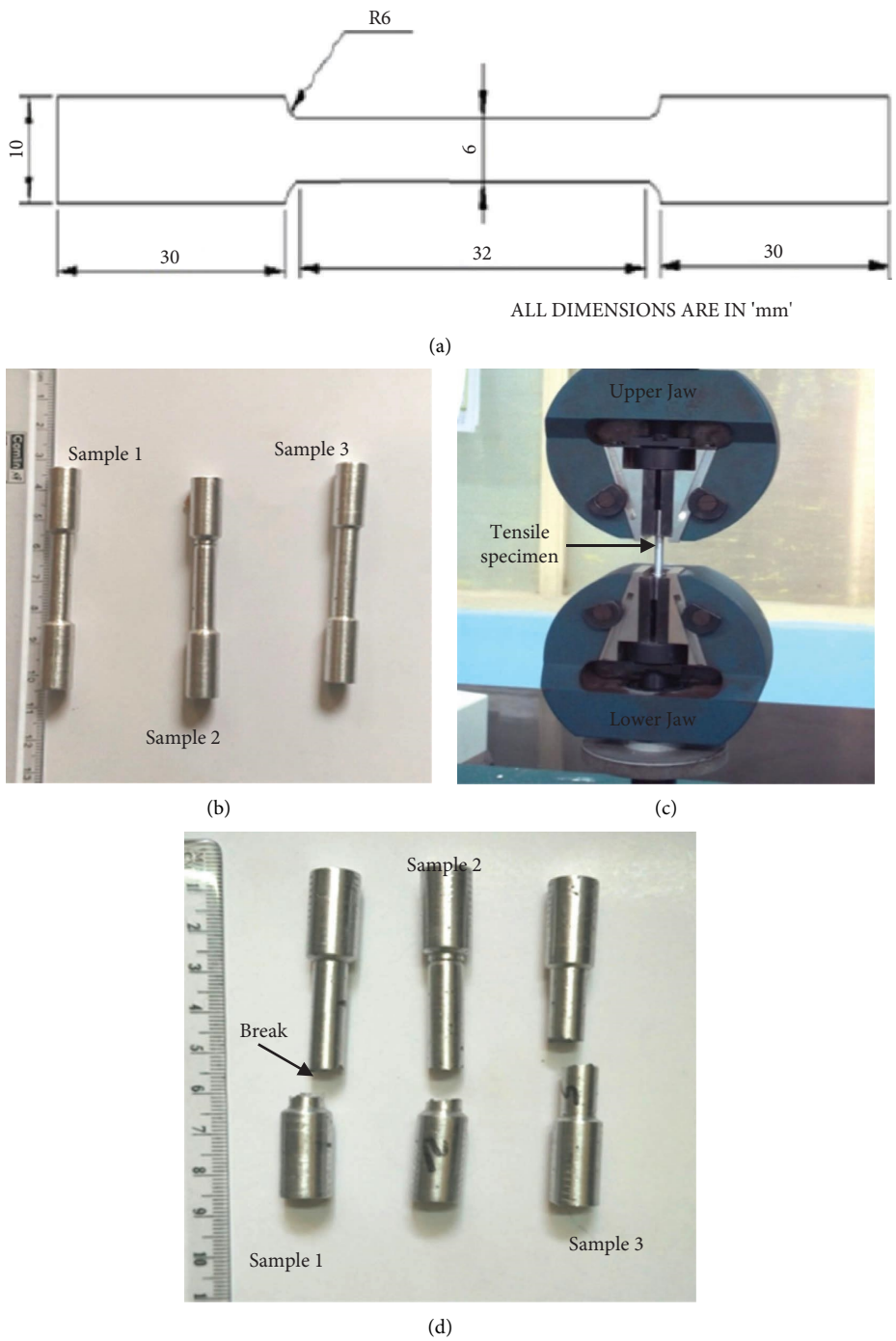

Figure 2: (a) Tensile sample dimension; (b) prepared cast samples for tensile testing; (c) tensile testing in the UTM machine; (d) specimen after tensile test.

3.6. Microstructure. The scanning electron microscope (SEM) that was used for this study is shown in Figure 10(a). By utilizing a concentrated electron beam across the surface of the material, the image is shown in Figure 10(b) was taken at 25 μm size on the surface of the finished specimen to analyze its surface properties and access the dispersion of flyash and graphite. From the microstructure analysis, the distribution of flyash on the surface of the composite is observed. It also shows the formation of pores and graphite accumulation on the surface. The accumulation of graphite on the surface forms a lubricating layer so that it reduces the wear rate by reducing the contact area and reducing the strength and hardness also.

3.7. Thermal Analysis. The prepared hybrid composite can be used in the application of disc brakes in automotive applications. Thermal analysis (Figures 11(a)–11(d)) was carried out for a disc brake using SOLIDWORKS software. Thermal analysis was done for finding out the temperature

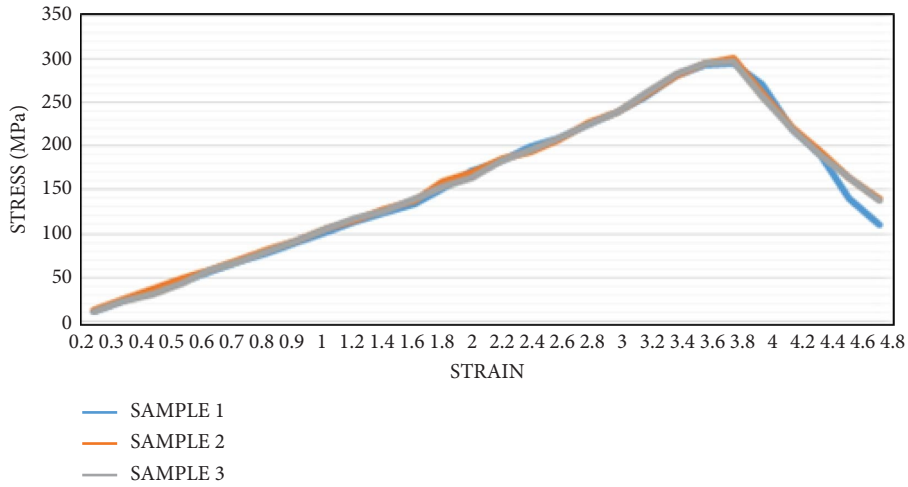

(a)

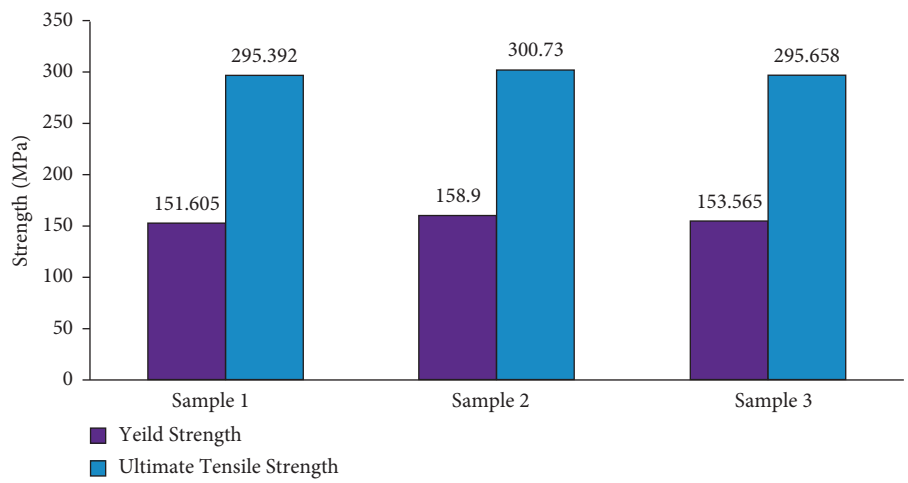

(b)

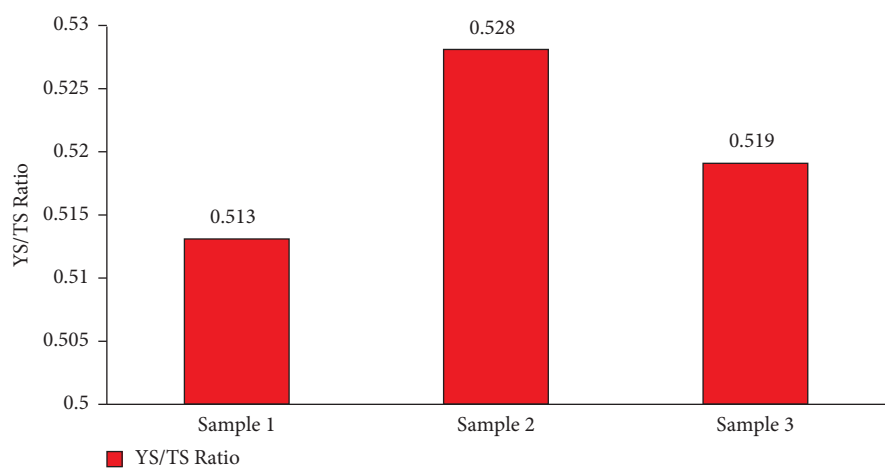

(c)

Figure 3: Continued.

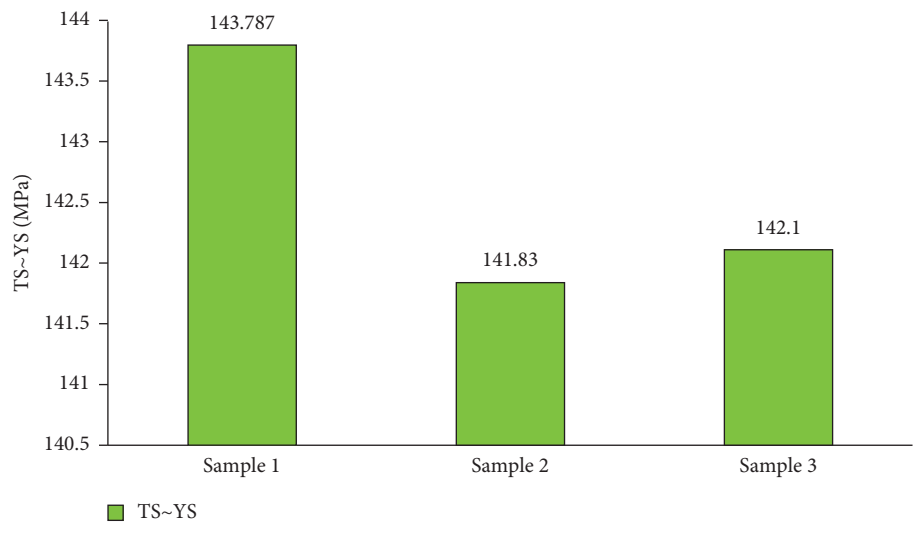

(d)

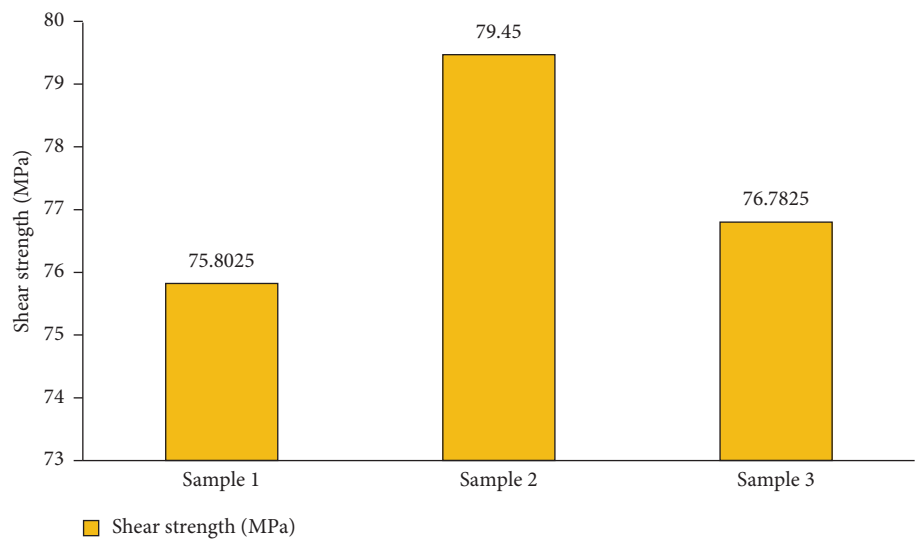

(e)

Figure 3: (a) Stress vs. strain curve for 3 specimens; (b) tensile and yield strength; (c) YS/TS ratio; (d) TS–YS variation; (e) estimated shear strength.

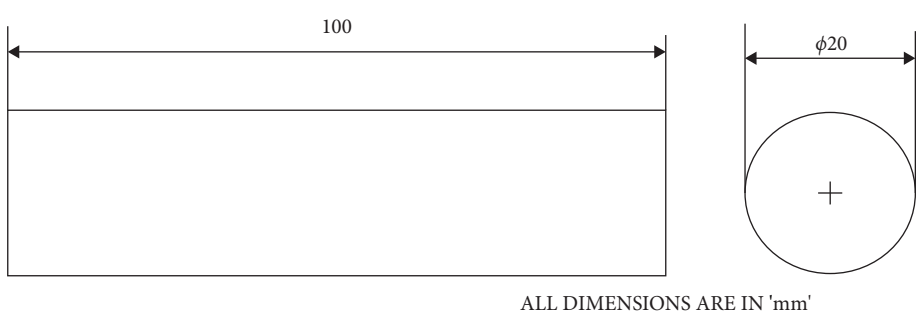

(a)

Figure 4: Continued.

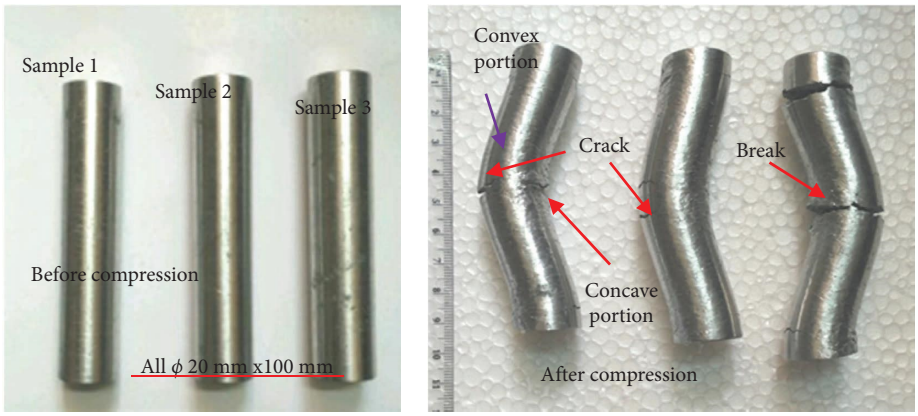

(b) (c)

Figure 4: (a) Compression test specimen dimension; (b) specimen prepared for the compressive test; (c) samples after compression test.

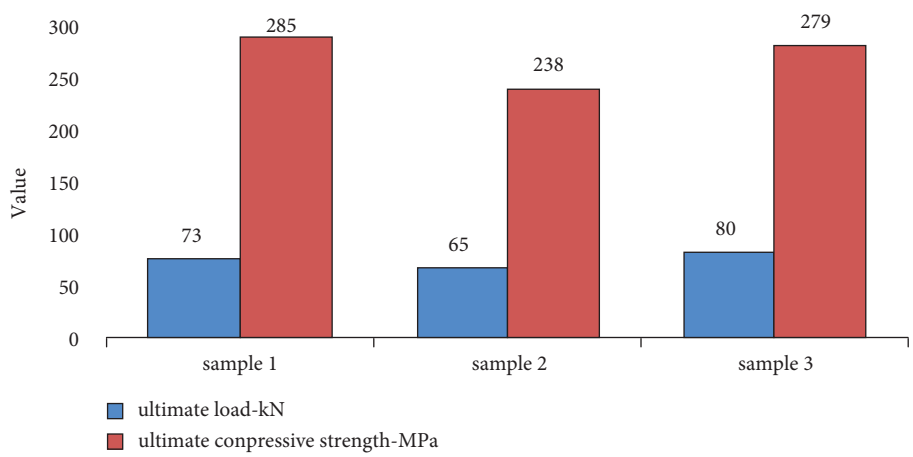

(a)

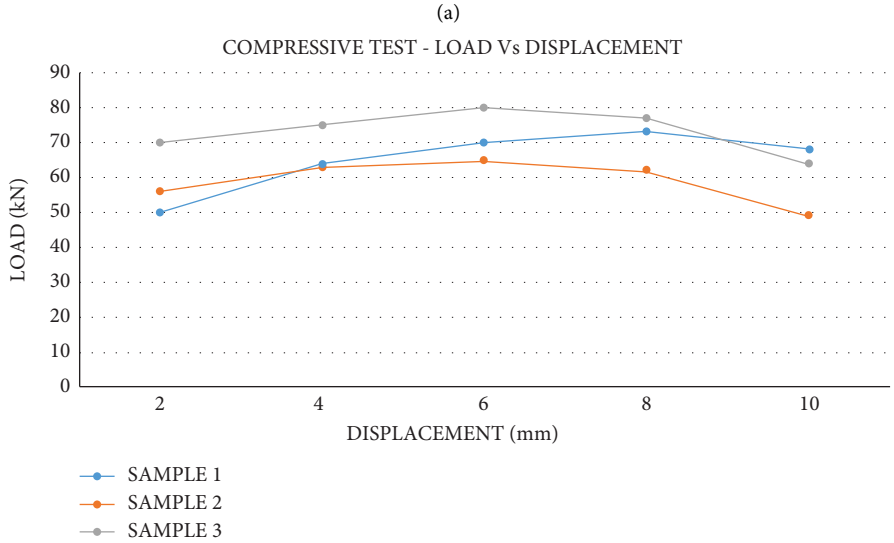

(b)

Figure 5: Continued.

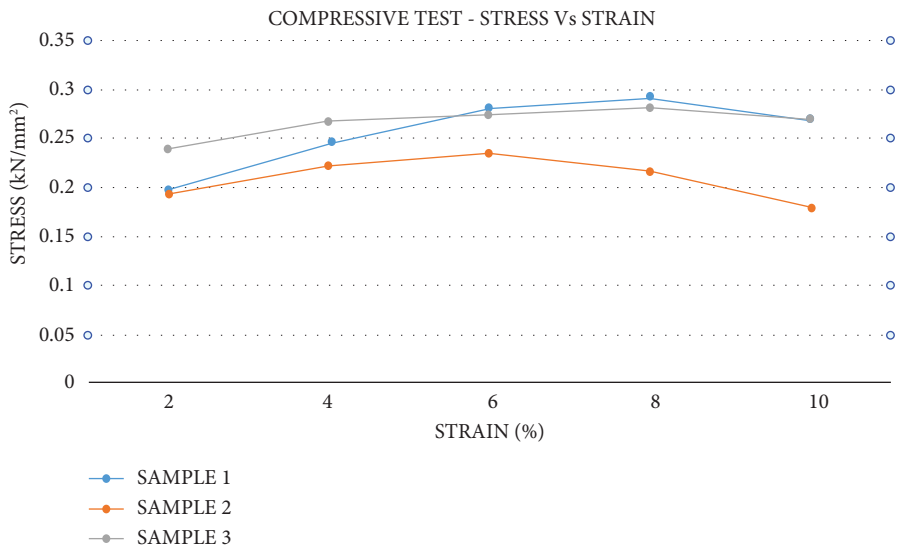

(c)

Figure 5: (a) Compressive test results; (b) relationship of load and displacement for the composites; (c) stress vs. strain curve for the compressive test.

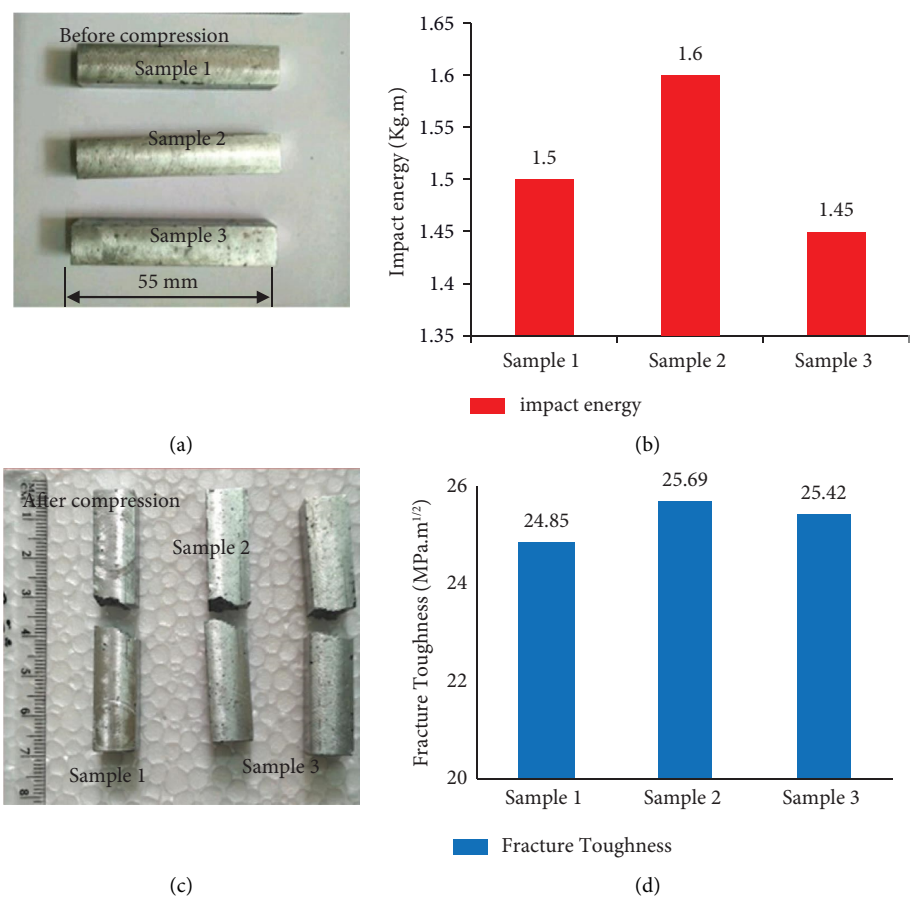

Figure 6: (a) Charpy test specimen before V-notching; (b) impact energy values of the composite specimen; (c) specimen after Charpy test; (d) fracture toughness of composite specimens.

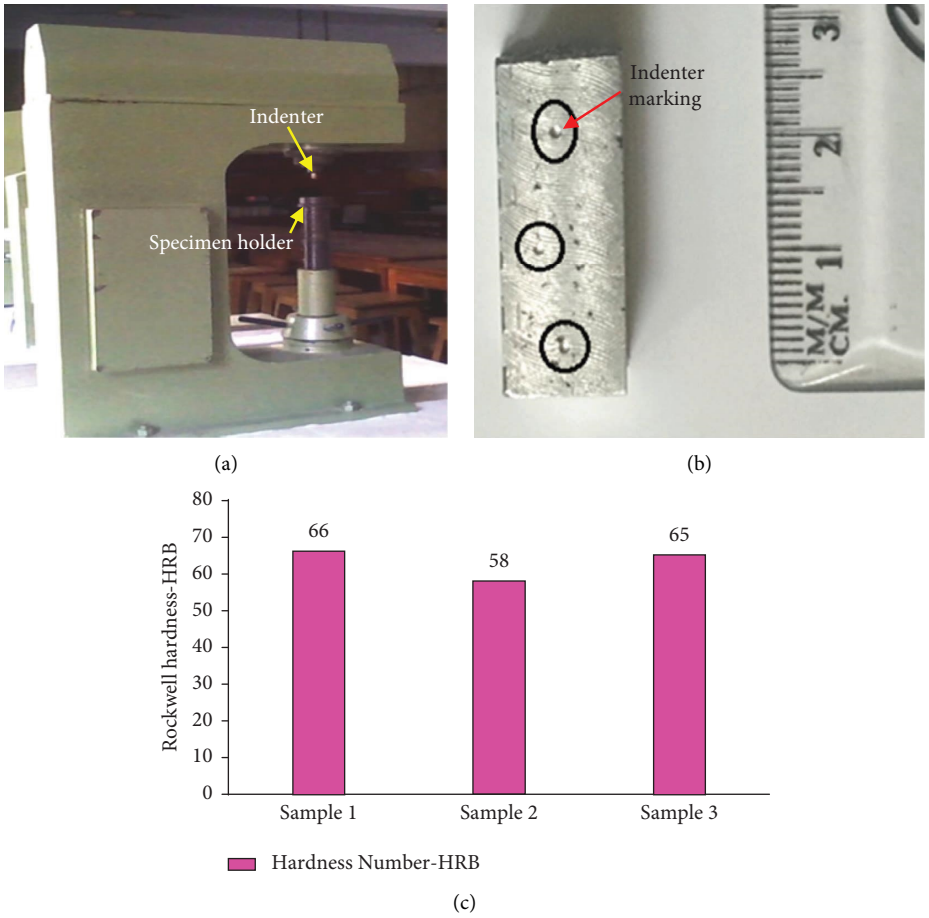

Figure 7: (a) Rockwell hardness tester; (b) hardness specimen; (c) hardness test results.

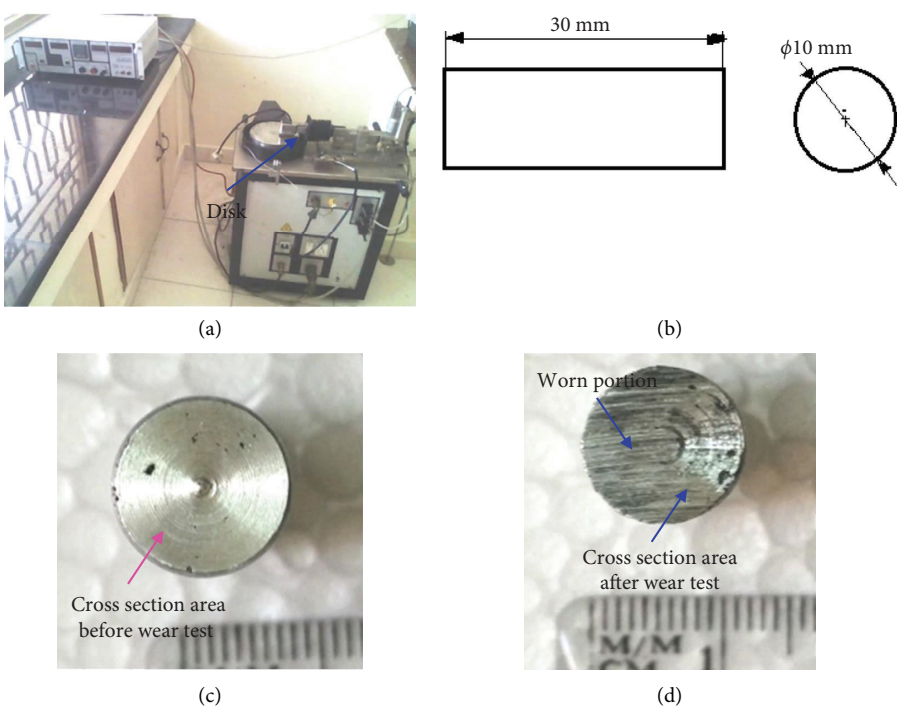

Figure 8: (a) Pin-on-disc apparatus; (b) wear test specimen design; (c) before wear test; (d) after wear test.

Table 3: Wear test readings.

Specimen	Initial weight (gm)	Final weight (gm)	Weight loss (gm)	Coefficient of friction	Wear rate (mm^3/Nm)
Sample 1	6.3250	6.3130	0.0120	0.325	0.00028888
Sample 2	6.4877	6.4754	0.0123	0.285	0.0002961
Sample3	6.3487	6.3360	0.0127	0.185	0.0003057

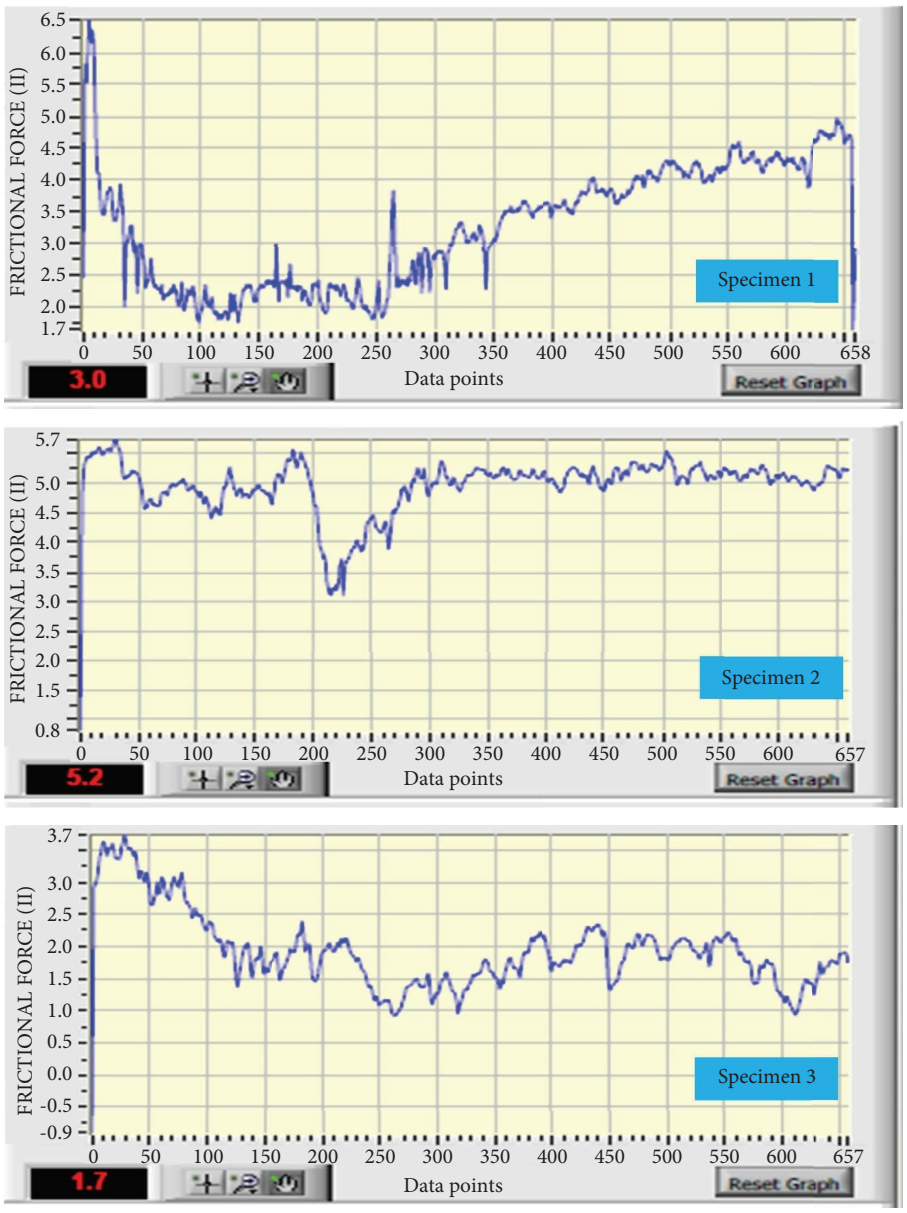

Figure 9: Frictional force vs. sliding distance curve recorded for the specimens.

distribution in the disc brake plate during the braking action. The steps such as model creation, the meshing of the model, and boundary conditions were involved in the analysis. Initially, a model of a disc brake plate was created using solid works software then the properties of the model are fed into the software using custom properties. The model creation of the disc brake plate involved extrusion, revolved cut, chamfering, etc. The model created using the standard dimensions of the disc brake plate in motorbikes is shown in Figure 11(a). The created model was in turn meshed and the mesh information was given in the figure. The maximum aspect ratio is around 4. It was done to divide the object into a fine number of elements so that the properties required can be analyzed in each element. Meshing is the primary for

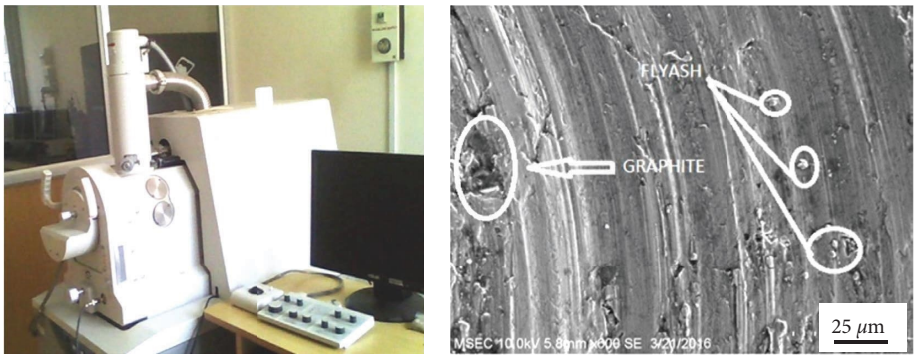

(a) (b)

Figure 10: (a) Scanning electron microscope (SEM); (b) SEM image of composite.

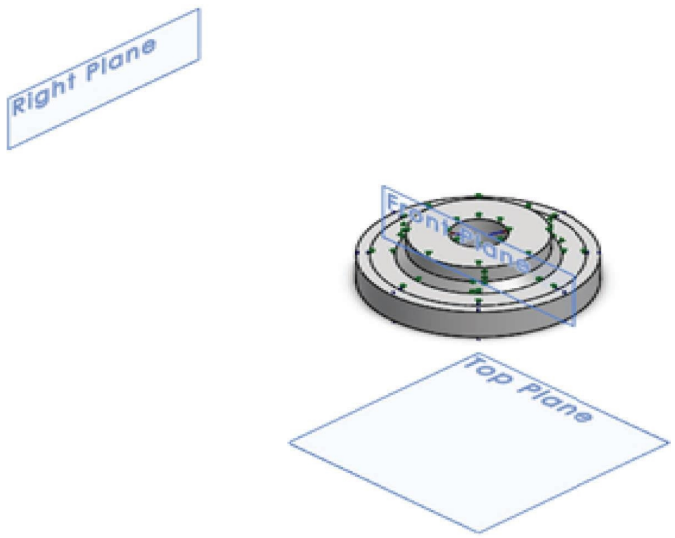

(a)

Mesh Information - Details

Total Nodes	116198
Total Elements	69940
Maximum Aspect Ratio	4.1135
% of elements with Aspect Ratio < 3	99.8
% of elements with Aspect Ratio > 10	0
% of distorted elements(Jacobian)	0
Time to complete mesh(hh;mm;ss):	00:00:07
Computer name:	KRISHNAN

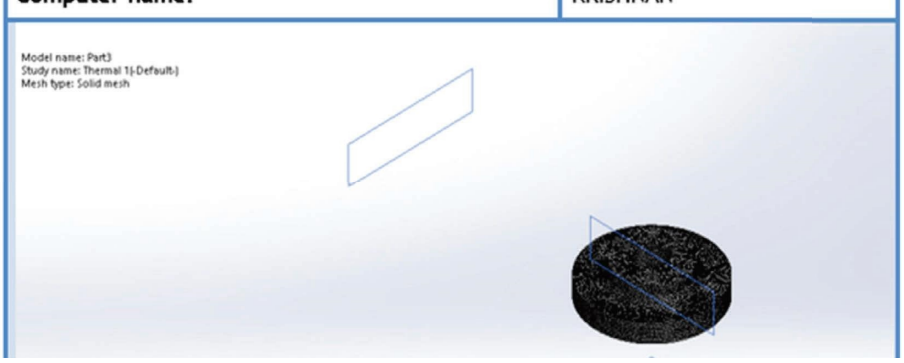

(b)

Figure 11: Continued.

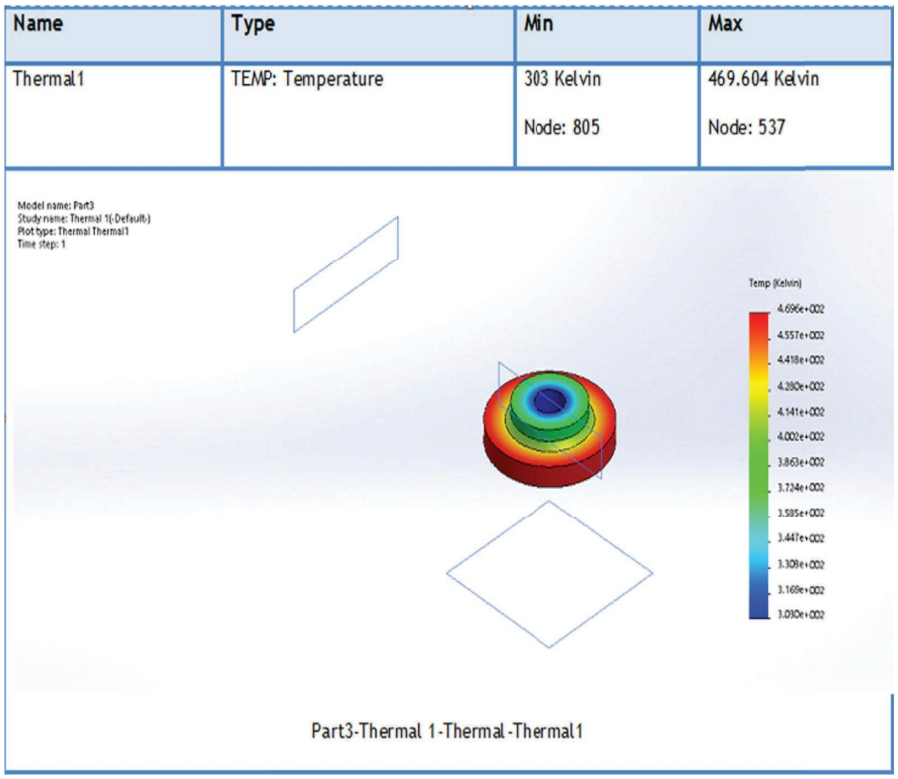

(c)

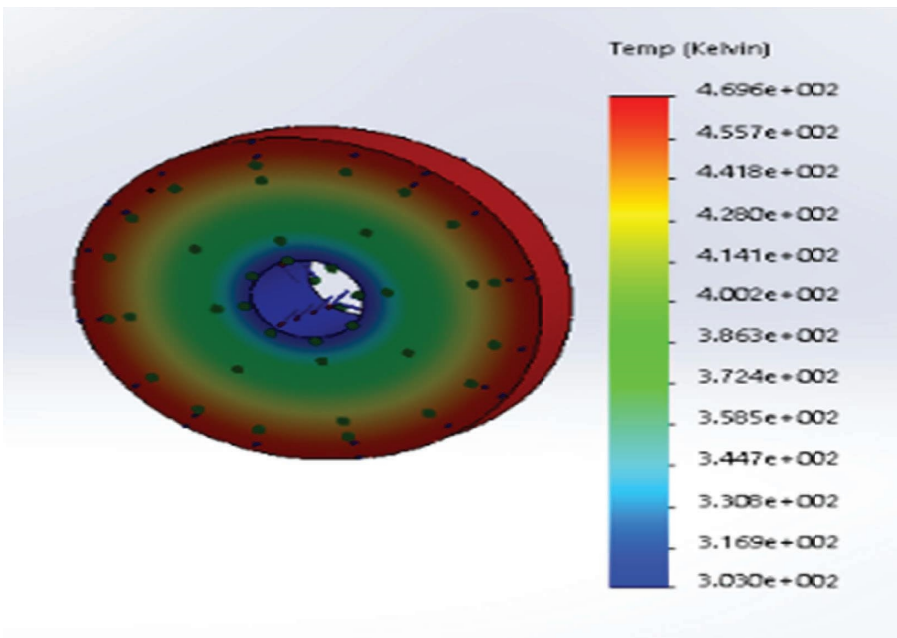

(d)

Figure 11: (a) Disc brake plate model; (b) meshing of disc brake plate model; (c) thermal analysis (top view); (d) thermal analysis (bottom view).

finite element analysis. Nevertheless, the base portion of the plate (i.e.,) hub portion was fixed as to boundary conditions while the analysis. The specified area was the area of the brake pad that was to be in contact with the plate. This particular area is sensitive and bears the pressure of braking, so a pressure of 1 MPa was applied in that area, and the results were analyzed. A maximum temperature of 469 Kelvin was recorded.

4. Conclusions

The AA2024-fly ash-graphite hybrid composite was successfully manufactured utilizing the stir casting technique, and the cast specimens were evaluated for analyzing their mechanical and tribological characteristics. The following observations are made based on the experimental findings:

(a) Addition of 10 wt. % flyash reduces the density of the composite, thereby reducing the overall weight.

(b) Excessive graphite content increases the porosity and cracks leading to a reduction in the mechanical performance of the hybrid composite.

(c) Incorporated graphite particles act as a lubricant during the abrasion process, reducing wear. The wear rate increases with applied stress, and at 5% graphite weight, the wear rate and coefficient of friction are reduced.

(d) The AA2024-flyash-graphite hybrid composite can be used in low-strength, less-weight, and high-wear applications such as low-weight gears in marine applications and low-duty motor and bike disc brakes. It could also be used for making low-strength fasteners in aerospace applications.

Data Availability

The data supporting the findings of the study are available from the corresponding author upon request.

Conflicts of Interest

The authors declare that they have no conflicts of interest.

Acknowledgments

The authors appreciate the technical assistance to complete this experimental work from the Department of Mechanical Engineering, K. Ramakrishnan college of Technology, Trichy, Tamilnadu, India. The authors would like to thank the technical assistance to complete this experimental work.

References

[1] T. Matsunaga, J. K Kim, S. Hardcastle, and P. K. Rohatgi, "Crystallinity and selected properties of flyashparticles," *Materials Science and Engineering A*, vol. 325, no. 1-2, pp. 333–343, 2002.

[2] M. K. Marichelvam, S. Senthil Murugan, K. Maheswaran, and D. ShyamprasadVarma, "Processing and Characterization of Eco-Friendly Cutting Fluid with Nano Additives for Turning Operation," *Surface Review Letters*, vol. 28, 2021.

[3] P. K. Rohatgi and B. C. Pai, "Seizure resistance of cast aluminium alloys containing dispersed graphite particles of various sizes," *Wear*, vol. 59, no. 2, pp. 323–332, 1980.

[4] P. K. Rohatgi, S. Ray, and Y. Liu, "Tribological properties of metal matrix–graphite particle composites," *International Materials Reviews*, vol. 37, no. 1, pp. 129–152, 1992.

[5] J. Zhang, R. J. Perez, and E. J. Lavernia, "Effect of SiC and graphite particulates on the damping behavior of metal matrix composites," *Acta Metallurgica et Materialia*, vol. 42, no. 2, pp. 395–409, 1994.

[6] M. K. Surappa and P. K. Rohatgi, "Technical note," *Metals Technology*, vol. 5, no. 1, pp. 358–361, 1978.

[7] B. P. Krishnan, M. K. Surappa, and P. K. Rohatgi, "The UPAL process: a direct method of preparing cast aluminium alloy-graphite particle composites," *Journal of Materials Science*, vol. 16, no. 5, pp. 1209–1216, 1981.

[8] S. Basavarajappa, G. Chandramohan, A. Mahadevan, M. Thangavelu, R. Subramanian, and P. Gopalakrishnan, "Influence of sliding speed on the dry sliding wear behaviour and the subsurface deformation on hybrid metal matrix composite," *Wear*, vol. 262, no. 7–8, pp. 1007–1012, 2007.

[9] C. B. Lin, R. J. Chang, and W. P. Weng, "A study on process and tribological behavior of Al alloy/Gr. (p) composite," *Wear*, vol. 217, no. 2, pp. 167–174, 1998.

[10] J. N. Wei, H. F. Cheng, Y. F. Zhang, F. S. Han, Z. C. Zhou, and J. P. Shui, "Effects of macroscopic graphite particulates on the damping behavior of commercially pure aluminium," *Materials Science & Engineering, A: Structural Materials: Properties, Microstructure and Processing*, vol. 325A, pp. 444–453, 2002.

[11] S. S. Murugan and T. P. D. Rajan, "Characterization of graphite-reinforced LM30-aluminium matrix composite processed through gravity and vertical centrifugal casting processes," *J. Inst. Eng. India Ser. D*, vol. 102, no. 1, pp. 19–26, 2021.

[12] S. S. Murugan, P. Sathiya, and A. N. Haq, "Mechanical properties estimation from tensile testing of aa6063-aisi304l bimetal joints friction welded with different joining methods," *Surface Review and Letters*, vol. 28, no. 04, Article ID 2150013, 2021.

[13] P. Zhang, S. X. Li, and Z. F. Zhang, "General relationship between strength and hardness," *Materials Science and Engineering A*, vol. 529, pp. 62–73, 2011.

[14] D. Norris, J. Reaugh, and W. Server, "A fracture-toughness correlation based on Charpy initiation energy," in *Fracture Mechanics*, R. Roberts, Ed., pp. 207–217, ASTM International, West Conshohocken, PA, USA, 1981.

[15] G. T. Méndez, S. I. C. Colindres, J. C. Velazquez, D. A. Herrera, E. T. Santillan, and A. Q Bracarense, "Fracture toughness and Charpy CVN data for A36 steel with wet welding," *Soldagem&Inspeção*, vol. 22, no. 3, pp. 258–268, 2017.

[16] J. R. Dougan, *Relationships between Charpy V-Notch Impact Energy and Fracture Toughness*, Web, [PWR; BWR], USA, 1982.

[17] J. Kapp and J. H. Underwood, "Correlation between Fracture Toughness, Charpy V-Notch Impact Energy, and Yield Strength for ASTM A723 Steel," *Me-Morandum Report ARCCB-MR-92008*, 1992.

[18] M. V. Krishna and A. M. Xavior, "An investigation on the mechanical properties of hybrid metal matrix composites," *Procedia Engineering*, vol. 97, pp. 918–924, 2014.

[19] A. Saravanakumar, P. Sasikumar, and S. Sivasankaran, "Synthesis and mechanical behavior of AA 6063-X wt% Al2O3- 1% Gr (X = 3, 6, 9 and 12 wt%) hybrid composites," *Procedia Engineering*, vol. 97, pp. 951–960, 2014.

[20] J. O. Bird, P. J. Chivers, 28 - Friction, J. O. Bird, and P. J. Chivers, *Newnes Engineering and Physical Science Pocket Book*, Elsevier, Amsterdam, Netherlands, 1993.

[21] R. N. Rao and S. Das, "Effect of sliding distance on the wear and friction behavior of as cast and heat-treated Al–SiCp composites," *Materials & Design*, vol. 32, no. 5, pp. 3051–3058, 2011.

Hindawi
Advances in Materials Science and Engineering
Volume 2023, Article ID 8573440, 9 pages
https://doi.org/10.1155/2023/8573440

Research Article

Effect of ZrB_2 Particles on Machining Parameters of AA7475 Alloy-Based Composites by Optimization Technique

C. R. Mahesha,[1] R. Suprabha,[1] R. Suresh Kumar,[2] Chirumamill Mallika Chowdary,[3] Viyat Varun Upadhyay,[4] M. Soumya,[5] Essam A. Al-Ammar,[6] Sivasankar Palaniappan,[7] and Abdi Diriba[8]

[1]*Department of Industrial Engineering and Management, Dr. Ambedkar Institute of Technology, Bangalore, Karnataka 560056, India*
[2]*Department of Mechanical Engineering, Sri Eshwar College of Engineering, Coimbatore 641202, India*
[3]*Department of Civil Engineering, Koneru Lakshmaiah Education Foundation, Guntur, Andhra Pradesh 522302, India*
[4]*Department of Mechanical Engineering, GLA University, Mathura, UP 281406, India*
[5]*Department of Computer Science and Engineering, SR University, Warangal, Telangana 506001, India*
[6]*Department of Electrical Engineering, College of Engineering, King Saud University, Saudi Arabia*
[7]*Department of Environmental Engineering and Energy, Poznan University of Technology, Poznan, Poland*
[8]*Department of Mechanical Engineering, Mizan Tepi University, Tepi, Ethiopia*

Correspondence should be addressed to Abdi Diriba; abdi@mtu.edu.et

Received 10 September 2022; Revised 8 October 2022; Accepted 15 October 2022; Published 2 February 2023

Academic Editor: Pudhupalayam Muthukutti Gopal

ZrB_2 particle-reinforced AA7475 is a potential material for high-performance aeronautical engine blades because of its exceptional characteristics. The machinability of ZrB_2/AA7475 metal matrix composites (MMC) is still a challenge because of the influence of ZrB_2 particles. The impact of ZrB_2 particulates on the machined parameters of ZrB_2/aluminum matrix composites was explored experimentally in order to meet the needs of industry. Additionally, the best machining circumstances for this type of material matrix composites were studied in this research. A surface roughness (R_a) and metal removal rate (MRR) multiobjective optimization model was built, and a set of ideal parameter combinations was produced, with the surface roughness of ZrB_2/AA7475 material matrix composites being lower than that of the nonreinforced alloys at the same cutting speed.

1. Introduction

Aeronautics and other industries have greatly benefited from particle-reinforced metal matrix composites (PRMMC), a new family of materials with improved features such as a greater ratio of mass to strength, a greater elastic modulus, and better resistance to wear and tear [1–3]. There are two ways to make PRMMCs, ex situ and in situ. Ex situ processes use a subsequent technique, such as stir casting, to incorporate reinforcements into the matrix after they have been synthesized separately [4, 5]. Ex situ composites frequently exhibit particle segregation and poor interface adhesion [6]. However, in situ composites are made by directly synthesizing reinforcement phases inside the matrix, which improves adhesion at surfaces and hence increases mechanical characteristics [7, 8]. At the same time, the majority of studies concentrate on the in-situ particle-reinforced MMCs' material preparation method [9]. Engineers need to know how to machine these high-performance materials in order to use them in their designs. Strengthening particles in matrix are known to be extremely abrasive. Because of this, it is difficult to machine MMCs, and the most common difficulties are tool wear and low surface quality. Also, the physical qualities [10]. In commercial practice, silicon carbide-particle-strengthened MMCs are frequently utilized since the preparation method for ex situ material matrix composites is significantly less difficult [11, 12]. SiC particle-strengthened material matrix composites have been the

subject of much investigation on wear resistance, surface integrity, and the creation of chips [13].

Machining in situ MMCs, however, has received little attention. MMC grinding behaviour was investigated by [14, 15]. Surface quality was improved when removing PTMCs from titanium-6aluminium-4V by using a small depth of cut and a higher workpiece speed. The experimental results demonstrate that the brazed CBN wheel has a higher benefit in terms of higher polishing of PTMCs than the electroformed CBN wheel. MMCs with Al-6061-ZrB_2 were machined by [16, 17]. Cutting parameters were examined in relation to tool wear, force of cutting, and surface roughness. In terms of polishing PTMCs, it was observed that the brazed CBN wheel had an advantage over the electroformed CBN wheel [18, 19] for its machinability. The effect of factors on performance metrics and the built-up edge and chip creation are studied during turning operations. Using Al_2O_3 and Al_2O_3-SiC as a baseline [20, 21], evaluated the machinability of their innovative in situ ceramic strengthened aluminium MMC. An analysis by [22] examined the mechanical behavior of ZrB_2/Al7475MMC. Chip formation, tool wear, and surface quality are all discussed. Findings from a study showed that PCD tools were less prone to tool wear than PCBN and layered carbide tools. The most typical reasons for tool failure include wear from abrasion, adhesion, chipping, and peeling. Unlayered carbide tools have a tool life ranging from three to twenty minutes, with milling speed having the greatest impact [23, 24].

Cutting circumstances for MMCs are the most important part of a machining operation. When LM23 Al/SiC particle composites were turned by [25, 26], it was discovered that the surface finish was impacted by machining parameters. The best conditions for increasing metal removal rate while reducing surface roughness were found utilizing RSM. A want function technique was utilized by [27] to optimize machining parameters in order to decrease surface roughness. V, f, and a_p all affect flank wear and R_a in spinning aluminum/silicon carbide particle MMC with an unlayered WC addition in a dry environment [28]. A Taguchi approach was utilized to discover the optimum mixture of flank wear and R_a characteristics [29]. Soft computing has also been used by certain researchers to help them better optimize cutting parameters. The surface roughness of aluminum-silicon carbide (20p) was investigated by [30, 31] utilizing PCD additions under various cutting circumstances. ANOVA and ANN approaches were used to analyze the experimental data. Al/SiC MMCs were turned utilizing a PCD insert in an experiment conducted by [32] a link was found among speed of cutting, feed and cut depth as well as workpiece's surface finish and particular power [33]. GRA was utilized to determine the best machining constraints. For aluminum/SiCp MMCs being turned in a dry environment with an unlayered WC addition to cutting speed, feed rate, and cut depth have an effect on flank wear and surface roughness. The ideal combination of wear of flank and surface roughness properties was discovered utilizing the Taguchi technique. On the basis of these findings [34, 35], we studied the outcome of cutting speed, feed rate, depth of cut, and cutting force on Al6061-TiC surface roughness utilizing a Taguchi L27 orthogonal array and ANOVA. Numerous studies on the mechanical parameters and cutting characteristics of material matrix composites supplemented with ex situ particles have been conducted. Ex situ MMCs have different mechanical properties than in situ MMCs because of their distinct microstructures [36–38]. Due to these differences in machinability, only a small amount of research has been done on the machining parameters and cutting parameters for in situ material matrix composites. Additionally, for industrial purposes, machining efficiency is a significant metric. A ZrB_2-reinforced MMCs sample is machined with various cutting parameters to research the impact of reinforcement particles on machining force and surface roughness. We also developed, based on our experimental findings, an approach to finding the best machining parameter combinations that takes both MMR and surface roughness into consideration. To summarize the paper's organization, consider the following: Section 2 goes into great depth on the machining test circumstances. Section 3 presents and discusses the experimental outcomes. GA is used in Section 4 to establish and develop the multi-objective optimization model. Here are the final thoughts and plans for further research in Section 5.

2. Experimentation

2.1. Materials. Alloys of 7475 aluminium and ZrB_2 (ZrB_2 particles range in size from 50 nm to 200 nm) were employed in this experiment, and the mixed salts method was used to make the ZrB_2 particles. Table 1 shows the theoretical chemical composition (weight percentage) of a matrix alloy. It is tabulated in Table 2 that ZrB_2/AA7475 MMCs in situ have the following mechanical and physical properties. They were fashioned from square blocks of ZrB_2/AA7475 MMCs using the turning method, respectively.

2.2. Turning Criteria Used. A dry bar-turning approach was used on a computer numerical control turning center for the experiments. PCD tools were used in this experiment because the ZrB_2 particles were so aggressive in their ability to scratch and abrade surfaces. Table 3 contains the relevant turning conditions.

2.3. Evaluation. Figure 1 depicts the cut-off force metering apparatus. All forces are radial forces: Fc (cutting) and Ft (pushing). A surface roughness tester (T620A) was utilized to evaluate the roughness of the surface with a calculation and cut-off length of 0.8 mm. The average values of the measurements made at each position were calculated after they were repeated twice.

3. Analysis of Experimental Result

3.1. Machining Forces. For a variety of cutting speeds, feed rates, and cutting forces, the results are shown in Figures 2 and 3. In comparison to ZrB_2/Al MMCs, the nonreinforced 7475 aluminium alloy has a lower cutting force. The cutting and thrust forces for 7475 aluminium alloy and MMCs are

Table 1: Chemical arrangement of AA 7475 alloy.

Basics	Copper	Chromium	Magnesium	Zinc	Manganese	Silicon	Aluminium
wt%	1.9	0.22	2.3	5.7	0.06	1.50	Remaining

Table 2: ZrB_2/AA 7475 MMCs mechanical and physical characteristics.

Properties	Elastic modulus (GPa)	Yield strength (MPa)	Density (g/cc)	Elongation	Hardness (HB)	Poisson ratio
Range	71.7	462	2.81	12%	140	0.33

Table 3: Turning criteria.

Turning criteria	Description
Cutting speed (V) (m/min)	30, 60, 90, 120
Feed rate (f) (m/min)	30, 60, 90, 120
Depth of cut (a_p) (mm)	0.5, 1, 1.5, 2
Cutting edge angle (°)	−5
Cutting condition	Dry
Cutting tool	Polycrystalline diamond
Nose radius (mm)	0.6
Clearance angle (°)	5

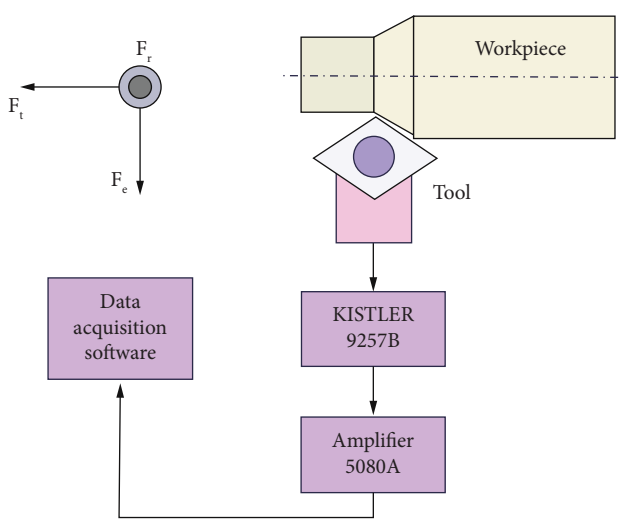

Figure 1: Illustration of cutting force arrangement.

illustrated in Figures 2(a) and 2(b). Cutting speed has an important impact on both cutting and pushing forces. While MMCs are travelling at speeds of less than 60 m/min, the forces diminish rapidly as speed rises.

The force rises significantly as speed is increased further. The following is a summary of how this works:

(1) When cutting speed increases, the tool-to-workpiece friction ratio decreases.

(2) As cutting speed increases, the cutting temperature rises, softening the metal matrix. Because of the two factors outlined above, as the speed of cutting grows from 10 m/min to 60 m/min, the force becomes less significant.

Cutting and pushing forces are depicted in Figure 3 using various feeds. MMCs have a greater tensile strength than the aluminium alloy 7475. As feed increases, so do the pressures for both resources practically linearly. As feed rate rises, the MRR rises, which necessitates a greater amount of energy for chip creation. The cutting force is increased as a result. In contrast, MMCs have a far greater growth rate than the 7475 aluminium alloy. The forces exerted by the two materials are nearly equal at low feed rates. Because of the presence of reinforced particles in ZrB_2/Al 7475 MMCs, the shear stress rises with increasing feed rate. As inputs rise, the differential between MMCs and nonreinforced alloys widen. A nonreinforced alloy's thrust force is virtually unaffected by the feed.

To further our understanding of how reinforcements affect force generation, we analyzed the force signals from the dynamometer. Figure 4 depicts the highest forces generated while spinning MMCs and AA7475 at 90 m/min, 60 mm/min feed, and a 2 mm depth of cut at these various speeds. When MMCs are turned, the force of cutting is greater than radiated force. In contrast, when spinning AA7475, the highest force of cutting is less than the radiated force. This may have been caused by turning AA7475. AA7475 is less rigid than ZrB_2/AA7475 MMCs, which makes the workpiece more prone to vibration during the machining procedure. As an outcome, the cutting force will be greater than the maximum radial force. The V is greater than average radiated force while turning 7475 alloy. Cutting force during the turning of MMCs differs significantly from thrust force compared to AA7475, suggesting that ZrB_2/AA7475 MMCs are more heterogeneous due to the reinforcements. When turning both materials, the radiated force variation is greater than the force of the cutting and thrust force variations. This could be because of vibrations that occur throughout the turning operation.

3.2. Surface Roughness (R_a). Figure 5 illustrates how cutting speed influences surface roughness. ZrB_2/Aluminum material matrix composites have a lower roughness than nonreinforced 7475 aluminium alloy at all cutting speeds. Because of the reinforcing particles, ZrB_2/Al7475 MMCs are less ductile and more prone to fracture when turned. On the other hand, as seen in Figure 5, raising the cutting speed leads to lessened surface roughness. When cutting at a faster speed, there may be a decrease in material flow on the side. Figure 6 illustrates the surface roughness is influenced by feed rate. Maintaining a constant feed rate results in a linear increase in surface roughness. While the roughness of MMC is lower when fed at low speeds, the opposite is true when fed at high speeds.

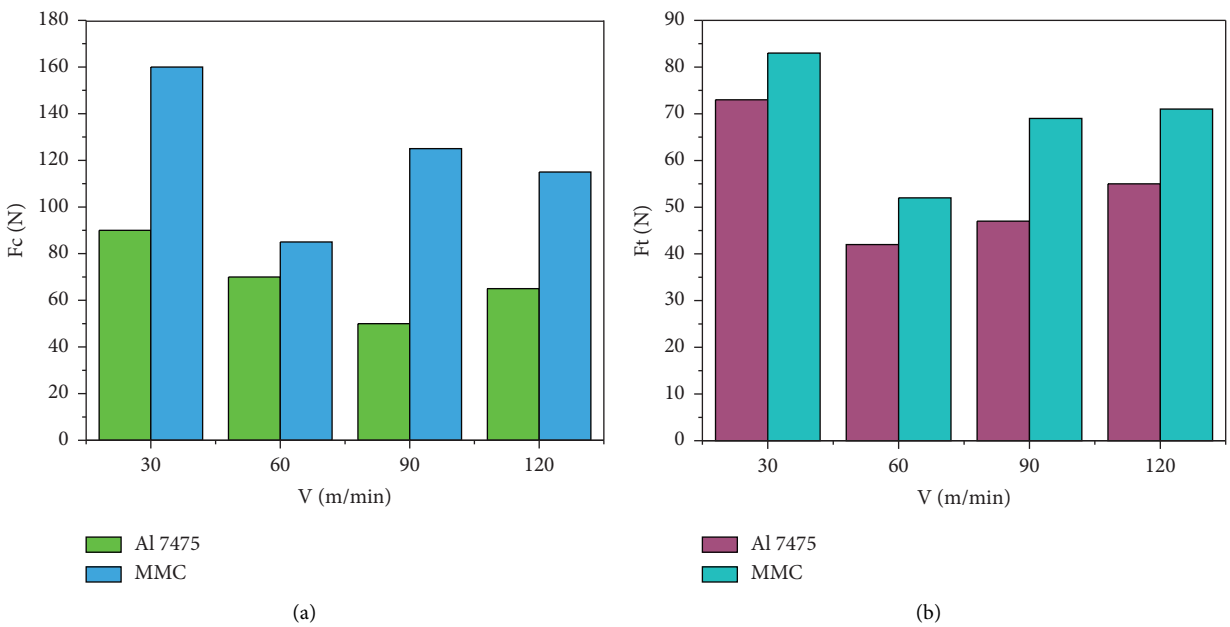

Figure 2: Comparison of (a) cutting force and (b) thrust force with speed (at $f = 60$ mm/min and $a_p = 2$ mm).

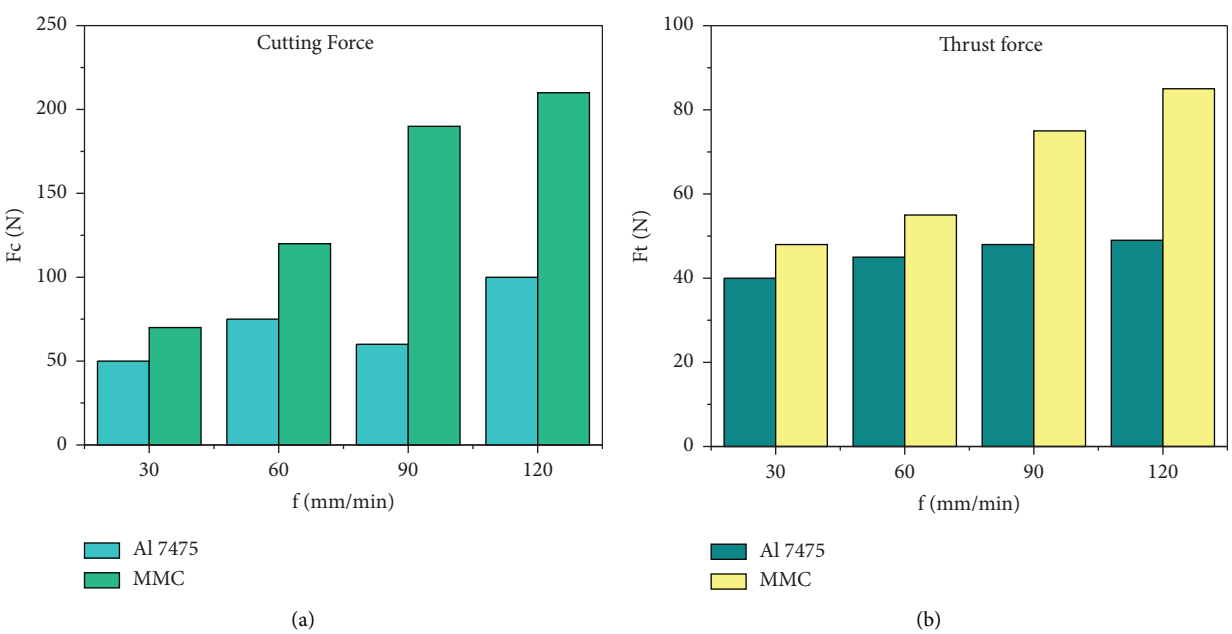

Figure 3: Comparison of forces with feed rate (at $V = 90$ m/min and $a_p = 2$ mm).

Feed marks on nonreinforced 7475 aluminium alloy are inconsistent because the material softens during cutting. When it comes to MMC, the feed markings are plainly visible, and the f marks become more severe as V increases. Reinforcement particles may be too little to have an effect on this. Because the ZrB_2 particle is so small, it has a small effect on the machining process.

4. Surface Roughness and Metal Removal Rate Improved by Optimizing Turning Parameters

Surface roughness is a more critical factor in determining the quality of a workpiece's surface, since abnormalities in the surface can serve as the nucleation point for fractures or corrosion. This section examined experimentally the

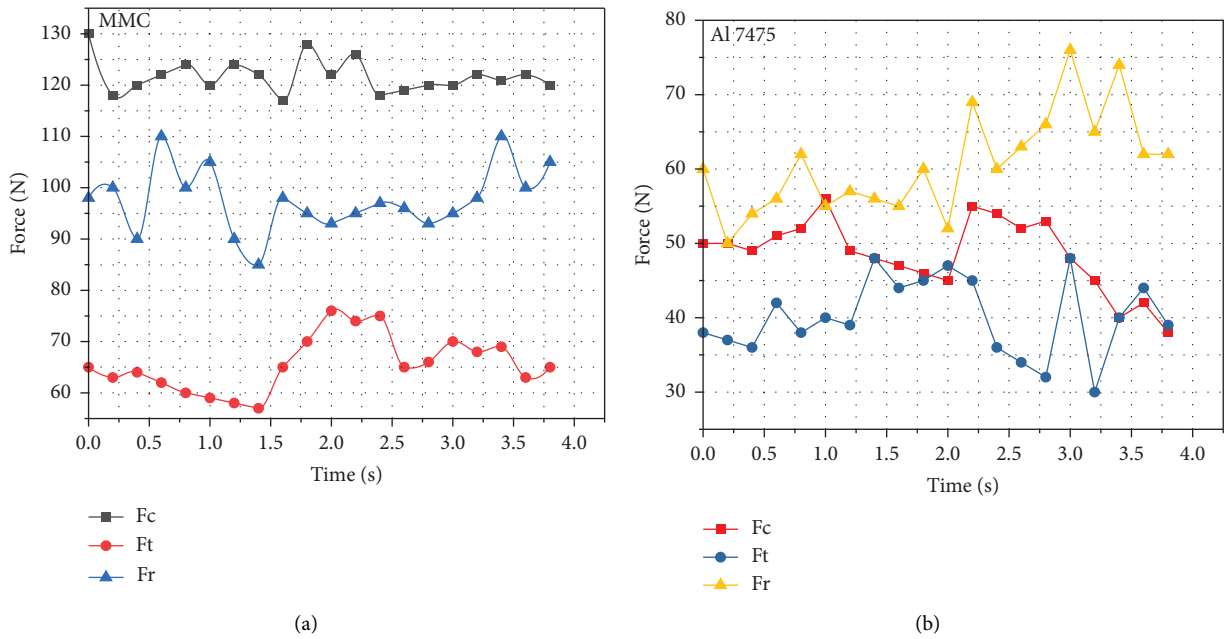

Figure 4: Comparison of force signals. (a) MMCs. (b) 7475 ($V = 90$ m/min, $f = 60$ mm/min, $a_p = 2$ mm).

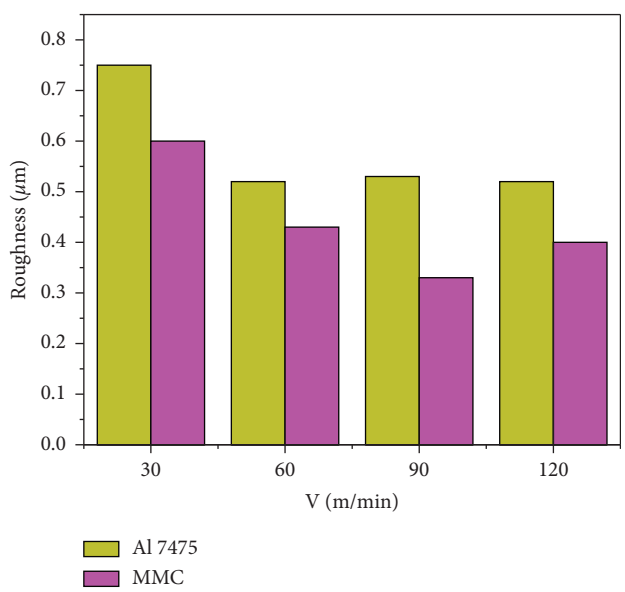

Figure 5: Comparison of V on R_a ($f = 60$ mm/min, $a_p = 2$ mm).

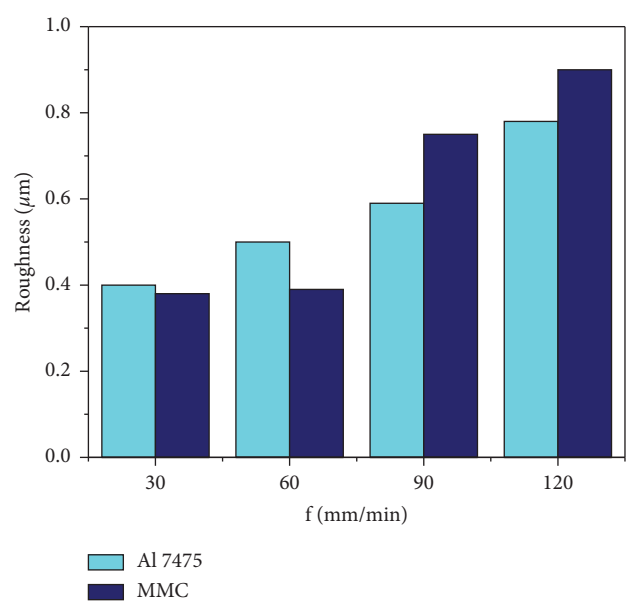

Figure 6: Impact of f (mm/min) on R_a ($V = 90$ m/min, $a_p = 2$ mm).

connection between V and R_a. The surface roughness model was built with RSM 32 to allow for quantitative comparisons between cutting settings and surface roughness. Real-world data can be depicted as a two- or three-dimensional hypersurface, utilizing RSM as a major tool for discovering and visualizing the relationship between variables. Surface roughness and MRR were also taken into consideration when optimizing the cutting parameters.

4.1. Development of the Surface Roughness Model. There are fewer design points in a Box–Behnken design than in central composite designs, making it more efficient at estimating first- or second-order coefficients. There are usually three layers of each element in a Box–Behnken design. The speed of the cutting range starts at 110 to 300 m/min, feed rates range from 30 to 120 mm/min, and the depth of cut ranges from 0.5 to 1.5 mm, making this machine versatile enough to handle a varied range of resources and applications. Table 4 shows the link among surface roughness and machine properties as follows:

According to earlier studies, a second-sort quadratics model can be used to approximate the true functional connection between R_a and cutting properties, which can be represented as

Table 4: Experimentation outcome on R_a.

S. no.	Cutting factor			Surface roughness (μm)
	V (m/min)	F (mm/min)	a_p (mm)	
1	30	120	0.5	3.12
2	60	90	0.5	4.64
3	90	120	1.5	2.21
4	120	120	1	1.72
5	120	90	1	1.63
6	90	30	1	0.31
7	60	90	1	1.84
8	30	60	1.5	0.86
9	60	120	1	8.24
10	90	30	1	0.62
11	120	60	1	1.74
12	120	90	1	0.63
13	90	120	0.5	0.63
14	30	30	0.5	0.53
15	60	60	1	1.75
16	120	90	1.5	3.53
17	90	120	1	1.72

Table 5: The model's statistical summary.

Basis	S.D.	R^2	Adj. R^2	Pred. R^2	Press
2FI	0.136496	0.9617	0.9526	0.9474	1.18614
Linear	0.160973	0.9458	0.9492	0.9304	1.59635
Quadratic	0.097193	0.9945	0.9872	0.9863	0.45731

$$R_a = \beta + \sum_{i=1}^{k} \beta_i x_i + \sum_{i=1}^{k} \beta_{ii} x_i^2 + \sum \sum_{i<j} \beta_{ij} x_i x_j + \varepsilon, \quad (1)$$

where R_a is surface roughness of workpiece, β is regression coefficients, x_i is values of ith cutting parameter, and ε is observation's mistake due to the experiment.

ANOVA was used to examine the effect of input variables on surface roughness in order to confirm the findings of past experiments. Models were compared using the linear, 2FI, and quadratic models to determine which one was the most accurate. Table 5 demonstrates that the quadratic model is a great fit, and hence the surface response function should be a quadratic model. Second order is the response surface model (RSM) data. The regression equation for R_a is shown as

$$R_a = -2.33 - 0.0044V + 0.091f + 1.26a_p - 0.00038Vf + 0.0026Va_p + 0.00062fa_p + 0.000048V^2 + 0.00016f^2 - 1.11a_p^2. \quad (2)$$

The original data used to create the regression model were utilized to verify the model's accuracy. In addition, three roughness values of the surface were utilized to verify the accuracy of RSM. Table 6 displays the results of the testing. There was good distribution in the space of cutting parameter selection for the checking data. As a result, the RS model's accuracy may be tested using these data. Table 6 shows that the maximum inaccuracy is less than 10%. As a result, the regression model has been proven to be accurate.

4.2. Optimum Results and Discussion. Both objectives of this research are at odds with one another. For example, the MRR increases as the feed rate rises, yet surface roughness also rises as the feed rate rises. The other goal (raising the MRR) would never be achieved if all efforts were directed just at smoothing the surface texture. With so many competing goals, it is essential to find a middle ground. Problems with several objectives are frequently tackled using the sum of weighted elements approach. There is typically just one answer per run, and the weights are normalized so that the sum of the weights equals 1. Initializing, evaluating, crossover and mutation, selection, and other GA processes are just a few of the many facets that go into the algorithm's construction. In order to optimize the multiobjective optimization model, commercial software was used. A relative experiment was conducted in order to confirm the best outcomes. It was necessary to use both optimal cutting parameters and conventional cutting parameters to achieve the appropriate surface roughness while cutting ZrB_2/AA7475. Table 7 shows the outcomes. Surface roughness has

Table 6: RS model's accuracy was tested using this collection of data.

Trial	Cutting factor			R_a		
	V	F	a_p	Measurement	Rs model	Error (%)
1	60	90	0.6	1.193	1.36212	7.909
2	90	120	0.8	1.805	1.97563	9.969
3	120	60	1.2	0.478	0.46119	6.415

Table 7: Comparison of experimental results.

Cutting type	Cutting factor			Surface roughness (μm)	MRR (mm^3/min)
	V (m/min)	F (mm/min)	a_p (mm)		
Conventional	120	120	1	1.72	14090000
Optimal	90	90	1	0.765	12143000

been demonstrated to improve with increasing cutting speed. When cutting at a faster speed, there may be a decrease in material flow on the side. As the feed rate rises, the roughness of the finished product also rises.

5. Conclusions and Scope of Future Work

The machining parameters of 6% ZrB_2/AA7475 material matrix composites must be studied for engineering applications because it is a new material. The nonreinforced 7475 aluminium alloy was utilized as a comparison to find the effect of in situ produced ZrB_2elements on the machining parameters of material matrix composites. Surface roughness and machining force were examined in relation to ZrB_2 particles. A surface roughness response surface model was created. The following are the study's most important findings:

(1) ZrB_2/AA7475 MMCs have a somewhat higher machining force than 7475 aluminium alloy without reinforcement. As the speed increased, so did the cutting and pushing forces for both substances. The machining force rose gradually after a specific speed of 60 m/min. The machining force rose in direct proportion to the feed rate. The forces generated by the two materials are almost equal when the feed rates are relatively low. Although the nonreinforced alloy has a higher initial machining force than ZrB_2/aluminum matrix materials, this increase is slower.

(2) Both materials saw significant reductions in surface roughness as the cutting speed was increased. Fewer cuts are made after a specific speed is reached. When fed at a low rate, ZrB_2/AA7475 MMCs have a rougher surface than 7475 aluminium alloy, but as the feed rate is increased, ZrB_2/AA7475 MMCs' surface roughness increases faster. On the other hand, the feed marks on ZrB_2/Al7475 MMCs are clearly visible. For this novel material, there is still much work to be done before a complete understanding of machinability can be acquired. In the near future, we plan to investigate the mechanisms that cause material loss and chip creation.

Data Availability

The data used to support the findings of this study are included within the article. Further data or information is available from the corresponding author upon request.

Conflicts of Interest

The authors declare that there are no conflicts of interest.

Acknowledgments

The authors appreciate the supports from Mizan Tepi University, Ethiopia for the research and preparation of the manuscript. The authors would like to acknowledge the Researchers Supporting Project Number (RSP2023R492), King Saud University, Riyadh, Saudi Arabia.

References

[1] S. R. Ruban, K. L. Dev Wins, J. D. Raja Selvam, and R. S Rai, "Influence of turning parameters on the machinability of Al6061/ZrB2 & ZrC hybrid in-situ Aluminium Matrix Composite," *Australian Journal of Mechanical Engineering*, vol. 2021, 2021.

[2] M. M. Nasr, S. Anwar, A. M. Al-Samhan, M. Ghaleb, and A. Dabwan, "Milling of graphene reinforced ti6al4v nanocomposites: an artificial intelligence based industry 4.0 approach," *Materials*, vol. 13, no. 24, pp. 1–22, 2020.

[3] D. Srinivasan, M. Meignanamoorthy, A. Gacem et al., "Tribological behavior of Al/Nanomagnesium/Aluminum nitride composite synthesized through liquid metallurgy technique," *Journal of Nanomaterials*, vol. 2022, pp. 1–12, Article ID 7840939, 2022.

[4] Z. Liao, A. Abdelhafeez, H. Li, Y. Yang, O. G. Diaz, and D. Axinte, "State-of-the-art of surface integrity in machining of metal matrix composites," *International Journal of Machine Tools and Manufacture*, vol. 143, pp. 63–91, 2019.

[5] V. Mohanavel, K. Ashraff Ali, S. Prasath, T. Sathish, and M. Ravichandran, "Microstructural and tribological characteristics of AA6351/Si3N4 composites manufactured by stir casting," *Journal of Materials Research and Technology*, vol. 9, no. 6, pp. 14662–14672, 2020.

[6] A. Pugazhenthi, I. Dinaharan, G. Kanagaraj, and J. D. R. Selvam, "Predicting the effect of machining parameters on turning characteristics of AA7075/TiB2 in situ

aluminum matrix composites using empirical relationships," *Journal of the Brazilian Society of Mechanical Sciences and Engineering*, vol. 40, no. 12, p. 555, 2018.

[7] T. Chwalczuk, D. Przestacki, P. Szablewski, and A. Felusiak, "Microstructure characterisation of Inconel 718 after laser assisted turning," *MATEC Web of Conferences*, vol. 188, p. 02004, 2018.

[8] R. Singh, M. Shadab, and R. N. Rai, "Optimization of machining process parameters in conventional turning operation of Al5083/B4C composite under dry condition," *Materials Today Proceedings*, vol. 5, no. 9, pp. 19000–19010, 2018.

[9] A. Pugazhenthi, G. Kanagaraj, I. Dinaharan, and J. David Raja Selvam, "Turning characteristics of in situ formed TiB2 ceramic particulate reinforced AA7075 aluminum matrix composites using polycrystalline diamond cutting tool," *Measurement*, vol. 121, pp. 39–46, 2018.

[10] C. Yan, W. Lifeng, and R. Jianyue, "Multi-functional SiC/Al composites for aerospace applications," *Chinese Journal of Aeronautics*, vol. 21, no. 6, pp. 578–584, 2008.

[11] S. Natarajan, R. Narayanasamy, S. P. Kumaresh Babu, G. Dinesh, B. Anil Kumar, and K. Sivaprasad, "Sliding wear behaviour of Al 6063/TiB2 in situ composites at elevated temperatures," *Materials & Design*, vol. 30, no. 7, pp. 2521–2531, 2009.

[12] L. M. Tham, M. Gupta, and L. Cheng, "Effect of limited matrix-reinforcement interfacial reaction on enhancing the mechanical properties of aluminium-silicon carbide composites," *Acta Materialia*, vol. 49, no. 16, pp. 3243–3253, 2001.

[13] I. Aziz, Z. Qi, and X. Min, "Corrosion inhibition of SiCp/5A06 aluminum metal matrix composite by cerium conversion treatment," *Chinese Journal of Aeronautics*, vol. 22, no. 6, pp. 670–676, 2009.

[14] C.-G. Zhou, L.-D. Wang, J.-W. Shen, C.-H. Chen, Y. Ou, and H.-T. Feng, "Wear characterization of raceway surface profiles of ball screws," *Journal of Tribology*, vol. 14411 pages, 2022.

[15] X. Liu, L. Cai, and H. Chen, "Residual stress indentation model based on material equivalence," *Chinese Journal of Aeronautics*, vol. 35, no. 8, pp. 304–313, 2022.

[16] X. F Liu, W. H Wang, R. S Jiang, Y. F Xiong, and C. W. Shan, "Comparative investigation on surface integrity for conventional and ultrasonic vibration–assisted cutting of in situ TiB2/7050Al MMCs," *International Journal of Advanced Manufacturing Technology*, vol. 120, no. 3–4, pp. 1949–1965, 2022.

[17] P. Maurya, N. Kota, J. Gibmeier, A. Wanner, and S. Roy, "Review on study of internal load transfer in metal matrix composites using diffraction techniques," *Materials Science and Engineering A*, vol. 840, p. 142973, 2022.

[18] L. Lü, M. O. Lai, Y. Su, H. L. Teo, and C. F. Feng, "In situ TiB2 reinforced Al alloy composites," *Scripta Materialia*, vol. 45, no. 9, pp. 1017–1023, 2001.

[19] X. Pan, W. He, Z. Cai et al., "Investigations on femtosecond laser-induced surface modification and periodic micro-patterning with anti-friction properties on Ti6Al4V titanium alloy," *Chinese Journal of Aeronautics*, vol. 35, no. 4, pp. 521–537, 2022.

[20] F. Zhao, B. Lin, Y. He, and T. Sui, "Interference mechanism and damage accumulation in high-speed cross scratches on hard brittle materials," *Chinese Journal of Aeronautics*, vol. 35, no. 3, pp. 579–591, 2022.

[21] Ü. A. Usca, M. Uzun, S. Sap et al., "Tool wear, surface roughness, cutting temperature and chips morphology evaluation of Al/TiN coated carbide cutting tools in milling of Cu–B–CrC based ceramic matrix composites," *Journal of Materials Research and Technology*, vol. 16, pp. 1243–1259, 2022.

[22] X. Han, Z. Liao, G. G. Luna, H. N. Li, and D. Axinte, "Towards the understanding the effect of surface integrity on the fatigue performance of silicon carbide particle reinforced aluminium matrix composites," *Journal of Manufacturing Processes*, vol. 73, pp. 518–530, 2022.

[23] T. Tayeh, J. Douin, S. Jouannigot et al., "Hardness and Young's modulus behavior of Al composites reinforced by nanometric TiB2 elaborated by mechanosynthesis," *Materials Science and Engineering A*, vol. 591, pp. 1–8, 2014.

[24] M. Wang, D. Chen, Z. Chen et al., "Mechanical properties of in-situ TiB2/A356 composites," *Materials Science and Engineering A*, vol. 590, pp. 246–254, 2014.

[25] R. Aghababaei, M. Malekan, and M. Budzik, "Cutting depth dictates the transition from continuous to segmented chip formation," *Physical Review Letters*, vol. 127, pp. 235502–235523, 2021.

[26] S. Kesarwani and R. K. Verma, "Ant Lion Optimizer (ALO) algorithm for machinability assessment during Milling of polymer composites modified by zero-dimensional carbon nano onions (0D-CNOs)," *Measurement*, vol. 187, p. 110282, 2022.

[27] A. Dttmann and J. d. O. Gomes, "Evaluation of additive manufacturing parts machinability using automated gmaw er70s-6 with nodular cast iron," *U.Porto Journal of Engineering*, vol. 7, no. 2, pp. 88–97, 2021.

[28] M. El-Gallab and M. Sklad, "Machining of Al/SiC particulate metal-matrix composites Part I: tool performance," *Journal of Materials Processing Technology*, vol. 83, no. 1–3, pp. 151–158, 1998.

[29] X. Ding, W. Y. H. Liew, and X. D. Liu, "Evaluation of machining performance of MMC with PCBN and PCD tools," *Wear*, vol. 259, no. 7–12, pp. 1225–1234, 2005.

[30] N. H. Ononiwu, C. G. Ozoegwu, N. Madushele, and E. T. Akinlabi, "Characterization, machinability studies, and multi-response optimization of AA 6082 hybrid metal matrix composite," *International Journal of Advanced Manufacturing Technology*, vol. 116, no. 5–6, pp. 1555–1573, 2021.

[31] N. H. Ononiwu, C. G. Ozoegwu, N. Madushele, and E. T. Akinlabi, "Machinability studies and optimization of aa 6082/fly ash/carbonized eggshell matrix composite," *Revue des Composites et des Matériaux Avancés*, vol. 31, no. 4, pp. 207–216, 2021.

[32] S. Mohanty, G. K. Mohanta, S. R. Das, and J. J. Behera, "The effect of process parameters while turning AL based MMC with waste reinforcement in CNC machine in wet condition by using Taguchi optimization technique," *MATERIALS, MECHANICS & MODELING (NCMMM-2020)*, vol. 2341, 2021.

[33] R. K. Bhushan, S. Kumar, and S. Das, "Effect of machining parameters on surface roughness and tool wear for 7075 Al alloy SiC composite," *International Journal of Advanced Manufacturing Technology*, vol. 50, no. 5–8, pp. 459–469, 2010.

[34] Y. Xiong, W. Wang, Y. Shi et al., "Investigation on surface roughness, residual stress and fatigue property of milling in-situ TiB2/7050Al metal matrix composites," *Chinese Journal of Aeronautics*, vol. 34, no. 4, pp. 451–464, 2021.

[35] X. Liu, W. Wang, R. Jiang et al., "Analytical model of cutting force in axial ultrasonic vibration-assisted milling in-situ TiB2/7050Al PRMMCs," *Chinese Journal of Aeronautics*, vol. 34, no. 4, pp. 160–173, 2021.

[36] M. El-Gallab and M. Sklad, "Machining of Al/SiC particulate metal matrix composites Part II: workpiece surface integrity," *Journal of Materials Processing Technology*, vol. 83, no. 1–3, pp. 277–285, 1998.

[37] N. Muthukrishnan, M. Murugan, and K. Prahlada Rao, "Machinability issues in turning of Al-SiC (10p) metal matrix composites," *International Journal of Advanced Manufacturing Technology*, vol. 39, no. 3–4, pp. 211–218, 2008.

[38] S. S. Joshi, N. Ramakrishnan, and P. Ramakrishnan, "Analysis of chip breaking during orthogonal machining of Al/SiCp composites," *Journal of Materials Processing Technology*, vol. 88, no. 1-3, pp. 90–96, 1999.

Hindawi
Advances in Materials Science and Engineering
Volume 2023, Article ID 9002743, 12 pages
https://doi.org/10.1155/2023/9002743

Research Article

An Optimisation Method of Construction for Warping Copper Plates and Engines Using Complete Block Designs with Some Special Types of Graphs

P. Karthikeyan,[1] K. Kalaiselvi,[1] M. Pachamuthu,[2] Kanulla Karthik,[3] and A. Johnson Santhosh[4]

[1]*Department of Mathematics, Sri Vasavi College of Arts and Science College, Erode, Tamilnadu, India*
[2]*Department of Statistics, Periyar University, Salem, Tamil Nadu, India*
[3]*Department of Mechanical Engineering, Lakireddy Bali Reddy College of Engineering, NTR District, Mylavaram, Krishna, Andhra Pradesh, India*
[4]*Faculty of Mechanical Engineering, Jimma Institute of Technology, Jimma University, Jimma, Ethiopia*

Correspondence should be addressed to A. Johnson Santhosh; johnson.antony@ju.edu.et

Received 15 July 2022; Revised 1 October 2022; Accepted 3 October 2022; Published 31 January 2023

Academic Editor: Vijayananth Kavimani

The application of bipartite and regular graphs plays a vital role in the area of engineering, mathematical sciences, design of experiments, and medical fields. This study proposes an optimization method for constriction of randomized block design and Latin square design using bipartite and regular graphs with applications of warping copper plates in specimens and comparing them to burners and engines on different days. The construction methods and analysis are performed as follows: the first method is a construction of randomized block design using bipartite and complete bipartite graphs with applications for the amount of warping copper plates and different laboratories are taken to test any significant difference that exists between the mean number of responses for the labs and copper specimens. The second method is the construction of a Latin square design using regular graphs to test whether there is any significant difference between the burners, engines, and some days in statistical analysis of interaction plots, contour plots, and 3D surface plots.

1. Introduction

In this modern scientific electronic world, mathematical sciences and engineering for a method of construction in complete block designs are randomized block design (RBD) and latin square design (LSD) which have been developed by graph theory. To meet the current trend of warping copper plates and specimens, compared to burners, engines with the statistical analysis problem have become a critical issue, which occurs from the residual stress accumulated from various methods of construction. In this situation inevitable for a method of construction using graph theory incomplete block designs. The first study in graph theory was written by Euler in 1936 when he settled the famous unsolved problem of his day, known as the Konigsberg bridge problem. The graphs over a framework answer issues with several preparations, networking, optimization, matching, and operational problems. For illustration, Google maps use graphs for structure alteration systems, where the connexion of two or more roads is measured to be a vertex, and the road joining two vertices is deemed to be an edge, thus their steering system is based on the procedure to calculate the shortest path between two vertices. In graph theory, as described by Bondy and Murty [1], a component that allows exhibiting a series of data on a chart is known as a bar graph. Any binary vertices combined by more than one edge are known as a multigraph. A graph without loops and with at most one edge between two vertices is called a simple graph. Each vertex is associated by an edge to each other vertex is called a complete graph. Direction may be allocated to each edge to

produce is known as a directed graph. A tree suggests splitting out from a root and never implementing a cycle. The applications of trees in data storage, searching, complete block designs, etc. A graph with no cycle is acyclic, a forest is an acyclic graph. A tree is connected acyclic graph. A leaf or pendant vertex is a vertex of degree. A spanning subgraph G is a subgraph with vertex set $V(G)$. A spanning tree is a spanning subgraph that is a tree. For example, a tree is a connected forest, and every component of a forest is a tree. A graph with no cycles has no odd cycles; hence trees and forests are bipartite. The path is a tree, and a tree is a path if and only if its maximum degree is 2. A star is a tree consisting of one vertex adjacent to all the others. The n-vertex star is a biclique $K_{1,n-1}$. A graph that is a tree that has exactly one spanning tree; the full graph itself. In an experimental design, by Das and Giri, [2], the designs containing the basic principle of blocking are called block designs and may be categorized into two types, complete and incomplete block designs. In a complete block design, all the treatments are allocated to every block. That is $k = v$ and hence $b = r$ otherwise incomplete block designs. The experimental material is to be homogeneous, then the design is known as a completely randomized design (CRD). In a CRD, there is no local control measure adopted, and the total variation is divided into two components, treatment and error. An improvement of CRD is obtained by providing local control measures through a blocking design called RBD. Blocking basic principles can be extended more to advance RBD by eliminating more sources of variation. LSD is an improved design with binary sources of variation in two directions, namely, blocks and treatments. Some methods for construction and analysis developed by various researchers concerning such designs are discussed; Bose [3], has discussed the construction of balanced incomplete block designs with an example. Yamamoto et al.[4] has discussed the claw decomposition of complete graphs and complete bipartite graphs. Zhang and Zhu [5] have discussed Hilton's theorem and proved that graph G is a 2-connected, k-regular, nonbipartite graph of order at most $3k - 3$, and x, y is a pair of distinct vertices. If $G\ \{x, y\}$ is connected, then G contains an (x, y)-Hamilton path. Zhang et al. [6] have developed the effect of underfilled epoxy on warpage in flip-chip assemblies. Jacobs et al. [7] constructed protein flexibility predictions using graph theory. Gavrilyuk and Makhnev [8] have discussed the amply regular graphs and block designs. Tseng et al. [9] have discussed the analysis of the formability of aluminum and copper-clad metals with different thicknesses by the finite element method and experiment. Rizzo and Mansano [10] have developed the electrooptically sensitive diamond-like carbon thin films deposited by reactive magnetron sputtering for electronic device applications. Miyajima et al. [11] have presented the electrophoretic deposition onto an insulator for thin film preparation for electronic device fabrication. Yang et al. [12] have developed the chip warpage model for reliable prediction of delamination failures. Pachamuthu M and Jaisankar R [13] have discussed the construction methodology of lattice designs using *MOLS* using Galois field. Gupta et al. [14] have proved the reduction of out-of-plane warpage in surface micromachined beams using corrugation. Federer and Wright [15] have constructed the lattice square designs. Hwang and Tzou [16] have studied an analytical approach to asymmetrical cold- and hot-rolling of clad sheets using the slab method. Lee et al. [17], analyzed the differential speed rolling to reduce warping in the bimetallic slab. Zhu et al. [18] have discussed the experimental identification of warpage origination during the wafer-level packaging process. Kim et al. [19] have discussed the warpage analysis of electroplated Cu films on fibers-reinforced polymer packaging substrates. The analysis method is performed using the following sequence: fabricate specimens for scanning 3D contours, transform 3D data into curvatures, compute the built-in stress of the film using a stress-curvature analytic model, and verify it through comparisons of the finite element method (FEM) simulations with the measured data also calculate residual stress, and predict curvatures using FEM simulation throughout the reflow process temperature ranging between 25 and 180°C are proven to be accurate by the comparison of the FEM simulations and experimental measurements. Lee [20] have developed the decomposition of the complete bipartite multigraph into cycles and stars. Mandal and Dash [21] have discussed the balanced incomplete Latin square designs with proposed three methods of construction of balanced incomplete latin square designs. Particular classes of Latin squares, namely, Knut Vik designs, semi-Knut Vik designs, and crisscross Latin squares play a key role in the construction. Sumaiya et al. [22] have constructed a generation of complete bipartite graphs using normalized Hadamard matrices. Ramya and Pachamuthu [23] have constructed the balanced incomplete block designs through factorization and coloring graphs using mutually orthogonal Latin square designs with numerical examples. Ilayaraja and Muthusamy [24] have discussed the essential and adequate conditions for the existence of a decomposition of complete bipartite graphs into cycles and stars with four edges of the problems. Sivamaran et al. [25] have studied the effect of chemical vapor deposition parameters on the diameter of multiwalled carbon nanotubes. Sivamaran et al. [26] have discussed optimizing chemical vapor deposition parameters to attain minimum diameter carbon nanotubes by response surface methodology. Nemitallah et al. [27] have reviewed frontiers in combustion techniques and burner designs for emissions control and CO_2 capture. Sivamaran et al. [28] have identified of appropriate catalyst system for the growth of multiwalled carbon nanotubes via a catalytic chemical vapor deposition process in a single-step batch technique. Reddy and Hemavathi [29] have described several characterizations of k-distance bipartite graphs with an example. Saurabh and Singh [30] have discussed a note on the construction of Latin square-type designs. Ozkan [31] has performed a comparative study on the investigation of the electromagnetic shielding performance of copper plate and copper composite fabrics. Electromagnetic shielding performances of copper plate and metal composite in woven/knitted fabrics were compared. For this purpose, the electromagnetic shielding effectiveness of single and double-layer copper plates and metal composite fabrics were measured in vertical and horizontal directions. As a result,

the copper plate showed better performance than composite fabric samples for both measurement directions. In general, the EMSE of the composite fabrics was lower than 10 dB for horizontal directions. Only the copper plates provided electromagnetic shielding at a significant level (up to 60 dB) against horizontally polarized waves. EMSE behavior of copper plate was similar for both directions due to the isotropic structure and this performance was maintained at a higher frequency level. On the other hand, gaps in the structure of composite fabrics caused a decrease in EMSE performance against increasing frequency. Raza and Asif Masood [32] have discussed the efficiency of Lattice design in relation to randomized complete block design in agricultural field experiments. Richthammer [33] has derived the bunkbed conjecture for complete bipartite graphs and related classes of graphs. Braun and Tyagi [34] have proved the minimax optimal clustering of bipartite graphs with a generalized power method. Sivamaran et al. [35] have developed multiresponse optimization on tribomechanical properties of CNTs/nSiC reinforced hybrid Al MMC through response surface method approach and also studied the optimum parameters were found load at 2.00 kg, speed 200 rpm, 7.50% of SiC reinforcement results in wear rate of 20.50 μm/g with the hardness of 161.43 HV. Moreover, the L32 orthogonal array and hierarchical clustering were established to understand and validate the relationship between the process parameters and responses of this investigation. In this study, an optimization method for the construction of complete block designs is RBD and LSD. The method of construction for RBD and LSD with numerical examples is to test whether there is any significant difference between labs and warping copper plates with specimens, compare three burners, engines and three days is discussed, construing the graphs of results is an interaction plot for response lines around parallel, the R^2 value is nearest to 1, the noise signal is greater than 4, the variables are associated with changes in the response variable, and the contour plot the association between the variables excellence. Also, the graph of three-dimensional (3D) surface plot is related to the response variable, so our hypothesis of the study is valid and significant.

2. Preliminaries

2.1. A Bipartite Graph. A graph $G = (V, E)$ is said to be a bipartite graph if vertices set V can be separated into two subsets V_1 and V_2, such that each edge of G connects a vertex of V_1 to V_2. These graphs are meant by $K_{m,\,n}$, where m and n are the numbers of vertices in V_1 and V_2, respectively.

2.2. A Complete Bipartite Graph. A graph $G = (V, E)$ is a complete bipartite graph if vertices set V can be separated into two subsets V_1 and V_2, so each vertex of V_1 is connected to each vertex of V_2. The number of edges in a complete bipartite graph is $m \times n$ as each of the m vertices is connected to each of the n vertices.

2.3. Randomized Block Design (RBD). The RBD of each treatment is repeated the same number of times. Suppose that there are v treatments, and each v is to be repeated r times and the total number of the experimental units is vr; then, these are arranged into b groups, each of size k, and these groups are made homogeneous using the error control measure, and then the v treatments are allotted at random to the k plots in each block. This type of homogeneous grouping of the experimental units and the random allocation are the features of RBD.

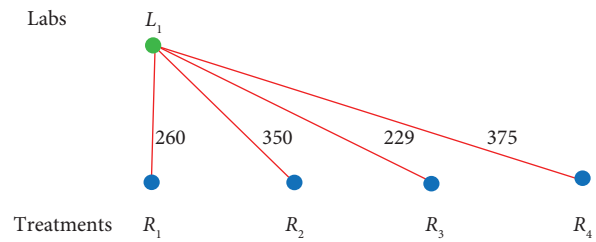

Figure 1: First bipartite graph.

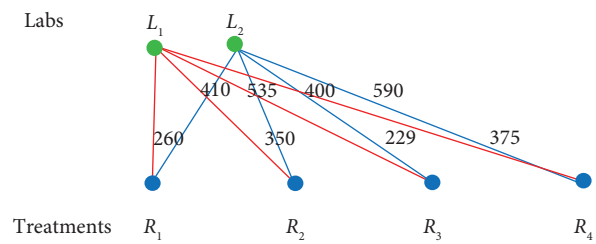

Figure 2: Second bipartite graph.

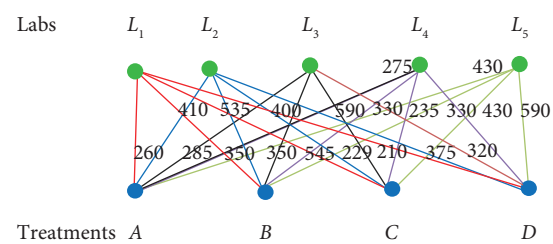

Figure 3: Third bipartite graph.

Table 1: Labs and warping copper plates and specimens.

Labs	Warping copper plates and specimens (treatments)			
	A	B	C	D
L_1	260	350	229	375
L_2	410	535	400	590
L_3	285	350	210	320
L_4	275	330	235	330
L_5	430	545	430	590

2.4. Latin Square Design (LSD). A Latin square is designed to arrange $(n \times n)$ different treatments so that each treatment occurs exactly once in each row and each column.

2.5. Regular Graph. The degree of a vertex v in graph G written as $d_g(v)$ is the number of edges incident to v, except

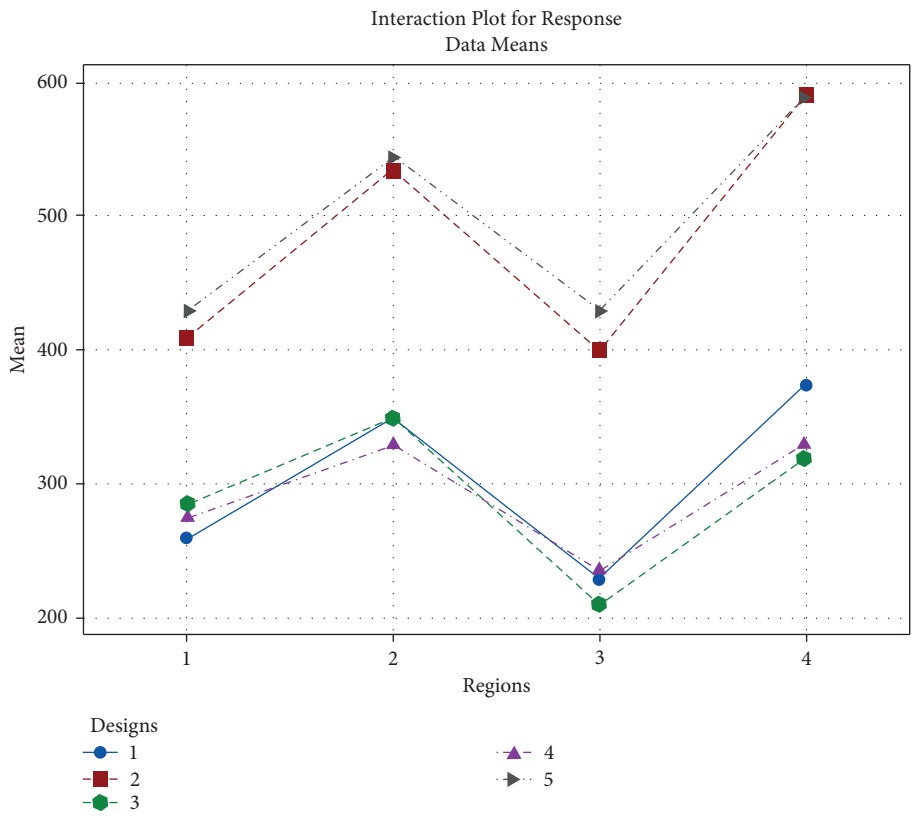

Figure 4: Interaction plot for response.

Table 2: Model summary.

S	R^2 (%)	Adj. R^2 (%)	Predicted R^2 (%)
27.0372	96.66	94.71	90.72

Table 3: Coefficients of response.

Term	Coeff	SE. Coeff	T-value	P value	VIF
Constant	373.95	6.05	61.85	0.01	
		Labs			
1	−70.5	12.1	−5.83	0.01	1.60
2	109.8	12.1	9.08	0.01	1.60
3	−82.7	12.1	−6.84	0.01	1.60
4	−81.4	12.1	−6.74	0.01	1.60
		Treatments			
1	−42.0	10.5	−4.01	0.02	1.50
2	48.0	10.5	4.59	0.01	1.50
3	−73.1	10.5	−6.99	0.01	1.50

that each loop at v is counted twice. The maximum degree is $\triangle(G)$, the minimum degree is $\delta(G)$, and G is regular if $\triangle(G) = \delta(G)$.

3. Main Results

3.1. An Optimisation of Techniques for Warping Copper Plates and Specimens Method of Construction for RBD Using Bipartite and Complete Bipartite Graphs

Step 1: Let us consider any RBD order layout $(b \times v)$ and take rows considered blocks (b) and columns considered treatments (v). Complete the vertices of the graph set V and separate the vertices set into two subsets V_1 and V_2.

Step 2: connect every vertex in V_1toV_2 by using the edges for both the bipartite and complete bipartite graphs

Step 3: if the number of v is equal to the number of blocks $(b = v)$, then the complete bipartite graph is used instead of a portion of the bipartite graph

Step 4: all edges in a complete bipartite graph is $(b \times v)$

Step 5: thus, the same procedure is used to draw a graph for all the different orders $(b \times v)$ of *RBD*

3.2. Applications

3.2.1. Example 1. An experiment to determine the amount of warping (mm) of copper plates was conducted in five different laboratories (L_1, L_2, L_3, L_4, and L_5) using four copper specimens (treatments) with different percentage of copper compositions (A, B, C, and D).

Step 1: Construction of the above experiment is to form an RBD layout of five laboratories and four copper specimens . Consider the first lab (L1) to be given four treatments (A=R_1, B=R_2, C=R_3, and D=R_4); the amount of warping (mm) of copper plates value is R_1=260,

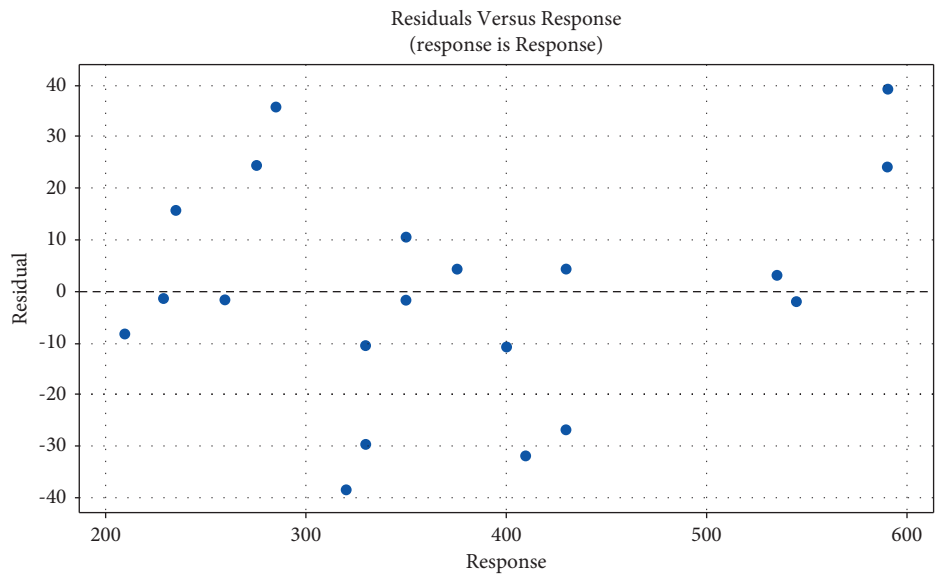

Figure 5: Residuals versus response.

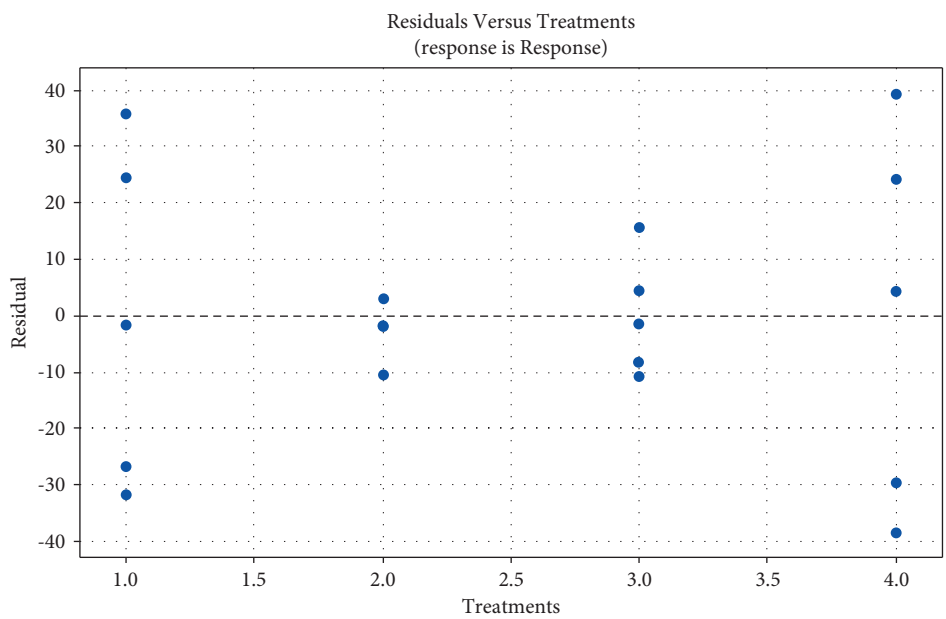

Figure 6: Residuals versus treatments.

$R_2 = 350$, $R_3 = 229$, and $R_4 = 375$, and resulting Figure 1 is known as first bipartite graph as follows:

Step 2: Consider the second lab (L2) given for four treatments (A, B, C, and D) the amount for warping (mm) of copper plates in 410, 535, 400, and 590 respectively. Using complete bipartite graphs and construction of separate the vertices set V into four subsets $A = V_1 = R_1, B = V_2 = R_2, C = V_3 = R_3$ and $D = V_4 = R_4$, the labs and specimens (treatments) are given the second bipartite graph in Figure 2 as follows;

Step 3: Similarly, using the above steps of the same procedure for constructing the third, fourth, and fifth labs (L3, L5, and L5) in four treatments. Observe the data of the third lab value is 285, 350, 210, and 320; the fourth lab value is 275, 330, 235, and 330; the fifth lab value is 430, 545, 430, and 590. Using complete bipartite graphs and constructing to separate the vertices set V into four subsets $A = V_1 = R_1, B = V_2 = R_2, C = V_3 = R_3$ and $D = V_4 = R_4$, the labs and specimens (treatments) given the third bipartite graph in Figure 3 are as follows;

Since there are five labs and four specimens, the amount of warping (mm) of copper plates is shown in Table 1.

Discuss if any significant difference exists between the mean number of responses for the five labs and four copper specimens.

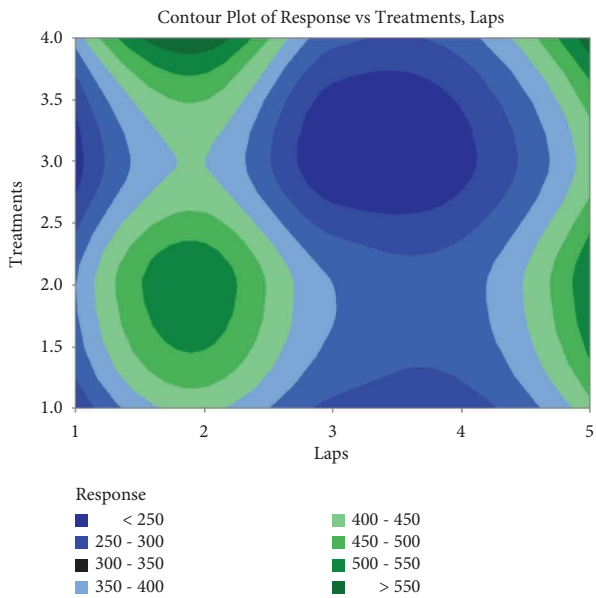

Figure 7: Contour plot of response vs. treatments vs. labs.

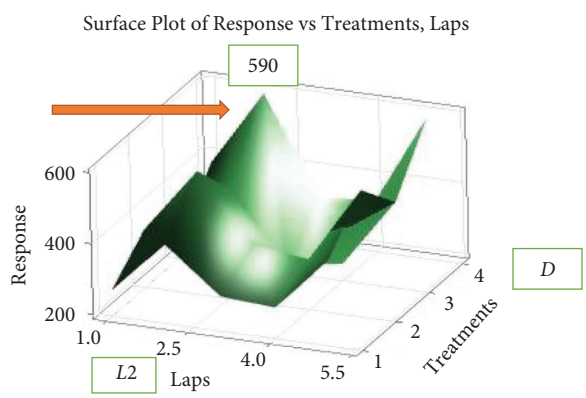

Figure 8: Surface plot of response vs. treatments vs. labs.

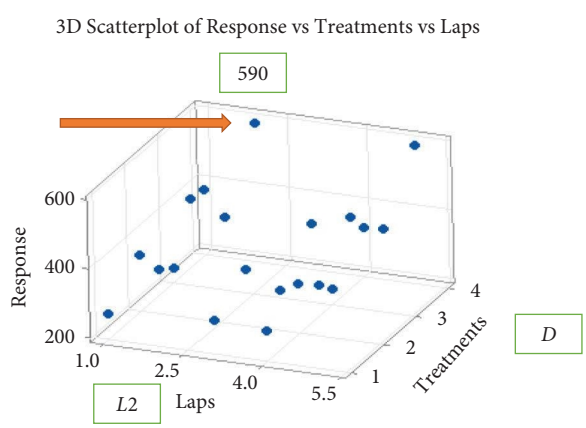

Figure 9: 3D scatterplot of response vs treatments vs labs.

Solution: constructing the graphs. The below interaction plot Figure 4 for response lines around parallel. So, our hypothesis of the study is valid and continues with the analysis.

Table 4: ANOVA for response.

SV	df	Adj. SS	Adj. MS	F-value	P value	Remarks
Labs	4	184271	46067.7	63.02	0.01	Significant
Copper specimens	3	69576	23192.0	31.73	0.01	Significant
Error	12	8772	731.0	—	—	—
Total	19	262619	—	—	—	—

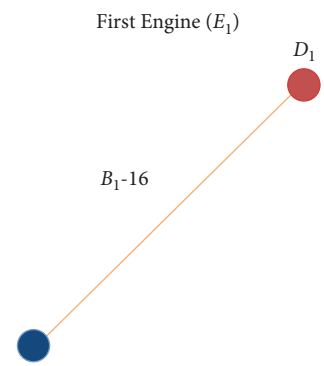

Figure 10: First regular graph.

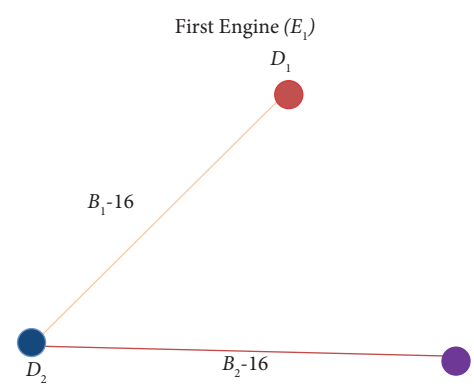

Figure 11: Second regular graph.

Null hypothesis (H_0): there is no significant difference between labs and copper specimens.

In Table 2, the R^2 value is nearest to 1 (0.9666) and the model is fitted to our problem. The R^2 probability value is 0 to 1. The difference is very close R^2 to the adjusted R^2 of 0.9072 and the noise signal is greater than 4 (27). A predicted R^2 value is 90.72% which is substantially less than the R^2 value of 96.66% which may indicate the overall model is fitted in the abovementioned example.

The coefficient response in Table 3 for two factors labs and copper specimens is significant at a 5% level of significance and concludes that the variables are associated with changes in the response variable.

3.2.2. General Linear Model: Response versus Labs and Treatments. In Figures 5 and 6 the normality and equal variance (treatments, residual response) assumptions are responsible. There is no concern, however, about the

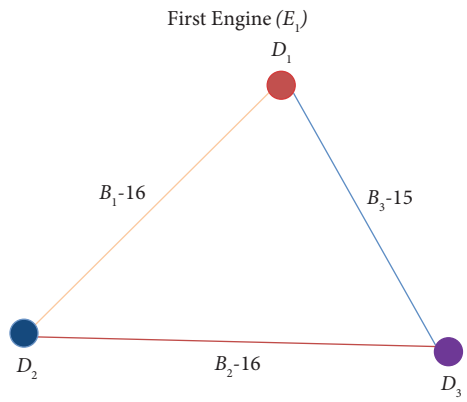

Figure 12: Third regular graph.

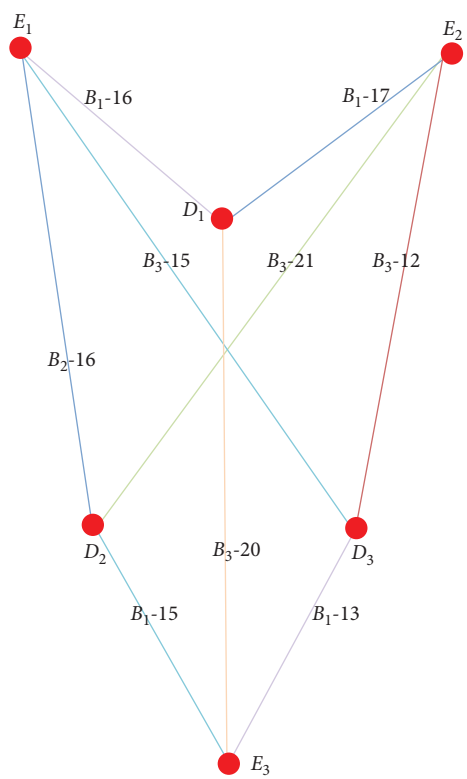

Figure 13: Fourth regular graph.

Table 5: Burners, engines, and days.

-	Engine 1	Engine 2	Engine 3
Day 1	Burner 1-016	Burner 2-017	Burner 3-020
Day 2	Burner 2-016	Burner 3-021	Burner 1-015
Day 3	Burner 3-015	Burner 1-012	Burner 2-013

appropriateness of the no interaction assumption. The data appear to be randomly distributed at the center line zero. Now, we perform an analysis for a randomized block design.

3.2.3. Contour Plot of Response vs. Treatments vs. Labs. The contour plot (Figure 7) indicates two predictor variables and shows the association between the variables labs

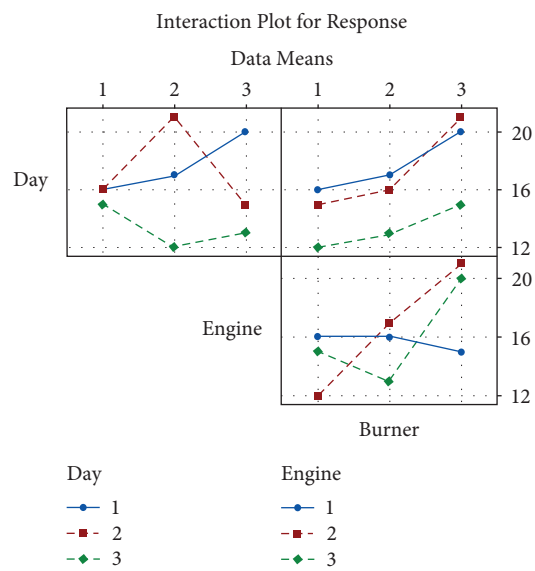

Figure 14: Interaction plot for response.

Table 6: Model summary.

S	R^2 (%)	Adj. R^2 (%)	Predicted R^2 (%)
0.881917	97.74	90.97	54.27

Table 7: Coefficients of response.

Term	Coef	Coef	T-value	P value	VIF
Constant	16.111	0.294	54.80	0.001	1.33
		Days			
1	1.556	0.416	3.74	0.065	1.33
2	1.222	0.416	2.94	0.099	1.33
		Engines			
1	−0.444	0.416	−1.07	0.397	1.33
2	0.556	0.416	1.34	0.313	1.33
		Burners			
1	−1.778	0.416	−4.28	0.051	1.33
2	−0.778	0.416	−1.87	0.202	1.33

(L_2) and treatment (D) used for the amount of warping (mm) of copper plates. The dark areas of the plot specify excellence. Figure 8 indicates three dimensional (3D) and Figure 9 is a surface plot of illustration into two predictor variables and related the response variable is normal as follows.

3.2.4. The 3D Surface Plot of Response vs. Treatments vs. Labs. The conclusion of the plots in Figures 8 and 9 shows that the relationship between the two variables labs and treatments for the amount of warping (mm) of copper plates occurs at nearly the second lab = 590 and treatments = D. All the sum of squares are presented in Table 4 and an inference is drawn.

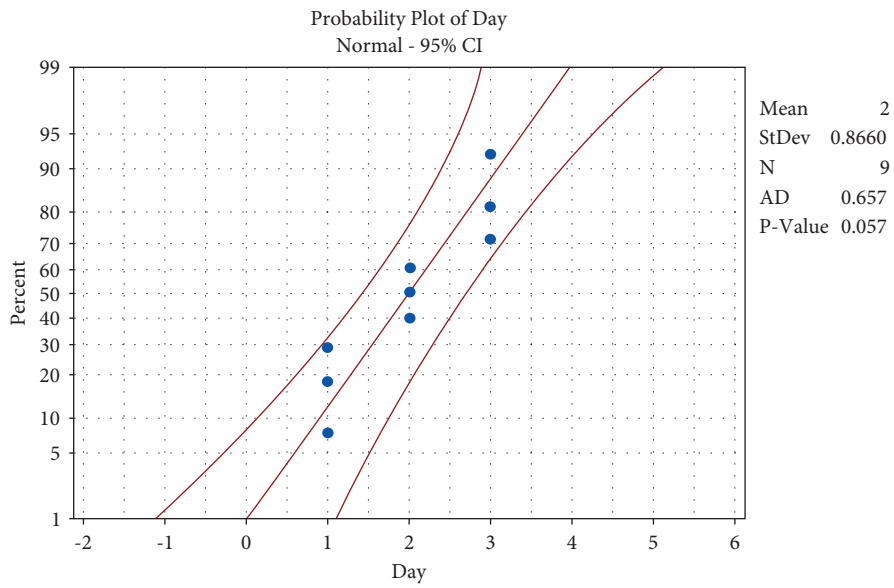

Figure 15: Probability plot of day.

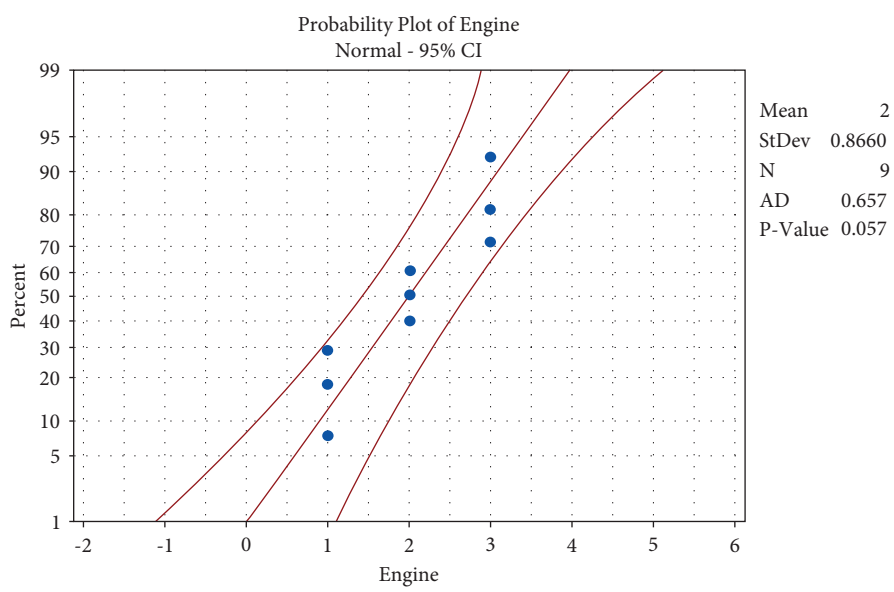

Figure 16: Probability plot of engine.

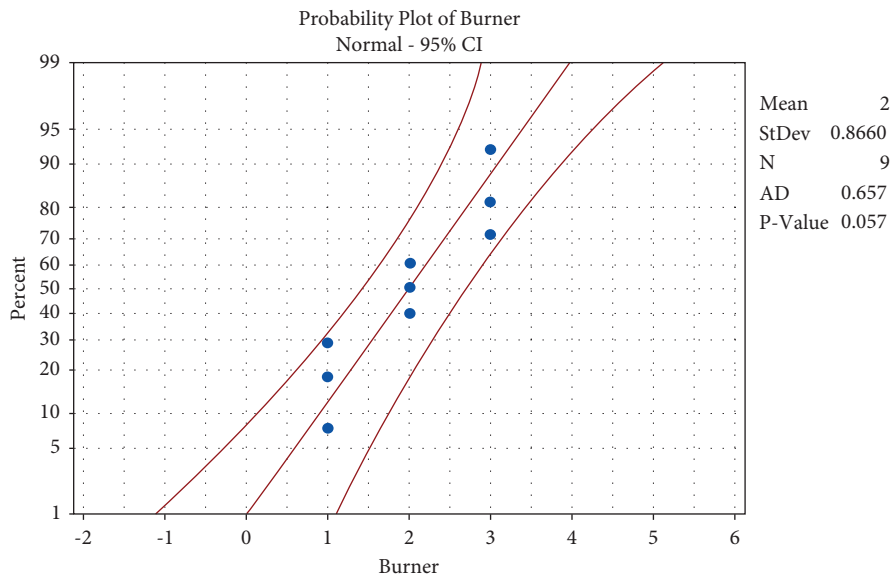

Figure 17: Residuals versus burner.

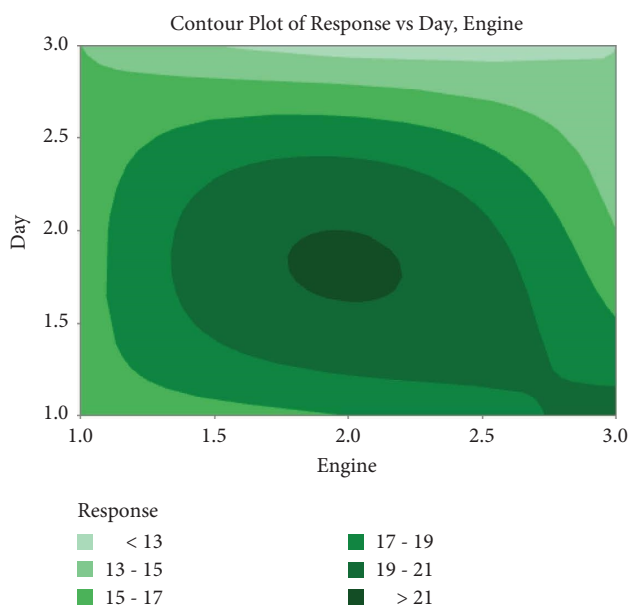

Figure 18: Contour plot of response vs. day vs. engine.

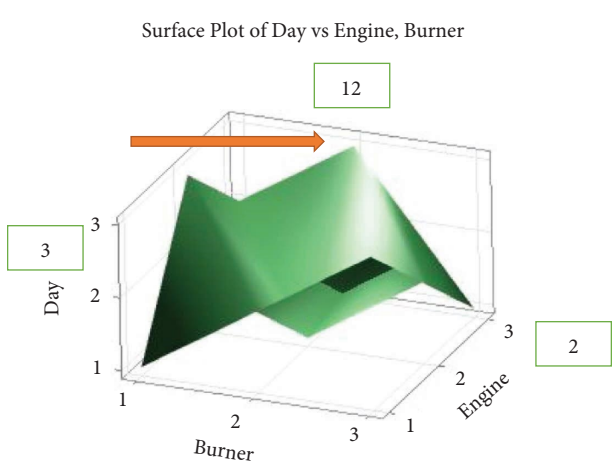

Figure 19: 3D plots of day vs. engine and burner.

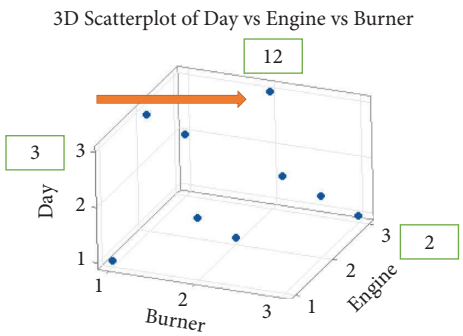

Figure 20: 3-D day vs engine vs. burner.

Table 8: ANOVA for the response.

sv	df	Adj. SS	Adj. MS	F-value	P value	Remarks
Days	2	34.889	17.4444	22.43	0.043	Significant
Engines	2	1.556	0.7778	1.00	0.500	Not significant
Burners	2	30.889	15.4444	19.86	0.048	Significant
Error	2	1.556	0.7778	—	—	—
Total	8	68.889	—	—	—	—

(1) Inference. Since P is 0.0, the model F-value (63.02) suggests that the model is significant. There is only a 0.01% chance that an F-value this large could occur due to noise.

3.3. An Optimisation Method of Construction for Burners and Engines using LSD with Regular Graph

Step 1: Take any LSD of order $(n \times n)$, the rows and treatments are considered as two sets of vertices, and then differentiate both by using vertex coloring.

Step 2: The regular graph has the same degree of vertices. Each vertex is connected to other vertices with the same number of edges.

Step 3: If the treatment numbers are equal to the blocks $(b = v)$, then the complete bipartite graph is used instead of a portion of the bipartite graph, and the edge numbers in the regular graph are $(n \times n)$.

Step 4: Thus, the same procedure is used to draw the graph for all the different orders n of *LSD*.

3.4. Applications

3.4.1. Example 2. A trial to compare three burners B_1, B_2, and B_3, three engines E_1, E_2, and E_3,, and three days D_1, D_2, and D_3 is given as follows:

Step 1: let us consider the first day (D1), first burner (B1), and first engine (E1) and are taken two sets of vertices and differentiate both of them by using vertex coloring of the regular graph to construct these three directions of factors for the results is 16 hours are shown in Figure 10 as follows;

Step 2: Consider the second day (D2), second burner (B2), and second engine (E2) and are taken as two sets of vertices and differentiate both of them by using vertex coloring of the regular graph to the construction of these three directions of factors for the results is 16 hours are shown in Figure 11 as follows;

Step 3: The third day (D3), third burner (B3), and third engine (E3) are taken as two sets of vertices and differentiated of them by using vertex coloring of the regular graph to the construction of these three directions of factors for the results is 15 hours are shown in Figure 12 as follows;

Step 4: Similarly, the same procedure to constriction of the regular graph using the remaining day, burner, and two engines the resulting diagram is known as the regular graph has the same degree of all vertices that is every vertex connected to any other vertices with the same number of edges are shown in Figure 13 as follows;

Step 5: The days are equal to the engines $(b = v)$ and number of burners; then, the complete bipartite graph is used instead of the bipartite graph, and the number of edges in the regular graph is (3×3). A LSD was formed as the tests were made on three engines (E1, E2, and E3) and were spared over three days (D1, D2, and D3). Since there are three burners, three engines, and three days values are shown below in Table 5.

To check whether the null hypothesis is that there is any significant difference between the burners, engines, and number of days.

(1) Solution: constructing the graphs. The plot in Figure 14 is referred to as the interaction of the lines that are not parallel and the interaction result specifies that the association between burners and engines depends on the value of days.

Null hypothesis (H_0): there is no significant difference between burners, days, and engines.

Table 6 represents that the model is fitted because the R^2 value is nearest to 1 (0.9774). The probability R^2 value is 0 to 1. The difference is very close R^2 to the adjusted R^2 of 0.9072 and the noise signal is greater than 4 (88). A predicted R^2 value is 54.27% which is substantially less than the R^2 value of 97.74% which may indicate that the overall model is fitted in the abovementioned example.

The coefficient response in Table 7 for three factors day and burner is significant, but the engine is not significant at a 5% level of significance and concludes that the variables are associated with changes in the response variable.

3.4.2. Probability Plot of Day. In the probability plot of the day (Figure 15), the null hypothesis states that the data follow a normal distribution. The fitted distribution line is the straight middle line on the plot. The outer solid lines on the plot are confidence intervals for the individual percentiles, not for the distribution as a whole, and should not be used to assess distribution fit.

3.4.3. Probability Plot of Engine. In the probability plot of the engine (Figure 16), the null hypothesis states that the data follow a normal distribution. The fitted distribution line

is the straight middle line on the plot. The outer solid lines on the plot are confidence intervals for the individual percentiles, not for the distribution as a whole, and should not be used to assess distribution fit.

3.4.4. Probability Plot of Burner. In the probability plot of the burner (Figure 17), the null hypothesis states that the data follow a normal distribution. The fitted distribution line is the straight middle line on the plot. The outer solid lines on the plot are confidence intervals for the individual percentiles, not for the distribution as a whole, and should not be used to assess distribution fit.

The contour plot (Figure 18) indicates two predictor variables and shows the association between the variables which are days, burners, and engines that are used for the treatments. The dark areas of the plot specify excellence.

3.4.5. The 3D Scatterplot Plot of Response vs. Day vs. Engine Surface Plot of Day vs. Engine vs. Burner. The graph of three dimensional (3D) graph (Figure 19) and surface plot (Figure 20) of illustration into two predictor variables and related the response variable is represented above the maximum quality scores and occur at about the second engine of the third day of the second burner treatment is 12.

All the sum of squares is presented in the ANOVA Table 8 and inference is given below.

(1) Inference. Since the p values are 0.043, 0.5, and 0.048, there is a difference between the burners and the days, but the difference between engines is not significant.

4. Conclusion

(i) This study proposed an optimization method of construction for warping copper plates and engines using complete block designs with bipartite and complete bipartite graphs.

(ii) The first method of construction for RBD with the numerical example is to test whether there is any significant difference between labs and warping copper plates with specimens discussed, construing the graphs of results is an interaction plot for response lines around parallel, so our hypothesis of the study is valid and significant.

(iii) Therefore, inference of P is 0.001 and the model F-value (63.02) suggests that the model is significant and only a 0.001% chance that an F-value this large could occur due to noise.

(iv) Also, the calculated R^2 value is nearest to 1 (0.9666) and the model is fitted to our problem, and the R^2 probability value is 0 to 1 and the difference is very close, i.e, R^2 to adjusted R^2 (0.9072) and the noise signal is greater than four (27) and also the predicted R^2 value is 90.72% which is substantially less than R^2 value of 96.66% which may indicate overall warping copper plates and engines are fitted.

(v) Finally, it was concluded that the relationship between the variables of labs and treatments for the amount of warping (mm) of copper plates occurs at nearly the second lab = 590 and warping copper plates and specimens D is efficient with the 3D surface.

(vi) The second optimization method of construction for burners and engines using LSD with a regular graph is to test whether there is any significant difference between burners, days, and engines.

(vii) The interaction graphs of the lines are not parallel, and the inference is that the P values are 0.043, 0.5, and 0.048 (less than 0.05, reject the hypothesis). Hence, the conclusion is that the burners and the days are different. The difference between engines is insignificant, but the model fits because the R_2 value is nearest to 1 (0.9774, and the probability R_2 value is 0 to 1).

(viii) The difference is very close R^2 to the adjusted R^2 (0.9072) and the noise signal is greater than 4 (88) and also the predicted R^2 value is 54.27% which is substantially less than the R^2 value of 97.74% which may indicate that the overall model is fitted.

(ix) The 3D scatterplot and the 3D surface plot show the three predictor variables (days, burners, and engines). In our study, the maximum quality score at about the second engine on the third day of the second burner treatment is 12.

(x) This methodology can also be applied in the case of factorial experiments, confounding, fractional replicated designs, balanced incomplete block designs, lattice designs, and so on.

Data Availability

The data that support the findings of this study are available from the corresponding author on request.

Conflicts of Interest

The authors declare that they have no conflicts of interest.

References

[1] J. A. Bondy and U. S. R. Murty, *Graph Theory with Applications"*, Elsevier Science Publishing Co Inc, New York, NY, USA, 1976.

[2] M. N. Das and N. C Giri, *Design and Analysis of Experiment"*, New Age International (P) Limited, New Delhi, India, 1979.

[3] R. C. Bose, *On the Construction of Balanced Incomplete Block Designs", Human Genetics*, UCL and Blackwell Publishing Ltd, Hoboken, NJ, USA, 1939.

[4] S. Yamamoto, H. Ikeda, S. Shige-Eda, K. Ushio, and N. Hamada, "On claw decomposition of complete graphs and complete bipartite graphs," *Hiroshima Mathematical Journal*, vol. 5, no. 1, pp. 33–42, 1975.

[5] C.-Q. Zhang and Y.-J. Zhu, "Factorizations of regular graphs," *Journal of Combinatorial Theory - Series B*, vol. 56, no. 1, pp. 74–89, 1992.

[6] W. Zhang, D. S. Wu, Y. Lee, and B. Masterson, "The effect of underfill epoxy on warpage in flip-chip assemblies," *IEEE Transactions on Components Packaging and Manufacturing Technology Part A*, vol. 21, no. 2, pp. 323–329, 1998.

[7] D. J. Jacobs, A. Rader, L. A. Kuhn, and M. Thorpe, "Protein flexibility predictions using graph theory," *Proteins: Structure, Function, and Genetics*, vol. 44, no. 2, pp. 150–165, 2001.

[8] A. L. Gavrilyuk and A. A. Makhnev, "Amply regular graphs and block designs," *Siberian Mathematical Journal*, vol. 47, no. 4, pp. 621–633, 2006.

[9] H. C. Tseng, C. Hung, and C. C. Huang, "An analysis of the formability of aluminum/copper clad metals with different thicknesses by the finite element method and experiment," *International Journal of Advanced Manufacturing Technology*, vol. 49, no. 12, pp. 1029–1036, 2010.

[10] V. Z. Rizzo and R. D. Mansano, "Electro-optically sensitive diamond-like carbon thin films deposited by reactive magnetron sputtering for electronic device applications," *Progress in Organic Coatings*, vol. 70, no. 4, pp. 365–368, 2011.

[11] S. Miyajima, S. Nagamatsu, S. S. Pandey, S. Hayase, K. Kaneto, and W. Takashima, "Electrophoretic deposition onto an insulator for thin film preparation toward electronic device fabrication," *Applied Physics Letters*, vol. 101, no. 19, Article ID 193305, 2012.

[12] S. Y. Yang, W. S. Kwon, and S. B. Lee, "Chip warpage model for reliability prediction of delamination failures," *Microelectronics Reliability*, vol. 52, no. 4, pp. 718–724, 2012.

[13] M. Pachamuthu and R. Jaisankar, "Construction of lattice designs using MOLS," *Malaya Journal of Matematik*, no. 1, pp. 11–16, 2013.

[14] A. Gupta, L. Barron, M. Brainin, and J. B. Lee, "Reduction of out-of-plane Warpage in surface Micromachined beams using corrugation," *Journal of Micromechanics and Microengineering*, vol. 24, no. 6, Article ID 065023, 2014.

[15] W. T. Federer and J. Wright, *Construction of Lattice Square Designs"*, Technical Report Series of the Biometrics Unit, Cornell University, Ithaca, NY, USA, 1986.

[16] Y. M. Hwang and G. Y. Tzou, "An analytical approach to asymmetrical cold- and hot-rolling of clad sheet using the slab method," *Journal Of Materials Processing Technology*, vol. 62, no. 1–3, pp. 249–259, 1996.

[17] C. H. Lee, J. P. Park, and Y. H. Moon, "Differential speed rolling to reduce warping in bimetallic slab," *Advances in Mechanical Engineering*, vol. 6, pp. 375162–375167, 2014.

[18] C. Zhu, W. Ning, H. Lee, J. Ye, G. Xu, and L. Luo, "Experimental identification of warpage origination during the wafer level packaging process," in *Proceedings of the IEEE 64th Electronic Components And Technology Conference (ECTC)*, pp. 815–820, IEEE, Lake Buena Vista, Florida, USA, May 2014.

[19] C. Kim, T. I. Lee, M. Kim, and T. S. Kim, "Warpage analysis of electroplated Cu films on fiber- reinforced polymer packaging substrates," *Polymers*, vol. 7, no. 6, pp. 985–1004, 2015.

[20] H. C. Lee, "Decomposition of the complete bipartite multigraph into cycles and stars," *Discrete Mathematics*, vol. 338, no. 8, pp. 1362–1369, 2015.

[21] B. N. Mandal and S. Dash, "On balanced incomplete Latin square designs," *Communications in Statistics - Theory and Methods*, vol. 46, no. 13, pp. 6258–6263, 2017.

[22] M. N. F. Sumaiya, W. V. Nishadi, K. D. E. Dhananjaya, A. A. I. Perera, and D. Uththamawadu, "Generation of compete bipartite graphs using normalized hadamard matrices," *Elixir Appl. Math.*vol. 113, pp. 49269–49271, 2017.

[23] A. Ramya and M. Pachamuthu, "On the construction of balanced incomplete block designs through factorization and coloring graphs using mutually orthogonal Latin square designs," *International Journal of Agricultural Statistics Science*, vol. 15, no. 2, pp. 807–813, 2019.

[24] M. Ilayaraja and A. Muthusamy, "Decomposition of complete bipartite graphs into cycles and stars with four edges," *AKCE International Journal of Graphs and Combinatorics*, vol. 17, no. 3, pp. 697–702, 2020.

[25] V. Sivamaran, B. Visvalingam, G. Mannathusamy, and V. Viswanathan, A. G. Rao, Effect of chemical vapor deposition parameters on the diameter of multi-walled carbon nanotubes," *International Nano Letters*, Springer, vol. 8, no. 4, pp. 1–12, 2018.

[26] V. Sivamaran, V. Balasubramanian, M. Gopalakrishnan, V. Viswabaskaran, and A. Gouravrao, "Optimizing chemical vapor deposition parameters to attain minimum diameter carbon nano tubes by response surface methodology," *Journal of Advanced Microscopy Research*, vol. 13, no. 2, pp. 181–189, 2018.

[27] M. A. Nemitallah, A. A. Abdelhafez, A. Ali, I. Mansir, and M. A. Habib, "Frontiers in combustion techniques and burner designs for emissions control and CO2 capture- A Review," *International Journal Of Energy Research*, pp. er.4730–33, 2019.

[28] V. Sivamaran, V. Balasubramanian, M. Gopalakrishnan, V. Viswabaskaran, and A. G. Rao, "Identification of appropriate catalyst system for the growth of multi-walled carbon nanotubes via catalytic chemical vapor deposition process in A single step batch technique," *Materials Research Express*, vol. 6, no. 10, pp. 105620–105716, 2019.

[29] P. S. K. Reddy and P. S. Hemavathi, "Generalization of bipartite graphs," *Journal of Discrete Mathematical Sciences and Cryptography*, vol. 23, no. 3, pp. 787–793, 2020.

[30] S. Saurabh and M. K. Singh, "A note on the construction of Latin square type designs," *Communications in Statistics - Theory and Methods*, vol. 51, no. 10, pp. 3434–3437, 2020.

[31] I. Ozkan, "Investigation on the electromagnetic shielding performance of copper plate and copper composite fabrics: a comparative study," *Tekstil ve Konfeksiyon*, vol. 30, no. 2, pp. 156–162, 2020.

[32] I. Raza and M. Asif Masood, "Efficiency of lattice design in relation to randomized complete block design in agricultural field experiments," *Pakistan Journal Of Agricultural Research*, vol. 22, no. 3-4, pp. 150–153, 2009.

[33] T. Richthammer, "Bunkbed conjecture for complete bipartite graphs and related classes of graphs," 2022, https://arxiv.org/abs/2204.12931.

[34] G. Braun and H. Tyagi, "Minimax optimal clustering of bipartite graphs with a generalized power method," 2022, https://arxiv.org/abs/2205.12104.

[35] V. Sivamaran, V. Kavimani, M. Bakkiyaraj, and S. T. Selvamani, "Multi response optimization on tribo-mechanical properties of CNTs/nSiC reinforced hybrid Al MMC through RSM approach," *Forces in Mechanics*, Elsevier, vol. 6, pp. 1–17, Article ID 100069, 2022.

Hindawi
Advances in Materials Science and Engineering
Volume 2022, Article ID 7592552, 13 pages
https://doi.org/10.1155/2022/7592552

Research Article

Investigations on the WEDM of Friction Stir Processed Magnesium/Graphene-Boron Nitride Hybrid Surface Composite through the Entropy-COPRAS Approach

V. Kavimani,[1] **P. M. Gopal**,[1] **V. Sivamaran**,[2] **and K. Anand Babu**[3]

[1]*Centre for Material Science, Department of Mechanical Engineering, Karpagam Academy of Higher Education, Coimbatore 641021, India*
[2]*Department of Mechanical Engineering, Audisankara College of Engineering and Technology (Autonomous), Gudur, India*
[3]*Department of Production Engineering, National Institute of Technology, Tiruchirappalli 620015, India*

Correspondence should be addressed to V. Kavimani; manikavi03@gmail.com

Received 28 July 2022; Revised 22 September 2022; Accepted 1 October 2022; Published 17 October 2022

Academic Editor: Dhanesh G. Mohan

In this research, friction stir processing (FSP) is utilized to develop the graphene-boron nitride-reinforced hybrid magnesium surface composite with varying volume percentages of reinforcements. A Taguchi-coupled Entropy-COPRAS approach is adopted to understand the influence of control factors of wire electrical discharge machining on the developed magnesium surface composite. An optimal combination of machining factors to attain maximum material removal rate (MRR) along with minimal kerf width and surface roughness is to be finalized. The Taguchi method is utilized for planning the experiments with three levels and four factors, namely, reinforcement volume %, pulse off time, wire feed rate, and pulse on time. ANOVA results show that pulse on time and reinforcement volume % act as the most significant factors for output responses. Using the Entropy-COPRAS approach, an optimal combination for output response was found for a maximum MRR of 16.20 mm^3/min; minimal surface roughness of 3.86 μm; and 0.29 μm of kerf width.

1. Introduction

Growing demand for lightweight structural materials in the aerospace and transport industries has resulted in a major interest in magnesium and its alloys. Compared with aluminium and steel, magnesium is one of the engineering materials that weighs the least, which helps with boosted fuel economy and a reduction in pollutants [1, 2]. Likewise, it exhibits a better strength-to-weight ratio, toughness, high damping capacity, and easier machinability. However, these materials have some major limitations, such as low creep, stiffness, low resistance to wear, and increased reactivity towards chemicals that frequently limit their industrial applications. It also has poor ductility, characterized by a brittle-like performance at ambient temperature owing to its HCP crystal structure and a limited slip system [3–5]. Composite development is considered one of the key ways to enhance the desired strength of Mg matrix material by the addition of selected reinforcements. The inclusion of carbide and carbon-based reinforcement such as SiC, TiC, CNT, graphene, etc. in the magnesium matrix enhances the mechanical characteristics and functional properties [6, 7]. In several industrial applications, material life is mainly dependent on surface mechanical qualities, and hence the development of surface composites has been adopted by several researchers.

Friction stir processing is a surface modification technique used to develop surface composites at a temperature below the substrate's melting point, and there is little literature available based on Mg FSP [8]. Qiao et al. adopted FSP with different passes to develop a ZrO_2-reinforced magnesium surface composite [9]. Investigation over mechanical behaviour depicts improved tensile strength (~15.9%) while compared with base material. Likewise,

increases in FSP pass decrease its grain size. An SiC-reinforced Mg surface composite was developed by Lu et al. through the FSP approach, and optimization was done for the FSP parameters to attain better mechanical properties [10]. Results revealed that FSP of three passes showcases better tensile and hardness properties. A graphene-reinforced Mg surface composite was developed by Zang et al. and its effects on mechanical properties were analyzed [11]. Observed results show that higher rotation speed and three passes increase the tensile and microhardness of the Mg matrix and also found that the addition of graphene up to 6.43 volume % showcased improved strength compared to the base material. Because composite materials are harder, tougher, and more resistant to wear and fatigue, they are more difficult to machine. Though these composites have better properties, the existence of reinforcement particles in the matrix phase harms the cutting tool life during traditional machining, which results in a deprived surface quality of machined engineering parts. Additionally, the inclusion of reinforcement reduces the tool life of traditional tungsten carbide and high-speed steel tools due to abrasion. As a result of their high hardness, composite materials are challenging to process using traditional techniques, particularly where complex geometry and dimensional accuracy are needed.

These composites are easily processed using nontraditional techniques like abrasive water jet machining. However, they can only be cut in one direction with these techniques. Consequently, WEDM has become a good method for shaping complicated materials made of composites. Herein, material removal takes place by erosion formed by sparks in-between the work samples and wire. Conversely, the formation of an immediate rise in temperature due to sparks and variation in melting point among the matrix and reinforcement will affect the surface of machined components. Another fact is that the presence of reinforcement phase in composite forms limits electrical conductivity, which results in damage due to anisotropic thermal distribution. Furthermore, wire breaking owing to the limited build-up current and variation in hardness of the composite is also a limiting factor to reducing the production rate in WEDM. Hence, there is a need for an hour to optimize the control factors to improve the quality of machined surfaces by maintaining higher material removal. It was found that only minimal studies discussed the WEDM of Mg surface composites. Kavimani et al. examined the consequences of WEDM parameters on graphene magnesium composite, and the results revealed that a surge in pulse on time increases MRR [12]. Further, observation revealed that pulse off time and pulse on time have more domination in influencing control parameters over output response. Vijayabhaskar and Rajmohan et al. developed a nano SiC-reinforced Mg composite and discussed the consequences of WEDM control factors on the developed composite [13]. Reinforcement percentage, pulse off time, voltage, pulse on time, and wire feed rate are chosen as input parameters. The results reveal that an increase in reinforcement percentage decreases the surface finish. Progress in newer soft computing techniques results in the development of different optimization approaches to attain solutions for complex objectives and uncertain situations. For predicting and attaining optimal machining parameters, researchers adopted various mathematical and statistical techniques such as Taguchi, ANN, GA, PSO, etc. [14, 15]. Additionally, a multiresponse optimization strategy was utilized to address the competing natural responses brought on by material removal rate, surface roughness, kerf taper, etc., which prevented the individually optimized settings from accomplishing their goals [16, 17]. From an industrial viewpoint, the ideal combination is necessary to ensure that the defined reactions are obtained in the best possible balance.

This fact made the researchers adopt hybrid optimization techniques, and a little literature on these techniques is discussed in detail. An analytical hierarchy process coupled genetic algorithm approach was adopted by Kumar et al. to optimize WEDM parameters. Input parameters such as wire tension, spark gap-set voltage, pulse on time, pulse peak current, pulse off time, wire feed rate, and other input parameters are selected and optimized for MRR and roughness [18]. At the optimal combination, 13.79% and 19.16% improvements have been attained while compared with discrete optimal solutions. A PCA-coupled ANN approach was adopted by Phate et al. to understand the WEDM behaviour of the developed composite. The results reveal that integrated form optimization techniques deliver an effective optimal solution. Based on available literature, it can be noted that wire feed rate, pulse off time, and pulse on time are the major influencing parameters in WEDM [19]. Machinability analysis of graphene-based surface composites has rarely been reported. Multiobjective optimization techniques deliver better results when compared with traditional techniques. Utilization of Entropy-coupled CORPUS for WEDM analysis is not yet reported. On the basis of the obtained evidence, an attempt has been made to understand the machinability characteristics of graphene-reinforced surface composite. The Entropy-coupled CORPUS methodology is adopted to understand and optimize the machining parameters to improve the quality of the machined surface and production rate in a single unique solution.

2. Materials and Methods

AZ31 Mg alloy substrate with dimensions of $150 \times 100 \times 8$ mm is selected as the base material. Graphene and boron nitride particles are selected as reinforcements to improve the basic and functional properties of the AZ31 Mg alloy. Herein, graphene and boron nitride particles are mixed in equal proportion by the assistance of an ultrasonic assisted stirring process. Herein, the calculated amount of graphene and BN particles are ultrasonicated separately with organic solvent for 1 h, and then the samples are further sonicated for 3 h. After that, the samples are stirred using a magnetic stir coupled with a hot plate for 3 h at 1000 rpm. Then the attained mixtures are vacuum dried for 24 h and the resultant samples are used as reinforcement. The profile of the FSP tool used and the step-by-step procedure for FSP are illustrated in Figures 1(a) and 1(b). As a first step in FSP,

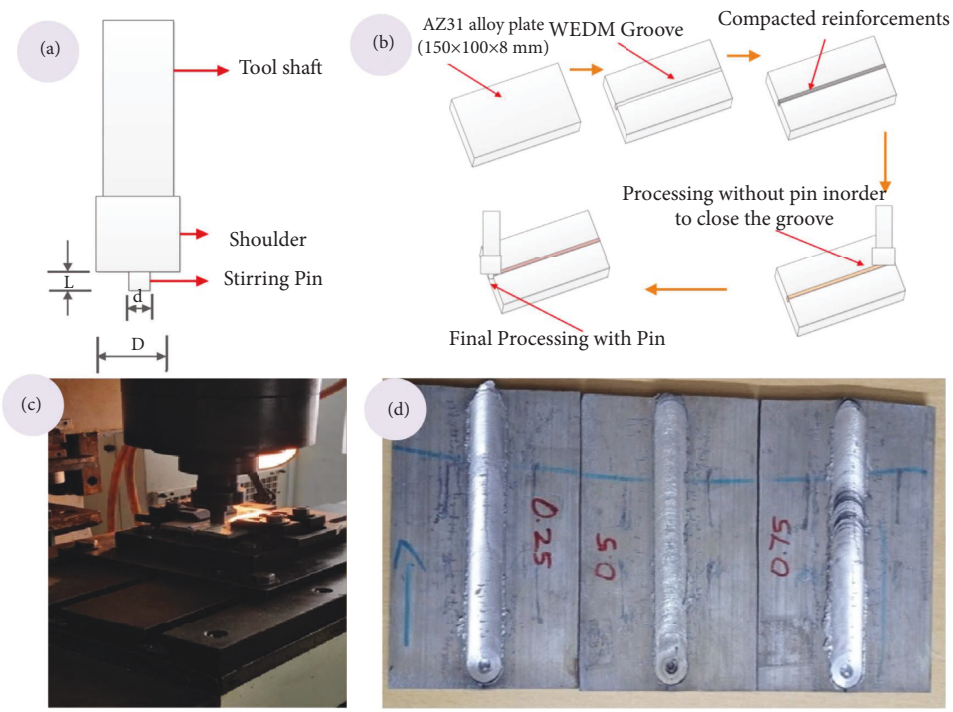

Figure 1: (a) Dimension of tool profile. (b) Schematic sketch of FSP. (c) Modified milling machine for the FSP approach. (d) Developed surface composite.

a groove has been made at the center of the Mg plate parallel to its longest side, as shown in Figure 1(b) using the WEDM process. The groove depth is fixed at 5 mm and its width is varied based on volume % of reinforcement (1, 3, and 5). A double-tempered H13 steel tool with a 5 mm pin length (L), a 20 mm diameter shoulder (D), and a 6 mm diameter pin (d) was utilized for FSP. Friction stir processing was conducted in a modified vertical milling machine with an optimized rotation speed and traverse feed of 1200 rpm and 20 mm/min (Figure 1(c)). Initially, the reinforcement mixture is filled in the groove gap and the pin-less tool is allowed to pass for compacting, followed by the passing of the pin-headed tool [20]. The developed surface composite is shown in Figure 1(d).

3. Experimental Design

The Taguchi approach was adopted for the experimental plan with three levels and four factors with the L27 orthogonal array. Based on available literature, pulse off time, pulse on time, and wire feed rate are found to be the most important control factors in WEDM and hence they are chosen as input parameters (Table 1). Similarly, the production rate of a material and the surface quality of mechanical components are mainly based on MRR, surface roughness, and kerf width, respectively, and so these parameters are chosen as output responses (Table 2). Herein, procedures for MRR, surface roughness, and kerf width measurement are already shown in our previous reports [20, 21]. While larger is better condition, it is designated for MRR and smaller is better condition, it is designated for kerf width (KW) and surface roughness during SN ratio analysis, since higher surface roughness (Ra) decreases the surface quality.

Table 1: Machining parameters and respective levels.

Parameters	Notation	Unit	Level 1	Level 2	Level 3
Reinforcement %	A	Wt. %	1	3	5
Pulse off time	B	Ms	4	8	12
Pulse on time	C	Ms	10	15	20
Wire feed rate	D	m/min	4	6	8

4. Results and Discussion

To determine the correlation among the set of variable pairings, a scatter-plot matrix is utilized (Figure 2). It is possible to arrange these pairwise correlations into a matrix. In general, the diagonal arrangement of the current matrix pair shows a stronger correlation between the matrix pairs and a lack of outliers in the obtained output data. Further relations between the various control factors and their respective output responses can also be understood with the help of a matrix plot. It can also be used to observe the clustering of data by control factors in the dataset for a specific response variable. Herein, the correlation set of variables can be identified based on the mirror images. For example, the eighth row fifth column and the ninth row sixth column of the scatter plot resemble the mirror image of the fifth row eighth column and the sixth row ninth column of the scatter plot, which denotes the correlation among data sets. Likewise, the influence of each control factor over other output responses can also be examined using a scatter plot. For example, the fifth column in the first row implies the

Table 2: Experimental trails along with output response.

Reinforcement (%)	Pulse off time (μs)	Pulse on time (μs)	Wire feed rate (m/min)	MRR (mm^3/min)	Ra (μm)	KW (μm)
1	4	10	4	12.0765	3.6730	0.2877
1	4	15	6	14.8180	3.7540	0.2905
1	4	20	8	16.2010	3.8610	0.2967
1	8	10	6	12.3505	3.6830	0.2972
1	8	15	8	14.6605	3.7270	0.3027
1	8	20	4	13.4580	3.7630	0.3010
1	12	10	8	11.8400	3.6540	0.3049
1	12	15	4	11.5170	3.6980	0.3053
1	12	20	6	13.3415	3.7670	0.3093
3	4	10	4	10.0170	3.7280	0.2870
3	4	15	6	13.7505	3.8130	0.2948
3	4	20	8	14.8505	3.8960	0.2963
3	8	10	6	10.9015	3.6820	0.2967
3	8	15	8	12.8680	3.7680	0.3014
3	8	20	4	12.2725	3.7750	0.3004
3	12	10	8	11.3505	3.7280	0.3023
3	12	15	4	11.1015	3.7220	0.3032
3	12	20	6	13.1340	3.7960	0.3079
5	4	10	4	9.2265	3.7260	0.2873
5	4	15	6	12.6765	3.8290	0.2897
5	4	20	8	13.9850	3.8820	0.2916
5	8	10	6	9.9400	3.7430	0.2930
5	8	15	8	13.2080	3.8110	0.2947
5	8	20	4	11.3830	3.8230	0.2969
5	12	10	8	10.0180	3.7480	0.2972
5	12	15	4	9.6890	3.7590	0.3002
5	12	20	6	10.9415	3.8250	0.3010

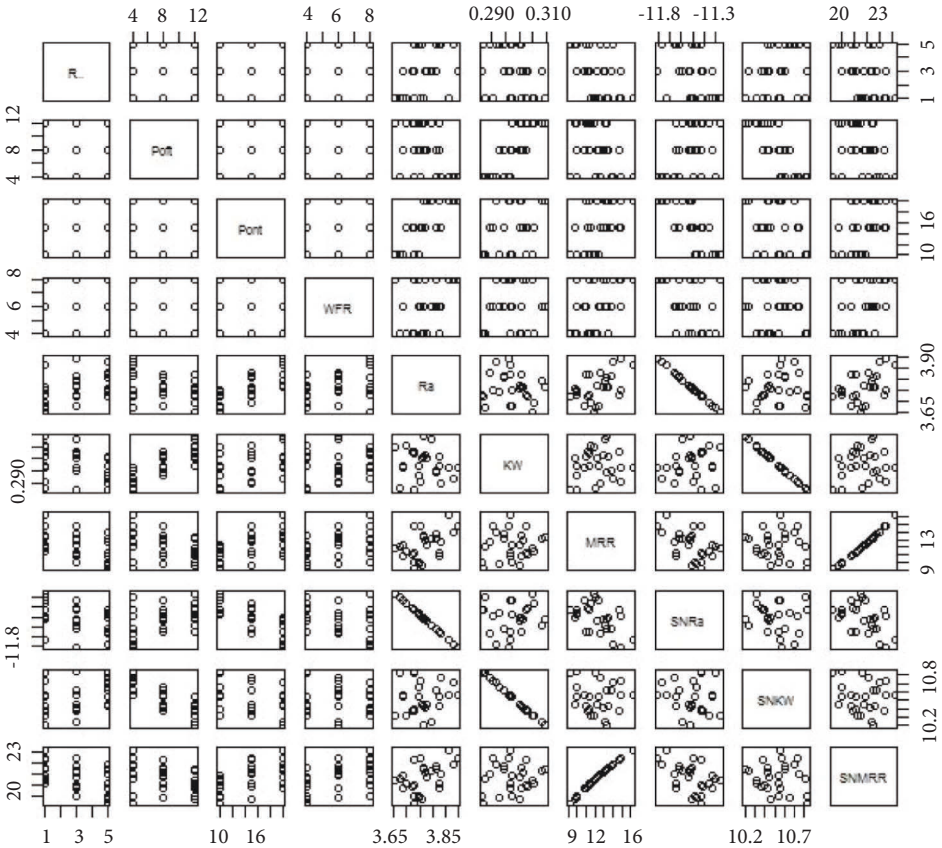

Figure 2: Matrix scatter plot of the L27 OA dataset.

relation between surface roughness and reinforcement percentage. In this, the x-axis denotes the surface roughness, and the y-axis denotes the reinforcement percentage. The movement of variables from left to right indicates that surface roughness increases with respect to reinforcement increment.

An algorithmic analysis known as a "hierarchical cluster" groups the related data into clusters. Each cluster, in this case, differs from the others, and the values are very close to one another. Figure 3 shows that the output parameter values are clustered into four groups using the expressive colours of blue and brown (dark and lighter). According to the input parameter, these are ranked from −1 to 1. The output parameter values are presented in lighter and darker shades of blue and brown in a top-to-bottom arrangement.

4.1. Effect of Control Factors on Surface Roughness. In Figure 4 depicts the influence of control factors on surface quality. It can be noted that increases in reinforcement decrease the surface roughness as the presence of reinforcement particles promotes the hardness values of the developed composite that results in breakage of wires during the WEDM process, thus decreasing the surface finish. The thermal mismatch between the matrix and reinforcement also plays a vital role in surface roughness. During pulse on time, the creation of sparks results in the melting of base material due to its low melting point. Compared with reinforcement (Graphene: BN), further gets flushed out by the dielectric medium at pulse off time. These reinforcement particles do not melt and stick to the matrix, increasing its surface roughness [12].

Another reason is the presence of BN, which is a well-known wide band gap semiconductor that decreases the chance for the production of sparks and results in improper cuts during machining. It can also be shown that increases in pulse off time increase the surface quality of developed samples. This upsurge in pulse off time results in the absence of spark generation and splashing of dielectric fluid. This fact removes the burs and debris formed over the machined surface. Thus, surface quality increases. Likewise, an increase in the pulse on time upsurges surface roughness that might be owing to the effect of spark generation that creates harder heat affected zones near the machined surface, thus increasing the surface roughness [22]. A rise in wire feed rate decreases the surface quality since the surge in wire feed rate results in newer wire recovery at a faster phase during the machining process. This fact increases the quality and efficiency of generated sparks that form deeper craters over the machined surface, thus reducing the surface finish. Among the available control factors, pulse on time acts as the key parameter in governing the surface quality of the developed composite, followed by reinforcement percentage in second position (Table 3). Wire feed rate has low significance on surface finish [23].

Further, the contribution percentage of individual parameters and their significance can be confirmed by the ANOVA results shown in Table 4. In general, P values of control factor less than 0.05 are deliberated as significant parameters.

It can be observed from Table 4 that all the P values are less than 0.05, which implies that selected parameters have an influence over the surface quality of the developed composite. The individual contributions of machining parameters are shown in Table 4, that indicates that pulse on time has the major contribution of 58.53% followed by reinforcement volume percentage with a contribution percentage of 18.18%. Herein, wire feed rate delivers a lower contribution of 9.3%. Furthermore, the attained results well coincide with the output response table. The obtained ANOVA results showcase an R square value of 93.2% significance. A mathematical model was developed based on the attained values to predict the surface roughness (equation (1)) of the developed sample with an R square value of 93.41%. The variation in experimental and predicate values is implied in Figure 5.

$$\begin{aligned} \mathrm{SR} = {} & 3.53036 + 0.0157444\,\text{reinforcement\%} \\ & -0.00645972\,\text{pulse off} + 0.0113478 \\ & \text{pulse on} + 0.0113222\,\text{wire feed}. \end{aligned} \tag{1}$$

The optimal parameters can be attained from the response table. It states that lower values of wire feed rate, pulse on time, and reinforcement volume % with a higher value of pulse off time are optimal solutions for higher surface quality.

4.2. Influence of Control Factors on Kerf Width. Figure 6 infers the impact of control factors on kerf width in the WEDM slot on the developed composite. It can be observed that increases in reinforcement percentage decrease the kerf width of the samples. The addition of reinforcement improves the hardness, which decreases the chances of widening of the sample during the machining process. Further, graphene and BN have better thermal stability that decreases the intensity and heat dissipation over the composite at spark generation, thus decreasing the kerf width. Increment in pulse on time increases the kerf width as more pulse on time maximises the discharge current or energy over the electrode that results in more dielectric supply which causes material evaporation. Likewise, higher pulse on time improves the transfer dissipation inside near the workpiece and dielectric fluid, thus increasing the kerf width. This fact initiates confined heat over the material that erodes a large portion of the material and causes widening of the kerf and profounder craters. During machining, an increase in pulse off time increases flushing time that results in debris and burs over the machined surface that results in a higher kerf width. Lower pulse off time causes inadequate flushing time, which results in the creation of a recast layer over the surface of the machined component that decreases the kerf width. Herein, lower kerf width can be obtained during minimal energy discharge that improvises exactness in dimension [13]. Likewise, an increase in wire feed rate increases kerf width; this might be due to an increase in the intensity of generated sparks. Another reason is increment in wire feed rate increases wire tension and vibration of the wire that causes irregular cuttings on the machined surface [24].

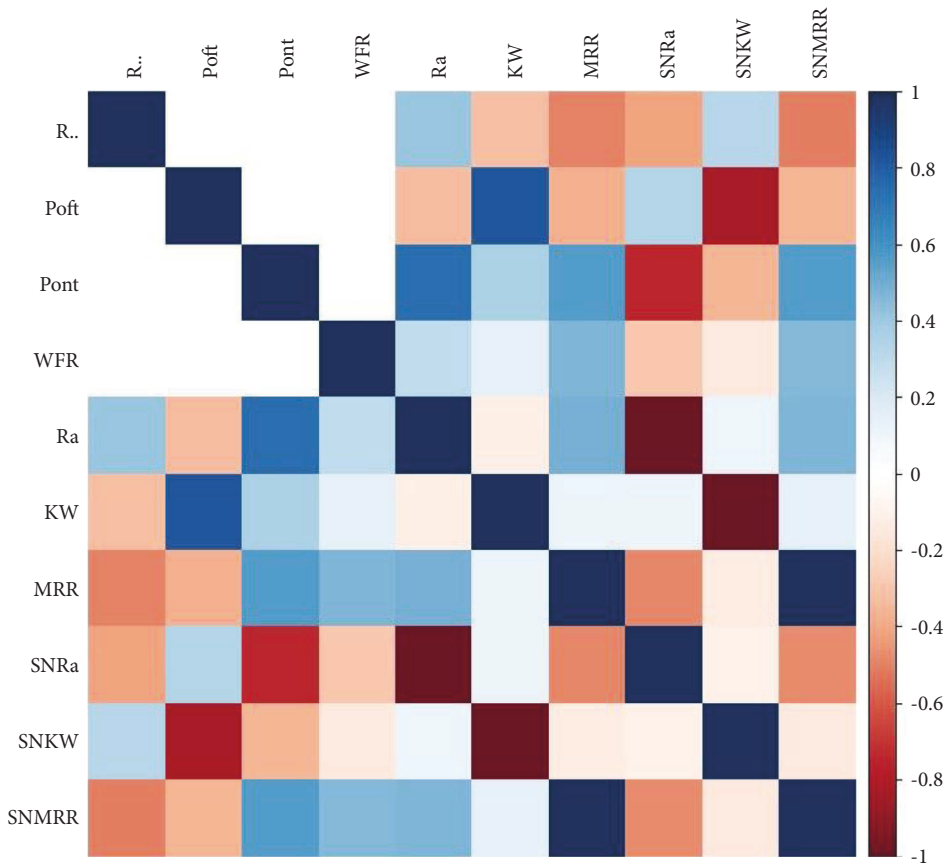

Figure 3: Hierarchical clustering of the correlation coefficient matrix of input variables.

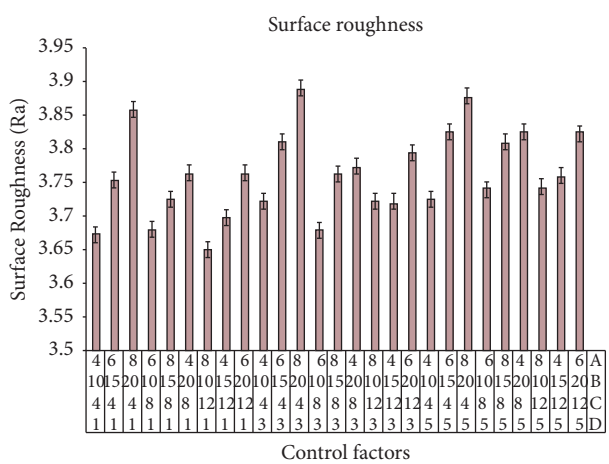

Figure 4: Effect of control factors on surface roughness.

Table 3: Response table for surface roughness.

Level	Reinforcement %	Pulse off time	Pulse on time	Wire feed rate
1	−11.44	−11.58	−11.38	−11.46
2	−11.52	−11.49	−11.51	−11.52
3	−11.58	−11.47	−11.64	−11.56
Delta	0.15	0.12	0.26	0.1
Rank	**2**	**3**	**1**	**4**

Table 4: ANOVA table for surface roughness.

Source	DF	Seq. SS	Adj. SS	MS	F	P	Contribution (%)
Reinforcement vol.%	2	0.017996	0.017996	0.008998	33.1	0	17.32
Pulse off time	2	0.013792	0.013792	0.006896	25.37	0	13.28
Pulse on time	2	0.057949	0.057949	0.028974	106.59	0	55.78
Wire feed rate	2	0.009264	0.009264	0.004632	17.04	0	8.92
Error	18	0.004893	0.004893	0.000272			
Total	26	0.103893					
			***R*-square–93.20%**				

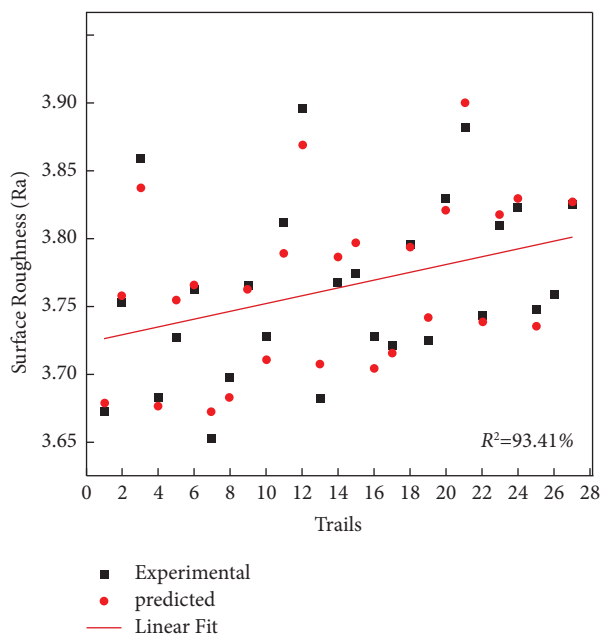

Figure 5: Variation between experimental and predicated values of surface roughness.

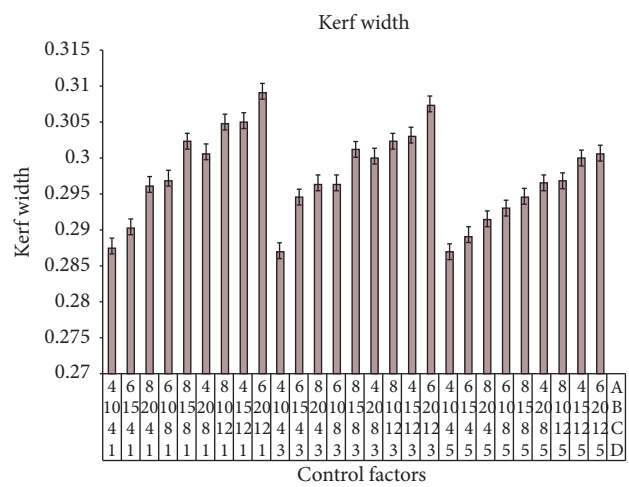

Figure 6: Effect of machining parameters on kerf width.

Table 5: Response table for kerf width.

Levels	Reinforcement %	Pulse off time	Pulse on time	Wire feed rate
1	10.47	10.71	10.61	10.56
2	10.49	10.51	10.52	10.52
3	10.62	10.36	10.46	10.5
Delta	0.14	0.36	0.16	0.06
Rank	3	1	2	4

The response table revealed that pulse off time acts as more dominating parameter in governing kerf width (Table 5), followed by pulse on time. Herein, wire feed rate depicts lower influence over kerf width. From the response table, it can be noted that an increasing percentage of reinforcement and minimal values of control factors is the optimal parameter combination. 10 μs of pulse on time with a pulse off time of 4 μs and a 4 m/mm of wire feed rate is the optimal solution for obtaining a lower kerf width. From Table 6, it can be inferred that P value is lower than that of 0.05 for every control parameter, which depict that all the machining parameters has significant effect over the output response. The contributions of individual parameters are computed by dividing the sequential sum of square values of each parameter by total sequential sum of square values. The attained values are illustrated in Table 6. The obtained results have a 95.3% significant confidence level. As shown early in the response table, pulse off time has a higher contribution percentage of 70.9% followed by pulse on time and reinforcement volume % that contribute more or less equal percentages of 13.6 & 13.3%, respectively. As inferred from ANOVA results, wire feed rate acts as the lower significant parameter with a 2.09% contribution. A mathematical model has been developed to predict the kerf width as illustrated in equation (2). The variation in experimental and predicated values is shown in Figure 7.

$$\begin{aligned}\text{Kerf width} = {} & 0.278016 - 0.00121389\ \text{reinforcement \%} \\ & + 0.00152361\ \text{pulse off time} \\ & + 0.000531111\ \text{pulse on time} \\ & + 0.000522222\ \text{wire feed rate.}\end{aligned} \tag{2}$$

4.3. Effect of Control Factors on MRR. Figure 8 shows the consequence of control factors on the rate of material removal. It can be observed from the figure that an increase in volume % of reinforcement decreases MRR values. This might be due to the presence of graphene and BN particles that decrease the intensity of spark generation, so the machining rate decreases. Further, these particles have varying electrical conductivity when

Table 6: ANOVA table for kerf width.

Source	DF	Seq. SS	Adj. SS	MS	F	P	Contribution (%)
Reinforcement	2	0.0001264	0.0001264	6.32E−05	24.81	**0**	12.72
Pulse off time	2	0.0006728	0.0006728	0.000336	132.06	**0**	67.69
Pulse on time	2	0.000129	0.000129	6.45E−05	25.32	**0**	12.98
Wire feed rate	2	0.0000198	0.0000198	9.9E−06	3.9	**0.039**	1.99
Error	18	0.0000459	0.0000459	0.0000025			
Total	26	0.0009939					
				R^2 = 95.39%			

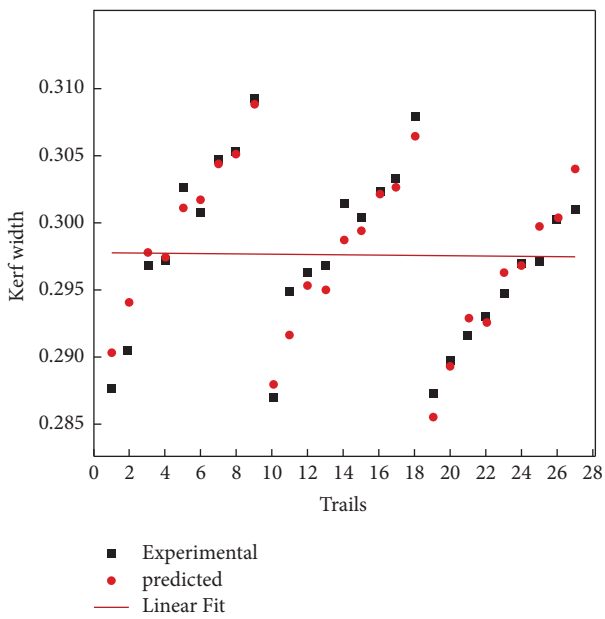

Figure 7: Variation between experimental and predicted values of Kerf width.

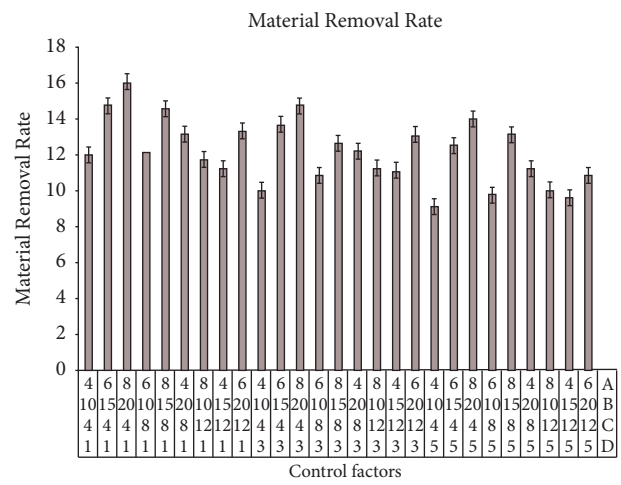

Figure 8: Influence of machining parameters on MRR.

compared with the base matrix material, which thus decreases the generation of sparks. The hybrid reinforcement has higher thermal stability. This fact decreases the chances of melting of composite material, which increases the machining time. Similarly, an increment in pulse off time decreases MRR values. During pulse off time, the machining process will be in idle condition and no spark generation will happen, which decreases the production rate. An increase in pulse on time increases the MRR value since an increase in the pulse on time promotes the spark cohort time that increases the MRR. It could be shown that increases in wire feed rate increase MRR [12, 23]. During machining conditions, increases in the wire feed rate increase the chance of changeover on new wires that increase the intensity of the spark generated near the work piece, which results in higher MRR. The response table shows that pulse on time is the key dominant parameter for governing the MRR, and pulse off time attains the last position in influencing the MRR. From the response table, the optimal solution for MRR can be attained. Herein, higher values of pulse on time and wire feed followed by lower addition of reinforcement and pulse off time is the optimal condition for a better production rate (Table 7).

Table 7: Response table for MRR.

Levels	Reinforcement (%)	Pulse off time	Pulse on time	Wire feed rate
1	22.46	22.19	20.67	20.92
2	21.7	21.77	22	21.83
3	20.92	21.12	22.41	22.34
Delta	1.54	1.07	1.73	1.42
Rank	2	4	1	3

The significance of machining parameters and their respective contributions are inferred from ANOVA (Table 8). Based on ANOVA results, P value < 0.05 indicated that all the control parameters have an influence over the output response. It can be illustrated from Table 8 that pulse on time has more contribution (36.03%) in dominating the output response followed by reinforcement volume % and wire feed rate with more or less equal contribution over materials removal rate. Herein, pulse off time showcases a minimal contribution of 14.9% in governing the output response. An empirical model has been established by the linear regression method to foresee the MRR of a composite as shown in equation (3). The developed model has better predictability with an R square value of 93.18%, as shown in Figure 9.

Table 8: ANOVA for MRR.

Source	DF	Seq. SS	Adj. SS	MS	F	P	Contribution (%)
Reinforcement %	2	20.483	20.483	10.242	62.41	0	24.65
Pulse off time	2	11.998	11.998	5.999	36.56	0	14.44
Pulse on time	2	28.876	28.876	14.438	87.98	0	34.75
Wire feed rate	2	18.778	18.778	9.389	57.22	0	22.60
Error	18	2.954	2.954	0.164			
Total	26	83.089					
R^2 = 96.45%							

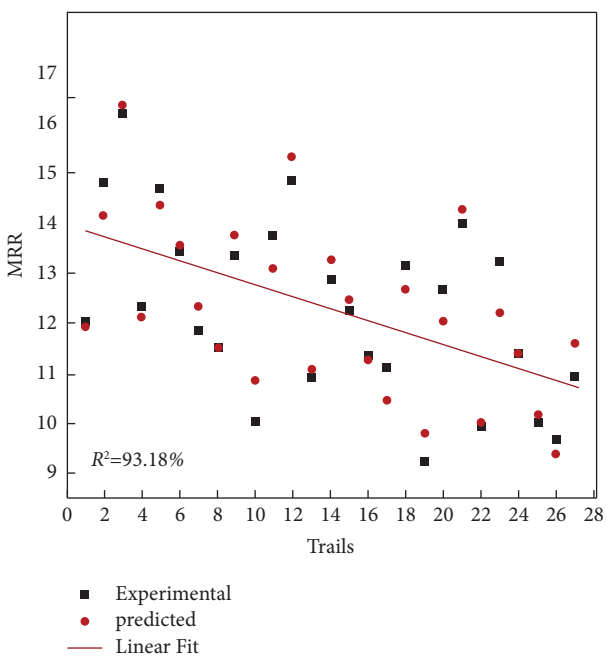

Figure 9: Experimental versus predicted values of MRR.

$$\begin{aligned} \text{MRR} = {} & 8.8289 - 0.533208 * \text{reinforcement \%} \\ & - 0.203729 * \text{pulse off time} \\ & + 0.242739 * \text{pulse on time} \\ & + 0.506681 * \text{wire feed rate.} \end{aligned} \tag{3}$$

4.4. Multiresponse Optimization of Control Factors. Mutual optimal parameter combinations for two or more output parameters can be obtained with the assistance of multiobjective optimization. The determination of an accurate weight for the output response is the foremost difficulty in multiresponse optimization. Researchers determined the weightage for the response based on their familiarity with and trial and error method related to the control factors' significance [25]. Hence, there is a need to develop a new approach for computing the weightage for the output response. In this proposed research, the entropy method was adopted for allotting individual weightage on output response, which was earlier used for several multicriteria decision making problems. Most of the time, the decision maker expresses their ideas by taking into account choice variables in order to determine the weights for their traits and to parallelize comparisons with actual-world circumstances. Since entropy weight is a quantity that represents a criterion's relevance in terms of the relative weights of criteria, the entropy method does not require such a choice. When more factors are taken into account, the entropy idea might be used to reduce the human errors involved in assigning weights. The steps involved in the entropy approach are illustrated as follows [26]:

Step 1: normalization of decision matrix EI:

$$Eij = \frac{Kij}{\sum_{i=1}^{p} Kij}, \tag{4}$$

$$Eij = \frac{1/Kij}{\sum_{i=1}^{p} 1/Kij}. \tag{5}$$

Herein, (4) is used for maximization function, and (5) is used for normalizing the minimization function (refer to Table 9)

Step 2: calculation of entropy index:

$$Ie = -\left[\frac{\sum_{i=1}^{l} Eij ln(Eij)}{\ln(l)}\right]. \tag{6}$$

Entropy index of the normalized values can be obtained from equation (6). The calculated values are illustrated in Table 10.

Step 3: determination of weightage:

$$We = \frac{1 - Ie}{\sum_{e=1}^{n} (1 - Ie)}. \tag{7}$$

The values attained for individual parameters from (7) can be used as weightage for the hybrid optimization approaches as shown in Table 10. In this research, entropy-coupled Complex Proportional Assessment (COPRAS) was adopted to attain an optimal solution for better MRR with better surface quality.

4.5. Multiobjective Optimization by the Entropy-Coupled Complex Proportional Assessment Approach. The COPRAS approach involves proportional and direct confidence in the significance and effectiveness of substitutions available in the existence of equally conflicting parameters [27]. COPRAS incorporates the success of alternatives in relation to several control factors and connects the weights by ranking and suggesting the optimal parameters. The

Table 9: Entropy modelling for output variables.

Maximize function	Minimization function		Normalization			Entropy index (EI)		
MRR	Ra	KW	MRR	Ra	KW	EIMRR	EIRa	EiKW
12.0765	3.673	0.2877	0.0364	0.0027	0.0383	−0.1206	−0.0159	−0.1250
14.818	3.754	0.2905	0.0447	0.0026	0.0379	−0.1389	−0.0156	−0.1241
16.201	3.861	0.2967	0.0489	0.0025	0.0371	−0.1475	−0.0152	−0.1223
12.3505	3.683	0.2972	0.0372	0.0027	0.0371	−0.1226	−0.0158	−0.1222
14.6605	3.727	0.3027	0.0442	0.0026	0.0364	−0.1379	−0.0157	−0.1206
13.458	3.763	0.3010	0.0406	0.0026	0.0366	−0.1301	−0.0155	−0.1211
11.84	3.654	0.3049	0.0357	0.0027	0.0361	−0.1190	−0.0159	−0.1200
11.517	3.698	0.3053	0.0347	0.0027	0.0361	−0.1167	−0.0158	−0.1199
13.3415	3.767	0.3093	0.0402	0.0026	0.0356	−0.1293	−0.0155	−0.1188
10.017	3.728	0.2870	0.0302	0.0026	0.0384	−0.1057	−0.0157	−0.1252
13.7505	3.813	0.2948	0.0415	0.0026	0.0374	−0.1320	−0.0154	−0.1229
14.8505	3.896	0.2963	0.0448	0.0025	0.0372	−0.1391	−0.0151	−0.1224
10.9015	3.682	0.2967	0.0329	0.0027	0.0371	−0.1123	−0.0158	−0.1223
12.868	3.768	0.3014	0.0388	0.0026	0.0366	−0.1261	−0.0155	−0.1210
12.2725	3.775	0.3004	0.0370	0.0026	0.0367	−0.1220	−0.0155	−0.1213
11.3505	3.728	0.3023	0.0342	0.0026	0.0365	−0.1155	−0.0157	−0.1207
11.1015	3.722	0.3032	0.0335	0.0026	0.0363	−0.1137	−0.0157	−0.1205
13.134	3.796	0.3079	0.0396	0.0026	0.0358	−0.1279	−0.0154	−0.1192
9.2265	3.726	0.2873	0.0278	0.0026	0.0384	−0.0997	−0.0157	−0.1251
12.6765	3.829	0.2897	0.0382	0.0026	0.0380	−0.1248	−0.0153	−0.1244
13.985	3.882	0.2916	0.0422	0.0025	0.0378	−0.1335	−0.0152	−0.1238
9.94	3.743	0.293	0.0300	0.0026	0.0376	−0.1051	−0.0156	−0.1234
13.208	3.811	0.2947	0.0398	0.0026	0.0374	−0.1284	−0.0154	−0.1229
11.383	3.823	0.2969	0.0343	0.0026	0.0371	−0.1158	−0.0153	−0.1223
10.018	3.748	0.2972	0.0302	0.0026	0.0371	−0.1057	−0.0156	−0.1222
9.689	3.759	0.3002	0.0292	0.0026	0.0367	−0.1032	−0.0156	−0.1213
10.9415	3.825	0.301	0.0330	0.0026	0.0366	−0.1126	−0.0153	−0.1211

Table 10: Calculated weighted entropy values.

Degree of divergence			Entropy weights		
MRR	Ra	Kw	MRR	Ra	Kw
0.0031	0.8726	0.0001	0.00352832	0.99639944	0.00007224

following steps are involved in the COPRAS approach as follows [28]:

Step 1: The initial step involves formation of decision matrix followed by normalization of output parameter.

$$NOij = \frac{Qij}{\sqrt{\sum_{i=1}^{m} Qij^2}}. \quad (8)$$

Step 2: This involves multiplication of calculated individual weight to create a normalized decision matrix. Herein, weightage calculated from the entropy approach will be multiplied with a normalized matrix (equation (9)) to form a weighted matrix as shown in Table 9.

$$NWij = We\,X\,NOij. \quad (9)$$

Step 3: calculation of Pi

In this, Pi is maximization function calculated by

$$Pi = \sum_{j=1}^{n} Qij. \quad (10)$$

Here, n is number of maximizing response.

Step 4: calculation of Ri.

In this Ri, denote the minimization function calculated by

$$Ri = \sum_{j=m+1}^{n} Qij. \quad (11)$$

The calculated values are summarized, and the calculated values are illustrated in Table 11.

Step 5: Observing the diminutive value of R.

$$\mathrm{Rmin} = \mathrm{minRi}. \quad (12)$$

Step 6: Determination of weight for attained individual response Qi

The Qi values are calculated by using equation (13), and the maximum value in Qi is termed as $Q_{\max}$.

$$\mathrm{Qi} = \mathrm{Pi} + \frac{\mathrm{Rmin}\ \sum_{\mathrm{J}=1}^{\mathrm{m}} \mathrm{Ri}}{\mathrm{Ri} \sum_{\mathrm{j}=1}^{\mathrm{m}} \mathrm{Rmin/Ri}}\ . \quad (13)$$

Table 11: Computed attributes values.

Weighted normalized matrix			Pi	Ri
MRR	Ra	KW	MRR	Ri
0.00012851	0.03600936	0.00000259	0.00012851	0.03601194
0.00015768	0.03680347	0.00000261	0.00015768	0.03680608
0.00017240	0.03785247	0.00000267	0.00017240	0.03785514
0.00013142	0.03610740	0.00000267	0.00013142	0.03611007
0.00015600	0.03653876	0.00000272	0.00015600	0.03654148
0.00014321	0.03689170	0.00000271	0.00014321	0.03689441
0.00012599	0.03582309	0.00000274	0.00012599	0.03582583
0.00012255	0.03625445	0.00000274	0.00012255	0.03625720
0.00014197	0.03693092	0.00000278	0.00014197	0.03693370
0.00010659	0.03654857	0.00000258	0.00010659	0.03655115
0.00014632	0.03738189	0.00000265	0.00014632	0.03738454
0.00015802	0.03819561	0.00000266	0.00015802	0.03819827
0.00011600	0.03609759	0.00000267	0.00011600	0.03610026
0.00013693	0.03694072	0.00000271	0.00013693	0.03694343
0.00013059	0.03700935	0.00000270	0.00013059	0.03701205
0.00012078	0.03654857	0.00000272	0.00012078	0.03655128
0.00011813	0.03648974	0.00000273	0.00011813	0.03649247
0.00013976	0.03721523	0.00000277	0.00013976	0.03721799
0.00009818	0.03652896	0.00000258	0.00009818	0.03653154
0.00013489	0.03753875	0.00000260	0.00013489	0.03754136
0.00014882	0.03805835	0.00000262	0.00014882	0.03806097
0.00010577	0.03669562	0.00000263	0.00010577	0.03669826
0.00014055	0.03736228	0.00000265	0.00014055	0.03736493
0.00012113	0.03747993	0.00000267	0.00012113	0.03748260
0.00010660	0.03674464	0.00000267	0.00010660	0.03674731
0.00010310	0.03685249	0.00000270	0.00010310	0.03685518
0.00011643	0.03749954	0.00000271	0.00011643	0.03750224

Table 12: Optimal criteria and ranking.

Rimin/Ri	Qi	Ni (%)	Ranking
0.994832	0.001497	92.92797	23
0.973367	0.001557	96.61189	7
0.946393	***0.001611***	***100***	***1***
0.992128	0.001504	93.3404	19
0.980415	0.001545	95.8837	12
0.971037	0.001546	95.92208	11
1	0.001488	92.33272	26
0.988102	0.001501	93.13701	21
0.970004	0.001546	95.93782	10
0.980156	0.001496	92.8398	24
0.958306	0.001567	97.27148	4
0.937891	0.00161	99.91754	2
0.992398	0.001488	92.3603	25
0.969748	0.001541	95.64807	14
0.96795	0.001537	95.41665	15
0.980152	0.00151	93.7208	16
0.981732	0.001505	93.41761	17
0.962594	0.001554	96.47144	8
0.980682	0.001487	92.27149	27
0.954303	0.001562	96.93211	5
0.941275	0.001595	99.02206	3
0.976227	0.001501	93.13598	22
0.958809	0.001561	96.86694	6
0.955799	0.001546	95.93924	9
0.974924	0.001503	93.30322	20
0.97207	0.001504	93.3404	18
0.955298	0.001542	95.694	13

Step 7: Determination of the utility degree Ni %.

$$Ni = 100\,X\,(Q)i/Qmax). \quad (14)$$

Based on the utility degree, the maximum value is ranked as the optimal parameter and the calculated values are shown in Table 12.

Based on the entropy-coupled corpus method, optimal control factors to attain better MRR along with minimal Ra and kerf width are attained. Herein, lower pulse off time and volume percentage of reinforcement with higher values of wire feed rate and pulse on time are the optimal machining parameters for attaining a good quality machined surface and production rate for the developed composite. The optimal parameter attained based on the hybrid approach (highlighted in bold font) yields the outcome values of 16.20 mm^3/min of MRR with 0.29 μm of kerf width and minimal surface roughness of 3.86 μm.

5. Conclusion

A magnesium surface composite with varying volume percentages of hybrid reinforcement was developed by the friction stir processing route. The WEDM process was used to understand the machinability of magnesium surface composites. The Taguchi approach was utilized for planning the experiment. The obtained results are as follows:

(i) Pulse on time and reinforcement volume percentage act as the dominating factors to influence MRR, kerf width, and surface roughness.

(ii) Lower values of pulse on time and reinforcement volume %; higher values of wire feed rate and pulse off time are the optimal machining control factors for attaining better surface integrity

(iii) Wire feed rate has the least significance over output responses.

(iv) Entropy-coupled COPRAS was adopted to attain an optimal solution, viz. a wire feed rate of 8 m/min, 1 volume % of reinforcement, 20 μs of pulse on time, and 4 μs of pulse off time.

(v) mathematical model has been developed based on the correlation between the output and input parameters with better predictability.

(vi) In the future, artificial neural networks can be used to develop models for composite machining and to predict the output response without wasting the work sample with various experimental trials.

(viii) The developed composite can be used in potential industrial applications where lightweight structures with high hardness and wear-resisting surfaces are needed.

Data Availability

The raw/processed data required to reproduce these findings cannot be shared at this time as the data also form part of an ongoing study.

Conflicts of Interest

The authors declare that they have no conflicts of interest.

References

[1] S. Banerjee, S. Poria, G. Sutradhar, and P. Sahoo, "Dry sliding tribological behavior of AZ31-WC nano-composites," *J Magnes Alloy*, vol. 7, pp. 315–327, 2019.

[2] S. Zhang, X. Ma, R. Wu, Q. Ji, F. Zhong, and X. Wang, "Effect of Sn alloying and cold rolling on microstructure and mechanical properties of Mg[sbnd]14Li alloy," *Materials Characterization*, vol. 182, Article ID 111491, 2021.

[3] M. Y. Zhou, L. B. Ren, L. L. Fan, Y. W. X. Zhang, T. H. Lu, and G. F. Quan, "Progress in research on hybrid metal matrix composites," *Journal of Alloys and Compounds*, vol. 838, 2020.

[4] F. Guo, L. Liu, Y. Ma, L. Jiang, D. Zhang, and F. Pan, "Mechanism of phase refinement and its effect on mechanical properties of a severely deformed dual-phase Mg–Li alloy during annealing," *Materials Science and Engineering A*, vol. 772, Article ID 138792, 2020.

[5] M. S. Jalali, A. Zarei-Hanzaki, M. Mosayebi, H. R. Abedi, M. Malekan, and M. Kahnooji, "Unveiling the influence of dendrite characteristics on the slip/twinning activity and the strain hardening capacity of Mg-Sn-Li-Zn cast alloys," *J Magnes Alloy*, 2022.

[6] K. Dharmalingam, G. Padmavathi, A. B. Kunnumakkara, and R. Anandalakshmi, "Microwave-assisted synthesis of cellulose/zinc-sulfate-calcium-phosphate (ZSCAP) nanocomposites for biomedical applications," *Materials Science and Engineering: C*, vol. 100, pp. 535–543, 2019.

[7] V. Kavimani, K. S. Prakash, M. S. Starvin, B. Kalidas, V. Viswamithran, and S. R. Arun, "Tribo-surface characteristics and wear behaviour of SiC@r-GO/Mg composite worn under varying control factor," *Silicon*, vol. 12, no. 1, pp. 29–39, 2020.

[8] Q. Liu, Q. x Ma, G. q Chen et al., "Enhanced corrosion resistance of AZ91 magnesium alloy through refinement and homogenization of surface microstructure by friction stir processing," *Corrosion Science*, vol. 138, pp. 284–296, 2018.

[9] K. Qiao, T. Zhang, K. Wang et al., "Effect of multi-pass friction stir processing on the microstructure evolution and corrosion behavior of ZrO2/AZ31 magnesium matrix composite," *Journal of Materials Research and Technology*, vol. 18, pp. 1166–1179, 2022.

[10] Y. Lu, W. Li, F. Luo et al., "Mechanical properties and corrosion behavior of a friction stir processed magnesium alloy composite AZ31B–SiC," *Materials Testing*, vol. 64, no. 3, pp. 314–322, 2022.

[11] Q. Zang, H. Chen, J. Zhang, L. Wang, S. Chen, and Y. Jin, "Microstructure, mechanical properties and corrosion resistance of AZ31/GNPs composites prepared by friction stir processing," *Journal of Materials Research and Technology*, vol. 14, pp. 195–201, 2021.

[12] V. Kavimani, K. S. Prakash, and T. Thankachan, "Influence of machining parameters on wire electrical discharge machining performance of reduced graphene oxide/magnesium composite and its surface integrity characteristics," *Composites Part B: Engineering*, vol. 167, pp. 621–630, 2019.

[13] S. Vijayabhaskar and T. Rajmohan, "Experimental investigation and optimization of machining parameters in WEDM of nano-SiC particles reinforced magnesium matrix composites," *Silicon*, vol. 11, no. 4, pp. 1701–1716, 2019.

[14] Y. Al-Dunainawi, M. F. Abbod, and A. Jizany, "A new MIMO ANFIS-PSO based NARMA-L2 controller for nonlinear dynamic systems," *Engineering Applications of Artificial Intelligence*, vol. 62, pp. 265–275, 2017.

[15] A. C. Y. Yuen, T. B. Y. Chen, C. Wang et al., "Utilising genetic algorithm to optimise pyrolysis kinetics for fire modelling and characterisation of chitosan/graphene oxide polyurethane composites," *Composites Part B: Engineering*, vol. 182, Article ID 107619, 2020.

[16] V. Kavimani, K. S. Prakash, T. Thankachan, S. Nagaraja, A. K. Jeevanantham, and J. P. Jhon, "WEDM parameter optimization for silicon@r-GO/magneisum composite using taguchi based GRA coupled PCA," *Silicon*, vol. 12, no. 5, pp. 1161–1175, 2020.

[17] P. M. Gopal, "Wire electric discharge machining of silica rich E-waste CRT and BN reinforced hybrid magnesium MMC," *Silicon*, vol. 11, no. 3, pp. 1429–1440, 2019.

[18] A. Kumar, N. Grover, A. Manna et al., "Multi-objective optimization of WEDM of aluminum hybrid composites using AHP and genetic algorithm," *Arabian Journal for Science and Engineering*, vol. 47, no. 7, pp. 8031–8043, 2021.

[19] M. R. Phate, S. B. Toney, and V. R. Phate, "Multi-parametric optimization of WEDM using artificial neural network (ANN)-based PCA for Al/SiCp MMC," *Journal of the Institution of Engineers*, vol. 102, no. 1, pp. 169–181, 2021.

[20] T. Thankachan, K. Soorya Prakash, and M. Loganathan, "WEDM process parameter optimization of FSPed copper-BN composites," *Materials and Manufacturing Processes*, vol. 33, no. 3, pp. 350–358, 2018.

[21] R. Gopal, K. Thirunavukkarasu, V. Kavimani, and P. M. Gopal, "Measurement and multi-response optimization of spark erosion machining parameters for titanium alloy using hybrid taguchi–grey relational analysis–principal component analysis approach," *Journal of Materials Engineering and Performance*, vol. 30, no. 4, pp. 3129–3143, 2021.

[22] K. Mouralova, L. Benes, R. Zahradnicek et al., "Analysis of cut orientation through half-finished product using WEDM," *Materials and Manufacturing Processes*, vol. 34, no. 1, pp. 70–82, 2019.

[23] V. Kavimani, K. Soorya Prakash, and T. Thankachan, "Multi-objective optimization in WEDM process of graphene – SiC-magnesium composite through hybrid techniques," *Measurement*, vol. 145, pp. 335–349, 2019.

[24] K. Mouralova, J. Kovar, L. Klakurkova, T. Prokes, and M. Horynova, "Comparison of morphology and topography of surfaces of WEDM machined structural materials," *Measurement*, vol. 104, pp. 12–20, 2017.

[25] P. M. Gopal, K. S. Prakash, and S. Jayaraj, "WEDM of Mg/CRT/BN composites: effect of materials and machining parameters," *Materials and Manufacturing Processes*, vol. 33, no. 1, pp. 77–84, 2018.

[26] K. Anand Babu and R. Jeyapaul, "Process parameters optimization of electrical discharge wire cutting on AA6082/Fly Ash/Al2O3 hybrid MMC using taguchi method coupled with hybrid approach," *Journal of the Institution of Engineers*, vol. 102, no. 1, pp. 183–196, 2021.

[27] R. Krishankumar, H. Garg, K. Arun, A. Saha, K. S. Ravichandran, and S. Kar, "An integrated decision-making COPRAS approach to probabilistic hesitant fuzzy set information," *Complex Intell Syst*, vol. 7, no. 5, pp. 2281–2298, 2021.

[28] A. R. Mishra, P. Liu, and P. Rani, "COPRAS method based on interval-valued hesitant Fermatean fuzzy sets and its application in selecting desalination technology," *Applied Soft Computing*, vol. 119, Article ID 108570, 2022.

Hindawi
Advances in Materials Science and Engineering
Volume 2022, Article ID 5320363, 8 pages
https://doi.org/10.1155/2022/5320363

Research Article

Mechanical and Wear Studies on AA7075/Nano TiC/Graphite Hybrid Composites for Tribological Applications

Clement Tom Scaria,[1] R. Pugazhenthi,[1] Ajith Arul Daniel,[1] and K. Santhosh[2]

[1]*Department of Mechanical Engineering, Vels Institute of Science Technology and Advanced Studies, Chennai 600117, India*
[2]*Department of Mechatronics Engineering, Wollo University, Kombolcha Institute of Technology, Post Box No. 208, Kombolcha, Ethiopia*

Correspondence should be addressed to R. Pugazhenthi; pugal4@gmail.com and K. Santhosh; santhosh@kiot.edu.et

Received 22 August 2022; Accepted 22 September 2022; Published 14 October 2022

Academic Editor: Pudhupalayam Muthukutti Gopal

The current paper aims to study wear behaviour of AA7075 reinforced with different weight percentage of nano-TiC and graphite particles under dry sliding condition. TiC particles are taken in different weight percentages (5%, 10%, and 15%), and graphite was chosen as (3%, 4%, and 5%) along with three different levels of sliding speed, applied load, and sliding velocity. The fabrication was conducted using stir casting equipment, and the experiments were done using Taguchi's L27 orthogonal array. The Taguchi and ANOVA results applied load and percentage of TiC are the most influencing parameters which influences wear loss and friction coefficient

1. Introduction

Metal matrixes in unstructured foams and MMCs have the potential to be employed as steel and cast iron component substitutes, especially when matrix materials are light. Aluminium is the common material used in the manufacturing process. These composites have grown in popularity due to its overwhelmed corrosion resistance, enhanced strength, and reduced density. Over base alloys, it has better resistivity and rigidity [1–4]. In a wide range of applications, these composites are replacing traditional aluminium alloys. Recent advancements in aluminium-based composites have made them increasingly useful and important in the automobile and space industries. One of the most significant developments in composite studies is the inclusion of nanoreinforcement in aluminium alloys. One of the keys to success in nanocomposites is good strength even at low volume fraction [5, 6]. Composites are made utilising a variety of traditional techniques, including solid state and liquid state fabrication. Among the various fabrication techniques, ultrasonic stir casting was among the most advantageous methods for achieving good dimensional precision and homogeneous dispersion of reinforcing particles to attain the final product [7]. Depending on the application, different types of reinforcing particles are employed to make the composites. Ceramic particles have a higher level of stability and rigidity, making them ideal for use as reinforcement particles in specific applications. The addition of hard cermet carbide particles to an aluminium alloy increases mechanical and tribological qualities as well as hardness at ambient and increased temperatures [8, 9]. There are various alternative techniques to improving composite characteristics. Lowering of matrix grain size and reinforcing particle size is among them. Traditional metal matrix composites are projected to have substantially superior microstructure stability and mechanical properties than nanocrystalline matrices enhanced by nanoreinforcements [10]. Mohan et al. investigated aluminium LM4-based composites reinforced with TaC ceramic powder, with reinforcements percentages ranging from 0.5 to 2 wt%. The materials were created using a powder metallurgy process. The dry sliding wear behaviour of the proposed composites was evaluated using a pin-on-disc apparatus, and the Taguchi design of experiment was adopted. It was also

discovered that the percentage of Ta/NbC (tantalum niobium carbide) reinforcement has an effect on the dry sliding wear rate. The results reveal that the use of hard ceramic composites in alloys has a significant impact on the dry slide wear resistance qualities [4]. Ramanaiah et al. conducted an experiment using Al7075 reinforced with TiC (2, 4, 6, 8, and 10) wt%, with a mean particle size of 2 m, using the stir casting method. It was also discovered that composites had a lower wear rate than alloys. With 8 wt% TiC, superior wear qualities and COF have been observed [11]. Priyaranjan Samal et al. conducted an experiment on AA5052 and TiC as matrix and reinforcing elements. When compared to the base material, the 9% TiC-reinforced MMCs showed a significant improvement, with a 32 percent rise in hardness, 78% increase in the tensile value. The COF values for the composites declined linearly as the TiC content and applied stress increased as a result of the formation of deep grooves with no plastic deformation at the 9% TiC-reinforced composites [12]. The composite is made by utilising a two-step stir casting method with volume fractions of silicon carbide and titanium carbide ranging from 5% to 15%. Dry sliding wear tests with a pin-on-disc wear tester were used to investigate the wear and frictional qualities. At room temperature without a lubricant, differing loads of 10N, 20N, and 30N were applied with varying sliding velocities (1 m/s, 2 m/s, and 3 m/s). TiC-reinforced composites had a microhardness rating that was 18.8% greater than SiC-reinforced composites. TiC had a wear rate of 2.1103 mm^3/m, while SiC had a wear rate of 6.4103 mm^3/m, according to the wear rate forecast. The wear rate increases as the load and sliding velocities increases [13, 14]. The friction and wear properties of the 15% SiC / 5% Gr/AI composites with various-size graphite additions were examined using squeeze casting technology. The friction coefficient of composites dropped after the addition of graphite, and wear resistance rose by 170 to 340 times [15]. The tribological behaviour of AMMCs reinforced with SiC and MoS2 in a variety of temperatures. The hybrid MMC were made using the compo casting method, which involved reinforcing different sizes of SiC (10, 20, 40 m) with 5059 aluminium alloy at various weight fractions (5, 10, and 15%), with the addition of MoS2 set at 2%. In addition to particle size and SiC weight percentage, process parameters such as load, sliding velocity, sliding distance, and temperature were evaluated, and the L27 orthogonal array was used to conduct the experiments. The best sliding condition was determined using the Taguchi and the ANOVA approach. When fine particles are reinforced at their maximum percentages, the wear rate is shown to be strong at 15% [16].

2. Experimental Details

2.1. Materials Used. The matrix material selected is an AA7075 with great ductility; tremendous strength, hardness, and good fatigue endurance are only a few of its remarkable mechanical properties. Due to microsegregation, it is more susceptible to embrittlement than several alloys[17]. The chemical composition of AA7075 is shown in Table 1. Titanium carbide (TiC) is chosen as a primary reinforcement due to its good wear and corrosion resistance. Graphite is chosen as a secondary reinforcement because of its self-lubrication properties. The EDS image of AA7075 hybrid composites is shown in Figure 1.

Table: 1: Composition for aluminium alloy 7075.

Si	Fe	Cu	Mn	Mg	Zn	Ti	Cr	Al
1.12	0.35	1.4	0.81	2.4	5.8	0.25	0.56	Bal

2.2. Experimental Set-Up. AA7075 alloy is fabricated using the liquid casting method is used to create graphite and TIC composite. An electrical furnace with a graphite crucible is used to melting the base material AA7075. The process is kept at 850°C in temperature. The melted aluminium is mixed with the warmed graphite particles. Then, it is swirled at 500 rpm with the aid of an impeller connected to a speed control motor. Continue swirling until all of the particles are distributed equally [18]. In order to solidify, the charge is deposited into a temporary steel mould after being removed from the graphite crucible. The same procedure is repeated for AA7075/5% Gr is mixed with 5% and 10% of TiC. The casted composites have undergone T6 heat treatment. In order to improve the wettablity of matrix and reinforcement, magnesium is added to about 2% during the casting process. Test specimens are prepared as per the requirements of the testing methods. The process parameters and their levels are shown in Table 2.

2.3. Dry Sliding Wear. A pin-on-disc method was employed at various parameters, including applying force, sliding speed, and sliding distance, to assess the sliding wear behaviour of Al based hybrid composite. The tests were carried out in dry conditions in accordance with ASTM G9995 standards [19]. The test specimens, which had measurements of 10 mm × 10 mm × 30 mm, were clamped against a spinning sharpened disc made of EN32 steel and hardened to RC60.

3. Result and Discussion

The experimental results for the input parameters are given in Table 3. Figure 2 shows the S/N ratio graph for wear loss. From the figure, it can be found that the load is the most influencing parameter for wear loss. When the load is minimum, the wear loss also decreases, and the wear loss is maintained between 15N and 30N. At 10N of applied load, the wear loss is very low. The weight percentage of TiC is the second most influencing parameter for wear loss. At the maximum percentage of TiC, the wear loss is deceased [20]. At 3%, the loss of particles in the composites is very low. At 15% of nano TiC and 3% of graphite, the hardness value of the developed composites is very high. In this case, the harder particles have high strength to with stand the wear loss. From this experiment, the optimum combination to attain maximum wear loss is 3% of graphite and 15% of TiC, 400 rpm of sliding distance, 10 N of applied load,

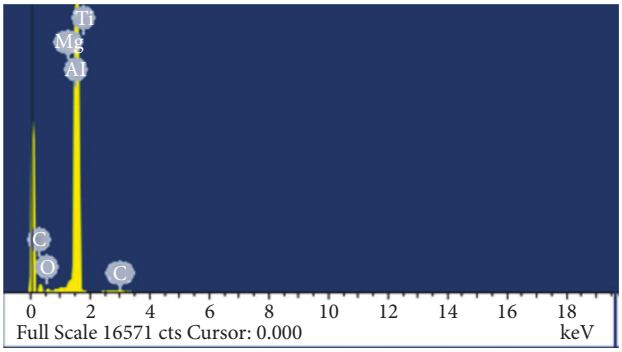

Figure 1: EDS image of AA7075 MMCs.

Table 2: Process parameters and their levels.

Variable	Factor	Notation	Unit	Range	
				Low	High
A	Titanium carbide	TiC	Wt. %	5	15
B	Graphite	Gr	Wt. %	3	5
B	Sliding speed	N	Rpm	400	600
D	Applied load	L	N	10	20
E	Sliding velocity	V	m/s	0.5	1.5

and 0.5 m/sec of sliding velocity has minimum wear loss. The ANOVA table shows significant of wear loss in Table 4.

Figure 3 shows the coefficient of friction for the developed composites. The graph represents that the sliding velocity is the most affecting parameter which influencing the coefficient of friction. Increasing the sliding velocity increases the friction value. Next, the percentage of titanium carbide is the second influencing parameter for coefficient of friction. At 15% of TiC, the hardness of the developed composite is high, so that in that level, the friction is very low. When the applied load decreases, the coefficient of friction also decreases. At 10 N of applied load, the COF value is very low. At 400 rpm of sliding speed, the COF values decreases. This is due to the distance travelled between the pin and the disc ratio is very low so at that level the friction between the pin and the disc decreases [21]. The results shows that the optimum parameters to attain maximum coefficient of friction is 3% of graphite and 15% of TiC, 400 rpm of sliding distance, 10 N of applied load, and 0.5 m/sec of sliding velocity. Table 5 shows the ANOVA table significance for coefficient of friction.

Regression equation can be given as

$$\begin{aligned}\text{wear loss} = &-0.000637593 + 0.000652222\,\text{Graphite}\,\% \\ &- 0.000114333\,\text{TiC}\,\% + 5.38333e \\ &- 006\,\text{Sliding Speed} + 7.26667e \\ &- 005\,\text{Load} + 0.00101222\end{aligned} \tag{1}$$

Sliding velocity can be given as

$$\begin{aligned}\text{COF} = &\ 0.167846 + 0.00842222\,\text{Graphite}\,\% \\ &- 0.00411444\,\text{TiC}\,\% + 4.91111e \\ &- 005\text{Sliding Speed} + 0.00263889\,\text{Load} \\ &+ 0.0429778\,\text{Sliding Velocity}\end{aligned} \tag{2}$$

Figure 4 shows the surface plot graph of titanium carbide and graphite weight percentage on wear loss during dry sliding wear behaviour. Increase in wt % of both reinforcement decreases the wear loss [22]. When the graphite percentage is 3% and 15%, then it increases the hardness of the composites. In that case, during dry sliding wear, the wear loss is very less.

Figure 5 shows the surface plot graph of sliding speed and load on wear loss. When the load and sliding speed increases, the wear loss in the composites increases. When the load is at 10 N, the wear loss is minimum; meanwhile, the wear loss increases at 15 N and sliding speed 500 rpm. In this work, the wear loss is suddenly low at 20N and the relation between sliding speed along and load along with material properties. The reading in that level during the experimentation the TiC 5% and Graphite is 5%, the hardness value is lower, and the wear loss is lower in this connection the wear loss was nearer to 15 N.

The relation between load and the sliding velocity is shown in Figure 6. The least domineering factor is for the wear loss. When the sliding velocity and load is higher and increases, the wear loss is higher in the developed composites. At 1.5 m/sec and when 20 N is the applied load, the wear loss is higher.

Figure 7 shows the surface plot for coefficient of friction between the weight percentage of titanium carbide and graphite. When the percentage of TiC increases, the COF increases. When the graphite percentage increases, the friction increases in a slow manner. The minimum influence on the graphite material is due to its self-lubrication properties and the friction between the pin and the disc decreases [23].

Figure 8 shows the interaction plot for coefficient of friction between load and sliding speed. When the load is at 10 N, the friction between the pin and the disc decreases; this is due to that the impact between the pin and the disc is low [24]. Meanwhile, when the load increases to 15N, the coefficient of friction increases. Meanwhile, when the load increases to 20%, the coefficient of friction slightly increases at that level. This is because of the presence of the graphite around 5% in this case, then the hardness of the composite material decreases due to the self-lubricant properties of graphite. Also, when the sliding distance of composites increase at 500 RPM, then the friction value also increases.

Figure 9 shows the interaction plot for coefficient of friction between load and sliding velocity. When the load and sliding velocity increases, the coefficient of friction increases. In this case, when load 10 N and sliding velocity increases, the friction values increases. Gradually, when the friction increases at 1.5 m/sec of sliding velocity and 20 N, the friction between the pin and disc is higher.

Table 3: Results of experiments.

S. no	Graphite %	TiC %	Sliding speed	Load	Sliding velocity	Wear loss	COF
1	3	5	400	10	0.5	0.0041	0.241
2	3	5	400	10	1	0.0051	0.253
3	3	5	400	10	1.5	0.005	0.29
4	3	10	500	15	0.5	0.0049	0.232
5	3	10	500	15	1	0.0049	0.25
6	3	10	500	15	1.5	0.0056	0.291
7	3	15	600	20	0.5	0.0044	0.226
8	3	15	600	20	1	0.0051	0.258
9	3	15	600	20	1.5	0.0066	0.286
10	4	5	500	20	0.5	0.0056	0.288
11	4	5	500	20	1	0.0056	0.309
12	4	5	500	20	1.5	0.006	0.317
13	4	10	600	10	0.5	0.0055	0.243
14	4	10	600	10	1	0.0048	0.269
15	4	10	600	10	1.5	0.0062	0.283
16	4	15	400	15	0.5	0.0048	0.215
17	4	15	400	15	1	0.0054	0.233
18	4	15	400	15	1.5	0.0048	0.261
19	5	5	600	15	0.5	0.0074	0.288
20	5	5	600	15	1	0.0082	0.281
21	5	5	600	15	1.5	0.0089	0.313
22	5	10	400	20	0.5	0.0054	0.274
23	5	10	400	20	1	0.0063	0.285
24	5	10	400	20	1.5	0.0066	0.305
25	5	15	500	10	0.5	0.0045	0.222
26	5	15	500	10	1	0.004	0.239
27	5	15	500	10	1.5	0.006	0.271

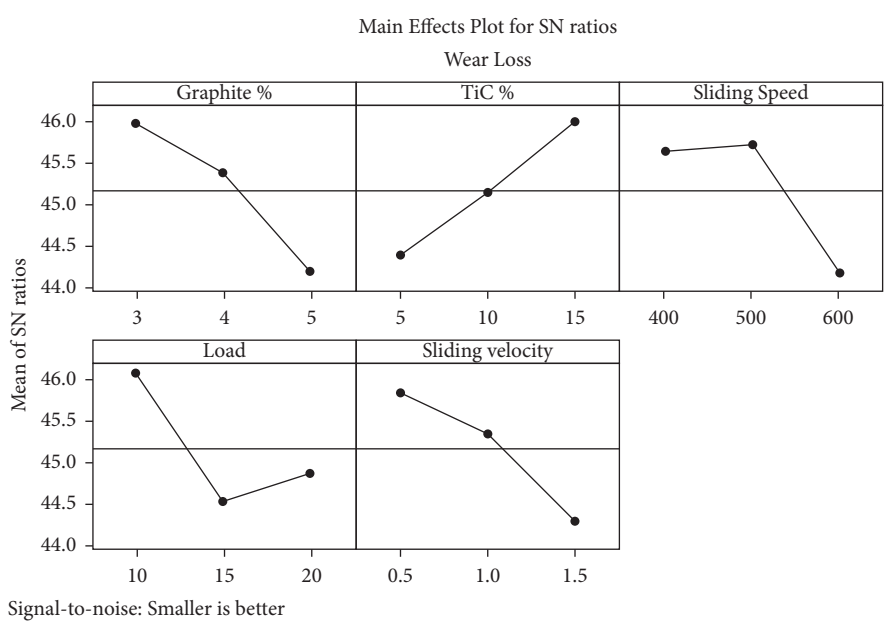

Figure 2: S/N ratio for wear loss.

Table 4: ANOVA for wear loss.

Source	DF	Seq SS	Adj SS	Adj MS	F	P
Graphite %	2	0.0000083	0.0000083	0.0000041	16.19	0
TiC %	2	0.0000059	0.0000059	0.000003	11.62	0.001
Sliding speed	2	0.0000073	0.0000073	0.0000037	14.37	0
Load	2	0.0000055	0.0000055	0.0000027	10.75	0.001
Sliding velocity	2	0.0000048	0.0000048	0.0000024	9.44	0.002
Error	16	0.0000041	0.0000041	0.0000003		
Total	26	0.0000359				

Table 5: ANOVA for COF.

Source	DF	Seq SS	Adj SS	Adj MS	F	P
Graphite %	2	0.0012998	0.0012998	0.0006499	9.68	0.002
TiC %	2	0.0077158	0.0077158	0.0038579	57.44	0
Sliding speed	2	0.0004563	0.0004563	0.0002282	3.4	0.059
Load	2	0.0034588	0.0034588	0.0017294	25.75	0
Sliding velocity	2	0.0084748	0.0084748	0.0042374	63.1	0
Error	16	0.0010745	0.0010745	0.0000672		
Total	26	0.02248				

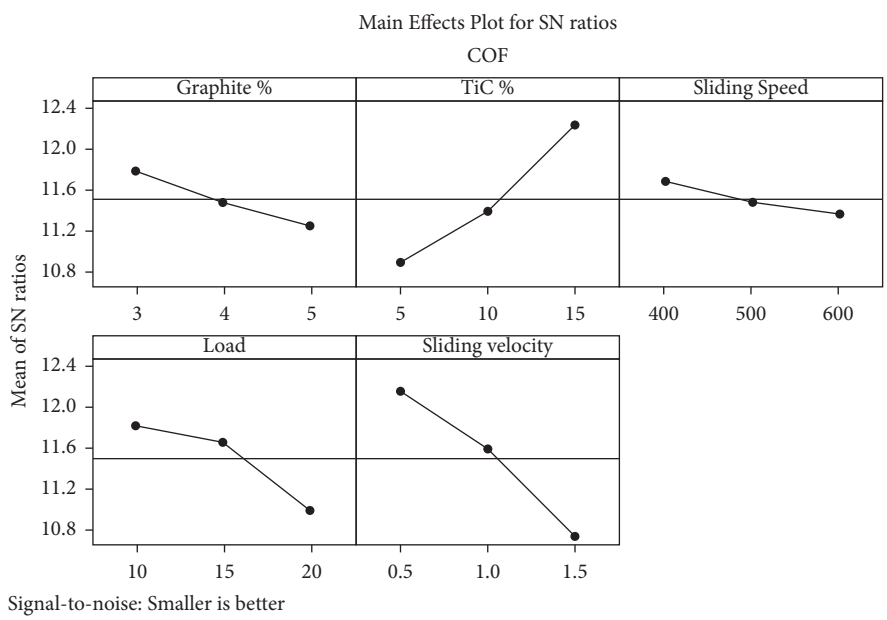

Figure 3: S/N ratio for coefficient of friction.

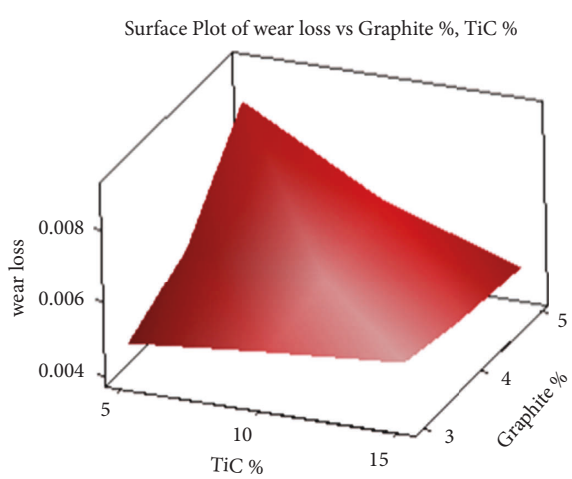

Figure 4: Surface plot graph for TiC % VS graphite % to wear loss.

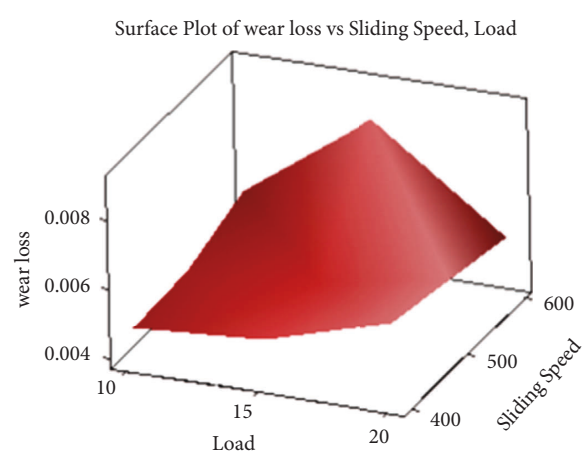

Figure 5: Surface plot graph for load % VS sliding speed to wear loss.

4. Wornout Analysis

Figure 10 shows the wornout surface of the after wear composites. Figure 10(a) shows the presence of 15% of TiC and 3 % of graphite with the load of 10 N. The wornout surfaces are very low, and this is due to the hardness of the composite. In this case, at that level, the reinforcement particles are strongly bonded with the matrix phase, then the surface is very smooth. Also, it is clearly observed that the 3%

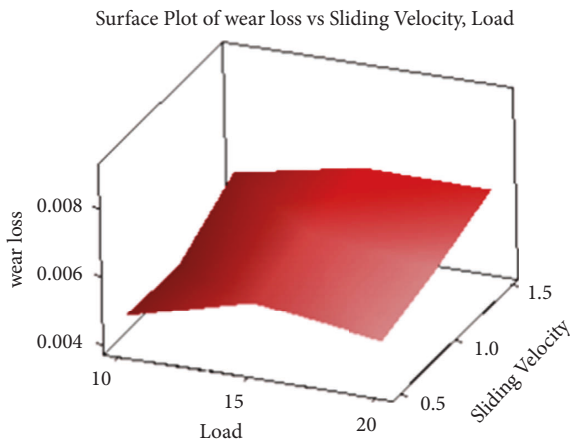

Figure 6: Surface plot graph for load % VS sliding velocity to wear loss.

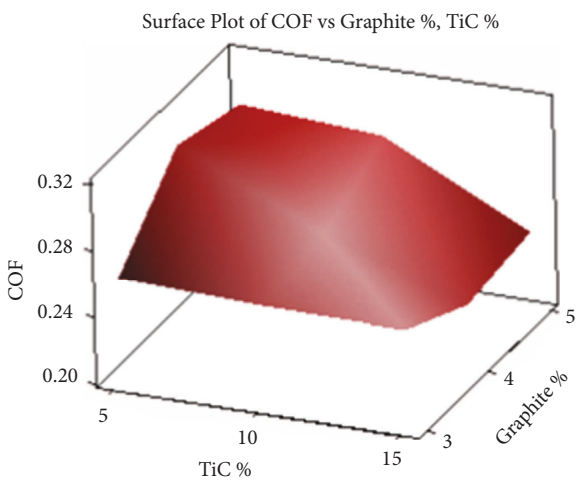

Figure 7: Surface plot graph for graphite % vs TiC to COF.

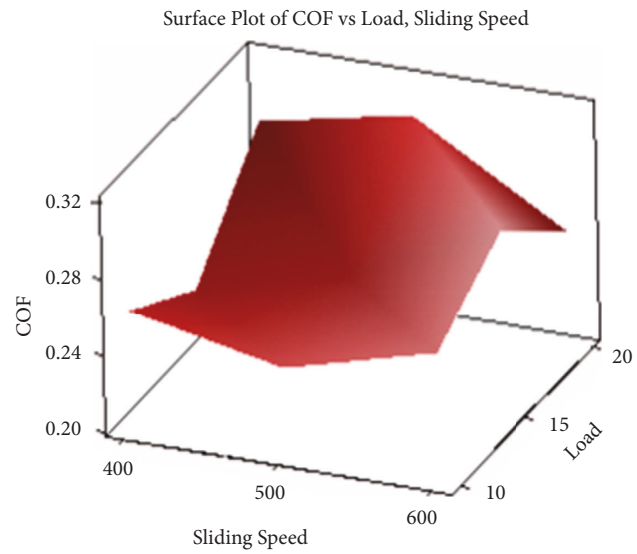

Figure 8: Surface plot graph for load % VS sliding speed to COF.

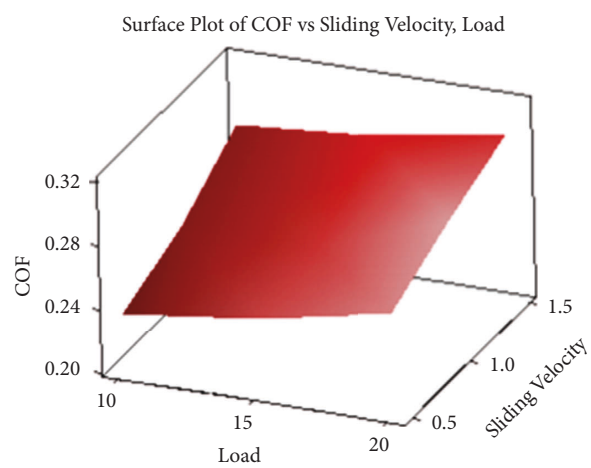

Figure 9: Surface plot graph for load % vs sliding distance to COF.

of graphite have experienced a minimal wear. This is due to the self-lubrication effect of graphite on the tribo surface [25]. Figure 10(b) shows the presence of 10% TiCi and 4% of Graphite with the load capacity of 15 N. In this case, the wornout surface has a mild groove on the surface of the matrix. Due to the increase in load and 2% of graphic particles, the hardness of the composites is low at that level. Figure 10(c) shows the presence of 5% of TiC with 4% of graphite and at 15 N of the applied load, the wear debris is very high. This shows severe plastic flow of material at low applied loads. At high applied load and high sliding velocity, the flake-like debris is formed as an outcome of delamination of the tribo surface [26]. Figure 10(d) shows the presence of TiC at 5% and 5% of graphite and applied load at 20 N. During the maximum load, the delamination of the reinforcement from the matrix is very high due to the 5% of TiC presence in the material. In the graphite 5% case, the

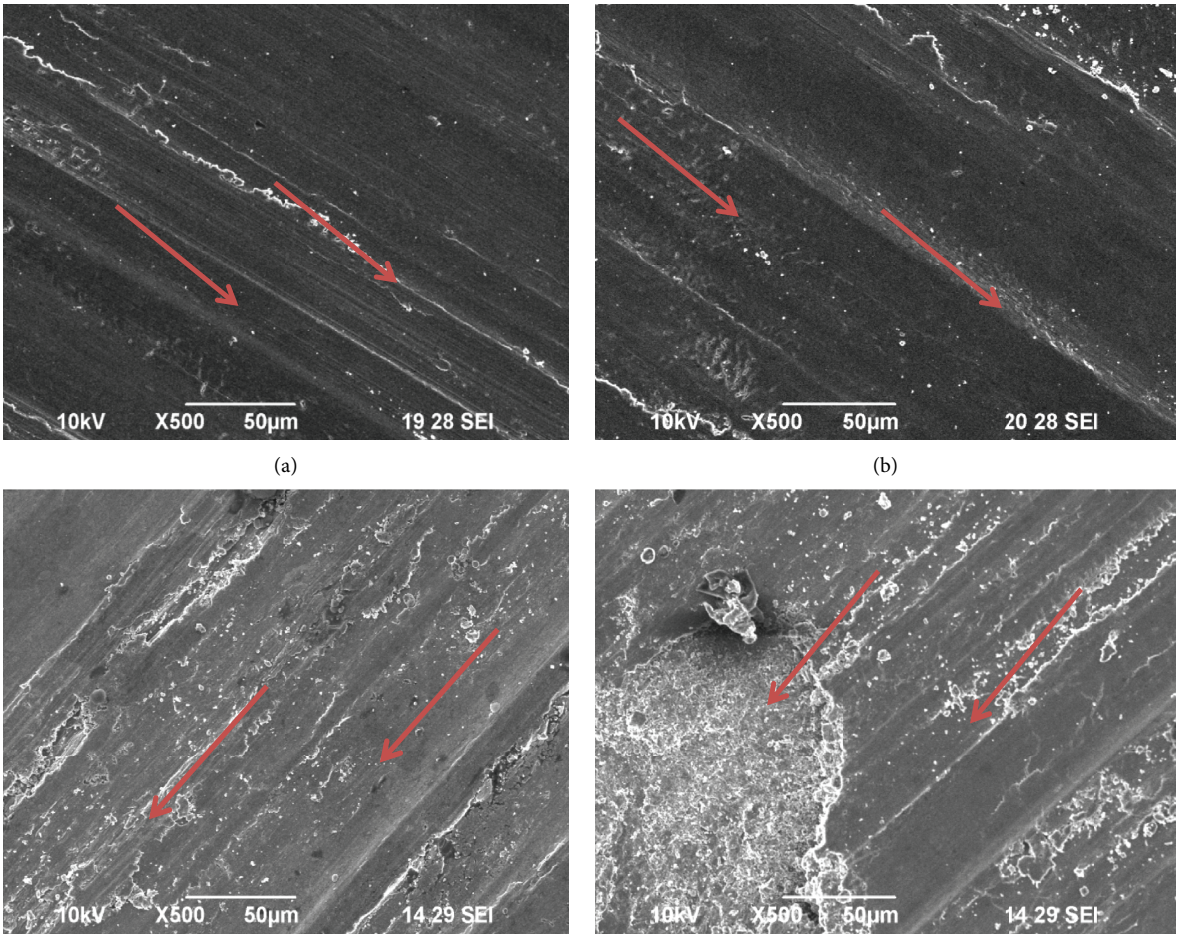

Figure 10: (a) TiC 15%, graphite 3%, and load 10N; (b) TiC 10%, graphite 4%, and load 15N; (c) TiC 5%, graphite 4%, and Load 15N (d). TiC 5%, graphite 45%, and load 20N.

hardness of the composite is very low and also it provides self-lubricant properties which cause slowly decrease and leads to the maximum delamination of the reinforcement.

5. Conclusion

(1) Al7075/TiC/Gr was fabricated using the liquid metallurgy process, and Taguchi method was adapted to find the optimum combination of input parameters.

(2) Load and TiC % are the most influencing parameters for wear loss, At 20N of applied load and 15% of TiC, the wear loss decreases. The optimum combination for minimum wear loss is 3% of graphite and 15% of TiC, 10 N of applied load, 400 rpm of sliding distance, and 0.5 m/s of sliding velocity offers minimum wear loss.

(3) Coefficient of friction is minimum when TiC percentage increases. Load is the maximum parameter, which increases the friction between the pin and the disc. The optimum combination for lower coefficient of friction is 3% of graphite and 15% of TiC, 10 N of applied load, 400 rpm of sliding distance, and 0.5 m/s of sliding velocity offers minimum friction in developed Al7075/TiC/Gr composites.

(4) The wornout images shows the different consequences of various influencing parameters which affects the wear loss and coefficient of friction using SEM images. Through which, it is identified as 15% of TiC and 3% of graphite, which shows minimum delamination and small groove in after wear composites.

Data Availability

All the associated data are provided in the article.

Conflicts of Interest

The authors declare that they have no conflicts of interest.

References

[1] S. Mosleh-Shirazi, F. Akhlaghi, and D. Y. Li, "Effect of SiC content on dry sliding wear, corrosion and corrosive wear of

Al/SiC nanocomposites," *Transactions of Nonferrous Metals Society of China*, vol. 26, no. 7, pp. 1801–1808, 2016.

[2] D. Jeyasimman, R. Narayanasamy, R. Ponalagusamy, V. Anandakrishnan, and M. Kamaraj, "The effects of various reinforcements on dry sliding wear behaviour of AA 6061 nanocomposites," *Materials & Design*, vol. 64, pp. 783–793, 2014.

[3] D. M. Shinde, S. Poria, and P. Sahoo, "Dry sliding wear behavior of ultrasonic stir cast boron carbide reinforced aluminium nanocomposites," *Surface Topography: Metrology and Properties*, vol. 8, no. 2, Article ID 025033, 2020.

[4] T. S. Sachit, N. Mohan, R. Suresh, and M. A. Prasad, "Optimization of dry sliding wear behavior of aluminum LM4-Ta/NbC nano composite using Taguchi technique," *Materials Today Proceedings*, vol. 27, pp. 1977–1983, 2020.

[5] G. Cao, H. Konishi, and X. Li, "Mechanical properties and microstructure of Mg/SiC nanocomposites fabricated by ultrasonic cavitation based nanomanufacturing," *Journal of Manufacturing Science and Engineering*, vol. 130, no. 3, 2008.

[6] K. J. Joshua, S. J. Vijay, and D. P. Selvaraj, "Effect of nano TiO2 particles on microhardness and microstructural behavior of AA7068 metal matrix composites," *Ceramics International*, vol. 44, no. 17, pp. 20774–20781, 2018.

[7] U. K. G. Annigeri Veeresh Kumar, "Method of stir casting of aluminum metal matrix composites: a review," *Materials Today Proceedings*, vol. 4, no. 2, pp. 1140–1146, 2017.

[8] M. P. Reddy, M. Himyan, F. Ubaid et al., "Enhancing thermal and mechanical response of aluminum using nanolength scale TiC ceramic reinforcement," *Ceramics International*, vol. 44, no. 8, pp. 9247–9254, 2018.

[9] V. Khalili, A. Heidarzadeh, S. Moslemi, and L. Fathyunes, "Production of Al6061 matrix composites with ZrO2 ceramic reinforcement using a low-cost stir casting technique: microstructure, mechanical properties, and electrochemical behavior," *Journal of Materials Research and Technology*, vol. 9, no. 6, pp. 15072–15086, 2020.

[10] A. Siddique, Z. Iqbal, Y. Nawab, and K. Shaker, "A review of joining techniques for thermoplastic composite materials," *Journal of Thermoplastic Composite Materials*, Article ID 089270572210966, 2022.

[11] V. R. Rao, N. Ramanaiah, and M. M. M. Sarcar, "Dry sliding wear behavior of Al7075 reinforced with titanium carbide (TiC) particulate composites," in *Proceedings of the International Conference on Advances in Materials, Manufacturing and Applications*, AMMA, NIT,Tiruchirapally, April 2015.

[12] K. Hemadri, S. Ajith Arul Daniel, A. Parthiban, and T. Vinod kumar, "Investigation on the response parameters in electric discharge machining of developed aluminium metal matrix composites," *Materials Today Proceedings*, 2022.

[13] R. Gukendran, M. Sambathkumar, K. S. K. Sasikumar, K. Ponappa, and S. Gopal, "Investigation of dry sliding wear behavior of al 7075–(SiC/TiC) hybrid metal matrix composites," *Surface Review and Letters*, vol. 28, no. 07, Article ID 2150065, 2021.

[14] S. Basavarajappa, G. Chandramohan, K. Mukund, M. Ashwin, and M. Prabu, "Dry sliding wear behavior of Al 2219/SiCp-Gr hybrid metal matrix composites," *Journal of Materials Engineering and Performance*, vol. 15, no. 6, pp. 668–674, 2006.

[15] L. Jinfeng, J. Longtao, W. Gaohui, T. Shoufu, and C. Guoqin, "Effect of graphite particle reinforcement on dry sliding wear of SiC/Gr/Al composites," *Rare Metal Materials and Engineering*, vol. 38, no. 11, pp. 1894–1898, 2009.

[16] S. A. A. Daniel and PM. Gopal, "Study on tribological behaviour of Al/SiC/MoS2 hybrid metal matrix composites in high temperature environmental condition," *Silicon*, vol. 10, no. 5, pp. 2129–2139, 2018.

[17] A. Kumar, V. Kumar, A. Kumar, B. Nahak, and R. Singh, "Investigation of mechanical and tribological performance of marble dust 7075 aluminium alloy composites," *Materials Today Proceedings*, vol. 44, pp. 4542–4547, 2021.

[18] K. Almadhoni and S. Khan, "Review of effective parameters of stir casting process on metallurgical properties of ceramics particulate Al composites," *IOSR Journal of Mechanical and Civil Engineering*, vol. 12, no. 6, pp. 2278–1684, 2015.

[19] A. A. Daniel, S. Murugesan, and S. Sukkasamy, "Dry sliding wear behaviour of aluminium 5059/SiC/MoS 2 hybrid metal matrix composites," *Materials Research*, vol. 20, no. 6, pp. 1697–1706, 2017.

[20] M. Azadi, A. S. Rouhaghdam, S. Ahangarani, and H. H. Mofidi, "Mechanical behavior of TiN/TiC multilayer coatings fabricated by plasma assisted chemical vapor deposition on AISI H13 hot work tool steel," *Surface and Coatings Technology*, vol. 245, pp. 156–166, 2014.

[21] K. Hemadri, S. Ajith Arul Daniel, V. Kukanur, S. Vijayananth, and R. Kumar, "Investigation on mechanical characterization of Al/Mos2/WC hybrid composite," *Materials Today Proceedings*, 2022.

[22] J. Lakshmipathy and B. Kulendran, "Reciprocating wear behavior of 7075Al/SiC in comparison with 6061Al/Al2O3 composites," *International Journal of Refractory Metals and Hard Materials*, vol. 46, pp. 137–144, 2014.

[23] A. Baradeswaran and A. E. Perumal, "Wear and mechanical characteristics of Al 7075/graphite composites," *Composites Part B: Engineering*, vol. 56, pp. 472–476, 2014.

[24] A. Kovalchenko, O. Ajayi, A. Erdemir, G. Fenske, and I. Etsion, "The effect of laser texturing of steel surfaces and speed-load parameters on the transition of lubrication regime from boundary to hydrodynamic," *Tribology Transactions*, vol. 47, no. 2, pp. 299–307, 2004.

[25] L. Wang, G. Zhang, Y. Wang, Y. Wang, X. Sun, and Q. Xue, "TiC/aC: H nanocomposite coatings as substitute for MoS2-based solid lubrication in helium atmosphere," *Journal of Non-Crystalline Solids*, vol. 358, no. 1, pp. 65–71, 2012.

[26] P. Loganathan, A. Gnanavelbabu, and K. Rajkumar, "Analysis and characterization of friction behaviour on AA7075/ZrB2 composite under dry sliding condition," *Materials Research Express*, vol. 6, no. 2, p. 026576, 2018.

Hindawi
Advances in Materials Science and Engineering
Volume 2022, Article ID 1920810, 11 pages
https://doi.org/10.1155/2022/1920810

Research Article

Multiobjective Optimization of WEDM Parameters on the Mg-HNT-Zr Hybrid Metal Matrix Composite Using Taguchi-Coupled GRA

A. Jayaganthan,[1] M. Manickam,[2] S. Prathiban,[3] M. Amarnath,[4] Karthikeyan Subramanian,[5] M. Babu,[6] P. Dharmadurai,[7] and Yesgat Adamassu[8]

[1]*Department of Automobile Engineering, Sathyabama Institute of Science and Technology, Chennai, Tamil Nadu 600119, India*
[2]*Department of Mechanical Engineering, Bharath Institute of Higher Education and Research, Chennai 600073, India*
[3]*Department of Mechanical Engineering, Annamalai University, Chidambaram, Tamil Nadu, India*
[4]*Department of Mechatronics Engineering, Sathyabama Institute of Science and Technology, Chennai, Tamil Nadu 600119, India*
[5]*Department of Mechanical Engineering, Dhanalakshmi Srinivasan College of Engineering and Technology, Chennai, Tamil Nadu, India*
[6]*Department of Mechanical Engineering, SRM Easwari Engineering College, Chennai, India*
[7]*Department of Aeronautical Engineering, Mahendra Engineering College, Namakkal, Tamil Nadu, India*
[8]*Defence University College, Bishoftu, Ethiopia*

Correspondence should be addressed to Yesgat Adamassu; yesgat.admassu@dec.edu.et

Received 6 July 2022; Accepted 4 September 2022; Published 13 October 2022

Academic Editor: Pudhupalayam Muthukutti Gopal

The current research deals with Taguchi-coupled grey relational analysis (GRA) multiobjective optimization of wire electric discharge machining (WEDM) for better surface roughness (Ra) and the material removal rate (MRR) over magnesium/halloysite nano tube/zirconium (Mg/HNT/Zr) metal matrix composite (MMC). Hybrid composites are created through the powder metallurgy route by varying the weight percentage of reinforcements HNT (5 and 10%) and Zr (0.5 and 1%) to the weight of the base material magnesium. Machining is carried out by varying the factors such as reinforcement's weight percentage, pulse OFF time, pulse ON time, and wire feed (WF) based on Taguchi's L27 orthogonal array. The response surface roughness (Ra) and the material removal rate (MRR) were studied through Taguchi-coupled GRA to evaluate the optimized machining parameters. ANOVA results reveal the percentage contribution of certain factors over the machining of composites. The developed regression model proved that the predicted values were merely similar to the experimental values of MRR and Ra. The best parametric combinations obtained from optimization are inline as the minimum weight percentage of reinforcements, and higher Pon, higher WF, and the lowered Poff are used to attain the best rate of MRR during machining and for minimized surface roughness.

1. Introduction

MMCs are excellent materials in which high-strength and hard refractory ceramics are reinforced with the ductile metal matrix. Aluminum, magnesium, copper, titanium, and zinc are the commonly used lightweight matrix material and carbides, nitrides, oxides, and borides are the commonly used reinforcements in the form of particulates, whiskers, or fibers [1]. Strong attention to the evolution of MMCs is due to the improved properties such as strength, hardness, wear resistance, corrosion resistance, higher thermal, and electrical conductivities combined with significant weight-reducing over alloys. Due to these superior properties of MMCS, they are widely used in automotive, aerospace, construction, and marine industries [1]. Amongst the several matrix materials used in MMCs, aluminum and magnesium matrices are used as the most common materials due to their low density, less weight, good corrosion resistance, high electrical and thermal conductivity, and low cost [2].

The MMCs can be fabricated by the different techniques such as the selection of suitable processing techniques on matrix material, quantity, and the nature of reinforcements and application. Liquid state, vapor state, and solid-state processing are the three major types of composite fabrication methods widely used. The solid-state handling approach incorporates the creation of MMC in the strongest state itself without softening the components, which results in the holding of the lattice stage and the support stage by common dispersal taking place among them in strong positions at discernible temperature and are lower than the exceptional weight. The fundamental preferred position of this procedure is that the collection of metals that can be dealt with is progressively broad and the assistant handling is negligible. Powder metallurgy and diffusion bonding methods are the most commonly used methods to make solid-state processing [3].

Powder metallurgy involves powders for manufacturing metal in the metal matrix composite with the sequence of blending, compaction, and sintering. This technique involves three main processes as shown in Figure 1.

The reinforcement and matrix powders are combined to develop a homogenous mixture with the help of a ball milling or mechanical stirrer or magnetic stirrer or ultrasonicator, etc. Then, the mixed powders are cold-pressed in a die to make the mixtures turn into a solid green composite, and this process is called compaction. The final step is the sintering process; here, the green composite is kept in a furnace at below-melting temperature to make a full solid composite. Sometimes the compaction process is carried out at an increased temperature, which is called hot pressing. Powder metallurgy permits minimizing machining operation on account of forming parts with minimum tolerance. Powder metallurgy allows the development of materials, which cannot be made by using any other technologies such as hard materials, refractory materials, porous metals, wear-resistant materials, blends of dissimilar metals, permanent magnets, possessing various melting points or are insoluble in the molten state, and different combinations of metals with nonmetals [4].

Machining is one of the important aspects of manufacturing processes by which excess materials are constantly removed by trimming from a preformed object that takes place in the form of solid chips or metal powders to get the desired shape, finish, and tolerance. The materials cannot be commercialized into applications directly without machining, as a minimum machining process is needed to get the required shape [5]. Traditional and nontraditional machining are the two different ways of machining. The major hindrance in the growth of MMCs was that of machining by using traditional techniques due to the property of superior hardness and the presence of reinforcement. The use of customary machinery to machine hard composite materials causes severe tool wear owed to the rough nature of the reinforcement. At the same time, with their various sophisticated technologies and features, nonconventional machining methods, also known as noncontact metal removal methods, have gained a reputation for successfully machining MMCs in industries [6]. Nontraditional machining processes are used to machine MMCs including electrical discharge machining (EDM), abrasive jet machining (AJM), electrochemical machining (ECM), and laser beam machining (LBM). The wire electrical discharge machining (WEDM), a commonly accepted nontraditional machining technology for complicated precision components, discovered an effective metal removal approach for MMCs to enhance the cut quality at a specified cost. For a composite material that is made of different materials with different properties, the WEDM process is recommended for a more precise and accurate resulting surface finish.

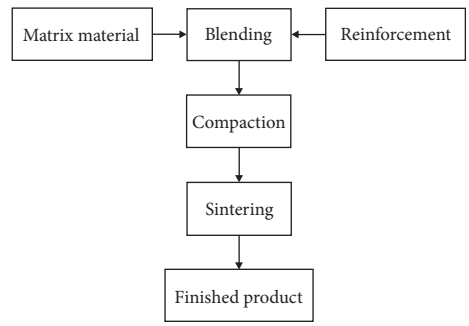

Figure 1: Powder metallurgy process.

WEDM is an unconventional machining process that is defined as a method in which materials are removed from the workpiece in a maximum accurate and effective manner [7]. WEDM is a high-precision cutting procedure that may be used on practically on any electrically conductive material. A thin, electrically charged wire usually made of a brass material gripped between the lower and upper mechanical guides constructs one electrode, while the material remaining cut forms another electrode. Electrical discharge between material and wire creates sparks that instantly cuts the excess material. Then, the debris are being flushed away by sinking the wire and workpiece in deionized water. Among the spoke explores broadly held in this field, just the sinking EDM process was commonly revealed, and significant on WEDM [8].

2. Materials and Methods

2.1. Materials. Hybridized Mg composites are often made by using the powder metallurgy (PM) process, which involves adding Zr and HNT particles to the basic material Mg in varying weight percentages. Aluminum and silica-rich double-layered aluminosilicate HNT were taken as a primary reinforcement for its ecofriendly, nontoxic, high strength, corrosion resistance, and wear-withstanding properties [9, 10]. HNT is a multiwalled kaolin clay with the structural formula ($H_4AL_2O_9Si_2.2H_2O$) that was purchased from Sigma-Aldrich Company (USA).

Zr was selected as the reinforcing material for its wear resistance and high corrosion resistance properties such as high temperatures [11]. Zr compounds are used extensively in biomedical uses, including hip replacements, knee, and dental implants. It is also used in some prosthetic and therapeutic devices. As a result, Zr was chosen as a reinforcing material for hybrid biocompatible magnesium MMCs [1, 12].

2.2. Composite Fabrication. Powder metallurgy, which comprises the processes of sintering, compression, and blending, is the most efficient method of producing MMCs. Blending is one of the dynamic methods in PM, as the metallic powder particles are combined with reinforcing particles [13, 14]. The weight level of essential HNT fortification is fluctuated in the scope of 5 and 10, though the weight percent of optional Zr support is changed in the range of 0.5 and 1.0. In light of the writing review and starter trial examination results, the measure of reinforcements is fixed [15]. Nine distinctive magnesium MMCs were arranged by differing HNT and Zr percentages as specified in Table 1 alongside an unadulterated Mg sample.

The mixed powders were crushed under pressure in a die, then sintering was carried out in a hot furnace. Furthermore, as compared to the ingot metallurgical method, powder metallurgy has the ability to eliminate reinforcement separation. Figure 2 shows the powder metallurgy process for composite fabrication.

The blending process was performed by mixing the base material and reinforcement at a steady speed for 2 hours by using a magnetic stirrer. Figure 3 illustrates the SEM image of the base material and reinforcement's well-blended powder composition.

The sample was compressed using a hydraulic press machine with a 40 mm diameter die, a 560 Mpa load, and a 10-minute dwell time. Finally, under an argon gas atmosphere, the compressed green composite was sintered at 550°C in a muffle furnace, and sintered samples were then cooled down in the furnace [3]. Images of sintered composite material samples are displayed in Figure 2.

Density and hardness are the important physical property of the material corresponding to lightweight applications. The variation of density and microhardness for the unreinforced and as well as HNT and Zr reinforced in the various composition of composites is given in Table 1. Since the density of HNT (2.53 g/cm^3) and Zr (6.49) is higher than the matrix material Mg (1.738 g/cm^3), the addition of reinforcements leads to an increase in the density of the material. An increment in hardness with the increase in HNT and Zr weight rate might be ascribed to the higher hardness of support. Thus, both material phases with the great bonding illustrations have higher hardness.

2.3. Machining Condition and Measurement. Taguchi's DOE approach based on OA was used for designing the experiment by varying considerations at different levels. Minitab programming was utilized for this reason and the L27 symmetrical cluster was planned by using five factors that is the weight proportion of HNT and Zr over the pure Mg, pon, poff, and WF having three stages revealed in Table 2 were selected for this study in light of the writing review, specialists' recommendations, and preliminary trials. The response parameters were the material removal rate (MRR) and surface roughness (Ra). The appropriated experimental design obtained by using the L27 orthogonal array (OA) chosen for the considered WEDM process parameters is shown in Table 3 and 4.

Surface roughness (Ra) and the material removal rate (MRR) are considered response parameters because the surface roughness value plays an important role in any newer material and likewise the MRR is also most important to commercialize the material economically. PCE-RT 1200 (the UK make) surface roughness tester was used to determine the roughness value over the surface of the machined composites for each trial. The parameter MRR during the WEDM process was determined by the following equation which incorporates the measure of material evacuated.

$$MRR = \frac{Wa - Wb}{t} \frac{g}{\min}, \tag{1}$$

where Wa is the mass of workpiece material prior to machining, Wb is the mass of workpiece material in the wake of machining, and t is the duration of machining.

The machining process for the newly developed composites was carried out by using the EXETEKEX40 WEDM setup, as displayed in Figure 4. The machine had a brass wire of diameter 0.25 mm and the wire material was fed into the workpiece material so as to machine the surface with precise dimensions and all other relative fundamental machine specifications and other relevant general process parameters are provided in Table 4.

To know the deviation between test esteems and ideal cutting qualities, a quality misfortune capacity approach was prescribed by Taguchi. In the Taguchi strategy, the reaction factors were broken down as far as signal-to-noise (S/N) proportions, which records the affectability of yield estimated to the clamor factor or wild factor. The best possible S/N proportions figuring criteria must be picked from the three criteria in particular "larger is better," "nominal is better," and "smaller is better." The difference between measured data and the ideal value is expected to be as small as possible. The generic form of the S/N ratio then becomes small for surface roughness (Ra) so the equation can be described as follows:

$$n = -10 \log_{10} \left(\frac{1}{n} \sum_{i=1}^{n} yi^2 \right). \tag{2}$$

The difference between measured data and the ideal value is expected to be as large as possible. The generic form of S/N ratio then becomes maximum for the material removal rate (MRR) so the equation can be represented as follows:

$$n = -10 \log_{10} \left(\frac{1}{n} \sum_{i=1}^{n} \frac{1}{yi^2} \right). \tag{3}$$

ANOVA was performed to recognize the noteworthiness of every parameter over the reaction factors. Furthermore, the rate impact of each factor over the response variable was additionally distinguished from the ANOVA study by utilizing a consecutive aggregate of square values. And a p value of under 0.05 had a significant effect. Taguchi S/N proportions investigation was constrained to take care of just

Table 1: Results of hardness and density tests.

S. No	Composition	Hardness value for (100 gm.)	Density (g/cm^3)
1	Pure Mg	28.4	1.636
2	Mg-HNT 5%	34.8	1.638
3	Mg-HNT 10%	36.7	1.675
4	Mg-Zr 0.5%	32.7	1.619
5	Mg-Zr 1%	33.4	1.645
6	Mg-HNT 5%-Zr 0.5%	35.3	1.658
7	Mg-HNT 5%-Zr 1%	36.4	1.630
8	Mg-HNT 10%-Zr 0.5%	36.7	1.696
9	Mg-HNT 10%-Zr 1%	38.1	1.659

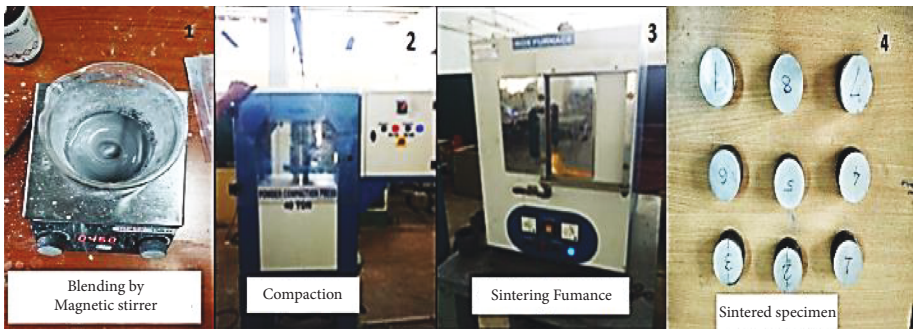

Figure 2: Composite development steps and prepared specimens.

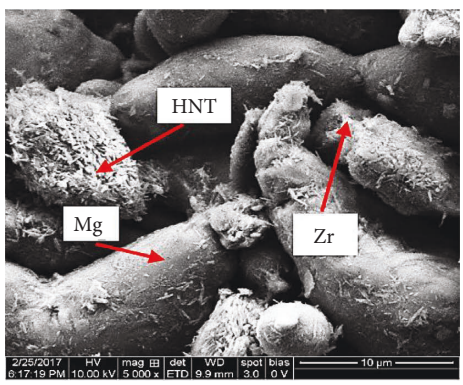

Figure 3: SEM micrograph of the well-mixed powder structure.

Table 2: Machining factors and levels (WEDM).

Factors	Codes	Level 1	Level 2	Level 3
HNT %	*A*	0	6	11
Zr %	*B*	0	0.6	1
Pulse on time (μs)	*C*	10	11	12
Pulse off time (μs)	*D*	15	16	17
Wire feed (m/min)	*E*	4	5	6

single-objective optimization issues. To advance the information parameters for multiobjective such as the material removal rate and surface roughness, a multiobjective streamlining named grey relational investigation with Taguchi configuration is a superior arrangement through GRA [16]. First, multiresponse parameters could be changed into a solitary target capacity, and afterwards, qualities of the ensuing ideal arrangement of parameters can be resolved.

Table 3: L27 experimental design with response variables.

Trial no.	HNT wt.%	Zr wt. %	*P* on	*P* off	Wire feed	MRR (g/min)	Ra (μm)	SNRA MRR	SNRA Ra
1	0	0	10	15	4	1.734	2.168	4.7809819	−6.7212
2	0	0	10	15	5	1.789	2.203	5.0522068	−6.8603
3	0	0	10	15	6	1.814	2.264	5.1727457	−7.0975
4	0	0.5	11	16	4	1.712	2.379	4.6700752	−7.5279
5	0	0.5	11	16	5	1.735	2.412	4.7859896	−7.6475
6	0	0.5	11	16	6	1.777	2.478	4.9937486	−7.882
7	0	1	12	17	4	1.695	2.454	4.5833941	−7.7975
8	0	1	12	17	5	1.715	2.496	4.6852825	−7.9449
9	0	1	12	17	6	1.732	2.597	4.7709578	−8.2894
10	5	0	11	17	4	1.603	2.452	4.0986704	−7.7904
11	5	0	11	17	5	1.639	2.497	4.2915791	−7.9484
12	5	0	11	17	6	1.698	2.532	4.5987537	−8.0693
13	5	0.5	12	15	4	1.664	3.053	4.4230664	−9.6945
14	5	0.5	12	15	5	1.69	3.126	4.5577341	−9.8998
15	5	0.5	12	15	6	1.703	3.197	4.624293	−10.095
16	5	1	10	16	4	1.498	2.788	3.5102363	−8.9059
17	5	1	10	16	5	1.513	2.867	3.5967786	−9.1486
18	5	1	10	16	6	1.542	2.947	3.7616875	−9.3876
19	10	0	12	16	4	1.659	2.769	4.3969277	−8.8465
20	10	0	12	16	5	1.684	2.815	4.5268417	−8.9896
21	10	0	12	16	6	1.692	2.874	4.5680072	−9.1697
22	10	0.5	10	17	4	1.412	2.489	2.9966939	−7.9205
23	10	0.5	10	17	5	1.498	2.543	3.5102363	−8.1069
24	10	0.5	10	17	6	1.545	2.612	3.7785697	−8.3395
25	10	1	11	15	4	1.568	3.102	3.9069212	−9.8328
26	10	1	11	15	5	1.594	3.178	4.0497663	−10.043
27	10	1	11	15	6	1.623	3.256	4.2063704	−10.254

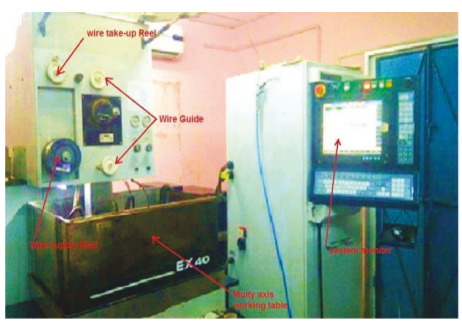

Figure 4: Wire cut EDM machine setup.

Table 4: Key features of selected WEDM machine.

S. No.	Parameters of WEDM	Range/values
1.	Discharge current	10 A
2.	Gap voltage	20 V
3.	Pulse ON time	10–12 μs
4.	Pulse OFF time	15–17 μs
5.	Wire material	Cu
6.	Wire diameter	0.25 mm
7.	Wire feed (WF)	4–6 m/min
8.	Wire tension	8 N
9.	Workpiece height	30 mm
10.	Dielectric fluid	Deionized water

Furthermore, the Taguchi plan with grey relational analysis is a strong technique to take care of the multiobjective issues.

The primary stage is to standardize the deliberate yield work independently and it is fundamentally the same as the S/N proportions computation in the Taguchi strategy where various models are pursued. The "smaller is better" standardization condition was chosen for normalizing surface roughness and the corresponding formula can be represented as follows:

$$Y_{ij} = \frac{\left(\max\left(z_{ij}\right) - (zij)\right)}{\max\left(z_{ij}\right) - \min\left(z_{ij}\right)}. \quad (4)$$

If there should arise an occurrence of MRR, the criteria picked for normalizing is "larger is better" and the equation is as follows:

$$Y_{ij} = \frac{\left(Z_{ij} - \min\left(z_{ij}\right)\right.}{\max\left(z_{ij}\right) - \min\left(z_{ij}\right)}, \quad (5)$$

where Z_{ij} is the worth acquired from the trial information and min (Z_{ij}) is the base of an incentive from the investigation. Correspondingly, max (Z_{ij}) is the most extreme worth obtained from the analysis for that specific reaction.

The subsequent step is to figure out grey relational coefficient for the standardized information utilizing the following equation.

$$GRC_{ij} = \frac{\left(\delta_{\min} + \gamma\delta_{\max}\right)}{\left(\delta_{ij} + \gamma\delta_{\max}\right)}, \quad (6)$$

where, $i = 1, 2, 3, \ldots, n$ and $j = 1, 2, 3, \ldots, m$.

GRC_{ij} is grey relational coefficients for the i_{th} explore/preliminary and j_{th} subordinate variable/reaction esteem. δ outright is unique among y_{oj} and y_{ij}, which is a distinction from the objective worth and can be treated as a quality misfortune. γ is the distinctive coeffective which is ordinarily fixed at 0.5.

The last step is to create a grey relational assessment for the test data. Besides, this is the most astonishing estimation of GRG which suggests the best parameters. The GRG is settled by using the equation as shown

$$GRG_{ij} = \frac{1}{n}\sum_{i=0}^{n} GRC_{ij}. \quad (7)$$

3. Results and Discussion

The response parameters such as MRR and Ra were analyzed through Taguchi single-objective optimization and ANOVA. The responses were converted into a regression equation to evaluate the optimized parameters from Taguchi analysis by using a multiobjective optimization technique called grey relational analysis (GRA). Table 4 demonstrates the attained MRR and Ra values with their respective signal-to-noise ratio. We then determined the S/N to maximize the MRR and minimize the Ra by larger the better and smaller the better criteria. The optimal level for MRR and Ra was found by the mean S/N ratio.

3.1. Main Effect on MRR. Figure 5 depicts the effect of input parameters such as reinforcement wt. %, *p*on, *p*off, and WF in the response to MRR during WEDM of developed composites in Taguchi's analysis.

It is seen from Figure 5 that the expansion in weight level of fortifications to the base material fundamentally diminishes the MRR and the elements, for example, *p*on and WF at more elevated levels work on the MRR, while the expansion in *p*off adds to the lessening in MRR. The principle justification behind the reduction in MRR during machining is because of an expansion in hardness of the composites on the expansion of the support to a specific rate over the base material and furthermore because of the low electrical conductive nature of the essential support HNT.

The results from the previous experiment on WEDM regarding MRR decreased due to their hardness and electrical conductivity of the material, but the factor wire feed rate kept at a higher level the MRR increased, whereas the presence of larger particles in composites tends to decrease MRR by protecting the matrix material from melting [17, 18]. It is quite obvious that the increase in the wire feed rate from lower to higher level increases the spark energy verification and the material removal significantly causes an increase in MRR.

3.2. Main Effect on Ra. Figure 6 reveals that better surface roughness characteristics are obtained from factors such as the increase in poff and other factors. *P*on, WF, and reinforcements are at lower levels.

The main factor to increase the surface roughness value is the addition of hard reinforcements over the base material, which makes the machining a complicated process in which the increase in poff reduces the spark supply over the wire causing a decrease in Ra. Both the reinforcements HNT and Zr in material base magnesium significantly cause a decrease in MRR and an increase in Ra during the WEDM process.

3.3. ANOVA. Table 5 shows the ANOVA results for MRR, it reveals that the weight percentage of HNT in magnesium MMC's majorly contributes to MRR in WEDM as 49% and Zr weight percentage contributes 15.48% and other factors *P*on 17.576% and *P*off 8.9% and WF 7.2% during the machining process. It can also be seen from Table 5 the % of contribution in various factors for determining the Ra, where the presence of reinforcements HNT and Zr contributes 46% and 20.2%, respectively, in determining the Ra of Magnesium MMCs. WF shows the least contribution as 2.5% and Pon contributes 13% to the Ra on machining of Magnesium MMC's and the main machining parameter P off shows a major contribution as 17.3% over that of another machining parameter in determining the Ra value.

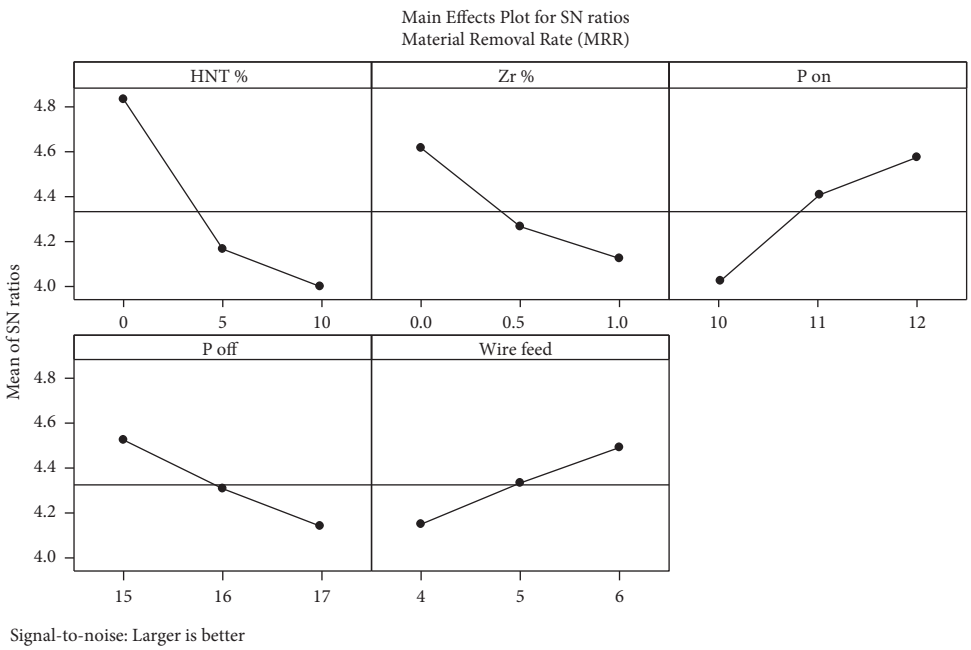

Figure 5: Result of input process parameters on MRR.

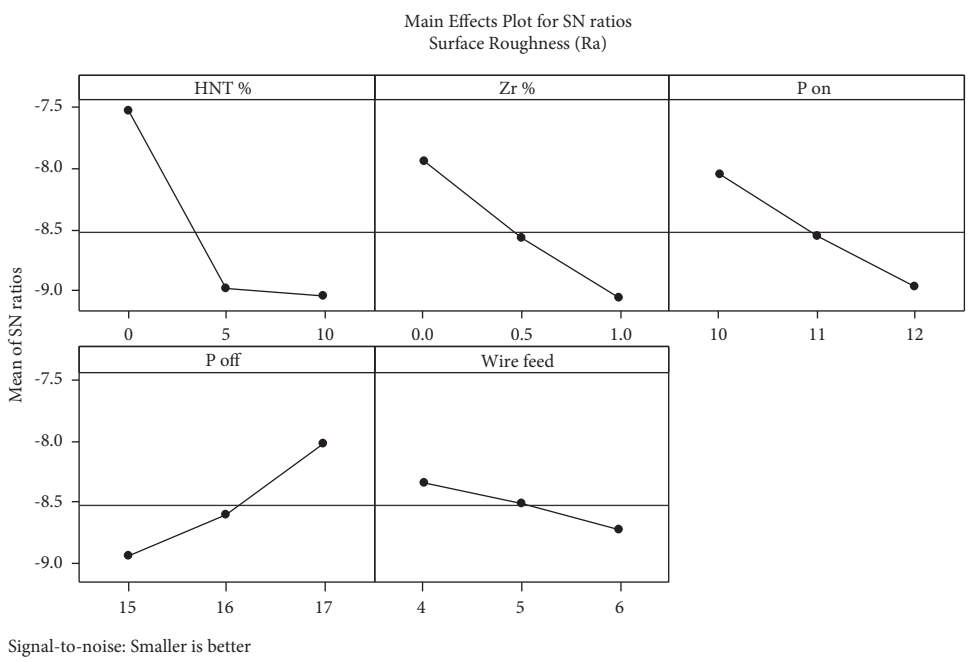

Figure 6: Result of input process parameters on Ra.

3.4. Mathematical Modeling. The regression equation has been formulated with the aid of the statistical software Minitab 16 to evaluate the optimized parameters from Taguchi's method and ANOVA. The regression equation for MRR and Ra is given as follows:

$$MRR = 1.64 - 0.0159 \times A - 0.0924 \times B + 0.0494 \times C - 0.0357 \times D + 0.0323 \times E, \quad (8)$$

$$Ra = 3.00 + 0.0465 \times A + 0.346 \times B + 0.139 \times C - 0.160 \times D + 0.0613 \times E. \quad (9)$$

Table 5: Analysis of variance for MRR and Ra.

Source of variance	DF	*Sum of squares* Sequential	Adjusted	Adjusted MS	*F* value	*P*-value	%C
		Material removal rate-MRR ($R^2 = 0.9808$, adj. $R^2 = 0.9687$)					
HNT %	2	0.127564	0.127564	0.063782	203.46	$p \leq 0.001$	48.956
Zr %	2	0.040353	0.040353	0.020177	64.36	$p \leq 0.001$	15.486
P on	2	0.045791	0.045791	0.022896	73.04	$p \leq 0.001$	17.576
P off	2	0.023055	0.023055	0.011527	36.77	$p \leq 0.001$	8.848
WF	2	0.018788	0.018788	0.009394	29.97	$p \leq 0.001$	7.210
Error	16	0.005016	0.005016	0.009394			
Total	26	0.260566					
		Surface roughness-Ra ($R^2 = 0.9985$, adj. $R^2 = 0.9976$)					
HNT %	2	1.24545	1.24545	0.62272	2556.27	$p \leq 0.001$	46.670
Zr %	2	0.53957	0.53957	0.26978	1107.46	$p \leq 0.001$	20.219
P on	2	0.34900	0.34900	0.17450	716.32	$p \leq 0.001$	13.077
P off	2	0.46277	0.46277	0.23139	949.83	$p \leq 0.001$	17.341
WF	2	0.06794	0.06794	0.03397	139.44	$p \leq 0.001$	2.545
Error	16	0.00390	0.00390	0.00024			
Total	26	2.66862					

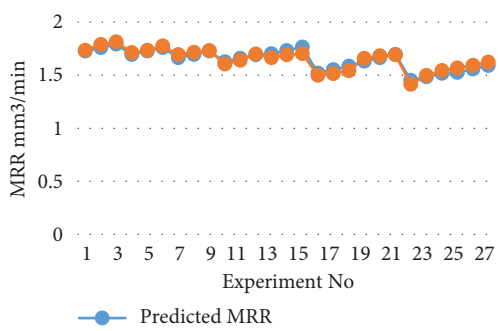

Figure 7: Actual Vs predicted MRR.

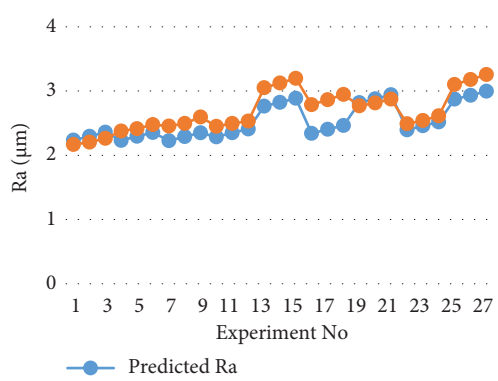

Figure 8: Actual Vs predicted Ra.

Figures 7 and 8 uncover the analysis results and their anticipated consequences of MRR and Ra values for the arrangement of preliminary courses of action. It is evident that trial and anticipated outcomes present a superior relationship with one another addressing an ostensible blunder deviancy among the exploratory and anticipated aftereffects of both MRR and Ra. From now, in light of Figures 7 and 8, it tends to be nitty gritty that equations (8) and (9) have a superior arrangement in determining the MRR and Ra values with the trial values, consequently used capably to expect the recently referenced output response inside the possibility of scattering.

3.5. Multiobjective Optimization

3.5.1. GRA. The GRA method was used to normalize the response parameters by "Smaller the better" and "Larger the

Table 6: Calculated GRG and its order in the optimization process.

Trial. No	*Normalized values*		*Grey relational coefficient*		Grey relational grade	Rank
	MRR	Ra	MRR	Ra		
1	0.800995	1	0.715302	1	0.857651	3
2	0.937811	0.967831	0.889381	0.939551	0.914466	2
3	1	0.911765	1	0.85	0.925	1
4	0.746269	0.806066	0.663366	0.72053	0.691948	6
5	0.803483	0.775735	0.717857	0.690355	0.704106	5
6	0.90796	0.715074	0.844538	0.637002	0.74077	4
7	0.70398	0.737132	0.628125	0.655422	0.641773	8
8	0.753731	0.698529	0.67	0.623853	0.646927	7
9	0.79602	0.605699	0.710247	0.559096	0.634671	9
10	0.475124	0.738971	0.487864	0.657005	0.572434	12
11	0.564677	0.69761	0.534574	0.623139	0.578857	11
12	0.711443	0.665441	0.634069	0.599119	0.616594	10
13	0.626866	0.186581	0.57265	0.380686	0.476668	21
14	0.691542	0.119485	0.618462	0.362184	0.490323	17
15	0.723881	0.054228	0.644231	0.345836	0.495033	16
16	0.21393	0.430147	0.388781	0.467354	0.428068	22
17	0.251244	0.357537	0.400398	0.437651	0.419025	24
18	0.323383	0.284007	0.424947	0.411187	0.418067	25
19	0.614428	0.44761	0.564607	0.475109	0.519858	15
20	0.676617	0.405331	0.607251	0.456759	0.532005	13
21	0.696517	0.351103	0.622291	0.4352	0.528746	14
22	0	0.704963	0.333333	0.628902	0.481118	20
23	0.21393	0.655331	0.388781	0.591948	0.490365	18
24	0.330846	0.591912	0.42766	0.550607	0.489133	19
25	0.38806	0.141544	0.449664	0.368065	0.408865	27
26	0.452736	0.071691	0.477435	0.350064	0.41375	26
27	0.524876	0	0.512755	0.333333	0.423044	23

Table 7: A typical response for GRG.

Level	HNT wt.%	Zr wt.%	Pulse on time	Pulse OFF time	Wire feed
1	0.7508	0.6717	0.6025	0.6005	0.5643
2	0.4763	0.5622	0.5723	0.5536	0.5766
3	0.4995	0.4927	0.5518	0.5724	0.5857
Delta	0.2745	0.1790	0.0508	0.0469	0.0214
Rank	1	2	3	4	5

better" and calculate the GRC as shown in Table 6. The GRG value was calculated by the average value of GRC concerning MRR and Ra. (0.5 weight was given for both MRR and RA). The parameter combination which has the highest value of GRG was considered as an optimum condition. The results attained from Taguchi coupled GRA were identical. From Table 6, it very well may be distinguished that the reinforcement wt. % increases when the MRR decreases and Ra increases. At lower p ON the Ra was decreased, and p ON and wire feed was high. Maximum MRR was reached at the machining of Mg MMC which strengthened with the base degree of reinforcements.

Table 7 shows the optimal conditions for better MRR and Ra values using the mean table or response table for GRG. According to the study, the parameter level which has the most elevated mean worth was considered as the optimal parameter level. For simple portrayals, optimum parameter levels are mentioned in bold figure in Table 7, and Figure 9 also graphically represents the effects of process parameters.

Table 8 shows the ANOVA results for GRG and it confirmed that each process parameter attained a significant effect over response parameters and it also revealed that the percentage of the weight of HNT has the maximum influence on GRG (70.561%) followed by Zr weight percentage

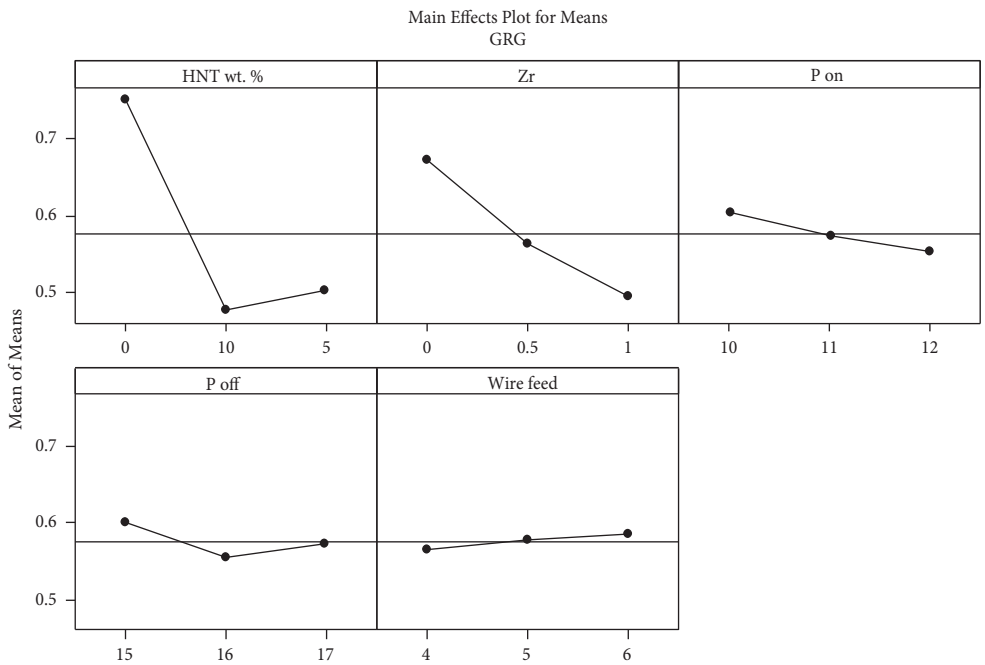

Figure 9: Main effects plot of the mean of means on GRG.

Table 8: Analysis of variance for GRG.

Source of variance	DF	*Sum of squares*		Adjusted MS	F value	*P*-value	% C
		Sequential	Adjusted				
HNT %	2	0.417190	0.417190	0.208595	946.07	$p \leq 0.001$	70.561
Zr %	2	0.146672	0.146672	0.073336	332.61	$p \leq 0.001$	24.807
P on	2	0.011741	0.011741	0.005870	26.63	$p \leq 0.001$	1.985
P off	2	0.010033	0.010033	0.005016	22.75	$p \leq 0.001$	1.70
WF	2	0.002079	0.002079	0.001040	4.72	$p \leq 0.001$	0.351
Error	16	0.003528	0.003528	0.000220			0.596
Total	26	0.591242					100
$R^2 = 0.994$, adj. $R^2 = 0.9903$							

(24.807%), Pulse ON time (1.98%), Pulse OFF time(1.20%), and wire feed (0.351%).

4. Conclusion

The WEDM studies were performed on the freshly evolved hybrid Mg-based MMCs and the accompanying conclusions were made.

(i) The addition of HNT and Zr into the Mg causes a small percentage increase in density because of the higher solidity of reinforcements.

(ii) An increase in hardness was accomplished by the addition of reinforcements with the Mg matrix.

(iii) Machinability of composite decreases as the Wt. % of reinforcements increases.

(iv) The optimal combination of input parameters identified by Taguchi-coupled GRA is lower level reinforcement percentage, pulse OFF time, pulse ON time, and higher-level wire feed rate.

(v) The developed regression equation predicts a nominal error deviancy among the predicted and experimental results of both Ra and MRR.

(vi) The optimal conditions recommended by GRA for attained higher MRR and lower Ra is revealed that the percentage of the weight of HNT has the greatest influence on GRG (70.561%), followed by Zr weight percentage (24.807%), pulse ON time (1.98%), pulse OFF time (1.20%), and wire feed (0.351%).

Data Availability

The data supporting the current study are given in the article.

Disclosure

The authors wish to declare and acknowledge that this article is available as a pre-print in Research Square and the same is cited in this study.

Conflicts of Interest

The authors declare that they have no conflicts of interest.

References

[1] R. Casati and M. Vedani, "Metal matrix composites reinforced by nano-particles—a review," *Metals*, vol. 4, no. 1, pp. 65–83, 2014.

[2] L. Dobrzanski and M. Adamiak, "Mechanically milled aluminium matrix composites reinforced with halloysite nanotubes," *Journal of Achievements in Materials and Manufacturing Engineering*, vol. 55, p. 654, 2012.

[3] A. Jayaganthan and K. S. Prakash, "Influence of machining parameters of electrochemical micromachining process over magnesium based hybrid metal matrix composite," *Materials Research Express*, vol. 6, no. 2, Article ID 026510, 2018.

[4] V. Kavimani and K. S. Prakash, "Tribological behaviour predictions of R-GO reinforced Mg composite using ANN coupled Taguchi approach," *Journal of Physics and Chemistry of Solids*, vol. 110, pp. 409–419, 2017.

[5] V. Kavimani, K. S. Prakash, M. S. Starvin, B. Kalidas, V. Viswamithran, and S. R. Arun, "Tribo-surface characteristics and wear behaviour of SiC @ r-GO/Mg composite worn under varying control factor," *Silicon*, vol. 12, 2019.

[6] L. Liu, X. Chen, F. Pan, S. Gao, and C. Zhao, "A new high-strength Mg-Zn-Ce-Y-Zr magnesium alloy," *Journal of Alloys and Compounds*, vol. 688, pp. 537–541, 2016.

[7] S. Mohanty, B. Routara, and R. Bhuayan, "Experimental investigation of machining characteristics for Al-SiC12% composite in electro-discharge machining," *Materials Today Proceedings*, vol. 4, no. 8, pp. 8778–8787, 2017.

[8] P. M. Gopal and K. S. Prakash, "Wire electric discharge machining of silica rich E-waste CRT and BN reinforced hybrid magnesium MMC," *Silicon*, vol. 11, no. 3, pp. 1429–1440, 2019.

[9] K. Ravindra, G. Manasi, G. Sheetal, and P. B. Kumar, "Halloysite nanotubes and applications: a review," *Journal of Advanced Scientific Research Available*, vol. 3, no. 2, pp. 25–29, 2012.

[10] A. Pramanik and G. Littlefair, "Wire EDM mechanism of MMCs with the variation of reinforced particle size," *Materials and Manufacturing Processes*, vol. 31, no. 13, pp. 1700–1708, 2016.

[11] A. Prasad, K. Siva, M. Tamil, and A. krishnaiah, "parametric optimization in wire electrical discharge machining of titanium alloy using response surface methodology," *Materials Today Proceedings*, vol. 4, no. 2, pp. 1434–1441, 2017.

[12] J. Singh, "Fabrication characteristics and tribological behavior of Al/SiC/gr hybrid aluminum matrix composites: a review," *Friction*, vol. 4, no. 3, pp. 191–207, 2016.

[13] K. P. Somashekhar, N. Ramachandran, and J. Mathew, "Material removal characteristics of micro slot (kerf) geometry in μ-WEDM on aluminum," *International Journal of Advanced Manufacturing Technology*, vol. 51, no. 5–8, pp. 611–626, 2010.

[14] J. Soyama, M. Oehring, W. Limberg, T. Ebel, K. U. Kainer, and F. Pyczak, "The effect of zirconium addition on sintering behaviour, microstructure and creep resistance of the powder metallurgy processed alloy Ti–45Al–5Nb–0.2B–0.2C," *Materials & Design*, vol. 84, pp. 87–94, 2015.

[15] D. Veerabrahmam, "Optimization of process parameters of wire-cut electric discharge machining of A356 . 2 aluminum alloy," *International Journal of Advanced Mechanical Engineering*, vol. 8, no. 1, pp. 173–180, 2018.

[16] K. Vetri Velmurgan and K. Venkatesan, "Experimental investigation and optimization of machining parameters using grey-relational analysis approach and fuzzy based Taguchi loss function method," *Indian Journal of Science and Technology*, vol. 9, no. 44, 2016.

[17] H. Zhang, Y. Zhao, Y. Yan et al., "Microstructure evolution and mechanical properties of Mg matrix composites reinforced with Al and Nano SiC particles using spark plasma sintering followed by hot extrusion," *Journal of Alloys and Compounds*, vol. 725, pp. 652–664, 2017.

[18] J. Anandan, K. S. Prakash, L. Jino, E. Manoj, A. Jacob, and S. A. Suthan, *Multi-objective optimization of WEDM parameters on Mg-HNT-Zr hybrid metal matrix composite using Taguchi coupled GRA*, Research Square Preprint, Durham, NC, USA, 2022.

Hindawi
Advances in Materials Science and Engineering
Volume 2022, Article ID 4475605, 6 pages
https://doi.org/10.1155/2022/4475605

Research Article

Optimization of Crashworthiness Parameters of Thin-Walled Conoidal Structures

K. Vinayagar,[1] P. Ganeshan,[2] P. Nelson Raja,[1] M. S. Zakir Hussain,[3] P. Vengala Kumar,[4] P. Ramshankar,[5] V. Mohanavel,[6,7,8] N. Mathankumar,[9] K. Raja,[10] and Tesfaye Tefera Bezabih[11]

[1]*Department of Mechanical Engineering, Fatima Michael College of Engineering & Technology, Madurai, India*
[2]*Department of Mechanical Engineering, Sri Eshwar College of Engineering, Coimbatore 641202, Tamil Nadu, India*
[3]*Department of Mechanical Engineering, AAA College of Engineering & Technology, Sivakasi, Tamil Nadu, India*
[4]*Department of Mechanical Engineering, University VOC College of Engineering, Thoothukudi, Tamil Nadu, India*
[5]*Department of Civil Engineering, University College of Engineering Dindigul, Dindigul 624622, Tamil Nadu, India*
[6]*Centre for Materials Engineering and Regenerative Medicine, Bharath Institute of Higher Education and Research, Chennai 600073, Tamil Nadu, India*
[7]*Department of Mechanical Engineering, School of Technology, Glocal University, Delhi-Yamunotri Marg, Saharanpur, Uttar Pradesh 247121, India*
[8]*Department of Mechanical Engineering, Chandigarh University, Mohali 140413, Punjab, India*
[9]*Department of Mechanical Engineering, NPR College of Engineering and Technology, Natham, Dindigul 624401, Tamil Nadu, India*
[10]*Department of Mechanical Engineering, University College of Engineering Dindigul, Dindigul 624622, Tamil Nadu, India*
[11]*Department of Mechanical Engineering, Ambo University, Ambo, Ethiopia*

Correspondence should be addressed to Tesfaye Tefera Bezabih; tesfaye.tefera@ambou.edu.et

Received 15 July 2022; Revised 22 August 2022; Accepted 5 September 2022; Published 12 October 2022

Academic Editor: Pudhupalayam Muthukutti Gopal

This paper aims to identify the optimum level of factors or parameters that affect the energy absorption of conoidal structures by grey relational examination. To optimize crashworthiness parameters of conical structures, the L9 orthogonal array has been adopted to design the experiments. The tailor-made thin-walled conical structures were fabricated by three most important factors, such as base diameter, height, and thickness, as design variables, and they were subjected to axial compression in a quasi-static method. The important responses of crashworthiness indicators such as the mean crushing force and specific energy absorption (SEA) were calculated with the help of a load-displacement curve. Experimental results showed that the crushing behaviours of conical structures were fairly significant. Grey relational analysis (GRA) and analysis of variance are used toobtain the optimal levels of parameters. From the results, the optimum levels of parameters are found to be a base diameter of 180 mm, a height of 120 mm, and a thickness of 1.5 mm.

1. Introduction

Energy absorbers with lightweight are widely used to develop the crashworthiness of vehicles at the time of collisions. The thin-walled formations or structure are normally used as energy absorbers in all types of transport systems owing to their properties like very less weight and the capacity to absorb more impact energy. By determining the mean crushing power, the energy lost until the substance or material was compressed-honeycomb structures' ability to absorb energy is assessed. Several studies have been carried out to develop theoretical models to forecast the mean or average crushing force for thin-walled structures. Significant analysis has been carried out by the authors in [1] intended for out-of-plane axial crushing confrontation of hexagonal honeycomb. The wall thickness and diameter of hexagonal

wall structures were compared to the crushing strength and folding wave's wavelength and the submitted solutions were based on the design's convenience. Crushing strength, flow stress, curvature effects, and wavelength are considered and evaluated in the model. This folding model was again improved by considering more detailed structures and changing the structural loading in that deformation [2]. For honeycomb structures, analytical and experimental results are compared with each other [3–6].

In the past decade, the hexagonal structure has been modified by other structures like square and circular structures. It has been investigated by numerical, theoretical, and experimental methods under axial compression or impact [7–12]. To improve the energy absorber performance, a number of researchers have modified several odd and even numbers of polygonal sections and star sections. The tubes offered their own performance in axial loading, and the results were compared [13–18]. Several researchers have identified several alternative approaches, including single cell various cross-sectional tubes, multicell tubular sections, and filler materials [19, 20]. Single and multi-cell hollow columns' capacities for absorbing energy were compared analytically and quantitatively, and it was determined that the multi-cell available columns outperformed the single columns [21, 22]. The experimental findings, the circular cylinder's capacity to absorb energy, and the development of empirical relationships for concertina or axisymmetric structures [23]. Multicell square columns compressed axially using analytical and numerical techniques [24]. In hexagonal honeycombs and circular honeycombs, the influence of the central angle and the boundary effect is found to be an important factor in the crushing strength of the structure when the number of cells is very small [25, 26]. Analysis was carried out to develop the crashworthiness of thin-walled sections, and the circular honeycombs with the square package and hexagonal package were examined numerically and experimentally [27, 28].

Although many researchers and series of experiments mainly concentrated on polygonal sections (square, pentagon, hexagon, octagon, and circular) as energy absorbers, in this work, conical structures have been used as energy absorbers. The thin-walled conical ribs are fabricated in sheet metal in various types, and then, we study the performance of energy absorption of tubes type wise using the crashworthiness indicators. The study and investigation of energy absorption capabilities of conical ribs were experimentally performed, and the Taguchi method with the grey relational method was used to find out the optimal parameters for multiresponse such as the mean crushing force and specific energy absorption. This proposed work is useful for the design of engineering structures, which are used as energy absorbers.

2. Parameters of the Crashworthiness Study

In crashworthiness, basic parameters such as total energy absorption (TEA), specific energy absorption (SEA), and average or mean crushing force (F_{mean}) are delineated underneath with numerical equations. This study aims to determine the optimal level of factors or operating parameters for the maximum of (output) objectives of SEA and F_{mean}. Specific energy absorption (SEA) is portrayed as held vitality per unit mass. This is a basic criterion for looking at the vitality retention limit with particular mass, which is expressed as follows:

$$SEA = \frac{EA}{m}, \tag{1}$$

where m refers to the mass of the specimen and EA is the total energy absorption of crushing force. EA evaluated with the help of the load/force-displacement curve by applying direct integration is expressed as follows:

$$EA = \int_0^{\delta} F(\delta) d\delta. \tag{2}$$

F_{mean} is the average or mean crushing force which is calculated as follows:

$$F_{\text{mean}} = \frac{EA}{\delta}. \tag{3}$$

2.1. Taguchi Method with Grey Relational Analysis (GRA). The Taguchi method is one of the simplest and most popular methods to obtain the optimum set/level of factors or parameters for a single objective optimization problem To solve and analyze a multiresponse problem, Taguchi-based grey relational analysis is identified as a suitable method.

The main objective of crashworthiness analysis is the maximization of SEA and CFE. To evaluate the quality of experimental results, in Taguchi analysis, the signal to noise (S/N) ratio is considered larger than the best characteristic response, which is calculated as follows:

$$\frac{S}{N}\text{Ratio } x_i(k) = -10\log_{10}\left(\frac{1}{j}\right)\sum_{i=1}^{j}\left(\frac{1}{y_i^2(k)}\right), \tag{4}$$

where $y_i(k)$ is the observed response value for the kth response in the Ith trial, $x_i(k)$ is the S/N ratio value for the kth response in the Ith trial, and j is the number of experiments.

Optimum parameters can be obtained from Taguchi's method after obtaining discrete datasets from experimental results. The responses are normalized across the range from 0 to 1. The normalized S/N ratios can be obtained as follows:

$$x_i'(k) = \frac{x_i(k) - \min x(k)}{\max x(k) - \min x(k)} \text{For better response,} \tag{5}$$

where $k = 1$ to n, n is the performance characteristic kth response at all trials, and $i = 1$ to 9.

After calculating the normalized S/N values, the grey relational coefficient can be calculated as follows:

$$\xi_i(k) = \frac{\left(\min_k \min_i \left\|x_i(0) - x_i'(k)\right\|\right) + \psi\left(\max_k \max_i \left\|x_i(0) - x_i'(k)\right\|\right)}{\left|x_i(0) - x_i'(k)\right| + \psi\left(\max_k \max_i \left\|x_i(0) - x_i'(k)\right\|\right)}, \tag{6}$$

where ψ is the resolution coefficient, and its value is taken as 0.5.

Table 1: Factors and levels of parameters.

Notation of factor	Factors (mm)	Levels		
		1	2	3
A	Base diameter	160	170	180
B	Height	120	130	140
C	Thickness	0.5	1	1.5

Table 2: Chemical composition of Al5052.

Composition	Percentage
Al	96.35
Mg	2.2
Si	0.25
Mn	0.1
Fe	0.4
Cu	0.1
Zn	0.1
Residuals	0.5

Grey relational grade can be obtained as follows:

$$\gamma_i = \frac{1}{n}\sum_{k=i}^{n}\xi_i(k). \tag{7}$$

2.2. Analysis of Variance. GRA is simple and easy to understand, and it is based on range analysis. However, the range analysis cannot distinguish experimental errors and data fluctuations caused by level changes in parameters or factors. For this problem, ANOVA is used to design the optimized levels of parameters, which significantly affect the characteristics. The predicted optimum condition of grey relational grade using crashworthiness can be evaluated as follows:

$$\hat{\gamma} = \gamma_{\text{avg}}(m) + \sum_{i=1}^{n}\left(\gamma_i(m) - \gamma_{\text{avg}}(m)\right), \tag{8}$$

where n is the number of experiments, $\gamma_{\text{avg}}(m)$ is the mean of grey relational grade, and $\gamma_i(m)$ is the mean of grey relational grade at optimum level.

3. Experimental Procedures

3.1. Selection of Section Geometry and Parameters. In this work, the average or mean crushing force (F_{mean}) and specific energy absorption (SEA) were taken as output responses of crashworthiness with respect to the following parameters, such as base diameter, height, and thickness. Experiments were conducted on these three parameters/control factors (base diameter, height, and thickness) at three levels, and hence, the L9 orthogonal array (OA) was selected. The levels of factors for the experimental process are described in Table 1.

3.2. Materials. Aluminum alloy Al 5052 was selected for lightweight, high strength, cost-effectiveness, and greater formability. Chemical composition of aluminum alloy Al 5052 is listed in Table 2. Mechanical properties of materials are shown in Table 3. Experimental design using the L9 orthogonal array is mentioned in Table 4. Sample specimens are shown in Figure 1.

Table 3: Mechanical properties of Al 5052.

Property	Value
Young's modulus (E)	69.3 GPa
Ultimate tensile load	228 MPa
Elongation	15%
Density (ρ)	2.68 g/cm^3
Shear modulus (τ)	25.9 GPa
Poisson's ratio (μ)	0.33

Table 4: Experimental design using the L9 orthogonal array.

Test no	Base diameter (mm)		Height (mm)		Thickness (mm)	
	Level	Value	Level	Value	Level	Value
1	1	160	1	120	1	0.5
2	1	160	2	130	2	1
3	1	160	3	140	3	1.5
4	2	170	1	120	2	1
5	2	170	2	130	3	1.5
6	2	170	3	140	1	0.5
7	3	180	1	120	3	1.5
8	3	180	2	130	1	0.5
9	3	180	3	140	2	1

Figure 1: Samples of specimens before loading.

Figure 2: Crushed patterns of cones.

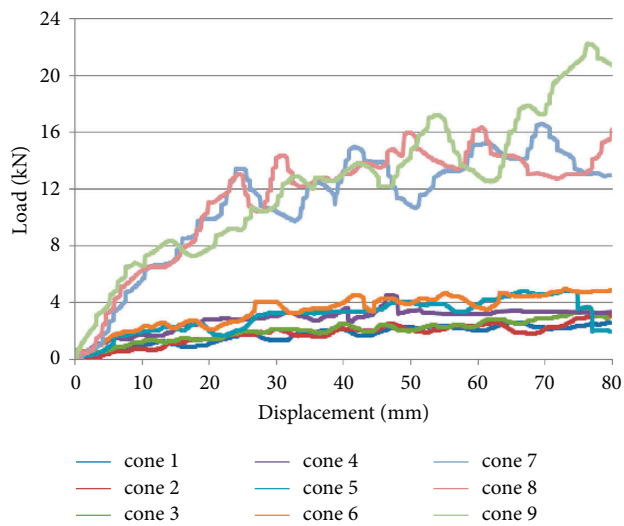

Figure 3: Load-displacement curves.

Table 5: Experimental results.

Code	Mass (kg)	Base diameter (mm)	Height (mm)	Thickness (mm)	F_{mean} (kN)	TEA (N-m) $F * d\delta$	SEA (kJ/kg) TEA (m)
Cone 1	0.046	160	120	0.5	1.48	118.4	2.574
Cone 2	0.1	160	130	1	3.51	280.8	2.808
Cone 3	0.16	160	140	1.5	7.98	638.4	3.990
Cone 4	0.104	170	120	1	4.86	388.8	3.738
Cone 5	0.16	170	130	1.5	8.65	692	4.325
Cone 6	0.065	170	140	0.5	2.76	220.8	3.397
Cone 7	0.175	180	120	1.5	9.59	767.2	4.384
Cone 8	0.074	180	130	0.5	3.45	276	3.730
Cone 9	0.146	180	140	1	6.15	492	3.370

3.3. Experimental Process. The compression test was carried out by using a computerized universal testing machine. The test specimen was vertically put between the lower movable table and the fixed cross head. The compressive axial force was applied to the samples, and the rate of compression was 10 mm/min. The crushed samples of specimens are shown in Figure 2. Specimens were compressed up to 80 mm displacement.

4. Results and Discussion

4.1. Experimental Results. A force/load-displacement curve is obtained during the test and is clearly shown in Figure 3. From the curves, all the patterns have more number of peaks. The number of peaks indicates the number of folds in each section. Based on the results, the crashworthiness effects of conical sections with base diameter, height, and thickness of thin-walled sections are studied, and the results are tabulated in Table 5.

4.2. Optimization Results. In the Taguchi method, the S/N ratios for better characteristics were chosen for the mean crushing force and specific energy absorption. Corresponding values of S/N ratios were calculated, and the results of multiple responses are tabulated in Table 5. Based on the S/N ratios, the normalized S/N ratios could be calculated for each parameter level.

Table 6 reveal that the test number 7 has the highest grey relational grade of the nine combinations, with the reference diameter 180 mm, height 120 mm, and thickness 1.5 mm.

The average grey relational grade and optimum level of controllable factors are calculated and tabulated in Table 7. Base diameter level 3, height level 1, thickness level 3, and the combination of the optimum process parameters are the optimum levels of the parameters. Optimum values of parameters at each level are indicated as stars in Table 7, and the variation of maximum to minimum is also indicated.

In multiperformance characteristics, the most affecting parameter has the maximum max-min value, and the highest value of max-min for thickness in response to the average grey relational grade is 0.456. The max-min value for base diameter is 0.195 and that for height is 0.02. The order of importance of factors in this study is listed as follows: factor C (thickness), factor A (base diameter), and factor B (height) such that $0.456 > 0.195 > 0.020$. Results of grey relational analysis (GRA) and importance of parameters were tested and listed by ANOVA, and the results are presented in Table 8. The analysis of variance also proved that the most significant and controllable factor is thickness, followed by base diameter and height of the conical structures.

Table 6: Taguchi and grey relational analysis results.

Specimen no.	Response I-F_{mean}			Response II-SEA			Grey rational grade	Rank
	S/N ratio	Normalized S/N ratio	Grey rational coefficient	S/N ratio	Normalized S/N ratio	Grey rational coefficient		
Cone 1	3.41	0.00	0.333	8.212	0	0.333	0.333	9
Cone 2	10.91	0.46	0.482	8.968	0.163	0.374	0.428	8
Cone 3	18.04	0.90	0.835	12.019	0.823	0.739	0.787	3
Cone 4	13.73	0.64	0.579	11.454	0.701	0.626	0.602	4
Cone 5	18.74	0.94	0.900	12.720	0.975	0.952	0.926	2
Cone 6	8.82	0.33	0.427	10.622	0.521	0.511	0.470	7
Cone 7	19.64	1.00	0.999	12.837	1.00	1	1.00	1
Cone 8	10.76	0.45	0.477	11.343	0.677	0.608	0.543	6
Cone 9	15.78	0.76	0.677	10.552	0.506	0.503	0.590	5

Table 7: Response of the average/mean grey relational grade.

Notation of factor	Control factors (mm)	Average grey relational grade			Max-min
		Level 1	Level 2	Level 3	
A	Base diameter	0.516	0.666	0.711*	0.195
B	Height	0.645*	0.632	0.625	0.020
C	Thickness	0.449	0.540	0.904*	0.456

The symbol * indicates optimum level of factors.

Table 8: ANOVA results.

Notation of factor	Control factor	DoF	Sum of squares	Mean squares	F value	% contribution
A	Base diameter (mm)	2	0.062	0.0312	21.996	15.055
B	Height (mm)	2	0.000626	0.000313	0.221	0.151
C	Thickness (mm)	2	0.349	0.1743	122.89	84.109
D	Error	2	0.00283	0.00142		0.684
Total		8	0.415	0.207		100

5. Conclusion

In this research, an optimization value of important crashworthiness parameters for conical structures was analyzed and presented by using the Taguchi-based grey relational method. Based on the grey relational approach, some key findings and conclusions were summarized:

(1) This analysis presents the significant effects of the base diameter, height, and thickness of a conical structure on crashworthiness.

(2) The optimum process parameters are a base diameter of 180 mm, a height of 120 mm, and a thickness of 1.5 mm, i.e, Test No. 7.

(3) Order of significance of various factors is as follows: thickness 84%, base diameter 15%, and height 0.15%, respectively.

(4) According to the influencing factor or parameter analysis, it was concluded that thickness and base diameter have a significant effect on the energy absorption/crashworthiness performance.

Obtained results can give some useful guidance to design thin-walled and lightweight structures for crashworthiness applications.

Experimental analysis described in this work would be useful for the development of energy absorption structural components in the field of aircraft, marine, and automobile applications.

Data Availability

The data used to support the findings of this study are included within the article, and the data can be made available from the corresponding author upon request.

Conflicts of Interest

The authors declare that there are no conflicts of interest regarding the publication of this article.

References

[1] S. S. Hsu and N. Jones, "Quasi-static and dynamic axial crushing of thin-walled circular stainless steel, mild steel and aluminium alloy tubes," *International Journal of Crashworthiness*, vol. 9, pp. 195–217, 2004.

[2] N. Saravanan, V. Yamunadevi, V. Mohanavel et al., "Effects of the interfacial bonding behavior on the mechanical properties of E-glass fiber/nanographite reinforced hybrid composites," *Advances in Polymer Technology*, vol. 2021, Article ID 6651896, 9 pages, 2021.

[3] M. Shakeri, S. Salehghaffari, and R. Mirzaeifar, "Expansion of circular tubes as impact energy absorbers: experimental and

theoretical investigation," *International Journal of Crashworthiness*, vol. 12, pp. 493–501, 2007.

[4] R. Rajendran, K. Prem Sai, B. Chandrasekar, A. Gokhale, and S. Basu, "Impact energy absorption of aluminium foam fitted AISI 304L stainless steel tube," *Materials and Design*, vol. 30, pp. 1777–1784, 2009.

[5] S. Hou, Q. Li, S. Long, X. Yang, and W. Li, "Crashworthiness design for foam filled thin-walled structures," *Materials and Design*, vol. 30, pp. 2024–2032, 2009.

[6] H. F. Yin, G. L. Wen, S. J. Hou, and K. Chen, "Crushing analysis and multi-objective crashworthiness optimization of honeycomb-filled single and bi-tubular polygonal tubes," *Aterials and Design*, vol. 32, pp. 4449–4460, 2011.

[7] E. Acar, M. A. Guler, B. Gerçeker, M. E. Cerit, and B. Bayram, "Multi-objective crashworthiness optimization of tapered thin-walled tubes with axisymmetric indentations," *Thin-Walled Structures*, vol. 49, pp. 94–105, 2011.

[8] Y. Zhang, G. Y. Sun, G. Y. Li, Z. Luo, and Q. Li, "Optimization of foam-filled bitubal structures for crashworthiness criteria," *Materials and Design*, vol. 38, pp. 99–109, 2012.

[9] M. Haghi Kashani, H. Shahsavari Alavijeh, H. Akbarshahi, and M. Shakeri, "Bitubular tubes with different arrangements under quasi-static axial compression loading," *Materials and Design*, vol. 51, pp. 1095–1103, 2013.

[10] H. Wu, H. Fan, Z. Xia, F. Jin, and Q. Zhou, "Axial crushing behaviors of multi-cell tubes with triangular lattices," *International Journal of Impact Engineering*, vol. 63, pp. 106–117, 2014.

[11] M. Yamashita, M. Gotoh, and Y. Sawairi, "Axial crush of hollow cylindrical structures with various polygonal cross-sections: numerical simulation and experiment," *Journal of Materials Processing Technology*, vol. 140, pp. 59–64, 2003.

[12] S. Sharifi, M. Shakeri, H. Ebrahimi Fakhari, and M. Bodaghi, "Experimental investigation of bitubal circular energy absorbers under quasi-static axial load," *Thin-Walled Structures*, vol. 89, pp. 42–53, 2015.

[13] K. Vinayagar and A. Senthilkumar, "Crashworthiness analysis of double section bi-tubular thin-walled structures," *Thin-Walled Structures*, vol. 112, pp. 184–193, 2017.

[14] P. Raju, K. Raja, and K. Lingadurai, "Glass/Caryota urens hybridized fibre-reinforced nanoclay/SiC toughened epoxy hybrid composite: mechanical, drop load impact, hydrophobicity and fatigue behaviour," *Biomass Conv. Bioref*, vol. 2021, 2021.

[15] K. Vinayagar and A. Senthil Kumar, "Multi-response optimization of crashworthiness parameters of bi-tubular structures," *Steel and Composite Structures*, vol. 23, no. 1, pp. 31–40, 2017a.

[16] M. A. Nagaraj, K. Vinayagar, and S. P. samy, "Enhancing performance of cell formation problem using hybrid efficient swarm optimization, Soft Computing," *A Fusion of Foundations, Methodologies and Applications*, Springer, Berlin/Heidelberg, Germany, 2021.

[17] S. Azarakhsh and A. Ghamarian, "Collapse behaviour of thin-walled conical tube clamped at both ends subjected to axial and oblique loads," *Thin-Walled Structures*, vol. 112, pp. 1–11, 2017.

[18] P. Raju, K. Raja, K. Lingadurai, T. Maridurai, and S. C. Prasanna, "Mechanical, wear, and drop load impact behavior of glass/Caryota urens hybridized fiber-reinforced nanoclay/SiC toughened epoxy multihybrid composite," *Polymer Composites*, vol. 42, no. 3, pp. 1486–1496, 2020.

[19] G. Sun, P. Tong, J. Fang, G. Li, and Q. Li, "Parameterization of criss-cross configurations for multi-objective crashworthiness optimization," *International Journal of Mechanical Sciences*, vol. 2017, 2017.

[20] X. Zhang and H. Zhang, "Experimental and numerical investigation on crush resistance of polygonal columns and angle elements," *Thin-Walled Structures*, vol. 57, pp. 25–36, 2012.

[21] G. Venkatesh, V. Vignesh, and K. Vinayagar, "Extraction and characterization of agricultural discarded Sesbania aculeata stem waste as potential alternate for synthetic fibers in polymer composites," *Journal of Natural Fibers, Taylor and Francis*, vol. 2021, 2021.

[22] V. Jeyabalaji, G. R. Kannan, P. Ganeshan, K. Raja, B. NagarajaGanesh, and P. Raju, "Extraction and characterization studies of cellulose derived from the roots of acalypha indica L," *Journal of Natural Fibers*, Taylor & Francis, vol. 59, pp. 1508–1512, 2021.

[23] B. Jiang, X. Chen, J. Yu, Y. Zhao, Z. Xie, and H. Tan, "Energy-absorbing properties of thin-walled square tubes filled with hollow spheres," *Thin-Walled Structures*, vol. 180, 2022.

[24] N. Bhanu Teja, P. Ganeshan, V. Mohanavel et al., "Performance and emission analysis of watermelon seed oil methyl ester and n-butanol blends fueled diesel engine," *Mathematical Problems in Engineering*, vol. 2022, Article ID 2456338, 12 pages, 2022.

[25] N. Mohanraj, N. Mathan Kumar, P. Prathap et al., "Mechanical properties and electrical resistivity of the friction stir spot-welded dissimilar Al–Cu joints," *International Journal of Polymer Science*, vol. 2022, Article ID 4130440, 7 pages, 2022.

[26] M. S. Ravi Theja, P. Ramshankar, M. C. Sashikkumar et al., "Investigation into mechanical properties of EPDM/SBR-nanoclay nanocomposites Materials," *Today's Office: Proceedings*, 2022.

[27] M. Vijayakumar, P. Navaneethakrishnan, and G. Kumaresan, "Thermal characteristics studies on sintered wick heat pipe using CuO and Al2O3 nanofluids," *Experimental Thermal and Fluid Science*, vol. 79, pp. 25–35, 2016.

[28] N. A. kumar and D. Subbulekshmi, "Online auto selection of tuning methods and auto tuning PI controller in FOPDT real time process-pH Neutralization," *Energy Procedia*, vol. 117, pp. 1109–1116, 2017.

Hindawi
Advances in Materials Science and Engineering
Volume 2022, Article ID 7783967, 10 pages
https://doi.org/10.1155/2022/7783967

Research Article

A Beam Steering Dielectric Resonator Antenna Designed Using Rogers RO4003C Material for S-Band Applications

Manisha Kumari,[1] Tavanam Venkata Rao,[2] S. Arun Jayakar,[3] D. Srinivas,[4] Dola Gobinda Padhan,[5] A. Kishore Reddy,[6] P. Rahul Reddy,[7] and Amanuel Diriba Tura[8]

[1]*Department of Electronics and Communication Engineering, Gokaraju Rangaraju Institute of Engineering and Technology, Hyderabad-500090, Telangana, India*
[2]*Department of Electronics and Communication Engineering, Sreenidhi Institute of Science and Technology, Hyderabad 501301, India*
[3]*Department of Electronics and Instrumentation Engineering, Bannari Amman Institute of Technology, Erode 638401, India*
[4]*School of Business, SR University, Warangal-506371, India*
[5]*Department of Electrical and Electronics Engineering, Gokaraju Rangaraju Institute of Engineering and Technology, Hyderabad-500090, Telangana, India*
[6]*Department of Electrical and Communication Engineering, Andhra Engineering College, Nellore 524322, Andhra Pradesh, India*
[7]*Department of Electronics and Communication Engineering, Geethanjali Institute of Science and Technology, Nellore-524137, Andhra Pradesh, India*
[8]*Faculty of Mechanical Engineering, Jimma Institute of Technology, Jimma University, Jimma, Ethiopia*

Correspondence should be addressed to Amanuel Diriba Tura; diriba.amanuel@ju.edu.et

Received 1 September 2022; Accepted 23 September 2022; Published 10 October 2022

Academic Editor: Vijayananth Kavimani

A pattern reconfigurable dielectric resonator antenna emitting at 3.1 GHz is presented in this study. The beam can be steered at 6 degrees, 8 degrees, 14 degrees, and 171 degrees. Three P-i-N diodes are employed in the slots of the ground plane to help steer the beam direction. By changing the state of the three diodes, five states can be obtained. The $TE_{01\delta}$ mode is excited using a differential feed technique. Differential feed helps in increasing the gain and reducing the size of the structure. The return loss of each state is less than −25 dB. The gain of the first state is 7.65 dBi, the second and fifth state's gain is 8.22 dBi, third and fourth state's gain is 10.6 dBi. This Antenna is designed using Rogers RO4003C material which has low Electrical gravity, low voltage, and high oxidation resistance that makes it appropriate for RF applications. The properties required for RF microwave circuits, matching networks, and controlled impedance transmission lines are present in the RO4003C material. Annealed copper is used for designing the ground plane and feedline which provides excellent conductivity. The antenna is fabricated using the chemical etching process which employs a positive photoresist that gives a higher resolution accuracy for the designed antenna. This process of fabrication has another advantage of inculcating structures from simpler to complex.

1. Introduction

With the advent of wireless communication, the demand for reconfigurable antennas is increasing. Reconfigurable antennas are advantageous as they are compact, economical, and versatile, and they may replace an antenna array or several antennas. Reconfigurability can be categorized into frequency, pattern, polarization, and bandwidth. Pattern reconfiguration can be done by mechanical tuning or electrical tuning. A pattern-reconfigurable multidirectional microstrip antenna for wireless communication was studied [1]. Utilizing switchable directors, a pattern-reconfigurable dielectric resonator antenna is created [2]. A straightforward arc dipole-based planar beam steerable antenna is presented [3]. Pattern reconfigurability using spherical shaped dielectric patch operating on higher order mode is designed

[4]. An antenna having five switchable beams in the elevation plane was investigated for pattern reconfiguration [5]. A cylindrical dielectric resonator antenna with pattern-reconfigurable components was developed [6]. The investigation of a gain-enhanced, pattern-reconfigurable planar Yagi-Uda antenna on a coplanar construction was proposed [7]. Wideband antennas with a reversible broadside and end-fire patterns were studied [8]. A reconfigurable pattern is produced by utilizing H-shaped components [9]. Demonstration of a dielectric liquid-based reconfigurable antenna with adjustable radiation pattern and polarization was proposed [10]. A wideband gravitational ball lens-based dielectric resonator antenna for circular polarization was investigated [11].

Dielectric resonator antenna is advantageous over microstrip patch antenna in terms of efficient radiation, bandwidth enhancement, and lesser conductor loss. At microwave and millimeter-wave frequency, the surface waves dominate in the case of microstrip patch antenna which eventually deteriorates the antenna efficiency, whereas DRAs do not suffer from surface waves and hence are more suitable at a higher frequency. Dielectric resonators with relative permittivity of 100 and higher are used in applications such as oscillators and filters. The higher the permittivity, the more the fields are tightly bound inside the material.

To make dielectric resonators work as an antenna the relative permittivity has to be between 3 and 50. When the relative permittivity is decreased, the fields when excited by the RF signal can escape and radiate. The DRAs have a distinct property of having distinct modes which when excited create distinct radiation patterns. DRAs offer simple feeding techniques such as microstrip feed, coaxial cable, and coplanar waveguide. They may therefore be integrated with many planar techniques. By adjusting the location of the DRA with regard to the line, it is simple to modify the coupling between a DR and a planar transmission line. By carefully selecting resonator settings, a DRA antenna's working bandwidth may be adjusted throughout a broad range. For instance, by selecting the right resonator material's dielectric constant, the bandwidths of a DR antenna's lower order modes may be readily changed from a tiny percentage to 10% or more.

The frequency range in which the antenna's input VSWR is smaller than a certain number of S is known as the impedance bandwidth of an antenna. The relationship between the entire unloaded Q-factor Q of the resonator and the impedance bandwidth of a resonant antenna, which is perfectly matched to a transmission line at its "resonant frequency," is as follows:

$$BW = \frac{(S-1)}{Q\sqrt{S}}. \quad (1)$$

In this paper, a differential feed is used to excite the fundamental $TE_{01\delta}$ mode. Differential feed helps in reducing the cross-polarization and increases the gain of the antenna. Three slots are etched in the ground plane in which three p-i-n diodes are inserted. Altered states (on/off) of diode results in beam steering. This antenna's DR construction is straightforward, and its switching speed is quick. Various studies are done on material specifications and antenna band selections [12–22].

The material, Rogers RO4003C is used as the substrate which provides low electrical gravity, low voltage, and high oxidation resistance that makes it appropriate for RF applications. All of the RO4003C laminates available configurations, which use both 1080 and 1674 glass fabric types, adhere to the same laminate electrical performance criteria. While using the same production procedure as ordinary epoxy/glass laminates, RO4003C laminates offer tight control over the dielectric constant (Dk) and minimal loss at a quarter of the cost of traditional microwave laminates. There are no additional through-hole treatments or handling techniques necessary, in contrast to PTFE-based microwave materials. Materials in the RO4003C category are not UL 94 V-0 certified and are not brominated.

The ground plane and the feedline are designed using annealed copper metal for better conductivity. The antenna is fabricated using the chemical etching process which employs a positive photoresist that gives higher resolution accuracy for antenna and other RF circuits. This process of fabrication has another advantage of inculcating structures from simpler to complex.

1.1. Antenna Configuration and Material Specifications. The schematic of the antenna structure is depicted in Figure 1. The structure consists of a DP, substrate 1, ground plane, substrate 2, and a feed. The dielectric constant of the cylindrical DP is $\varepsilon_{rd} = 45$, the loss tangent is tan $\delta = 1.9 \times 10^{-4}$, and the volume is $\pi \times r \times r \times h\,\text{mm}^3$ (where r = radius and h = height of the patch). Both substrates 1 and 2 are Rogers RO4003 C with $\varepsilon_{rs} = 3.38$, size of $L \times L\,\text{mm}^2$ (L = length of the substrate. The thickness of substrate1 is 1.524 mm and substrate 2 is 0.813 mm with tan δ of 0.0027 is chosen for the present design. The length and width of the two substrates and ground plane are $60 \times 60\,\text{mm}^2$. The radius of the dielectric patch is 20.6 mm. The height of substrate 1 is 1.524 and substrate 2 is 0.813 mm. The length of feedback 1 is 14.5 mm and feedback 2 is 31 mm. The gap between the slots in the ground plane is 2.15 mm and the length of the slot is 8.5 mm. The relative permittivity of both substrates is 3.38 and that of the dielectric patch is 45.

All of the RO4003C laminates available configurations, which use both 1080 and 1674 glass fabric types, adhere to the same laminate electrical performance criteria. While using the same production procedure as ordinary epoxy/glass laminates, RO4003C laminates offer tight control over the dielectric constant (Dk) and minimal loss at a quarter of the cost of traditional microwave laminates. There are no additional through-hole treatments or handling techniques necessary, in contrast to PTFE-based microwave materials. Materials in the RO4003C category are not UL 94 V-0 certified and are not brominated. Hydrocarbon ceramic laminates with the RO4000 brand name are intended to provide improved high-frequency performance and

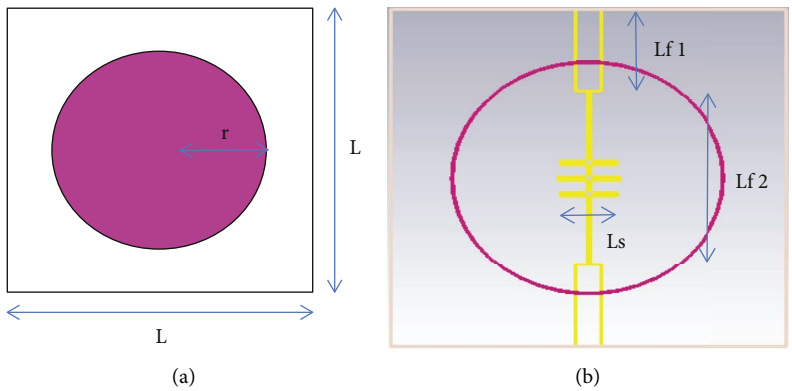

Figure 1: Schematic diagram of the pattern reconfigurable DP antenna. (a) The radius of the cylindrical DP. (b) Substrate along with feedline, diodes, and ground plane slots.

inexpensive circuit manufacturing. The outcome is a low-loss material that can be manufactured using common epoxy/glass (FR-4) techniques.

Once working frequencies reach 500 MHz and beyond, there are much less number of laminates to choose from. Higher operating frequencies prevent the use of traditional circuit board laminates in many applications, but reduced dielectric loss enables RO4000 series material to be utilized in such applications. Superior high-frequency performance and affordable circuit fabrication are two features of RO4000 hydrocarbon ceramic laminates. The properties required for RF microwave circuits, matching networks, and controlled impedance transmission lines are present in the RO4000 material. Figure 2 presents a variation of the relative permittivity of Rogers R04003C with temperature and frequency.

The Three connection slots are etched in parallel while the ground plane is positioned on the top layer of substrate 2. The area of slot 1 and slot 3 for simulation is $8.5 \times 0.9\,\text{mm}^2$, while slot 2 is $9.4 \times 0.6\,\text{mm}^2$. Three P-i-N diodes are kept in the coupling slots to provide the beam steering operation. The spacing, d, between the slots is 2.15 mm. The metal used for feedline and ground plane is annealed copper as they retain impact resistance to 20 K. Copper becomes flexible after being annealed. Annealing restores electrical conductivity by enhancing the crystal lattice's uniformity. The resistivity of annealed copper is 1.72×10^{-8} ohm-m and its specific gravity is 8.89. The modulus of elasticity is 17,000000 psi. Table 1 presents the specifications of annealed copper and Figure 3 shows the variation of stress with respect to strain for annealed copper (Table 2).

1.2. Mathematical Analysis of TE_{mn} Mode. For the purpose of directing the ensuing design, a mathematical study of the TEmn mode is necessary. The theoretical analytical model of the DP resonator is depicted in Figure 4 beneath.

As magnetic walls, four side planes that are perpendicular to the z-axis direction are considered. The resonator is half-cut by using the ground plane as an electric wall. In accordance with the Helmholtz equation and boundary conditions [23].

$$\begin{aligned} \nabla^2 . E_z + k^2 . E_z &= 0 \\ \nabla^2 . H_z + k^2 . H_z &= 0. \end{aligned} \tag{2}$$

It is possible to retrieve the TEmn mode's field element expressions.

For the DP

$$\left(|z| \le \frac{h_d}{2}\right)$$
$$H_{z1}(x, y, z) = A_1 \sin(k_x x) \sin(k_y y) \cos[k_z z + \varphi_z]. \tag{3}$$

For air $(z > h_d/2)$

$$H_{z2}(x, y, z) = A_1 \cos\left(\frac{k_z h_d}{2} + \varphi_z\right) \times \sin(k_x x) \sin(k_y y) e^{-\alpha_1\left(z - \frac{h_d}{2}\right)}. \tag{4}$$

For the substrate $(-h_d/(2 - h_{s1}) \le z \le -h_d/2)$

$$H_{z3}(x, y, z) = \frac{A_1 \cos(k_z h_d/2 - \varphi_z)}{\sin h(\alpha_2 h_{s1})} \sin(k_x x) \sin(k_y y) \times \sinh\left[\alpha_2\left(z + \frac{h_d}{2} + h_{s1}\right)\right]. \tag{5}$$

The wave numbers of the z-axis dissipation mode in air and substrate, respectively, are represented in the aforementioned formulas by $\alpha 1$ and $\alpha 2$, respectively. The wave numbers on the x, y, and z axes are denoted by the letters k_x, k_y, and k_z.

$$\begin{aligned} k_x &= \frac{m\pi}{w_d}, \\ k_y &= \frac{n\pi}{w_d}. \end{aligned} \tag{6}$$

The following equations are used to obtain the remaining field components in the DP, air, and substrate.

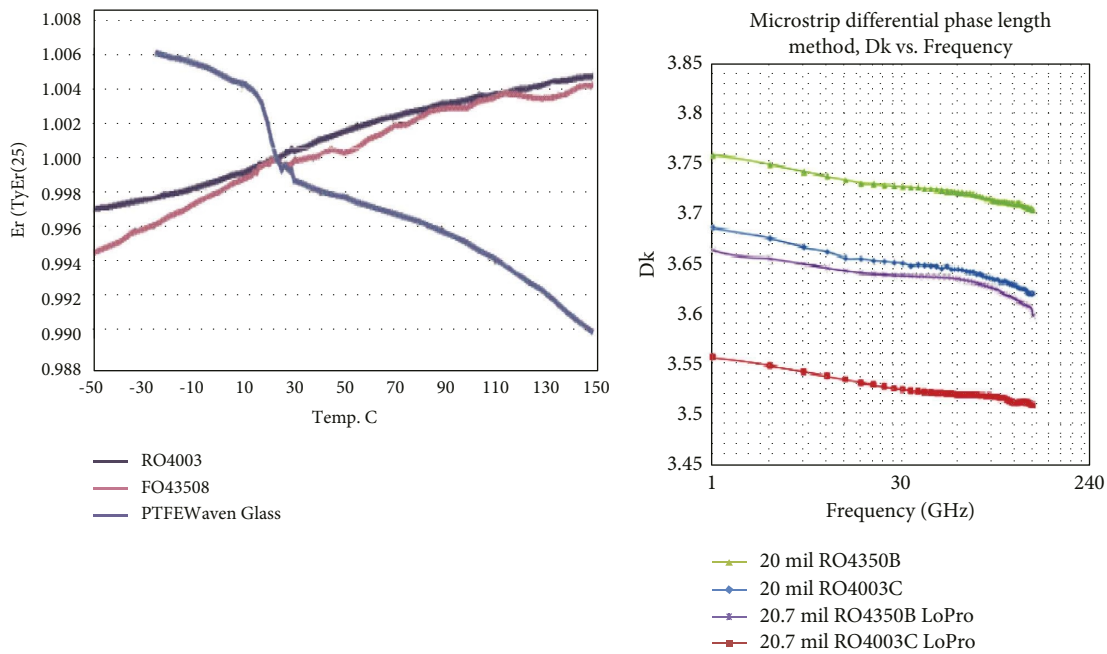

(a) (b)

Figure 2: Variation of RO4003C relative permittivity with (a) temperature and (b) frequency.

Table 1: Specification of annealed copper.

Specific gravity	8.89
Density	0.322 lb./cu. In. At 68°F
Thermal conductivity	226 BTU/Sq Ft/Ft/Hr°F at 68°F
Coefficient of thermal expansion	0.0000098/°F from 68°F to 572°F
Modulus of elasticity	17,000,000 psi
Tensile strength	32,000 psi min
Yield strength (0.5% extension)	20,000 psi min
Elongation in 2″ approx	30%
Shear strength	25,000 psi
Hardness, rockwell	54 min

Table 2: Parameter dimensions.

Parameters	Dimension (mm)
L	60
R	20.6
Lf1	14.5
Lf2	31
Ls	8.5
h1	1.524
h2	0.813
D	2.15

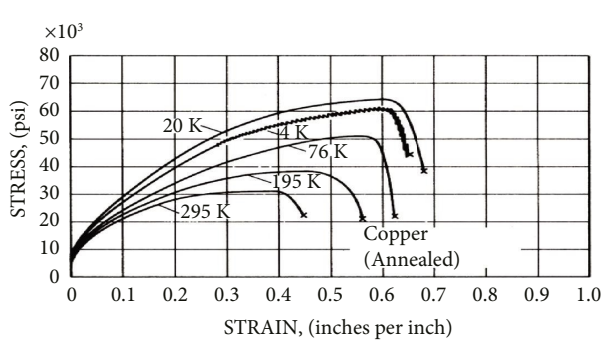

Figure 3: Stress vs strain variation of annealed copper.

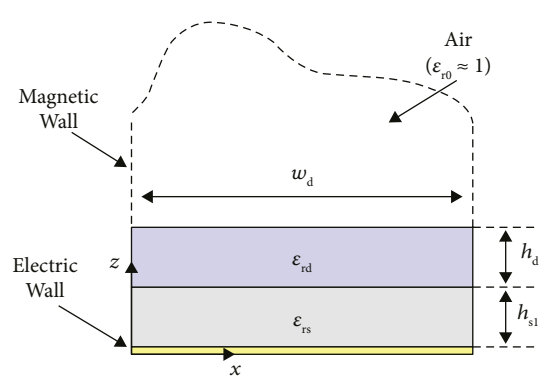

Figure 4: Modeling of DP resonator.

$$E_x = -\frac{j\omega\mu_0}{k_c^2}\frac{\partial H_z}{\partial x},$$
$$E_y = -\frac{j\omega\mu_0}{k_c^2}\frac{\partial H_z}{\partial x},$$
$$H_x = \frac{1}{k_c^2}\frac{\partial^2 H_z}{\partial x \partial z},$$
$$H_y = \frac{1}{k_c^2}\frac{\partial^2 H_z}{\partial y \partial z}. \quad (7)$$

The following formula is therefore derived in accordance with the continuous criterion for the tangential H-field and E-field at the DP interfaces:

$$k_z.h_d = \tan^{-1}\left(\frac{\alpha_1}{k_z}\right) + \tan^{-1}\left(\frac{\alpha_2 \coth(\alpha_2 h_{s1})}{k_z}\right),$$
$$\varphi_z = \frac{\tan^{-1}(\alpha_1/k_z) - \tan^{-1}(\alpha_2 \coth(\alpha_2 h_{s1})/k_z)}{2}. \quad (8)$$

Lastly, when paired with classical electromagnetism's preservation of wavelength range

$$k_x^2 + k_y^2 + k_z^2 = \varepsilon_{r\,d} k_0^2$$
$$k_x^2 + k_y^2 - \alpha_1^2 = \varepsilon_{r0} k_0^2 \quad (9)$$
$$k_x^2 + k_y^2 - \alpha_2^2 = \varepsilon_{rs} k_0^2.$$

1.3. Reconfigurability Principle. Three coupling slots loaded with P-i-N diodes are placed in the ground plane to provide beam steering, as depicted in Figure 1. Five switching states that function at roughly 3.1 GHz can be accomplished by adjusting the ON-/OFF state of the P-i-N diodes, as listed in Table 3. BAR64-02V P-i-N diode is used whose equivalent diagram is shown in Figure 5. Conventional silicon fabrication techniques, such as oxidation, photolithography, ion implantation, aluminum sputter deposition, and passivation, were used to create the diodes. Boron was implanted into the bare wafer to create the diode's front side ($p+$ active area). For an n + contact, the phosphorous was doped on the back side. State 1 is established when D_1 is ON and D_2 and D_3 are OFF. In this instance, as depicted in Figure 6, the E-field of the $TE_{01\delta}$ mode is evenly spread across the DP resonator.

The half-power beamwidth (HPBW) is 87.6 degrees, while the main beam orientation is 8 degrees. State 1 has a 7.65 dBi peak gain. State 2 has a primary beam direction of 14 degrees and an HPBW of 88.6 degrees when D_1 and D_2 are OFF and D_3 is ON. State 2 has an 8.22 dBi peak gain. State 3 is when just D_3 is OFF but D_1 and D_2 are ON. In this situation, the HPBW is 66.5 degrees, while the main beam direction is 171 degrees. 10.6 dBi is added to the peak gain. In the fourth condition, D_1 and D_3 are OFF while D_2 is ON, producing a gain of 10.6 dBi and a relatively high HPBW of 171 degrees in comparison with the other modes.

2. Results and Discussion

The E field distribution of $TE_{01\delta}$ mode at 3.1 GHz as shown in Figure 6 is derived by using the Eigenmode solver in CST Microwave studio. This $TE_{01\delta}$ mode generates a distinct radiation pattern that is broadside. A differential feed is given to the designed structure which results in higher gain. A differential feed excites the cylindrical DRA in such a way that $TE_{01\delta}$ mode is excited. For a differential feed to work, both the ports carry the same amplitude but 180 degrees out of phase Rf signal. The ON state of the P-i-N diode is given by providing a 2.1 ohm Resistor. The OFF state is a parallel RC circuit of $R = 500$ Ohm and $C = 2.1$ pF. A parametric analysis has been carried out in terms of the distance between the slots (d) for each state and state 2 by varying d from 0.15 to 2.15 mm The return loss for state 1 and state 2 as shown in Figure 7 below can be read to be ranging from −25 dB to −32 dB for state 1. The return loss for state 2 with varying d ranges from −25 to −28 dB. A second parametric analysis was carried out with the radius (r) of the cylindrical DP. The radius varied from 10.6 mm to 20.6 mm showing a return loss ranging from −31 to −33 dB. Finally, the structure was optimized at $d = 2.15$ mm and a radius, $r = 20.6$ mm.

Figure 8 depicts return loss for different radius values of the dielectric patch. The designed structure provides a return loss of −28 dB and a wide bandwidth as can be seen in Figure 9. State 1 provides a return loss of −28 dB, while state 2 and state 4 provide a S11 Value of −30 dB. The return loss of state 3 is < −40 dB. The major lobe direction of state 1 is 8 degrees whereas that of state 2 is 14 degrees as shown in Figure 10. Figure 11 represents the 3D radiation plot of state 1, state 2, and state 3. States 1 and 2 have a broadside radiation pattern. The gain of state 1 is 7.65 dBi, while that of state 3 and state 4 is 10.6 dBi. State 2 and state 5 provide a gain of 8.22 dBi. A comparison of different techniques of pattern reconfiguration using the switching method has been carried out in Table 4. [1] A microstrip patch antenna is studied which consists of 6 switches and 6 states at 3.7 GHz with a gain of 6 dBi. A DRA [4] is investigated with 3 switches comprising of 3 states at 5.8 GHz providing a gain of 7.48 dBi. An MPA with 20 switches and 5 states operating at 2.4 GHz providing a gain of 6.5 dBi is studied [5]. With an increase in the number of switches, the loss increases, and it makes the structure bulkier. [8] An MPA with 8 switches and 9 states resonating at 2.5 GHz with a gain of 7.26 dBi is investigated. [11] presents an MPA with 17 switches and only 3 states radiating at 3.5 GHz and providing a gain of 9 dBi. A DRA [24] with 8 switches and 8 states operating at 5.8 GHz with a gain of 7.27 dBi is studied. The present antenna structure provides better efficiency compared to the other structures in terms of the implementation of the number of diodes and the maximum number of states attainable. The gain as compared to previous structures is also higher which makes it suitable for indoor wireless communication. Many researchers have used various techniques to engineer the devices along with suitable antennas to accommodate for better performance [25–34].

Table 3: Switching states of the proposed antenna.

State	D1	D2	D3	S11 (dB)	Gain (dBi)	Beam direction	HPBW	Side lobe (dB)
1	ON	OFF	OFF	−28	7.65	8^0	87.6^0	−5
2	OFF	ON	OFF	−37	8.22	14^0	88.6^0	−2.7
3	ON	ON	OFF	−30	10.6	171^0	66.5^0	−2
4	OFF	ON	ON	−30	10.6	-171^0	171^0	−2
5	OFF	OFF	ON	−30	8.22	6^0	83.3^0	−4.7

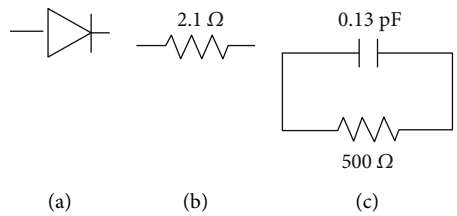

Figure 5: (a) P-i-N diode; (b) on state; (c) off state.

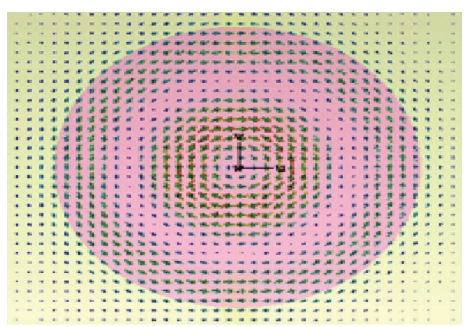

Figure 6: E field distribution of $TE_{01\delta}$ mode at 3.1 GhZ.

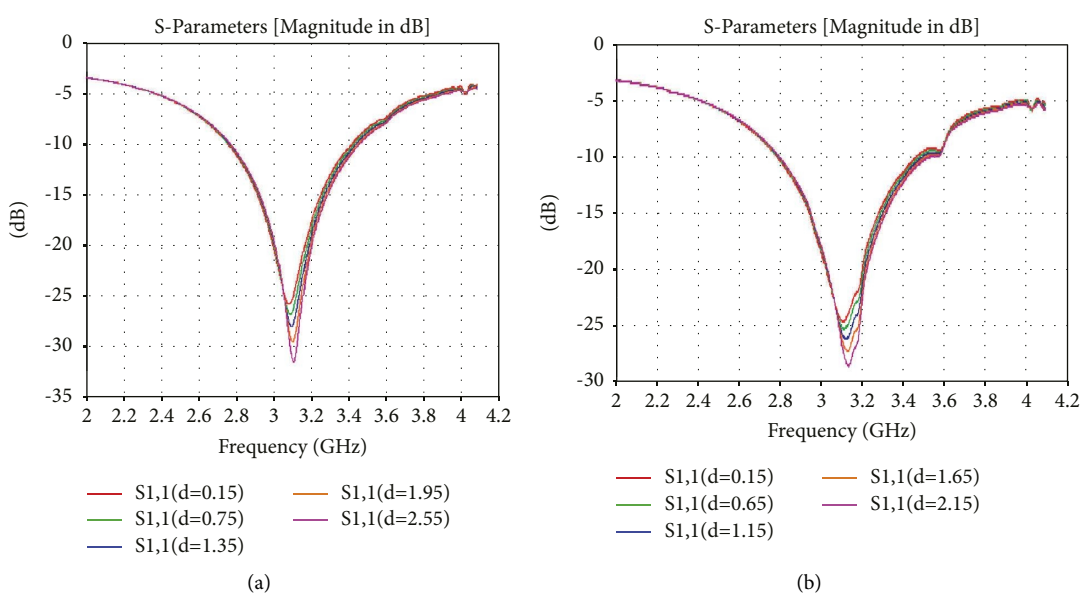

Figure 7: Parametric analysis of the distance between the slots of (a) state 1 and (b) state 2.

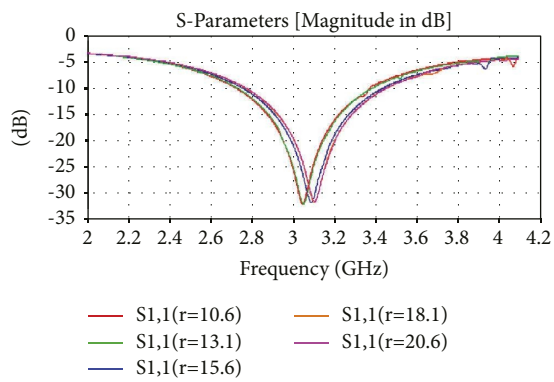

Figure 8: Parametric analysis of the return loss for different radius values of the dielectric patch.

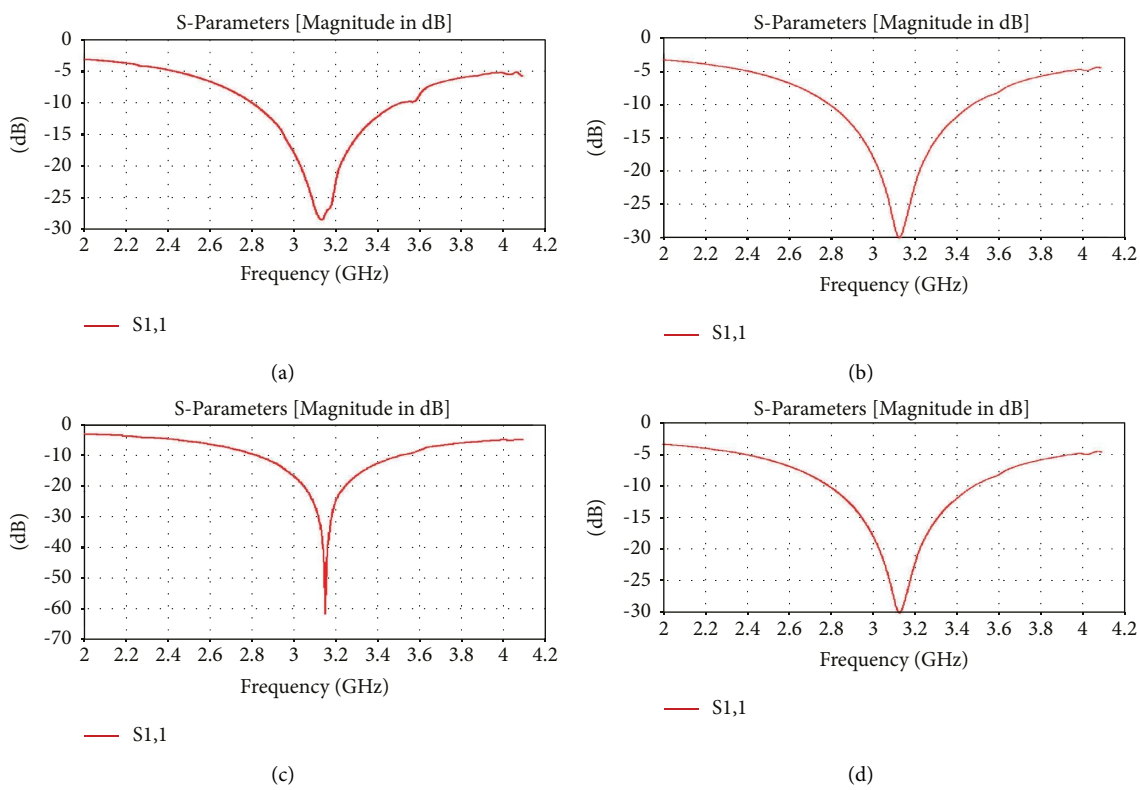

Figure 9: Return loss of (a) state 1, (b) state 2, (c) state 3, and (d) state 4.

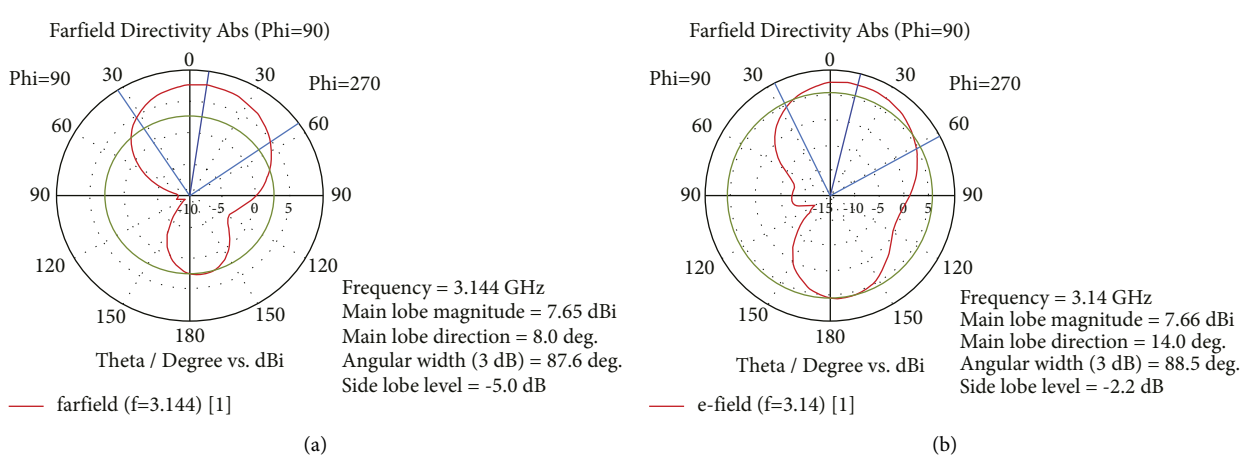

Figure 10: Polar plot of (a) state 1 and (b) state 2.

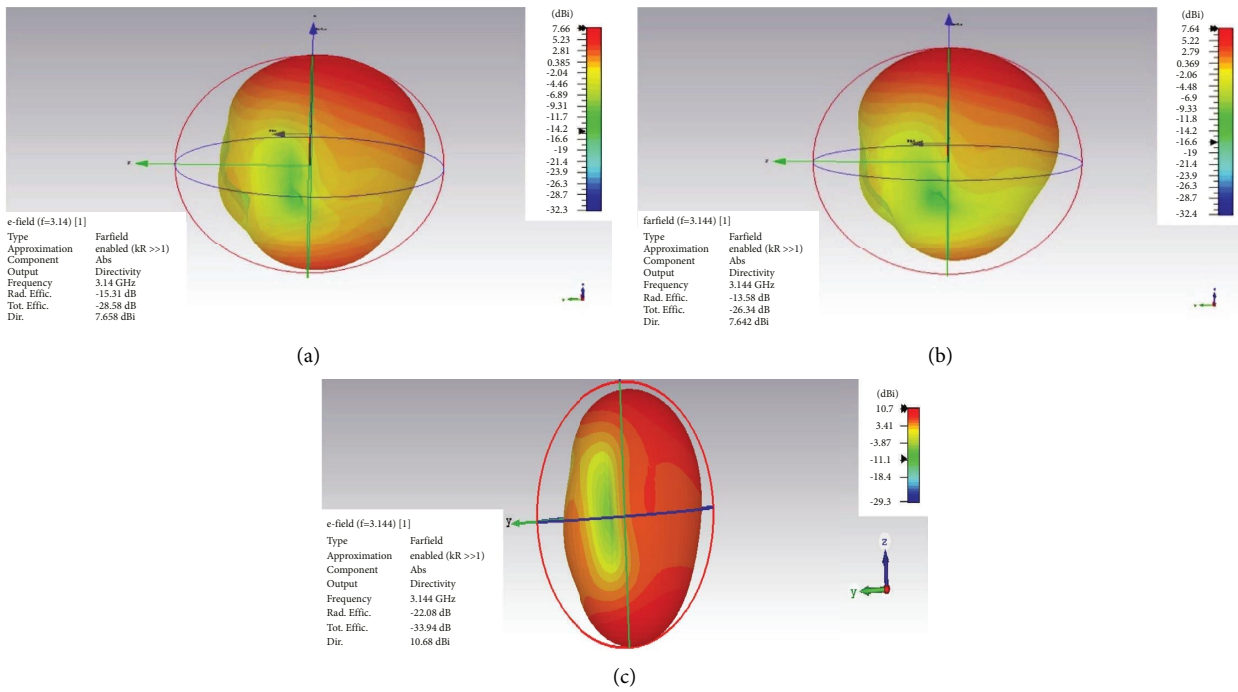

Figure 11: 3D radiation pattern of (a) state 1, (b) state 2 and (c) state 3.

Table 4: Comparison of different pattern reconfiguration techniques.

Reference	Antenna type	Number of switches	Number of states	F0 (GHz)	Gain (dBi)
[1]	MPA	6	6	3.7	6
[4]	DRA	3	3	5.8	7.48
[5]	MPA	20	5	2.4	6.5
[8]	MPA	8	9	2.5	7.26
[10]	MPA	8	4	3.4	7.3
[11]	MPA	17	3	3.5	9
[24]	DRA	8	8	5.8	7.27
Present work	DRA	3	5	3.1	10.6

3. Fabrication Process

An appropriate material must be prepared before the process of fabrication. Both the electrical requirements for antenna applications and the requirements for deep lithography manufacturing should be met by the material. Permittivity and dielectric loss are two crucial electrical properties of the material. Direct/indirect manufacturing techniques may be thought of to create effective and feasible antenna structures depending on the material qualities. The direct procedure prioritizes lithography fabrication suitability; as a result, pure photoresist materials with/without a minimal amount of additives are acceptable.

The indirect technique relies heavily on the material's electrical qualities, allowing for the use of significant amounts of non-photoresist materials with superior electrical capabilities. Direct manufacturing is simpler and easier than indirect fabrication, which involves first creating a high-aspect-ratio photoresist frame before utilizing a robotic machine to inject microwave material into the frame. Here the substrate used is Rogers RO4003C having a relative permittivity of 3.38 and $\tan\delta = 0.0027$. Organic polymers used as photoresist materials undergo chemical changes when exposed to UV light. The photoresist is positive when the exposed region becomes more soluble in the developer. If it becomes less soluble, the substance is regarded as a negative resist. The exposed areas of negative resists increase as the developer dissolves the counterpart, which impairs the process's ability to resolve itself.

The developer solution seeps into the photoresist material, causing swelling, which in turn causes a distortion in the patterned area.

As a result, positive resists are being used more frequently than negative ones in photolithography-based antenna fabrication because they offer superior resolution.

4. Conclusion

A pattern reconfigurable dielectric resonator antenna emitting at 3.1 GHz is presented in this paper. The beam can be steered at 6 degrees, 8 degrees, 14 degrees, and 171 degrees. Three P-i-n diodes are employed in the slots of the

ground plane to help steer the beam direction. By changing the state of the three diodes, five states can be obtained. The return loss of each state is less than −25 dB. The gain of the first state is 7.65 dBi, the second and fifth state's gain is 8.22 dBi, and the third and fourth state's gain is 10.6 dBi. A differential feed excites the $TE_{01\delta}$ mode, reduces the design complexity, makes it low profile, and enhances the gain. A mathematical analysis of TE_{mn} is elaborated which forms the basis for understanding the working of the antenna. The E field of the excited $TE_{01\delta}$ is presented which in turn generates a broadside radiation Pattern. The Antenna can be a good contender for S-band applications. The structure is designed using Rogers RO4003C which offers higher longevity, Low electrical gravity, low voltage, and high oxidation resistance making it useful in RF applications including airplane and media domains. The relative permittivity of the substrate (Rogers RO4003C) is 3.38 with $\tan\delta = 0.0027$.. They are low-loss materials that can be produced using common epoxy/glass (FR-4) fabrication techniques that are reasonably priced. Once operational frequencies reach 500 MHz and above, the range of laminates typically available is significantly constrained. The properties of RF microwave circuits, matching networks, and controlled impedance transmission lines are present in the RO4000 material. Annealed copper is used to design the ground plane and feedline which provides excellent conductivity. The Antenna is fabricated using the chemical etching process which employs a positive photoresist that inculcates structures from simpler to complex while giving a higher resolution accuracy for the designed Antenna. [35–41]

Data Availability

The data used to support this study are included within the article.

Ethical Approval

This article does not contain any studies with human or animal subjects.

Conflicts of Interest

The authors declare that they have no conflicts of interest regarding the publication of this paper.

Acknowledgments

The authors are thankful to Jimma Institute of Technology, Jimma University, Jimma, Ethiopia for their cooperation and support during this research work. The publication of this research work is only for the academic purpose of Jimma University, Ethiopia.

References

[1] G. Yang, J. Li, D. Wei, S.-G. Zhou, and R. Xu, "Pattern reconfigurable microstrip antenna with multidirectional beam for wireless communication," *IEEE Transactions on Antennas and Propagation*, vol. 67, no. 3, pp. 1910–1915, 2019.

[2] Y. H. Ke, L.-L. Yang, and J.-X. Chen, "A pattern-reconfigurable dielectric resonator antenna based on switchable Directors," *IEEE Antennas and Wireless Propagation Letters*, vol. 21, no. 3, pp. 536–540, 2022.

[3] G. Jin, M. Li, D. Liu, and G. Zeng, "A simple planar pattern-reconfigurable antenna based on arc dipoles," *IEEE Antennas and Wireless Propagation Letters*, vol. 17, no. 9, pp. 1664–1668, 2018.

[4] B. K. Ahn, H.-W. Jo, J.-S. Yoo, J.-W. Yu, and H. L. Lee, "Pattern reconfigurable high gain spherical dielectric resonator antenna operating on higher order mode," *IEEE Antennas and Wireless Propagation Letters*, vol. 18, no. 1, pp. 128–132, 2019.

[5] S.-L. Chen, P.-Y. Qin, W. Lin, and Y. J. Guo, "Pattern-reconfigurable antenna with five switchable beams in elevation plane," *IEEE Antennas and Wireless Propagation Letters*, vol. 17, no. 3, pp. 454–457, 2018.

[6] B.-J. Liu, J.-H. Qiu, C.-L. Wang, and G.-Q. Li, "Pattern-reconfigurable cylindrical dielectric resonator antenna based on parasitic elements," *IEEE Access*, vol. 5, Article ID 25584, 2017.

[7] S. Raman, N. Timmons, and J. Morrison, "Gain enhanced pattern reconfigurable planar Yagi-Uda antenna on coplanar structure," *Electronics Letters*, vol. 49, no. 25, pp. 1593–1595, 2013.

[8] X. Ding and B.-Z. Wang, "A novel wideband antenna with reconfigurable broadside and endfire patterns," *IEEE Antennas and Wireless Propagation Letters*, vol. 12, pp. 995–998, 2013.

[9] J. Ren, X. Yang, J. Yin, and Y. Yin, "A novel antenna with reconfigurable patterns using H-shaped structures," *IEEE Antennas and Wireless Propagation Letters*, vol. 14, pp. 915–918, 2015.

[10] J. Ren, Z. Zhou, Z. H. Wei et al., "Radiation pattern and polarization reconfigurable antenna using dielectric liquid," *IEEE Transactions on Antennas and Propagation*, vol. 68, no. 12, pp. 8174–8179, 2020.

[11] Z. Chen, Q. Liu, B. Sanz-Izquierdo, H. Liu, J. Yu, and X. Chen, "A wideband circular-polarized beam steering dielectric resonator antenna using gravitational ball lens," *IEEE Transactions on Antennas and Propagation*, vol. 69, no. 5, pp. 2963–2968, 2021.

[12] R. Deepa, M. P. Devi, N. A. Vignesh, and S. Kanithan, "Implementation and performance evaluation of ferroelectric negative capacitance FET," *Silicon*, vol. 14, no. 5, pp. 2409–2419, 2022.

[13] E. S. Kumar, S. Kumar P, N. Arun Vignesh, and S. Kanithan, "Design and analysis of junctionless FinFET with Gaussian doped for non-polar structure," *Silicon, vol. 14, pp. 8439–8447*, 2022.

[14] S. Kanithan, N. ArunVignesh, E. Karthikeyan, and N. Kumaresan, "An intelligent energy efficient cooperative MIMO-AF multi-hop and relay based communications for Unmanned Aerial Vehicular networks," *Journal of Computer and Communications*, vol. 154, pp. 254–261, 2020.

[15] R. Senthil, G. M. Tamil selvan, S. Kanithan, and N. Arun Vignesh, "Routing in WSNs powered by a hybrid energy storage system through a CEAR protocol based on cost welfare and route score metric," *International Journal of Computers, Communications & Control*, vol. 14, no. 2, pp. 233–252, 2019.

[16] B. Shilpa, L. K. Rao, N. A. Vignesh, and V. V. Kumar, "Design of inset fed circular dual band patch antenna for WLAN

frequencies," *International Journal of Systems, Control and Communications*, vol. 13, no. 1, pp. 56–66, 2022.

[17] N. Arun Vignesh and P. Poongodi, "Analysis of localized quality of service improvement architecture for wireless LAN," *Wireless Personal Communications*, vol. 90, no. 2, pp. 701–711, 2016.

[18] N. A. Vignesh and P. Poongodi, "A cluster-based network architecture scheme for QoS improvement in WLAN," *International Journal of Networking and Virtual Organisations*, vol. 17, no. 2/3, pp. 158–169, 2017.

[19] S. Kanithan, A. Ananthanarayanan, N. Arun Vignesh, and T. Kannapiran, "Improved imperialist competitive algorithm based energy efficient peak to average power ratio (papr) in cooperative mimo-af systems," in *Proceedings of the International Conference on Computer Communication and Informatics (ICCCI)*, pp. 1–5, Coimbatore, India, January 2022.

[20] K. Murali, N. A. Vignesh, S. Kanithan, N. Kumareshan, P. Vidyullatha, and D. V. Babu, "Two stage signal processing of channel valuation and recognition for millimeter MIMO systems," in *Proceedings of the International Conference on Computer Communication and Informatics (ICCCI) Coimbatore, India*, pp. 1–5, January 2022.

[21] N. S. Kiran, N. A. Vignesh, S. Kanithan et al., "Cross coupled power effective quick level shifter," in *Proceedings of the International Conference on Computer Communication and Informatics (ICCCI) Coimbatore, India*, pp. 1–5, January 2022.

[22] L. G. N. S. Pratyusha, K. Keerthi, K. S. Reddy, and E. S. Sushma, "A study on wideband spectrum monitoring using NI USRP," in *Proceedings of the International Conference on Computer Communication and Informatics (ICCCI) Coimbatore, India*, pp. 1–4, January 2022.

[23] K. M. Luk and K. W. Leung, *Dielectric Resonator Antennas*, "Research Studies", Press Ltd, Hertfordshire, England, UK, 2003.

[24] L. Zhong, J.-S. Hong, and H.-C. Zhou, "A novel pattern-reconfigurable cylindrical dielectric resonator antenna with enhanced gain," *IEEE Antennas and Wireless Propagation Letters*, vol. 15, pp. 1253–1256, 2016.

[25] S. S. P. Tammireddy, M. Samson, P. R. Reddy et al., "An energy-efficient reconfigurable accelerators in multi-core systems using PULP-NN," *Applied Nanoscience, vol. 21*, pp. 1–14, 2021.

[26] A. L. Narayana, B. Prasad, P. R. Kapula, D. Prasad, A. K. Panigrahy, and D. N. V. S. L. S. Indira, "Enhancement in performance of DHTprecoding over WHT for EC companded OFDM in wireless networks," *Applied Nanoscience*, pp. 1–16, 2021.

[27] M. D. Prakash, B. G. Nelam, S. Ahmadsaidulu, A. Navaneetha, and A. K. Panigrahy, "Performance analysis of ion-sensitive field effect transistor with various oxide materials for biomedical applications," pp. 1–11, Silicon, 2021.

[28] M. D. Prakash, S. L. Nihal, S. Ahmadsaidulu, R. Swain, and A. K. Panigrahy, "Design and modelling of highly sensitive glucose biosensor for Lab-on-chip applications," pp. 1–7, Silicon, 2022.

[29] A. Kumar Panigrahi and K.-N. Chen, "Low temperature Cu-Cu bonding Technology in 3D integration: an extensive review," *Journal of Electronic Packaging*, vol. 140, no. 1, Article ID 010801, 2018.

[30] A. K. Panigrahy, T. Ghosh, S. R. K. Vanjari, and S. G. Singh, "Surface density gradient engineering precedes enhanced diffusion; drives CMOS in-line process flow compatible Cu–Cu thermocompression bonding at 75° C," *IEEE Transactions on Device and Materials Reliability*, vol. 19, no. 4, pp. 791–795, 2019.

[31] N. A. Vignesh, R. Kumar, R. Rajarajan et al., "Silicon wearable body area antenna for speech-enhanced IoT and nanomedical applications," *Journal of Nanomaterials*, vol. 2022, Article ID 2842861, 9 pages, 2022.

[32] A. K. Panigrahi, T. Ghosh, S. R. K. Vanjari, and S. G. Singh, "Oxidation resistive, CMOS compatible copper-based alloy ultrathin films as a superior passivation mechanism for achieving 150 C Cu–Cu wafer on wafer thermocompression bonding," *IEEE Transactions on Electron Devices*, vol. 64, no. 3, pp. 1239–1245, 2017.

[33] S. Bonam, A. K. Panigrahi, C. H. Kumar, S. R. K. Vanjari, and S. G. Singh, "Interface and reliability analysis of Au-passivated Cu–Cu fine-pitch thermocompression bonding for 3-D IC applications," *IEEE Transactions on Components, Packaging, and Manufacturing Technology*, vol. 9, no. 7, pp. 1227–1234, 2019.

[34] A. K. Panigrahi, T. Ghosh, C. H. Kumar, S. G. Singh, and S. R. K. Vanjari, "Direct, CMOS in-line process flow compatible, sub 100° C Cu–Cu thermocompression bonding using stress engineering," *Electronic Materials Letters*, vol. 14, no. 3, pp. 328–335, 2018.

[35] C. Song, E. L. Bennett, J. Xiao et al., "Passive beam-steering gravitational liquid antennas," *IEEE Transactions on Antennas and Propagation*, vol. 68, no. 4, pp. 3207–3212, 2020.

[36] B. Li and K. W. Leung, "On the differentially fed rectangular dielectric resonator antenna," *IEEE Transactions on Antennas and Propagation*, vol. 56, no. 2, pp. 353–359, 2008.

[37] Z.-L. Lu, X.-X. Yang, and G.-N. Tan, "A multidirectional pattern reconfigurable patch antenna with CSRR on the ground," *IEEE Antennas and Wireless Propagation Letters*, vol. 16, pp. 416–419, 2017.

[38] W.-Q. Deng, X.-S. Yang, C.-S. Shen, J. Zhao, and B.-Z. Wang, "A dual polarized pattern reconfigurable Yagi patch antenna for microbase stations," *IEEE Transactions on Antennas and Propagation*, vol. 65, no. 10, pp. 5095–5102, 2017.

[39] M. A. Towfiq, A. Khalat, S. Blanch, J. Romeu, L. Jofre, and B. A. Cetiner, "Error vector magnitude, intermodulation, and radiation characteristics of a bandwidth- and pattern-reconfigurable antenna," *IEEE Antennas and Wireless Propagation Letters*, vol. 18, no. 10, pp. 1956–1960, 2019.

[40] R. L. Haupt and M. Lanagan, "Reconfigurable antennas," *IEEE Antennas and Propagation Magazine*, vol. 55, no. 1, pp. 49–61, 2013.

[41] J. Costantine, Y. Tawk, S. E. Barbin, and C. G. Christodoulou, "Reconfigurable antennas: design and applications," *Proceedings of the IEEE*, vol. 103, no. 3, pp. 424–437, 2015.

Hindawi
Advances in Materials Science and Engineering
Volume 2022, Article ID 7341201, 9 pages
https://doi.org/10.1155/2022/7341201

Research Article

Investigation on Wear and Corrosion Behavior of Cu, Zn, and Ni Coated Corten Steel

D. Kumaravel,[1] **V. K. Bupesh Raja**,[1] **Kabasker Balthaser**,[2] **A. Jayaganthan**,[1] **S. Sahas**,[1] **S. Muralidharan**,[1] **and Tariku Achamyeleh**[3]

[1]*School of Mechanical Engineering, Sathyabama Institute of Science and Technology, Chennai, India*
[2]*DMI St. Eugene University, Chibombo, Zambia*
[3]*Department of Mechanical Engineering, Debre Tabor University, Debra Tabor, Ethiopia*

Correspondence should be addressed to V. K. Bupesh Raja; bupesh.v.k@gmail.com and Tariku Achamyeleh; tariku.achamyeleh@mu.edu.et

Received 20 July 2022; Accepted 21 September 2022; Published 8 October 2022

Academic Editor: Pudhupalayam Muthukutti Gopal

Corten steel is a low-carbon alloy steel. It is widely used in architecture, the transport sector, and industrial applications, where the steel is exposed to harsh environments. It is very much sought after due to its auto protection from corrosive environments through the formation of patina (rust). The specialty of patina formed on the corten steel is that it can self-heal itself and stop the spreading of corrosion. Generally, steels are given protective coatings to enhance resistance to corrosion, wear, abrasion, etc. One of the popular protective coating techniques is electroplating. In this study, the effect of electroplating of copper (Cu), zinc (Zn), and nickel (Ni) on the wear and corrosion behavior of Corten ASTM A242 grade steel is investigated. It was observed that the Cu coating yielded poor corrosion and wear protection performance. The Zn coating exhibited a moderate improvement. The Ni electroplating produced excellent results and, the wear and corrosion resistance was improved in the corten steel. Thus, when compared with Cu, Zn, and Ni coatings, the Ni-coated corten steel is an ideal candidate in applications where there is a need for good resistance to wear, abrasion, and corrosion.

1. Introduction

The corten steel belongs to the family of weathering steels. The corten steel's uniqueness lies in its ability to instantaneously form a stable rust layer called as patina. This patina gives corten steel the aesthetically pleasing appearance and also makes it immune to corrosion. The rust formed on the corten steel prevents further corrosion of the underlying corten steel, by forming an impervious passivation layer. Furthermore, corten steel has good combination of mechanical properties with minimal alloying in the low alloyed steels segment. Since it has good weight to strength ratio, it is widely used in fabrication of railway coaches, transport industry, bridges, structures, etc. The corten steel is the work horse of the railway coach building industry. Corten steel is inherently capable to serve in harsh environments and climatic conditions. The versatility of corten steel lies in its ability to be welded, formed, and undergo processing and heat treatments, and thus its properties could be engineered to produce various products, equipment, structures etc.

The presence of Ni in corten steel makes it unique among the weathering steel, as the Ni present in it enhances the corrosion resistance as observed by other investigators [1]. The uniqueness of corten steel lies in the proper combination of alloying elements in it. Several investigators have observed that, if the quantity of elements like Mn increases, the corrosion rate will increase and also the structure of the rust formed will be poor [2, 3]. Ni-based coatings through electroplating route has enhanced the wear and corrosion resistance of the steel substrate and mechanical properties, as discussed elsewhere [4–8]. Copper, as a corrosion and wear resistant coating, is effective only when coupled with elements like Cr as discussed elsewhere [9–11]. The Ni coating is nonpervious to corrosion than the Cu coating as observed by other investigators [12]. Several investigators have tried to explore the corrosion behavior of corten steel and other

weathering steels and observed that the corten steel possesses good immunity to corrosion [13–16]. The Zn-based coatings provide good immunity in salty environments as discussed elsewhere [17, 18]. The Zn-based coating offers good corrosion resistance but the passivation layer shall be porous and hence likely to form pitting as discussed by Protsenko and Danilov [19]. The coating of Cu and Ni imparts immunity from wear, stress corrosion cracking, erosion, abrasion, etc. as studied by other investigators [20]. Most of the investigators have studied coating of other steels through techniques other than electroplating, like jet electrodeposition and dipping, for studying corrosion behavior, ballistic response, etc. [17–20]. There is scant work reported in literature on the electroplating behavior in corten steel and thus, necessitating this investigation.

2. Materials and Methods

The Corten ASTM A242 Grade Steel of 3 mm thickness was taken for this investigation. The composition of the corten steel was determined using a vacuum spark spectrometer. The micro Vickers hardness test was carried out conforming to ASTM E384—10e2 using Wilson Wolpert micro Vickers hardness testing machine on the Corten steel with 0.5 kg load and dwell of 5 sec. The metallurgical specimens are prepared by polishing with various grades of emery paper, polished with lavigated alumina (0.0013 μm particle size) and final polishing was done using diamond polishing compound (0.25 μm particle size) and then etched with Nital. The microstructural analysis was performed using a Zeiss Axio Scope optical microscope. The Cu, Zn, and Ni coating were done individually on corten steel in AK Finishing Technologies, Chennai, India. The scratch test was performed using Ducom, Bangalore, India, scratch tester. The scratch test was carried out with a Rockwell diamond stylus indenter of 120 degrees, length of 45 mm, friction accuracy of 0.1 N for a depth range of 0–300 mm, and a working load of 5 N. The surface roughness (Ra) was measured using a Mitutoyo roughness tester. The coating thickness was measured using an optical microscope scale. The bend test was performed using a universal testing machine (UTM). The corrosion test was carried out in a salt spray setup for 48 hours conforming to ASTM B117. The corrosion test setup was maintained at a temperature of $33 \pm 1^{\circ}$C with 5% NaCl. The weight loss was measured every 12 hours. The surface morphology of the corroded corten steel was studied using Jeol—scanning electron microscope (SEM). The elemental composition of the corroded surface was determined using the energy dispersive spectroscopy (EDS) attached with the SEM machine. The dry pin on disk wear test were carried out on the electroplated specimens with an applied load of 20 N, sliding velocity of 1 m/sec, and sliding distance of 300 m, at 637 rpm; for 300 seconds.

3. Results and Discussion

3.1. Chemical Composition. The elemental composition conforms to Corten Steel—ASTM 242 and is shown in Table 1. The presence of Nickel and chromium contributes to its inherent corrosion resistance. The unique blend of alloying elements gives the corten steel good mechanical properties and corrosion resistance. Furthermore, due to its low alloying content, it is a cheap deal over its functionality.

3.2. Microstructure. The microstructure shows mill normalized condition with uniform grains of pearlite in ferrite matrix. The rolling bands are observed along the longitudinal direction of the sheet. The grain size corresponds to ASTM grain size No; as per ASTM E-112. The average grain size measured as grain size No; 6 as per the standard. No stringers observed between the grain flow. The microstructure shows resolved grain boundaries and the precipitated pearlite between the grain boundaries which is shown in Figure 1. The grains of pearlite show no elongated grains.

3.3. Hardness Test. The microhardness of the corten steel in pristine condition and electroplated condition is shown in Figure 2. The Cu-coated corten steel specimens exhibited an increase of around 197.1% in microhardness when compared with the uncoated corten steel. Similarly, the Ni-coated specimens showed an increase of around 400.2% in microhardness. However, the Zn-coated specimens showed a decrease of around 47.6% in microhardness. This behavior vindicates the nature of the coating in terms of density of the coating. From these observations, it can be inferred that the Ni coating has potential to resist wear and abrasion, whereas the Zn coating has the least wear resistance.

3.4. Coating Thickness. When comparing the macrostructure images in Figure 3, and coating thickness measurements in Figure 4, the Zn coating thickness is observed to be considerably more than Cu and Ni coating. The Cu coating has the least thickness and the Ni coating higher than Cu; and the Zn coating has the highest thickness. This nonuneven distribution of coating thickness among Cu, Zn, and Ni, shall be attributed to the electro chemical reaction and the reduction potential of the respective elements involved in the electroplating process.

From (1), it could be observed that the oxygen forms hydroxyl ions when reacted with water during electroplating. The following reactions take place in nickel, copper, and zinc; equations (2)–(4), where the respective metal hydroxides are formed on the cathode (carton steel) during electro plating, as discussed elsewhere [4, 21, 22]. The reduction potential of copper is 0.337 V, nickel is −0.25 V, and zinc is −0.7628 V. By virtue of their reduction potential, zinc has greater reduction potential and hence easily gets deposited on the cathode (corten steel), whereas copper has least deposition rate and the deposition rate of nickel is moderate. This is responsible for their respective thickness of coating through the electroplating process. Hence, Zn in the presence of iron (Fe) tends to produce thick coating, as observed by other investigators [23].

Table 1: Chemical composition of corten steel (conforming to ASTM 242).

Elements	C	Si	Mn	P	S	Cr	Ni	Mo	V	W	Ti	Al	C	N	Fe
Weight (%)	0.108	0.262	0.366	0.092	0.013	0.555	0.188	0.005	0.003	<0.01	0.003	0.030	0.005	0.0341	Remainder

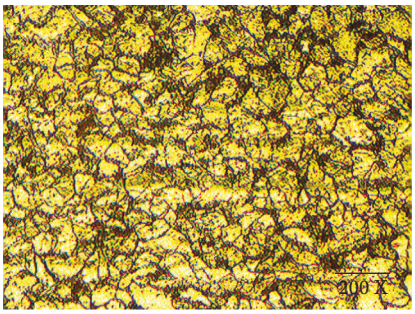

Figure 1: Microstructure of corten steel.

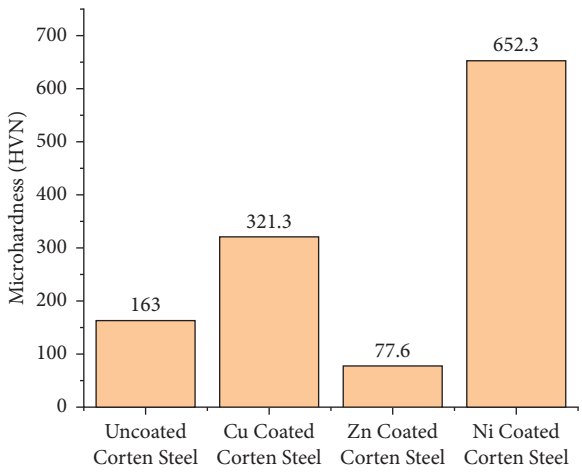

Figure 2: Microhardness of uncoated and coated corten steel specimen.

$$\frac{1}{2o_2} + 2H_2O + 2E - \longrightarrow 2OH \quad (1)$$

$$Ni^{2+} + 2OH^- \longrightarrow Ni(OH)_2 \quad (2)$$

$$Cu^{2+} + 2OH^- \longrightarrow Cu(OH)_2 \quad (3)$$

$$Zn^{2+} + 2OH^- \longrightarrow Zn(OH)_2 \quad (4)$$

3.5. Scratch Test. The scratch test is carried out to determine the vulnerability of the coating to abrasion. From Figure 5, it is clear that Zn shows a poor performance, and Cu has slightly better scratch resistance. However, Ni coating offers good scratch resistance to the underlying corten steel and thus proves that the coating is coherent and could resist abrasions and shall be durable.

3.6. Surface Roughness (R_a). The Cu coating produces a rough finish, followed by Ni-coated corten steel surface and is shown in Figure 6. The Zn-coated corten steel surface exhibits around half of the roughness R_a values when compared with other two coatings. When compared with Cu and Ni, the Zn coating produces a smooth surface with lower R_a value.

3.7. Adhesive Bend Test. A gradual linear increase in the adhesive bend strength is observed in Figure 7. This trend indicates that there is not much effect of coating on the ultimate bending strength. Furthermore, it is obvious from the Figure that the adhesion of the coating is good in Ni when compared with Cu and Zn. This behavior shall enhance the durability of the coating in functional field applications.

3.8. Corrosion Test. The weight loss due to the corrosion of Cu, Zn, and Ni is very much low when compared with the uncoated corten steel and is shown in Figure 8. This indicates that the coatings offer the corten steel surface, immunity from corrosion [24–27]. Among the three coatings, Ni had the least corrosion-induced material weight loss. The corrosion rate of Cu spiked when compared to the uncoated corten steel due to the Fe surface catalyzed reaction of Cu, which causes accelerated corrosion. The Ni-coated carton steel exhibited least corrosion rate compared to other corrosion coupons. Zn exhibited a slightly higher corrosion rate than the Ni-coated carton steel coupons. The reason behind the minimal corrosion rate of Ni-coated carton steel is its strong bonding with the substrate and its capability to plug the pores and holes in the surface of the carton steel, and thereby sealing all paths from corrosion attack.

Furthermore, the Ni has strong affinity towards Fe and hence the bonding between the corten steel substrate is good. However, in the case of Cu, this affinity is less and hence the bonding is poor, as discussed by Singh and Singh [28].

The Fe in the corten steel substrate surface triggers the chemical reduction of Cu. This surface catalyzed chemical reduction reaction is shown in (5) as formulated by investigators elsewhere [20].

$$Cu^{2+}_{(aq)} + Fe_{(s)} \longrightarrow Cu_{(s)} + Fe^{2+}_{(aq)} \quad (5)$$

It can be observed from (1), that the chemical reduction reaction results in poor adherence, and a less dense coating of Cu on the corten steel.

Zn exhibits a spontaneous dense passivation layer in the presence of Fe in the corten steel substrate, which imparts corrosion resistance to the substrate as discussed by other investigators [23].

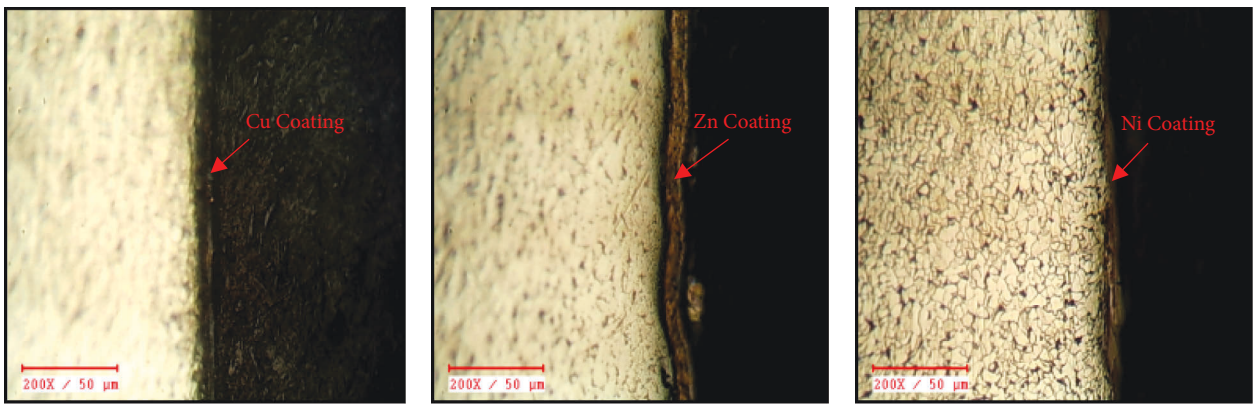

(a) (b) (c)

Figure 3: Macrostructure of electroplated corten steel (a) Cu coated (b) Zn coated (c) Ni coated.

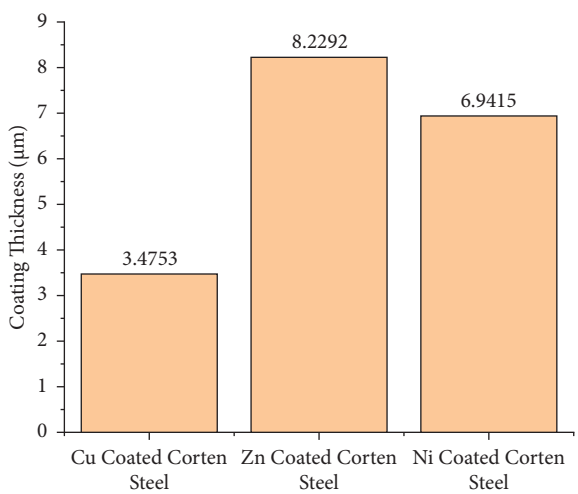

Figure 4: Coating thickness of electroplated corten steel.

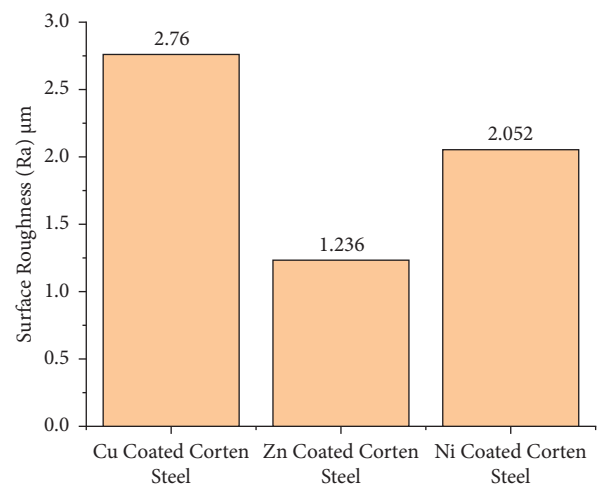

Figure 6: Roughness (R_a) of electroplated corten steel.

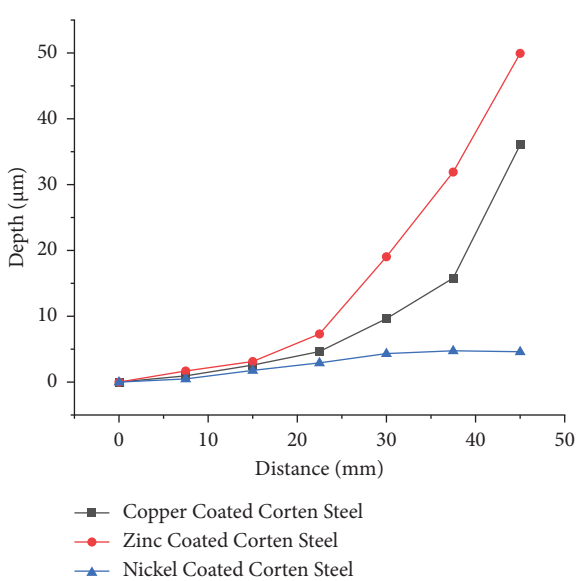

Figure 5: Scratch penetration depth of electroplated corten steel.

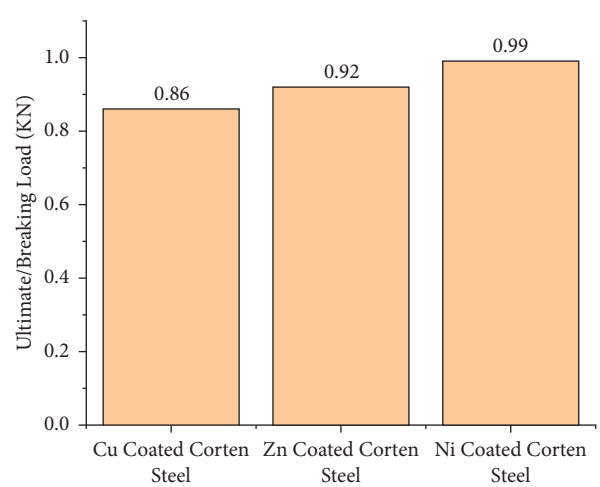

Figure 7: Adhesive bend strength of electroplated corten steel.

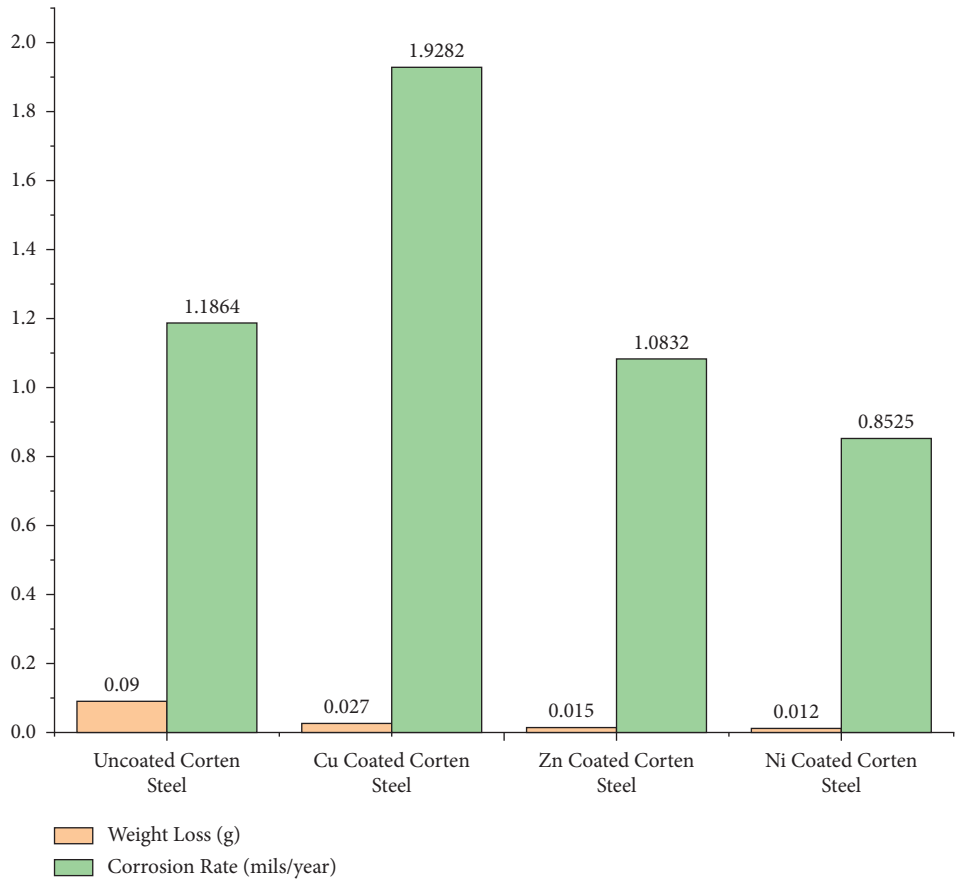

Figure 8: Salt spray test result of uncoated and coated corten steel.

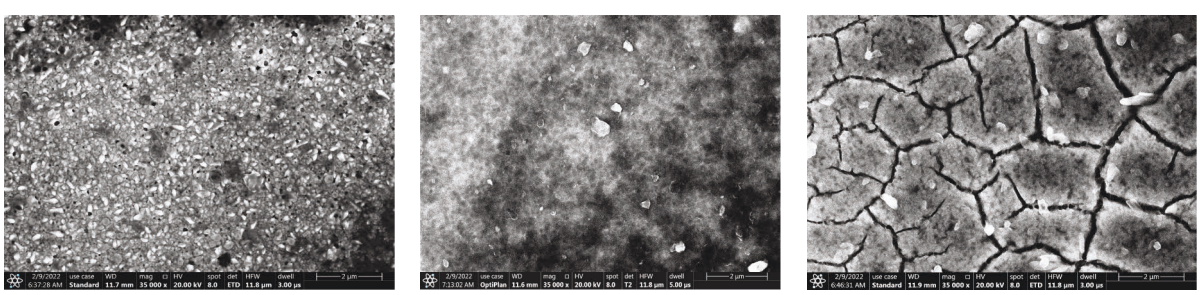

(a) (b) (c)

Figure 9: SEM surface morphology images of electroplated corten steel (a) Cu coated (b) Zn coated (c) Ni coated.

The SEM image in Figure 9(a) shows numerous pores in the Cu-coated layer leading to pitting and increased corrosion rate. The presence of pores in the Cu coating leads to leaching out of Fe and thus aggravating the corrosion and it is evident from the EDS report shown in Figure 10(a).

The SEM image in Figure 9(b) shows a uniform coating of Zn and a dense passivation layer formation, which protects the substrate from corrosion and is visible from the EDS report in Figure 10(b).

The SEM image in Figure 9(c) shows a dense passivation layer formation upon exposure to corrosive medium, which leads to good corrosion resistance and is seen from the elemental spectrum in EDS report shown in Figure 10(c), as observed elsewhere [29]. The Ni coating was effective as it was able to form a coherent layer which seals the pores in the corten steel substrate and prevents outward migration of elements from the substrate as discussed elsewhere [30–33]. The presence of Mo in the Corten steel matrix works synergistically with Ni coating to prevent growth of pits during the formation of the passivation layer as discussed by other investigators [34].

3.9. Wear Test. The inherent behavior of Zn upon electroplating, is to reduce the ductility of the steel and form incoherent coating, this in turn makes the corten steel susceptible to wear as observed by other investigators [35]. This shall be attributed to the higher wear induced weight loss of Zn-coated corten steel than the Cu and Ni-coated substrates, as shown in Figure 11.

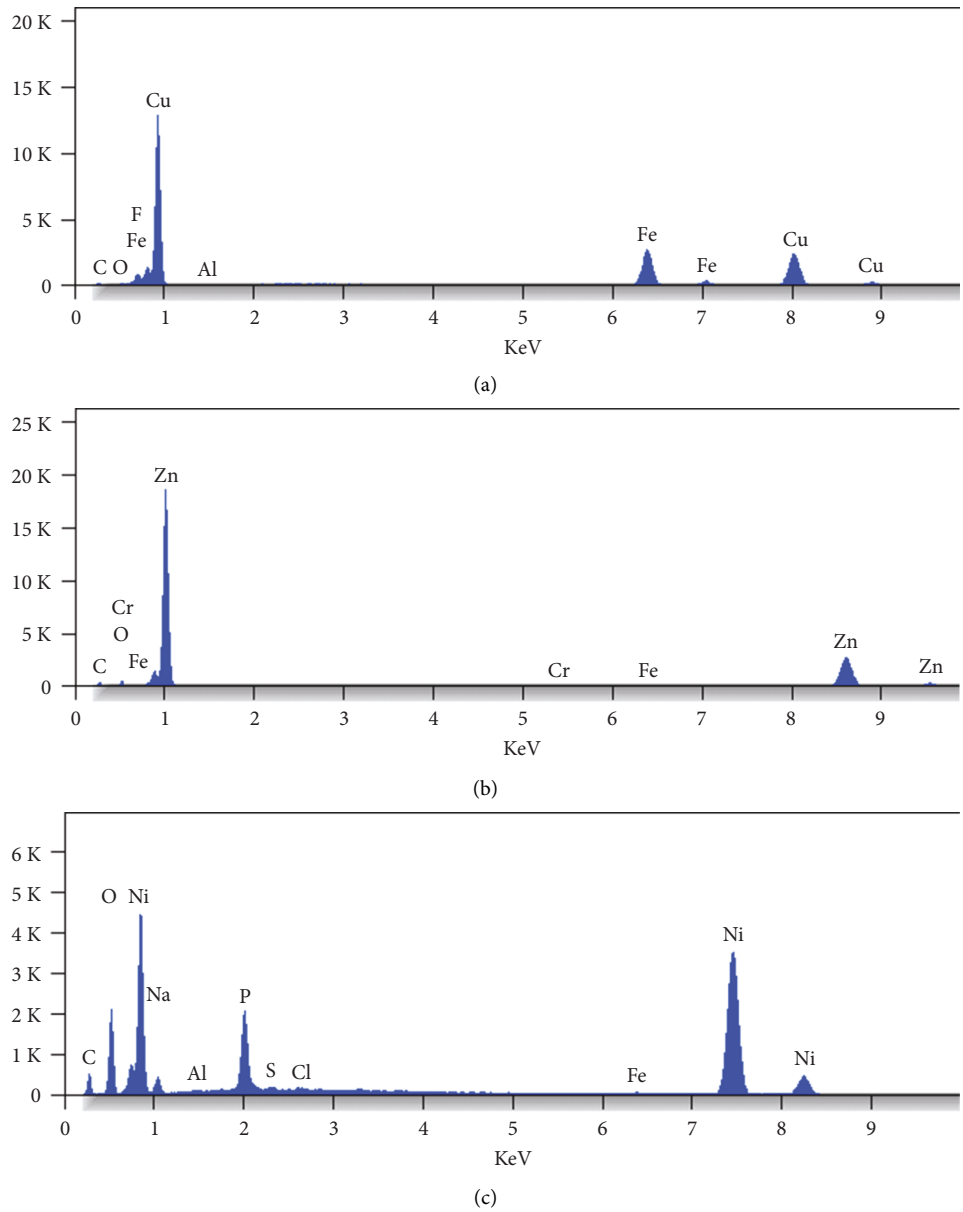

Figure 10: Energy dispersive spectroscopy (EDS) report of (a) Cu electroplated corten steel, (b) Zn electroplated corten steel, and (c) Ni electroplated corten steel.

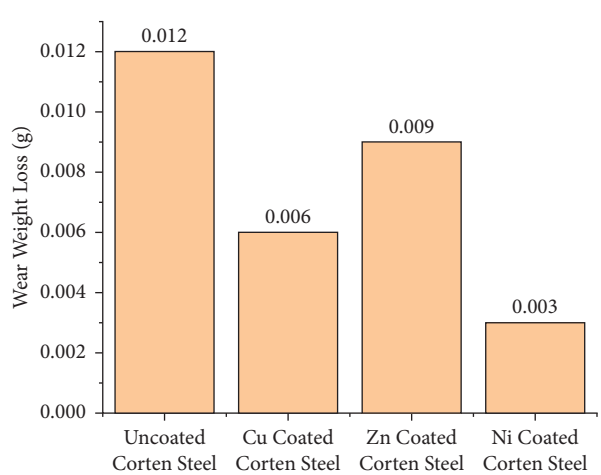

Figure 11: Wear test weight loss of uncoated and coated corten steel.

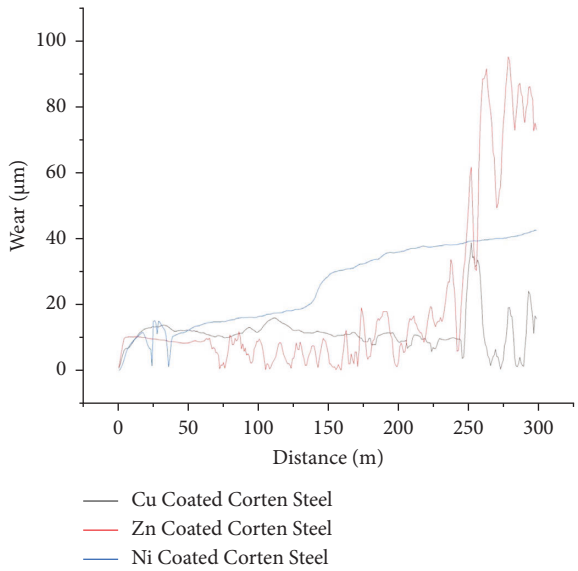

Figure 12: Wear rate of electroplated corten steel.

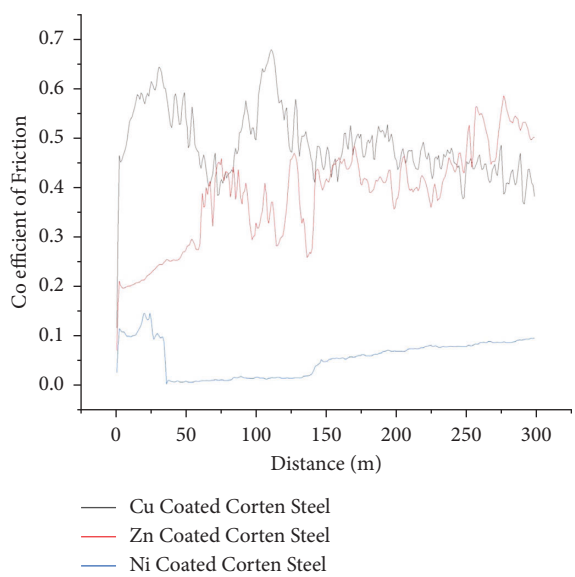

Figure 13: Coefficient of friction of electroplated corten steel.

The wear rate of the three electroplated specimens is shown in Figure 12, where it is observed that Zn exhibits a spike in wear rate; Cu has a steady trend in wear rate; and Ni has a moderate wear rate. The coefficients of friction (COF) of the three electroplated specimens are shown in Figure 13. The COF of Ni-coated corten steel specimens is less when compared with Cu and Zn-coated corten steel specimens. The low COF of Ni indicates its inherent immunity to wear and vice versa in the case of Cu and Zn-coated corten steel specimens. A similar trend is observed in the Figure 14, which depicts the wear frictional force during the wear test on the Cu, Zn, and Ni electroplated corten steel specimens. As the frictional force is lower in the Ni-plated surface, the wear also is low.

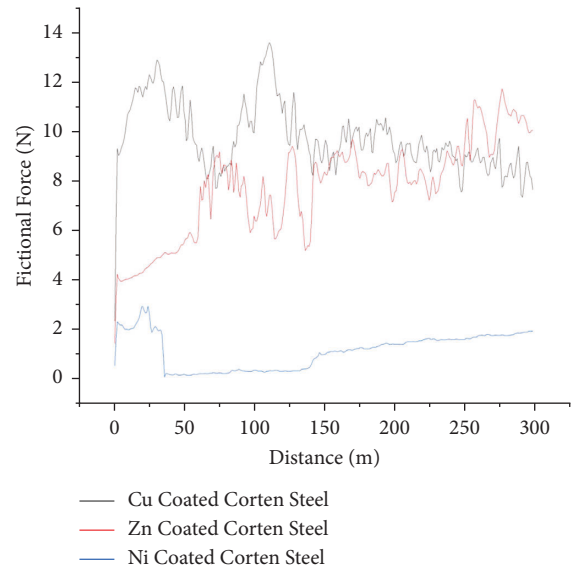

Figure 14: Wear frictional force of electroplated corten steel.

4. Conclusion

Corten steel is inherently resistant to corrosion and wear, due to its unique blend of alloying elements. As it is cheap and is the staple raw material for architectural applications, in this investigation, an effort has been taken to enhance its corrosion and wear resistance and also improve its durability, through electroplating. This study yielded good insight into the mechanism behind the improvement of properties by the electroplating of corten steel with Cu, Zn, and Ni. The Ni-coated corten steel specimens exhibited the lowest corrosion rate of 0.8525 mils/year and wear weight loss of 0.003 g, when compared with Cu and Zn-coated specimens. Ni was found to be the ideal coating that can impart resistance to corten steel–ASTM 242 from wear, abrasion, and corrosion.

Data Availability

The data used to support the findings of this study are available from the corresponding author upon request.

Conflicts of Interest

The authors declare that there are no conflicts of interest regarding the publication of this article.

Acknowledgments

The authors would like to thank the International Research Centre (IRC), Sathyabama Institute of Science and Technology, India and Metmech Engineers, India, for providing the test facilities required for this study. The authors wish to state that this study was not funded by any grant or agency. This study was carried out as part of Ph.D research work.

References

[1] C. Chiavari, E. Bernardi, C. Martini, F. Passarini, A. Motori, and M. C. Bignozzi, "Atmospheric corrosion of Cor-Ten steel with different surface finish: accelerated ageing and metal release," *Materials Chemistry and Physics*, vol. 136, no. 2–3, pp. 477–486, 2012.

[2] J. Jia, X. Cheng, X. Yang, X. Li, and W. Li, "A study for corrosion behavior of a new-type weathering steel used in harsh marine environment," *Construction and Building Materials*, vol. 259, Article ID 119760, 2020.

[3] V. K. Bupesh Raja, K. Palanikumar, R. Rohith Renish, A. N. Ganesh Babu, J. Varma, and P. Gopal, "Corrosion resistance of corten steel—a review," *Materials Today Proceedings*, vol. 46, pp. 3572–3577, 2021.

[4] C. s. Liu, F. h. Su, and J. z. Liang, "Fabrication of Co–Ni–P film with excellent wear and corrosion resistance by electroplating with supercritical CO2 emulsion," *Transactions of Nonferrous Metals Society of China*, vol. 28, no. 12, pp. 2489–2498, 2018.

[5] C. Y. Bai, J. L. Lee, T. M. Wen, K. H. Hou, M. S. Wu, and M. D. Ger, "The characteristics of chromized 1020 steel with electrical discharge machining and Ni electroplating pretreatments," *Applied Surface Science*, vol. 257, no. 8, pp. 3529–3537, 2011.

[6] H. H. Zhou, Z. W. Liao, C. X. Fang et al., "Pulse electroplating of Ni-W-P coating and its anti-corrosion performance," *Transactions of Nonferrous Metals Society of China*, vol. 28, no. 1, pp. 88–95, 2018.

[7] T. M. Meißner, C. Oskay, A. Bonk et al., "Improving the corrosion resistance of ferritic-martensitic steels at 600°C in molten solar salt via diffusion coatings," *Solar Energy Materials and Solar Cells*, vol. 227, Article ID 111105, 2021.

[8] D. J. Raj, V. K. B. Raja, T. S. Savan, and S. Babu, "Development of novel tricoated CuNiCr filler for welding weathering steel," *AIP Conference Proceedings*, vol. 2311, 2020.

[9] C. A. Huang, C. K. Lin, and Y. H. Yeh, "The corrosion and wear resistances of magnesium alloy (LZ91) electroplated with copper and followed by 1 μm-thick chromium deposits," *Thin Solid Films*, vol. 519, no. 15, pp. 4774–4780, 2011.

[10] C. A. Huang, C. K. Lin, and Y. H. Yeh, "Increasing the wear and corrosion resistance of magnesium alloy (AZ91D) with electrodeposition from eco-friendly copper- and trivalent chromium-plating baths," *Surface and Coatings Technology*, vol. 205, no. 1, pp. 139–145, 2010.

[11] J. R. Deepak, V. K. Bupesh Raja, and G. S. Kaliaraj, "Mechanical and corrosion behavior of Cu, Cr, Ni and Zn electroplating on corten A588 steel for scope for betterment in ambient construction applications," *Results in Physics*, vol. 14, Article ID 102437, 2019.

[12] M. Weinstein, C. Falconer, W. Doniger et al., "Environmental degradation of electroplated nickel and copper coated SS316H in molten FLiNaK salt," *Corrosion Science*, vol. 191, Article ID 109735, 2021.

[13] Abdel Halim, K. S., Ramadan, M., Sherif, E. S. M. et al., "Enhancement of surface and interface properties of low carbon steel by hybrid ZnO and NiO nanoparticles reinforced iin coating. Crystals," *Surface and Coatings Technology*, vol. 12, 332, 2022, 2016.

[14] Q. Zhang, Y. Feng, Z. Chen et al., "Preparation and corrosion resistance of Ni-W-cf composite coating on P110 steel," *Coatings*, vol. 12, no. 2, p. 231, 2022.

[15] C. Barile, C. Casavola, G. Pappalettera, and V. P. Kannan, "Designing a deep neural network for an acousto-ultrasonic investigation on the corrosion behaviour of CORTEN steel," *Procedia Structural Integrity*, vol. 37, pp. 307–313, 2022.

[16] M. Rohmah, P. A. Paristiawan, and T. B. Romijarso, "Effect of forging load and heat treatment process on the corrosion behavior of A588-1% NI for weathering steel application in a marine environment," vol. 26, no. 2, pp. 237–248, 2022.

[17] M. M. Karimi Azar, H. Shooshtari Gugtapeh, and M. Rezaei, "Evaluation of corrosion protection performance of electroplated zinc and zinc-graphene oxide nanocomposite coatings in air saturated 3.5 wt. % NaCl solution," *Colloids and Surfaces A: Physicochemical and Engineering Aspects*, vol. 601, Article ID 125051, 2020.

[18] W. Wu, R. Chen, Z. Yang, Z. He, Y. Zhou, and F. Lv, "Corrosion resistance of 45 carbon steel enhanced by laser graphene-based coating," *Diamond and Related Materials*, vol. 116, Article ID 108370, 2021.

[19] V. S. Protsenko and F. I. Danilov, "The corrosion-protective traits of electroplated multilayer zinc-iron-chromium deposits," *Metal Finishing*, vol. 108, no. 5, pp. 28–32, 2010.

[20] Y. Reda, A. M. El-Shamy, and A. K. Eessaa, "Effect of hydrogen embrittlement on the microstructures of electroplated steel alloy 4130," *Ain Shams Engineering Journal*, vol. 9, no. 4, pp. 2973–2982, 2018.

[21] J. Gong and G. Zangari, "Increased metallic character of electrodeposited Mn coatings using metal ion additives," *Electrochemical and Solid-State Letters*, vol. 7, no. 9, pp. 91–94, 2004.

[22] Y. I. Supriyatna, R. Noviyana, E. G. Suka, B. N. Hidayah Kambuna, S. Sumardi, and Sudibyo, "Influence of current density in Cu-Mn electroplating of AISI 1020 steel corrosion rate," *Materials Today Proceedings*, vol. 44, pp. 3289–3295, 2021.

[23] Y. I. Choi, E. S. Shin, K. Kuroda, M. Okido, and C. J. Park, "Improved surface morphology and corrosion resistance for galvannealed coatings by pre-electroplating iron," *Corrosion Science*, vol. 58, pp. 152–158, 2012.

[24] M. A. Abdulrahaman, O. K. Abubakre, S. A. Abdulkareem, J. O. Tijani, A. Aliyu, and A. S. Afolabi, "Effect of coating mild steel with CNTs on its mechanical properties and corrosion behaviour in acidic medium," *Advances in Natural Sciences: Nanoscience and Nanotechnology*, vol. 8, no. 1, Article ID 15016, 2017.

[25] S. Kordzangeneh, S. Naghibi, and H. Esmaeili, "Coating of steel by alkyd resin reinforced with Al2O3 nanoparticles to improve corrosion resistance," *Journal of Materials Engineering and Performance*, vol. 27, no. 1, pp. 219–227, 2018.

[26] H. Cheng, B. Xu, J. Zhao et al., "High-performance nickel coating on SLM 316L stainless steel processed by jet electrochemical machining and jet electrodeposition," *Proceedings of the Institution of Mechanical Engineers - Part B: Journal of Engineering Manufacture*, vol. 236, no. 4, pp. 462–472, 2022.

[27] D. Chu, Z. Li, K. Yao et al., "Studying the strengthening mechanism and thickness effect of elastomer coating on the ballistic-resistance of the polyurea-coated steel plate," *International Journal of Impact Engineering*, vol. 163, Article ID 104181, 2022.

[28] S. Singh and H. Singh, "Effect of electroplated interlayers on bonding mechanism of cold-sprayed copper on SS316L steel substrate," *Vacuum*, vol. 172, Article ID 109092, 2020.

[29] H. H. Sheu, H. B. Lee, S. Y. Jian, C. Y. Hsu, and C. Y. Lee, "Investigation on the corrosion resistance of trivalent chromium conversion passivate on electroplated Zn–Ni alloy," *Surface and Coatings Technology*, vol. 305, pp. 241–248, 2016.

[30] P. Niranatlumpong and H. Koiprasert, "Improved corrosion resistance of thermally sprayed coating via surface grinding and electroplating techniques," *Surface and Coatings Technology*, vol. 201, no. 3–4, pp. 737–743, 2006.

[31] Q. Zhao, S. Geng, G. Chen, and F. Wang, "Comparison of electroplating and sputtering Ni for Ni/NiFe2 dual layer coating on ferritic stainless steel interconnect," *Corrosion Science*, vol. 192, Article ID 109837, 2021.

[32] Y. Zhang, "Mechanical properties and corrosion resistance of pulse electrodeposited Ni-B/B4C composite coatings," *Surface and Coatings Technology*, vol. 421, 2021.

[33] Y. Li, P. Song, W. Wang, M. Lei, and X. Li, "Microstructure and wear resistance of a Ni-WC composite coating on titanium grade 2 obtained by electroplating and electron beam remelting," *Materials Characterization*, vol. 170, Article ID 110674, 2020.

[34] S. Mosayebi, M. Rezaei, and Z. Mahidashti, "Comparing corrosion behavior of Ni and ni-mo electroplated coatings in chloride mediums," *Colloids and Surfaces A: Physicochemical and Engineering Aspects*, vol. 594, Article ID 124654, 2020.

[35] T. Mehner, I. Scharf, P. Frint et al., "Hydrogen embrittlement of a quenching and partitioning steel during corrosion and zinc electroplating," *Materials Science and Engineering A*, vol. 744, pp. 247–254, 2019.

Hindawi
Advances in Materials Science and Engineering
Volume 2022, Article ID 3002481, 9 pages
https://doi.org/10.1155/2022/3002481

Research Article

Fabrication and Analysis of the HLM Method of Layered Polymer Bumper with the Fracture Surface Micrographs

P. V. Narashima Rao,[1] P. Periyasamy,[1] A. Bovas Herbert Bejaxhin,[2] E. Vetre Selvan,[3] N. Ramanan,[4] N. Vasudevan,[5] R. Elangovan,[6] and Mebratu Tufa[7]

[1]*Department of Mechanical Engineering, St. Peter's Institute of Higher Education and Research, Avadi, Chennai, India*
[2]*Department of Mechanical Engineering, Saveetha School of Engineering, SIMATS, Thandalam, Chennai, India*
[3]*Department of Mechanical Engineering, Sri Sairam Engineering College, West Tambaram, Chennai, India*
[4]*Department of Mechanical Engineering, PSN Engineering College, Tirunelveli, India*
[5]*Department of Electronics and Communication Engineering, K. Ramakrishnan College of Technology, Samayapuram, Trichy, India*
[6]*Department of Mechanical Engineering, Mookambigai College of Engineering, Kalamavur, Pudukkottai 622502, Tamil Nadu, India*
[7]*Department of Mechanical Engineering, Faculty of Manufacturing, Institute of Technology, Hawassa University, Hawassa, Ethiopia*

Correspondence should be addressed to Mebratu Tufa; mebratu.tufa@hu.edu.et

Received 9 July 2022; Revised 24 August 2022; Accepted 29 August 2022; Published 4 October 2022

Academic Editor: Vijayananth Kavimani

Bumpers are essential components that shield passenger cars from slow-speed collisions. Automobiles have them mounted on the front and rear ends. It is believed that bumpers would be crucial in avoiding or restricting damage to automobiles. Various composite material combinations are being researched when a car frontal accident occurs in light of the impact requirements. By comparing it to the parent material, the unique hybrid fibre-metal laminate production clarifies problems such as deformation and stress. This research focuses on identifying the hybrid material composed of basalt fibre with aluminium and glass fibre combinations, inducing it with the properties of the existing parent material and fusing it together to form a laminated composite. It also focuses on identifying its specific features and mapping them with those of the existing ones. This project's peculiarity strives to give the best bumper with a range of deformation between 0.017378 m and 0.03114 m for the 38 MPa tensile strength with a maximum stress prediction of 2.424×10^2 MPa that shows advantageous in day-to-day operations, and this is done by comparing simulation results.

1. Introduction

The world's attention is currently concentrated on rapid breakthroughs in industries such as aerospace, space, automotive, electronics, and defence, as well as infrastructure and power generation. The automotive industry has emerged as a major economic booster for countries all over the world. Automobile manufacturers are attempting to introduce light-weight, fuel-efficient vehicles to the market. As a result, there is ongoing research towards lowering car costs by adopting light-weight composites that have similar mechanical properties to metal parts used in automobiles. The current research focuses on the usage of aluminium and basalt fibre composites in the manufacture of automotive bumpers. This aluminium basalt fibre composite is expected to absorb lateral or transverse loading caused by accidents or intentionally occurring occurrences. It is inferred that the fibre metal laminate (FML) exhibits greater bonding strength, exhibiting superior properties [1]. It is noted how composite lamination should be performed [2]. It explains

how reinforcement happens in the FML and explains its characteristics [3]. The paper explains the review of different FML conditions [4]. It explains the conceptual and computational approaches of the FML and how it is performed [5]. It explains the analysis and the methodology adopted to analyse the bumper in Ansys software, and it explains the 3-point bending approach to bumper analysis [6]. For a bumper barrier impact, it explains the presence of an equivalent curved-beam element for the analysis of the bumper [7]. It describes how to analyse a bumper's whole frontal crash barrier and half frontal impact barrier. It also explains how to use ANSYS explicit dynamics for crash analysis [8]. It describes the impact analysis on the wind using finite element analysis with Abaqus software and an auto-towing hook with a steel ball at the end. It describes the parameters for designing and analysing an automotive front end, such as material, thickness, shape, and impact conditions of the beam with bumpers [9, 10]. The tribological behaviour of nonferrous-related material composites has been verified by the experimental verification of wear resistance among the Al6063 metal matrix composite by using the single pass ECAPA route [11]. Better particulate dispersion and more bondage levels can be achieved frequently by using the squeeze casting technique [12]. The defects in casting and grain boundary strengthening have been found through SEM and NDT methods of testing [13]. The tensile and flexural characteristics of natural fibre-reinforced polymer composites have been the focus of Ngo et al.'s research [14]. In this investigation, polylactic acid (PLA), polystyrene (PS), and epoxy (EP) were employed as the matrices to manufacture composites by using Kenaf (KE) and palm empty fruit bunch fibre (EFB) with volume fractions, Vf, of 20, 40, and 60%. Because of the high proportion of fibre, the tensile strength was at least 29 MPa. According to Luis Angel Lara-González et al.'s discussion in [15], the tensile strength was around 22.88 MPa and reached a high of 56.47 MPa. The mixed fibre composite made of basalt and aluminium has a minimum strength of 38 MPa. [16] Even while this method appears to be successful, it ignores important mechanical characteristics such as fracture toughness. Hybrid PFC has much lower fracture toughness than dentine which has been discussed by Manhart et al.

References [17] Kim and Okuno have discussed that dentine is made up of collagen fibres encased in a hydroxyapatite matrix, whereas hybrid PFC is made out of filler particles embedded in a resin matrix. High fracture toughness materials can more effectively withstand crack initiation and spread. As a result, flexural strength and fracture toughness are crucial factors in determining how long a dental material will last. [18, 19] Garoushi et al. and Lassila et al. have conferred that due to their near resemblance to dentine in terms of microstructure and mechanical characteristics, composite resins reinforced with millimeter-scale short glass fibres (SFRC) are currently the most intriguing materials [20]. It has been established that the material's fibre and matrix-related properties can be used to explain the material's improved resistance to crack propagation also known as fracture toughness, and flexural strength has been identified by St. Georges et al. [21] Lastumäki et al. have discussed that the UDMA cross-linked matrix, which is plasticized to some extent by using the linear PMMA polymer chains, boosts the flexural strength of composite resin.

In this research work, the absence of strength in metal matrix composites can be determined, and it has been replaced with a novel method of composite preparation, especially from the categories of fibre reinforcements. For superior mechanical qualities, basalt fibre/glass fibres were mixed with nonferrous aluminium alloys to create hybrid polymer composites. The combined form of crash test and deformation simulations can be used with the novelty function, and their comparisons are carried out here. Experimental results based on predictions have been taken into account. These elevated values of tensile and flexural strengths have been obtained, which can be useful for the sustainable development of the fibre-oriented composite. In addition, the applications are huge in size for the implementation of light-weight, high-strength materials which can be used for automotive and aircraft body applications. The simulations are held in hands to step up to the next level based on their predicted stresses and deformations, and they can fulfill the future scope.

2. Materials and Methods

2.1. Fabrication of FML with Layers. The hand lay-up method of composite processing is the most basic. This strategy also has a low infrastructure need. The processing steps are simple to follow. To begin with, a release gel is sprayed on the mould surface to keep the polymer from sticking. Reinforcement in the form of woven mats or chopped strand mats is trimmed to meet the dimensions of the mould and then put on the surface of the mould. The liquid thermosetting polymer is then thoroughly mixed with a predetermined hardener (curing agent) and poured onto the surface of the previously prepared mat in the mould as shown in Figure 1. The ASTM D 790 criteria are followed in the preparation of the flexural specimens. The test specimens of each laminate of aluminium basalt fibre reinforced epoxy composites are manufactured and evaluated by using the same UTM to apply the three-point flexural stress. The 3-point flexural test is the most frequent flexural test, and it was employed in this experiment to determine the composite materials' bending strength. Placing the test specimen in the UTM and applying force to it until it fractures and breaks is the testing procedure. The result of the specimen's flexural strength is seen. Table1 shows the results of the experiments. A hand layup is depicted in Figure 2. The capital and infrastructure needs are reduced as compared to other alternatives. The manufacturing rate of treated composites is reduced, and attaining a large volume fraction of reinforcement is difficult.

2.2. Tensile Testing. The characteristics of fibres and their orientation, which determine the quality of the produced composite laminate, are influenced by a variety of factors.

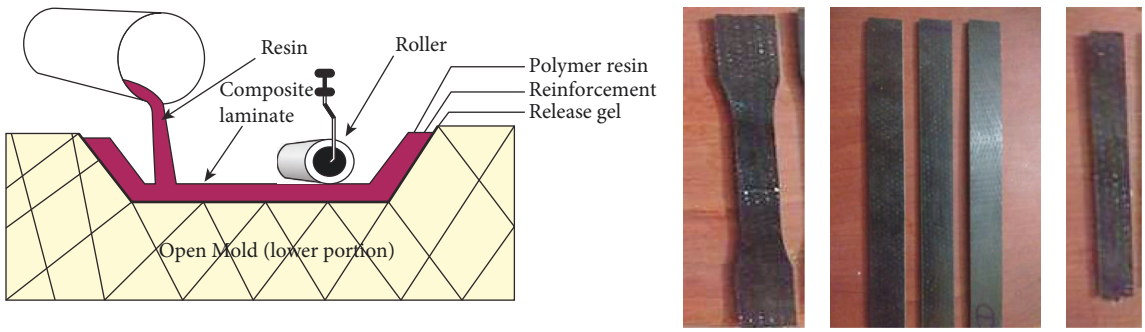

(a) (b) (c) (d)

Figure 1: (a) Hand lay-up method of fibre metal laminate [22], (b) specimen for tensile testing, (c) samples of the impact test, and (d) sample for the flexural test.

Table 1: experimental value for flexural strength.

Specimen	Sample (KN)
Basalt fibre	161
Basalt and aluminium fibre	192
Glass fibre	120
Aramid fibre	192

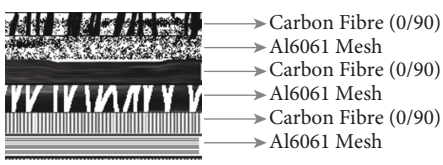

Figure 2: FML layers of the laminate.

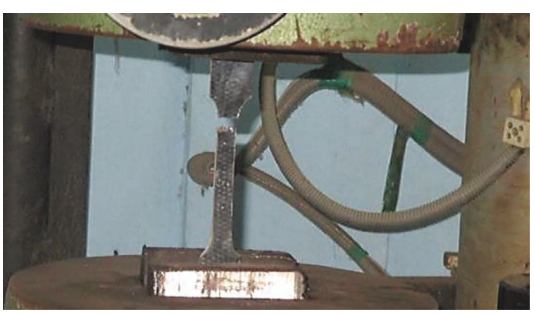

Figure 3: UTM tensile testing of the sample specimen.

The impact of fibre parameters is discussed further down. The dimensions of the tensile test specimens are taken into consideration. It is made in accordance with ASTM-D638 methods and standards. The laminate specimen is used to test the tensile behaviour of composite laminates. On the Universal Testing Machine (UTM), as depicted in Figure 3, the tensile test is carried out by applying load to the specimen until it fails, and the results are recorded. The constructed laminate as shown in Figure 3 was put through a tensile test in accordance with ASTM-D638. After the test, the trials provided tensile strength results. Table 2 shows the results of the experiments.

Table 2: experimental value for tensile strength.

Specimen	Tensile load (KN)	Tensile strength (N/mm^2)
Basalt fibre	3.2	34
Basalt fibre and aluminium fibre	3.6	38
Glass fibre	2.8	22
Aramid fibre	3.8	44

Figure 4: Flexural testing of the specimen sample.

2.3. Flexural Testing. Flexural specimens are prepared in accordance with ASTM D 790 standards. Each laminate of aluminium basalt fibre reinforced epoxy composite is fabricated and assessed by using the same UTM to apply the three-point flexural stress. The 3-point flexural test is the most common flexural test, and it was used in this experiment to evaluate the bending strength of the composite materials, as shown in Figure 4. The testing process consists of placing the test specimen in the UTM and exerting force on it until it fractures and breaks. The flexural strength of the specimen is demonstrated, and the outcomes of the trials are shown in Table 1.

2.4. Impact Testing. Impact test specimens are constructed to the necessary dimensions in accordance with the ASTM-A370 standard as depicted in Figure5. During the testing procedure, the test specimen is inserted into the UTM. The

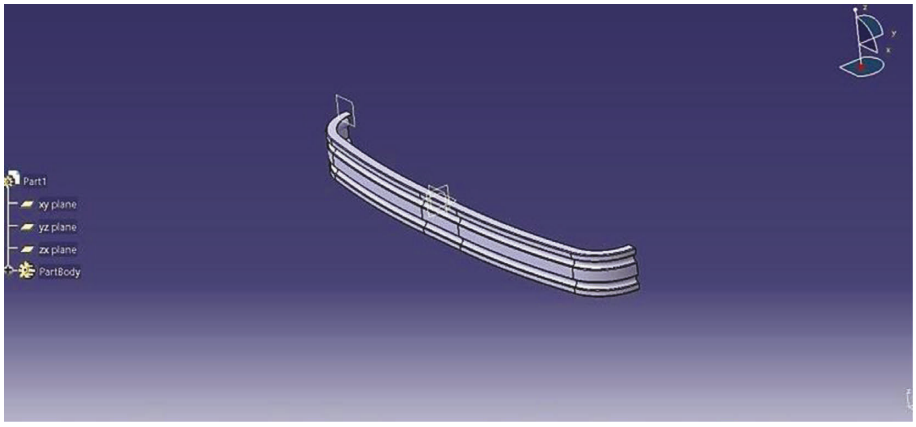

Figure 5: CATIA V5 model of the bumper.

Figure 6: Impact testing of the sample specimen.

Table 3: Experimental values of absorbed energy using the impact test.

Specimen	Absorbed energy (J)
Basalt fibre	7
Basalt and aluminium fibre	8
Glass fibre	7
Aramid fibre	14

specimen must be inserted into the testing apparatus, allowing the pendulum to fracture the specimen as mentioned in Figure 6. The impact test can simply determine the maximum energy necessary to shatter the material. The maximum energy absorbed by the various specimens, particularly aramid fibre, has been determined to be 14 J, as shown in Table 3.

3. Design and Analysis of the Modelled Bumper

3.1. Modelling of the Bumper. CATIA (computer-assisted three-dimensional interactive application) is a multiplatform computer-aided design (CAD), computer-aided manufacturing (CAM), and computer-aided engineering (CAE) software package developed by Dassault Systemes. CATIA has unrivalled capabilities for modelling any product in the context of its real-world behaviour: design in the age of experience. System architects, engineers, designers, and all other stakeholders may define, conceive, and shape the linked world. To build 3D CAD models of the aluminium specimen as shown in Figure 5, CATIA V5 is utilized.

The finite element approach is a numerical approximation method in which a complicated structure is broken down into a number of little bits or pieces, which are referred to as finite elements. These microscopic elements are linked together by nodes, which are small points that connect them with the incorporation of a convergence type of mesh generation. The finite element approach is also known as structural analysis because it uses matrix algebra to solve simultaneous equations. It is quickly becoming the major analytical tool for designers and analysts.

3.2. Stress and Total Deformation. Total deformation and directional deformation are phrases that are used interchangeably in finite element methods, regardless of the software employed. Directional deformation refers to the movement of the system along a certain axis or in a user-defined direction. The total deformation is the vector sum of all the directional displacements of the systems. Figures 7(a) and 7(b) show a detailed comparison of the deformation levels of the basalt fibre bumper and basalt aluminium fibre under 3-point bending. The complete deformation of the basalt fibre bumper under 3-point bending is shown in Figures 7 and 8.

The comparison between the tensile strength and load for various fibre and composite materials is mentioned in Figure 9. Here, the tensile strength of 44 N/mm^2 is recorded in aramid fibre under a load condition of 3.6 kN. In comparison, the tensile strength of glass fibre, basalt, and aluminium fibre composites was attained with higher entities. The loads have tensile strengths of 3.6 kN and 3.8 kN, respectively, which have been identified through the peaks obtained in Figure 9. If the load becomes a maximum of 3.5 kN or greater, the basalt fibre and aluminium fibre composites produce higher tensile strength values.

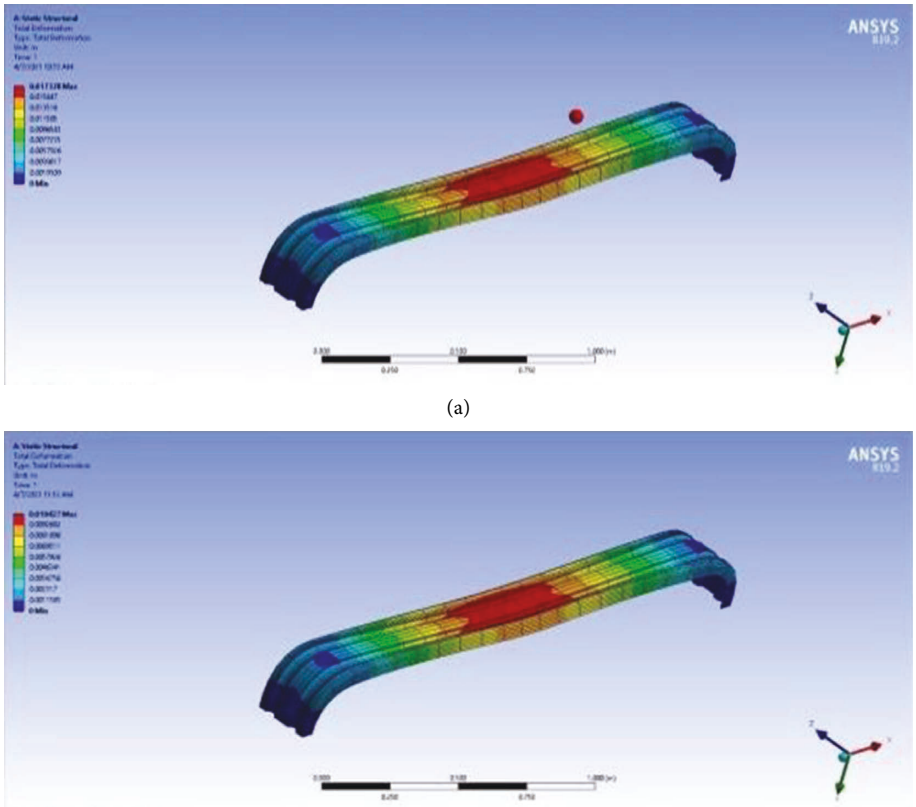

(a)

(b)

Figure 7: Total deformation of (a) basalt fibre bumper and (b) basalt aluminium fibre.

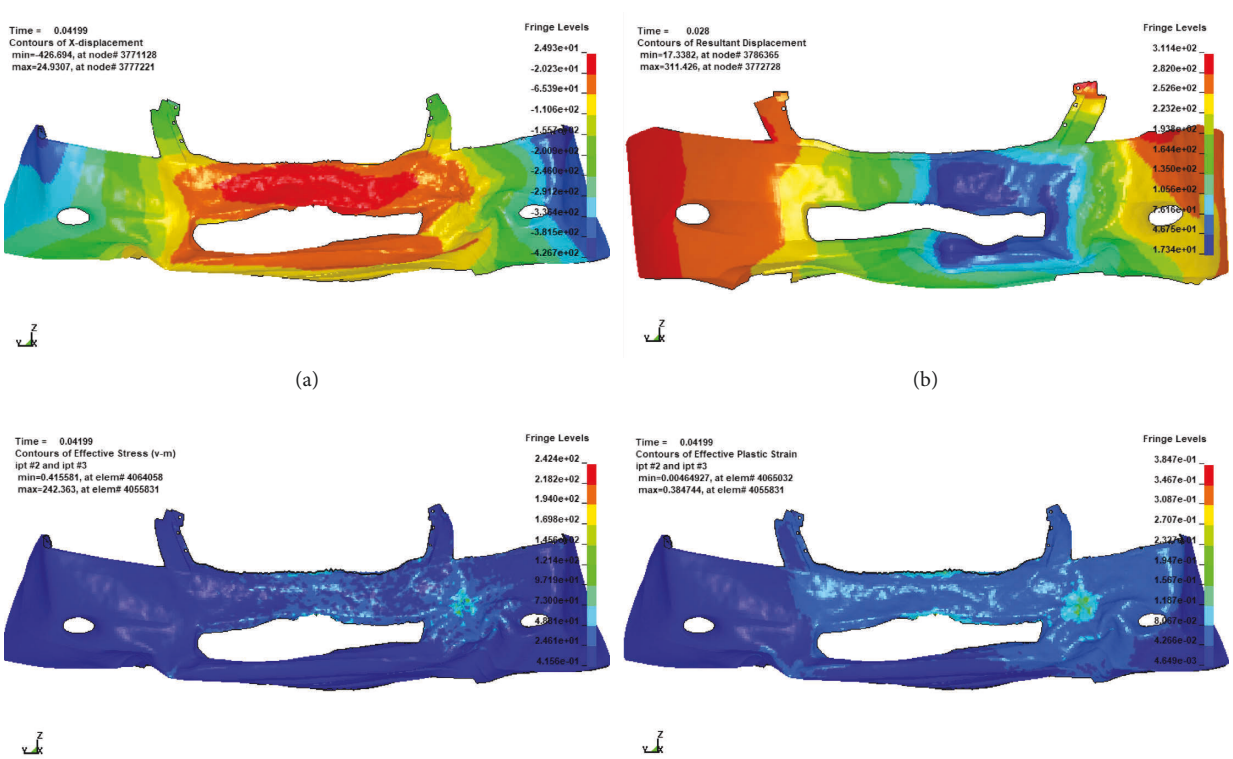

(a) (b)

(c) (d)

Figure 8: Crash test simulation results by using FEA (a) resultant displacement of the frontal crash of basalt fibre (b) resultant displacement of the frontal crash of basalt fibre with aluminium (c) effective von Mises stress (d) effective plastic strain.

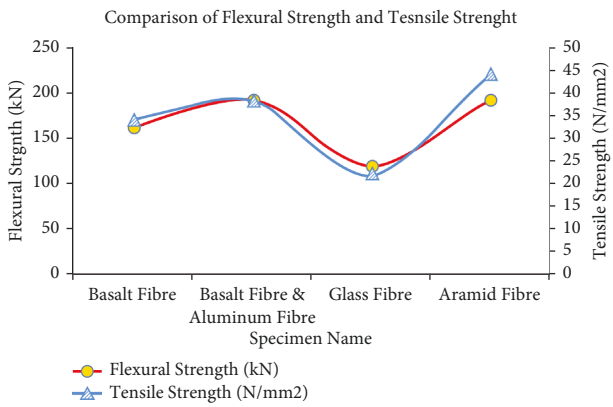

Figure 9: Comparison of flexural strength and tensile strength.

The strong bonding of fibre reinforcement can provide an effective bending moment while also withstanding more fluctuations. The material contribution was obtained among the layerwise specimens, which can reveal remarkable strength in both tensile as well as impact testing. Figures 7 and 8 show that the curvature area of the basalt aluminium fibre bumper showed more and less deformation of 0.03114 and 0.017378 m. More concentration of stress was obtained at its centre. A higher stress of 2.424×10^2 MPa can be obtained by using the basalt fibre bumper during the frontal crash simulation. [14] Ngo et al. have focused on the tensile and flexural properties of natural fibre reinforced polymer composites. In this study, Kenaf (KE) and palm empty fruit bunch fibre (EFB) with volume fractions of Vf of 20%, 40%, and 60% were used in this study to prepare composites that comprised polylactic acid (PLA), polystyrene (PS), and epoxy (EP) as the matrices. The tensile strength was attained at a minimum of 29 MPa due to the percentage of fibre addition up to 20% according to the discussion of [15] Lara-González et al. The tensile strength was found to be nearly 22.88 MPa, with a maximum of 56.47 MPa. Comparatively, the basalt fibre and aluminium combined fibre composite has attained a 38 MPa as minimum. It can withstand more tensile loads compared with other fibre composites.

A crash test is a type of destructive testing that is frequently carried out to guarantee that crashworthiness and crash compatibility standards are met for various means of transportation, automobile safety, or associated systems and components. The front panel body of the vehicle can be involved in this crash test. The real-time structural damages can be verified through the simulation platform by applying some trail loads for the required boundary conditions. The body dynamics and materials involved in any automotive components based upon the unchanging or nonidentical pressures can be analysed through this software tool.

The impacts of strain rate sensitivity of CFRE, BFRE, and their mixes were investigated, according to Yao et al. [23]. Cross-sections of the cracked specimens were analysed. The findings showed that all of the hybrid composites were sensitive to the stacking order. In the quasistatic condition, the peak forces of two hybrid constructions were between those of basalt fibre reinforced composite and carbon fibre reinforced composite, with H1 and H2 improved by 3 MPa and 29 MPa, respectively, compared to BFRE. [24] According to Zuzana Marcalikova et al., the augmentation of fibre content in the composite construction boosted tensile strength. [25] Tensile tests revealed that laminates with modified F584-epoxy matrix had better mechanical characteristics than laminates with F155-epoxy matrix. The F584/PW family has the greatest tensile strength, while the F584/8HS family has the highest modulus.

The frontal crash of the polymer bumper has been identified with the simulation outcomes such as deformation and von Mises stress. The resultant displacement of the front crash of the bumper shown in Figure 8(a) indicates that more deformation 2.493×10^{-2} mm has occurred at the exact centre region of the basalt fibre composite front bumper. Similarly, as shown in Figure 8(b), a reasonable deformation of 3.114×10^{-2} mm has been identified for the aluminium-combined basalt fibre bumper. In addition to that, the effective von Mises stress and strain were obtained for the applied load, which can be considered for the fixed boundary conditions. Because of the safe load and its extreme level, this design fails. Utilizing CATIA V5 simulation studies, the composite bumper solid model with the simply supported type was developed utilizing the parameters for determining the safe design and loading. Since both ends are fixed, there is zero displacement. In this research investigation, the static mode of analysis was used.

Load: 3 KN to 5 KN (based on tensile, impact, and flexural strength)

Model: composite bumper solid model (CATIA-V5)

Type of model: simply supported

Boundary conditions: both the ends of the bumper as the fixed position for static and front crash test (zero displacement at the fixed ends)

Figure 10 depicts the relationship of tensile strength to tensile load for the basalt fibre, basalt fibre and aluminium fibre composite, glass fibre, and aramid fibre. The triangular yellow marker represents the range of tensile strength, which has been connected with the curved red lines. The bar represented the value of the tensile load acting on the specimen while conducting the test. Tensile properties vary depending on the closeness of the polymer structure in the specimen. Basalt and glass fibre, in particular, were recognized as having no previous reinforcements. However, in aramid and basalt-aluminium fibres, the impact of homogeneous reinforcements is combined. This might be demonstrated by the excellent tensile results indicated in Figure 11 microstructures.

Due to the changes in material composition or composite matrix, nearly identical ranges of flexural and tensile strength have been attained. Probably, the basalt fibre and aluminium combined form of the specimen have attained a secondary level of better outcomes in tensile strength. The aramid fibre was observed as a robust material composite which will be used for more applications. On the other hand, comparative analyses have been carried out over the same materials for the parameters of flexural strength and tensile

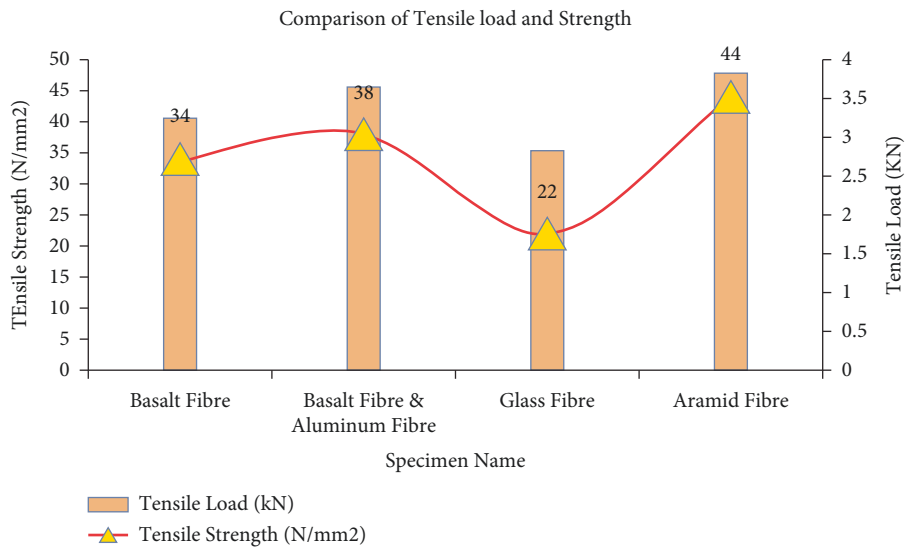

Figure 10: Comparison of tensile strength for different tensile loads.

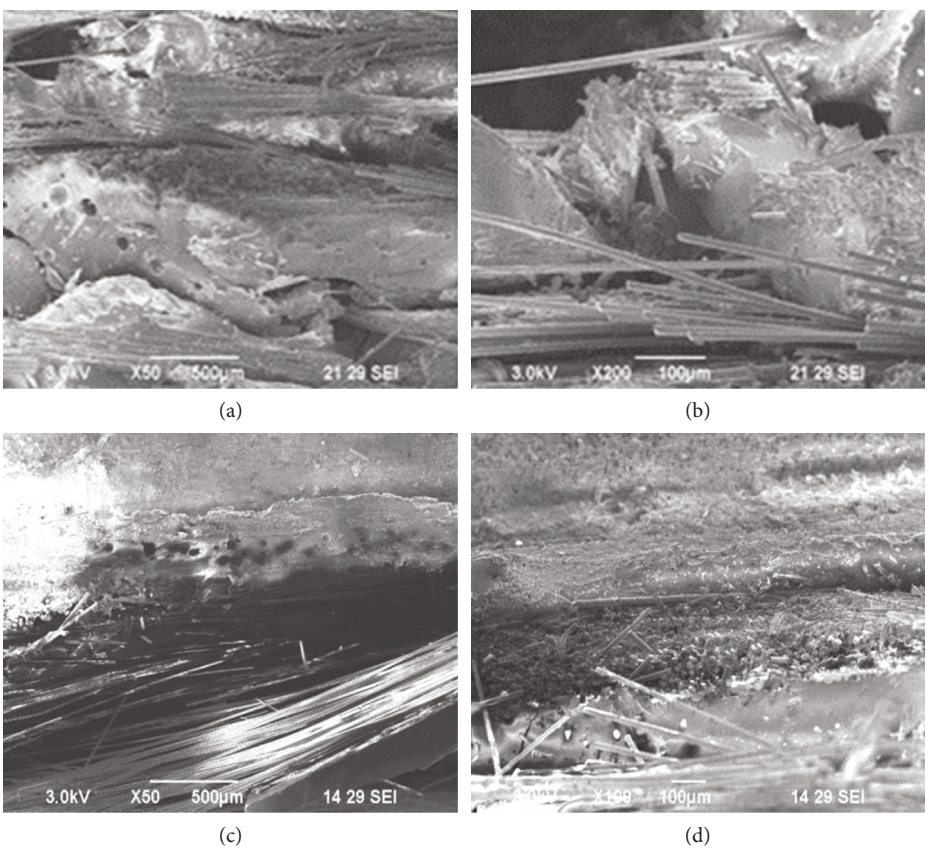

Figure 11: SEM images of fractures and surfaces of the FLM layer composite of (a) basalt fibre, (b) basalt-aluminium fibre, (c) glass fibre, and (d) aramid fibre.

strength. The blue smooth line curve represents the tensile strength, and the red-lined yellow bullets depict the flexural strength. Figure 9 depicts the intermittent coincident between tensile and flexural strength.

The exact same coincidence happened for the basal fibre and aluminium fibre, which shows that it can withstand higher load applications with acceptable flexural and equivalent tensile strength. The same conditions are suitable

which have been obtained for thearamid fibre with elevated tensile properties.

4. Microstructural Evidence of Fracture Surface Images

The topography of the surface is determined by the interaction between the tool and the properties of the material being machined. Mechanical testing showed that during the extruded profile, the tested material's mechanical properties changed. Microscopical analysis of the material's structure revealed the heterogeneity of the composite and the presence of small fractures where the wood particles and polymer matrix contacted one another. SEM creates image samples that are used to examine the specimen's topography and morphology. It depicts the cracked surfaces of test specimens that are examined by using a scanning electron microscope (SEM). The relationship between the tool and the quality of the machined material determines the topography of the surface. Mechanical tests demonstrated that the material's mechanical characteristics change throughout the extruded profile. The composite's heterogeneity was revealed by microscopic examination of the material's structure, which also revealed the presence of tiny fissures at the points where the wood particles and polymer matrix came into contact.

The damage caused by the specimen's tensile test is depicted in Figure 11. Various magnification levels have been maintained for taking these observations as 50X, 100X, and 200X with a size factor of 100 μm and 500 μm, respectively. Simple basalt fibre having major white spots indicated as a pure form of basalt fibre. Figure 11(b) clearly shows that fibre breakage occurs in basalt-aluminium fibre as a result of a sheer action that is not uniform across the surface due to the presence of twisted fibres that oppose each other in the opposite direction, eventually achieving stability. Figure 11(c) shows that the distribution of brittle-rich glass particles is clearly indicated bythe dark and closely spaced lines structure. Figure 11(d) depicts the particle distribution of aramid fibres by using solid coloured even surfaces. A scanning electron microscope was used to create the images. A ductile fracture is depicted in this illustration. Porosity is caused by the generation of exothermal heat.

5. Conclusion

Automobile manufacturers are attempting to introduce light-weight, fuel-efficient vehicles to the market. As a result, there is ongoing research towards lowering car costs by adopting light-weight composites that have similar mechanical properties to metal parts used in automobiles. The following conclusions have been made:

(i) The current research focuses on the usage of aluminium and basalt fibre composites in the manufacture of automotive bumpers. This aluminium glass fibre composite is expected to absorb lateral or transverse loading caused by accidents or intentionally occurring occurrences.

(ii) The performance of composite materials is examined using a three-point bending technique in this study. It is a type of internal mode failure caused by fibre layer separation in a composite laminate. The delaminated specimen with its voids and blowholes is shown in the illustration. It has also been discovered that during the separation of layers, the medium's adhesion is not greatly changed, resulting in less damage to the laminate.

(iii) The specimen was subjected to a two-fold shear test, which resulted in this damage. Because of the twisted fibres resisting each other in the opposite direction, the shear effect causes fibre breakage that is not uniform over the surface, so it achieves a stable condition.

(iv) In CATIA V5, the proposed fibre metal laminate of basalt and aluminium was conceived as a bumper. The design was loaded into ANSYS APDL software, and a three-point bending technique was used on both the basalt fibre bumper and the basalt-aluminium fibre bumper. Equivalent stress and deformation values were obtained and compared.

Data Availability

The data used to support the findings of this study are included within the article. Should further data or information be required, these are available from the corresponding author upon request.

Disclosure

It was performed as a part of the Employment Hawassa University, Ethiopia.

Conflicts of Interest

The authors declare that they have no conflicts of interest.

Acknowledgments

The authors would like to thank the Saveetha School of Engineering, SIMATS, Chennai 602 105, Tamil Nadu, India, for their excellent support for the submission of their papers.

References

[1] E. A. TamerSinmazçelik and M. ÖzgürBora, "OnurÇoban A Review: Fibre Metal Laminates," *Background, Bonding Types and Applied Test Methods*, vol. 32, 2011.

[2] K. Kavitha, R. Vijayan, and T. Sathishkumar, "Fibre-metal laminates," *A review of reinforcement and formability characteristics*, vol. 22, 2020.

[3] R. Khan, "Fiber Bridging in Composite Laminates," *A Literature Review*, vol. 229, 2019.

[4] M. Chandrasekar, M. R. Ishak, M. Jawaid, Z. Leman, and S. M. Sapuan, "An Experimental Review on the Mechanical Properties and Hygrothermal Behaviour of Fibre Metal Laminates," *Journal of Reinforced Plastics and Composites*, vol. 36, 2016.

[5] Kreja Ireneusz, "A Literature Review on Computational Models for Laminated Composite and sandwich Panels," *Open Engineering*, vol. 25, 2011.

[6] P. B Biradar and Kajol Kamat, "Dhammadeep Sarkate , Sagar Jamdade, Design and analysis of Bumper," vol. 34, 2018.

[7] D.-K. Park, "Bumper Impact Using the Dynamically Equivalent Beam Approach," *International Journal of Automotive Technology*, vol. 25, 2011.

[8] M. Karthikeyan, M. P. Jenarthanan, R. Giridharanl, and K. Shunmugesh, "Investigation on Crash Analysis of a Frontal Car Bumper," *Transactions of the Indian Institute of Metals*, vol. 12, 2011.

[9] A. Calienciug and N. Radu, "Design and FEA Crash Simulation for a Composite Car Bumper," *Engineering Sciences*, vol. 5, 2012.

[10] J. Marzbanrad and M. Alijanpour, "Mahdi Saeid Kiasat Design and Analysis of an Automotive Bumper Beam in Low-Speed Frontal Crashes," *Elsiver*, vol. 47, 2009.

[11] P. Sureshkumar, T. Jagadeesha, L. Natrayan, M. Ravichadran, D. Veeman, and S. M. Muthu, "Electrochemical corrosion and tribological behaviour of AA6063/Si_3N_4/Cu $(NO_3)_2$ Composite processed using single-pass ECAPA route with 120° die angle," *Journal of Materials Research and Technology*, vol. 16, pp. 715–733, 2022.

[12] L. Natrayan and M. Senthil Kumar, "A novel feeding technique in squeeze casting to improve reinforcement mixing ratio," *Materials Today Proceedings*, vol. 46, pp. 1335–1340, 2021.

[13] A. Bovas Herbert Bejaxhin, G. Paulraj, and M. Prabhakar, "Inspection of casting defects and grain boundary strengthening on stressed Al6061 specimen by NDT method and SEM micrographs" Journal of Materials," *Research and Technology*, vol. 8, no. 3, pp. 2674–2684, 2019.

[14] W. L. Ngo, M. Pang, L. Yong, and K. Y. Tshai, "Mechanical properties of natural fibre (Kenaf, oil palm empty fruit bunch) reinforced polymer composites," *Advances in Environmental Biology*, vol. 8, pp. 2742–2747, 2014.

[15] L. Á. Lara-González, W. Guillermo-Rodríguez, Y. Pineda-Triana, G. Peña-Rodríguez, and H. F. Salazar, "Optimization of the tensile properties of polymeric matrix composites reinforced with magnetite particles by experimental design," *TecnoLógicas*, Mayo-Agosto, vol. 23, no. 48, 2020.

[16] J. Manhart, K. H. Kunzelmann, H. Y. Chen, and R. Hickel, "Mechanical properties and wear behavior of light-cured packable composite resins," *Dental Materials*, vol. 16, pp. 33–40, 2000.

[17] K. H. Kim and O. Okuno, "Microfracture behaviour of composite resins containing irregular-shaped fillers," *Journal of Oral Rehabilitation*, vol. 29, pp. 1153–1159, 2002.

[18] S. Garoushi, P. K. Vallittu, and L. V. J. Lassila, "Short glass fiber reinforced restorative composite resin with semi-interpenetrating polymer network matrix," *Dental Materials*, vol. 23, pp. 1356–1362.

[19] L. Lassila, S. Garoushi, P. K. Vallittu, and E. Säilynoja, "Mechanical properties of fiber reinforced restorative composite with two distinguished fiber length distribution," *Journal of the Mechanical Behavior of Biomedical Materials*, vol. 60, pp. 331–338, 2016.

[20] A. J. Georges, E. J. Swift, J. Y. Thompson, and H. O. Heymann, "Irradiance effects on the mechanical properties of universal hybrid and flowable hybrid resin composites," *Dental Materials*, vol. 19, pp. 406–413.

[21] T. M. Lastumäki, L. V. Lassila, and P. K. Vallittu, "Thesemi-interpenetrating polymer network matrix offiber-reinforced composite and its effect on the surface adhesive properties," *Journal of Materials Science: Materials in Medicine*, vol. 14, pp. 803–809, 2003.

[22] https://www.eppcomposites.com/hand-layup-process.html.

[23] Y. Yao, J. Cui, S. Wang et al., "Comparison of tensile properties of Carbon fiber, basalt fiber and hybrid fiber reinforced composites under various strain rates," *Applied Composite Materials*, vol. 29, 2022.

[24] Z. Marcalikovaa, M. Racek, P. Mateckova, and R. Cajka, "Comparison of tensile strength fiber reinforced concrete with different types of fibers," *Procedia Structural Integrity*, vol. 28, pp. 950–956, 2020.

[25] Jane Maria Faulstich de Paiva, S. . Mayer, and M. Cerqueira Rezende, "Comparison of tensile strength of different Carbon fabric reinforced epoxy composites," *Materials Research*, vol. 9, no. No. 1, pp. 83–89, 2006.

[26] M. Nasiruddin, A. Hambali, J. Rosidah, W. S. Widodo, and M. N. Ahmad, "A review of energy absorption of automotive bumper beam," *International Journal of Applied Engineering Research*, vol. 12, no. 2, p. 12, 2017.

[27] P. Kumar Uddandapu, "Impact Analysis on Car Bumper by Varying Speeds Using Materials ABS Plastic and Poly Ether Imide by Finite Element Analysis Software Solid Works," *International Journal of Modern Engineering Research (IJMER)*, vol. 3, 2013.

Hindawi
Advances in Materials Science and Engineering
Volume 2022, Article ID 1684169, 8 pages
https://doi.org/10.1155/2022/1684169

Research Article

Investigation of Mechanical and Tribological Properties of AA6061/MWCNT/B_4C Hybrid Metal Matrix Composite

P. Satishkumar,[1] N. Natarajan,[2] Rajasekaran Saminathan,[3] J. Justin Maria Hillary,[4] Biru Birhanu,[5] Arnold C. Alguno,[6] Rey Y. Capangpangan,[7] Vishnu Raj,[8] and Stephen Livingston[9]

[1]*Department of Mechanical Engineering, Study World College of Engineering, Coimbatore, Tamil Nadu 641105, India*
[2]*Department of Mechanical Engineering, Muthayammal Engineering College, Rasipuram, Namakkal, Tamil Nadu 637408, India*
[3]*Mechanical Engineering College of Engineering, Jazan University, Jizan, Saudi Arabia*
[4]*Department of Mechanical Engineering, Sri Krishna College of Engineering and Technology, Coimbatore, Tamil Nadu 641105, India*
[5]*Motor Vechicle Engineering, Defense University College of Engineering, Oromia, Ethiopia*
[6]*Department of Physics, Mindanao State University, Lligan Institute of Technology, Lligan, Phillippines*
[7]*Department of Physical Science and Mathematics, College of Science and Environment, Mindanao State University, Naawan, Misamis Oriental, Phillippines*
[8]*Department of Aeronautical Engineering, Manav Rachna International Institute of Research and Studies, Fabidabad, India*
[9]*Department of Mechanical Engineering, Study World College of Engineering, Coimbatore, Tamil Nadu 641105, India*

Correspondence should be addressed to Biru Birhanu; biru.birhanu@dec.edu.et

Received 21 July 2022; Accepted 5 September 2022; Published 30 September 2022

Academic Editor: Pudhupalayam Muthukutti Gopal

Carbon nanotubes (CNTs) and graphene, in particular, have been the subject of many recent studies since their discovery in the early 2000s. Because of their unusual properties, carbon nanotubes (CNTs) have piqued the interest of scientists across a wide range of disciplines. An Al matrix was reinforced with powder metallurgy-fabricated B_4C and CNT composites. The nanocomposite aluminium matrix was examined for tribological behaviour, density, stiffness, and compressive strength before and after hot isostatic pressing (HIP). Scanning electron microscopy and TEM were used to analyze the carbon nanotubes and their hybrid counterparts (SEM). The density of nanocomposites was reduced by 38% without HIP but by 45% after it was added to the mixture. Hardness was also increased by 40%, but following HIP, the hardness rose to 67%. Before and after HIP, the compression strength increased by 39% and 60%, respectively. HIP improves the wear rate by 45%, and B_4C and CNTs improve the coefficient of friction by 20% in all volume fractions but only by 48% in the case of nanocomposites.

1. Introduction

Composite materials have replaced monolithic substances in the minds of material scientists looking to improve mechanical qualities and develop high-tech equipment [1]. A clean interface separates the components of composite materials, which are made up of two or more chemically stable materials [2–4]. Due to their superior rigidity and strength, composites have replaced traditional materials [5]. Continuous fibres, discontinuous fibres, and particles can reinforce composites consisting of metal or polymer components [6, 7].

Among carbon nanotube's mechanical properties are stiffness and strength measurements in the 1000 GPa range and heat conductivity measurements in the 100 GPa range [8, 9]. Carbon nanotubes were used by [10] to strengthen magnesium alloy powder composites. They utilized a zwitterionic surfactant solution to evenly disperse the CNTs throughout the magnesium alloy. While CNTs have been proven to increase tensile and yield stress, they have also been

demonstrated to reduce elongation. The researchers [4] investigated wet sliding wear on hybridized nanocomposites of AlSi–2.5wt% CNTs–10wt% SiCp. Hybrid nanocomposites can be used as reinforcement to increase wear resistance [11].

To make MWCNTs/Ti composites, they employed sorted coacervation and SPS (spark plasma sintering) (3 wt.%) [12]. MWCNT reinforcements and a dense structure worked together to reduce yield strength before a considerable increase in sintering temperature was reached [13, 14]. For this hypoeutectic AA356–Si alloy, [15] researchers studied its microstructure and dry sliding wear characteristics. Compared to monolithic alloys, A356/MWCNT alloys showed superior wear resistance [15]. In a CNT alloy composite, [16] used squeeze casting to examine Al and Mg. Nanostructures enable new features and capabilities that are more efficient or impossible with more extensive structures and machinery [17, 18].

HMMC with nano/microsized strengthening has only been studied in the literature for a modest amount [19–22]. The authors [23] examined the squeeze casting of Al/SiC/graphite hybrid MMCs. Compounds reinforced with boron carbide-reinforced graphite exhibited identical coefficients of thermal expansion, even after adding graphite to improve dimensional stability [24, 25]. Increased graphite content condensed the heat conduction of hybridized composites. Researchers [26] investigated the wear resistance of B_4C/Sic/Al hybrid composites. They initiate that the coefficients of friction of the mixtures gradually rise as the reinforcing weight percentage increases [27, 28].

There was a slight decrease in wear resistance with an increase in B_4C wt %, but the friction coefficient did not change [29]. The impact of hybridizing carbon nanotubes and B_4C on the mechanical properties of Al 6061 composites has not previously been studied using powder metallurgy [30]. Consequently, powder metallurgy was employed in the current investigation to generate the aluminium matrix reinforced with boron carbide and multiwalled carbon nanotubes [31]. Powder metallurgy has used a range of aluminium powders and CNT volume fractions to significant effect. For pre- and post-HIP, the tribological, density, stiffness, and compressive strength performance of the aluminium matrix nanocomposite were studied [32–34].

2. Material

The multi-walled carbon nanotubes (CNTs) employed in this study were synthesized using an electric arc discharge with 99%. The average diameter of MWCNTs is 10–12 nm, and the length is 1–20 m. Boron carbide (B_4C) has a Young's modulus of 300 GPa, a tensile strength of 150 GPa, and a density of 3.3 g/cm^3. This project uses an aluminium matrix with a purity of 99.36%. Nanotech Corporation provided the MWCNTs and B_4C. Table 1 lists the chemical compositions of various types of boron carbide (B_4C).

3. Experimentation

3.1. Manufacturing of B_4C/MWCNT Composites. The initial stage was to manufacture the samples by employing ball milling at 280 rpm for 30 hours on six samples of Al 6061 and hybridized strengthening (CNT and B_4C) with various attentiveness proportions, as indicated in Table 2.

The cylinder-shaped specimens, 12 mm long and 10 mm wide, were physically crushed using hydraulic pressing with a volume of 40,000 kg and a pressure of 500 MPa utilizing a double-action die. This was followed by 0.5 hours of degassing at 200°C and 2 hours of sintering at 600°C. The samples were kept in the oven until they reached room temperature for this experiment. Samples were then subjected to a HIP (Figure 4) for two hours at 600°C under 250 MPa. An hour of heating at 600°C at a pace of 20°C/min brought the process to a close.

3.2. Hardness Test. The mechanical properties of composite materials can be defined in part by their hardness. A Vickers hardness machine is used to conduct the hardness test (Figure 5). Six readings were collected along the polished specimen's cross-section with a Zwick/Roell model hardness tester to get the average result. ASTM −17 was used to conduct the tests on the specimens.

3.3. Compression and Density. We used SHIMADZU universal testing equipment to evaluate the samples to conduct a compressive strength test (UH-F500KN). In this investigation, the cross-head speed of the universal test machine employed was 3 mm/min, which is the area of the specimen. The temperature was set at 25°C for the experiment. According to ASTM D1217-15, Archimedes' rule was used to determine the density of the specimens [35]. Specimens were weighed in air and distilled water according to MPIF standard 42, 1998, and the density (D) was then calculated using the Archimedes methodology with water as the floating liquid.

$$D = \frac{\text{specimen de nsity}}{\text{water de nsity}} = \frac{\text{weight in air}}{\text{weight in air} - \text{weight in water}}. \quad (1)$$

3.4. Tests on Wear. A pin-on-disc tribometer was employed to conduct wear tests on the sintered specimens (Figure 6). According to Figure 6, materials can be tested for friction and wear under various loads using the T.E. 79 multi-axis tribometer. The machine can execute ASTM G99 [36] tests in pin-on-disc mode. Cylinders of 12 mm and a diameter of 10 mm were employed in the experimentation.

4. Results and Discussions

Figure 1 depicts the XRD form of the CNT, as shown in the figure. According to the diffraction peaks, graphene sheets buckle together and form multiwalled nanotubes due to their concentric cylindrical structure. The reflection is seen as a sharp peak at 26.5 in the pattern [37].

Nanoadditive dispersion in aluminium was tested using SEM. The SEM was utilized for characterizing powder metallurgy-produced aluminium composites for microstructure and dispersion. A scanning electron microscope

Table 1: Chemical arrangement of Al 6061.

Elements	Silicon	Iron	Magnesium	Copper	Chromium	Zinc	Titanium	Manganese	Aluminium
wt %	0.7	0.6	0.9	0.30	0.25	0.20	0.10	0.05	Balance

Table 2: Al 6061 and hybridized reinforcement (MWCNT + B_4C) with variant mixtures.

Specimen	Composition
1	Al 6061
2	Al 6061 + 10% B_4C
3	Al 6061 + 10% B_4C + 1% CNT
4	Al 6061 + 10% B_4C + 1.5% CNT
5	Al 6061 + 10% B_4C + 2% CNT
6	Al 6061 + 10% B_4C + 2.5% CNT

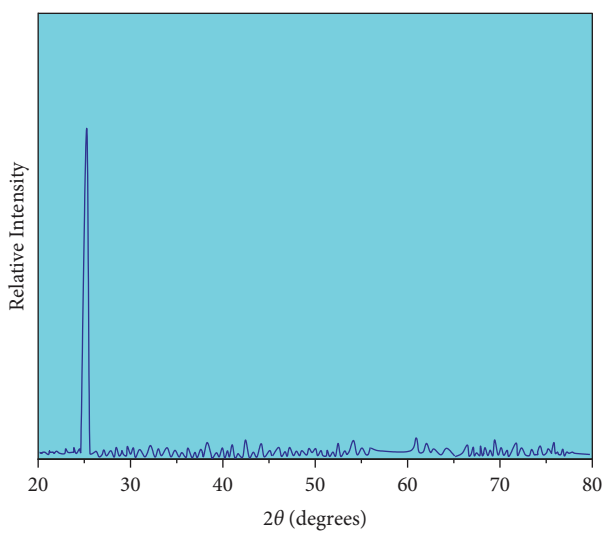

Figure 1: XRD form of CNTs.

(SEM) image of Al 6061 can be seen in Figures 2(a). Figure 2(b) shows a scanning electron microscope image of Al 6061 in the presence of boron carbide. Table 1 displays the oxidation states of aluminium and MWCNTs at various molar concentrations, as seen in Figure 2. (1, 1.5, 2, and 2.5 % wt.). Figure 2(b) shows that the Al 6061 contains a small amount of boron carbide (10wt. %). The compressive strength of the composites can be improved with the help of the B_4C [38].

Boron carbide and its various concentrations have been studied using the Energy Dispersive X-ray (EDX). As shown in Figure 3, the EDX of Al 6061 looks like this. Figure 3(b), on another end, shows that the atomic contribution of element O is 8% due to the inclusion of B_4C in the matrix. A carbon nanotube composite was used to add the element of C to Figures 3(c)–3(f). Each of these graphs has a different percentage of C: 5, 12, 21, and 37%. Boron carbide, which promotes interfacial attachment and increases the mechanical characteristics of hybridized composites, was shown to have been formed by the high carbon peak [39].

4.1. Comparison of Density before and after HIP. By comparing the densities before and after hot isostatic pressing, the actual density of hybrid composites was calculated. When compared with aluminium alloy and B_4C, the concentration of multiwalled carbon nanotubes was increased by decreasing the density, as shown in Figure 4. On the other hand, the actual density of the composite before HIP is less than the density of hybrid composites after HIP. It also clearly reveals that the ideal percentage of MWCNT was 2% by giving the best value of density.

4.2. Actual Density before and after Hot Isostatic Pressing. Figure 5 shows the experimental results of AA 6061/B_4C/MWCNT composites in the Vickers hardness test. It clearly shows that raising the volume fraction of MWCNT results in a higher value for hardness after HIP and before HIP which gives the best optimum result of about 2.5% volume fraction. The high hardness value and hard B_4C/MWCNT particles mat attribute to the strengthening effect. It is shown in the table that the maximum hardness value before hot isostatic pressing is 42.31 HV at 2.5% of multiwalled carbon nanotube and after hot isostatic pressing is 50.1 HV at 2.5% of MWCNT. The low hardness value before hot isostatic pressing is 37.39 HV at 1% of multiwalled carbon nanotube and 46.12 HV at 1% of MWCNT after HIP, respectively.

4.3. Variation of Reinforcement Particles in Volume Fractions. Table 3 shows compression test results for AA6061/boron carbide/multiwalled carbon nanotube nanocomposites before and after hot isostatic pressing. By increasing MWCNT, the value of the compression stroke decreases, as shown in Table 3. In all scenarios, the compression value attained after HIP is comparable to that of the value attained before HIP. The before and after compressed specimens are ductile materials meant for AA6061/B_4C/MWCNT.

4.4. Effect of Reinforcement Particles on the Friction Coefficient and Wear of Hybrid Composites. After 15 minutes at 250 rpm and 20 N of force applied, the coefficient of friction for the powder metal was calculated by calculating the pin on the disc setup. Figure 6 illustrates the COF of produced hybrid composites. From Figure 6, by adding B_4C to aluminium the COF of hybrid composites was reduced. Also, with the addition of various concentrations of MWCNT to B_4C and aluminium, the COF shows high improvement after HIP [40, 41]. In the case of with and without HIP, the COF for nanocomposites is raised by 39% and 48%, respectively. Whereas with HIP, wear rates were improved by 45% at all volume concentrations, and with B_4C and CNT, wear rates were improved by 20% at all volume fractions. Figure 7 shows the wear rates before and after hot isostatic pressing.

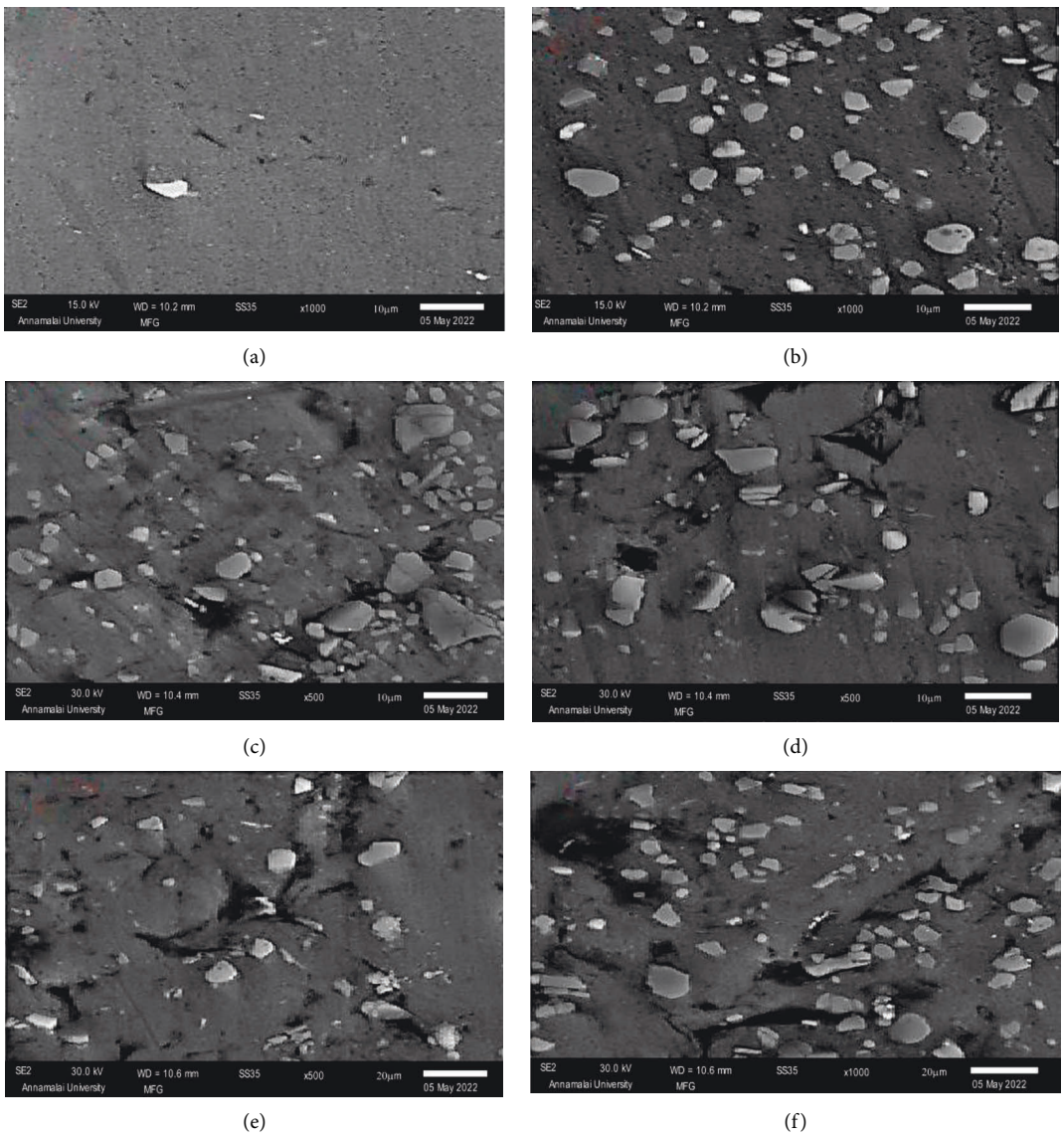

Figure 2: SEM images of (a) Al 6061, (b) Al 6061 + 10% B_4C, (c) Al 6061 + 10% B_4C + 1% CNT, (d) Al 6061 + 10% B_4C + 1.5% CNT, (e) Al 6061 + 10% B_4C + 2% CNT, and (f) Al 6061 + 10% B_4C + 2.5% CNT.

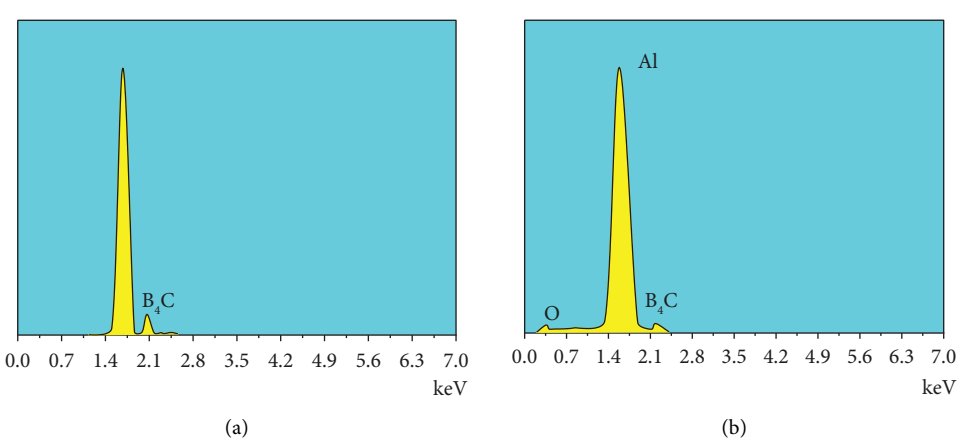

Figure 3: Continued.

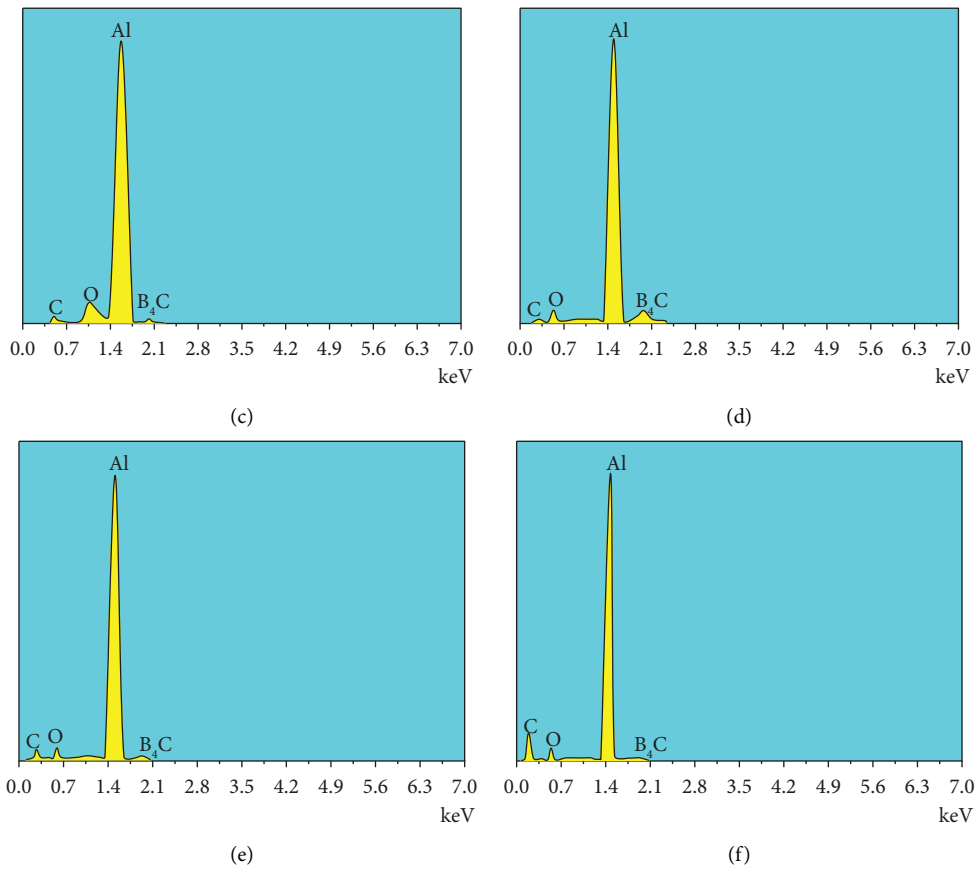

Figure 3: EDX of (a) Al 6061, (b) Al 6061 + 10%B_4C, (c) Al 6061 + 10% B_4C + 1% CNT, (d) Al 6061 + 10% B_4C + 1.5% CNT, (e) Al 6061 + 10% B_4C + 2% CNT, and (f) Al 6061 + 10% B_4C + 2.5% CNT.

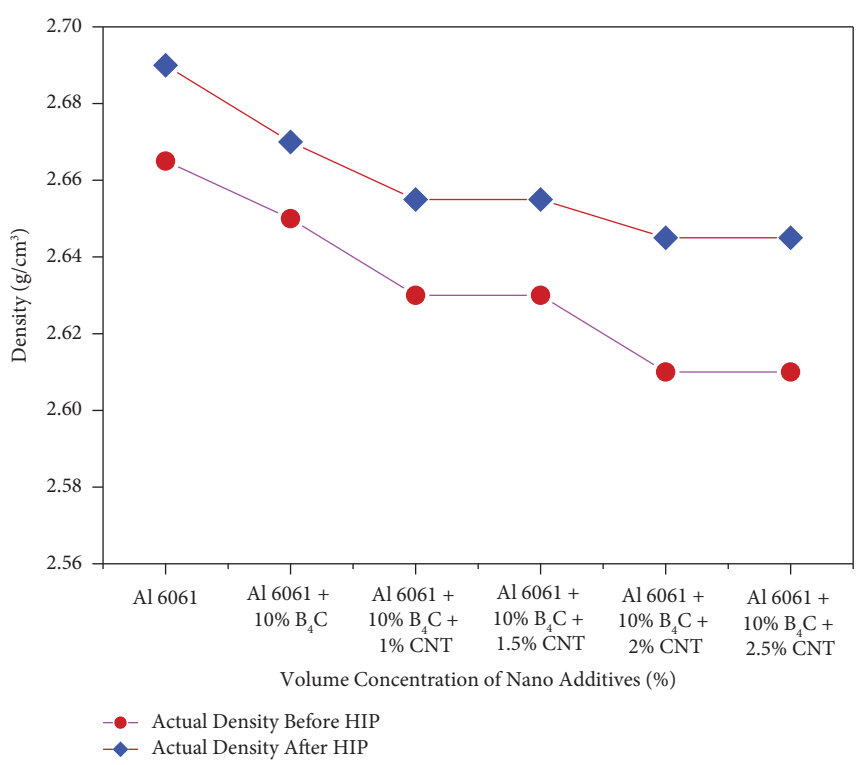

Figure 4: Before and after measurements of actual densities HIP.

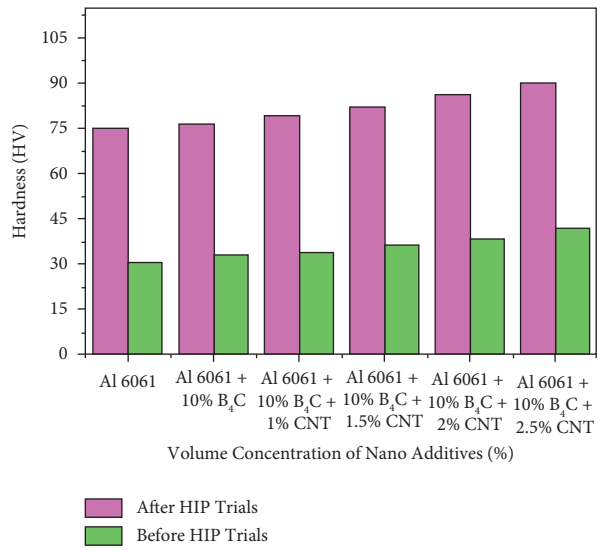

Figure 5: Hardness before and after hot isostatic pressing.

Table 3: Pre-HIP and post-HIP compressive stroke of AMC with varied CNT wt %.

Specimen	Stroke pre-HIP (mm)	Stroke post-HIP (mm)
Al 6061	5.723	4.4
Al 6061 + B_4C	5.341	3.9
Al 6061 + 10% B_4C + 1% CNT	5.234	3.5
Al 6061 + 10% B_4C + 1.5% CNT	4.82	2.9
Al 6061 + 10% B_4C + 2% CNT	4.787	2.7
Al 6061 + 10% B_4C + 2.5% CNT	3.599	2.4

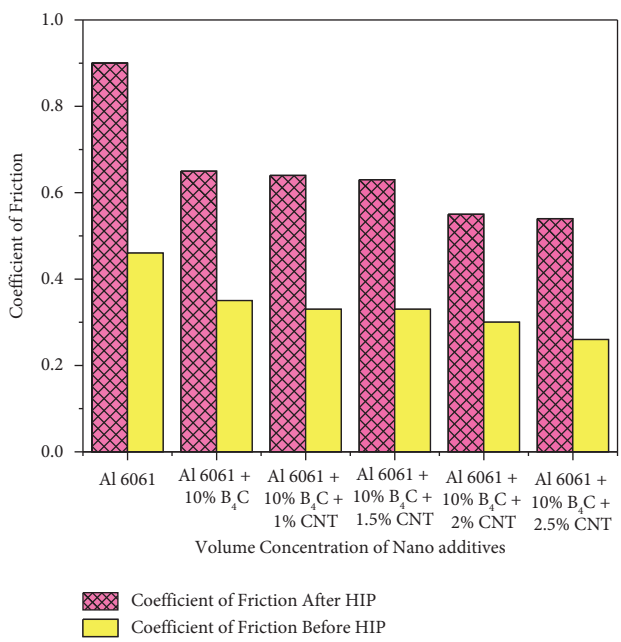

Figure 6: The friction coefficient of before and after HIP.

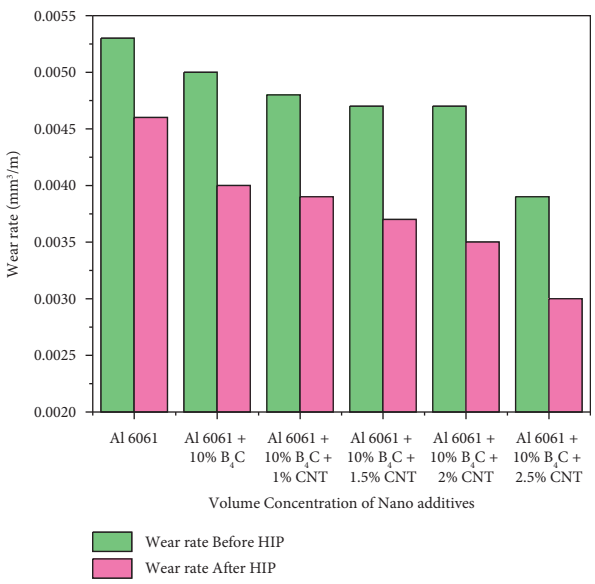

Figure 7: Before and after HIP wear rates.

5. Conclusion

By using a powder metallurgy process, AA6061 with hybrid composites was fabricated and characterized by compression, tribology, hardness, and density tests before and after HIP. Based on morphological and test results, the tribological and mechanical characteristics were enhanced, and multiwalled carbon nanotubes and boron carbide were dispersed uniformly and homogeneously in AA6061. The self-lubricating effect of B_4C and the creation of a carbon coating on the surface increases the tribological and mechanical characteristics of hybridized composites compared to AA6061. In all the experimental results, the best percent of multiwalled carbon nanotube was 2.5wt%. The excess B_4C and MWCNT were added to the composites, which inimically affect the composites due to the lack of wettability of the matrix. The tribological and mechanical characteristics of hybrid composites were increased by 39%, 45%, and 65%, respectively. Qualities of the composites like friction, wear, hardness, and compression strength were enhanced by hot isostatic pressing. As a result, HIP showed more effectiveness in composites without heat treatment due to sealed pores in the samples.

Data Availability

All required data are available within the manuscript.

Conflicts of Interest

The authors declare that they have no conflicts of interest.

References

[1] A. Gnanavelbabu, V. Arunachalam, K. T. Sunu Surendran, and K. Rajkumar, "Optimization of machining parameters in CNC turning of AA6061-B4C-CNT hybrid composites using grey-fuzzy method," *IOP Conference Series: Materials Science and Engineering*, vol. 764, no. 1, p. 012010, 2020.

[2] A. Gnanavelbabu, P. Saravanan, K. Rajkumar, S. Karthikeyan, and R. Baskaran, "Effect of abrasive waterjet machining parameters on hybrid AA6061-B4C- CNT composites," *Materials Today Proceedings*, vol. 5, no. 5, pp. 13438–13450, 2018.

[3] L. Yang, B. Pu, X. Zhang, J. Sha, C. He, and N. Zhao, "Manipulating mechanical properties of graphene/Al composites by an in-situ synthesized hybrid reinforcement strategy," *Journal of Materials Science & Technology*, vol. 123, pp. 13–25, 2022.

[4] X. Wang, Y. Su, C. Qiu et al., "Mechanical behavior and interfacial micro-zones of SiCp(CNT) hybrid reinforced aluminum matrix composites," *Materials Characterization*, vol. 189, p. 111982.

[5] J. Sun, P. Zhai, Y. Chen, J. Zhao, and Z. Huang, "Hierarchical toughening of laminated nanocomposites with three-dimensional graphene/carbon nanotube/SiC nanowire," *Materials Today Nano*, vol. 18, p. 100180.

[6] D. Bommana, T. R. K. Dora, N. P. Senapati, and A. S. Kumar, "Effect of 6 Wt.% particle (B4C + SiC) reinforcement on mechanical properties of AA6061 aluminum hybrid MMC," *Silicon*, vol. 14, no. 8, pp. 4197–4206, 2022.

[7] P. Van Trinh, J. Lee, B. Kang, P. N. Minh, D. D. Phuong, and S. H. Hong, "Mechanical and wear properties of SiCp/CNT/Al6061 hybrid metal matrix composites," *Diamond and Related Materials*, vol. 124, p. 108952.

[8] R. Narasimmalu and R. Sundaresan, "Experimental study on surface characteristics in μeD milling of Al6063%-5%B4C-5% ZrSiO4composite using TOPSIS method," *Surface Topography: Metrology and Properties*, vol. 10, no. 1, p. 015040, 2022.

[9] E. B. Moustafa, A. Melaibari, G. Alsoruji, A. M. Khalil, and A. O. Mosleh, "Tribological and mechanical characteristics of AA5083 alloy reinforced by hybridising heavy ceramic particles Ta2C & VC with light GNP and Al2O3 nanoparticles," *Ceramics International*, vol. 48, no. 4, pp. 4710–4721, 2022.

[10] H. Riaz, T. Mnazoor, and A. Raza, "Fabrication and characterization of AA6061/CNTs surface nanocomposite by friction stir processing," *International Journal of Advanced Manufacturing Technology*, vol. 105, no. 1–4, pp. 749–769, 2019.

[11] P. Singh, R. K. Mishra, and B. Singh, "Mechanical characterization of eggshell ash and boron carbide reinforced ZA-27 hybrid metal matrix composites," *Proceedings of the Institution of Mechanical Engineers - Part C: Journal of Mechanical Engineering Science*, vol. 236, no. 3, pp. 1766–1779, 2022.

[12] S. Das, M. Chandrasekaran, S. Samanta, P. Kayaroganam, and J. Paulo Davim, "Fabrication and tribological study of AA6061 hybrid metal matrix composites reinforced with SiC/B4C nanoparticles," *Industrial Lubrication & Tribology*, vol. 71, no. 1, pp. 83–93, 2019.

[13] P. Thamizhvalavan, N. Yuvaraj, and S. Arivazhagan, "Abrasive water jet machining of Al6063/B4C/ZrSiO4 hybrid composites: a study of machinability and surface characterization analysis," *Silicon*, vol. 14, no. 3, pp. 1093–1121, 2022.

[14] M. Ganesh, N. Arunkumar, K. Elavarasan, and R. Sathish, "Experimental investigation of friction and wear behavior of al7075-TiO2-B4C using RSM, ANN and desirability function," *International Journal of Vehicle Structures & Systems*, vol. 14, no. 1, pp. 41–46, 2022.

[15] S. Dharmalingam, P. Satishkumar, P. Pitchandi, and N. Natarajan, "Investigation of mechanical, morphological studies and electrochemical micro holing process parameters on Al6061-SiC-Gr hybrid metal matrix composites,"

International Journal of Heavy Vehicle Systems, vol. 25, no. 3/4, pp. 430–441, 2018.

[16] C. Qiu, Y. Su, J. Yang et al., "Microstructural characteristics and mechanical behavior of SiC(CNT)/Al multiphase interfacial micro-zones via molecular dynamics simulations," *Composites Part B: Engineering*, vol. 220, p. 108996.

[17] K. G. Chandrashekhar, D. P. Girish, and K. A. Ashok, "Optimization and prediction on the mechanical behavior of granite particle reinforced Al6061 matrix composites using deer hunting optimization based DNN," *Silicon*, 2022.

[18] M. Muniyappan and N. Iyandurai, "Structural morphology, elemental composition, mechanical and tribological properties of the effect of carbon nanotubes and silicon nanoparticles on A.A. 2024 hybrid metal matrix composites," *SAE International Journal of Materials and Manufacturing*, vol. 15, no. 2, 203 pages, 2022.

[19] B. Radha Krishnan, R. Theerkka Tharisanan, V. Arumuga Prabu, P. Immanuel, and A. Ramakrishnan, "Experimental investigation of mechanical properties of Al7075-Al2O3-B4C composite via stir route," *Materials Today Proceedings*, vol. 64, pp. 1721–1724, 2022.

[20] A. Abebe Emiru, D. K. Sinha, A. Kumar, and A. Yadav, "Fabrication and characterization of hybrid aluminium (Al6061) metal matrix composite reinforced with SiC, B4C and MoS2 via stir casting," *International Journal of Metalcasting*, 2022.

[21] K. Rajkumar, K. Ramraji, M. Aamir Qureshi, and A. Gnanavelbabu, "Tribo-effectiveness of co-equal concentration of hard and soft particulates in aluminium matrix," *Materials Today Proceedings*, vol. 62, pp. 1233–1237, 2022.

[22] J. J. M. Hillary, R. Sundaramoorthy, R. Ramamoorthi, and S. J. S. Chelladurai, "Investigation on microstructural characterization and mechanical behaviour of aluminium 6061 – CSFA/sicp hybrid metal matrix composites," *Silicon*, 2022.

[23] Q. Xu, Q. Shan, J. Hu et al., "The oxidation resistance mechanism of SiC-B4C-xAl2O3 ceramics at 1400 ℃ in air atmosphere," *Journal of the European Ceramic Society*, vol. 42, no. 6, pp. 2618–2629, 2022.

[24] N. Ramadoss, K. Pazhanivel, A. Ganeshkumar, and M. Arivanandhan, "Microstructural, mechanical and corrosion behaviour of B4C/BN-reinforced Al7075 matrix hybrid composites," *International Journal of Metalcasting*, 2022.

[25] A. Kareem, J. A. Qudeiri, A. Abdudeen, T. Ahammed, and A. Ziout, "A review on aa 6061 metal matrix composites produced by stir casting," *Materials*, vol. 14, no. 1, pp. 175–222, 2021.

[26] N. R. J. Hynes, S. Raja, R. Tharmaraj, C. I. Pruncu, and D. Dispinar, "Mechanical and tribological characteristics of boron carbide reinforcement of AA6061 matrix composite," *Journal of the Brazilian Society of Mechanical Sciences and Engineering*, vol. 42, no. 4, p. 155, 2020.

[27] J. Anwar, M. Khan, M. U. Farooq et al., "Effect of B4C and CNTs' nanoparticle reinforcement on the mechanical and corrosion properties in rolled Al 5083 friction stir welds," *Canadian Metallurgical Quarterly*, pp. 1–10, 2022.

[28] J. Suthar and K. Patel, "Corrosion behaviour of Mg, graphite-, B4C and Ti-reinforced hybrid aluminium composites," *Journal of The Institution of Engineers (India): Series C*, 2022.

[29] S. Chand, P. Chandrasekhar, S. Roy, and S. Singh, "Influence of dispersoid content on compressibility, sinterability and mechanical behaviour of B4C/BN reinforced Al6061 metal matrix hybrid composites fabricated via mechanical alloying," *Metals and Materials International*, vol. 27, no. 11, pp. 4841–4853, 2021.

[30] S. Ayyanar, A. Gnanavelbabu, K. Rajkumar, and P. Loganathan, "Studies on high-temperature wear and friction behaviour of AA6061/B4C/hBN hybrid composites," *Metals and Materials International*, vol. 27, no. 8, pp. 3040–3057, 2021.

[31] O. Carvalho, G. Miranda, M. Buciumeanu, M. Gasik, F. S. Silva, and S. Madeira, "High temperature damping behavior and dynamic Young's modulus of AlSi–CNT–SiCp hybrid composite," *Composite Structures*, vol. 141, pp. 155–162, 2016.

[32] P. Satishkumar, C. Saravana Murthi, R. Chebolu et al., "Optimizing the mechanical and microstructure characteristics of stir casting and hot-pressed AA 7075/ZnO/ZrO2 composites," *Advances in Materials Science and Engineering*, vol. 2022, pp. 1–18, 2022.

[33] G. Dirisenapu, L. Dumpala, and S. P. Reddy, "Parametric optimisation of tribological characteristics of novel Al7010/B4C/BN hybrid metal matrix nanocomposites using taguchi technique," *Australian Journal of Mechanical Engineering*, pp. 1–13, 2021.

[34] B. Tomiczek, L. A. Dobrzañski, and M. Macek, "Effect of milling time on microstructure and properties of AA6061/MWCNTS composite powders/wpływ czasu mielenia Na strukturę I własności proszk ów kompozytowyc H AA6061/MWCNTS," *Archives of Metallurgy and Materials*, vol. 60, no. 4, pp. 3029–3034, 2015.

[35] Z. Du, M.-J. Tan, J.-F. Guo, and J. Wei, "Friction stir processing of Al-CNT composites," *Proceedings of the Institution of Mechanical Engineers - Part L: Journal of Materials: Design and Applications*, vol. 230, no. 3, pp. 825–833, 2016.

[36] D. N. Travessa, G. V. B. da Rocha, K. R. Cardoso, and M. Lieblich, "Carbon nanotube-reinforced aluminum matrix composites produced by high-energy ball milling," *Journal of Materials Engineering and Performance*, vol. 26, no. 6, pp. 2998–3006, 2017.

[37] L. P. e. a. L Prabhu et al and S. Satish Kumar, "An application of CCD in RSM to obtain optimize treatment of eccentric-weave friction stir welding between polyether-ether-ketone polymer and AA 6061-T6 with reinforced multiwall," *International Journal of Mechanical and Production Engineering Research and Development*, vol. 8, no. 6, pp. 739–754, 2018.

[38] A. Sharma, H. Fujii, and J. Paul, "Influence of reinforcement incorporation approach on mechanical and tribological properties of AA6061- CNT nanocomposite fabricated via FSP," *Journal of Manufacturing Processes*, vol. 59, pp. 604–620, 2020.

[39] K. S. Sridhar Raja and V. K. Bupesh Raja, "Optimization of wear behaviour in aluminium reinforced boron carbide composite using Taguchi technique," *International Journal of Applied Engineering Research*, vol. 10, no. 8, pp. 6390–6395, 2015, ISSN 0973-4562.

[40] K. S. Sridhar Raja and V. K. Bupesh Raja, "The Corrosion behaviour of boron carbide reinforced aluminium metal matrix composite," *ARPN Journal of Engineering and Applied Sciences*, vol. 10, no. 22, pp. 10392–10394, December 2015, ISSN 1819-6608.

[41] K. S. Sridhar Raja and V. K. Bupesh Raja, "Production and characterization of boron carbide reinforced aluminium A356 composites," *International Journal on Design and Manufacturing Technologies*, vol. 7, no. 2, pp. 29–32, 2013, ISSN 0973-9106.

Hindawi
Advances in Materials Science and Engineering
Volume 2022, Article ID 2494750, 9 pages
https://doi.org/10.1155/2022/2494750

Research Article

Heat Index Based Optimisation of Primary Process Parameters in Friction Stir Welding on Light Weight Materials

Stephen Leon Joseph Leon,[1] N. Manikandan,[2] R. Santhanakrishnan,[3] Mohsin O. Al-Khafaji,[4] Hayder Mahmood Salman,[5] Harishchander Anandaram,[6] R. Malkiya Rasalin Prince,[7] L. Karthick,[8] and R. Rajesh Sharma[9]

[1]*Engineering Department, University of Technology and Applied Sciences-Ibri, Ibri, Oman*
[2]*Department of Mechanical Engineering, SRM Institute of Science and Technology, Ramapuram, Chennai, India*
[3]*School of Engineering and Technology, CMR University, Bengaluru, Karnataka, India*
[4]*Air Conditioning and Refrigeration Techniques Engineering Department, Al-Mustaqbal University College, Babylon 51001, Iraq*
[5]*Department of Computer Science, Al-Turath University College, Al Mansour, Baghdad, Iraq*
[6]*Centre for Excellence in Computational Engineering and Networking, Amrita Vishwa Vidyapeetham, Coimbatore, India*
[7]*Department of Mechanical Engineering, Karunya Institute of Technology and Sciences, Coimbatore, India*
[8]*Department of Mechanical Engineering, Hindusthan College of Engineering and Technology, Coimbatore, India*
[9]*Adama Science and Technology University, Nazrēt, Ethiopia*

Correspondence should be addressed to R. Rajesh Sharma; sharmaphd10@gmail.com

Received 23 July 2022; Accepted 8 September 2022; Published 25 September 2022

Academic Editor: Pudhupalayam Muthukutti Gopal

In friction stir welding, tool shoulder diameter and its rotational speed are the major influencing parameters than others. A simple novel correlation is proposed to select the optimum range of tool shoulder diameter with respect to the chosen rotational speed and vice versa. The conditions to apply derived correlation were defined through process heat index number as the joint efficiency in the friction stir welding depends on the effective heat supply to the volume of material deformed in the stir zone. Weld speed is the key parameter through which generated heat can be regulated towards optimum heat supply to attain defect-free weld in the stir zone. Effective heat input also has obvious effect on grain growth and corresponding property eradication in the heat affected zone. The experimental study was carried out on AA2024-T3 plates to understand the effect of process heat index on the prescribed optimum range of tool shoulder and rotational speed defined in the correlation. Eventually, a novel relationship was attained between the first order process influencing parameters to deliver maximum joint efficiency.

1. Introduction

Friction stir welding is the most preferable solid state joining technique for several high strength-to-weight ratio materials like aluminium alloys. In this welding, high-strength recrystallised metal structure weld joints are formed without cracking defects as the entire joining process is carried out above the recrystalisation temperature and below the melting point [1]. On the other hand, when the process is carried out in a temperature lower than the recrystallisation temperature, it results in defects like voids and tunnels in the stir zone [2], while higher process temperature leads to other defects, such as pores and flashes [2]. This indicates that the process parameters should be selected to induce optimum heat supply to ensure the entire joining process to be carried out in the temperature range, which produces a defect-free weld joint. Tool/matrix contact surface area and the relative velocity between the tool and the matrix are responsible for heat generation during this joining process (Figure 1).

Being major influencing factors of heat generation, appropriate selection of tool rotation speed and traverse speed can optimise heat generation rate in friction stir

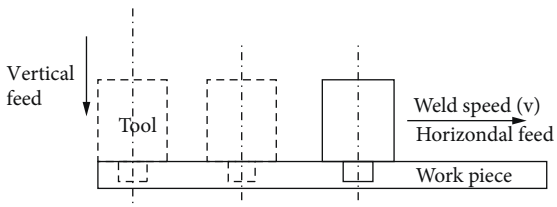

Figure 1: Tool movement at various stages.

welding [3]. Apart from this, contact conditions along the tool/matrix interface is also a major influencing factor on the effective heat supply [4]. Among all the heat supply boundaries, the tool shoulder/matrix is the major contributor in total heat generation. In order to optimise the heat generation rate, appropriate selection of shoulder diameter with respect to the tool rational speed and traverse speed is highly recommended.

Many researchers have tried to optimise tool shoulder diameter with respect to pin diameter, tool rotation speed, and welding speed [5–7]. These researches concluded an optimum shoulder diameter on the basis of constrained input parameter limits. For instance, even though the proven optimal tool shoulder pin ratio is 3, the combined effect of low tool rotational speed and high welding speed resulted in weld defects due to insufficient heat supply [8]. This reveals that the geometrical tool dimensions cannot be optimised without considering the tool rotation as well as welding speed.

The simplest way of optimising shoulder diameter with respect to the chosen process parameters is through the analysis of maximum utilisation of available torque. Arora et al. [9] developed a new criterion to optimise shoulder diameter on the basis of maximum utilisation of available torque. Nandan et al. [10] proposed a model which reveals that excess tool rotational speed or excess tool shoulder diameter leads to excess softening of material along the tool/matrix contact interface. This leads to poor mixing of material along the weld line and causes weld defects. Apart from this, it leads to excess material spill out on the top surface of the weldment, leading to excess flash weld defect. From this, it can be understood that there is always need for a simple correlation that can reveal the basic information for the selection of shoulder diameter range with respect to the tool rotational speed, and vice versa. Although the welding speed is an important factor to be considered in the estimation of effective heat supply during the joining process, its effect on heat generation is less comparing with the tool rotational speed. Many researchers [11–13] optimised weld speed with respect to the thickness and other properties on the workpiece to be joined. In this paper, a simple novel correlation is proposed to select the optimum range of tool shoulder diameter with respect to the chosen rotational speed and vice versa. The obtained correlation was related with the heat index value to attain to relate primary process parameters with other process conditions like absolute thermal resistance of the base metal. Derived conditions were validated through experimental analysis.

2. Optimum Values

The maximum utilisation of available torque depends on the design of appropriate tool geometry. The amount of heat generation in the tool/matrix interface depends on the friction between the contact surfaces. Friction in turn depends on the local velocity difference between the rotating tool and metal flow, which is quantified by the slip rate (δ) given by [14]

$$\delta = \exp\left[-\frac{E_{eff}}{E_{\max}}\right], \tag{1}$$

where the ratio between effectively transferred energy (E_{eff}) and maximum available energy ($E_{\max}$) is termed as transfer efficiency.

If $E_{\text{eff}} = E_{\max}$ then $T_{\max} = T_s$ [14].

Assuming 90% transfer efficiency.

$E_{\text{eff}} = 0.9E_{\max}$ then the minimum attainable slip rate $\delta_{\min} = 0.4$.

The slip rate can also be estimated by [15]

$$\delta = 0.3\exp\left[\frac{\omega r}{1.87}\right] - 0.026, \tag{2}$$

where r is the radial distance from the axis to the point at which slip rate is to be estimated.

Substituting $\delta_{\min} = 0.4$ in Equation (2), the maximum value of,

$$\omega r = 0.59. \tag{3}$$

Local heat generation analysis done by the Schmidt et al. [13] recorded maximum heat generation at the shoulder edge of the tool. It indicates that $\delta_{\min}$ is achieved at the point where $r = R_{\text{Shoulder}}$. So Equation (3) can be rewritten as,

$\omega R_{\text{shoulder}} = 0.59$ in which optimum energy transfer can be achieved.

Although Equation (3) gives a minimum optimum value of shoulder radius, during the welding stage, for higher welding velocity, the heat generated by the optimum shoulder radius may not be sufficient. The obtained optimum values by Arora et al. [9] reveal that sliding and sticking torque increase with an increase in shoulder diameter. In a particular diameter, the total toque developed is equally shared by sliding and sticking. Beyond that, the sticking torque reduces, and the sliding torque increases with a further increase in shoulder diameter. In other words, at a particular diameter for a given tool rotational speed, when the slip factor is 0.5, sticking torque reaches its maximum value and the maximum value of shoulder radius can be optimised at this limit.

Applying the conditions, equation (3) can be rearranged for its maximum value as,

$$\omega R_{\text{Shoulder}} = 1.05. \tag{4}$$

So depending on the forward motion of the tool per rotation, the required heat index value changes, and based on the required heat index value, the value of $\omega R_{\text{Shoulder}}$ should be opted in the range of 0.59 to 1.05.

2.1. Least Values. Equations (3) and (4) explain the range of the combined values of the tool shoulder and its rotational velocity. These two factors individually have their lower limits, which cannot be reduced beyond that. Every researcher tried to reduce the values of R_{shoulder} and ω to improve the property eradication in thermo-mechanically affected zone (TMAZ) as these two factors are directly proportional to the heat supply. Too much reduction in these two parameters leads to improper material flow around the tool pin and results in weld defects in the stir zone (SZ). A coupled thermal/material flow model developed by Hamilton et al. [14] suggests that

$$\text{Maximum effective strain rate}\dot{\varepsilon} = \frac{R_{\text{Shoulder}}\sqrt{6}\omega}{3h}. \quad (5)$$

Here, h refers to the workpiece thickness.

Equation (5) reveals that when $R_{\text{shoulder}} = 1.2\,\text{h}$, effective strain equals the tool rotational velocity and it reduces to its minimum value at the tool pin tip. From this, it can be understood that R_{shoulder} should always be more than 1.2 times of workpiece thickness to ensure proper material flow till its extreme depth of the Stir zone.

Minimum tool rotational speed can be explained using the required effective heat input during the process. Peak temperature during the process can be expressed as [15]

$$\frac{T_{\max}}{T_m} = K\left(\frac{\omega^2}{10^4 v}\right)^{\gamma}. \quad (6)$$

Here, T_m is the melting temperature of the material, v is the weld speed, and K and γ are coefficients suggested by Chen et al. [15].

When $T_{\max} = T_{\text{sat}} \approx 0.9\ T_m$ temperature-dependent yield strength of the parental metal becomes the minimum value, and it can be considered as extreme condition in frictional heat generation during the joining process. And for the extreme values of K and γ,

$$\text{Minimumheatindex (HI)} = \frac{\omega 2}{104 v} = 20.89. \quad (7)$$

Considering all, optimum range can be written as,

$$\omega R_{\text{SHoulder}} = 0.59\, to 1.05 \left| \begin{array}{l} R_{\text{Shoulder}} \geq 1.2h \\ HI \geq 20.89 \end{array} \right. . \quad (8)$$

2.2. Model Consistency with Literature Data. From the previous studies, it is evident that an increase in shoulder diameter increases the heat generation rate. But the effective heat flux delivered to the workpiece depends on process variables like rotational speed and welding speed. Apart from these process variables, temperature-dependent material properties like yield strength, which is responsible for the flow stress, have a direct impact on effective heat supply. Variation in yield stress results in a nonuniform slip factor throughout the tool/matrix interface. This reveals that, even though the heat generation increases with an increase in shoulder diameter, it attains a saturation point where the slip factor attains its maximum value as temperature-dependent flow stress of material that plays a significant role in self-limiting heat generation in friction stir welding. This reveals that, even though the heat generation increases with an increase in shoulder diameter, it attains a saturation point where the slip factor attains its maximum value. Figure 2 illustrates experimental results on optimum shoulder radius done on various ranges of tool rotational speed and tool shoulder radius [7, 16–19–21]. [22–25] On these results, optimum values are concluded based on the microstructure and mechanical property analysis of the joined work pieces. It can be observed that, concluded optimum values on their findings corresponding to their opted tool rotational speed are within the suggested maximum and minimum range. Experiments carried out by Padmanaban et al. [7] did not observe any considerable change in the post-weld microstructure with the change in shoulder diameter. It clearly indicates that the increase in the shoulder radius beyond the suggested maximum value ($\omega R_{shoulder} = 1.05$) does not make any difference in the weld quality.

2.3. Minimum Heat Index. Effective heat input during the joining process has an obvious effect on grain growth and property eradication in the heat affected zone. Reducing heat input beyond a limit leads to poor material flow under the tool shoulder in the stir zone and results in wormhole as well as tunnel defects. To attain a defect-free weld, the torque developed by the tool shoulder on the top tool/matrix contact surface should be sufficient to overcome the flow resistance given by the material on the bottom most surface. Reducing the yield strength of the material is a unique way to improve material flow in the stir zone. As the material yield strength is a temperature-dependent property (Figure 3), selection of the minimum possible heat index with respect to the optimum process peak temperature will result in a defect-free weld in the stir zone and improve post-weld property in the heat affected zone.

Extracted values from Figure 3 suggest that the peak temperature should be maintained at 78% of its melting point in order to reduce the yield strength of the base metal (AA2024-T3) to its lowest value [24]. From this, it can be concluded that the lowest possible operating temperature during the friction stir welding of AA2024-T3 is 0.78 T_m. Reducing temperature lower than 0.78 T_m may lead to the insufficient material flow in the stir zone.

From Equation (6), when $T_{\max} = 0.78 T_m$, HI = 2.68.

The selection of process conditions that deliver a heat index of 2.68 is sufficient to develop a maximum flow in the stir zone for the plates with negligible thickness. For thin AA2024-T3 plates, this analytically estimated minimum heat index value (2.68) is closely aligned with the experimental results obtained by Fu et al. [25]. In their experiment, friction stir welding done on 1.6 mm thickness AA2024-T3 plates delivered its maximum joint efficiency when the heat index value was 2.45. The above condition is valid for thin plates, whereas for thick plates, the temperature gradient in the stir zone depends on the thermal resistance and the lowest temperature can be obtained by

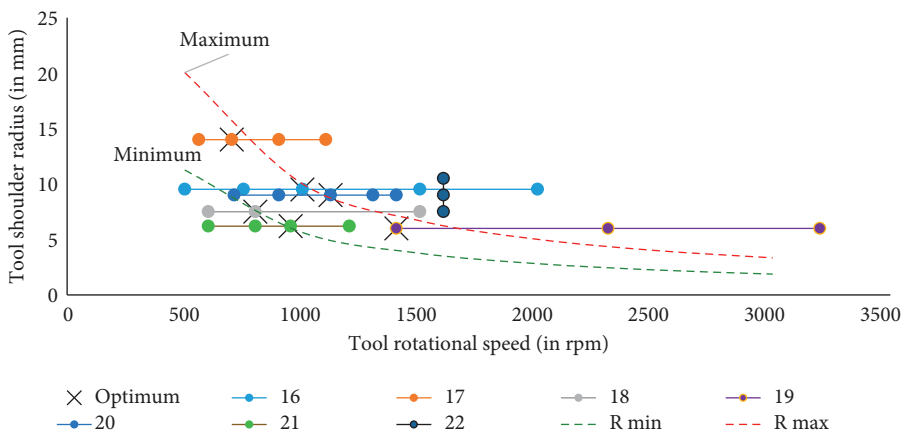

Figure 2: Optimum shoulder radius obtained through different experiments.

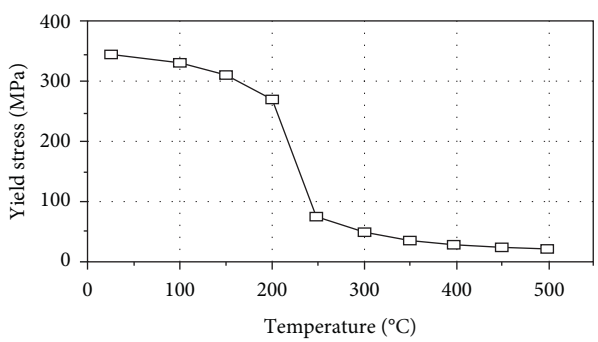

Figure 3: Yield strength of AA2024-T3 at different temperature [21].

$$T_{\max} = (R_{\theta} Q_{\text{eff}}) - T_{\min}. \quad (9)$$

Here, absolute thermal resistance $R_{\theta} = h/k$ for a unit cross-sectional area of the base metal. Being far away from the heat input boundary, the minimum temperature under the tool shoulder can be expected in the interface of the stir zone and the thermo-mechanically affected zone at the bottom surface of the workpiece. From Equation (9), it can be understood that the minimum heat index value depends on thermal resistance in the stir zone and the opted heat index value for the process to rise the peak temperature ($T_{\max}$) along the top contact surface should be sufficient to rise the temperature at the bottom surface ($T_{\min}$) equal to the critical temperature at which the base metal material loses its yield strength completely to facilitate the material flow. For the given absolute thermal resistance of the base metal, in order to define the required heat index conditions for the proposed "$R_{\text{shoulder}}\omega$" range in Equation (8), thermal history during the joining process with respect to the weld speed (v) has to be analysed.

3. Experimental Steady

AA2024-T3 plates of 6 mm thick were used as the base metal for the current experimental studies. Experimentally attained yield and ultimate strength of base metal properties are listed in Table 1. Process parameters used in the joining process are given in (Table 2). Tool pin diameter is kept constant and tool shoulder diameter is increased in such a way that the ratio between tool shoulder and pin diameters are 2.5, 3, 3.5, and 4. Maximum temperature rise during the welding stage was recorded using K-type thermocouples embedded inside the drilled holes at approximately 2 mm distance for the top and bottom surfaces at different locations as shown in Figure 4. In view of considering the minor deviation in the temperature rise on advancing and

Table 1: Properties of base metal (AA2024-T3).

Property	Values
Thermal conductivity (W/mK)	151
Yields strength (MPa) (obtained through tensile test)	343
Ultimate strength (MPa) (obtained through tensile test)	457
Saturation temperature (°C)	510

Table 2: Levels of process variables for friction stir welding on AA2024-T3.

Parameter	Levels
Shoulder radius (mm)	7.5, 9, 10.5, & 12
Tool rotation speed (rpm)	800, 900, 1000, 1100, & 1200
Weld speed (mm/min)	60, 70, & 80
Tool pin shape	Cylindrical
Tool pin radius (mm)	3

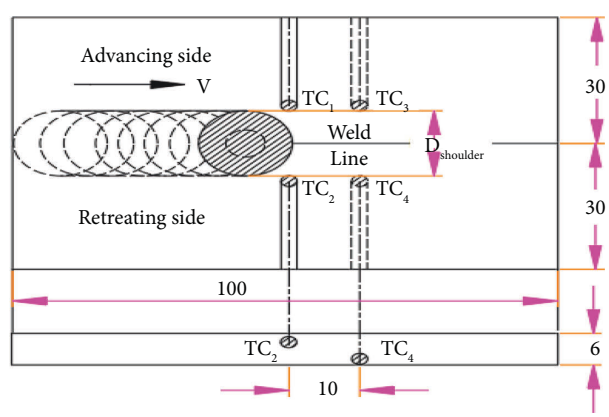

Figure 4: Experiment layout.

Table 3: Defects identified.

$R_{\text{Shoulder}}\omega$	Heat index	Weld defects due to insufficient heat supply	$R_{\text{Shoulder}}\omega$	Heat index	Weld defects due to excess heat supply (excess flash)
0.63	8.00		1.51	24.00	
0.75	8.00		1.51	20.57	
0.63	9.14	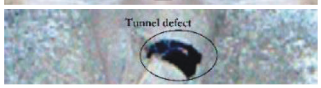	1.38	20.17	
0.71	10.13	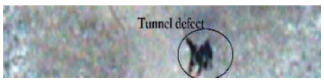	1.26	16.67	
0.75	9.14	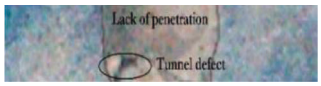	1.32	24.00	
0.88	8.00	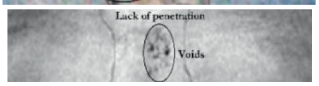	1.21	20.17	
0.85	10.13	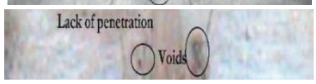	1.10	16.67	
0.79	12.50		1.13	24.00	

retreating sides, average values of temperature recorded by the thermocouples TC_1 and TC_2 were considered for the top surface, and average values of TC_3 and TC_4 were considered for the bottom surface. Macrostructure analysis was carried out to analyse the quality of the weld joint. Defects identified on different trails are given in Table 3.

4. Results and Discussions

4.1. Thermal Analysis. Comparing Table 3 and Figure 5, it can be concluded that the temperature gradient in the stir zone has an obvious influence over weld defects. Weld defects due to insufficient material flow were recorded when the bottom surface temperature was lesser than 410°C (equal to $0.78T_m$). The levels of defects were increasing from small voids to tunnels when the lowest temperature in the stir zone was reduced further. The lowest temperature of 374.3°C was recorded for the heat index value of 8 on the usage of the 7.5 mm shoulder radius tool. It indicates that even though $R_{\text{shoulder}}\omega = 0.63$ which is well within the recommended optimal range (Equation (8)), the chosen heat index value was not sufficient to overcome the absolute thermal resistance given by the base metal to rise the temperature of the material more than $0.78T_m$ at the bottom surface. On the other hand, surface defects developed by the excess heat supply were not identified in the top surface in the optional range of $R_{\text{shoulder}}\omega$ (0.59 to 1.05) even though the heat index value is maximum (20.89). From this, it can be concluded that irrespective of base metal thickness, defects due to excess heat supply can be avoided if the operating conditions match the recommended values in Equation (8). And also it is evident that for thin plates, the derived condition in Equation (8) is valid to obtain a defect-free weld joint even in the lowest recommended heat index value (2.68) as thermal resistance is negligible. For thicker plates, the optimal range of $R_{\text{shoulder}}\omega$ should be related to the heat index in order to consider the effect of absolute thermal resistance to attain the minimum heat index value which can provide a defect-free weld joint. Figure 4 explains the variation in the temperature at the bottommost surface of the workpiece with respect to the temperature rise at the top surface for a 6 mm thick AA2024-T4 plate. From the extracted values of temperatures using the best curve fit method, the relationship between the temperatures at the top and bottom surfaces can be expressed as

$$T_{\max} = 0.9551T_{\min} + 27.358. \quad (10)$$

From this Equation, it can be understood that a minimum of 419°C should be maintained at the top surface of the workpiece to ensure a $0.78T_m$ temperature at the bottom surface that shall enhance sufficient material flow to attain a defect-free joint.

4.2. Quantitative Analysis. Although the qualitative analysis with respect to the recorded thermal history provides a path to attain a defect-free weld, quantitative analysis is the unique way to optimise process parameters towards maximum joint strength. Joint strength was quantitatively analysed using the Vickers hardness test and tensile test. Obtained yield strength results for every trail are listed in Table 4. The ultimate strength of every specimen collected from different trails was compared with the ultimate strength of the base metal (Table 1) to estimate its joint efficiency. The lowest hardness value observed on every trail and corresponding joint efficiency are compared in Figure 6.

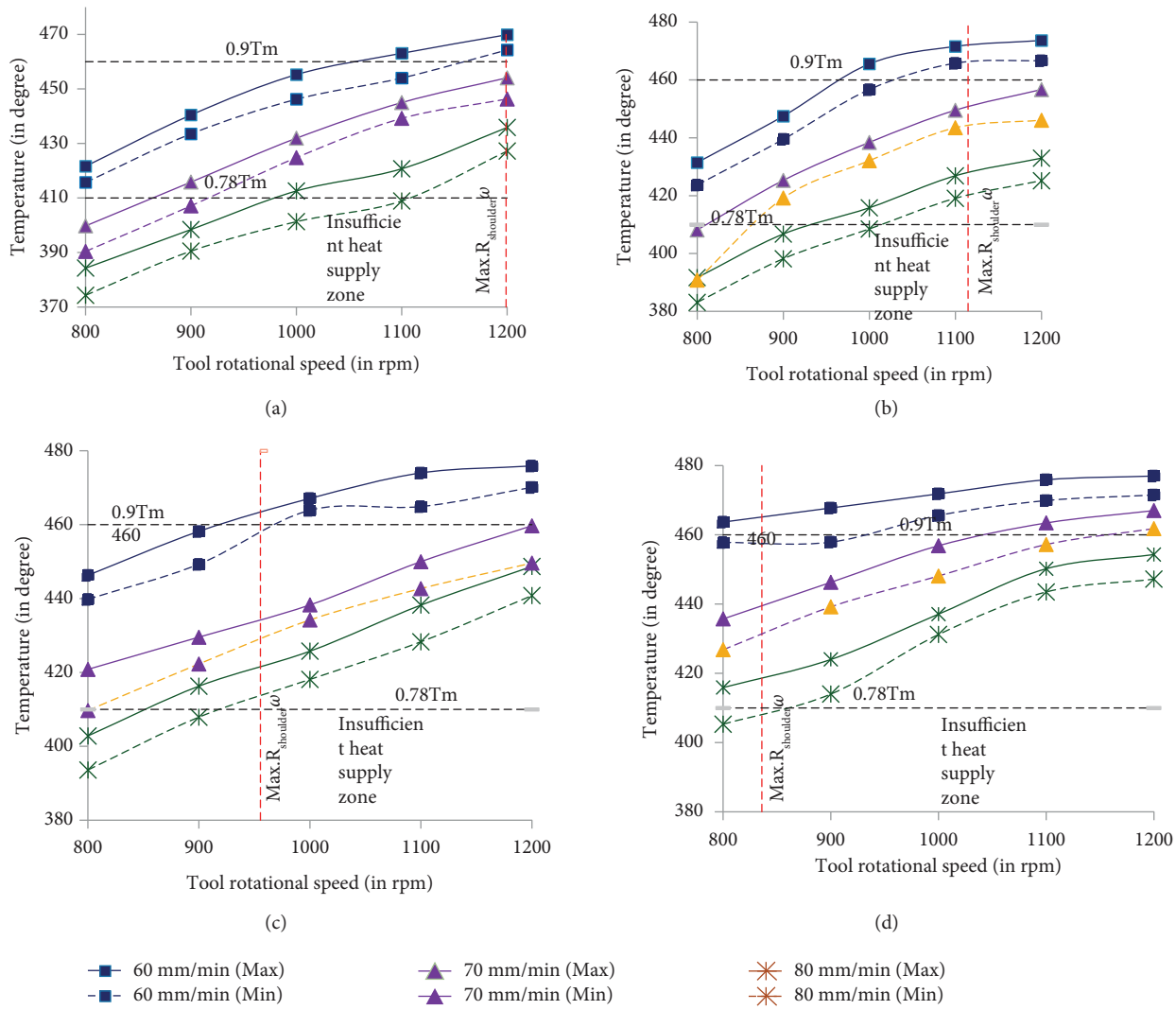

Figure 5: Temperature recorded at the top and bottom surfaces during the welding stage. (a) $R_{shoulder} = 7.5$ mm; (b) $R_{shoulder} = 9$ mm; (c) $R_{shoulder} = 10.5$ mm; (d) $R_{shoulder} = 12$ mm.

Table 4: Experimental results on mechanical property (yield strength in MPa).

Shoulder radius	Tool rotational speed (rpm)	Weld speed		
		60 mm/min	70 mm/min	80 mm/min
7.5	800	311.2	286.7	278.9
	900	303.2	300.8	287.3
	1000	300.1	308.3	296.7
	1100	297.3	305.6	297.1
	1200	294.9	301.9	308.3
9	800	308.8	287.4	284.7
	900	305.1	311.4	295.5
	1000	299.5	307.2	299.2
	1100	299.3	303.5	312.8
	1200	296.3	302.1	312.1
10.5	800	307.1	313.1	294.6
	900	300.9	311.9	313.1
	1000	295.5	305.9	312.4
	1100	293.3	301.3	308.1
	1200	292.9	300.1	304.1

Table 4: Continued.

Shoulder radius	Tool rotational speed (rpm)	Weld speed 60 mm/min	70 mm/min	80 mm/min
	800	300.1	310.1	298.5
	900	298.3	307.2	312.4
12	1000	296.5	302.9	308.3
	1100	294.4	301.1	304.5
	1200	293.9	299.3	303.6

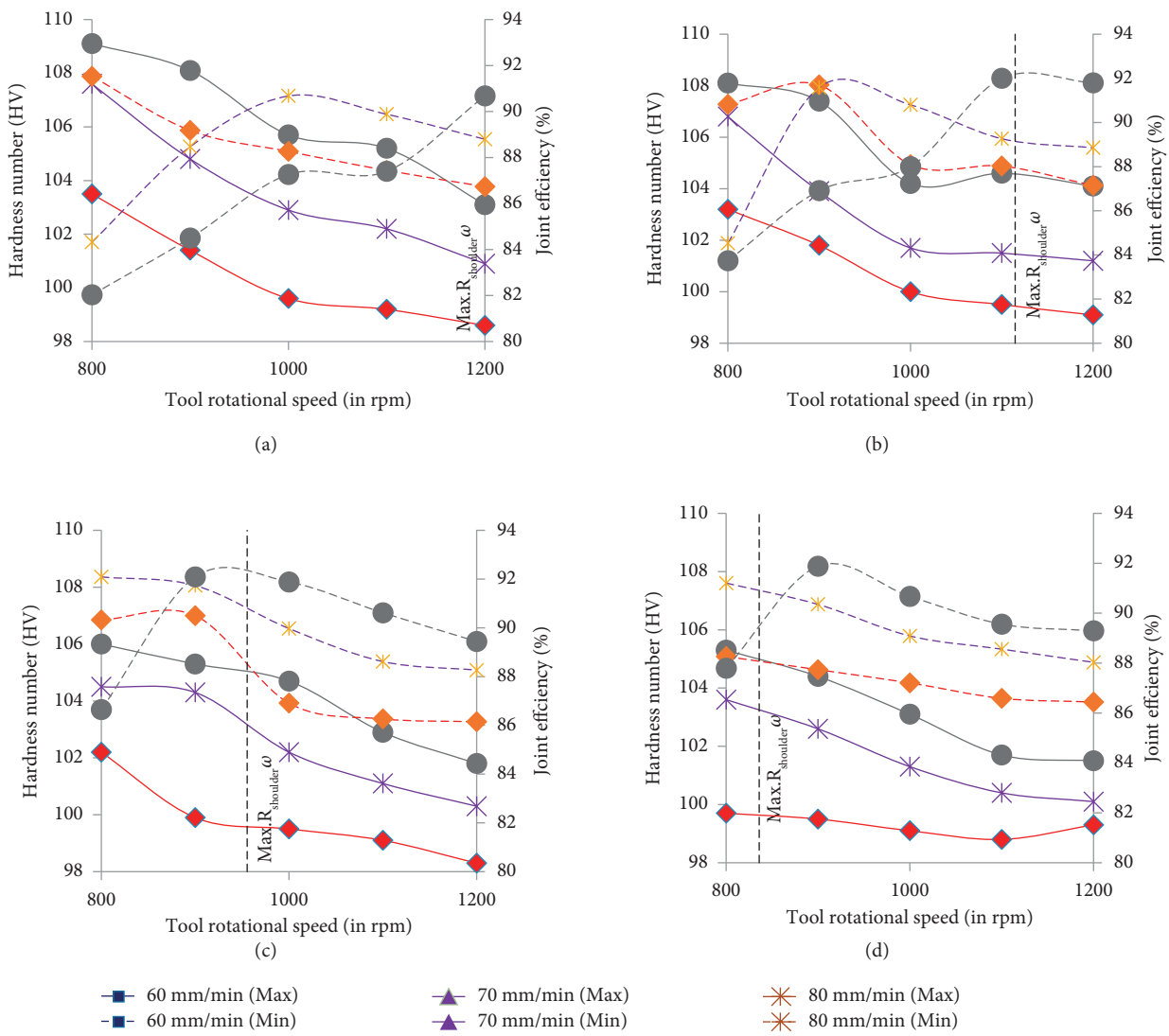

Figure 6: Joint efficiency and lowest hardness value. (a) $R_{shoulder} = 7.5$ mm; (b) $R_{shoulder} = 9$ mm; (c) $R_{shoulder} = 10.5$ mm; (d) $R_{shoulder} = 12$ mm.

As expected, the lowest hardness of 99.2 was recorded while using a 7.5 shoulder diameter tool as the heat generation rate is very low. Input heat flux is a function of relative motion between the tool and the base metal. An increase in tool rotational speed with respect to the tool feed could lead to recrystalisation of material, which in turn alters the hardness value of the base metal in the heat affected zone. As expected, the attained lowest hardness values on each trail in Figure 6 indicate that the decrease in hardness value is a direct function of tool rotational speed and the indirect function of weld speed. In a simplified form, it can be concluded that the increase in heat index value reduces the hardness value as higher heat input induces grain growth and leads to property eradication in the heat-affected zone.

From Figure 6, it can be understood that joint efficiency is a direct function of hardness value when the $R_{shoulder}\omega > 1.05$, whereas in the optimal range (from 0.59 to 1.05), the relationship between the lowest hardness value and the joint

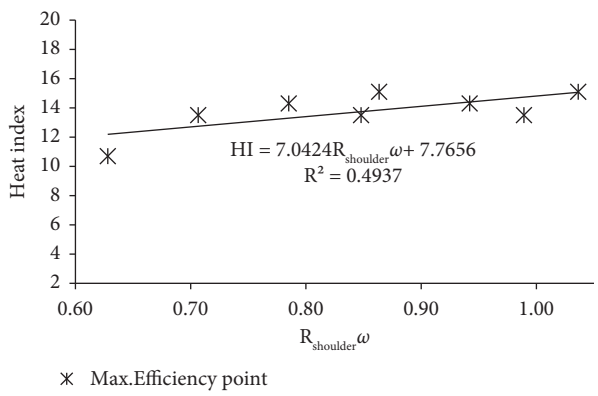

Figure 7: Heat index for the chosen tool shoulder radius and rotational speed.

efficiency is irregular due to the weld defect in the stir zone. Higher weld speed reduces the process heat index value. Even though trials done with low heat index pacified recrystallisation of material in the heat affected zone, it led to weld defects caused by insufficient heat supply in the stir zone (Table 3). It is also understood that the lowest heat index value at which defect-free weld can be obtained for the chosen "$R_{shoulder}\omega$" is the optimal value towards maximum joint efficiency as it reduces property eradication in the heat affected zone.

4.3. Optimisation of Heat Index Conditions. Tool shoulder radius and rotational speed are the key parameters to be considered to optimise total heat generation during friction stir welding. However, weld speed is the deciding factor for effective heat supply during the joining process to build a comfortable thermal environment in the stir zone to induce sufficient material flow. With the proper selection of weld speed, total heat generated can be regulated towards the optimum heat supply to attain better joint strength. From the qualitative and quantitative analysis, it is understood that process parameter optimisation can be done by relating "$R_{shoulder}\omega$" value with the heat index to define the optimum process peak temperature which could overcome the absolute thermal resistance in the stir zone and deliver a defect-free joint.

Figure 7 reveals the maximum efficiency points for the chosen key parameters. Using the best curve fit, the relationship between heat index and "$R_{shoulder}\omega$" to facilitate an amiable environment to achieve maximum joint efficiency for the prescribed circumstance can be expressed as

$$\text{Heat index} = 7.0424\text{R}_{\text{shoulder}}\omega + 7.7656. \quad (11)$$

This equation relates all key parameters toward maximum joint strength based on the process needs. The heat index in Equation (11) denotes the effective heat supply during the process as it indicates the number of tool rotations per one millimeter forward movement and Rshoulderω defines the total heat generation controlling parameters. Here, the term "$R_{shoulder}\omega$" decides the total heat generation during the process, and the selection of the prescribed heat index value regulates the heat supply to achieve better joint efficiency. This derived equation defines the heat index value for the prescribed "$R_{shoulder}\omega$" optimal range from 0.6 to 1.05 (equation (8)). For higher tool shoulder radius and rotational speed, the volume of material to be deformed on each revolution is higher and hence the required heat index value increases. The obtained conditions in equation (8) define the optimal conditions for heat generation, and equation (11) leads towards the optimal heat index to facilitate an amiable thermal environment based on the total heat generation.

5. Conclusions

A correlation is proposed to relate the optimum range of tool shoulder radius with respect to its rotational speed. Correlation was optimised to avoid property eradication in TMAZ and a possible selection of the least shoulder radius was obtained to ensure effective strain rate at its maximum depth in SZ. Further possible minimum value of tool rotational speed was attained through the effective heat index value to avoid surface defects. Prescribed correlation and conditions were examined through friction stir welding on AA2024-T3 plates. Based on the obtained results, the following were concluded:

(i) Obtained correlation is valid as the maximum joint efficiency is observed well within the recommended range in the correlation. There was a gradual decrease in joint efficiency when $R_{shoulder}\omega$ was greater than 1.05, irrespective of the weld speed.

(ii) Weld defects were identified at higher weld speeds when the $R_{shoulder}\omega$ value is lesser than 1.05 and the intensity of defect was increasing with a further decrease in $R_{shoulder}\omega$ value. On the other hand, excess flash defects were identified at lower weld speeds. The optimum weld speed range to attain defect-free weld was defined by the heat index number, and it was found that the maximum heat index number should not exceed 20.67.

(iii) It was identified that the minimum heat index number to be maintained according to the absolute thermal resistance of the base metal to facilitate the required effective heat supply to the volume of material to be deformed in the stir zone.Minimum heat index number was identified as 2.68 for thin AA2024-T3 plates and a correlation was obtained for thicker plates to estimate the minimum process temperature to be maintained to attain a defect-free weld in the view of relating the minimum heat index with the process peak temperature.

(iv) A novel relationship is achieved between the heat index and "$R_{shoulder}\omega$" to facilitate an amiable environment to achieve maximum joint efficiency for the prescribed circumstance.

Data Availability

The data used to support the findings of this study are included in the article. Should further data or information be

required, these are available from the corresponding author upon request.

Conflicts of Interest

The authors declare that they have no conflicts of interest regarding the publication of this paper.

Acknowledgments

The authors thank Adama Science and Technology University, Nazrēt, Ethiopia for providing characterization support to complete this research work.

References

[1] M. M. Mijajlovic, N. T. Pavlovic, S. V. Jovanovic, D. S. Jovanovic, and M. D. Milcic, "Experimental studies of parameters affecting the heat generation in friction stir welding process," *Thermal Science*, vol. 16, no. suppl. 2, pp. S351–S362, 2012.

[2] S. Bocchi, G. D'Urso, and C. Giardini, "The effect of heat generated on mechanical properties of friction stir welded aluminum alloys," *International Journal of Advanced Manufacturing Technology*, vol. 112, no. 5-6, pp. 1513–1528, 2021.

[3] A. S. Sedmak, R. Kumar, S. Chattopadhyaya et al., "Heat input effect of friction stir welding on aluminium alloy AA 6061-T6 welded joint," *Thermal Science*, vol. 20, no. 2, pp. 637–641, 2016.

[4] D. M. Veljic, B. L. Medjo, M. P. Rakin, Z. M. Radosavljevic, and N. S. Bajic, "Analysis of the tool plunge in friction stir welding - comparison of aluminium alloys 2024 T3 and 2024 T351," *Thermal Science*, vol. 20, no. 1, pp. 247–254, 2016.

[5] S. W. Park, T. J. Yoon, and C. Y. Kang, "Effects of the shoulder diameter and weld pitch on the tensile shear load in friction-stir welding of AA6111/AA5023 aluminum alloys," *Journal of Materials Processing Technology*, vol. 241, pp. 112–119, 2017.

[6] F. Sarsilmaz, "Relationship between micro-structure and mechanical properties of dissimilar aluminum alloy plates by friction stir welding," *Thermal Science*, vol. 22, no. Suppl. 1, pp. S55–S66, 2018.

[7] G. Padmanaban and V. Balasubramanian, "Selection of FSW tool pin profile, shoulder diameter and material for joining AZ31B magnesium alloy – an experimental approach," *Materials & Design*, vol. 30, no. 7, pp. 2647–2656, 2009.

[8] S. A. Khodir and T. Shibayanagi, "Friction stir welding of dissimilar AA2024 and AA7075 aluminum alloys," *Materials Science and Engineering: B*, vol. 148, no. 1-3, pp. 82–87, 2008.

[9] A. De Arora, A. De, and T. DebRoy, "Toward optimum friction stir welding tool shoulder diameter," *Scripta Materialia*, vol. 64, no. 1, pp. 9–12, 2011.

[10] R. Nandan, G. Roy, T. Lienert, and T. Debroy, "Three-dimensional heat and material flow during friction stir welding of mild steel," *Acta Materialia*, vol. 55, no. 3, pp. 883–895, 2007.

[11] C. Hamilton, S. Dymek, and A. Sommers, "A thermal model of friction stir welding in aluminum alloys," *International Journal of Machine Tools and Manufacture*, vol. 48, no. 10, pp. 1120–1130, 2008.

[12] Q. Li and M. Lovell, "On the critical interfacial friction of a two-roll CWR process," *Journal of Materials Processing Technology*, vol. 160, no. 2, pp. 245–256, 2005.

[13] H. B. Schmidt and J. H. Hattel, "Thermal modelling of friction stir welding," *Scripta Materialia*, vol. 58, no. 5, pp. 332–337, 2008.

[14] C. Hamilton, M. Kopyściański, O. Senkov, and S. Dymek, "A coupled thermal/material flow model of friction stir welding applied to Sc-modified aluminum alloys," *Metallurgical and Materials Transactions A*, vol. 44, no. 4, pp. 1730–1740, 2013.

[15] Y. Chen, H. Ding, J. z. Li, J. w. Zhao, M. j. Fu, and X. h. Li, "Effect of welding heat input and post-welded heat treatment on hardness of stir zone for friction stir-welded 2024-T3 aluminum alloy," *Transactions of Nonferrous Metals Society of China*, vol. 25, no. 8, pp. 2524–2532, 2015.

[16] X. Cao and M. Jahazi, "Effect of tool rotational speed and probe length on lap joint quality of a friction stir welded magnesium alloy," *Materials & Design*, vol. 32, pp. 1–11, 2011.

[17] M. Fazel-Najafabadi, S. F. Kashani-Bozorg, and A. Zarei-Hanzaki, "Joining of Cp-Ti to 304 stainless steel using friction stir welding technique," *Materials & Design*, vol. 31, no. 10, pp. 4800–4807, 2010.

[18] H. Fujii, L. Cui, M. Maeda, and K. Nogi, "Effect of tool shape on mechanical properties and microstructure of friction stir welded aluminum alloys," *Materials Science and Engineering A*, vol. 419, no. 1-2, pp. 25–31, 2006.

[19] H. Khalatbari and I. Lazoglu, "Friction stir incremental forming of polyoxymethylene: process outputs, force and temperature," *Materials and Manufacturing Processes*, vol. 36, no. 1, pp. 94–105, 2021.

[20] H. Nami, H. Adgi, M. Sharifitabar, and H. Shamabadi, "Microstructure and mechanical properties of friction stir welded Al/Mg2Si metal matrix cast composite," *Materials & Design*, vol. 32, no. 2, pp. 976–983, 2011.

[21] A. R. Cisko, J. B. Jordon, R. L. Amaro et al., "A parametric investigation on friction stir welding of Al-Li 2099," *Materials and Manufacturing Processes*, vol. 35, no. 10, pp. 1069–1076, 2020.

[22] J. Stephen Leon, G. Bharathiraja, and V. Jayakumar, "Analytical and experimental investigations of optimum thermo-mechanical conditions to use tools with non-circular pin in friction stir welding," *The International Journal of Advanced Manufacturing Technology*, vol. 107, no. 11, pp. 4925–4937, 2020.

[23] J. Stephen Leon and V. Jayakumar, "Effect of tool shoulder and pin cone angles in friction stir welding using non-circular tool pin," *Journal of applied and computational mechanics*, vol. 6, no. 3, pp. 554–563, 2020.

[24] S. S. Sabari, S. Malarvizhi, and V. Balasubramanian, "Influences of tool traverse speed on tensile properties of air cooled and water cooled friction stir welded AA2519-T87 aluminium alloy joints," *Journal of Materials Processing Technology*, vol. 237, pp. 286–300, 2016.

[25] R. D. Fu, J. F. Zhang, Y. J. Li, J. Kang, H. J. Liu, and F. C. Zhang, "Effect of welding heat input and post-welding natural aging on hardness of stir zone for friction stir-welded 2024-T3 aluminum alloy thin-sheet," *Materials Science and Engineering: A*, vol. 559, pp. 319–324, 2013.

Hindawi
Advances in Materials Science and Engineering
Volume 2022, Article ID 2788479, 8 pages
https://doi.org/10.1155/2022/2788479

Research Article

Effect of Friction Stir Welding on the Mechanical and Microstructural Behaviour of AA7075 Aluminium Alloy

C. R. Mahesha,[1] R. Suprabha,[1] Nellore Manoj Kumar,[2] Koushik Kosanam,[3] Harishchander Anandaram,[4] S. C. V. Ramana Murty Naidu,[5] M. Kalyan Chakravarthi,[6] and Venkatesan Govindarajan[7]

[1]*Department of Industrial Engineering and Management, Dr. Ambedkar Institute of Technology, Bangalore 560056, India*
[2]*Department of Mathematics, Saveetha School of Engineering, Saveetha Institute of Medical and Technical Sciences (SIMATS), Thandalam, Chennai, Tamilnadu 602105, India*
[3]*Department of Manufacturing Systems Engineering & Management, California State University, 18111 Nordhoff St, Northridge, CA 91330, USA*
[4]*Centre for Excellence in Computational Engineering and Networking, Amrita Vishwa Vidyapeetham, Coimbatore, Tamil Nadu 641112, India*
[5]*Department of Mechanical Engineering, Sri Venkateswara College of Engineering and Technology, Srikakulam, Andhra Pradesh 532001, India*
[6]*School of Electronics Engineering, VIT-AP University, Amaravathi 522237, India*
[7]*Department of Mechanical Engineering, Haramaya Institute of Technology, Haramaya University, Dawa, Ethiopia*

Correspondence should be addressed to Venkatesan Govindarajan; venkatesanggg2011@gmail.com

Received 21 June 2022; Accepted 25 August 2022; Published 10 September 2022

Academic Editor: Pudhupalayam Muthukutti Gopal

In this research work, an attempt was made to weld AA7075 alloy using the friction stir welding (FSW) technique. The experimental runs were designed using the Taguchi L18 orthogonal array and welds were obtained by varying tilt angle, tool rotation speed, tool feed rate, and axial load, whereas weld quality was accessed in terms of tensile strength and microhardness. The microstructure was examined using an optical microscope. The studies revealed that the tool angle was the most influential factor followed by the tool feed rate as both the parameters impacted the intensity of heat developed. It was observed that the tool tilt decreased the microhardness of the welds. The UTS values and macrostructure imply that the weld should be subjected to higher tool torque conditions. The material flow was not periodic nor coordinated, as seen by the tool-tilted weld's macrostructure. With a tool tilt, the weld pressure is lowered, and the lower pressure could not be enough to prevent volumetric defects. The reduced pressure at quicker welding rates may have had an effect on the development of flaws.

1. Introduction

AA7075, an aerospace aluminium alloy, has found its application in the manufacturing of aircraft structural wings and fins [1]. Zinc, a major alloying element of seven series aluminium alloy, possess a melting point of 420°C and boiling point of 907°C [2]. When joined utilizing the fusion welding technique, these zinc particles get evaporated, which alters the elemental composition of the aluminium alloy [3]. To overcome these issues, it was preferred to machine the aerospace aluminium alloy with solid state welding techniques [4]. Friction stir welding (FSW), cold metal transfer (CMT), ultra-sonic welding (USW), and hot pressure welding (HPW) are the distinct solid state welding process [5]. In joining innovation, FSW has drawn in an extraordinary consideration as a strong-state welding procedure used to join comparable and different ferrous and nonferrous metals with practically no deformities [6]. FSW can stay away from the vast majority of the issues related to unique nonferrous materials joined by fusion welding processes [7].

Tool geometry, rotation speed, feed rate, and dwell time are the distinct process parameters deciding the quality of the welded joints [8]. While the tool is being translated, the material being stirred is being moved from the front to the rear of the tool probe while it is being rotated [9]. The quality of the weld is also impacted by the tool's axial pressure [10]. It means that extremely high pressures cause excessive heating and joint thinning, whereas extremely low pressures result in inadequate heating and voids [11]. Another crucial factor, particularly for creating welds with "smooth" tool shoulders, is the tool's tilt angle, as measured in relation to the work piece surface [12]. The Al (6061) and (1018 steel) sheets were joined by Chen et al. using Friction Stir Welding to create a 6 mm thick layer of each alloy. They employed a steel welding instrument to complete the butt joint. The sizes for the shoulder and pin were chosen to be 24 mm and 5.5 mm, respectively. On the side facing forward, they utilized aluminium sheet, and on the side facing back, steel. An optical microscope was used to find the metallographic analysis. They claimed that intermetallic compounds are present in the joint region, especially in the nugget field. At a distance of 100 mm and a rotational speed of 917 rpm, the tool snapped [13].

Muthu and Jayabalan focused on the microstructure and temperature dispersion of the weld produced by the friction mix welding technique between Al (6061-T6) and 99.9% copper [14]. They observed that there existed metallic mixes such as CuAl2, CuAl, and, furthermore, Cu9Al4 buried in the joint field. According to them, there is a range of temperature conveyance and a high level of strong dissolvability in the bottom portion of the chunk location. Conductivity is a problem when welding copper in contact with other metals. They discovered that copper, due to its strong conductivity, diffuses the intensity created by the sponsorship blacksmith's iron, resulting in an inadequate welding temperature in the joint field. They discovered that the aluminium side's most severe temperature is 580 °C, which is greater than the softening point of the Al-Cu amalgam. They used 95 mm/min travel speed and 914 rpm rotating speed as the welding boundaries in this investigation. The friction mix welding apparatus used for this project was composed of steel [15]. From the above literature review, it was clear that a lot of research has been conducted on the welding of the aluminium alloy utilizing the FSW technique, research related to the FSW of AA7075 alloy and analysing its microstructural behaviour was very scarcely available. Hence, in this research work, an attempt was made to FSW AA7075 alloy by varying the input variables tilt angle, speed, feed, and axial load. The impact of these axial loads on the mechanical and microstructural behaviour was exploited deeply.

2. Experimental Work

The base metal utilized in the analyses was AA 7075 aluminium alloy with the chemical composition as depicted in Table 1. The experimental results are shown in Table 2 [16]. The following parametric limits were considered for the FSW; tool rotational speed (N), feed rate (S), axial force (F), and tilt angle. Other variables, viz shoulder and pin diameter, were kept consistent to concentrate the impact of tool angle on weld arrangement. As a thumb rule, the instrument pin width was proposed as equivalent to the thickness of the parent metal, and the shoulder measurement was three times that of the pin diameter. In accordance with shoulder distance and pin, they were fixed at 18 mm and 6 mm separately. The trial grid was designed as per the Taguchi L18 symmetrical cluster. FSW was done on an 11 kV/440 V (AC) direct FSW machine. The table showed the exploratory plan lattice, which is a symmetrical exhibit with two degrees of boundaries. Three samples were sheared crossover to the weld crease from each example in a processing machine. The samples were prepared in conformance with American Society for Testing and Materials (ASTM) standard E8M-04 for the tensile tests. The typical worth of the elasticity was considered for each example. For microstructure, specimens were sheared wise to the weld line and cleaned and carved with Keller's reagent. A Trinocular metallurgical magnifying lens (TMM) was utilized to inspect the microstructure of the weld. The difference in mechanical properties of the weld joints was analysed through hardness estimations across the crossover, the cross part of the weld. Estimations were taken by a Vicker's hardness analyser at 0.5 kgf load with a dwell time of 10 sec. Readings were taken 1.5 mm beneath the weld zone and at an interval of 1 mm.

Table 1: Chemical composition of the AA7075 alloy (Spectrum analysis).

Element	Si	Fe	Cu	Mn	Mg	Cr	Zn	Al
Composition	0.07	0.25	1.6	0.07	2.6	0.3	5.9	Remaining

3. Results and Discussion

To validate the absence of potential flaws such as blazes and surface passage as depicted in Figure 1(a) and the tensile specimen as portrayed in Figure 1(b), all welds underwent a visual inspection. Welded seams had smooth surfaces and were clearly free of defects. Due to weld fusions that were formed at higher temperatures, the weld surface was rough and contained tiny aluminium particles that gave it a rough, paper-like look. However, upon ocular inspection, low temperature welds seemed to have smooth surfaces.

The ultimate tensile strength (UTS) for the joints manufactured at different parametric levels is shown in Figure 2. The outcomes showed that elasticity experienced a critical plunge as the instrument was shifted by a point of +1.50. The most extreme elasticity was accounted for a tilt angle of 0° indeed, even at a higher device travel speed of 600 mm/min. This movement speed is one of the greatest qualities at any point announced for AA7075 amalgam at a thickness of 6 mm. The microhardness for two instances is shown in Figure 3 as a delegate model; one with a tool angle of 0, 700 mm/min, and the other with 1.50, 600 mm/min, and 700 rpm. Welds made with 1.50 slant points revealed lower values for hardness, and the microhardness appropriation amply demonstrated the influence of tool angle.

Table 2: Experimental runs and its results.

S.No	Tilt angle	Tool rotation (rpm)	Tool feed rate (mm/min)	Axial load	Tensile strength (MPa)	Microhardness (HV)
1	0	500	16	10	248	63
2	0	500	20	15	311	68
3	0	500	24	20	272	71
4	0	600	16	10	299	59
5	0	600	20	15	342	66
6	0	600	24	20	322	70
7	0	700	16	15	287	64
8	0	700	20	20	261	68
9	0	700	24	10	339	72
10	1.5	500	16	20	304	43
11	1.5	500	20	10	352	48
12	1.5	500	24	15	278	47
13	1.5	600	16	15	255	51
14	1.5	600	20	20	286	39
15	1.5	600	24	10	322	55
16	1.5	700	16	20	347	44
17	1.5	700	20	10	326	42
18	1.5	700	24	15	303	49

(a) (b)

Figure 1: (a) Visual inspection of the FSW joint. (b) FSW tensile specimen.

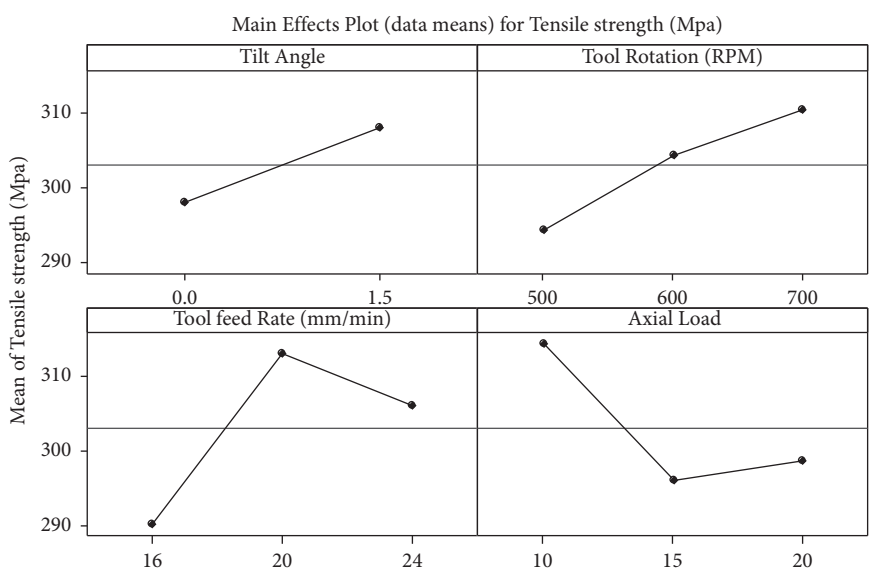

Figure 2: Main effect plot for tensile strength of FSW joints.

According to distinct research, the value of hardness is higher on the progressive side. In the case of a 0° tool angle, it is observed that the microhardness of the welds is approximately 70 Hv, resulting in a condition of up to 63 percent comparable with the base material hardness, while the microstructure hardness value is reduced to 45 in the case of a 1.50 tool angle.

The modification of the welds' mechanical characteristics with different process variables was demonstrated by variance in UTS and MH. For welds delivered with a tool tilt at a point of 1.5°, a significant decline in rigidity was observed. A similar trend was observed for the FSW of polyethylene. However, the general consensus was that increased strength for FSW joints of aluminium composites is favoured by a

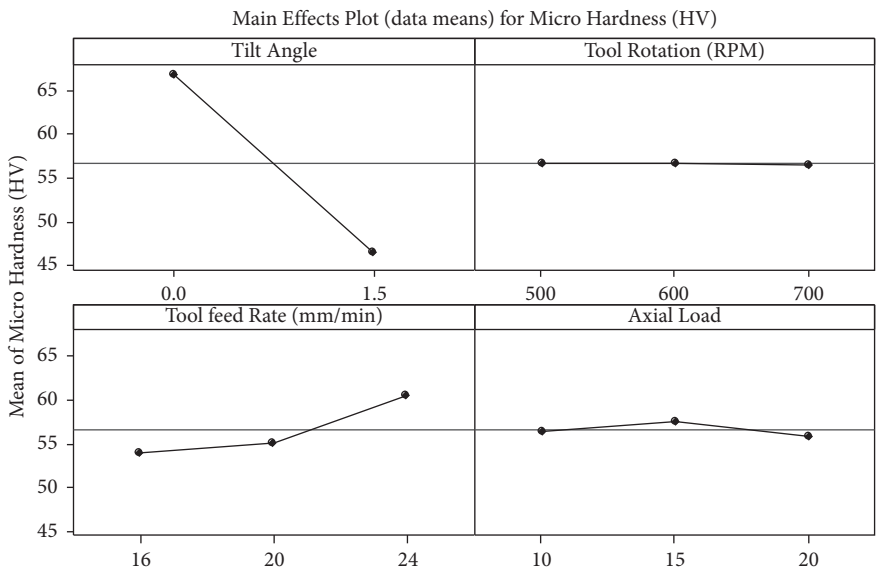

Figure 3: Main effect plot for microhardness of FSW joints.

tool tilt. The elasticity of the welds is improved by an instrument slant, according to a miniature underlying depiction of rubbing mix welded steel joints [17]. The device slant is the most effective boundary for the rigidity of the weld joints. Research promoting the notion that a tilt angle encourages blending and periodic replenishment of material in the weld joint, and the suppression of discharged material in the weld line by the tool shoulder has been taken into account [18]. In any event, a tool offset at higher rates may not be successful in achieving constraint and blending of extruded material, as seen by the drop in the weld strength included in this investigation. The microstructure has been used to assess the variation in UTS and microhardness.

The microstructure demonstrated precipitation solidification of the base metal following solution treatment. As shown in Figure 4(a), the main aluminium strong arrangement included fine, uniform Mg2Si eutectic particles that had accelerated. The material was rolled, as seen by the direction of the grain. The grain direction might be observed along the path of the equal lines. The micrograph also shows a small amount of the insoluble intermetallic complex Al6 (Fe Mn) in the base metal structure. In both the cases, fracture of the eutectic particles happened at the shoulder zone (SZ) because of the strain of the turning shoulder. The insoluble buried metallic compounds have shaped a bunch at the shoulder zone, as found in Figures 4(b) and 4(c).

In the optical microscope, the nugget zones (NZ) of the two instances are identical. The NZ exhibit split eutectic Mg2Si particles that have undergone distinctive recrystallization, as expected from Figures 5(a) and 5(b). The lack of grain direction, which was present in the parent metal, is thought to be the reason for the evidence of recrystallization. The eutectic particles would have disintegrated and quickly reprecipitated due to the mixing pressure and heated impact. For various welds produced under distinct input variables, the microstructure did not demonstrate a striking distinction. Therefore, it seems sensible to assume that heat input was crucial for the welders, and errors in certain welds may be attributed to a shortage in the material stream. This notion is supported by the welds' macrostructure at various interfaces. The FSW joining system may be understood in terms of material forging and extrusion. As the pin spins, heat generated by friction softens the material, which is then released around the pin and produced by shoulder motion. For this activity to be viable, the rotational and crossover speeds must be combined properly. It is essential to add heat to the material in order to soften it so that the ejected material may be blended properly. It was determined that low intensity input was the main cause of kissing bond or poor passage.

A consistent and steady state FW was performed under fractional tacky and sliding interface contact conditions aside from the device plunge stage [19]. All things considered, at higher speeds, tacky contact conditions overwhelm the cycle. Thus, at higher velocities, tool force will be high. Different examinations have recommended that, besides in the instances of overheating, tool force has a direct relation to work piece hardness, yield strength, and ductility. As the welding speed increments, heat input diminishes, and power consumed builds, in view of the decreased time for material deformation and dispensation. In addition, at higher welding speeds, the material ahead of the pin gets an extension period to preheat the material in the encompassing, and this retards the material softening for the welding system, which requires higher axial force. In such a condition, the intensity input depends generally on the plastic deformity of the encompassing mass material. In FSW, the info power is changed over into plastic softening energy, which is to some degree put away in the microstructure and to some extent changed over into heat. The consequences of mathematical re-enactments uncover that the heat energy gotten from plastic twisting shifts from 2 to 20% [20]. These perceptions prove low heat contribution at higher welding speeds. The general pattern of low UTS in all welds was

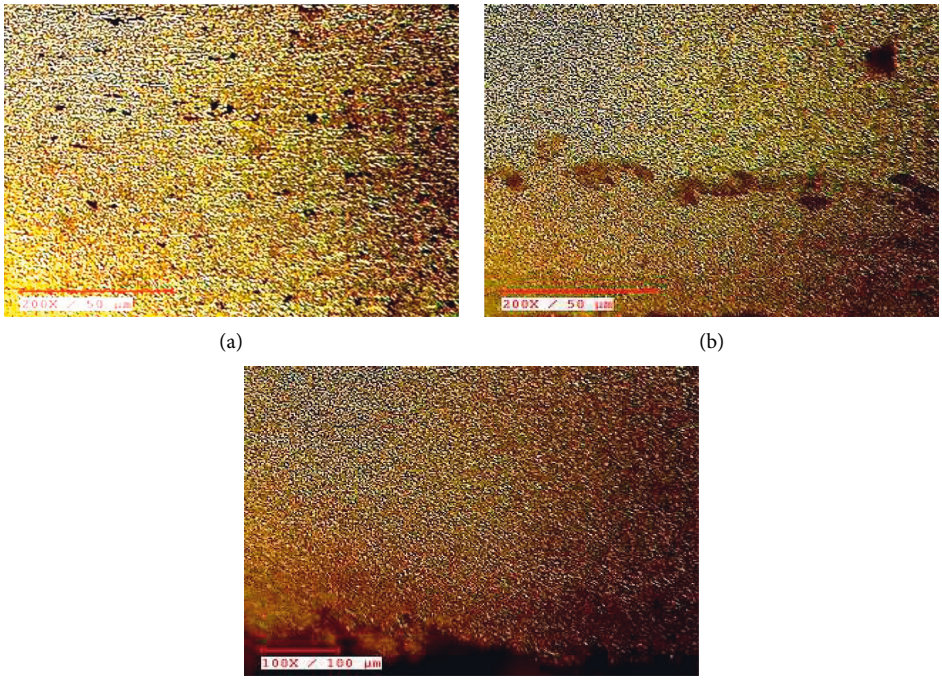

(a) (b) (c)

Figure 4: Microstructure of the (a) base metal, (b) shoulder zone with 0° tool angle, and (c) shoulder zone with 1.5° tool angle.

characteristic of low heat input for the scope of welding speed.

The majority of the heat in FSW was produced by shoulder activity, and the material stream was also impacted by the shoulder's crucial stress on plasticized material. The pin action regulates the material union and sporadic material filling of the joint. The substance is transported upward on the withdrawing side while being pushed downward on the pushing side [21]. The device strings pull the material below while moving the material in front of the pin upward [22]. The tool tilts in favour of the material's vertical growth in front of the pin. Other limits, such as pivotal power, rotational speed, and welding speed, have an impact on the union through the intermittent interchange of material. Although the shoulder driven stream and pin driven stream procedures are unaffected, the single stream volume and then the full mix zone are factors in welding speed [23]. The welding speed may thus have a greater influence on the material stream.

The device activity's material evolution in FSW is challenging. The split of the material handling zone into a revolution zone and a progress zone was suggested by Behera et al. [24]. The material stream is a combination of crossover, longitudinal, and exact, as for the device hub in the revolution zone, which is promptly located on the device pin surface. The progress zone was identified as the shear layer of material located between the rotational zone and the material framework. Heat input is a factor in the overall grinding mix volume.

In FSW, the weld formation proceeds while the material filling is delayed. By filling the material holes sporadically to provide a weld without deformities, a successful mix of boundaries overcomes this time delay. Due to this period of time where the grooves are not compensated by the compelling material stream, passage swindles have developed. Weld zones can be divided into shoulder-affected zones (SAZ), pin impacted zones (PIZ), and weld base zones (WBZ) depending on the material stream. Trench deformation is thought to be caused by a time delay in material filling in the PAZ. The descending material stream in the SAZ is reduced and surrenders are therefore created if the material stream from the withdrawing side to the pushing side and/or the crucial power are insufficient. It was explained that the material stream in the SAZ is persistent because the material in contact with the shoulder pivots at the same speed as the equipment. The material streams in the PAZ spin with the hardware and also move in an upward and downward orientation. As a result, the material stream in the PAZ is variable. The WBZ, which is located between the equipment tip and the parent metal's base surface, typically has a low stream speed of material. During the instrument's direct development, the WBZ is filled with material. WBZ is always filled at the point where the equipment passes the weld line at any given time. The weld setup in the WBZ needed more time in this fashion [25, 26].

The weld's macrostructure reveals an extremely sizable amount of void at the pin's bottom portion. Such malformations have been caused by inadequate intensity input that led to a viral weld situation [27, 28]. This situation, and the development of the vacuum into a passage or worm opening defect, may have been energised by a higher welding rate. The material around the FSW pin creeps around it, and it also streams upward in a roughly spherical form in layers [29, 30]. Ineffective material mixing is seen in Figure 5. 8 at

(a) (b)

Figure 5: Microstructure of the NZ (a) at 0° tool angle and (b) at 1.5° tool angle.

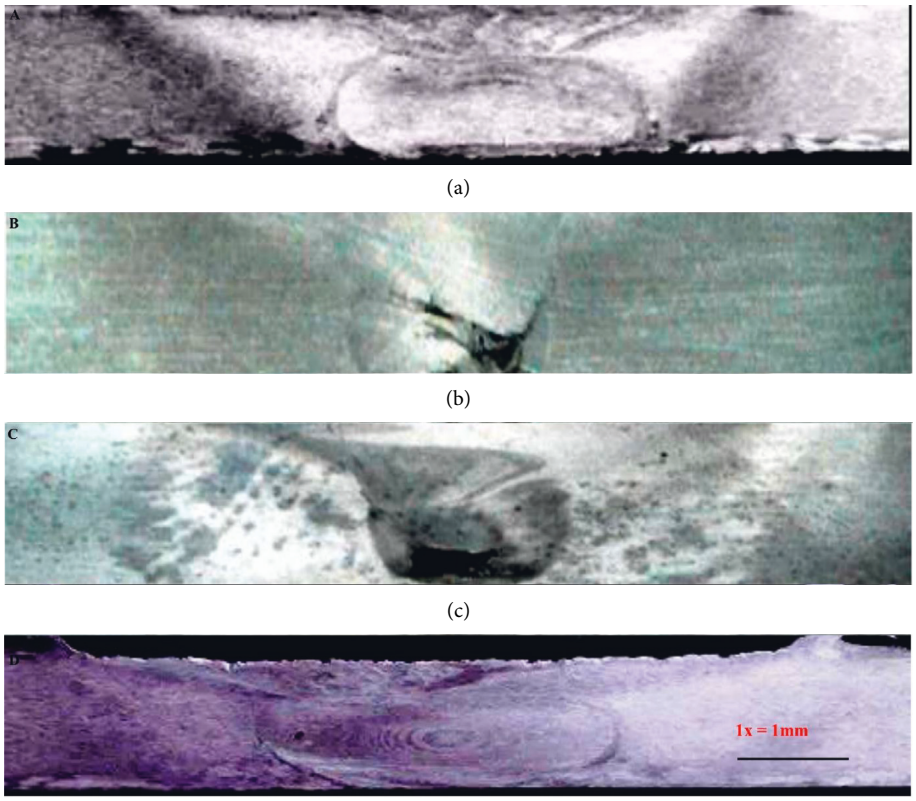

(a)

(b)

(c)

(d)

Figure 6: Macroscopic view of (a) weld at 0° tool angle, (b) weld at 1.5° tool angle, (c) weld with tunnel, and (d) distinct weld zones.

various contact levels. Possible causes include inadequate material flow around the pin and a lack of sufficient SAS, PAZ, and WBZ manufacturing activity by the shoulder. The mathematical components of the strung pin will probably not be an option for the device to tilt at greater rates in order to achieve the proper material stream. It may have resulted in the interior crumbling and regenerating.

In Figure 6(a), the macrostructure of the weld created at a 0° tilt angle is shown. The macrostructure demonstrates that the weld was freed from substantial flaws. The NZ was typically better than other weld types. It was explained that the pivoting pin, which in FSW is referred to as the turning shear material, deforms the material immediately adjacent to the apparatus surface (TSM). When a threaded pin profile is offered, the forcefully deformed material from the apparatus pin string surface pulls the surrounding material by the pinning activity. This surrounding stream, TSM, and the shoulder-driven material sporadically fill the hole when the tool progression occurs to prevent the development of volumetric defects. The size of the NZ determines the

superior material stream and mechanical qualities since larger NZs display suitable shoulder-driven streams. The material stream in the macrostructure showed the formation of onion rings. When compared to other welds, the superior material transformation and combination of this one may be to blame for the improved mechanical characteristics.

Inadequate material stream caused deformities of insufficient filling, as seen in Figures 6(b) and 6(c), in the macrostructure of the welds generated at a 1.5° device tilt angle. To prevent the creation of deformities, shoulder-driven material has to be properly convergent with pin-driven material [31, 32]. This material flow strategy relies heavily on temperature and axial power. It is logical to assume that the slanted point of the instrument, at the higher crossing speed, adversely influences the material stream and consolidation of layered material during welding and causes deformity arrangement because the tilt angle affects the shoulder-driven material stream and hydrostatic tension. According to FSW of AA 7075, the material stream is supposedly sensitive to the shoulder [33, 34]. The vertical power following up on the weld line is altered as the instrument is adjusted. This might affect the amount of material sucked in by the shoulder and the intensity that is generated. This effect could be anticipated to become significant at a faster rate. This might provide an explanation for the age of flaws that appear when the device is moved, as seen in the macrograph in Figure 6(d).

4. Conclusion

Along with other process factors, the impact of tool tilt angle on the high-speed FSW of 7075 aluminium alloy was investigated. An ideal set of process parameters was then provided. The outcomes of the research showed that

(1) The most important factor influencing weld strength is tool tilt angle, which has been demonstrated to have a negative impact on weld strength at faster tool travel speeds.

(2) Although the welds made at faster rates appeared to be free of defects, it was found that they had relatively weak welds, especially when the tool is tilted.

(3) The tool tilt was found to reduce the microhardness of the welds. Higher tool torque conditions for the weld are suggested by the UTS values and macrostructure. The macrostructure of the tool-tilted weld demonstrates that the material flow was neither periodic nor coordinated.

(4) Weld pressure is decreased with a tool tilt, and the reduced pressure may be less than the limiting amount needed to prevent volumetric flaws. The creation of defects may have been impacted by the lower pressure at faster welding speeds.

Data Availability

The data used to support the findings of this study are included within the article.

Conflicts of Interest

The authors declare that there are no conflicts of interest.

References

[1] S. Rajakumar, C. Muralidharan, and V. Balasubramanian, "Influence of friction stir welding process and tool parameters on strength properties of AA7075-T6 aluminium alloy joints," *Materials & Design*, vol. 32, no. 2, pp. 535–549, 2011.

[2] A. Nishimoto, J. I. Inagaki, and K. Nakaoka, "Influence of alloying elements in hot dip galvanized high tensile strength sheet steels on the adhesion and iron-zinc alloying rate," *Tetsu-To-Hagane*, vol. 68, no. 9, pp. 1404–1410, 1982.

[3] H. Nagaseki and K. I. Hayashi, "Experimental study of the behavior of copper and zinc in a boiling hydrothermal system," *Geology*, vol. 36, no. 1, pp. 27–30, 2008.

[4] E. Akca and A. Gürsel, "Solid state welding and application in aeronautical industry," *Periodicals of Engineering and Natural Sciences*, vol. 4, no. 1, 2016.

[5] A. Nassiri, T. Abke, and G. Daehn, "Investigation of melting phenomena in solid-state welding processes," *Scripta Materialia*, vol. 168, pp. 61–66, 2019.

[6] R. Ranjith and B. Senthil Kumar, "Joining of dissimilar aluminium alloys AA2014 T651 and AA6063 T651 by friction stir welding process," *WSEAS Transactions on Applied and Theoretical Mechanics*, vol. 9, pp. 179–186, 2014.

[7] D. Kumar Rajak, D. D. Pagar, P. L. Menezes, and A. Eyvazian, "Friction-based welding processes: friction welding and friction stir welding," *Journal of Adhesion Science and Technology*, vol. 34, no. 24, pp. 2613–2637, 2020.

[8] D. Mishra, R. B. Roy, S. Dutta, S. K. Pal, and D. Chakravarty, "A review on sensor based monitoring and control of friction stir welding process and a roadmap to Industry 4.0," *Journal of Manufacturing Processes*, vol. 36, pp. 373–397, 2018.

[9] M. Abbasi, A. Abdollahzadeh, B. Bagheri, A. Ostovari Moghaddam, F. Sharifi, and M. Dadaei, "Study on the effect of the welding environment on the dynamic recrystallization phenomenon and residual stresses during the friction stir welding process of aluminum alloy," *Proceedings of the Institution of Mechanical Engineers - Part L: Journal of Materials: Design and Applications*, vol. 235, no. 8, pp. 1809–1826, 2021.

[10] F. Lambiase, H. A. Derazkola, and A. Simchi, "Friction stir welding and friction spot stir welding processes of polymers—state of the art," *Materials*, vol. 13, no. 10, p. 2291, 2020.

[11] K. P. Mehta, R. Patel, H. Vyas, S. Memon, and P. Vilaça, "Repairing of exit-hole in dissimilar Al-Mg friction stir welding: process and microstructural pattern," *Manufacturing Letters*, vol. 23, pp. 67–70, 2020.

[12] R. Ranjith, P. K. Giridharan, and K. B. Senthil, "Predicting the tensile strength of friction stir welded dissimilar aluminum alloy using ann," *International Journal of Civil Engineering & Technology*, vol. 8, no. 9, pp. 345–353, 2017.

[13] G. Chen, S. Zhang, Y. Zhu, C. Yang, and Q. Shi, "Thermo-mechanical analysis of friction stir welding: a review on recent advances," *Acta Metallurgica Sinica*, vol. 33, no. 1, pp. 3–12, 2020.

[14] M. F. X. Muthu and V. Jayabalan, "Tool travel speed effects on the microstructure of friction stir welded aluminum–copper joints," *Journal of Materials Processing Technology*, vol. 217, pp. 105–113, 2015.

[15] Y. Sun, W. Gong, J. Feng, G. Lu, R. Zhu, and Y. Li, "A review of the friction stir welding of dissimilar materials between

aluminum alloys and copper," *Metals*, vol. 12, no. 4, p. 675, 2022.

[16] K. S. Arora, S. Pandey, M. Schaper, and R. Kumar, "Effect of process parameters on friction stir welding of aluminium alloys 2219-T87," *The International Journal of Advanced Manufacturing Technology*, vol. 50, no. 9, pp. 941–952, 2010.

[17] S. M. Senthil, R. Parameshwaran, S. Ragu Nathan, M. Bhuvanesh Kumar, and K. Deepandurai, "A multi-objective optimization of the friction stir welding process using RSM-based-desirability function approach for joining aluminum alloy 6063-T6 pipes," *Structural and Multidisciplinary Optimization*, vol. 62, no. 3, pp. 1117–1133, 2020.

[18] H. Jafari, H. Mansouri, and M. Honarpisheh, "Investigation of residual stress distribution of dissimilar Al-7075-T6 and Al-6061-T6 in the friction stir welding process strengthened with SiO2 nanoparticles," *Journal of Manufacturing Processes*, vol. 43, pp. 145–153, 2019.

[19] W. Zhao and C. Wu, "Constitutive equation including acoustic stress work and plastic strain for modeling ultrasonic vibration assisted friction stir welding process," *International Journal of Machine Tools and Manufacture*, vol. 145, Article ID 103434, 2019.

[20] R. Saha and P. Biswas, "Current Status and Development of External Energy-Assisted Friction Stir Welding Processes: A Review," *Welding in the World*, pp. 1–33, Springer, Berlin, Germany, 2022.

[21] T. A. Shehabeldeen, M. A. Elaziz, A. H. Elsheikh et al., "A novel method for predicting tensile strength of friction stir welded AA6061 aluminium alloy joints based on hybrid random vector functional link and henry gas solubility optimization," *IEEE Access*, vol. 8, pp. 79896–79907, 2020.

[22] E. T. Akinlabi and R. M. Mahamood, *Solid-state Welding: Friction and Friction Stir Welding Processes*, Springer International Publishing, New York, NY, USA, 2020.

[23] G. Chen, G. Wang, Q. Shi, Y. Zhao, Y. Hao, and S. Zhang, "Three-dimensional thermal-mechanical analysis of retractable pin tool friction stir welding process," *Journal of Manufacturing Processes*, vol. 41, pp. 1–9, 2019.

[24] R. K. Behera, B. P. Samal, S. C. Panigrahi, and K. K. Muduli, "Microstructural and mechanical analysis of sintered powdered aluminium composites," *Advances in Materials Science and Engineering*, vol. 2020, pp. 1–7, Article ID 1893475, 2020.

[25] M. Shunmugasundaram, A. Praveen Kumar, L. Ponraj Sankar, and S. Sivasankar, "Optimization of process parameters of friction stir welded dissimilar AA6063 and AA5052 aluminum alloys by Taguchi technique," *Materials Today Proceedings*, vol. 27, pp. 871–876, 2020.

[26] R. K. Behera, B. P. Samal, S. C. Panigrahi et al., "Erosion wear characteristics of novel ammc produced using powder metallurgy," *Archives of Metallurgy and Materials*, vol. 67, no. 3, 2022.

[27] A. Janeczek, J. Tomków, and D. Fydrych, "The influence of tool shape and process parameters on the mechanical properties of AW-3004 aluminium alloy friction stir welded joints," *Materials*, vol. 14, no. 12, p. 3244, 2021.

[28] R. K. Behera, B. P. Samal, S. C. Panigrahi et al., "Experimental analysis on machinability aspects of sintered aluminium metal matrix (Al+ Si+ Mg+ Cu+ SiC) composite-a novel product produced by powder metallurgy method," *International Journal of Materials Engineering Innovation*, vol. 13, no. 1, pp. 1–22, 2022.

[29] K. P. Mehta, P. Carlone, A. Astarita, F. Scherillo, F. Rubino, and P. Vora, "Conventional and cooling assisted friction stir welding of AA6061 and AZ31B alloys," *Materials Science and Engineering*, vol. 759, pp. 252–261, 2019.

[30] B. P. Samal, R. K. Behera, A. Behera et al., "Fuzzy logic application on dry sliding wear behavior of matrix aluminum composite produced by powder metallurgy method. Composites: mechanics, computations, applications," *Composites: Mechanics, Computations, Applications, An International Journal*, vol. 13, no. 1, pp. 49–62, 2022.

[31] S. Jayaprakash, S. Siva Chandran, T. Sathish et al., "Effect of tool profile influence in dissimilar friction stir welding of aluminium alloys (AA5083 and AA7068)," *Advances in Materials Science and Engineering*, vol. 2021, pp. 1–7, Article ID 7387296, 2021.

[32] R. K. Behera, B. P. Samal, S. C. Panigrahi, K. Muduli, A. Mohamed, and A. Samal, "Evaluation of magnesium recovery in Al-Mg alloys produced by modified stir casting method using genetic algorithm optimisation technique," *International Journal of Materials Engineering Innovation*, vol. 12, no. 2, pp. 134–148, 2021.

[33] K. Fuse and V. Badheka, "Bobbin tool friction stir welding: a review," *Science and Technology of Welding & Joining*, vol. 24, no. 4, pp. 277–304, 2019.

[34] G. H. S. F. L. Carvalho, I. Galvão, R. Mendes, R. M. Leal, and A. Loureiro, "Friction stir welding and explosive welding of aluminum/copper: process analysis," *Materials and Manufacturing Processes*, vol. 34, no. 11, pp. 1243–1250, 2019.

Hindawi
Advances in Materials Science and Engineering
Volume 2022, Article ID 8622510, 16 pages
https://doi.org/10.1155/2022/8622510

Research Article

Unsteady Radiative Maxwell Fluid Flow over an Expanding Sheet with Sodium Alginate Water-Based Copper-Graphene Oxide Hybrid Nanomaterial: An Application to Solar Aircraft

S. Chandrasekaran,[1] **M. Satyanarayana Gupta**,[2] **Sanju Jangid**,[3] **K. Loganathan**,[3,4] **B. Deepa**,[5] **and Dinesh Kumar Chaudhary**[6]

[1]*Department of Mathematics, Government Arts and Science College, Idappadi 637102, Tamil Nadu, India*
[2]*Department of Aeronautical Engineering, MLR Institute of Technology, Hyderabad, Telangana, India*
[3]*Department of Mathematics and Statistics, Manipal University Jaipur, Jaipur 303007, India*
[4]*Research and Development Wing, Live4Research, Tiruppur 638106, Tamil Nadu, India*
[5]*Department of Mathematics, Faculty of Engineering, Karpagam Academy of Higher Education, Coimbatore, Tamil Nadu, India*
[6]*Department of Physics, Amrit Campus, Tribhuvan University, Kathmandu, Nepal*

Correspondence should be addressed to M. Satyanarayana Gupta; msngupta.m@gmail.com and Dinesh Kumar Chaudhary; din.2033@gmail.com

Received 18 July 2022; Revised 6 August 2022; Accepted 10 August 2022; Published 5 September 2022

Academic Editor: Pudhupalayam Muthukutti Gopal

The primary heat source from the sunlight is solar energy, which is used in photovoltaic panels, solar power plates, photovoltaic streetlights, and solar-based hybrid nanocomposites. A hybrid nanofluid is traversing an expanding sheet in this investigation. Maxwell fluid stream with two nanoparticles is going towards a trough with a parabolic form and is situated within the solar aircraft wing to investigate the phenomena of heat transfer rate. The term solar thermal radiation was introduced to describe heat transfer occurrence. The effectiveness of heat transmission from airplane wings is assessed by taking into account unique phenomena such as magnetic field and heat source. The bvp4c procedure was applied to quantitatively explain the energy and motion equations with MATLAB software. The copper (Cu) and graphene oxide (GO) nanosolid particles are mixed with sodium alginate (SA), a common liquid, to form the nanosolid particles. Numerous control variables are thoroughly examined, including temperature, shear stress, motion, friction component, and Nusselt number. The skin-friction coefficient upsurges with a growing magnetic impression. The upsurge in Deborah number reduces the skin-friction coefficient. The heat source impression declines the heat transport rate but upsurges the skin-friction coefficient. The skin-friction coefficient and heat transport rate increase with growing magnetic impression. When it comes to heat transfer analysis, hybrid nanofluid efficiency is substantially superior to that of regular nanofluid.

1. Introduction

The primary cause of pollution and increase in atmospheric CO2 concentrations is the production and consumption of energy; hence, lowering CO2 emissions and transitioning to carbon-free energy sources are essential for the sustainability of life on Earth. Experts are actively investigating the use of nanotech and solar radiation to improve the efficiency of flying. Analysts are now investigating how to use nanotech and sunshine radiation to increase the productivity of aircraft. Brewster [1] analysed and reported the nature of radiative heat transfer. By embedding microparticles in standard heat exchangers, Choi and Eastman [2] suggested that a whole new class of heat exchangers may be developed. Suresh et al. [3] studied heat transfer effects on laminar convective flow in a pressure droplet features past an unvaryingly rounded tube via Al_2O_3–Cu/water hybrid nanofluid. The power management plan for solar-powered

high-level long-endurance aircraft was researched by Gao et al. [4]. The size of a solar/hydrogen structure for high altitudes and long-endurance airplanes was covered by Barbosa et al. [5]. The flow and energy transport in top-convective Maxwell fluid above an exponentially stretched surface with the Cattaneo–Christov heat flux were subjected by Ahmad et al. [6]. As described in Das et al.'s [7] study, the computational analysis of the time-dependent laminar hydromagnetic boundary layer flow and energy transport of nanofluids across an accelerated convective heat heated stretched sheet. Current research on the production, thermal physical features, heat transmission, pressure drop features, potential uses, and limitations of hybrid nanofluids was compiled by Sarkar et al. [8]. An experiment on temperature and nanosized particles volume with thermal conductivity of $ZnO–TiO_2/EG$ hybrid nanofluid was investigated by Toghraie et al. [9].

Efficacy in energy transport is currently the most important requirement from an industry standpoint. Modern businesses will not be able to function with conventional cooling solutions. Nanofluids have great promise as effective heat transfer devices. Microchooses, 100 nm metering, are involved in this phenomenon and can be detected in ethylene, water, oil, or glycol. Typically, the metals, oxide, carbon graphite, nitrides, carbides, and nanotubes are confined in nanostructures. Since then, numeral techniques have been established in a direction to increase the heat exposure of nanofluids. Nanoparticles, heat diffusion, Brownian motion, thermophoresis, and other techniques are among them. Using the Buongiorno model, Farooq et al. [10] examined hydromagnetic Maxwell fluid with nanomaterials on a surface that is extending exponentially while also accounting for thermophoretic and Brownian motion phenomena. Loganathan et al. [11] cast off the Cattaneo–Christov heat flux model to study the impact of second-order slip, reaction rate, and cross-diffusion properties on the hydromagnetic convective Oldroyd-B liquid flow towards a stretchable surface. Maleki et al. [12] inspected the impression of the Eckert amount, temperature and motion slipping parameters, radiation, suction or blowing, heat source/sink, and tiny particle volume fraction on the motion and heat transmission on the flow and heat transmission over a porous plain plate.

The research about non-Newtonian fluids has recently attracted a lot of interest. This is due to their wide range of industrial product applications. A most crucial factor in geoscience, biomechanics, and industries is how fluids flow through the porous material, including water through rock, to regulate skin temperature and filter out impurities. Typically, more than one fundamental equation cannot adequately describe these fluids. Due to the variety of these fluids, many constitutive equations are therefore presented. The three primary categories of non-Newtonian fluids are integral, rate, and differential kinds. The nonviscous fluids rate type includes Maxwell fluid. This lesson highlights the benefits of downtime. Abdelmalek et al. [13] analyzed the double-diffusion occurrence in Carreau liquid transient, a wedge-formed frame with strain relations and connections for heat physical features. The advancements in the primary cycles and relevant features, CSP (Concentrated Solar Power) techniques, heat exchange, and phase transition substance applied for thermal energy storage were the main topics of Khandelwal et al.'s [14] study of the integrated solar combined cycle system. The thermally stratiform flow of Oldroyd-B liquid caused by a stretchable sheet was explored by Loganathan et al. [15] with the effects of radiation and chemical reactions. To perform better, Rubbi et al. [16] developed a working fluid from soybean oil and Ti_3C_2 particles for use in a hybrid photovoltaic-thermal (PV-T) solar gatherer. Loganathan et al. [17] discovered the entropy investigation of third-order nanofluid flow with the impression of inclined magnetic impact across a convective surface. Loganathan et al. [18] addressed the impression of hydromagnetic Darcy–Forchheimer third-grade nanofluid flow towards a linear elastic sheet. Waini et al. [19] evaluated the constant mixed convective for both assisting and opposing flows over an erect surface immersed in a porous mode with Al_2O_3–Cu/water hybrid nanofluid. Through the development of a total energy optimizing model that incorporates the connection of increased energy conversion and additional energy usage, Wu et al. [20] concentrated on evaluating the energy concert of a symmetrical Λ-formed movable arm solar aircraft.

Usage for the impacts of magnetic influence on non-Newtonian fluids is expanding in a variety of industries, including chemical engineering, polymeric technologies, MHD generators, nuclear reactors, petroleum industries, and acceleration, geothermal heat, and plasma investigations. Ahmad et al. [21] studied an applied magnetic field, thermal dissipation, a heat source, and convective boundary circumstances; heat transfer is theoretically enhanced for graphene oxide/kerosene oil and graphene oxide-silver/kerosene oil hybrid nanofluids over a porous stretchable sheet. By employing hybrid nanofluid (CNT (carbon nanotube)-Al_2O_3/water and CNT-Fe3O4/water) as a cooling under the encouragement of an external magnetic field, Anitha et al. [22] inspected the energy transference performance of an advanced manufacturing double-tube heat exchanger. Gul et al. [23] discovered the heat insulation of the hybrid nanofluid flow in four distinct scenarios of conical gap between a cone and disc flow, involving 1st static cone revolving disc, 2nd static cone spinning disc, 3rd cone and disk rotation in much the same way, and 4th cone and disc rotation in the opposite direction. In the company of the convective situation, Hussain et al. [24] concentrated on hybrid nanoliquid flow through an exponentially extending spinning surface. The thermal characteristics of the moving copper-iron (II, III)/oxide-engine oil Casson fluid with nanoparticles in the solar parabolic trough absorber were explored by Jamshed et al. in [25]. To deepen the experiments of the sunlight aircraft wings with different assets like porous mode, Cattaneo–Christov heat flux, viscosity dissipation, heating and flow of energy, and entropy creation, Jamshed et al. [26] researched heat exchange by utilizing the tangent hyperbolic nanocomposite past inside solar wings

solar parabolic trough receiver. Jamshed et al. [27] evaluated the flow and heat transmission characteristics of a Cu–TiO_2/tangent hyperbolic hybrid nanofluid of this sort across a slippery surface. The temperature distribution and entropy creation analysis of third-grade nanofluid flow forward into stretchy sheet with oriented magnetic impacts, thermal radiation, heat source/sink, and convective thermal influences was researched by Jamshed [28]. Loganathan et al. [29] utilized a third-grade fluid flow with nanoparticles with zero mass flux and a non-Fourier model to analyze entropy and heat transfer. With the assistance of Cattaneo–Christov dual diffusion, Loganathan et al. [30] defined the effect of the hydrodynamic radiative Maxwell fluid model on a hot surface. Jamshed et al. [31] investigated radiative Prandtl–Eyring hybrid nanofluid in a parabolic trough surface within a solar water pump to analyze the viscid dissipation, heat generation, and entropy. Muhammad et al. [32] researched the time-dependent squeezing flow of a hybrid nanofluid (having CNTs + CuO/water) and a nanofluid (having CNTs/water) with the melting impact and viscid dissipation to designate the behavior of heat exchange, entropy formation, and bean amount. To optimize the creation of entropy of Williamson fluid flow towards a plain and stretchy surface, Qayyum et al. [33] tested the influence of hydromagnetic, nonlinear thermal radiation, Darcy–Forchheimer porous mode, viscous dissipation, 1st-order motion slip, and convective boundary circumstance. To manage the flow system heat transfer, Saeed et al. [34] employed the slip conditions created by a whirling disc, thermal stratification, and nonlinear thermal radiation in the solution of the Darcy–Forchheimer flow for TiO_2–Ag/H_2O hybrid nanofluid. The time-dependent Maxwell Cu–Al_2O_3/sodium alginate hybrid nanofluid approaching a stretchy/shrinking surface with radiative heat action and energy transmission was researched by Zainal et al. [35].

Several academics have been interested in the flow of a viscous caused by a stretched sheet. This is a result of their many uses in the polymeric industry worldwide, environmental contamination, biological processes, aerodynamic extraction of plastic sheets, manufacture of glass fiber along a liquid film and condensation process, chilling and/or dryness of papers and textile, and so on. Ahmad et al. [36] investigated the effects of brick-shaped nanostructured materials made of cerium oxide (CeO_2) and zinc oxide (ZnO) on the time-dependent three-dimensional water-driven hybrid nanofluid flow. In addition to the benefits of thermal defeat and the non-Fourier concept for energy flux, Algehyne et al. [37] revealed the heat transport in Maxwell MoS_2–Ag/engine oil hybrid nanofluid past across an endless stretchy erect porous sheet. Bhattacharyya et al. [38] inspected an electrically conducted Maxwell hybrid nanofluid fluid covering Cu and graphene oxide nanoparticles with time-dependent aligned magnetic field and velocity slip conditions over a linearly stretched sheet. On a convectively heated Riga plate with Cattaneo–Christov theory, Eswaramoorthi et al. [39] deliberated the effects of glycerin-based carbon nanotubes with motion slip in a porous material described by Darcy and Forchheimer. Ouni et al. [40] discussed the heat generation and viscous dissipation impression of Oldroyd-B fluid flow with copper-gold/engine oil hybrid nanoparticles with a parabolic trough surface collector within a solar water pump. Ali et al. [41] discussed the heat transportation and energy creation of carboxymethyl cellulose water-based cross hybrid nanofluid flow. Iftikhar et al. [36] researched the influence of heat generation/absorption of three-dimensional time-dependent brick from zinc-oxide hybrid nanofluid. A study on MHD radiative bidirectional hybrid nanofluid flow to analyze thermal performance was deliberated by Iftikhar et al. [42]. Iftikhar et al. [43] inspected the heat transference of blade-formatted cadmium telluride-graphite nanocomposites hybrid nanofluid flow under electromagnetohydrodynamics. Iftikhar et al. [44] studied an entropy creation of sphere-sized bidirectional hybrid nanofluid along with varying thermal performance. Using the Williamson model, Hussain [45] investigated the viscous dissipation, thermal radiation, and entropy creation of a hybrid nanofluid (Cu-graphene oxide/sodium alginate) that was situated within solar airplane wings and moved into a trough with a parabolic form. According to Jamshed et al. [46], time-independent hybrid nanofluid (Cu-silicon dioxide/engine oil) flow and thermal transport properties are affected by nanosolid particle morphologies, porosity substantial, heat generator, viscid dissipative, and radiative flux.

In solar aircraft wings, a trough with a parabolic shape called (PTSC) captures solar thermal energy in the system of solar radiative sprinkling. The quest for more expensive and alternative fuel sources will be significantly impacted by aviation studies. The heat transference rate increases when established hybrid nanofluids are used in place of conventional nanofluids. Because they were obtained under entirely cutting-edge substantial circumstances, the research findings will be helpful to fresh scientists.

The latest results can aid in future advancements by allowing for the assessment of the thermal system heat effect while taking into consideration various non-Newtonian hybrid nanofluids (Carreau, second-grade, tangent hyperbolic fluid, Casson, micropolar nanofluids, etc.). Furthermore, the extending approach may be used to simulate the effects of magneto-slip movement as well as temperature-dependent fluidity and porosity.

The research model may plug the space in heat transmission by utilizing radiative Maxwell hybrid nanofluid flows on a penetration stretchable surface, changing thermal conductivity, heat source, and MHD (magnetohydrodynamic) impact. The theoretical motion of the nanofluids is represented using the Tiwari and Das model. In this study, copper (Cu) and graphene oxide (GO) hybrid nanoparticles are used, with sodium alginate (SA) serving as the regular fluid. The Maxwell hybrid nanofluid's leading equation will be converted into ordinary differential equations with the proper parallel transformations.

2. Mathematical Formulation

The following are the circumstances and guiding principles that govern the flow model:

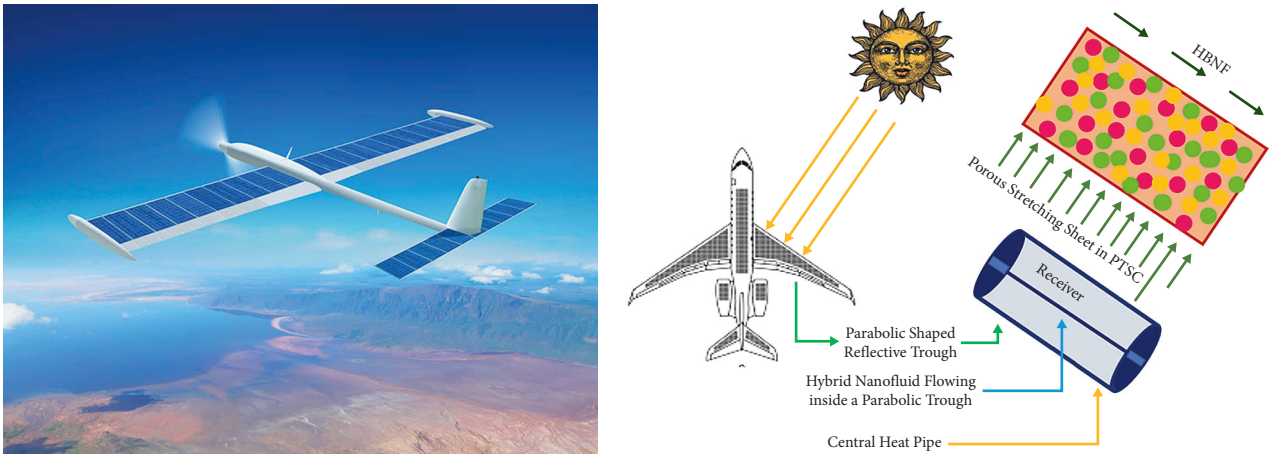

(a) (b)

Figure 1: Methodical picture of existing theoretic research.

(i) Two-dimensional unsteady laminar flow.
(ii) Boundary layer guesstimates.
(iii) Tiwari–Das model (single stage system).
(iv) Radiative Maxwell hybrid nanofluid.
(v) Piercing mode.
(vi) On the x-axis, a magnetic field $B(t) = B_0(1-\xi t)^{-(1/2)}$ is applied.
(vii) Flow with heat source and viscous dissipation.

The solar aircraft application modelling and flow diagram are given in Figures 1 and 2, respectively. Below mentioned equations are the governing equation [21, 45] for existing research work:

Equation of continuity:

$$\frac{\partial u}{\partial x} + \frac{\partial v}{\partial y} = 0. \tag{1}$$

Equation of motion:

$$\rho_{hbnf}\left(\frac{\partial u}{\partial t} + u\frac{\partial u}{\partial x} + v\frac{\partial u}{\partial y}\right) = \mu_{hbnf}\frac{\partial^2 u}{\partial y^2} - \lambda\left(u^2\frac{\partial^2 u}{\partial x^2} + v^2\frac{\partial^2 u}{\partial y^2} + 2uv\frac{\partial^2 u}{\partial x \partial y}\right) - \sigma_{hbnf}B_0(t)^2 u - \mu_{hbnf}\frac{u}{k}. \tag{2}$$

Equation of temperature:

$$(\rho C_p)_{hbnf}\left(\frac{\partial T}{\partial t} + u\frac{\partial T}{\partial x} + v\frac{\partial T}{\partial y}\right) = k_{hbnf}\frac{\partial^2 T}{\partial y^2} - \frac{\partial q_r}{\partial y} + \mu_{hbnf}\left(\frac{\partial u}{\partial y}\right)^2 + Q_0(T - T_\infty). \tag{3}$$

The boundary situations for the present situation are as tracks [31, 40]:

$$u = U_w + N_w\frac{\partial u}{\partial y}, v = V_w, -k_0\left(\frac{\partial T}{\partial y}\right) = h_f(T_w - T), at\ y = 0, u \longrightarrow 0, T \longrightarrow T_\infty, at\ y \longrightarrow \infty. \tag{4}$$

The apparatuses of velocity in the consistent coordinates of y and x are meant by v (m/s) and u (m/s), respectively, where T (K) is the fluid temperature, λ is the relaxation time, N_w depicts the slip length, V_w signifies the encompassing plate porosity, and k_0 shows the material porousness. Furthermore, *hbnf* stands for hybrid nanofluid, *nf* stands for nanofluid, *Bf* stands for base fluid, $(\rho C_p)_{hbnf}$ denotes the heat capacity of the hybrid nanofluid, B_0 (Tesla-T) depicts the magnetic field strength, σ_{hbnf} depicts the electrical conductivity, k_{hbnf} denotes the thermal conductivity of the hybrid nanofluid, ρ_{hbnf} denotes the hybrid nanofluid density, and μ_{hbnf} denotes the hybrid nanofluid dynamic

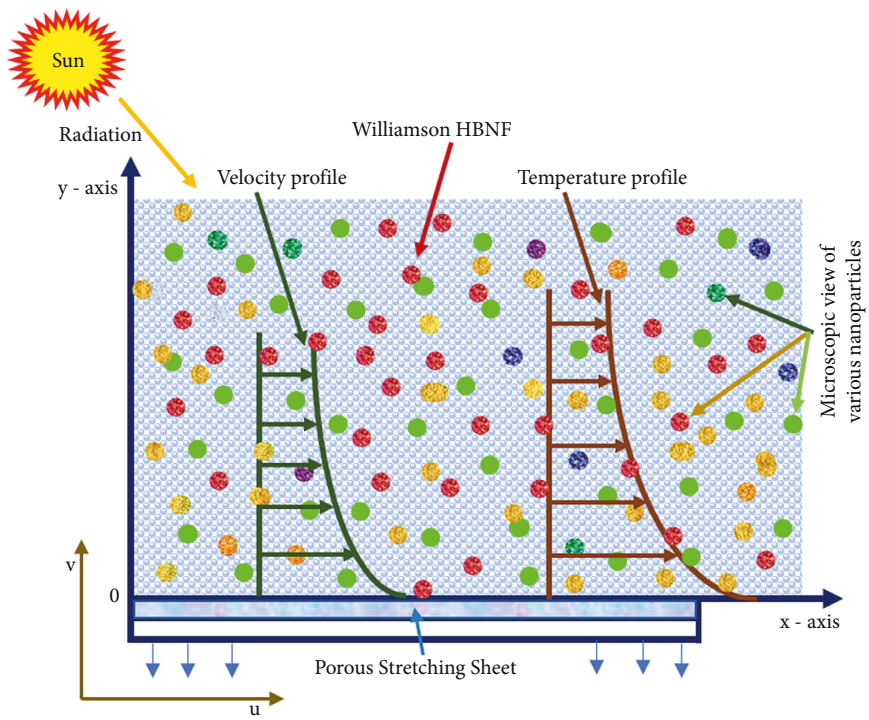

Figure 2: Movement model picture.

viscosity.C_p is the specific heat at unvarying pressure, M depicts the shape factor (3 for sphere), ϕ_{Cu} depicts the volume fraction of Cu, ϕ_{GO} depicts the volume fraction of GO, and $k_{Bf}, \mu_{Bf}, \rho_{Bf}$, and σ_{Bf} denote the thermal conductivity, dynamic viscosity, density, and electrical conductivity of the SA base fluid, respectively. The subscripts Bf, Cu, and GO denote the amounts of base fluid, Cu nanoparticle, and GO nanoparticle, respectively. As a result, Table 1 contains information on the working pure fluid as well as two different nanomaterials Cu and GO, and the hybrid nanoparticle physical properties are given in Table 2.

The penultimate term in energy (3), where q_r indicates the radiative heat flux and is delineated using the Rosseland guesstimate [38, 45], represents thermal radiation

$$q_r = \frac{-4\sigma^*}{3k^*}\frac{\partial T^4}{\partial y}, \tag{5}$$

where σ^* is the Stefan–Boltzmann constant and k^* corresponds to the coefficient of mean absorption. Now, using the Taylor series for the term T^4 at a location T_∞ and disregarding the higher order terms in approximation, the following final form may be obtained.

Here, T^4 is a linear connection of temperature through Taylor's arrangement extension about T_∞ and disregarding progressive terms; thus,

$$T^4 \approx 4T_\infty^3 T - 3T_\infty^4. \tag{6}$$

In the current situation, we may simplify our model analysis by taking into account the following nondimensional variables [19, 38, 45]:

$$\eta = \sqrt{\frac{b}{\nu_{Bf}(1-\xi t)}}y, \psi = \sqrt{\frac{\nu_{Bf} b}{(1-\xi t)}}x f, \theta(\eta) = \frac{T - T_\infty}{T_w - T_\infty}, u = \frac{\partial \psi}{\partial y} = \frac{bxf'}{(1-\xi t)} \text{ and } v = -\frac{\partial \psi}{\partial x} = -\sqrt{\frac{\nu_{Bf} b}{(1-\xi t)}}f. \tag{7}$$

The primes now stand for differentiation of the pseudosimilarity variables. According to the scientific flow model, a traveling flat plate with an uneven expansion motion and an isolating surface temperature is summarized as follows [38, 45]:

$$U_w = \frac{bx}{(1-\xi t)} \text{ and } T_w = T_\infty + \frac{b^* x}{(1-\xi t)}, \tag{8}$$

where the initial expansion rate and heat variance, respectively, are denoted by b and b^*. The temperatures of the surface and surroundings are represented, respectively, by

Table 1: The formulation and limitations for the nanofluid and hybrid nanofluid in the aforesaid system of equations [21, 45].

Thermal properties	Nanofluid	Hybrid nanofluid
Thermal diffusivity	$\alpha_{nf} = k_{nf}/(\rho C_p)_{nf}$	$\alpha_{hbnf} = k_{hbnf}/(\rho C_p)_{hbnf}$
Viscosity	$\mu_{nf}/\mu_{Bf} = 1/(1-\phi_{Cu})^{2.5}$	$\mu_{hbnf}/\mu_{Bf} = 1/(1-\phi_{Cu})^{2.5}(1-\phi_{GO})^{2.5}$
Heat capacity	$(\rho C_p)_{nf}/(\rho C_p)_{Bf} = ((1-\phi_{Cu}) + \phi_{Cu}(\rho C_p)_{Cu}/(\rho C_p)_{Bf})$	$(\rho C_p)_{hbnf}/(\rho C_p)_{Bf} = \phi_{GO}(\rho C_p)_{GO}/(\rho C_p)_{Bf} + (1-\phi_{GO})((1-\phi_{Cu}) + \phi_{Cu}(\rho C_p)_{Cu}/(\rho C_p)_{Bf})$
Density	$(\rho)_{nf}/(\rho)_{Bf} = ((1-\phi_{Cu}) + \phi_{Cu}(\rho)_{Cu}/(\rho)_{Bf})$	$(\rho)_{hbnf}/(\rho)_{Bf} = \phi_{GO}(\rho)_{GO}/(\rho)_{Bf} + (1-\phi_{GO})((1-\phi_{Cu}) + \phi_{Cu}(\rho)_{Cu}/(\rho)_{Bf})$
Thermal conductivity	$k_{nf} = k_{Cu} + (M-1)k_{Bf} - (M-1)\phi_{Cu}(k_{Bf} - k_{Cu})$ $/k_{Cu} + (M-1)k_{Bf} + \phi_{Cu}(k_{Bf} - k_{Cu})k_{Bf}$	$k_{hbnf} = k_{GO} + (M-1)k_{nf} - (M-1)\phi_{GO}(k_{nf} - k_{GO})/k_{GO}$ $+(M-1)k_{nf} + \phi_{GO}(k_{nf} - k_{GO})k_{nf}$
		where, $k_{nf} = k_{Cu} + (M-1)k_{Bf} - (M-1)\phi_{Cu}(k_{Bf} - k_{Cu})/k_{Cu} + (M-1)k_{Bf} + \phi_{Cu}(k_{Bf} - k_{Cu})k_{Bf}$
Electrical conductivity	$\sigma_{hbnf} = (1 + 3(\phi_{Cu}\sigma_{Cu}/\sigma_{Bf} - (\phi_{Cu}))/(\phi_{Cu}\sigma_{Cu}/(\phi_{Cu})\sigma_{Bf} + 2)$ $-(\phi_{Cu}\sigma_{Cu}/\sigma_{Bf} - (\phi_{Cu})))$	$\sigma_{hbnf} = (1 + 3(\phi_{Cu}\sigma_{Cu} + \phi_{GO}\sigma_{GO}/\sigma_{Bf} - (\phi_{Cu} + \phi_{GO}))$ $/(\phi_{Cu}\sigma_{Cu} + \phi_{GO}\sigma_{GO}/(\phi_{Cu} + \phi_{GO})\sigma_{Bf} + 2) - (\phi_{Cu}\sigma_{Cu} + \phi_{GO}\sigma_{GO}/\sigma_{Bf} - (\phi_{Cu} + \phi_{GO})))$

Table 2: $Cu - GO/SA$ hybrid nanoparticle physical properties [38, 45].

Physical characteristics	SA	Cu	GO
ρ	989	8933	1800
C_p	4175	385.0	717
k	0.6376	401.00	5000
σ	2.6×10^{-4}	5.96×10^{7}	1.1×10^{-5}
Pr	6.5	-	-

Table 3: Evaluation concerning the values of $-\theta'(0)$ with Pr, when $Bi \longrightarrow \infty$, and absenteeism of further remaining parameters.

Pr	Das et al. [7]	Jamshed et al. [25]	Hussain [45]	Current work
1	1.00000000	1.00000000	1.00000000	1.00000000
3	1.92357431	1.92357420	1.92357420	1.923682566
7	3.07314679	3.07314651	3.07314651	3.072250191
10	3.72055436	3.72055429	3.72055429	3.720673886

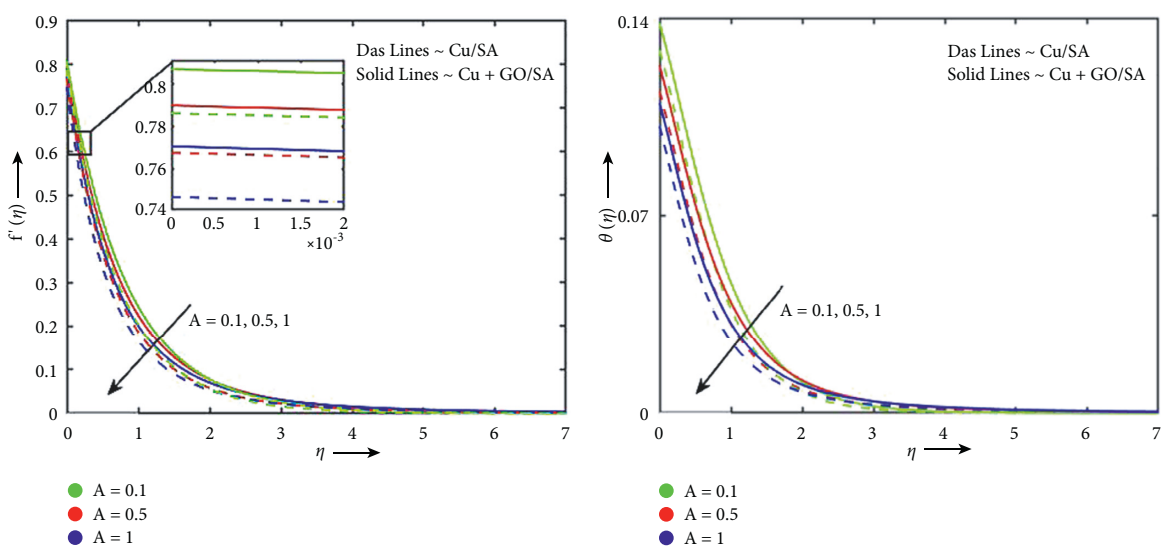

(a) (b)

Figure 3: A variances in velocity and temperature.

T_w and T_∞. Temperature fluctuation puts the plate surface in harm because it is designed to be slick.

Using the similarity modifications (7), create controlling equations (1)–(4), where continuity (1) is completely fulfilled and the other required equations adopt the dimensionless form shown as follows:

$$f''' + \phi_a\phi_b f f'' - \phi_a\phi_b (f')^2 - \phi_a\phi_b \frac{\xi}{b} f' - \phi_a\phi_b \frac{\xi}{b}\frac{\eta}{2} f'' - K f' - \beta\left(\phi_a\phi_b f^2 f''' - 2\phi_a\phi_b f f' f''\right) - \phi_a\phi_e M n^2 f' = 0, \tag{9}$$

$$\theta''\left(1 + \frac{1}{\phi_d} PrNr\right) + \Pr\frac{\phi_c}{\phi_d}\left(f\theta' - f'\theta - A\left(\theta + \frac{\eta}{2}\theta'\right) + \frac{Ec}{\phi_a\phi_c} f''^2 + \frac{1}{\phi_c} Q\theta\right) = 0, \tag{10}$$

with the boundary circumstances

$$\begin{aligned} f(0) = S,\ f'(0) &= 1 + \Lambda f'',\ \theta'(0) \\ &= -Bi(1-\theta), at\ \eta = 0.\ f'(\infty) \\ &\longrightarrow 0, \theta(\infty) \longrightarrow 0, at\ \eta \longrightarrow \infty. \end{aligned} \tag{11}$$

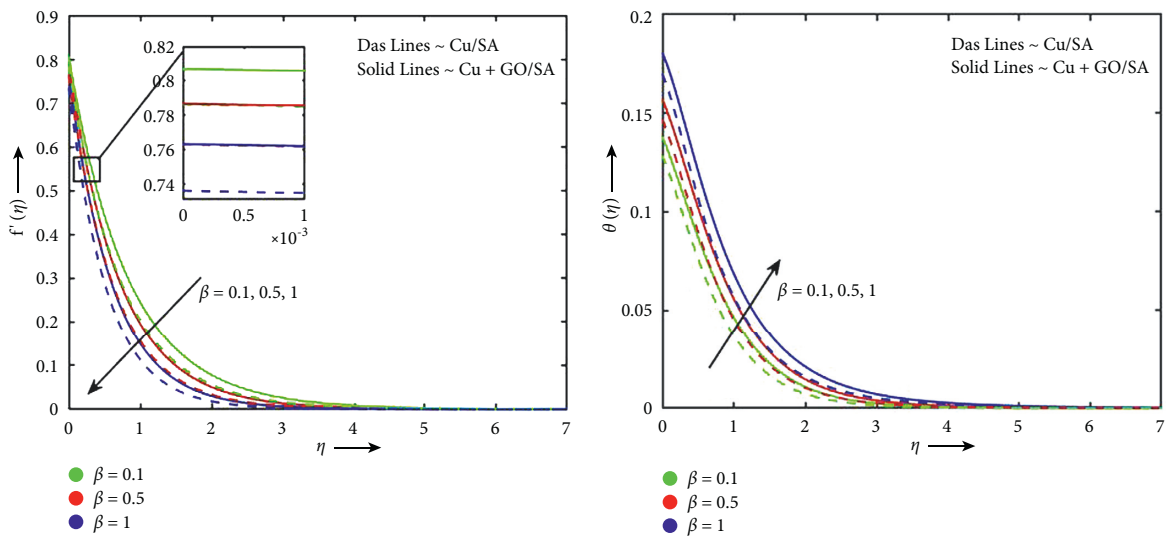

Figure 4: β variances in velocity and temperature.

The unsteadiness parameter (A), porous medium parameter (K), Deborah number (β), Hartmann (magnetic) parameter (Mn), Eckert number (Ec), heat source parameter (Q), Prandtl number (Pr), radiation parameter (Nr), suction/injection parameter (S), velocity slip parameter (Λ), and Biot number (Bi) are all terms used to describe the participation of dimensionless restrictions in equations (9)–(11). These variables are stated numerically as

$$\phi_a = \frac{\mu_{Bf}}{\mu_{hbnf}}, \phi_b = \frac{(\rho)_{hbnf}}{(\rho)_{Bf}}, \phi_e = \frac{(\sigma)_{hbnf}}{(\sigma)_{Bf}}, \phi_c = \frac{(\rho C_p)_{hbnf}}{(\rho C_p)_{Bf}},$$

$$\phi_d = \frac{(k)_{hbnf}}{(k)_{Bf}}, A = \frac{\xi}{b}, K = \frac{\nu_{Bf}(1-\xi t)}{bk}, \beta = \frac{\lambda U_w}{x},$$

$$Mn^2 = \frac{\sigma_{Bf} B_0^2}{\rho_{Bf} b}, Ec = \frac{U_w^2}{(C_p)_{Bf}(T_w - T_\infty)}, Q = \frac{Q_0 x}{(\rho C_p)_{Bf} U_w}, \quad (12)$$

$$\Pr = \frac{\nu_{Bf}}{\propto_{Bf}}, Nr = \frac{16\sigma^* T_\infty^3}{3k^* \nu_{Bf}(\rho C_p)_{Bf}}, S = -V_w\sqrt{\frac{(1-\xi t)}{b\nu_{Bf}}},$$

$$\Lambda = \sqrt{\frac{b}{(1-\xi t)\nu_{Bf}}} N_w, Bi = \frac{h_f}{k_0}\sqrt{\frac{\nu_{Bf}(1-\xi t)}{b}}.$$

The shear stress and heat transport rate are the physical quantities of engineering practical significance, and they are delineated as follows.

The shear stress is $C_f = \tau_w/\rho_{Bf}U_w^2$, and the Nusselt number is well-defined as $\mathrm{Nu_x} = \mathrm{xq_w}/\mathrm{k}_{Bf}(T_w - T_\infty)$.

The surface shear stress τ_w is assumed by $\tau_w = \mu_{hbnf}(\partial u/\partial y)_{y=0}$, and we get

$$C_f Re_x^{1/2} = \frac{1}{\phi_a}[f''(0)]. \quad (13)$$

The rate of heat transfer q_w is assumed by $q_w = -k_{hbnf}(\partial T/\partial y)_{y=0} + (q_r)_{y=0}$, and we get

$$Nu_x Re_x^{-1/2} = -\phi_d[1 + Nr]\theta'(0), \quad (14)$$

where $Re_x = xu_w/\nu_{Bf}$ is the Reynolds number.

3. Numerical Structure

Equations are solved via the bvp4c technique. All numerical values and graphs are found with MATLAB software which is discussed in through tables and graphs. Let

$$f = y(1), f' = y(2), f'' = y(3), \theta = y(4), \theta' = y(5). \quad (15)$$

Equations (9)–(11) are reduced into a new form as

$$f''' + \phi_a\phi_b y(1)y(3) - \phi_a\phi_b(y(2))^2 - \phi_a\phi_b\frac{\xi}{b}y(2) - \phi_a\phi_b\frac{\xi}{b}\frac{\eta}{2}y(3) - Ky(1)$$
$$-\beta\left(\phi_a\phi_b(y(1))^2 f''' - 2\phi_a\phi_b y(1)y(2)y(3)\right) - \phi_a\phi_e Mn^2 y(2) = 0, \theta''\left(1 + \frac{1}{\phi_d}PrNr\right) \quad (16)$$
$$+\Pr\frac{\phi_c}{\phi_d}\left(y(1)y(5) - y(2)y(4) - A\left(y(4) + \frac{\eta}{2}y(5)\right) + \frac{Ec}{\phi_a\phi_c}(y(3))^2 + \frac{1}{\phi_c}Qy(4)\right) = 0,$$

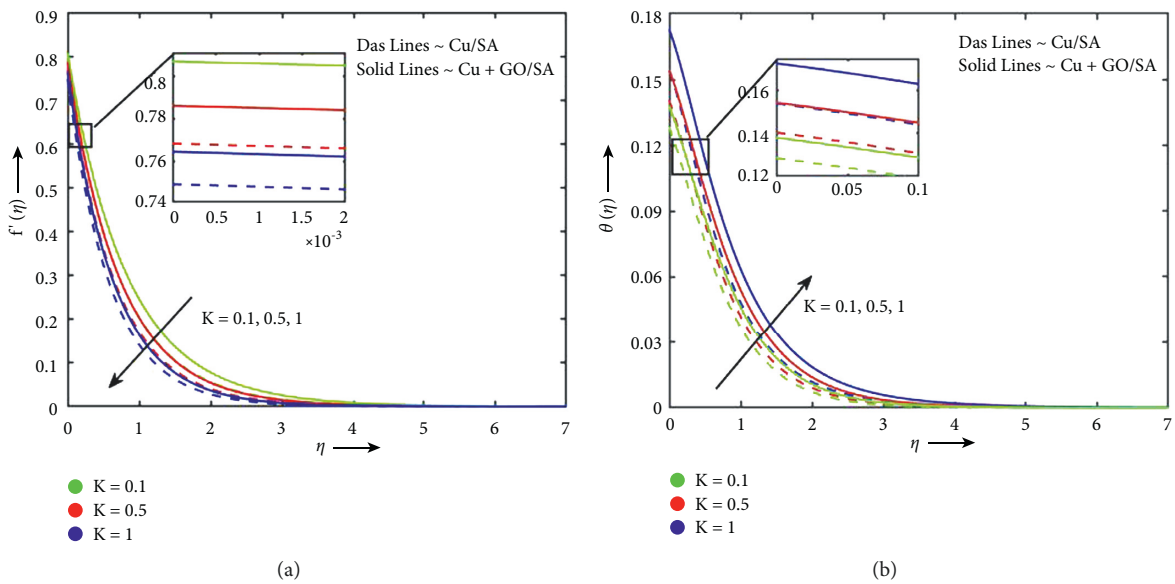

Figure 5: K variances in velocity and temperature.

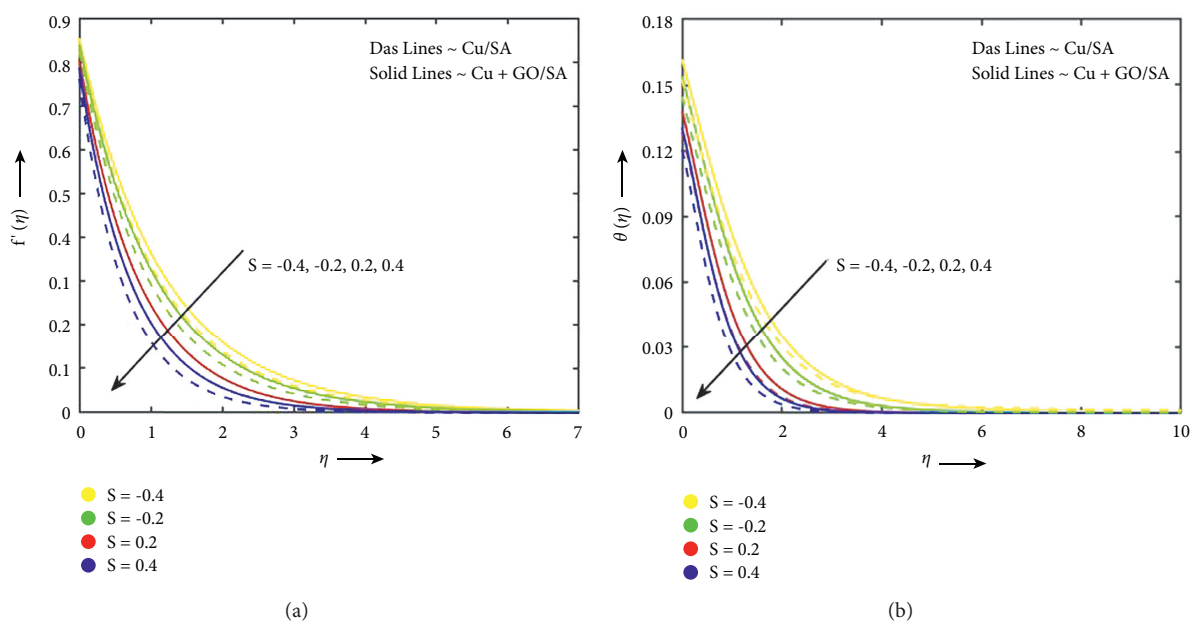

Figure 6: S variances in velocity and temperature.

with the boundary conditions

$$y0(1) = S, y0(2) = 1 + \Lambda y0(3), y0(5) = -Bi(1 - y0(4)), at\ \eta = 0 y\infty(2) \longrightarrow 0, y\infty(4) \longrightarrow 0, at\ \eta \longrightarrow \infty. \quad (17)$$

The choice $\eta(\infty) = 7$ or 10 indicates that each numerical output approaches asymptotic assets ideally in this technique.

3.1. Code Validation. Validation of present findings is carried out with the use of contrast to current research. Table 3 provides a comparison of the known research

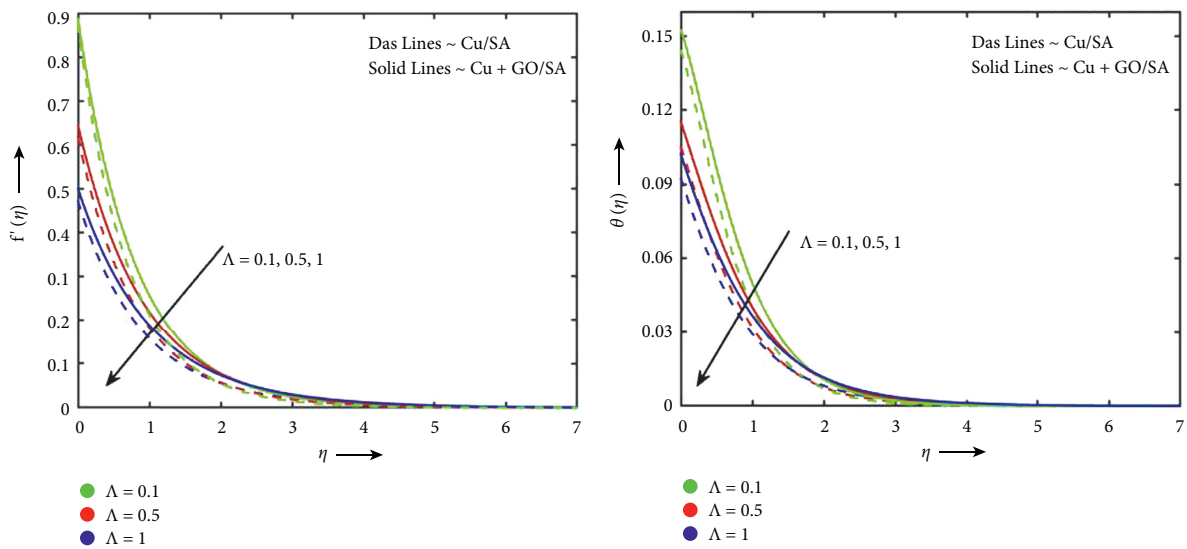

(a) (b)

Figure 7: Λ variances in velocity and temperature.

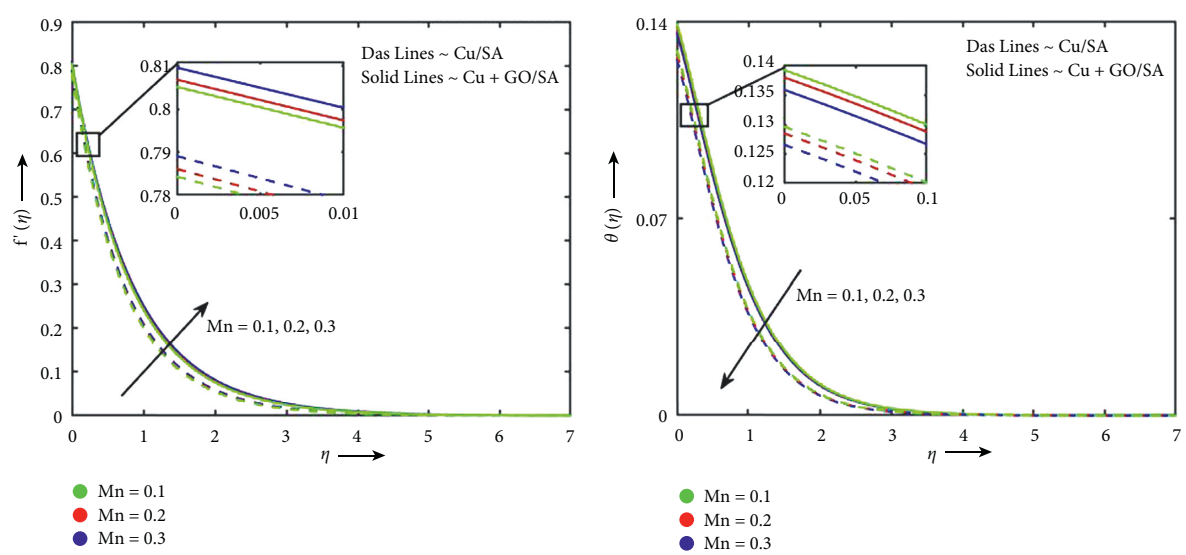

(a) (b)

Figure 8: *Mn* variances in velocity and temperature.

consistencies. However, extremely accurate results for the current analysis are found.

4. Result and Discussion

Using the bvp4c technique, the characteristics of two different sodium alginate-based nanofluids, namely, $Cu - SA$ and $GO - Cu/SA$, are quantitatively examined. We compare our performance of the model to the analytical ones for the limited situation of standard Newtonian flow in the current configuration to validate our mathematical model. The effects of emerging flow characteristics are listed using various graphs and table data that have been compiled. The impact of multiple physical parameters on motion, temperature, skin-friction coefficient, and Nusselt parameter values obtained with MATLAB software is exposed in Figures 2–11 and Table 1. For the current research, we measured the values of physical parameters as $\beta = K = A = Nr = Ec = Q = Bi = 0.1$, $Mn = S = \Lambda = 0.2, \phi_{GO} = 0.09, \phi_{Cu} = 0.18$, and $\Pr = 6.5$.

Figures 3(a) and 3(b) show the decline behavior of motion and temperature of increasing unsteadiness parameter, respectively, for both Cu/SA and $Cu - GO/SA$. Figure 3(b) shows how the unsteadiness affects the heat distribution, and it can be understood that as the unsteadiness number is raised, the temperature distribution drastically diminishes. This is true since a reduction in the temperature profile is brought on by an increase in heat

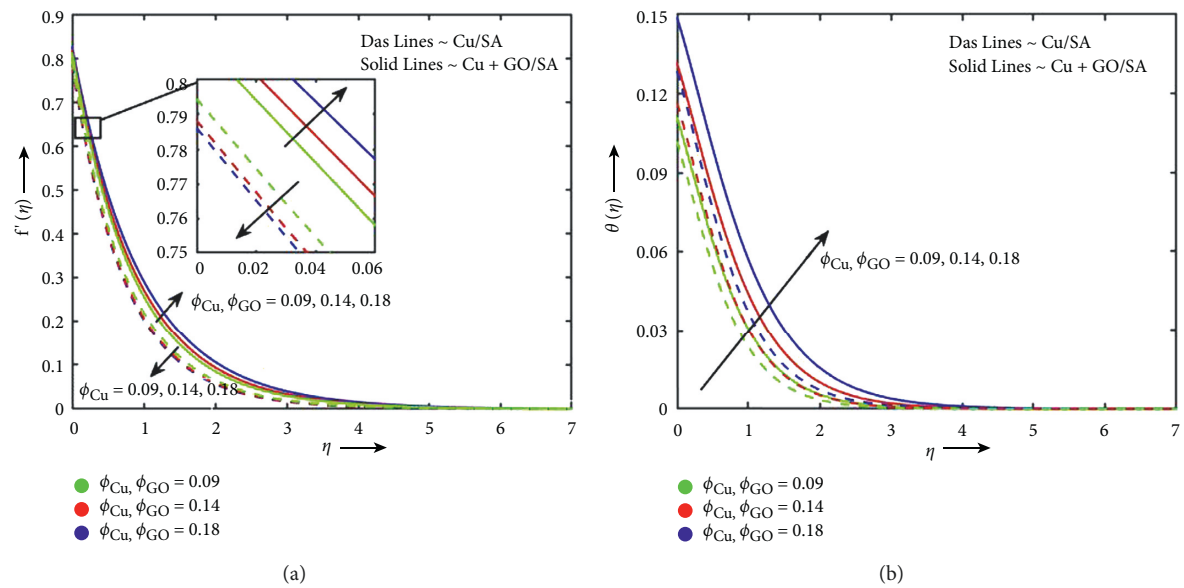

Figure 9: ϕ variances in velocity and temperature.

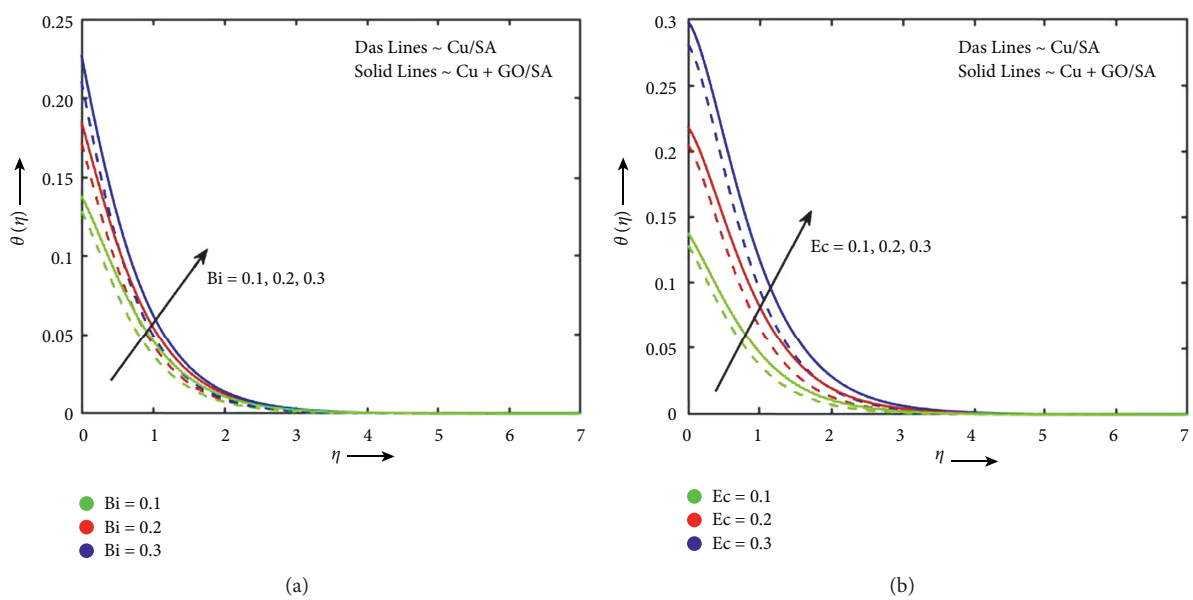

Figure 10: *Bi* and *Ec* variances in temperature.

losses of the sheet being stretched. Due to the reduction in the heat transference rate from the sheet to the fluid for larger quantities of the unsteady parameter, this suggests that the cooling rate is significantly greater than the rate of chilling for the steady flow.

Figures 4(a) and 4(b) depict the impression of the growing Deborah number on the velocity and temperature for both Cu/SA and $Cu - GO/SA$, respectively. Figure 4(a) shows how hybrid nanomaterials and nanostructures, as well as motion curves, are affected by the Deborah number. In comparison to the change in Deborah, the movement of nanoparticles and hybrid nanomaterials is decreased. This decrement flow behavior is caused by its elastic nature (Maxwell fluid). In light of fluid flow, Maxwell liquid repairs greater deformation as a result of this property. By using greater values of the Deborah number, momentum boundary layers are reduced. Additionally, it is looked at whether hybrid nanoparticles are more effective than approach-related nanomaterials in terms of maximum flow phenomena. Due to its elastic nature, flow properties are decreasing. Also, it is shown that Maxwell liquid is warmed up more than viscous fluid. In comparison to the instance of the technique associated with nanomaterials, it is noticed that the strategy associated with nanomaterials is much more effective in obtaining the greatest thermal energy (see Figure 4(b)).

In terms of flow behaviors, porosity has always played a key role. However, in nanolevel streaming settings, the

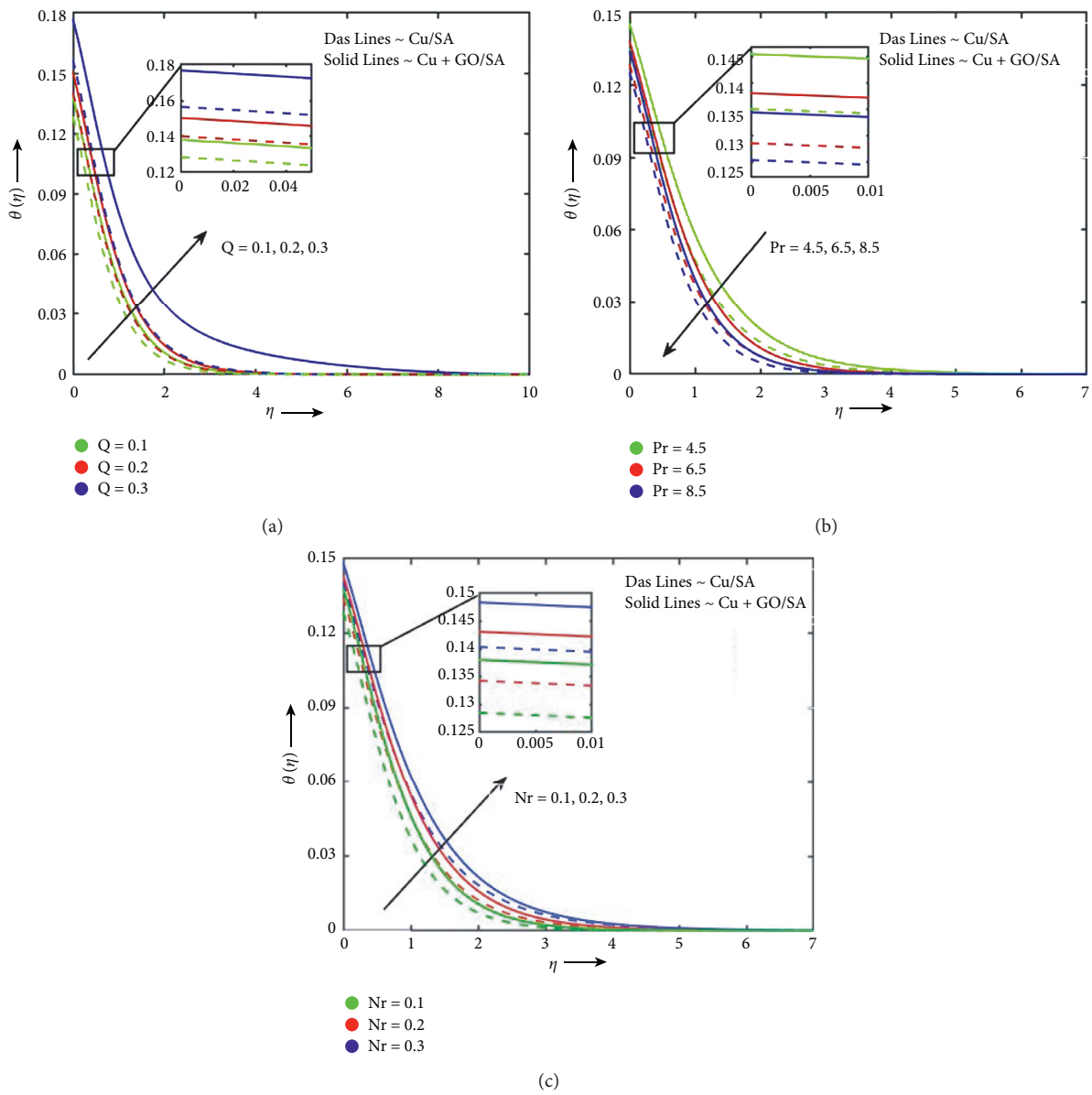

Figure 11: Q, Pr, and Nr variances in temperature.

porous nature of the material is critical for the passage of nanoparticles and thermal issues. $Cu-GO/SA$ hybrid nanofluid fluids continue to flow ahead of Cu/SA nanofluid fluids, as seen in Figure 5(a) when the porosity values increase. Fluids prefer to flow through the higher porosity rather than over it as the parameter continues to rise in value. In Figure 5(a), the flow rate for $hbnf$ is slower than that of nanolevel fluid because the flow seeks to flow into the porous mode more as there are more particles present. Both the $Cu-GO/SA$ mixture and the Cu/SA nanomixture of fluids are shown in Figure 5(b) in their most advanced thermal states. Two factors might be to blame for this increase: the first is the well-known explanation for lower fluidity absorbing more heat, the second is the special thermal transmitting properties of nanomaterials, and the $Cu-GO/SA$ hybrid is taking control of the Cu/SA by absorbing more heat, encouraging thermal dispersion of the hybrid. Because of the porous surface's ability to diminish fluidity, which lowers the fluid velocity and raises its heat, the porosity of the used fluid is directly related to its viscosity.

The impact of the suction ($+ve$ values) and injection ($-ve$ values) on the motion and temperature characteristics of both Cu/SA and Cu- GO/SA is depicted in Figure 6. As can be observed in Figure 6(a), as the suction impression is increased, the motion graphs and the thickness of the momentum boundary layer both decrease. However, when the injection parameter is increased, the velocity and momentum boundary layers are improved. Similar to this, as the suction variable is increased, the temperature profiles

Table 4: The skin-friction and Nusselt number values for Pr = 6.5.

β	Mn	K	A	Pr	Ec	Nr	Q	Bi	S	Λ	ϕ_{Cu}	ϕ_{GO}	$Cf_x Re_x^{1/2}$	$Nu_x Re_x^{-1/2}$
														0.203399471
														0.198911995
														0.193351315
														0.203103094
														0.203399471
														0.203900759
														0.203399471
														0.199526545
														0.195200657
													−2.007929558−2.218466432	0.203399471
													−2.462615810−2.025015280	0.206948785
													−2.007929558−1.978850427	0.210061001
													−2.007929558−2.224604383	0.201634394
													−2.449624474−2.007929558	0.203399471
													−2.186074026−2.386574079	0.204265376
													−2.007929543−2.007929558	0.203399471
	0.2	0.1	0.1	6.5	0.1	0.1		0.1		0.2	0.18	0.09	−2.007929560−2.007929558	0.184438877
0.1	0.1	0.1	0.1	4.5	0.1	0.1	0.10.1	0.1	0.2–0.4	0.1	0.09	0.09	−2.007929562−2.007929562	0.165478283
0.5	0.2	0.5	0.5	6.5	0.2	0.2	0.20.3	0.2	−0.2 0.2	0.5	0.14	0.14	−2.007929558−2.007929548	0.203399471
1	0.3	1	1	8.5	0.3	0.3		0.3	0.4	1	0.18	0.18	−2.007929543−2.007929558	0.220592104
													−2.007929554−2.007929541	0.237506074
													−2.007929558−2.007929556	0.203399471
													−2.007929554−1.512755614	0.200507438
													−1.658541706−2.007929558	0.194257513
													−2.215655645−2.304959505	0.203399471
													−1.470390874−1.036070950	0.384590061
													−1.504092052−1.924981668	0.547020898
													−2.330362054	0.197777437
														0.199618121
														0.203399471
														0.205201976
														0.199947269
														0.208729347
														0.211806558
														0.164188753
														0.21118982 9
														0.256863623

and the width of the thermal boundary layer decrease, but the reverse tendency is seen in the situation of blowing, as seen in Figure 6(b).

Fluid flow with $Cu - GO/SA$ and Cu/SA can have their flow rates restricted by the velocity slip constraint. The slip parameter slipperiness is overshadowed by the strength of solid materials, which is what would be causing the slow flow rate seen in Figure 7(a) for its boosted amounts. Figure 7(b) depicts the decline in temperature profiles of the upsurge velocity slip parameter.

As understood in Figure 8(a), the velocity rises as the magnetic field increases as a result of both Cu/SA and $Cu - GO/SA$ flow. Opposite impression is shown for temperature; that is, the temperature declines with growing magnetic (see Figure 8(b)).

Figure 9(a) depicts the influence of both Cu/SA and $Cu - GO/SA$ volumetric fraction parameters on velocity. The nanofluid flow slows down as the intensity increases. This occurrence occurs as a result of friction escalating, and fluid viscidness increases with increasing nanofluid volume fraction. As enhanced, the hybrid nanofluid has a faster motion than regular nanofluid. With increases in volume fraction, the fluid temperature rises noticeably, as seen in Figure 9(b). These conclusions support our concept that adding nanomaterials to regular fluids recovers thermal conductivity and increases thermal efficacy.

Figure 10(a) illustrates how the Biot quantity Bi raises the heat of the Maxwell graphene hybrid nanofluid and nanofluid. This may be explained by pointing out that an increase in Biot number grows in convective heat transport at the surface, which raises the temperature. It is evident from Figure 10(b) that raising Eckert quantities causes the heat flow to increase. The relationship Eckert establishes between enthalpy and kinetic energy and the reality that the

overall process is completed in the presence of viscidness while kinetic energy is converted to internal energy can both be used to clarify this characteristic of Maxwell fluid with copper and graphene nanospheres. As a result, viscous dissipation can raise a fluid temperature more quickly.

The thermal scatter in the $Cu-GO/SA$ and Cu/SA nanofluids is explained in Figure 11(a) to increase the heat generation constraint. According to the parameter, it tends to increase the flow's surrounding thermal conditions. This will demonstrate improved thermal diffusion for the two fluid flow combinations. The heat is seen to be decreasing in tendency while the Prandtl number is increasing in Figure 11(b). Failures in the heat curve are seen because the greater Prandtl number denotes the lower thermal diffusivity. The temperature of the $hbnf$ and nf grows better with an increase in radiation parameter, as shown in Figure 11(c). In reality, the radiation goes up the fluid ability to transfer heat, which causes the thermal boundary layer to expand and, as a consequence, lowers the fluid temperature.

Table 4 illustrates the various physical parameters values with skin-friction coefficient and heat transfer rate. The velocity declines and temperature increase when both nanoparticles have the same volume fraction value. The skin-friction coefficient declines with Deborah, unsteadiness, and porosity parameters, while the opposite behavior shows for the magnetic parameter. The Nusselt number upsurges with Prandtl, radiation, and Biot number. Both the thermal and motion impressions increase with the velocity slip parameter. The skin-friction declines, and temperature grows with suction/bowing influence.

5. Conclusions

The goal of the existing research is to boost the solar energy phenomenon, which will increase aircraft endurance and be employed in solar aviation for a variety of uses. Maxwell hybrid nanofluid is taken into consideration for this goal. Graphs and tables are thoroughly examined for many parametrical influences, including heat source, magnetic field, viscous dissipation, thermal liquid on PTSC, and solar-powered aircraft. The following are the findings that result from the issue mentioned:

(i) The upsurge in Deborah number reduces the skin-friction coefficient.

(ii) The heat source parameter declines the heat transfer rate but upsurges the skin-friction coefficient.

(iii) The skin-friction coefficient and heat transfer rate increase with growing magnetic impression.

(iv) The motion profile declines with Cu/SA and raises with $Cu-GO/SA$, while temperature grows for both hybrid nano- and nanofluids.

Data Availability

The raw data supporting the conclusions of this article will be made available by the corresponding author without undue reservation.

Conflicts of Interest

The authors declare that they have no conflicts of interest.

Authors' Contributions

All authors listed have made a substantial, direct, and intellectual contribution to the work and approved it for publication.

References

[1] M. Q. Brewster, *Thermal Radiative Transfer and Properties*, John Wiley & Sons, Hoboken, NJ, USA, 1992.

[2] S. U. Choi and J. A. Eastman, *Enhancing thermal Conductivity of Fluids with Nanoparticles (No. ANL/MSD/CP-84938; CONF-951135-29)*, Argonne National Lab. (ANL), Argonne, IL, USA, 1995.

[3] S. Suresh, K. P. Venkitaraj, P. Selvakumar, and M. Chandrasekar, "Effect of Al2O3–Cu/water hybrid nanofluid in heat transfer," *Experimental Thermal and Fluid Science*, vol. 38, pp. 54–60, 2012.

[4] X. Z. Gao, Z. X. Hou, Z. Guo, J. X. Liu, and X. Q. Chen, "Energy management strategy for solar-powered high-altitude long-endurance aircraft," *Energy Conversion and Management*, vol. 70, pp. 20–30, 2013.

[5] R. Barbosa, B. Escobar, V. M. Sanchez, J. Hernandez, R. Acosta, and Y. Verde, "Sizing of a solar/hydrogen system for high altitude long endurance aircrafts," *International Journal of Hydrogen Energy*, vol. 39, no. 29, Article ID 16637, 2014.

[6] J. Ahmad Khan, M. Mustafa, T. Hayat, and A. Alsaedi, "Numerical study of Cattaneo-Christov heat flux model for viscoelastic flow due to an exponentially stretching surface," *PLoS One*, vol. 10, no. 9, Article ID e0137363, 2015.

[7] S. Das, S. Chakraborty, R. N. Jana, and O. D. Makinde, "Entropy analysis of unsteady magneto-nanofluid flow past accelerating stretching sheet with convective boundary condition," *Applied Mathematics and Mechanics*, vol. 36, no. 12, pp. 1593–1610, 2015.

[8] J. Sarkar, P. Ghosh, and A. Adil, "A review on hybrid nanofluids: recent research, development and applications," *Renewable and Sustainable Energy Reviews*, vol. 43, pp. 164–177, 2015.

[9] D. Toghraie, V. A. Chaharsoghi, and M. Afrand, "Measurement of thermal conductivity of ZnO–TiO2/EG hybrid nanofluid," *Journal of Thermal Analysis and Calorimetry*, vol. 125, no. 1, pp. 527–535, 2016.

[10] U. Farooq, D. Lu, S. Munir, M. Ramzan, M. Suleman, and S. Hussain, "MHD flow of Maxwell fluid with nanomaterials due to an exponentially stretching surface," *Scientific Reports*, vol. 9, no. 1, pp. 7312–7411, 2019.

[11] K. Loganathan, S. Sivasankaran, M. Bhuvaneswari, and S. Rajan, "Second-order slip, cross-diffusion and chemical reaction effects on magneto-convection of Oldroyd-B liquid using Cattaneo–Christov heat flux with convective heating," *Journal of Thermal Analysis and Calorimetry*, vol. 136, no. 1, pp. 401–409, 2019.

[12] H. Maleki, J. Alsarraf, A. Moghanizadeh, H. Hajabdollahi, and M. R. Safaei, "Heat transfer and nanofluid flow over a porous plate with radiation and slip boundary conditions," *Journal of Central South University*, vol. 26, no. 5, pp. 1099–1115, 2019.

[13] Z. Abdelmalek, U. Nazir, M. Nawaz, J. Alebraheem, and A. Elmoasry, "Double diffusion in Carreau liquid suspended

with hybrid nanoparticles in the presence of heat generation and chemical reaction," *International Communications in Heat and Mass Transfer*, vol. 119, Article ID 104932, 2020.

[14] N. Khandelwal, M. Sharma, O. Singh, and A. K. Shukla, "Recent developments in integrated solar combined cycle power plants," *Journal of Thermal Science*, vol. 29, no. 2, pp. 298–322, 2020.

[15] K. Loganathan, K. M. Prabu, E. Elanchezhian, R. Nirmalkumar, and K. Manimekalai, "Computational analysis of thermally stratified mixed convective non-Newtonian fluid flow with radiation and chemical reaction impacts Journal of Physics: conference Series," *Journal of Physics: Conference Series*, vol. 1432, no. 1, Article ID 012048, 2020.

[16] F. Rubbi, K. Habib, R. Saidur, N. Aslfattahi, S. M. Yahya, and L. Das, "Performance optimization of a hybrid PV/T solar system using Soybean oil/MXene nanofluids as A new class of heat transfer fluids," *Solar Energy*, vol. 208, pp. 124–138, 2020.

[17] K. Loganathan, K. Mohana, M. Mohanraj, P. Sakthivel, and S. Rajan, "Impact of third-grade nanofluid flow across a convective surface in the presence of inclined Lorentz force: an approach to entropy optimization," *Journal of Thermal Analysis and Calorimetry*, vol. 144, no. 5, pp. 1935–1947, 2021.

[18] K. Loganathan, N. Alessa, K. Tamilvanan, and F. S. Alshammari, "Significances of Darcy–Forchheimer porous medium in third-grade nanofluid flow with entropy features," *The European Physical Journal - Special Topics*, vol. 230, no. 5, pp. 1293–1305, 2021.

[19] I. Waini, A. Ishak, T. Groşan, and I. Pop, "Mixed convection of a hybrid nanofluid flow along a vertical surface embedded in a porous medium," *International Communications in Heat and Mass Transfer*, vol. 114, Article ID 104565, 2020.

[20] M. Wu, Z. Shi, H. Ang, and T. Xiao, "Theoretical study on energy performance of a stratospheric solar aircraft with optimum Λ-shaped rotatable wing," *Aerospace Science and Technology*, vol. 98, Article ID 105670, 2020.

[21] F. Ahmad, S. Abdal, H. Ayed, S. Hussain, S. Salim, and A. O. Almatroud, "The improved thermal efficiency of Maxwell hybrid nanofluid comprising of graphene oxide plus silver/kerosene oil over stretching sheet," *Case Studies in Thermal Engineering*, vol. 27, Article ID 101257, 2021.

[22] S. Anitha, K. Loganathan, and M. Pichumani, "Approaches for modelling of industrial energy systems: correlation of heat transfer characteristics between magnetohydrodynamics hybrid nanofluids and performance analysis of industrial length-scale heat exchanger," *Journal of Thermal Analysis and Calorimetry*, vol. 144, no. 5, pp. 1783–1798, 2021.

[23] T. Gul, M. Bilal, M. Bilal, W. Alghamdi, M. I. Asjad, and T. Abdeljawad, "Hybrid nanofluid flow within the conical gap between the cone and the surface of a rotating disk," *Scientific Reports*, vol. 11, no. 1, pp. 1180–1219, 2021.

[24] A. Hussain, M. H. Alshbool, A. Abdussattar et al., "A computational model for hybrid nanofluid flow on a rotating surface in the existence of convective condition," *Case Studies in Thermal Engineering*, vol. 26, Article ID 101089, 2021.

[25] W. Jamshed, S. Uma Devi S, R. Safdar, F. Redouane, K. S. Nisar, and M. R. Eid, "Comprehensive analysis on copper-iron (II, III)/oxide-engine oil Casson nanofluid flowing and thermal features in parabolic trough solar collector," *Journal of Taibah University for Science*, vol. 15, no. 1, pp. 619–636, 2021.

[26] W. Jamshed, K. S. Nisar, R. W. Ibrahim, F. Shahzad, and M. R. Eid, "Thermal expansion optimization in solar aircraft using tangent hyperbolic hybrid nanofluid: a solar thermal application," *Journal of Materials Research and Technology*, vol. 14, pp. 985–1006, 2021.

[27] W. Jamshed, K. S. Nisar, S. S. P. M. Isa, S. Batool, A. H. Abdel-Aty, and M. Zakarya, "Computational case study on tangent hyperbolic hybrid nanofluid flow: single phase thermal investigation," *Case Studies in Thermal Engineering*, vol. 27, Article ID 101246, 2021.

[28] W. Jamshed, "Thermal Augmentation in Solar Aircraft Using tangent Hyperbolic Hybrid Nanofluid: A Solar Energy Application," *Energy & Environment*, 2021.

[29] K. Loganathan, G. Muhiuddin, A. M. Alanazi, F. S. Alshammari, B. M. Alqurashi, and S. Rajan, "Entropy optimization of third-grade nanofluid slip flow embedded in a porous sheet with zero mass flux and a non-Fourier heat flux model," *Frontiers in Physics*, vol. 8, p. 250, 2020.

[30] K. Loganathan, N. Alessa, N. Namgyel, and T. S. Karthik, "MHD flow of thermally radiative Maxwell fluid past a heated stretching sheet with Cattaneo–Christov dual diffusion," *Journal of Mathematics*, vol. 2021, Article ID 5562667, 10 pages, 2021.

[31] W. Jamshed, N. A. A. M. Nasir, S. S. P. M. Isa et al., "Thermal growth in solar water pump using Prandtl–Eyring hybrid nanofluid: a solar energy application," *Scientific Reports*, vol. 11, no. 1, Article ID 18704, 2021.

[32] K. Muhammad, T. Hayat, A. Alsaedi, and B. Ahmad, "Melting heat transfer in squeezing flow of basefluid (water), nanofluid (CNTs+ water) and hybrid nanofluid (CNTs+ CuO+ water)," *Journal of Thermal Analysis and Calorimetry*, vol. 143, no. 2, pp. 1157–1174, 2021.

[33] S. Qayyum, M. I. Khan, F. Masood, Y. M. Chu, S. Kadry, and M. Nazeer, "Interpretation of entropy generation in Williamson fluid flow with nonlinear thermal radiation and first-order velocity slip," *Mathematical Methods in the Applied Sciences*, vol. 44, no. 9, pp. 7756–7765, 2021.

[34] A. Saeed, M. Jawad, W. Alghamdi, S. Nasir, T. Gul, and P. Kumam, "Hybrid nanofluid flow through a spinning Darcy–Forchheimer porous space with thermal radiation," *Scientific Reports*, vol. 11, no. 1, pp. 16708–16715, 2021.

[35] N. A. Zainal, R. Nazar, K. Naganthran, and I. Pop, "Unsteady flow of a Maxwell hybrid nanofluid past a stretching/shrinking surface with thermal radiation effect," *Applied Mathematics and Mechanics*, vol. 42, no. 10, pp. 1511–1524, 2021.

[36] I. Ahmad, M. Faisal, Q. Zan-Ul-Abadin, T. Javed, and K. Loganathan, "Unsteady 3D heat transport in hybrid nanofluid containing brick shaped ceria and zinc-oxide nanocomposites with heat source/sink," *Nanocomposites*, vol. 8, no. 1, pp. 1–12, 2022.

[37] E. A. Algehyne, E. R. El-Zahar, S. H. Elhag et al., "Investigation of thermal performance of Maxwell hybrid nanofluid boundary value problem in vertical porous surface via finite element approach," *Scientific Reports*, vol. 12, no. 1, pp. 2335–2412, 2022.

[38] A. Bhattacharyya, R. Sharma, S. M. Hussain, A. J. Chamkha, and E. Mamatha, "A numerical and statistical approach to capture the flow characteristics of Maxwell hybrid nanofluid containing copper and graphene nanoparticles," *Chinese Journal of Physics*, vol. 77, pp. 1278–1290, 2022.

[39] S. Eswaramoorthi, K. Loganathan, R. Jain, and S. Gyeltshen, "Darcy-forchheimer 3D flow of glycerin-based carbon nanotubes on a Riga plate with nonlinear thermal radiation and cattaneo-christov heat flux," *Journal of Nanomaterials*, vol. 2022, Article ID 5286921, 20 pages, 2022.

[40] M. Ouni, L. M. Ladhar, M. Omri, W. Jamshed, and M. R. Eid, "Solar water-pump thermal analysis utilizing copper–gold/engine oil hybrid nanofluid flowing in parabolic trough solar collector: thermal case study," *Case Studies in Thermal Engineering*, vol. 30, Article ID 101756, 2022.

[41] F. Ali, K. Loganathan, S. Eswaramoorthi, K. Prabu, A. Zaib, and D. Kumar Chaudhary, "Heat transfer analysis on Carboxymethyl Cellulose water-based cross hybrid nanofluid flow with entropy generation & quot," *Journal of Nanomaterials*, vol. 2022, Article ID 5252918, 11 pages, 2022.

[42] I. Ahmad, Q. Zan-Ul-Abadin, M. Faisal, K. Loganathan, T. Javed, and D. Kumar Chaudhary, "Quot; prescribed thermal activity in the radiative bidirectional flow of magnetized hybrid nanofluid: keller-box Approach & quot," *Journal of Nanomaterials*, vol. 2022, Article ID 5531041, 16 pages, 2022.

[43] I. Ahmad, Q. Zan-Ul-Abadin, M. Faisal, K. Loganathan, T. Javed, and N. Namgyel, "Convective heat transport in bidirectional water driven hybrid nanofluid using blade shaped Cadmium Telluride and graphite nanoparticles under electromagnetohydrodynamics process," *Journal of Mathematics*, vol. 2022, Article ID 4471450, 14 pages, 2022.

[44] I. Ahmad, Q. Zan-Ul-Abadin, M. Faisal, K. Loganathan, T. Javed, and S. Gyeltshen, "Entropy analysis in bidirectional hybrid nanofluid containing nanospheres with variable thermal activity," *Journal of Nanomaterials*, vol. 2022, Article ID 1915185, 15 pages, 2022.

[45] S. M. Hussain, "Dynamics of radiative Williamson hybrid nanofluid with entropy generation: significance in solar aircraft," *Scientific Reports*, vol. 12, no. 1, pp. 8916–8923, 2022.

[46] W. Jamshed, S. U. DeviS, M. Prakash et al., "Entropy amplified solitary phase relative probe on engine oil-based hybrid nanofluid," *Chinese Journal of Physics*, vol. 77, pp. 1654–1681, 2022.

Hindawi
Advances in Materials Science and Engineering
Volume 2022, Article ID 2876643, 12 pages
https://doi.org/10.1155/2022/2876643

Research Article

Production of Mycoblock from the Mycelium of the Fungus *Pleurotus ostreatus* for Use as Sustainable Construction Materials

Digafe Alemu,[1,2] **Mesfin Tafesse**,[1,2] **and Yohannes Gudetta Deressa**[3]

[1]*Department of Biotechnology, College of Biological and Chemical Engineering, Addis Ababa Science and Technology University, P.O. Box 16417, Addis Ababa, Ethiopia*
[2]*Biotechnology and Bioprocess Center of Excellence, Addis Ababa Science and Technology University, P.O. Box 16417, Addis Ababa, Ethiopia*
[3]*College of Architecture and Civil Engineering, Department of Civil Engineering, Addis Ababa Science and Technology University, P.O. Box 16417, Addis Ababa, Ethiopia*

Correspondence should be addressed to Digafe Alemu; digafe.alemu@aastu.edu.et

Received 12 April 2022; Revised 27 May 2022; Accepted 24 June 2022; Published 31 August 2022

Academic Editor: Vijayananth Kavimani

As the global population rises, resource depletion and environmental pollution also aggravate. To meet the needs of the population, different products have been manufactured. However, most industrially manufactured products are not eco-friendly, costly, and locally unavailable. To solve these problems, using and enhancing locally available biomaterials are the key option. Three substrates sawdust, bagasse, and coffee husk and the fungus *Pleurotus ostreatus* were used. Mycelium was fully colonized by 9, 14, and 27 days on potato dextrose agar (PDA), sorghum grain, and substrate, respectively. The mycelium growth on coffee husk showed the fastest growth rate whereas that of the sawdust was slowest. The fully colonized substrates were molded for 7, 14, and 21 days by plastic mold to maintain their regular 3D structure. The result shows that the block made with sawdust at 21 molding period has higher compressive strength and density of 750 kPa and 343.44 Kg/m^3, respectively, followed by bagasse and coffee husk. These variations were due to the mycelium density difference between the substrates. Physicochemical and mechanical characteristics such as mycelium morphology, bimolecular and elemental analysis of substrates, density, water absorption, and compressive strength of the block were analyzed. This technology has the potential to replace conventional construction and packaging materials used for indoor applications such as insulation, partition walls, and other design and architectural applications. It also benefits in terms of its low cost, green synthesis approach, nontoxicity, low environmental emission, recyclability, and local availability.

1. Introduction

The rapid rate of global population growth leads to environmental pollution and natural resource depletion. The human population increase could aggravate both resource depletion and environmental pollution. Similarly, the rise of the human population is also the main cause of urbanization. The United Nations study projection showed that about 66% of the world population will live in urban areas by 2050 [1]. The increasing urban population will lead to a significant increase in urban energy consumption and urban emissions [2]. Modernization of the construction sector has a significant role to play in reducing urban emissions [2]. Most construction materials nowadays are made of cement, gypsum, metals, wood products, and polymer products. These materials need high cost, consume energy, are environmentally unfriendly, and are nonrecyclable. A recent study shows that about 8.7 gigatons, which is about 10% of the world emission, of carbon dioxide, is from the construction sector [3], either from demolition or construction [4]. To minimize the environmental effect caused by the construction sector, applications of innovative materials (low/zero carbon buildings) are the key options [2].

As compared to others, cement is one of the most widely used construction materials worldwide [5–7]. Cement-based materials are hydrophobic, high strength, and durable [7].

However, they are not subject to decomposition, create environmental pollution, are susceptible to cracking, and require high-cost. Eight to ten percent of the global total carbon dioxide emissions were released from the manufacturing of cement only [8]. To keep the construction sector clean and sustainable, technological improvement should be needed.

The practice of business as usual in the construction sector will not create a sustainable environment and circular economy. The advancement of technology in construction materials has become one of the most important recent issues in the field of Biotechnology and Civil Engineering research studies. There is a possibility of making sustainable construction material from a complex of fungal mycelium and organic substrates [9, 10]. Mycelium is a vegetative part of fungi that has a long, branching, and filamentous structure called hyphae and acts as a natural adhesive and is used to create a network of extremely dense fibers, attached to the organic substrate (sawdust, straw, coffee grounds, wheat bran, and bagasse) [11, 12]. The organic matter bounds with this hyphal structure and forms fungal skin. When this process is ceased through drying or heating, the incomplete process results in a mycelium-based block (Mycoblock). Mycoblock is a block made of organic substrates and uses mycelium as a natural adhesive. In addition to being applied in biocomposite production, the fungal mycelium can also be applied in a variety of other environmental technologies [13, 14].

Existing research shows that Mycoblock is used in a variety of applications such as packaging materials, insulations, partition walls, utensils, furniture, and different design and architectural [15]. It can significantly reduce the reliance on fossil fuels and the embodied energy required for construction and lower waste left at the end of buildings' life cycles [16]. Because it is entirely biodegradable, does not produce waste when appropriately discarded, and produces a lower carbon footprint *s* compared to conventionally manufactured building materials [16], the quality of the product can be enhanced through methodological diversifications such as types of substrate, types of strain, length of cultivation time, molding type, and molding temperature [17].

The genera belonging to Pleurotus are widely used and studied by different scholars for the application of Mycoblock followed by *Trametes* and *Ganoderma genera* due to their contamination resistance and faster growth than other fungal genera [16, 17]. Hot-pressing shifts the property of blocks from foam-like to wood-like by enhancing their stiffness and homogeneity [16]. The current study is mainly focused on the production of noncement-based biomaterials from organic wastes for alternative and low-cost construction materials by using fungal mycelium as a natural adhesive. The study also identifies the comparative strength of different substrates (bagasse, sawdust, and coffee husk) for better mycelium-based blocks.

2. Materials and Methods

2.1. Strain Cultivation. The fungal strain *Pleurotus ostreatus* (P. *Ostreatus*) was obtained from Shitaki international mushroom plc. In Addis Ababa., PDA (39 g/L) was used for the growth of the strain after autoclaving at 121°C for 15 minutes (min). The warm liquid media (50–60°C) was poured carefully into a sterile Petri plate until 2/3 of the plates were filled [18]. A piece of mass of mycelium was picked using an inoculation loop and placed at the center of a cooled PDA agar plate under an aseptic condition to refresh the strain. The fully colonized refreshed strain was triplicated by taking a disk of (6 x 6) mm2 mycelium grown on agar. Finally, the plates were incubated at 28°C until grown mycelia fully cover the Petri plate. Mycelia growth was visually observed and measured using a ruler in terms of diameter on the culture plate every three days intervals, and growth rate (GR) was calculated using equation (equation (1)) [19]. The pure culture was stored for further study according to the preservation method used by [20].

2.1.1. Spawn Preparation. Sorghum grain locally called (ZENGADA) purchased from the local market was cleaned and soaked. Then, the cleaned and soaked grain was spread on a water permeable cloth to remove the excess water until 50% moisture (Equation (2)). To maintain the pH, 2% lime on a dry weight basis of grain was added and mixed thoroughly [21–23]. Glass bottles filled with 100 g (on a wet weight basis) grain lime mixture were autoclaved at 121°C for 60 min and allowed to cool overnight in aseptic condition. After cooling a quarter (1/4) of 9-days-old culture from the Petri dish was inoculated and incubated at 28°C until the substrate was fully colonized. The mycelia invasion rates were inspected every three days' intervals.

2.1.2. Substrate Collection, Preparation, and Inoculation. Three substrates were collected from the following places: coffee husk (CH) and sawdust (SD) from Addis Ababa around Haile garment and Bagasse (Bg) from the Metehara sugar factory. These substrates were selected due to their abundance and local availability. The average size of the substrate was obtained by homogenizing it manually with a scissor below 2 cm [24, 25], and other unwanted materials such as plastics, metals, and stones were cleaned out from the substrate manually.

About 10% Teff bran (on a dry weight basis) was added to each prepared substrate as a supplement and to provide adequate void space between substrate substances [9, 21, 25]. The substrate-supplement mixture was soaked separately in excess tap water overnight to soften the substrate. Then, the soaked mixture was drained off the excess water until moisture content become 60% to 70% [26, 27]. For moisture measurement, about 40 g samples from each type were taken randomly [9], and the result was analyzed according to Equation (2) [21].

For the purpose of buffering, preventing substrate adhesion and facilitating air circulation between substrates, 3% of calcium sulfate (on a dry weight basis) was added to each mixture and mixed thoroughly [22, 27, 28]. The adequate amount of substrate mixture was sterilized in an autoclave at 121°C for 60 min and allowed to cool overnight under aseptic conditions [22, 29]. Each substrate (1000 g) with 60 to 70% moisture was inoculated with 10% spawn (100 g) [25, 30].

Then, the sample bags were kept in a dark room at (22 + 1°C) until mycelium fully colonized the substrate. The mycelium growth rate was inspected every five days to determine mycelium quality and density.

2.2. Production Phase. Blocks were made after passing the following three phases: molding, incubation, and denaturation. About 200 g of fully colonized mycelium of each substrate was added to 11 cm × 8 cm *x* 4 cm size plastic mold for three incubation periods (7, 14, 21 days) [26, 31], under aseptic conditions. The incubation temperature was adjusted to 22 + 1°C. At the end of each growth period, the sample was taken out of the mold and ready for weight measurement and denaturation. To terminate the mycelium overgrowth, for dehydration, and decrease the toxicity level of the strain, heat of about 50°C for 48 h was applied [32].

2.3. Physico-Chemical and Mechanical Characterization Techniques

2.3.1. pH Level. pH was measured after taking 1 : 10 w/w of the sample from the fully colonized substrate and control and soaked for one hour (hr) [33, 34].

2.3.2. Water Content. To ensure mycelium development, the moisture content of both inoculated substrate and control were measured by taking a 40 g sample from each bag, and the result was analyzed by (equation (2)) [35].

2.3.3. Elemental Analysis. The substrate elemental content was evaluated by a device EA 1112 Flash CHNS/O- analyzer by taking 0.2 g of samples' powder grinded with the size of below 150 μm.

2.3.4. Scanning Electron Microscopy (SEM). The surface morphology of the mycelium fibers grown on PDA and different substrates were analyzed using SEM (INSPECT F50, Japan).

2.3.5. Fourier-Transform Infrared Spectroscopy (FT-IR). The chemical composition of fungi mycelium fiber grown on different existed substrates was analyzed by FT-IR spectroscopy (Perkin Elmer, USA) in the range of 4000 to 500 cm 1. Then, 0.5 g of sample grinded below ≤150 μm in size was taken for analysis.

2.3.6. Water Absorption. After dry weight was obtained, each block was submerged in excess water for 32 hrs. Weight was recorded every 8, 24, and 32 hours until stable weights were obtained [18, 36]. Then, the data were analyzed with the (equation (3)) [35].

2.3.7. Density. Densities were calculated by measuring the weight and volume of each block after heating 50°C for 48 h as per equation (4) [37].

2.3.8. Compressive Strength. A compressive strength test was carried out by a compressive testing machine (3000 kN) with a pace rate of 2.4 kN/s. The samples were gently placed on the lower beam and compressed till the specimens fractured completely.

2.4. Statistical Analysis. The experimental design was completely randomized in a 3 x 3 factorial method with three substrates and three cultivation periods. Each test was triplicated and the result was taken from the mean:

$$\text{Growthrate} = \frac{Df - Di}{di}, \tag{1}$$

$$\text{moisturecontent}\,(\%) = \frac{(Mw - Dw)}{Mw} \times 100, \tag{2}$$

$$\text{Waterabsorption}\,(\%) = \left(\frac{Wf - Wi}{Wf} \times 100\right), \tag{3}$$

$$\text{Density} = \frac{m}{y}. \tag{4}$$

where *Df* is diameter at the last evaluation day, Di is diameter at the initial evaluation day, di is the evaluation day interval, Dw is dry weight of the substrate, M is mass, Mw is moistened weight of the substrate, V is volume, Wf is final weight of the Mycoblock (after 24 hr submerged in water), and Wi is initial weight of the Mycoblock (dry weight before submerged to water).

3. Results and Discussion

3.1. Growth Conditions and Morphological Analysis of Mycelium Fibers. The growth condition of *P. ostreatus* mycelium fibers on PDA, grains, and three substrates (CH, SD, Bg) were illustrated in Table 1 and Figures 1(a)–1(c). The mean growth rate of mycelium grown on PDA was higher than grain and substrates as indicated in (Table 2). The color of the cotton-like structure of mycelium fibers grown on PDA covered the entire Petri dish (90 mm in diameter) within 9 days (Figure 2(a)), whereas that of the spawn takes 14 days for entire growth (Figure 2(b)), which showed similar results with the study of [21]. The mycelium growth rate for culture and spawn decreased as incubation time increased (Figures 1(a) and 1(b)); whereas the mycelium growth rate between different substrates was varied (Figure 1(c)). This is might be due to nutrient limitations.

The highest running rate was observed in coffee husk followed by bagasse and sawdust numerically 25, 26, and 27 days, respectively. These growth differences might be due to variation of aeration between substrate particles and nutritional content [21]. The mycelium growth rate of the current study is comparable with the study of [22] which took 25 and 27 days for full colonization of *P. ostreatus* mycelium on the coffee bulb and wood chips supplemented with Teff straw, respectively. Figure 3 shows the mycelium growth condition on different substrates. The figure illustrates that the growth rate was inversely proportional to the

Table 1: Growth features of mycelium grown on PDA and different substrates.

	Growth length (mm)	Growth period (days)	Growth rate (mm/day)
Plate culture	90	9	10.00
Spawn	120	14	8.19
Coffee husk	175	25	7.00
Bagasse	167	26	5.82
Sawdust	152	27	5.14

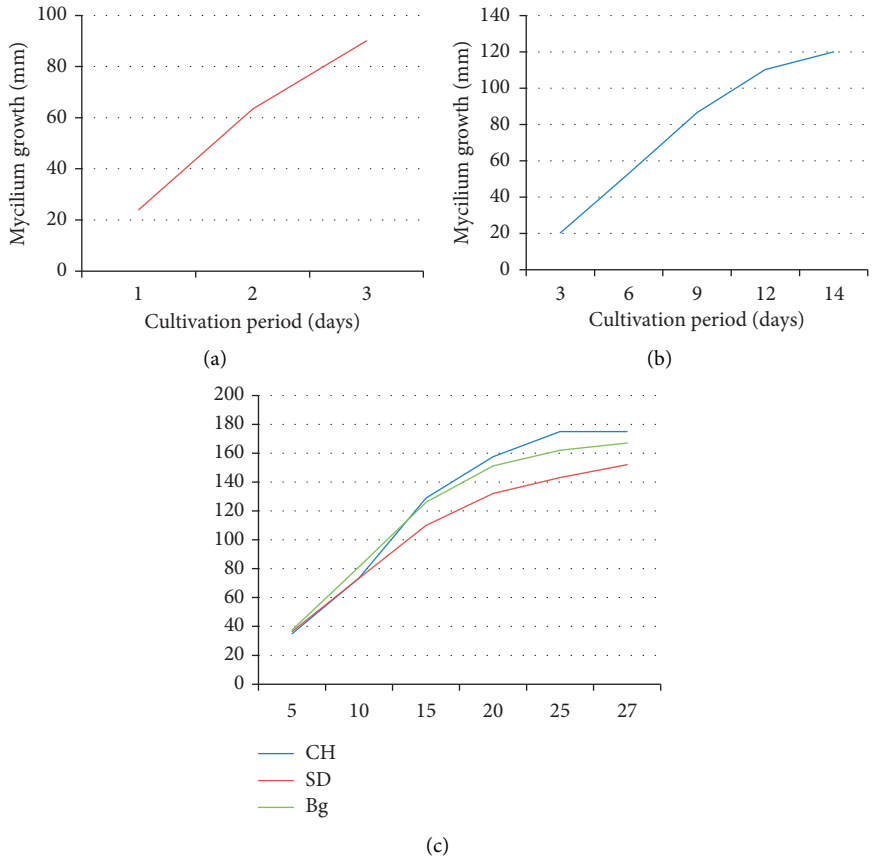

Figure 1: Mycelium growth rate grown on (a) PDA, (b) grain (spawn), and (c) different substrates: CH (coffee husk), SD (sawdust), and Bg (bagasse).

Table 2: Mean and standard deviation of mycelium growth rate at different growth media.

Statistical measurements	PDA	Spawn	CH	SD	Bg
Mean growth rate (mm/day)	10.00	8.19	7.00	5.14	5.82
Std. deviation	2.19	2.78	2.79	2.02	3.04

length of the incubation period and height of growing materials and directly proportional to the density of mycelium, which might be due to aeration difference across a height [37] and difficulty in nutrient extraction out of compacted substrates [18]. No mycelium growth was observed in control samples.

Unlike the growth rate, the density of the mycelium at each substrate was inversely proportional to the incubation period which is in agreement with [38], which might have happened due to substrate elemental content (Table 3). The elemental composition of the substrate has a high effect on fungal mycelium development[39].

Mycelium-based blocks were formed at 7, 14, and 21 days of incubation with different physico-chemical characteristics. The skin on the surface of the block was formed through growing radial direction and stimulated the generation of the outer skin when the expanding biomass of mycelium came in contact with the molds and formed a fairly strong protective layer on the surface of the sample [7] (Figures 4(a)–4(c)). In contrast, the block made with control had no mycelium skin and had an indefinite structure. Mycoblock with no heat applied was spongy in texture, was white in color, and increased in size. Whereas Mycoblock exposed to heat was strong, was brown in color, and showed reduction in size. Block made with coffee husk was fractured when exposed to heat, which might be due to low mycelium density. A similar result was reported in [40].

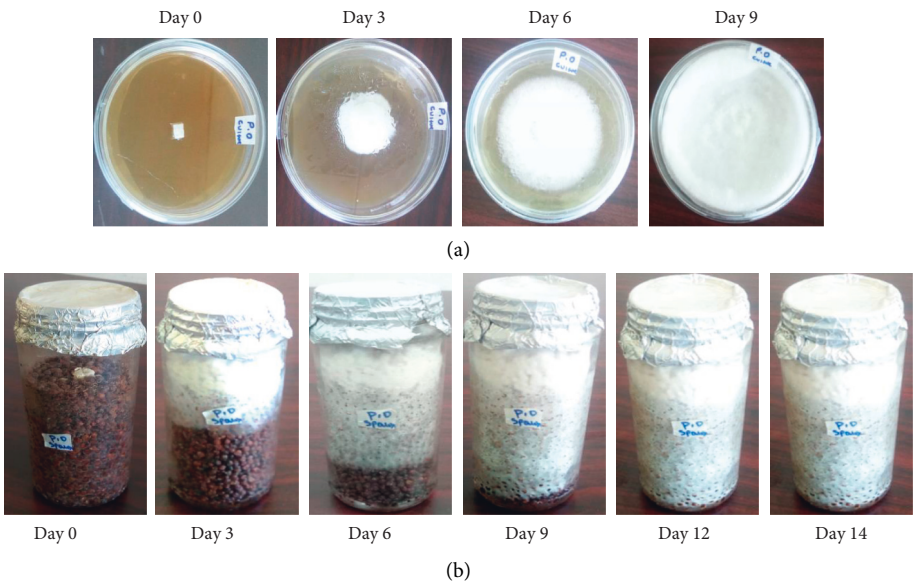

Figure 2: Mycelium growth on (a) PDA and (b) spawn.

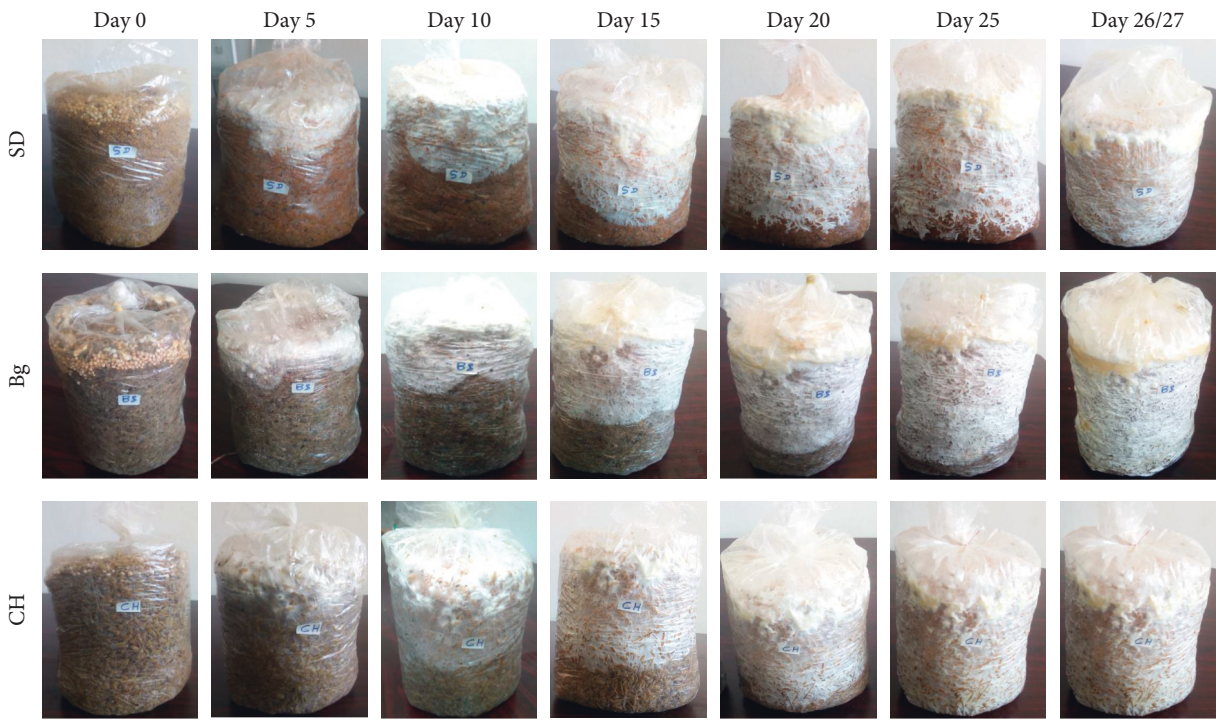

Figure 3: Mycelium growth conditions on Bg, SD, and CH at different growth periods.

Table 3: Elemental content of the substrates.

Substrates	N (%)	C (%)	C/N ratio
SD	1.67	48.21	28.87
Bg	1.86	35.73	19.21
CH	1.87	35.21	18.83

3.1.1. Morphological Analysis. The morphology of P. ostreatus hyphae grown on PDA and different substrates were identified by light microscope and SEM (Figures 5(a) and 5(b)). Figure 5(a) illustrated that the light microscope image of hyphae grown on PDA had septa, anastomosis, and clamp connections in their filaments which is similar to [41] study report. Clamp connections are more common in most of Basidiomycota which is formed during cell division of secondary hyphae [42], whereas anastomosis helps the hyphae to attach to one another [37]. SEM images of pure mycelium clearly show the tubular hyphae and the interwoven network (Figure 5(b)). The SEM image for the control sample has more air voids in between the substrates

Figure 4: Image showing Mycoblock made from different substrates: (a) heat exposed, (b) nonheat exposed, (c) control, (d) block side view, and (e) rectangular sheets.

(Figure 5(c)). In contrast, SEM images for mycelium colonized substrates have interwoven hyphae networks between substrate particles with less air voids (Figures 5(d)–5(f)). The difference in voids spaces might be due to the network of hyphae.

3.2. Physical and Chemical Characterization of Mycelium Fibers. Mycelium development on each substrate was evaluated through selected properties such as pH and water content, as shown in Figures 6(a)and 6(b). There were changes in pH and water content values in mycelium-developed substrates and the control [43, 44]. The pH of the control samples was higher than mycelium-developed samples (Figure 6(a)), which is probably due to enzymatic digestion [33]. Similarly, the water content of each substrate inoculated with *P. ostreatus* had higher water content than substrate without fungi (Figure 6(b)). This variation might be due to mycelium density variation between substrates [44].

Mycelium chemical composition and the chemical nature of different substrates were analyzed by FT-IR spectra. Mycelium-based materials (MBm) made from selected substrates are expected to inherit the microstructure and properties of the feeding material [45]. All expected essential biomolecules such as polysaccharides, proteins, lipids, and Chitin were observed (Figure 7), which is in line with the result reported in [18]. The author's report shows that all the essential characteristic biomolecules such as proteins (1644 to 1546 cm^{-1}), lipids (3000–2800 cm^{-1}, 1740 cm^{-1}), nucleic acids (1255–1245 cm^{-1}), chitin (1318–1415), and polysaccharides (1200–900 cm^{-1}) were observed from Mycoblock made of agricultural wastes. The presence of chitin in fungal mycelia even at minor fractions is crucial for the material's

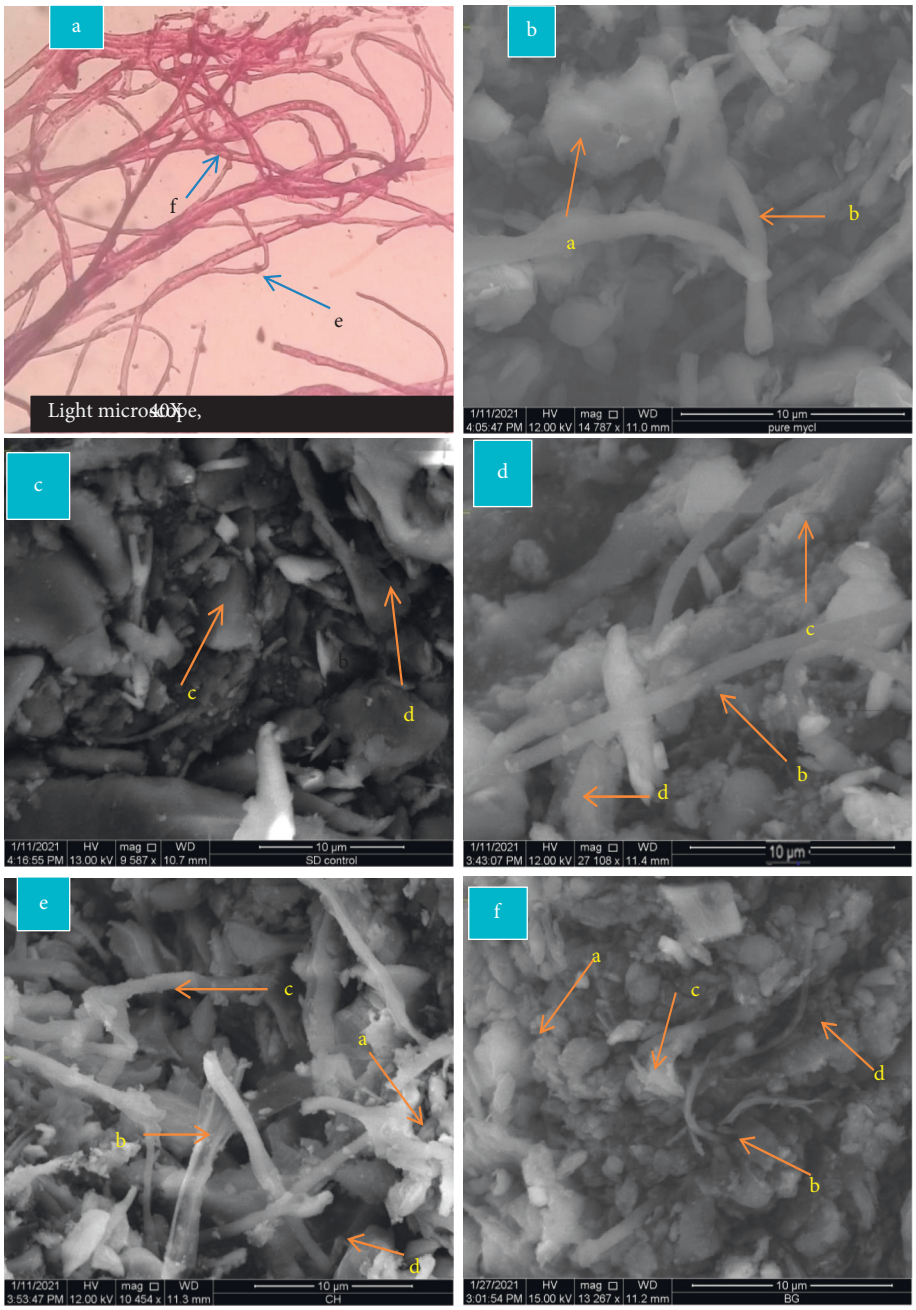

Figure 5: Microscopic images of mycelium grown on different substrates. (a) Electro microscopic image of pure mycelium. (b) SEM image of pure mycelium. (c) SEM image of pure SD. (d) SEM image of inoculated SD. (e) SEM image of the inoculated coffee husk. (f) SEM image of inoculated Bg, where (A) fused hyphae, (B) mycelium, (C) substrate, (D) air voids, (E) hyphae septa, and (F) hyphae anastomosis under a light microscope.

structural and mechanical properties [46, 47]. Chitin is a long-chain polymer of N-acetyl glucosamine. This long-chain polymer forms into antiparallel chains and reinforces by being crossed-linked to β (1, 3) glucan with covalent bonds [35].

3.3. Physical Characterizations of Mycoblock. The physical properties of the current Mycoblock were affected by two factors, incubation time and substrate type. As incubation time increased, the density of the block had increased and decreased water absorption up to 11.95% and 1.9% respectively (Figure 8). This result agrees with the previous study made in [7] that the density of Myco block prepared using sawdust mycelium composite increased from 195 kg/m3 to 280 kg/m3 as the incubation period increased because the voids between the fibers are filled as the mycelium continues to grow and the substrate is bonded more strongly together which in turn increases the density [46]. Similarly, longer inoculation time increased mycelium composition

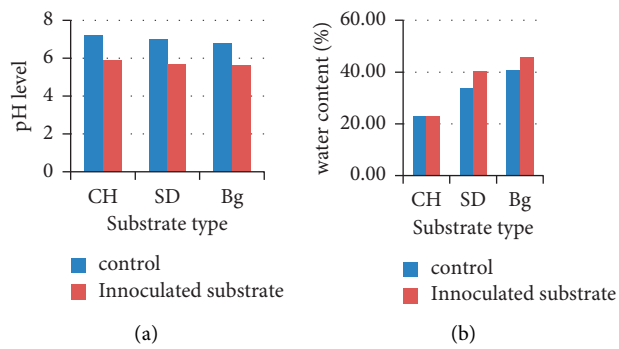

Figure 6: Effect of mycelium development on pH and water content.

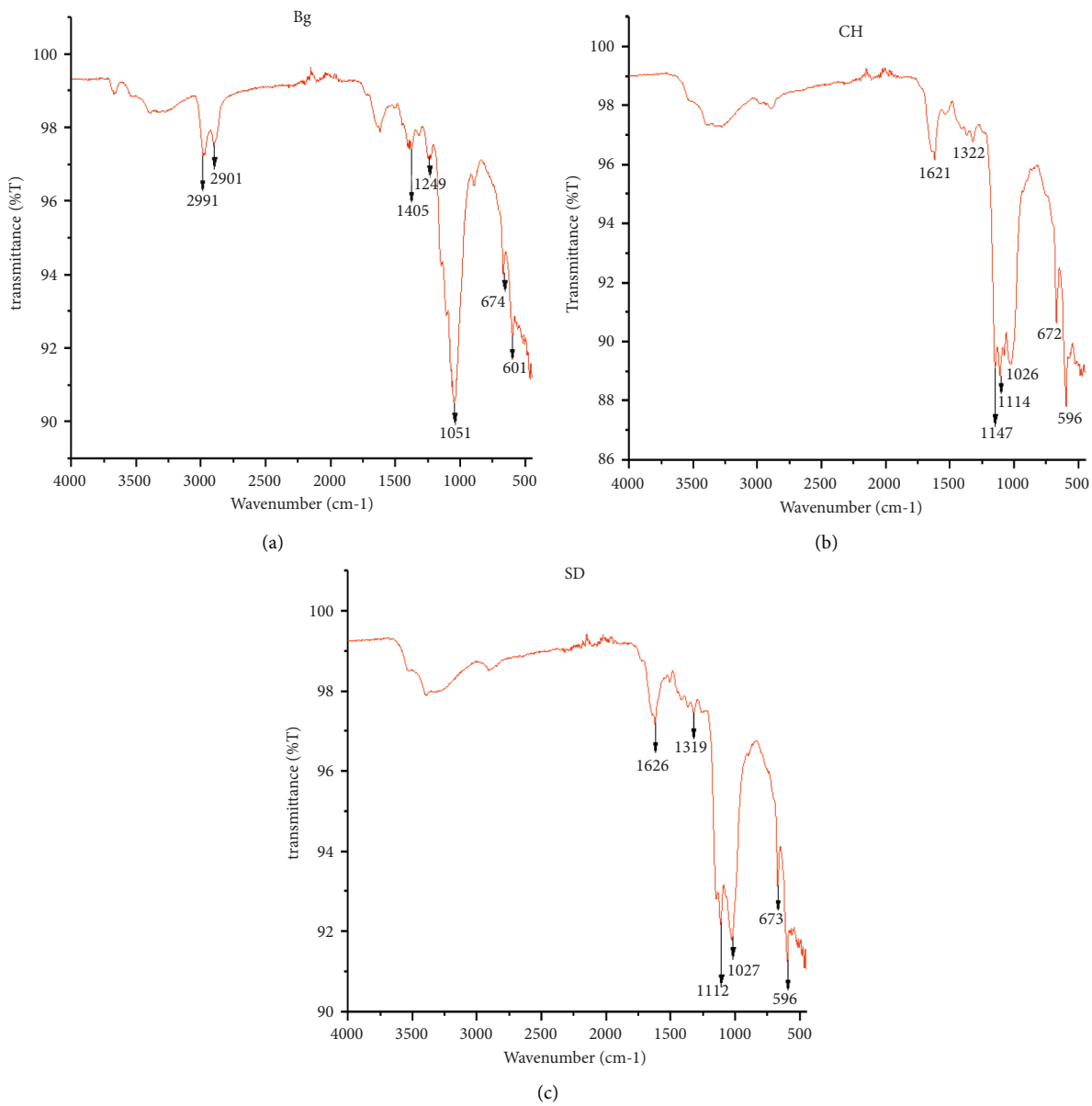

Figure 7: FT-IR spectra band grown on different substrates (a) Bg, (b) CH, and (c) SD.

such as chitin [48], which positively affects the compressive strength of the materials [49]. On the contrary, an extensive incubation period leads to complete degradation of the feeding substrate, which causes a decrease in compressive

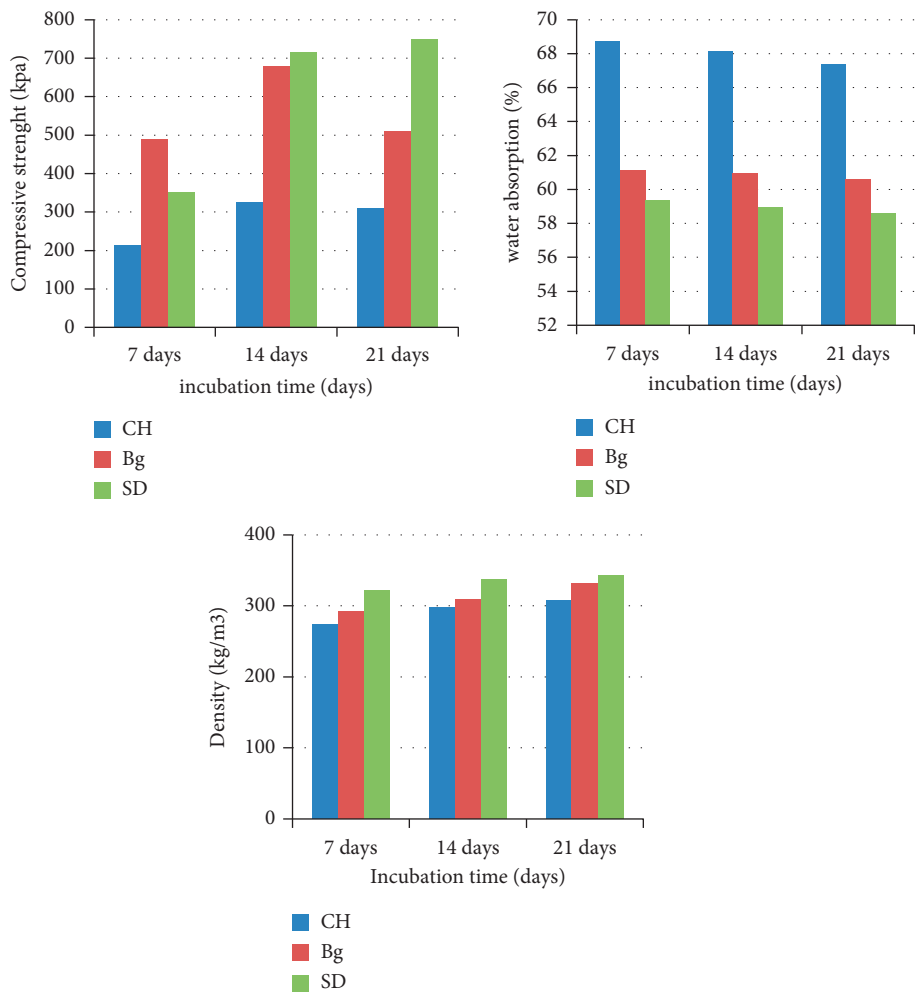

Figure 8: Mycoblock physical and mechanical characteristics with varying substrates and incubation period.

strength [19, 50]. A study report done in [51] also strongly agree with the current study that, as the incubation period increases further, it causes more organic substrate degradation, and results in less substrate and more hyphal structures. Since most of the compressive strength of Mycoblock is from the substrates, longer growth times result in less compressive strength.

The current study shows that the compressive strength of Mycoblock increased up to 53.07% as the incubation period increased depending on substrate type. The strength of Mycoblock prepared using both coffee husk (CH) and bagasse (Bg) decreased from 309 kPa to 352 kPa, and 679 kPa to 511 kPa, respectively, as the incubation period increased from 14 days to 21 days, while saw dust (SD) Mycoblock remained increased from 352 kPa to 750 kPa. The mean strengths of CH, Bg, and SD were 283 kPa, 559.67 kPa, and 605.33 kPa, respectively.

This result agrees with the work in [7]; the compressive strength of Mycoblock increased from 350 kPa to 570 kPa as incubation time increased from one week to three weeks. Result reported in [19] also supports the current study report; the authors conclude that an extensive growth period of sawdust above 4 weeks resulted in decreased material strength. The main reason might be due to the physical nature of the substrate [50] and its chemical contents [9]. Glucan-forming substrate (sawdust) is stronger than non-glucans-forming (softwoods) substrates [9] due to a thick layer of lignin that holds together laminates of cellulose fibrils in cross-orientation [50].

The maximum values in density and compressive strength of Mycoblock for sawdust and bagasse were 343.44 kg/m^3 and 750 kPa and 331.65 kg/m^3 and 511 kPa, respectively. The current study finding is a better result in compressive strength and density than the recent studies report, which has the maximum compressive strength and density of 498 kPa and 249 kg/m^3 Mycoblock made from mycelium substrate complex [51, 52]. In contrast, coffee husk had lower density and compressive strength which was about 292.35 kg/m^3 and 283.00 kPa, respectively. The vice versa was true for water absorption. SD had minimum water absorption capacity followed by Bg and CH, numerically 58.96%, 60.87%, and 68.07%, respectively. The same study also supports the current study that Mycoblock made from mycelium and saw dust has higher compressive strength and density than bagasse [18]. The same author reported that the lower strength and density of bagasse as compared to sawdust was because it has maximum substrate size and low mycelium penetration. The overall mean and standard

Table 4: The mean and standard deviation of Mycoblock at different properties and substrates.

Properties	Statistics	CH	SD	Bg
Water absorption (%)	Mean	68.07	58.96	60.87
	Std. deviation	0.67	0.27	0.39
Compressive strength (kPa)	Mean	283.00	605.33	559.67
	Std. deviation	60.36	220.13	103.93
Density (kg/m3)	Mean	292.35	334.11	310.92
	Std. deviation	17.47	10.99	19.89

deviation of physical properties of Mycoblock for three substrates are illustrated in Table 4.

The compressive strength of SD was 9.47% and 56.53% higher than Bg and CH, respectively. Similarly, the density of SD was 10.49% and 9.72% higher than Bg and CH, respectively. Based on this, it can be concluded that the compressive strength of Mycoblock is highly affected by substrate type rather than incubation time differences. The variations between substrate types were due to particle size, particle density, particle water holding capacity, and particle nutritional content. Improving molding type and heat application during the fabrication method could increase the density and compressive strength of Mycoblock by 2 to 3 folds than cold press [50, 53].

Mycoblock obtained in the current study fulfills the mechanical standards for applications in partition, architectural design, and insulation. It could replace polymer-based materials such as expanded polystyrene; the most widely used material for construction, which has the density in the range of 16–48 kg/m3 [54] and compressive strength in the range of 69–400 kPa [7]. The current finding which is about above two folds higher in compressive strength than polystyrene could help in substituting conventional nonecofriendly materials. The mycelium-based block is 49 times cheaper than cement and gypsum-based blocks [55]. It was pointed out that only 18.92 USD is needed per m3 of Mycoblock, whereas 936.87 USD per m3 was needed for cement-based block [18, 55]. Even though it is below the standard of cement-based materials in strength, density, and water absorption, it has also additional, and most significant benefits are the green synthesis approach, local availability, and nontoxicity [13]. The main challenge with Mycoblock technology is the sensitivity issue. Because it is growing rather than manufacturing, the life cycle of the selected strain for the technology is affected by different environmental factors. Know a day's mycelium-based composite is applied in a variety of applications such as packaging, insulation, partition wall, design, and architecture [13].

4. Conclusion

In this study, three substrates such as sawdust, bagasse, and coffee husk were used to produce Mycoblock using a fungal strain *Pleurotus ostreatus*. Aseptic conditions were strictly considered and pH and water contents were managed for the growth of the mycelium and compared with the control. Important parameters including substrate elemental analysis, SEM, FT-IR, density, compressive strength, and water absorption were analyzed to confirm the standard of the Mycoblock. The values obtained from physico-chemical and mechanical analysis varied with different substrates and incubation time periods. Maximum compressive strength and density were 750 kPa and 343.44 kg/m^3, respectively, with a 21 incubation period. Mycelium-based block most significantly benefits due to its low cost, green synthesis approach, nontoxicity, and low environmental emission. Apart from this, mycelium-based blocks have the potential to replace synthetic polymers used for construction materials. Furthermore, the development and expansion of the current study could be used for several renewable and sustainable applications such as wall insulating panels, packaging material, and production of furniture materials, as biodegradable and zero waste alternatives.

Data Availability

All data presented or analyzed during this study are included within the article.

Conflicts of Interest

The authors declare they have no conflicts of interest.

Authors' Contributions

DA contributed to the writing of the article. MT and YG contributed as advisors.

Acknowledgments

The authors wish to acknowledge all who have participated in this study.

References

[1] United Nations, "World urbanization Prospect," 2014, https://www.un.org/en/development/desa/publications/2014-revision-world-urbanization-prospects.html.

[2] S. Riffat, R. Powell, and D. Aydin, "Future cities and environmental sustainability," *Future Cities and Environment*, vol. 2, p. 1, 2016.

[3] United Nations environment Programme, "Global status report for buildings and construction," in *Global alliance for Building and Construction*, UNEP, Nairobi, Kenya, 2021.

[4] M. Dougoud, "Mycelium infrastructures for impermanent futures: revitalization of an industrial site through the manufacturing and research of mycelium based bio composite materials," 2018, https://digital.lib.washington.edu/researchworks/bitstream/%20handle/1773/41701/%20Dougoud%20washington_0250O18369.pdf?sequence=1&isAllowed=y.

[5] S. Panchal, M. M. Khan, and A. Sharma, "Stabilization of soil using bio-enzyme," *International Journal of civil engineering and technology*, vol. 8, no. 1, pp. 234–237, 2017.

[6] R. Siddique, K. Singh, M. Singh, M. Singh, V. Corinaldesi, and A. Rajor, "Properties of bacterial rice husk ash concrete,"

Construction and Building Materials, vol. 121, pp. 112–119, 2016.

[7] Z. J. Yang, M. White, F. Zhang et al., "Physical and mechanical properties of fungal mycelium-based Biofoam," *Journal of Materials in Civil Engineering*, vol. 29, no. 7, pp. 1–9, 2017.

[8] H. P. Italia and J. Shah, "Experimental study of bacterial Self-healing effect on concrete: a review," *Journal of Civil Engineering and Environmental Technology*, vol. 3, no. 1, pp. 78–81, 2016.

[9] A. Ghazvinian, P. Farrokhsiar, F. Vieira, J. Pecchia, and B. Gursoy, "Mycelium-based bio-composites for architecture: Assessing the effects of cultivation factors on compressive strength," *Mater Stud Innovation*, vol. 2, 2019.

[10] J. Maximino C Ongpeng, E. Inciong, V. Sendo, C. Soliman, and A. Siggaoat, "Using waste in producing bio-composite mycelium Bricks," *Applied Sciences*, vol. 10, no. 15, p. 5303, 2020.

[11] W. A. Elkhateeb and G. M. Daba, "The Amazing potential of fungi in human life," *Journal of Pharmaceutical Sciences*, vol. 5, no. 3, pp. 12–16, 2019.

[12] F. Heisel, K. Schlesier, J. Lee et al., "Design of a load-bearing mycelium structure through informed structural engineering," in *Proceedings of the World Congress on Sustainable Technologies WCST-2017*, Cambridge, UK, December 2017.

[13] D. Alemu, A. Ayele, S. Haile, and M. Kamaraj, "Comparative utilization of Dead and live fungal biomass for the removal of Heavy metal: a Concise review," *The Scientific World Journal*, vol. 2021, Article ID 5588111, 10 pages, 2021.

[14] D. Alemu, A. Ayele, S. Haile, T. Tesfaye, and M. Kamaraj, "Mycoremediation: fungal-based technology for Biosorption of Heavy metals—a review," *Strategies and Tools for Pollutant Mitigation*, pp. 355–373, 2021.

[15] D. Alemu, M. Tafesse, and A. K. Mondal, "Mycelium based composite: the future sustainable biomaterial; A Review," *International Journal of Biomaterials*, vol. 2022, 2022.

[16] A. Ghazvinian and B. Gursoy, "Basics of building with mycelium-based bio-composites: a review of Built Projects and Related material research," *Journal of Green Building*, vol. 17, no. 1, pp. 37–69, 2022.

[17] H. Vašatko, L. Gosch, J. Jauk, and M. Stavric, "Basic research of material properties of mycelium-based composites," *Biomimetics*, vol. 7, no. 2, p. 51, 2022.

[18] K. Joshi, M. K. Meher, and K. M. Poluri, "Fabrication and characterization of bio-blocks from agricultural waste using fungal mycelium for renewable and sustainable applications," *ACS Applied Bio Materials*, vol. 3, no. 4, pp. 1884–1892, 2020.

[19] M. P. Matos, J. L. Teixeira, B. L. Nascimento, and S. Griza, "Production of biocomposites from the reuse of coconut powder colonized by Shiitake mushroom," *Agricultural Sciences*, vol. 10, p. 1590, 2019.

[20] J. S. Paul, K. L. Tiwari, and S. K. Jadhav, "Long term preservation of commercial important fungi in glycerol at 4°C," *International Journal of Biological Chemistry*, vol. 9, no. 2, pp. 79–85, 2015.

[21] A. Tesfaw, A. Tadesse, and G. Kiros, "Optimization of oyster (*Pleurotus ostreatus*) mushroom cultivation using locally available substrates and materials in Debre Berhan , Ethiopia," *Journal of Applied Biology & Biotechnology*, vol. 3, pp. 15–20, 2015.

[22] Z. Tsegaye, "Growing of oyster mushrooms using agricultural residues at Ethiopian Biodiversity Institute Addis Ababa, Ethiopia," *Academia Journal of Microbiology Research*, vol. 3, no. 1, pp. 14–21, 2015.

[23] M. W. Khan, M. A. Khan, and A. Rehman, "Effect of different levels of lime and pH on mycelial growth and production efficiency of oyster mushroom (Pleurotus spp)," *Pakistan Journal of Botany*, vol. 45, no. 1, pp. 297–302, 2013.

[24] A. Getachew, A. Keneni, and M. Chawaka, "Production of oyster mushroom (*Pleurotus ostreatus*) on substrate composed from wheat straw, waste Paper and cotton seed waste," *International Journal of Microbiology and Biotechnology*, vol. 4, no. 2, pp. 38–44, 2019.

[25] C. Sánchez, "Cultivation of Pleurotus ostreatus and other edible mushrooms," *Applied Microbiology and Biotechnology*, vol. 85, no. 5, pp. 1321–1337, 2016.

[26] J. L. Teixeira, M. P. Matos, B. L. Nascimento, S. Griza, F. S. R. Holanda, and R. H. Marino, "Production and mechanical evaluation of biodegradable composites by white rot fungi," *Ciencia E Agrotecnologia*, vol. 42, no. 6, pp. 676–684, 2018.

[27] F. R. Vieira and M. C. N. de Andrade, "Optimization of substrate preparation for oyster mushroom (*Pleurotus ostreatus*) cultivation by studying different raw materials and substrate preparation conditions (composting: phases I and II)," *World Journal of Microbiology and Biotechnology*, vol. 32, no. 11, p. 190, 2016.

[28] P. Stamets, "Growing gourmet and medicinal mushrooms," 2000, https://www.amazon.com/Growing-Gourmet-Medicinal-Mushroo%20ms-Stamets/dp/1580081754.

[29] F. Alemu and M. Fisseha, "Cultivation of pleurotus ostreatus mushroom on Ficus vasta Leaves (Solid waste of plant) at Dilla university, Ethiopia," *International Journal of Applied Sciences*, vol. 2, no. 1, 2015.

[30] R. J. J. Lelivelt, "The mechanical possibilities of mycelium materials," 2015, https://research.tue.nl/en/studentTheses/the-mechanical-possibilities-of-mycelium-materials.

[31] B. S. Santhosh, D. R. Bhavana, and M. G. Rakesh, "Mycelium composites : an emerging green building material," *International Research Journal of Engineering and Technology*, vol. 5, no. 6, pp. 3066–3068, 2018.

[32] L. Jiang, G. McIntyre, D. Walczyk, and R. Bucinell, "A new approach to manufacturing biocomposite sandwich structures: mycelium-based cores," in *Proceedings of the ASME 2016 International Manufacturing Science and Engineering Conference*, pp. 1–11, ASME, Blacksburg, Virginia, USA, June 2016.

[33] N. Attias, O. Danai, N. Ezov, E. Tarazi, and Y. J. Grobman, "Developing novel applications of mycelium based biocomposite materials for design and architecture," in *Proceedings of the Building with bio-based materials: Best practice and performance specification*, Zagreb, Croatia, September 2017, https://tcode.net.technion.ac.il/files/2017/09/FP1303-paper-Noam-Attias_31_7_17.pdf.

[34] I. A. Zakarya, S. N. B. Khalib, N. Mohd Ramzi, and N. M. Ramzi, "Effect of pH, temperature and moisture content during composting of rice straw burning at different temperature with food waste and effective microorganisms," *E3S Web of Conferences*, vol. 34, pp. 1–8, 2018.

[35] Y. Tsao, "Characterization of mycelium-based composites as foam-like wall insulation material," 2020, https://research.tue.nl/en/studentTheses/characterization-of-mycelium-based-composites-as-foam-like-wall-i.

[36] W. Sun, M. Tajvidi, C. G. Hunt, G. Mcintyre, and D. J. Gardner, "Fully bio-based Hybrid composites made of wood, fungal mycelium and cellulose Nanofibrils," *Scientific Reports*, vol. 9, pp. 1–12, 2019.

[37] E. O. Precious, "Design and testing of mycelium bio-composite," 2019, https://kth.diva-portal.org/smash/get/diva2:1096048/FULLTEXT01.pdf.

[38] M. Haneef, L. Ceseracciu, C. Canale, I. S. Bayer, J. A. Heredia-Guerrero, and A. Athanassiou, "Advanced materials from fungal mycelium: fabrication and tuning of physical properties," *Scientific Reports*, vol. 7, no. 1, Article ID 741292, 2017.

[39] H. T. Hoa, C. L. Wang, and C. H. Wang, "The effects of different substrates on the growth, yield, and nutritional composition of two oyster mushrooms (Pleurotus ostreatus and Pleurotus cystidiosus)," *Mycobiology*, vol. 43, no. 4, pp. 423–434, 2015.

[40] F. V. W. Appels, "The use of fungal mycelium for the production of bio-based materials," 2020, https://www.uu.nl/agenda/the-use-of-fungal-mycelium-for-the-production-of-bio-based-materials.

[41] I. Milovanović, I. Brčeski, M. Stajić, A. Korać, J. Vukojević, and A. Knežević, "Potential of pleurotus ostreatus mycelium for selenium absorption," *The Scientific World Journal*, vol. 2014, Article ID 681834, 8 pages, 2014.

[42] N. T. P. Dung, D. B. Tuyen, and P. H. Quang, "Morphological and genetic characteristics of Oyster mushrooms and conditions effecting on its spawn growing," *The International Food Research Journal*, vol. 19, pp. 347–352, 2012.

[43] N. Attias, O. Danai, T. Abitbol et al., "Mycelium bio-composites in industrial design and architecture: comparative review and experimental analysis," *Journal of Cleaner Production*, vol. 246, Article ID 119037, 2020.

[44] E. Elsacker, S. Vandelook, J. Brancart, E. Peeters, and L. De Laet, "Mechanical, physical and chemical characterisation of mycelium-based composites with different types of lignocellulosic substrates," *PLoS One*, vol. 14, no. 7, 2019.

[45] M. R. Islam, G. Tudryn, R. Bucinell, L. Schadler, and R. C. Picu, "Mechanical behavior of mycelium-based particulate composites," *Journal of Materials Science*, vol. 53, no. 24, pp. 16371–16382, 2018.

[46] E. Elsacker, S. Vandelook, A. Van Wylick et al., "A comprehensive framework for the production of mycelium-based lignocellulosic composites," *Science of the Total Environment*, vol. 725, Article ID 138431, 2020.

[47] Z. Tacer-caba, J. J. Varis, P. Lankinen, and K. S. Mikkonen, "Comparison of novel fungal mycelia strains and sustainable growth substrates to produce humidity-resistant bio-composites," *Materials & Design*, vol. 192, no. 8, Article ID 108728, 2020.

[48] M. A. Shakir, B. Azahari, Y. Yusup, M. F. Yhaya, and A. Salehabadi, "Preparation and characterization of mycelium as a bio-Matrix in fabrication of bio-composite," *Journal of Advanced Research in Fluid Mechanics and Thermal Sciences*, vol. 65, no. 2, pp. 253–263, 2020.

[49] C. Girometta, A. M. Picco, R. M. Baiguera et al., "Physico-mechanical and Thermodynamic properties of mycelium-based biocomposites: a review," *Sustainability*, vol. 11, no. 1, 2019.

[50] N. Attias, O. Danai, T. Abitbol et al., "Mycelium bio-composites in industrial design and architecture: comparative review and experimental analysis," *Journal of Cleaner Production*, vol. 246, Article ID 119037, 2020.

[51] A. Ghazvinian and B. Gürsoy, "Mycelium-based composite Graded materials: Assessing the effects of time and substrate mixture on mechanical properties," *Biomimetics*, vol. 7, no. 2, p. 48, 2022.

[52] A. Rigobello, C. Colmo, and P. Ayres, "Effect of composition Strategies on mycelium-based composites Flexural Behaviour," *Biomimetics*, vol. 7, no. 2, p. 53, 2022.

[53] M. Y. Nurain Izzati, A. Suraya Hani, S. Shahiron et al., "Strength and water absorption properties of lightweight concrete brick," *IOP Conference Series: Materials Science and Engineering*, vol. 513, no. 1, Article ID 012005, 2019.

[54] R. Mirski, D. Dukarska, A. Derkowski, R. Czarnecki, and D. Dziurka, "By-products of sawmill industry as raw materials for manufacture of chip-sawdust boards," *Journal of Building Engineering*, vol. 32, Article ID 101460, 2020.

[55] J. C. V. Empelen, "A study into more sustainable, alternative in tropical climates," 2010, https://repository.tudelft.nl/islandora/object/uuid:fcb0418d-5816-4073-9042-b7ff84c10362/datastream/OBJ3/download.

Hindawi
Advances in Materials Science and Engineering
Volume 2022, Article ID 6022550, 10 pages
https://doi.org/10.1155/2022/6022550

Research Article

Optimization on Material Removal Rate and Surface Roughness of Stainless Steel 304 Wire Cut EDM by Response Surface Methodology

Sathishkumar Seshaiah,[1] Deepak Sampathkumar,[1,2] Mathanbabu Mariappan,[1] Ashokkumar Mohankumar,[1] Guruprasad Balachandran,[3] Murugan Kaliyamoorthy,[4] Barathiraja Rajendran,[1] and Rajendiran Gopal[5]

[1]*Department of Mechanical Engineering, Government College of Engineering, Bargur, Krishnagiri 635 104, Tamil Nadu, India*
[2]*Department of Mechanical and Automation Engineering, Agni College of Technology, Thalambur, Chennai 600 130, Tamil Nadu, India*
[3]*Department of Mechanical Engineering, Alagappa Chettiar Government College of Engineering and Technology, Karaikudi 630 003, India*
[4]*Department of Mechanical Engineering, Government Polytechnic College, Thiruvarur 612 804, India*
[5]*Department of Motor Vehicle Engineering, Defence University College of Engineering, Bishoftu, Ethiopia*

Correspondence should be addressed to Deepak Sampathkumar; deepak.mae@act.edu.in and Rajendiran Gopal; razaautoirtt@gmail.com

Received 2 May 2022; Accepted 29 July 2022; Published 29 August 2022

Academic Editor: Vijayananth Kavimani

In this work, wire cut electrical discharge machining (WEDM) is used for the material removing processes; it is utilized for machining conductive parts where it is required to produce complicated shapes, new profiles, new geometry, new product development, and high-accuracy components. This machining process is best suitable for high-end applications such as aerospace, automations, automobile, and medical devices. At present, most of the industrial sectors choose the WEDM process because it is used to develop products in a very short development cycle and at a better economic rate. In this paper, the selected complex geometry of the metal sample was eroded away from the wire during the WEDM process, which eliminates mechanical tensions during machining. The effect of different WEDM operation variables set as wire speed, wire tension, discharge current, dielectric flow rate, and pulse on and off time on the parameter, stainless steel 304 material removing rate (MRR) using RSM, has been studied. The MRR will be maximized if the optimum sets of operational variations are used and also achieve a superior surface finish.

1. Introduction

WEDM, also called as "spark," is a machining technique that employs electrical output to obtain a variety of shapes. WEDM is a unique variation of the traditional EDM technique that starts the electrical sparking process using an electrode. The thin continuous brass, copper, or tungsten made wire electrode with a diameter of 0.05-0.3 mm moves constantly, which makes use of that may attain a better tiny corner radius of WEDM. Using a series of rapidly recurring current outputs among the two electrodes separated by a dielectric solution and placed at an electric voltage, the material is removed from the workpiece. The tool-electrode, or simply the "tool" or "electrode," is one of the electrodes, whilst the workpiece-electrode [1, 2], or just the "workpiece", is the other electrode.

As the distance between the electrodes decreases, the intensity of the electric field in the volume between them

exceeds the strength of the [3–5] dielectric (at least at few point(s), that breakup the allowed current to flow among the two electrodes). This is analogous to the breaking of the capacitor. From this, the material is removed from the two electrodes [6].

When the current flow slows (or stops—based on the generator), fresh solution-based dielectric is frequently introduced into the internal-electrode volume, allowing solid elements to be removed and the dielectric's insulating characteristics to be recovered [7]. Flushing is the process of replenishing the interelectrode volume with a new liquid dielectric. Additionally, following a current flow, the potential differentiation among the two electrodes [8] is recovered to its prebreakdown state, allowing for another liquid dielectric breakdown. Wire EDM is used in various manufacturing industrial applications: soft armors shaping, hybrid composite, and mainly in the coating industries (thermal spray processes) for cutting the base materials into the desired shape [9–20].

The mechanism of wire EDM process parameters is most similar to conventional EDM. The conventional EDM process will create an erosion effect on the sample surfaces to remove the material. The basic mechanism involved in the electric discharge machining (EDM) process is that the tool electrode is the cathode and the sample material is the anode. The developed voltage is passed between the two electrodes, and dielectric medium is passed between them to create a strong electrostatic effect. This effect produces a spark gap between the tool and sample. Huge thermal energy is created, and it melts material and vaporizes the material from the sample. The modification of pulse energy and current durations in the dielectric medium can determine the dimensional accuracy and quality of the machining samples [21–25].

To improve the dimensional accuracy and quality of the wire EDM process, it has many working parameters: surface roughness, metal removal rate, wire feed rate, pulse on time, pulse off time, peak current, pulse current, applied voltage, etc.

These all parameters mostly influence the performance of wire EDM machining processes. The proper selection of optimal parameters plays a very important role in the wire EDM machining process; it leads to dimensional accuracy and a quality surface finish. The improper selection of process parameters will lead to dimensional inaccuracy, poor quality, and surface finish; it also leads to wire breakage in the continued machining process; and it affects the performance of the process [26–29].

The most accurate optimization technique is the response surface methodology (RSM) based linear regression model is used in this work. The popularity and simplicity of this technique needed to control various parameters in the wire EDM process. In the present work, surface roughness, MRR, pulse on time, pulse off time, and peak current values are chosen for performance measurement. The selected parameters are the most essential things to get dimensional accuracy and quality finishing in the WEDM process. Many researchers have proved that using the RSM technique is most helpful in carrying out experiments with this technique, which leads to minimal experimental effort [30–33].

2. Experimentation

2.1. 304 Grade Stainless Steel. The most popular stainless steel is SAE 304, commonly known as A2 stainless steel (A2 steel tool not to be confused) with or stainless steel (18/8), standard 1.4301. The major noniron components of steel are chromium (typically 18%) and nickel (usually 8%). Its steel is made of austenite. It is nonmagnetic and not particularly electrically or thermally conductive. It is extensively used because it is easy to mold into different forms and has a better corrosion resistance than ordinary steel. Screws, machinery components, textiles, and other household and industrial items are made of stainless steel 304. These SS 304 grade materials are also used in defense applications like aircraft, armors, and shields as well. But the machining operations performed with this material are very difficult in traditional methods, and there are many proven literature studies available [34–37]. The experiment runs in the WEDM process with various optimized parameter values fed into the machine, and the machined sample design is shown in Figure 1.

2.2. Stainless Steel: Grade 304 (Uns S30400). Standard chemical formula: Fe, <0.08% C, 17.5-20% Cr, 8-11% Ni, <2% Mn, <1% Si, <0.045% P, and <0.03% S. Detailed chemical compositions are shown in Table 1.

2.3. Tool for Machining. The experiment findings were achieved using an Electronica Machine Tools Ltd wire-cut EDM machine (ULTRACUT S2), as shown in Figure 2. The technical specifications of the ULTRACUT S2 WEDM are shown in Table 2.

2.4. Performance Measures. WEDM performance is often assessed using the following criteria, independent of the electrode material and dielectric fluid used.

2.4.1. Material Removal Rate (MRR). Its greatest is a key indicator of the WEDM process' efficiency and cost-effectiveness. However, increasing MRR is not necessarily desired for all applications, since it may compromise the work piece's surface integrity. Fast removal rates result in a rough surface finish.

The expression of material removal rate (MRR) can be obtained from the WEDM. MRR = cutting velocity × wire diameter × material thickness.

2.4.2. Roughness of the Surface (Ra). The WEDM process creates a huge number of craters on the surface, which are created by the discharge energy. The quality of the surface is mostly determined by the amount of energy per spark.

2.5. Parts Programming in Machine. The component programming system receives the profile's geometry and the mobility of the wire electrode cutter along its

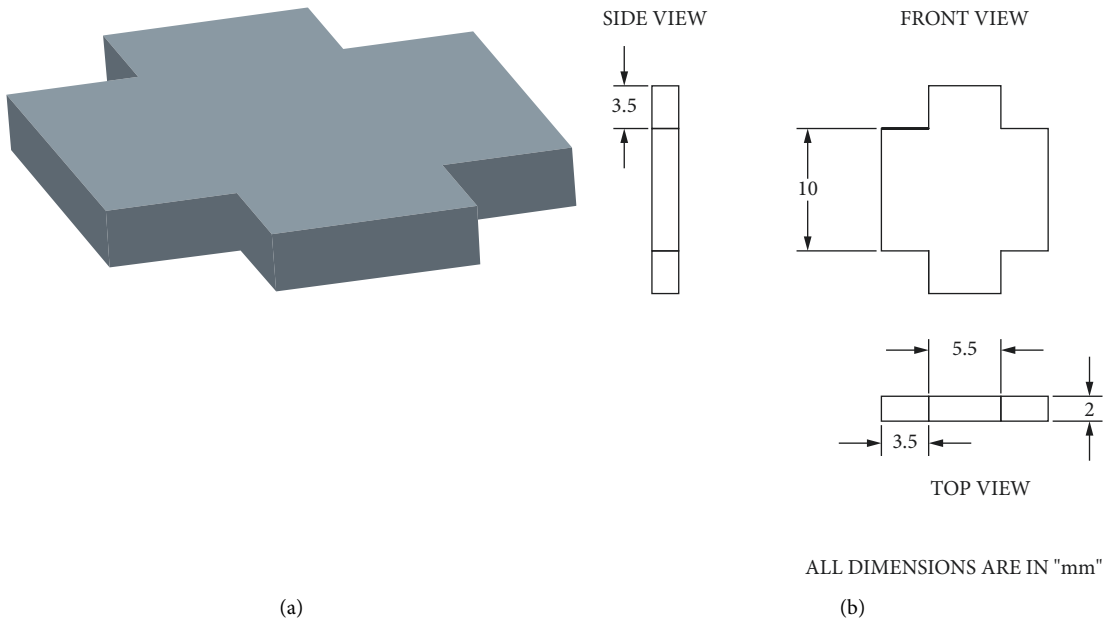

Figure 1: (a) Component 3D model and (b) detail 2D drawing.

Table 1: Chemical composition.

C%	0.017
Si%	0.41
Mn%	1.80
Cr%	18.08
Mo%	0.57
Cu%	0.56
Ni%	8.02
Co%	0.113
P%	0.031
S%	0.026
N%	0.087

Figure 2: Wire-cut EDM machine ULTRACUT S2.

keyboard, in terms of different definitions of points, lines, and circles as tool path elements, in a completely menu-driven, conversational manner. Each path element's wire compensation and taper gradient may be customized individually. After feeding the profile into the computer, all of the path's numerical information is automatically computed, and a printout is produced. On the visual display panel, the entered profile may be checked. The computer records the successful profile definition, which is subsequently sent into the generator for programmed execution. The machine input data are detailed in Tables 3 and 4.

Table 2: Technical specification of the ULTRACUT WEDM.

Model	ULTRACUT S2
Make	Electrica, Pune
Generator	El pulse 50 S
Travel range	
Main table traverse (X, Y)	X 600 mm, Y 400 mm
Auxiliary table traverse (Uv)	U ± 40 mm, V ± 40 mm
Vertical	Z 325 mm
Max. table size	860 × 580 mm
Max. work piece size	1150 × 810 x 300
Max. work piece weight	1000 kg
Feed	
Main table feed rate	900 mm/min
Resolution	0.001 mm
Wire feed rate	0.15 m/min
Max. taper cutting range	±15°/100 mm
Dielectric supply unit	
Dielectric fluid	DM water
Dirty tank	900 ltr
Clean tank	300 ltr
Wire diameter	0.25 mm
Program	El cam V1.14 with hardware
Lock	(USB-3049-2943)

2.6. Surface Roughness Tester. The surface roughness value for specified experimental components is measured using

Table 3: Input parameters and their levels.

Factor	A	B	C
Input parameter	Pulse ON, (T-ON)	Pulse OFF, (T-OFF)	Peak current(IP)
Units	µs	µs	Amps
Level 1	105	115	125
Level 2	43	53	63
Level 3	170	190	210

Table 4: Response surface methodology design.

Sl. no.	X1 (T –ON)	X2 (T- OFF)	X3 (IP)
1	1	0	0
2	0	1	0
3	0	0	0
4	0	−1	0
5	−1	1	−1
6	0	0	1
7	1	−1	1
8	0	0	−1
9	0	0	0
10	0	0	0
11	0	0	0
12	−1	−1	−1
13	1	1	1
14	−1	0	0
15	1	−1	−1
16	−1	−1	1
17	0	0	0
18	0	0	0
19	1	1	−1
20	0	1	−1

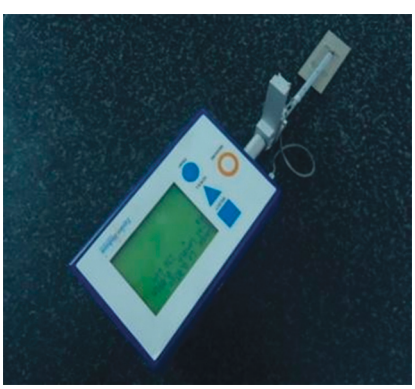

Figure 3: Roughness tester.

Taylor Hobson, Surtronic25 Roughness Testers. The surface roughness tester used is presented in Figure 3 and its specifications are listed in Table 5.

2.7. Material Removal Rate: Calculations. The MRR surface finish has conducted 20 experiments with various parameters like cutting velocity, MRR, and surface roughness. Various machining parameters were selected to perform this work. The obtained Ra value of all these experiments is shown in Table 6.

Table 5: Taylor Hobson.

Model	Surtronic25
Range	00-300 µm
Evaluation length	2.50 mm–25.0 mm
Cutoff	0.25 mm–2.50 mm

Table 6: Result of MRR and surface finish.

Wire diameter (mm)	0.25	Material thickness (mm)	2.052
Sl. no.	Cutting velocity. (mm/min)	MRR (mm^3/min)	Ra,(µm)
1	7.8	3.933	2.711
2	8.2	4.303	2.939
3	8.9	4.557	2.92
4	9.2	4.507	2.802
5	8.6	4.214	2.919
6	9.4	4.474	3.012
7	8	4.325	2.807
8	9.8	4.716	2.946
9	9.6	4.523	2.922
10	8.3	4.572	2.968
11	8.4	4.567	2.926
12	7.6	4.104	2.848
13	7.9	3.807	3.021
14	8.8	4.209	2.784
15	7.4	3.687	2.352
16	9	4.565	2.894
17	9.1	4.557	2.92
18	8.9	4.572	2.938
19	7.8	4.326	2.915
20	7.2	3.736	2.707

$$\begin{aligned}&\text{Material Removal Rate (MPR)}\\&= Vc\ x\ \text{Wire Dia}\ x\ \text{Material Thickness}\\&= 7.8 \times 0.25 \times 2.052.\\&= 3.933\,\frac{\text{mm}^3}{\text{min}}.\end{aligned} \tag{1}$$

3. Results and Discussions

These experimental results were obtained using a specific WEDM process. The wire diameter is 0.25 mm, the material is brass, and the dielectric fluid is di-ionized water. The experimental design matrix results are displayed in Tables 7–11. The obtained results from experiments are conducted with the specific input process parameters such as pulse on time (T-on),µs; pulse off time (T-off), µs; and peak current(IP), amps, with various levels of experiments shown in Table 7.

From Table 8, it is evaluated that the coefficients of estimated regression for surface roughness are very close to the unity value of (R^2 or R-Sq = 0.9860) and the adjusted coefficient is (R^2 or R-Sq Adj. = 0.9730). This RSM model indicates the estimators of acceptable values with the proper

Table 7: Results obtained from experiment.

Exp. no.	Input process parameter					
	Pulse on time(T-on),μs		Pulse off time (T- off),μs		Peak current(IP), amps	
	Coded	Actual	Coded	Actual	Coded	Actual
1	1	125	0	53	0	190
2	0	115	1	63	0	190
3	0	115	0	53	0	190
4	0	115	−1	43	0	190
5	−1	105	1	63	−1	170
6	0	115	0	53	1	210
7	1	125	−1	43	1	210
8	0	115	0	53	−1	170
9	0	115	0	53	0	190
10	0	115	0	53	0	190
11	0	115	0	53	0	190
12	−1	105	−1	43	−1	170
13	1	125	1	63	1	210
14	−1	105	0	43	0	190
15	1	125	−1	43	−1	170
16	−1	105	−1	43	1	210
17	0	115	0	53	0	190
18	0	115	0	53	0	190
19	1	125	1	63	−1	170
20	−1	105	1	63	1	210

Table 8: Coefficients of estimated regression for surface roughness, Ra.

Term	Coef	SE coef	T	*P*
Constant	0.682524	2.10589	0.324	0.753
A	0.201951	0.03963	5.096	0.000
B	−0.00411	0.02071	−0.198	0.847
C	−0.099919	0.01431	−6.982	0.000
A ∗ A	−0.001524	0.00017	−9.011	0.000
B ∗ B	−0.000403	0.00016	−2.553	0.029
C ∗ C	0.000184	0.00003	5.286	0.000
A ∗ B	0.001104	0.00008	13.35	0.000
A ∗ C	0.000455	0.00004	10.638	0.000
B ∗ C	−0.00379	0.00004	−8.86	0.000
S	R-Sq		R-Sq (Adj)	
0.02419	98.60%		97.30%	

Table 9: Variance analysis for surface roughness, Ra.

Source	DF	Seq-SS	Adj-SS	Adj-MS	F	*P*
Regression	9	0.413512	0.413512	0.04592	78.52	0.000
Linear	3	0.109886	0.03622	0.012134	20.63	0.000
Square	3	0.087207	0.10881	0.036395	61.99	0.000
Interactions	3	0.21642	0.21642	0.072064	123.29	0.000
Residual error	10	0.005851	0.005851	0.000573	-	-
Lack of fit	5	0.004096	0.004096	0.000807	2.33	0.187
Pure error	5	0.001755	0.001755	0.00034	-	-
Total	19	0.419363	-	-	-	-

Table 10: Coefficients of estimated regression for material removal rate (MRR).

Term	Coef	SE coef	T	*P*
Constant	−53.3003	6.42397	−8.297	0.000
A	0.986	0.1209	8.155	0.000
B	0.2197	0.06317	3.477	0.006
C	−0.0424	0.04366	−0.971	0.354
A ∗ A	−0.0046	0.00052	−8.963	0.000
B ∗ B	−0.0009	0.00048	−1.901	0.087
C ∗ C	0.0003	0.00011	2.509	0.031
A ∗ B	0.001	0.00025	4.082	0.002
A ∗ C	0.0001	0.00013	0.652	0.529
B ∗ C	−0.0013	0.00013	−10.043	0.000
S	R-Sq		R-Sq(Adj)	
0.07379	97.00%		94.40%	

Table 11: Variance analysis of material removal rate (MRR).

Source	DF	Seq SS	Adj SS	Adj MS	F	*P*
Regression	9	1.78682	1.78682	0.198536	36.46	0.000
Linear	3	0.09402	0.76464	0.254879	46.81	0.000
Square	3	1.0506	1.09863	0.366211	67.26	0.000
Interactions	3	0.6422	0.6422	0.214067	39.32	0.000
Residual error	10	0.05445	0.05445	0.005445	-	-
Lack of fit	5	0.05275	0.05275	0.010549	31.03	0.001
Pure error	5	0.0017	0.0017	0.00034	-	-
Total	19	1.84127	-	-	-	-

degree of freedom and ideal architecture for reactive extraction process predictive simulations shown in Table 8. The ANOVA predicted results shown in Tables 9–11 give a T-value of 0.324, −8.297; *P*-value of 0.753; and an F-value of 78.52, 36.46 in the RSM model outlined as significant.

The significance to look at the obtained values in the model is that they correspond to peak current, pulse on time, and pulse off time. The surface roughness values are controlled with pulse on time and pulse off-time set input mean values shown in Tables 8 and 9. The material removal rate will be controlled with peak current modifications shown in Tables 10 and 11. The optimized output responses are shown in Figures 4 to 8.

3.1. Regression Analysis for Material Removal Rate. The findings of the experiments were used to create a mathematical model that expressed the connection between process parameters and MRR. Multiple regressions are used to calculate the coefficients of mathematical models, as shown in Figure 4.

$$\begin{aligned} \mathrm{MRR} = {} & -53.3033 + 0.986 \times \mathrm{Ton} + 0.2197 \times \mathrm{Toff} \\ & - 0.042 \times \mathrm{IP} - 0.0046 \times \mathrm{Ton}^2 - 0.0009 \times \mathrm{Toff}^2 \\ & + 0.0003 \times \mathrm{IP}^2 + 0.001 \times \mathrm{Ton}\, x\, \mathrm{Toff} + 0.0001 \\ & \times \mathrm{Ton}\, x\, \mathrm{IP} - 0.0013 \times \mathrm{Toff}\, x\, \mathrm{IP}. \end{aligned} \tag{2}$$

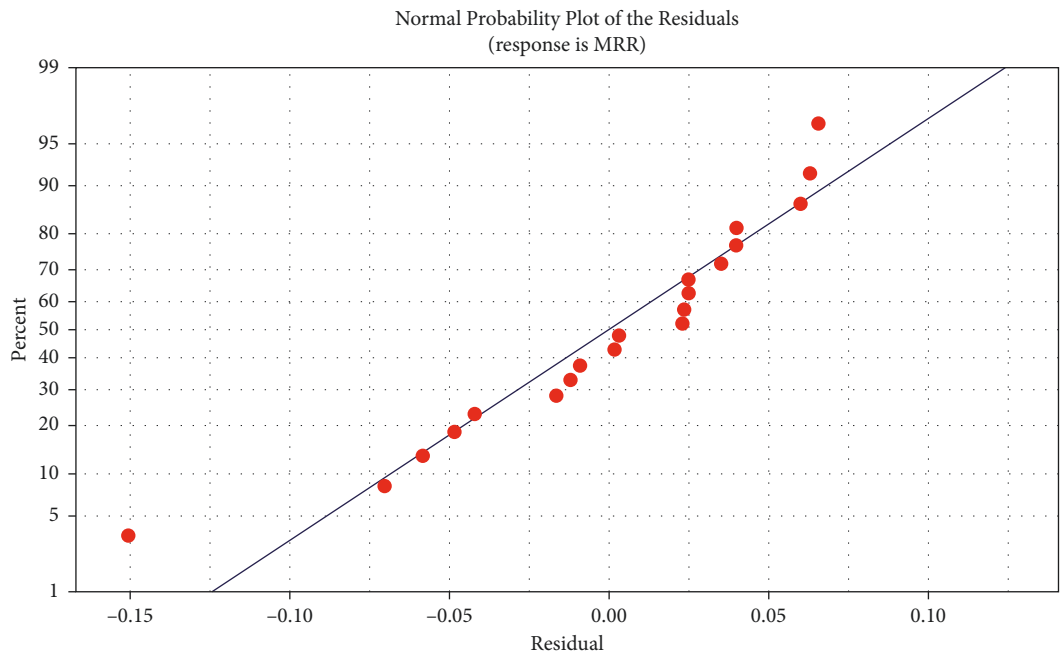

Figure 4: Normal probability plot of the residuals of the MRR.

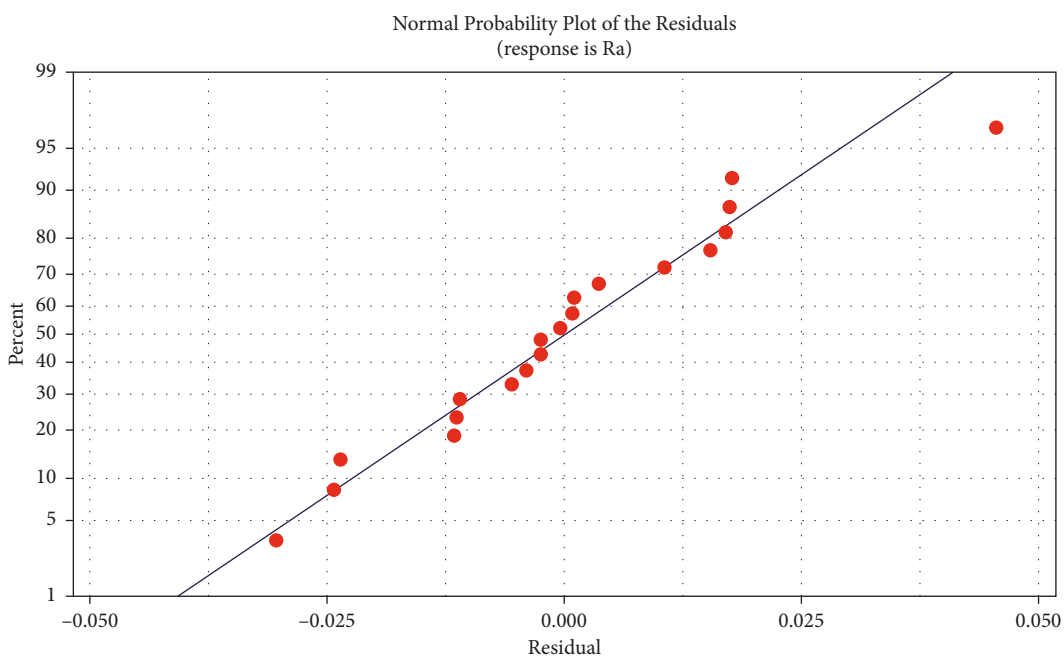

Figure 5: Normal probability plot of the residuals of surface roughness. The wire EDM process completed the given input process parameter. Shapes of component profile are shown in Figure 6.

3.2. Regression Analysis for Surface Roughness. The findings of the experiments were utilized to create a mathematical model that expressed the connection between process parameters and surface roughness, as shown in Figure 5. Multiple regressions are used to calculate the coefficients of mathematical models.

$$\begin{aligned} SR = {} & 0.682524 + 0.201951\, x\, \mathrm{Ton} - 0.\,00411\, x\, \mathrm{Toff} \\ & - 0.099919\, x\, IP - 0.001524\, x\, \mathrm{Ton}^2 0.000403\, x\, \mathrm{Toff}^2 \\ & + 0.000184\, x\, IP^2 + 0.001104\, x\, \mathrm{Ton}\, x\, \mathrm{Toff} \\ & + 0.0004551\, x\, \mathrm{Ton}\, x\, IP - 0.000379\, x\, \mathrm{Toff}\, x\, IP. \end{aligned} \tag{3}$$

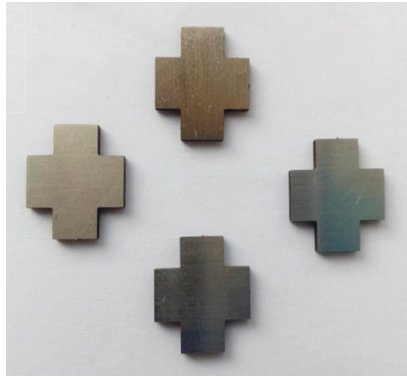

Figure 6: Wire EDM component profile.

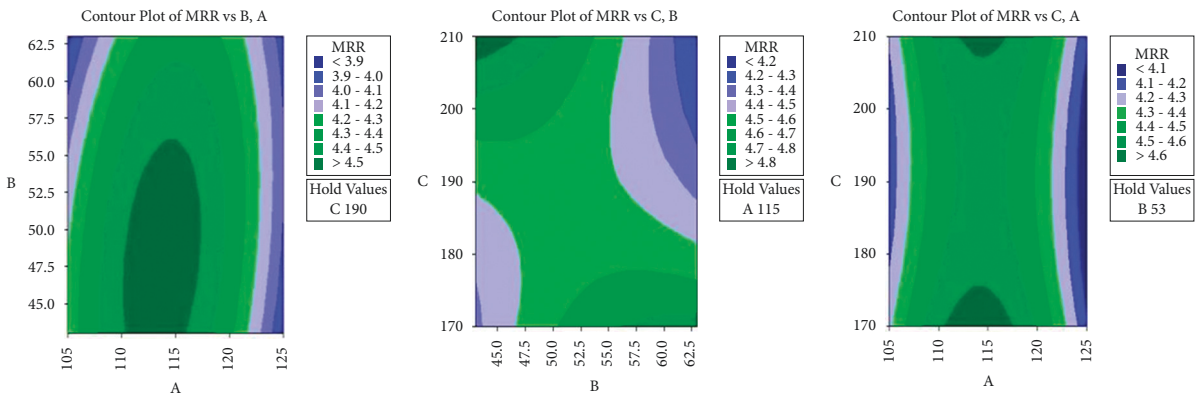

(a) (b) (c)

Figure 7: (a) Contour plot Of MRR vs (B) A., (b) contour plot of MRR vs (C) B., and (c) contour plot Of MRR vs C, A.

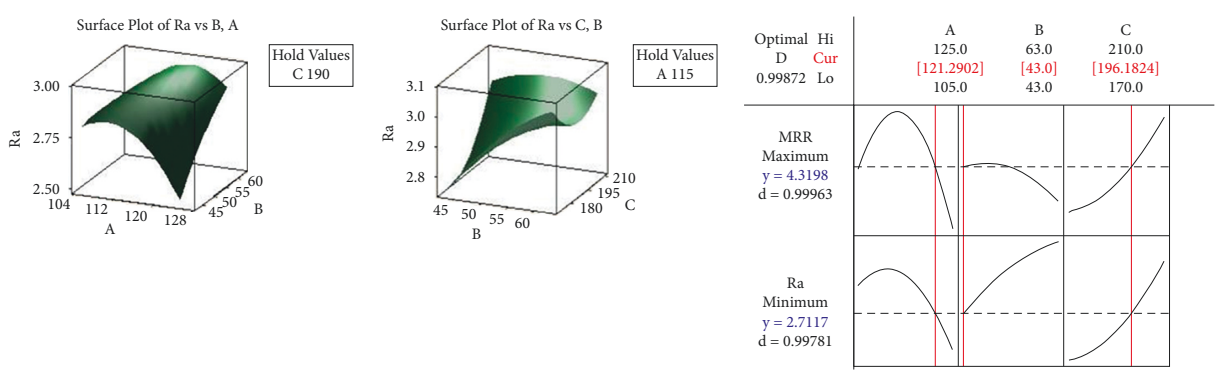

(a) (b) (c)

Figure 8: (a) Surface plot of Ra vs (C) A., (b) surface plot of Ra vs (C) B., and (c) optimization plot of MRR, Ra.

The response optimization plot for MRR and Ra is shown in Figures 7 and 8. The ultimate goal of our research is to increase MRR while reducing surface roughness.

Figure 7 shows the 2D contour response surface of MRR, and Figure 8 shows the 3D response surface of Ra. The MRR values vary with the changes in the discharge voltage and peak current. The Ra value leads to an electrode spark energy gap between the tool and the sample material. There are many combinations selected with MRR and Ra parameters, to opt with the graphs. This graph shows the increasing MRR value has a tendency to decrease surface roughness (Ra) [38–42].

In order to evaluate whether the maximum value of MRR and Ra is minimum, the desirability method was utilized to determine the optimal value of variables (Ra). The greatest values of MRR = 4.3198 and Ra = 2.7117 are achieved for the following combination of variables, as shown in the graph [43–45].

$$T\,\text{On} = 121.2902\,(\mu s),$$
$$T\,\text{Off} = 43\,(\mu s), \quad (4)$$
$$IP = 196.182\,(\text{amp}).$$

4. Conclusion

(i) As a consequence, the tests were performed on a WEDM machine, and the experimental research findings were derived from the work completed.

(ii) The pulse on time increases with respect to the surface roughness.

(iii) To achieve a superior surface finish for the specified test range in a 304 stainless steel material, utilize a high pulse on time of 121.2902 (s), a low pulse off time of 43.00 (s), and a peak current of 196.182 (amps) in the WEDM Process. The surface roughness optimal value is 2.7117, while the material removal rate is 4.3198.

(iv) The stainless steel 304 material has better corrosion resistance, high strength in mechanical properties, and is best suited for many chemical industries, automobiles, and customized machine spare manufacturing applications. The hardened stainless steel 304 work materials during re-machining is a major problem in mechanical industries. The wire-cut electric discharge machining process will solve that problem easily.

Data Availability

The data used to support the findings of this study are available from the author upon request.

Conflicts of Interest

The authors declare that they have no conflicts of interest.

Acknowledgments

The authors wish to express their sincere thanks to Dr. S. K. Nayak, Director General, and Dr. K. Prakalathan, Director (Academics), Central Institute of Petrochemicals Engineering and Technology (CIPET), Chennai, Tamil Nadu, India, for the help rendered during characterization, polymer testing lab facilities. The authors also wish to thank Dr. K. P. Bhuvana, Scientist, and R. Joseph Bensingh, Senior Scientist, CIPET : School for Advanced Research in Polymers (SARP)—Advanced Research School for Technology and Product Simulation (ARSTPS), Chennai, Tamil Nadu, India, for their help in carrying out this investigation, and the authors dedicated this work to the Government of India.

References

[1] A. Goswami and J. Kumar, "Investigation of surface integrity, material removal rate and wire wear ratio for WEDM of Nimonic 80A alloy using GRA and Taguchi method," *Engineering Science and Technology, an International Journal*, vol. 17, no. 4, pp. 173–184, 2014.

[2] F. Kausar, S. Kumar, M. Azam, S. Suman, A. Sharma, and A. Sethi, "Optimization of machining parameter for surface roughness on WEDM of En36 alloy steel," *Journal of Mechanical and Civil Engineering*, vol. 12, no. 6, pp. 101–104, 2015.

[3] A. Biloria and R. Singh, "Optimizing the parameters influence the performance of wire cut EDM machining," *International Journal of current Engineering and Technology*, vol. 4, no. 5, 2014, http://inpressco.com/category/ijcet.

[4] F. Klocke, D. Welling, A. Klink, D. Veselovac, T. Nöthe, and R. Perez, "Evaluation of advanced wire-EDM capabilities for the manufacture of fir tree slots in Inconel 718," *Procedia CIRP*, vol. 14, pp. 430–435, 2014.

[5] C. D. Shah, J. R. Mevada, and B. C. Khatri, "Optimization of process parameter of wire electrical discharge machine by response surface methodology on Inconel-600," *International Journal of Emerging Technology and Advanced Engineering*, vol. 3, no. 4, pp. 2250–2459, 2013.

[6] K. Kumar and R. Ravikumar, "Modeling and optimization of wire EDM process," *International Journal of Modern Engineering Research*, vol. 3, no. 3, pp. 1645–1648, 2013.

[7] F. Han, J. Jiang, and D. Yu, "Influence of discharge current on machined surfaces by thermo-analysis in finish cut of WEDM," *International Journal of Machine Tools and Manufacture*, vol. 47, no. 7-8, pp. 1187–1196, 2007.

[8] K. Kanlayasiri and S. Boonmung, "Effects of wire-EDM machining variables on surface roughness of newly developed DC 53 die steel: design of experiments and regression model," *Journal of Materials Processing Technology*, vol. 192-193, pp. 459–464, 2007.

[9] K. Mathivanan, D. Thirumalaikumarasamy, M. Ashokkumar, S. Deepak, and M Mathanbabu, "Optimization and prediction of AZ91D stellite-6 coated magnesium alloy using box behnken design and hybrid deep belief network," *Journal of Materials Research and Technology*, vol. 15, pp. 2953–2969, 2021.

[10] M. Ashokkumar, D. Thirumalaikumarasamy, C. Ramachandran et al., "Enhancing the corrosion resistance of low pressure cold sprayed metal matrix composite coatings on AZ31B Mg alloy through friction stir processing," *Coatings*, vol. 12, no. 2, p. 135, 2022.

[11] M. Mathanbabu, D. Thirumalaikumarasamy, P. Thirumal, and M. Ashokkumar, "Study on thermal, mechanical, microstructural properties and failure analyses of lanthanum zirconate based thermal barrier coatings: a review," *Materials Today Proceedings*, vol. 46, pp. 7948–7954, 2021.

[12] M. Ashokkumar, D. Thirumalaikumarasamy, P. Thirumal, and R. Barathiraja, "Influences of Mechanical, Corrosion, erosion and tribological performance of cold sprayed Coatings A review," *Materials Today Proceedings*, vol. 46, pp. 7581–7587, 2021.

[13] M. Kannan, T. Duraisamy, T. Pattabi, and A. Mohankumar, "Investigate the corrosion properties of stellite coated on AZ91D alloy by plasma spray technique," *Thermal Science*, vol. 26, no. 2, pp. 911–920, 2022.

[14] S. Deepak, D. Thirumalaikumarasamy, M. Ashokkumar, and S. K. Nayak, "Experimental analyzing the static puncture resistance performance of shear thickening fluid impregnated polypropylene hybrid composite target structures for armour application," *Journal of the Textile Institute*, pp. 1–13, 2022.

[15] S. Deepak, D. Thirumalaikumarasamy, P. Thirumal, and M. Ashokkumar, "Static puncture resistance characteristics with various indenter nose shape geometry perforation of shear thickening fluid impregnated polypropylene fabric for soft armour application," *Polymers and Polymer Composites*, vol. 30, Article ID 096739112110633, 2022.

[16] S. Deepak, D. Thirumalaikumarasamy, P. Thirumal et al., "Preparation and characterization of shear thickening fluid coated polypropylene fabric for soft armour application," *Journal of the Textile Institute*, vol. 112, no. 10, pp. 1555–1567, 2021.

[17] M. Ashokkumar, D. Thirumalaikumarasamy, S. Deepak, and T. Sonar, "Electrochemical corrosion performance of friction stir processed cold spray metal matrix composite coatings on AZ31B magnesium alloy under sodium chloride environment," *Surface Topography: Metrology and Properties*, vol. 10, no. 3, Article ID 035010, 2022.

[18] Ľ. Straka and S. Hašová, "Optimization of material removal rate and tool wear rate of Cu electrode in die-sinking EDM of tool steel," *International Journal of Advanced Manufacturing Technology*, vol. 97, no. 5-8, pp. 2647–2654, 2018.

[19] S. Deepak, K. P. Bhuvana, R. J. Bensingh, K. Prakalathan, and S. K. Nayak, "Development of hybrid composites and joining technology for lightweight structures," *Advances in Polymer Sciences and Technology*, pp. 123–131, 2018.

[20] S. Dinesh, A. G. Antony, K. Rajaguru, and V. Vijayan, "Experimental investigation and optimization of material removal rate and surface roughness in centerless grinding of magnesium alloy using grey relational analysis," *Mechanics and Mechanical Engineering*, vol. 21, no. 1, pp. 17–28, 2017.

[21] V. Gaikwad and V. S. Jatti, "Optimization of material removal rate during electrical discharge machining of cryo-treated NiTi alloys using Taguchi's method," *Journal of King Saud University - Engineering Sciences*, vol. 30, no. 3, pp. 266–272, 2018.

[22] P. M. Abhilash and D. Chakradhar, "Wire EDM failure prediction and process control based on sensor fusion and pulse train analysis," *International Journal of Advanced Manufacturing Technology*, vol. 118, no. 5-6, pp. 1453–1467, 2022.

[23] P. M. Abhilash and D. Chakradhar, "Failure detection and control for wire EDM process using multiple sensors," *CIRP Journal of Manufacturing Science and Technology*, vol. 33, pp. 315–326, 2021.

[24] K. Rajmohan and A. S. Kumar, "Experimental investigation and prediction of optimum process parameters of micro-wire-cut EDM of 2205 DSS," *International Journal of Advanced Manufacturing Technology*, vol. 93, no. 1-4, pp. 187–201, 2017.

[25] T. Bergs, U. Tombul, T. Herrig, M. Olivier, A. Klink, and F. Klocke, "Analysis of characteristic process parameters to identify unstable process conditions during wire EDM," *Procedia Manufacturing*, vol. 18, pp. 138–145, 2018.

[26] T. Muthuramalingam and B. Mohan, "A review on influence of electrical process parameters in EDM process," *Archives of Civil and Mechanical Engineering*, vol. 15, no. 1, pp. 87–94, 2015.

[27] D. Jafari, T. H. Vaneker, and I. Gibson, "Wire and arc additive manufacturing: opportunities and challenges to control the quality and accuracy of manufactured parts," *Materials & Design*, vol. 202, Article ID 109471, 2021.

[28] A. Alias, B. Abdullah, and N. M. Abbas, "Influence of machine feed rate in WEDM of titanium Ti-6Al-4V with constant current (6A) using brass wire," *Procedia Engineering*, vol. 41, pp. 1806–1811, 2012.

[29] K. H. Ho, S. T. Newman, S. Rahimifard, and R. D. Allen, "State of the art in wire electrical discharge machining (WEDM)," *International Journal of Machine Tools and Manufacture*, vol. 44, no. 12-13, pp. 1247–1259, 2004.

[30] A. Mandal and A. R. Dixit, "State of art in wire electrical discharge machining process and performance," *International Journal of Machining and Machinability of Materials*, vol. 16, no. 1, pp. 1–21, 2014.

[31] A. Chaudhary, S. Sharma, and A. Verma, "Optimization of WEDM process parameters for machining of heat treated ASSAB '88 tool steel using Response surface methodology (RSM)," *Materials Today Proceedings*, vol. 50, pp. 917–922, 2022.

[32] B. Choudhuri, R. Sen, S. K. Ghosh, and S. C. Saha, "Modelling and multi-response optimization of wire electric discharge machining parameters using response surface methodology and grey-fuzzy algorithm," *Proceedings of the Institution of Mechanical Engineers - Part B: Journal of Engineering Manufacture*, vol. 231, no. 10, pp. 1760–1774, 2017.

[33] A. Çiçek, T. Kıvak, and E. Ekici, "Optimization of drilling parameters using Taguchi technique and response surface methodology (RSM) in drilling of AISI 304 steel with cryogenically treated HSS drills," *Journal of Intelligent Manufacturing*, vol. 26, no. 2, pp. 295–305, 2015.

[34] V. N. Gaitonde, M. Manjaiah, S. Maradi, S. R. Karnik, P. M. Petkar, and J. P. Paulo Davim, "Multiresponse optimization in wire electric discharge machining (WEDM) of HCHCr steel by integrating response surface methodology (RSM) with differential evolution (DE)," *Computational Methods and Production Engineering*, , pp. 199–221, Woodhead Publishing, 2017.

[35] K. Ishfaq, N. Ahmad, M. Jawad, M. A. Ali, and A. Al-Ahmari, "Evaluating material's interaction in wire electrical discharge machining of stainless steel (304) for simultaneous optimization of conflicting responses," *Materials*, vol. 12, no. 12, p. 1940, 2019.

[36] G. Ugrasen, M. Bhagawan Singh, and H. V. Ravindra, "Optimization of process parameters for SS304 in wire electrical discharge machining using taguchi's technique," *Materials Today Proceedings*, vol. 5, no. 1, pp. 2877–2883, 2018.

[37] T. Chaudhary, A. N. Siddiquee, and A. K. Chanda, "Effect of wire tension on different output responses during wire electric discharge machining on AISI 304 stainless steel," *Defence Technology*, vol. 15, no. 4, pp. 541–544, 2019.

[38] M. Ashokkumar, D. Thirumalaikumarasamy, T. Sonar, S. Deepak, P. Vignesh, and M. Anbarasu, "An overview of cold spray coating in additive manufacturing, component repairing and other engineering applications," *Journal of the Mechanical Behavior of Materials*, vol. 31, no. 1, pp. 514–534, 2022.

[39] P. M. Gopal and K. Soorya Prakash, "Minimization of cutting force, temperature and surface roughness through GRA, TOPSIS and Taguchi techniques in end milling of Mg hybrid MMC," *Measurement*, vol. 116, pp. 178–192, 2018.

[40] S. Karthik, K. S. Prakash, P. M. Gopal, and S. Jothi, "Influence of materials and machining parameters on WEDM of Al/AlCoCrFeNiMo0.5 MMC," *Materials and Manufacturing Processes*, vol. 34, no. 7, pp. 759–768, 2019.

[41] P. M. Gopal, K. S. Prakash, and S. Jayaraj, "WEDM of Mg/CRT/BN composites: effect of materials and machining parameters," *Materials and Manufacturing Processes*, vol. 33, no. 1, pp. 77–84, 2018.

[42] G. R, K. V, G. P.M, and S. D, "Multi-response optimization and surface integrity characteristics of wire electric discharge machining α-phase Ti-6242 alloy," *Process Integration and Optimization for Sustainability*, vol. 5, no. 4, pp. 815–826, 2021.

[43] R. Prasanna, P. M. Gopal, M. Uthayakumar, and S. Aravind, "Multicriteria optimization of machining parameters in WEDM of titanium alloy 6242," *Lecture Notes in Mechanical Engineering*, , pp. 65–75, Springer, 2019.

[44] M. Ashokkumar, D. Thirumalaikumarasamy, S. Deepak et al., "Optimization of cold spray process inputs to minimize porosity and maximize hardness of metal matrix composite coatings on AZ31B magnesium alloy," *Journal of Nanomaterials*, vol. 2022, Article ID 7900150, 17 pages, 2022.

[45] R. Pradeep Raj, D. Thirumalaikumarasamy, C. Ramachandran et al., "Optimisation of HVOF spray process parameters to achieve minimum porosity and maximum hardness in WC-10Ni-5Cr coatings," *Coatings*, vol. 12, no. 3, p. 339, 2022.

Hindawi
Advances in Materials Science and Engineering
Volume 2022, Article ID 7134991, 8 pages
https://doi.org/10.1155/2022/7134991

Research Article

Green Synthesis of *Datura stramonium* (Asaangira) Leaves Infusion for Antibacterial Activity through Magnesium Oxide (MgO) Nanoparticles

Abel Saka,[1] Leta Tesfaye Jule,[1,2] Lamessa Gudata,[1] Adugna Gindaba,[3] Soressa Shuma Abdisa,[4] N Nagaprasad,[5] and Krishnaraj Ramaswamy[2,6]

[1]*Dambi Dollo University, College of Natural and Computational Science, Department of Physics, Dembi Dolo, Ethiopia*
[2]*Centre for Excellence-Indigenous Knowledge, Innovative Technology Transfer and Entrepreneurship, Dambi Dollo University, Ethiopia*
[3]*College of Natural and Computational Science, Department of Biology, Dambi Dollo University, Dembi Dolo, Ethiopia*
[4]*Department of Animal Science, College of Agriculture and Veterinary Medicine, Dambi Dollo University, Dembi Dolo, Ethiopia*
[5]*Department of Mechanical Engineering, ULTRA College of Engineering and Technology, Madurai 625 104, Tamilnadu, India*
[6]*Department of Mechanical Engineering, Dambi Dollo University, Dembi Dolo, Ethiopia*

Correspondence should be addressed to Abel Saka; latiyejesus@gmail.com, Leta Tesfaye Jule; laterajule@gmail.com, and Krishnaraj Ramaswamy; prof.dr.krishnaraj@dadu.edu.et

Received 30 April 2022; Revised 16 June 2022; Accepted 30 July 2022; Published 25 August 2022

Academic Editor: Pudhupalayam Muthukutti Gopal

The biosynthesized magnesium oxide nanoparticles were pigeon-holed with X-ray diffraction (XRD), ultraviolet-visible (UV-Vis) spectrophotometer, scanning electron microscope (SEM), and photoluminescence spectrometer (PLs) and antibacterial activity. *Datura stramonium* leaves extract has been used in the present work,; which has medicinal value, and we have synthesized magnesium oxide nanoparticles from both chemical and biosynthesis techniques. The XRD result indicates the realization of crystalline magnesium oxide nanoparticles, and again it is also inveterated with an ultraviolet-visible (UV-Vis) spectrophotometer. The superficial morphology expresses that magnesium oxide nanoparticles have a bulbous morphological shape for both biosynthesis and chemosynthesis. The antibacterial activity of magnesium oxide nanoparticles obtained from *Datura stramonium* leaves against *E. coli* and *S. aureus* was studied. The antibacterial activity also shows a good zone of inhibition. Both techniques are promising for the preparations of MgO nanoparticles in antibacterial activity and show the same result. This outcome demonstrates that the biosynthesized nanoparticles originate from having some medicinal uses and are biodegradable.

1. Introduction

Microbial infection endures enticement municipal consideration. It is predicted that almost 48 million gears of pathogenic ailments arise in the US [1]. Consequently, in demand to resolve this delinquency, it is essential to grow effective antimicrobial proxies to control the bacteriological populace [2]. Mostly, antibacterial proxies can be classified as carbon-based or mineral antibacterial proxies. Biological antibacterial proxies such as carbon-based acids, vital oils, bacteriocin, and enzymes have been extensively considered. Nevertheless, they have particular limitations, such as little confrontation to dispensation situations, which provides their solicitations. The foremost compensations of mineral antibacterial proxies, associated with carbon-based antibacterial proxies, are the enriched steadiness under exacting dispensation situations [3].

Nanotechnology is mostly apprehensive about the production of nanoparticles of flexible sizes, characters, chemical configurations, and controlled disproportion and possible use for human welfare [4]. The application of biological creatures such as microbes, plant extracts, or plant

biomass could be a substitute for biochemical and physical techniques for the fabrication of nanoparticles in a sustainable way [5, 6]. The organic production technique of nanoparticles is easy, effective, and biodegradable in contrast to a chemical-mediated combination [7].

Metallic nanoparticles have been prepared using different approaches comprising physical, chemical, and biosynthesis techniques that involve the use of microbials like bacteria, yeast, and fungi [8] and plant extracts [9]. The physical and chemical techniques of metal nanoparticle synthesis use very large amounts of energy, toxic solvents, and dangerous chemicals [10]. The biological techniques of using microbials in the metallic nanoparticle approach are eco-friendly and cost-effective because of the intricate laboratory procedure of preparing and upholding the microbial cultures, complex extractions, and purification procedures [11].

It is important to pay special attention to metallic oxides such as NiO, zinc oxide, and CuO because not only are they reliable under harsh method conditions, but they are also widely perceived as safe materials [12]. However, several chemical approaches exist for metallic nanoparticle production; abundant reactants and raw materials are applicable in the reactions that are poisonous and theoretically dangerous. Nanostructured mesoporous zinc oxide is also of study interest due to its miscellaneous characteristics, which initiate from its structural appearances [13]. Nowadays, there have been some approaches for the production of nanostructured mesoporous zinc oxide, e.g., gel template method [14], modified citrate precursor method [15], microwave plasma torch method [16], and burning method [17]. Currently, certain mineral antibacterial constituents in specific mineral metallic oxides like titanium oxide (TiO_2), zinc oxide (ZnO), magnesium oxide (MgO), and calcium oxide (CaO) have been investigated [18].

Among the researched mineral metallic oxides, zinc oxide, magnesium oxide, and calcium oxide are of specific attention due to harsh procedure circumstances and are largely observed as nontoxic resources to mortals [19]. Furthermore, they have antimicrobial action deprived of sunlight activation, associated with titanium oxide that needs sunlight [20]. Lately, nanosciences, as well as nanotechnology, have been foremost to a scientific rebellion in the biosphere, which is apprehensive with resources with meaningfully new as well as developed physical (somatic), chemical, and organic characteristics [21]. In this esteem, nanoparticles are renowned as antibacterial proxies because of their sizes, configuration, and superficial behaviours [22]. Therefore, nanotechnology compromises a way to upgrade the action of mineral antibacterial proxies. Metallic oxide nanoparticles like zinc oxide, magnesium oxide, and calcium oxide have been studied as mineral antibacterial proxies [23].

Magnesium oxide (MgO) is a significant mineral substantial with a widespread energy bandgap [24]. This metallic oxide has been applied in numerous ways such as catalysis, catalyst supports, poisonous wastes remediation, headstrong constituents as well as adsorbents, preservatives in weighty petroleum oils, shiny and antireflecting coverings, superconducting and ferroelectric thin films as the substrate, and superconductors and lithium-ion batteries [25]. In medical fields, magnesium oxide is used for the respite of indigestion, painful stomach, and bone renewal. Magnesium oxide nanoparticles also have an extensive perspective as an antibacterial proxy. So, in this work, the main preparation techniques, antibacterial action, and antibacterial types of using magnesium oxide nanoparticles are argued.

In this current work, we have used the *Datura stramonium* leaves extract which has therapeutic value and we have manufactured magnesium oxide nanoparticles from it by green deposition production technique. These green synthesized nanoparticles were tested by X-ray diffraction (XRD) characterization to calculate their magnitude and properties. The antibacterial activity of magnesium oxide nanoparticles obtained from *Datura stramonium* leaves is in contradiction to *E. coli*, *S. aureus*, and bacillus studied. The antibacterial activity also illustrates a good zone of inhibition.

2. Materials and Methods

2.1. Materials. All the reagents utilized in this research were of analytical grade. Magnesium nitrate ($Mg(NO_3).3H_2O$) and NaOH were obtained from Sigma-Aldrich. All solutions were prepared from double-distilled water.

2.2. Groundwork of Datura stramonium Foliage Extraction. *Datura stramonium* leaves of about 30–35 g were collected from East Wollega Zone, Gudaya Bila District, carefully washed away with double-distilled water, and cut into slight pieces; then, the foliage was heated in 250 ml cut-glass beaker with 150 ml of double-distilled water for 45 min at 300°C using a magnetic stirrer through the hot dish. After reheating, the pigment of the aqueous mixture was transformed from waterlogged to chocolate color and then the solution was allowed to refrigerate at 37°C.

The aqueous extract of *Datura stramonium* (Asaangira, Oromo) foliage was unglued by percolation with Whatman No. 50 filter paper. The deposits were cast off for the preparation of magnesium oxide (MgO) nanoparticles. *Datura stramonium* flowers, leaves, and fruit were taken from East Wollega Zone, Gudaya Bila District, Darbes Kebele, Oromia, Ethiopia, as illustrated in Figure 1.

2.3. Synthesis of Magnesium Oxide Nanoparticles. The sources utilized for the deposition of magnesium oxide nanoparticles are magnesium nitrate ($Mg(NO_3).3H_2O$) and NaOH. The magnesium oxide nanoparticles were produced by the chemosynthesis technique. 30 ml of $Mg(NO_3).3H_2O$) 0.2 M was dissolved with a volume of 30 ml of 0.2 M NaOH in a 150 ml beaker. Double-distilled water was added to fill the total volume required. The pH value of the solution was 2 (pH = 2), which is categorized under an acidic bath. Then, the solution was kept on the heater and stirred for 2 hr at a temperature of 50°C. Then, after it was allowed to cool down, the powder form of MgO nanoparticles was formed. Then, the powder was transferred to a plate and reserved for

Figure 1: *Datura stramonium* flowers, leaves, and fruit are taken from East Wollega Zone, Gudaya Bila District, Darbes Kebele, Oromia, Ethiopia.

application. The deliberation of ($Mg(NO_3).3H_2O$) 0.2 molarity, aqueous were dissolved with capacity (30 millilitres) of the *Datura stramonium*foliage except for the preparation. After some minutes, 30 ml of 0.2M sodium hydroxide (NaOH) was added drop by drop to the solution. Then, the mixture is maintained for a few hours. The pigment of the compound transformed from chocolate to yellow, representing the development of MgO nanoparticles.

The compacted manufactured goods were cleaned, and then, the separate precipitate was bare to return to the situationby placing it in the furnace at 50°C for about 60 min; then, it was allowed to cool at room temperature, and we obtained the crushed powder using a motor and pestle, before adding Mg $(NO_3).3H_2O$, and after adding Mg $(NO_3).3H_2O$, respectively.

3. Results and Discussion

3.1. X-Ray Diffraction. The XRD pattern of MgO nanoparticles derived from the sol-gel technique is illustrated in Figure 2. For biosynthesis or *Datura stramonium* extract MgO nanoparticle, few peaks but the longest peaks were observed; the presence of prominent and sharp diffraction peaks positioned at the 2θ values of 30, 32, 35, 37, 48, 56, 64, and 69 corresponding to (211), (110), (111), (200), (100), (210), (220), and (320) planes, respectively, indicated the formation of MgO with bulbous crystalline shape. For chemosynthesis MgO nanoparticles, many peaks were the same except no peak formed at 2theta values of less than 30 and some crystalline impurities were detected that fluctuated the intensities of peaks; this result shows the prepared nanoparticle formation with a spherical (bulbuls) shape. The findings demonstrated that the structure resembled cubic shape in nature. These results agreed with reported works [26, 27]. Debye–Scherrer's formula was used to compute the crystalline size of zinc oxide, as shown in Table 1:

$$D = \frac{0.94\lambda}{\beta \cos\theta}, \quad (1)$$

where D = crystalline size (nm), $K = 0.9$ (Scherrer constant), $\lambda = 0.15406$ nm (wavelength of the X-ray sources), β = FWHM (radians), and θ = peak position (radians).

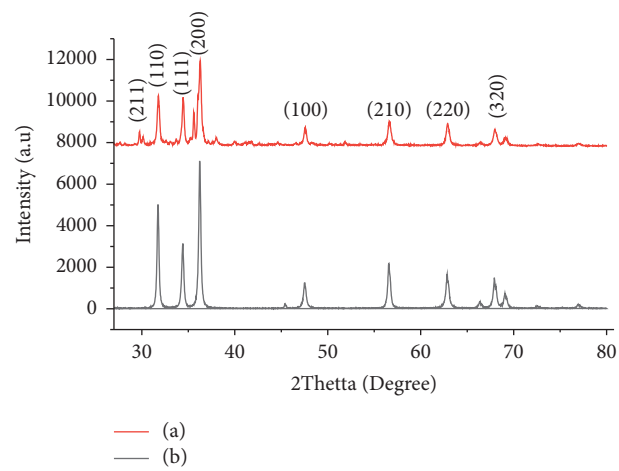

Figure 2: X-ray diffraction pattern of (a) biosynthesized magnesium oxide (MgO) from *Datura stramonium* leaves extract and (b) chemosynthesized nanoparticles.

Table 1: XRD data and calculation of peaks parameters: 2theta, FWMH, and crystalline size (nm).

Sl. no.	2theta (degree)	FWMH (radians)	D (nm)
1	30	6.86465	0.337219
2	32	8.93974	0.295582
3	35	0.87978	0.285169
4	37	1.01812	0.173284
5	48	0.69772	0.148195
6	56	0.62852	0.134706
7	64	0.00513	0.136776
8	69	0.00513	0.13690

The average crystalline size of magnesium oxide nanoparticles was revealed to be 0.17 nm.

3.2. Scanning Electron Microscopy (SEM). An instrument used for the analysis of surface morphology was scanning electron microscope (SEM). A well-established method for investigating the topography, texture, and surface

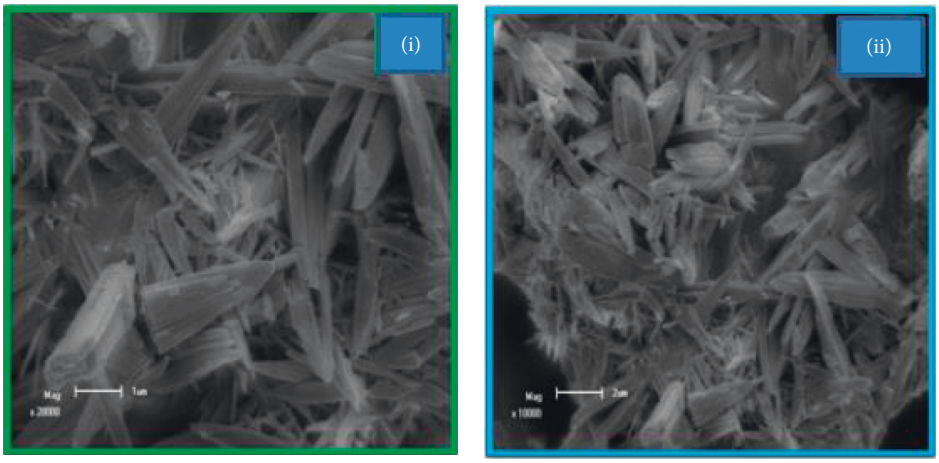

(a) (b)

Figure 3: Scanning electron microscopy of (a) biosynthesized magnesium oxide (MgO) from *Datura stramonium* leaves extract at 20000 magnification and (b) chemosynthesized nanoparticles at 10000 magnification.

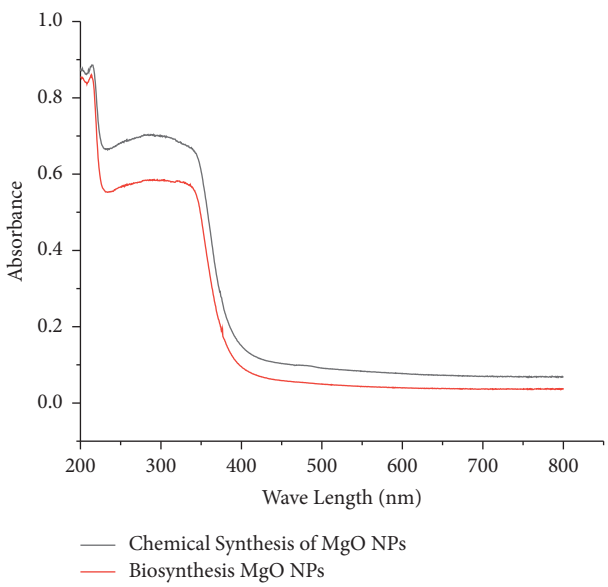

Figure 4: Absorbance measured by UV-Vis of biosynthesized magnesium oxide (MgO) nanoparticles derived from *Datura stramonium* leaves extract.

characteristics of powders has been developed. The scanning electron microscope (SEM) generates a three-dimensional picture of the specimen, which is extremely useful when evaluating the shape and structure of a sample. The SEM images were analyzed, and a topographical analysis was carried out on the basis of the surface study results. The morphology of both biosynthesized and chemosynthesized magnesium oxide nanoparticles was determined by scanning electron microscopy. As shown in Figures 3(a) and 3(b), the SEM micrographs of these materials at different magnification designate a wood cracked-like structure and no agglomeration was found. This shape is relatively spherical or bulbuls; this result is in good agreement with reported works [28–30].

3.3. UV-Visible Spectrophotometer Analysis. UV-visible spectroscopy shows the preoccupation spectroscopy in the ultraviolet-visible phantom area [31]. It customs sunny in the noticeable region and head-to-head near-infrared (NIR) arrays. In this section of the electromagnetic spectrum, molecules experience electronic changeovers. Nanoparticles have convinced optical assets such as sizes, shapes, concentrations, and accumulation state, as well as a refractive index which can be acknowledged with a UV-vis spectrometer. Nanoparticles prepared from certain metals powerfully interrelate with a convinced wavelength of light as well, as their sole optical characters indicate a singularity known as surface plasmon timbre [32, 33]. In the current research, UV-vis is used for both biosynthesized and chemosynthesized magnesium oxide nanoparticles prepared from *Datura stramonium* leaf extracts. Figures 4 and 5 show the absorbance and transmittance spectra of biosynthesized MgO nanoparticles and chemosynthesized MgO nanoparticles between wavelengths of 250 nm to 800 nm, respectively.

Broad peaks were perceived at 325 nm, as shown in Figure 5, for biosynthesized and chemosynthesized ones. As it can be seen, a black line shift occurs because of leaf extracts and chemical grounded variation. Broadening and shift are attributed to agglomeration or an upsurge in the size of the particles [34].

The transmittance spectra which are shown in Figure 5 were evaluated from the absorbance. The outcomes show that the optical transmittance of the MgO nanoparticles prepared by biosynthesis MgO nanoparticle with blue colour is greater than that of chemically prepared MgO nanoparticle with red colour, for wavelength greater than 450 nm. The higher transmittance also indicates a lower defect density of the MgO nanoparticle since absorption of light in the longer wavelength region (>500 nm) is frequently caused by crystalline faults such as grain boundaries and dislocations [35, 36].

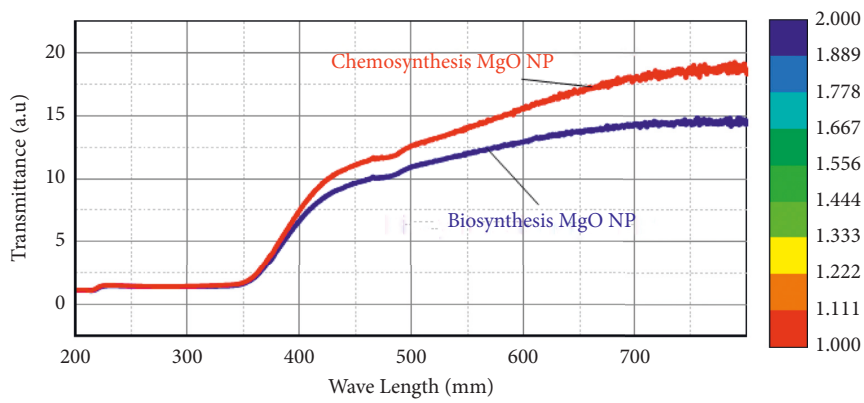

Figure 5: Transmittance measured by UV-Vis of biosynthesized and chemosynthesized magnesium oxide (MgO) nanoparticles derived from *Datura stramonium* leaves extract.

3.4. Photoluminescence (PL) Analysis. The PL continuum of magnesium oxide nanoparticles was chronicled at 37°C through a Xe spotlight as an excitation sunlit foundation at an excitation wavelength of 450 nanometers. Photo-luminescence emanation continuums are portrayed in Figure 6. Fleabags from the valence posse and electrons (e-) from the electronic states composite with each other, and this is accountable for the emanation properties of conversion metals [37]. The recombination of photo-excited electron (e-) and hole (h) sets at the energy situations would persuade the photo-emission [38]. The natural surroundings of the imperfections cause light emanation. Photo-luminescence stretches the evidence around the froths and imperfections in nanoparticles. The defect middles create changed electronic states in the widespread bandgap. The emanation variety shows emission at different techniques because of their different colour centres on the magnesium oxide nanoparticles shown in Figure 6. It is evident from the highest emission spectrum that the magnesium oxide nanoparticles emit at several wavelengths due to the presence of multiple colour centres on the particles. It has risen to the UV-visible region. PL spectra revealed UV (389 nm), violet (390 nm, 391 nm), blue (451 nm), green (455 nm), and orange (462 nm) emissions. The presence of oxygen vacancies in MgO nanoparticles causes them to glow in the ultraviolet (389 nm) area (surface defects). If there is a lot of imperfection, there will also be a lot of strength. Because of the F centres, there has been an increase in green emissions [39, 40].

3.5. Antibacterial Activity Analysis. The antibacterial commotion of biosynthesis and chemosynthesis MgO nanoparticles resulting from *Datura stramonium* (Asaangira) leaves extracts was applied for Gram-negative(G−) *Escherichia coli* and Gram-positive (G+) bacteria *Staphylococcus aureus* and bacillus by tabloid discuss dispersal procedure [41]. Nutrient agar cultures were cast off to develop bacteria.

3.6. Preparation of Inoculums. The bacterial investigation concerns were shifted away from the conventional beliefs represented by the nutrient culture (NC) dishes and also

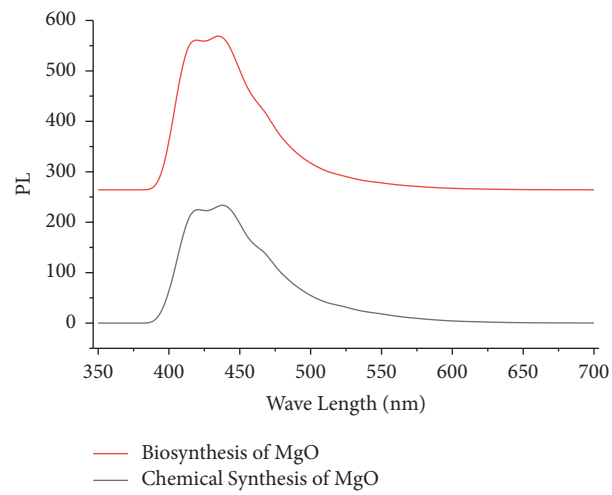

Figure 6: Photoluminescence (PL) spectrum of biosynthesized and chemosynthesized magnesium oxide (MgO) nanoparticles derived from *Datura stramonium* leaves extract.

hatched for a period of forty-eight hours. After that, more discrete bacteriological groups that were not connected were used as inoculums [42]. The bacteriological ring was used to transfer the microorganisms to the autoclaved nutrient culture, which was then moderately whirled while being heated to approximately 500 degrees Celsius in a distilled water bath with a variety of other miscellaneous ingredients. After that, the culture was transferred to sterile Petri plates, where it was given time to coagulate and was also subjected to a biological evaluation.

A new instance was created by marking inoculums from each of the existing media on nutrient agar means in a Petri dish. Aliquots of magnesium oxide were freshly synthesized in the following volumes: 25 μL, 45 μL, 65 μL, 85 μL, and 100 μL. On tabloid discusses, with a radius of 2.5 millimetres, nanoparticles were saturated with the help of a micropipette [39].

3.7. Development Sketch of Bacteria. After that, new groups began occupying the incubation space and were used to research the development of inoculations using

Table 2: Bacterial activities of biosynthesized MgO nanoparticles.

Treatment	Concentration (μg/mL)	Percentage of inhibition
Magnesium oxide nanoparticles	25	17.16 ± 1.02
	45	25.12 ± 1.30
	65	26.43 ± 1.23
	85	38.46 ± 1.32
	100	58.67 ± 1.09

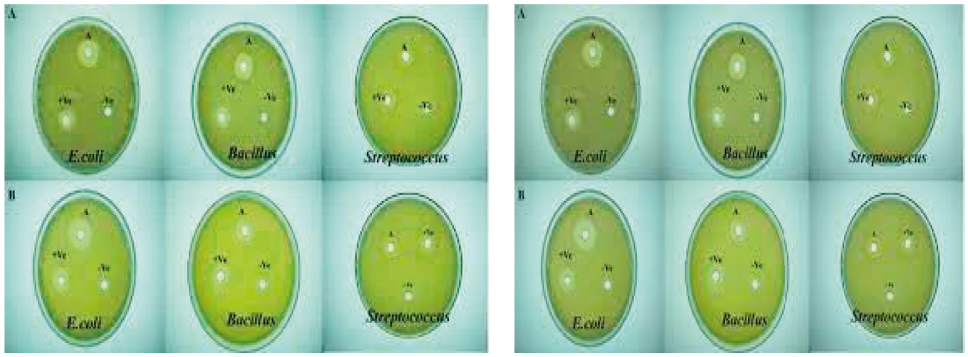

(a) (b)

Figure 7: (a, b) Antibacterial activity of biosynthesized and chemosynthesized MgO nanoparticles derived from *Datura stramonium* (Asaangira), respectively.

Table 3: Bacterial activities of chemosynthesized MgO nanoparticles.

Treatment	Concentration (μg/mL)	Percentage of inhibition
Magnesium oxide nanoparticles	25	14.23 ± 1.12
	45	18.14 ± 1.25
	65	19.43 ± 1.00
	85	28.24 ± 1.14
	100	38.54 ± 1.05

microorganisms. We made sure the media potage solution was checked for turbidity, and we kept the OD (optical density) at 500 nm between 0.08% and 0.10% throughout the process.

3.8. Preparation of Media Culture. Both nutrient culture agar, as well as nutrient potage, was used as components of the development media that were investigated in this study. The nutrient agar was sterilised for the purpose of pasteurisation by being subjected to 15 Ibs pressure at 120°C for 20 minutes and then maintaining at 37°C.

3.9. Evaluation of Antibacterial Properties. Before the investigation, the plates were sterilised in an autoclave and dehydrated in a dry furnace overall. Kirby–Bauer's discussion of a dissemination method that uses the postponement of microorganisms feasting on nutrient culture agar provides evidence that antibacterial negotiator has the potential to estrange the microbial cell [43]. Bacterial activities of biosynthesized MgO nanoparticles are listed in Table 2. The examinations were done for both biosynthesized MgO and chemosynthesized MgO NPs set for an outstanding result. Utilizing two different methods produces the same outcome for all of the bacterial types that were tested. So, under the right conditions and in the right environment, eco-friendly biosynthesis is safe and promises antibacterial activity. After vaccination, the plates were kept in an incubator at a temperature of 30 degrees Celsius for a period of 48 hours. The antibacterial action was achieved by measuring the embarrassment zone. The antibacterial bustle of genuine MgO Nanoparticles was powerful by the Kirby–Bauer disc dispersal methodology, which is demonstrated in Figures 7(a) and 7(b). Bacterial activities of chemosynthesized MgO nanoparticles are listed in Table 3.

As it is seen from Tables 2 and 3 concerning Figures 7(a) and 7(b), the antibacterial activities (*E. coli*, bacillus, and *Streptococcus*) are analyzed. The biosynthesized MgO nanoparticle shows a high inhibition zone, which is promising for antibacterial applications. The result also agrees with reports [44, 45].

4. Conclusion

The biosynthesis and chemosynthesis of MgO nanoparticles were studied in an aqueous medium using *Datura stramonium* leaves extract for biosynthesis. The prepared biosynthesized nanoparticles of magnesium oxide are

established by colour variations, and it has been tested by XRD, SEM, PL, UV-Vis, and antibacterial activity. Its size, approximately 0.17 nm, was definitely by X-ray diffraction analysis. The different peaks confirm the presence of different functional groups and bonding. SEM shows that the biosynthesized nanoparticles had rod-like structure, PL analysis reveals that the prepared material was crystalline, and it has strong peaks at a higher wavelength for the biosynthesis of MgO nanoparticles derived from *Datura stramonium* , and UV-Vis also confirmed this output. The antibacterial activity shows that the biosynthesized nanoparticles show the bacterial activity against Gram-negative *Escherichia coli* and Gram-positive bacteria *Staphylococcus aureus* and bacillus by the paper disc diffusion method and show a good zone of inhibition. Both techniques are promising for the preparations of MgO nanoparticles in antibacterial activity and show the same result. This outcome demonstrates that the biosynthesized nanoparticles originate from having some medicinal uses and are biodegradable.

Data Availability

The data used to support the findings of this study are included within the article.

Disclosure

This study was performed as a part of the employment of the authors (Dambi Dollo University, Ethiopia).

Conflicts of Interest

The authors declare that they have no conflicts of interest.

References

[1] E. F. El-Belely, M. M. S. Farag, H. A. Said et al., "Green synthesis of zinc oxide nanoparticles (ZnO-NPs) using Arthrospira platensis (Class: cyanophyceae) and evaluation of their biomedical activities," *Nanomaterials*, vol. 11, no. 1, p. 95, 2021.

[2] T. Gur, I. Meydan, H. Seckin, M. Bekmezci, and F. Sen, "Green synthesis, characterization and bioactivity of biogenic zinc oxide nanoparticles," *Environmental Research*, vol. 204, Article ID 111897, 2022.

[3] K. V. Karthik, A. V. Raghu, K. R. Reddy et al., "Green synthesis of Cu-doped ZnO nanoparticles and its application for the photocatalytic degradation of hazardous organic pollutants," *Chemosphere*, vol. 287, Article ID 132081, 2022.

[4] H. Sadiq, F. Sher, S. Sehar et al., "Green synthesis of ZnO nanoparticles from Syzygium Cumini leaves extract with robust photocatalysis applications," *Journal of Molecular Liquids*, vol. 335, Article ID 116567, 2021.

[5] A. Jayachandran, T. R. Aswathy, and A. S. Nair, "Green synthesis and characterization of zinc oxide nanoparticles using Cayratia pedata leaf extract," *Biochemistry and Biophysics Reports*, vol. 26, Article ID 100995, 2021.

[6] K. Hamidian, M. Sarani, E. Sheikhi, and M. Khatami, "Cytotoxicity evaluation of green synthesized ZnO and Ag-doped ZnO nanoparticles on brain glioblastoma cells," *Journal of Molecular Structure*, vol. 1251, Article ID 131962, 2022.

[7] M. Rafique, R. Tahir, S. S. A. Gillani et al., "Plant-mediated green synthesis of zinc oxide nanoparticles from Syzygium Cumini for seed germination and wastewater purification," *International Journal of Environmental Analytical Chemistry*, vol. 102, no. 1, pp. 23–38, 2022.

[8] H. S. Lalithamba, M. Raghavendra, K. Uma, K. V. Yatish, D. Mousumi, and G. Nagendra, "Capsicum annuum fruit extract: a novel reducing agent for the green synthesis of ZnO nanoparticles and their multifunctional applications," *Acta Chimica Slovenica*, vol. 65, no. 2, pp. 354–364, 2018.

[9] S. Umavathi, S. Mahboob, M. Govindarajan et al., "Green synthesis of ZnO nanoparticles for antimicrobial and vegetative growth applications: a novel approach for advancing efficient high quality health care to human wellbeing," *Saudi Journal of Biological Sciences*, vol. 28, no. 3, pp. 1808–1815, 2021.

[10] M. Ahamed, M. Javed Akhtar, M. Majeed Khan, and H. A. Alhadlaq, "Facile green synthesis of ZnO-RGO nanocomposites with enhanced anticancer efficacy," *Methods*, vol. 199, pp. 28–36, 2022.

[11] P. Ramesh, K. Saravanan, P. Manogar, J. Johnson, E. Vinoth, and M. Mayakannan, "Green synthesis and characterization of biocompatible zinc oxide nanoparticles and evaluation of its antibacterial potential," *Sensing and Bio-Sensing Research*, vol. 31, Article ID 100399, 2021.

[12] S. Rajendrachari, P. Taslimi, A. C. Karaoglanli, O. Uzun, E. Alp, and G. K. Jayaprakash, "Photocatalytic degradation of Rhodamine B (RhB) dye in waste water and enzymatic inhibition study using cauliflower shaped ZnO nanoparticles synthesized by a novel One-pot green synthesis method," *Arabian Journal of Chemistry*, vol. 14, no. 6, Article ID 103180, 2021.

[13] N. Bhattacharjee, I. Som, R. Saha, and S. Mondal, "A critical review on novel eco-friendly green approach to synthesize zinc oxide nanoparticles for photocatalytic degradation of water pollutants," *International Journal of Environmental Analytical Chemistry*, vol. 2022, Article ID 2022130, 28 pages, 2022.

[14] A. Nagar, A. Kumar, U. Tyagi et al., "Ultrafast, trace-level detection of NH3 gas at room temperature using hexagonal-shaped ZnO nanoparticles grown by novel green synthesis technique," *Physica B: Condensed Matter*, vol. 626, Article ID 413595, 2022.

[15] S. Khoso, S. Mehar, I. Anam et al., "Green synthesis of zno nanoparticles from foeniculum vulgare, its characterization and biological potential against bacteria," *Journal of Animal & Plant Sciences*, vol. 32, no. 1, pp. 229–237, 2022.

[16] M. Golmohammadi, M. Honarmand, and A. Esmaeili, "Biosynthesis of ZnO nanoparticles supported on bentonite and the evaluation of its photocatalytic activity," *Materials Research Bulletin*, vol. 149, Article ID 111714, 2022.

[17] L. Regni, D. Del Buono, M. Micheli, S. L. Facchin, C. Tolisano, and P. Proietti, "Effects of biogenic ZnO nanoparticles on growth, physiological, biochemical traits and antioxidants on olive tree in vitro," *Horticulturae*, vol. 8, no. 2, p. 161, 2022.

[18] M. Murugan, K. B. Rani, J. A. Wins et al., "Green synthesized ZnO NPs as effective bacterial inhibitor against isolated MDRs and biofilm producing bacteria isolated from urinary tract infections," *Journal of King Saud University Science*, vol. 34, no. 1, Article ID 101737, 2022.

[19] S. Hayat, A. Ashraf, M. Zubair et al., "Biofabrication of ZnO nanoparticles using Acacia arabica leaf extract and their antibiofilm and antioxidant potential against foodborne

pathogens," *PLoS One*, vol. 17, no. 1, Article ID e0259190, 2022.

[20] H. Subramanian, M. Krishnan, and A. Mahalingam, "Photocatalytic dye degradation and photoexcited antimicrobial activities of green zinc oxide nanoparticles synthesized via Sargassum muticum extracts," *RSC Advances*, vol. 12, no. 2, pp. 985–997, 2022.

[21] G. A. Otunola, A. J. Afolayan, E. O. Ajayi, and S. W. Odeyemi, "Characterization, antibacterial and antioxidant properties of silver nanoparticles synthesized from aqueous extracts of Allium sativum, Zingiber officinale, and Capsicum frutescens," *Pharmacognosy Magazine*, vol. 13, no. 50, p. S201, 2017.

[22] S. Al-Musawi, S. Albukhaty, H. Al-Karagoly et al., "Antibacterial activity of honey/chitosan nanofibers loaded with capsaicin and gold nanoparticles for wound dressing," *Molecules*, vol. 25, no. 20, p. 4770, 2020.

[23] J. S. Jayan, A. S. Sethulekshmi, and G. Venu, "Appukuttan Saritha and Kuruvilla Joseph 2 1Department of Chemistry, School of Arts and Sciences, Amrita Vishwa vidyapeetham, amritapuri, kollam, India, 2Department of chemistry, Indian Institute of Space Science and Technology, Valiyamala, India," *Antimicrobial Textiles from Natural Resources*, vol. 8, p. 619, 2021.

[24] B. S. Panda, M. A. Ahemad, and L. N. Mishra, "Green Synthesized Nanoparticles & an Approach towards Antibacterial & Antimicrobial Activities: A Review," *International Journal of ChemTech Research*, vol. 14, no. 1, pp. 16–41, 2021.

[25] N. Raura, A. Garg, A. Arora, and M. Roma, "Nanoparticle technology and its implications in endodontics: a review," *Biomaterials Research*, vol. 24, no. 1, pp. 21–28, 2020.

[26] A. Amir, S. Bibi, A. Nawaz et al., "In Vitro Antibacterial Response of ZnO-MgO Nanocomposites at Various Compositions," *International Journal of Applied Ceramic Technology*, vol. 18, no. 5, pp. 1417–1429, 2021.

[27] H. Beyzaei, M. Mirzaei, N. H. Fakhrabadi, and B. Ghasemi, "Synergistic effects of dual antimicrobial combinations of synthesized N-heterocycles or MgO nanoparticles with nisin against the growth of Aspergillus fumigatus: in vitro study," *Veterinary Research Forum*, vol. 12, no. 2, pp. 241–246, 2021.

[28] H. Bardania, R. Mahmoudi, H. Bagheri et al., "Facile preparation of a novel biogenic silver-loaded Nanofilm with intrinsic antibacterial and oxidant scavenging activities for wound healing," *Scientific Reports*, vol. 10, no. 1, pp. 6129–6214, 2020.

[29] Y. M. Jawad and M. F. H. Al-Kadhemy, "Enhancement optical properties of CMC/PAA polymer blend by MgO, SiO2 and bacteriocin for antimicrobial packaging application," *Journal of Global Scientific Research (ISSN: 2523-9376)*, vol. 6, no. 9, pp. 1715–1725, 2021.

[30] B. R. Mohammad, A. Algburi, and Z. M. Alzubaidy, "Antibacterial Activity of CuO and MgO nanoparticles in combination with levofloxacin against multidrug resistant escherichia coli causing urinary tract infections," *Journal of Research in Ecology*, vol. 8, no. 1, pp. 2654–2663, 2020.

[31] R. A. Ulwali, N. K. Abass, M. D. Majed, and H. A. Alwally, "Green synthesis of MgO NPs by olea europeae leaves extract from bulk MgO and study physical properties," *Neuro-Quantology*, vol. 19, no. 5, pp. 114–119, 2021.

[32] S. K. R. Namasivayam, D. Shyamsundar, M. M. Prabanch, R. A. Bharani, and G. P. Avinash, "Inhibitory Potential of Molecular Mechanism of Pathogenesis with Special Reference to Biofilm Inhibition by Chemogenic Zinc Oxide Nanoparticles," *Letters in Applied NanoBioScience*, vol. 10, no. 1, pp. 1862–1870, 2020.

[33] S. Mazraedoost and G. Behbudi, "Basic Nano magnetic particles and essential oils: biological applications," *Journal of Environmental Treatment Techniques*, vol. 9, no. 3, pp. 609–620, 2021.

[34] R. Supreetha, S. Bindya, P. Deepika, H. M. Vinusha, and B. P. Hema, "Characterization and biological activities of synthesized citrus pectin-MgO nanocomposite," *Results in Chemistry*, vol. 3, Article ID 100156, 2021.

[35] P. N. H. Diem, T. N. M. Phuong, N. Q. Hien, D. T. Quang, T. T. Hoa, and N. D. Cuong, "Silver, gold, and silver-gold bimetallic nanoparticle-decorated dextran: facile synthesis and versatile tunability on the antimicrobial activity," *Journal of Nanomaterials*, vol. 202011 pages, Article ID 7195048, 2020.

[36] Z. Jannah, L. Rohmawati, and W. Setyarsih, "Synthesis and Characterization of Nanoparticles CaCO3/MgO as Antibacterial," in *Proceedings of the 7th Mathematics, Science, and Computer Science Education International Seminar, MSCEIS 2019*, Bandung, Indonesia, October 2019.

[37] P. Dandapat, "Studies on biologically synthesized nanoparticles; their antibacterial, antifungal & anticancer activities and applications in nano-medicine," *International Journal of Advanced Multidisciplinary Scientific Research*, vol. 3, no. 12, pp. 50–62, 2020.

[38] S. Sharmin, M. M. Rahaman, C. Sarkar, O. Atolani, M. T. Islam, and O. S. Adeyemi, "Nanoparticles as antimicrobial and antiviral agents: a literature-based perspective study," *Heliyon*, vol. 7, no. 3, Article ID e06456, 2021.

[39] A. Kumar, A. Choudhary, H. Kaur, S. Mehta, and A. Husen, "Metal-based nanoparticles, sensors, and their multifaceted application in food packaging," *Journal of Nanobiotechnology*, vol. 19, no. 1, pp. 256–325, 2021.

[40] N. Baniasadi, A. Kariminik, and S. M. R. Khoshroo, "Synthesis and study of bactericidal effects of iron oxide nanoparticles on bacteria isolated from urinary tract infections," *Avicenna Journal of Clinical Medicine*, vol. 27, no. 1, pp. 37–44, 2020.

[41] S. Patil and R. Chandrasekaran, "Biogenic nanoparticles: a comprehensive perspective in synthesis, characterization, application and its challenges," *Journal of Genetic Engineering and Biotechnology*, vol. 18, no. 1, pp. 67–23, 2020.

[42] M. Sheikhpour, M. Arabi, A. Kasaeian, A. Rokn Rabei, and Z. Taherian, "Role of nanofluids in drug delivery and biomedical technology: methods and applications," *Nanotechnology, Science and Applications*, vol. 13, pp. 47–59, 2020.

[43] W. Ahmad and D. Kalra, "Green synthesis, characterization and anti microbial activities of ZnO nanoparticles using Euphorbia hirta leaf extract," *Journal of King Saud University Science*, vol. 32, no. 4, pp. 2358–2364, 2020.

[44] M. S. Saif, A. Zafar, M. Waqas et al., "Phyto-reflexive zinc oxide nano-flowers synthesis: an advanced photocatalytic degradation and infectious therapy," *Journal of Materials Research and Technology*, vol. 13, pp. 2375–2391, 2021.

[45] M. I. Rahmah, N. M. Saadoon, A. J. Mohasen, R. I. Kamel, T. A. Fayad, and N. M. Ibrahim, "Double hydrothermal synthesis of iron oxide/silver oxide nanocomposites with antibacterial activity," *Journal of the Mechanical Behavior of Materials*, vol. 30, no. 1, pp. 207–212, 2021.

Hindawi
Advances in Materials Science and Engineering
Volume 2022, Article ID 1399618, 8 pages
https://doi.org/10.1155/2022/1399618

Research Article

Impact of AlN-SiC Nanoparticle Reinforcement on the Mechanical Behavior of Al 6061-Based Hybrid Composite Developed by the Stir Casting Route

S. Kaliappan,[1] A. Shanmugam,[2] Pradeep Johnson,[3] M. Karthick,[4] S. Sekar,[5] Pravin P. Patil,[6] M. K. S. Sai,[7] K. P. Yuvaraj,[8] and Venkatesan Govindaraajan[9]

[1]*Department of Mechanical Engineering, Velammal Institute of Technology, Chennai 601204, Tamil Nadu, India*
[2]*Mechanical Engineering, SAMS College of Engineering and Technology, Chennai, Tamil Nadu, India*
[3]*Department of Mechatronics Engineering, Hindustan College of Engineering and Technology, Coimbatore, India*
[4]*Department of Mechanical Engineering, Velammal Engineering College, Velammal New-Gen Park, Ambattur-Redhills Road, Chennai 600066, Tamil Nadu, India*
[5]*Department of Mechanical Engineering, Rajalakshmi Engineering College, Rajalakshmi Nagar Thandalam, Chennai 602105, Tamil Nadu, India*
[6]*Department of Mechanical Engineering, Graphic Era Deemed to be University, Bell Road, Clement Town, Dehradun 248002, Uttarakhand, India*
[7]*Department of Mechanical Engineering, Vignana Bharathi Institute of Technology, Hyderabad, Telangana, India*
[8]*Department of Mechanical Engineering, Sri Krishna College of Engineering and Technology, Coimbatore, Tamil Nadu, India*
[9]*Department of Mechanical Engineering, Haramaya Institute of Technology, Haramaya University, Dire Dawa, Ethiopia*

Correspondence should be addressed to Venkatesan Govindaraajan; venkatesanggg2011@gmail.com

Received 11 June 2022; Revised 11 July 2022; Accepted 20 July 2022; Published 25 August 2022

Academic Editor: Pudhupalayam Muthukutti Gopal

The enhancement of composites' mechanical characteristics (tensile, compressive, and hardness) is a constant demand for technological advancement. The stir casting process is used to make the hybrid aluminium alloy metal matrix composites Al 6061-SiC-AlN in our present study. To create mechanical qualities such as tensile, compressive, and hardness, silicon carbide and aluminium nitride (both 3% and 6%) were utilized as the reinforcement. The tensile strength, compressive strength, and hardness of the Al 6061-SiC-AlN hybrid composites samples were determined. The tensile, compressive, and hardness parameters of Al 6061-SiC-AlN hybrid composites are estimated and evaluated to those of the matrix Al 6061 alloy. With the inclusion of silicon carbide and AlN nanoparticles, the tensile strength, compressive strength, and hardness increased from 328 to 385 MPa, 145 to 178 Mpa, and 302 to 724 VHN, respectively.

1. Introduction

Aluminum and alloy hybrid nanocomposites (AAHNCs) are industrialized materials with desirable properties including strong tensile, compressive, hardness, and stiffness. In comparison to unreinforced alloys, these materials have a higher abrasion resistance. These materials are used in a variety of structural applications in a variety of sectors, including marine, aircraft, and automobiles [1, 2]. Rail coaches, towers, pylons, military and commercial bridges, aerospace applications, shipbuilding operations rivets, truck frames, and transportation are just a few of the heavy-duty structural uses for aluminium alloy 6061 [3]. Al 6061 is the repeatedly utilized matrix material owing to its low density and electrical resistance, high and good strength, superior corrosion resistance, and greater machinability [4].

Aluminium oxide (Al2O3), tungsten carbide (WC), titanium diboride (TiB2), silicon carbide (SiC), zirconium

boride (ZrB2), titanium carbide (TiC), and boron carbide (B4C) are commonly utilized as nanoscale reinforcements in aluminium hybrid composites to improve mechanical properties like tensile, compressive, and hardness [5]. The current investigation used two reinforcements, one is SiC and another one AlN. Silicon carbide nanoparticles are possible a nano reinforcement for aluminium alloy 6061 matrix owing to its high hardness, low density, high wear, impact resistance, high melting point, and good chemical and thermal stability [6]. Aluminium alloy 6061 composites containing silicon carbide nanoparticles have improved toughness, machinability, and self-lubricating properties [7].

AlN is a high-hardness refractory compound with excellent corrosion and wear resistance, a low coefficient of thermal expansion, and high electrical resistivity. It has a wide range of applications in electrical and semiconductor devices, as well as corrosive and molten metal handling [8]. In recent years, the tribological and mechanical properties of nanoparticles and fiber-reinforced Al 6061 composites are greatly enhanced. Sun et al. investigated Al1060/Al6061-0.5SiC/Al1060 laminates with a hot roll bonding process and heat treatment. After heat treatment, the Goss and *R* components dominated the texture of the Al6061-0.5SiC composite. The tensile strength of the as-rolled laminates increased as the rolling reduction was lowered, but the elongation first increased and then decreased [9]. Using the powder metallurgy approach and the effect of SiC clusters, Mulugundam Siva Surya developed Al6061/SiC composites with high interfacial bonding between Al6061/SiC composites. It was discovered that diffusion-controlled grain formation had a detrimental influence on mechanical characteristics and resulted in improved features [10]. For the aerospace sector, Ishfaq et al. specified the Al6061-7.5% SiC composite. Although the SiC reinforcement in the Al-substrate greatly improves mechanical properties, it makes difficulties machining as the Al6061-7.5% SiC composite allows outstanding hardness and strength [11]. Halil et al. explored and improved the mechanical characteristics of Al6061-SiC-B4C hybrid composites made via powder metallurgy extrusion. Wear resistance, tensile strength, transverse rupture strength, hardness, and density of the Al6061-SiC-B4C hybrid composites were evaluated. Al6061-SiC-B4C hybrid composites with SiC particle reinforcement had the highest tensile strength [12]. Bhat and Kakandikar customized the Al6061-5% SiC-50 mm sized composite by the stir casting process and investigated hardness and wear characteristics of the new composite. The output of the new composite was obtained with a lower wear rate and superior hardness [13]. Veeresh Kumar et al. used particulate SiC with the Al6061 composite prepared by the liquid metallurgy route. The particulate SIC used in Al6061 enhanced the mechanical and tribological properties. Especially hardness, ultimate tensile strength, wear resistance, and density of the composites augment with the augmented SiC content [14].

The aluminium matrix with aluminium nitride particle composites is frequently employed in electrical and electronics equipment. Chemically, aluminium nitride is more stable than SiC, however, it has a poorer thermal conductivity. Aluminum does not react with aluminium nitride [15], but when Al interacts with SiC in Al–SiC composites, the Al4C3 phase forms, which affects the tensile, compression, and hardness properties of the aluminium silicon carbide composite [16, 17]. AlN has an excellent combination with aluminium alloys, outstanding heat treatment and physical properties, high thermal conductivity, high specific strength and stiffness, high electrical resistivity, low dielectric constant, a tailorable coefficient of thermal expansion [15]. As a result, the Al–AlNp composite is a fantastic material for electronic packaging [18, 19]. Ashok Kumar and Murugan developed the Al6061 (T6)-AlNp composite by the stir casting process and improved wettability, ultimate tensile strength, yield strength, microhardness, and macrohardness [20]. SiCp/Al composites were created by Xie et al., who also studied how the phase composition, densification behaviour, and mechanical characteristics of the composites were related. The findings showed that raising the laser power density improved the density, microhardness, and friction resistance of the SLM produced SiCp/Al composites. This improvement may be attributed to the higher molten pool temperature at higher laser power densities [21].

In generally aluminium alloy hybrid composites are prepared by stir casting [22, 23], squeeze casting [24, 25] and powder metallurgy [26, 27]. Stir casting has a number of advantages, including being trouble-free, supple, and affordable, as well as producing multifunctional, bulk-manufacturing, and contour composite components that are free of dangerous reinforcing particles. Due to these distinguishing characteristics of the stir casting technique, a slew of new efforts has been made to create a variety of composites using this method [28, 29]. The tensile, compression, and hardness properties of the stir cast Al-SiC-AlN hybrid composites with varied reinforcements have received only a cursory examination. This paper describes the mechanical properties of an Al-SiC-AlN hybrid composite made in a static ambiance utilizing a stir casting process.

2. Experimental Work

2.1. Materials. Nice Chemicals Limited, Telangana, India, provided the aluminium 6061 matrix alloy, and the reinforcements of aluminium nitride (50 nm) and silicon carbide (50 nm) nanoparticles used in this work. The SEM morphology of aluminium 6061, aluminium, and nitride silicon carbide powders is shown in Figures 1(a)–1(c). The chemical composition and mechanical characteristics of the matrix (Al6061 alloy) and reinforcements are shown in Tables 1 and 2. (AlN & SiC).

The distribution of aluminium nitride, silicon carbide, and aluminium 6061 matrix alloy is studied morphologically using a scanning electron microscope because this, in a sequence, resolves significantly to affect the mechanical characteristics of the composites and determination and also to verify their effective manufacturing. Aluminium nitride and silicon carbide nanoparticles have a stone-like shape and are 50 nm in size. The distribution of reinforcement and the matrix alloy is in uniform distribution. The distribution of aluminium nitride and silicon carbide in the aluminum 6061

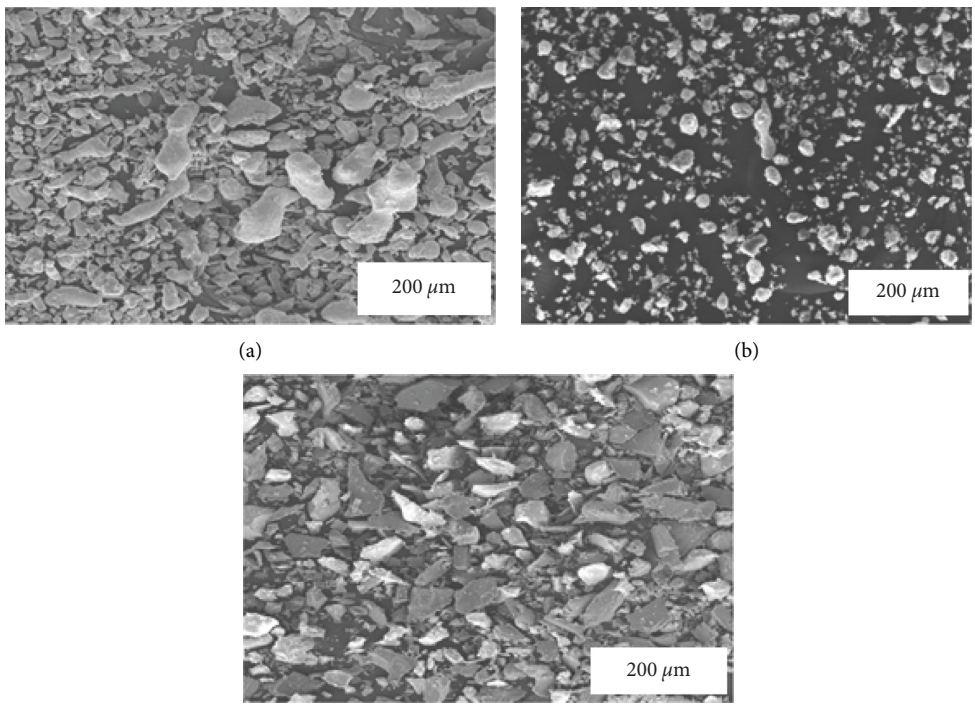

(a) (b) (c)

Figure 1: SEM morphology of (a) Al 6061, (b) AlN, (c) SiC.

Table 1: Chemical composition of the matrix (Al6061 alloy) [7, 9, 13].

Elements	Mg	Si	Fe	Mn	Cu	Cr	Zn	Ni	Ti	Al
Wt (%)	0.85	0.65	0.26	0.22	0.20	0.04	0.06	0.02	0.01	Balance

Table 2: Mechanical properties of the matrix (Al6061 alloy) and reinforcements (AlN & SiC) [3, 10, 20].

Properties	Ultimate tensile strength (Mpa)	Hardness (HRB)	Melting temperature (°C)	Modulus of elasticity (GPa)	Density (g/cm^3)
Al6061 alloy	320	80	650	70	2.7
AlN	270	1100	2,200	310	3.26
SiC	250	2800	2730	410	2.52

matrix alloy, which determines the substantial impact on the composites, and in addition, substantiate the victorious fabrication of composites.

2.2. Composite Preparations. The matrix AA6061 aluminium alloy was melted in a graphite clay crucible in a stir casting furnace and heated to a temperature of around 750°C. The nano particles of aluminium nitride (AlN) and silicon carbide (SiC), with a particle size of 50 nm were chosen as the reinforcement. The molten AA6061 was continually agitated at 500 rev/min to integrate the known amounts of preheated AlN and SiC filler components. The Al-AlN-SiC molten mixture was put into cast iron moulds when the procedure was completed. Castings were made using the Al 6061 alloy, with AlN and SiC filler percentages of 3% and 6%, respectively. Figure 2 shows experimental illustrations of a stir casting setup. The fashioned hybrid composites were cut and prepared into the desired forms. To prepare samples for FESEM and mechanical testing, they were machined. The prepared samples were polished and etched with Keller's reagent using normal metallographic procedures.

The casted samples, one matrix Al 6061 alloy sample, and two other samples with different wt. % SiC-AlN nano reinforcements were utilized to construct test specimens for tensile, compression, hardness, and FESEM examination analysis, and their dimensions are shown in Table 3.

3. Result and Discussion

3.1. Tensile Test. The tensile test was performed in accordance with the ASTM–E8 standard, using the tensile test. The digital tensometer setup is depicted in Figure 3. The specimen dimension was 14 mm diameter and 10 mm length as shown in Figure 4. The tensile test experiments were performed at the atmospheric temperature. The readings of Al 6061 alloy, 3% Al 6061-SiC-AlN hybrid composites, and 6% Al 6061-SiC-AlN hybrid composites sample were taken. The difference in tensile strength with an increase in SiC/AlN microparticle entitlement is shown in Figure 5. The

Figure 2: Experimental setup of the stir casting process.

Table 3: ASTM for tensile, compression, hardness, and FESEM.

S.No	ASTM	Test	Dimensions (in mm)
1	ASTM E8	Tensile test	Dia 14 × length 100
2	ASTM E9	Compression test	Dia 14 × length 20
3	ASTM: E384-10	Hardness test	Dia 14 × length 10
4	ASTM E3-11	FESEM	Dia 14 × length 10

Figure 3: Tensile test-digital tensometer setup.

tensile strength of the Al 6061-SiC-ALN hybrid composite material augments by a quantity of 90% as the substance of SiC/AlN nano particulates augment from 3 to 6 wt%. The SiC/AlN nano particulates reinforcement arrangement and properties regulate the mechanical characteristics of hybrid composites, resulting in a highly strong interface that transfers and relocates stress from the Al 6061 matrix to the SiC/AlN microparticle reinforcement, exhibiting improved strength and elastic modulus [30]. The elastic modulus, tensile strength, and fatigue strength of Al 6061-SiC-AlN

Figure 4: Tensile specimen.

hybrid composites reinforced by SiC/AlN nanoparticles are all greater than monolithic alloys [31]. By raising the volume proportion of the nano phase and lowering the size of the nano reinforcement at the price of concentrated ductility, the strength of SiC/AlN nanoparticles reinforced Al 6061-SiC-AlN hybrid composites is improved [32].

3.2. Compression Test. The compression test specimen samples were produced according to ASTM E9, as stated in Table 3. The compression testing machine was used to test the samples, as illustrated in Figure 6. It depicts the effects of varying compression strength with a weight percent of reinforcements. An Al 6061 alloy sample has a compressive strength of 145 MPa. The Al 6061-SiC-AlN hybrid composites sample with 3 percent SiC-AlN reinforcement and 6 percent SiC-AlN reinforcement has compressive strengths of 165 MPa and 178 MPa, respectively (Figure 7). When contrasted to the original matrix of the Al 6061 alloy, the organized Al 6061-SiC-AlN hybrid sample demonstrates an increase in compressive strength. This indicates that the aluminum ductile character has been gradually giving way to brittleness. This transformation was made possible through the absorption of hard nanoparticles into the soft and ductile aluminium metal matrix [33, 34].

3.3. Hardness. The microhardness of complicated samples of the Al 6061 alloy and its Al 6061-SiC-AlN hybrid composites (Figure 8) was examined using an ASTM-approved standard testing approach. The hardness of the Al 6061-SiC-AlN hybrid composites was determined using a Vickers microhardness tester in accordance with ASTM: E384-10. A weight of 1 kgf was applied on all of the samples for 15 seconds. The test was carried out at three different locations to avoid the indenter resting on the hard reinforcement particles. All ten measurements' averages were computed and reported. Figure 9 displays the hardness value in relation to the weight percent of nano reinforcements and summarizes the findings of the hardness tests.

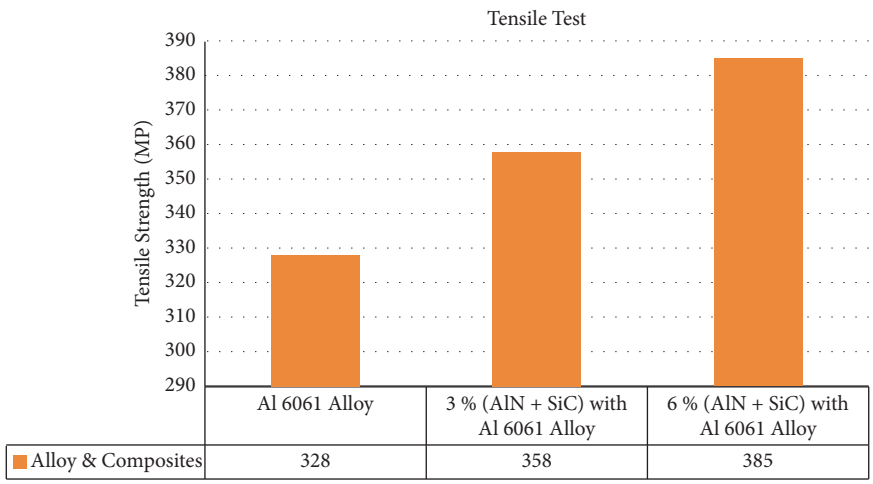

Figure 5: Tensile strength of the Al 6061 alloy and Al 6061 alloy-SiC-AlN hybrid composites.

Figure 6: Compression specimen.

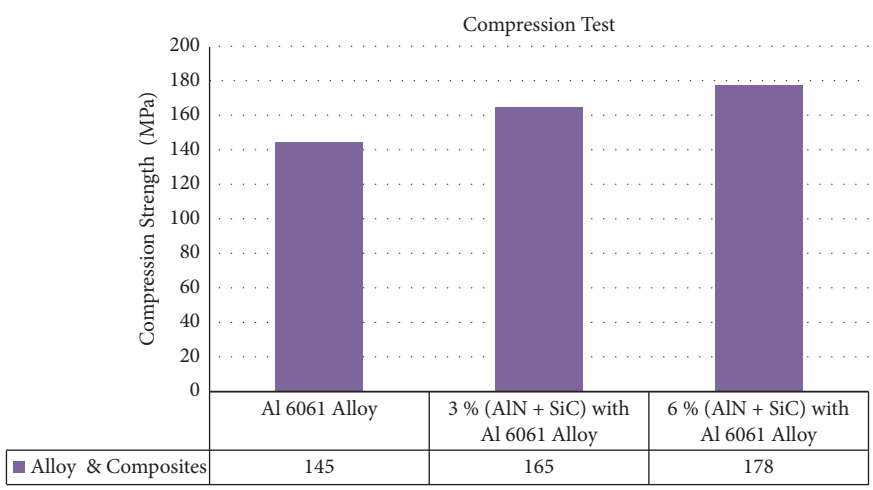

Figure 7: Compression test results.

In comparison to the Al 6061 matrix material, the hardness of composite specimen-2 was found to be higher than that of the Al 6061 matrix material. This might be due to a lack of nano reinforcement dispersion mixed with extra porosity. When compared to other test specimens, the hardness of composite specimen-3 was found to be larger than that of the matrix Al 6061 alloy[35], with a maximum hardness of 724 VHN. This might be due to the Al 6061 matrix material having the fewest holes and shrinkage cavities, as well as a better distribution of nano reinforcements. As a result, combining a hybrid composite of the Al 6061 alloy reinforced with 6% SiC-AlN proved to be the most effective way to achieve maximal hardness.

3.4. Fractured Surface Analysis. A FESEM is an electron microscope that uses a focused stream of electrons to create images of a substance. Electrons react with atoms in the

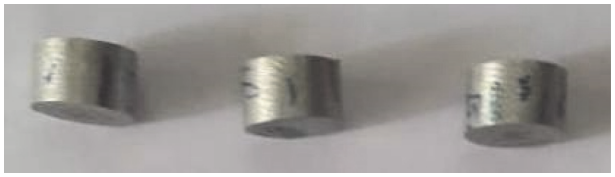

Figure 8: Hardness test specimen.

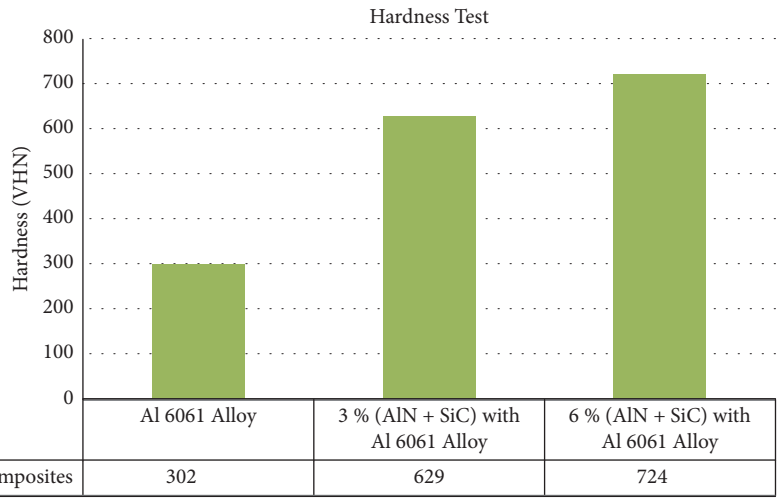

Figure 9: Hardness test results.

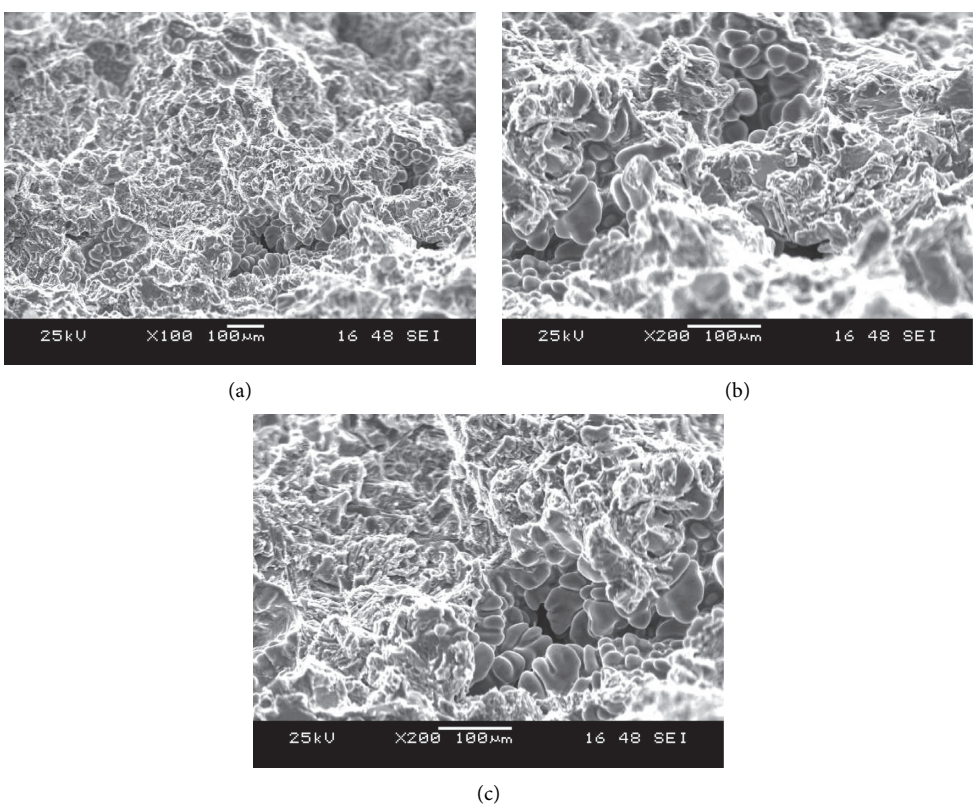

Figure 10: (a–c) FESEM of alloy and composites. (a) Al 6061 alloy; (b) 3% (AlN + SiC) with Al 6061 alloy; (c) 6% (AlN + SiC) with the Al 6061 alloy.

sample to produce a variety of signals that convey information about the sample's topography and composition. To create the image, the electron beam is scanned in a raster scan pattern and the location of the beam is combined with the signal received. FESEM has a resolution of over 1.5 nanometers.

Figure 10 shows the FESEM pictures of the aluminium composite. It is plain to see that the fracture is ductile. The grains are easily visible, and they are evenly scattered. As a result of this finding, it may be deduced that the fracture begins at the corroded area mentioned in the optical micrograph. The ductility of the material is marginally reduced as the amount of boron carbide increases, resulting in a considerable rise in hardness.

The dispersion of particles throughout the matrix was found to be very homogeneous as a black zone, as seen by these FESEM pictures. The uniform dispersion of AlN-SiC-reinforced particles with aluminium alloy can easily be seen in these pictures. The consistency of the cast composites can also be seen in these photos. The matrix particle and weight percentage, as well as the distribution of reinforcing particles and the particle-matrix interface bonding, determine the properties of aluminium MMCs [36, 39].

4. Conclusion

Stir casting was used to effectively cast Al 6061- AlN-SiC hybrid composites in this study. The impacts of aluminum nitride (AlN) and silicon carbide (SiC) on the composites tensile, compression, hardness, and FESEM characteristics were planned and reported. According to the tensile test, increasing the volume fraction of the nano phase and lowering the size of the nano reinforcement at the price of focused ductility improves the strength of SiC-AlN nanoparticles-reinforced Al 6061-SiC-AlN hybrid composites. The compression test, compressive strength of the Al 6061-SiC-AlN hybrid composite sample with 3% SiC-AlN reinforcement and 6% SiC-AlN reinforcement is 165 MPa and 178 MPa, respectively. When compared to the original matrix Al 6061 alloy, the organized Al 6061-SiC-AlN hybrid sample demonstrates an increase in the compressive strength. The hardness test combining a hybrid composite of Al 6061 alloy reinforced with 6% SiC-AlN proved to be the most effective way to achieve maximal hardness. The dispersion of particles throughout the matrix was found to be very homogeneous as a black zone, as seen by these FESEM pictures. The uniform dispersion of AlN-SiC reinforced particles with the aluminium alloy can easily be seen in these pictures.

Data Availability

The data used to support the findings of this study are included in the article. Should further data or information be required, these are available from the corresponding author and upon request.

Conflicts of Interest

The authors declare that they have no conflicts of interest.

References

[1] S. Vellingiri, "An Experimental and Investigation on the Micro-structure Hardness andTensile properties of Al-gr-Fe3O4 hybrid metal matrix composites," *FME Transactions*, vol. 47, no. 3, pp. 511–517, 2019.

[2] S. Suresh, G. H. Gowd, and M. L. S. Devakumar, "Mechanical and wear characteristics of aluminium alloy 7075 reinforced with nano-aluminium oxide/magnesium particles by stir casting method," *Materials Today Proceedings*, vol. 24, pp. 273–283, 2020.

[3] I. Sabry, M. A. Ghafaar, A. H. I. Mourad, and A. H. Idrisi, "Stir casted SiC-Gr/Al6061 hybrid composite tribological and mechanical properties," *SN Applied Sciences*, vol. 2, no. 5, p. 943, 2020.

[4] S. K. Soni, D. Ganatra, P. Mendiratta, C. S. K. A. Reddy, and B. Thomas, "Microstructure and mechanical characterization of Al2O3/graphene reinforced Al6061 based hybrid nanocomposites," *Metals and Materials International*, vol. 28, no. 2, pp. 545–555, 2022.

[5] V. Suresh, N. Hariharan, and S. Vellingiri, "An investigation on the tensile properties and micro-structure of hybrid metal matrix composites," *International Journal of Materials and Product Technology*, vol. 56, no. 1/2, pp. 84–94, 2018.

[6] P. Paulraj and R. Harichandran, "The tribological behavior of hybrid aluminum alloy nanocomposites at High temperature: role of nanoparticles," *Journal of Materials Research and Technology*, vol. 9, no. 5, pp. 11517–11530, 2020.

[7] T. Arunkumar, T. Selvakumaran, R. Subbiah, K. Ramachandran, and S. Manickam, "Development of high-performance aluminium 6061/SiC nanocomposites by ultrasonic aided rheo-squeeze casting method," *Ultrasonics Sonochemistry*, vol. 76, Article ID 105631, 2021.

[8] J. R. Xavier and N. Jeeva, "Evaluation of newly synthesized nanocomposites containing thiazole modified aluminium nitride nanoparticles for aerospace applications," *Materials Chemistry and Physics*, vol. 286, Article ID 126200, 2022.

[9] H. Y. Sun, Z. J. Wang, P. Du, J. X. Zhang, and W. C. Liu, "Effect of rolling reduction and heat treatment on the microstructure and mechanical properties of Al1060/Al6061-0.5SiC/Al1060 laminates," *Materials Science and Engineering: A*, vol. 830, Article ID 142328, 2022.

[10] M. S. Surya, "Effect of SiC weight percentage and sintering duration on microstructural and mechanical behaviour of Al6061/SiC composites produced by powder metallurgy technique," *Silicon*, vol. 14, no. 6, pp. 2731–2739, 2021.

[11] K. Ishfaq, M. U. Farooq, S. Anwar, M. A. Ali, S. Ahmad, and A. M El-Sherbeeny, "A comprehensive investigation of geometrical accuracy errors during WEDM of Al6061-7.5%SiC composite," *Materials and Manufacturing Processes*, vol. 36, no. 3, pp. 362–372, 2020.

[12] K. Halil, O. İsmail, D. Sibel, and Ç. Ramazan, "Wear and mechanical properties of Al6061/SiC/B4C hybrid composites produced with powder metallurgy," *Journal of Materials Research and Technology*, vol. 8, no. 6, pp. 5348–5361, 2019.

[13] A. Bhat and G. Kakandikar, "Manufacture of silicon carbide reinforced aluminium 6061 metal matrix composites for enhanced sliding wear properties," *Manufacturing Review*, vol. 6, p. 24, 2019.

[14] G. B. Veeresh Kumar, C. S. P. Rao, and N. Selvaraj, "Studies on mechanical and dry sliding wear of Al6061–SiC composites," *Composites Part B: Engineering*, vol. 43, no. 3, pp. 1185–1191, 2012.

[15] Y. Q. Liu, H. T. Cong, W. Wang, C. H. Sun, and H. M. Cheng, "AlN nanoparticle-reinforced nanocrystalline Al matrix composites: fabrication and mechanical properties," *Materials Science and Engineering: A*, vol. 505, no. 1-2, pp. 151–156, 2009.

[16] J. Vicens, M. Chedru, and J. L. Chermant, "New Al–AlN composites fabricated by squeeze casting: interfacial phenomena," *Composites Part A: Applied Science and Manufacturing*, vol. 33, no. 10, pp. 1421–1423, 2002.

[17] Q. Zhang, G. Chen, G. Wu, Z. Xiu, and B. Luan, "Property characteristics of a AlNp/Al composite fabricated by squeeze casting technology," *Materials Letters*, vol. 57, pp. 1453–1458, 2003.

[18] Y. B. Tang, Y. Q. Liu, C. H. Sun, and H. T. Cong, "AlN nanowires for Al-based composites with high strength and low thermal expansion," *Journal of Materials Research*, vol. 22, no. 10, pp. 2711–2718, 2007.

[19] D. F. Lii, J. L. Huang, and S. T. Chang, "The mechanical properties of AlN/Al composites manufactured by squeeze casting," *Journal of the European Ceramic Society*, vol. 22, no. 2, pp. 253–261, 2002.

[20] B. Ashok Kumar and N. Murugan, "Metallurgical and mechanical characterization of stir cast AA6061-T6–AlNp composite," *Materials & Design*, vol. 40, pp. 52–58, 2012.

[21] H. Xie, J. Zhang, F. Li et al., "Selective laser melting of SiCp/Al composites: densification, microstructure, and mechanical and tribological properties," *Ceramics International*, vol. 47, no. 21, pp. 30826–30837, 2021.

[22] P. P. Awate and S. B. Barve, "Microstructural observation and mechanical properties behavior of Al2O3/Al6061 nanocomposite fabricated by stir casting process," *Engineering. Research. Express*, vol. 4, no. 1, Article ID 015023, 2022.

[23] V. Suresh, P. Vikram, R. Palanivel, and R. F. Laubscher, "Mechanical and wear behavior of LM25 Aluminium matrix hybrid composite reinforced with Boron carbide, Graphite and Iron oxide," *Materials Today Proceedings*, vol. 5, no. 14, pp. 27852–27860, 2018.

[24] A. Gnanavelbabu, K. T. S. Surendran, and S. Kumar, "Process optimization and studies on mechanical characteristics of AA2014/Al2O3 nanocomposites fabricated through ultrasonication assisted stir–squeeze casting," *Inter Metalcast*, vol. 16, no. 2, pp. 759–782, 2022.

[25] T. Arunkumar, V. Pavanan, V. A. Murugesan, V. Mohanavel, and K. Ramachandran, "Influence of nanoparticles reinforcements on aluminium 6061 alloys fabricated via novel ultrasonic aided rheo-squeeze casting method," *Metals and Materials International*, vol. 28, no. 1, pp. 145–154, 2022.

[26] V. S. S. Venkatesh and A. B. Deoghare, "Microstructural characterization and mechanical behaviour of SiC and kaoline reinforced aluminium metal matrix composites fabricated through powder metallurgy technique," *Silicon*, vol. 14, no. 7, pp. 3723–3737, 2022.

[27] P. H. Syeddu Masooth, G. Bharathiraja, V. Jayakumar, and K. Palani, "Microstructure and mechanical characterisation of ZrO2 reinforced Ti6Al4V metal matrix composites by powder metallurgy method," *Materials Research Express*, vol. 9, no. 2, Article ID 020003, 2022.

[28] A. M. Sánchez de la Muela, J. Duarte, J. Santos Baptista et al., "Stir casting routes for processing metal matrix syntactic foams: a scoping review," *Processes*, vol. 10, no. 3, p. 478, 2022.

[29] P. Samal, P. R. Vundavilli, A. Meher, and M. M. Mahapatra, "Multi-response modeling for sliding wear behavior of AA5052/TiC composites by stir casting: a comparative analysis using response surface methodology and fuzzy logic system," *Proceedings of the Institution of Mechanical Engineers - Part E: Journal of Process Mechanical Engineering*, vol. 236, no. 2, pp. 254–266, 2021.

[30] A. Abebe Emiru, D. K. Sinha, A. Kumar, and A. Yadav, "Fabrication and Characterization of Hybrid Aluminium (Al6061) Metal Matrix Composite Reinforced with SiC, B4C and MoS2 via Stir Casting," *International journal Metalcasting*, 2022.

[31] J. J. M. Hillary, R. Sundaramoorthy, R. Ramamoorthi, and S. J. S. Chelladurai, "Investigation on Microstructural Characterization and Mechanical Behaviour of Aluminium 6061 – CSFA/Sicp Hybrid Metal Matrix Composites," *Silicon*, 2022.

[32] K. S. A. Ali, V. Mohanavel, S. A. Vendan et al., "Mechanical and microstructural characterization of friction stir welded SiC and B4C reinforced aluminium alloy AA6061 metal matrix composites," *Materials*, vol. 14, no. 11, p. 3110, 2021.

[33] V. A. Kumar, M. P. Anil, G. L. Rajesh, V. Hiremath, and V. Auradi, "Tensile and compression behaviour of boron carbide reinforced 6061Al MMC's processed through conventional melt stirring," *Materials Today Proceedings*, vol. 5, no. 8, pp. 16141–16145, 2018.

[34] N. Lokesh, B. Manoj, K. Srikanth, P. kumar, P. K. V. Ramanayya, and M. Rao, "Mechanical characterization of stir cast Al 6063 TiO2-cu reinforced hybrid metal matrix composites," *Materials Today Proceedings*, vol. 5, no. 9, pp. 18383–18392, 2018.

[35] G. S. Pradeep Kumar, P. G. Koppad, R. Keshavamurthy, and M. Alipour, "Microstructure and mechanical behaviour of in situ fabricated AA6061–TiC metal matrix composites," *Archives of Civil and Mechanical Engineering*, vol. 17, no. 3, pp. 535–544, 2016.

[36] Y. B. Mukesh, T. P. Bharathesh, R. Saravanan, and R. Keshavamurthy, "Effect of hot extrusion on mechanical behaviour of boron nitride reinforced aluminium 6061-based metal matrix composites," *International Journal of Materials Engineering Innovation*, vol. 10, no. 2, pp. 135–151, 2019.

[37] V. K. Anand, A. Aherwar, M. Mia, O. Elfakir, and L. Wang, "Influence of silicon carbide and porcelain on tribological performance of Al6061 based hybrid composites," *Tribology International*, vol. 151, Article ID 106514, 2020.

[38] V. Suresh, N. Hariharan, S. Paramesh, M. P. Kumar, and P. A. Prasath, "Tribological behaviour of aluminium/boron carbide (B4C)/graphite (Gr) hybrid metal matrix composite under dry sliding motion by using ANOVA," *International Journal of Materials and Product Technology*, vol. 53, no. 3/4, pp. 204–217, 2016.

[39] V. Suresh, A. D. Praneet, and J. Anoop, "Ingenious analysis on machining parameters of aluminium alloy (LM25)/graphite (Gr)/boron carbide (B4C) hybrid composites using wire electrical discharge machining (WEDM)," *Materials Today Proceedings*, vol. 37, pp. 3112–3117, 2021.

Hindawi
Advances in Materials Science and Engineering
Volume 2022, Article ID 7210265, 14 pages
https://doi.org/10.1155/2022/7210265

Research Article

Parameter Optimization and Machining Performance of Inconel 625 with Nanoparticles Dispersed in Biolubricant

T. Mohanraj,[1] N. Radhika,[1] S. Aswin Nanda,[1] V. Vignesh,[1] B. Jayaraman,[1] K. R. Ratana Selvan,[1] and Yesgat Admassu[2]

[1]*Department of Mechanical Engineering, Amrita School of Engineering, Amrita Vishwa Vidyapeetham, Coimbatore, India*
[2]*Institute of Research Development, Defence University College of Engineering, Bishoftu, Ethiopia*

Correspondence should be addressed to Yesgat Admassu; yesgat.admassu@dec.edu.et

Received 17 June 2022; Accepted 20 July 2022; Published 24 August 2022

Academic Editor: Pudhupalayam Muthukutti Gopal

Productivity and cost-effectiveness are essential components of any long-term manufacturing system. While quantity and quality are linked to productivity, the economy focuses on energy-efficient processes that produce a high output-to-input ratio. Hard-to-cut materials have always been difficult to machine because of more significant tool wear and power losses. Inconel 625 is a hard material used in aerospace and underwater applications and is milled using biolubricants with nanoparticles. Palm oil is considered a biolubricant, and titanium dioxide (TiO_2) and copper oxide (CuO) are selected as nanoparticles. When the combination of biolubricants and nanoparticles is added to the workpiece's surface, it enhanced some properties while machining. Experiments involving four factors with four levels were carried out using the Taguchi design of experiments (DoE). The feed, depth of cut, speed, and coolant with nanoparticle additives were all factors. The responses were surface roughness, spindle vibration along *X*, *Y*, and *Z* axes, and material removal rate. Technique for Order of Preference by Similarity to Ideal Solution (TOPSIS) was used to alter the multiresponse optimization problem to a single-response optimization problem. The S/N of TOPSIS closeness coefficients was calculated, and the optimal machining conditions were determined. Surface roughness, material removal rate, and spindle vibration were reduced by 3.10%, 6.14%, 7.54% (Vx), and 6.78% (Vz), respectively, due to the TOPSIS optimization.

1. Introduction

Inconel 625's enhanced mechanical properties, outstanding weldability, and high oxidation and corrosion resistance, nickel-based aerospace alloys have gained popularity. Inconel 625 is widely used in manufacturing, especially for aircraft structures, springs, turbine blades, submarine bellows, steam power plants, and oceanographic devices [1]. Due to its meager thermal conductivity, the formation of built-up edges, and a greater sticking or welding propensity to cutting edges, Inconel 625's machinability is considered poor [2] and classified as a difficult-to-machine material. Furthermore, due to Inconel 625's low heat transfer rate, a large portion of the cutting energy is converted into heat during machining, which remains in the tool-workpiece interface for a longer time. High localized temperatures in the machining region result from heat generation, causing tool material softening and rapid tool wear, decreasing tool life, and compromising machined surface integrity. The use of cutting fluids is required to solve these issues. Most traditional machining fluids contain hazardous chemical constituents that can pollute the environment, cause biological problems for workers, contaminate soil, and pollute water during disposal [3, 4]. Furthermore, cutting fluids account for roughly 17% of machining costs, while tooling costs account for only 8% [5, 6]. Many attempts have been made to reduce cutting fluids to make material removal processes more environmentally friendly [7]. The growing interest in tracking all elements of the material removal process has resulted from the metal-based industry's main challenge of increasing the quality and productivity of machined parts [8].

Dry cutting, or machining without the need for any cutting fluid, is one of the best machining options for achieving green manufacturing. However, when dry-machining Inconel, the work material bonds firmly to the tool surface, resulting in early tool failure and poor surface quality. Furthermore, Inconel's high mechanical strength and poor thermal conductivity result in unfavorable residual stresses, surface irregularities, and burning/overheating in the cutting zone when machining without coolant [9]. The surface roughness of the machined product can affect various areas of its operation, including gentle friction, heat generation, the ability to distribute and hold a lubricant, wear, and a material's ability to withstand fatigue [10]. Dry cutting also necessitates using unique cutting tool materials such as ceramic, PCD, PCBN, and careful tool geometry and specific coatings. Therefore, to facilitate heat transfer from the tool–chip interface, these tacky alloys are typically machined under wet cutting conditions, which results in high manufacturing costs, worker health risks, and severe environmental problems [11]. Due to the specific inherent properties and their capacity to biodegrade, vegetable oils are seen as alternatives to mineral oils in lubricant formulations.

Vegetable oils have a high flash point, viscosity index, lubricity, and lower evaporative loss than mineral oils [12]. Plant oils are extracted by applying pressure to the pertinent part of a plant and squeezing the oil out [13]. Plant oils (edible and nonedible) can also be extracted by dissolving plant parts in water, distilling the oil, or infusing plant parts with a base oil. Various studies have demonstrated the value of edible vegetable oils such as coconut oil [14], palm oil [15], soya bean oil [16], and canola oil [17] as an environmentally friendly lubricant for machining. The novelty was premised on the fact that using cooling/lubrication circumstances and depth of cut as input variables improved the manufacturing system's sustainability and efficiency. This study is based on the idea that productivity results from quality, utilization, and efficiency working together.

The utilization of nanoparticles in various base fluids has received a lot of interest in the last decade [18]. The nanoparticles dispersed in water, for instance, can improve the thermal conductivity, and it is a suitable heat transfer fluid, especially for solar collectors [19]. Nano coolants (the dispersal of nanoparticles in water or ethylene glycol) have been studied for real-world problems since the early 2000s [20]. Nanoparticles added to the lubricant are thought to provide antifriction and antiwear properties. On the other hand, the improved characteristics are entirely determined by nanoparticle characteristics like shape, size, and concentration. Moreover, it has been reported that adding a suitable amount of nanoparticles to lubricating oil improves antifriction and antiwear characteristics [21]. These terms cover the manufacturing process, including surface roughness, material removal rate, and spindle vibration. These responses are optimized by combining constructive process parameters like feed speed and cutting depth. Taguchi design of experiment (DoE) is used to optimize the input parameters collectively, as they would alternatively behave differently in different responses. The goal is to optimize the input parameters based on the responses that are both sustainable and constructive at the same time.

Table 1: Properties of palm oil.

Oils	Color	Density (g/cm^3)	Dynamic viscosity (mPa·s)
Palm oil	Light yellow	0.89	77.19

Taguchi's DoE is an excellent tool for optimization because it is simple and efficient. Taguchi assists in selecting a control variable combination that significantly reduces the impact of noise. Minimizing tool costs is necessary to be cost-effective in manufacturing [22]. Variations recommended that machining irregularity could be reduced if appropriate values and requirements were used [23]. Technique for Order of Preference by Similarity to Ideal Solution (TOPSIS) selects the alternative closest to the ideal solution and farthest from the ideal negative alternative. It is helpful in cases where there are a lot of requirements and substitutes [24]. It is based on the theory of an optimum moving solution from which it tries to negotiate the result that is the closest. The smallest distance from the positive ideal solution (PIS) and the greatest distance from the negative ideal solution (NIS) are used to rank the options. TOPSIS explores the ranges of both PIS and NIS, ranking candidates based on their relative proximity and combining the two distance measurements [25]. Taguchi's DoE was combined with the TOPSIS to identify the processing parameters for milling the Inconel 625 alloy. Surface roughness, spindle vibration, and MRR were all taken into account. They discovered that, after optimization, machining performance improved [26]. The novelty of this research lies in the combination of biolubricants and nanoparticles that are used. Inconel 625 has not been machined with the current choice of biolubricants and nanoparticles. The responses such as surface roughness (Ra), material removal rate (MRR), and vibration have not been recorded for this particular combination.

2. Materials and Method

2.1. Oils and Nanoparticles. After carefully considering the literature review and availability of the materials, palm oil has been chosen. The nanoparticles chosen are TiO_2 and CuO. The nanoparticles are biocompatible with oils and do not cause adverse effects on the lubricant. The properties of palm oil are given in Table 1.

2.2. SEM Images. SEM image was used to examine the surface morphology of the nanoparticles. SEM images of the nanoparticles TiO_2 and CuO have been observed and shown in Figure 1. It ensures that the nanoparticles are in the nanometer size range and that the size is marked on the image. Figure 1(a) shows that CuO nanoparticles are in the range of 124 to 215 nm. According to the SEM image, as

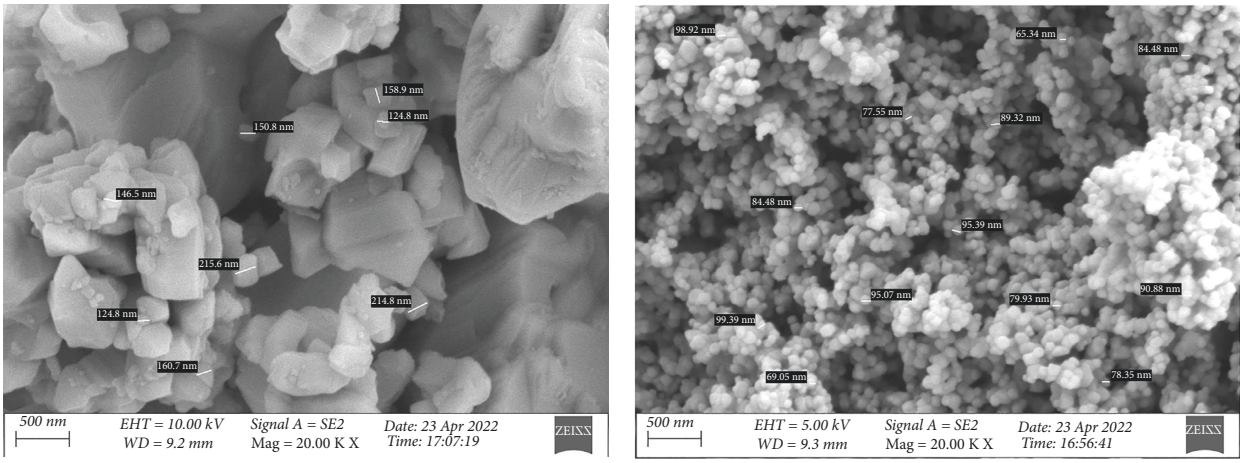

(a) (b)

Figure 1: (a) SEM image of CuO. (b) SEM image of TiO_2.

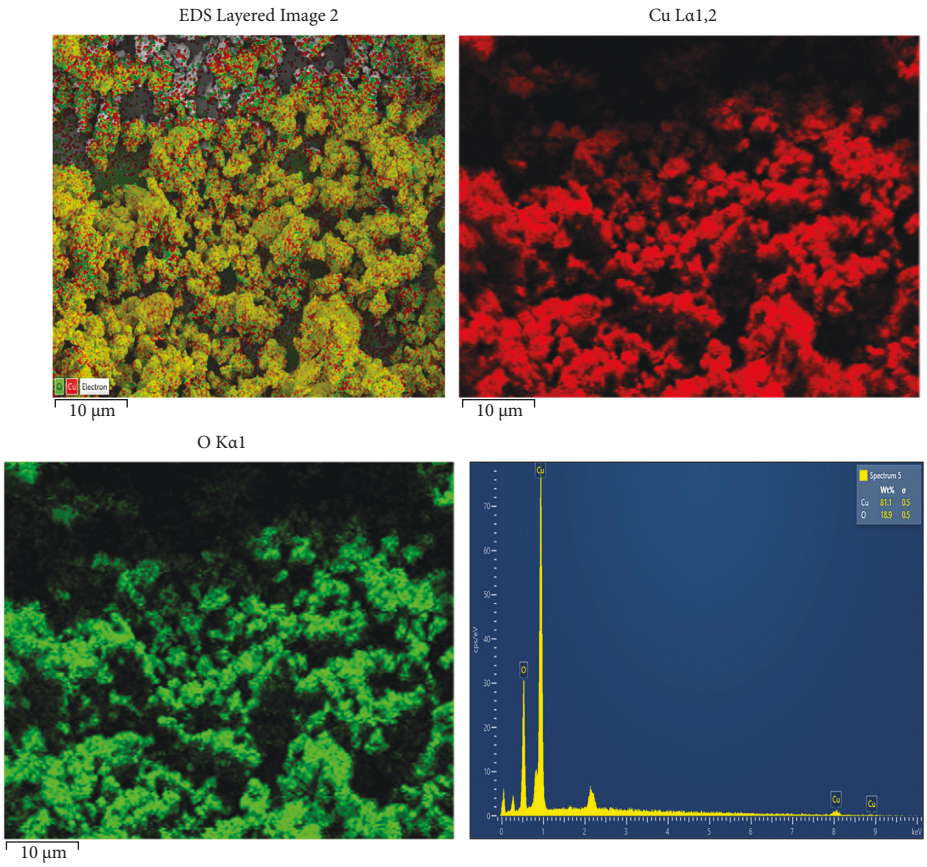

Figure 2: EDX analysis and elemental mapping of CuO.

shown in Figure 1(b), the TiO_2 nanoparticles are 60 to 100 nm in size, and the TiO_2 nanoparticles have a homogeneous spherical morphology.

2.3. EDX of CuO and TiO_2. The energy dispersive X-ray (EDX) analysis is used to characterize the elemental composition and chemical composition of a specimen with an atomic number. Elemental mapping is a technique for obtaining high-resolution imaging by accumulating detailed elemental composition data across a sample area. Every pixel in the image is examined to preserve the rudimentary spectrum.

The EDX spectrum of CuO Nanoparticles is shown in Figure 2. The spectrum depicts the chemical components of the sample. The dissemination of Cu (red dots) and O (green dots) components, which make up the whole body of the

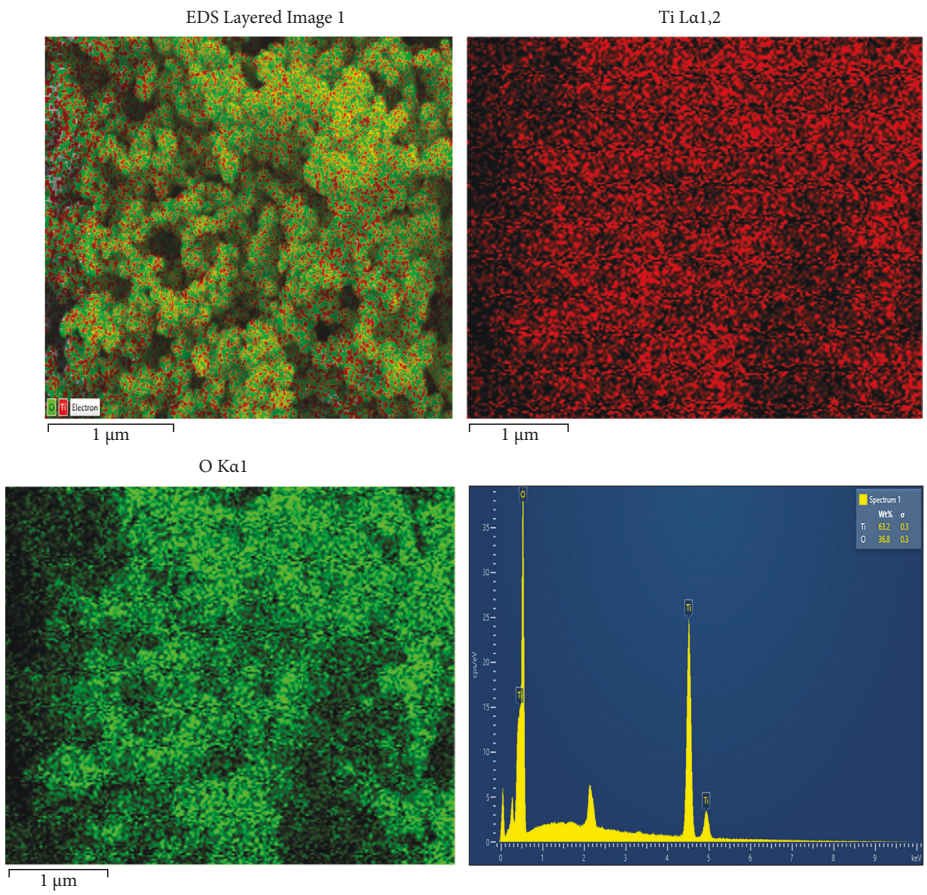

Figure 3: EDX analysis and elemental mapping of TiO_2.

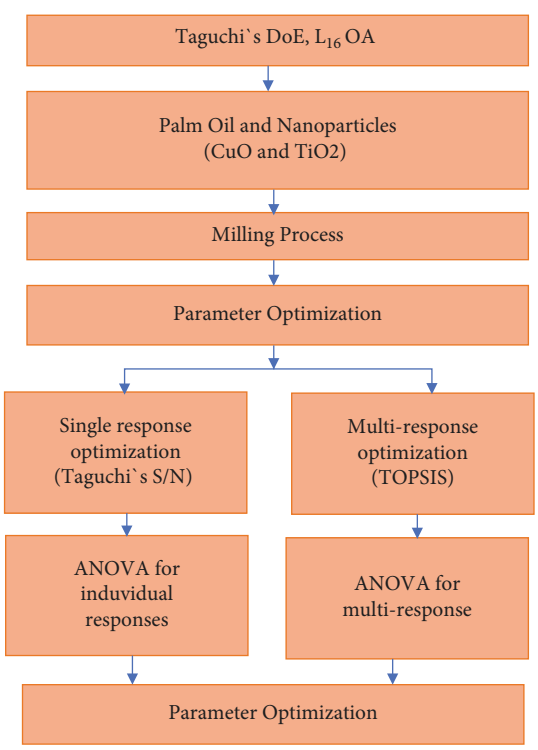

Figure 4: Flowchart for methodology.

processed sample, is homogeneous in Figure 2. For each element, the corresponding findings are shown separately. The presence of oxygen and copper is demonstrated by the change in the distribution of both elements. Figure 2 indicates that 81.1% of Cu and 18.9% of O were presented in the sample. The elemental mapping shows that elements are correctly dispersed in aggregated Cu and O nanoparticles [27]. Figure 2 shows no CuO nanoparticle impurities, and only Cu and O elements are present [28, 29].

Figure 3 shows EDX analysis of TiO_2 nanoparticles. Figure 3 reveals that 63.2% of Ti and 36.8% of O were presented in the sample. The distribution of Ti (red dots) and O (green dots) elements, which make up the entire body of the processed samples, is homogeneous [30, 31]. The results of EDS revealed that no other impurities were present in the nanoparticles. From Figure 3, it was observed that there is no impurity in the TiO_2 nanoparticle, and only the elements Ti and O were present [32, 33].

2.4. Methodology. The flowchart of the methodology for this research is given in Figure 4.

2.4.1. Experimental Setup. Milling operations were completed on a high-rigidity Computer Numerical Control (CNC) BMV35 T12 with a machine with specifications: maximum spindle rpm 8000, spindle power 5.5 kW, and

Table 2: Factors and their levels.

Levels	Spindle speed (rpm)	Feedrate (mm/min)	Depth of cut(mm)	Coolant
Level 1	1500	125	0.10	1 (palm oil)
Level 2	2000	150	0.15	2 (palm oil with 0.5 wt% of CuO)
Level 3	2500	175	0.20	3 (palm oil with 0.5 wt% of TiO_2)
Level 4	3000	200	0.25	4 (palm oil with 0.25 wt% of CuO and 0.25wt% of TiO_2)

(a) (b) (c)

Figure 5: (a) 0.5wt% of CuO, (b) 0.5wt% of TiO_2 nanoparticles, (c) hybrid (0.25 wt% of CuO + 0.25wt% of TiO_2).

maximum traverse distance in *x-y-z* axis are 450-350-350 mm, respectively. Commercially available Inconel 625 block (150 × 50 × 50 mm) was used as the workpiece material for machining. End milling operation was selected as the machining process. The cutting tool used for machining Inconel 625 was PVD-coated carbide (Grade: VP15TF; designated as SEMT13T3AGSN-JM).

2.4.2. DoE. Feed rate, spindle speed, cut depth, and palm oil are process parameters. At the same time, the surface roughness, spindle vibration, and material removal rate are considered responses. An orthogonal array (OA) matrix helps the machine operator decide the best parameters with the fewest possible experiments. The four-parameter system has a total of 15 degrees of freedom. An OA's Degree of Freedom (DoF) should be equal to or larger than the total DoF. As a result, L_{16} OA was used in this study because it has a DoF of 15 and allows fewer experiments to identify the best milling parameters. The selected parameters and their levels are shown in Table 2. There are sixteen experiments in total. Experiments are carried out after the OA has been defined, and the S/N for every experiment is calculated [34].

2.4.3. Preparation of Coolant. A beaker of 200 ml was taken, and 99.5 ml of palm oil was poured into it. 0.5 g of nanoparticles was measured using a highly sensitive electronic

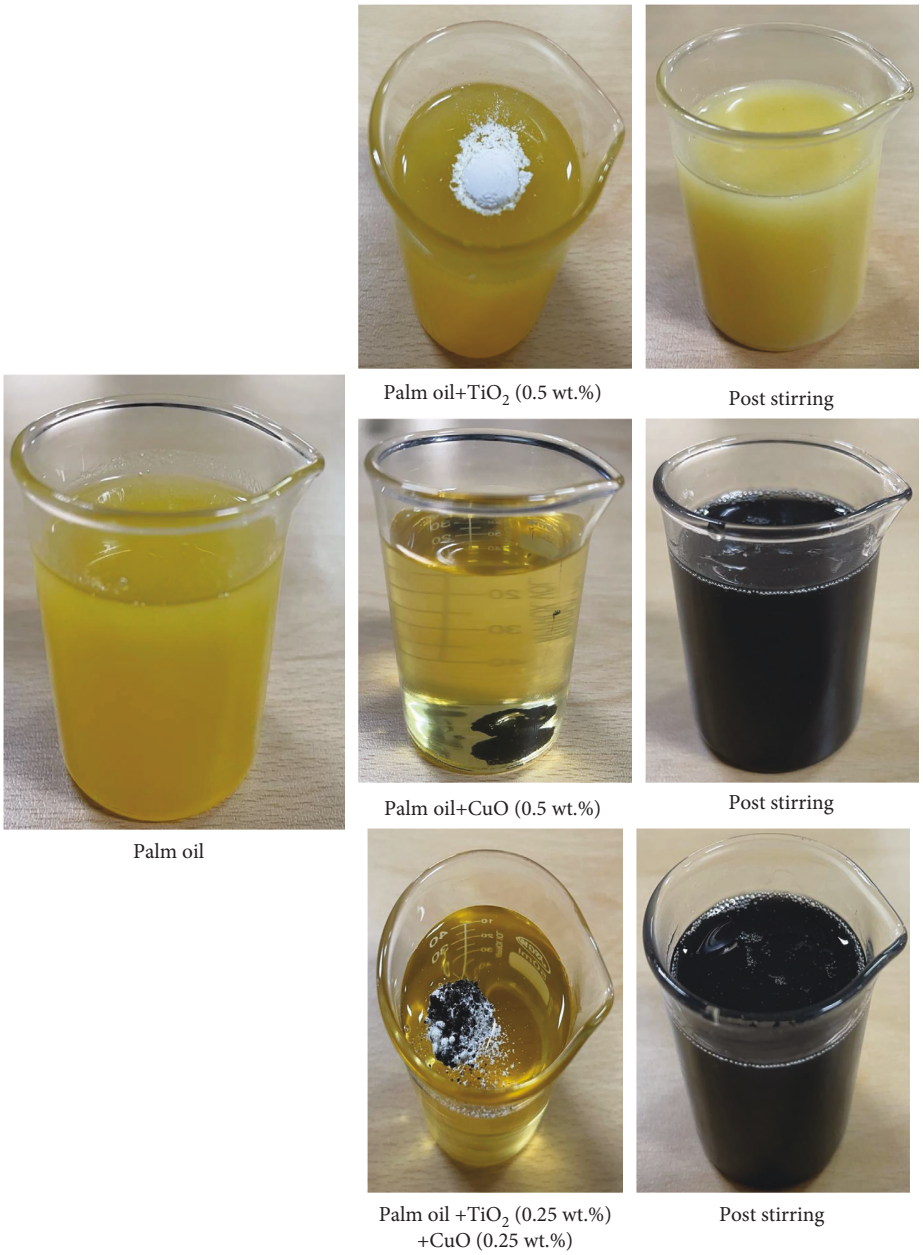

Figure 6: Preparation of nano lubricant.

balance. The electronic balance was air-tight to ensure minimal error. The nanoparticle was poured into the beaker, and constant stirring was done for thirty seconds using a spatula. The stirring ensures that the oil has 0.5 wt% of nanoparticles uniformly [35]. The nanoparticles and preparation of nanolubricant are shown in Figures 5 and 6.

2.4.4. Milling Procedure. The CNC machine BMV35 T12 was used for all milling operations on Inconel 625, as shown in Figure 7. The vibration sensor MPU 6050 has been soldered to the Arduino UNO board using jumper cables. The Arduino UNO board acts as an interface between the sensor and the system and is connected to a laptop using a USB-A cable.

The vibration sensor MPU 6050 has been attached to the spindle using double-sided tape. Using the Arduino IDE, vibration in the spindle's *x*-, *y*-, and *z*-axes during the milling process has been recorded. The workpiece is cleaned with a neat cloth before fitting inside the CNC machine. Facing the workpiece has been done to 0.1 mm. After facing the material, the tool holder is removed and replaced with milling inserts. The mixture of oils and nanoparticles has been poured uniformly over the material using a dropper (10 ml). The end milling operation has been carried out according to the DoE design matrix. After machining, the surface roughness was measured using a surface roughness testing instrument (Make- Carl Zeiss. Model- E-35B). Three surface roughness values were recorded, and the average surface roughness was noted. The material removal rate (MRR) was

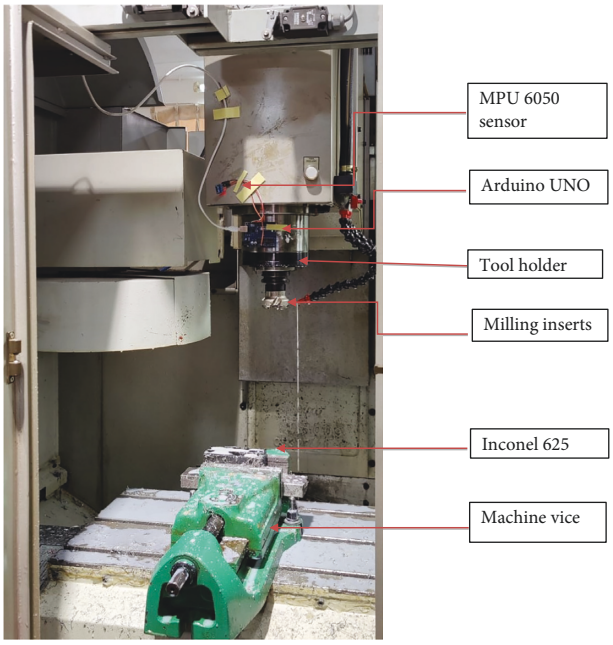

Figure 7: Machining process.

computed using the weight-loss method, and the weight of the material was recorded before and after each pass. The formula for the weight-loss method has been given as follows:

$$\text{Loss of material weight}\,(g) = \textit{original weight} - \textit{measured weight},$$

$$\textit{Volume of workpiece} = \frac{\text{mass (Loss of material)}}{\text{density}}, \quad (1)$$

$$\text{MRR} = \frac{\textit{Volume of workpiece}}{\text{machining time}}.$$

The density of Inconel 625 is 8.4 g/cc. The same procedure is repeated for all experiments.

2.5. Process Parameter Optimization

2.5.1. Taguchi's S/N. Using Taguchi signal-to-noise (S/N), the optimal factors were analyzed. Larger is better (LB) and Smaller is better (SB) are the two characteristics available for optimization. LR characteristics were applied for MRR and SR characteristics for Ra and *Vx*, *Vy*, and *Vz*. Using the formula, S/N values for different responses were recorded [36–38].

$$SB\text{:}\ \eta = -10\log\frac{1}{n}\sum_{i=1}^{n} y_i^2,$$
$$LB = -10\log\frac{1}{n}\sum_{i=1}^{n} y_i^2. \quad (2)$$

The S/N ratio was used to determine the best conditions for each response. The ideal situation is the level at which the maximum S/N is reached.

2.6. TOPSIS. To turn a multiresponse optimization problem into a single-response optimization problem, TOPSIS is used. The steps involved in the TOPSIS approach are depicted below. A normalized matrix is utilized in TOPSIS. Calculate the PIS and NIS using normalized weighted values and Euclidean distance using formulae [39, 40]. The S/N for closeness coefficient was computed from that the optimal parameter for multiresponse was identified.

(1) Normalization matrix r_{ij} is calculated out using

$$r_{ij} = \frac{x_{ij}}{\sqrt{\sum_{i=1}^{m} x_{ij}^2}}, \quad (3)$$

where $i = 1, 2, 3, \ldots, m$, $j = 1, 2, 3, \ldots, n$ and a_{ij} represent the ith value of the jth experimental run. r_{ij} represents the normalized data for the corresponding test.

(2) Compute the weight w_{ij} of each response.

(3) The weighted normalized data is computed by multiplying the normalized data with its equivalent weight. The weighted normalized data V_{ij} is computed using

$$V_{ij} = w_i * r_{ij}, \quad (4)$$

where $i = 1, 2, \ldots, m$, $j = 1, 2, \ldots, n$ and w_j represents the weight of the jth criterion

$$\sum_{j=1}^{n} w_j = 1. \quad (5)$$

(4) The PIS (V^+) and NIS (V^-) are estimated from the weighted normalized data:

$$V^+ = (V_1^+, V_2^+, \ldots, V_n^+)\max \textit{values}, \quad (6)$$

$$V^- = (V_1^-, V_2^-, \ldots, V_n^-)\max \textit{values}. \quad (7)$$

(5) The separation value of the PIS and NIS is computed from (6) and (7):

$$S_i^+ = \sqrt{\sum_{j=1}^{n}\left(V_{ij} - V_j^+\right)^2},$$
$$S_i^- = \sqrt{\sum_{j=1}^{n}\left(V_{ij} - V_j^-\right)^2}, \quad (8)$$

where $i = 1, 2, \ldots, m$.

(6) The closeness coefficient to the ideal solution is estimated using equation (11):

Table 3: Surface roughness, spindle vibration, and MRR for palm oil.

Speed	Feed	DoC	Coolant	Ra	MRR	ax	ay	az
1500	125	0.1	1	0.103	1.191198	0.173359	0.417925	0.396441
1500	150	0.15	2	0.149	1.435532	0.166886	0.406583	0.358339
1500	175	0.2	3	0.159	3.361345	0.176182	0.442583	0.396144
1500	200	0.25	4	0.229	3.494976	0.213174	0.406836	0.375259
2000	125	0.15	3	0.076	2.021427	0.164513	0.422058	0.393962
2000	150	0.1	4	0.163	2.436054	0.178955	0.414779	0.391988
2000	175	0.25	1	0.161	7.510504	0.114595	0.42088	0.377286
2000	200	0.2	2	0.35	7.809087	0.180548	0.435534	0.406443
2500	125	0.2	4	0.103	1.155101	0.220654	0.432775	0.409345
2500	150	0.25	3	0.081	1.392031	0.200459	0.429581	0.381369
2500	175	0.1	2	0.12	3.571429	0.166229	0.425354	0.386759
2500	200	0.15	1	0.111	3.713412	0.184046	0.427508	0.39247
3000	125	0.25	2	0.108	1.010714	0.179596	0.416428	0.36319
3000	150	0.2	1	0.11	1.218027	0.178492	0.43709	0.393807
3000	175	0.15	4	0.07	2.258403	0.148024	0.422805	0.367047
3000	200	0.1	3	0.107	2.348187	0.191256	0.437669	0.384296

Table 4: S/N values for individual responses.

	Level	Speed	Feed	DoC	Coolant
Smaller is better					
Ra	1	16.26	20.3	18.33	18.47
	2	15.78	18.32	20.28	15.85
	3	19.77	18.34	16	19.9
	4	20.25	15.11	17.46	17.85
	Delta	4.47	5.19	4.28	4.05
	Rank	2	1	3	4
Vx	1	14.82	14.73	15.03	15.93
	2	16.08	14.86	15.63	15.23
	3	14.34	16.52	14.51	14.77
	4	15.21	14.34	15.28	14.52
	Delta	1.73	2.18	1.12	1.4
	Rank	2	1	4	3
Vy	1	7.572	7.489	7.456	7.416
	2	7.468	7.497	7.542	7.518
	3	7.355	7.375	7.191	7.272
	4	7.363	7.397	7.569	7.552
	Delta	0.217	0.122	0.378	0.28
	Rank	3	4	1	2
Vz	1	8.376	8.16	8.182	8.193
	2	8.146	8.42	8.448	8.446
	3	8.184	8.396	7.912	8.25
	4	8.459	8.19	8.623	8.277
	Delta	0.314	0.261	0.711	0.253
	Rank	2	3	1	4
Larger is better					
MRR	1	6.515	2.244	6.931	8.035
	2	12.303	3.865	6.931	8.020
	3	6.644	11.544	7.837	6.733
	4	4.074	11.883	7.834	6.733
	Delta	8.229	9.638	0.906	1.303
	Rank	2	1	4	3

Table 5: Analysis of variance.

Source	DF	Adj SS	Adj MS	F-Value	*P*-Value	% Contribution
Surface roughness						
Speed	3	0.02259	0.007529	21.92	0.015	31.02
Feed	3	0.02261	0.007535	21.94	0.015	31.04
DoC	3	0.0136	0.004534	13.2	0.031	18.68
Coolant	3	0.01298	0.004326	12.59	0.033	17.82
Error	3	0.00103	0.000344			
Total	15	0.0728				
S		R-sq		R-sq(adj)		R-sq(pred)
0.018534		98.58%		92.92%		89.74%
MRR						
Speed	3	24.28	8.0932	21.08	0.016	37.06
Feed	3	31.03	10.3433	26.94	0.011	47.36
DoC	3	3.98	1.3267	3.46	0.168	6.07
Coolant	3	5.065	1.6883	4.4	0.128	7.73
Error	3	1.152	0.384			
Total	15	65.506				
S		R-sq		R-sq(adj)		R-sq(pred)
0.61964		98.24%		91.21%		49.98%
Vx						
Speed	3	0.00235	0.000784	16.72	0.022	25.66
Feed	3	0.00388	0.001292	27.57	0.011	42.31
DoC	3	0.00107	0.000356	7.6	0.065	11.65
Coolant	3	0.00173	0.000575	12.27	0.034	18.83
Error	3	0.00014	0.000047			
Total	15	0.00916				
S		R-sq		R-sq(adj)		R-sq(pred)
0.006846		98.47%		92.33%		86.35%
Vy						
Speed	3	0.00029	0.000096	10.26	0.044	16.48
Feed	3	0.00011	0.000037	4.01	0.142	6.43
DoC	3	0.00086	0.000288	30.81	0.009	49.56
Coolant	3	0.00045	0.00015	16.12	0.024	25.90
Error	3	2.8E-05	0.000009			
Total	15	0.00174				
S		R-sq		R-sq(adj)		R-sq(pred)
0.0030549		98.39%		91.96%		84.27%
Vz						
Speed	3	0.00073	0.000243	9.64	0.048	22.54
Feed	3	0.0003	0.000099	3.93	0.145	9.20
DoC	3	0.00182	0.000607	24.04	0.013	56.23
Coolant	3	0.00031	0.000104	4.13	0.137	9.66
Error	3	7.6E-05	0.000025			
Total	15	0.00324				
S		R-sq		R-sq(adj)		R-sq(pred)
0.0063477		96.66%		85.31%		83.06%

$$CC_i^+ = \frac{S_i^-}{S_i^+ + S_i^-}. \quad (9)$$

3. Results and Discussion

3.1. Single Response Optimization Using Taguchi's S/N. The surface roughness, MRR, and spindle vibrations are tabulated in Table 3.

Taguchi's S/N values were used to find the best parameters for individual responses. The SB characteristics were used for surface roughness and vibration signals. Maximizing the MRR is a critical criterion in metal removal processes [41]. The MRR must be determined to attain excellent machinability. As a result, for MRR, the LB characteristic was used. From Table 4, it can be seen that the highest S/N value produces the best results. For palm oil, the minimum surface roughness can be obtained when the spindle speed is 3000 rpm, feed rate of 125 mm/min, depth of cut (DoC) of 0.15 mm, and palm oil, with CuO nanoparticles being used as a coolant. Minimal vibration on the *x*-axis during the machining operation was obtained with the spindle speed of 2000 rpm, feed rate of 175 mm/min, DoC of 0.15 mm, and palm oil without nanoparticles. Similarly, for the *y*-axis and *z*-axis speeds of 1500 rpm and 3000 rpm, a feed rate of 150 mm/min for both DoC of 0.25 mm for both

and y-axis palm oil with both nanoparticles and z-axis palm oil, with TiO_2 being used as the coolant. For MRR, the optimal parameters are a speed of 2000 rpm, 200 mm/min feed, 0.20 mm DoC, and palm oil without nanoparticles.

3.2. ANOVA. Analysis of Variance (ANOVA) is used to find the most significant parameter influencing the response. When using ANOVA, the method is quite beneficial for determining the level of risk and the effect of milling parameters on a specific response. It is utilized to determine each control factor's relative influence in the response evaluation to ensure that the quality of the most critical aspects of the product should be carefully monitored [22, 42].

3.2.1. Surface Roughness. From Table 5, both speed and feed rate have the same level of contribution of 31% to surface roughness, followed by DoC of 18.68% and coolant of 17.82%, respectively. From the P-value ($P < 0.05$), it was found that all parameters have significantly impacted machining. The average surface roughness for the speed of 1500 rpm is 0.16 μm, and when the speed increases to 2500 rpm, the surface roughness is reduced by 18.75%. Similarly, for the speed of 3000 rpm, there is a 38.75% decrease in surface roughness. As the spindle speed increases, the built-up edge advancement slows down, and heat in the shear zone rises, making it more straightforward for machining and improving surface quality [43]. With an increase in feed, the surface roughness steadily increased, generating force on the machined surface that causes vibration, which raises the roughness. An identical pattern was observed in the literature [21, 44].

It is observed that when CuO and TiO_2 (hybrid mode) nanoparticles are mixed with palm oil, the lowest surface roughness is obtained when compared to all other combinations [45]. The mechanism could involve rolling CuO nanoparticles rather than forming a layer or repairing surfaces [46]. CuO nanoparticles act as a third body between the two mating parts, preventing metal-metal contact and thus reducing surface roughness, as evidenced by the lower coefficient of friction and roughness values observed [47].

3.2.2. MRR. From Table 5, it was observed that feed has a significant impact on the MRR, contributing 47.36%. Moreover, the speed gives 37.06% of the contribution to the machining process. DoC and coolant have an insignificant impact of 6.07% and 7.73%. The feed has more impact than speed and as the feed increases, machining the material to the desired length takes less time, increasing the MRR [48]. When palm oil is mixed with the hybrid combination of nanoparticles at a speed of 2000 rpm, a feed of 175 mm/min, and 0.15 mm DoC, the optimal results are obtained. The hybrid mode of nanoparticles formulates a third layer between the workpiece and the tool. The surface is slippery, will be long-lasting, and is ideal for machining for extended periods [49].

Table 6: Normalization table.

S. No.	Ra	MRR	V_x	V_y	V_z
1	0.168131	0.084796	0.242232	0.245895	0.256665
2	0.243218	0.102189	0.233188	0.239221	0.231997
3	0.259541	0.23928	0.246177	0.260403	0.256473
4	0.373805	0.248793	0.297865	0.23937	0.242951
5	0.124058	0.143897	0.229872	0.248327	0.25506
6	0.266071	0.173412	0.250051	0.244044	0.253782
7	0.262806	0.534641	0.160123	0.247633	0.244264
8	0.571318	0.555896	0.252278	0.256255	0.26314
9	0.168131	0.082227	0.308317	0.254632	0.26502
10	0.132219	0.099093	0.280098	0.252753	0.246907
11	0.19588	0.254235	0.232269	0.250266	0.250397
12	0.181189	0.264342	0.257165	0.251533	0.254094
13	0.176292	0.071948	0.250947	0.245014	0.235137
14	0.179557	0.086706	0.249405	0.257171	0.25496
15	0.114264	0.160766	0.206832	0.248766	0.237635
16	0.17466	0.167158	0.267239	0.257512	0.248802

3.2.3. Spindle Vibration. From Table 5, it can see that x-axis feed can have a significant impact of 42.31%, followed by a speed of 25.66%, and coolant of 18.83%. DoC also has a minimal impact of 11.65%. All parameters will have a significant impact on the machining process. For the y-axis, the DoC had a significant contribution of 49.56%, followed by coolant with 25.9% and speed with 16.48%, and feed had an insignificant impact of 6.43% [50]. For the z-axis, DoC had a significant impact of 56.23%, followed by a speed of 22.54%, and both the coolant and depth of cut had an insignificant impact of 9.6% and 9.2%, respectively. The spindle moves in the same direction as the z-axis. As a result, the contribution of the DoC is more on the z-axis [34, 51].

It is observed that when using vibration on the x-axis, the values are lower when TiO_2 is mixed with palm oil [52]. Similarly, for the z-axis, the values are lower when TiO_2 is mixed with palm oil [53]. Similar research discovered that adding nanoparticles to the lubricant can decrease friction and wear, increase allowable bearing capacity, and remove heat under higher temperatures and high load conditions, reducing bearing wear and achieving vibration suppression [54].

4. Multiresponse Optimization Using TOPSIS

TOPSIS can be used to conduct multiresponse optimization. Table 6 displays the normalized data. (3) can be used to conduct data normalization. Table 7 shows the weighted normalization and separation measures. (4) is used to calculate the weighted normalization. Equations (8), (9), and (11) calculate the separation measures and the closeness coefficient CC_i. Table 8 shows the S/N values of CC_i. From Table 8, it can see that the optimal parameter can be identified. The optimal parameters are the speed of 2000 rpm, feed of 175 mm/min feed, DoC of 0.15 mm, and palm oil with 0.25 wt% of CuO and 0.25wt% of TiO_2 nanoparticles. From Table 9, it can be seen that the feed had a contribution of 43.93%, followed by a speed of 25.10%, the coolant of 23.3%, and DoC of 6.08%. Speed, feed, and coolant significantly impacted the machining process. From this, it can be observed that the multiresponse characteristics are impacted by feed speed and coolant.

Table 7: Weighted normalization. Measures of separation and closeness coefficient values.

Ra	MRR	V_x	V_y	V_z	S^+	S^-	CC_i
0.033626	0.016959	0.048446	0.049179	0.051333	0.096381	0.081822	0.459152
0.048644	0.020438	0.046638	0.047844	0.046399	0.09546	0.068043	0.416158
0.051908	0.047856	0.049235	0.052081	0.051295	0.072057	0.071872	0.499357
0.074761	0.049759	0.059573	0.047874	0.04859	0.085033	0.053413	0.385803
0.024812	0.028779	0.045974	0.049665	0.051012	0.083742	0.092004	0.523504
0.053214	0.034682	0.05001	0.048809	0.050756	0.084362	0.065501	0.437072
0.052561	0.106928	0.032025	0.049527	0.048853	0.030158	0.115207	0.792536
0.114264	0.111179	0.050456	0.051251	0.052628	0.09352	0.097441	0.510264
0.033626	0.016445	0.061663	0.050926	0.053004	0.100111	0.080672	0.446237
0.026444	0.019819	0.05602	0.050551	0.049381	0.094613	0.088256	0.482618
0.039176	0.050847	0.046454	0.050053	0.050079	0.064289	0.084919	0.569133
0.036238	0.052868	0.051433	0.050307	0.050819	0.0631	0.087642	0.581406
0.035258	0.01439	0.050189	0.049003	0.047027	0.099266	0.080116	0.446623
0.035911	0.017341	0.049881	0.051434	0.050992	0.096586	0.079316	0.45091
0.022853	0.032153	0.041366	0.049753	0.047527	0.079607	0.095493	0.545362
0.034932	0.033432	0.053448	0.051502	0.04976	0.081696	0.082064	0.501122

Table 8: S/N for TOPSIS.

Level	Speed	Feed	DoC	Coolant
1	−7.17	−6.749	−6.392	−5.215
2	−5.281	−7.012	−5.803	−6.339
3	−5.887	−4.666	−6.602	−6.176
4	−6.477	−6.388	−6.018	−5.085
Delta	1.889	2.347	0.799	1.871
Rank	2	1	4	3

Table 9: ANOVA for CC_i.

Source	DF	Adj SS	Adj MS	F-value	P-value	% contribution
Speed	3	0.02949	0.009828	15.94	0.024	25.10
Feed	3	0.05159	0.017197	27.89	0.011	43.93
DoC	3	0.00715	0.002382	3.86	0.148	6.08
Coolant	3	0.02737	0.009122	14.8	0.027	23.30
Error	3	0.00185	0.000617			
Total	15	0.11744				

Table 10: Confirmation test results.

Responses	Optimal parameters	Measured values	TOPSIS	Measured values	Variation	% improvement
Ra	A4-B1-C2- D3	0.170975		0.16567	0.00530	3.10
MRR	A2-B4-C3-D1	3.58		3.80	0.22	6.14
V_x	A2-B3-C2-D1	0.176825	A2-B3-C2-D4	0.16348	0.0133	7.54
V_y	A1-B2-C4-D4	0.42075		0.44364	−0.02289	−5.44
V_z	A4-B2-C4-D2	0.38335		0.35735	0.026	6.78

4.1. Confirmation Test. A calculation test was used to verify the significance of the solution parameters. The experiments were repeated three times, with the average result used for the analysis. For further investigation, the value was used. Table 10 showed the confirmation test results and discovered that the surface roughness decreased by 3.10%. The MRR was increased by 6.14%. The spindle vibration in the x & z-axis decreased by 7.54% and 6.78%. On the other hand, vibration in the y-axis increased by 5.44%.

The consumption of nanoparticles (0.25 to 0.5 wt%) along with palm oil is significantly less, and the overall cost is also reasonably minimum. Further, it enhances the surface roughness, MRR, and vibration features. This will significantly enhance the life span of the machine.

5. Conclusion

Inconel 625 was machined with SEMT-13T3AGSN-JM VP15 TF with palm oil and CuO and TiO_2 nanoparticles as additives. Taguchi's DoE was applied to design the experiments. Taguchi's DoE coupled with TOPSIS was used to optimize the process parameters. The following conclusions have been drawn from the experimentation:

(i) Surface roughness was measured as a feed and speed function and depended on it.

(ii) Both the speed and feed significantly impact MRR.

(iii) The spindle speed vibration in the x-axis depends on the speed and feed. Similarly, the y-axis depends on the DoC and coolant, and the z-axis depends on the depth of cut and speed.

(iv) Taguchi's S/N analysis was used to find the best parameters for individual responses.

(v) TOPSIS was used to perform the multiresponse optimization, with the best parameters being 2000 rpm, 175 mm/min feed, 0.15 mm depth, and coolant of palm oil with 0.25 wt% of CuO and 0.25wt% of TiO_2 nanoparticles.

(vi) According to ANOVA for the closeness coefficient, speed and feed have physical significance, with 25.10% and 43.93%, respectively.

(vii) Surface roughness, material removal rate, and spindle speed vibration were reduced by 3.10%, 6.14 percent, 7.54% (Vx), and 6.78%(Vz) due to TOPSIS optimization. This will significantly improve the machining performance.

Data Availability

The data used to support the findings of this study are included within the article.

Conflicts of Interest

The authors declare that they have no conflicts of interest.

References

[1] O. Çolak, "Investigation on machining performance of inconel 718 under high pressure cooling conditions," *Strojniški vestnik-Journal of Mechanical Engineering*, vol. 58, no. 11, pp. 683–690, 2012.

[2] J. S. Senthilkumaar, P. Selvarani, and R. M. Arunachalam, "Intelligent optimization and selection of machining parameters in finish turning and facing of Inconel 718," *International Journal of Advanced Manufacturing Technology*, vol. 58, no. 9-12, pp. 885–894, 2012.

[3] D. G. Thakur, B. Ramamoorthy, and L. Vijayaraghavan, "Investigation and optimization of lubrication parameters in high speed turning of superalloy Inconel 718," *International Journal of Advanced Manufacturing Technology*, vol. 50, no. 5-8, pp. 471–478, 2010.

[4] N. Dhar, M. Kamruzzaman, and M. Ahmed, "Effect of minimum quantity lubrication (MQL) on tool wear and surface roughness in turning AISI-4340 steel," *Journal of Materials Processing Technology*, vol. 172, no. 2, pp. 299–304, 2006.

[5] A. K. Sharma, A. K. Tiwari, and A. R. Dixit, "Effects of Minimum Quantity Lubrication (MQL) in machining processes using conventional and nanofluid based cutting fluids: a comprehensive review," *Journal of Cleaner Production*, vol. 127, pp. 1–18, 2016.

[6] T. Singh, P. Singh, J. Dureja, M. Dogra, H. Singh, and M. S. Bhatti, "A review of near dry machining/minimum quantity lubrication machining of difficult to machine alloys," *International Journal of Machining and Machinability of Materials*, vol. 18, no. 3, pp. 213–251, 2016.

[7] J. P. Davim, P. S. Sreejith, and J. Silva, "Turning of brasses using minimum quantity of lubricant (MQL) and flooded lubricant conditions," *Materials and Manufacturing Processes*, vol. 22, no. 1, pp. 45–50, 2007.

[8] N. Radhika, A. Sudhamshu, and G. K. Chandran, "Optimization of electrical discharge machining parameters of aluminium hybrid composites using Taguchi method," *Journal of Engineering Science & Technology*, vol. 9, no. 4, pp. 502–512, 2014.

[9] A. Devillez, G. Le Coz, S. Dominiak, and D. Dudzinski, "Dry machining of Inconel 718, workpiece surface integrity," *Journal of Materials Processing Technology*, vol. 211, no. 10, pp. 1590–1598, 2011.

[10] H. Kumar, S. Ilangovan, and N. Radhika, "Optimization of cutting parameters for MRR, tool wear and surface roughness characteristics in machining ADC12 piston alloy using DOE," *Tribology in industry*, vol. 42, no. 1, pp. 32–40, 2020.

[11] D. Thakur, B. Ramamoorthy, and L. Vijayaraghavan, "Influence of minimum quantity lubrication on the high speed turning of aerospace material superalloy Inconel 718," *International Journal of Machining and Machinability of Materials*, vol. 13, no. 2/3, pp. 203–214, 2013.

[12] I. Choudhury and M. El-Baradie, "Machinability of nickel-base super alloys: a general review," *Journal of Materials Processing Technology*, vol. 77, no. 1–3, pp. 278–284, 1998.

[13] M. Mia, M. K. Gupta, J. A. Lozano et al., "Multi-objective optimization and life cycle assessment of eco-friendly cryogenic N2 assisted turning of Ti-6Al-4V," *Journal of Cleaner Production*, vol. 210, pp. 121–133, 2019.

[14] M. K. Gupta, M. Mia, G. Singh, D. Y. Pimenov, M. Sarikaya, and V. S. Sharma, "Hybrid cooling-lubrication strategies to improve surface topography and tool wear in sustainable turning of Al 7075-T6 alloy," *International Journal of Advanced Manufacturing Technology*, vol. 101, no. 1–4, pp. 55–69, 2019.

[15] M. Sarıkaya, V. Yılmaz, and A. Güllü, "Analysis of cutting parameters and cooling/lubrication methods for sustainable machining in turning of Haynes 25 superalloy," *Journal of Cleaner Production*, vol. 133, pp. 172–181, 2016.

[16] Ç V. Yıldırım, T. Kivak, M. Sarikaya, and F. Erzincanli, "Determination of MQL parameters contributing to sustainable machining in the milling of nickel-base superalloy waspaloy," *Arabian Journal for Science and Engineering*, vol. 42, no. 11, pp. 4667–4681, 2017.

[17] Y. Su, L. Gong, B. Li, Z. Liu, and D. Chen, "Performance evaluation of nanofluid MQL with vegetable-based oil and ester oil as base fluids in turning," *International Journal of Advanced Manufacturing Technology*, vol. 83, no. 9–12, pp. 2083–2089, 2016.

[18] N. C. Sidik and O. A. Alawi, "Computational investigations on heat transfer enhancement using nanorefrigerants," *Journal of Advanced Research Design*, vol. 1, pp. 35–41, 2014.

[19] M. Jamil, N. C. Sidik, and M. M. Yazid, "Thermal performance of thermosyphon evacuated tube solar collector using TiO2/water nanofluid," *Journal of Advanced Research in Fluid Mechanics and Thermal Sciences*, vol. 20, no. 1, pp. 12–29, 2016.

[20] S. Zainal, "ANSYS simulation for Ag/HEG hybrid nanofluid in turbulent circular pipe," *Journal of Advanced Research in Applied Mechanics*, vol. 23, no. 1, pp. 20–35, 2016.

[21] S. R. Das, D. Dhupal, and A. Kumar, "Experimental investigation into machinability of hardened AISI 4140 steel using TiN coated ceramic tool," *Measurement*, vol. 62, pp. 108–126, 2015.

[22] A. C. Mitra, M. Jawarkar, T. Soni, and G. Kiranchand, "Implementation of Taguchi method for robust suspension design," *Procedia Engineering*, vol. 144, pp. 77–84, 2016.

[23] V. Vignesh, S. Ilangovan, and N. Radhika, "Statistical analysis of process parameters in drilling of SS410 stainless steel," *Materials Today Proceedings*, vol. 46, pp. 3313–3319, 2021.

[24] H.-S. Shih, H.-J. Shyur, and E. S. Lee, "An extension of TOPSIS for group decision making," *Mathematical and Computer Modelling*, vol. 45, no. 7-8, pp. 801–813, 2007.

[25] S. V. Alagarsamy, P. Raveendran, and M. Ravichandran, "Investigation of material removal rate and tool wear rate in spark erosion machining of Al-Fe-Si alloy composite using taguchi coupled TOPSIS approach," *Silicon*, vol. 13, no. 8, pp. 2529–2543, 2021.

[26] M. Thangamuthu, J. Yerchuru, N. A. R. Shanmugam, Y. Ravi, and A. K. Gur, "Multi-response optimization of end-milling parameters for inconel 625 using taguchi coupled with topsis," *Surface Review and Letters*, vol. 28, no. 10, Article ID 2150096, 2021.

[27] S. I. Al-Saeedi, G. M. Al-Senani, O. H. Abd-Elkader, and N. M. Deraz, "One pot synthesis, surface and magnetic properties of Cu2O/Cu and Cu2O/CuO nanocomposites," *Crystals*, vol. 11, no. 7, p. 751, 2021.

[28] M. Verma, V. Kumar, and A. Katoch, "Sputtering based synthesis of CuO nanoparticles and their structural, thermal and optical studies," *Materials Science in Semiconductor Processing*, vol. 76, pp. 55–60, 2018.

[29] D. Rehana, D. Mahendiran, R. S. Kumar, and A. K. Rahiman, "Evaluation of antioxidant and anticancer activity of copper oxide nanoparticles synthesized using medicinally important plant extracts," *Biomedicine & Pharmacotherapy*, vol. 89, pp. 1067–1077, 2017.

[30] A. M. Alturki and R. Ayad, "Synthesis and characterization of titanium dioxide nanoparticles with a dosimetry study of their ability to enhance radiation therapy using a low energy X-ray source," *Indian Journal of Science and Technology*, vol. 12, pp. 1–5, 2019.

[31] D. Cabaleiro, M. J. Pastoriza-Gallego, C. Gracia-Fernandez, M. M. Pineiro, and L. Lugo, "Rheological and volumetric properties of TiO2-ethylene glycol nanofluids," *Nanoscale Research Letters*, vol. 8, no. 1, pp. 1–3, 2013.

[32] M. Hamadanian, A. Reisi-Vanani, and A. Majedi, "Sol-gel preparation and characterization of Co/TiO2 nanoparticles: application to the degradation of methyl orange," *Journal of the Iranian Chemical Society*, vol. 7, no. S2, pp. S52–S58, 2010.

[33] M. B. Askari, Z. Tavakoli Banizi, M. Seifi, S. Bagheri Dehaghi, and P. Veisi, "Synthesis of TiO2 nanoparticles and decorated multi-wall carbon nanotube (MWCNT) with anatase TiO2 nanoparticles and study of optical properties and structural characterization of TiO2/MWCNT nanocomposite," *Optik*, vol. 149, pp. 447–454, 2017.

[34] S. Shankar, T. Mohanraj, and A. Pramanik, "Tool condition monitoring while using vegetable based cutting fluids during milling of inconel 625," *Journal of Advanced Manufacturing Systems*, vol. 18, no. 04, pp. 563–581, 2019.

[35] A. Das, O. Pradhan, S. K. Patel, S. R. Das, and B. B. Biswal, "Performance appraisal of various nanofluids during hard machining of AISI 4340 steel," *Journal of Manufacturing Processes*, vol. 46, pp. 248–270, 2019.

[36] J. Gokulachandran and K. Mohandas, "Prediction of cutting tool life based on Taguchi approach with fuzzy logic and support vector regression techniques," *International Journal of Quality & Reliability Management*, vol. 32, no. 3, pp. 270–290, 2015.

[37] A. S. Kang, G. S. Cheema, and V. Gandhi, "Optimization of surface roughness and metal removal rate in end milling using taguchi grey relational analysis," *Indian Journal of Science and Technology*, vol. 10, pp. 31–13, 2017.

[38] A. K. Gur, C.n. Ozay, and B. Icen, "Evaluation of B4c/Ti coating layer, investigation of abrasive wear behaviors using Taguchi technique and response surface methodology," *Surface Review and Letters*, vol. 27, no. 10, Article ID 1950225, 2020.

[39] H.-P. Nguyen, V.-D. Pham, and N.-V. Ngo, "Application of TOPSIS to Taguchi method for multi-characteristic optimization of electrical discharge machining with titanium powder mixed into dielectric fluid," *International Journal of Advanced Manufacturing Technology*, vol. 98, no. 5–8, pp. 1179–1198, 2018.

[40] A. Shanmugam, T. Mohanraj, K. Krishnamurthy, and A. K. Gur, "Multi-response optimization on abrasive waterjet machining of glass fiber reinforced plastics using taguchi method coupled with topsis," *Surface Review and Letters*, vol. 28, no. 12, Article ID 2150120, 2021.

[41] S. Shankar, T. Mohanraj, and S. K. Thangarasu, "Multi-response milling process optimization using the Taguchi method coupled to grey relational analysis," *Materials Testing*, vol. 58, no. 5, pp. 462–470, 2016.

[42] A. K. Gür, T. Yildiz, and B. Icen, "Theoretical evaluation of abrasive wear behavior of B4C/FeCrC coating layer evaluated by a Taguchi approach," *Materials Testing*, vol. 62, no. 7, pp. 733–738, 2020.

[43] M. Yasir, "Effect of cutting speed and feed rate on surface roughness of AISI 316l SS using end-milling," *ARPN Journal of Engineering and Applied Sciences*, vol. 11, no. 4, pp. 2496–2500, 2016.

[44] M. D. Morehead, Y. Huang, and J. Luo, "Chip morphology characterization and modeling in machining hardened 52100 steels," *Machining Science and Technology*, vol. 11, no. 3, pp. 335–354, 2007.

[45] A. Raina and A. Anand, "Influence of surface roughness and nanoparticles concentration on the friction and wear characteristics of PAO base oil," *Materials Research Express*, vol. 5, no. 9, Article ID 095018, 2018.

[46] S. Bhaumik and S. Pathak, "Analysis of anti-wear properties of CuO nanoparticles as friction modifiers in mineral oil (460cSt viscosity) using pin-on-disk tribometer," *Tribology in industry*, vol. 37, no. 2, p. 196, 2015.

[47] M. V. Thottackkad, R. K. Perikinalil, and P. N. Kumarapillai, "Experimental evaluation on the tribological properties of coconut oil by the addition of CuO nanoparticles," *International Journal of Precision Engineering and Manufacturing*, vol. 13, no. 1, pp. 111–116, 2012.

[48] S. Singhvi and M. Khidiya, "Effect of spindle speed and feed on material removal rate in turning operation," *Int. J. Sci. Res. Sci. Eng. Technol*, vol. 2, pp. 807–811, 2016.

[49] I. P. Okokpujie, O. S. Ohunakin, and C. A. Bolu, "Multi-objective optimization of machining factors on surface roughness, material removal rate and cutting force on end-milling using MWCNTs nano-lubricant," *Progress in Additive Manufacturing*, vol. 6, no. 1, pp. 155–178, 2021.

[50] T. Mohanraj, S. Shankar, R. Rajasekar, R. Deivasigamani, and P. M. Arunkumar, "Tool condition monitoring in the milling process with vegetable based cutting fluids using vibration signatures," *Materials Testing*, vol. 61, no. 3, pp. 282–288, 2019.

[51] T. Mohanraj, J. Yerchuru, H. Krishnan, R. Nithin Aravind, and R. Yameni, "Development of tool condition monitoring system in end milling process using wavelet features and Hoelder's exponent with machine learning algorithms," *Measurement*, vol. 173, Article ID 108671, 2021.

[52] S. Singh, X. Chen, C. Zhang, R. K. Gautam, R. Tyagi, and J. Luo, "Nickel-catalyzed direct growth of graphene on bearing steel (GCr15) by thermal chemical vapor deposition and its tribological behavior," *Applied Surface Science*, vol. 502, Article ID 144135, 2020.

[53] V. Bhardwaj, R. Pandey, and V. Agarwal, "Experimental investigations for tribo-dynamic behaviours of conventional and textured races ball bearings using fresh and MoS2 blended greases," *Tribology International*, vol. 113, pp. 149–168, 2017.

[54] D. Muller, C. Matta, R. Thijssen, M. bin Yusof, M. van Eijk, and S. Chatra, "Novel polymer grease microstructure and its proposed lubrication mechanism in rolling/sliding contacts," *Tribology International*, vol. 110, pp. 278–290, 2017.

Hindawi
Advances in Materials Science and Engineering
Volume 2022, Article ID 4254024, 11 pages
https://doi.org/10.1155/2022/4254024

Research Article

Experimental Investigation and Optimization of Material Removal Rate and Tool Wear in the Machining of Aluminum-Boron Carbide (Al-B_4C) Nanocomposite Using EDM Process

A. Arunnath,[1,2] S. Madhu,[3] and Mebratu Tufa[4]

[1]*Department of Mechanical Engineering, Saveetha School of Engineering, Saveetha Institute of Medical and Technical Sciences, Chennai 602105, India*
[2]*Department of Mechanical Engineering, Faculty of Engineering and Technology, Vadapalani Campus, SRM Institute of Science and Technology, Chennai, India*
[3]*Department of Automobile Engineering, Saveetha School of Engineering, Saveetha Institute of Medical and Technical Sciences, Chennai 602105, India*
[4]*Department of Mechanical Engineering, Faculty of Manufacturing, Institute of Technology, Hawassa University, Hawassa, Ethiopia*

Correspondence should be addressed to S. Madhu; mathumarine@gmail.com and Mebratu Tufa; mebratu.tufa@hu.edu.et

Received 14 June 2022; Accepted 19 July 2022; Published 21 August 2022

Academic Editor: Vijayananth Kavimani

Electrical discharge machining (EDM) is a cost-effective unconventional machining method used for machining any composites materials. EDM is based on the thermoelectric energy between the electrode and workpiece. In this work, boron carbide particles of 50 nm (6 wt.%) are reinforced with aluminum 7075 (94 wt.%) prepared using stir casting method. The stir casting process is carried out at speed of 700–800 rev/min. The fabricated aluminum-boron carbide nanometal matrix composites are used as workpiece (anode); copper electrode is used as tool (cathode). This work investigates the influence of EDM process parameters such as current (I), pulse on-time (t_{on}), and tool diameter (d) during machining of Al-B_4C composite on metal removal rate (MRR) and tool wear rate (TWR). The design of experimental plan is executed by Taguchi approach, and the responses of each parameter are influenced by analysis of variances (ANOVA). Response table for average value of MRR and TWR shows that the current is the significant parameter affecting MRR and TWR. From this work, it was observed that material removal rate increased with increasing the current, and the tool wear rate decreases.

1. Introduction

The input parameters were optimized by Box Behnken method, and quadratic model was suggested for output responses. The prepared specimen is machined using electrical discharge machining (EDM). The presence of graphite nanopowders in dielectric fluid notably improved the surface finish and enhanced MRR (material removal rate) and EWR (electrode wear rate) [1, 2]. The input process parameters were optimized using L18 orthogonal array of Taguchi Method on AISI D2 steel specimen machined by electrical discharge machining (EDM). The electrical spark vaporized on work material there after it has been flushed out through fluid medium. It has been observed that increasing current leads to increasing the surface roughness, and CuW electrode prepared through powder metallurgy is better than conventional Cu electrode [3, 4]. The silicon powder mixed in dielectric fluid gives more MRR and better surface roughness. EDM is a very important machining method that is extensively and effectively used for the machining of such materials, exactly and cost-effectively within the high advance in business [5]. The experimental

investigation has different characteristics to reduce machining time and cost. Dry EDM milling obtained superior function compared to oil EDM milling and oil die sinking EDM. This paper work is about the reduction of tool wear rate using boron doped CVD-diamond (B-CVD) and polycrystalline diamond (PCD). The results show lack of knowledge in the process behavior of B-CVD and PCD in micro-EDM as well as wear on tool electrode with surface formation process [6, 7]. It is clearly evident that it is the toughest material, specifically having high magnetic permeability and being difficult to make microhole. Moreover, severe tool wear rate can be observed using conventional machining compared to micro-EDM process [8].

Rotation of tools provides adequate flushing in the machining zone compared to nonrotational tools. In general, the classical experiment is too difficult to optimize and very complex. This can be overcome using Taguchi method [9, 10]. MRR by sterilization conductor polarity on a zirconia-based composite offers the foremost stable machining conditions and terminates that negative polarity with a perceptibly lower risk of arcing. This experimental investigation brought a new concept such as mixing of micro-MoS_2 powder in dielectric fluid along with ultrasonic vibration using μ-EDM processes. However, the most significant process needs to increase MRR without degrading the surface finish [11, 12]. Al7075 is employed within the production of M16 rifles for the army vehicles. The M16 rifle prime quality has lower and higher receivers. Moreover, extension tubes, square measure, are usually made of 7075-T6 alloy. Due to its greater strength, superior hardness, thermal properties, and potential to be extremely polished, 7075 is widely utilized in molding tool. Boron chemical compound (B_4C) is one amongst the toughest materials known, ranking third behind diamond and cubical component compound. It is the toughest material created in tariff quantities. Boron chemical compound powder is created by reacting carbon with B_2O_3 in an electrical arc chamber, through carbothermal reduction or by gas section reactions. Nowadays, although metal matrix composites have more advantages, they are not widely used as their plastic counterparts. This paper presents getting precision machining obtained by smaller overcut dimensions of crater resulting in low MRR with less energy desirable [13, 14]. Many combinations of metals, ceramics, and compounds are often used with matrices of low temperature alloys. In most of the cases, Taguchi approaches were broadly used to find optimized result performed by different characteristics through significant parameters and reduced sensitivity of the system performance to design a top-quality system. The improvement is to select the required parameters for machining Ti-6Al-4V superalloy on micro-EDM by victimization of the Taguchi technique with different responses on MRR, TWR, overcut, and taper. They conjointly know optimum combination levels of victimization ANOVA and S/N quantitative relation graphs. The Taguchi technique spots the optimal value to extend the removal rate of material in which fluid containing micropowder in micro-EDM victimization associates degree L18 orthogonal array. The different results were observed on EDM machining with multiple characteristics of MRR value and surface roughness. Analysis of variance is employed to review the importance of variables method on gray relative grade showing discharged current and duty cycle being the most needed parameters [15, 16].

The mechanical properties of composite material have been improved by introducing fly ash material. Filler material such as potassium titanium chloride is used to avoid wettability issues. Modern composite materials attract significant attention compared with aluminum alloys due to their high specific properties, reduced weight, corrosion resistance, and cost reduction used for aircraft structural parts [17, 18]. Aluminum alloy 6063 reinforcement of TiB_2 shows lower wear rate by increasing the % of TiB_2 particles improving the peak hardness and good interfacial bond in situ composites method. A new stir caster setup is introduced in this experimental work to get homogeneous dispersion of aluminum-based SiC composite used by four bladed 45° angular, and its position is 35% of material below and 65% of material above the stirrer. Aluminum alloy AA7075 is reinforced with different ratio of TiB_2 fabricated using in situ reaction of organic salts K_2TiF_6 and KBF_4 to molten aluminum. It also increases the exothermic reaction holding time which improves wear resistance [19–21]. Aluminum-TiB_2 composite material specimens were prepared by powder methodology, and the experiment was conducted through hipping treatment to improve CTE results. Three different particle sizes of B_4C (56.9 μm, 4.2 μm, and 2.0 μm) are investigated to study the morphology behaviour using Al7075/B_4C composites by plasma activated sintering. A high performance of light weight composite armor is produced with B_4C composite metal foams having adequate potential applications prepared by PM technique [22, 23]. The MMC material is prepared with Al6061 and different % of rice husk to improve the wear resistance because it reduces the plastic deformation on the worn surface and size of wear debris generated. The results of this investigation showed the superiority of Al7075/Al_2O_3/5 wt% of graphite composites for gaining their wear reduction [24]. The influence of plasma-activated sintering parameters was studied using Al7075/B_4C precipitating smooth interparticle bonding. Tribological and mechanical properties were studied on Al7075/graphite composites for the optimum wear rate. The manufacturing of low-cost material is always in demand and needed in most of the engineering fields. Those demands are overcome by using fly ash material taken from industrial waste, agricultural waste, etc. This reinforcement of MMC obtained superior mechanical properties [25]. The fabrication of aluminum with B_4C occurs poor wetting condition during liquid stage. It can be avoided by introducing flux material such that K_2TiF_6 improves good interfacing bonding and wettability due to the presence of TiC and TiB_2. Mechanical, tribology, and microstructure of Al7075 reinforced with nanoparticles were studied. It has been observed that the porosity level and hardness increase by increasing the wt% of nanoparticles [26].

From the previous research, it was noticed that current, pulse on-time, and pressure were selected as electrical discharge machining parameters to obtain response parameters

like material removal rate (MRR), tool wear rate, and surface roughness. As far as the optimization techniques related to Al-B_4C is concerned, researchers have mainly used response surface method. But the capability of other optimization techniques like Taguchi and ANOVA should also be examined. The present work is thus focused on EDM machining of aluminum-boron carbide composite. Stir casting method is used for fabricating aluminum-boron carbide (6 wt.%) with the particle size of 50 nm in Al7075 metal matrix. The effect of current, pulse on-time (T_{on}), and electrode diameter on MRR and TWR is investigated using Taguchi and ANOVA techniques. Experiments are performed as per L16 orthogonal array of Taguchi. The optimal setting of different process parameters is also found to maximize MRR and minimize EWR.

2. Experimental Setup

The experiments are conducted on the fabricated aluminum 7075 nano boron carbide metal matrix composites using EDM as shown in Figure 1. A mix between two propelled materials which are MMC of Al7075T6 as workpiece and copper I as terminal has been chosen in this investigation. The copper impregnated graphite is considered as a cross-breed material for the cathode, exponentially utilized as a part of hardware and shape making industry. The workpiece or occupation is secured and braced at a proper area on the x-y table [27]. The area of little gaps or fine profound openings to be penetrated might be set apart at work. The activity might be set with the assistance of dial stand and DRO. A reasonable anode of specific size and additionally a proper guide bramble are chosen, and the cathode is embedded into the hurl for holding it. The cathode is then tried for coolant stream at a weight of around 100 Kg/sq·cm. The cathode may now be positional on to occupation to begin drilling process.

2.1. Stir Casting of Al-B_4C Composite. The composite materials were fabricated by stir casting process route [28]. Commercially available aluminum Al7075 was chosen as the matrix and B_4C 50 nm selected as reinforcement. By liquid casting technique, the aluminum metal matrix is melted in the temperature of 850° about 1 kg. The preheated stirrer is introduced in the melt when the temperature of the melt is about 30°C above the pouring temperature. Agitation of the melt is started, and the preheated B_4C of 6 wt.% is added as reinforcement. Aluminum requires a temperature as high as 1100°C for wetting the B_4C surface completely. Aluminum alloy 7075T6 (94 wt.%) reinforced with boron carbide (6 wt. %) with the size of 50 nm is used in the current investigation. For the stir casting process, 470 grams 27 × 10 × 06 cm chunk of aluminum 7075 and 30 grams of nano boron carbide are taken in two cauldrons. The aluminum 7075 is cut into a pack of little pieces with the goal that it can fit into the cauldron no 4. Boron carbide is the hardest conventional abrasives. Its Mohs hardness is 9.36, melting point is 2350°C, and density is 2.51 g/cm^3. The boron carbide is taken in a different way, and both cauldrons are put in the muffle furnace. The most extreme warming capacity of the suppress heater is 900°–950°C considering 7075 at 635°C for softening purpose of aluminum and the boron carbide nanopowder at 2763°C. The mute heater is exchanged, and it begins to warm the metal and the clay powder. The stirrer turns at the very least to the most extreme speed of 750 to 1000 rpm. The stirrer measurements are 200 mm with neck length of 10 mm diameter, and wing/cutting-edge measurements are 15 mm width, 25 mm length, and 10 mm breadth. After the liquid fluids are blended in the cauldron utilizing stirrer, it was warmed to accomplish liquid state in the suppress heater to 950°C. Then, it is removed from the heater, and a pink hued powder named coverall is included over the best so the blend holds its temperature. At that point, the blend is made in to specific shape for testing with dimensions of 100 mm × 100 mm × 10 mm; before the charge is filled in the die, the die is heated to around 32°C. Figure 2 shows the surface of aluminum-boron carbide nanometal matrix composites using stir casting method. The fabricated composite material is having superior mechanical strength due to having more flexural strength and improved hardness. It can be used for several applications such as aerospace, transport, and automobile industries. It is the least expensive and high-performance material because it is more flexible and reliable in the fabricated part.

Figure 1: Electrical discharge machine used for this investigation.

2.2. Experimental Investigation. In this work, 16 holes were made on aluminum T6 alloy using EDM machine with the parameters of discharge current (7.5, 10, 12.5, 15 amps), pulse on-time (1, 2, 3, and 4 micro sec), and the tool diameter

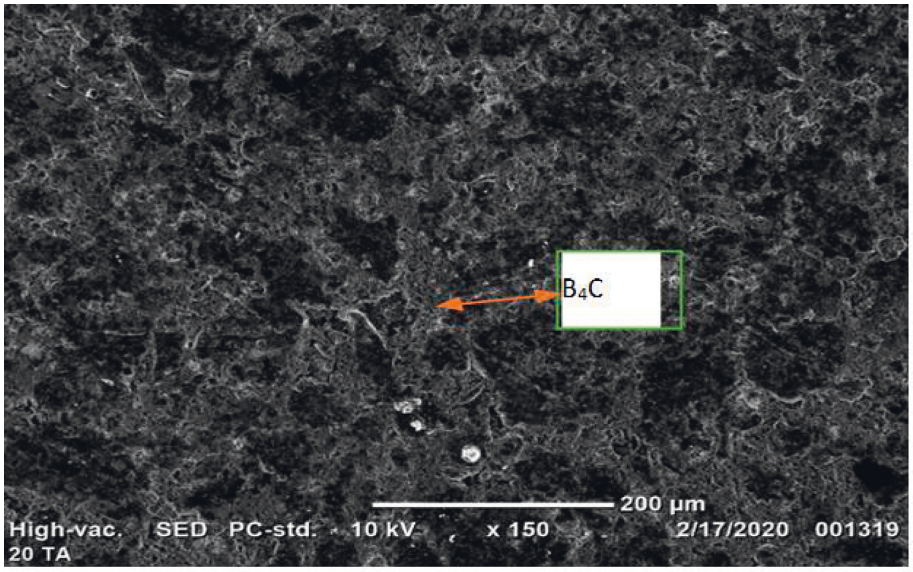

Figure 2: SEM images of fabricated aluminum (7075) B_4C nanocomposites.

(4, 6, 8, and 10 mm). Table 1 shows the electrical discharge machine input parameters and their levels. Figure 3 shows the machined samples and Figure 4 shows the tools used for this investigation [29].

2.3. ANOVA Method. In this work, it was embraced to decide the critical parameters impacting the unpleasantness in the MRF forms. The ANOVA is acquired by separating the deliberate aggregate of the squared deviations from the aggregate mean S/N proportion into commitments by every one of the control factors and the blunders. Table 2 demonstrates the outline of ANOVA for S/N proportions. Examination about the estimation of variety proportion (F), which is the fluctuation of the elements separated by the blunder difference for all control factors, demonstrated a considerably higher impact of pivoting speed and substantially less impact of cutting-edge by materials exploration infiltration profundity. The level of each factor commitment, P, on the aggregate of squared deviations from the aggregate mean S/N proportions delineated the level of impact on the outcome [30].

2.4. Mathematical Modelling and Optimization. The material removal rate and tool wear rate are conducted using fabricated composite material. The results of MRR as a function of tool diameter, current, and on-time were consolidated for machining optimization. This experiment is designed according to the selected 4 levels and 3 factors through the tools of Minitab software, and it is given in Tables 2–7. All the experimental results were analyzed by means of response surface methodology (RSM). RSM is the combination of mathematical and statistical technique which is used to model and analyze the problem. The main objective of the RSM is to optimize the response with respect to the given set of independent variables. ANOVA is a statistical tool which is used to investigate the nature of the input parameter and also identify which input parameter most significantly affects the output parameters. The mathematical expression for MRR and TWR for the composite material is shown in equations (1) and (2), respectively [31].

Table 1: Electrical discharge machining process parameters and their levels.

Electrical discharge process parameters	Levels			
	L1	L2	L3	L4
Tool diameter (mm)	4	6	8	10
Current (amps)	7.5	10	12.5	15
Pulse on-time (micro sec)	1	2	3	4

$$\text{Metal removal rate}\,(MRR) = \frac{W_1 - W_2}{T_d}, \tag{1}$$

where W1 is the weight of workpiece before machining, W2 is the weight of workpiece after machining, and Td is the time taken for machining.

$$\text{Tool wear rate}\,(TWR) = \frac{T_1 - T_2}{T_d}, \tag{2}$$

where W1 is the weight of tool before machining, W2 is the weight of tool after machining, and Td is the time taken for machining. The effects of input parameters of tool diameter, current, and pulse on-time and output parameters such as MRR and TWR are obtained during machining process and different outputs are found for different inputs.

3. Effect of Process Parameters on MRR

Electrical discharge machining was done on aluminum 70775 boron carbide nanometal matrix. Material removal rate was estimated, and the results were recorded in Table 8.

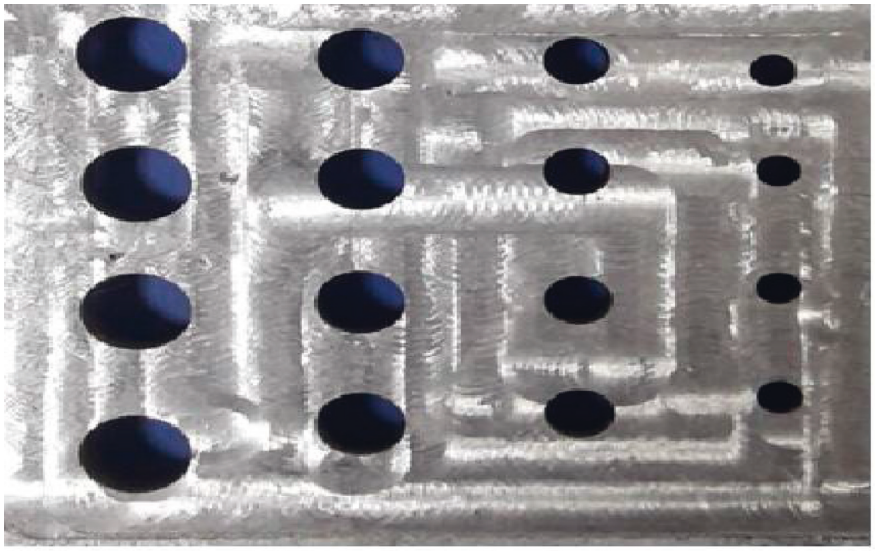

Figure 3: Holes made on T6 aluminum alloy.

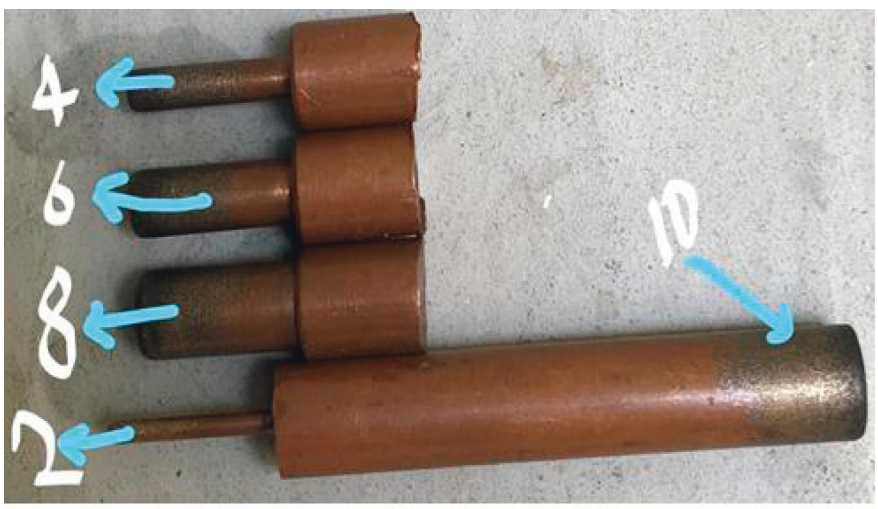

Figure 4: Tools used for EDM process.

Table 2: Larger S/N ratio Taguchi method.

Level	Tool diameter (mm)	Current (amp)	On-time (μ sec)
1	−53.10	−51.59	−50.09
2	−52.22	50.71	50.71
3	48.58	50.09	−51.59
4	48.58	50.09	−50.09
Delta	4.52	1.51	1.51
Rank	1	2	3

Table 3: Response table for means.

Level	Tool diameter (mm)	Current (amp)	On-time (μ sec)
1	0.002250	0.002750	0.003250
2	0.002500	0.003000	0.003000
3	0.003750	0.003250	0.002750
4	0.003750	0.000500	0.003250
Delta	0.001500	0.000500	0.000500
Rank	1	2	3

3.1. Effect of Tool Diameter on MRR. The material removal rate (MRR) has been increased by increasing current which is shown in Figure 5. Initially, there is no more effect on MRR in current 7.5 amps; thereafter, MRR rapidly increased from 0.039 mm to 0.252 mm obtained by increasing current in the range between 7.5 amps and 15 amps. In addition to this, MRR is more in the effect of current ranging between 10 amps and 15 amps [32].

3.2. Effect of Tool Diameter on MRR. TWR seems poor by using current in the range of 7.5–15 amps, as shown in Figure 6. The variations in tool diameter produced different MRR values. It was observed that there is no MRR by 2 mm diameter of tool due to more hardened precipitation matrix, and the MRR is attempted by 4 mm tool diameter [17, 18]. Again, the MRR value has effectively increased by increasing

Table 4: General linear model: MRR versus tool diameter, current, and on-time.

Factor	Type	Levels	Values
Tool diameter (mm)	Random	4	4, 6, 8, 10
Current (amp)	Random	4	1, 2, 3, 4
On-time (μ sec)	Random	4	1, 2, 3, 4

Table 5: Analysis of variance for MRR, using adjusted SS for tests.

Source	DF	Seq SS	Adj SS	Adj MS	F	P
Tool diameter (mm)	3	0.0536962	0.0536962	0.0178987	46.62	0.000
Current (amp)	3	0.0010337	0.030816	0.0010272	2.68	0.141
On-time (μ sec)	3	0.0073486	0.0073486	0.0024495	6.38	0.027
Error	6	0.0023035	0.0023035	0.0003839	—	—
Total	15	0.0643819	0.0941643	0.0217593	55.68	0.168

$S = 0.0195936$, R-Sq = 96.42%, and R-Sq (adj) = 91.06%.

Table 6: Smaller S/N ratio response for the Taguchi method.

Level	Tool diameter (mm)	Current (amp)	On-time (μ sec)
1	25.50	19.17	19.08
2	20.04	19.25	21.86
3	19.08	20.94	18.92
4	13.57	18.83	18.34
Delta	11.94	2.11	3.53
Rank	3	1	2

Table 7: Means response for the Taguchi method.

Level	Tool diameter (mm)	Current (amp)	On-time (μ sec)
1	0.05325	0.11775	0.12550
2	0.09950	0.12425	0.09075
3	0.12050	0.11100	0.13725
4	0.2125	0.13275	0.13725
Delta	0.15925	0.02175	0.04650
Rank	3	1	2

Table 8: MRR and TWR obtained during EDM of Al-B_4C.

S. no.	Tool diameter (mm)	Current (amps)	On-time (micro sec)	Wt. of W/P before (gm)	Wt. of W/P after (gm)	Wt. of tool before (gm)	Wt. of tool after (gm)	MRR (m^3/min)	TWR (m^3/min)
1	4	1	4	118.69	118.08	9.27	9.25	0.061	0.002
2	4	2	3	118.08	117.59	9.25	9.23	0.049	0.002
3	4	3	1	117.59	117.07	9.23	9.21	0.052	0.003
4	4	4	2	117.07	116.56	9.21	9.19	0.051	0.002
5	6	1	3	116.56	115.50	11.38	11.36	0.10	0.002
6	6	2	4	115.50	114.52	11.36	11.33	0.098	0.003
7	6	3	1	114.52	113.51	11.33	11.31	0.10	0.002
8	6	4	2	113.51	112.50	11.31	11.28	0.10	0.003
9	8	1	4	112.50	110.98	14.16	14.12	0.15	0.004
10	8	2	3	110.98	109.49	14.12	14.09	0.14	0.003
11	8	3	2	109.49	108.97	14.09	14.05	0.052	0.004
12	8	4	1	108.97	107.50	14.05	14.01	0.14	0.004
13	10	1	2	107.50	105.82	36.25	36.22	0.16	0.003
14	10	2	1	105.82	103.72	36.22	36.18	0.21	0.004
15	10	3	3	103.72	101.32	36.18	36.14	0.24	0.004
16	10	4	4	101.32	98.91	36.14	36.10	0.24	0.004

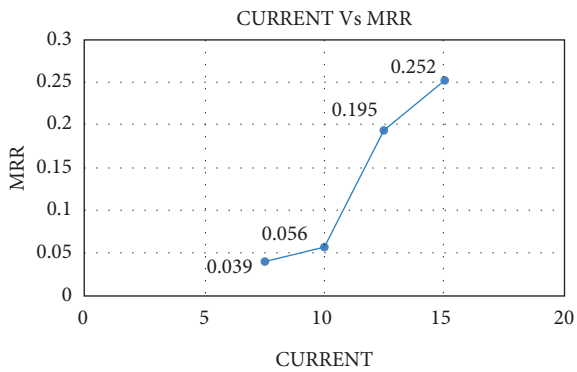

Figure 5: Current versus MRR.

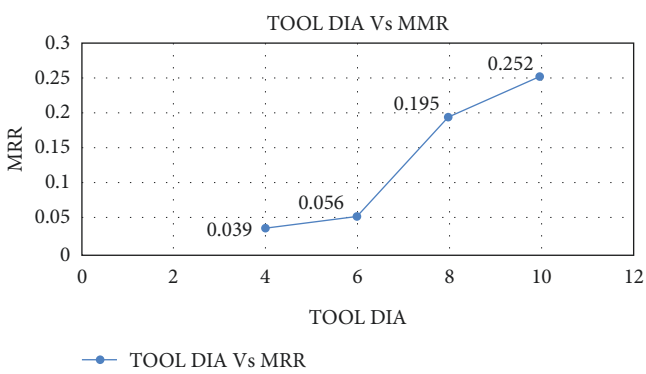

Figure 6: Tool DIA versus MRR.

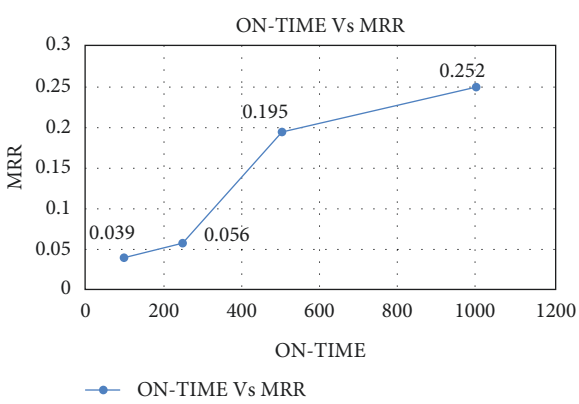

Figure 7: On-time versus MRR.

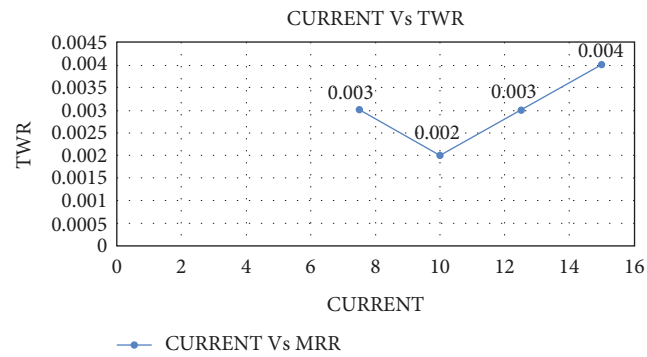

Figure 8: Current versus TWR.

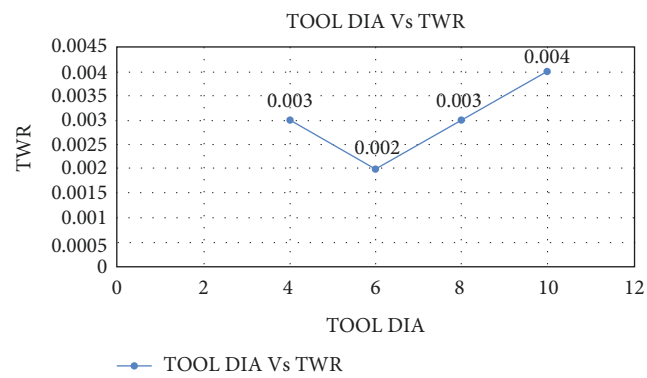

Figure 9: Tool diameter versus tool wear rate.

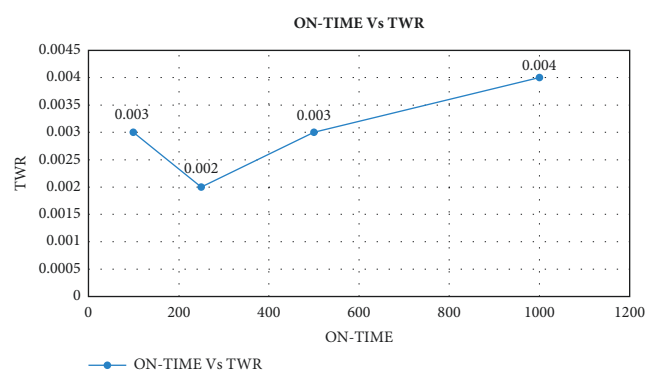

Figure 10: On-time versus TWR.

tool diameter 6 mm to 10 mm. The middle range of the current is more effective in gaining very less TWR. It can be obtained that the TWR values are having more variations with the current input.

3.3. Effect of On-Time on MRR. The MRR was also affected by on-time, as indicated in Figure 7 in the range from 100 to1000 μ·sec. MRR increases more between 400 and 600 μ·sec with increasing on-time sharply in the range from 200 to 500 μ·sec. The middle range of the on-time is more effective in gaining the high MRR than the first and last value [33]. It is shown that the MRR value is proportional to the on-time.

4. Effect of Process Parameters on TWR

Electrical discharge machining was done on the fabricated composites, and the electrode wear rate was calculated and recorded in Table 8.

4.1. Effect of Current on TWR. The effect of current on tool wear rate (TWR) is shown in Figure 8. TWR has been decreased at initial stage when the current ranged from 7.5 amps to 10 amps. The TWR was drastically increased (0.002 mm to 0.004 mm) by keeping on increasing current

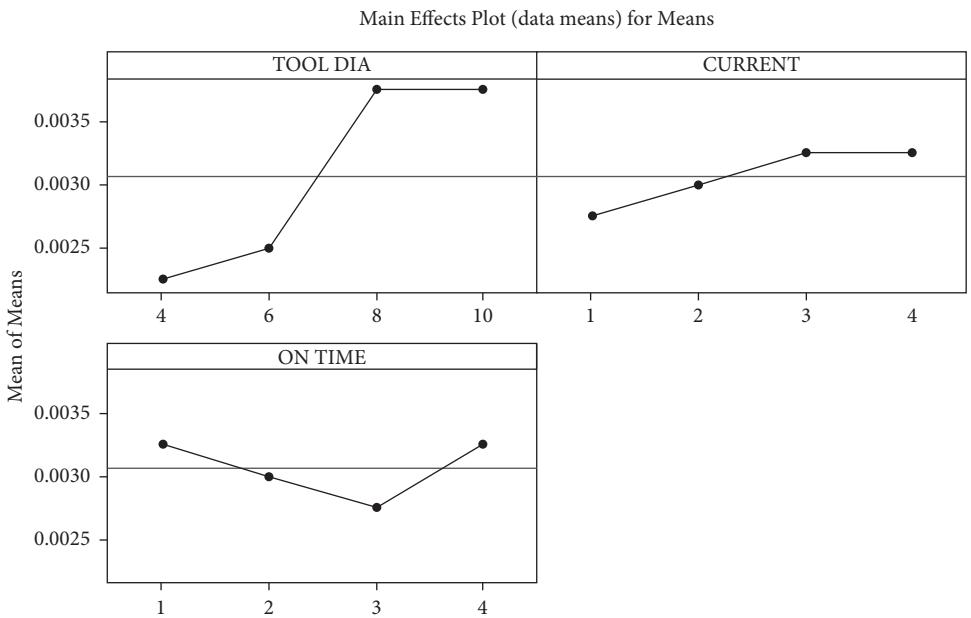

Figure 11: Main effect plot for means (ANOVA method).

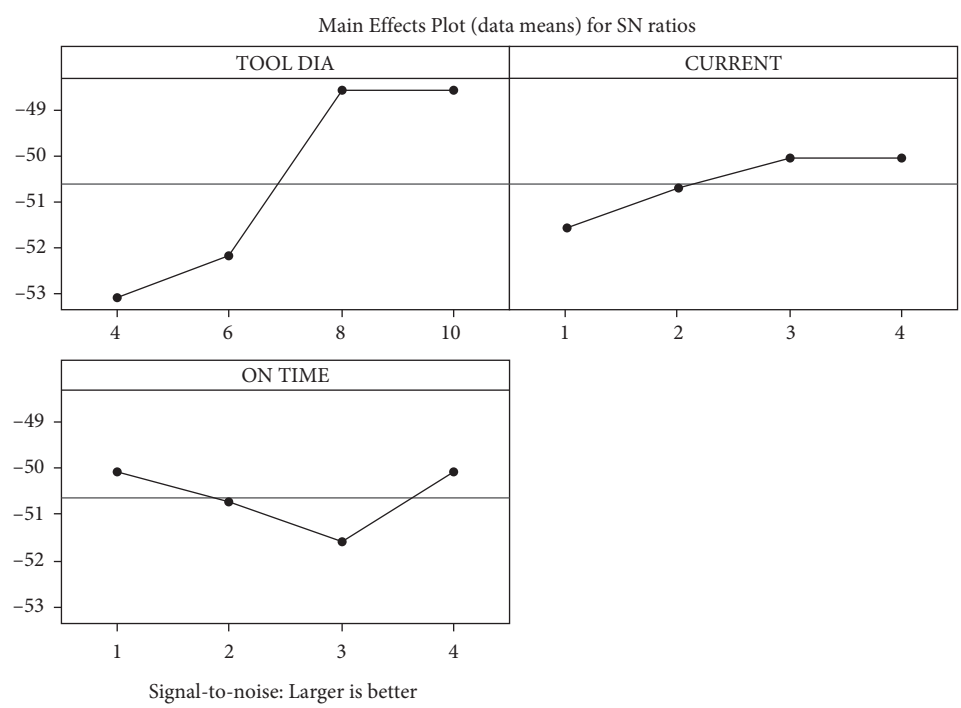

Figure 12: Main effect plot for SN ratio (ANOVA).

effect from 10 amps to 15 amps. It has been observed that one of the significant parameters was the current to control TWR [34].

4.2. Effect of Tool Diameter on TWR. The TWR was also affected by tool diameter as indicated in Figure 9. The variations of TWR have been observed by different tool diameters in the range from 4 mm to 10 mm. The less TWR was observed at 6 mm tool diameter, and more TWR was obtained in 10 mm tool diameter [23, 24]. Initially, it was noted that TWR decreased between 4 mm and 6 mm and after that increased. The middle range of the tool diameter was less effective and also gained less TWR, and the variation of TWR may be dependent on tool diameter [30].

4.3. Effect of On-Time on TWR. It was observed that TWR was also affected by on-time as represented in Figure 10 (ranging from 100 to 1000 μ·sec). TWR decreased with on-time ranging from 100 to 220 μ·sec. Moreover, it has been noted that TWR increased after decreasing as the function of

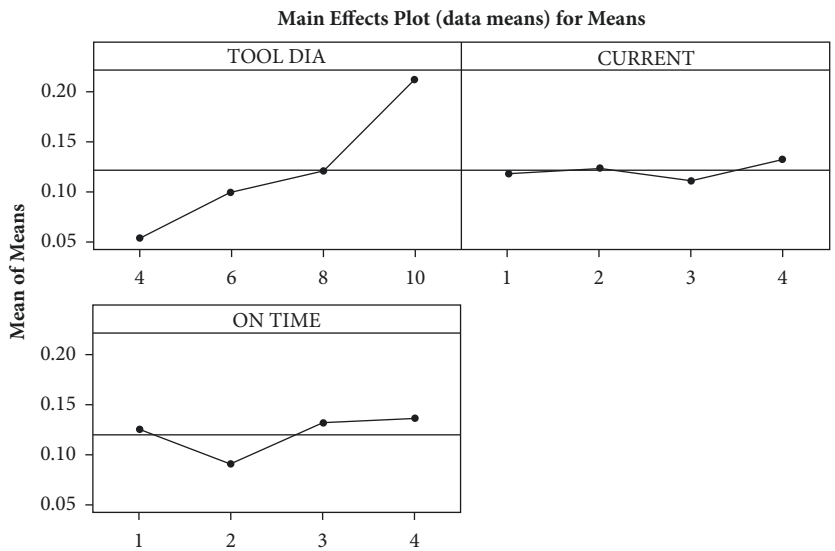

Figure 13: Main effect plot for mean.

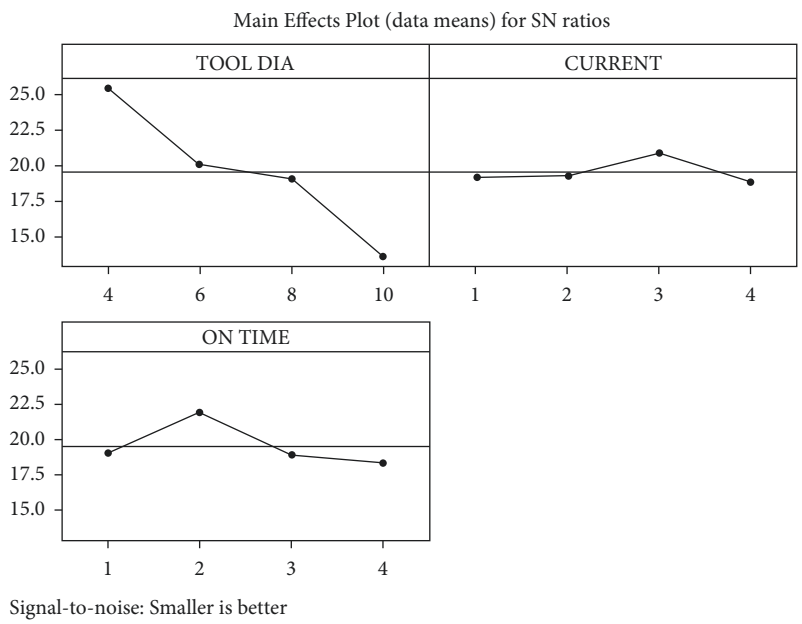

Figure 14: Main effect plot for S/N ratio.

on-time was in the range from 100 to 220 μ·sec. The middle range of the on-time was less effective and gained less TWR. It was shown that TWR obtained no significant result with the function of on-time at 220 μ·sec [19].

4.4. Optimization of Process Parameters. The analysis is based on S/N ratio and means as shown in Figures 11 and 12. This experimental work draws the effect of independent variables of tool diameter, current, and on-time for depending variables of MRR and TWR. Tables 2–7 provide the rank for the independent variables based on the response of MRR and TWR obtained in the prepared specimen. It is evident that the factors mainly considered are MRR and TWR. The concept of "larger is better" shows that the optimal parameter effect represents maximum MRR on the composite [27, 29]. According to this concept, the tool diameter plays a significant role in obtaining maximum material removal rate compared to factors influenced as current and pulse on-time. *F*-test value at 95% confidence level is used to indicate the independent parameters affecting the process. Analysis of variance for MRR using adjusted SS for tests provided that F-value is higher for tool diameter than other factors of machining. Under this optimal condition for minimum TWR, on-time plays a significant role followed by current then tool diameter.

It is evident that the optimum machining parameter is influenced by on-time with dependent parameters such as tool diameter as shown in Figures 11 and 12. Initially, the material removal rate is gradually increasing by varying tool

diameter from 4 mm to 8 mm; after that, it maintains constant material removal rate from 8 mm to 10 mm. Furthermore, the MRR gets increased by keeping on increasing current up to a certain range; after that, it obtains constant current ranging from 3 amps to 4 amps. It has been observed that the MRR gradually decreases to the 1, 2, 3 μ·seconds ranges of pulse on-time; then, it increases by increment of 4 μ·sec as shown in Figures 13 and 14. For TWR, the requirement is to minimize in order to improve the machining efficiency. The criterion selected using the Minitab statistical software is "smaller is better," which states that the output must be as low as possible. The TWR is gradually decreasing by the increment of tool diameter, and also it has been observed that there is less tool wear in the parameter of pulse on-time followed by current obtained by ANNOVA results [33, 34].

5. Conclusion

In the present work, the machining optimization parameters, MRR and TWR, were carried out on Al7075T6 reinforcement of B_4C composite. The fabricated specimen reveals uniform distribution of B_4C particles and very low agglomeration and segregation of particles and porosity. Based on the experimental results, the following conclusions can be observed:

(i) MMC specimen prepared from reinforced particles of nano boron carbide and AL7075T6 weight fraction ranged between 6 wt.% and 94 wt.% using stir casting process.

(ii) The optimized machining parameters were found by Taguchi method in order to increase productivity and minimize production cost. The optimized parameters are tool diameter (10 mm), on-time (3 μ·sec), and current (3 amps) for greater MRR considered as larger value is better.

(iii) The optimum machining parameters were found by Taguchi method in order to reduce tool wear rate with adequate material removal rate which helps to improve modern manufacturing era. Two more combinations provided minimum tool wear rate during machining. Tool diameter (6 mm), pulse on-time (1 μ·sec), and current (3 amps) were considered among the significant factors for minimized TWR.

(iv) The mathematical model was used to determine the MRR and TWR on the fabricated composite material Al7075T6 with B_4C being in the combination of independent factors like tool diameter, current, and on-time.

(v) The analysis of variance (ANOVA) was used to analyze the experimental results to know the percentage of contribution of each parameter on MRR and TWR. The main effect plots for means were used to study the effect of input process parameters on EDM responses, while the S/N plots helped to decide the optimal level of process parameters and their values. The most significant parameter was tool diameter compared to other influenced factors for better metal removal rate, and the specified current range and pulse on-time were important for tool wear rate.

(vi) Under this optimum condition, the prepared MMC was subjected to homogeneous mixing and had superior mechanical properties. MRR was affected due to increase in the pulse off-time, which is dependent on the proportional to the pulse on-time. Increase in pulse on-time for all peak current settings led to increase in MRR and decrease in TWR.

Data Availability

The data used to support the findings of this study are included in the article. Should further data or information be required, they can be obtained from the corresponding author upon request.

Disclosure

This research was performed as a part of the employment of Hawassa University, Ethiopia.

Conflicts of Interest

The authors declare that there are no conflicts of interest regarding the publication of this article.

Acknowledgments

The authors thank Annamalai University and Tamil Nadu Teachers Education University for providing facilities and support to complete this research work.

References

[1] L. Houman and E. C. Jameson, *Dearbern, Michigan, "Electrical Discharge Machining, Tooling, Methods and Applications*, pp. 5–19, Society of Manufacturing Engineers, Michigan, USA, 1983.

[2] M. P. Jahan, M. Rahman, and Y. S. Wong, "Study on the nanopowder mixed sinking and milling micro-EDM of WC-Co," *International Journal of Advanced Manufacturing Technology*, vol. 53, no. 1-4, pp. 167–180, 2011.

[3] N. Beri, S. Maheshwari, C. Sharma, and A. Kumar, *Performance Evaluation of Powder Metallurgy Electrode in Electrical Discharge Machining of AISI D2 Steel Using Taguchi Method*, International Journal of Mechanical and Mechatronics Engineering, 2008.

[4] B. R. Lazarenko, *To Invert the Effect of Wear on Electric Power Contacts,* Dissertation of the All-Union Institute of Electro Technique in Moscow/CCCP, Russian, 1943.

[5] W. J. Wang, P. Shen, J. H. Song, J. Guo, Q. Y. Liu, and X. S. Jin, *Experimental Study on Adhesion Behavior of Wheel/rail under Dry and Water Conditions*, pp. 2699–2705, Wear, 2011.

[6] Z.Bo Yu, J. Takahashi, and K. Masanori, "Dry electrical discharge machining of cemented carbide," *Journal of Materials Processing Technology*, vol. 149, pp. 353–357, 2004.

[7] E. Uhlmann and M. Roehner, "Investigations on reduction of tool electrode wear in micro-EDM using novel electrode

materials," *CIRP Journal of Manufacturing Science and Technology*, vol. 1, no. 2, pp. 92–96, 2008.

[8] H. S. Liu, B. H. Yan, F. Y. Huang, and K. H. Qiu, "A study on the characterization of high nickel alloy microholes using micro-EDM and their applications," *Journal of Materials Processing Technology*, vol. 169, no. 3, pp. 418–426, 2005.

[9] F. M. Hosking, F. F. Portillo, R. Wunderlin, and R. Mehrabian, "Composites of aluminium alloys fabrication and wear behaviour," *Journal of Materials Science*, vol. 17, no. 2, pp. 477–498, 1982.

[10] C. P. Hong, H. F. Shen, and I. S. Cho, "Prevention of macrosegregation in squeeze casting of an Al-4.5 wt pct Cu alloy," *Metallurgical and Materials Transactions A*, vol. 29, no. 1, pp. 339–349, 1998.

[11] T.-R. Lin, "Experimental design and performance analysis of TiN-coated carbide tool in face milling stainless steel," *Journal of Materials Processing Technology*, vol. 127, pp. 1–7, 2002.

[12] G. S. Prihandana, M. Mahardika, M. Hamdi, Y. S. Wong, and K. Mitsui, "Effect of micro-powder suspension and ultrasonic vibration of dielectric fluid in micro-EDM processes—Taguchi approach," *International Journal of Machine Tools and Manufacture*, vol. 49, no. 12-13, pp. 1035–1041, 2009.

[13] N. Tosun, C. Cogun, and G. Tosun, "A study on kerf and material removal rate in wire electrical discharge machining based on Taguchi method," *Journal of Materials Processing Technology*, vol. 152, no. 3, pp. 316–322, 2004.

[14] S. Mitra, G. Paul, and S. S. Nagahanumaiah, "Experimental study on influence of process variables on crater dimensions in micro-EDM of Y-Titanium aluminide"," *AIP Conference Proceedings*, pp. 1315–1181, 2011.

[15] M. S. Murali, G. B. Pavalarajan, and K. P. Rajurka, "A study on process parametrers of ultrasonic assisted micro EDM based on Taguchi Method," *Journal of Materials Engineering and Performance*, vol. 17, pp. 210–215, 2008.

[16] K. M. Patel, P. M. Pandey, and P. V. Rao, "Optimisation of process parameters for multi-performance characteristics in EDM of Al2O3 ceramic composite," *International Journal of Advanced Manufacturing Technology*, vol. 47, no. 9-12, pp. 1137–1147, 2010.

[17] V. Nishant, S. C. Vettivel, Characterization and experimental analysis of boron carbide and rice husk ash reinforced AA7075 aluminium alloy hybrid composite," *Journal of Alloys and Compounds*, vol. 741, pp. 981–998, 2018.

[18] T. Dursun and C. Soutis, "Recent developments in advanced aircraft aluminium alloys," *Materials and Design*, vol. 56, pp. 862–871, 2014.

[19] S. Natarajan, R. Narayanasamy, S. P. Kumaresh Babu, G. Dinesh, B. Anil Kumar, and K. Sivaprasad, "Sliding wear behaviour of Al 6063/TiB2 in situ composites at elevated temperatures," *Materials & Design*, vol. 30, no. 7, pp. 2521–2531, 2009.

[20] S. Manoj, D. Deepak Dwivedi, L. Singh, and V. Chawla, "Development of aluminium based silicon carbide particulate metal matrix," *Composite" Journal of Minerals & Materials Characterization & Engineering*, vol. 8, pp. 455–467, 2009.

[21] H. B. Michael Rajan, S. Ramabalan, I. Dinaharan, and S. J. Vijay, "Synthesis and characterization of in situ formed titanium diboride particulate reinforced AA7075 aluminum alloy cast composites," *Materials & Design*, vol. 44, pp. 438–445, 2013.

[22] C. Mallikarjuna, S. M. Shashidhara, U. S. Mallik, and K. I. Parashivamurthy, "Grain refinement and wear properties evaluation of aluminum alloy 2014 matrix-TiB2 in-situ composites," *Materials & Design*, vol. 32, no. 6, pp. 3554–3559, 2011.

[23] S. C. Tjong and K. F. Tam, "Mechanical and thermal expansion behavior of hipped aluminum–TiB2 composites," *Materials Chemistry and Physics*, vol. 97, no. 1, pp. 91–97, 2006.

[24] C. Wu, K. Ma, J. Wu et al., *Influence of Particle Size and Spatial Distribution of B_4C Reinforcement on the Microstructure and Mechanical Behavior of Precipitation Strengthened Al alloy Matrix Composites*, Materials Science and Engineering, Illinois, 2016.

[25] M. Garcia-Avila, M. Portanova, and A. Rabiei, *Ballistic Performance of Composite Metal Foams*, Composite Structures, California, 2015.

[26] J. Allwyn Kingsly Gladston, I. Dinaharanc, N. Mohamed Sheriff, and J. David Raja Selvam, *Dry Sliding Wear Behavior of AA6061 Aluminum alloy Composites Reinforced rice Husk Ash Particulates Produced Using Compocasting*, Journal of Asian Ceramic Societies, 2017.

[27] A. Baradeswaran, S. C. Vettivel, A. Elaya Perumal, N. Selvakumar, and R. Franklin Issac, *Experimental investigation on mechanical behaviour, modelling and optimization of wear parameters of B4C and graphite reinforced aluminium hybrid composites*, Materials and Design, vol. 63, pp. 620–632, 2014.

[28] A. Baradeswaran and A. Elaya Perumal, "Study on mechanical and wear properties of Al 7075/Al2O3/graphite hybrid composites," *Composites: Part B*, vol. 56, pp. 464–471, 2014.

[29] C. Wu, P. Fang, G. Luo et al., "Effect of plasma activated sintering parameters on microstructure and mechanical properties of Al-7075/B 4 C composites," *Journal of Alloys and Compounds*, vol. 615, pp. 276–282, 2014.

[30] A. Baradeswaran and E. Perumal, *Wear and Mechanical Characteristics of Al7075/Graphite Composites*, Composites: Part B, 2013.

[31] S. D. Saravanan and M. S. Kumar, "Effect of mechanical properties on rice husk ash reinforced aluminum alloy (AlSi10Mg) matrix composites," *Procedia Engineering*, vol. 64, pp. 1505–1513, 2013.

[32] G. Narasaraju and D. Linga Raju, "Characterization of hybrid rice husk and fly ash-reinforced aluminium alloy (AlSi10Mg) composites" materials today," *Proceedings*, vol. 3056, p. 3064, 2015.

[33] A. Baradeswaran and A. Elaya Perumal, "Influence of B4C on the tribological and mechanical properties of Al 7075–B4C composites," *Composites Part B: Engineering*, vol. 54, pp. 146–152, 2013.

[34] R. Amit, K. K. S. Mer, and P. Pawan Kumar, "Synthesis and characterization of mechanical, tribological and micro structural behaviour of Al 7075 matrix reinforced with nano Al2O3 particles," *Materials Today's Office: Proceedings*, vol. 4, pp. 2645–2658, 2017.

Hindawi
Advances in Materials Science and Engineering
Volume 2022, Article ID 1598868, 7 pages
https://doi.org/10.1155/2022/1598868

Research Article

Plastic Waste Management System Using Metal Shredder for Clean Environment

C. Jeyalakshmi,[1] **Manjunathan Alagarsamy**,[1] **R. Kalaiarasan**,[2] **M. Easwaran**,[3] **Yuvaraja Thangavel**,[4] **and Prabhu Paramasivam**[5]

[1]*Department of Electronics and Communication Engineering, K. Ramakrishnan College of Engineering, Trichy, Tamil Nadu, India*
[2]*Department of Electronics and Communication Engineering, M. Kumarasamy College of Engineering, Karur, Tamil Nadu, India*
[3]*Department of Electronics and Communication Engineering, Sastra University, Tanjore, Tamilnadu, India*
[4]*Department of Electronics and Communication Engineering, Kongunadu College of Engineering and Technology, Trichy, Tamilnadu, India*
[5]*Department of Mechanical Engineering, College of Engineering and Technology, Mettu University, Mettu 318, Ethiopia*

Correspondence should be addressed to Prabhu Paramasivam; drprabhu@meu.edu.et

Received 7 June 2022; Accepted 20 July 2022; Published 16 August 2022

Academic Editor: Pudhupalayam Muthukutti Gopal

With the high rise in population and a huge level of unwanted materials, conventional methods of waste disposal are becoming outdated as it involves more manual scavenging work and unwanted human potential. In order to overcome the above manual issues, there is a need to design a machine that can clear the litter and leftover wastes without much involvement of human indulgence. To overcome the above issues, the smart garbage collector was designed and implemented. It consists of a vacuum machine that sucks out leftover trash on the ground. Then, it is lifted to a certain height by servo motors to drop it into the shredding area. The shredder then cuts the waste into very tiny pieces. Then, the waste pieces are transferred to the storage box. This box is placed at an inclined angle to support the disposal of waste without human intervention. The box opening and closing actions are controlled by a servo motor that is placed outside the box and the slide opens vertically to avoid any unwanted residual waste in the storage box. The storage box consists of an ultrasonic sensor to notify the level of waste accumulated inside the box, and when the maximum threshold value is attained, the proposed machine has to dispose of the crushed waste. All the actions of the controller are monitored by a private server hosted on the Blynk platform that can be accessed only by the user. The server can be controlled through a mobile interface that acts as a remote control for the proposed machine. The Local Server is set up using Raspberrypi which enables ease of access to the Blynk server hosted in our home router IP.

1. Introduction

Currently, plastic waste crushers are available in many places, but they are large sized and their usage is best suited for waste processing centers or public places such as railway stations, malls, busy places, and so on. Although effective in plastic waste management, such crushers primarily serve the purpose of recycling the plastic waste that has been manually collected and brought to waste processing centers. For closed-area waste management, their effectiveness is limited because of their costly, bulky nature as well as maintenance requirements. Moreover, if there is no manual labor to collect and deposit waste due to a lack of resources, it presents a cleanliness hazard to the nearby environment.

Already portable waste bottle crusher is designed [1] but it is not moveable and we cannot control it with our mobile phone. For an efficient, affordable solution for plastic waste management in small spaces, a miniature low-cost mobile crusher will be the ideal option, and in this paper, we aim to design a prototype mobile crusher robot that will have the main features of reduced cost, small in size, and move in any direction with user friendly in maintaining plastic wastes. Hence, it provides an attractive design for waste collection in domestic areas. Many problems are arising due to plastics

even for the sea creatures like fish. Though our government is banning one-time use of plastic bags, most countries have made official announcements and warnings, to control the pollution caused by plastic materials.

So, this compact mobile crusher robot will be very valuable to society because of its affordable costs, autonomous functioning, and prevention of manual collection of waste thereby promoting a clean environment. At the national level, in India, used PET bottles are recycled into other useful products like polyester fibers which will be utilized in textiles. The Indian government is now keen on eliminating all single-use plastics from our country by 2022. At present, a common way to recycle plastic waste is mechanical recycling [2] only. At the International level, a documentary on National Geographic depicted a report [3] highlighting plastic waste; only 9% of the plastic has been recycled.

In India, the foremost thing is, in metropolitan cities and in small towns, we have to Install solid waste recycling units [4]. Types of solid plastic waste (SPW) and their origins are discussed [5]. Indian Railways [6] installed a 'PET bottle crushing machine' at many railway stations to minimize plastic waste. The railway authorities announced that if a passenger drops a bottle into the machine, they will avail of a cashback of Rs. 5 in their Paytm accounts. In this paper, we have designed a low-cost machine for a plastic waste crusher that can be utilized for recycling. There are so many products that are also there in the market designed by other inventors which are discussed here.

Once the dustbin is filled, immediately an interrupt signal is sent to a controller which switches on the moving system using RFID tags. And once it is activated, the current system stops and automatically the servo system starts its function to dispose of the collected waste material in some other place [7]. We know that GSM is advantage over ZigBee for short-range communication; here, author [8] uses GSM MODEM, and they used an Infrared (IR) sensor for garbage detection. Another smart bin [9] consists of observing the level of the bin, and it will automatically dispose the waste in the prescribed area and back to its original place. This automatic bin also contains a gas sensor to alarm the nearby people if harmful gas leaks. Multiple dustbins [10] from the various places of the city are connected through IOT. A mathematical formulation technique is introduced to maintain the whole system.

The work related to the current system [11] which was referred in this paper emphasis on dynamic models for collecting unwanted materials. Based on fuzzy credibility theory, the model is created. The author's [12] aim is to achieve a centralized real-time management system. Both the municipal and the residents thus benefit from an integrated program resulting in substantial cost savings and less urban emissions. The planned system would be able to simplify the cycle of solid waste disposal and the monitoring of the total collection method utilizing the IoT. In this paper [13], authors introduced 2 routing methods so as to fulfill solid waste disposal in a smart city. For detecting the level of the garbage, IR sensors are used in this [14] system. The pH sensor is also utilized to detect degradable or nondegradable material. Every such dustbin [15] is provided with a light sensor part at several distances from the base of the dustbin. Hence, as soon as the bin is completely filled, the GCV comes and such that there is no chance for spillage. In this paper [16], author has designed an electronic model to empty the bin as soon as it is filled. Hence, the waste can be managed efficiently using the proposed system. To manage the waste problem, IOT-based approach is proposed [17] by the author. To connect the sensor and the IOT module, an advanced microcontroller is utilized as a visual connecting device. This is also implemented in the native village of the author.

In order to overcome the difficulties such as the absence of channelization of collected waste and a mechanism to separate waste, in this paper, we proposed a wirelessly controlled garbage collector that operates only through a private server hosted in Raspberry Pi by using the Blynk controlling software. All the commands to the microcontroller are sent through the mobile user interface. The trash is sucked out by using a vacuum, and the servo motors navigate it to the crusher where the trash is crushed to fine pieces and dropped into the storage chamber beneath the board. The storage chamber consists of a sensor to monitor the level of trash accumulated in the storage and consists of a servo motor to open and close the cover of the chamber to get out the trash. The collector transports by 4 DC motors controlled by a motor driver given a power supply by 12 V batteries. The Smart Garbage Collector can be used in places of mass waste gathering such as railway stations, malls, and theatres.

2. Design Methodology and Implementation

Figure 1 shows the process diagram of the current device using an Arduino microcontroller. Initially, the plastic bottles are sucked by the garbage suction, and for this, most of the power is needed. These wastes are crushed in the shredder section and collected in the storage section. A plastic shredder shown in Figure 2 is a mechanical device that is used to cut the plastic into small pieces for recycling process. It consists of numerous steel blades which are capable of cutting the plastic pieces. There are two shafts structure in it. Each shaft consists of an equal number of blades in it. Both the shafts rotate towards them or away from them. The blades are correctly fixed perfectly so that they will not strike each other. The shafts are controlled by the AC motor. We power the motor using a single-phase AC power supply (240 V–50/60 Hz). Using many gears, the shafts and motor will be connected. In general, the shredding method produces raw material to be utilized further for manufacturing, at the same time finished products like landscape protection. Distinct terms are used to define size reduction devices, such as grinders, chippers, granulators, and hammer mills. The main motto is to reduce the size of the given input material.

Any automated system makes use of a microcontroller or digital signal processor to control the real-time signals received from the inputs. It is converted into appropriate data and controlled accordingly. The microcontroller used in this investigation is Arduino uno which is clearly shown in

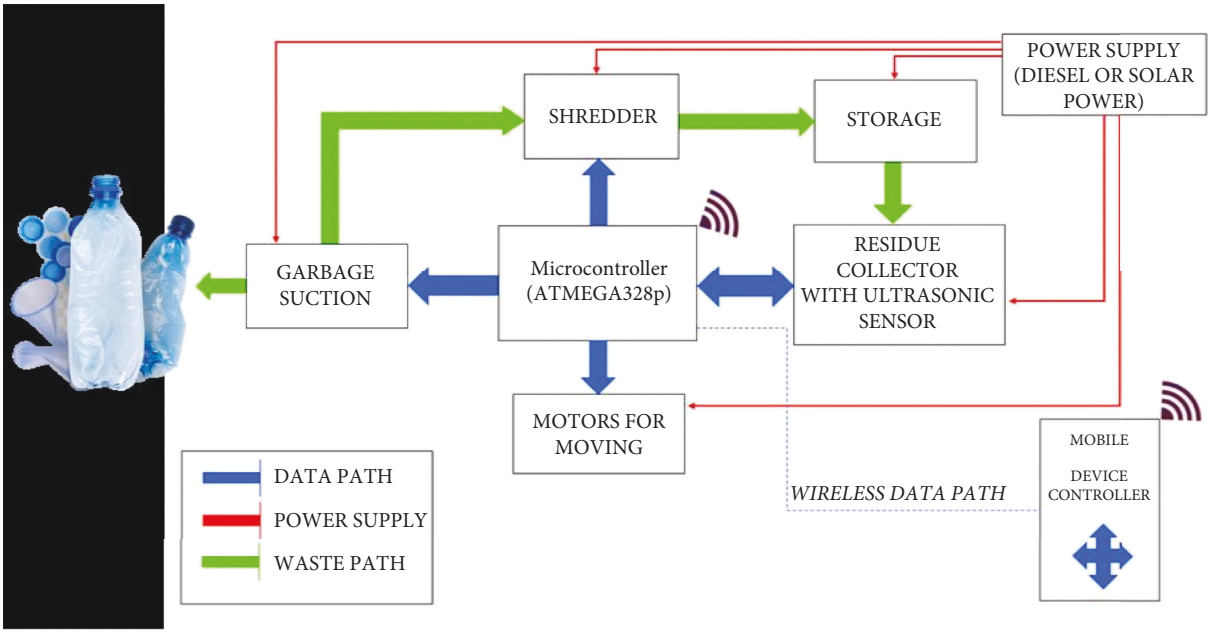

Figure 1: General process diagram of the smart garbage collector.

Figure 2: Front view of the shredder.

Figure 3 and has fourteen input and output pins. Out of these fourteen pins, six are utilized as pulse width modulated outputs, and six can be used as analog inputs. This board also contains a sixteen megahertz ceramic resonator, a universal serial bus connection, and a provision for reset function. In this Arduino board, there are two receivers and transmitter Light Emitting Diodes which can be flashed when required. i.e., when internally when data are transmitted via the USB to the serial chip and from the USB to the computer system. Through the Arduino digital pins, serial communication is made possible through the software serial library. It also supports the interintegrated circuit and serial peripheral interface protocol for serial data transfer. As we know, IIC is slower than SPI since it uses four wire protocols for data transfer.

Another microcontroller unit shown in Figure 4 is ESP8266 which can be automatically controlled through our local Wi-Fi network or from the Internet. The above ESP-01 module has general purpose input and output pins which will be suitably programmed to operate an LED or a relay via the Internet. The module will be programmed by an Arduino USB to TTL converter via the serial pins. The ESP8266 module works with 3.3 V only so that higher than this supply will damage the circuit.

Blynk shown in Figure 5 is a new platform that allows us to quickly build interfaces for controlling and monitoring our hardware projects from our iOS and Android device. After downloading the Blynk app, we can create a project dashboard and arrange buttons, sliders, graphs, and other widgets onto the screen. Using the widgets, we can turn pins on and off or display data from sensors. Blynk supports hardware platforms such as Arduino, Raspberry Pi, and similar microcontroller boards to build hardware for our projects.

The user mobile controller and the garbage collector will be connected to the same network. A private server is created using the desired microprocessor (Raspberry pi). The Raspberry pi will act as the private domain of the server (local server). We can also use a separate mobile application in order to give the control signals to the garbage collector. Once the garbage is detected by the user, they send the control signal from the mobile controller to this waste crusher unit using the desired mobile application. The signal will be detected by the transceiver module in the garbage collector. First, the user will send the moving commands to the crusher to move to the desired position and send the control signal for the movable handle which carries the suction pipe. The handle will move downwards making the suction pipe nearer to the garbage. Then, the user will send the control signal for the suction module such that the garbage will get stacked to the mouth of the suction pipe. By sending the signal to the suction pipe, the garbage will correctly fall in the area of the shredder. The shredder will be activated by the user control, such that it will move in a forward direction so that the garbage will be cut into small pieces. The output of the garbage will get

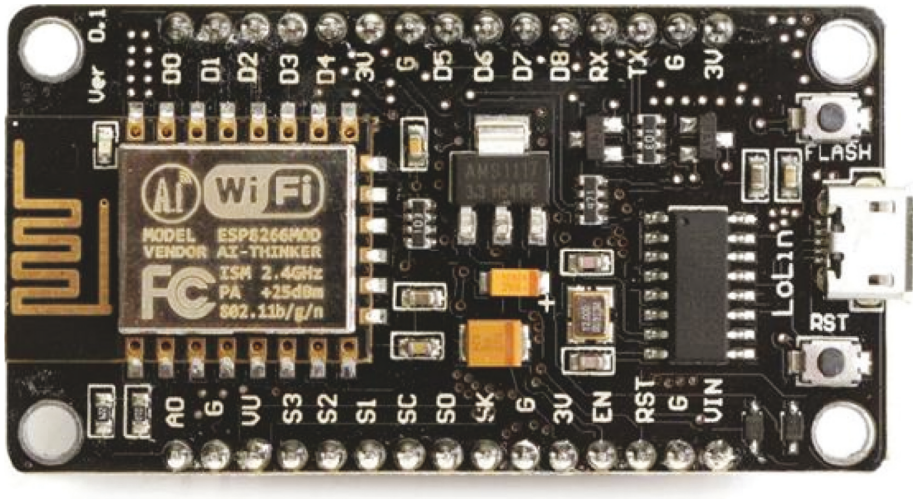

Figure 3: Arduino board.

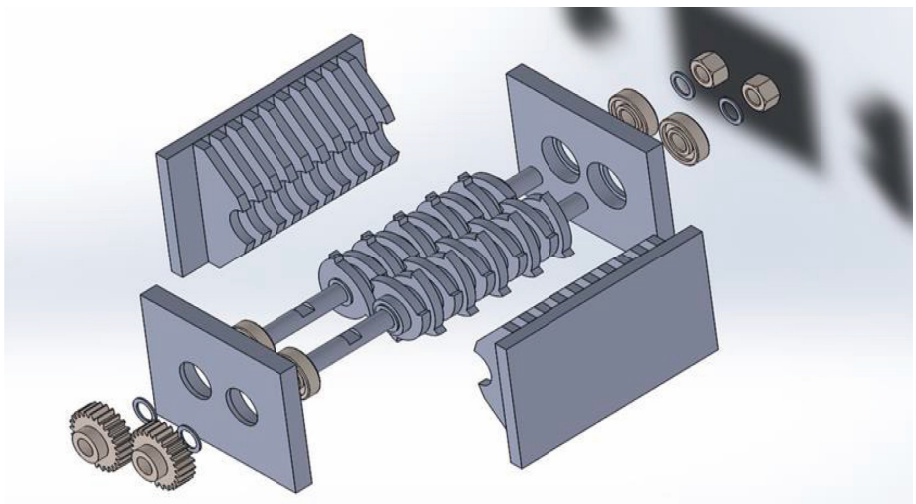

Figure 4: Node MCU ESP8266.

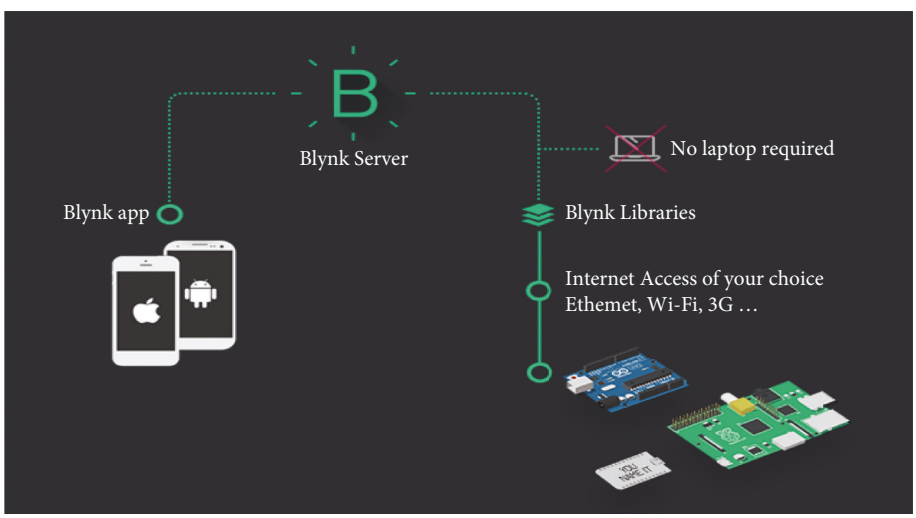

Figure 5: Front panel of Blynk app.

Figure 6: Suitable materials for crushing.

stored in the waste storage box below the crusher unit. Hence, our main motto will be completed. Once the waste storage box will get filled, the user will get a notification on the mobile device because we have employed an ultrasonic sensor in the waste storage box. So, the user can give the control signal to the waste storage box lid, which will be controlled by the servo motor. So that the lid will open and the wastes will fall outside, especially in the recyclable area. Then, the waste will be recycled into newer things. Specification of the proposed garbage collector device is given as follows:

(i) Suction power: 800 W
(ii) Waste storage: 0.45–1 kg of plastic
(iii) Shredder capacity: it can crush up to 0.25 mm to 1.5 mm bottle wall thickness
(iv) Weight machine can carry up to 20 kgs
(v) Battery power: 12 v 1.3 A

3. Results and Discussion

The input to the shredder consists of plastic, paper, and chart board materials that can be crushed to small pieces by the metal shredder, for example, paper cups, water bottles, broken chart boards, and plastic cans.

Any one of the trash shown in Figure 6 is first absorbed by a vacuum cleaner guided by a servo motor and it is lifted up to the level of falling into the shredder. The shredder then crushes the trash into pieces and drops it down on the storage box below the surface of the holder board. The controls are all manually monitored to avoid any situation that leads to accidental crushing up of any other materials not specified. The complete process is shown step by step in Figures 7–9. The minimum power to be used in the suction pump is 800 W.

The storage box below the surface of the holder board is placed at an angle such that when the door of the box is opened vertically upwards, the trash slides out of the chamber without any residual deposits.

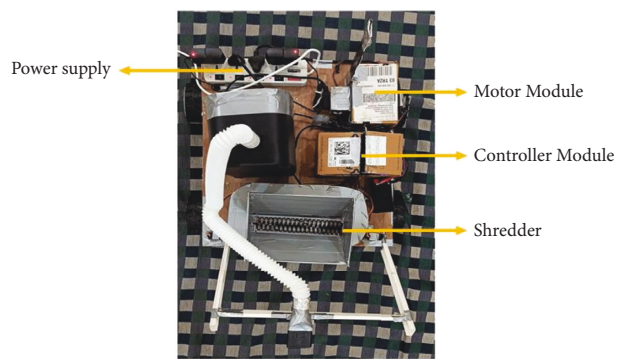

Figure 7: Shredder pickup path.

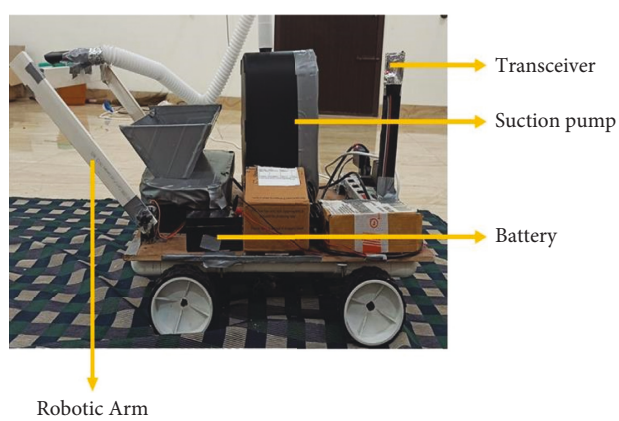

Figure 8: Full view of mobile crusher.

The box also contains an ultrasonic sensor to measure the amount of trash deposited into the storage box. Once the threshold level is reached, the system disposes of the waste into a baggage area. The method of disposal comprises of disposing the trash into a garbage area that arises after the microcontroller is notified of a threshold level of waste in the storage box. Then, it again returns to the left-off position and continues to clean off the remaining disposed wastes. To

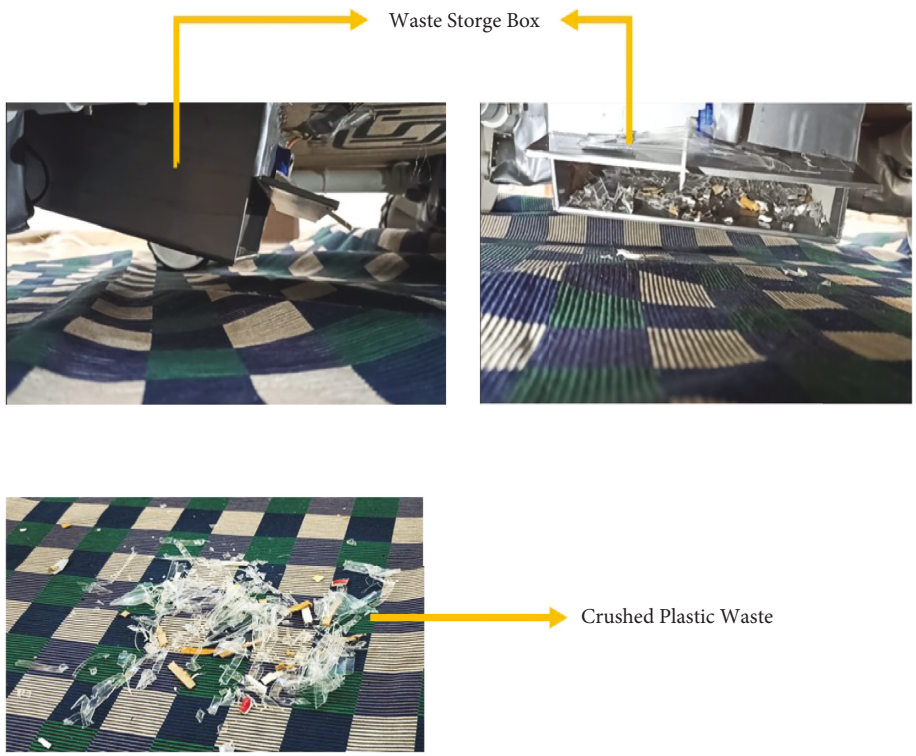

Figure 9: Sample of crushed output.

increase the capacity of the existing garbage collector, the following modifications can be done. (i) Normal Gear motors can be changed to planetary gear motor which will increase the torque so it can carry up to 100 kgs. (ii) Battery capacity needs to be increased from 1.2 A to 7.5 A and lead acid battery is changed to a lithium-ion battery. (iii) Storage capacity can also be increased. (iv) Advanced micro-controllers can be utilized to increase the processing speed.

4. Conclusion

This prototype model for waste collection is the order of the day. Last year only our government banned all plastic materials. However, for the current situation, again large number of plastic covers, masks, and virus protective dresses made the environment worse. So, this prototype is not just a hobby but a real-time useful environment-friendly device that will be utilized for real-time waste collection which will be made automatic with additional features in near future. Real-time application examples of the proposed compact mobile crusher are individual homes, small community areas, and small institutions such as temples, rural, or semiurban areas that are present within out-of-city limits. In order to fetch the waste in the interior places also, automatic control switch is provided, and whenever the machine is in on condition, it will move to the particular place and collect the waste. Hence, the proposed crusher behaves as a robot in cleaning the waste provided we can adjust the capacity according to our purpose. If we utilize the same for domestic purposes, it completely picks up the waste thereby reducing the burden of the manual workers. Initially, a prototype is designed to clean the plastic waste which will be extended to other materials also.

Data Availability

The data used to support the findings of this study are included in the article.

Disclosure

This study was performed as a part of the Mettu University, Mettu, Ethiopia.

Conflicts of Interest

The authors declare that they have no conflicts of Interest.

Acknowledgments

The authors would like to thank the K. Ramakrishnan College of Technology for their excellent support for the submission of their papers.

References

[1] R. Darshan and S. Gururaja, "Design and fabrication of crusher machine for plastic wastes," *International Journal of Mechanical and Production Engineering*, vol. 510 pages, 2017.
[2] 2022, https://greencleanguide.comindia-to-eliminate-single-use-plastic-by-2022.
[3] D. Oliver and A. Prieto, "Plastic Waste Management, a Matter for the Community," *Microbial Biotechnology*, vol. 12, pp. 1–3, 2018.

[4] R. Joshi and S. Ahmed, "Status and challenges of municipal solid waste management in India: a review," *Cogent Environmental Science*, vol. 2, no. 1, Article ID 1139434, 2016.
[5] K. Ragaert, L. Delva, and K. van Geem, "Mechanical and chemical recycling of solid plastic waste," *Waste Management*, vol. 69, pp. 24–58, 2017.
[6] 2019, https://swachhindia.ndtv.com›Plastic Waste.
[7] S. Thiyagesan, R. Shankaran, and V. Kumar, "Smart garbage collector and disposer," *International Journal Of Current Engineering And Scientific Research*, vol. 5, no. issue 2, 2018.
[8] P. Morajkar, V. Bhor, D. Pandya, and A. Deshpande, "Smart garbage management system," *International Journal of Engineering Research and Technology*, vol. 4, no. 3, 2015.
[9] S. Sreejith, R. Ramya, and A. Sanjay kumar, "Smart BIN for waste management system," in *Proceedings of the 5th International Conference on Advanced Computing & Communication Systems (ICACCS)*, Coimbatore, India, March 2019.
[10] H. Saha, S. Auddy, S. Pal et al., "Waste management using internet of things (IOT)," in *Proceedings of the 8th Annual Industrial Automation and Electromechanical Engineering Conference (IEMECON)*, Bangkok, Thailand, August 2017.
[11] T. Anagnostopoulos, A. Zaslavsky, and A. Medvedev, "Robust waste collection exploiting cost efficiency of IOT potentiality in smart cities," in *Proceedings of the 1st IEEE International Conference on Recent Advances in Internet of Things, RIoT*, Seoul Republic of Korea, June 2015.
[12] M. S. U. Maheswari, V. Rohini, G. Surdeep, and M. Varshini, "Smart waste management and predicting BINS with high waste index," *International Journal of Innovative Technology and Exploring Engineering*, vol. 9, no. 7, pp. 482–485, 2020.
[13] T. Vasileios, "Anagnostopoulos and arkady zaslavsky "effective waste collection with shortest path SEMI-STATIC and dynamic routing" 4," *LNCS*, vol. 8638, pp. 95–105, Department of InfocommunicationS Technologies, ITMO University, St. Petersburg, Russia, 2014.
[14] C. Ishwarya, S. Jayashree, and P. Yesodha, "Microtronics technologies," *GSM based garbage and waste collection BINS overflow indicator*, vol. 32 pages, 2017.
[15] K. G. Narendra, C. Swamy, and K. N. Nagadarshini, "Efficient garbage disposal management in metropolitan cities using VANETs," *Journal of Clean Energy Technologies*, vol. 2, no. 3, pp. 258–262, 2014.
[16] I. R. Khan, M. Alam, and A. Razdan, "Smart garbage monitoring system using IoT," *SSRN Electronic Journal*, 2021.
[17] A. Maheshwari, A. Tyagi, and N. Joshi, "To improve efficiency of garbage collection system for smart cities: review paper," in *Proceedings of the International Conference of Advance Research & Innovation (ICARI)*, Punjab, India, March 2020.

Hindawi
Advances in Materials Science and Engineering
Volume 2022, Article ID 8579180, 13 pages
https://doi.org/10.1155/2022/8579180

Research Article

Hybrid RSA-ROA Scheduling Algorithm for Minimization of Power Loss and Improving the Renewable with Sustainable Energy Harvesting in Power System

Cuddapah Anitha,[1] **Virendra Swaroop Sangtani**,[2] **Ajay Kumar Bansal**,[3] **Mahaveerakannan R.**,[4] **R. Rajesh Sharma**,[5] **and Saravanan M. S.**[6]

[1]*Department of Computer Science and Systems Engineering, Sree Vidyaniketan Engineering College, Tirupati, Andhra Pradesh, India*
[2]*Department of Electrical Engineering, Swami Keshvanand Institute of Technology, Management & Gramothan, Jaipur, Rajasthan, India*
[3]*Department of Electrical Engineering, Central University of Haryana, Mahendergarh, Haryana, India*
[4]*Department of Computer Science and Engineering, Saveetha School of Engineering, Saveetha Institute of Medical and Technical Sciences, Chennai, Tamil Nadu, India*
[5]*Adama Science and Technology University, Adama-1888, Ethiopia*
[6]*Department of Artificial Intelligence, Saveetha School of Engineering, Saveetha Institute of Medical and Technical Sciences, Chennai, India*

Correspondence should be addressed to R. Rajesh Sharma; sharmaphd10@gmail.com

Received 21 June 2022; Accepted 16 July 2022; Published 16 August 2022

Academic Editor: Vijayananth Kavimani

Recently, it has been very common for wireless sensor networks (WSNs) to be used in several applications (surveillance, home automation, and vehicle tracking), as well as in environmental monitoring and wildlife tracking. A typical sensor node has a limited amount of battery life. To overcome this, one method is to use an energy harvesting device to recharge the batteries of sensor nodes. Energy reaping WSNs still lack intelligent strategies for intelligently using both energy organization and harvesting systems, though. To maximize the harvesting of renewable energy sources (RES) and minimize power scheme losses, this study provides an optimal generation scheduling strategy for a power scheme combined with distributed generation (DG) and sustainable energy storage systems (ESSs). The major goal of this work is to make it possible to use RES in a power system while still maintaining a profit. By using ESS management, we are able to get the most out of our renewable energy resources and maximize our harvesting potential. It is also possible to reduce operating losses in the power system by scheduling ESS and controlled generation at the optimal times. Near global optimal solutions are sought using a hybrid algorithm combining Reptile Search Algorithm and Remora Optimization Algorithm (RSA-ROA). The power system operational restrictions are taken into account when formulating and evaluating the optimization issue. It has been tested in a variety of circumstances to see if the proposed strategy is effective. The proposed model has 0.260 J of remaining energy, when the number of rounds is 5000, but the existing techniques have only 0.110 J and 0.045 J for the same number of rounds.

1. Introduction

WSNs are made up of a limited sum of low-cost and low-power sensors. Multiple tasks such as data sensing and simple computing can be performed by the network, as well as short-distance transmission and storage for temporary data [1, 2]. In addition to health monitoring, transportation tracking, environmental monitoring, and border surveillance, it is employed in various uses of Internet of Things [3]. Energy consumption in sensor networks is closely connected

to their longevity because of the battery's major role in supplying power. Sensor nodes in traditional sensor networks have been batteries with a finite capacity. Although the sensor nodes have a partial battery life, the normal application will have a limited battery life as well. It takes a long time to replace the batteries of sensor nodes and making the network sustainable is often a challenging task, because they are often located in remote locations. As a result, prolonging the life of a network is a difficult task when faced with energy restrictions [4].

Researchers have found a way around the restrictions of energy harvesting technologies by adopting this method. An energy collecting technology can be used to power nodes indefinitely. The network's energy consumption can be optimized for maximum efficiency. Increasing the sampling frequency or duty cycle of a sensor node, for example, or increasing the transmission power to reduce the energy harvesting device is more favourable. Renewable energy resources include the energy gathering system [5]. A resource's ability to be replenished over time by natural processes is what is meant by the term "ambient energy resources." Sensor nodes are powered by a variety of sources, including photovoltaics, wind turbines, heat pumps, and other mechanically driven devices such as batteries [6–8]. Photoelectric cells transform the solar radiation into electrical energy, which is then used in an outdoor system during the daytime rather than at night or in overcast conditions [9]. Wind energy is rehabilitated into power energy by turbines in the wind energy-based system. There are two ways to shift the turbines: horizontally and vertically. It also uses piezoelectric or electrostatic devices to turn heat into electricity, as well as TEGs to convert mechanical electricity. As a result of the unpredictable nature of energy collecting, managing energy supplies is a difficult endeavour. Wind and solar energy harvesting systems [10–13] use prediction as a well-known approach of managing renewable resources. In contrast, several contemporary WSNs that harvest energy lack a smart approach for judiciously utilizing the management and harvesting systems. Energy harvesting and battery replacement will be discussed in detail in the following paragraphs.

Battery Replacement. An efficient and successful operating system requires regular battery replacement. The central remote station constantly monitors the battery's condition. Maintenance personnel or a team may be dispatched to the remote location to replace a low-battery device. To avoid this problem, an additional battery or energy source should be added to the sensor node. This solution is either practical, cost-efficient, or flexible for effective and sustainable WSNs because of the high energy consumption of sensor nodes in dynamic operations.

Energy Harvesting in Sustainable Manner. Wind, solar, water, and other natural energy bases can all be used to generate electricity, as well as pressure, heat, and vibration. Low-power sensor nodes can now last an indefinite amount of time thanks to energy harvesting, which has to be done in a sustainable manner. Single-source energy harvesting is a superior option for long-term WSN sustainability. When adopting single-source energy harvesting, however, irregular and insufficient battery charging might have a negative impact on the system's stability [14–16].

With the hybrid technique of energy harvesting, it is possible to build and execute an enhanced WSN that can increase the lifespan data collection, actuation, and processing, and transmission is another option for a WSN that is effective, long-lasting, and sustainable. We therefore need clever solutions. Optimal generation scheduling is the focus of this research, which examines the best way to maximize renewable energy gathering while minimizing power losses. It is possible to identify the most important variables in RES-based electricity generation with DG and ESS using the proposed method. In practice, however, DG accommodations and dimensions cannot be modified due to producer capacity restrictions and economic benefit. DGs, in particular, are always situated in a certain location that cannot be controlled. Producers expect maximum DG outputs, while the power system's loss may rise because of this. The output power of DGs is therefore adjusted in a way that maximizes the gathering of renewable energy. Thus, enough power can be given to the loads, and extra power can be stored in ESS (Excessive Power Storage).

1.1. Organization of This Paper. The related study of the existing technique, which is related to our research study is mentioned in Section 2. The brief explanation of the proposed model is depicted in Section 3, and the validation analysis is presented in Section 4. Finally, the conclusion of the research work is given in Section 5.

2. Related Works

WSN generation depends on duty cycle, deployment type, and battery state-run of charge (SoC), according to Sharma [17]. Using ambient energy reaping to charge WSN node batteries, we provide a novel solution to the design challenge of low energy availability (LEA). Nevertheless, solar energy harvesting is fraught with difficulties, such as the inconsistency of the power supply and the inability to accurately estimate the sun's output, as well as problems related to temperature and the efficiency of the solar panels. The goal of this research is to extend the lifespan of WSNs by gathering solar energy. As shown by our simulations, the sensor network lifetime can be extended to an indefinite level, with an optimum duty cycle of 100%, up to 115.75 days. SEH-WSNs also saw an increase in network speed from 100 to 160 kilobits per second.

Liu [18] suggests a two-stage strategy for dealing with the dynamics of renewable energy. As part of the network preparation phase, we apply the primal cut approach to resolve an RO (two-stage) problem and build an efficient data gathering tree. With minimum overhead, we offer an algorithm that may maximize the sample rates of nodes based on the observed recharge rates. Network performance is maximized under renewable energy uncertainty by not having to reconfigure routing structure during operational

phase. The proposed strategy is shown to be successful and robust in coping with the fluctuation of renewable energy through numerical findings.

According to Gupta [19], there is an adaptive. Multi-sensing solutions based on network and node-level partnerships are proposed to boost energy efficiency. Instead of relying on cross-correlation among the recorded strictures at each node, the latter relies on nodes with active sensors (as determined by MS). MS-sensing SP's quality can be improved by using a retraining logic. Multisensor data fusion is presented to estimate all parameters across field nodes utilizing undersampled signals from the MS-CC active sensors.

A new protocol was proposed by Sah [20] for energy harvesting clusters (NEHCP). An algorithm called hierarchical clustering routing is used to implement the NEHCP, which employs solar EH. It is the cluster head's job to convey data collected from the sensor nodes back to the central station. The beginning phase, setup phase, and data transmission phase are all parts of the NEHCP algorithm. The EH-WSN feature gives better results in terms of network longevity because it is unique. The EH-WSNs' energy consumption is balanced and network efficiency is increased by the simulation element of this technology.

Two-port hybrid diodes and an adaptive supercapacitor buffer energy management technique are presented by Qi [21] to accomplish combined optimization. In the hybrid diode semiactive topology, the bidirectional DC/DC converter is replaced by a unidirectional DC/DC converter and two diodes instead of the current two. As a result, 15.5 percent less energy is lost, and the control system's cost, size, and complexity are all reduced. Adaptive supercapacitor buffer energy organization is also being developed using the novel architecture to reduce battery degradation. There is a minimum threefold increase in battery life compared to the current hybrid energy storage devices in simulations and experiments. Sensor nodes powered by sunlight for the first time have been made possible.

A wearable medical sensor device was designed by Mohsen for long-term medical use [22]. The acceleration of a human body can all be monitored in real time using this method. There are two sensors in this system: one for temperature and one for pulse oximetry. There is also a microprocessor and a Bluetooth low energy module in there. Batteries are required to power this sensor system, but they only last so long. An energy harvester that can power an array of wearable medical sensors is therefore being developed. The sensor system's lifespan can be extended thanks to this harvester, which generates enough energy to run the scheme. The suggested hybrid energy harvester is made up of two supercapacitors, a DC-DC boost converter and two flexible solar panels. For a total of 46 hours of operation, the sensor system was put to the test in active-sleep mode, where it consumed an average of 2.13 mW over a single hour. Finally, the findings of the experiments show that the medical sensor system may be monitored for an extended period of time.

A multihop data forwarding algorithm and decision-making model for the selection of data forwarding nodes were developed by Wu [23] for WSN powered by solar cells and batteries. The Pareto optimal collection of solutions can be found using the particle swarm optimization method. Energy supply models are developed after an investigation of solar energy acquisition aspects. An algorithm for forwarding information in response to changes in network energy consumption and delay has been demonstrated in simulated results.

3. Proposed System

In this section, first mathematical models for sustainable ESS and RES are explained.

3.1. Mathematical Ideal. Equations (1) and (2) describe the optimal generation preparation problem for maximizing energy gathering and reducing losses.

$$\text{Maximize } f_1 = \max\left(P_{\text{DG dispatch}}\right), \tag{1}$$

$$\text{Maximize } f_2 = \min\left(P_{\text{Lossline}}\right). \tag{2}$$

There are two sets of proposed goal functions: f_1 and f_2. The power system's P (DG dispatch) harvests renewable energy. In a transmission line, P (Loss line) represents the amount of power lost (MW).

3.1.1. Renewable Energy Harvesting Model. It is a fact of life that DGs are continuously run at their supreme rated power production. This could lead to unfavourable conditions for the power system, such as increased power losses. On the other hand, DG power cannot be directly controlled by the utilities. Renewable energy harvesting includes two components: DG dispatch of power and storage of power, which is the amount of power that can be stored between P (DG dispatch) and the maximum power that can be generated. ESS will store the extra power. The following is the function for gathering renewable energy sources:

$$P_{DG\,\text{dispatch}} = P_{DG\,\text{dispatch}} - P_{\text{storage}}. \tag{3}$$

Excess power is stored in ESS, where it is closely linked to power loss. These losses can be broken down into battery and converter losses, respectively [24], for the electric energy storage system (ESS). The following formula can be used to compute the ESS's loss:

$$\begin{aligned} P_{\text{LossESS}} &= P_{\text{Lossbatter}} + P_{\text{Lossconverter}}, \\ P_{\text{Lossbatter}} &= I_{\text{battery}}^2 \times R_{\text{battery}}, \\ P_{\text{Lossconverter}} &= P_{sb} + \left(k\% \times P_{\text{storage}}\right), \end{aligned} \tag{4}$$

where the battery and converter losses are denoted by $P_{\text{Lossbatter}}$ and $P_{\text{Lossconverter}}$, respectively. The internal resistance of the battery is R_{battery}. Power storage (P_{storage}) determines I_{battery} charging current. Standby power loss due to components is known as P_{sb} (continuous standby loss). Losses in semiconductors and filters account for k percent of the total.

This research, on the other hand, examines the direct link of the highest amount of renewable energy gathering. As a result, ESS loss is treated as if it were a property of P_{storage} rather than I_{batter}y. As shown in (3), P_{storage} has a considerable impact on ESS's power loss. Therefore, the ESS losses can be expected to be stowed power and ESS as follows:

$$\begin{aligned} P_{\text{storage}} &= P_{DG\,\text{output}} - P_{DG\,\text{dispatch}}, \\ P_{\text{LossESS}} &= (1-\eta)P_{\text{storage}}. \end{aligned} \tag{5}$$

3.1.2. Power Loss in Line Ideal. The generalised power flow is used in this study to determine the power losses in the power system's line. When analyzing the steady state of a real, the power flow equation can be expressed as follows [25]:

$$\begin{aligned} S_i &= P_i + jQ_i, \\ P_i &= \sum k = 1n|V_i||V_k||Y_{ik}| \cos(\theta_i - \theta_k - \alpha_{ik}), \quad i = 1, 2, \ldots, n, \\ Q_i &= \sum k = 1n|V_i||V_k||Y_{ik}| \sin(\theta_i - \theta_k - \alpha_{ik}), \quad i = 1, 2, \ldots, n. \end{aligned} \tag{6}$$

Net apparent power injections to bus I are represented by Si, P^i, and Q^i, respectively. Number of buses in the system is n. The magnitudes of the voltages on buses I and k are V^i and V^k, respectively. Both I and k refer to the voltage angles at the two buses in question. The difference in admission between buses I and k is measured by Y^{ik}. When two buses are in phase with one another, they are called "ik" and "k."

This work only covers the active component power losses in lines due to a branch conductance (g_{ik}) among buses I and k, which can be expressed as follows:

$$P_{\text{Lossline}_{ik}} = g_{ik}\left[V_i^2 + V_k^2 - 2V_iV_k \cos(\theta_i - \theta_k)\right]. \tag{7}$$

3.2. Objective Function Formulation. Achieving maximum energy means maximizing the DG's power output or decreasing the amount of excess energy that can represent the least amount of power loss in the ESS, as discussed in Sections 3.1.1 and 3.1.2. The proposed method's objective function is the product of (1) and (2). As a result, the following may be said about it:

$$\text{Min } P_{\text{Loss}}^{\text{Total}} = \sum_{i=1}^{Nl} P_{\text{Lossline},i} + \sum_{j=1}^{\text{Nst}} P_{\text{LossESS},j}. \tag{8}$$

Loss line i is defined as the power loss, and loss line j as the ESS loss. To put it another way, Nl and Nst represent the total sum of energy transmission lines and storage facilities.

3.3. Operational Constraints

3.3.1. Power Flow Constraint. When power is transmitted between any two buses I and j, where each bus is represented by a row and a column in Tables 1 and 2. An illustration of a power flow restriction is the following:

$$I_{i-j} \le I_{i-j}^{\max}, \tag{9}$$

Table 1: Details of IEEE 14-bus standard test scheme.

Type	Cap. (MW)	Bus
Renewable DG unit 1	100	12
Conventional gen. unit 2	600	2
Renewable DG unit 2	100	10
Conventional gen. unit 1	750	1
Conventional gen. unit 3	400	3
ESS unit 1		12
ESS unit 2		10
ESS unit 3		9

Table 2: Details of IEEE 30-bus test system.

Type	Cap. (MW)	Bus
Conventional gen. 1	200	1
Conventional gen. 2	150	2
Conventional gen. 3	150	5
Renewable DG 1	50	5
Conventional gen. 5	50	11
Conventional gen. 6	50	13
Renewable DG 3	50	9
ESS unit 1		5
ESS unit 2		3
ESS unit 3		9

where $I_{(i-j)}$ is the present line among buses$I$ and j, as shown in the figure. The line between buses I and j has a maximum current capacity of $I_{i-j}^{\max}$.

3.3.2. Generator Constraints. The system's generators must be run within the bus voltage's rated active and reactive power restrictions. The voltage must also fall within the acceptable ranges of maximum and minimum. The following are possible generator constraints:

$$\begin{aligned} P_N^{\min} &\le P_N \le P_N^{\max}, \\ Q_N^{\min} &\le Q_N \le Q_N^{\max}, \\ V_N^{\min} &\le V_N \le V_N^{\max}. \end{aligned} \tag{10}$$

Generator bus N injects power (PN) both actively and reactively. Generator N's maximum active and reactive powers are referred to as PN max an d QN max. PN min an d QN min are generator N's minimal active and reactive powers. The voltage on the bus at which a generator is attached (bus N) is known as V_N. Voltages min are the generator bus's maximum and minimum operational voltages, respectively.

3.3.3. Renewable Distributed Generation Restraint. Only the maximum power output from the renewable DG source is taken into account. Here are some examples of how you can set a restriction:

$$0 \le P_{DG,N} \le P_{DG,N}^{\max}. \tag{11}$$

The active power transfer from DG to bus N is denoted by $P_{DG,N}$. DGs at bus N have a maximum active power of $P_{DG,N}^{\max}$.

3.3.4. Load Constraints. Distribute general load across system while maintaining voltage limitations as seen in (12). A voltage deviation (VD) limit must also be adhered to when operating the load. Difference in voltage between the maximum and minimum voltage limitations is referred to as *VD*. We can write *VD* down as follows:

$$\begin{aligned} &V_N^{\min} \le V_N \le V_N^{\max}, \quad N = 1, \ldots, n \text{ bus no,} \\ &VD_i = V_i^{\max} - V_i^{\min}, \quad i = 1, \ldots\ldots, m \text{ scenarios no.} \end{aligned} \tag{12}$$

Maximum and minimum bus voltage limitations are $V_N^{\max}$ and $V_N^{\min}$, respectively. Maximum and lowest system voltages for scenario I are $V_i^{\max}$ and $V_i^{\min}$, respectively.

3.4. Proposed Model: Background. For minimizing the power loss and maximizing the renewable energy harvesting as presented in Sections 3.1 to 3.3, the optimal solutions are explored by applying the hybrid RSA-ROA. With regard to this hybrid algorithm, an entirely new transition mechanism has been proposed, and its primary technique has been described.

3.4.1. Reptile Search Algorithm (RSA). Here, we will discuss the Reptile Search Algorithm (RSA). Reptile Search Algorithm (RSA) is based on the natural behaviour of crocodiles in the wild, including their encircling mechanics, hunting tactics, and social interactions [26].

Encircling Phase. This section introduces the RSA's exploratory activity (encircling). Crocodiles have two distinct ways of encircling prey: high-walking and belly-walking.

Iteration number is divided into four equal parts, and the total sum of iterations is also divided into four equal parts. Based on these scenarios, RSA alternates between exploration and exploitation search stages. Two key search algorithms are used to uncover better answers in the RSA exploration mechanisms, which examine search regions and approaches.

During this step of the search, only one criterion must be met. High-walking and belly-walking search methods are carried out according to $tT/4$ an d $t2\,T/4$ and $t > T/4$, respectively. The following equation shows how the position is updated:

$$x_{(i,j)}(t+1) = \begin{cases} \text{Best}_j(t) \times \eta_{(i,j)}(t) \times \beta - R_{(i,j)}(t) \times \text{rand}, & t \le \dfrac{T}{4}, \\ \text{Best}_j(t) \times x_{(r_1,j)} \times ES(t) \times \text{rand}, & t \le 2\dfrac{T}{4} \text{ and } t > \dfrac{T}{4}. \end{cases} \tag{13}$$

Equation (14) yields the hunting parameter $\eta_{(i,j)}$. No matter what, b will always be equal to 0.01. Equation (15) determines the reduction function $R_{(i,j)}$. There are four random numbers in this problem: r_1, r_2, $x(i, j)$, and N. The sense of evolution equation (16) gives us the probability parameter $ES(t)$.

$$\eta_{(i,j)} = \text{Best}_j(t) \times P_{(i,j),}, \tag{14}$$

$$R_{(i,j)} = \frac{\text{Best}_j(t) - x_{(r_2,j)}}{\text{Best}_j(t) + \varepsilon}, \tag{15}$$

$$ES(t) = 2 \times r_3 \times \left(1 - \frac{1}{T}\right). \tag{16}$$

It is an integer with the value. The following equation determines the difference parameter $P_{(i,j),}$:

$$P_{(i,j),} = \alpha + \frac{x_{(i,j)} - M(x_i)}{\text{Best}_j(t) \times \left(UB_{(j)} - LB_{(j)}\right) + \varepsilon'}. \tag{17}$$

In (18), $M(x_i)$ indicates the average position. These are the highest and lower limits, respectively, where it has a value of 0.1.

$$M(x_i) = \frac{1}{n} \sum_{j=1}^{n} x_{(i,j),} \tag{18}$$

Hunting Phase. This section discusses RSA's predatory tendencies. Crocodiles hunt in two ways, depending on their hunting habits: coordination and teamwork.

$t \le T$ and t 3 $T/4$ are used for hunting coordination in this phase; if t T and t 3 $T/4$ are used, then the hunting cooperation is accomplished. Equation (19) depicts the position-updating procedures:

$$x_{(i,j)}(t+1) = \begin{cases} \text{Best}_j(t) \times P_{(i,j)}(t) \times \text{rand}, & t \le 3\frac{T}{4} \text{ and } t > 2\frac{T}{4}, \\ \text{Best}_j(4) - \eta_{(i,j)}(t) \times \varepsilon - R_{(i,j)}(t) \times \text{rand}, & t \le T \text{ and } t > 3\frac{T}{4}, \end{cases} \tag{19}$$

where the best solution is found, and the hunting parameter $\eta_{(i,j)}$ is defined by equation (14). According to equation (17), $P_{(i,j)}$, is the difference parameter. Equation (15) defines reduction function $R_{(i,j)}$.

3.4.2. Remora Optimization Algorithm (ROA). The detailed explanation of ROA [27] is given in the upcoming section.

Free Travel. SFO Strategy (20) provided the procedure's elite idea, which was used to model this algorithm's location update.

$$R_i^{t+1} = R_{\text{best}}^t - \left(\text{rand} \times \left(\frac{\left(R_{\text{best}}^t - R_{\text{ran d}}^t\right)}{2}\right) - R_{\text{rand}}^t\right), \tag{20}$$

where R_{rand}^t is a random location.

Experience Attack

The tuyu must take little steps around the host on a regular basis in order to regulate whether or not it is essential to replace the host. The following is the formula for simulating the aforementioned principles:

$$R_{\text{att}} = R_i^t - \left(R_i^t - R_{\text{pre}}\right) \times \text{rand}n. \tag{21}$$

In this example, R_{pre} is where the previous iteration left off, and R_{att} represents a tentative stride in that direction.

Because of this step's fitness evaluation, the current solution $f(R_i^t)$ and the attempted solution $f(R_{\text{att}})$ are described. If, for example, the proposed solution's fitness function value is lower than the fitness function value, then the proposed solution should be rejected.

$$f\left(R_i^t\right) > f\left(R_{\text{att}}\right). \tag{22}$$

This section shows how Remora uses a different technique for local optima than does the rest of Remora.

$$f\left(R_i^t\right) < f\left(R_{\text{att}}\right). \tag{23}$$

Eat Thoughtfully

WOA Strategy

As shown in the equations below, the location update formulation of Remora attached to the whale was reconstructed using the original WOA method:

$$\begin{aligned} R_{i+1} &= D \times e^{\alpha} \times \cos(2\pi\alpha) + R_i, \\ \alpha &= \text{rand} \times (a-1) + 1, \\ a &= -\left(1 + \frac{t}{T}\right), \\ D &= \left|R_{\text{best}} - R_i\right|. \end{aligned} \tag{24}$$

When a Remora is attached to a whale, their locations may be viewed as the same in the broader solution space. It is a number that decreases exponentially in the range of [−2, −1] and is chosen at random from the range of [−1, 1].

Host Feeding

Host feeding is a subcategory of the exploitation method. Host location can be reduced to the optimal solution at this stage. As a mathematical concept, travelling on or around the host is an appropriate way to describe incremental stages:

$$\begin{aligned} R_i^t &= R_i^t + A, \\ A &= B \times \left(R_i^t - C \times R_{\text{best}}\right), \\ B &= 2 \times V \times \text{rand} - V, \\ V &= 2 \times \left(1 - \frac{t}{T}\right). \end{aligned} \tag{25}$$

In this case, A was used to indicate a very small movement connected to the physical space occupied by the host and remora. To tell the difference between the host and Remora, researchers used a Remora factor (C). If the host has a volume of one, the Remora's volume is equal to one hundredth of that volume.

3.4.3. The Proposed Hybrid Method. RSA and ROA with a novel transition mechanism are combined in this part to present the primary technique for the proposed hybrid search algorithm.

In the suggested HRSA, a new mean transition mechanism and two major search strategies can alleviate many issues. Early global and local search algorithms are shortcomings of classical RSA. Nevertheless, it remains the most popular way to conduct a search. As a result, local search and early convergence are avoided by using the ROA search technique. ROA is used as a search engine as well as to

improve the efficiency of search. As a result, new ideas from other places can effectively broaden the search space. More robust approaches to achieving better results are inspired by these proposals for the proposed model.

Initialization Phase. Starting with a collection of candidates (X) generated stochastically, the optimization process in RSA commences. Nearly optimum solutions are found in each iteration.

$$X = \begin{bmatrix} x_{1,1} & \cdots & x_{1,j} & x_{1,n-1} & x_{1,n} \\ x_{2,1} & \cdots & x_{2,j} & \cdots & x_{2,n} \\ \cdots & \cdots & x_{i,j} & \cdots & \cdots \\ \vdots & \vdots & \vdots & \vdots & \vdots \\ x_{N-1,1} & \cdots & x_{N-1,j} & \cdots & x_{N-1,n} \\ x_{N,1} & \cdots & x_{N,j} & x_{N,n-1} & x_{N,n} \end{bmatrix}, \quad (26)$$

where $x(i, j)$ is the jth location of the ith solution and N is the total sum of solutions and n is the size of the dimension derived from the following equation:

$$x_{ij} = \text{rand} \times (UB - LB) + LB, \quad j = 1, 2, \ldots, n, \quad (27)$$

where rand is a random and LB and UB signify the bound, correspondingly. The flow chart of the proposed model is given in Figure 1.

The Projected Mean Transition Mechanism (MTM). At the beginning of this section, Algorithm 1 provides an explanation of the mean transition mechanism (MTM). Controlling the search and switching between the RSA and the MT are both possible with this method. It takes a lot of skill to move from one search method to the next. It calls for an efficient method of changing the update operations across multiple techniques. When the fitness does not improve after five iterations, the basic idea behind the MTM is to regulate the search approaches (I). The number of repetitions decreases if there are no benefits to be had through testing.

While the fitness function value and C serve as a counter in Algorithm 1, the TM variable can be switched from 0 to 1 to alter the search process between RSA and MT. There are a maximum number of repeats I that should be altered if no improvements are seen.

4. Simulation Results and Discussion

4.1. Test Systems Description. The projected technique is put to test using IEEE 14-bus and 30-bus test schemes, side by side. According to the test systems, the generation units include generation and renewable DG units. Each renewable DG unit has an ESS installed to collect any extra power generated. In each site, the DG power output is a combination of the electricity energy available from the DG dispatch and the extra power stored in the ESS unit, which has different standards. Tables 1 and 2 present the component data for the 14-bus and 30-bus test systems, respectively. The efficiency of ESS is assumed to be 90% in all deployed locations for the purpose of calculating ESS losses.

The proposed WSN is being tested using MATLAB 2014 software. Table 3 shows the results of two distinct simulations. Table 4 has further information. During the simulations, we measure efficiency, the sum of active nodes, the network's average energy consumption, the First Node Dies (FND), the loss of 10% and 20% of nodes, and the number of packages transferred.

Depending on their level of sophistication, energy collecting nodes can be classified as basic or sophisticated. During different simulations, the percentages of normal and advanced nodes in the network are 80 percent and 20 percent, respectively. Nodes in the advanced stage have three times the energy of those in the standard stage. We ran a number of simulations, and the mean results are shown here. Table 3 shows the simulations scenario of the proposed model; here we used 100 and 200 nodes for simulation, as well as the areas of $500 \times 500\,\text{m}^2$ and $300 \times 300\,\text{m}^2$, respectively.

Table 4 shows the different parameters used in simulation, which are used in the proposed model.

In the FND analysis, when the time is 44.4 s, the hybrid RSA-ROA method has 40439 packets for 100 noded. But the single algorithm such as RSA and ROA has only 2410 packets and 3986 packets for the same number of nodes (100). When the number of nodes is 80, the hybrid model has 125268 packets, where the single models have only 5213 and 6535 packets for the analysis of PND. Next, Table 5 presents the summary for FND and PND for network 2.

From the comparative analysis in Table 6, it is shown that different types of PND, 200, 180 and 160, are used. In the FND analysis on 200 nodes, when the time is 361.2 s, the hybrid RSA-ROA method has 72239 packets. But the RSA and ROA have only 3840 packets and it reaches around 19.2 s and 4140 packets in 20.7 s for the same node 100. When the number of nodes is 160, the hybrid model has 229453.5 packets in 1202 s, where the single models have only 17357.4 in 93.3 s and 14928.9 packets in 78.1 s for the analysis of PND. Table 7 and Figure 2 show the experimental analysis of total number of live nodes for network 1.

When the initial rounds start, all the techniques have 100 nodes, but when the rounds are high, all techniques have different number of nodes. For instance, when the number of rounds is 1500, the RSA has 28 nodes and ROA has 30 nodes, but the proposed model has 90 nodes. This is due to the integration of RSA model and ROA model. When the number of rounds is 3500, the RSA has only 30 live nodes, ROA has 35 live nodes, and the proposed model has 91 live nodes. Finally, when the number of rounds is 5000, the proposed model has 82 live nodes, ROA has 35 live nodes, and RSA has 30 live nodes. Figure 3 presents the number of live nodes for proposed network 2.

In this second network, the initial nodes are 200 for zero rounds. When the number of rounds is increased, the live nodes for existing technique are less, when compared with the proposed model. When the number of rounds is 4500, the RSA has 125 nodes, ROA has 130 live nodes, and the proposed model has 187 live nodes. When the number of rounds is 2000, the proposed model has 183 live nodes, the RSA model has 130 nodes, and ROA has 138 live nodes. This

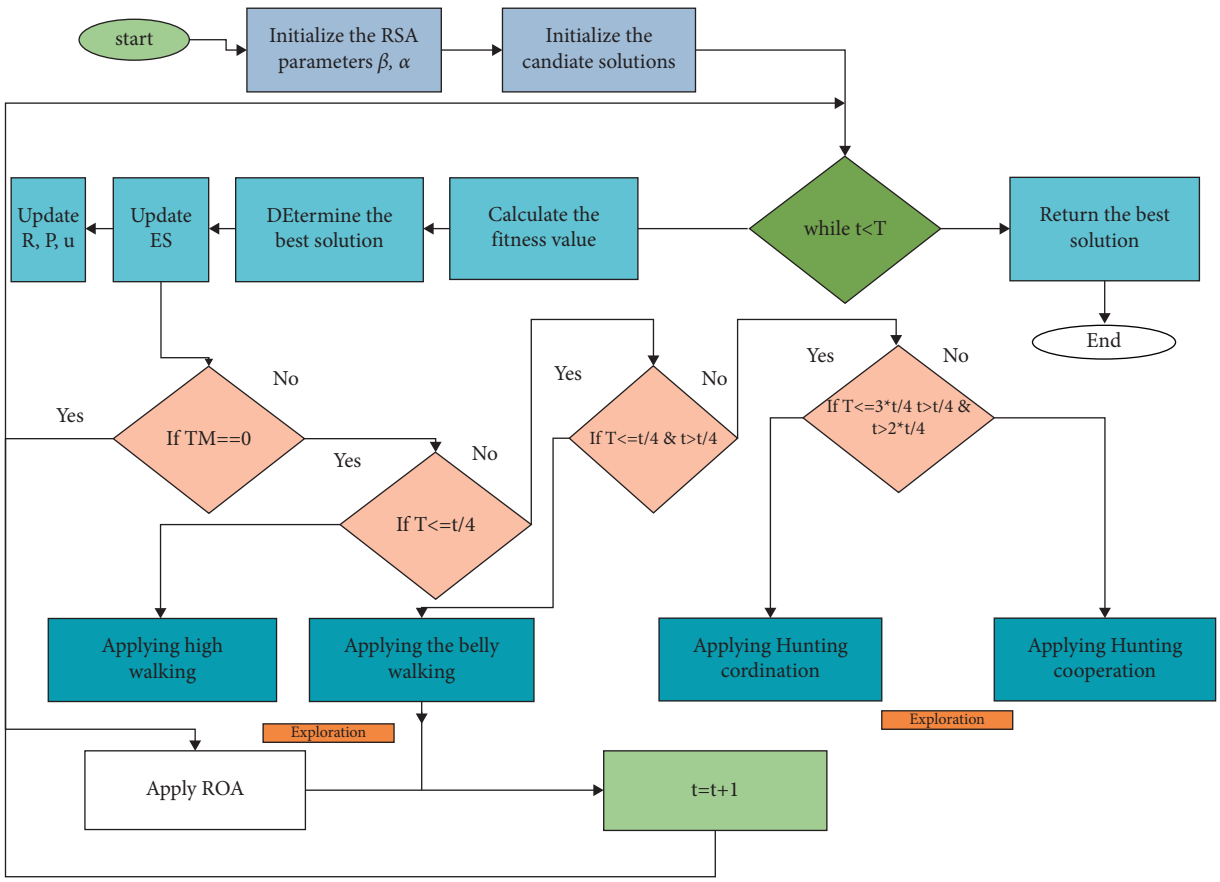

Figure 1: Flow chart of the proposed hybrid model.

(i) Initialize the TM parameter value ($TM = 0$).
(ii) sum$FF = 0$;
(iii) for ($t = 1$ to T)do
(iv) sumFF = sumFF + currentFF
(v) $C = (C + 1)$;
(vi) if (currentFF 6 = sumFF)then
(vii) if ($C > I$)then
(viii) TM = flip (TM);
(ix) sum$FF = 0$;
(x) $C = 0$;
(xi) end if
(xii) end if
(xiii) end for

Algorithm 1: The projected mean transition mechanism (MTM).

Table 3: Simulations scenario.

Network	Sink	Number of nodes	Area (m^2)
Proposed network 1	(0,0)	100	300 × 300
Proposed network 2	(250,250)	200	500 ×5 00

analysis shows that the number of lives nodes is higher for the proposed model compared to the existing techniques. Table 8 and Figure 4 show the remaining energy for network 1.

Initially, all models have 0.600 J, but when the number of nodes increases, the energy is also reduced. When the number of rounds is 500, the remaining energy of RSA is 0.111 J, that of ROA is 0.065 J, and that of the proposed model is 0.410 J. When the number of rounds is 2000, the remaining energy of RSA is 0.111 J, that of ROA is 0.055 J, and that of the proposed model is 0.340 J. When the number of rounds is 3500, the remaining energy of RSA is 0.111 J, that of ROA is 0.045 J, and that of the proposed model is 0.290 J. For the second network, the experimental values are shown in Table 9 and Figure 5.

When the number of rounds is 500, the proposed model has 0.360 J, ROA has 0.180 J, and RSA has 0.020 J. For all

Table 4: Parameters used in simulation.

Parameter	Value
$P_{DG\,\mathrm{dispatch}}$	5 nJ/bit/message
P_{storage}	50 nJ/bit
P_{ESS}	10 pJ/bit/m2
$P_{DG\,\mathrm{output}}$	0.0013 pJ/bit/m4
Packets size	8192 bits
Message size	100 bits
Energy of threshold down	0.01 J
Energy of threshold up	0.1 J

Table 5: Summary of FND and partial node death (PND) for proposed network 1.

Protocol	FND (100 nodes)		PND (90 nodes)		PND (80 nodes)	
	Time (s)	Packets	Time (s)	Packets	Time (s)	Packets
RSA	24.1	2410	53.2	5213.5	72.7	6901.2
ROA	40.1	3986.7	69.8	6535.6	95.5	8354.8
Hybrid RSA-ROA	44.4	40439	1288.6	125268.5	1150.8	12459

Table 6: Summary of FND and PND for proposed network 2.

Protocol	FND (200 nodes)		PND (180 nodes)		PND (160 nodes)	
	Time	Packets	Time	Packets	Time	Packets
RSA	19.2	3840	59.6	11584.3	93.3	17357.4
ROA	20.7	4140	50.4	9865.7	78.1	14928.9
Hybrid RSA-ROA	361.2	72239	868.5	170170	1202	229453.5

Table 7: Number of live nodes for proposed network 1.

Total no. of rounds	0	500	1000′	1500	2000	2500	3000	3500	4000	4500	5000
RSA	100	20	25	28	30	28	25	30	28	25	30
ROA	100	35	38	32	38	32	30	35	38	30	35
Hybrid RSA-ROA	100	90	88	90	83	87	90	91	90	87	82

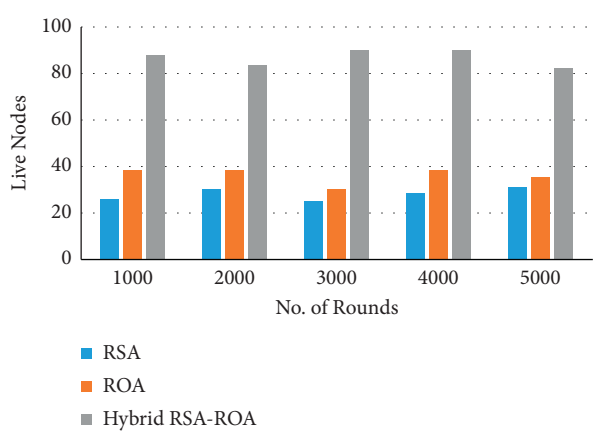

Figure 2: Graphical representation for network 1.

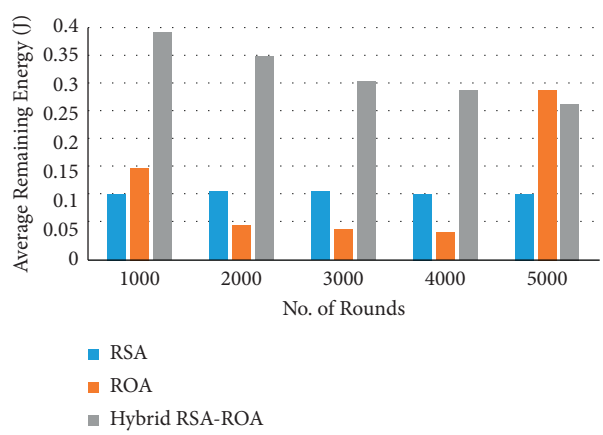

Figure 3: Graphical representation of the proposed model for energy.

different rounds, the existing RSA has stable remaining energy (i.e., 0.020 J). When the number of rounds is 1500, the proposed model has 0.200 J and ROA has 0.180 J. But, at one particular round, all techniques including the proposed model have stable remaining energy (i.e., 0.180 J). Table 10 shows the performance analysis of proposed model in terms of throughput.

The throughput of the proposed hybrid model is increased, when the number of nodes is also increased. In the throughput experiments for network 1, the RSA achieved 109 kbps, ROA achieved 114 kbps, and the proposed hybrid model achieved 157 kbps when the number of nodes reached 2000. These same techniques achieved 149 kbps, 170 kbps,

Table 8: Average remaining energy over different number of rounds for network 1.

Total no. of rounds	0	500	1000′	1500	2000	2500	3000	3500	4000	4500	5000
RSA	0.600	0.111	0.111	0.111	0.110	0.110	0.110	0.110	0.110	0.110	0.110
ROA	0.600	0.065	0.060	0.060	0.055	0.054	0.050	0.045	0.045	0.045	0.045
Hybrid RSA-ROA	0.600	0.410	0.380	0.360	0.340	0.32	0.300	0.290	0.280	0.270	0.260

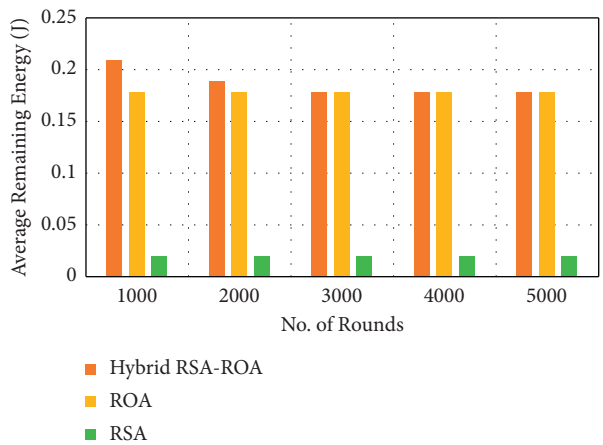

Figure 4: Graphical representation of the proposed model for remaining energy in network 2.

Table 9: Average remaining energy over different number of rounds for network 2.

Total no. of rounds	0	500	1000′	1500	2000	2500	3000	3500	4000	4500	5000
Hybrid RSA-ROA	0.60	0.360	0.210	0.200	0.190	0.180	0.180	0.180	**0.180**	0.180	0.180
ROA	0.60	0.180	0.180	0.180	0.180	0.180	0.180	0.180	0.180	0.180	0.180
RSA	0.60	0.020	0.020	0.020	0.020	0.020	0.020	0.020	0.020	0.020	0.020

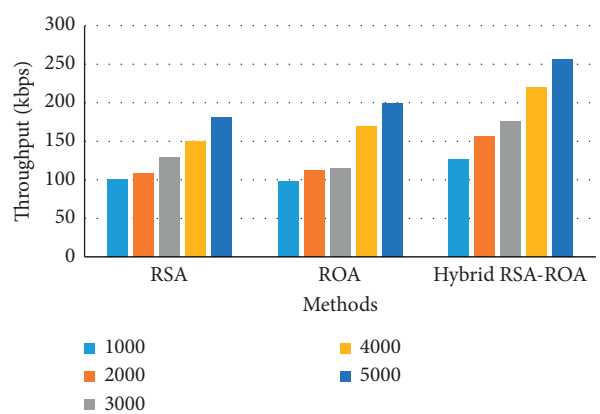

Figure 5: Graphical representation of the proposed method in terms of throughput for network 1.

and 220 kbps when the number of nodes reached 4000. Finally, when the number of nodes reached 5000, the RSA achieved 182 kbps, ROA achieved 200 kbps, and the proposed hybrid model achieved 255 kbps throughput. For proposed network 2, the RSA achieved 104 kbps, ROA achieved 119 kbps, and the proposed hybrid model achieved 136 kbps when the number of nodes reached 1000. These same techniques achieved 148 kbps, 159 kbps, and 189 kbps when the number of nodes reached 3000. Finally, when the number of nodes reached 5000, the RSA achieved 192 kbps, ROA achieved 220 kbps, and the proposed hybrid model achieved 263 kbps throughput. Figures 5 and 6 show the graphical analysis of the proposed hybrid model for both networks.

Table 11, Figure 7, and Figure 8show the experimental analysis of the proposed method for routing overhead for networks 1 and 2.

For proposed network 1, the routing overheads of RSA, ROA, and the hybrid model are 0.8, 0.7, and 0.5, respectively when the number of nodes is 2000. The RSA has 0.98, ROA has 0.9, and the proposed hybrid model consumed only 0.82 routing overhead when the number of nodes reached 4000. From this analysis, it is clearly proven that

Table 10: Validated analysis of the proposed method for throughput (kbps).

No. of nodes	Proposed network 1			Proposed network 2		
	RSA	ROA	Hybrid RSA-ROA	RSA	ROA	Hybrid RSA-ROA
1000	100	98	126	104	119	136
2000	109	114	157	120	128	166
3000	128	115	176	148	159	189
4000	149	170	220	159	190	234
5000	182	200	255	192	220	263

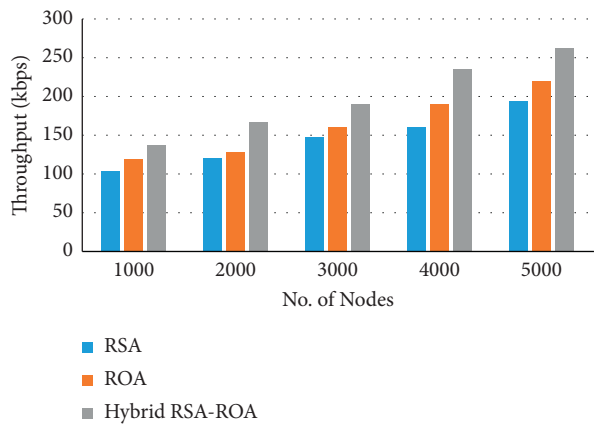

Figure 6: Graphical representation of the proposed method in terms of throughput for network 2.

Table 11: Performance analysis of the proposed method for routing overhead.

No. of nodes	Proposed network 1			Proposed network 2		
	RSA	ROA	Hybrid RSA-ROA	RSA	ROA	Hybrid RSA-ROA
1000	0.7	0.6	0.4	0.63	0.51	0.49
2000	0.8	0.7	0.5	0.70	0.58	0.46
3000	0.9	0.7	0.62	0.69	0.63	0.57
4000	0.98	0.9	0.82	0.71	0.69	0.74
5000	1.23	1.18	0.96	1.26	1.07	0.82

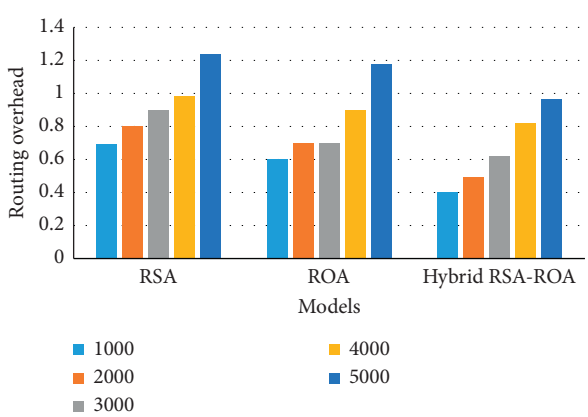

Figure 7: Graphical representation of the proposed method in terms of routing overhead for network 1.

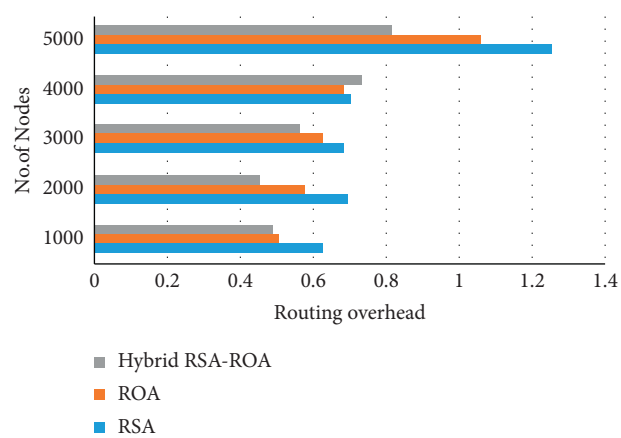

Figure 8: Graphical representation of the proposed method in terms of routing overhead for network 2.

the number of nodes influences the performance of routing overhead of each model. The hybrid model achieved 0.49 to 0.82 of routing overhead when the numbers of nodes were 1000 to 5000, while the single models, RSA and ROA, achieved 0.63 to 1.26 and 0.51 to 1.07 of routing overhead when numbers of nodes were 1000 to 5000. Figure 8 shows the graphical analysis of proposed network 2 in terms of routing overhead.

5. Conclusion

In this paper, the optimum generation programming was studied using the hybrid model in the power system. The proposed method was implemented keeping in mind maximum renewable energy harvest and minimization of energy losses. The optimal solutions for the proposed method were identified and obtained by integrating RSA and ROA algorithms. The comparative cases of single technique with hybrid model were made to exploit the potential and effectiveness of the proposed method in two different networks, where the single models, RSA and ROA, achieved 0.63 to 1.26 and 0.51 to 1.07 of routing overhead, respectively, when the numbers of nodes were 1000 to 5000. The simulation results showed the effectiveness and good performance of the proposed method for obtaining optimal solutions for generation programming, especially with maximum harvesting of renewable energy and minimizing energy losses. Energy losses were clearly low depending on the optimum storage power of the ESS and minimizing line losses with maximum renewable energy harvest. In addition, the maximum renewable energy harvest is greatly affected by the reduction of conventional generations and reduced ESS losses.

Data Availability

No data were used to support the findings of this study.

Conflicts of Interest

The authors declare that they have no conflicts of interest.

References

[1] D. Praveen Kumar, A. Tarachand, and A. C. S. Rao, "Machine learning algorithms for wireless sensor networks: a survey," *Information Fusion*, vol. 49, pp. 1–25, 2019.

[2] D. Praveen Kumar, A. Tarachand, and A. C. S. Rao, "ACO-based mobile sink path determination for wireless sensor networks under non-uniform data constraints," *Applied Soft Computing*, vol. 69, pp. 528–540, 2018.

[3] J. Yick, B. Mukherjee, and D. Ghosal, "Wireless sensor network survey," *Computer Networks*, vol. 52, no. 12, pp. 2292–2330, 2008.

[4] I. F. Akyildiz, W. Su, Y. Sankarasubramaniam, and E. Cayirci, "Wireless sensor networks: a survey," *Computer Networks*, vol. 38, no. 4, pp. 393–422, 2002.

[5] F. K. Shaikh and S. Zeadally, "Energy harvesting in wireless sensor networks: a comprehensive review," *Renewable and Sustainable Energy Reviews*, vol. 55, pp. 1041–1054, 2016.

[6] A. A. Babayo, M. H. Anisi, and I. Ali, "A review on energy management schemes in energy harvesting wireless sensor networks," *Renewable and Sustainable Energy Reviews*, vol. 76, pp. 1176–1184, 2017.

[7] H. Yu and Q. Yue, "Indoor light energy harvesting system for energy-aware wireless sensor node," *Energy Procedia*, vol. 16, pp. 1027–1032, 2012.

[8] D. Daniel, N. Preethi, A. Jakka, and S. Eswaran, "Collaborative intrusion detection system in cognitive smart city network (CSC-net)," *International Journal of Knowledge and Systems Science*, vol. 12, no. 1, pp. 60–73, 2021.

[9] F. Akhtar and M. H. Rehmani, "Energy replenishment using renewable and traditional energy resources for sustainable wireless sensor networks: a review," *Renewable and Sustainable Energy Reviews*, vol. 45, pp. 769–784, 2015.

[10] A. Cammarano, C. Petrioli, and D. Spenza, "Online energy harvesting prediction in environmentally powered wireless sensor networks," *IEEE Sensors Journal*, vol. 16, no. 17, pp. 6793–6804, 2016.

[11] H. Cheng, Z. Su, N. Xiong, and Y. Xiao, "Energy-efficient node scheduling algorithms for wireless sensor networks using Markov random field model," *Information Sciences*, vol. 329, pp. 461–477, 2016.

[12] D. A. Guimaraes, E. P. Frigieri, and L. J. Sakai, "Influence of node mobility, ˜ recharge, and path loss on the optimized lifetime of wireless rechargeable sensor networks," *Ad Hoc Networks*, vol. 97, Article ID 102025, 2020.

[13] A. Shawahna, M. E. Haque, and M. E. Tozal, "Energy harvesting in wireless sensor network with efficient landmark selection using mobile actuator," in *Proceedings of the: 2017 Annual IEEE International Systems Conference (SysCon)*, pp. 1–8, IEEE, Montreal, QC, Canada, April 2017.

[14] S. Sakya, "Design of hybrid energy management system for wireless sensor networks in remote areas," *Journal of Electrical Engineering and Automation (EEA)*, vol. 02, pp. 13–24, 2020.

[15] F. K. Shaikh and S. Zeadally, "Energy harvesting in wireless sensor networks: a comprehensive review," *Renewable and Sustainable Energy Reviews*, vol. 55, pp. 1041–1054, 2016.

[16] S. Kim, R. Vyas, J. Bito et al., "Ambient RF energy-harvesting technologies for self-sustainable standalone wireless sensor platforms," *Proceedings of the IEEE*, vol. 102, no. 11, pp. 1649–1666, 2014.

[17] H. Sharma, A. Haque, and Z. A. Jaffery, "Maximization of wireless sensor network lifetime using solar energy harvesting for smart agriculture monitoring," *Ad Hoc Networks*, vol. 94, Article ID 101966, 2019.

[18] R. S. Liu and Y. C. Chen, "Robust data collection for energy-harvesting wireless sensor networks," *Computer Networks*, vol. 167, Article ID 107025, 2020.

[19] V. Gupta and S. De, "Collaborative multi-sensing in energy harvesting wireless sensor networks," *IEEE Transactions on Signal and Information Processing over Networks*, vol. 6, pp. 426–441, 2020.

[20] D. K. Sah and T. Amgoth, "A novel efficient clustering protocol for energy harvesting in wireless sensor networks," *Wireless Networks*, vol. 26, no. 6, pp. 4723–4737, 2020.

[21] N. Qi, Y. Yin, K. Dai, C. Wu, X. Wang, and Z. You, "Comprehensive optimized hybrid energy storage system for long-life solar-powered wireless sensor network nodes," *Applied Energy*, vol. 290, Article ID 116780, 2021.

[22] S. Mohsen, A. Zekry, K. Youssef, and M. Abouelatta, "A self-powered wearable wireless sensor system powered by a hybrid energy harvester for healthcare applications," *Wireless Personal Communications*, vol. 116, no. 4, pp. 3143–3164, 2021.

[23] J. Wu, M. Xu, F. F. Liu, M. Huang, L. Ma, and Z. M. Lu, "Solar wireless sensor network routing algorithm based on multi-objective particle swarm optimization," *J. Inf. Hiding Multim. Signal Process.*vol. 12, no. 1, pp. 1–11, 2021.

[24] K. Panagiotou, C. Klumpner, and M. Sumner, *The Effect of Including Power Converter Losses when Modelling Energy Storage Systems: A UK Domestic Study*, EPE'16 ECCE Europe, Europe, 2016.
[25] J. Grainger and W. Stevenson, *Power System Analysis*, McGraw-Hill, New York, Ny, USA, 1994.
[26] L. Abualigah, M. Abd Elaziz, P. Sumari, Z. W. Geem, and A. H. Gandomi, "Reptile Search Algorithm (RSA): a nature-inspired meta-heuristic optimizer," *Expert Systems with Applications*, vol. 191, Article ID 116158, 2022.
[27] H. Jia, X. Peng, and C. Lang, "Remora optimization algorithm," *Expert Systems with Applications*, vol. 185, Article ID 115665, 2021.

Hindawi
Advances in Materials Science and Engineering
Volume 2022, Article ID 6559014, 18 pages
https://doi.org/10.1155/2022/6559014

Research Article

Optimizing the Mechanical and Microstructure Characteristics of Stir Casting and Hot-Pressed AA 7075/ZnO/ZrO_2 Composites

P. Satishkumar,[1] C. Saravana Murthi,[2] Rohinikumar Chebolu,[3] Yenda Srinivasa Rao,[4] Rey Y. Capangpangan,[5] Arnold C. Alguno,[6] Vishnu Prasad Yadav,[7] M. Chitra,[8] and Mahesh Gopal[9]

[1]*Anna University, Chennai, India*
[2]*Mechanical Engineering, United Institute of Technology, Coimbatore, Tamil Nadu, India*
[3]*Mechanical Engineering, Andhra University, Visakhapatnam, Andhra Pradesh, India*
[4]*Mechanical Engineering, Swamy Vivekananda Engineering College, Bobbili, Andhra Pradesh, India*
[5]*Department of Physical Science and Mathematics, College of Science and Environment, Mindanao State University, Naawan, Misamis Oriental, Philippines*
[6]*Department of Physics, Mindanao State University, Lligan Institute of Technology, Lligan City, Philippines*
[7]*Chemical Engineering, GGV, Bilaspur, India*
[8]*Electronic Communication Engineering, Kongu Engineering College, Tamil Nadu, India*
[9]*Mechanical Engineering, College of Engineering and Technology, Wollega University, Post Box No. 395, Nekemte, Ethiopia*

Correspondence should be addressed to Mahesh Gopal; doctorgmahesh@gmail.com

Received 24 May 2022; Revised 4 July 2022; Accepted 8 July 2022; Published 8 August 2022

Academic Editor: Vijayananth Kavimani

The composite was made using the stir cast manufacturing method. Many parameters, like stirring speed, stirring time, ZrO_2% reinforcement, and cast temperature, are evaluated in a Taguchi experimental design to see how they affected the composite properties. In terms of composite properties, ZrO_2% reinforcement and the stir speed have the most significant impact. There were 25.02% gains in ultimate tensile strength and hardness, as well as a decrease in composite wear loss, when the optimal stir casting parameters were used compared to the initial stir casting settings. To get insight into the process and the qualities of the composite, the hot-pressing parameters were studied. Pressure, followed by temperature, is the most critical factor in determining the properties of composites. When a hot-pressing setting was determined to reduce the wear loss by a significant 39.3%, it was deemed perfect by the superranking concept. Under ideal conditions, hot-pressing procedures reduced wear loss by 40.8% while boosting ultimate tensile strength and hardness by 19.83% and 9.6%, respectively. The resulting microstructures and worn surface morphologies from stir casting and hot pressing show vastly different properties.

1. Introduction

Al 7075-ZnO castings account for approximately 80% to 90% of the entire production of Al 7075 castings worldwide. There are a number of automotive and aerospace industries where Al 7075-ZnO castings have been used [1, 2]. These include the engine blocks, the cylinder heads of automobile engines, and transmission housings of automobile engines, as well as wheel rims, the powertrains, and suspension components of automobile engines [3–5]. Modern businesses have developed composites (including reinforcements) that have improved toughness and plasticity, as well as the aforementioned qualities, as a result of technological breakthroughs [6]. Red mud, fly ash, borides, nitrides, oxide, and carbides are some of the reinforcing elements used in metal matrix composites (MMC) [7]. When it comes to porosity in composites, organic reinforcements may be more cost-effective. Because of the high temperatures, dynamic loads, and wear, composite material parts in these applications must have a greater level of hardness and wear

resistance. For piston, cylinder liner, and connecting rod applications, zirconium oxide (ZrO_2) reinforcement is good [8]. Sintering, casting, infiltration methods, spray forming, roll bonding, and equal channel angular pressing are some of the methods used to make these composites [9–11]. The most cost-effective processing procedures for MMCs are stir-casting and penetration, which account for around 67% of total volume output. Al 6061 alloy was strengthened and hardened by stirring in carbides (SiC and B4C) before being cast. In Al 6063 stir-casting, SiC reinforcement of up to 12% increased hardness and strength [6]. Stir-cast hybrid composites with Silicon carbide and tungsten carbide reinforced Al6061 showed enhanced strength [3]. To some extent, the mechanical characteristics of composites are influenced by parameters related to stir-casting [12, 13]. Choosing the right variables to impact stir-casting parameters resulted in a better composite material's characteristics. When it comes to raising the quality of composites, it is assumed that conducting studies on all stir-casting factors one at a time is impractical [14, 15]. In addition to being time-consuming, tedious, wasteful, expensive, and energy-intensive, many methods are also inefficient. In addition, they produce regional solutions [16, 17]. For Al 7010 MMCs, Taguchi's statistical method limits practical testing to the lowest and most optimal stir-casting variables simultaneously [18]. The Taguchi method can be used to raise the hardness of MMC by adjusting the basal % of reinforcement, time, and size [19]. Silicon carbide reinforced AA6061 composites with the Taguchi technique's optimal parameter levels were shown to have improved wear resistance properties [20]. Stir-casting composites have varied densities because of the porosity created when reinforcing particles are added to the matrix material [20, 21]. Using porous materials in castings and composites can cause stress concentration and crack development [22]. When loaded, these components fail catastrophically due to their inferior tensile and fatigue strengths. MMC's with low porosity and a wide range of properties are still a problem to design using universal parametric criteria for novel matrix-reinforcement compositions. As a result, postprocessed composites require special attention to ensure that pores are sealed [23, 24]. Pores in composites can be minimized by some posttreatment methods such as extrusion, pressing, or rolling [25]. In 713LC superalloys subjected to hot pressing, this method increases fatigue life and decreases casting faults (porosity, microshrinkage, and inhomogeneity) [26, 27]. Cast Ti6Al4V exposed to various hot-pressing settings had their pore closure affected by pressure, temperature, and holding time. They discovered that the porosity of a hot-pressing material changes significantly depending on the parameters of the process [28–30]. It was found that using the Taguchi approach, pressure, temperature, and dwell time were all improved in Al 7075-5% TiC and that zirconium diboride composite density, grain size, and hardness were all improved using the Taguchi method [31]. The Taguchi approach was used to optimize the hot-pressing parameters and differences in silicon carbide percentage in ZrB_2 composites [32]. Differences in matrix-reinforcement compositions led Taguchi to calculate ideal hot pressing settings, which were found to be different from previous studies [33]. Furthermore, there has been no effort to identify a single set of hot-pressing parameters that may be used for numerous outputs. Al-metal matrix composites have likely seen an improvement in mechanical and wear qualities due to the addition of reinforcement in the form of zirconium oxide [34]. It is the fundamental goal of the current research to develop Al 7075/ZnO reinforced with ZrO_2 (ZnO reinforced Al 7075). Stir-casting was used to create the composites [35]. Analysis and optimization of stir-casting parameters using the Taguchi method were utilized to increase wear resistance and hardness of the composites by increasing the stirring speed, stirring time, cast temperature and reinforcement weight percentage of ZrO_2. The concept of super rank was used to optimize entire outputs [36]. Composites made with the concept of super ranking optimized stir-casting settings were hot pressed in order to close pores and increase their properties [34, 35]. Using the Taguchi approach, we were able to determine the best conditions for hot-pressing parameters in order to increase hardness and wear resistance [37]. Using the Pareto ANOVA technique, it is possible to identify the best possible conditions.

2. Materials and Methods

2.1. Materials. Matrix material for industrial applications using Al 7075/ZnO alloy: For use in load bearing applications, ZrO_2 has good hardness and wear resistance qualities as a reinforcing material. Stir-casting composites are created by adding ZrO_2 reinforcement to an Al 7075/ZnO alloy. At 50 um in diameter, the ZrO_2 particles were detected. According to an EDS analysis, the composite samples contain ZrO_2, Al 7075, and ZnO.

2.2. Stir-Casting Method. Many sectors were interested in MMC's liquid state processing technique (stir casting) because of its durability, simplicity, and economy. For the fabrication of Al 7075/ZnO-ZrO_2 composites, melt stirring was facilitated by die casting. Mechanical stirring was used to disseminate ZrO_2 particles (4,8 and 12%) into a molten Al 7075/ZnO matrix metal. The precise selection of stirring speed, stirring time, reinforcement preheating, and melt temperature are all important for superior mechanical characteristics and homogenous ZrO_2 particle dispersion in the molten matrix. FENFE Metallurgical Laboratory in Bangalore provided the Al 7075/ZnO ingot material, which was then chopped into small pieces and deposited in a graphite container fitted with an electric furnace. First, the temperature of the specimen was raised to 780°C. Hexachloroethane (C_2Cl_6) tablets, pulverized into powder, are dipped into the molten metal below using a Zr-coated Cr-steel rod. The ZrO_2 powder reinforcements were heated to 525°C in an electric muffle furnace for 30 minutes to remove humidity, deposits, and scales from particles. Using a funnel, heat up particles added to melt and mechanically agitated at 525–625 rpm for 25–30 g/min. Finally, the heated mould was filled with the prepared melt and it was poured into the

mould to set (say 700 to 780°C). Using a split die, the casting was expelled from the die once it had solidified to the desired level of rigidity. With the use of a total of nine Taguchi tests (stirring speed, time, and temperature), we were able to find the best combination of ZrO_2 wt% (4,8 and 12%) and casting temperature. The results of each experiment are duplicated three times to ensure that they are accurate. An experimental stir-cast arrangement is depicted in Figure 1.

2.3. Hot-Pressing Method. Reduction of porosity and refinement of grains in the components are two of the primary reasons why the hot-pressing technique outperformed Stir Casting in terms of overall performance. As a result of this negative pressure differential, a vortex is formed that pulls in reinforcement and air bubbles, which results in pores or other defects in cast composite materials. In a hot-pressing procedure, the cast specimens are concurrently subjected to both pressure and warmth. In order to provide pressure, a 100-ton hydraulic press was used. An electric muffle furnace was used to heat the collected stir-cast samples. The desired experimentation temperature is maintained by the temperature control device (say 420–500°C). It took two hours to guarantee that the warmth was evenly distributed throughout the specimens by keeping them in a hot furnace. Fragmented die goes halves made of H13 Hot Work Steel are used to press specimens (45 HRC). Before using the die or punch, they must be heated to the proper temperature. There was a wide range of pressures and temperatures utilized in the hot-pressing process. The dwell duration was also changed (40, 80, and 120 MPa) (refer to Table 1). Pressure and heat were removed from the process after the proper dwell time had been established. The specimens were reexamined once they had cooled down.

2.4. Vickers Hardness Assessment. According to the ASTM E384 standard, Vickers hardness equipment was used to measure microhardness in composites of stir-cast and hot-pressed. Following milling and polishing, the specimens were ready for the hardness test. Tests for hardness were carried out in stir casting on the side opposite to the pressing and pouring directions. The composite specimens were subjected to a 1 kgf load for 10 seconds using a rectangular pyramid diamond indenter with a 136° angle. During the Vickers hardness test, each sample received an average of eight indentations.

2.5. Wear Test. The wear test was carried out using a computerized pin-on-disc (TR-20LE, Ducom) system. An ASTM-G99 standard operating method was used to note wear rate values, which were recorded. To ensure accurate results, the specimens were first polished to a surface roughness of 0.25 m. Examples of pin materials utilized a range of stir-cast and hot-press processes. When the 8-inch-thick EN-24 steel disc is rubbed against the pin's substance, the hardness of the EN-24 steel (62 HRC) is maintained. Sliding at a speed of 2.5 meters per second and a distance of 1000 meters are utilized to record the wear rate data. Welding tests are conducted in a temperature-controlled setting. For each of the hot-pressing and stir-casting settings, three wear rate results are averaged.

2.6. Tensile Strength. ASTM E8 standards were used to create and evaluate cast and hot-pressed samples. The tensile strength measurements were recorded using a universal testing machine. Tensile tests on every specimen were performed at a strain rate of 0.5 mm/s, as can be seen. The mean of tensile strength readings for each stir-casting and hot-pressing condition is recorded for each specimen.

2.7. Metallographic Examination. The metallic material's microstructure and production method have an effect on the material's physical, mechanical, and wear behavior. When 316 stainless steel pieces were subjected to a different production route, they displayed differential attributes and a varied microstructure. There is a substantial correlation between the change in microstructure and the change in properties. There have been similar findings reported in the literature. As a result, samples produced by stir-cast and hot-press are subjected to microstructural studies. The samples are first polished to a glass finish in order to be studied using optical and scanning electron microscopes. Composites' worn surface structure is examined using SEM.

2.8. Taguchi Method. Any manufacturing process can benefit from determining a set of optimal circumstances that enhances its product's performance. A trial and error or one factor at a time strategy results in this. There is a loss of time and money in addition to undesirable results [38]. The Taguchi approach has proven to be successful because of its solid experimental design and ability to address real-world problems with a minimum number of trials, even when there are several elements influencing the process's performance. The wear rate, UTS, and hardness of the stir-cast made Al 7075/ZnO-ZrO_2 composites are examined in Taguchi L9 tests to see how various parameters affect these composites (stirring speed, stirring time, temperature, and ZrO_2 reinforcements). Stir casting components and their relative values could only be identified after a thorough literature review [39]. Taguchi L9 trials were used to measure hardness, ultimate tensile strength, and wear rate as a function of hot-pressing factors (such as dwell time, pressure, and temperature). The conditions for hot pressing were established by a pilot experiment and subsequent study [40]. Table 1 shows the stir-cast or hot-press operations, experimentation, and optimization parameters and its levels.

2.9. Super Ranking Concept. Product/process performance can be improved using a Taguchi approach, although this method can only analyze and optimize certain reactions. It is possible to solve engineering problems using MCDM (multi-criteria decision making) approaches when many factors influence the responses that are in conflict with one another. There are a number of weighting methods that can be used for allocating individual responses, including

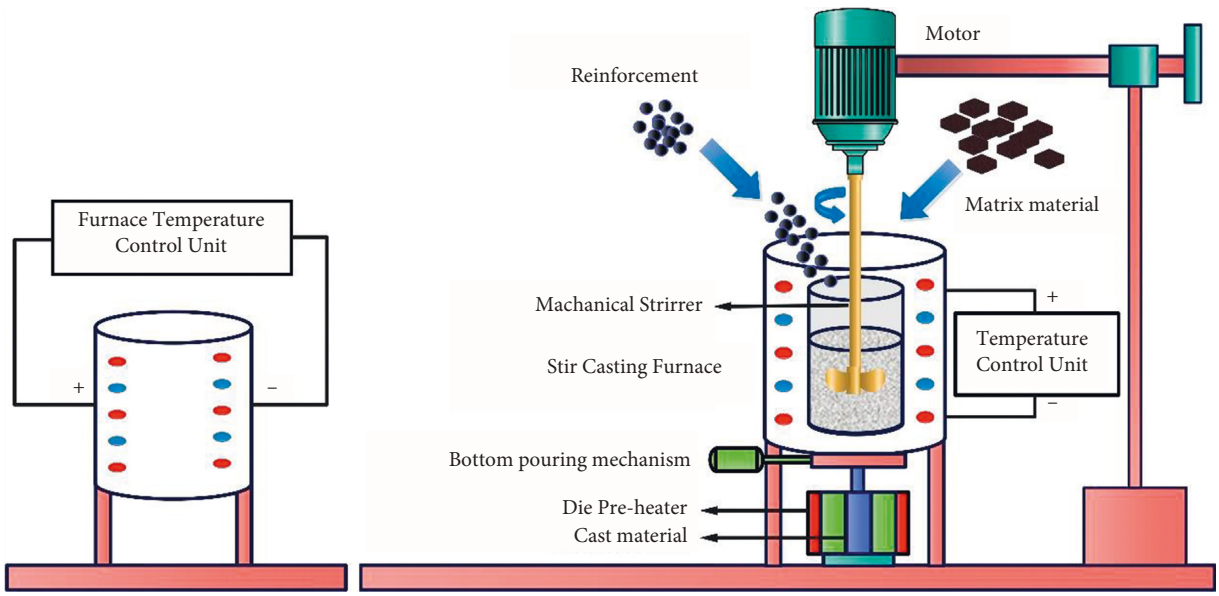

Figure 1: Schematic view of the stir-casting arrangement.

Table 1: Stir-cast progression and hot-press progression parameters.

Stir-cast progression		Hot-press progression	
Input parameters	Levels (1,2,3)	Input parameters	Levels (1,2,3)
A: Stirring speed, rev/min	525, 575,625	E: Temperature, C	420,460,500
B: Stirring time, min	5, 10,15	F: Pressure, MPa	40,80,120
C: Casting temperature, C	700,740,780	G: Dwelling time, min	15,30,45
D: ZrO_2 reinforcement, %	4,8,12	–	–

CRITIC, PCA, and Entropy, Fuzzy and AHP. A skilled mathematician is needed to perform critical computational steps when analyzing contradictory optimization parameters when using weight methods. In order to quickly discover the best solutions, those in the sector require forecasting tools that utilize simple mathematical principles. SRC can be used to solve multi-objective optimization problems without the usage of weighting methods or costly computing procedures.

3. Results and Discussion

Microfluidic chip testing was conducted using a variety of stir-cast and hot-press settings on the Taguchi L9 microfluidic chip. Pareto analysis is used to discover optimal values for each parameter in the case of contradicting outputs. SRC is used to find a single set of optimal variables for all outputs in a model. Microstructure tests were carried out to support this. Using Taguchi and SRC's ideal circumstances as a baseline, independent experiments verify their conclusions.

3.1. Stir-Casting Process. To create the Al 7075/ZnO-ZrO_2 composites, stir casting was used. Taguchi L9 experiment method was used to examine the effects of stirring speed, stirring time, cast temperature, and ZrO_2 reinforcements (4,8,12%) on wear loss, hardness, and Ultimate tensile strength. For each trial, average values of 24 hardness indents, three wear losses, and Ultimate tensile strength are shown in Table 2 based on a total of 36 indents. Using the actual output data, the S/N ratio was calculated. Quality parameters for hardness and UTS were employed with larger-the-better values, whereas wear loss was used with smaller values. Table 2 shows the S/N ratio statistics for the stir-casting process's output quality attributes.

In order to build the Pareto ANOVA, we used the S/N ratio data (Table 2). An analysis of variance using the Pareto principle helps researchers to find the elements that contribute and the best values for hardness and wear loss, as well as UTS.

3.1.1. Influence of Factors on Hardness. Using Signal to Noise ratio, Figure 2 depicts the hardness behavior for each factor and level. The results showed that adding ZrO_2 to the Al 7075/ZnO matrix at a higher percentage (after 12%) resulted in a significant decrease in hardness values. Possible explanations include an increase in trapped air within a ZrO_2 particle cluster when the ZrO_2 reinforcement percentage is increased, as well as the fact that ZrO_2 particles that have agglomerated during melting do not break apart. Some reinforced elements might aggregate on the melted surfaces to specific characteristics of MMCs. The shear action of rotating blade induced by a prolonged period of maximum stirring speed resulted in the deagglomeration of reinforcement particles in the melt mixture, resulting in a

Table 2: Experimental Input and output settings of stir-casting progression.

Trial. No	Input				Output			S/N ratio, dB		
	Stirring speed rpm	Stirring time Min	Casting temperature °C	ZrO_2 reinforcement %	Hardness HV	Ultimate tensile strength MPa	WL Mg	Hardness	UTS	WL
L1	525	5	700	4	63.8	162.7	13.8	36.10	44.23	−22.80
L2	525	10	740	8	64.4	176.2	12.9	36.18	44.92	−22.22
L3	525	15	780	12	61.8	141.2	15.1	35.82	43.01	−23.58
L4	575	5	740	8	63.6	153.4	14.7	36.07	43.72	−23.35
L5	575	10	780	12	66.5	174.6	13.2	36.46	44.84	−22.41
L6	575	15	720	4	66.8	180.1	10.1	36.50	45.11	−20.09
L7	625	5	780	12	64.9	178.3	12.2	36.24	45.02	−21.73
L8	625	10	740	8	64.3	169.9	13.3	36.16	44.60	−22.48
L9	625	15	720	4	67.0	198.1	8.8	36.52	45.94	−18.89

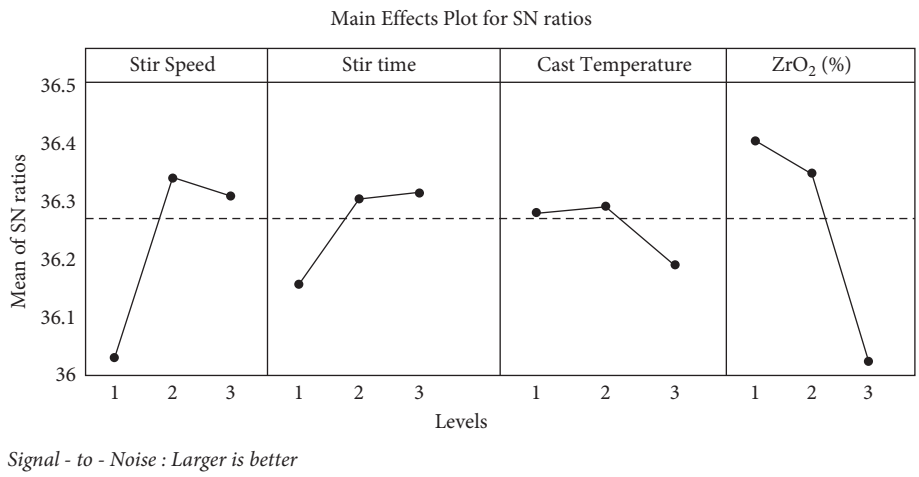

Figure 2: Main effect plot for hardness.

homogenous particle distribution in composites. Improved hardness values were achieved by increasing speed and stirring duration.

Observe that hardness ratings do not improve significantly once the stirring speed crosses the intermediate value. A possible explanation for the enhanced hardness values observed with a higher casting temperature is improved wettability and a more uniform mixing process. There was a strong correlation between ZrO_2 reinforcement and the effects of stirring rates, durations of stirs, and pouring temperatures (refer to Table 3). To maximize the hardness value, Pareto ANOVA indicated that A2B3C2D1 (i.e., 575 rpm, 15 min stir duration, 740°C cast temperature and ZrO_2: 4% ZrO_2) was found to be the best stir-casting conditions (refer Table 3). Owing to the multifactor structure of the studies (i.e., levels factors = 34 : 81 experimental set), the indicated ideal levels differ from those of L9 experiments.

3.1.2. Impact on Parameters on Wear Loss. Figure 3 illustrates the most important aspects that influence wear loss, as shown in the figure. After a 10% increase in ZrO_2 reinforcement to Al 7075/ZnO, wear loss increased. With an increase in the amount of ZrO_2 reinforcement, large particle clusters form that reduce matrix wetting and cause the reinforcement to pull away from the matrix under loading conditions, leading to the formation of large gaps or pores in the composites. When the stir speed and time are increased, the wear loss lowers, allowing for a more uniform dispersion of reinforcement particles and an improved interparticle distribution. Particle agglomeration, on the other hand, can occur at modest stirring speeds and times. Increased wear loss is caused by cast temperatures which are either very less or very high Over low pouring temperatures cause particle aggregation and premature solidification. Due to the long time it takes for the material to solidify at a high temperature, an undesirable microstructure can result. ZrO_2 reinforcement had the greatest impact on wear loss, followed by stirring time, stirring speed as well as pouring temperature. It was observed that A3B3C2D2 (i.e., 625 rpm, 15 minutes of stirring time, cast temperature of 740°C, and ZrO_2: 8% wt.) were the optimum parameter levels for decreasing wear loss in composites. In the Taguchi L9 trials, the optimal settings for minimising wear loss are not one of them.

3.1.3. Impact of Parameters on UTS. For the Al 7075/ZnO/ZrO_2 composites, the most important stir-casting factors were shown in Figure 4. From 4% to 12% ZrO_2 reinforcement, the ultimate tensile strength of the material did not

Table 3: Stir casting methodology for Pareto ANOVA results.

Output	Parameters	Levels	Stirring speed	Stirring time	Casting temperature		ZrO_2%	Total
Hardness (HV)	Mean	1	36.03	36.14	36.25		36.36	108.68
	Factor	2	36.34	36.27	36.26		36.31	—
	Levels	3	36.31	36.28	36.17		36.02	—
	Mean square deviation (MSD)		0.15	0.05	0.01		0.21	0.17
	% contribution		41.3	7.8	3.05		45.85	100
	Optimal levels		A2B3C2D1 (not at L9 experiments)					
Wear loss	Mean	1	−22.86	−22.62	−21.79	−21.37		−65.84
	Factor	2	−21.95	−22.37	−21.48	−21.34		—
	Levels	3	−21.03	−20.85	−22.57	−23.13		—
	MSD		5.05	5.48	1.92	6.32		18.77
	% contribution		27.93	28.4	11.12	32.78		100
	Optimum levels		A3B3C2D2 (not at L9 experiments)					
Ultimate tensile strength (MPa)	Mean	1	44.05	44.32	44.65	45.00		133.8
	Factor	2	44.56	44.79	44.86	45.02		—
	Levels	3	45.19	44.69	44.69	43.78		—
	MSD		1.96	0.34	0.47	3.06		5.84
	% contribution		34.29	5.15	7.34	53.22		100
	Optimum levels		A3B2C2D2 (not at L9 experiments)					

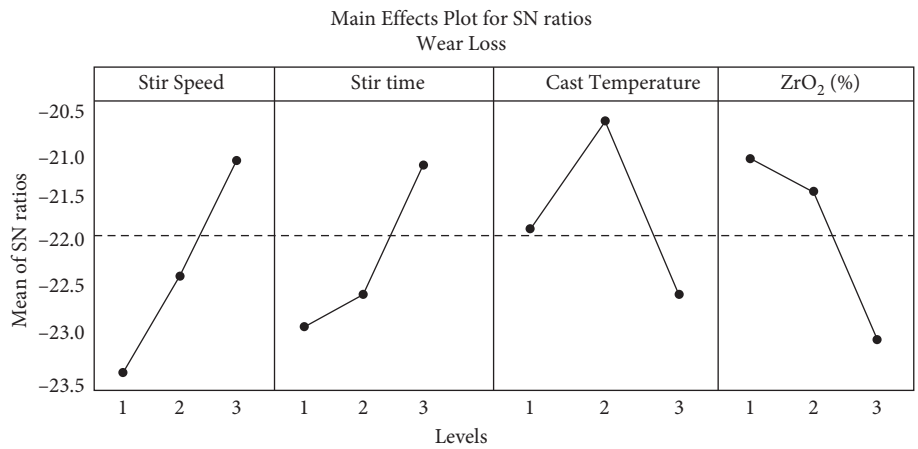

Figure 3: Main effect plot for wear loss.

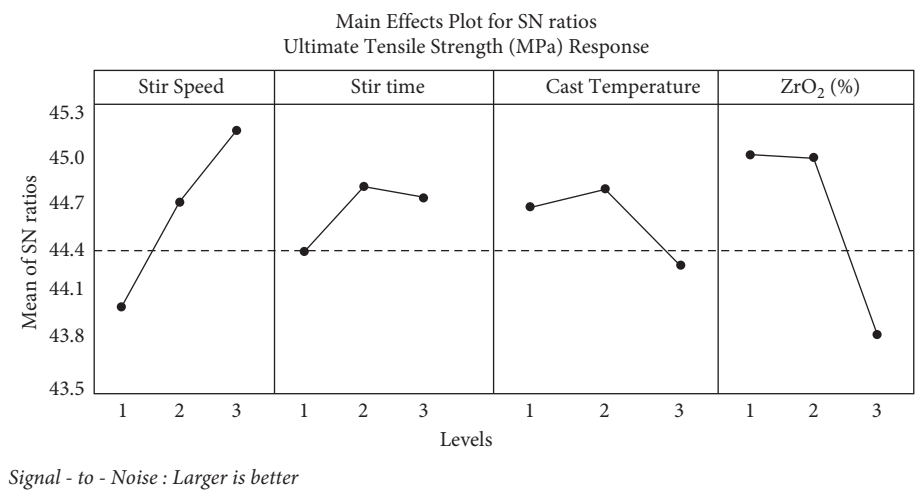

Figure 4: Main effect plot for ultimate tensile strength.

change at all. It is possible that the porosity or voids caused by clustered ZrO_2 particles reduces the value of UTS, which diminishes the advantages of reinforcing particles beyond the critical limit of reinforcement. Centrifugal currents are set up in an aluminium melt when the stirring speed is increased, resulting in a vortex. To increase the composites' UTS, this aids in dispersing the reinforcing particles evenly throughout the melt. The formation of a vortex by stirring speed and time is critical to the distribution of reinforced particles in an aluminium matrix. Because vortex have a greater ability to draw in air, prolonged stirring time results in composite porosity. The aluminium melt's viscosity and gas pick-up are influenced by the cast temperature. Low viscosities caused by low casting temperatures generally have difficulties stirring aluminium melt, while high viscosities lose control over particle movement, making it difficult to distribute particles uniformly throughout composites. As an example, value stating that zirconium oxide reinforcement accounted for more than any other factor. For a higher ultimate tensile strength, stir-casting conditions A3B2C2D2, which include a 600 rpm stir speed, an 8-minute stir period, and ZrO_2 weight percentage of 10%, should be used instead. The Taguchi L9 trials were the ideal sets for maximising UTS, which founded as optimum.

3.1.4. Optimization of Stir-Casting Process. Using the Taguchi method, it was not possible to simultaneously optimise many outputs due to limitations. Using a multi-objective optimization approach, WL was minimised while UTS and hardness are maximised using the stir-cast method. Based on the measured experimental results, the S/N ratio data is calculated (refer Table 2). The S/N ratio data of each response were used to assign a rank to each response. The top rank is given to the S/N ratio with the highest value, followed by the second and so on (refer to Table 4). Figure 5 shows the Main effect plot for responses of Signal to Noise ratio.

3.1.5. Confirmation Experiments. Table 5 shows the progress of Stir casting through Anova output results. Experiment results for the beginning and ideal conditions are shown in Table 6 and Figure 6 shows the contribution of parameters to

Table 4: Super ranking concept: stir-casting progression result summary.

Trial. No	S/N ratio, dB			Rank			Squaring rank			Sum of squared rank
	Hardness (Hv)	Ultimate tensile strength (MPa)	WL	Hardness (Hv)	Ultimate tensile strength (MPa)	WL	Hardness (Hv)	Ultimate tensile strength (MPa)	WL	
L1	36.10	44.23	-22.80	7	7	7	49	49	49	147
L2	36.18	44.92	−22.21	5	4	4	25	16	16	57
L3	35.82	43.01	−23.58	9	9	9	81	81	81	243
L4	36.07	43.72	−23.35	8	8	8	64	64	64	192
L5	36.46	44.84	−22.41	3	5	5	9	25	25	59
L6	36.50	45.11	−20.09	2	2	2	4	4	4	12
L7	36.24	45.02	−21.73	4	3	3	16	9	9	34
L8	36.16	44.60	−22.48	6	6	6	36	36	36	108
L9	36.52	45.94	−18.89	1	1	1	1	1	1	3

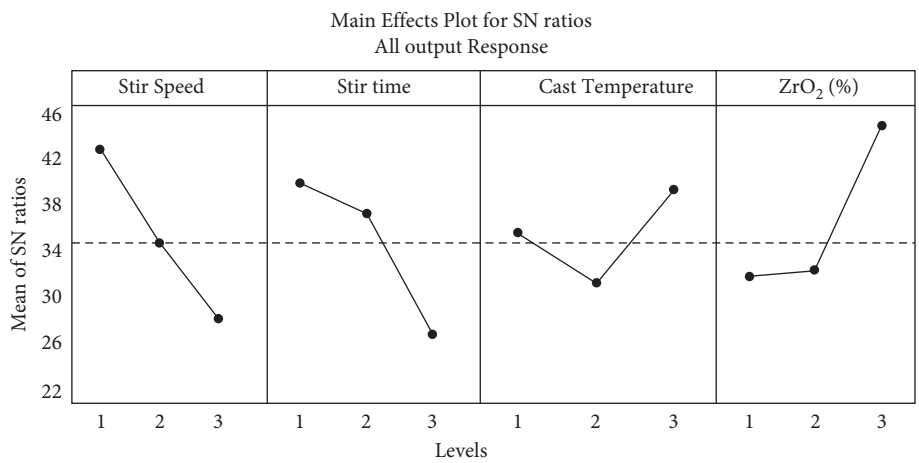

Figure 5: Main effect plot for responses of signal to noise ratio.

different responses. Note that the Taguchi technique was utilised to discover ideal conditions for stir-casting progression for a distinct response, but the SRC technique was utilised to find the optimum parameters for several reactions. Hardness, wear loss, and UTS were enhanced by 6.58%, 37.68%, and 29.26% using the Taguchi method, respectively. SRC yielded a 37.68% reduction in WL, a 25.02% increase in UTS, and a 5.64% increase in hardness associated with the starting experimental conditions of the stir-casting method. The better findings show that Taguchi and SRC are effective.

3.2. Hot-Pressing Technique. Stir-cast composite samples benefit from improved characteristics thanks to the use of the hot-pressing process (prepared as per optimized condition). SRC found the best results with a ZrO_2 reinforcement weight of 10% in an Al 7075-ZnO matrix. Consequently, the hot-pressing procedure was used on the Al 7075/ZnO and ZrO_2 specimens that had been stir-casted. By applying hot-press techniques with diverse sets of parameters, the WL, hardness, and ultimate tensile strength were studied. For hot-press, Taguchi L9 experiments were conducted to acquire the experimental input-output data. Table 7 shows the S/N ratio based on experimental results. Pareto analysis of variance was utilized to determine the impacts of hot-press factors and the ideal level. Table 8 summarises the hot-pressing technique's findings.

3.2.1. Effect of Hardness Factors. Figure 7 explains hot-pressing parameters affect the hardness of the material. As pressure was raised, the hardness values rose in a straight line. Full densification, which leads to higher hardness values, may be achieved by applying pressure to composite samples. Low temperatures allow composites to solidify prematurely before pressure is applied, whereas high temperatures produce significant grain growth and low hardness values as a result of the cooling process. Maximum time below pressure is constantly preferred to achieve full compaction and hence higher hardness values. Compared to pressure and temperature, dwell time or holding time has a negligible effect on hardness. The three most significant factors were found to be 69.08 % pressure, 19.47 % temperature, and 11.46 % dwell duration (refer to Table 8). Temperature, pressure, and dwell time at 400°C, 100 MPa, and 40 minutes were found to be the ideal hot pressing conditions for maximizing hardness values.

Table 5: Stir-casting progression: pareto ANOVA output results.

Parameters	Levels	Stirring speed	Stirring time	Casting temperature	ZrO_2%	Total
Mean	1	42.06	39.88	25.32	29.44	103.23
Factor	2	34.22	37.07	30.11	29.11	—
Levels	3	26.95	26.28	37.92	44.68	—
MSD		344.72	307.28	95.23	474.16	1221.39
% contribution		28.07	25.31	8.72	37.90	100
Optimum levels		A3B3C2D2(not at L18 experiments combination)				

Table 6: Validation of experimental outcome for optimum settings of stir-casting progression.

State	Stir-casting state	Responses	% Improvement
Optimum setting for hardness	Stirring speed: 575 rpm	Hardness: 68	6.58%
	Stirring time: 15 min	—	—
	Casting temperature: 740°C	—	—
	ZrO_2 wt.%: 4% wt	—	—
Optimum setting for wear loss	Stirring speed: 625 rpm	WL: 8.6 g	37.68%
	Stirring time: 15 min	—	—
	Casting temperature: 740°C	—	—
	ZrO_2 wt.%: 8% wt	—	—
Optimum setting for UTS	Stirring speed: 625 rpm	UTS: 210.3 MPa	29.26%
	Stirring time: 10 min	—	—
	Casting temperature: 740°C	—	—
	ZrO_2 wt.%: 8% wt	—	—
Optimum setting for all outputs	Stirring speed: 600 rpm	WL: 8.6 g	WL: 37.68%
	Stirring time: 12 min	UTS: 204.2 MPa	UTS: 25.02%
	Casting temperature: 740°C	Hardness: 68.1	UTS: 25.02%
	ZrO_2 wt.%: 8% wt	—	—

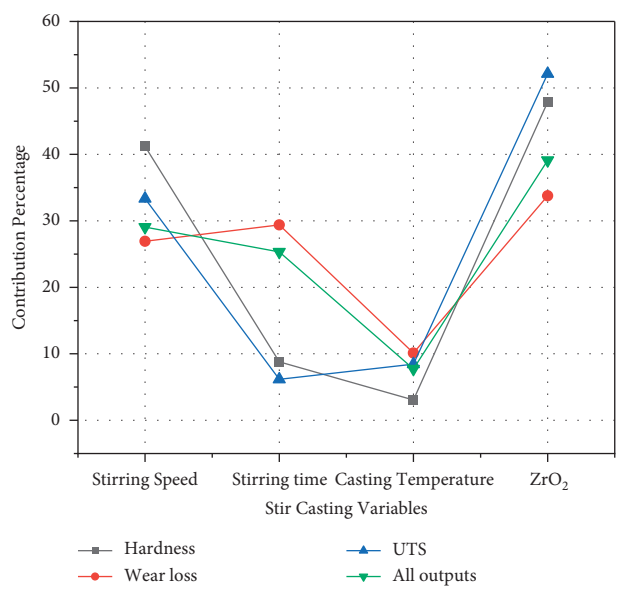

Figure 6: Contribution of parameters on variant responses in percentage.

3.2.2. Effect of Wear Loss Factors. As shown in Figure 8, hot-pressing circumstances have a significant impact on wear loss. Low wear loss can be attributed to high pressure and a shorter dwell duration. To optimise heat transmission, grain structure, and pore closure in pressurised composites, metal is forced closer to the die surface walls by increased pressure. The least amount of wear is found when the temperature is maintained at a consistent intermediate range. An early solidification and lower heat extraction capabilities result in minimal wear loss. Pressure, temperature, and dwell time are identified to contribute 48.77%, 38.07%, and 13.17% to wear loss,

Table 7: Hot-pressing progression's experimental input and output setting.

Trial. No.	Input			Output			S/N ratio, dB		
	Temperature(E)	Pressure(F)	Dwelling time	Hardness	Ultimate tensile strength	Wear loss	Hardness	Ultimate tensile strength	Wear loss
L1	420	40	15	70.2	216.1	8.4	36.93	46.69	−18.49
L2	420	80	30	72.3	233.6	7.5	37.18	47.37	−17.50
L3	420	120	45	72.7	236.5	7.1	37.23	47.48	−17.03
L4	460	40	30	71.7	227.5	8.0	37.11	47.14	−18.06
L5	460	80	45	72.8	239.1	6.6	37.24	47.57	−16.39
L6	460	120	15	73.3	241.9	5.2	37.30	47.67	−14.32
L7	500	40	45	70.6	220.9	8.3	36.98	46.88	−18.38
L8	500	80	15	71.3	233.4	7.9	37.06	47.36	−17.95
L9	500	120	30	72.3	228.9	8.2	37.18	47.19	−18.28

Table 8: Hot-pressing progression's Pareto ANOVA results.

Output	Parameters	Levels	E (°C)	F (MPa)	G (min)	Total
Hardness (Hv)	Mean	1	37.20	37.11	37.16	111.59
	Factor	2	37.25	37.19	37.21	—
	Levels	3	37.15	37.29	37.23	—
	MSD		0.015	0.048	0.008	0.071
	% Contribution		18.47	69.09	12.47	100
	Optimum levels		E2F3G3 (not at L9 assortment)			
Wear loss	Mean	1	−17.67	−18.31	−16.92	−52.13
	Factor	2	−16.26	−17.28	−17.95	—
	Levels	3	−18.20	−16.54	−17.27	—
	MSD		07.08	03.73	01.64	12.44
	% Contribution		49.76	36.07	14.18	100.00
	Optimum levels		E2F3G1			
Ultimate tensile strength (Mpa)	Mean	1	47.18	46.91	47.24	141.79
	Factor	2	47.46	47.43	47.23	—
	Levels	3	47.15	47.45	47.31	—
	MSD		0.19	0.56	0.02	0.77
	% Contribution		24.54	74.08	1.38	100
	Optimum levels		E2F3G3 (not the combination of L9 experiments)			

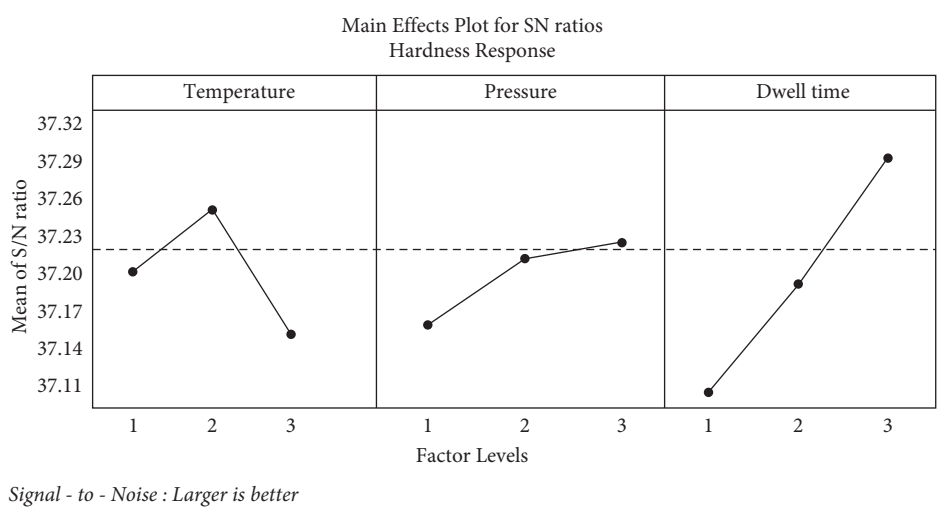

Figure 7: Main effect plot for ultimate tensile strength.

respectively. The optimum conditions (E2F3G1: 480°C, 100 MPa, and a dwell time of 20 minutes) result in the least amount of wear and tear.

3.2.3. Effect of Ultimate Tensile Strength Factors. Figure 9 depicts the UTS, which follows the same pattern as the values of hardness and Figure 10 shows the mean for overall output

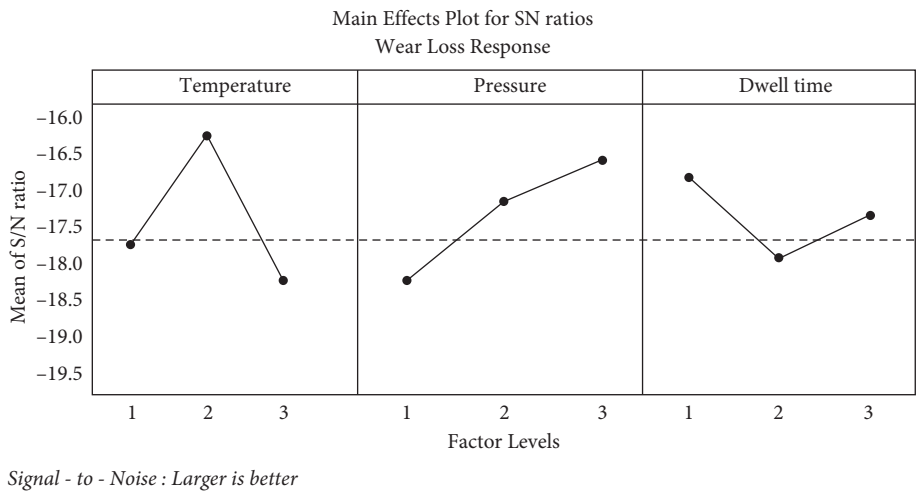

Figure 8: Main effect plot for wear loss responses.

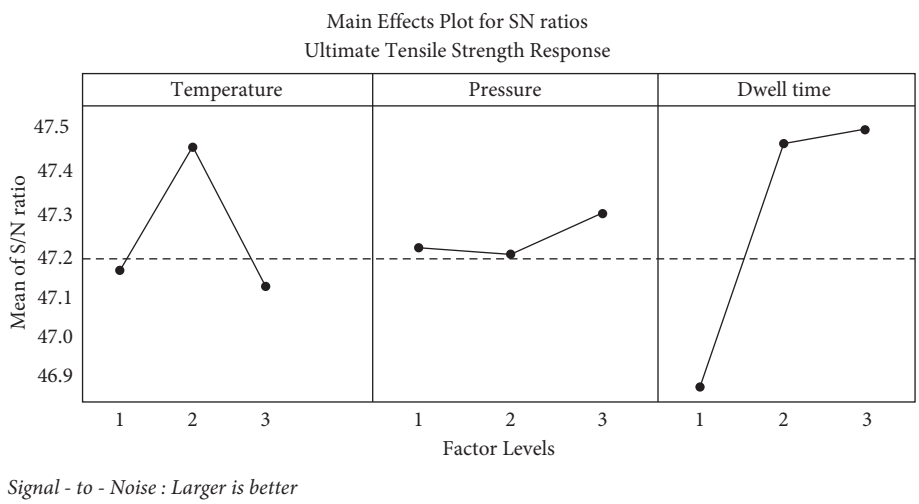

Figure 9: Main effect plot for wear loss.

responses. Figure 11 shows that hardness and ultimate tensile strength have a high link, which may explain why this is the case. There was no discernible increase in characteristics due to an increase in pressurization pressure after reaching the midpoint. When the temperature was kept in the medium range and the dwell time was increased, composites' ultimate tensile strength improved. A total of 75.09%, 1.39%, and 23.52% was provided by pressure, dwell time, and temperature. It was observed that E2F3G3 was the ideal combination of factors and levels to maximise the UTS of the composite.

3.2.4. Optimization of Hot-Pressing Process. Controversial comments can be prioritized using the "super ranking" idea. For hot-pressing conditions, the processes in the super ranking concept are similar to those for stir-cast conditions, and outcomes are exposed in Table 9. For higher-quality composites, the ideal hot-pressing settings were found to be E2F3G3 (440°C, 100 MPa, and a 40 minute dwell period). There was a maximum contribution of 73.18%, followed by a dwell time of 4.35% for pressure and temperature, respectively. For each individual output, the percentage involvement and ideal factor level were identified to be varied, which may be attributed to an input factor impact on the outcome of each individual. Individual outputs, as well as several outputs, have different optimal variables and levels than those found in L9 trials, according to research.

3.2.5. Experiments for Confirmation. Pareto output results for all the outputs were given in Table 10. Comparing outcomes of the starting and ideal hot-pressing experiments is shown in Table 11. Using the Taguchi method, a rise of 4.7% in hardness and a 13.05% increase in UTS were found (refer Table 11). An increase of 42.9% was achieved by creating the ideal circumstances to minimize wear (refer Table 11). The ideal circumstances for SRC resulted in a 39.29% decrease in WL, while an 11.54% rise in UTS and a 4.88% increase in hardness, respectively, were found (refer to Table 11). It is possible to conduct optimization work using Taguchi and SRC. Figure 12 shows the contribution of percentage at different parameters.

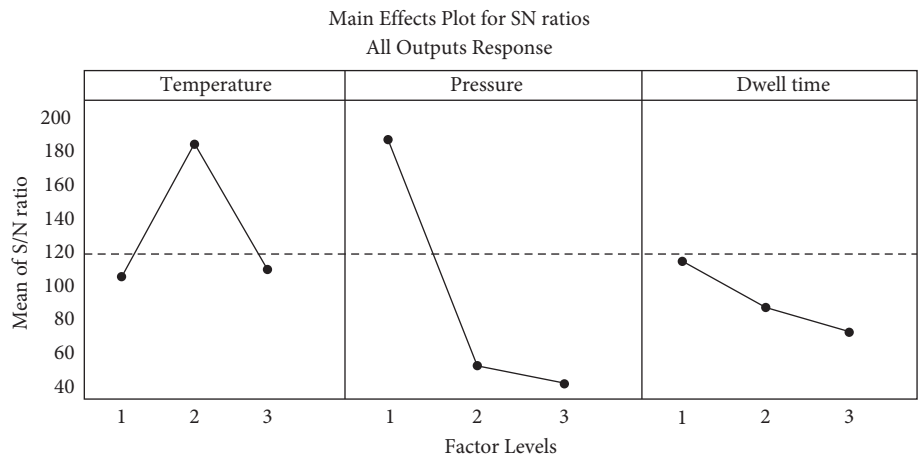

Signal - to - Noise : Smaller is better

Figure 10: Main effect plot for responses of signal to noise ratio.

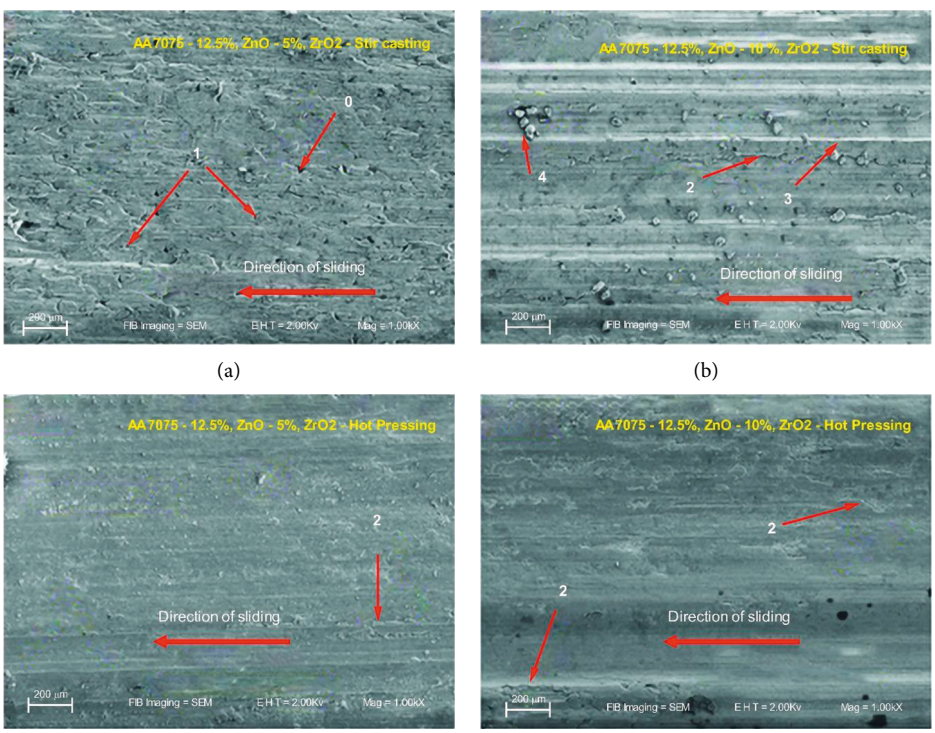

Figure 11: Wear Surface morphology of hot-pressed and stir-casting AA 7075/ZnO-ZrO_2 composites. (a) AA7075-12.5%, ZnO-5%, ZrO_2-stir casting. (b) AA7075-12.5%, ZnO-10%, ZrO_2-stir casting. (c) AA7075-12.5%, ZnO-5%, ZrO_2-hot pressing. (d) AA7075-12.5%, ZnO-10%, ZrO_2-hot pressing.

3.3. Hot-Pressing and Stir-Casting Comparison. Stir-cast and hot-press processes have been compared in Table 12 for their optimized qualities. The stir-casting process was used to create composites for hot-pressing under optimised parametric conditions. In comparison to the stir-casting process, the hot-pressing technique reduced WL by 40.8% while increasing UTS and hardness values by 19.83% and 9.6%, respectively.

3.4. Microstructure Characterisation. Figure 13 shows the microstructural characterization of Al 7075/ZnO-ZrO_2 composites made by stir-casting and hot-pressing. The surface morphology of ZrO_2 particles was studied using optical and SEM micrographs. ZrO_2 particles are similar in appearance to these bright silvery, almost spherical particles. Al 7075/ZnO-5% ZrO_2 and ZnO-10% ZrO_2 in stir-casted conditions are shown in Figures 13(a)–13(d). A dendritic

Table 9: Super ranking concept's result summary.

Trial. No	S/N ratio, dB			Ranking			Square ranking			Sum of squared rank
	Hardness	Ultimate tensile strength	Wear loss	Hardness	Ultimate tensile strength	Wear loss	Hardness	Ultimate tensile strength	Wear loss	
L1	36.93	46.69	−18.49	9	9	9	81	81	81	243
L2	37.18	47.37	−17.50	4	4	4	16	16	16	48
L3	37.23	47.48	−17.03	3	3	3	9	9	9	27
L4	37.11	47.14	−18.06	6	7	6	36	49	36	121
L5	37.24	47.57	−16.39	2	2	2	4	4	4	12
L6	37.30	47.67	−14.32	1	1	1	1	1	1	3
L7	36.98	46.88	−18.38	8	8	8	64	64	64	192
L8	37.06	47.36	−17.95	7	5	5	49	25	25	99
L9	37.18	47.19	−18.28	4	6	7	16	36	49	101

Table 10: Pareto ANOVA outcome for all outputs.

Parameters	Levels	E (°C)	F (MPa)	G (min)	Total
Mean	1	106	185.33	115	282
Factor	2	45.33	53	90	—
Levels	3	130.67	43.68	78	—
MSD		11570.67	37668.67	2238	51447.30
% contribution		23.49	72.18	4.34	100
Optimum levels		E2F3G3 (not the combination of L9 experiments)			

Table 11: Validation experimental outcome for optimum settings of hot-pressing progression.

Setting	Hot-pressing progression	Response	% Improvement
Primary (Table 7)	Temperature: 420°C Pressure: 40 MPa Dwell time: 15 min	WL: 8.5 g UTS: 216.2 MPa Hardness: 70.3	— — —
Optimum setting for hardness	Temperature: 460°C Pressure: 120 MPa Dwell time: 45 min	Hardness: 73.5 — —	4.7% — —
Optimum setting for wear loss	Temperature: 460°C Pressure: 120 MPa Dwell time: 15 min	WL: 4.8 g — —	42.9% — —
Optimum setting for UTS	Temperature: 460°C Pressure: 120 MPa Dwell time: 45 min	UTS: 244.3 MPa — —	13.05% — —
Optimum setting for all outputs	Temperature: 460°C Pressure: 120 MPa Dwell time: 45 min	WL: 5.1 g UTS: 244.3 MPa Hardness: 74.5	WL: 39.29% UTS: 11.54% Hardness: 4.91%

structure can be seen in Figures 13(a)–13(d) that grows in accordance with beneficial growth patterns. A columnar shape is influenced by the direction of heat flow in grains, which promotes the growth of some grains while inhibiting the growth of others. Figures 13(a)–13(d) depict the ZrO_2 particle dispersion in the Al 7075/ZnO matrix. The majority of ZrO_2 particles have a spherical shape. Additionally, the ZnO/Al 7075 alloy has a strong interfacial interaction with ZrO_2, which assists in achieving improved mechanical properties. Al 7075/ZnO-10% ZrO_2 composites S1-HT (Al 7075/ZnO) and S2-HT (Al 7075/ZnO) in hot-pressing conditions are shown in Figures 13(e)–13(h). To create a composite with good mechanical properties, the ZrO_2 reinforcement particles must be evenly distributed in the matrix alloy. If high pressure and hot pressing had been used, the lack of porosity and grain refinement in the composites would have indicated solid castings. ZrO_2 particle surface homogeneity is discovered. As shown in Figures 13(e)–13(h), the ZrO_2 particles are dispersed uniformly throughout the Al 7075/ZnO matrix. The mechanical properties of composites can be improved by having a more uniform dispersion of the matrix and the reinforcement. Al 7075/ZnO-ZrO_2 composites are examined by energy dispersive X-ray spectroscopy.

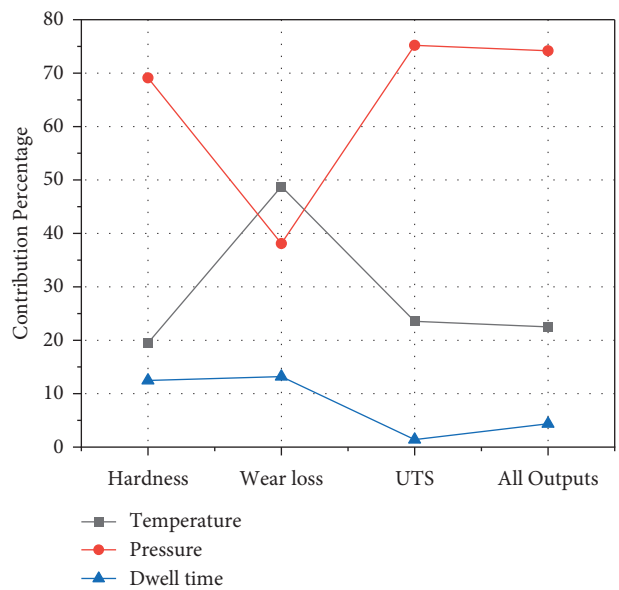

Figure 12: Hot-pressing constraint's percentage of contribution.

Table 12: Evaluation of Variant processing methodology Characteristics.

Optimal characteristics of variable processes		Improvement percentage (%)
Stir cast	Hot press	
WL: 8.7 g	WL: 5.2 g	40.80
Ultimate tensile strength: 204.2 MPa	Ultimate tensile strength: 244.3 MPa	19.83
Hardness: 68.1	Hardness: 74.5	09.60

3.5. Wear Surface Morphology. Figure 11 depicts the wear patterns of Al 7075/ZnO-ZrO_2 composites made using the stir-casting and hot-press conditions described above. From Figure 11, 2 indicates a delaminated area, 3 indicates dense, narrow abrasive grooves, 4 indicates debris, and 5 indicates an abrasion area. For Al 7075/ZnO-ZrO_2 composites exposed to stir cast Figures 11(a) and 11(b), hot pressing Figure 11(c), wear tracks had different wear profiles. These findings support the notion that abrasion wear has undergone a significant mechanism of wear change. In contrast to the Al 7075/ZnO-ZrO_2 composites surface exposed to the hot press and displays slim abrasive groove, less debris, and slight abrasive areas; a huge amount of delaminated areas, holes, and abundant grooves had been detected on the AA 7075-12.5% ZnO-ZrO_2 composite surface exposed to stir casting. Figure 11(a) indicates that the stir-cast S1 composite (Al 7075/ZnO-5% ZrO_2) has a higher degree of plastic deformation because of the impression of the pin and disc at maximum load. Observed maximum wear loss is substantially supplemented by achieved results, namely maximum wear loss at 30 N, with the width of the wear grooves. Table 13 shows the Validation experimental results for optimum settings for stir-casting process.

A small amount of plastic deformation can be seen in the stir-cast S2 composite (Al 7075/ZnO-10% ZrO_2) at the load of 30 N, as shown in the micrograph of Figure 11(b). Wear grooves are narrower with a lower wear loss of 8.7 g and a higher VHN hardness of 67.4; these findings are supported by the obtained results, which indicate negligible wear loss under a 30 N load. S2 composites, in contrast to S1 composites, include more hard and ceramic particles. Wear can be reduced by using ceramic elements as load-carrying material. Many researchers found the same thing. Hot-pressed S1-HP composite (Al 7075/ZnO-10% ZrO_2) reveals a slight abrasion region (Figure 11(c)), which is corroborated by SEM microscopy. Figure 11(c) shows that the wear groove widths are smaller than in Figures 11(a) and 11(b), with a nominal wear loss of 8.4 g. A higher hardness of 69.8 VHN, as opposed to that made by means of the stir-casting processes, could also account for improved wear resistance. In addition, samples produced by simultaneously applying high pressure and a lower dwell period result in low wear losses. As shown in Figure 11(c), the wear track surface had many slim and narrow grooves similar to the sliding track and some wear debris elements, which indicates mild abrasive wear. As shown in Figure 11(d), the SEM micrograph exhibits like surface to S1-HP composite. For comparison, the wear tracks in Figure 11(d) indicate the least wear loss of 5.1 grams in comparison to Figures 11(a)–11(c). Compared to other composites, the 73.8 VHN hardness and grain refinement because of the hot press may be a factor in the improved wear rate of hot-pressed carbon fibre.

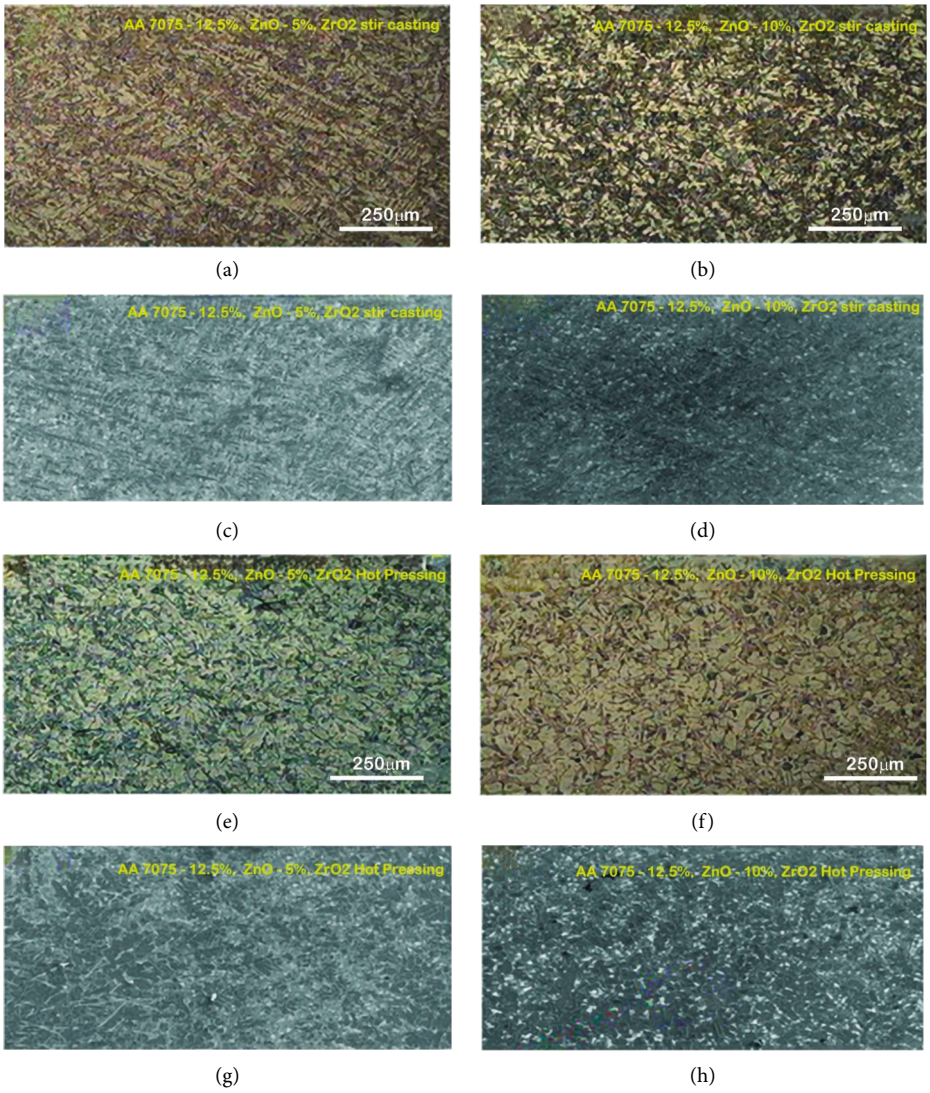

Figure 13: Microstructure of hot-pressed and stir-casting AA 7075/ZnO-ZrO_2 composite. (a, c) AA7075-12.5%, ZnO-5%, ZrO_2 stir casting. (b, d) AA7075-12.5%, ZnO-10%, ZrO_2 stir casting. (e, g) AA7075-12.5%, ZnO-5%, ZrO_2 hot pressing. (f, h) AA7075-12.5%, ZnO-10%, ZrO_2 hot pressing.

Table 13: Validation experimental outcome for optimum settings for stir-casting progression.

State	Processing parameters	Response	Composite specification
Primary	Stirring speed: 525 rpm	WL: 13.8 g	S1 (Al 7075/ZnO-5% ZrO_2)
	Stirring time: 5 min	UTS: 162.7 MPa	—
	Casting temperature: 700°C	Hardness: 63.8	—
	ZrO_2 wt.%: 4	—	—
Optimum setting for all outputs	Stirring speed: 625 rpm	WL: 8.5 g	S2 (Al 7075/ZnO-10% ZrO_2)
	Stirring time: 15 min	UTS: 204.2 MPa	—
	Casting temperature: 740°C	Hardness: 68.1	—
	ZrO_2 wt.%: 8% wt	—	—
Initial hot pressing	Temperature: 420°C	WL: 8.5 g	S1-HP (Al 7075/ZnO-10%ZrO_2)
	Pressure: 40 MPa	UTS: 217.2 MPa	—
	Dwell time: 15 min	Hardness: 70.3	—
Hot pressing optimum setting for all outputs	Temperature: 460°C	WL: 5.2 g	S2-HP (Al 7075/ZnO-10%ZrO_2)
	Pressure: 120 MPa	UTS: 244.3 MPa	—
	Dwell time: 45 min	Hardness: 74.5	—

4. Conclusions

Using a two-step procedure, which includes stir-casting and hot-pressing processes, the current work conserves natural resources while also healing or fixing cast faults. The following are some observations on the acquired results: [41–43].

(1) Al 7075/ZnO composites reinforced with ZrO_2 at different weight percentages can be made via stir casting. Casting properties were most strongly influenced by ZrO_2 reinforcements, succeeded by stirring speed, stirring time, and temperature.

(2) When the best stir-casting circumstances were determined, wear loss was reduced by 37.68% (13.8–8.4 g), 25.02%, and 5.64%, respectively, compared to the first stir-casting parameters, and hardness was increased by 63.8–67.4% compared to the original conditions. For stir casting, a Pareto analysis of variance found optimum conditions, which were not found in a set of L9 investigations, and their related properties show that the models constructed and analysis done were effective.

(3) A hot-pressing process is used to repair or decrease pores in samples that have been manufactured under stir-cast optimized conditions. Variables (such as temperature, pressure, and dwell time) that affect characteristics (such as wear loss, UTS, and hardness) during hot pressing have been experimentally investigated. Pressure, temperature, and dwell time all have a role in sealing pores, which results in enhanced characteristics.

(4) Wear loss was reduced by 39.29%, UTS increased 11.54%, and hardness values increased 4.88% as compared to the initial hot-pressing circumstances, according to the super ranking idea.

(5) The hot-pressing process used on the improved stir-cast components reduced wear loss by 40.8%, increased UTS by 19.83%, and increased hardness by 9.6%. Because of the results obtained, even stir-cast optimised condition have a greater possibility to enhance the characteristics when subjected to hot press.

Data Availability

The authors confirm that all the data are available in this research article.

Conflicts of Interest

The authors declare that they have no conflicts of interest.

References

[1] R. H. Oskouei, M. R. Barati, and R. N. Ibrahim, "Surface characterizations of fretting fatigue damage in aluminum alloy 7075-T6 clamped joints: the beneficial role of Ni-P coatings," *Materials*, vol. 9, no. 3, pp. 141–3, 2016.

[2] R. P. Udayagiri, S. B. Koppad, P. G. Gupta, M. Munishamaiah, K. Bontha, and S. Bontha, "The effect of heat treatment on the mechanical and tribological properties of dual size SiC reinforced A357 matrix composites," *Journal of Materials Research and Technology*, vol. 9, no. 3, pp. 6434–6452, 2020.

[3] F. Bedir, "Characteristic properties of Al-Cu-SiCp and Al-Cu-B4Cp composites produced by hot pressing method under nitrogen atmosphere," *Materials & Design*, vol. 28, no. 4, pp. 1238–1244, 2007.

[4] J. Hashim, L. Looney, and M. S. J. Hashmi, "Metal matrix composites: production by the stir casting method," *Journal of Materials Processing Technology*, vol. 92-93, no. 93, pp. 1–7, 1999.

[5] D. Bommana, T. R. K. Dora, N. P. Senapati, and A. S. Kumar, "Effect of 6 Wt.% particle (B4C + SiC) reinforcement on mechanical properties of AA6061 aluminum hybrid MMC," *Silicon*, vol. 14, no. 8, pp. 4197–4206, 2022.

[6] R. Srinivasan, B. Suresh Babu, P. Prathap, R. Whenish, R. Soundararajan, and G. Chandramohan, "Optimization of friction stir welding process parameters on AA 6063-SiC-B4C hybrid metal matrix composites by genetic algorithm," *Journal of Ceramic Processing Research*, vol. 22, no. 1, pp. 16–24, 2021.

[7] H. Xin, Y. Lu, L. Chen et al., "Heat propagation simulation of thin-walled Ti6Al4V alloy components fabricated by double-wire GTAW additive manufacturing," *Science and Technology of Welding & Joining*, vol. 27, no. 6, pp. 446–454, 2022.

[8] B. Prasanna Nagasai, S. Srikanth, and J. A. Ranga Babu, "Mechanical properties of AA 7075-nano ZrO_2 reinforced matrix composites," *Advances in Applied Mechanical Engineering*, Springer, Berlin, Germany, pp. 921–928, 2020.

[9] S. E. Hernández-Martínez, J. J. Cruz-Rivera, C. G. Garay-Reyes, and J. L. Hernández-Rivera, "Experimental and numerical analyses of the consolidation process of AA 7075–2 wt.% ZrO_2 powders by equal channel angular pressing," *Journal of Materials Engineering and Performance*, vol. 28, no. 1, pp. 154–161, 2019.

[10] M. Kaseem, Y. H. Lee, and Y. G. Ko, "Incorporation of MoO 2 and ZrO 2 particles into the oxide film formed on 7075 Al alloy via micro-arc oxidation," *Materials Letters*, vol. 182, pp. 260–263, 2016.

[11] A. Shanmugasundaram, "Experimental investigation of mechanical and tribological properties of Al 7075-MoS2/ZrO_2/Ni hybrid composite," *Advances in Materials and Metallurgy*, Springer, Berlin, Germany, 2019pp. 299–309, Lecture Notes in Mechanical Engineering.

[12] M. Feng, Y. Liao, M. Chen, S. Zhu, and F. Wang, "Crystallization and thermal shock behaviors of SiO2-Al2O3-ZnO-CaO-based glass with added different contents of CeO2 at 900°C," *Cailiao Yanjiu Xuebao/Chinese Journal of Materials Research*, vol. 36, no. 2, pp. 90–98, 2022.

[13] F. C. R. Hernandez, J. M. H. Ramírez, and R. Mackay, *Al-Si Alloys: Automotive*, Aeronautical, and Aerospace Applications, 2017.

[14] A. Lakshmikanthan, S. Bontha, M. Krishna, P. G. Koppad, and T. Ramprabhu, "Microstructure, mechanical and wear properties of the A357 composites reinforced with dual sized SiC particles," *Journal of Alloys and Compounds*, vol. 786, pp. 570–580, 2019.

[15] R. Piya, S. Krishnan, P. K. Muraliraja et al., "Optimization of stir-squeeze casting parameters for production of metal matrix composites using a hybrid analytical hierarchy

process-Taguchi-Grey approach," *Engineering Optimization*, vol. 52, no. 7, pp. 1166–1183, 2020.

[16] N. Barati, J. Jiang, and E. I. Meletis, "Microstructural evolution of ceramic nanocomposites coated on 7075 Al alloy by plasma electrolytic oxidation," *Surface and Coatings Technology*, vol. 437, Article ID 128345, 2022.

[17] S. Gangwar, P. Arya, and V. K. Pathak, "Optimal material selection for ship body based on fabricated zirconium dioxide/silicon carbide filled aluminium hybrid metal alloy composites using novel Fuzzy based preference selection index," *Silicon*, vol. 13, no. 8, pp. 2545–2562, 2021.

[18] A. N. Tiwari, V. Gopinathan, and P. Ramakrishnan, "Processing of modified ai (7010)-sic particulate composites by mechanical alloying and hot-pressing," *Materials and Manufacturing Processes*, vol. 6, no. 4, pp. 621–633, 1991.

[19] M. Shahedi Asl, M. Ghassemi Kakroudi, B. Nayebi, and H. Nasiri, "Taguchi analysis on the effect of hot pressing parameters on density and hardness of zirconium diboride," *International Journal of Refractory Metals and Hard Materials*, vol. 50, pp. 313–320, 2015.

[20] V. Sivamaran, V. Balasubramanian, M. Gopalakrishnan, V. Viswabaskaran, and A. G. Rao, "Combined synthesis of carbon nanospheres and carbon nanotubes using thermal chemical vapor deposition process," *Chemical Physics Impact*, vol. 4, Article ID 100072, 2022.

[21] C. N. Chakravarthy and S. Sathees Kumar, "Surface roughness measurement on Al-7075 reinforced with the ZRO_2 powder by using box-behnken analysis," *International Journal of Mechanical and Production Engineering Research and Development*, vol. 10, no. 2, pp. 859–866, 2020.

[22] A. Singh Rathaur, J. Kumar Katiyar, and V. Kumar Patel, "Experimental analysis of mechanical and structural properties of hybrid aluminium (7075) matrix composite using stir casting method," *IOP Conference Series: Materials Science and Engineering*, vol. 653, no. 1, Article ID 012033, 2019.

[23] V. B. Nathan, R. R.Soundararajan, C. B. Abraham, and F. Rahman.A, "Evaluation of mechanical and metallurgical properties on aluminium hybrid metal matrix composites," *Materials Today Proceedings*, vol. 18, pp. 2520–2529, 2019.

[24] P. N. Bellamkonda, "Wear and electrochemical corrosion behaviour of nano ZrO_2 reinforced AA7075 metal matrix composites," *International Journal of Mechanical and Production Engineering Research and Development*, vol. 9, no. 3, pp. 793–802, 2019.

[25] S. Venkatesan, B. Visvalingam, G. Mannathusamy, V. Viswanathan, and A. G. Rao, "Effect of chemical vapor deposition parameters on the diameter of multi-walled carbon nanotubes," *International Nano Letters*, vol. 8, no. 4, pp. 297–308, 2018.

[26] F. Zhu, Y. Jin, B. Ji et al., "CuO/ZrO_2 co-promoted by ZnO, Sn, and CuP shows high efficiency for dimethyldichlorosilane production in the Rochow-Müller reaction," *Applied Catalysis A: General*, vol. 636, Article ID 118582, 2022.

[27] J. S. Midala, I. H. Kamari, H. M. Al-Hada et al., "Effect of calcination temperature on the structural and optical properties of (ZnO)0.8 (ZrO_2)0.2 nanoparticles," *Journal of Inorganic and Organometallic Polymers and Materials*, vol. 32, no. 5, pp. 1755–1765, 2022.

[28] X. Shi, X. Chen, Z. Xu et al., "Efficient conversion of benzene and syngas to toluene and xylene over ZnO-ZrO_2&H-ZSM-5 bifunctional catalysts," *Chinese Journal of Chemical Engineering*, vol. 45, pp. 203–210, 2022.

[29] J. Ding, Z. Li, W. Xiong, Y. Zhang, A. Ye, and W. Huang, "Structural evolution and catalytic performance in CO2 hydrogenation reaction of ZnO-ZrO_2 composite oxides," *Applied Surface Science*, vol. 587, Article ID 152884, 2022.

[30] J. F. Ying, B. J. Flinn, M. Y. Zhou, P. C. Wong, K. A. R. Mitchell, and T. Fostert, "Optimization of zinc phosphate coating on 7075-T6 aluminum alloy," *Progress in Surface Science*, vol. 50, no. 1–4, pp. 259–267, 1995.

[31] S. E. Hernández Martinez, "Structure and properties of AA 7075 reinforced with nanometric ZrO 2 obtained by ball-milling," *Acta Metallurgica Sinica*, vol. 4, pp. 2703–2709, 2014.

[32] V. Sivamaran, D. V. Balasubramanian, D. M. Gopalakrishnan, D. V. Viswabaskaran, D. A. G. Rao, and D. G. Sivakumar, "Mechanical and tribological properties of Self-Lubricating Al 6061 hybrid nano metal matrix composites reinforced by nSiC and MWCNTs," *Surfaces and Interfaces*, vol. 21, Article ID 100781, 2020.

[33] V. Sivamaran, V. Kavimani, M. Bakkiyaraj, and S. T. Selvamani, "Multi response optimization on tribo-mechanical properties of CNTs/nSiC reinforced hybrid Al MMC through RSM approach," *Forces in Mechanics*, vol. 6, Article ID 100069, 2022.

[34] R. Karunanithi, K. S. Ghosh, and S. Bera, "Synthesis and characterization of TiO2 dispersed Al 7075 micro- and nanocomposite," *Advanced Materials Research*, vol. 984-985, pp. 313–318, 2014.

[35] N. Barati, E. I. Meletis, F. Golestani Fard, A. Yerokhin, S. Rastegari, and M. A. Faghihi-Sani, "Al_2O_3-ZrO_2 nanostructured coatings using DC plasma electrolytic oxidation to improve tribological properties of Al substrates," *Applied Surface Science*, vol. 356, pp. 927–934, 2015.

[36] S. E. Hernández-Martínez, J. J. Cruz-Rivera, C. G. Garay-Reyes, C. G. Elias-Alfaro, R. Martínez-Sánchez, and J. L. Hernández-Rivera, "Application of ball milling in the synthesis of AA 7075-ZrO_2 metal matrix nanocomposite," *Powder Technology*, vol. 284, pp. 40–46, 2015.

[37] V. Sivamaran, V. Balasubramanian, M. Gopalakrishnan, V. Viswabaskaran, and A. G. Rao, "Identification of appropriate catalyst system for the growth of multi-walled carbon nanotubes via catalytic chemical vapor deposition process in a single step batch technique," *Materials Research Express*, vol. 6, no. 10, Article ID 105620, 2019.

[38] J. F. Ying, M. Y. Zhou, B. J. Flinn, P. C. Wong, K. A. R. Mitchell, and T. Foster, "The effect of Ti-colloid surface conditioning on the phosphating of 7075-T6 aluminium alloy," *Journal of Materials Science*, vol. 31, no. 3, pp. 565–571, 1996.

[39] S. Shenbag, N. Moorthi, and V. Moorthi, "Aluminium-titanium diboride (Al-TiB2) metal matrix composites: challenges and opportunities," *Procedia Engineering*, vol. 38, pp. 89–97, 2012.

[40] M. Anil, V. C. Srivastava, M. K. Ghosh, and S. N. Ojha, "Influence of tin content on tribological characteristics of spray formed Al-Si alloys," *Wear*, vol. 268, no. 11-12, pp. 1250–1256, 2010.

[41] F. Muhaffel, M. Baydogan, and H. Cimenoglu, "A study to enhance the mechanical durability of the MAO coating fabricated on the 7075 Al alloy for wear-related high

temperature applications," *Surface and Coatings Technology*, vol. 409, Article ID 126843, 2021.

[42] S. E. Hernández-Martinez, J. J. Cruz-Rivera, C. G. Garay-Reyes, R. Martínez-Sánchez, I. Estrada-Guel, and J. L. Hernández-Rivera, "Comparative study of synthesis of AA 7075-ZrO_2 metal matrix composite by different mills," *Journal of Alloys and Compounds*, vol. 643, no. S1, pp. S107–S113, 2015.

[43] E. Tolun and S. Tolun, "On the comparison of the ballistic response of coated aluminum plates," *Materials & Design*, vol. 31, no. 7, pp. 3188–3193, 2010.

Hindawi
Advances in Materials Science and Engineering
Volume 2022, Article ID 7919532, 14 pages
https://doi.org/10.1155/2022/7919532

Research Article

Surface Flaw Detection of Plug Valve Material Using Infrared Thermography and Weighted Local Variation Pixel-Based Fuzzy Clustering Technique

V. Jacintha,[1] **S. Karthikeyan**,[2] **and P. Sivaprakasam**[3]

[1]*Department of Electronics & Communication Engineering, Sathyabama Institute of Science & Technology, Chennai 600119, India*
[2]*Department of Electronics & Communication Engineering, Sathyabama Institute of Science & Technology, Chennai, India*
[3]*Department of Mechanical Engineering, College of Electrical and Mechanical Engineering, Centre of Excellence-Nanotechnology, Addis Ababa Science and Technology University, Addis Ababa, Ethiopia*

Correspondence should be addressed to V. Jacintha; jacinthaece@gmail.com and P. Sivaprakasam; shiva@aastu.edu.et

Received 7 June 2022; Accepted 5 July 2022; Published 8 August 2022

Academic Editor: Vijayananth Kavimani

This study focuses on the identification and categorization of plug valve defects. We utilize a thermal fluke camera to obtain the plug valve thermal images. The thermal camera utilizes passive infrared thermography towards the identification of plug valve defects such as cracks, porosity, and internal defects. These flaws depict variation in surface temperature induced by heat flux. Infrared thermography is capable of identification of surface flaws such as cracks and subsurface flaws such as porosity. Its flaw identification range is effective only up to a certain depth in the metal. The heat flux variations are clearly visible for surface cracks and subsurface porosity. However, the heat flux shows no fluctuations for internal defects. Hence, to identify the internal defects in the metal, we opt for a combination of passive infrared thermography and dye penetrating test. In the dye penetrating test, a thinned paint is applied over the metal surface that aids in the identification of cracks, porosity, and internal defects as well. The PIT-DPT (passive infrared thermography-dye penetrating test) works in combination with weighted local variation pixel-based fuzzy clustering (WLVPBFC) to measure the depth of the defects. The defects were measured against parametric quantities such as F-value, precision, recall, accuracy, Jaccard index, TP, FP, TN, FN, FP rate, TP rate, and MCC. These parameters depict variations with regard to surface texture and extent of defect level. The PIT-DPT and WLVPBFC techniques identify metal flaws with 87.88% efficiency when evaluated against other existing algorithms.

1. Introduction

The plug valve utilized for defect evaluation is made of cast iron. Cast iron belongs to the family of iron-carbon alloys possessing carbon concentration of greater than 2%. The primary alloying substances of cast iron are carbon in the range of 1.8 to 4% and silicon in the range of 1 to 3%. Metal defects are obtained in times in the processing chain, while making the metal and yielding castings, during mechanical and pressure handling operations, because of thermal, chemical thermal, and electrochemical properties, and in tasks such as conjoining metals, storage, dispatch, and working. There are 3 major metal defects such as cracks, porosity, and internal defects that we are going to focus on. Several research works are carried out towards clustering diverse mathematical and data consisting of varied attributes. This is owing to its demand in real-time applications [1]. Cracks are surface or subsurface scissures that originate in a material. Cracks are caused due to utilizing hydrogen to weld ferrous metals, residuary stress, base metal contaminant, enhanced welding speed, reduced current, no preheating prior to welding, improper joint design, and huge amounts of sulphur and carbon in the metal. Cracks minimize the effectiveness of the weld by decreasing the weld dimension. They can develop and cause breakage of the entire metal part. There are a variety of cracks such as cooling, solidifying, centre crack, crater, abrasion, pickling, and heat treatment, machining ruptures, plating, fatigue,

creep, stress corrosion, and hydrogen cracks. Porosity is the occurrence of holes or voids in the weld. It happens due to freezing of gas expelled from the weld pool when it solidifies. The entrapped gas produces a hollow globule that gets feeble and can explode after certain duration. Porosity happens as an outcome of insufficient electrode oxidant, usage of longer arc, inappropriate gas cover, wrong surface treatment, usage of enhanced gas flow, polluted weld surface, presence of moisture, rust, paint, and oil. There are varied types of porosity: distributed porosity seems like fine pores. If they occur in huge quantities, they are termed as surface-breaking pores. If the pores are stretched, they are termed as wormholes. The existing NDT techniques enable the detection of pore flaws having a diameter of 0.13 mm and porosity flaws that are submerged at a depth of 1 mm [1]. In the final solidifying of the weld pool, we have crater pipe (gas porosity). Porosity will bring down the metal ductility and stiffness. Internal defects happen due to the following: welding current and welding speed are at their peak, use of faulty angle, heat distribution not uniform, diminution in fatigue strength, surface contaminants, misalignment, service failure, notch effect, hence preventing gas flow, porous and brittle weld joints, and material loss. The varied internal defects that happen in welds are undercut, incomplete fusion, incomplete penetration, slag inclusion, and spatter. The undercut is a furrow formed at the weld toe, scaling down the metal thickness. This ends up in a weak weld and workpiece. When the weld metal is not perfectly merged with the base metal, it results in incomplete fusion. When the weld metal does not completely go through the thickness of the joint, incomplete penetration takes place. When the solid covering material, flux thaws in the weld or weld surface, it causes slag inclusion to occur. Weld spatter comprises tiny particles of liquefied metal that are formed in proximity to the welding arc that binds to the gas shroud of the weld gun and thereby restricting gas flow.

Table 1 explains the novelty of the proposed technique.

(i) There are different types of nondestructive testing methods, among which we utilize dye penetrating test for identifying and categorizing metal defects. DPT is utilized for the detection of cracks and porosity.

(ii) To detect internal defects, we utilize passive infrared thermography. The testing of plug vales using DPT-PIT (dye penetrating test-passive infrared thermography) can be carried out on-site, on the very same premises of the plug valve.

(iii) In many instances, a combination of RGB and thermal imaging has enhanced the entire object detection process [2].

(iv) The experimentations are carried out on cast iron plug valves, showing effective outcomes to identify metal defects such as cracks, porosity, and internal defects.

2. Literature Survey

Srinivasan and Sadagopan studied the segmentation of the brain tissues during intensity nonuniformity and noise [4]. A similarity distance vector is used to estimate rough fuzzy regions based on both local spatial information and global spatial information. For weighted image estimation, the approach also uses a bounded support vector. The suggested algorithm's objective function is minimized for the segmentation of various brain tissues in MR images. Clustering algorithms for T1 and T2 MR images from the brain Web dataset are used to test the RFRBSFCM algorithm. Compared with other current state-of-the-art methods, the quantitative results show that the algorithm under consideration is more efficient. The fuzzy multi-characteristic clustering technique is based on fuzzy logic and clustering to achieve this objective. Fuzzy sets are utilized to express ambiguity in user query, similarity measure, and image content. Clustering is an unsupervised classification method that allows a tiny degree of control over clustering and dramatically enhances clustering performance. The preliminary results indicate that our suggested method is capable of attaining high precision and recall rates with improved computing efficiency [5]. Soft optimization techniques are used to detect liver cancer in abdominal liver imaging automatically. Performance is evaluated using entropy, energy, mean, standard deviation, accuracy, and elapsed time in this article. A novel automatic segmentation technique for detecting liver cancer is also being developed. Based on ROI and the adaptive watershed algorithm, a novel recommended technique is presented. Furthermore, the findings of this suggested study provide unambiguous information concerning normal and aberrant segmentation of the malignant region of the liver, allowing physicians to treat the problem in a consistent manner. To better segment tumours, region growth, intensity-based thresholding, and proposed statistical parameter-based segmentation approaches can be applied [6]. Fuzzy clustering enables effective segmentation even if the image to be processed is contaminated with noise [7]. To minimize the objective function, the algorithm requires an update on the membership function and cluster centres. Hence by linking the membership function, the number of iterations is reduced to a great extent. This procedure enables minimizing the objective function [8]. The key step in fuzzy clustering is selection of number of clusters and centroid initialization. Histogram smoothening automates this entire process. The number of peaks denotes the number of clusters. The gray level of each peak denotes the centroid of the cluster. Since this entire process is automated, it reduces the number of iterations and speeds up the procedure [9]. The segmentation of colour images is even more effective even in the presence of noise and requires a few number of iterations to complete the task [10]. Unsupervised learning is a procedure in which the data will not be labelled. The algorithm must automatically perform the clustering of data exclusively on its own. Here, fuzzy C-means clustering is an unsupervised learning procedure, which performs effectively except in the presence of noise. Hence to overcome this issue, the adaptive FCM algorithm is utilized that performs effectively even in the presence of noise [11]. The pixels in an image render sufficient details of the image. The image patch gives more information about the image, when compared to the pixels.

Table 1: Applicability and novelty of the proposed work.

Technique	Applicability	Remarks
Eddy current testing	Partially applicable	Detects subsurface flaws only up to 1 mm deep [1]
X-ray	Limited/not applicable	Flaws are not orthogonal to the radiation pattern. Operator at risk since exposed to radiation [1]
Ultrasonic inspection	Limited/ impossible	Lack of proper coupling between the probe and the material leads to severe echoing of signals and false alarms, thus misleading the inspection process [2]
Magnetic particle inspection	Not applicable	Inability to test nonferrous materials. Large currents are required that result in burning of the testing parts. Demagnetization is an issue [3]
Dye penetrant inspection	Applicable	Provides on-suite inspection. Lesser processing time with efficient results. Inexpensive in comparison with other NDT techniques

The image patch gives details about the image pixel and the cluster centre. Based on the distance of the image patch and the cluster centre, weights are assigned to each pixel in the image [12]. Kernel-based fuzzy clustering processes several features at the same time, thereby reducing the processing time [13]. The spatial or contextual data allow assigning labels to the pixels with the aid of the neighbouring pixels, thereby dealing with noise and other constraints [14]. The adaptive FCM possesses an adaptive factor that automatically changes the interval between the samples within every class and thereby extracts the features that belong to a particular sample. The greater the interval width between the samples, the more separable they are [15]. The spatial details are considered as a crucial attribute of the input image that needs to be classified. The spatial data of an image refer to the location of each and every pixel in the image. While getting to know the position of the pixel, the clustering is made happen more effectively [16]. Supervised FCM deals with the classification of defects utilizing labelled data, but unsupervised FCM refers to defect categorization when the data are not labelled. From the analysis, it is advisable to go for semi-supervised FCM in which part of the input data are labelled; utilizing this info, the algorithm is guided through the unsupervised areas of segmentation and classification [17]. FCM algorithm overcomes the effect of noise present in the image by assigning low membership values to those pixels that contain noise. Hence, those pixels containing noise get suppressed and do not enter the segmentation stage. The pixels that are noise-free are assigned with higher membership values, which further enter into the segmentation phase [18].

From the literature survey, the varied defects identify using various clustering algorithms. These other clustering algorithms are not adaptive to the local context, dependent on clustering parameters; hence, the clustering task becomes tedious. They need to update their contextual weight for each iteration. The objective is to propose a clustering algorithm that performs pixel-based fuzzy clustering using the weighted filter, in which the weights are automatically allocated to each pixel inside the local window, adaptive to the local context, independent of clustering parameters, thereby enabling the clustering task to be simplified with low computation cost.

3. Proposed System

There are various nondestructive testing (NDT) procedures utilized for the identification of defects in valves. Eddy current testing works on the principle of electromagnetic induction to identify flaws in the material under test. A current is passed through a coil adjacent to the test piece. Hence, the test piece starts generating Eddy currents that interfere with the current in the coil. As a result, a magnetic field is created in the coil. If a defect is present in the test piece, it causes variation in the Eddy current that in turn varies the amplitude and phase of the output signal. However, this technique can detect subsurface flaws submerged only up to 1 mm depth. Radiographic testing (RT) utilizes X-rays or gamma rays to evaluate the structure of the material under test towards detection of defects. However, the depth of penetration of X-rays is very low, capable to detect only surface flaws. This technique can also give misleading outcomes, in the presence of any dirt/foreign substances. Ultrasonic NDT testing utilizes sound waves for detecting defects in the test piece. The sound waves are generally high-frequency waves that traverse through a medium (piece of iron/steel) till they enter the border of another medium (air), at which instance gets reflected back. A detailed study of these reflections enables the evaluator to compute the test piece thickness and thereby detect surface and subsurface defects. If the surface of the specimen is not flat, it will create serious issues during probe coupling, which in turn results in echoes being generated. This will ultimately end up in erroneous measurements. Magnetic particle inspection (MPT) is a technique that involves magnetizing the material under test. Later magnetic substances are sprinkled over the surface of the test piece. If there is a defect in the test piece, the magnetic field gets disturbed, which causes magnetic flux leakage. Hence, the magnetic particles get grouped around the region of magnetic flux leakage, thereby indicating the defect. This technique is capable to detect only surface flaws and near subsurface flaws. Also, the specimen needs to be demagnetized at the end of the test, which becomes a time-consuming task.

In Figure 1, the three plug valve flaws, which are cracks, porosity, and internal defects, identify using the DPT-PIT method. This infrared method does not require an extraneous heat source.

The infrared emission radiated by the object is rather accumulating. Passive infrared thermography has the capability to render a temperature dispersion graph of the metal surface or joint throughout welding. Defective metal samples can induce unnatural temperature dispersion. If a particular area has an unnatural hot spot with respect to its

Figure 1: Block diagram of the proposed system.

surroundings, it points out to be a serious issue, where its temperature is in total variation with its surroundings. These data utilize to curb welding parameters to assure reliable joints, in materials. Infrared thermography (IRT) is a universally recognized condition-supervising tool where the temperature evaluates in a realistic noncontact fashion. Hence, there is no impairment to the metal test piece. It is applicable for defect detection in metal plug valves since the sizing and depth of defect can be identified by this method from one side by considering time evolution.

Dye penetrant inspection is a nondestructive testing method to detect flaws that are present in metals. The metal test piece is initially cleaned using SKC-S cleaner to get rid of dirt, paint, oil, grease, etc. If left uncleaned, it may lead to masking of defects and produce false results. The presence of dust/dirt/foreign substances may alter the thermal characteristics of the material and thereby result in erroneous NDT measurements [3]. The next step is application of penetrant, which is a bright coloured dye having high wetting capacity. The penetrant needs to douse into the flaws and requires a dwell time of 10–30 seconds. The following step is the removal of excess penetrant; if the excess penetrant is not removing properly, it may mask the defects and end up in false results during inspection, after which is the application of developer, which is available in aerosol spray tins that might employ acetone, isopropyl alcohol, or a mixed version of the two. The development time is generally 10 minutes to 120 minutes. There must be uniform coating of the developer, over the entire surface of the metal. The developer bleeds the penetrant out of the flaws onto the surface, to make it obviously visible. This process can figure out the location, orientation, and defect type. The dwell time is for the bloating action to occur.

3.1. Clustering. Clustering is the process of assigning the pixels of an image to clusters, in such a way that pixels in one cluster are alike, while pixels belonging to varied clusters are dissimilar. The objective is to form separate groups having similar attributes and allocate them into clusters. Clusters distinguish through similarity indices such as distance, connectivity, and intensity.

3.1.1. Fuzzy Clustering. Fuzzy clustering is a type of clustering in which each pixel can be a part of more than one cluster.

3.1.2. Fuzzy C-Means Clustering. Fuzzy c-means clustering algorithm was presented by Bezdek in 1981. It separates the image into clusters depending upon the distance of centre of cluster from the data points. It utilizes the Euclidean distance norm to separate the image into clusters. Normally, clustering algorithms are of four types: hierarchical, decomposing a

Step 1: Initialization of the window size, number of clusters, fuzzy membership matrix, and iteration counter.
Step 2: Initialization of centre of the cluster, for enhanced visualization of the segmented image; normally, cluster centre is in the range of cent = [0, 50,120,200].
Step 3: GRBF kernel
$K(x_i, v_j) = \exp\ (-\| x_i - v_j \|^2/2\sigma^2)$.
where "σ" denotes the kernel width.
Utilize maximum gray level as the kernel width. The kernel width of GRBF kernel is computed for improved accuracy.
Step 4: Computing "?" depending on the distance variances amidst all pixels:
$\sigma = [\sum_{i=1}^{N} (d_i - \overline{d})^2/N - 1]^{1/2}$,
where ?? = $\|x_i - x'\|$ is the distance from the grayscale of pixel ? to the grayscale mean of all pixels and ? is the mean of all distances ??.
Step 5: Computing the novel cluster centres
$v_j = \sum_{i=1}^{N} u_{ij}^m (K(x_i, v_j)x_i + \varphi_i K(\overline{x}_i, v_j)\overline{x}_i)/\sum_{i=1}^{N} u_{ij}^m (K(x_i, v_j) + \varphi_i K(\overline{x}_i, v_j))$.
Step 6: Computing the novel membership matrix
A membership function for a fuzzy set A on the universal set X is denoted as $\mu_A : X \to [0, 1]$, where every factor of X is mapped out to a value in the range of 0 and 1. Membership functions enable to render a pictorial representation of a fuzzy set.
$u_{ij} = ((1 - K(x_i, v_j)) + \varphi_i (1 - K(\overline{x}_i, v_j)))^{-1/(m-1)} / \sum_{k=1}^{c} (1 - K(x_i, v_k) + \varphi_i (1 - K(\overline{x}_i, v_k)))^{-1/(m-1)}$.
Step 7: Computing the objective function

$$J_{\text{ARKFCM}} = 2[\sum_{i=1}^{N}\sum_{j=1}^{c} u_{ij}^m (1 - K(x_i, v_j)) + \sum_{i=1}^{N}\sum_{j=1}^{c} \varphi_i u_{ij}^m (1 - K(\overline{x}_i, v_j))].$$

Step 8: Computing local average of each pixel, local variance of each pixel, local variation coefficient
$\text{LVC}_i = \sum_{k \in N_i} (x_k - \overline{x}_i)^2/N_R * (\overline{x}_i)^2$,
where x_k is the grayscale of any pixel present in the local window N_i around the pixel I, N_R is the cardinality of N_i, and x_i' is its average grayscale.
Step 9: Computing local sum of LVC and exponential function
LVC is applied to an exponential function to deduce the weights inside the local window
$\zeta_i = \exp\ (\sum_{k \in N_i, i \neq k} \text{LVC}_k)$.
Step 10: Computing weight for each pixel. PixWgt: this function computes the weight for every pixel depending on the local variation coefficient
$\omega_i = \zeta_i / \sum_{k \in N_i} \zeta_k$.
The ultimate weight allotted to each pixel is related to mean grayscale of the local window

$$\varphi_i = \begin{cases} 2 + \omega_i, & \overline{x}_i < x_i \\ 2 - \omega_i, & \overline{x}_i > x_i \\ 0, & \overline{x}_i = x_i \end{cases}.$$

The parametric quantity ?? allots greater values for pixels having high LVC and lesser values for pixels with low LVC. When the local mean grayscale is the same as the central pixel grayscale, ?? is zero and the algorithm will function similarly to the standard FCM algorithm.
? can be substituted with the grayscale of the novel weighted image ?:
$\overline{\xi}_i = 1/2 + \max(\varphi_i)(x_i + 1 + \max(\varphi_i)/N_R - 1 \sum_{r \in N_i} x_r)$,
where x_r and N_i are the grayscale and neighbourhood of pixel i and N_R is the cardinality of N_i. The above formula ensures that the weighted image is free from parametric quantities that are difficult to adjust.
Step 11: Computing the final weights

Algorithm 1: Initializations.

density function, graph theoretic, and minimizing an objective function. The main concentration of this technique is on clustering by minimizing the objective function.

3.1.3. WLVPBFC. The weighted local variation pixel-based fuzzy clustering framework is proposed for the segmentation of plug valve defects. In the framework, the local average grayscale is substituted by grayscale of weighted filter, to obtain the contextual information. The standard Euclidean distance is substituted by the Gaussian radial basis function (GRBF) to obtain good accuracy. The regularization of parametric quantity will bring to increase segmentation robustness, conserve image particulars, and formulate a weighted image. The local variation coefficient is computed for each of the weighted image pixels. The primary advantages are adaptive to the local context, independency of clustering parameters, and reduced computational costs (Algorithm 1).

4. Results and Discussions

Figure 2 depicts the clustering results of a plug valve obtained using a median filter. The median filter is a nonlinear

Figure 2: ARKFCM outputs using the median filter for defective and healthy thermal images.

digital filtering method and is commonly utilized to get rid of noise present in an image.

The median filter substitutes a pixel by the median, of all pixels in the neighbouring window. Since the median must generally be the value of one of the pixels in the neighbouring window, the median filter does not produce novel impractical pixel values when the filter extends over an edge. Hence, the performance of the median filter is enhanced in maintaining incisive edges. One of the primary issues with the median filter is that it is relatively costly and complicated to calculate.

$$y[m,n] = \text{me di an}\ \{x[i,j], (i,j) \in w\}. \quad (1)$$

The defective plug valve thermal images are shown to contain defects such as cracks, porosity, and internal defects. The process is repeated from one iteration to the next by varying the window size (WS) and the cluster number (CN). The defective plug valve thermal images having WS = 1 and CN = 2 show cracks; WS = 5 and CN = 3 shows porosity defects; and WS = 21 and CN = 15 shows internal defects. However, the default window size (size of the local window) is 3. The clustering results of healthy plug valve thermal images do not contain any of the abovementioned defects. This clustering process enables to detect the plug valve defects in a more efficient manner but requires updating their contextual weights for every iteration, which is the primary cause of their greater computational cost.

Figure 3 shows the clustering results of plug valve that are obtained using the average filter. The average filter performs by passing across the image pixel by pixel, substituting every value with the mean value of the pixels in the neighbourhood, considering itself.

Even if one of the pixels has an untypical value, it can drastically disturb the mean value of all the neighbouring pixels. When the filter spans across an edge, the filter will extrapolate novel values for edge pixels, resulting in blurred edges. This becomes an issue if sharp edges are expected in the output.

The defective plug valve thermal images are shown to contain defects such as cracks, porosity, and internal defects. The process is repeated from one iteration to the next by varying the window size (WS) and the cluster number (CN). The defective plug valve thermal images having WS = 3 and CN = 2 shows cracks; WS = 7 and CN = 4 shows porosity defects; and WS = 15 and CN = 8 shows internal defects. However, the default window size (size of the local window) is 3. The clustering results of healthy plug valve thermal images do not contain any of the abovementioned defects. This clustering process enables to detect the plug valve defects in a more efficient manner but require updating their contextual weights for each iteration, which is the primary cause of their greater computational cost. The above drawback can be overcome using the weighted filter.

Figure 4 shows the clustering outputs of healthy and defective plug valve thermal images, obtained using the weighted filter.

The type of clustering used is weighted local variation pixel-based fuzzy clustering. In this technique, we compute the weight for every pixel depending on the local variation coefficient. Initially, the local average/mean of every pixel is computed. Then, the local variance of each pixel is computed. Using this, the local variation coefficient (LVC) is determined. Further, the summation of the LVC is

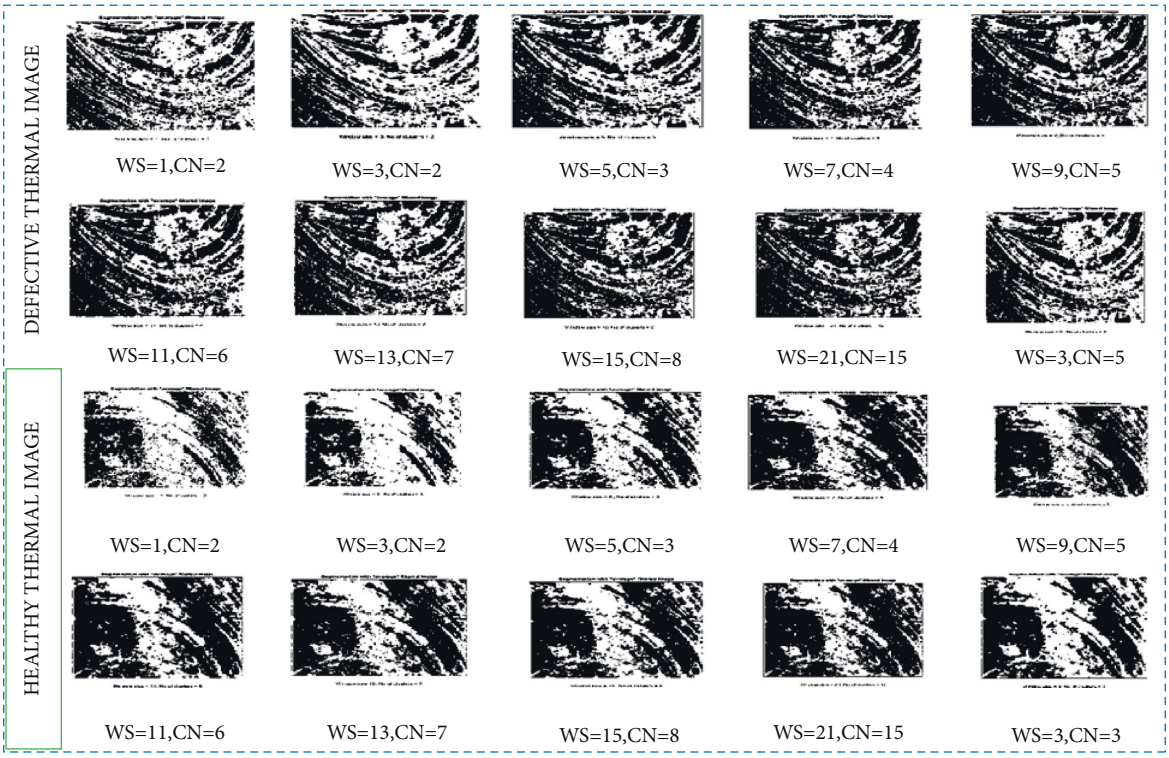

Figure 3: ARKFCM outputs using the average filter for defective and healthy thermal images.

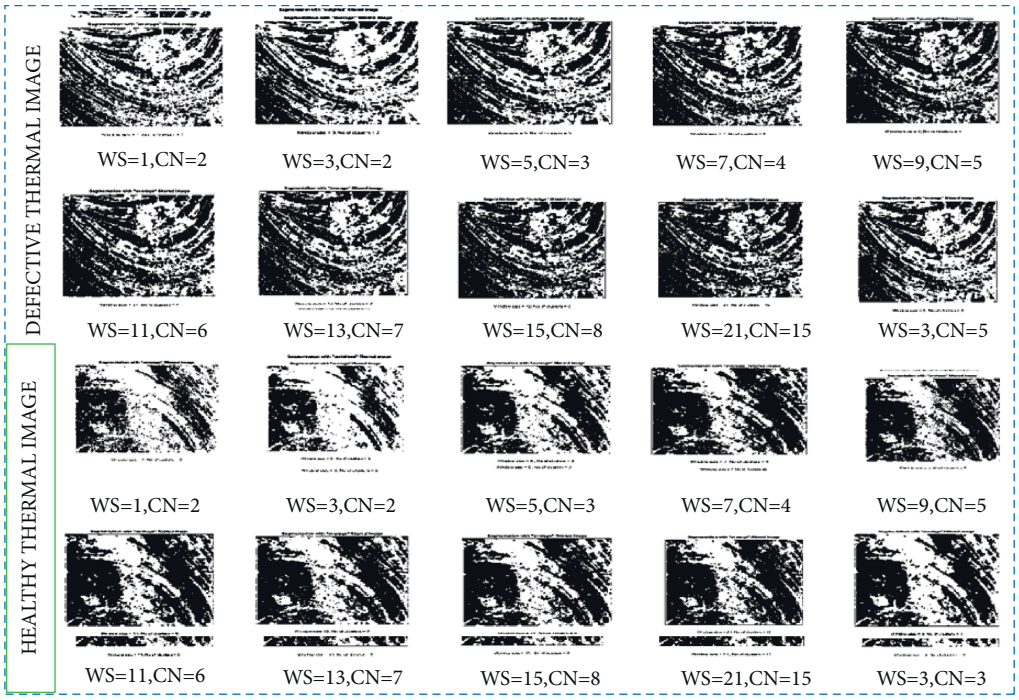

Figure 4: ARKFCM outputs using the weighted filter for defective and healthy thermal images.

computed. Finally, we apply this summation to an exponential function, to determine the weights of the pixel inside a local window. At last, we compute the weight for every individual pixel. The pixel that seems to be brighter when compared to the mean grayscale of its neighbouring pixels will possess a higher LVC value, and hence, greater weight is allotted to that pixel. Similarly, the pixel that seems to be less bright when compared to the mean grayscale of its neighbouring pixels will possess a lower LVC value, and hence, lesser weight is allotted to that pixel. When the local mean

grayscale equals the central pixel grayscale, the weight allotted to that pixel is zero. However, in this manner weights are allotted to every pixel inside the local widow. This allocation of weights simplifies the clustering task, and hence, segmentation is performed much effectively and easily, with less computational cost and at a much faster manner. Other FCM algorithms require updating their contextual weights for each iteration, which is the primary cause of their greater computational cost and time consumption.

Table 2 shows the various evaluation parameters that are considered to prove that the weighted filter is very efficient when compared with the median and average filters.

4.1. True Positive, True Negative, False Positive, and False Negative. A true positive is a result where the framework accurately anticipates the positive category. Likewise, a true negative is a result where the framework perfectly anticipates the negative category. A false positive is a result where the framework fallaciously anticipates the positive category. False negative is a result where the framework wrongly anticipates the negative category.

4.2. Accuracy. Accuracy is the ratio of correct anticipations (both true positives and true negatives) among the entire instances studied.

$$\text{Accuracy} = \frac{(\text{TP} + \text{TN})}{(\text{TP} + \text{TN} + \text{FP} + \text{FN})}. \tag{2}$$

4.3. Precision and Recall. Precision (also termed as positive predictive value) is the ratio of relevant cases to the retrieved cases, while recall (alias sensitivity) is the ratio of the total number of relevant cases actually retrieved.

$$\begin{aligned} \text{Precision} &= \frac{\text{TP}}{(\text{TP} + \text{FP})} \\ \text{Recall} &= \frac{\text{TP}}{\text{P}} \\ \text{P} &= \text{TP} + \text{FN} \\ \text{N} &= \text{FP} + \text{TN} \\ \text{FP rate} &= \frac{\text{FP}}{\text{N}} \\ \text{TP rate} &= \frac{\text{TP}}{\text{P}}. \end{aligned} \tag{3}$$

4.4. F-Measure. The F_{value} (F-score or F-measure) is a valuation metric for a test's exactitude. A standard that merges precision and recall is the harmonic mean of precision and recall, the conventional F-measure, or balanced F-score:

$$\text{Fvalue} = 2 * \frac{((\text{precision} * \text{recall})}{(\text{precision} + \text{recall}))}. \tag{4}$$

Table 2: Evaluation metrics.

S. no	Evaluation standards	Adaptive regularized kernel-based FCM		
		Weighted filter	Average filter	Median filter
		Window size 3 cluster number 2		
1	Accuracy	0.6944	0.6878	0.6800
2	FN	3637	3010	3831
3	FP	3239	3790	3368
4	F prate	0.6207	0.6289	0.6087
5	F value	0.7987	0.7984	0.78i9
6	Jaccard index	0.6649	0.6644	0.6430
7	MCC	0.1646	0.1572	0.1612
8	Precision	0.8082	0.7803	0.7959
9	Recall	0.7895	0.8173	0.7742
10	TN	1979	2236	2165
11	TP	13645	13464	13136
12	T prate	0.7895	0.8173	0.7742

This standard is roughly the mean of precision and recall and is normally the harmonic mean, which, for the context of two numbers, co-occurs with the square of the geometric average fractioned by the arithmetic average. F-measure is perfect when its value equals unity.

4.5. Jaccard Index. When comparing finite sample sets, the Jaccard coefficient measures similarity, and is defined as the size of the intersection fractioned by the size of the union of the sample sets:

$$J(A, B) = \frac{|A \cap B|}{A \cup B} = \frac{A \cap B}{|A| + |B| - |A \cap B|}. \tag{5}$$

4.5.1. MCC. The MCC is a correlation coefficient between the observed and anticipated binary classifications; it generates a value between −1 and + 1. A coefficient of +1 denotes a perfect anticipation, 0 denotes no better than stochastic anticipation, and −1 denotes total discrepancy between anticipation and observation. The coefficient considers true and false positives and negatives and is normally looked upon as a balanced measure that can be utilized even if the categories are of extremely varied sizes.

$$\text{MCC} = \frac{(\text{TP} * \text{TN} - \text{FP} * \text{FN})}{\sqrt{((\text{TP}+\text{FP}) * (\text{TP}+\text{FN}) * (\text{TN}+\text{FP}) * (\text{TN}+\text{FN}))}}. \tag{6}$$

5. Output Graphs

5.1. Neural Network Training Model. The neural network training model lists the following parameters. Epoch is the time taken to complete one full cycle in training the total number of samples in the neural network. It takes into account one forward pass and one backward pass. Iterations are the total number of passes required to train the samples. Time denotes the duration taken to train each sample. Performance indicates the efficiency of each of the three different types of images. Gradient represents the percentage

Table 3: Iteration parameters.

S. no	Parameters	Bad-bad image	Good-bad image	Good-good image
1	Epoch	11 iterations	25 iterations	14 iterations
2	Time	3 sec	5 sec	0 sec
3	Performance	0.546	0.56	0.599
4	Gradient	0.00729	0.0121	0.00875
5	Validation checks	6	6	6

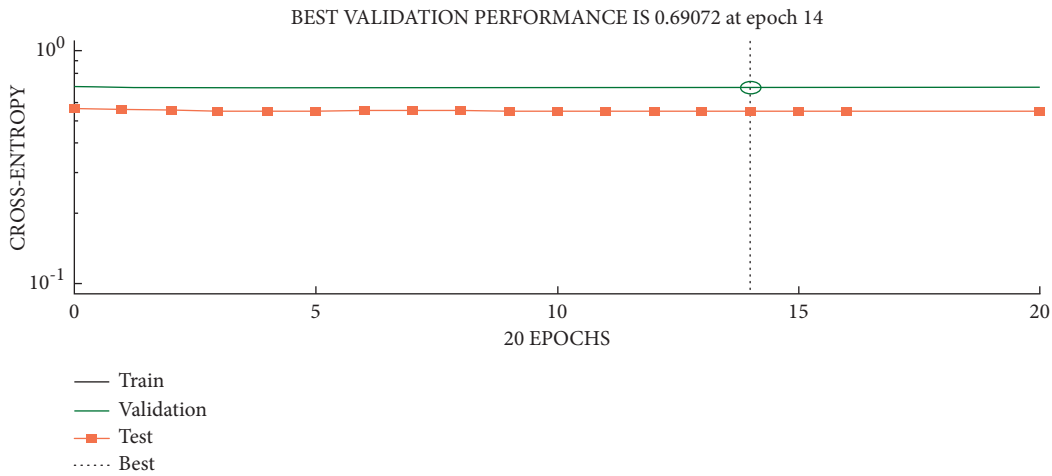

Figure 5: Performance plot.

amount of deviation that exists between the original input image and the output image. Validation checks indicate the number of times the verification has taken place. Table 3 shows the various iteration parameters utilized to evaluate the performance of the proposed technique.

5.1.1. Performance Plot. The performance plot shown in Figure 5 is the plot between the number of epochs on the X-axis and the cross-entropy values on the Y-axis. Epoch is the time taken to complete one full cycle. Cross-entropy evaluates the deviation amidst three probability distributions (training, validation, and testing) for a particular random variable or set of events. There are four lines, train, validation, test, and best. To affirm that training is performing effectively, the other three lines must lie on the best (dotted) line or in close proximity to it. If any of the three (training, validation, and testing) lines converge or pass beside the best (dotted) line, it reveals that convergence is taken place; else, the network is to be trained again. The training dataset is utilize to cultivate the candidate algorithms, and the validation dataset is utilized to analyze their operations and determine which one to choose and the test dataset is utilized to fetch the evaluation metrics such as accuracy, sensitivity, specificity, and F-measure. This plot enables us to determine the best fit among training, validation, and testing and also at what instance it occurs. In the case of defective-defective image, the best fit occurs at epoch 4 having a value equal to 0.5993. In the case of healthy-defective image, the best fit occurs at epoch 19 having a value equal to 0.53649. In the case of healthy-healthy image, the best fit occurs at epoch 8 having a value equal to 0.50936.

5.1.2. Training State. The training state graph shown in Figure 6 denotes the present advancement/training status at a particular instant while training is ongoing. In this case, six-validation errors are observed, and it denotes that when six-validation check faults are generated at the same time, then training will terminate. A validation check error is generated when the dataset has a few issues, such as certain instances that are not apprehensible by the training algorithm. The first training state graph is a plot between number of epochs on the X-axis and the gradient on the Y-axis. The gradient shows the amount of deviation of the healthy-defective image from the healthy-healthy image. For defective-defective image, initially at 0 epoch, the gradient had a higher value, which gradually decreases, and at epoch 11, the gradient has a least value equal to 0.0011818, which is approximately equal to zero. Hence, having a gradient value to be equal to zero indicates that there is not much deviation between the two images. For healthy-defective image, initially at 0 epoch, the gradient had a higher value, which gradually decreases, and at epoch 25, the gradient has a least value equal to 0.00064096, which is approximately equal to 0. For healthy-healthy image, initially at 0 epoch the gradient had a higher value, which gradually decreases, and at epoch 14, the gradient has a least value equal to 0.0028701, which is approximately equal to zero.

5.1.3. Error Histogram. Error histogram shown in Figure 7 is the graph of the errors between target values and anticipated values after a feed-forward neural network is trained. There are completely 20 bins. Bins denote the count of vertical bars observed on the histogram. The zero error line represents the

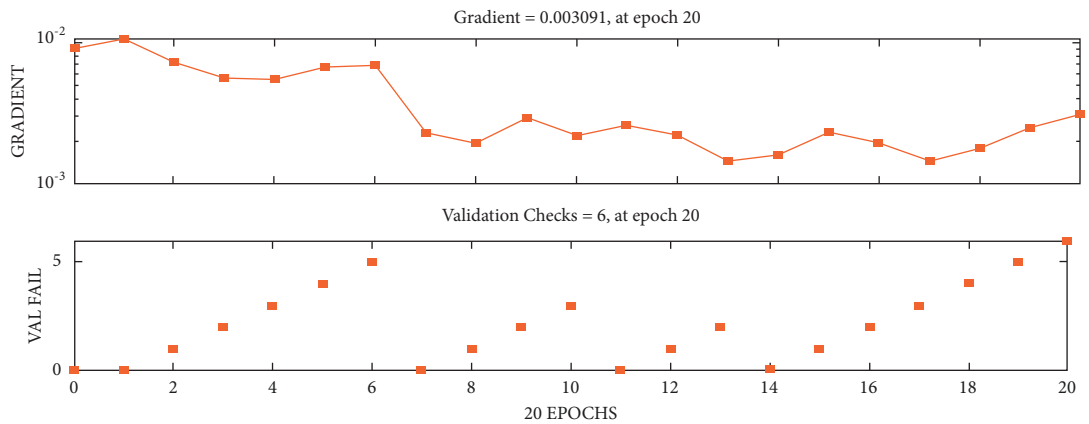

Figure 6: Training state for healthy-healthy image.

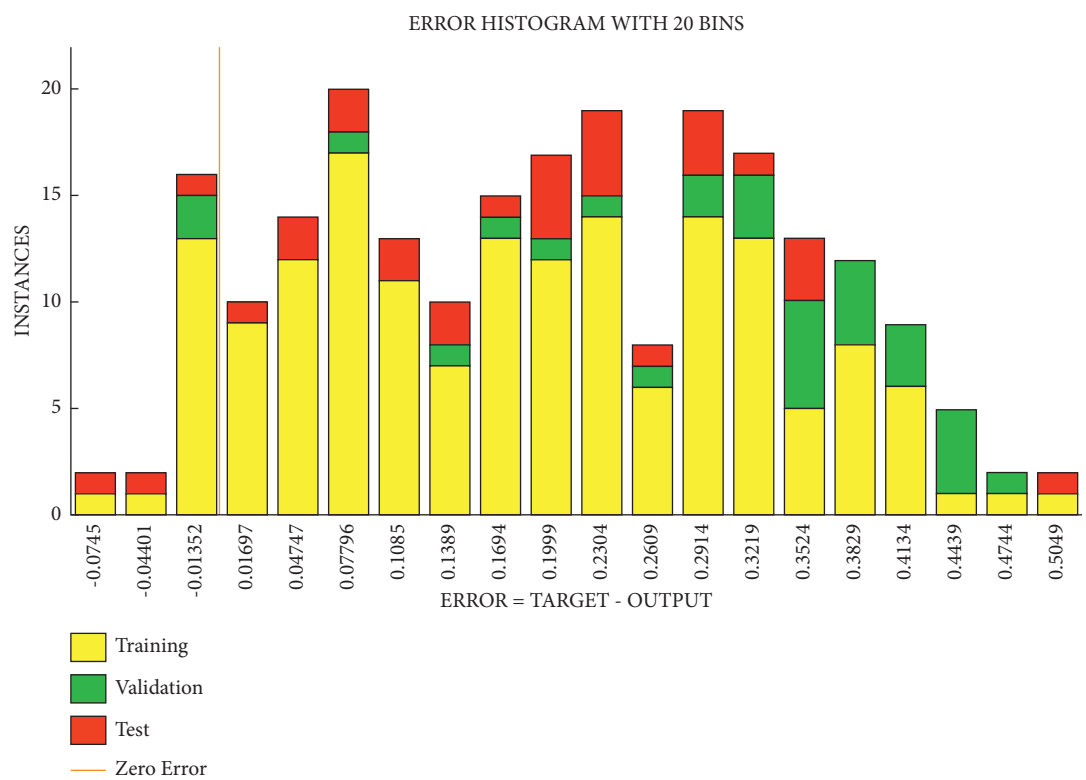

Figure 7: Error histogram for healthy-healthy image.

zero error value on the error axis (i.e., X-axis). For defective-defective image, the aggregate neural network error is in the range of -0.1318 to 0.4742. This range is fractioned into 20 bins, so that the width of every bin is (0.4742-(−0.1318))/20 = 0.0303. Every vertical bar denotes the count of the dataset samples that belongs to specific bin. For instance, in the middle of the histogram, there exists a bin representing the error of -0.00418 and the height of that bin for the validation dataset is 16. It implies that 16 samples from the validation dataset have an error lying in that range. Likewise, for healthy-defective image, the smallest amount of error 0.003858 roughly equals 0 and the height of that bin for the validation dataset is 16. For healthy-healthy image, the smallest amount of error -0.0099 roughly equals zero and the height of that bin for the validation dataset is 17.

5.1.4. Confusion Matrix. A confusion matrix (or error matrix) is generally utilized as a quantifiable technique for characterizing image classification precision. It brings out the parallelism between the classification output and the image taken as reference. A confusion matrix is an nxn matrix in which every row depicts the real classification of a particular data and every column depicts the anticipated classification. The precision of an image can be checked by viewing the diagonal cells of the confusion matrix, which

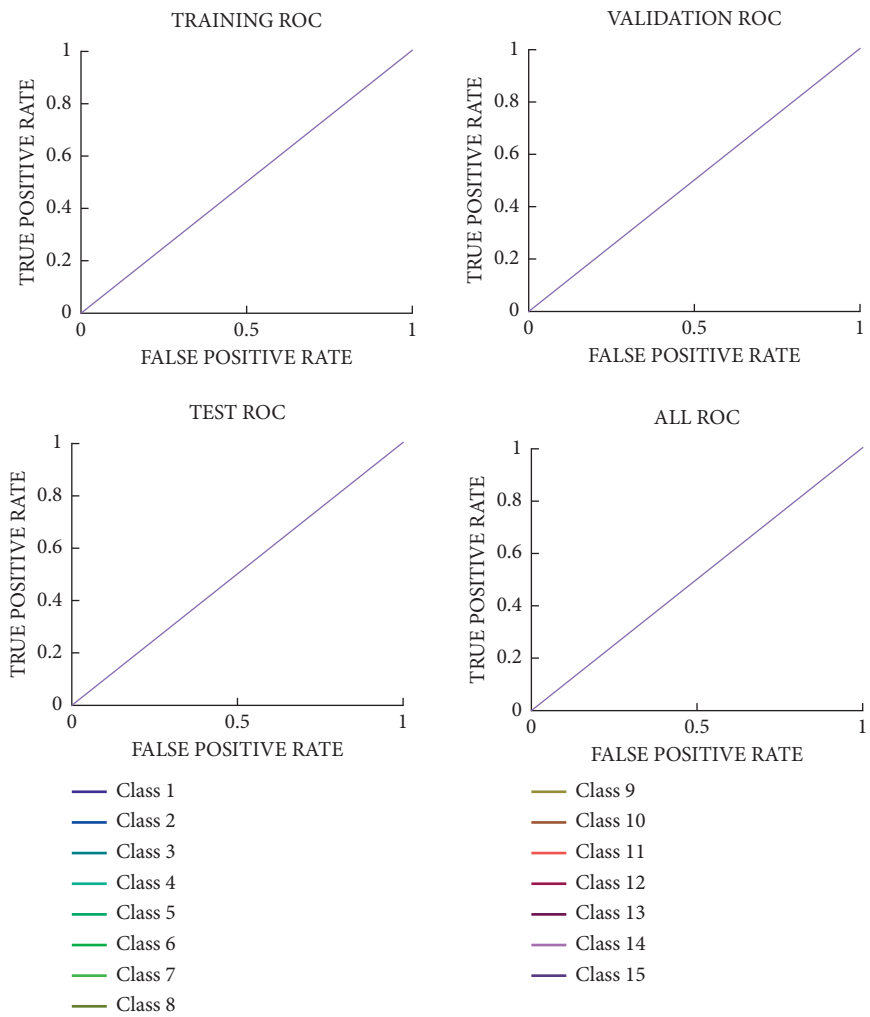

Figure 8: Receiver output characteristics graph for healthy-healthy image.

indicate the count of the perfect classifications. A healthy image will have greater values along the diagonal and lesser values in the cells apart from the diagonal. In addition, one can determine whether the model is not performing well, by evaluating the greater values on the non-diagonal cells in the matrix. If so, these cells comprise classification errors, i.e., instances in which there exists no correspondence between the reference image and classified image. However, these evaluations can be utilized to detect instances in which the precision is great, but the prototype is continuously performing the wrong classification of similar information.

5.2. Receiver Output Characteristic Graph. A receiver operating characteristic curve shown in Figure 8, or ROC curve, is a graphical representation that exemplifies the efficiency of a binary classification model as its discriminating threshold is altered. Classification accuracy is the total number of perfect classifications. The ROC curve is generated by plotting the true-positive rate (TPR) versus the false-positive rate (FPR) at varying threshold levels. ROC analysis renders tools to choose optimum models and cast aside suboptimal models. Bringing down the threshold level

25	54	12	23	31
41	32	42	64	25
24	46	50	55	65
49	53	56	61	60
57	61	66	71	76

Figure 9: Matrix to compute magnitude and orientation.

classifies many pixels as positive, thereby enhancing both false positives and true positives. Hence, the ROC curve can be utilized to choose a threshold for a classification model that enhances the true positives and reduces the false positives. The ROC curves for the training state, validation state, and test state are obtained individually. Then, a combined version of all the states and the final ROC curve are obtained.

5.2.1. SIFT. An image-matching algorithm recognizes the primal characteristics from an image and is capable of matching these characteristics to a novel image of the similar object. SIFT aids in locating these primal features generally

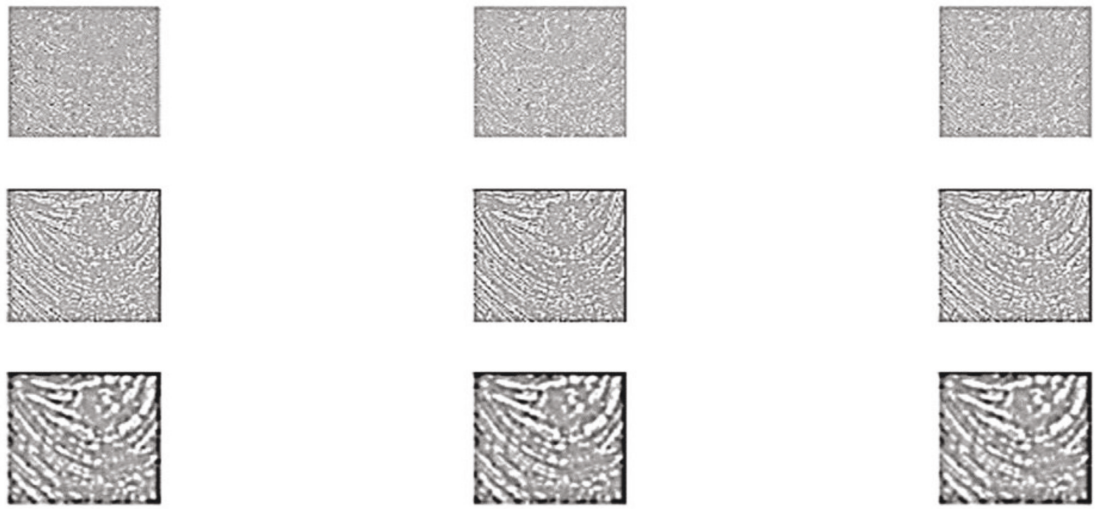

Figure 10: Output graph showing key points that do not match.

Figure 11: Output graph showing key points that perfectly match.

termed as "key points" of the plug valve image. These key points must be robust in such a way that, even if there is any variation in the scale, rotation, or angle of the image, key points are utilized for varied computer vision applications, such as image matching and object identification. The next phase is the construction of the scale space. Scale space is a grouping of several plug valve image possessing varied scales, which are obtained from an individual plug valve thermal image. This is performed to identify the unique features that show no variation in all the images whose scale has been varying. Difference-in-Gaussian function is utilized to remove or lessen image noise. Post-utilizing Gaussian blurs the texture, and less vital particulars are withdrawn from the image and only applicable data such as shape and edges are retained. The difference in Gaussian is a feature enhancement algorithm that deals with subtracting the blurred version of an original image from a less blurred version of the same image. Hence, we have confidently enhanced the vital features. Key point localization (selection) determines the primal key points from the image that can be utilized for feature matching. The aim is to determine the local maxima and minima for the images. It is performed by equating each image pixel with its adjacent pixels. This enables to get rid of low contrast key points, those that lie in close proximity to the edge, not sturdy to noise. Next is to specify an orientation to every key point so that their alignment does not vary, even if the image is rotated or slightly changed in angle. The magnitude and orientation are computed using the matrix shown in Figure 9.

To determine the magnitude and orientation for the central pixel highlighted in yellow, for this, initially the gradients in x and y directions are computed by fetching the difference between 55 and 46 and 56 and 42. The gradient values are $G_X = 9$ and $G_Y = 14$, respectively.

$$\text{Magnitude} = \sqrt{((G_X)^2+(G_Y)^2)} = 16.64$$

$$\Phi = \tan\,(G_Y/G_X) = \tan\,(1.55) = 57.17$$

The magnitude denotes the pixel intensity, and the orientation gives the pixel direction.

5.2.2. Histogram for Magnitude and Orientation. The bins for the angle values, such as 0–9, 10–19, 20–29, till 360, are plotted on the X-axis. In our case, the angle value is 57, and

hence, it will lie in the 6th bin. The 6th bin value will be proportional to the pixel magnitude, 16.64. This computation is performed for all the pixels surrounding the key point. At one particular instance, the graph would elevate to its maximum level. The bin at which we view this elevation is considered to be the key point orientation. In addition, if there exists a second elevation (viewed between 80 and 100%), then another key point is yielded. In this manner, the number of key points is increased. We utilize the neighbouring pixels, their magnitude, and orientation, to create a distinct fingerprint for this key point termed a "descriptor." In the given outputs, the gray images shown in Figure 10 denote those in which the key points do not match. The blue and green outputs shown in Figure 11 denote those in which the key points match perfectly.

6. Conclusions

This research work is based on weighted local variation pixel-based fuzzy clustering (WLVPBFC), in which the clustering task becomes easy by allocating/calculating the weights of each pixel. This is performed by computing the local variation coefficient. This enables the segmentation to be carried out more effectively, easily, faster, and with lesser computational cost. The clustering results of normal FCM using average filter and median filter are utilized for comparison purpose. It is determined that the FCM using average and median filter requires updating their contextual information for each iteration, which results in greater computational cost and time consumption. The WLVPBFC using weighted filter for plug valve thermal images outperforms the normal FCM using average filter and median filter in terms of accuracy of 69.44%, precision of 80.82%, Jaccard index of 0.6649, and MCC of 0.1646. The evaluation graphs show that the best results are obtained for healthy-healthy plug valve thermal images. In addition, using SIFTS the matching features/key points are obtained with a magnitude of 16.64 and phase value of 57.17. In future, this concept can be applied using deep learning algorithms.

Data Availability

The data used to support the findings of this study are included within the article.

Conflicts of Interest

The authors declare that they have no conflicts of interest regarding the publication.

References

[1] M. Machado, L. F. S. G. Rosado, N. A. M. Mendes, R. M. M. Miranda, and d. J. G. Santos, "New directions for inline inspection of automobile laser welds using non-destructive testing," *International Journal of Advanced Manufacturing Technology*, vol. 118, no. 3-4, pp. 1183–1195, 2022, Page No :1183–1195.

[2] S. B. Kera, A. Tadepalli, and J. J. Ranjani, *A Paced Multi-Stage Block-wise Approach for Object Detection in thermal Images*, The Visual Computer, 2022.

[3] R. Shrestha, S. Sfarra, S. Ridolfi, G. Gargiulo, and W. Kim, "A numerical–thermal–thermographic NDT evaluation of an ancient marquetry integrated with X-ray and XRF surveys," *Journal of Thermal Analysis and Calorimetry*, vol. 147, no. 3, pp. 2265–2279, 2021.

[4] A. Srinivasan and S. Sadagopan, "Retracted article: rough fuzzy region based bounded support fuzzy C-means clustering for brain MR image segmentation," *Journal of Ambient Intelligence and Humanized Computing*, vol. 12, no. 3, pp. 3775–3788, 2021.

[5] P. K. Kavitha and V. P. Saraswathi, "Retracted article: content based satellite image retrieval system using fuzzy clustering," *Journal of Ambient Intelligence and Humanized Computing*, vol. 12, no. 5, pp. 5541–5552, 2021.

[6] V. Hemalatha and C. Sundar, "Retracted article: automatic liver cancer detection in abdominal liver images using soft optimization techniques," *Journal of Ambient Intelligence and Humanized Computing*, vol. 12, no. 5, pp. 4765–4774, 2021.

[7] J. Miao, X. Zhou, and T. Z. Huang, "Local segmentation of images using an improved fuzzy C-means clustering algorithm based on self-adaptive dictionary learning," *Applied Soft Computing*, vol. 91, p. 106200, 2020.

[8] Q. Wang, X. Wang, C. Fang, and W. Yang, "Robust fuzzy c-means clustering algorithm with adaptive spatial & intensity constraint and membership linking for noise image segmentation," *Applied Soft Computing*, vol. 92, Article ID 106318, 2020.

[9] P. Valsalan, P. Sriramakrishnan, S. Sridhar et al., "Knowledge based fuzzy c - means method for rapid brain tissues segmentation of magnetic resonance imaging scans with CUDA enabled GPU machine," *Journal of Ambient Intelligence and Humanized Computing*, Article ID 0123456789, 2020.

[10] V. M. Dante, J. M. V. Kinani, and J. d. J. Rubio, "Color-based image segmentation by means of a robust intuitionistic fuzzy C-means algorithm," *International Journal of Fuzzy Systems*, vol. 22, no. 3, pp. 901–916, 2020.

[11] Y. Gao, D. Wang, J. Pan, Z. Wang, and B. Chen, "A novel fuzzy c-means clustering algorithm using adaptive norm," *International Journal of Fuzzy Systems*, vol. 21, no. 8, pp. 2632–2649, 2019.

[12] Y. Tang, F. Ren, and W. Pedrycz, "Fuzzy C-Means clustering through SSIM and patch for image segentation," *Applied Soft Computing J.*, p. 2019, 105928.

[13] P. Das and A. Das, "A fast and automated segmentation method for detection of masses using folded kernel based fuzzy c-means clustering algorithm," *Applied Soft Computing*, vol. 85, Article ID 105775, 2019.

[14] A. Halder and N. Talukdar, "Robust brain magnetic resonance image segmentation using modified rough-fuzzy C-means with spatial constraints," *Applied Soft Computing*, vol. 85, Article ID 105758, 2019.

[15] G. Feng, M. Ni, S. Ou, W. Y, and J. Xu, "A Preferential Interval-Valued Fuzzy C-means algorithm for remotely sensed imagery classification," *International Journal of Fuzzy Systems*, vol. 21, no. 7, pp. 2212–2222, 2019.

[16] G. Feng, M. Ni, S. Ou, and W. Yan, "Means algorithm for remotely sensed imagery classification," *International Journal of Fuzzy Systems*, 2019.

[17] C. Wan, X. Yuan, X. Dai, T. Zhang, and Q. He, "A self-adaptive multi-objective harmony search based fuzzy clustering technique for image segmentation," *Journal of Ambient Intelligence and Humanized Computing*, vol. 1-16, 2018 [14].

[18] P. Kaur, "Intuitionistic fuzzy sets based credibilistic fuzzy C-means clustering for medical image segmentation," *International Journal of Information Technology*, vol. 9, no. 4, pp. 345–351, 2017.

Hindawi
Advances in Materials Science and Engineering
Volume 2022, Article ID 2411848, 10 pages
https://doi.org/10.1155/2022/2411848

Research Article

Investigation of Mechanical Behavior and Microstructure Analysis of AA7075/SiC/B4C-Based Aluminium Hybrid Composites

HassabAlla M. A. Mahmoud,[1] P. Satishkumar,[2] Yenda Srinivasa Rao,[3] Rohinikumar Chebolu,[4] Rey Y. Capangpangan,[5] Arnold C. Alguno,[6] Mahesh Gopal,[7] A. Firos,[8] and Murthi C. Saravana[9]

[1]*Department of Physics, Faculty of Sciences and Arts, Dhahran Al Janoub, King Khalid University, Abha, Saudi Arabia*
[2]*Anna University, Chennai, Tamilnadu, India*
[3]*Mechanical Engineering, Swamy Vivekananda Engineering College, Bobbili, Andhra Pradesh, India*
[4]*Mechanical Engineering AUCE(A), Andhra University, Visakhapatnam, Andhra Pradesh, India*
[5]*Department of Physical Science and Mathematics, College of Science and Environment, Mindanao State University, Naawan, Misamis Oriental, Marawi, Philippines*
[6]*Department of Physics, Mindanao State University, Lligan Institute of Technology, Lligan City, Philippines*
[7]*Mechanical Engineering, College of Engineering and Technology, Wollega University, Post Box No. 395, Nekemte, Ethiopia*
[8]*Department of Computer Science and Engineering, Rajiv Gandhi University, Doimukh, Arunachal Pradesh, India*
[9]*Mechanical Engineering, United Institute of Technology, Coimbatore, Tamil Nadu, India*

Correspondence should be addressed to Mahesh Gopal; doctorgmahesh@gmail.com

Received 4 June 2022; Accepted 5 July 2022; Published 22 July 2022

Academic Editor: Pudhupalayam Muthukutti Gopal

The microstructure and mechanical properties of an MMC based on AA 7075 and strengthened through silicon carbide (SiC) as well as boron carbide (B_4C) elements were studied. The ($SiC + B_4C$) combination was used in various weight percentages of 4, 8, 12, and 16% to create the hybrid composites utilizing the traditional stir casting procedure. XRD and SEM measurements were used to investigate the dispersion of the reinforced particles. For example, microhardness, impact strength, and ultimate tensile strength were measured on hybrid composites at room temperature. The density and porosity of the materials were also studied. The researchers found that increasing the weight percentage of the ($SiC + B_4C$) mixture resulted in a small drop in % elongation. However, hybrid composites comprising 16% ($SiC + B_4C$) weight reduction showed some decrease in hardness and tensile strength. Equated to unreinforced alloys, the hardness and tensile strength of hybrid composites rise by 8% and 21%, respectively. Reinforcement also resulted in a decrease in impact strength and density, as well as an increase in porosity.

1. Introduction

Metal matrix composites (AMCs) made of aluminium have gained popularity in recent decades because of their amazing qualities such less weight, higher strength, modulus of elasticity, exceptional restraining, and good wear resistance. When the number of reinforced particles in a matrix composition grows, ductility often suffers [1]. In transportation and structural applications, where high-stress resistance is critical, 6082 T6 tweaked AA provides good mechanical qualities and high strength [2]. Aluminium composites have undergone a great deal of development in the last few decades to improve their qualities [3].

Hybrid aluminium AMCs are the next generation of AMCs, and they have the ability to fulfill the growing demands of high-tech applications in the future [4]. Additionally,

researchers have experimented with creating hybrid metal matrix composites by combining two or more reinforcing materials, in an effort to get better mechanical qualities, such as increased dimensional stability and improved heat and corrosion resistance for the final invention [5]. A number of researchers have explored the mechanical properties of a range of hybrid composites. As per the proportion of strengthening in the metal matrix increases, tensile strength, stiffness, and porosity all improve. However, when the proportion of reinforcement rises, the composite's impact energy and density both fall significantly. Ultrasonic cavitation solidification was used in [6] to create a hybrid composite utilizing AA6061 as a base metal and (SiC + B_4C) as reinforcement. They found that the porosity boosted the hardness and tensile strength of the alloy. When [7]used a traditional stir casting method to create a hybrid composite, they used an aluminium alloy containing boron carbide (B_4C) and graphite reinforcing particles (Gr). For better strength, hardness, and wear resistance, researchers added B_4C to the matrix, but the material became more brittle as a result. Alumina nanoparticles (Al_2O_3) were created via powder metallurgy, and the strengthening mechanism was discovered to be the most important strength mechanism [8, 9]. The solidification of a substance is linked to the program of dislocations inside that material. Strengthening mechanisms must be introduced to limit dislocation movement and thus boost the material's strength in order to improve material attributes like yield strength. Researchers evaluated the wear as well as the mechanical characteristics of reinforcement combinations on the surface of composites for wear [10]. An increase in microhardness is attributed to the occurrence of silicon carbide and alumina particles in hybrid composites made of Al, SiC, and Gr. SiC and Al_2O_3 reinforcement added to aluminium hybrid composites boosted tensile strength and hardness while decreasing the elongation percentage, according to a study by Davis et al. [11]. It was found that the ultimate tensile and hardness of hybrid composites made with boron carbide particles and calcium carbide with the main alloy of AA 6063 were improved, while the impact strength was somewhat reduced. A two-step stir casting procedure was used to create a dual-reinforced particle AA composite in [12]. LM-13 AA was used in the experiments. Silicon carbide and zircon sand ($ZrSiO_4$) particles were used in the study. The composites outperform the unreinforced alloy in terms of wear resistance, according to the authors.

It is stated in the literature that several researchers have evaluated the mechanical and structural properties of composite materials using SiC, Gr. Ca_2O_3, $ZrSiO_4$, TiC, and Al_2O_3. There has been no study done on AA6082 to make hybrid composites employing (SiC + B_4C) as reinforcement. Aluminum and silicon carbide (SiC) particles are chemically compatible and create strong bonds in the matrix [13]. There are a number of advantages to using SiC as a reinforcement in AMCs because of its outstanding workability, easy machining, and inexpensive cost. B_4C must be added to aluminium composites in order to increase their mechanical qualities. B_4C is a great reinforcement material because of its high rigidity and hardness, as well as its low density. Because of B_4C and aluminum's similar densities, the settling problem is reduced while solidifying a molten matrix due to its low density [14]. An initial investigation of the (SiC + B_4C)-reinforced AA6082 hybrid composites' microstructure and mechanical characteristics was carried out. Many different techniques, including liquid state production, stir casting, intrusion, and squeeze casting, can be utilized to make composites. The stir casting process is the most commonly used technique for composite manufacturing because it can generate complex shapes at a low cost. Using a graphite crucible to melt a molten matrix metal requires 10–15 minutes of vigorous stirring in order to produce a homogeneous composite [15]. When it comes to liquid state manufacturing, stir casting is the most easy and cost-effective process. Another benefit of the stir casting technology is its capacity to produce composites with a volume proportion of up to 30%. [16–18]. The swirling motion of the particles in the stir casting process enhances the chemical interactions between the matrix and reinforcing particles [19]. Experimental data on microhardness, impact strength, elongation percentage, and tensile strength of stir-cast hybrid metal matrix composites were collected [20].

2. Materials and Experimentation

2.1. Base Material. A 6 mm thick AA7075 plate was chosen as the basis material in this study. The matrix alloy's chemical and mechanical properties are listed in Tables 1 and 2. At a temperature of roughly 180°C, the alloy was artificially aged to achieve the T6 state. Table 3 lists the specifics of the SiC and B_4C particles utilized as reinforcement in this study. The particles used in this investigation were 35 μm in diameter. By adding 4, 8, 12, and 16wt % of the (SiC + B_4C) mixture in equal proportions, we were able to create Al-SiC-B_4C hybrid composites.

2.2. Composite Fabrication. The specimen was prepared employing the standard stir-casting method. Figure 1 depicts the experimental setup employed in this study. For the production of each sample, a graphite crucible was used to melt 1000 grams of aluminium in an electric furnace with an argon environment at 8000°C. As a way to improve the matrix alloy's wettability with reinforcements, magnesium (2 wt%) was infused into the molten metal. Magnesium is considered a better wettability agent for SiC. To oxidize the surface of the B_4C particles, they were baked for 3–4 hours at a temperature of 2000°C in a baking oven. Using a graphite stirrer set to 400 rpm for roughly 10 minutes, this preheated powder was fed into the molten metal at a consistent feed rate using SiC. This ensured a uniform distribution of the powder throughout the metal. A 300 mm long, 80 mm wide, and 40 mm deep injection mold was utilized to pour the liquid combination.

The hybridized composite was allowed to harden at ambient temperature before being taken from the mold and subjected to various mechanical tests. Samples containing 4%, 8%, 12%, and 16% (SiC + B4) were prepared using the same procedure.

Table 1: Chemical arrangement of AA7075.

Component	Magnesium	Silicon	Manganese	Iron	Copper	Zinc	Aluminium
(wt%)	2.5	0.08	0.04	0.3	1.5	5.6	Remaining

Table 2: Mechanical properties of AA7075.

Tensile strength (MPa)	Density (g/cm^3)	Vickers hardness (HV)	% elongation (%)
228	2.81	175	17

Table 3: Particulars of **SiC** and **B_4C** particulate.

Reinforcement	Mean particle size (μm)	Hardness (kg/mm^2)	Density (g/cm^3)	Melting point °C
SiC	35	2,800	3.20	2,700
B_4C	35	2450	2.52	2,450

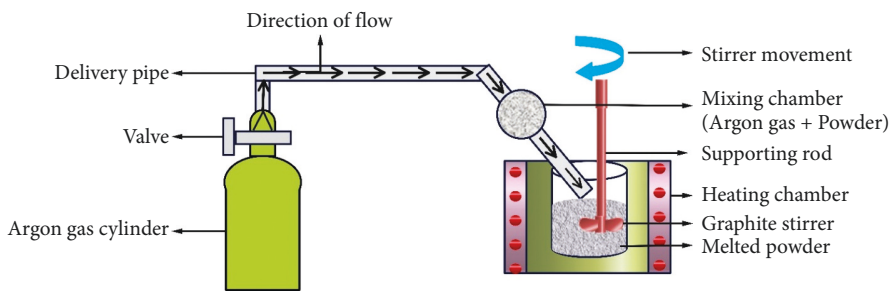

Figure 1: Diagram of experimental arrangement.

2.3. Measurements. Microstructural investigation was performed by producing cylindrical samples with 6 mm diameters and 20 mm heights. The microstructure samples depicted in Figure 2 were used in the research. An SEM was utilized to examine the microstructure of the Al-SiC-B_4C mixture. Keller's Reagent (HF/HF/HCl/HNO3/H2O) and Emery paper (400, 600, and 1000 grades) were utilized to etch samples using Keller's Reagent (H2O). Nikon's Eclipse MA-100 optical microscope and JOEL's JSM-6510LV scanning electron microscope were utilized for the microstructure study.

All samples were subjected to a 15-second microhardness test on a Vickers hardness testing method and a force of 1 kg. The hardness of small cuboids was determined using an electric discharge machine. Samples were indented by a diamond indenter, which had square bases and an angle of 136° between them. The Charpy tests, which used specimens $56 \times 10 \times 10$ mm in size, with notch depths of 3 mm, tip radius of 0.30 mm, and angles of 45°, were performed on impact testing machines using these specimens. As shown in Figure 3, the samples used in this study are schematically depicted. All specimens were evaluated three times for hardness and impact strength in order to acquire an average result.

The hybrid composites' tensile behaviour was examined and tested in accordance with the ASTM-E8 standard. Temperatures ranged from 25°C to 30°C and relative humidity ranged from 40 to 60% during the tests on the universal testing equipment. Using the schematic diagram indicated in Figure 4(a), the flat specimens with a thickness

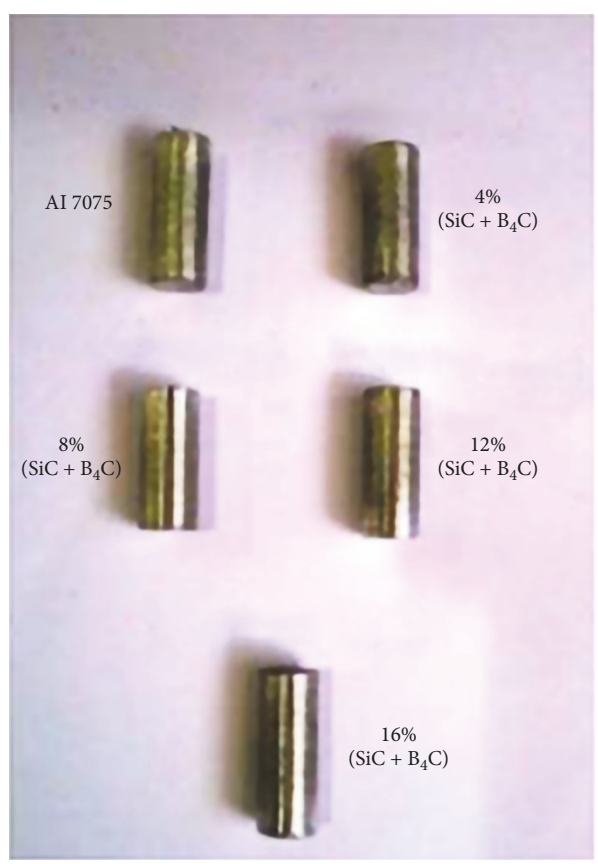

Figure 2: Samples for microstructure evaluation.

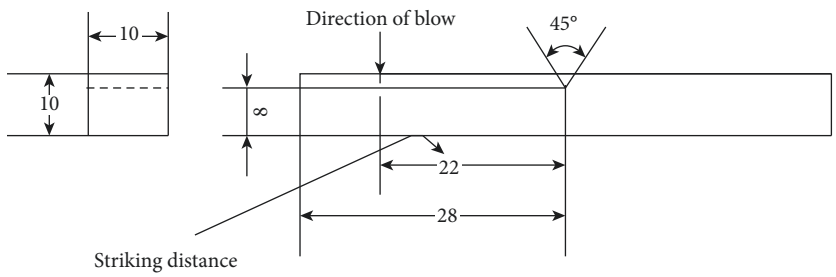

Figure 3: Diagram of specimen for impact strength.

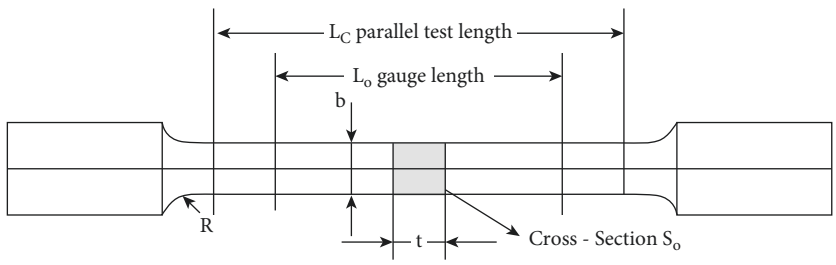

(a)

(b)

Figure 4: Tensile test. (a) Diagram and (b) sample.

of 6 mm were machined to match the dimensions of the schematic diagram. Figure 4(b) shows the tensile test specimens.

The mass and volume of a sample were utilized to calculate the density of the specimen. Equation (1) can be used to determine the density by using the measurements of mass and volume:

$$\text{density}\left(\frac{\text{g}}{\text{cm}^3}\right) = \frac{\text{mass}}{\text{volume}}. \quad (1)$$

The following equation can be used to determine the specimen's porosity using a straightforward relationship:

$$\text{porosity} = 1 - \frac{d}{d_a}, \quad (2)$$

whereas d is the mass of the specimen and d_a is the density of the base material.

It will be possible to account for even closed porosity using this straightforward approach.

3. Results and Discussion

3.1. XRD and Microstructural Study. By using XRD patterns, Figures 5(a)–5(e) depict the matrix alloy and hybridized composites. The prominent peaks in the XRD data belong to aluminium, which is the parent material. Hybrid composites' lower peaks show their SiC and B_4C content. At the goniometer receiving slit station, the diffractometer uses a graphite curved single crystal monochromator to select CuK radiation ($\lambda = 1.54$A). During the XRD investigation, a diffraction angle (2θ) of 20–1100 was maintained. Figures 5(a)–5(e) depict the occurrence of Si, Al_4C_3, and Al_3BC, all of which were found in the final samples. The hybrid composites' Al_3BC and Al_4C_3 maxima, on the other hand, were incredibly low. In an electric furnace, aluminium and boron carbide interacted directly to produce Al_3BC and Al_4C_3 [21–23].

Figures 6(a) and 6(b) show scanning electron microscope images of silicon carbide and boron carbide particles,

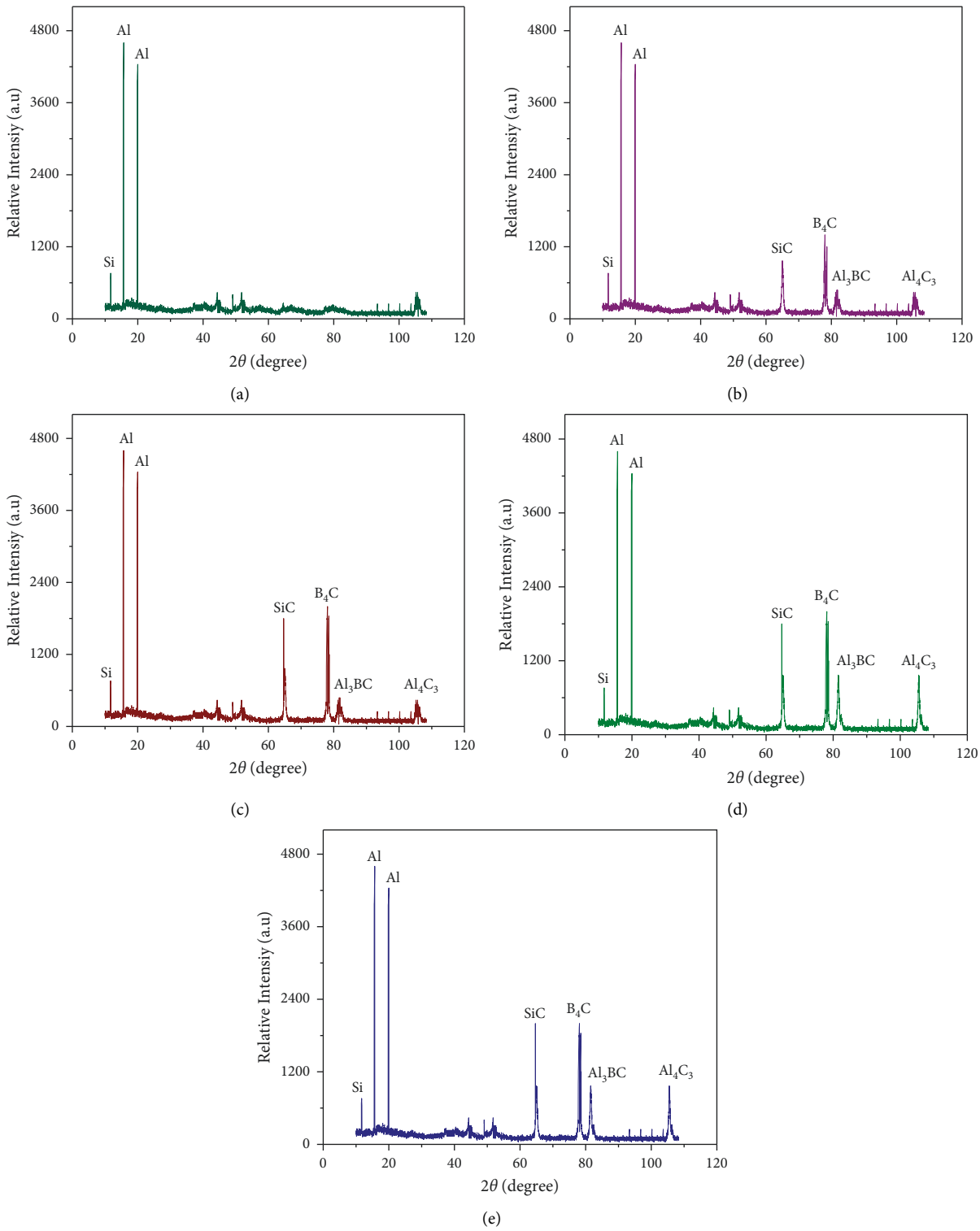

Figure 5: X-ray diffraction forms of (a) 0%, (b) 4%, (c) 8%, (d) 12%, and (e) 16% of (silicon carbide + boron carbide) strengthened hybridized composites.

respectively. First-generation Al 7075 grains developing dendritically reveal the interdendritic zone between aluminium and silicon grains in the microstructure of the Al 7075 silicate eutectic. The temperature mismatch between the molten matrix and the reinforcing particles results in the formation of aluminium. Due to the ceramic particles' weaker heat conductivity compared to Al 7075 melt, the molten matrix is hotter than the temperature of the ceramic particles.

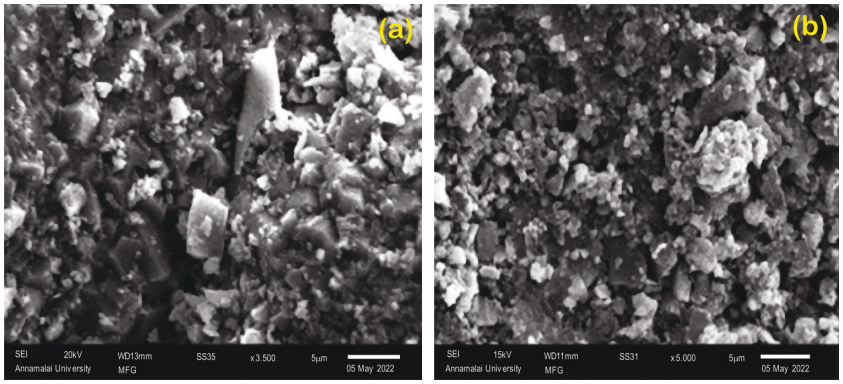

Figure 6: (a, b) SEM images of silicon carbide and boron carbide particles.

As a result, the solidification process requires more time to cool hotter particles, which in turn heats the liquid alloy around them. When the hybrid composites were cooled during solidification, they formed dendritic regions. In regions where the dispersion of reinforced particles is not as good, the particle clusters were also detected. No cavities in the interface indicate that the interfacial connection between particles and matrix is strong. According to [20, 24], the reinforcing particulate can prevent dendritic development. Increasing the weight percentage of reinforcement leads to an increased degree of cluster agglomeration as well. In contrast, well-placed agglomerations in the composites can reinforce the composite [25].

3.2. Impact Strength and Microhardness. Samples of substrate metal AA7075 and hybridized composites are shown in Table 4. Hybrid composites have higher hardness values than their unreinforced counterparts, and this hardness rises in direct proportion to the weight percentage of reinforcement added. This is in accordance with the investigation that took place previously [26]. The matrix's hardness and resistance to plastic deformation are both improved by the inclusion of hard reinforcing particles [27]. As shown in Figure 7, the hardness increases up to 12%wt fraction, which is shown in the graph. Increasing the density of the particulate mixture within the matrix reduces the hardness of the SiC and B_4C particles [28]. The ideal hardness of reinforced composites with a (SiC + B_4C) mixture of 12%wt is 8% greater than the hardness of unreinforced alloys.

Table 5 summarizes the impact test findings for unreinforced alloys and hybrid composites. As shown in Figure 8, as compared to the unreinforced alloy, the impact strength of composites falls as the weight percentage of particles rises in the metal matrix. However, despite the fact that hybrid composites' impact strength tends to decrease, the reduction amount was quite small. One possible explanation for the decrease in strength is the modest change in material properties from ductile to brittle caused by the reinforcement of hard particles [29].

Cracking and decohesion of reinforcing particles lead to the loss of impact strength in composites because of microstructural defects. A reduction in impact strength occurs as a wt% increase in reinforcement occurs, which leads to a rise in failure rates.

3.3. Tensile Behavior of Hybrid Composites. Hybrid composites exhibited a surge in UTS with an increasing weight percentage of the (silicon carbide + boron carbide) mixture in the tensile behavior when the reinforcing mixture was present. Table 6 shows the tensile values as well as the % elongation. Figure 4(b) shows that all samples, even the unreinforced ones, did not break at the center of the gauge length. Because the midsection of a tensile specimen is the weakest when subjected to tensile stresses, it is common for the specimen to shatter. Due to particle concentration, defects, or minute impurities, the center may not be shattered in some cases. For example, the UTS went from 319 MPa at 0% addition to 386 MPa at 12% addition, an increase of 21%. In terms of UTS, the hybrid composite with 12%wt of reinforcement outperforms its 16%wt counterpart. The increased porosity and excessive aggregation of reinforcing particles in the microstructures could be the cause [30]. Porosity in hybrid composites that have been cured reduces material strength, which is caused by the aggregation of tiny particles.

The % elongation of hybrid composites declines as the weight percentage of reinforcement increases in comparison to AA7075. Figure 9 demonstrates how the UTS and elongation percentage change when the wt% of strengthening in the aluminium matrix increases. With the inclusion of strengthening particles and a decrease in the ductility of Al 7075 composition, the percentage elongation decrease may be attributed to these factors.

3.4. Density and Porosity. Figures 10 and 11 show the outcome of the measurements of density and porosity. Hybrid composite density decreased after 2.7 g/cm^3 at 0% (silicon carbide + boron carbide) towards 2.61% at 16% (SiC + B_4C) addition, indicating that the inclusion of reinforcing particles in the metal matrix has little influence on density. There was a recorded 5.2% reduction in density. With the addition of strengthening, the porosity ranges of the strengthened hybridized composites marginally rise. There is an increase in value from 0.35 to 2.14

Table 4: Results on microhardness.

Terms of specimen	Hardness1	Hardness2	Hardness 3	Average hardness
AA7075	170	172	168	170
AA7075 + 4% (SiC + B_4C)	168	169	170	173
AA7075 + 8% (SiC + B_4C)	171	173	175	173
AA7075 + 12%(SiC + B_4C)	170	172	173	172
AA7075 + 16% (SiC + B_4C)	168	173	172	171

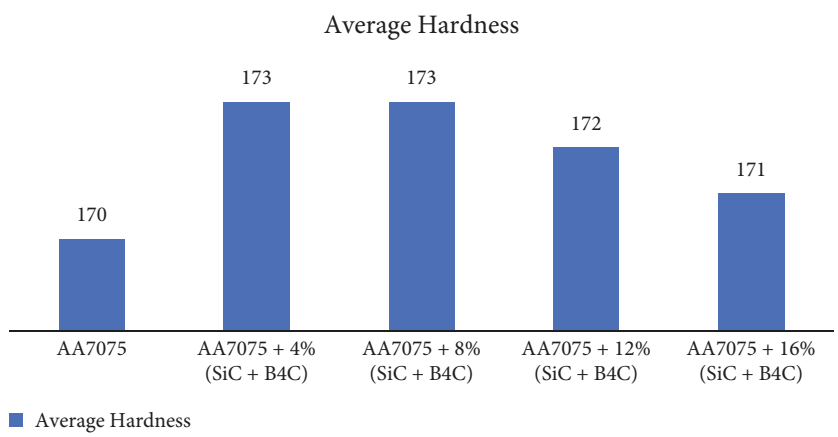

Figure 7: Hardness of unreinforced alloy and hybridized composites.

Table 5: Impact tests results.

Terms of specimen	Test 1(Nm)	Test 2 (Nm)	Test 3 (Nm)	Mean impact
AA 7075	9.5	9.8	9.5	9.6
AA 7075 + 4% (SiC + B_4C)	9.4	9.4	9.2	9.33
AA 7075 + 8% (SiC + B_4C)	8.7	8.75	8.8	8.75
AA 7075 + 12% (SiC + B_4C)	8.4	8.4	8.2	8.33
AA 7075 + 16% (SiC + B_4C)	7.9	7.95	7.9	7.92

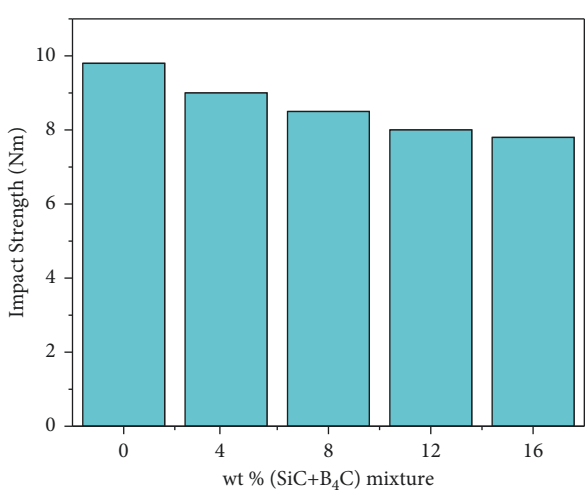

Figure 8: Impact strength on variant wt% of (SiC + B_4C) mixture.

Table 6: Results of tensile strength along with % elongation.

Terms of specimen	Ultimate tensile strength (MPa)	% enhancement	% elongation
AA 7075	319	—	8.42
AA 7075 + 4% (SiC + B_4C)	335	4.8	7.91
AA 7075 + 8% (SiC + B_4C)	358	12.31	7.32
AA 7075 + 12% (SiC + B_4C)	386	21.07	6.89
AA 7075 + 16% (SiC + B_4C)	372	16.7	6.9

when adding 16% (SiC + B_4C) to the mixture. The authors in [31, 32] found similar results in terms of density and porosity.

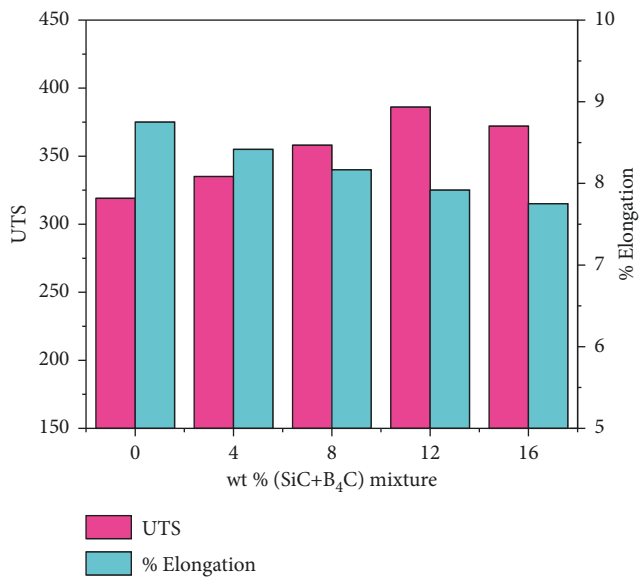

Figure 9: Ultimate tensile strength and % elongation for different weight percentages of ($SiC + B_4C$) mixture.

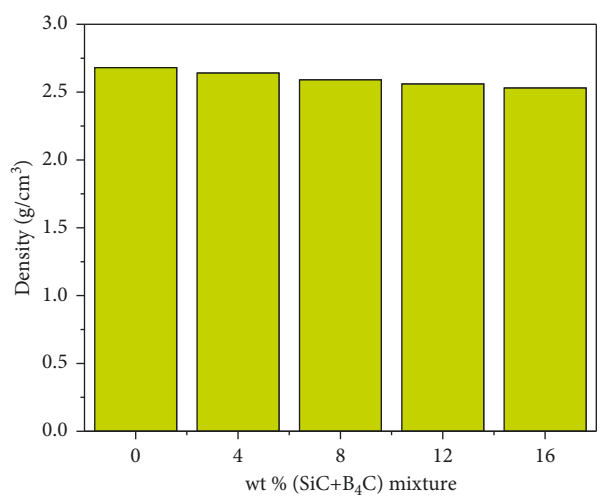

Figure 10: Density with variant weight percentage of ($SiC + B_4C$) mixture.

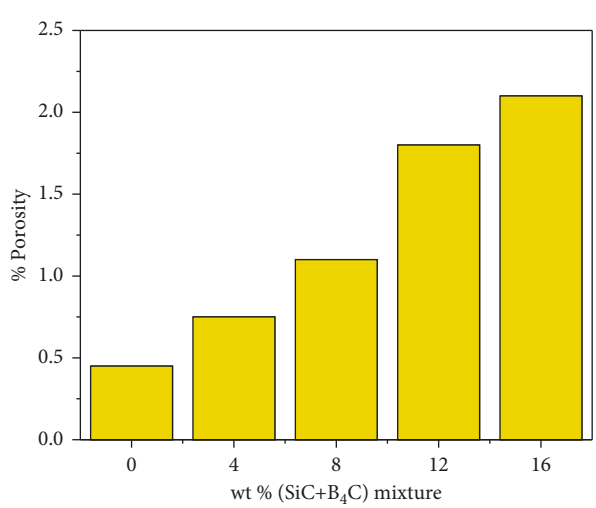

Figure 11: Porosity with variant wt% of ($SiC + B_4C$) mixture.

4. Conclusion

In summary, the stir casting process was employed to create AA7075 reinforced with 4, 8, 12, and 16 weight percentages of ($SiC + B_4C$) particulates, and experimental results led to the conclusions listed below:

(1) The existence of Al 7075, silicon carbide (Sic), aluminum carbide (Al4C3), ternary alumina-boron carbide (Al_3BC), boron carbide(B_4C), and silicon (Si) in the hybridized composites was confirmed by XRD, and SEM micrographs showed good dispersion of the reinforced particles. As the weight percentage of strengthening rises, so does the particle agglomeration.

(2) It went from 170 HV for an unreinforced alloy to 175 HV for a hybridized component with 12wt% of strengthening in microhardness. An 8% increase in hardness was seen. There was also a minor drop in hardness over 12%wt of reinforcing.

(3) The impact strength of hybridized composites steadily decreases as reinforcement is added at a marginal rate.

(4) The ultimate tensile strength of hybrid composites is significantly improved by the addition of reinforcement. When equated to unreinforced alloy, the UTS increases in strength by 21%, from 318 to 386 MPa. With the addition of 16%wt strengthening, however, the hybridized composite's strength decreased slightly.

(5) With increasing AA matrix composition, the % elongation was identified to be decreased as the strengthening percentage improved.

(6) A decrease in density and an increase in porosity were noted when reinforcing particulate was added. At 0% $SiC + B_4C$ adding to 16% Silicon Carbide + Boron Carbide in the metal matrix, the density decreases between 2.7 g/cm^3 and 2.61 g/cm^3, and the porosity increases between 0.4% and 2.21%.

Data Availability

No data were used to support this study..

Conflicts of Interest

The authors declare that they have no conflicts of interest.

References

[1] G. Chawla, V. K. Mittal, and S. Mittal, "Experimental investigation of process parameters of al-sic-b4c mmcs finished by a novel magnetic abrasive flow machining setup," *Walailak Journal of Science and Technology*, vol. 18, no. 18, 18 pages, 2021.

[2] R. Vijayakumar and R. Kirubaharan, "Mechanical behaviour of hybrid metal matrix composite with AL6063/B4C/river sand," *Pakistan Journal of Biotechnology*, vol. 14, pp. 181–184, 2017.

[3] B. Suresh Babu, "Investigations of the effect of the tool rotational speed on friction stir welded joint on aluminium

metal matrix hybrid composite. Investigations of the effect of the tool rotational speed on friction stir welded joint on aluminium metal matrix hybrid composite," *IOP Conference Series: Materials Science and Engineering*, vol. 988, no. 1, Article ID 012045, 2020.

[4] A. Z. Syahrial and M. A. Pratama, "The influence various boron carbide reinforcement on the microstructure and mechanical properties of ADC12/B4C composite by stir casting," *AIP Conference Proceedings. The influence various boron carbide reinforcement on the microstructure and mechanical properties of ADC12/B4C composite by stir casting*, vol. 2232, p. 2020, 2020.

[5] F. Ahmed, S. Srivastava, and A. B. Agarwal, "Synthesis & Characterization of Al-Ti-Cr MMC as friction material for disc brakes application," *Materials Today Proceedings*, vol. 4, no. 2, pp. 405–414, 2017.

[6] G. S. Matharou and B. K. Bhuyan, "Parametric analysis of electric discharge machining of hybrid composite materials," *Advances in Engineering Materials*, vol. 7, pp. 329–339, 2021.

[7] G. Chawla, V. Kumar, and R. S. Sharma, "Neural simulation of surface generated during magnetic abrasive flow machining of hybrid Al/SiC/B4C-MMCs," *Journal of Bio- and Tribo-Corrosion*, vol. 7, no. 4, p. 153, 2021.

[8] B. Suresh Babu, G. Chandramohan, C. Boopathi, T. Pridhar, and R. Srinivasan, "Production and characterization of mechanical and microstructural behaviour of friction stir welded Al6063 composites reinforced with Gr/B4C/SiC particles," *Journal of Ceramic Processing Research*, vol. 19, no. 1, pp. 69–74, 2018.

[9] Y. S. Bijjargi, V. M. Shinde, A. Mudgal, H. Kumar, and N. E. Prasad, "CFD modeling and optimal design of SiC deposition on the fuel combustion nozzle in a commercial CVD reactor," *Ceramics International*, vol. 48, no. 8, pp. 11043–11055, 2022.

[10] M. Rafiei, M. Salehi, M. Shamanian, and A. Motallebzadeh, "Preparation and oxidation behavior of B4C-Ni and B4C-TiB2-TiC-Ni composite coatings produced by an HVOF process," *Ceramics International*, vol. 40, no. 8, pp. 13599–13609, 2014.

[11] R. Davis, A. Singh, F. L. Amorim, M. J. Jackson, and W. F. Sales, "Effect of tool geometry on the machining characteristics amid SiC powder mixed electric discharge drilling of hybrid metal matrix composite," *Silicon*, vol. 14, no. 1, pp. 27–45, 2022.

[12] B. Varun, V. M. Kumar, L. Jery Rajkumar, and D. R. Medhunhashini, "Characterization of aluminium/(SiC+B4C) ceramic particles reinforced hybrid Surface Composites (SC) fabricated by friction stir processing," *IOP Conference Series: Materials Science and Engineering*, vol. 932, no. 1, Article ID 012119, 2020.

[13] C. T. Guerrero, F. González, T. E. Soto et al., "An overview of the interactions between reinforcements and Al matrices with Si, Cu and Mg as Alloying elements in Aluminum matrix composites: case of oxide reinforcements," *Materials Research*, vol. 25, 2022.

[14] V. K. Lagisetti, A. P. Reddy, and P. V. Krishna, "Dry sliding wear study on aa6061/SiCp nano and aa6061/SiCp/gr hybrid nanocomposites," *Silicon*, 2022.

[15] G. Gobinath and R. Ramachandran, "2nd international conference on sustainable energy resources, materials and technologies," in *Proceedings of the 2nd International Conference on Sustainable Energy Resources, Materials and Technologies*, vol. 979, ISERMAT, Beijing, China, 2019.

[16] O. Meydanoglu, B. Jodoin, and E. S. Kayali, "Microstructure, mechanical properties and corrosion performance of 7075 Al matrix ceramic particle reinforced composite coatings produced by the cold gas dynamic spraying process," *Surface and Coatings Technology*, vol. 235, pp. 108–116, 2013.

[17] T. Senthilvelan, S. Gopalakannan, S. Vishnuvarthan, and K. Keerthivaran, "Fabrication and characterization of SiC, Al2O3 and B4C reinforced Al-Zn-Mg-Cu alloy (AA 7075) metal matrix composites: a study," *Advanced Materials Research*, vol. 622-623, pp. 1295–1299, 2012.

[18] M. C Jo, J. H Choi, J Yoo et al., "Novel dynamic compressive and ballistic properties in 7075-T6 Al-matrix hybrid composite reinforced with SiC and B4C particulates," *Composites Part B: Engineering*, vol. 174, Article ID 107041, 2019.

[19] M. Pul, "Effect of sintering on mechanical property of SiC/B4C reinforced aluminum," *Materials Research Express*, vol. 6, no. 1, Article ID 016541, 2018.

[20] J. P. Ajithkumar and M. Anthony Xavior, "Flank and crater wear analysis during turning of Al 7075 based hybrid composites," *Materials Research Express*, vol. 6, no. 8, Article ID 086560, 2019.

[21] M. Karnam, A. Shivaramakrishna, R. Joshi, T. H. Manjunatha, and K. Veerabhadrappa, "Study of mechanical properties and drilling behavior of Al7075 reinforced with B4C," *Materials Today Proceedings*, vol. 5, no. 11, pp. 25102–25111, 2018.

[22] S. Gopalakannan and T. Senthilvelan, "Synthesis and characterisation of Al 7075 reinforced with SiC and B4C nano particles fabricated by ultrasonic cavitation method," *Journal of Scientific and Industrial Research*, vol. 74, no. 5, pp. 281–285, 2015.

[23] S. Sunil Kumar Reddy, C. Sreedhar, and S. Suresh, "Investigations on Al 7075/nano-SiC/B4C hybrid reinforcements using liquid casting method," *Materials Today Proceedings*, vol. 46, pp. 8540–8547, 2021.

[24] S. K. Tiwari, S. Pal, A. Sharma, A. Dasgotra, and J. K. Pandey, "Investigation of tribological properties of stir cast hybrid aluminum composites," *Lecture Notes in Mechanical Engineering*, pp. 125–132, 2022.

[25] V. C. Uvaraja and N. Natarajan, "Processing of stir cast Al-7075 hybrid metal matrix composites and their characterization," *International Review of Mechanical Engineering*, vol. 6, no. 4, pp. 724–729, 2012.

[26] J. P. Ajithkumar and M. Anthony Xavior, "Cutting force and surface roughness analysis during turning of Al 7075 based hybrid composites," *Cutting force and surface roughness analysis during turning of Al 7075 based hybrid composites. Procedia Manufacturing*, vol. 30, pp. 180–187, 2019.

[27] G. S. Matharou and B. K. Bhuyan, "Hybrid metal matrix composite development by stir casting and environmental concerns," *Advances in Engineering Materials*, pp. 377–386, 2021.

[28] S. Aksöz, S. Kaner, and Y. Kaplan, "Tribological and aging behavior of hybrid Al 7075 composite reinforced with B4C, SiC, and TiB2," *Science of Sintering*, vol. 53, no. 3, pp. 311–321, 2021.

[29] S. Thirumalai Kumaran, M. Uthayakumar, and S. Aravindan, "Analysis of dry sliding friction and wear behaviour of AA6351-SiC-B4C composites using grey relational analysis," *Tribology: Materials, Surfaces & Interfaces*, vol. 8, no. 4, pp. 187–193, 2014.

[30] G. Singh and S. Goyal, "Microstructure and mechanical behavior of AA6082-T6/SiC/B4C-based aluminum hybrid composites," *Particulate Science and Technology*, vol. 36, no. 2, pp. 154–161, 2018.

[31] D. Bandhu, A. Thakur, R. Purohit, R. K. Verma, and K. Abhishek, "Characterization & evaluation of Al7075 MMCs reinforced with ceramic particulates and influence of age hardening on their tensile behavior," *Journal of Mechanical Science and Technology*, vol. 32, no. 7, pp. 3123–3128, 2018.

[32] N. Ramadoss, K. Pazhanivel, A. Ganeshkumar, and M. Arivanandhan, "Effect of SiC and MoS2 Co-reinforcement on enhancing the tribological and anti-corrosive performance of aluminum matrix (Al6063-T6) nanocomposites," *Silicon*, 2021.

Hindawi
Advances in Materials Science and Engineering
Volume 2022, Article ID 6164599, 10 pages
https://doi.org/10.1155/2022/6164599

Research Article

Improving Sustainability of EDM Sector by Implementing Unconventional Competitive Manufacturing Approach

K. G Sagar,[1] P. K. Anjani,[2] Manju Shree Raman,[3] N. S. M. P. Latha Devi,[4] Kamakshi Mehta,[5] Jose Luis Arias Gonzales,[6] Nellore Manoj Kumar,[7] and Venkatesan S[8]

[1]*Department of Mechanical Engineering, Cambridge Institute of Technology, Bangalore, Karnataka 560036, India*
[2]*Department of Management Studies, Sona College of Technology, Salem, Tamil Nadu 636005, India*
[3]*Department of Management, College of Business & Economics, Debre Tabor University, East Africa, Postal Code: 272, Debre Tabor, Ethiopia*
[4]*Department of Engineering Physics, Koneru Lakshmaiah Education Foundation (KLEF), Vaddeswaram Pincode: 522 302, Guntur, Andhra Pradesh, India*
[5]*Amity College of Commerce, Amity University, Ashiana Angan,Pincode: 301019, Bhiwadi, Haryana, India*
[6]*Department of Business, University of British Columbia, Arequipa, Postal Code: 054, Peru*
[7]*Department of Physics, SCSVMV Deemed Univeristy, Enathur 631561, Kanchipuram, Tamil Nadu, India*
[8]*School of Mechanical Engineering, College of Engineering and Technology, Wachemo University, Hosaena, Ethiopia*

Correspondence should be addressed to Venkatesan S; profsvenkatesan@gmail.com

Received 6 May 2022; Accepted 23 June 2022; Published 11 July 2022

Academic Editor: Pudhupalayam Muthukutti Gopal

In this research work, an attempt was made to machine the titanium (Ti6Al4V) alloy utilizing electric discharge machining technique. The distinct process parameters and its impact on the machining performance were identified using the cause-and-effect diagram (CED). The key process parameters identified by CED diagram were current, pulse on time (Ton), aluminium oxide (Al_2O_3) powder concentration, and gap distance; experiments were conducted by varying the process parameters, experimental runs were designed using the Taguchi mixed orthogonal array. The experimental results revealed that improvement in material removal rate (MRR) was due to the bridging effect; reduction in tool wear rate (TWR) owing to the expansion of spark gap and enhancement in the surface roughness (Ra) was due to the complete flushing of machined debris. The interaction impact was analysed using the contour plot and with the aid of mathematical modelling experimental fits that were identified and the results were validated utilizing the sensitivity analysis. The obtained results were optimized using the technique for order of preference by similarity to ideal solution (TOPSIS) optimization technique.

1. Introduction

The life time of the product depends on the quality of the component used to assemble it. The manufacture of main landing gears from composites using conventional machining processes has distinguishing critical to excellent attributes [1]. The attributes include excessive tool wear due to the presence of abrasive particles in the composites, formation of build-up edges, and exhibiting poor surface as the removal of particles leaves the pits on the surface [2–4]. To resolve this issue, the composites were manufactured using the unconventional machining (UCM) technique, of which electric discharge machining (EDM) was preferred for producing components with utmost quality [5]. The EDM input variable which controls the outcome of the process includes current, spark gap, powder concentration, cycle time, and tool materials [6–8]. Tuning the parameters to the ideal level results in the manufacturing of high-quality items; failing to do so results in faulty products [9]. The route cause for the distinct defects was identified using the CED diagram. The CED, also known

Table 1: Chemical composition of Ti6Al4V (spectrum analysis).

Element	V	Al	Sn	Zr	Mo	C	Si	Fe	Ti
% Composition	4.24	5.48	0.614	0.0031	0.005	0.368	0.03	0.119	89.1409

as the Ishikawa graph or fish-bone investigation, is a directing approach that groups both ordinary and uncommon reasons under the umbrella of the 4M, man machine, methodology, and materials [10]. However, it is possible that the output value y is misled by the set of input quantity ratings (major categories) and other ambiguity elements (subcategories) [11]. There are several instances of CED with jumbled up quantity and uncertainty variables [12].

Current and Ton were the influential parametric setting which influences the machining performance, when the Al_2O_3 was incorporated in the dielectric medium [13]. The shorter Ton results in reduction of Ra value whereas longer current generates heat of high intensity [14]. Hybridisation of machining process enhances the flushing of machined debris and improves the quality of the machined surface [15]. Machined surface property was altered with the changes in the characteristics of dielectric fluid [16]. The optimum duty factor and thermography determine the productivity and quality of titanium alloy [17]. The MRR increased with the increment in the conductivity of the dielectric fluid and over the threshold limit reduces due to upsurge in gap distance [18]. Microcracks were decreased, and the permeability of machined surfaces was improved by suspending a significant quantity of powder at the right proportion [19]. The addition of hydroxyapatite to dielectric fluid changes the discharge gap significantly and affects various input variables as well as dielectric fluid deionization [20].

Selecting best solution from the available alternatives increases the productivity of the industry [21]. Grey relational analysis (GRA), technique for order of preference by similarity to ideal solution (TOPSIS), VIKOR, and multi-objective optimization on the basis of ratio analysis were the distinct optimization technique used for identifying the right parametric combination [22–24]. From the above literature, it was confirmed that the heaps of works were available on the EDM of titanium alloy. However, works related to the machining titanium alloy under Al_2O_3 incorporated dielectric medium were scarcely available. The work was carried out with the following objectives (i) to identify the most influential process parameters through CAD; (ii) to analyse the machining performance by varying the parameters; and (iii) to optimize the process variable through TOPSIS optimization technique.

2. Materials and Methods

Ti6Al4V, a medical grade titanium alloy procured from the Ragavendra Engineering having the chemical composition as depicted in Table 1, was selected for investigation. The process parameters which influence the quality of the manufactured product was identified using the CED. The selected process parameters were varied for four levels, and

Table 2: Input variables and its levels.

Process parameters	Levels
Tool	Cu
Powder concentration (g/l)	5, 10, 15, 20
Polarity	Positive (1), Negative (2)
Pulse ON time (μs)	15
Current (A)	05, 10, 15, 20
Gap distance (mm)	1, 2, 3, 4
Pulse OFF time (μs)	4
Dielectric fluid	EDM oil
Machined time (mins)	10

DOE was designed using the Taguchi orthogonal array as depicted in Table 2. The machining performance was accessed in terms of MRR and TWR, determined according to equations (1) and (2). The Ra was measured utilizing the device SJ210 surface roughness tester, in which the value was computed at 10 different places and the average value was recorded as the Ra value. The copper was used as the electrode, hydro carbon oil as dielectric, and specimens were machined for 10 mins. The results were optimized through TOPSIS technique, a mathematical model was developed, the obtained results were compared with the experimental, and valediction of the model was done through sensitivity analysis.

$$\mathrm{MRR} = \left(\frac{(X_b - X_a)}{z}\right). \quad (1)$$

$$\mathrm{TWR} = \left(\frac{(Y_b - Y_a)}{z}\right). \quad (2)$$

X_b: weight of the work piece before machining
X_a: weight of the work piece after machining
Y_b: weight of the work piece before machining
Y_a: weight of the work piece after machining
z: machined time

The unit of MRR and TWR was mg/min.

2.1. Cause and Effect Diagram. The EDM process parameters were broadly classified into electrical parameters, nonelectrical parameters, electrode parameters, dielectric parameters, powder parameters, and integrated process as shown in Figure 1. The assisted EDM viz. ultrasonic, magnetic was used to facilitate the flushing of the machined debris as well as electrical parameters, gap distance was varied for the same effect, gap distance was picked as one of the input variables keeping the cost in mind. Because dielectric characteristics influence heat generation and changing current results in the same output, several researchers found that current was the

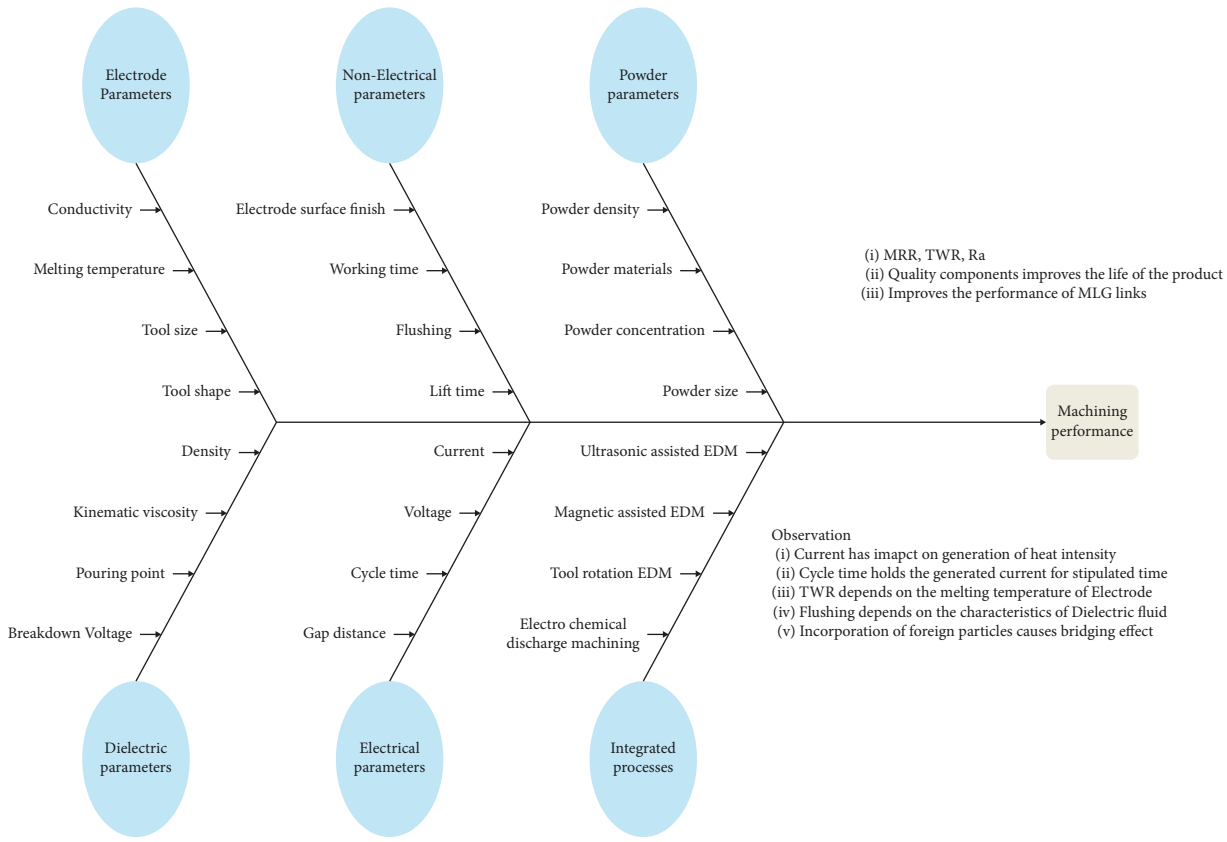

Figure 1: Cause and effect diagram of EDM.

most affecting EDM parameter [25, 26]; hence, current was chosen as the variable. The electrode material characteristics influence the TWR, corner wear, and Ra, whereas change of polarity can yield good surface; hence, these two parameters were selected for investigation.

3. Results and Discussion

3.1. Influence of Distinct Process Parameters on EDM Performance of Ti6Al4V Alloy. Traditionally in EDM, positive polarity was maintained for the effective machining of materials; in special cases, negative polarity was preferred to attain the best Ra value. The MRR of titanium alloy linked to the negative polarity was 18% lower than that of the positive polarity connected electrode as shown in Figure 2; similar result was reported by the distinct researchers [27, 28]. The electrons stream in a straight way and are fit for making secondary electrons while moving to the anode zone and impacting more. It tends to be surmised that the positive polarity zone gets more thermal power than the negative extremity zone. In this way, the emphatically charged anode procures more thermal power than the adversely charged electrode terminal. The MRR upsurges with the raise in concentration of the powder particles in the dielectric fluid; when incorporated with the applied voltage, these particles get energised and travel in a zigzag form. It reduces the spark gap between the electrodes and causes bridging; hence, more heat strucks the work piece, results in the increase in MRR. With the change in current, initially MRR decreases until the 10 A; thereafter, it increases. The reduction in MRR was attributed to the fact that the remove material was remelted over the surface; hence, reduction in volume occurs. The MRR increases with raise in gap distance, as it facilitates the complete flushing of the machined debris.

The interaction effect of various process parameters on the MRR of titanium alloy is shown in Figure 3. When connected to the positive polarity, a maximum MRR of 2.38 mg/min was attained for the current of 15 A and it was reduced to 1.88 mg/min when the polarity was shifted to negative. With regard to the powder concentration, when the volume was 15 g/l at positive polarity, a MRR of 1.59 mg/min was recorded and it was drastically reduced to the 0.82 mg/min, without incorporating powders at negative polarity. The interaction impact of gap voltage and the polarity was very low, as the MRR changes only with the changes in the gap voltage. In case of current and powder concentration, a minimum MRR of 0.86 mg/min was documented at 10 A current under pure dielectric fluid; it was increased to 2.33 mg/min when 20 g/l was added to the fluid at the current of 15 A. Irrespective of the interaction between the gap distance to the either electrical or non-electrical process parameters, MRR varies only with the value of the gap voltage.

The TWR increases with raise in the powder concentration until the saddle point of 5 g/l; thereafter, it declines sharply as shown in Figure 4. The results confirmed that

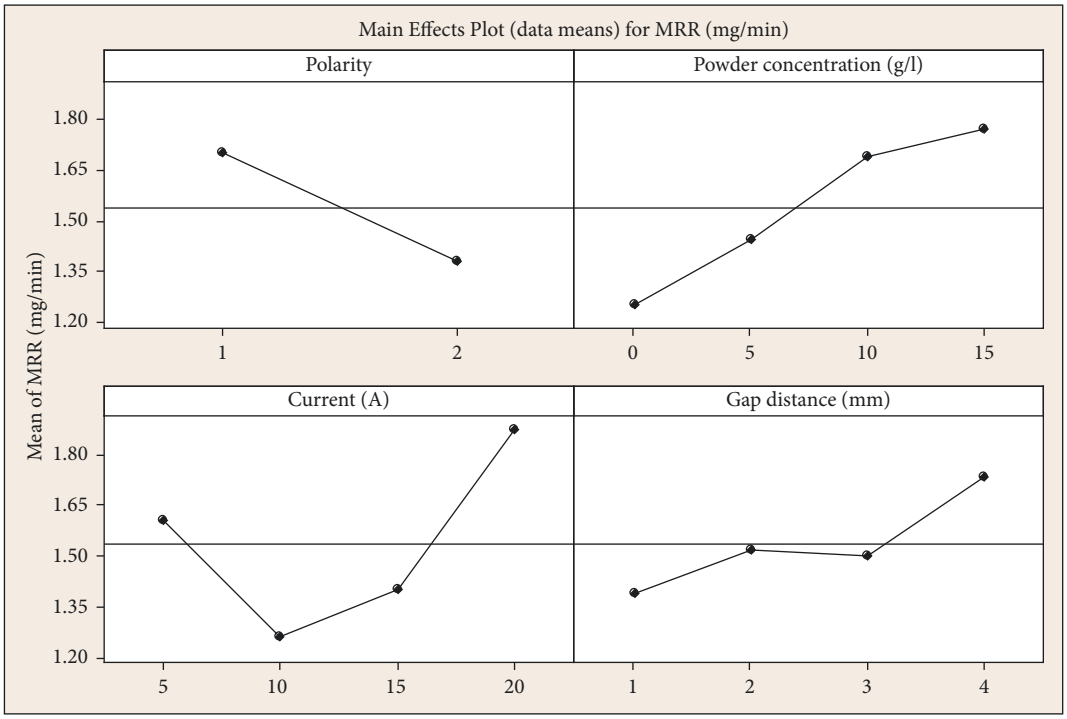

Figure 2: Influence of various process parameters on MRR of Ti6Al4V.

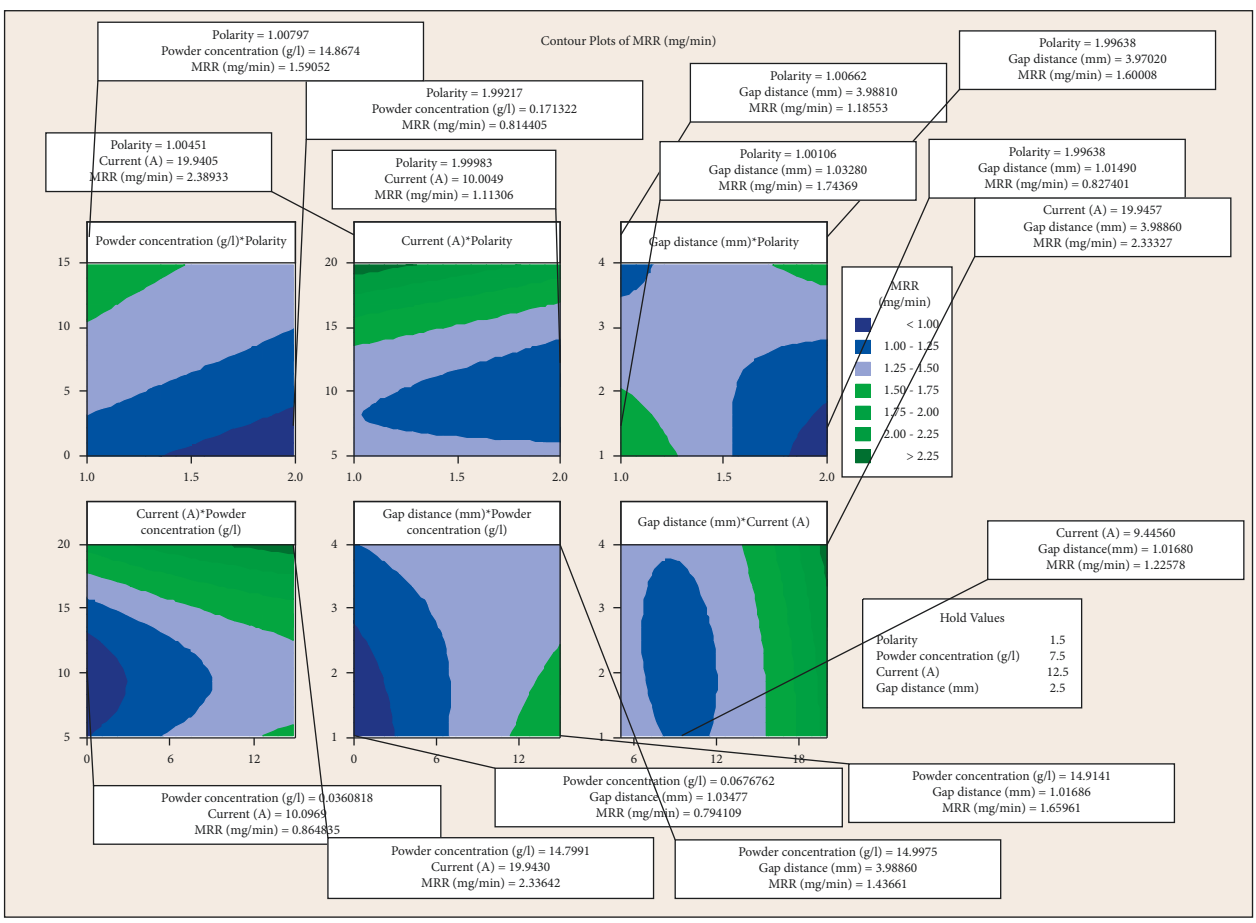

Figure 3: Interaction impact of various process parameters on MRR of Ti6Al4V.

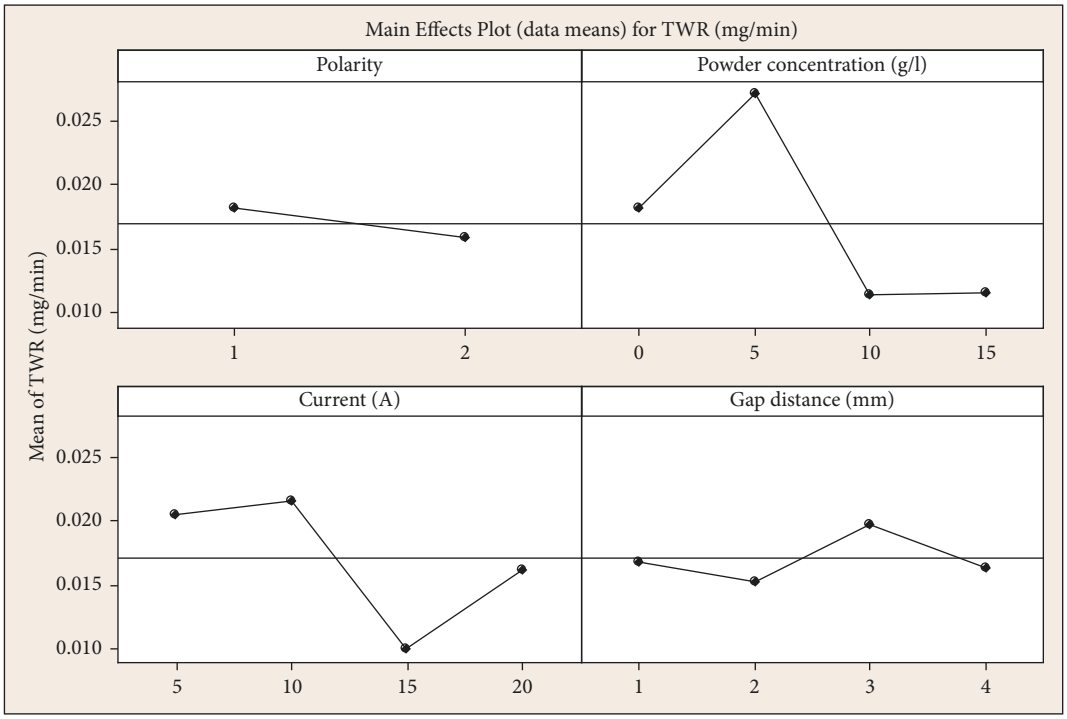

Figure 4: Influence of various process parameters on TWR.

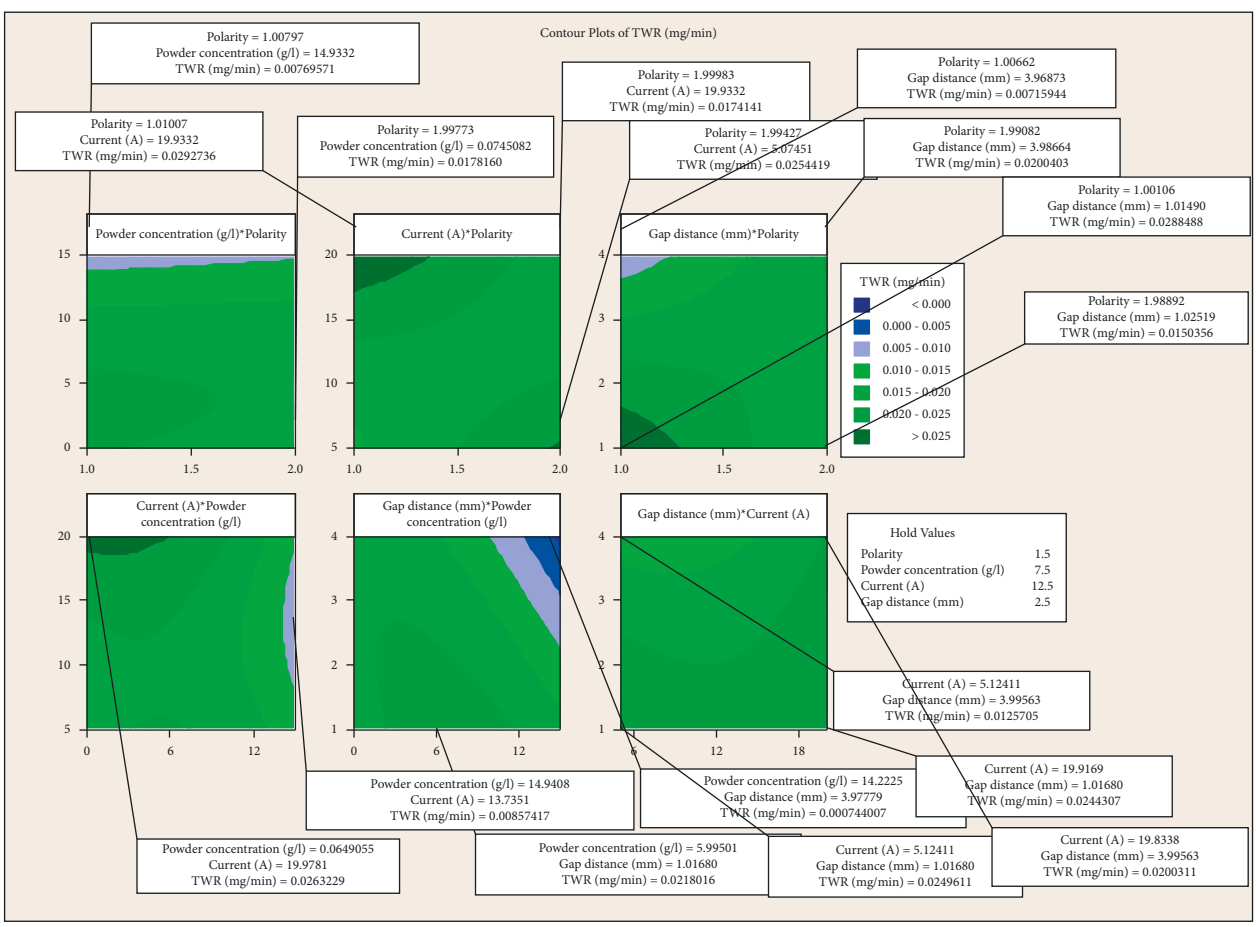

Figure 5: Interaction impact of various process parameters on TWR.

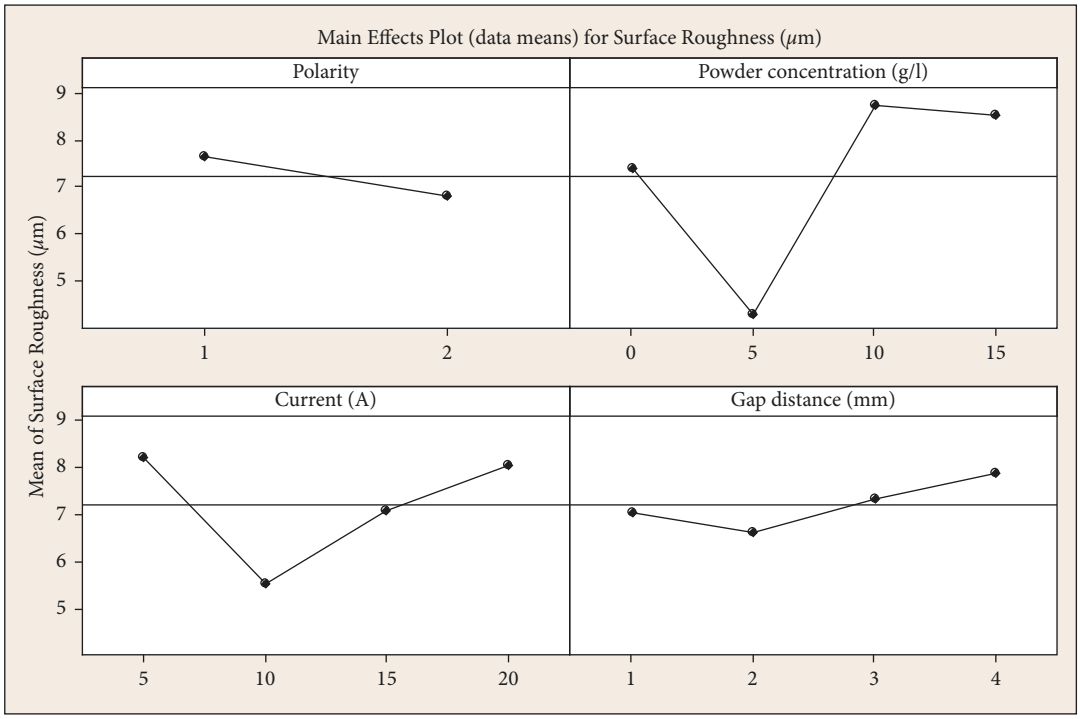

Figure 6: Influence of various process parameters on Ra of Ti6Al4V.

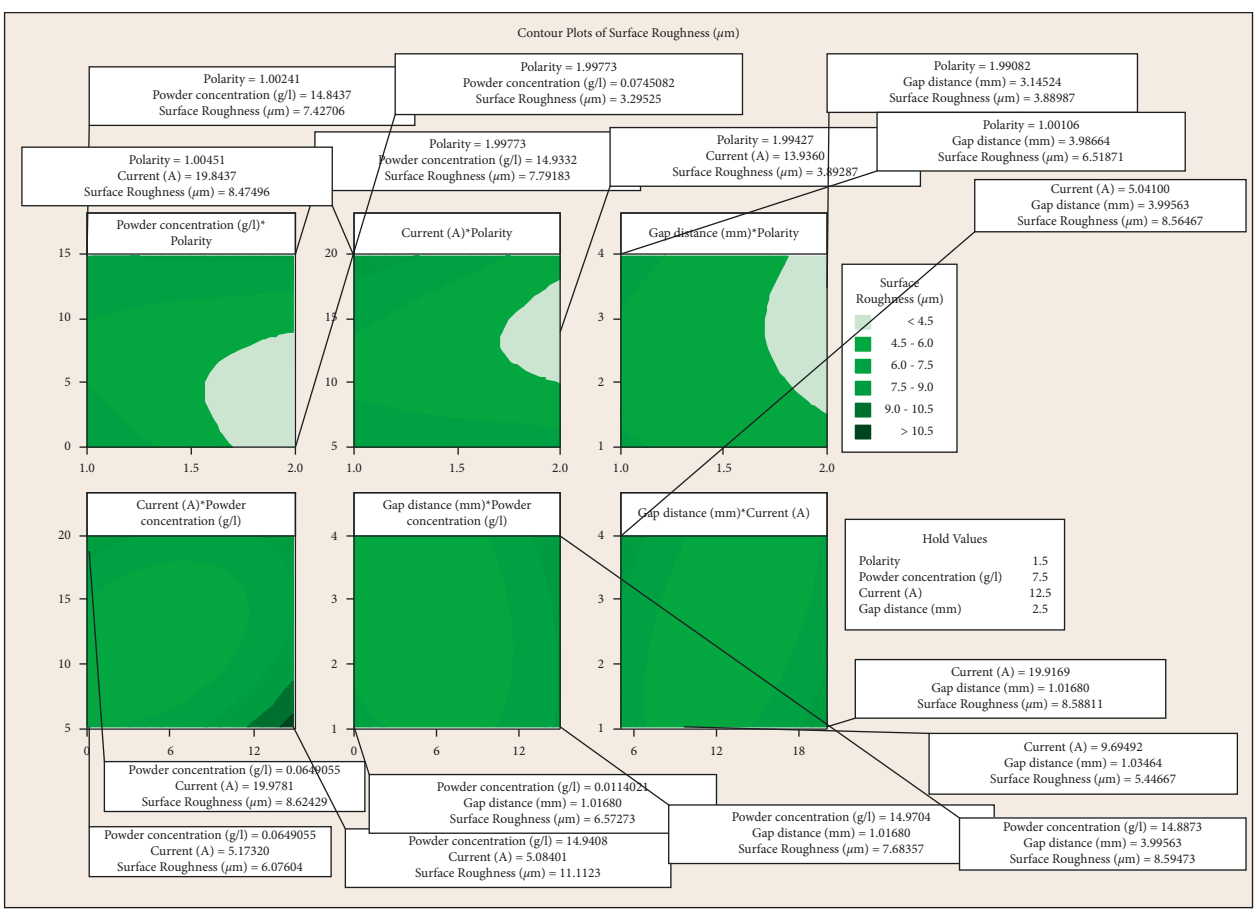

Figure 7: Interaction impact of various process parameters on R_a of Ti6Al4V.

Table 3: Experimental and predicted results of EDM of titanium alloy.

S. No	Polarity	Powder concentration (g/l)	Current (A)	Gap distance (mm)	Experimental results			Predicted results		
					MRR (mg/min)	TWR (mg/min)	Surface roughness (μm)	MRR (mg/min)	TWR (mg/min)	Surface roughness (μm)
1	1	0	5	1	1.12104	0.012881	5.0937	1.26368	0.020663	7.2194
2	1	0	10	2	0.50058	0.030237	5.8203	1.02499	0.01967	6.9701
3	1	0	15	3	1.43855	0.02453	10.1135	1.31362	0.022126	8.0418
4	1	0	20	4	1.96354	0.030574	12.6365	2.12957	0.028032	10.4347
5	1	5	5	1	1.77329	0.035335	8.0071	1.60445	0.025552	6.3456
6	1	5	10	2	1.78704	0.022969	3.7106	1.28392	0.021378	5.7672
7	1	5	15	3	2.01383	0.01143	4.8048	1.49072	0.020655	6.5099
8	1	5	20	4	2.54455	0.026035	4.259	2.22483	0.023381	8.5737
9	1	10	5	2	2.06776	0.001671	9.9741	1.55979	0.01721	7.4412
10	1	10	10	1	1.58518	0.023168	12.2281	1.78501	0.026541	5.9321
11	1	10	15	4	1.31203	0.000234	10.0442	1.45341	0.005816	6.8738
12	1	10	20	3	1.3193	0.014017	5.9908	2.39122	0.022318	8.1542
13	1	15	5	2	0.946	0.016271	8.8559	1.71661	0.01119	9.6801
14	1	15	10	1	2.33251	0.026658	1.6505	2.01041	0.021442	7.2901
15	1	15	15	4	1.44726	0.00321	6.284	1.44657	-0.00656	8.4546
16	1	15	20	3	2.99926	0.01105	13.0695	2.45294	0.010858	8.8541
17	2	0	5	4	1.82468	0.026262	6.1482	1.49891	0.026343	5.4697
18	2	0	10	3	0.44802	0.01432	1.5727	0.93737	0.020672	3.1891
19	2	0	15	2	1.56279	0.004438	5.4497	0.76502	0.014777	4.2318
20	2	0	20	1	1.1429	0.001447	12.2119	0.98187	0.008656	8.5978
21	2	5	5	4	1.48571	0.02871	6.1791	1.64737	0.026629	6.8881
22	2	5	10	3	0.16613	0.039399	1.6682	1.1544	0.021879	3.7265
23	2	5	15	2	1.01663	0.02699	4.2928	1.05062	0.016904	3.8883
24	2	5	20	1	0.7439	0.025968	1.4748	1.33603	0.011704	7.3733
25	2	10	5	3	1.85968	0.030637	9.9594	1.51639	0.024087	8.6801
26	2	10	10	4	1.83308	0.001335	9.1525	1.57665	0.017975	6.2266
27	2	10	15	1	1.14958	0.0049	5.8941	1.08967	0.012393	5.8469
28	2	10	20	2	2.36929	0.015075	6.7705	1.86251	0.013451	6.1829
29	2	15	5	3	1.78266	0.01264	11.7626	1.63131	0.017565	12.6594
30	2	15	10	4	1.46302	0.014237	8.3857	1.60973	0.008273	9.8768
31	2	15	15	1	1.2776	0.003594	9.8181	1.34173	0.007712	8.0643
32	2	15	20	2	1.90664	0.004657	8.2322	2.03273	0.00559	8.0712

when 5 g/l concentration of powder particles was added, most of the generated heat was transferred to the tool materials; hence, TWR increases. With further increase in powder concentration, densification of machined debris occurred, and in case of current, a minimum TWR was obtained at 15 A. The gap distance has predominant impact on the TWR; 20% deviation was observed when there is shift in parametric value from 2 mm to 3 mm. At positive polarity, without mixing particles in the dielectric fluid, a TWR of 0.020 mg/min was observed and it was reduced to 0.017 mg/min when electrodes were connected to negative polarity as depicted in Figure 5. In particle mixed dielectric condition, change in polarity has no impact on the TWR which is evident that incorporation of particles transfers more volume of heat to workpiece [29]. When the current was tuned at lower parametric value, the TWR increases when there is changeover in polarity from positive to negative extreme, and at higher current, TWR reduces with change in polarity. Irrespective of the gap distance, 100% raise in TWR was noted, when electrodes were connected to the positive terminal. The minimum TWR of 0.008 mg/min and 0.007 mg/min was obtained for the current and gap distance of 15 A and 4 mm, respectively, at the powder concentration of 15 g/l.

The impact of various process parameters on the Ra of the Ti6Al4V is depicted in Figure 6. The results showed that sample machined at negative polarity exhibits least Ra, as reported by the various researchers [30, 31]. Attributable to the higher thermal power, the materials eliminated from the cathodes were totally flushed away; henceforth, it dispenses with the formation of remelted layer. As the Ra of the workpiece was impacted by the recast layer, it was evident that the tool extremity influences the Ra of the machined workpiece in EDM process. With regard to the raise in current, a minimum Ra of 5.52 μm was attained; further raise in current worsens the surface quality. At higher current, densification of plasma channel occurred, which results in the formation of material dooms and uneven machined surface; hence, Ra reduces. The best surface quality was attained, when 5 g/l of Al_2O_3 particles were added to the dielectric fluid. When the powder particles were incorporated, owing to the bridging effect, the gap between the tool and electrode increases which facilitates the thorough flushing of machined debris resulting in the reduction of Ra.

Table 4: Assessment values obtained through TOPSIS optimization technique.

Nomalised decision matrix			Weighted normalized decision matrix						
MRR (mg/min)	TWR (mg/min)	Surface roughness (μm)	MRR (mg/min)	TWR (mg/min)	Surface roughness (μm)	D-positive	D-negative	Accessment value	Rank
0.1199	0.11157	0.11291	0.03957	0.03682	0.03839	0.117271631	0.056450115	0.67505	5
0.05354	0.26189	0.12902	0.01767	0.08642	0.04387	0.10699767	0.092552134	0.5362	19
0.15386	0.21246	0.22418	0.05077	0.07011	0.07622	0.073054442	0.105253284	0.40971	26
0.21001	0.26481	0.28011	0.0693	0.08739	0.09524	0.044533921	0.136459488	0.24605	32
0.18966	0.30605	0.17749	0.06259	0.101	0.06035	0.058846878	0.125328922	0.31951	30
0.19113	0.19894	0.08225	0.06307	0.06565	0.02797	0.094926739	0.088202181	0.51836	20
0.21539	0.099	0.10651	0.07108	0.03267	0.03621	0.107145522	0.076856782	0.58231	12
0.27215	0.2255	0.09441	0.08981	0.07441	0.0321	0.078267866	0.113691088	0.40773	27
0.22116	0.01447	0.22109	0.07298	0.00478	0.07517	0.11512605	0.092870605	0.5535	15
0.16954	0.20067	0.27106	0.05595	0.06622	0.09216	0.068435923	0.115644263	0.37177	29
0.14033	0.00203	0.22265	0.04631	0.00067	0.0757	0.128831103	0.076203257	0.62834	6
0.14111	0.12141	0.1328	0.04657	0.04006	0.04515	0.107820655	0.066082988	0.62	7
0.10118	0.14093	0.1963	0.03339	0.04651	0.06674	0.103104204	0.077157048	0.57197	14
0.24947	0.2309	0.03659	0.08233	0.0762	0.01244	0.096366091	0.107483112	0.47273	21
0.15479	0.0278	0.13929	0.05108	0.00917	0.04736	0.127731077	0.058572297	0.68561	3
0.32079	0.09571	0.28971	0.10586	0.03158	0.0985	0.081027368	0.136349355	0.37275	28
0.19516	0.22747	0.13628	0.0644	0.07506	0.04634	0.076482091	0.101005403	0.43092	25
0.04792	0.12403	0.03486	0.01581	0.04093	0.01185	0.144064501	0.041477884	0.77645	1
0.16715	0.03844	0.1208	0.05516	0.01268	0.04107	0.125913007	0.058922437	0.68122	4
0.12224	0.01253	0.2707	0.04034	0.00414	0.09204	0.12689348	0.088027666	0.59042	11
0.1589	0.24867	0.13697	0.05244	0.08206	0.04657	0.080523304	0.100253612	0.44543	24
0.01777	0.34125	0.03698	0.00586	0.11261	0.01257	0.131843672	0.111952472	0.54079	18
0.10873	0.23377	0.09516	0.03588	0.07715	0.03235	0.102616392	0.084857683	0.54736	16
0.07956	0.22492	0.03269	0.02626	0.07422	0.01112	0.124283811	0.076330059	0.61952	8
0.1989	0.26536	0.22077	0.06564	0.08757	0.07506	0.052861489	0.12334375	0.3	31
0.19606	0.01157	0.20288	0.0647	0.00382	0.06898	0.120008661	0.082581885	0.59237	10
0.12295	0.04244	0.13065	0.04057	0.01401	0.04442	0.130037263	0.049920733	0.7226	2
0.25341	0.13057	0.15008	0.08362	0.04309	0.05103	0.087073113	0.097155019	0.47264	22
0.19067	0.10948	0.26074	0.06292	0.03613	0.08865	0.08826448	0.10258889	0.46247	23
0.15648	0.12331	0.18588	0.05164	0.04069	0.0632	0.096739333	0.080062546	0.54716	17
0.13665	0.03113	0.21763	0.04509	0.01027	0.074	0.121517372	0.07473374	0.61919	9
0.20393	0.04033	0.18248	0.0673	0.01331	0.06204	0.112592846	0.080791928	0.58222	13

Table 5: Sensitivity analysis and validectory of results.

Max	2.812236	0.029483	14.66625	0.866997
Min	0.70141	0.01219	4.44156	0.569453
Mean	1.01563	0.007278	4.597194	0.726892
Std	0.514458	0.00611	2.654605	0.045471

When the gap distance was maintained at 2 mm, machined surface with minimum Ra was attained and it increases with further increase in gap distance.

The interaction impact of various input variables on the Ra of the titanium alloy is shown in Figure 7. Regardless of the process parameters, when machined at negative polarity, the samples exhibit 150% better Ra value due to the uniform heat distribution. The ideal powder concentration to attain best Ra ranges between 5 g/l to 10 g/l and exceeds beyond the limit; it leads to the densification of machined debris results in reduction of Ra. Tuning the powder concentration and gap distance to the higher parametric levels results in worsening of surface quality.

3.2. TOPSIS. The TOPSIS technique was applied to choose the best from the available option. The streamlining method starts with the arrangement of the choice network; for the ongoing exploratory run, a choice framework of 32×4 is shaped as displayed in Table 3. The standardization of the choice network was determined as per the following equation:

$$\text{Aij} = \frac{\text{Yij}}{\sum_{i=1}^{n} \sqrt{(Yij)^2}}. \tag{3}$$

$$\text{Bij} = wj * \text{Aij}. \tag{4}$$

The subsequent stage was the arrangement of a weighted standardized choice grid, as displayed in condition (4), from which the Eigen values ($\square^{+}$, $\square^{-}$)were formed where the weight (wj) of the MRR, TWR, and Ra are 0.33, 0.33, and 0.34, respectively. For beneficiary ascribed, $\square^{+}$ and $\square^{+}$ are most extreme and least upsides of weighted standardized choice framework as well as the other way around for nonbeneficiary credits, as displayed in condition (5) and (6).

For beneficiaries,

$$\text{\textbf{\textbf{\textbf

$$\text{\textcircled{?}}^{+} = \text{Min}\,(\text{Bij})_{i=1}^{n}, \quad \text{\textcircled{?}}^{-} = \text{Max}\,(\text{Bij})_{i=1}^{n}. \tag{6}$$

The ideal (P^+) and nonideal (P^-) arrangements are determined utilizing condition (7). The scatterings between the standards and the nonstandards by the equivalent Euclidean distances as shown in the situations 8 and its qualities are depicted in Table 4.

$$\begin{aligned} (P^+, P^-) &= \sum_{j=1}^{n} \sqrt{\left(\text{Bij} - \text{\textcircled{?}}^{+}\right)^2 + \left(\text{Bij} - \text{\textcircled{?}}^{n}\right)^2}, \\ D^i &= \left(\frac{P^-}{(P^+ + P^-)}\right). \end{aligned} \tag{7}$$

In view of the overall closeness esteem, the best blend of trial was discharge current of 10 A and gap distance of 3 mm, with the negative polarity under unmixed dielectric medium. The sensitivity analysis was conducted, and it was found that the optimal value results in highest assessment value, as depicted in Table 5.

4. Conclusion

(1) The MRR increases with the incorporation of Al_2O_3 particles, owing to the bridging effect, and positive polarity proffers high MRR, owing to the formation of the secondary electrons. Due to the increase in spark gap, machined debris were completely flushed away, which results in improvement of MRR.

(2) The most impact input variables of TWR were gap distance, as PMEDM change of polarity has no impact on TWR. At lower parametric value of gap distance, 100% raise in TWR with change in polarity was observed.

(3) Addition of particles reduces Ra accredited to the fact complete flushing of machined debris. Because of the increased thermal energy, the materials removed from the cathodes were completely flushed away, eliminating the need for the development of a remelted layer.

(4) The TOPSIS technique was utilised for the obtaining optimal solution, with the aid of mathematical modelling, the predicted results were obtained, and the optimal results were validated using the sensitivity analysis.

Data Availability

All the data are included within the manuscript.

Conflicts of Interest

The authors declare that they have no conflicts of interest.

References

[1] P. Gangidi, "A systematic approach to root cause analysis using 3 × 5 why's technique," *International Journal of Lean Six Sigma*, 2018.

[2] Y. Nagaraj, N. Jagannatha, and N. Sathisha, "Hybrid nonconventional machining of glass - a review," *Applied Mechanics and Materials*, vol. 895, pp. 8–14, 2019.

[3] R. Muhammad, M. S. Hussain, A. Maurotto, C. Siemers, A. Roy, and V. V. Silberschmidt, "Analysis of a free machining $\alpha+\beta$ titanium alloy using conventional and ultrasonically assisted turning," *Journal of Materials Processing Technology*, vol. 214, no. 4, pp. 906–915, 2014.

[4] S. Gürgen and M. A. Sofuoğlu, "Advancements in conventional machining: a case of vibration and heat-assisted machining of aerospace alloys," in *Advanced Machining and Finishing*, pp. 143–175, Elsevier, Amsterdam, Netherlands, 2021.

[5] S. Vigneshwaran, K. M. John, R. Deepak Joel Johnson, M. Uthayakumar, V. Arumugaprabu, and S. T. Kumaran, "Conventional and unconventional machining performance of natural fibre-reinforced polymer composites: a review," *Journal of Reinforced Plastics and Composites*, vol. 40, no. 15-16, pp. 553–567, 2021.

[6] R. Ranjith, P. K. Giridharan, and J. Devaraj, "Influence of titanium-coated (b4c + sic) particles on electric discharge machining of aa7050 hybrid composites," *High Temperature Material Processes An International Quarterly of High-Technology Plasma Processes*, vol. 20, no. 2, pp. 93–105, 2016.

[7] P. Kuppan, A. Rajadurai, and S. Narayanan, "Influence of EDM process parameters in deep hole drilling of Inconel 718," *International Journal of Advanced Manufacturing Technology*, vol. 38, no. 1-2, pp. 74–84, 2008.

[8] N. Pragadish and M. Pradeep Kumar, "Optimization of dry EDM process parameters using grey relational analysis," *Arabian Journal for Science and Engineering*, vol. 41, no. 11, pp. 4383–4390, 2016.

[9] M. Patel Gowdru Chandrashekarappa, S. Kumar, J. JagadishJagadish, K. Pimenov, and K. Giasin, "Experimental analysis and optimization of EDM parameters on HcHcr steel in Context with different electrodes and dielectric fluids using hybrid Taguchi-based PCA-utility and Critic-utility approaches," *Metals*, vol. 11, no. 3, 419 pages, 2021.

[10] D. H. Yoo and C. G. Song, "Inundation accident analysis using hydrodynamic model and consideration of disaster roots using cause and effect diagram," *Journal of Convergence for Information Technology*, vol. 10, no. 10, pp. 128–134, 2020.

[11] D. D. Shinde, S. Ahirrao, and R. Prasad, "Fishbone diagram: application to identify the root causes of student-staff problems in technical education," *Wireless Personal Communications*, vol. 100, no. 2, pp. 653–664, 2018.

[12] M. F. Suárez-Barraza and F. G. Rodríguez-González, "Cornerstone Root Causes through the Analysis of the Ishikawa Diagram, Is it Possible to Find Them? A First Research Approach," *International Journal of Quality and Service Sciences*, 2018.

[13] R. Ranjith, M. Prabhakar, P. K. Giridharan, and M. Ramu, "Influence of Al203 particle mixed dielectric fluid on machining performance of Ti6Al4V," *Surface Topography: Metrology and Properties*, vol. 9, no. 4, Article ID 045052, 2021.

[14] T. T. Hong, N. V. Cuong, B. T. Danh et al., "Multi-objective optimization of PMEDM process of 90CrSi alloy steel for minimum electrode wear rate and maximum material removal rate with silicon carbide powder," *Materials Science Forum*, vol. 1018, pp. 51–58, 2021.

[15] M. Prabhakar, R. Ranjith, and S. Venkatesan, "Characterization of electric discharge machining of titanium alloy utilizing MEIOT technique for orthopedic implants," *Materials Research Express*, vol. 8, no. 8, Article ID 086505, 2021.

[16] S. Mohanty, A. K. Das, and A. R. Dixit, "Surface integrity of tribo-adaptive layer prepared on Ti6Al4V through μEDC process," *Surface and Coatings Technology*, vol. 429, Article ID 127922, 2022.

[17] S. Jeavudeen, H. S. JailaniJailani, and M. Murugan, "Enhancement of machinability of titanium alloy in the Eductor based PMEDM process," *SN Applied Sciences*, vol. 3, no. 4, 490 pages, 2021.

[18] T. T. Hong, N. H. Linh, N. V. Cuong et al., "Effect of process parameters on machining time in PMEDM cylindrical shaped parts with silicon carbide powder suspended dielectric," *Materials Science Forum*, vol. 1018, pp. 97–102, 2021.

[19] C. Somu, R. Ranjith, P. K. Giridharan, and M. Ramu, "A novel Cu-Gr composite electrode development for electric discharge machining of Inconel 718 alloy," *Surface Topography: Metrology and Properties*, vol. 9, no. 3, Article ID 035025, 2021.

[20] P. K. Rout and P. C. Jena, "A review of current researches on powder mixed electrical discharge machining (PMEDM) technology," *Lecture Notes in Mechanical Engineering*, pp. 489–497, 2021.

[21] R. Ranjith and S. N. Vimalkumar, "Integrated MOORA-ELECTRE approach for solving multi-criteria decision problem," *World Journal of Engineering*, vol. 19, no. 4, pp. 510–521, 2021.

[22] S. M. Shaaban and Y. I. Mesalam, "SVC parameters optimization using a novel integrated MCDM approach," *Symmetry*, vol. 14, no. 4, 702 pages, 2022.

[23] G. Poongavanam, V. Sivalingam, R. Prabakaran, M. Salman, and S. C. Kim, "Selection of the best refrigerant for replacing R134a in automobile air conditioning system using different MCDM methods: a comparative study," *Case Studies in Thermal Engineering*, vol. 27, Article ID 101344, 2021.

[24] A. Maji, T. Deshamukhya, G. Choubey, and A. Choubey, "Performance evaluation of perforated pin fin heat sink using particle swarm optimization and MCDM techniques," *Journal of Thermal Analysis and Calorimetry*, vol. 147, no. 8, pp. 5133–5150, 2022.

[25] E. Pujiyulianto, "Effect of pulse current in manufacturing of cardiovascular stent using EDM die-sinking," *International Journal of Advanced Manufacturing Technology*, vol. 112, no. 11-12, pp. 3031–3039, 2021.

[26] L. Jiang and M. Kunieda, "High rising speed discharge current pulse for EDM generated by inductive boosting voltage circuit," *CIRP Annals*, vol. 70, no. 1, pp. 147–150, 2021.

[27] S. Lakra and R. C. Francis, "A technique of tool manufacturing by changing the polarity of EDM," *International Journal*, vol. 9, no. 5, 2021.

[28] J. Sahu, S. Shrivastava, C. Mohanty, S. Mishra, and T. K. Mahanta, "Effect of polarity on MRR and TWR in electric discharge machining," in *Advances in Mechanical Processing and Design*, pp. 543–550, Springer, Singapore, 2021.

[29] K. Ishfaq, M. A. Maqsood, S. Anwar, M. Harris, A. Alfaify, and A. W. Zia, "EDM of Ti6Al4V under nano-graphene mixed dielectric: a detailed roughness analysis," *International Journal of Advanced Manufacturing Technology*, vol. 120, no. 11-12, pp. 7375–7388, 2022.

[30] J. Lei, X. Wu, Z. Zhou, B. Xu, L. Zhu, and Y. Tang, "Sustainable mass production of blind multi-microgrooves by EDM with a long-laminated electrode," *Journal of Cleaner Production*, vol. 279, Article ID 123492, 2021.

[31] B. Xu, M. Q. Lian, S. G. Chen et al., "Combining PMEDM with the tool electrode sloshing to reduce recast layer of titanium alloy generated from EDM," *International Journal of Advanced Manufacturing Technology*, vol. 117, no. 5-6, pp. 1535–1545, 2021.

Hindawi
Advances in Materials Science and Engineering
Volume 2022, Article ID 2748908, 9 pages
https://doi.org/10.1155/2022/2748908

Research Article

Synthesis and Characterization of Iron Doped Titanium Dioxide (Fe: TiO_2) Nanoprecipitate at Different pH Values for Applications of Self-Cleaning Materials

Tizazu Abza,[1] Abel Saka,[2] Jule Leta Tesfaye,[2,3] Lamessa Gudata,[2] N. Nagaprasad,[4] and Ramaswamy Krishnaraj[3,5]

[1]*Hawassa University, College of Natural and Computational Sciences, Physics Department, Hawassa, Ethiopia*
[2]*Dambi Dollo University, College of Natural and Computational Science, Department of Physics, Ethiopia*
[3]*Centre for Excellence-Indigenous Knowledge, Innovative Technology Transfer and Entrepreneurship, Dambi Dollo University, Ethiopia*
[4]*Department of Mechanical Engineering, ULTRA College of Engineering and Technology, Madurai - 625 104, Tamilnadu, India*
[5]*Department of Mechanical Engineering, College of Engineering, Dambi Dollo University, Ethiopia*

Correspondence should be addressed to Abel Saka; latiyejesus@gmail.com, Jule Leta Tesfaye; laterajule@gmail.com, and Ramaswamy Krishnaraj; prof.dr.krishnaraj@dadu.edu.et

Received 1 May 2022; Revised 27 May 2022; Accepted 10 June 2022; Published 8 July 2022

Academic Editor: Pudhupalayam Muthukutti Gopal

Fe:TiO_2 nano particles were deposited through sol-gel techniques, and the influence of pH values on structural, morphological, optical, and photoluminescence spectral behaviors was studied. Iron doped titanium dioxide nanopowders were analyzed using XRD, SEM, UV–ViS, and PL. Nano crystallized samples of titanium dioxide (72 nm, 77 nm, 78 nm, and 83 nm) were gained from X-Ray diffraction data and showed that there was the creation of unalloyed anatase and ructile segment with tetragonal configuration. The average crystal size was 77.5 nm. pH values provide the alteration of segments from anatase to ructile. The crystal size of prepared iron doped titanium dioxide nanoparticles was greater than before as pH value rises from 2 to 6 while FWHM and scrap sizes declined. Homogeneously disseminated cylindrical forms of iron doped titanium dioxide nanoparticles were perceived from scanning electron microscope graphics and rises in size with growing pH values from 2 to 6 in an acidic medium. Extremely translucent nanopowders are witnessed in the observable region by visible and redshifts near advanced wavelengths with rising pH values because of an increase in the size of particles from XRD data and SEM micrographs. The band gap of energy produced by nano concentrates was reduced with growing pH values that resemble the redshift of optical absorption superiority. The structural behaviors of deposited nanoparticles were also analyzed by Raman spectra and disclosed the existence of tetragonal anatase and ructile segments. EDS results confirmed that the dopant of pH values of the solutions might affect the size distributions of the Fe: TiO_2 nanoparticles. The general decrement intensity was witnessed from photoluminescence outcomes.

1. Introduction

Nanoscience and nanotechnology are developing and exponentially mounting areas with large solicitations in modern technology. The nanoparticle is an interdisciplinary part of an investigation by using essential methods of different aspects like chemicals, engineering, physical and biological knowledge, and foremost to the expansion of new approaches to operating small size particles consequential in the manufacture of nanoparticles. These Nanoparticles might describe as units approximately ranging from 1 to 100 nanometers. Nanotechnology deals with the depositions, growth, and solicitations of a multiplicity of nanoparticles [1]. Nanoparticles of (Fe:TiO_2) are hopeful resources and broadly used in numerous claims because of their extremely useful and actual devices, different sensors; reagents, optoelectronic, structural and current belongings; antimicrobial, brilliant gas-sensitive, and dielectric assets; optical and electrical possessions; best chemical constancy; and the dilapidation of contamination. Because of admirable

thermal stability, extraordinary sunlight reactivity, and sensitivity, comparatively cheaper tools, iron doped titanium dioxide nanoparticles are applicable in numerous manufacturing. In addition, iron doped titanium dioxide nanoparticles are brilliant photocatalysts because of their nontoxicity, higher photo sensitivity, solid corroding power, easy obtainability, and sustainability [2, 3]. According to the meaning of the term, water repellent fabrics are those that resist water from their surface [4]. The fluoro-alkyl-silanes are the chemicals that are most frequently utilized for hydrophobization because of their extremely low surface free energy and the facile interaction of the silane clusters and the hydroxyl groups on coverings. Additionally, the hydrophobization of a perfluorinated substance [5] is responsible for the formation of the majority of superoleophobic surfaces. Wettability is among the essential features of a solid surface, as well as the contact angle has now been widely utilized to examine the wettability of a solid surface in many applications.

A great deal of interest has been generated in superhydrophobic surfaces as a result of its possible practical uses, which include anti-sticking, anticontamination, as well as self-cleaning coatings. The mechanism is comparable to the lotus effect, which occurs naturally in the environment. *Lotus* plants have extremely hydrophobic surfaces that are rough and textured, making them ideal for growing in water. When water droplets land on them, the droplets condense and, if the surface slopes sufficiently, roll off the surface into the surrounding air. As a result, even during a torrential downpour, the surfaces remain dry. Furthermore, because the droplets pick up microscopic bits of dirt as they roll down the leaves of the lotus plant, the leaves of the plant remain clean even when it is raining lightly [6]. Also known is that nanosized Fe: TiO_2 and ZnO particles are much more highly effective at absorbing and scattering UV light than conventionally sized Fe: TiO_2 and ZnO particles, and as a result, they were significantly able to block UV radiation due to their significantly greater surface area to volume ratio. A great deal of effort has been put into the application of UV bulking treatment to fabrics with the use of nanotechnology. The sol-gel process has been used to generate UV blocking treatments for fabric, which were developed by Xin and colleagues. On the surface of treated cotton fabric, a thin layer of Fe: TiO_2 nanoparticles is created, which provides good UV protection. The finish is durable and may withstand up to 50 items of washings in the washing machine. As an alternative to Fe: TiO_2, ZnO nanorods ranging in length from 10 to 50 nm were also put into the cotton fabric to give UV protection. The rods provided good ultraviolet protection [7].

In nanoparticles of iron doped titanium dioxides, the electronic arrangements, as well as the charge behaviors, are powerfully exaggerated by crystalline segment. Iron doped titanium dioxides nanoparticles can exist as anatase, rutile, and brookite phases. The structure of anatase and rutine is tetragonal, and orthorhombic is for brookite [8]. From these types, anatase is meta-stable with maximum photocatalytic movement and completely transformed to the rutile phase at a maximum temperature [9]. In another way, increases in pH value sort phase alterations, that is, amorphous to anatase, anatase to rutile. Maximum chemical constancy and fewer activities of iron doped titanium dioxides were perceived in rutile behaviors [10]. As well, some iron doped titanium dioxides have a huge magnitude of anatase, and a minor magnitude of rutile exhibitions a more sophisticated photocatalytic action than in the rutile types. Among absorption spectrum, the advantageous semiconductors for sunlight catalysis involve a bandgap analogous to the energy of that of the energy of photons of visible or ultraviolet light, containing a value below 3.5 eV. The mainstream of investigators make sure definite that in iron doped titanium dioxide, the rutile partakes an unintended bandgap of three-point one zero electron volt and a direct energy band gap of three-point zero one electron volt, and anatase has only an indirect energy bandgap 3.23 eV [11].

Nevertheless, Reddy's work [12] reports that the bandgap of anatase segment from the conspiracy for indirect conversion is quite small (2.9–2.98 eV), which commanded them, conflicting with the other scholars, to generalize that the direct conversion is more promising for iron doped titanium dioxide nanoparticles with anatase type. The reported standards in numerous literature that 2.86–3.34 electron volt for the anatase type are the modifications being qualified to deviations in the stoichiometry of the preparations, the crystal size, the impurities compositions, and the kind of electronic conversion [13]. Various techniques have been published in the literature that iron doped titanium dioxide nanoparticles were deposited by chemical-precipitation [14], the sol-gel techniques [15, 16], hydrothermal [17], and solvothermal progressions [18], combustion techniques [2], a microemulsion, mediated techniques, electro-chemical preparations, fungus-mediated preparations, and chemical vapor synthesis [19]. Works [20] reported that iron doped titanium dioxide nanoparticles were equipped through the sol-gel technique by varying reaction constraints, such as hydrolyzing agents, molar ratio, and string time. Nanocrystals of Fe: $TiO_2$with maximum surface area and varying ratios of anatase or rutile were achieved from X-ray diffraction data, prepared via sol-gel techniques. Other literature [20] also published on the synthesis of anatase Fe: TiO_2 nanocrystals found by the sol-gel technique using titanium tetra-iso-pro-peroxide in ethylene glycol leads to maximum surface area standards as well as preserved anatase per small crystal size. Sol-gel techniques are the most significant and hopeful methods working in the manufacture of nanoparticles [21]. This technique yields high crystal oxides by permitting governor in particle size, surface morphology, and phase configuration in pH values. pH values have a vital role in the creation of Fe: TiO_2 crystalline phases. Hence, the objective of this research was to study the influence of pH values on structural, optical, and morphological behaviors of deposited iron doped titanium dioxide Nanoparticles through sol-gel techniques for self-cleaning application.

2. Materials and Methodology

2.1. Chemicals Used. In preparation of iron doped titanium dioxide Nanoparticles, the chemical used as glacial acetic

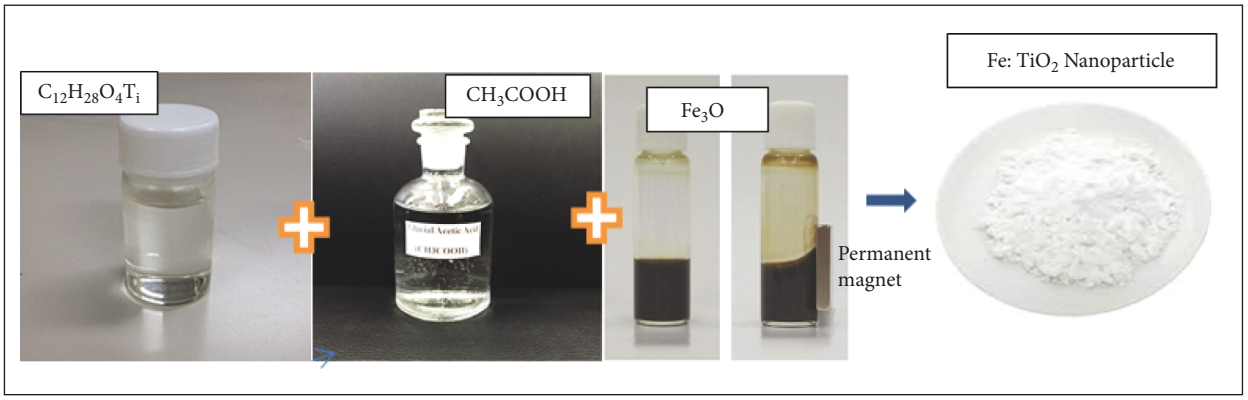

Figure 1: The procedure of material preparation.

acid (CH_3COOH) (98% LyondellBase Acetayls, LLC) and titanium (IV) iso-prop-oxide ($C_{12}H_{28}O_4Ti$) (99.9% Hebei, China) and Ferrous Oxide (Fe_3O) (98%, Zhejiang, China).

2.2. Instruments Used. Instruments used in the laboratory were magnetic stirrer, heater, thermometer, pH meter, Teflon pot, metallic pestle, and mortar auto-claves and beakers.

2.3. Sample Preparation Techniques. For the present study, Sol-gel techniques of Fe: TiO_2 nanoparticles were produced according to the process developed [22] by varying pH values of 2, 4, 5, and 6. The solution was administered by the ratio of 6Fe: TiO_2: $30CH_3COOH$: $320H_2O$. 72 ml of glacial acetic acid was slowly added to 32 ml of titanium (IV) iso-prop-oxide in a water bath at zero degrees Celsius by unceasing stirring. Then and there, 320 ml of distilled water was moderately added to the solution under stable stirring by using a magnetic stirrer, and 20 ml of ferrous Oxide was added to the solution. Ultrasonic conduct took place for 20 hr after dynamic anxiety (45 min). All over again, dynamic agitation was pragmatic for 3 hr. The mixture was decanted into a Teflon pot and located in stainless steel autoclaves. Next, step by step, iron doped titanium dioxide nanopowders were produced at 2, 4, 5, and 6 PH values, as shown in Figure 1. Lastly, the solid trials gained were ground by using a metallic pestle and mortar and kept in sample container glass.

2.4. Physical Characterizations. The consequential powders were analyzed by using instruments like X-ray diffraction, Scanning electron microscope, UV/Visible, and Fluorescence Spectroscopy. X-ray Diffraction (XRD) analysis was carried out utilizing a D8 Advance Bruker system using CuKα ($\lambda = 0.154056$ nm) radiation. The average crystalline size of produced Fe: TiO_2 Nanoparticle was determined from the peaks of XRD augmentation by using the Debye–Scherer formula [23].

$$dhkl = \frac{0.9\,\lambda}{\beta \cos\theta,} \tag{1}$$

where d_{hkl} is the average crystallite size, λ is the wavelength of the X-ray (0.15425 nm for Cu-Kα), β is the Full width at half maxima in radian, and θ is Braggs diffraction angle (? = 2dsinθ) agrees to the peak position. The grain magnitude (ε), lattice constraints "a"and "c" and the distance of the space d_{hkl} aimed at anatase and ructile phase of iron doped titanium dioxide nanoparticles could be deliberated by using equations (2)–(4) [24, 25].

$$\varepsilon = \frac{\beta}{4\tan\theta}, \tag{2}$$

$$a = \sqrt{\frac{1}{3}}\,\frac{\lambda}{\mathrm{Sin}\,\theta}\mathrm{c} = \frac{\lambda}{\mathrm{Sin}\,\theta}, \tag{3}$$

$$\mathrm{dhkl} = \frac{\mathrm{ac}}{2}\sqrt{\frac{3}{\mathrm{c}^2\left(\mathrm{h}^2 + \mathrm{hk} + \mathrm{k}^2\right) + 3\left((\mathrm{al})^2|4\right)}}. \tag{4}$$

The unit cell volume (V) and O-Ti-O bond length (L) are given by [26]

$$V = 0.866\mathrm{a}^3 cl = \frac{\mathrm{a}^3}{3} + \left(\frac{1}{2} - \mathrm{z}\right)^2 \mathrm{c}^2 Z = \frac{\mathrm{a}^2}{3\mathrm{c}^2} + \frac{1}{4}. \tag{5}$$

The surface morphology, as well as the nanostructure of the occasioning iron doped titanium dioxide (Fe: TiO_2) Nanoparticles, was analyzed with the help of a scanning electron microscope. The structural characteristics of synthesized Fe: TiO_2 powders were examined by a Raman shift (RAM, HR Spectrometer). Optical absorption spectra were recorded with a Perkin–Elmer Lambda-19 spectrophotometer in the 300–800 nm range. The bandgap energy of Fe: TiO_2NPs is calculated using equation (6) [1].

$$\mathrm{E} = \frac{\mathrm{hc}}{\lambda}, \tag{6}$$

where h is plank's constant ($h = 6.626\mathrm{x}10^{-34}$Js) C is the speed of light ($\mathrm{c} = 3 \times 10^8$ m/s, and λ is the wavelength. Photoluminescence (PL) quantities were accomplished at normal temperature by using an instrument called fluorescence spectrophotometer (LS-45) with an excitation wavelength of 260 Nanometer.

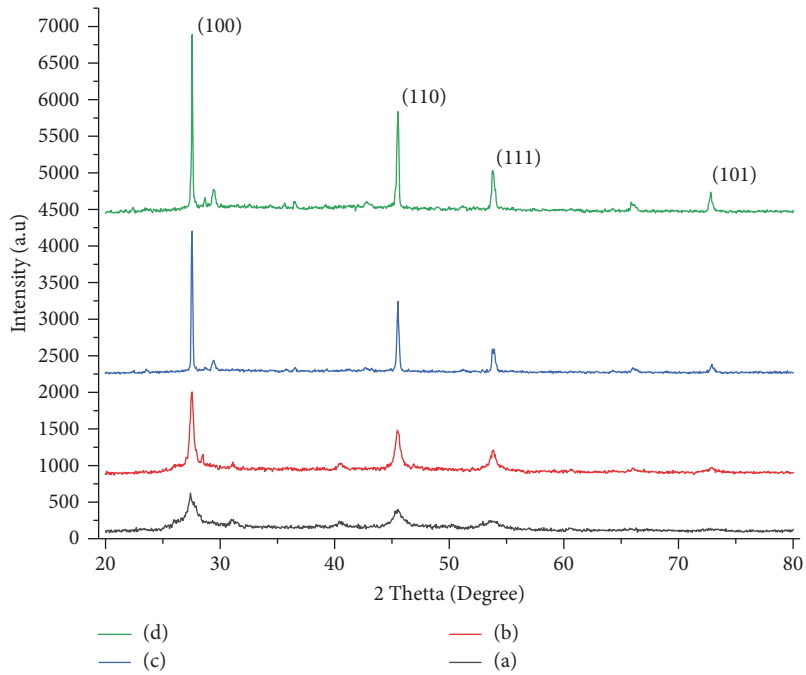

Figure 2: XRD graph of prepared iron doped titanium dioxide at different pH values of (a) pH = 2, (b) pH = 4, (c) pH = 5, and (d) pH = 6.

Table 1: The full width at half maxima (FWHM), average particle size and average crystal values of Fe: TiO_2 NPs at different pH values (2, 4, 5, and 6)

Sample	pH value	2Theta (Degree)	Theta (θ(degree)	FWHM (Radian)	Crystal Size (nm)
1	2	27.29508	13.64	0.11341	72
2	4	45.31616	22.65	0.11153	77
3	5	53.44262	26.72	0.11325	78
4	6	66.22951	33.11	0.11406	83

3. Results and Discussion

3.1. Structural Analysis of Fe: TiO2 Nanoparticles. Figure 2 expresses X-ray diffraction spectra of the produced iron doped titanium dioxide nanoparticles following sol-gel techniques at pH values of 2, 4, 5, and 6, which contracts the existence of anatase and ructile phase of iron doped titanium dioxide liable on pH values. The spectrum displays well-defined peaks of iron doped titanium dioxide nanoparticles. Nearby six analytical peaks were perceived at $2\theta = 27.295^{o}$, 45.31^{o}, $53.44^{o,}$ and $66.22^{o,}$ and their corresponding reflection of miller indices (100), (110), (111), and (101), respectively, for these pH values. Phase transformation is observed from anatase to rutine as the pH value increases from two to six. In other ways, anatase phases were evidently performed at 2 and 4 while ructile phases were observed at 5 and 6. All diffraction angles were well indexed to ructile and anatase configuration, which is nicely in agreement with that of reported works [27]. The strength peaks of deposited micromaterials become shriller with increasing pH values because of an increase in crystal size and crystalline structure.

The crystal sizes of prepared iron doped titanium dioxide nanoparticles were evaluated by using a Debye–Scherer equation with equation (1) depending on the deflection angle and full width at half-maximum (FWHM) of the peaks as described in Table 1 below. The average crystal size of prepared Fe: TiO_2 nanoparticles at pH values of 2, 4, 5, and 6 are 77.5, and the crystal sizes of Fe: TiO_2 nanoparticle were increased with pH value increased for both anatase and ructile phase, which is in good agreement with the result reported [28]. Additionally, Full Width at Half Maxima (FWHM), as well as middling grain size of produced Fe: TiO_2 Nanoparticles, declined with increasing pH value from 2 to 6. The crystal sizes are gained from Debye–Scherer's formula.

The influence of pH value on prepared titanium nanoparticles was evaluated by using equations (3)–(5). The lattice constraints of Fe: TiO_2 Nanoparticles were increased with pH value. Lattice constraints of prepared nanoparticles had agreed with that of TiO_2 previously [15]. The pH rate leads to perfection in crystalline size, deflection strength, oxygen–titanium–oxygen bond length, and volume of the unit cell.

3.2. Scanning Electron Microscope (SEM) Characterization of Fe: TiO_2 Nanoparticles. Figure 3 shows the morphology of deposited iron doped titanium dioxide nanoparticles samples at pH values of 2, 4, 5, and 6 using a scanning electron

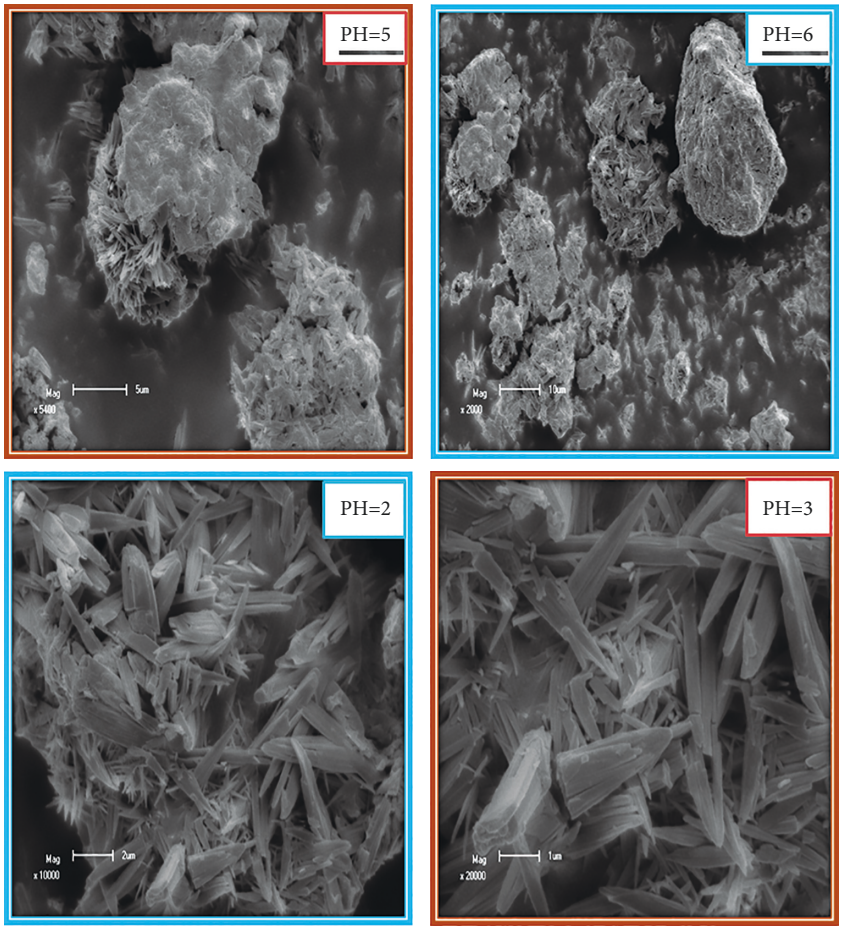

Figure 3: SEM images of synthesized Fe : TiO_2NPs at PH values of 2, 4, 5, and 6.

microscope (SEM) (Model CamScan MV2300). Homogenously disseminated cylindrical structure iron doped titanium dioxide NPs were perceived from Scanning electron microscope (SEM) micrographs. As shown in Figure 2 the middling size of deposited iron doped titanium dioxide nanoparticles was rising with pH tenets. SEM images at pH 2 and pH 3 are somewhat similar to fixed wood images as well as micrographs at pH 5 and 6 are also similar, and the image is like broken rocks. An accumulation of prepared iron doped titanium dioxide nanoparticles happened throughout pH values because of in height surface energy of nanoparticles.

3.3. Optical Characterization of Fe: TiO_2 NPs. The optical analysis of Fe TiO_2 nanoparticles using UV–Vis spectrophotometer (Schimadzu UV-1800) in the wavelength range of 250–700 nm. Figure 4 displays the absorbance spectrum of samples prepared at different pH values. The highly transparent nanopowders are seen in the visible region. The observed redshift towards higher wavelengths with a rising pH value is owing to an increase in particle size, as evidenced by XRD and SEM pictures [16]. Because oxygen vacancies form deep levels in the bandgap, the existence of oxygen vacancies at greater pH values may also be related to the aforesaid effect [29].

The energy band gap values of synthesized Fe : TiO_2 NPs are obtained by using the equation. UV/Visible studies show that the energy band gap decreases with increasing pH values of Fe : TiO_2NPs, corresponding to a redshift of the optical absorption edge [30]. This is due to an increase in pH value and a lowers inter-atomic spacing. It is noteworthy here that values of energy band gap obtained are lesser in comparison to the energy band gap 3.1 eV for pure anatase, 3 eV for rutile phase, and the data reported for the mixed-phase Fe : TiO_2 nanopowders exhibiting as a capable candidate for self-cleaning application [31].

3.4. Photoluminescence (PL) Spectral Analysis of Fe: TiO2 NPs. The optical behaviors of deposited Nanoparticles are also studied by using photoluminescence. Photoluminescence spectra of the prepared specimens were documented at room temperature in the range of wavelength between 400 nm and 700 nm, as depicted in Figure 5. The overall photoluminescence intensity decreases as the pH value increases from 2 to 6. The highest PL intensity at pH values 4 and 5 is mainly due to self-trapped exciton recombination, generated from oxygen vacancy and particle size which is known as defect centers [32]. The PL intensity decreases steadily with the increasing pH value from 2 to 6. The behavior of increment and decrement behavior is mainly due to isolated

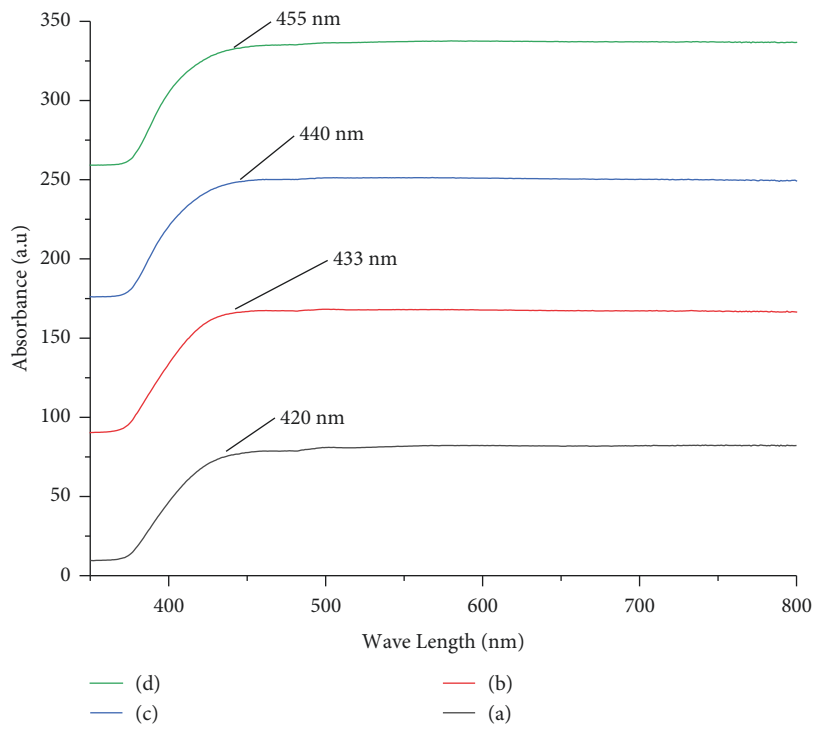

Figure 4: Absorbance spectra of Fe TiO_2NPs at PH value of (a) PH = 2, (b) pH = 4, (c) pH = 5, and (d) pH = 6.

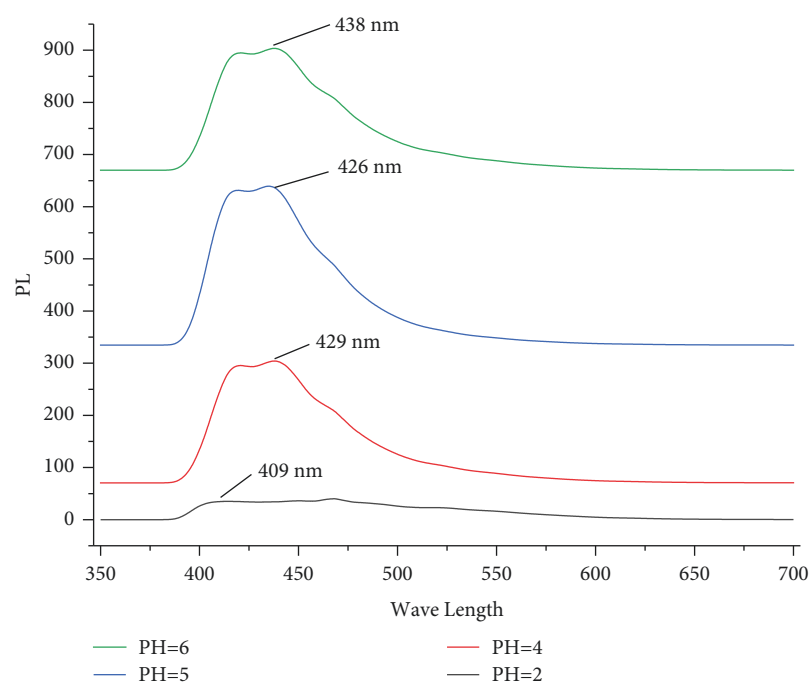

Figure 5: Photoluminescence spectra of prepared Fe TiO_2 Nanoparticles at pH values of 2, 4, 5, and 6. Energy-dispersive X-ray spectroscopy (EDS) characterization.

phases of anatase and rutile. As shown in Figure 5, Due to the increment of pH value, a new radioactive transition occurs, which leads to a new PL peak at the rutile phase [33–35]. The Photoluminescence strength of the peaks increases as the pH increases; this result shows that oxygen vacancies appear slowly with pH value. An anatase phase is perceived at pH = 2 and pH = 4 whereas the rutile phase looks at maximum pH value. The concentration of anatase and rutine peaks declines and then gradually appears for higher pH values. The growth of other peaks around the

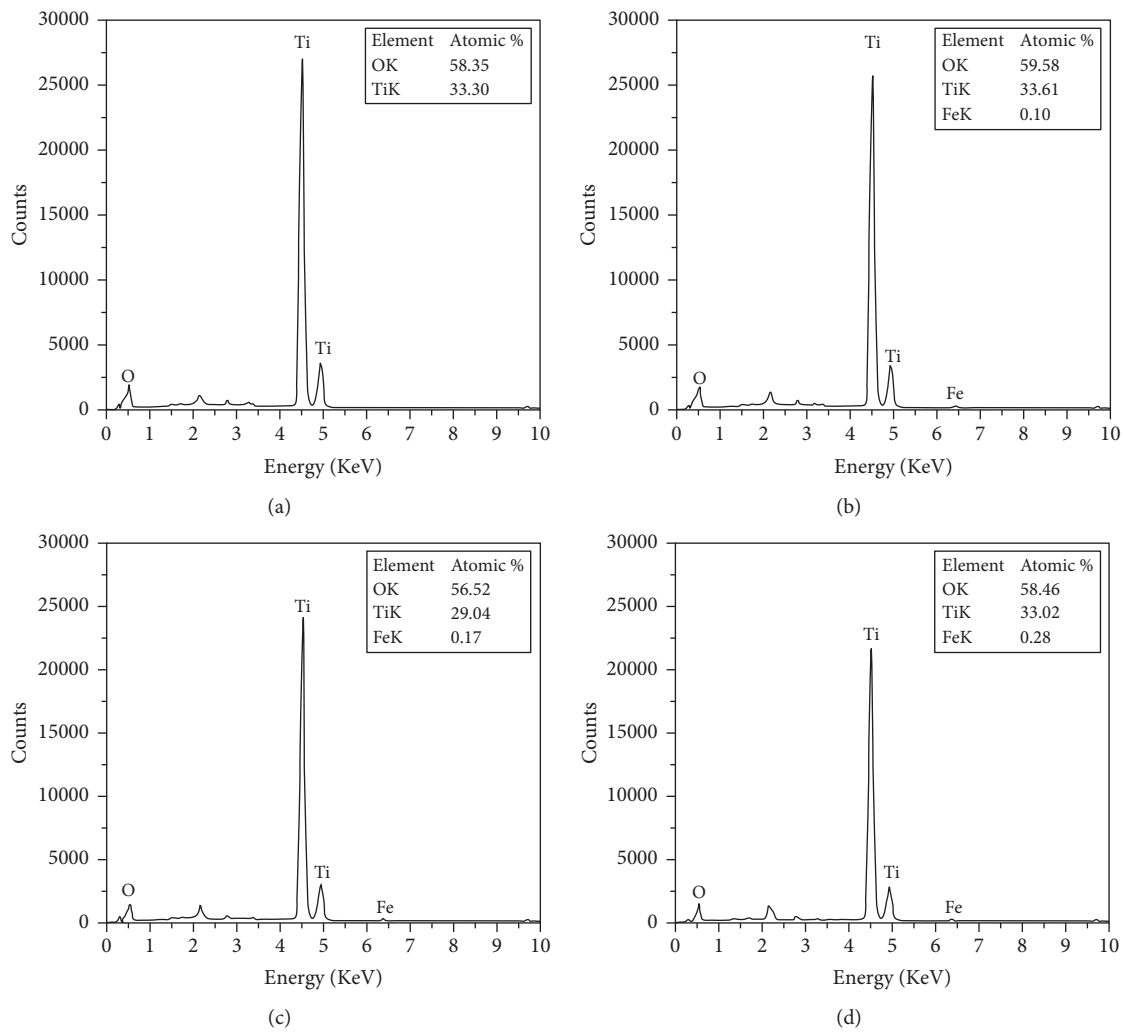

Figure 6: EDS patterns of Fe TiO_2 Nanoparticles at different pH values (a) pH = 2, (b) pH = 4, (c) pH = 5, and (d) pH = 6.

438 nm peak may indicate the existence of other voids inside the bandgap and narrow traps mainly basis on the surface morphology dissemination nanostructures [36].

EDS measurements were performed for all samples in a Hitachi TM3000 Tabletop microscope at the NTNU nano lab. The impact of iron ions doping on the chemical configuration was studied by energy-dispersive X-ray spectroscopy (EDS). Figure 6 displays the energy-dispersive X-ray spectroscopy (EDS) patterns of Fe : TiO_2 Nanoparticles at different pH values, varied as 2, 4, 5, and 6. The chemical configuration of four EDS arrays (Figures 4(a)–4(d)) was calculated, and it is initiated that the chemical elemental contents of oxygen and titanium have not altered significantly. At similar times, we can find that the elemental chemical components of iron were gradually growing. The chemical elemental contents of C are not displayed; they can arise from showing resin. Thus, EDS results in supplementary confirmed that the dopant of pH values of the solutions might affect the size distributions of the Nanoparticles. Figure 6 displays the sono-catalytic activities of Fe doped TiO_2 nanoparticles with different Fe^{3+} ion contents. It can be seen that the Fe dopant content has no noticeable influence on the degradation rate under our study circumstances. So, we chose pH = 5 as the best quantity of iron for TiO_2 due to its larger specific surface area [37].

4. Conclusions

Iron doped titanium dioxide nanoparticles with chemical formula Fe TiO_2 were produced through sol-gel technique from (CH_3COOH) and titanium (IV) iso-prop-oxide ($C_{12}H_{28}O_4Ti$) at pH values of 2, 4, 5, and 6. The prepared nanoparticles were analyzed by X-ray diffraction, scanning electron microscope, UV/Visible spectroscopy, and photoluminescence and were perceived from XRD data and revealed that there was the formation of anatase and rutine phase with hexagonal structure. A pH value gives the alteration of phases from anatase to rutine. Uniformly distributed hexagonal shapes of nanoparticles were shown from scanning electron microscope micrograph and increased in size with increasing pH values from 2 to 6. Extremely transparent nanopowders are witnessed in the visible region from UV/Visible and a slight red shift in the UV/Visible peaks towards higher wavelength as rising pH value. The PL

intensity of the peaks increases as the pH value increases. EDS results confirmed that the dopant of pH values of the solutions might affect the size distributions of the Fe TiO_2 Nanoparticles. This result indicates that oxygen vacancies appeared slowly with pH value; all results show Fe TiO_2 nanoparticles are promising for self-cleaning materials [38–41].

Data Availability

The data used to support the findings of this study are included in the article.

Disclosure

This study was performed as a part of the employment of the authors, Dambi Dollo University,Ethiopia.

Conflicts of Interest

The authors declare that there are no conflicts of interest regarding the publication of this article.

References

[1] S. Dai, Y. Wu, T. Sakai, Z. Du, H. Sakai, and M. Abe, "Preparation of highly crystalline TiO2 nanostructures by acid-assisted hydrothermal treatment of hexagonal-structured nanocrystalline titania/cetyltrimethyammonium bromide nanoskeleton," *Nanoscale Research Letters*, vol. 5, no. 11, pp. 1829–1835, 2010.

[2] K. Vijayalakshmi and V. Rajendran, "Synthesis and characterization of nano-Fe: TiO2 via different methods," *Archives of Applied Science Research*, vol. 4, pp. 1183–1190, 2012.

[3] J. Lin, M. Guo, C. T. Yip et al., "High temperature crystallization of free-standing anatase TiO2Nanotube membranes for high efficiency dye-sensitized solar cells," *Advanced Functional Materials*, vol. 23, no. 47, pp. 5952–5960, 2013.

[4] K. Shankar, J. I. Basham, N. K. Allam et al., "Recent advances in the use of TiO2 nanotube and nanowire arrays for oxidative photoelectrochemistry," *Journal of Physical Chemistry C*, vol. 113, no. 16, pp. 6327–6359, 2009.

[5] N. K. Allam and M. A. Ei-Sayed, "Effective photocatalytic properties of N-doped Iron doped Titanium dioxide nanotube arrays prepared by anodization," *Journal of Physical Chemistry C*, vol. 112, p. 12687, 2010.

[6] H. I. Hsiang and S. C. Lin, "Effects of aging on the phase transformation and sintering properties of TiO2 gels," *Materials Science and Engineering A*, vol. 380, no. 1-2, pp. 67–72, 2004.

[7] P. Roy, S. Berger, and P. Schmuki, "TiO2 nanotubes: synthesis and applications," *Angewandte Chemie International Edition*, vol. 50, no. 13, pp. 2904–2939, 2011.

[8] J. K. Tsai, W. D. Hsu, T. C. Wu, T. H. Meen, and W. J. Chong, "Effect of compressed Fe: TiO2 nanoparticle thin film thickness on the performance of dye-sensitized solar cells," *Nanoscale Research Letters*, vol. 8, pp. 79–85, 2013.

[9] G. K. Mor, O. K. Varghese, M. Paulose, K. Shankar, and C. A. Grimes, "A review on highly ordered, vertically oriented TiO2 nanotube arrays: fabrication, material properties, and solar energy applications," *Solar Energy Materials and Solar Cells*, vol. 90, no. 14, pp. 2011–2075, 2006.

[10] S. Kathirvel, C. Su, C. Y. Yang, Y. J. Shiao, B. R. Chen, and W. R. Li, "The growth of TiO2 nanotubes from sputter-deposited Ti film on transparent conducting glass for photovoltaic applications," *Vacuum*, vol. 118, pp. 17–25, 2015.

[11] V. Galstyan, E. Comini, G. Faglia, and G. Sberveglieri, "TiO2 nanotubes: recent advances in synthesis and gas sensing properties," *Sensors*, vol. 13, no. 11, pp. 14813–14838, 2013.

[12] Y. J. Park, J. M. Ha, G. Ali, V. Kim, Y. Addad, and S. O. Cho, "Controlled fabrication of nanoporous oxide layers on zircaloy by anodization," *Nanoscale Research Letters*, vol. 10, no. 1, p. 377, 2015.

[13] Y. Li, H. Yu, C. Zhang et al., "Effect of water and annealing temperature of anodized TiO2 nanotubes on hydrogen production in photoelectrochemical cell," *Electrochimica Acta*, vol. 107, pp. 313–319, 2013.

[14] O. Khatim, M. Amamra, K. Chhor et al., "Amorphous-anatase phase transition in single immobilized TiO2 nanoparticles," *Chemical Physics Letters*, vol. 558, pp. 53–56, 2013.

[15] D. Yoo, I. Kim, S. Kim, C. H. Hahn, C. Lee, and S. Cho, "Effects of annealing temperature and method on structural and optical properties of TiO2 films prepared by RF magnetron sputtering at room temperature," *Applied Surface Science*, vol. 253, no. 8, pp. 3888–3892, 2007.

[16] C. V. R. Vasantkumar and A. Mansingh, "Structural evolution and optical properties of Fe: TiO2 thin films prepared by thermal oxidation of sputtered Ti films," *Seventh IEEE International Symposium on Application of Ferroelectrics*, IEEE, vol. 88, pp. 713–716, 1990.

[17] V. Chaudhary, A. Srivastava, and J. Kumar, "On the sol-gel synthesis and characterization of titanium oxide nanoparticles," *Materials Research Society Symposia Proceedings*, vol. 1352, p. 759, 2011.

[18] A. Cesnovar, P. Paunovic, A. Grozdanov, and E. Fidanchevska, "Preparation of nano-crystalline Fe: TiO2 by sol-gel method using titanium tetraisopropoxide (TTIP)," *Adv. Nat. Sci. Theory Appl.*vol. 1, pp. 133–142, 2012.

[19] S. Dai, Y. Wu, T. Sakai, Z. Du, H. Sakai, and M. Abe, "Preparation of highly crystalline Fe: TiO2 nanostructures by acid-assisted hydrothermal treatment of hexagonal-structured nanocrystalline titania/cetyltrimethyammonium bromide nanoskeleton," *Nanoscale Research Letters*, vol. 11, pp. 1829–1850, 2017.

[20] H. Kominami, J. Kato, Y. Takada et al., "Novel synthesis of microcrystalline titanium (IV) oxide having high thermal stability and ultra-high photocatalytic activity, thermal decomposition of titanium(IV) alkoxide in organic solvents," *Catalysis Letters*, vol. 46, no. 3/4, pp. 235–240, 1997.

[21] H. Li, T. Xie, H. Wang, and Z. Du, "A facile solution-phase synthesis of high quality water soluble anatase Fe: TiO2 nanocrystals," *Journal of Colloid and Interface Science*, vol. 314, pp. 337–340, 2007.

[22] A. L. Linsebigler, G. Lu, and J. T. Yates, "Photocatalysis on TiO2 surfaces: principles, mechanisms, and selected results," *Chemical Reviews*, vol. 95, no. 3, pp. 735–758, 1995.

[23] K. Nagaveni, G. Sivalingam, M. S. Hegde, and G. Madras, "Solar photocatalytic degradation of dyes, high activity of combustion synthesized nano Fe: TiO2," *Applied Catalysis B: Environmental*, vol. 48, pp. 83–93, 2003.

[24] S. Pavasupree, J. Jitputti, S. Ngamsinlapasathian, and S. Yoshikawa, "Hydrothermal synthesis, characterization, photocatalytic activity and dye-sensitized solar cell performance of mesoporous anatase TiO2 nanopowders," *Materials Research Bulletin*, vol. 43, no. 1, pp. 149–157, 2008.

[25] C. Weiwei, Y. Hui, and G. Xingzhong, "A facile synthesis of nanocrystalline spherical Fe: TiO2 particles and its photoluminescent properties," *Procedia Engineering*, vol. 94, pp. 71–75, 2014.

[26] S. Bakardjieva, J. Šubrt, V. Štengl, M. J. Dianez, and M. J. Sayagues, "Photoactivity of anatase-rutile TiO2 nanocrystalline mixtures obtained by heat treatment of homogeneously precipitated anatase," *Applied Catalysis B: Environmental*, vol. 58, no. 3-4, pp. 193–202, 2005.

[27] A. K. Tripathi, M. K. Singh, M. C. Mathpal, S. K. Mishra, and A. Agarwal, "Study of structural transformation in TiO2 nanoparticles and its optical properties," *Journal of Alloys and Compounds*, vol. 549, pp. 114–120, 2013.

[28] A. Zareen, S. Ali, and M. Irfan, "The effect of PH values on phase and optical properties of Fe: TiO2 nanoparticles for solar cell applications," *ESJ*, vol. 2, pp. 447–450, 2014.

[29] S. Pawar, M. Chougule, S. Patil et al., "Fabrication of nanocrystalline TiO₂ thin film ammonia vapor sensor," *Journal of Sensor Technology*, vol. 01, no. 01, pp. 9–16, 2011.

[30] S. G. Pawar, M. A. Chougule, P. R. Godse et al., "Effect of annealing on structure, morphology, electrical and optical properties of nanocrystalline Fe: TiO2 thin films," *J. Nano Electron Phys*, vol. 3, pp. 185–192, 2011.

[31] H. C. Choi, Y. M. Jung, and S. B. Kim, "Size effects in the Raman spectra of TiO2 nanoparticles," *Vibrational Spectroscopy*, vol. 37, no. 1, pp. 33–38, 2005.

[32] C. Y. Xu, P. X. Zhang, and L. Yan, "Blue shift of Raman peak from coated TiO2 nanoparticles," *Journal of Raman Spectroscopy*, vol. 32, no. 10, pp. 862–865, 2001.

[33] C. Rath, P. Mohanty, A. C. Pandey, and N. C. Mishra, "Oxygen vacancy induced structural phase transformation in Fe: TiO2 nanoparticles," *Journal of Physics D: Applied Physics*, vol. 42, P. 205101, 2009.

[34] H. Zhang and J. F. Banfield, "New kinetic model for the nanocrystalline anatase-to-rutile transformation revealing rate dependence on number of particles," *American Mineralogist*, vol. 84, no. 4, pp. 528–535, 1999.

[35] M. C. Mathpal, A. K. Tripathi, M. K. Singh, S. P. Gairola, S. N. Pandey, and A. Agarwal, "Effect of annealing temperature on Raman spectra of TiO2 nanoparticles," *Chemical Physics Letters*, vol. 555, pp. 182–186, 2013.

[36] C. K. Chung, M. W. Liao, and C. W. Lai, "Effects of oxygen flow ratios and annealing temperatures on Raman and photoluminescence of titanium oxide thin films deposited by reactive magnetron sputtering," *Thin Solid Films*, vol. 518, no. 5, pp. 1415–1418, 2009.

[37] R. H. Waghchaure, P. B. Koli, V. A. Adole, T. B. Pawar, and B. S. Jagdale, "Transition metals Fe3+, Ni2+ modified titanium dioxide (TiO2) film sensors fabricated by CPT method to sense some toxic environmental pollutant gases," *Journal of the Indian Chemical Society*, vol. 98, no. 9, p. 100126, 2021.

[38] T. Bezrodna, T. Gavrilko, G. Puchkovska, V. Shimanovska, J. Baran, and M. Marchewka, "Spectroscopic study of TiO2 (rutile)-benzophenone heterogeneous systems," *Journal of Molecular Structure*, vol. 614, no. 1-3, pp. 315–324, 2002.

[39] T. Ohsaka, "Temperature dependence of the Raman spectrum in anatase TiO2," *Journal of the Physical Society of Japan*, vol. 48, no. 5, pp. 1661–1668, 1980.

[40] I. Sta, M. Jlassi, M. Hajji et al., "Structural and optical properties of TiO2 thin films prepared by spin coating," *Journal of Sol-Gel Science and Technology*, vol. 72, no. 2, pp. 421–427, 2014.

[41] M. C. Mathpal, A. K. Tripathi, M. K. Singh, S. P. Gairola, and S. N. Pandey, "Effect of PH value on Raman spectra of Fe: TiO2 nanoparticles," *Chemical Physics Letters*, vol. 500, pp. 82–112, 2011.

Hindawi
Advances in Materials Science and Engineering
Volume 2022, Article ID 6110591, 11 pages
https://doi.org/10.1155/2022/6110591

Research Article

Optimization of Abrasive Wear Characteristics of Polyethylene/Acrylate Copolymer Nanocomposites

S. Chockalingam,[1] G. Gopalarama Subramaniyan,[2] Anand Bisen,[3] S. Kaliappan,[4] S. Sekar,[5] Pravin P. Patil,[6] T. Ch. Anil Kumar,[7] B. Ramesh,[8] and S. Venkatesan[9]

[1]*Department of Mechanical Engineering, E.G.S. Pillay Engineering College, Nagapattinam, India*
[2]*Department of Mechanical Engineering, Saveetha Engineering College, Chennai, India*
[3]*Mechanical Engineering Department, Kalaniketan Polytechnic College Jabalpur (M.P.), Pin:482001, Jabalpur, India*
[4]*Department of Mechanical Engineering, Velammal Institute of Technology, Chennai 601204, Tamil Nadu, India*
[5]*Department of Mechanical Engineering, Rajalakshmi Engineering College, Rajalakshmi Nagar Thandalam, Chennai 602 105, Tamilnadu, India*
[6]*Department of Mechanical Engineering, Graphic Era Deemed to be University, Bell Road, Clement Town 248002, Dehradun, Uttarakhand, India*
[7]*Department of Mechanical Engineering, Vignan's Foundation for Science Technology and Research, Vadlamudi 522213, India*
[8]*Institute of Mechanical Engineering, Saveetha School of Engineering, Saveetha Institute of Medical and Technical Sciences, Chennai 602 105, Tamil Nadu, India*
[9]*School of Mechanical Engineering, College of Engineering and Technology, Wachemo University, Hosaena, Ethiopia*

Correspondence should be addressed to S. Venkatesan; profsvenkatesan@gmail.com

Received 7 April 2022; Accepted 7 June 2022; Published 27 June 2022

Academic Editor: Vijayananth Kavimani

Polymer nanocomposites are being used more widely in a variety of industries. As the compatibilizer, Elvaloy-AC-3427 (EAC) was used in addition to Cloisite 30B (C3B) as the reinforcement of filler in this research. For the production of Polyethylene/Cloisite 30B/Elvaloy AC-3427 nanomaterials, a twin-screw extruder is employed. Cloisite 30B was added to the Polyethylene matrix in the range of 2%, 3%, 4%, and 5%. The mechanical and thermal characteristics of the compounds have been examined. Nanocomposites were tested for their tribological properties utilizing abrasive wear load, C3B, and sliding distance which were all taken into consideration while performing the abrasive wear evaluations. Specific wear rate (SWR), coefficient of friction (COF), and weight loss were the abrasive wear test's output metrics (SWR). For the purpose of enhancing the abrasive wear characteristics, grey relational analysis and grey fuzzy were used. An ANOVA was carried out to examine the connection between input parameters and output variables. Finally, the Polyethylene/Cloisite 30B/Elvaloy AC-3427 nanocomposites abraded wear samples were evaluated microscopically.

1. Introduction

Researchers have been investigating Polyethylene-coated composite with supplements for the production of polymer nanoparticles for the last several decades. Additives are used to enhance several characteristics of the polymer matrix, including mechanical, thermal, and optical properties [1, 2]. Glass fibers, CNTs, nanoclays, and other traditional fillers can make up to 40% of the polymer matrix's weight, whereas nanotype fillers can make up to 5% of the weight. The manufacture of polymer nanocomposites may be made more cost-effectively by using fillers with low molecular weight [3]. Polymer nanocomposites may be made using a variety of ways, although the melt intercalation approach is the most common. To do melt intercalation, extruders (either single or twin) must be used [4]. Owing to the low

price, simplicity of processing, and availability in the marketplace, Polyethylene is the most commonly utilized substance [5]. For its better physical and thermal qualities, [6] determined that PE is the most frequently used substance. Even while PE has several advantages, its weak strength and poor stiffness render it inapplicable in most cases. Fillers such as mica and other fillers have been used in the PE to counteract its shortcomings. Additional abrasion resistance was needed to compensate for the higher strength and stiffness that fillers provided [5, 7]. According to earlier research, reinforcing nanoclays into the PE matrix is advantageous. Due to the hydrophobic nature of PE, it is difficult to spread nanoclays inside it. PE nanoclays were not well dispersed as a result of this occurrence [8]. Several writers have utilized various kinds of compatibilizers to circumvent this limitation [9, 10].

The study of polymer nanocomposites' tribological properties is essential for determining the materials' friction and wear. The pace of substance ejection may be sluggish, but it is a recurring one [11, 12]. Poly was the study's compatibilizer (ethylene co-glycidyl methacrylate) where load, abrading distance, and grit size were all considered input factors. The results showed that the inclusion of a compatibilizer increased abrasion resistance. An abrasive wear test that used worn surface morphology revealed microploughing as a wear process [13–15]. Because of this, they came to the conclusion that adding ZnO nano to ultrahigh molecular weight PE had a lower rate of wear than doing so in microform. According to microzno, the worn surface morphology shows that nanozinc oxide adds rather homogenous layers.

Grey Relational Analysis is a technique that uses black to represent a dearth of information and white to represent a surplus of data. There are a variety of descriptive terms for the region that is just outside of these two extremes [16]. There are sections of the system that are recognized, and there are parts of the system that do not have any information at all. GRA defines information quality and quantity as either finished or not yet finished, i.e., from black to white through the grey scale [17, 18]. When it comes to GRA, there is always a degree of ambiguity because of a wide range of possible data points. It is possible to go to the end of the GRA process with almost no information at all, and at the other end, there will be a unique answer. The optimal answer cannot be found by using GRA, but it may be used to identify a suitable solution [19, 20].

During the time of abrasive wear procedure, the input constraints of abrasive wear have a significant impact. Optimizing the input settings is essential to want better outcomes. These days, fuzzy logic, scatter search, and a host of other approaches are the most often utilized optimization methods. According to [21, 22], an optimization approach was developed to improve the multiple bead shape during submerged arc welding. For the optimization of various answers, the study in [23, 24] used a combined approach known as the Taguchi method and artificial intelligence.

GRA has been utilized in recent years to improve operations like welding, machining, and turning. When the fuzzy logic theory was applied to the GRA, it became even better. Research by [25–27] examined the drilling properties of CFRP compound plates. Optimizing the drilling experiment's result was done using GRA and grey fuzzy. Grey fuzzy's grade values were discovered to be higher than GRA's.

Despite the fact that a variety of other fillers have been used to strengthen the PE matrix, no one has reported on the usage of EAC as a compatibilizer [28–30]. Even though only limited research reports were available on the abrasive wear properties of the Polyethylene/Cloisite 30B/Elvaloy AC-3427 NCs, a twin-screw extruder was utilized to make the Polyethylene/Cloisite 30B/Elvaloy AC-3427 NCs which was used in this investigation. Cloisite 30B concentrations in the PE matrix were changed from 1% to 5%. They were made using the injection molding method. The tests used C3B (weight percentage), load (N), and sliding distance (m) as input factors and examined COF, SWR, and weight loss as output features [31–33]. GRA and grey fuzzy analysis were used to improve the abrasive wear findings.

2. Experimental Procedure

2.1. Selection of Materials. Repol H110 MA, as purchased from reliance industries, was chosen as the substance for the matrix because of its melting rate index of 11 g 10 min^{-1} and density of 0.88 g cubic $centimeter^{-1}$. Cloisite 30B was the nanoclay supplied by the southern clay products employed in this investigation (C3B). It was found that EAC has a melting rate of 4 grams per minute and a density of 0.926 grams per cubic $centimeter^{-1}$. C3B dispersion in the PE matrix was improved by the addition of this ingredient.

2.2. Production of Nanocomposites of Polyethylene/C3B/EAC. Polyethylene/Cloisite 30B/Elvaloy AC-3427 NCs were made utilizing a twin-screw extruder and intercalation of the melting process. The parameters for the twin-screw extrusion procedure used to make PE/C3B/EAC nanocomposites were chosen from earlier research [34] and are listed in Table 1.

Figure 1 shows that a twin-screw extruder's temperature may be adjusted at various zones. Injection molding was used to obtain the samples for testing, and the temperature was kept between 170°C and 190°C (from inlet to die area). In the PE matrix, C3B was finely dispersed at 2 wt % and with a high density at 5 wt %, as illustrated in Figures 2(a) and 2(b). The earlier research [35–37] explored the mechanical characteristics of treated materials in terms of their tensile, flexural, impact, and Shore *D* hardness measurements, as well as their thermal properties (DSC, TGA, and dynamic analysis).

3. Tribological Studies

A tribo testing equipment was utilized to conduct tribological investigations based on the ASTM G-99-05 two-body-abrasive wear test. Figure 2 depicts a schematic diagram of the machine. The upper part of a D3 steel disc was covered with 320-grit abrasive paper. A constant sliding velocity of 0.5 m s was used in the wear studies, and input

factors such as C3B weight percentage, load, and sliding distance were also used. According to the abrading direction, the PE/C3B/EAC nanocomposite sample illustrated in Figure 3 is parallel and antiparallel to 320 grit paper. For abrasive wear testing of Polyethylene/Cloisite 30B/Elvaloy AC-3427 NCs, the following assumptions were made: (i) samples with damage were excluded, (ii) there is surface roughness, and (ii) the load is delivered directly to the point of contact.

Experiments were performed to see how much weight was lost. An equation was used to determine the SWR.

$$\text{Specific wear rate}\left(K_s\right) = \frac{m_1 - m_2}{\rho \times N \times S}\,\frac{\text{mm3}}{\text{min}}. \quad (1)$$

In order to calculate the COF, the following equation was used:

$$\text{COF}\,(\mu) = \frac{\text{frictional force}\,(F)}{\text{load}\,(N)}. \quad (2)$$

Samples that had been scratched were examined using a scanning electron microscope.

4. Design of Experiments

Input parameter increases make parameter optimization more challenging. There was a direct correlation between an increase in the number of experiments and an increase in the input parameters. Taguchi techniques employed orthogonal arrays to lessen this complexity. Wear experiments were conducted using parameters such as C3B, load, and sliding distance at 0.5 min/s^{-1} with a constant sliding velocity. For the sake of clarity, the levels and parameters investigated are listed in Table 2. The L′16 orthogonal array was used to construct and conduct the current study's two-body abrasive wear testing. We saw a decrease in body weight, a rise in COF, and a decrease in SWR. Relational analysis in the dark of an efficient method for managing uncertainty and discrete data was presented by grey relational analysis (GRA). Black implies a lack of information, whereas white indicates that there is something there. Between white and black, a grey system contains data. Both the absolute value of the sequences and the connection between the sequences may be measured using the GRA method. Using this method, one may examine the link between sequences with the fewest data points, as well as the number of elements that influence a relationship.

Testing for two-body abrasion was carried out in an orthogonal array. A comparability sequence is a series of sixteen wear trials, each of which was treated as an independent subsystem during GRA. Weight loss, SWR, and COF were all lower under the settings with greater GRG levels. It turns into a single-objective optimization utilizing GRA as a result of this.

4.1. S/N Ratio for Computing Abrasive Wear Characteristics. Weight loss, SWR, and COF were all taken into account while testing the abrasive wear resistance of Polyethylene/Cloisite 30B/Elvaloy AC-3427 NCs. The equation shows the S/N ratio for attributes where the smaller the value, the better:

$$\frac{S}{\text{N ratio}\ \ (\eta)} = -10\log_{10}\frac{1}{n}\sum_{i=1}^{n}\frac{1}{y_i^2}. \quad (3)$$

Table 1: Process parameters for the production of PE/C3B/EAC nanocomposites.

Parameters	Range
Barrel temperature	180°C–230°C
Speed	70 rev/min
Volumetric feed	8 rev/min
Length of cooling	45 cm
Degassing pressure	50 mm Hg

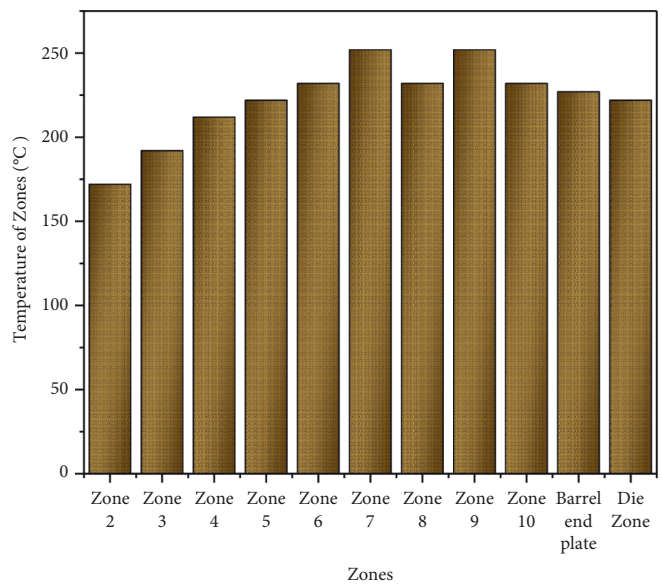

Figure 1: Different temperature zones of TSE.

4.2. Preprocessing of Data. Data pretreatment was a phrase used to describe the first normalization of experimental data in preparation for GRA. Data preparation is required since each response will have a distinct range and unit. The original sequence was transferred to the equivalent sequence once data preparation was completed. The range of zero to one is used to normalize them for this purpose. Based on the data sequence properties, the preprocessing was done.

It was referred to as "higher-the-better" when the initial value was regarded as infinite and normalized using the following equation:

$$x_i^*\,(k) = \frac{x_i^0\,(k) - \min x_i^0\,(k)}{\max x_i^0\,(k) - \min x_i^0\,(k)}. \quad (4)$$

The normalization of sequence may be done using equation (5) if the lower-the-better qualities are regarded.

$$x_i^*\,(k) = \frac{m\,x_i^0 - x_i^0\,(k)}{m\,x_i^0\,(k) - \text{m}\,x_1^0\,(k)}. \quad (5)$$

As an alternative to this, a normalization of the original sequence using the following would get the desired result.

$$x_i^*(k) = 1 - \frac{\| x_i^0(k) - x^0 \|}{m x_i^0(k) - x^0}. \quad (6)$$

As an alternative method, the original sequence value may be used and divided by the first digit of the new sequence to arrive at the desired result.

$$x_i^*(k) = \frac{x_i^*(k)}{x_i^0(1)}. \quad (7)$$

4.3. Calculation of GRG and GRC. GRA is used to assess the relevance of the systems to each other. For the GRA, the sequences employed might be called "grey relational coefficient ξ(k) " which was determined using

$$\xi(k) = \frac{\Delta m + \xi \Delta m}{\Delta oi(k) + \xi \Delta m}. \quad (8)$$

$$\Delta oi - \| x_o^*(k) - x_i^0(k) \|. \quad (9)$$

$$\Delta \min = \min_{\forall jei} \min_{\forall k} \| x_0^*(k) - x_j^0(k) \|. \quad (10)$$

$$\Delta m = \max_{\forall jzi} \max_{\forall k} \| x_0^*(k) - x_j^0(k) \|. \quad (11)$$

Accordingly, GRG was produced by taking the average values of grey the relational coefficient.

$$\gamma_i = \frac{1}{n} \sum_{k=1}^{n} \xi_i(k). \quad (12)$$

Real-time conditions change the relevance of many system variables [30]. Formula (12) can be expanded as follows:

$$\gamma_i = \frac{1}{n} \sum_{k=1}^{n} W_k \xi_i(k). \quad (13)$$

In (13), W_k represents the standardized wt of the element k. Equations (12) and (13) are the same if the values of W_k are the same for all the components. GRG compares the order of the reference sequence to indicate the extent of the effect. Sequences with higher values than the reference sequence will have better GRG values for that sequence, and the reverse is true if the reference sequence has lower values.

4.4. Grey Fuzzy Logic. In order to compute the GRG, three requirements must be met: (i) lower, (ii) higher, and (iii) nominal. To express the problem's ambiguity or lack of knowledge, grey fuzzy logic is used. According to [38–40], when dealing with ambiguity, a set of membership functions is critical. More than one hundred membership functions in the fuzzy set may be used to represent any item in the world that falls inside this range. Fuzzy logic was used to overcome the GRG's flaws.

In the TA part of the fuzzy logic technique, input values are fuzzified before rules are inferred and defuzzified after they have been inferred to provide better results. The comparison of input values with a defuzzification output value yields great prediction accuracy. Fuzzification is the process of applying linguistic factors to a clear number in order to make it fuzzy. In order to answer ambiguous and confusing inquiries, the fuzzy system is utilized, as well as to describe the certainty degree. The fuzzy variables can be assigned membership values using logical techniques. According to prior research, the numerous methods for assigning tasks include inference, rank ordering, intuition, natural networks, angular fuzzy sets, fuzzy statistics, and evolutionary algorithms. A Gaussian, trapezoidal, or triangle membership function is all viable options.

It is possible to derive the rules from the structure presented below by satisfying the following condition.

For linguistic variables, this type of information is known as superficial information. The fuzzy complication operation may be used to determine the membership function of values of fuzzy relations using a variety of ways. Mamdani's complication technique is the implication method of inference used in this study. Applied to fuzzy rule aggregation, it was dubbed max-min inference technique. This is followed by a defuzzification using the maximum membership approach.

Because of the use of fuzzy logic, GRG is more accurate than GRA and has lower levels of uncertainty. As a result, grey fuzzy logic's output is always greater than GRG. As a result, many kinds of applications can benefit from increasing the values of grey fuzzy logic.

Every input and output variable may be accounted for by using ANOVA to determine the proportion of their impact. ANOVA utilized in this investigation will focus on the impact of wear parameters on the SWR and COF output characteristics.

5. Results and Discussion

This part discusses the results of the abrasive wear experiments that were conducted. Grey Relational Analysis and GFL (Grey Fuzzy Logic) are also used to optimize the experimental parameters.

Table 3 shows the sliding distance (m), load (N), and weight loss (weight %) for C3B. Figures 4(a) and 4(b) show the major effect plots for COF and SWR (b). When Cloisite 30B was introduced to Polyethylene matrix NCs at a concentration of 1 weight %, the weight loss was the greatest associated with other concentrations of Cloisite 30B. Cloisite 30B added to the diet resulted in much more weight loss. When C3 B was added to 5 N, the weight loss was found to be lower, and it increased when the load was improved.

Specific wear rate readings were at their highest up to a sliding distance of 150 meters, and as the distance increased, the SWR decreased. In order to build the transfer layer, the PE/C3B/EAC NCs pin had to glide more often over the same surface, which increased the length of time it spent there. SWR values are reduced due to the data of a

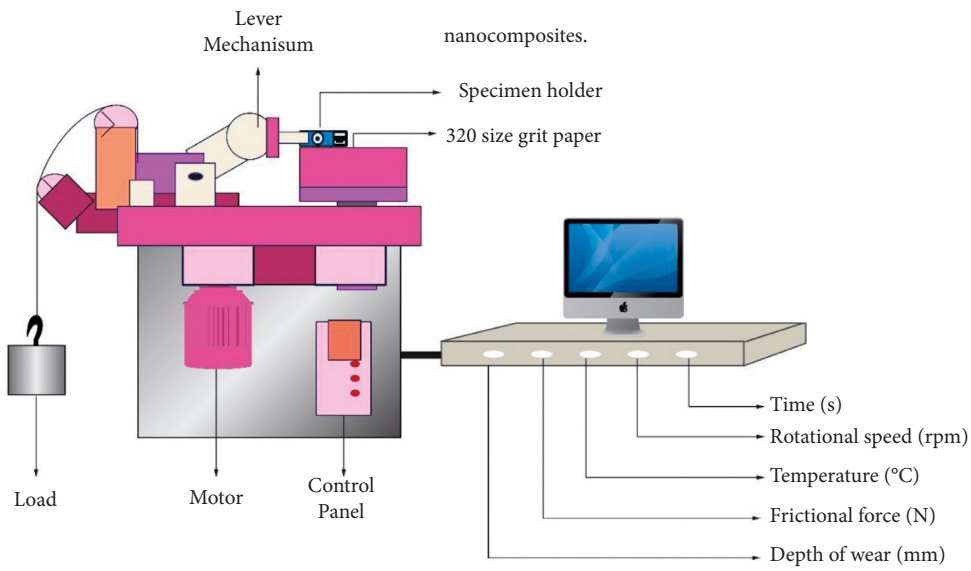

Figure 2: Schematic view of a pin on disc setup.

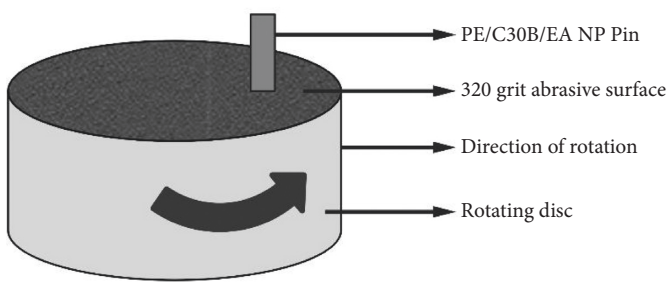

Figure 3: Rotating disc with Polyethylene/C3B/EAC nanocomposite.

Table 2: Control factors and their levels.

Control factors	Levels			
	1	2	3	4
C3B (*wt* %)	2	3	4	5
Load (N)	10	15	20	25
Sliding distance (m)	100	200	300	400

transfer layer on the surface. Specific wear rate values drop when the load is added. Polyethylene/Cloisite 30B/Elvaloy AC-3427 NCs is separated from the surface at 20Nload because of the heat generated at the contact surface. Adding Cloisite 30B at a very low increased the value of specific wear rate, whereas increasing the amount of C3B increased the value of SWR.

Cloisite 30B and Polyethylene composite bear the bulk of the burden. The COF values peaked at 1 weight % of PE/C3B/EAC and dropped as the amount of Cloisite 30B increased to the Polyethylene matrix increased. The rise in thermal stability values at 5 wt % of Polyethylene/Cloisite 30B/Elvaloy AC-3427 NCs, as validated by thermogravimetric testing, is another possible explanation for the lower COF values. When the load was raised, the COF value fell. At the contact zone, there was a temperature shift in the nanocomposite specimen PE/C3B/EAC. The PE/C3B/EAC NC surface partially melts at the 25 N load condition, lubricates the surface, and decreases the coefficient of friction value. A sliding distance of 200 m increases COF readings; however, the values drop as the distance increases. Polyethylene/Cloisite 30B/Elvaloy AC-3427 NCs on the 320-grit surface were clogged when the sliding distance was large, resulting in lower COF values.

5.1. GRA for Abrasive Wear. Analyzing output characteristics, this study used lower-the-better performance characteristics. Polyethylene/Cloisite 30B/Elvaloy AC-3427 NCs SWR, COF, and weight loss as results are shown in Table 4 with grey relationship coefficients of abrasive wear characteristics therein. For each trial, the grey relationship coefficients have a different value. For abrasive wear characteristics, there was a necessity to compute the GFRG.

GRG was determined by averaging the values indicated in Table 4 for each of the input parameters.

With a load of 25 N and an overall sliding distance of 100 meters, the response table determined that the optimal C3B addition was 5 wt %. The computed GRG major effect plot is shown in Figure 5. A GRG value exceeding 0.5 is seen in all three output abrasive wear characteristics.

Table 3: Results for COF, loss of weight, and SWR.

Sl. no.	Cloisite 30B (wt%)	Load (N)	Sliding distance (m)	COF (μ)	Loss of weight (g)	Wear rate (mm^3/Nm)
1	2	10	100	0.302	0.0025	0.007214
2	2	15	200	0.289	0.0089	0.006909
3	2	20	300	0.276	0.0101	0.003501
4	2	25	400	0.252	0.0152	0.002814
5	3	10	200	0.279	0.0049	0.007136
6	3	15	100	0.271	0.0041	0.006142
7	3	20	400	0.249	0.0145	0.003516
8	3	25	300	0.251	0.0114	0.002814
9	4	10	300	0.244	0.0050	0.004679
10	4	15	400	0.239	0.0115	0.004312
11	4	20	100	0.237	0.0107	0.004980
12	4	25	200	0.251	0.0110	0.004012
13	5	10	400	0.247	0.0095	0.004112
14	5	15	300	0.239	0.007	0.003914
15	5	20	200	0.239	0.008	0.003642
16	5	25	100	0.231	0.0039	0.003124

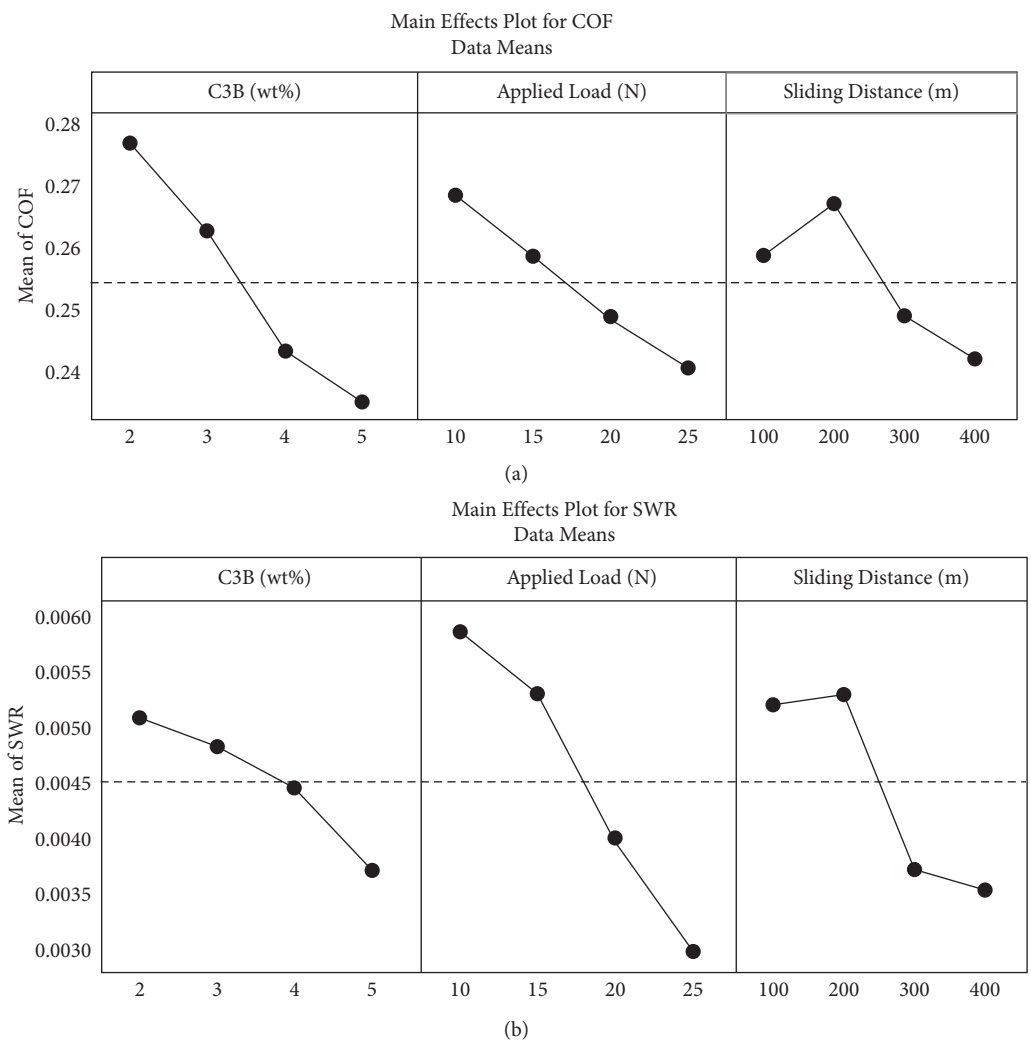

Figure 4: (a) Main effect plots of coefficient of friction. (b) Main effect plots of specific wear rate.

Table 4: The grey relation coefficient and grey relational grade for abrasive wear responses.

Sl. no.	Cloisite 30B (wt%)	Load (N)	Sliding distance (m)	GRC of COF (μ)	GRC for weight loss	GRC for SWR (mm^3/Nm)	GRG	Rank
1	2	10	100	0.329	0.998	0.329	0.542	12
2	2	15	200	0.349	0.481	0.349	0.389	14
3	2	20	300	0.462	0.449	0.741	0.552	16
4	2	25	400	0.679	0.342	1.000	0.669	15
5	3	10	200	0.384	0.719	0.328	0.481	4
6	3	15	100	0.471	0.784	0.401	0.549	11
7	3	20	400	0.609	0.339	0.742	0.574	13
8	3	25	300	0.641	0.421	0.998	0.679	6
9	4	10	300	0.668	0.728	0.531	0.640	2
10	4	15	400	0.739	0.409	0.608	0.580	10
11	4	20	100	0.756	0.442	0.491	0.571	8
12	4	25	200	0.682	0.419	0.642	0.576	7
13	5	10	400	0.712	0.469	0.619	0.612	9
14	5	15	300	0.841	0.519	0.661	0.669	3
15	5	20	200	0.745	0.569	0.728	0.678	5
16	5	25	100	0.998	0.781	0.879	0.881	1

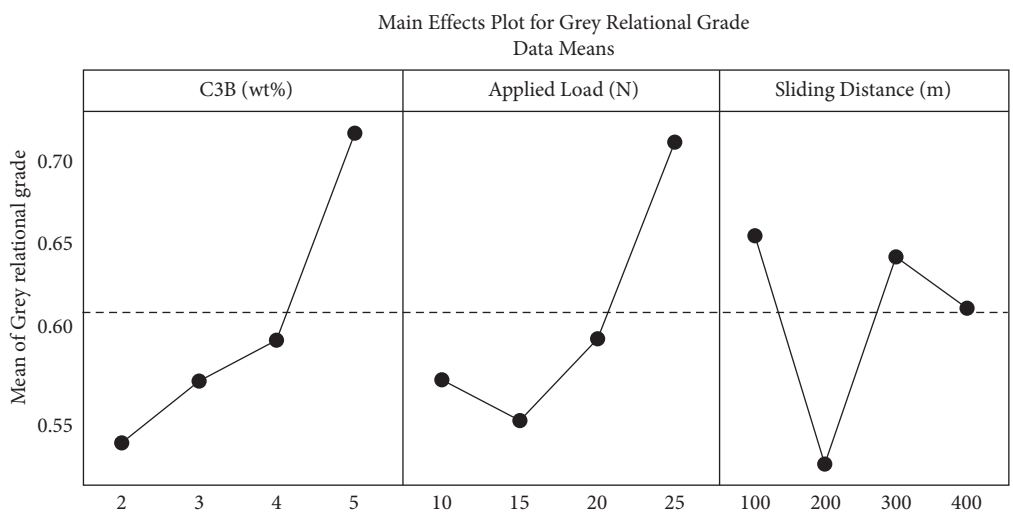

Figure 5: Main effect plots for GRG.

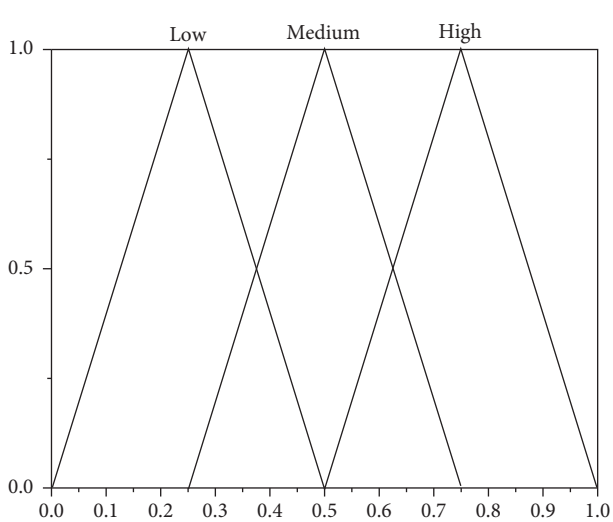

Figure 6: Output characteristics like weight loss, coefficient of friction, and specific wear rate.

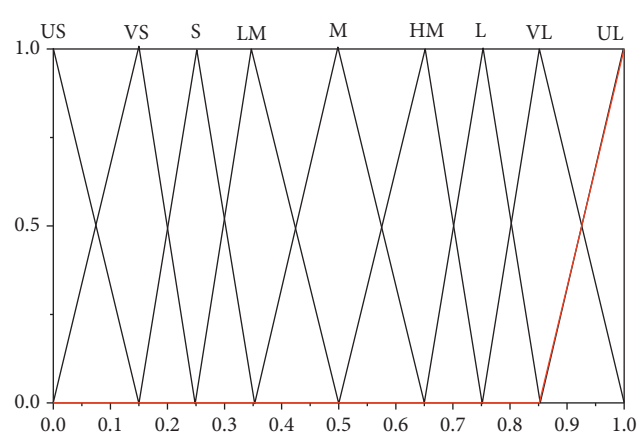

Figure 7: The nine fuzzy subsets for grey fuzzy reasoning grade.

Table 5: The abrasive wear responses at grey fuzzy reasoning grade.

Sl. no.	Cloisite 30B (wt%)	Load (N)	Sliding distance (m)	Grey fuzzy grade	Rank
1	2	10	100	0.571	16
2	2	15	200	0.406	12
3	2	20	300	0.554	4
4	2	25	400	0.679	14
5	3	10	200	0.510	13
6	3	15	100	0.558	15
7	3	20	400	0.569	2
8	3	25	300	0.689	11
9	4	10	300	0.651	8
10	4	15	400	0.602	6
11	4	20	100	0.578	9
12	4	25	200	0.590	10
13	5	10	400	0.612	5
14	5	15	300	0.690	7
15	5	20	200	0.671	1
16	5	25	100	0.897	3

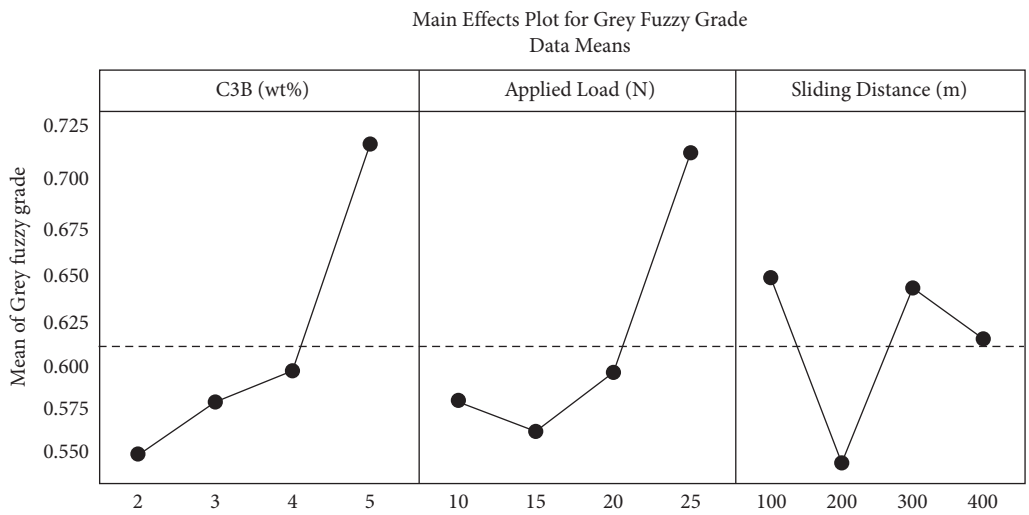

Figure 8: Main effect plots for the grey fuzzy grade.

Table 6: Confirmation test results.

Setting level	Abrasive wear characteristics at an optimum level		
	Parameter	Prediction	Experimental
C3B	10 weight %		
Load	25 Newtons		
Sliding distance	100 meters		
Grey relational grade		0.852	0.895
Grey fuzzy grade		0.858	0.986

When it comes to COF, SWR, and weight loss, the triangle membership function applied in Figure 6 demonstrates the customary nine fuzzy subclasses utilized for the GFRG.

All abrasive wear studies were predicted using the Fuzzy Interface System as shown in Figure 7, which was triggered by establishing a set of guidelines.

Table 5 lists the actual GFR values that were predicted by FIS. Table 4's values were compared to those in Table 5's tables. Compared to GRG, the grey fuzzy reasoning grade went up in terms of performance. The highest grey fuzzy relational grade was recorded in the 16th experiment, which reduced the experiment's uncertainty. Tables 4 and 5 illustrate how much higher the GFRG climbed when associated with GRA. The GRG value has moved to the reference value 1, which reduces fuzziness.

Figure 8 depicts the major impact plot of the abrasive wear features GFRG (Grey fuzzy Reasoning Grade). Cloisite

Table 7: ANOVA table for grey fuzzy grade.

Source	DOF	Adj. SS	Adj. MS	F_{cal}	F_{table}
C3B (wt%)	3	0.07214	0.02861	5.62	3.35
Load (N)	3	0.06187	0.02146	4.75	3.35
Sliding distance (m)	3	0.03214	0.01210	2.57	3.35
Error	6	0.02614	0.00436		
Total	15	0.18960			

03B and load were kept at stage 4, and sliding distance was kept at stage 1 in experiment sixteen, according to the table of results of the grey fuzzy technique.

Once the best circumstances were discovered, the theoretical prevision of GFRG was critical. The equation was used to get the fuzzy reasoning grade (14) where η_{om} is the GFRG mean value and $\overline{\eta_{ol}}$ is the GFRG at the optimal level. Table 6 displays the findings of the confirmation experiment. When compared to GRG, grey fuzzy bond values originated to be greater.

$$\eta_{\text{pre di ctal}} = \eta_{\text{om}} + \sum_{i=1}^{k} \overline{\eta_{ol}} - \eta_{om}, \tag{14}$$

5.2. Analysis of Variance for Grey Fuzzy Grade. Table 7 shows the Analysis of Variance results for the GFG. Each input abrasive wear feature was evaluated using ANOVA to determine the importance of the wear characteristics on the wear characteristics of the output abrasive material. When it came to defining abrasive wear characteristics, C3B addition had the greatest influence, in addition to load and sliding distance.

5.3. Worn Surface Structure. Abrasive wear resistance was improved when Cloisite 30B was introduced at 5% in Polyethylene/C3B/Elvaloy AC-3427 NCs. Abraded surfaces of 5 wt % PE/C3 B/EAC nanocomposites were smooth and less damaged, with indications of PE/C3B/EAC nanocomposites. To remove the matrix from the surface, PE/C3B/EAC nanocomposites must be processed in an agglomerated structure. The abraded surface shows patches of C3B, which enhance the properties' wear resistance. PE/C3B/EAC nanocomposites with a 5-weight % content increased wear resistance significantly due to their improved thermal stability.

The worn surface of Polyethylene/C30B/Elvaloy AC-3427 NCs contains 1 weight %. When C3 B was introduced to the PE matrix at 1 wt %, the abraded surface suffered greater damage than when C3B was applied to the PE matrix at any other concentration. When the PE/C3B/EAC nanocomposites were subjected to ductile fracture, the level of matrix damage was far greater than in any other nanocomposites created. Surface fatigue is the existence of huge, deep grooves on a worn surface. The microploughing and microcracking on the surface of 1 weight % Polyethylene/C30B/Elvaloy AC-3427 NCs were caused by poorer heat stability. The Cloisite 30B element has a proclivity to become free and be eliminated as wear debris where the network of fractures crosses. These nanocomposites were shown to be more susceptible to wear, which may be explained by the reduced ductility of the matrix, which deforms the matrix due to deterioration of the surface at 1weight %. Microcracking and microploughing were the wear processes discovered in this investigation.

6. Conclusion

A twin-screw extruder was utilized to make Polyethylene/Cloisite 30B/Elvaloy AC-3427 NCs. On the basis of abrasion wear testing, the Polyethylene/Cloisite 30B/Elvaloy AC-3427 NCs were defined. Grey Fuzzy and GRA were used to optimize the abrasive wear test results. The following are the findings:

(i) As part of the two-body abrasive wear testing, numerous performance metrics were taken into consideration in order to get the best results. GRA and grey fuzzy were used to optimize the results of two-body abrasive wear testing.

(ii) Grey's fuzzy reasoning grade was boosted by 25 N load, 5 wt % C3B addition, and a sliding distance of 100 m, which was near to the reference value of 0.897 for fuzzy reasoning grade.

(iii) Following sliding distance and load, the quantity of (wt %) addition of C3B was shown to be the most key aspect in inducing the abrasive wear characteristics.

(iv) Abrasive wear test results showed reduced damage to abraded wear surfaces when Cloisite 30B was applied at 5 wt % because more C3B was made public. Microcracking and microploughing were determined to be the abrasive wear mechanisms.

Data Availability

All the available data are included within the manuscript.

Conflicts of Interest

The authors declare that they have no conflicts of interest.

References

[1] D. Jafrey Daniel and K. Panneerselvam, "Modeling of tensile properties, dispersion studies, and hardness evaluation of cloisite 30B in polypropylene with Elvaloy AC 3427 as compatibilizer," *Journal of Composite Materials*, vol. 50, no. 23, pp. 3219–3227, 2016.

[2] A. Singh, S. Datta, S. S. Mahapatra, T. Singha, and G. Majumdar, "Optimization of bead geometry of submerged arc weld using fuzzy based desirability function approach," *Journal of Intelligent Manufacturing*, vol. 24, no. 1, pp. 35–44, 2013.

[3] D. J. Daniel and K. Panneerselvam, "Mechanical and thermal behaviour of polypropylene/cloisite 30B/Elvaloy AC 3427 nanocomposites processed by melt intercalation method," *Transactions of the Indian Institute of Metals*, vol. 70, no. 4, pp. 1131–1138, 2017.

[4] J. C. Rodríguez Hernández, M. Salmerón Sánchez, J. L. Gómez Ribelles, and M. Monleón Pradas, "Polymer-silica nanocomposites prepared by sol-gel technique: nanoindentation and tapping mode AFM studies," *European Polymer Journal*, vol. 43, no. 7, pp. 2775–2783, 2007.

[5] T. V. Sibalija and V. D. Majstorovic, "An integrated approach to optimise parameter design of multi-response processes based on Taguchi method and artificial intelligence," *Journal of Intelligent Manufacturing*, vol. 23, no. 5, pp. 1511–1528, 2012.

[6] H. Baniasadi, A. Ramazani S A, and S. Javan Nikkhah, "Investigation of in situ prepared polypropylene/clay nanocomposites properties and comparing to melt blending method," *Materials & Design*, vol. 31, no. 1, pp. 76–84, 2010.

[7] A. Krishnamoorthy, S. Rajendra Boopathy, K. Palanikumar, and J. Paulo Davim, "Application of grey fuzzy logic for the optimization of drilling parameters for CFRP composites with multiple performance characteristics," *Measurement*, vol. 45, no. 5, pp. 1286–1296, 2012.

[8] D. J. Daniel and K. Panneerselvam, "Manufacturing issues of polypropylene nanocomposite by melt intercalation process," *Materials Today Proceedings*, vol. 4, no. 2, pp. 4032–4041, 2017.

[9] D. J. Daniel and K. Panneerselvam, "Mechanical properties of polypropylene nanocomposites: dispersion studies and modelling," *Transactions of the Indian Institute of Metals*, vol. 71, no. 1, pp. 225–230, 2018.

[10] M. Kato, A. Usuki, and A. Okada, "Synthesis of polypropylene oligomer-clay intercalation compounds," *Journal of Applied Polymer Science*, vol. 66, no. 9, pp. 1781–1785, 1997.

[11] H.-L. Lin, "The use of the Taguchi method with grey relational analysis and a neural network to optimize a novel GMA welding process," *Journal of Intelligent Manufacturing*, vol. 23, no. 5, pp. 1671–1680, 2012.

[12] P. S. Kao and H. Hocheng, "Optimization of electrochemical polishing of stainless steel by grey relational analysis," *Journal of Materials Processing Technology*, vol. 140, no. 1-3, pp. 255–259, 2003.

[13] M. Grzenda, A. Bustillo, and P. Zawistowski, "A soft computing system using intelligent imputation strategies for roughness prediction in deep drilling," *Journal of Intelligent Manufacturing*, vol. 23, no. 5, pp. 1733–1743, 2012.

[14] A. N. Haq, P. Marimuthu, and R. Jeyapaul, "Multi response optimization of machining parameters of drilling Al/SiC metal matrix composite using grey relational analysis in the Taguchi method," *International Journal of Advanced Manufacturing Technology*, vol. 37, no. 3–4, pp. 250–255, 2008.

[15] C. L. Lin, J. L. Lin, and T. C. Ko, "Optimisation of the EDM process based on the orthogonal array with fuzzy logic and grey relational analysis method," *International Journal of Advanced Manufacturing Technology*, vol. 19, no. 4, pp. 271–277, 2002.

[16] Y.-C. Lin and H.-S. Lee, "Optimization of machining parameters using magnetic-force-assisted EDM based on gray relational analysis," *International Journal of Advanced Manufacturing Technology*, vol. 42, no. 11–12, pp. 1052–1064, 2009.

[17] S. Datta, A. Bandyopadhyay, and P. K. Pal, "Grey-based taguchi method for optimization of bead geometry in submerged arc bead-on-plate welding," *International Journal of Advanced Manufacturing Technology*, vol. 39, no. 11–12, pp. 1136–1143, 2008.

[18] S. Kumar and R. Singh, "Optimization of process parameters of metal inert gas welding with preheating on AISI 1018 mild steel using grey based Taguchi method," *Measurement*, vol. 148, Article ID 106924, 2019.

[19] R. Nalini, S. Nagarajan, and B. S. R. Reddy, "Polypropylene-blended organoclay nanocomposites - preparation, characterisation and properties," *Journal of Experimental Nanoscience*, vol. 8, no. 4, pp. 480–492, 2013.

[20] N. Tosun, "Determination of optimum parameters for multi-performance characteristics in drilling by using grey relational analysis," *International Journal of Advanced Manufacturing Technology*, vol. 28, no. 5-6, pp. 450–455, 2006.

[21] S.-H. Lim, A. Dasari, G. T. Wang et al., "Impact fracture behaviour of nylon 6-based ternary nanocomposites," *Composites Part B: Engineering*, vol. 41, no. 1, pp. 67–75, 2010.

[22] A. C. Chinellato, S. E. Vidotti, G.-H. Hu, and L. A. Pessan, "Compatibilizing effect of acrylic acid modified polypropylene on the morphology and permeability properties of polypropylene/organoclay nanocomposites," *Composites Science and Technology*, vol. 70, no. 3, pp. 458–465, 2010.

[23] W. Lertwimolnun and B. Vergnes, "Influence of compatibilizer and processing conditions on the dispersion of nanoclay in a polypropylene matrix," *Polymer*, vol. 46, no. 10, pp. 3462–3471, 2005.

[24] R. Ranjith, P. K. Giridharan, J. Devaraj, and V. Bharath, "Influence of titanium-coated (B4Cp+ SiCp) particles on sulphide stress corrosion and wear behaviour of AA7050 hybrid composites (for MLG link)," *Journal of the Australian Ceramic Society*, vol. 53, no. 2, pp. 1017–1025, 2017.

[25] S. Zhang, T. R. Hull, A. R. Horrocks et al., "Thermal degradation analysis and XRD characterisation of fibre-forming synthetic polypropylene containing nanoclay," *Polymer Degradation and Stability*, vol. 92, no. 4, pp. 727–732, 2007.

[26] R. Ranjith, P. K. Giridharan, C. Velmurugan, and C. Chinnusamy, "Formation of lubricated tribo layer, grain boundary precipitates, and white spots on titanium-coated graphite–reinforced hybrid composites," *Journal of the Australian Ceramic Society*, vol. 55, no. 3, pp. 645–655, 2019.

[27] R. Ranjith and P. K. Giridharan, "Experimental investigation of surface hardness and dry sliding wear behavior of AA7050/B 4 C p," *High Temperature Material Processes: An International Quarterly of High-Technology Plasma Processes*, vol. 19, no. 3-4, pp. 291–305, 2015.

[28] K. Palanikumar, "Experimental investigation and optimisation in drilling of GFRP composites," *Measurement*, vol. 44, no. 10, pp. 2138–2148, 2011.

[29] R. Ranjith and P. K. Giridharan, "Influence of high temperature on surface hardness of AA7050 hybrid composites," *Journal of Materials and Environmental Science*, vol. 8, pp. 1168–1172, 2017.

[30] L. A. Zadeh, "Fuzzy sets," *Information and Control*, vol. 8, no. 3, pp. 338–353, 1965.

[31] R. Ranjith, P. K. Giridharan, J. Devaraj, and S. Balamurugan, "Frictional behavior of the aa7050/b 4 c p aluminum

composites," *Composites: Mechanics, Computations, Applications, An International Journal*, vol. 9, no. 1, pp. 17–25, 2018.

[32] K.-T. Chiang, N.-M. Liu, and C.-C. Chou, "Machining parameters optimization on the die casting process of magnesium alloy using the grey-based fuzzy algorithm," *International Journal of Advanced Manufacturing Technology*, vol. 38, no. 3–4, pp. 229–237, 2008.

[33] D. D. Jafrey and K. Panneerselvam, "Study on tensile strength, impact strength and analytical model for heat generation in friction vibration joining of polymeric nanocomposite joints," *Polymer Engineering & Science*, vol. 57, no. 5, pp. 495–504, 2017.

[34] S. Shokoohi, A. Arefazar, and G. Naderi, "Compatibilized Polypropylene/Ethylene-Propylene-Diene-Monomer/Polyamide6 ternary blends: effect of twin screw extruder processing parameters," *Materials & Design*, vol. 32, no. 3, pp. 1697–1703, 2011.

[35] H. M. Akil, M. F. A. Rasyid, and J. Sharif, "Effect of compatibilizer on properties of polypropylene layered silicate nanocomposite," *Procedia Chemistry*, vol. 4, pp. 65–72, 2012.

[36] V. Kumar, J. Ramkumar, S. Aravindan, S. K. Malhotra, K. Vijai, and M. Shukla, "Fabricationand characterization of ABS nano composite reinforced by nano sized alumina particulates," *Int. J. Plast. Technol*, vol. 13, no. 2, pp. 133–149, 2009.

[37] B.-P. Chang, H. M. Akil, and R. B. M. Nasir, "Comparative study of micro- and nano-ZnO reinforced UHMWPE composites under dry sliding wear," *Wear*, vol. 297, no. 1–2, pp. 1120–1127, 2013.

[38] K. R. Sumesh, V. Kavimani, G. Rajeshkumar, P. Ravikumar, and S. Indran, "An investigation into the mechanical and wear characteristics of hybrid composites: influence of different types and content of biodegradable reinforcements," *Journal of Natural Fibers*, vol. 17, pp. 1–13, 2020.

[39] H. S. Lu, C. K. Chang, N. C. Hwang, and C. T. Chung, "Grey relational analysis coupled with principal component analysis for optimization design of the cutting parameters in high-speed end milling," *Journal of Materials Processing Technology*, vol. 209, no. 8, pp. 3808–3817, 2009.

[40] S. Keerthiveettil Ramakrishnan, K. Vijayananth, G. Pudhupalayam Muthukutti, P. Spatenka, A. Arivendan, and S. P. Ganesan, "The effect of various composite and operating parameters in wear properties of epoxy-based natural fiber composites," *Journal of Material Cycles and Waste Management*, vol. 24, no. 2, pp. 667–679, 2022.

Hindawi
Advances in Materials Science and Engineering
Volume 2022, Article ID 9594798, 7 pages
https://doi.org/10.1155/2022/9594798

Research Article

Investigations on Wear Behavior of Aluminium Composites at Elevated Temperature

B. R. Senthil Kumar,[1] G. Gopalarama Subramaniyan,[2] N. Pragadish,[3] P. M. Venkatesh,[4] Soni Sanjay,[5] C. M. Velu,[6] G. Navaneethakrishnan,[7] Suresh Vellingiri,[8] and Venkatesan Govindarajan[9]

[1]*Nehru Institute of Engineering and Technology, Coimbatore, Tamil Nadu, India*
[2]*Saveetha Engineering College, Chennai, Tamil Nadu, India*
[3]*Vel Tech Multitech, Avadi, Chennai, Tamil Nadu, India*
[4]*Vignan's Foundation for Science Technology and Research, Guntur, India*
[5]*Jabalpur Engineering College, R.G.P.V.Bhopal, Jabalpur, Madhya Pradesh, India*
[6]*Saveetha School of Engg, Saveetha Institute Medical and Technical Sciences, Saveetha University, Chennai, Tamil Nadu, India*
[7]*QIS College of Engineering and Technology, Ongole 523272, Andhra Pradesh, India*
[8]*Department of Mechanical Engineering, Adhi College of Engineering and Technology, Kanchipuram, Tamil Nadu, India*
[9]*Department of Mechanical Engineering, Haramaya Institute of Technology, Haramaya University, Dire Dawa, Ethiopia*

Correspondence should be addressed to Venkatesan Govindarajan; venkatesanggg2011@gmail.com

Received 13 April 2022; Revised 19 May 2022; Accepted 10 June 2022; Published 27 June 2022

Academic Editor: Vijayananth Kavimani

The aerospace aluminium alloy AA7050 was reinforced with Al_2O_3 of average particle size 5 m in this study using the stir casting method. To eliminate surface imperfections, AA7050/Al_2O_3 composites with varied weight percentages (0, 2, 4, 6) were manufactured, and wear tests on composites were carried out utilizing a pin-on-disc apparatus that varied load, velocity, temperature, and weight %. The tensile and hardness tests were carried out at a high temperature. The inclusion of particles enhances wear resistance by establishing a mechanically mixed layer (MML), according to the findings. The wear resistance at 300°C was 100% higher in comparison with resistance at 150°C. Because of the Orowan strengthening and Hall–Petch effect, the tensile strength and hardness of composites enhanced. Temperature, tracked by the weight % of strengthening powders, was the most important factor that influences the wear resistance of the composites. The findings showed that the material properties of AA7050/4wt%Al_2O_3 at 150°C and AA7050/2wt%Al_2O_3 at 300°C are superior than base alloy.

1. Introduction

AA7050 alloy has piqued attention across the globe in latest generations as the extremely ideal material for aerospace application, owing to its enhanced mechanical, tribological, and corrosion behavior [1]. Due to the growing need for lightweight materials in both developed and developing nations, defect-free composite materials are in high demand [2]. The quality of the materials used in any aerospace system determines its effectiveness. Some of the aerospace components manufactured by aluminium alloy are the hot plate collector, isolator, mount, thermal ducts, header pipeline, and moulding [2–5]. Since the sunlight-based header pipelines were accessible to high temperatures, it was necessary to investigate their viability at elevated temperatures [6].

Particles such as B_4C, SiC, WC, Al_2O_3, and Gr are used to strengthen aluminium alloys [7–9]. Sintering, moulding, and in situ production are the most often utilized composite manufacturing procedures [10–12]. The stir casting method was the most suitable of the numerous manufacturing procedures for mass production and uniform particle

Table 1: Elemental proportion of AA7050 aluminium alloy.

Zn	Mg	Cu	Fe	Cr	Si	Mn	Al
6.30	2.58	1.83	0.28	0.27	0.06	0.05	Balance

dispersion [13, 14]. The molten metal was stirred at a constant speed for a specified period of time utilizing a mechanical mixer [15]. The wettability of composites was improved by adding preheated particles [16].

The wear of the materials is governed by the velocity, sliding distance, load, temperature, and counterface hardness [17–19]. The impact of addition of SiC particles on the wear rate of aluminium composites was investigated. The addition of SiC particles increases the tribological capabilities, according to the findings. B_4C particles upsurge the strength, stiffness, and wear endurance of the AA2020 alloy [20]. When the load was increased over 60 N, the mild to severe regime transitioned. Sardar et al. found that hybrid composites had superior wear resistance than single-reinforced composites [21]. Increased matrix fortification improves elasticity, yield strength, and hardness [22]. The microhardness of the composite rises as the Al-N proportion in the alloy matrix increases [23]. The amalgamation of SiC and Al_2O_3 increases the composites' hardness, tensile strength, and density [24].

From the above survey, it was revealed that a significant amount of research has been done on the tribological performance of composites. However, only a few analyses have been performed on the tribological behavior of AA7050 composite materials at high temperatures. The objective of this study was to reinforce AA7050 alloy with Al_2O_3 particles and test wear behavior on reinforced composite materials at elevated temperatures. The mechanical and tribological properties of the composites were studied at high temperatures. With the use of an ANOVA table, the most influential factor was identified.

2. Experimental Procedure

Table 1 displays the elemental position of the AA7050 aluminium alloy as established by spectrochemical analysis. The liquid stir casting process was used to strengthen the AA7050 alloy with aluminium oxide (Al_2O_3) grains with a mean size of 5 μm. Around 1 kg of alloy was placed in a graphite receptacle and charged to 870°C in an electric furnace made by TSR instruments and solutions, according to the process parameters listed in Table 2.

Before being introduced to the charge, Al_2O_3 was charged to a temperature of 250°C to eradicate any moisture. The liquid was stirred for 4 minutes at 600 rpm using a sieve shaker. To increase wettability, an equivalent weight percentage of potassium titanium fluoride (K_2TiF_6) was introduced to the melt. The combination was agitated for additional 3 minutes after the flux was added. Figure 1 depicts the step-by-step technique entangled in the manufacture of composites.

Composites with dimensions of (−12 mm × L−105 mm) were made from the combined slurry which was put into a warmed die steel mould. To eliminate the surface defects, the specimens were turned and faced to a dimension of diameter 10mm × length 100mm. Wear tests on composites were completed as per ASTM-G99 principles by differing the temperature, stress, speed, and weight % of the composites utilizing a pin on plate contraption created by Ducom instruments; exploratory runs were arranged utilizing a Taguchi blended symmetrical exhibit.

Table 2: Casting variables.

Parameters	Value
Pouring temperature	870°C
Preheating temperature of Al_2O_3	250°C
Preheating temperature of mould	250°C
Stirring time	7 min
Stirring speed	600 rpm

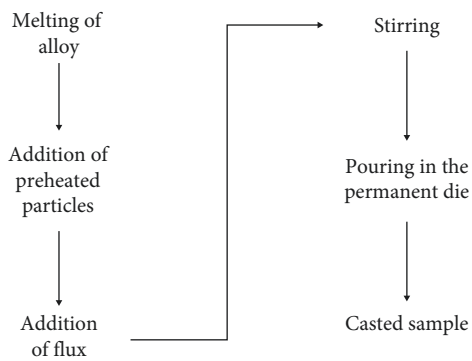

Figure 1: Steps involved in the production of composites.

The worn track was 100 mm in diameter, and the counterface was made up of EN-31 steel. The Taguchi orthogonal array was used to create the wear trial runs, which were then repeated three times. A Rockwell hardness tester and a universal testing machine were utilized to assess the composites' hardness and tensile strength at increased temperatures, according to ASTM-E18 and ASTM-E21 standards, respectively. The Rockwell hardness tester and UTM were manufactured by Xtreme Engineering Equipment Private Limited and Hualong, respectively. The hardness of nonferrous alloys was evaluated with a load of 100 N and a dwell time of 15 seconds, as specified by ASTM, and the outcomes were documented in Rockwell B-Scale. The specimen was placed in the UTM with a notch radius of 12.5 mm and a length and width of 50 mm and 4 mm, respectively. The load was added progressively until the material broke down at the specified temperature. Each experiment was conducted on three separate samples, with the average value being documented as the investigational findings. The most influential factor was revealed using an ANOVA (Table 3).

Table 3: Wear process parameters and their levels.

Process parameters	Levels
Reinforcement percentage	0, 2, 4, 6
Applied load (N)	15, 30
Speed (m/s)	15, 30
Temperature (°C)	150, 300

3. Results and Discussion

Figure 2 illustrates the microstructure of the composites. The Al2O3 particles were equally spread over the matrix material, according to the structure. The presence of a white film surrounding the reinforced particles suggests that Ti was applied to the reinforced particles. K2TiF6 flux was used to remove this titanium. The wear proportion of composites diminishes with the incorporation of reinforcing particles till four weight percent, after which it increases, according to the experimental data. The average wear proportion of amalgams was 7% inferior than that of unreinforced alloy, 629 mg for pure metal and 588 mg for composites reinforced with 4% Al_2O_3 particles, according to the Archard equation (equation (1)). The particles on the surface of the composites get dislodged during sliding and reach the contact region. Both metals are abraded by the ceramic particles, resulting in the formation of a MML [25]. The presence of Fe in the worn surface was confirmed through EDAX analysis, which reveals that the materials were mechanically mixed and averts direct metal surface contact as depicted in Figure 3. This MML hangs between the contact surfaces, averting metal surface contact and thereby reducing wear. When the temperature is rapidly increased from 150°C to 300°C, the wear rate increases by 100% as shown in Figure 4.

When sliding at 300°C, the material achieves its deformation state and becomes significantly deformed, resulting in increased material loss. At high temperatures, the parameters load and velocity have little effect on wear rate. The friction coefficient (COF) decreases to 0.166 as a result of the deformation condition, which is 40% less than materials sliding at 150°C as shown in Figure 5. All other variables have a minor or no effect on COF.

$$W = K\left(\frac{PLV}{3H}\right), \tag{1}$$

where P represents the applied load in N, L represents the sliding distance in m, V represents the applied velocity in m/s, H represents the hardness in HRB, and K represents the experimental constant.

The tensile strength of the AA7050/Al_2O_3 composites at high temperatures is shown in Figure 6. The composites with 4% reinforcement exhibited the highest tensile strength at 150°C. Orowan strengthening [26] induced the rise in strength, which indicates that the particles in the matrix give resistance to the movement of dislocation. The alloy reinforced with 2 weight % provides good tensile strength at 300°C.

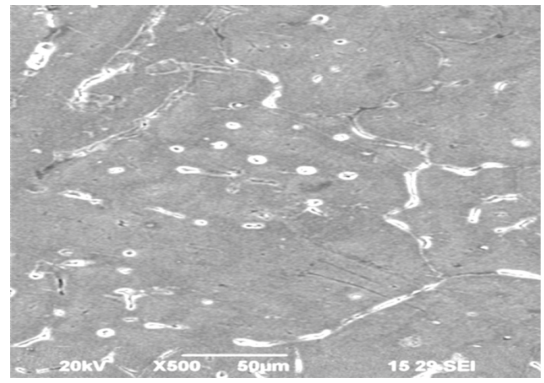

Figure 2: Microstructure of AA7050/Al2O3 composites.

$$\begin{aligned}\text{Wear} = {} & 163.000 + 15.5625\ \text{Weight percentage} \\ & - 1.13333\ \text{Load (N)} + 1.25000\ \text{Velocity (m/s)} \\ & - 0.348333\ \text{Temperature (C)} \\ & - 0.843750\ \text{Weight percentage} * \text{Weight percentage} \\ & - 0.483333\ \text{Weight percentage} * \text{Velocity (m/s)} \\ & + 0.0111111\ \text{Load (N)} * \text{Velocity (m/s)}.\end{aligned} \tag{2}$$

When the temperature is increased from 150°C to 300°C, the tensile strength is reduced by 95%. When a material is heated to a high temperature, its viscosity drops, resulting in an increase in percent elongation and a loss in tensile strength [27, 28]. The findings revealed that adding reinforcement had the least impact on tensile strength at high temperatures, and that material property loss was linked to viscosity drop at high temperatures [29, 30].

Figure 7 shows how adding Al_2O_3 particles increases the composites' toughness [31, 32]. The flux's titanium element encircles the reinforcing particles, prompting them to bind together. The titanium element refines the grain size due to the Hall–Petch effect, which raises the hardness value. The hardness of AA7050/6Al_2O_3 was 16% higher at 150°C than that of the unreinforced alloy and 11% higher at 300°C. When the temperature was raised to 300°C, the hardness value dropped by 75% [33, 34]. As indicated in Table 4, the most influential factor influencing material property is temperature, followed by weight reinforcement.

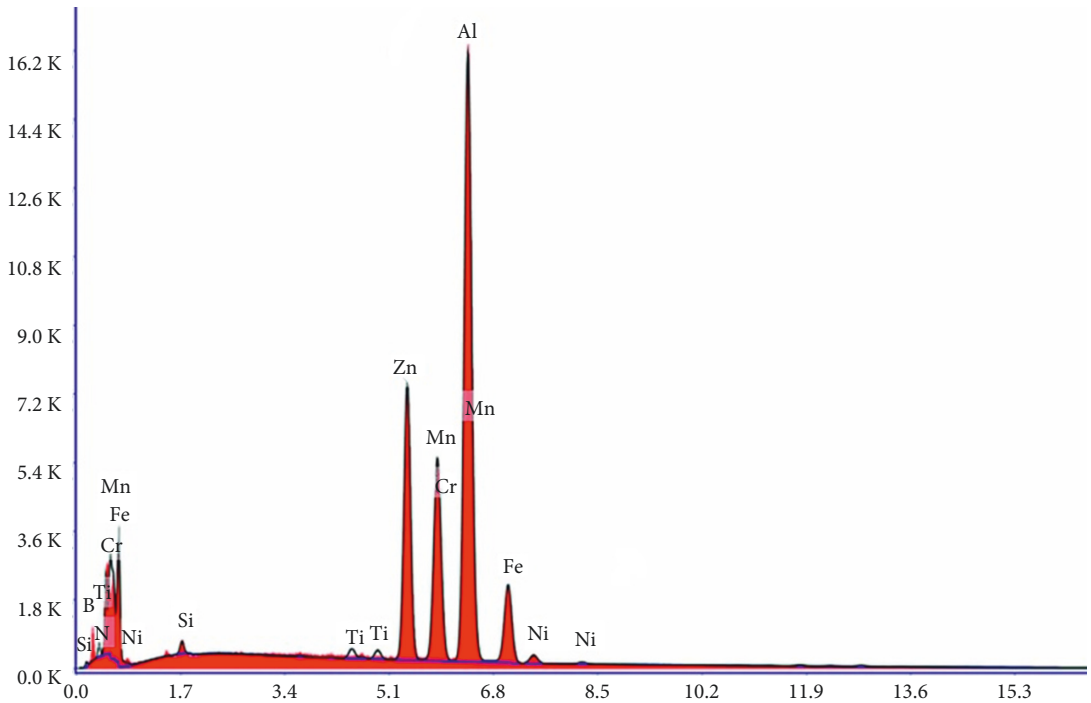

Figure 3: EDAX of worn surface of AA7050 composites.

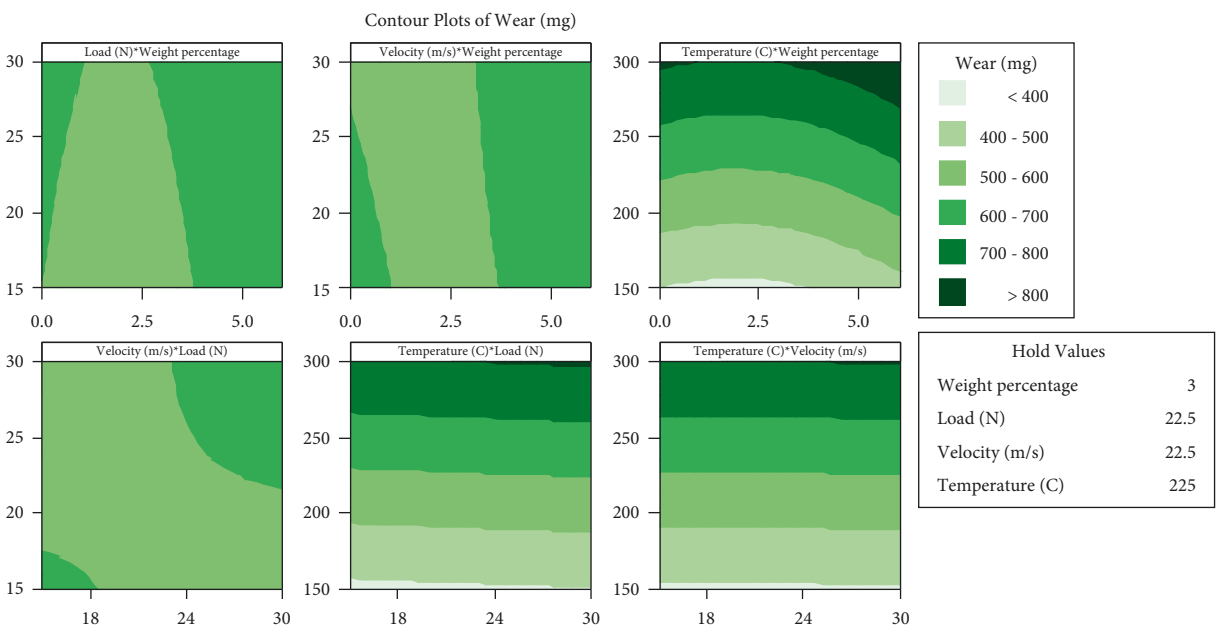

Figure 4: Interaction impact of various process parameters on wear of AA7050/Al2O3 composites.

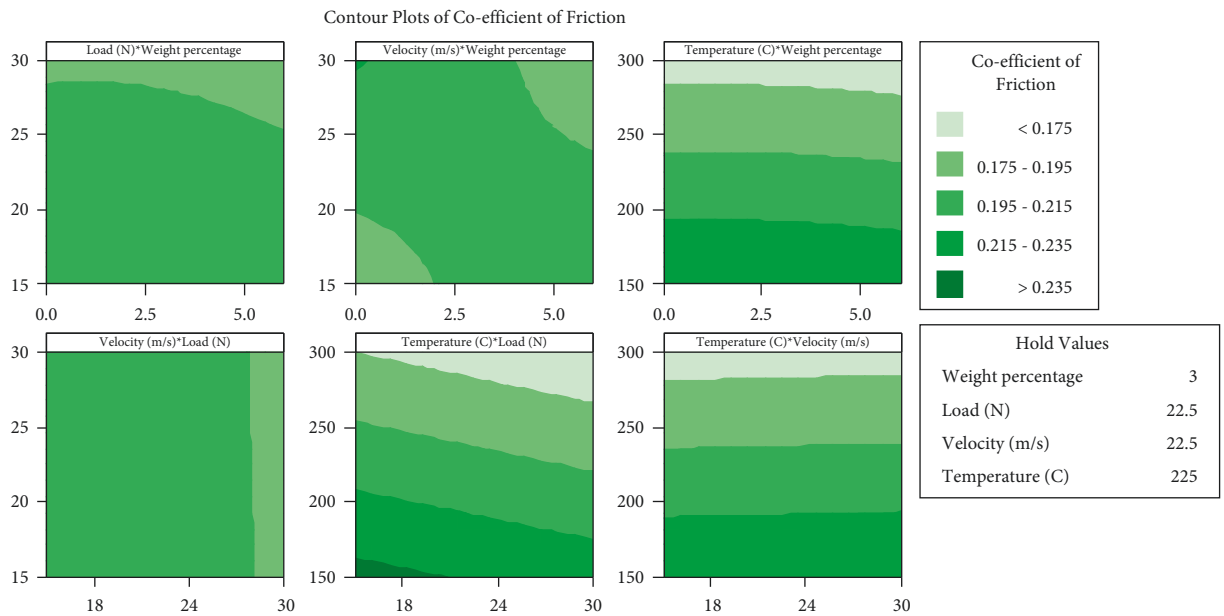

Figure 5: Interaction impact of various process parameters on COF of AA7050/Al2O3 composites.

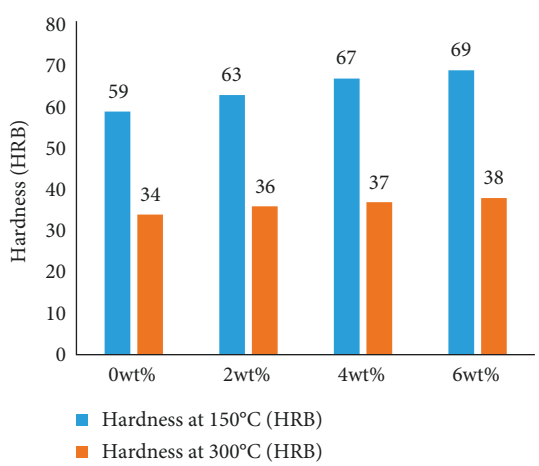

Figure 6: Effect of reinforcing particles on tensile strength of AA7050/Al_2O_3 composites.

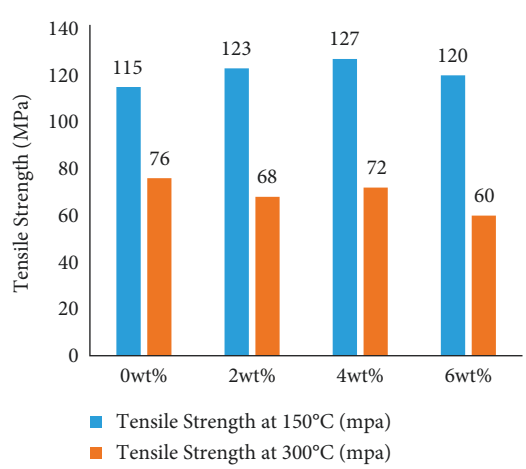

Figure 7: Effect of reinforcing particles on hardness of AA7050/Al_2O_3 composites.

Table 4: ANOVA for altered process parameter.

Level	Reinforcement percentage	Speed (m/s)	Load (N)	Temperature (°C)
1	191.5	191.5	190.8	151.1
2	191.0	191.0	192.8	232.2
3	183.7			
4	198.4			
Delta	14.6	0.5	1.6	82.1
Rank	2	4	3	1

When compared to other composite materials, the AA7050/4Al2O3 composites have a net flow value of 0.386 and have improved material properties at 150°C. The composite AA7050/2Al2O3 performed best at 300°C, with a net flow value of −0.287 [35, 36]. At increased temperatures, the composites show improved mechanical and tribological properties in all cases. The mathematical model for wear was constructed by connecting the results, as indicated in equation (2).

4. Conclusion

The liquid stir casting method was used to successfully create AA7050/Al2O3 composites. Tribological and metallurgical testing on composites was conducted, and the ensuing observations were obtained.

(1) Leading to the generation of a MML, the wear resistance of composites was 7% superior than pure aluminium alloy. When the temperature rises quickly from 150°C to 300°C, the wear rate increases from trivial to severe. At high temperatures, COF decreases as temperature rises, whereas velocity and load have little effect on wear rate.

(2) The insertion of reinforcing particles increases the tensile strength due to Orowan strengthening. When

the temperature is increased to 300°C, the viscosity is reduced by 95%, resulting in a 95% fall in tensile strength.

(3) Because of the Hall–Petch effect, the presence of hard ceramic particles (Al2O3) increases hardness. The ANOVA table revealed that temperature has the utmost impact on material properties, trailed by percent reinforcement. It was important for solar header pipes to use the composite because it has excellent strength at high temperatures.

5. Scope for Future Studies

In the future, tests may be conducted by varying the geometry of the particles and manufacturing them using diverse processes such as Compo casting and squeeze casting.

Data Availability

The data used to support the findings of this study are included within the article.

Conflicts of Interest

The authors declare that they have no conflicts of interest.

References

[1] T. K. Ghosh and M. A. Prelas, "Bioenergy," in *Energy Resources and Systems*, pp. 327–418, Springer, Dordrecht, Netherlands, Europe, 2011.

[2] A. Ummadisingu and M. Soni, "Concentrating solar power - technology, potential and policy in India," *Renewable and Sustainable Energy Reviews*, vol. 15, no. 9, pp. 5169–5175, 2011.

[3] A. Kaminski, B. Vandelle, A. Fave et al., "Aluminium BSF in silicon solar cells," *Solar Energy Materials and Solar Cells*, vol. 72, no. 1-4, pp. 373–379, 2002.

[4] M. Brogren, B. Karlsson, A. Roos, and A. Werner, "Analysis of the effects of outdoor and accelerated ageing on the optical properties of reflector materials for solar energy applications," *Solar Energy Materials and Solar Cells*, vol. 82, no. 4, pp. 491–515, 2004.

[5] R. Bravo, C. Ortiz, R. Chacartegui, and D. Friedrich, "Hybrid solar power plant with thermochemical energy storage: a multi-objective operational optimisation," *Energy Conversion and Management*, vol. 205, Article ID 112421, 2020.

[6] J. Soares and A. C. Oliveira, "Numerical simulation of a hybrid concentrated solar power/biomass mini power plant," *Applied Thermal Engineering*, vol. 111, pp. 1378–1386, 2017.

[7] C. Fenghong, C. Chang, W. Zhenyu, T. Muthuramalingam, and G. Anbuchezhiyan, "Effects of silicon carbide and tungsten carbide in aluminium metal matrix composites," *Silicon*, vol. 11, no. 6, pp. 2625–2632, 2019.

[8] L. Tesfaye, B. Bekele, A. Saka, N. Nagaprasad, K. Sivaramasundaram, and R. Krishnaraj, "Investigating spectroscopic and structural properties of Cr doped TiO2 NPs synthesized through sol gel deposition technique," *Tierarztliche Praxis*, vol. 41, pp. 860–872, 2021.

[9] N. K. Bhoi, H. Singh, and S. Pratap, "Developments in the aluminum metal matrix composites reinforced by micro/nano particles - a review," *Journal of Composite Materials*, vol. 54, no. 6, pp. 813–833, 2020.

[10] P. K. Krishnan, J. V. Christy, R. Arunachalam et al., "Production of aluminum alloy-based metal matrix composites using scrap aluminum alloy and waste materials: influence on microstructure and mechanical properties," *Journal of Alloys and Compounds*, vol. 784, pp. 1047–1061, 2019.

[11] V. Chak, H. Chattopadhyay, and T. L. Dora, "A review on fabrication methods, reinforcements and mechanical properties of aluminum matrix composites," *Journal of Manufacturing Processes*, vol. 56, pp. 1059–1074, 2020.

[12] M. Hoseini and M. Meratian, "Tensile properties of in-situ aluminium-alumina composites," *Materials Letters*, vol. 59, no. 27, pp. 3414–3418, 2005.

[13] J. Hashim, L. Looney, and M. S. J. Hashmi, "Metal matrix composites: production by the stir casting method," *Journal of Materials Processing Technology*, vol. 92-93, pp. 1–7, 1999.

[14] R. Ranjith, P. K. Giridharan, J. Devaraj, and V. Bharath, "Influence of titanium-coated (B4Cp + SiCp) particles on sulphide stress corrosion and wear behaviour of AA7050 hybrid composites (for MLG link)," *Journal of the Australian Ceramic Society*, vol. 53, no. 2, pp. 1017–1025, 2017.

[15] A. Kumar, R. S. Rana, and R. Purohit, "Effect of stirrer design on microstructure of MWCNT and Al alloy by stir casting process," *Advances in Materials and Processing Technologies*, vol. 6, no. 2, pp. 320–327, 2020.

[16] A. Kareem, J. A. Qudeiri, A. Abdudeen, T. Ahammed, and A. Ziout, "A review on AA 6061 metal matrix composites produced by stir casting," *Materials*, vol. 14, no. 1, p. 175, 2021.

[17] S. Sardar, S. Kumar Karmakar, and D. Das, "Tribological properties of Al 7075 alloy and 7075/Al2O3 composite under two-body abrasion: a statistical approach," *Journal of Tribology*, vol. 140, no. 5, Article ID 051602, 2018.

[18] R. Ranjith, P. K. Giridharan, C. Velmurugan, and C. Chinnusamy, "Formation of lubricated tribo layer, grain boundary precipitates, and white spots on titanium-coated graphite-reinforced hybrid composites," *Journal of the Australian Ceramic Society*, vol. 55, no. 3, pp. 645–655, 2019.

[19] S. Sardar, S. K. Karmakar, and D. Das, "Microstructure and tribological performance of alumina–aluminum matrix composites manufactured by enhanced stir casting method," *Journal of Tribology*, vol. 141, no. 4, 2019.

[20] A. Abdollahi, A. Alizadeh, and H. R. Baharvandi, "Comparative studies on the microstructure and mechanical properties of bimodal and trimodal Al2024 based composites," *Materials Science and Engineering A*, vol. 608, pp. 139–148, 2014.

[21] S. Sardar, S. K. Karmakar, and D. Das, "Evaluation of abrasive wear resistance of Al2O3/7075 composite by Taguchi experimental design technique," *Transactions of the Indian Institute of Metals*, vol. 71, no. 8, pp. 1847–1858, 2018.

[22] S. J. S. Chelladurai, R. Arthanari, N. Nithyanandam, K. Rajendran, and K. K. Radhakrishnan, "Investigation of mechanical properties and dry sliding wear behaviour of squeeze cast LM6 aluminium alloy reinforced with copper coated short steel fibers," *Transactions of the Indian Institute of Metals*, vol. 71, no. 4, pp. 813–822, 2018.

[23] S. Sardar, S. K. Pradhan, S. K. Karmakar, and D. Das, "Modeling of abraded surface roughness and wear resistance of aluminum matrix composites," *Journal of Tribology*, vol. 141, no. 7, 2019.

[24] H. Vasudev, L. Thakur, H. Singh, and A. Bansal, "Erosion behaviour of HVOF sprayed Alloy718-nano Al2O3 composite coatings on grey cast iron at elevated temperature conditions,"

Surface Topography: Metrology and Properties, vol. 9, no. 3, Article ID 035022, 2021.

[25] L. Tesfaye Jule, K. Ramaswamy, B. Bekele, A. Saka, and N. Nagaprasad, "Experimental investigation on the impacts of annealing temperatures on titanium dioxide nanoparticles structure, size and optical properties synthesized through sol-gel methods," *Materials Today Proceedings*, vol. 45, pp. 5752–5758, 2021.

[26] M. Vyshakh, R. Krishnaraj, A. P. Sayooj, and M. Afzal, "Experimental investigation on aluminium gravity die casting," *International Journal of Applied Environmental Sciences*, vol. 9, no. 2, pp. 213–222, 2014.

[27] R. Ranjith and P. K. Giridharan, "Experimental investigation of surface hardness and dry sliding wear behavior of AA7050/B4Cp," *High Temperature Material Processes An International Quarterly of High-Technology Plasma Processes*, vol. 19, no. 3-4, pp. 291–305, 2015.

[28] B. Bulcha, J. Leta Tesfaye, D. Anatol et al., "Synthesis of zinc oxide nanoparticles by hydrothermal methods and spectroscopic investigation of ultraviolet radiation protective properties," *Journal of Nanomaterials*, vol. 2021, Article ID 8617290, 10 pages, 2021.

[29] V. Sivamaran, V. Balasubramanian, M. Gopalakrishnan, V. Viswabaskaran, and A. G. Rao, "Identification of appropriate catalyst system for the growth of multi-walled carbon nanotubes via catalytic chemical vapor deposition process in a single step batch technique," *Materials Research Express*, vol. 6, no. 10, Article ID 105620, 2019.

[30] R. Ranjith, P. K. Giridharan, J. Devaraj, and S. Balamurugan, "Frictional behavior of the AA7050/B4cp aluminum composites," *Composites: Mechanics, Computations, Applications, An International Journal*, vol. 9, no. 1, pp. 17–25, 2018.

[31] V. Sivamaran, V. Balasubramanian, M. Gopalakrishnan, V. Viswabaskaran, and A. G. Rao, "Combined synthesis of carbon nanospheres and carbon nanotubes using thermal chemical vapor deposition process," *Chemical Physics Impact*, vol. 4, Article ID 100072, 2022.

[32] S. Venkatesan, B. Visvalingam, G. Mannathusamy, V. Viswanathan, and A. G. Rao, "Effect of chemical vapor deposition parameters on the diameter of multi-walled carbon nanotubes," *International Nano Letters*, vol. 8, no. 4, pp. 297–308, 2018.

[33] S. Venkatesan, B. Visvalingam, G. Mannathusamy, V. Viswanathan, and A. G. Rao, "In situ synthesis of multi-walled carbon nanorings by catalytic chemical vapor deposition process," *International Nano Letters*, vol. 9, no. 2, pp. 119–126, 2019.

[34] V. Sivamaran, D. V. Balasubramanian, D. M. Gopalakrishnan, D. V. Viswabaskaran, D. A. G. Rao, and D. G. Sivakumar, "Mechanical and tribological properties of Self-Lubricating Al 6061 hybrid nano metal matrix composites reinforced by nSiC and MWCNTs," *Surfaces and Interfaces*, vol. 21, Article ID 100781, 2020.

[35] V. Sivamaran, V. Kavimani, M. Bakkiyaraj, and S. T. Selvamani, "Multi response optimization on tribo-mechanical properties of CNTs/nSiC reinforced hybrid Al MMC through RSM approach," *Forces in Mechanics*, vol. 6, Article ID 100069, 2022.

[36] V. Sivamaran, V. Balasubramanian, M. Gopalakrishnan, V. Viswabaskaran, and A. Gouravrao, "Optimizing chemical vapor deposition parameters to attain minimum diameter carbon nano tubes by response surface methodology," *Journal of Advanced Microscopy Research*, vol. 13, no. 2, pp. 181–189, 2018.